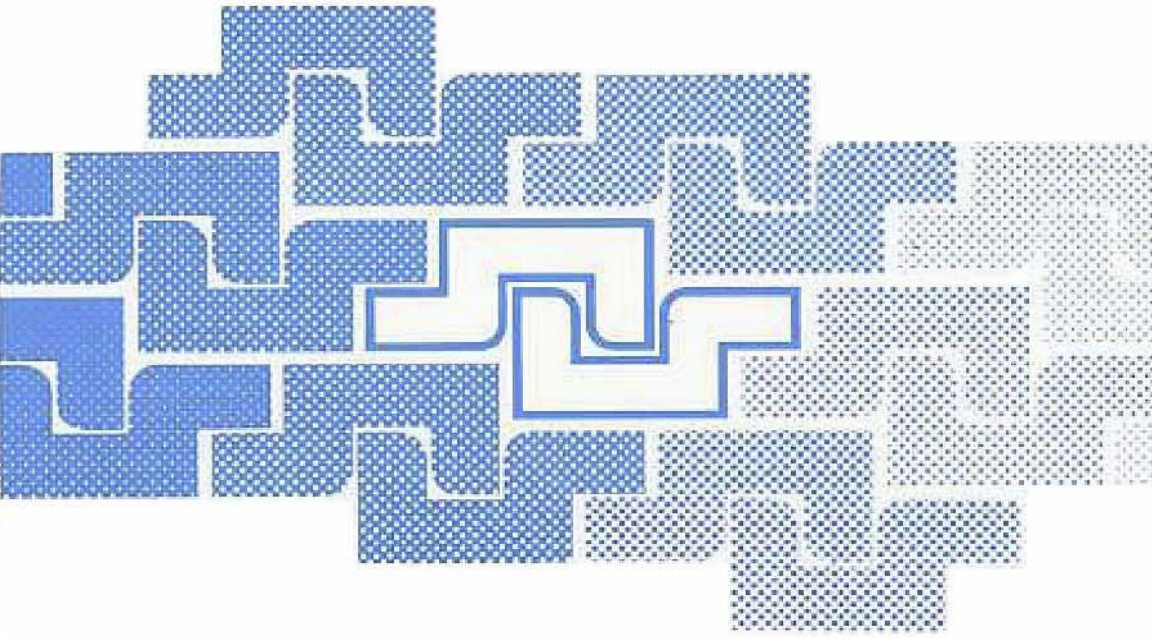

Electron Kinetics and Applications of Glow Discharges

Edited by

Uwe Kortshagen and

Lev D. Tsendin

NATO ASI Series

Series B: Physics Vol. 367

Electron Kinetics and Applications of Glow Discharges

NATO ASI Series

Advanced Science Institutes Series

A series presenting the results of activities sponsored by the NATO Science Committee, which aims at the dissemination of advanced scientific and technological knowledge, with a view to strengthening links between scientific communities.

The series is published by an international board of publishers in conjunction with the NATO Scientific Affairs Division

A	**Life Sciences**	Plenum Publishing Corporation
B	**Physics**	New York and London
C	**Mathematical and Physical Sciences**	Kluwer Academic Publishers Dordrecht, Boston, and London
D	**Behavioral and Social Sciences**	
E	**Applied Sciences**	
F	**Computer and Systems Sciences**	Springer-Verlag
G	**Ecological Sciences**	Berlin, Heidelberg, New York, London,
H	**Cell Biology**	Paris, Tokyo, Hong Kong, and Barcelona
I	**Global Environmental Change**	

PARTNERSHIP SUB-SERIES

1. Disarmament Technologies	Kluwer Academic Publishers
2. Environment	Springer-Verlag
3. High Technology	Kluwer Academic Publishers
4. Science and Technology Policy	Kluwer Academic Publishers
5. Computer Networking	Kluwer Academic Publishers

The Partnership Sub-Series incorporates activities undertaken in collaboration with NATO's Cooperation Partners, the countries of the C/S and Central and Eastern Europe, in Priority Areas of concern to those countries.

Recent Volumes in this Series:

Volume 365 — Techniques and Concepts of High-Energy Physics IX
edited by Thomas Ferbel

Volume 366 — New Developments in Quantum Field Theory
edited by Poul Henrik Damgaard and Jerzy Jurkiewicz

Volume 367 — Electron Kinetics and Applications of Glow Discharges
edited by Uwe Kortshagen and Lev D. Tsendin

Volume 368 — Confinement, Duality, and Nonpetturbative Aspects of QCD
edited by Pierre van Baal

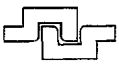

Series 5: Physics

Electron Kinetics and Applications of Glow Discharges

Edited by

Uwe Kortshagen

University of Minnesota
Minneapolis, Minnesota

and

Lev D. Tsendin

St. Petersburg State Technical University
St. Petersburg, Russia

Kluwer Academic Publishers

NEW YORK, BOSTON, DORDRECHT, LONDON, MOSCOW

eBook ISBN 0-306-47076-4
Print ISBN 0-306-45822-5

Created in the United States of America

Visit Kluwer Online at: http://www.kluweronline.com
and Kluwer's eBookstore at: http://www.ebooks.kluweronline.com

PREFACE

This book resulted from the NATO Advanced Research Workshop on "Electron Kinetics and Applications of Glow Discharges," held in St. Petersburg, Russia, on May 19-23, 1997. Glow discharges have found widespread applications in many technological processes from the manufacture of semiconductors, to recent developments in nano-technology, to the traditional fields of gas lasers, and discharge lamps. Consequently, the interest in the physics of glow discharges has experienced yet another resurgence of interest.

While the non-equilibrium character of glow discharges is widely accepted, the opinion still prevails that the main features can be captured by fluid models, and that kinetic treatments are only required for the understanding of subtle details. The erroneousness of this belief is demonstrated by the failure of fluid models to describe many basic features of glow discharges such as, for instance, electrode phenomena, striations, and collisionless heating effects. An adequate description of glow discharges thus has to be of kinetic nature.

The organizers and participants of the workshop were united in the belief that a critical assessment of the state-of-the-art of kinetic methods for the description of glow discharges was overdue. In particular, two different "schools" have developed over the past decades: analytical and semi-analytical approaches are favored by researchers mostly from Eastern countries while strongly computer-based methods are mostly used in the Western countries. The objectives of the workshop were: a) to bring together representatives of these different schools to propel research of glow discharge kinetics by creating synergistic effects between these different approaches, and b) to assess a broad spectrum of theoretical and experimental studies of glow discharge kinetics.

The authors of this book are well-known experts in the field of glow discharge research. The book presents a state-of-the-art review of our understanding of the kinetic nature of glow discharges.*

The workshop organizers want to thank all speakers and participants of the workshop for their scientific contributions and their support, which was invaluable in making this workshop a successful event. We are particularly thankful to

NATO Division of Scientific and Environmental Affairs

for its generous support of the workshop. In particular, we thank Dr. L. Veiga da Cunha and his staff for the excellent cooperation. We gratefully acknowledge co-sponsoring of the workshop by

*Articles resulting from poster presentations given during the workshop are published in *Plasma Physics Reports*, Volume 24, No. 7 (1998).

The Russian Foundation of Basic Research,
Applied Materials, Inc., and
OSRAM Sylvania, Inc.

We also wish to thank Drs. Anatoliy Kudryavtsev and Alexander Smirnov and Mrs. Karon Mooney for their support in organizing this workshop, and Dr. C. Eggs for the technical assistance provided in editing this book.

Uwe Kortshagen
University of Minnesota
Minneapolis

Lev D. Tsendin
St. Petersburg State Technical University
St. Petersburg, Russia
March 1998

CONTENTS

ANALYTICAL AND SEMI-ANALYTICAL MODELING APPROACHES

BASICS OF NUMERICAL PLASMA MODELING

DC DISCHARGES I

DC DISCHARGES II

STOCHASTIC ELECTRON HEATING I

INDUCTIVELY COUPLED PLASMAS

DISCHARGE KINETICS IN MOLECULAR MASS

MAGNETIZED DISCHARGES, SURFACE WAVE DISCHARGES

ADVANCED DIAGNOSTICS I

ADVANCED DIAGNOSTICS II

This Page Intentionally Left Blank

PRINCIPLES OF THE ELECTRON KINETICS IN GLOW DISCHARGES

L.D.Tsendin

Russia, St.-Petersburg State Technical University, St.-Petersburg, Polytechnicheskaja 29, 195251.

INTRODUCTION

The glow discharge physics, or, more widely speaking, the physics and technology of low-temperature plasmas, are undergoing a sort of the Renaissance nowadays. Numerous applications greatly stimulated interest in various topics of this problem.

First of all, the main working parameters - temperature and pressure - of the vast majority of technological processes are inevitably increasing. It follows that more and more considerable part of a processed material converts into the plasma state, and an opinion arises that in the coming century the considerable, if not the main, part of the materials and surface processing will inevitably use the plasma technology. The second reason of extreme rise of interest in this field follows from the fact that, among the more or less easily obtainable objects, the low-temperature gas discharge plasmas are the most remote ones from the thermodynamic equilibrium. As a result, a great variety of the plasma objects are widely used as active media of optical quantum generators and amplifiers. This extremely non-equilibrium property of glow discharge plasmas is the reason, also, why the most exotic chemical syntheses, which cannot be performed otherwise, are possible in the plasma state.

All these (and numerous other) reasons make it imperatively necessary to develop such a branch of knowledge, which can be called as the “plasma engineering”. In other words - how to design and to construct the plasma objects with the beforehand prescribed properties, where the useful processes are optimized, the treatment and reactions rates are maximal, etc. The central challenge consists in the fact that all the problems of such a sort are in some sense the inverse ones. They can be typically formulated as follows: how to combine the external parameters - the gas pressure and composition, current, voltage, frequency, vessel and electrode geometry, regime of the hydrodynamic flow, etc. - in order to achieve these technologic goals. But up to now the progress in this direction is rather slow. Notwithstanding to the fact that the intensive investigations, both of academic and of applied character, are carried out for many decades, it is difficult to point out any important technology which was predicted and developed theoretically - most part, if not all, of the glow discharge applications were found and optimized more or less empirically. The experiments and calculations have pursued, as a rule, a more modest aim - how to explain and to justify the existing technological processes, and not to optimize the existing

Electron Kinetics and Application of Glow Discharges
Edited by U. Kortshagen and L. D. Tsendin, Plenum Press, New York, 1998

and to predict new ones. Up to now most by the direct problems are solved - what are the plasma properties in a given device or installation, why it is so effective, what are the reasons for formation of a given product, etc. There are several explanations of such a situation.

First of all, the self-consistent character of problems makes it practically hopeless to seek for any analytic solutions, and forces an explorer to use some form of the numeric simulation. From the other side, a great variety of external parameters, complexety of the involved processes, and low accuracy and reliability of the data about the elementary processes, often lead to the fact that any separate calculation is in essence useless. In order to formulate and solve the inverse problems, first of all, it is necessary to have a rather good experience and intuition. The latter are acquired in process of solution of a considerable variety of the direct problems in a wide parameters range and subsequent detailed analysis of them. What we need for formulation and solution of the inverse problems are the scaling laws, i. e. the dependencies of the internal plasma parameters on the external ones.

One of the central difficulties which is met in pursuing of such a strategy is connected with proper account of the electron kinetics. Since the gas discharge plasmas represent extremely non-equilibrium systems, correct description of the kinetics, and especially of kinetics of the electron sub-system, which is, as a rule, the most remote from the thermodynamic equilibrium one, is of the vital importance for the glow discharge physics. The electron distribution function (EDF), and especially its high-energy tail, which usually depends exponentially on the discharge parameters, determines practically all the main plasma properties. Since the electron energies usually far exceed the energies of other discharge sub-systems (neutral gas, walls, electrodes, etc.), the EDF is formed predominantly in competition between the energy gain in the electric field (the simplest situation corresponds to the standard Ohmic heating), and energy losses in different electron collisions with all species of the charged and neutral particles which are present in a plasma, and with solid boundary surfaces. The simplest condition of 100% surface recombination is assumed usually for description of the latter process. The most important sources of the violation of thermodynamic equilibrium are connected usually with influence of the electromagnetic field, and of the cold solid surfaces.

The electromagnetic field in plasma is always self-consistent - it is not prescribed by an external circuit and geometry of discharge, but is created by the charged particles of a plasma itself. This fact makes it extremely desirable to obtain relatively simple analytic expressions for the EDF which are valid for rather wide variety of the field profiles. As in every self-consistent problem, it is impossible to obtain a numerical solution of any separate part of it - if you have started to simulate such a problem numerically, you are forced to perform it throughout up to the end. After performing great volume of calculations and obtaining plenty of graphs and tables, it is not too easy to extract out of them the understanding of an underlying physics, derivation of the scaling laws, prediction of the solution variation with external parameters, etc..

The great simplification of the electron kinetics is possible, if the dominant processes are characterized by comparatively long time scales and by smooth spatial profiles of plasma parameters and fields. For such conditions the collisions of plasma particles result in the formation of equilibrium between the particles and the local and instantaneous values of the external fields. Even if this partial equilibrium significantly differs from the genuine thermodynamic equilibrium, and the electron distribution function drastically differs. from the Maxwellian one, an average particle is representative for description of the behavior of the all ensemble of plasma particles in a given place and moment. The particles of each species can be described in terms of their density, mean velocity (or momentum), and mean energy. Such averaged description is usually called a fluid approximation, and the closed

set of equations for these values is known as fluid, or transport equations.

The characteristic peculiarity of the field profiles arising in gas discharges consists in their extreme inhomogeneity. As a rule, the typical such profiles can be subdivided into the weak plasma field, which occupies the main volume of a discharge, and the strong field regions in the space charge sheaths. In the cathode region of the dc discharge, for example, the small portion of energetic electrons is accelerated by the space charge field; influence of the weak plasma field on these electrons is negligible. On the other hand, the vast majority of the bulk plasma electrons cannot reach the high field sheath region, and their EDF is determined by the low plasma field. It means that both these fields are of equal importance for the EDF formation: simply they are responsible for formation of different parts of the EDF. And one of the central problems consists in the proper account of this fact. Up to now in a lot of publications the traditional fluid approximation is used for description of the whole electronic ensemble. It becomes more and more clear nowadays that the extremely non-equilibrium and non-uniform state of the glow discharge plasmas makes it absolutely hopeless to use this approach in qualitative estimates, to say nothing about calculations and modelling. The great number of phenomena which are specific and characteristic for the glow discharges cannot be understood properly even on a descriptive qualitative level in the framework of such an approach - i.e. in terms of an average electron. Since in the partially ionized glow discharge plasma the collisions between electrons which Maxwellize the electron distribution function are relatively seldom, the different parts of the EDF are very flexible and almost independent. It follows that the whole electronic ensemble in typical situations can be subdivided into several weakly connected populations, which can be formed by different segments of the field profile. In other words, the situation is possible, when for the parts of the EDF which correspond to various energies the spatially different parts of the field profile are responsible. To assign to the EDF in a given point one unique value of directed velocity and one value of the average energy, as it is made in the fluid approach, means the rough oversimplification, and often results in qualitatively erroneous results. Practically always the characteristic energy scales of different parts of the EDF differ drastically. It means that the real relative abundance of electrons in different energy regions can differ in orders of magnitude from the values calculated in the fluid model. Numerous situations exist, when it is absolutely evident that the low-pressure discharges can be described properly only on the kinetic level. At the higher pressure, such the most characteristic discharge phenomena, as the cathode and anode sheaths properties, potential profiles in sheaths, the Faraday dark space formation, generation and propagation of striations, stochastic electron heating, electron runaway in strong electric fields, etc., demand self-consistent kinetic description of electrons, too. Just now the opinion becomes more and more popular that the glow discharge physics, as a whole, is to be formulated essentially kinetically. To succeed in this challenge, efficient solution methods of the electron Boltzmann equation, both numerical and analytic, are to be developed.

We shall discuss here briefly the main physical mechanisms which determine the EDF in spatially and temporally inhomogeneous plasmas. We restrict ourselves by the simplest case of pure atomic gases and by the most characteristic limiting examples of the EDF formation.

CLASSIFICATION OF COLLISIONS. BULK ELECTRONS.

Under typical gas discharge conditions it is possible to divide the electrons unambiguously into two groups. The kinetic analysis of these groups is to be performed on essentially different lines. The first of these groups corresponds usually to the vast major-

ity of electrons. These bulk electrons are produced, as a rule, by ionization in a plasma volume. Their kinetic energy w does not exceed significantly the energy of the first electron excitation level ε_1. In this case, for not too high electric field intensities, which are characteristic for the discharge plasmas, the EDF can be subdivided into the EDF "body" ($w \lesssim \varepsilon_1$) and the exponentially decreasing EDF tail ($w > \varepsilon_1$).

In a discharge volume a relatively small fraction of high-energy electrons with $w >> \varepsilon_1$ is often present. These electrons are produced by acceleration of γ-electrons in cathode sheaths of DC discharges, or in electrode sheaths of RF capacitive discharges, where a strong electric field exists, by externally injected electron beams; sometimes such fast electrons are generated in resonance points of electromagnetic waves, etc.

We shall enlist here the main types of collisions which are relevant in simplest cases to the EDF formation. We start first from the bulk electrons.

The simplest and the most widely discussed is the situation when only elastic electron-atomic collisions are present. The energy relaxation in these collisions is extremely suppressed. It means that, if the probability of the energy gain $\delta\varepsilon$ from the field sufficiently fast decreases with $\delta\varepsilon$, the process of energy exchange with electromagnetic field corresponds to diffusion in energy. The energy diffusion coefficient equals to $D_\varepsilon = \left(\overline{\delta\varepsilon}\right)^2 \nu/3$, where $\nu = \nu(v)$ - the transport collision frequency, $\overline{\delta\varepsilon}$ - the average step in the random walk in energy. In the uniform stationary DC field, for example, $\overline{\delta\varepsilon} = eE\lambda$. The slow, practically continuous, energy losses in the elastic collisions can be described in terms of the negative convective flux along the kinetic energy axis w with "velocity" $V_\varepsilon(w) = -2(m/M)\nu w = -\delta_{el}\nu w$; $w = mv^2/2$. Since the isotropisation of the EDF in the elastic collisions occurs orders of magnitude faster than the energy relaxation, the resulting EDF is almost isotropic, and the expansion in the Legendre polynomials turns out very effective. In this expansion (which corresponds in our case of energy relaxation only in elastic collisions to the expansion in powers of $\sqrt{\delta}$ << 1) only the first two terms are important. The relatively small anisotropy of the EDF results from combined action of the electric field and smooth (with respect to the mean free path) variation of the plasma density. The kinetic equation for the isotropic part of the EDF in a uniform case is of the form

$$div_w \Gamma_\varepsilon = \frac{1}{v}\frac{\mathrm{d}}{\mathrm{d}w} v \left[D_\varepsilon \frac{\mathrm{d}f_0}{\mathrm{d}w} + V_\varepsilon f_0 \right] = 0$$

where Γ_ε - the flux of electrons in the energy space, v, $1/v$ - the Lame coefficients in this space. The solution of (1) with zero flux Γ_ε, when the diffusive flux upwards in energy is totally compensated by the convective flux due to the energy loss $V_\varepsilon(w)$, corresponds to the famous Druyvesteyn-Davydov's EDF [1, 2, 3]. It decreases exponentially with the characteristic energy scale $\triangle\varepsilon(w) = 1/\left[\frac{\mathrm{d}\ln f_0(w)}{\mathrm{d}w}\right]$:

$$f_0^{(0)}(w) = A \exp\left(\int_0^w \frac{V_\varepsilon(w')}{D_\varepsilon(w')} dw' \right) \qquad (2)$$

The average electron energy of the EDF (2) is of the order of $\bar{\varepsilon} \sim \triangle\varepsilon(\bar{\varepsilon}) \sim D_\varepsilon(\bar{\varepsilon})/V_\varepsilon(\bar{\varepsilon})$. This result can be interpreted as the energy gain from the DC electric field on the energy relaxation length $\lambda_\varepsilon(\bar{\varepsilon}) = \lambda(\bar{\varepsilon})/\sqrt{\delta_{el}}$. If the spatial scale of the field or plasma density inhomgeniety exceeds λ_ε, and the corresponding temporal scale exceeds $\tau_\varepsilon(\bar{\varepsilon}) = 1/(\delta_{el}\nu(\bar{\varepsilon}))$, the EDF in the inhomogeneous non-stationary plasma is close to (2), and the fluid description is valid. A lot of important and interesting situations cannot be described in these terms.

The situation with inelastic collisions is more complicated, and even more or less rigorous classification of possible situations is not formulated yet. First of all, in the self-sustained gas discharges plasma is created by the electron collisions with neutral particles - i.e. in some sort of the inelastic collisions, - and is removed in comparatively slow processes of ambipolar diffusion and recombination. In other words, without a proper account of the inelastic collisions it is impossible even to describe the plasma profile formation itself.

A simplified description of the inelastic collisions can be formulated, it the EDF 'body' in the electric field is described by a single characteristic energy scale $\bar{\varepsilon}$(in plasmas of self-sustained gas discharges this energy scale is of the order of 1 eV - up to the order of magnitude less, than the ionization potential). In this case the inelastic collisions can be subdivided into two groups. The collisions with relatively small (with respect to $\bar{\varepsilon}$) electron energy loss, as a rule, can be treated as continuous, or quasielastic. The expansion of the inelastic collision integral in powers of $\varepsilon_k/\bar{\varepsilon} << 1$ can be performed in this case, and these collisions can be taken into account by introducing, instead of δ_{el} = 2m/M, of the effective value δ_{eff} which now becomes energy-dependent[4, 5] . It means that in the molecular gases the electron collisions which are accompanied by the exchange with rotational and vibrational molecular levels with quanta energies ε_k of the order of 10^{-3} eV and 10^{-1} eV), are usually quasielastic. In typical molecular gases the inequality $\delta_{eff} << 1$ still holds, and the two-term expansion for the EDF is usually valid. The fluid approach with account of these collisions is applicable, if the problem scales exceed λ_ε, τ_ε with δ_{eff} (w) instead of δ_{el}. But such a simple criterion with δ_{eff}, which is determined by the electron energy balance, can be strongly misleading when applied to the electron collisions with great (with respect to $\bar{\varepsilon}$) energy loss. In this case the distinction between the spatial and temporal scales of the energy relaxation and of the EDF relaxation can be very significant[6 - 10].

In typical discharge situations for the bulk plasma electrons with energies below and slightly above the first electronic excitation potential the transport collision frequency ν_{tr} and the frequencies of the electronic excitation ν_k usually satisfy the inequalities

$$\nu_{tr}(w) >> \nu_k(w), \qquad \nu_k(w) >> \delta_{eff}\nu_{tr}(w) \tag{3}$$

At relatively low field intensities (it corresponds to relatively high pressure), when $\bar{\varepsilon}$ is small with respect to the energy of the first electronic level ε_1, the distribution of majority of electrons is determined by (2). The diffusive and convective fluxes in energy at $w < \varepsilon_1$ almost compensate each other, and the resulting flux Γ_ε is exponentially small. The collisions with excitation of the electronic states, which are accompanied by loss of practically all energy of the plasma electrons, determine only the EDF tail at $w \geq \varepsilon_1$. The energy scale of this tail is

$$\triangle^*\varepsilon \sim \sqrt{D_\varepsilon/\nu_1} \ll \bar{\varepsilon}. \tag{4}$$

From (3) it follows that this scale is considerably less, than the scale of the EDF "body" $\bar{\varepsilon}$ at $w < \varepsilon_1$. It means that the tail of EDF is also described by the two-term approximation, and that it decreases with energy considerably faster than the function (2). In other words, the income terms in the kinetic equation, which describe electrons after they have undergone the inelastic collisions with excitation of the k-th electronic level (the terms with the shifted energy $(w + \varepsilon_k)$, as an argument), are significant only in small region of the order of (4) at small energies. In the main part of the EDF body, and at its tail these terms are negligible.

Hence, the problem is reduced to the diffusion on energy in vicinity of an boundary with an absorbing media which is situated at $w \geq \varepsilon_1$, and in rough approximation the zero "black wall" boundary condition at $w = \varepsilon_1$ can be imposed on the distribution function f_0

in the energy diffusion equation (1). The electrons, which are "absorbed" at the EDF tail due to the excitation of the electronic states, reappear at low energies; in the intermediate energy region the flux in energy Γ_ε is small due to the fact that the diffusive flux here is almost compensated by the convective one. The electron energy in this case is lost mainly in the quasielastic collisions. The relaxation of the tail electrons with $w \geq \varepsilon_1$ in time and space is fast with respect to $\lambda_\varepsilon, \tau_\varepsilon$, and the fluid description is valid, if the same criteria of the smooth variation of the field and density, as for the EDF "body" $w < \varepsilon_1$ (of course, with δ_{eff} (w) instead of δ_{el}) are fulfilled. The source terms in the continuity and energy balance equations, which are determined, as a rule, by the tail of EDF, depend only on intensity of the local electric field. It means that the closed equations set for the plasma density in the fluid approximation can be written down in this case.

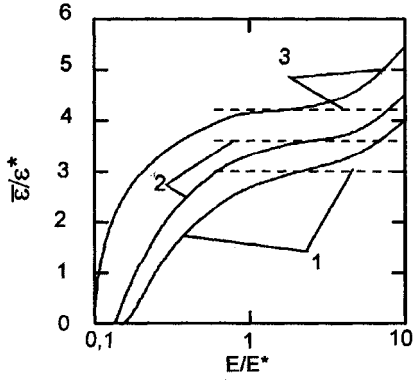

Figure 1. The field dependence of the average electron energy for 1) helium, 2) neon, 3) argon. The field is plotted as E/E^*, where E^*/p = 6.4 V/cm Torr for He, 2.0 V/cm Torr for Ne, 9.0 V/cm Torr for Ar. The horizontal dashed lines correspond to the distribution function in the black-wall approximation, when the energy loss in elastic collisions is ignored and the mean electron energy is $\bar{\varepsilon}/\varepsilon^*$ = 0.3 for He, 0.36 for Ne, and 0.43 for Ar.

Value of $\bar{\varepsilon}$ which corresponds to the scale of the exponential decrease of the EDF (2) due to the quasielastic collisions, increases with the field intensity, and at moderate fields becomes of the order of ε_1. At such fields the transition occurs to the regime in which the electron energy balance is controlled by the "genuine" inelastic collisions with large energy losses. Since the inequality (3) is fulfilled usually with significant margin, in considerable range of the electric fields the characteristic energy scale of the EDF tail remains small with respect to ε_1, which corresponds now to the energy scale of the "distribution body" at $w < \varepsilon_1$. is possible in this case to neglect the quasielastic energy losses (the second term in (1)), but to retain the approximate "absorbing wall" boundary condition $f_0 = 0$ at $w = \varepsilon_1$. This situation is illustrated at Fig. 1[10] , where the average electron energy $\bar{\varepsilon}$ versus electric field intensity is presented for several noble gases (He, Ne, Ar). The ascending branches of the curves at low fields correspond to the case when the energy balance is determined by the elastic collisions (2). The plateau, when $\bar{\varepsilon}$ practically doesn't depend on the field and remains of the order of ε_1, corresponds to the situation when the electron energy is lost mainly in inelastic collisions (in excitations of the electronic states), but the distribution tail decreases fast, and the contribution of the electrons with $w > \varepsilon_1$ to the total density and energy is small. According to (1), the energy diffusion flux is conserved up to $w = \varepsilon_1$, and is absorbed fast at $w > \varepsilon_1$. The inelastic collisions are accompanied by

considerable losses of electron energy of the order of several eV, and discreteness of these energy losses is sometimes crucial [6 - 10]. In such a situation it is necessary to distinguish between the spatial and temporal scales of the energy relaxation, and the scales of the relaxation of the electron distribution function. Some aspects of this problem are discussed lower. Frequently used is an approach, when the value of δ_{eff}, averaged over all the collisions, is introduced. The relaxation scales, which are calculated according to λ_ε, τ_ε, are identified with the scales in the criterion of applicability of the fluid approach. It follows, that in the presence of the inelastic collisions with large discrete energy losses, the real such criterion, which demands that the characteristic scale is to exceed the scale on which electrons "forget their biography", is considerably more stringent [10]. Since the distribution tail decreases fast, only several first electronic excitation levels determine the EDF. In the limiting case when only one electronic level is important, for example, the electron energy loss in collisions does not correspond to the relaxation of the EDF at all - the EDF in arbitrary DC electric field in the total energy scale reproduces an EDF in an injection point, shifted on an integer number of energy steps ε_1 [6 - 10].

The scale ε^*(4) increases with the field strength, and becomes of the order of ε_1. If $\Delta^*\varepsilon$ (E) exceeds ε_1, the corresponding collisions become quasielastic - and the equation (1) of the energy diffusion with new definition of the quasicontinuous energy loss rate V_ε (w) is applicable again.

For the approximate account of collisions in the electron Boltzmann equation for the bulk plasma electrons such a strategy can be proposed. If the energy loss in the an individual act of collision is small with respect to the EDF energy scale, the processes can be treated as quasielastic, and treated in the approximation of continuous energy losses. In the opposite case, at the moderate field strength, the EDF body in the energy interval $\Delta^*\varepsilon < w < \varepsilon_1$, where the majority of electrons is contained, is extremely simple. It corresponds to the conservation of the flux in energy Γ_ε. The energy scales of the EDF tail, and of the small region at low energy, where the energy flux conservation is violated, are both equal to (4).

Such an approach exhausts, in principle, the possible formation scenaria of the EDF of the bulk plasma electrons. They are essentially based on assumption about the EDF isotropy which follows from the condition (3), that the electron scattering dominates over their slowing down. The second assumption which was used in the derivation of (1), (2) consists in concept of the energy diffusion. It is based on the model that the energy exchange of electrons with electromagnetic field corresponds to random walk in energy with relatively small stochastic steps. For case of a DC electric field and energy-independent electron-neutral cross-section, for example, the probability of an energy step, which exceeds ($eE\lambda$), is exponentially small. What remains unclear - what is the situation, when these basic assumptions are violated.

If the scattering cross section for inelastic collisions with large energy loss is comparable with the transport one, the EDF anisotropy becomes significant. Hence, the two-term expansion for the EDF is not applicable in this case. Various numerical approaches which are based on straightforward solution of the Boltzmann equation [11, 12], or on the expansion of the EDF into spherical harmonics up to a high number [13, 14] were proposed. In [15] the situation was considered, when the transport cross-section is small with respect to the inelastic one. The simple analytic expressions for the extremely anisotropic "needle-like" EDF were derived. Its dependence on the angle ϑ between the DC electric field and electron velocity $\vec{v}$ is close to the Gaussian one. To our knowledge, the work on regular application of such an approach, and on the description of different mechanisms of the EDF relaxation, especially in the molecular gases, up to now is in an embrional state. It seems reasonable, accordingly, to discuss various possible scenaria of the EDF formation in this important

and complicated field for the simplest one-level model when only one type of the inelastic collisions is present, even if up to now no definite cross-section data are available in order to prefer one of them in a given experimental situation.

In the Fig.2 in the plane of variables λ^*/λ, $eE\lambda^*/\varepsilon_1$, where λ,λ^* are the transport and inelastic mean free paths, the various possibilities are presented.

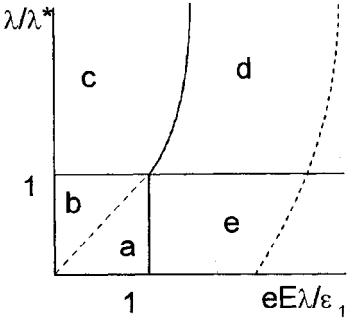

Figure 2.

In the domain *a* both the EDF body $w < \varepsilon_1$, and the tail, which decreases as $\exp\left(-\int_{\varepsilon_1}^{w} \frac{dw'}{eE\lambda^*(w')}\right)$, are highly anisotropic.

This case arises when the scattering is altogether negligible. In a weak field $\varepsilon_1 >> eE\lambda(\varepsilon_1) = eE\sqrt{2\varepsilon_1/m}/\nu_1$ it corresponds to the widely known Drude-Lorenz model. The extremely anisotropic electron motion in this case is analogous to the relay-race ion motion in the similar gas which is determined by the resonant charge-exchange [15].

In the region b the EDF body can be described in the two-term approximation $f_0(w) + \mu f_1(w); \mu = \cos(\vartheta)$:

$$f_0(w) = A\int_{w}^{w^*} \frac{dw'}{v' D_\varepsilon(w')}; \quad D_\varepsilon(w) = \frac{1}{3}(eE\lambda)^2\nu; \quad f_1(w) = -eE\lambda\frac{\partial f_0}{\partial w} \tag{5}$$

It corresponds to the energy flux Γ_ε conservation. At energies $eE\sqrt{2\varepsilon_1/m}/\nu_1 \gg \varepsilon_1$ this isotropy is violated, and the needle-like highly anisotropic EDF emerges [15]. Analogously to the standard diffusion theory [16], at $w = \varepsilon_1$ the approximate matching condition which demands absence of the averaged over angles influx in energy of the energetic electrons which are moving against the field at $w = \varepsilon_1$

$$\int_{-1}^{0}(f_0 + \mu f_1)\mu d\mu = -\frac{f_0}{2} + \frac{f_1}{3} = 0; \qquad f_0 = -\frac{2}{3}eE\lambda\left.\frac{\partial f_0}{\partial w}\right|_{w=\varepsilon_1} \tag{6}$$

From (6) the expression for w^* in (5) follows, which doesn't depend on characteristics of the inelastic collisions:

$$w^* = \varepsilon_1\left(1 + \frac{2}{3}\frac{eE\lambda}{\varepsilon_1}\right). \tag{7}$$

In the energy region $0 < (w - \varepsilon_1) \ll \varepsilon_1$, which contains the majority of the tail electrons, the electron trajectories can be considered as straight, and $f(w > \varepsilon_1, \mu < 0) = 0$;

$$f(w > \varepsilon_1, \mu > 0) = A\left(\frac{2}{3} + \mu\right)\left(\frac{eE\lambda}{vD_\varepsilon}\right)\Big|_{w=\varepsilon_1} \exp\left(-\int_{\varepsilon_1}^{w} \frac{dw'}{eE\lambda^*(w')\mu}\right). \qquad (8)$$

The domain c (Fig.2) corresponds to the above-mentioned case of the almost isotropic EDF, for which the energy balance is determined by the inelastic collisions, and the EDF at the tail fast decreases, as

$$\sim \exp\left(-\int_{\varepsilon_1}^{w} \frac{dw'}{eE\sqrt{\lambda\lambda^*}}\right). \qquad (9)$$

The energy scale of the tail is

$$\triangle^* \varepsilon = eE\sqrt{\lambda\lambda^*} < \varepsilon_1. \qquad (10)$$

If the integral (9) converges at $w \to \infty$, the so-called runaway in energy occurs - the EDF remains almost isotropic, but doesn't tend to zero at high energy. In other words, the stationary distribution in an electric field cannot be reached, and unlimited heating (i.e. the rise of the chaotic energy) of the electron gas takes place.

The domain d corresponds to situation, when the tail scale exceeds ε_1. In this case the inelastic collisions can be approximated as continuous, and the approach Eqs. (1), (2) becomes valid again. The runaway in energy in this case occurs, if the integral $\int dw \frac{V_\varepsilon}{D_\varepsilon} \sim \int \frac{\nu^*}{\lambda} dv$ converges at the upper limit.

In the domain e the relaxation of energy occurs faster than relaxation of momentum. It means that the action of collisions is equivalent to the velocity-dependent friction force $\varepsilon_1/\lambda^*(w)$. This force can compensate the electric field only if the friction force increases with energy. In the opposite case the genuine runaway [17 - 19] arises - the electron gas is accelerated infinitely by the electric field, and influence of the collisions becomes negligible. This phenomenon becomes possible, if the integral $\int \frac{dw}{\lambda^*(w)}$ converges at the upper limit, i. e. the mean free path $\lambda^*(w)$ increases with energy.

FAST ELECTRONS.

From the other side, at sufficiently high electron energies all the scattering events between electrons and atomic systems become asymptotically Rutherford-like. In other words, from the point of view of a fast free electron all the binding energies of the bound molecular electrons are negligible, and with increase of the projectile energy both the scattering and slowing down of a fast electron by gas molecules more and more resemble its interaction with a fully ionized plasma which consists of free slow electrons and bare nuclei [20, 21].

Due to the peculiarities of the Coulomb scattering, all the above-mentioned assumptions of domination of the scattering over the energy loss, of diffusion in energy, and of absence of the any form of the runaway, which are extremely efficient for description the bulk electrons, are violated at high electron energy and/or in intense electric fields. First of all, the Rutherford cross-section steeply decreases with the electron energy. It follows that in a DC electric field, for example, the probability of large energy gain remains finite. It manifests in the widely-known phenomenon of the electron runaway occurs [17 - 18]. This

phenomenon exists not only in fully ionized plasmas, but in a neutral gas too[19]. In strong enough electric field all electrons become the runaway ones. In the everyday gas discharge practice so high the fields are seldom. The more interesting (but far more difficult for analysis, as it can be seen from the only existing solution for the fully ionized plasma[18]) is the situation in relatively weak field, when portion of the runaway electrons is exponentially small. The additional difficulty is connected with the fact that the most interesting for gas discharges are the electrons of intermediate energies, at which the asymptotic law of the Coulomb collisions is inapplicable yet. The situation in this field is unclear now. It is aggravated by the fact that the straightforward numerical simulation is hampered by the lack of the experimental data, especially on the angular dependencies of the inelastic collisions. It can be stated, in any case, that in a rather intense electric fields the condition (3) of the EDF isotropy, and the approximation of the diffusion in energy are violated.

In [22] the simple model which allows an analytic solution was proposed for this situation. At high energies the ratio of the scattering to the slowing down doesn't exceed the atomic number Z. It means that the scattering is not too significant at least in light gases. At lower energies experimental evidences exist, too, that the EDF anisotropy is very significant. It manifests, for example, in the fact that the density of the fast electrons rises significantly at an axis of a cylindrical hollow cathode[23]. Hence, in [22] it was supposed that the model, which altogether neglects the scattering, and assumes delta-like angular dependence of the EDF, should be not too bad an approximation. Since the retarding force, which results due to the inelastic collisions, at $w \gtrsim \varepsilon_1$ increases with energy, and at high energies it decreases [21] with it, in the energy region of interest the maximum of this force is situated. According to some of the existing data [24] , this maximum is rather flat. Consequently, the simplest assumption of velocity-independent retarding force was made in [22].

THE EDF NON-LOCALITY.

One of the most pronounced and important kinetic effects consists in the EDF non-locality. Under this term we shall understand all the complex of phenomena, which are connected with the plasma and field inhomogeneity, and result in distinction between the real EDF, and the EDF in homogeneous plasma and field. Many aspects of this problem are discussed in detail in many other contributions to this book; see also the last review papers [25 - 27]. We shall discuss here briefly only several characteristic examples of numerous situations, in which the fluid approach is in principle misleading, and a rigorous kinetic treatment is necessary.

The radial electron fluxes in the nonlocal DC positive column.

In the local limit, when the EDF is formed by the momentum and energy balance in a given place, it is determined by the local values of plasma density and field. The small corrections to the local EDF which are proportional to small gradients of these parameters manifest themselves in formation of the particles and energy fluxes which are proportional to these gradients. In this (fluid) approximation the direction of the differential fluxes (i.e. of the contributions of different EDF parts to the total particles and energy fluxes) coincide with direction of the total fluxes. As plasma becomes more inhomogeneous, these fluxes increase, and the differential fluxes become more "independent".

If the radius of the discharge tube is small with respect to the electron energy relaxation length, the EDF isotropic part f_0 (w, r) for the electrons, which are trapped by the radial space charge field with potential $\Phi(r)$, depends only on total energy $\varepsilon = w + e\Phi(r)$.

Radially directed anisotropic part of EDF

$$f_{1r} = -\lambda(w)\left(\frac{\partial f_0}{\partial r}\right)_{\varepsilon}, \tag{11}$$

which determines the differential radial fluxes, paradoxically vanishes in this approximation, with $f_0 = f_0^{(0)}(\varepsilon)$. It means simply that due to the large radial plasma inhomogeneity, the gradient of the small radially-dependent corrections $f_0^{(1)}(\varepsilon, r)$ results in considerable radial fluxes, both integral and differential. In other words, in the local regime the energy gain from the Ohmic heating is balanced by the collisional losses locally in every point of the tube cross-section, and in the nonlocal regime - such a balance exists only in average. Since the spatial displacement occurs fast, the total energy is approximate integral of motion, and the main part of the EDF depends on it, according to the Liouville theorem. The radial fluxes are leveling up the local energy disbalance, forcing the EDF to depend on ε only. Since the rate of the EDF relaxation at different kinetic energies can be extremely different, the disbalance at various energies can differ significantly, and even be oppositely directed. Any attempts to apply the fluid approximation in this case are equivalent to pouring of new wine into an old wineskin, and are in principle misleading.

Neglecting the energy losses in elastic collisions, in the two-term approximation the kinetic equation in the variables $\tilde{\varepsilon} = \varepsilon/\varepsilon_1$, $\tilde{r} = r/R$ for the isotropic part of the EDF at energies above $\sqrt{D_\varepsilon \nu^*}$ reduces to:

$$A^2 \frac{1}{\tilde{r}} \frac{\partial}{\partial \tilde{r}} r\lambda v^2 \frac{\partial f_0}{\partial \tilde{r}} + \frac{\partial}{\partial \tilde{\varepsilon}} \lambda v^2 \frac{\partial f_0}{\partial \tilde{\varepsilon}} = \frac{3v\varepsilon_1^2}{c^2 E_z^2} \sum_k \nu_k f_0(\varepsilon, r)$$

The parameter $A = \varepsilon_1/(eE_z R)$ characterizes in this case the nonlocality of problem. We'll consider nonlocal case $A >> 1$. In order to equalize the electron and ion ambipolar radial fluxes, the radial potential profile arises which consists of the smooth plasma profile $\Phi(r)$, and of potential jump in the sheath. A typical $\Phi(r)$ dependence in the positive column is presented in the Fig. 3; Φ_w - the wall potential. It corresnonds to the outward directed net electron flux $\left\langle \Gamma_r^{(e)} \right\rangle$ in the fluid model.

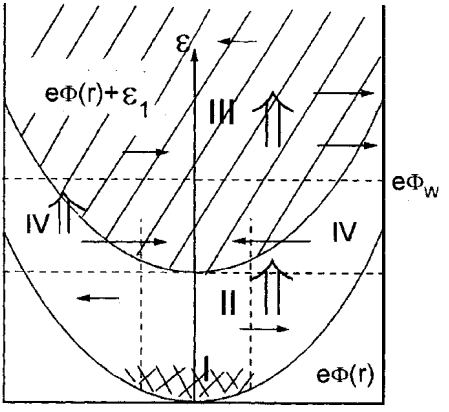

Figure 3.

The inelastic collisions occur in the dashed region $w = \varepsilon - e\Phi > \varepsilon_1$ (III in the Fig. 3). After such an event, which is described by the dashed arrows in the Fig. 3, an electron

emerges at low energies (in the doubly-dashed region I), and starts to gain energy from the longitudinal electric field. This process of the energy diffusion due to the Ohmic heating corresponds to the double vertical arrows. In the region II the main isotropic radially independent part of the EDF is close to (5) with only two replacements. The kinetic energy w is to be replaced for the full one ε, and the products $\nu V_\varepsilon\ (w), \nu D_\varepsilon\ (w)$ are to be replaced for the value of the same products which are averaged over the part of the tube cross-section available for an electron with a total energy ε [25, 26] . In other words, the problem coincides with the problem of thermal conductivity in long radially inhomogeneous rod with insulated side walls. The diffusion in energy with conserving radially-integrated energy flux Γ_ε generates in this region II the radial differential fluxes due to two main reasons. Since the available region increases with energy, the outward directed flux arises. The second reason follows from the fact that the genuine energy diffusion coefficient depends on the kinetic energy w and in order to level up the EDF at given total energy and at different r, the radial transport is necessary.

As the energy ε approaches the inelastic threshold ε_i, the inward directed differential flux arises, since the probability of the inelastic collisions (as well, as the kinetic energy) at given ε is maximal in the tube center. It means that the fast electrons sink is maximal here, and such a flux arises to maintain the EDF dependence on the total energy.

And at ε values, which exceed the wall potential Φ_w, the electrons can leave a plasma to tube wall, and strong outward directed flux results. In contrast to the average radial flux, which is determined by the ambipolar (i.e. by the ion) diffusion, this outward flux of the energetic electrons is not restricted by the quasineutrality condition, and is determined by the extremely fast electron diffusion. It leads to strong exponential depletion of the EDF tail, in competition with the exponential depletion caused by the inelastic collisions. It follows, in particular, that within logarithmic accuracy the values of $e\Phi_w$, and of ionization potential are close to each other. If not so, it is impossible to maintain the stationary state, in which the ionization rate is balanced by the wall escape.

Results of the recent publications [27, 28] agree with these considerations.

At the distance of the order of the mean free path in vicinity of the wall the anisotropy of the EDF which is caused by the fast recombination on the cold tube wall becomes significant. In a result, at $\varepsilon > e\Phi_w$; $r = R$ the backward flux of the energetic electrons which move almost normally towards plasma from the wall in the “anti-loss cone” is absent. For the majority of the tail electrons with $\varepsilon > e\Phi_w$ the solid angle of this cone is small. The approximate solution for this case was obtained in [30] . This cone is filled due to the elastic collisions and vanishes deep in the plasma. This phenomenon was investigated in detail in [31] . Since the elastic collisions were considered as isotropic, up to distance of the order of λ the step-wise dependence $f\ (\vartheta)$ was obtained, where ϑ - angle between an electron velocity and normal to the wall.

Striations.

Since the gas discharge represents an extremely non-equilibrium system, the uniform stationary state very often turns out to be unstable. Correspondingly, the DC positive column very often exists in the striated form, when all the plasma parameters are strongly longitudinally modulated. It is more or less widely known, that this phenomenon results from the development of a some form of ionization instability [32, 33] . But the variety of different forms of the striations is overwhelming, and up to now even satisfactory classification of them is absent. This situation demonstrates our poor understanding of the ionization phenomena even in such relatively simple and thoroughly explored an object.

In [34, 35] the 1D fluid model of running striations was proposed. It turned out that the propagation of unstable and/or weakly damping ionization signals in the DC positive column

is possible only if the wavelength is small with respect to the length of energy relaxation T_e/eE_z. The instability is caused by non-linear dependence of the ionization rate on the plasma density due to influence of the electron-electron collisions on the form of the EDF tail, or due to step-wise ionization. But, as it was stated above, the fluid description of a plasma, especially of so subtle processes, as of the EDF tail formation and of the ionization, is, generally speaking, impossible on such a short spatial scale. Such an approach can be justified only at rather high plasma density, when the frequent electron-electron collisions maintain the Maxwellian EDF, at least in the EDF "body" $w < \varepsilon_1$. Comparison of this model with the experimental results at high current values demonstrates good agreement [34, 35]. The extension of the fluid theory for non-linear and 2D fluid problems was performed in [36 - 38].

In practically all other situations, in our opinion, the phenomenon of striations cannot be described properly in the framework of the fluid model, and the rigorous kinetic approach is necessary.

One of the most striking properties of the standing striations, for example, consists in the fact, that:

1) the striations are fixed with respect to cathode (all the periodic structure of stratified column is shifted, if the cathode is displaced), and

2) the striations are equally sharp practically at arbitrary distance from the cathode [32, 33].

The alternating bright and dark layers imply that the EDF tail in the neighboring points contain strikingly different portions of energetic electrons. Since the same electrons are drifting from the cathode towards the anode, it means that the electrons "remember" their starting point, and "know", what energy to have at a given distance from it. The question arises, what is the microscopic mechanism of this "genetic memory"? How an electron, which have undergone thousands of stochastic collisions of various types, with the accuracy up to centimeters, if not to millimeters, "remembers" what energy to have? Especially if it is not the same electron which was emitted by the cathode, but its remote offspring?

In [10] the mechanism of the EDF "bunching" by the spatially periodic electric field $E_z(z)$ was proposed. This mechanism is characterized by many necessary properties. The situation was considered, when in the energy balance the inelastic collisions dominate. In absence of the energy losses in the quasielastic collisions the EDF at $w < \varepsilon_1$ in an arbitrary (!) monotone potential $\Phi(z)$ is extremely simple [6,7]:

$$f_0(\varepsilon, z) = \Psi(\varepsilon) \int^{z} \frac{dz' \nu(\varepsilon, z')}{v^3(\varepsilon, z')}. \qquad (12)$$

Here the total energy $\varepsilon = w + e\Phi(z)$ is introduced. In the simplest one-level approximation we have

$$\Psi(\varepsilon - \varepsilon_1) = \Psi(\varepsilon). \qquad (13)$$

Since in the one-level approximation the relaxation of the EDF is absent, the resulting EDF simply reproduces the differential fluxes $\Psi(\varepsilon)$, which are injected into field from the cathode. This situation reminds the widely known experiment of Franck and Hertz. It is natural to expect, that account of the small (of the order of $\varkappa$) energy losses in the elastic collisions, and/or of other levels of the electronic excitation, results in the stochastisation of the EDF. In other words, the combined action of the elastic and inelastic collisions smoothes down any steep injected EDF. It was shown in [10] that in the spatially periodic fields with the potential fall on the wavelength of the order of

$$\varepsilon_1 (1 + \varkappa)/k, \qquad (14)$$

where k - an integer number, an arbitrary smooth injected EDF, under combined influence of energy loss in the elastic and inelastic collisions (in the one-level model), and of the field, is transformed into a combination of delta-like peaks. It can be shown that the account of several excitation levels, at least in some simple models, can be described in terms of introducing of the parameter $\varkappa_{eff}$, instead of $\varkappa$.

The self-consistent solution of the problem of striations was given in [39] only for small signals and for case, when small energy losses in the elastic collisions are present. But it seems more or less evident, that the field profiles, which exhibit the "bunching" property, can arise self-consistently in numerous situations. The field profile in a plasma is determined by the quasineutrality condition, i.e. by the motion of ions. If, for example, the excitations in the one-level model are accompanied, with some probability, by ionization, the source terms in the ion equation, which, in fact, is the equation for the potential profile, will posses the same periodicity. Accordingly, such a potential profile arises automatically, if the plasma density is controlled by the step-wise ionization. In the noble gases difference between the first excitation and ionization potentials is not too significant, and such a scenario seems also possible, even. if the direct ionization dominates.

Formation of the cold electron population in the low pressure discharges.

Since the diffusive lifetime of the charged particles decreases at low pressure, the ionization rate, which is necessary for maintenance of a stationary discharge, rises. It follows that the EDF tail at the lower pressures is more pronounced. Usually it implies, that all the electrons are characterized by higher energy, too. On the other hand, the abundant population of the cold electrons is frequently observed. The most popular example of such a kind presents the Faraday dark space (FDS) in the DC discharges. In [40] it was observed, that in capacitively coupled RF (RFC) discharges, due to generation of the numerous slow electrons, sometimes the average electron energy even falls with the pressure decrease. In [41] the occurrence of the abundant cold electron population in ECR discharge was reported. The microscopic mechanism of these surprising phenomena remains in detail unclear, but numerous evidences exist of their essentially kinetic nature.

The FDS in a DC discharge arises in the following manner. The fast electrons, which incorporate the primary ones, emitted by cathode surface, and these of the secondaries, tertiaries, etc., are generated in the strong field of the cathode sheath. They penetrate deep into plasma, where the field is weak. A considerable part of the net ionization owes its existence to this nonlocal mechanism. The ions, which are generated in the plasma, are to be transported to cathode by the slow process of ambipolar diffusion. As a result, a rather high plasma density maximum arises in the vicinity of the range end of these fast electrons. In order to suppress the anode-directed electron current from this density peak, the inverse electric field arises, which traps the main fraction of electrons in vicinity of this maximum. The trapped electrons are distributed according to the Boltzmann's law. Accordingly, the potential minimum coincides with the density maximum. The electron current on the anode side of it is transported by the intermediate electrons with EDF (12). The only heating mechanism of the trapped electrons consists in their seldom collisions with the intermediate ones. Consequently, numerous population of the slow electrons emerges. Three distinct electron groups are responsible for different plasma properties in a cathode region of DC discharge. Fast electrons produce ionization, intermediate - are transporting current, and the slow trapped ones determine plasma density in the FDS[22] . The situation is presented schematically at the Fig. 4.

It is to be noted, that the popular phenomenological division of the cathode region into the FDS and negative glow seems, in some sense, rather superficious and misleading. The division into the ion space charge sheath, and into the plasma region of weak field, seems to be more consistent with the underlying physics. The sheath occupies, roughly speaking, only the part of the negative glow (NG), where the “fertile” electrons are born, The plasma region consists of the FDS and of the part of the NG, where only the ingoing electrons are capable of multiplication.

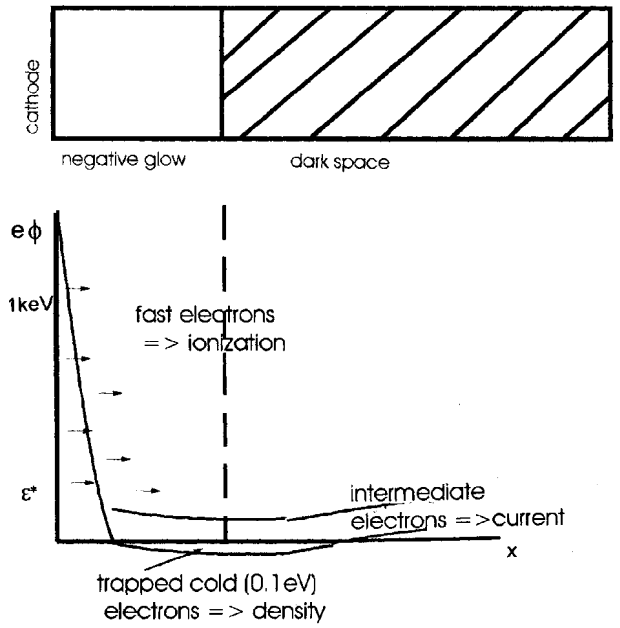

Figure 4.

In any low pressure currentless discharge, due to the EDF nonlocality, the EDF depends on the total energy $\varepsilon = \frac{mv^2}{2} + e\Phi(\vec{r})$ only, and the plasma density $N(x)$ is to be maximal in the discharge geometric center. It implies that the potential minimum arises in the plasma center. If the energy input is by any reason maximal in any other point but the geometric center of the discharge vessel, the trapped electrons cannot reach the energy source, and the population of the cold electrons arises.

The possible scenario in the RFC discharge is sketched in the Fig.5 The plasma density profile, and the stationary space charge potential correspond to the curves a), b). Since in the plasma the electron conductivity current dominates, due to the current conservation the oscillatory RF field $\widetilde{E} \sim 1/N$ is minimal in center, c). It follows, that

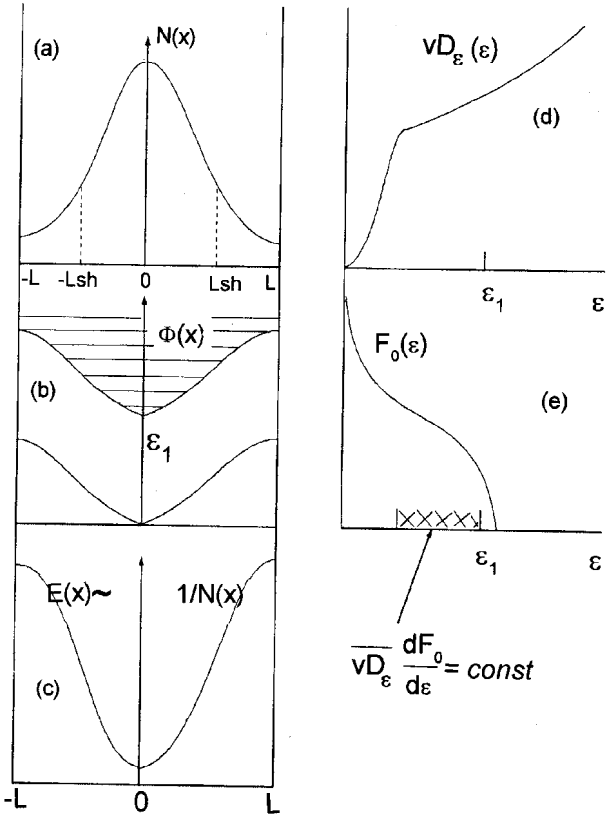

Figure 5.

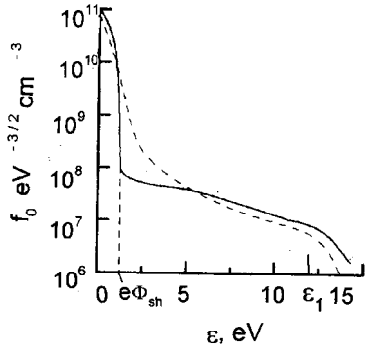

Figure 6.

the spatially averaged over the available for an electron with energy $\varepsilon = \frac{mv^2}{2} + e\Phi(\vec{r})$ area energy diffusion coefficient steeply rises with energy (Fig. 4d). Such a dependence of the energy diffusion coefficient results, according to (5), in the EDF of the type of Fig.5e. The stochastic electron heating, which is produced by the electron collisions with the oscillating plasma-sheath boundary, becomes significant with the pressure decrease. Since the low energy electrons cannot reach this boundary, the stochastic heating presents an additional mechanism which enhances the energy diffusion at high energies. Comparison of the experimental (dashed line)[42] , and of calculated [43] EDFs is given in the Fig.6.

Due to presence of strong and non-uniform magnetic field, of complicated electrodynamics, low collisionality, etc., in the case of ECR discharges the situation is considerably more complex. Nevertheless, it seems relatively evident, that if the point of the cyclotron resonance is situated far from the geometric center of a vessel, the population of cold electrons inevitably arises.

Acknowledgment. This work was supported by INTAS grant N940740 and by International Atomic Energy Agency research contract N9238/Regular Budget Fund.

REFERENCES

1. M. Druyvesteyn, Der Niedervoltbogen, *Zs. Phys.*, 64:781, (1930).
2. B. I. Davydov, Uber die Geschwindigkeitsverteilung der sich im elektrischen Felde bewegenden Elektronen, *Phys. Zeits. Sovjetunion*, 859, (1935).
3. W. P. Allis, "*Motion of ions and electrons*", in "*Handbuch der Physik*", Springer, Berlin, (1935).
4. T. Holstein, Energy distribution of electrons in high frequency gas discharges, *Phys. Rev.*, 70:367, (1946).
5. I. P. Shkarofsky, T. W. Johnston, M. P. Bachinsky, "*The particle kinetics of plasmas*", Addison-Wesley, Reading, (1966).
6. H. Bender, K. G. Muller, Striations als Eigenloesungen der Eletktronenbewegung im elektrischen Feld, *Zs. Phys.*, 263:299, (1973).
7. H. G. Lergon, K. G. Muller, Oertiche Relaxation der Elektronen-Energieverteilung in hohen Elektrischen Feldem, *Zs. Phys.*, 268: 157, (1973).
8. K. G. Muller, W. O. Muller, Simulation of the electron energy relaxation in a weakly ionized plasma, *Zs. Naturforsch.*, 30a:1553, (1975).
9. T. Ruzichka, K. Rohlena, On the non-hydrodinamic properties of electron gas in the plasma of a dc discharge, *Czech. J. Phys*, B22:906, (1972).
10. L. D. Tsendin, Electron distribution function of weakly ionized plasmas in nonuniform electric fields I,II , *Sov. J. Plasma. Phys*, 8:96; 8:228, (1982).
11. L. C. Pitchford, S. V. ONeil, J. R. Rumble, Extended Boltzmann analysis of electron swarm experiments, *Phys. Rev. A*, 23:294, (1981).
12. L. C. Pitchford, A. Phelps, Comparative calculations of electron-swarm properties in N_2 at moderate E/N values, *Phys. Rev. A*, 25:540, (1982).
13. A. Phelps, B. M. Jelenkovic, L. C. Pitchford, Symplified models of electron exitation and ionization at very high E/N, *Phys. Rev. A*, 36:5327, (1987).
14. R. Winkler, G. L. Braglia, A. Hess, J. Wilhelm, Fundamentals of a technique for determining electron distribution functions by multi-term even-order expansion in Legendre polinomials, *Beitr. Plasmaphysik*, 24:657, (1984).
15. A. P. Dmitriev, L. D. Tsendin, Distribution function of electrons scattered with a large energy loss in an electric field, *Sov. Phys.-JETP*, 54: 1071, (1981).
16. P. Morse, H. Feshbach, "*Methods of theoretical physics*", §2.4, Mc. Graw-Hill, NY, (1953).
17. H. Dreicer, Electron and ion runaway in a fully ionized gas I,II, *Phys. Rev.*, 115:238, (1959); *Phys. Rev.*, 117:329, (1960);
18. A. V. Gurevich, On the theory of the electron runaway effect, *Sov. Phys.-JETP*, 39: 1296, (1960). (in Russian)
19. A. B. Parker, P. C. Johnson, The dielectric breakdown of low-density gases, *Proc. Roy. Soc. Lond*, A325:511, (1971).
20. L. D. Landau, E. M. Lifshitz, "*Quantum mechanics - non relativistic theory*", §139, §148, Addison-Wesley, Reading, (1965).

21. L. D. Landau, E. M. Lifshitz, *"Electrodinamics of condensed media"*, §113.
22. V. I. Kolobov, L. D. Tsendin, Analytic model of short gas discharge in light gases, *Phys. Rev. A,* 46:7837, (1992).
23. I. Kuen, F. Howorka, and H. Störy, Population of excited He states (3 n 8) by dielectronic Hė recombination in dc hollow-cathode discharge, *Phys. Rev. A,* 23:829, (198 1).
24. W. T. Miles, R. Tompson, A. E. S. Green, Electron-Impact cross sections and energy deposition in molecular Hydrogen, *J. Appl. Phys.,* 43(2):678, (1972).
25. L. D. Tsendin, Electron kinetics in non-uniform glow discharge plasmas, *Plasma Sources Sci.&Techn.,* 4:200, (1995).
26. V. A. Godyak, V. I. Kolobov, Nonlocal electron kinetics in collisional gas discharge plasma, *IEEE Tr.,* PS-23:503, (1995).
27. U. Kortshagen, C. Busch ,L. D. Tsendin, On simplifying approaches to the solution of the Boltzman equation in spatially inhomogeneous plasmas, *Plasma Sources Sci. & Techn.,* 5(1):1, (1996).
28. D. Uhrlandt, R. Winkler, Radially inhomogeneous electron kinetics in the DC column plasma, *J. Phys.* D, 29: 115, (1996).
29. L. L. Alves, G. Gousset, M. Ferreira, Self-contained solution to the spatially inhomogeneous electron Boltzmann equation in a plamsa cylindrical positive column, *Phys. Rev. E,* 55(1):890, (1997).
30. L. D. Tsendin, Yu. B. Golubovsky, Positive column of a low-density, low-pressure discharge, *Sov. Phys.-Techn. Phys.,* 22: 1068, (1977).
31. U. Kortshagen, G. J. Parker, J. E. Lawler, Comparison of Monte-Carlo simulations and non-local calculations of the electron distribution function in a positive column plasma, *Phys. Rev. E,* 54:6746, (1996).
32. A. V. Nedospasov, Striations, *Sov. Phys.-Uspekhi,* 11:174, (1968).
33. L. Pekarek, Ionization waves (striations), *Sov. Phys.-Uspekhi,* 11:201, (1968).
34. K. Wojaczek, Der Positive Soule in Ar in Ubergangsbereich, IV, *Beitrage Plasmaphys.,* 6:319, (1966).
35. L. D. Tsendin, On propogation of longitudinal low-frequency waves in gas discharge plasma, *Sov. Phys.-Techn. Phys.,* 14:1013, (1969).
36. M. S. Gorelik, L. D. Tsendin, Hydrodinamic theory of large-amplitude ionization waves, *Sov. Phys.-Techn. Phys.,* 18:479, (1973).
37. L. D. Tsendin, Ionization and drift-temperature waves in media with hot electrons, *Sov. Phys.-Techn. Phys.,* 15:1245, (1970).
38. Yu. B. Golubovsky, V. I. Kolobov, L. D. Tsendin, 2D theory of ionization waves in constricted discharge, *Sov. Phys.-Techn. Phys.,* 31:31, (1985).
39. L. D. Tsendin, Ionization kinetics and ionization waves in Ne I,II, *Sov. Phys.-Techn. Phys.,* 27:407, (1982).
40. V. A. Godyak. R. B. Piejak, Abnormal low electron energy and heating-mode transition in a low-pressure Ar RF discharge at 13.56MHz, *Phys. Rev. Lett,* 65:996, (1990).
41. K. Wiesemann, Characterisation of plasmas by advanced diagnostic methods, *Pure. Appl. Chem.,* 68: 1029, (1996).
42. V. A. Godyak, Statistical heating of electrons at an oscillating plasma boundary, *Sov. Phys.-Techn. Phys.,* 16:1013, (1972).
43. I. D. Kaganovich, L. D. Tsendin, Spatial-temporal averaging procedure and modelling of RFC discharge, *IEEE Tr.,* PS-20:66, PS-20:86, (1992).

SPHERICAL SYMMETRICAL APPROACH TO THE THEORY OF RUNAWAY BREAKDOWN

A. V. Gurevich,[1] A. V. Lukyanov,[1] K. P. Zybin,[1] and R. A. Roussel-Dupre[2]

[1]P. N. Lebedev Institute of Physics
Russian Academy of Sciences
117924 Moscow, Russia
[2]Space and Science Technology Division
Los Alamos National Laboratory
Los Alamos, NM

1. INTRODUCTION

The notion that secondary electrons generated by cosmic rays could be accelerated over kilometer distances by thunderstorm electric field was first proposed by Wilson.[1] The frictional force F of fast nonrelativistic electrons moving in air diminishes with the kinetic energy of electrons ε (Fig. 1) until a minimum value,

$$F_{\min} \simeq \frac{4\pi N_m Z e^4}{mc^2} a, \qquad a \simeq 11 \tag{1}$$

is reached at $\varepsilon_{\min} \simeq 3\text{–}4mc^2$. At relativistic energies $\varepsilon >> mc^2$ the force F is slowly growing $(\sim \ln(\varepsilon/\varepsilon_1), \varepsilon_1 \simeq 270\text{eV})$ This specific behavior of friction force F in nonrelativistic region is a cause of runaway effect in a constant electric field.[2] Clearly, if an electric field E, applied to the medium, exceeds the minimum value $F_{\min}$:

$$E > E_c = F_{\min}/e = \frac{4\pi N_m Z e^3}{mc^2} a \tag{2}$$

then the electrons with the energies ε greater than characteristic value $\varepsilon_c = mc^2(\gamma_{1c}-1)$ (Fig. 1) will runaway. In other words electrons will be accelerated up to very high energies.

Runaway electrons in the context of thunderstorm electric fields in air were studied previously by a number of authors.[3,4] A fundamental new idea proposed by Gurevich, Milikh and Roussel-Dupree in 1992 showed how the generation of an avalanche of runaway electrons could lead to the air breakdown.[5] As is well known impact ionization of the air by energetic electrons leads to the production of newborn electrons with a wide spectrum of energies. Those secondary electrons whose energy exceeds the characteristic value ε_c become a part of runaway population and contribute

Electron Kinetics and Application of Glow Discharges
Edited by U. Kortshagen and L. D. Tsendin, Plenum Press, New York, 1998

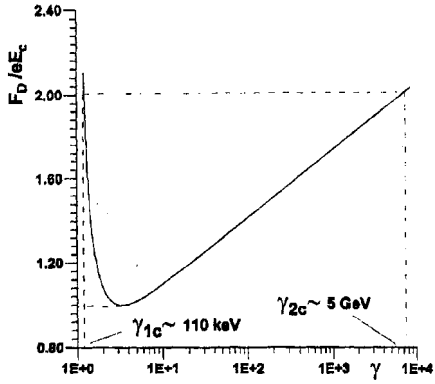

Figure 1. Dynamical friction force. The normalized energy loss per unit length ($F_d/Ec0$) for electrons in air is plotted as a function of the electron Lorentz factor γ.

to further acceleration and ionization that again populates the runaway regime. The net result is an avalanche in which the number of runaway electrons and with them of electrons of all other energies grows exponentially. This process was called runaway breakdown. It proceeds in electric fields $E > E_c$ (2) and in the presence of high-energy electrons (produced as a results of cosmic-ray interaction with atmosphere). It is important to note, that the critical field for runaway breakdown is about an order of magnitude lower than the threshold field for conventional breakdown E_{cth}:

$$E_c \approx 0.1 E_{cth} \tag{3}$$

This fact makes it possible for runaway breakdown to take place in relatively low electric fields $E_c \leq E << E_{cth}$ and as a result to determine fast charge transfer process in thundercloud, which can have important implication for lightning preconditioning and overall development of thunderstorm electricity.

Runaway breakdown proceeds as a beam of fast electrons having maximum energies of the order of 1 MeV.[6] A detailed kinetic theory[7] for the runaway process permitted a precise determination of the intensive fluxes of X-rays produced by bremsstrahlung emission in the 10–500 keV energy range.

The experimental observations of intensive X-rays by McCarthy and Parks[8] could be considered as a first manifestation of runaway breakdown during thunderstorm. These effects were recently confirmed and studied in details by Eack, Beasley et al..[9–11] Even more convincing were the observation of very intensive γ-ray bursts by' BATSE.[12] These observations indicate the direct connection between spectacular high-altitude lighting and runaway breakdown.

Nevertheless, it is worthy to note that the Earth's magnetic field B can substantially affect the runaway breakdown process at the altitudes above $z \sim 20$ km. At $z \simeq 40$ km, this influence already dominates. That is why, the influence of magnetic field B on high-altitude lighting should turn out to be significant even though it strongly depends on the angle between E and B.[13, 14]

Moreover, the role of lighting emission is not completely understood. For instance, in Refs. 15, 16 is supposed that alternating electromagnetic field is just a source of air ionization growth produced by high altitude lighting at $z \sim 60$–80 km. While, in such a case in Refs. 15–17 only conventional breakdown in gas was considered. From the one hand it gives rise to some difficulties in interpretation of the breakdown — the field is usually less than needed for conventional breakdown. From the other hand conventional mechanism of gas breakdown can not explain strong γ-emission which as usually supposed to appear under high-altitude lightnings.

It is pertinent to remember in connection with this fact that runaway process of electrons may appear not only in constant electric field. In particularly, runaway of electrons and ions may occur under stochastic Fermi acceleration. This process playing possibly a marked role in injection mechanisms of cosmic ray generation[18] leads to chaotic acceleration and manifests itself as a substantial distortion of the spherically-symmetrical part of a distribution function.[19] In this case, a chaotic (thermal) tail in the distribution function and symmetrically spreading in all directions particle flux are observed. One can say that effective temperature $T = T(\varepsilon)$ depends on the particle energy ε, growing infinitely with increasing of the energy ε. Clearly, this process could be called spherical-symmetrical or "thermal" mechanism of runaway. The process may be evolved effectively not only under the Fermi acceleration mechanism, but also under the action of a constant electric field on a plasma in case of strong electron scattering by ions (i.e. at $Z >> 1$, where Z is an ion charge) or by isotropically excited ion-sound plasma oscillations.[20, 21]

It is natural to expect that the same thermal runaway effect arises in motion of fast electrons in air if chaotic alternative electric field is applied or in constant electric and magnetic fields under strong scattering by nuclei $Z >> 1$. In air $Z \simeq 7.25$ (in reality, the effective value Z_{eff} could be slightly lower because of electron shielding on low levels[7]). Undoubtedly, that the value of Z in air is insufficient for total stochastization of electron motion in a constant electric field. In the same time, in the first approximation, even in this case consideration of chaotic acceleration could be useful. It simplifies significantly the kinetic theory of the air breakdown and gives it possible to solve the problem in different conditions: with and without magnetic field, in oscillating electric field a.s.o. However, what are the conditions, when spherical symmetrical (thermal) approach is correct? Can that thermal mechanism of runaway give rise to gas breakdown? Is that process significant in air, i.e. what is the relationship between critical field of thermal mechanism of runaway breakdown in crossed electric and magnetic fields or in oscillating electric field and the critical field of conventional breakdown?

This paper is just devoted to the investigation of these problems.

2. TRANSFORMATION OF KINETIC EQUATION

To describe the breakdown on runaway particles in electric field **E** and magnetic field **B** we start from kinetic equation[7]:

$$\frac{\partial f}{\partial t} + \mathbf{v}\boldsymbol{\nabla} f + e\mathbf{E}\frac{\partial f}{\partial \mathbf{p}} + \frac{e}{c}[\mathbf{v}, \mathbf{B}]\frac{\partial f}{\partial \mathbf{p}} = \hat{S}_1(f) + \hat{S}_{\text{ion}}(f), \tag{4}$$

here $\hat{S}_{\text{ion}}$ is an ionization integral which describe the production of new electrons due to collisions with molecules of the air, $\hat{S}_1 = \hat{S}_0 + \hat{L}$. The term $\hat{S}_0$ describes electron energy loses and the term $\hat{L}$ is a pitch-angle scattering. The classical integrals $\hat{S}_0$ and $\hat{L}$ and a model integral $\hat{S}_{\text{ion}}$ were determined in the paper Ref. 7. In arbitrary coordinate system, terms $\hat{S}_0$ and $\hat{L}$ could be presented in a form:

$$\hat{S}_0(f) = \frac{\partial}{\partial \mathbf{p}}\left(\frac{\mathbf{p}}{p}F_D f\right)$$

$$\hat{L}(f) = \nu(p)p^2\frac{\partial}{\partial p_i}\left[\left(\delta_{ij} - \frac{p_i p_j}{p^2}\right)\frac{\partial f}{\partial p_j}\right]. \tag{5}$$

Here

$$F_D = \frac{4\pi Z e^4 n_m}{mc^2}\frac{\gamma^2}{\gamma^2-1} \times \left\{\ln\left[\frac{mc^2(\gamma^2-1)^{1/2}(\gamma-1)^{1/2}}{\sqrt{2}I}\right] - \left[\frac{2}{\gamma}-\frac{1}{\gamma^2}\right]\frac{\ln 2}{2} + \frac{1}{2\gamma^2} + \frac{(\gamma-1)^2}{16\gamma^2}\right\}$$

is a dynamical friction force,

$$\nu = \frac{F_D(Z/2+1)}{p\gamma}$$

is a collision frequency, I = 80.5 eV for air, N_m is the molecular density,

$$\gamma = (1/\sqrt{1-(v/c)^2}),$$

v is the electron speed. Note, that here $Z \approx 14.5$, as we denote it as the average charge of air molecules N_2 and O_2.

There are several characteristic times in the equations (4), (5). One of them is defined by energy losses t_E and the other one by the pitch-angle scattering t_θ.

$$t_E \approx \frac{p}{F_D} \qquad t_\theta \approx \frac{p\gamma}{F_D(Z/2+1)} \tag{6}$$

If the effective charge Z is large enough, then depending on the considered energy range it could be different relation between t_E and t_θ. If

$$\gamma \ll 1 + \frac{Z}{2} \tag{7}$$

then

$$t_\theta \ll t_E$$

and distribution function in this region should be close to spherical symmetrical due to dominant angular scattering. On the contrary for high energy electrons

$$\gamma \gg 1 + \frac{Z}{2} \tag{8}$$

angular scattering is weak enough and distribution function is determined mainly by energy losses and angular distribution of a new born electrons.

We will start our analyses, considering the low energy range, where conditions (7) is fulfilled. Introducing a new small parameter of the problem $\epsilon = t_\theta/t_E$ we rewrite equations (4) and (5) in the form:

$$\frac{\partial f}{\partial t} + \mathbf{v}\boldsymbol{\nabla} f + e\mathbf{E}\frac{\partial f}{\partial \mathbf{p}} - \hat{S}_0(f) - \hat{S}_{\text{ion}}(f) = \frac{1}{\epsilon}\left[\hat{L}(f) - \frac{e}{c}[\mathbf{v},\mathbf{B}]\frac{\partial f}{\partial \mathbf{p}}\right]. \tag{9}$$

Let us seek for the solution to equation (9) in a power series on the parameter ϵ:

$$f = f_0 + \epsilon f_1 + \ldots .$$

In zero approximation we have

$$f(\mathbf{p},\mathbf{r},t) = f_0(|\mathbf{p}|,\mathbf{r},t).$$

On the next step of this procedure, after averaging of equation (9) on the momentum direction, one can find:

$$\frac{\partial f_0}{\partial t} + \epsilon \nabla \langle \mathbf{v} f_1 \rangle + \epsilon \langle e\mathbf{E} \frac{\partial f_1}{\partial \mathbf{p}} \rangle = S_0(f_0) + S_{\text{ion}}(f_0). \tag{10}$$

It is seen from (10), that the term $\frac{\partial f_0}{\partial t} \sim \epsilon$. Taking this. fact into account, we have in the first approximation on $\in$:

$$\hat{L}(f_1) - \frac{e}{c}[\mathbf{v}, \mathbf{B}] \frac{\partial f_1}{\partial \mathbf{p}} = \mathbf{p}\hat{\mathbf{H}} f_0, \tag{11}$$

here

$$\hat{\mathbf{H}} = \frac{v}{p}\nabla + e\frac{\mathbf{E}}{p}\frac{\partial}{\partial p}.$$

It is naturally to seek for a solution to the equation (11) in a form:

$$f_1 = p_i A_{ik} \hat{H}_k f_0. \tag{12}$$

It is easy to check, that f_1 (12) is an eigenfunction of the operator $\hat{L}$,

$$\hat{L} f_1 = -\nu f_1.$$

That is why, the equation (11) is identical to another more simple equation[22]

$$-\nu f_1 - [\mathbf{p}, \boldsymbol{\omega}_B] \frac{\partial f_1}{\partial \mathbf{p}} = \mathbf{p}\hat{\mathbf{H}} f_0 \qquad \omega_B = \frac{eBv}{cp}. \tag{13}$$

As follows from equation (13) the matrix A_{ik} has a form:

$$\begin{aligned} A_{xx} = A_{yy} = -\frac{\nu}{\nu^2 + \omega_B^2} \qquad A_{zz} = -\frac{1}{\nu} \\ A_{xz} = A_{zx} = A_{yz} = A_{zy} = 0 \qquad A_{xy} = -A_{yx} = -\frac{\omega_B}{\nu^2 + \omega_B^2}. \end{aligned} \tag{14}$$

Substituting (12) into (10) we result in the equation for isotropic part of the distribution function f_0:

$$\begin{aligned} &\frac{\partial f_0}{\partial t} + \frac{1}{3p^2}\frac{\partial}{\partial p}\left[p^2 e E_i A_{ik}\left(v\frac{\partial f_0}{\partial r_k} + eE_k\frac{\partial f_0}{\partial p}\right)\right] \\ &+ \frac{\partial}{\partial r_i}\left[\frac{v}{3}A_{ik}\left(v\frac{\partial f_0}{\partial r_k} + eE_k\frac{\partial f_0}{\partial p}\right)\right] = S_0(f_0) + S_{\text{ion}}(f_0). \end{aligned} \tag{15}$$

Equation (15) describes both thermal runaway effects and diffusive spreading of breakdown in the space. The analogous equation in nonrelativistic limit was derived in Ref. 22. If the magnetic field is negligible the distribution function in (15) is cylindrically symmetrical $f = f(t, p, r_\perp, z)$ and equation (15) could be rewritten in a form:

$$\frac{\partial f}{\partial t} + I_1(f) + I_2(f) + I_3(f) = S_0(f) + S_{\text{ion}}(f) \tag{16}$$

where

$$I_1 = \frac{1}{3p^2}\frac{\partial}{\partial p}\left(p^2 e^2 E^2 A_{zz}\frac{\partial f}{\partial p}\right)$$
$$I_2 = \frac{\partial}{\partial \mathbf{r}}\left(\frac{v^2}{3}A_{zz}\frac{\partial f}{\partial \mathbf{r}}\right) \tag{17}$$
$$I_3 = \frac{1}{3p^2}\frac{\partial}{\partial p}\left(p^2 v e E_z A_{zz}\frac{\partial f}{\partial z}\right) + \frac{\partial}{\partial z}\left(\frac{v}{3}eEA_{zz}\frac{\partial f}{\partial p}\right)$$

The first term in (16), (17) describe the heating of electrons by electric field, the second one describe the diffusive spreading of breakdown in space and the third term describe the motion and acceleration of particles in discharge along electric field direction. The coefficient 1/3 in (16), (17) appears because of scattering and angle averaging. Previously Ref. 6 was demonstrated that the breakdown discharge is spreading in space due to the scattering of a new born fast particles. Now we see that there is another process (angle scattering) which affect the diffusive spreading of breakdown discharge also.

Below, we restrict our consideration by a space uniform problem and neglect the dependence of f on the variable **r.** Equation (15) in these conditions has a form:

$$\frac{\partial f_0}{\partial t} = \frac{1}{p^2}\frac{\partial}{\partial p}\left\{p^2\left[F_D f_0 + \frac{e^2E^2}{3\nu}\left(\frac{\nu^2+\omega_B^2\cos^2\beta}{\nu^2+\omega_B^2}\right)\frac{\partial f_0}{\partial p}\right]\right\} + \hat{S}_{\text{ion}}(f_0). \tag{18}$$

Here $\cos\beta = \frac{\mathbf{EB}}{EB}$, β is an angle between electric and magnetic fields.

It is necessary to note that in spite of the equation (18) was derived in conditions of strong angle scattering of electrons in constant electric field, the quite analogous equation could be obtained in the case of oscillating or stochastic electric field.[22]

3. QUALITATIVE ANALYSIS

We will begin from the analysis of the general kinetic equation (4). Since equation (4) is a linear one we can search for its solution in a form quite analogous to the one used in conventional breakdown theory[23, 24]:

$$f(\mathbf{p},t) = f(\mathbf{p})e^{\lambda_i t} \tag{19}$$

Here parameter $\lambda_i = \frac{1}{\tau_i}$ — is the ionization growth rate and $f(\mathbf{p})$ is a stationary distribution function which is established in the process of breakdown. It is determined by the stationary equation (4) with $\frac{\partial f}{\partial t} = \lambda_i f$.

Boundary conditions to this equation at the low energies are determined by the following physical process. Low energy electrons are generated by fast runaway electrons, they lose their energy in collisions and then disappear at very low energies due to dissociative or three body attachment of electrons to O_2 molecules. That mean, that boundary conditions at $p \to 0$ is determined by the balance of the model ionization term $S_{\text{ion}}(f)$ and electron energy loss term $\hat{S}_{10}(f)$:

$$S_{\text{ion}} + \hat{S}_0(f) = 0\,, \qquad p \to 0 \tag{20}$$

As we will see below this condition determines quite definite mode of solution.

At the high energies when $p \to \infty$ it is natural to expect that:

$$f \to 0\,, \qquad p \to \infty \tag{21}$$

Qualitatively the structure of the solution of stationary equation (4), (19) with boundary conditions (20), (21) could be understood basing on the parameters (7), (8) and the concrete form of distribution function for runaway problems obtained in previous works.[19–22, 25] At the low energy region $\gamma \leq 3$–4 (see (7)) distribution function is close to the spherically symmetric and gradually falls down with the energy of electrons[7] $f \propto (\gamma - 1)^{-1}$. At the high energies $\gamma >> 8$ (see (8)) function $f(\mathbf{p})$ became directed along the direction of electric field (or in presence of a strong magnetic field — along the drift direction, analyzed in Ref. 13). Its directivity is high, but not too high determined by the combined action of electric field and ionization integral $S_{\text{ion}}(f)$. The distribution function can here effectively grow up with γ. It reaches maximum value at the second critical point γ_{2c} (see Fig. 1) and then rapidly falls down at $\gamma > \gamma_{2c}$ analogous to Ref. 25.

It should be emphasized, that according to this analysis the range of energies were the stationary distribution function is determined is extremely large growing exponentially with E/E_c (see Fig. 1). It means that in reality stationary distribution could be established at $E \sim E_c$ only. At $E \geq 2\,E_c$ it is nonstationary and breakdown essentially depend on the process of developing and establishing of a stationary distribution function. The last process depends strongly on the form of initial distribution function $f_0(\gamma)$. In our case of the runaway breakdown in the atmosphere the initial distribution of fast electrons is determined by a cosmic ray secondaries, which have in most part the low energies $\varepsilon \leq (1$–$2)$ MeV. So we can consider:

$$f_0 = \begin{cases} F_0(\gamma), & \gamma \leq \gamma_m \\ 0, & \gamma \geq \gamma_m \end{cases} \qquad \gamma_m \approx 5 \tag{22}$$

It will be shown below, that in this case the quasi stationary distribution function is rapidly established at $\gamma \leq \gamma_m$, but in the high energy range $\gamma > \gamma_m$ it is stretching out very slowly. It means in reality that breakdown process in initial conditions (22) is determined mainly by low energy electrons $\gamma \leq \gamma_m$. For this electrons condition (7) is well fulfilled and kinetic equation could be significantly simplified (16). Below we will use this equation to describe runaway air breakdown.

It should be notified also that as the full stationary solution is not established during runaway breakdown process in initial conditions (22), the electron distribution is stretching out with time in energies, what means that the number of electrons — fast and slow is growing in time not strictly exponentially. This make it different from the classical breakdown process which is always growing exponentially in time.[23, 24]

4. RUNAWAY AIR BREAKDOWN

Let us investigate now the problem of air breakdown, considering spherically symmetrical kinetic equation (18). Since equation (18) is a linear one, we can search for its solution in a form:

$$f_0(\gamma, t^*) = e^{\lambda_i^* t^*} f_0(\gamma) \tag{23}$$

γ and t^* are nondimensional variables

$$\gamma = \sqrt{\left(\frac{p}{mc}\right)^2 + 1}\,, \qquad t^* = \frac{t}{t_0}\,, \qquad \lambda_i^* = t_0 \lambda_i\,, \qquad t_0 = \frac{m^2 c^3}{4\pi e^4 Z n_m a} \tag{24}$$

Substituting (23) in (18) and introducing parameters $\delta_E = E/E_{c_0}$, $h = B/E_{c_0}$ and $\delta_z = (1 + Z/2)^{-1}$, one can find from (18)

$$\frac{d}{d\gamma}\left\{(\gamma^2 - 1)\phi_D(\gamma)\left[f_0 + \frac{T_{\text{eff}}}{\gamma}\frac{df_0}{d\gamma}\right]\right\} = \gamma\sqrt{\gamma^2 - 1}\,\lambda_i^* f_0 - S_i(f_0). \tag{25}$$

Here γ is Lorentz-factor of electron,

$$\phi_D = \frac{1}{a}\frac{\gamma^2}{\gamma^2-1} \times \left\{8.4 + \frac{1}{2}\ln(\gamma^2-1) + \frac{1}{2}\ln(\gamma-1) - 0.347\left(\frac{2}{\gamma} - \frac{1}{\gamma^2}\right) + \frac{1}{2\gamma^2} + \frac{(\gamma-1)^2}{16\gamma^2}\right\}$$

— is a friction force determined by interaction of electron with air molecules, and

$$T_{\text{eff}} = \frac{\delta_E^2(\nu^2 + \omega_B^2\cos^2\beta)}{3\delta_z(\omega_B^2+\nu^2)\nu^2\gamma} \tag{26}$$

— is a parameter which we will call effective temperature, $\omega_B = h/\gamma$, $\nu = \phi_D\delta_z^{-1}(\gamma^2-1)^{-1/2}\gamma^{-1}$, $a \approx 11.2$ — is a fundamental constant.[6] Model ionization integral S_i in (4) takes a form [6, 7]:

$$S_i = \frac{1}{2a}\int_{2(\gamma-1)+1}^{\infty} \gamma'^2 d\gamma' f_0(\gamma')\left[\frac{1}{(\gamma-1)^2} - \frac{2\gamma'-1}{\gamma'^2(\gamma'-\gamma)(\gamma-1)} + \frac{1}{(\gamma'-\gamma)^2} + \frac{1}{\gamma'^2}\right] \tag{27}$$

Note, that effective temperature T_{eff} according to (26) depend significantly on the energy of electrons $\varepsilon = mc^2(\gamma-1)$. Thus, in the absence of magnetic field ($h = 0$) temperature T_{eff} in nonrelativistic limit $\gamma - 1 < 1$ is proportional to ε^3. Directly this strong grows of T_{eff} with ε lead to thermal runaway effect.

The equation (4) has two asymptotics in the limit $\gamma \to 1$. They have different behavior at $\gamma \to 1$: first one is $f_0 \sim \exp\frac{1}{(\gamma-1)^2}$ and the second one $f_0 \sim 1/(\gamma-1)$. The first asymptotic corresponds to equipartition between two terms in LHS of the equation (4) and is equivalent to zero flux condition at $\gamma \to 1$. The second one is defined by the balance of friction force term in LHS and particle source $S(f_0)$ at RHS, it behaves as

$$S(f_0) \propto \frac{1}{(\gamma-1)^2}, \qquad f_0 \propto \frac{1}{\gamma-1}. \tag{28}$$

Only the second solution has a physical meaning in our case. Really, the fast particles from runaway region $\gamma - 1 > 2/\delta_E$ generate a wide range of electrons with low energies ε, which under the action of friction force lose their energy and disappear at $\varepsilon \to 0$ due to attachment to the air molecules. So the $\gamma \to 1$ asymptotic of distribution function is determined by the balance of particle generation and friction force, as was already noted in Section 2.

Integrating equation (25) over γ we obtain the following expression for nondimensional ionization rate λ_i^* (24):

$$\lambda_i^* = \frac{\int_1^{\gamma_\infty}\left\{S_i(f) + \frac{d}{d\gamma}[(\gamma^2-1)\phi_D f]\right\}d\gamma}{\int_1^{\gamma_\infty}\gamma\sqrt{\gamma^2-1}f\,d\gamma} \tag{29}$$

Here we took into account asymptotic behavior of distribution function at $\gamma \to 1$ (28). We supposed also in accordance with (21), (22) that $f \equiv 0$ at $\gamma \geq \gamma_\infty$. Note that close to the threshold conditions

$$\lambda_i \to 0 \qquad \text{at} \qquad E = E_{th}, \qquad \text{or} \qquad \delta_E = \delta_{th} \tag{30}$$

runaway breakdown process is always well described by the equations (18), (29)

As it was shown in Section 2 the equation (18) strictly speaking has no exponential growth rate. To clarify this point let us consider the solution of equation (25) in a limit

$$1 \ll \gamma \ll \gamma_{2c}$$

here γ_{2c} is a second root of equation

$$eE = F_D(\gamma)$$

(see Fig. 1) In this limit the equation (25) has following asymptotics the first one

$$f^{(1)} \propto \gamma^{-\frac{3}{2}-\frac{1}{2}\sqrt{9+4\lambda_i/\phi_\infty T_\infty}}$$

and the second one

$$f^{(2)} \propto \gamma^{-\frac{3}{2}+\frac{1}{2}\sqrt{9+4\lambda_i/\phi_\infty T_\infty}}$$

were

$$\phi_\infty = \frac{8.5}{a} \qquad T_\infty = \frac{\delta_E^2 \delta z}{3\phi_\infty^2}$$

Numerical and analytical analysis show that the first asymptotic can not satisfy the boundary condition (28). The second asymptotic gives a growing up solution $f^{(2)}$ which contradict to the restriction (21). It means that in rigorous theory to obtain exponentially growing in time solution we should consider an extremely spread in energies solution of the full kinetic equation (4), taking into account directional part of distribution function analogous to Refs. 20, 25. But as it was shown earlier in real situation for runaway breakdown in atmosphere this solution is not realized.

Really, runaway breakdown arises only in the presence of a high energy electrons. In the air conditions these electrons are cosmic ray secondaries with the energy $\varepsilon \leq 1$ MeV. So, the initial distribution function is not too spread in energies and could-be supposed as a beam which have an energy cut at $\varepsilon = \varepsilon_m$ (22).

Now, we will estimate the contribution of various parts of distribution function in growth rate (29). Let us suppose, that the main contribution is defined by the range of $\gamma \sim \gamma_0$ and $\gamma_0 >> 1$. Taking into account (28) one can find from (29):

$$\lambda_i^* \approx \frac{7}{4a\gamma_0} \tag{31}$$

So, we see, that contribution into the growth rate (31) decrease with increasing of γ_0. It means that the bulk part of distribution function $f(\gamma)$ for $\gamma \leq 1$–2 gives the main contribution into the λ_i^*.

Let us estimate now the spreading of the initial beam in time. The equation (18) is diffusive type in energy. For simplicity we restrict our consideration on relativistic limit. In this limit the simplified equation (18) takes a form:

$$\frac{\partial f}{\partial t} = \frac{D}{\gamma^2}\frac{\partial}{\partial \gamma}\left(\gamma^4 \frac{\partial f}{\partial \gamma}\right) + \delta(t)\delta(\gamma - \gamma_m) \qquad D = T_\infty \phi_{D\infty} \approx 0.43\delta_E^2 \delta_z. \tag{32}$$

The solution of (32) has a following form:

$$f \propto \frac{\exp\left\{-\frac{(\ln\gamma - \ln\gamma_b + 3Dt)^2}{\sqrt{Dt}}\right\}}{\sqrt{Dt}} \tag{33}$$

We see from (33) that the spreading of this beam and the motion of its maximum is rather slow (in limit $\delta_z << 1$). If the speed of maximum D is lower, than λ_i^* ,

$$\lambda_i^* > D \tag{34}$$

we will have quasi-exponential growth rate. Using this condition we obtain from (32), (34) restrictions on critical field:

$$\frac{E}{E_c} < 1.5\sqrt{\frac{\lambda_i^*}{\delta_z}} \tag{35}$$

It should be noted that λ_i^* depend on E/E_c. This dependence was obtained previously [6, 7]

$$\lambda_i^* = \lambda_{i0}^* \left(\frac{E}{E_c}\right)^{3/2} \qquad \lambda_{i0}^* \approx \frac{1.6}{a}$$

Using this relations one can find:

$$\frac{E}{E_c} < 3\left(\frac{1.6}{\alpha}\right)^2 \tag{36}$$

here $1 \le \alpha \le 1.3$ is a shielding parameter[7] ($Z_{\text{eff}} = Z/\alpha$). If condition (36) is fulfilled the growth rate should be quasi-exponential.

We resume the results of analytical analysis in this section.

1. For atmospheric conditions the runaway air breakdown process could be described by simplified time dependent kinetic equation (18) with boundary conditions (28), (21) and initial distribution function (22).

2. The solution of equation (18) effectively depends on the form of initial distribution function and generally speaking does not grow exponentially in time. But for the initial conditions (22) and for not very high values of electric field (36) it could be close to exponential.

5. NUMERICAL RESULTS

Conventional air breakdown always grow in time exponentially. It is fully described by the threshold electric field E_{cth} and growth rate time τ_i which is rapidly diminishing function of E/E_{cth}.

Runaway breakdown in general case is not growing exponentially in time. Its growth rate and threshold electric field depend significantly on the initial form of distribution function. Not far from the threshold runaway air breakdown process could be quite analogous to conventional, though it has much lower threshold electric field.

Here we will discuss the numerical solution of equation (18) with boundary conditions (21), (28) and a model ionization integral. First of all it is necessary to mention that numerical simulations justify analytical predictions about the behavior of the solution. We see (Figs. 2 and 3), that if the electric field is close to the threshold ($\delta_{th} \approx 1.3$) the electron density is growing up exponentially, but the exponent depends on the energy of initial beam ε_b.

5.1. Comparison with exact solution. Previously in the absence of magnetic field $B = 0$ the solution of kinetic equation (4) with the model ionization integral S_{ion} was investigated numerically.[7] It is shown at Fig. 4 for $\delta_E = 2$. One can see from the figure that the main bulk of electron distribution function is close to spherically

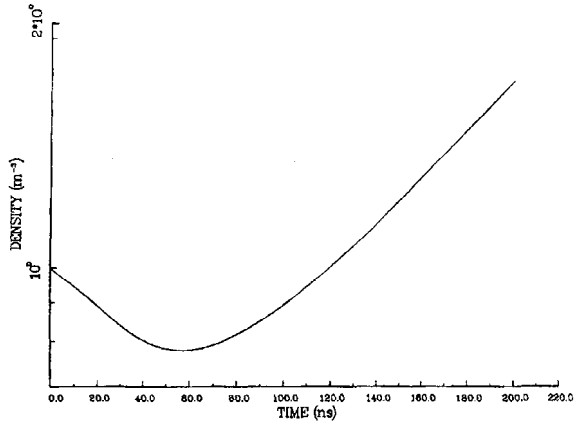

Figure 2. Spherically symmetric solution with ε_b = 10 MeV. The electron density is plotted as a function of time for δ_E = 1.4, h = 0 and ε_b = 10 MeV.

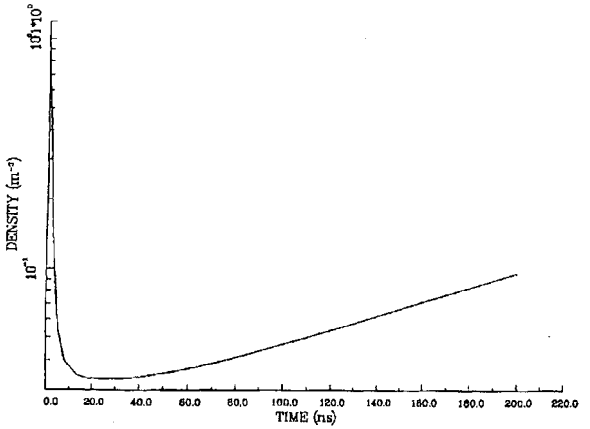

Figure 3. Spherically symmetric solution with ε_b = 1 MeV. The electron density is plotted as a function of time for δ_E = 1.4, h = 0 and ε_b = 1 MeV.

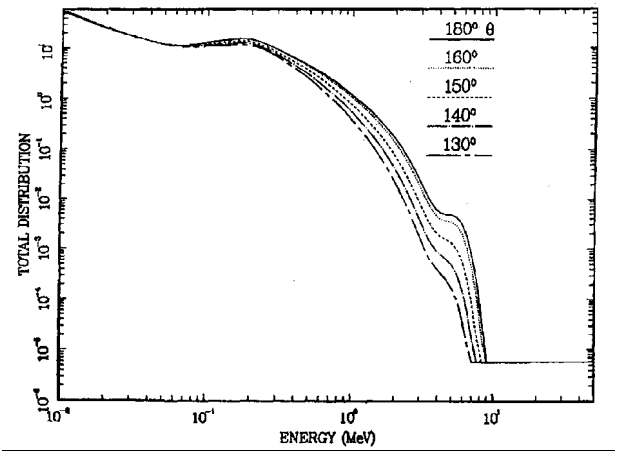

Figure 4. General solution of Boltzmann equation. The magnitude of the self-similar electron distribution function $\delta_E = 2$ and no magnetic field ($h = 0$) is plotted as a function of the electron energy and the angle θ between the applied electric field and the electron momentum vector. These results were obtained in Ref. 7.

symmetrical. Quite analogous statement could be made about the form of distribution function f for higher electric fields $\delta_E = 5, 8$, obtained in Ref. 7, though at the high energies $\varepsilon \geq 1$ MeV we see there, that the distribution function takes more directional character.

The solution of simplified spherically symmetrical equation (18) with boundary conditions (21), (28) and the same model ionization integral and initial distribution function as in Ref. 7 for $\delta_E = 2$ is demonstrated at the Fig. 5. One can see quite a reasonable agreement with Fig. 4. The dependence of the growth rate λ_i on electric field δ_E is presented in Table 1. As we expected for the low value of δ_E the growth rate of electron density is close enough to the previous one and the difference between them is increasing with increasing of δ_E.

The solution of equation (18) allowed to determine the threshold electric field for runaway breakdown with $B = 0$, which was found to be $\delta_{th} \approx 1.3$. We see from Figs. 4, 5 and Table 1, that not far from the threshold the form of distribution function and breakdown growth rate is well enough described in spherical symmetrical approach, what is in a full agreement with the results of analytical analysis, presented in the previous section. It allows us to explore the influence of magnetic field and oscillating electrical field on runaway breakdown in the same spherical symmetrical approximation.

5.2. Influence of magnetic field. The exact kinetic equation (4) is quite complicated for numerical analysis if magnetic field **B** is fully taken into account. The

Table 1. Avalanche Time for Spherical Symmetric τ_i^{sp} and Exact τ_i Kinetic Equations

δ_0	$\tau_i^{(sp)}$ (ns)	τ_i (ns)
2	19.6	27
5	2.4	7
8	0.6	2.9

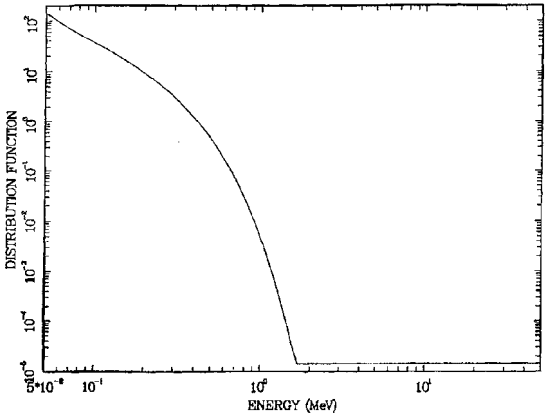

Figure 5. Spherically symmetric approach. The magnitude of the self-similar electron distribution function for $\delta_E = 2$ and no magnetic field ($h = 0$) is plotted as a function of the electron energy. These results were obtained using the spherically symmetric approach and can be compared directly with the general solution obtained in Ref. 7 (see Fig. 4).

5.2. Influence of magnetic field. The exact kinetic equation (4) is quite complicated for numerical analysis if magnetic field **B** is fully taken into account. The above both analytical and numerical analysis shows that spherically symmetrical approach (18) is very useful if one consider solution not far from the threshold. Let us analyze now using this approach the dependence of the threshold electric field $\delta_{E_{th}}$ on magnetic field **B.** It is characterized by two parameters: normalized value of magnetic field $h = B/E_{c0}$ and angle β between **B** and **E.** The influence of magnetic field is mostly strong for $\beta = 90°$, when $\mathbf{E} \perp \mathbf{B}$. The dependence of δ_{Eth} on h for $\beta = 90°$ is shown on Fig. 6 and in Table 2. One can see from the figure and Table 2 that $\delta_{E_{th}}$ is growing with h. This result seems quite natural: as one can see from equations (18), (26) the growth of magnetic field at $\beta = 90°$ diminishes the effective electron temperature T_{eff}. It means that the effective width of distribution function is decreasing with increasing magnetic field and one need to apply more strong electric field to achieve breakdown conditions. It is interesting to note that obtained in Ref. 13 analogous growth of breakdown electric field $\delta_{E_{th}}$ with h based on the analysis of the pure electron runaway process without heating, was much stronger. It means that the influence of thermal effects on runaway breakdown is enhancing with the increasing of normalized magnetic field h. This fact agrees with the form of distribution function in the presence of magnetic field obtained in Ref. 14 which is more close to the spherical symmetrical one (note that the amplification of breakdown time constant λ_i with h^{14} does not agree with our results).

The dependence of $\delta_{E_{th}}$ on h for different values of the angle β are presented at Table 3. One can see that $\delta_{E_{th}}$ for given h is diminishing with diminishing β and the relation

$$\delta_{E_{th}}(0°) < \delta_{E_{th}}(\beta) < \delta_{E_{th}}(90°), \qquad \delta_{E_{th}}(0°) \approx 1.3 \tag{37}$$

Table 2. Threshold Electric Field for Runaway Breakdown with a Magnetic Field ($\beta = 90°$)

h	0	1	2	5	10	30	100
δ_{th}	1.30	1.66	1.70	1.80	2.25	3.30	5.25

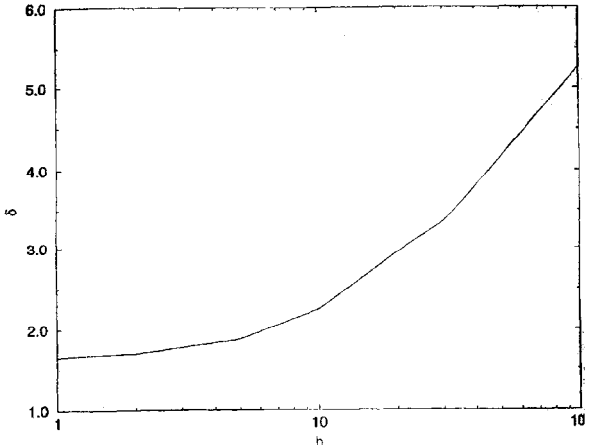

Figure 6. Threshold electric field vs. normalized magnetic field for $\beta = 90°$. The normalized threshold electric field for runaway breakdown ($\delta_{E_{th}}$) is plotted as a function of the normalized magnetic field (h) for an angle $\beta = 90°$ between the electric and magnetic fields.

is always fulfilled. This behavior of $\delta_{E_{th}}$ naturally follows from the formulae for T_{eff} in Eq. (18).

5.3. Alternating electric field. Spherical symmetrical approach and equation (18) gives the possibility to analyze breakdown in alternating and stochastic electric fields.

It is possible to show that in the case of stochastic field the equation (18) is not changed if one substitute averaged $\langle E^2 \rangle$ instead E^2. Because of this all previous results for constant electric field are valid for stochastic field too.

The results of numerical solution of equation (18) for the case of alternating electric field are shown on Fig. 7 and 8. The solution in this case depends on relation between frequency of electric field ω and ionization rate λ_i. If

$$\omega < \lambda_i \tag{38}$$

the situation is quasistationary (see Fig. 7) and the total number of secondary electrons is following to the change of electric field oscillating with the frequency ω. In opposite case when

$$\omega > \lambda_i \tag{39}$$

Table 3. Avalanche Time as a Function of Angle β for $\delta_E = 2.0$, $\delta_B = 10$

β (degree)	$\tau_i^{(sp)}$ (ns)
0	19.6
15	72.1
30	100
45	273
60	∞

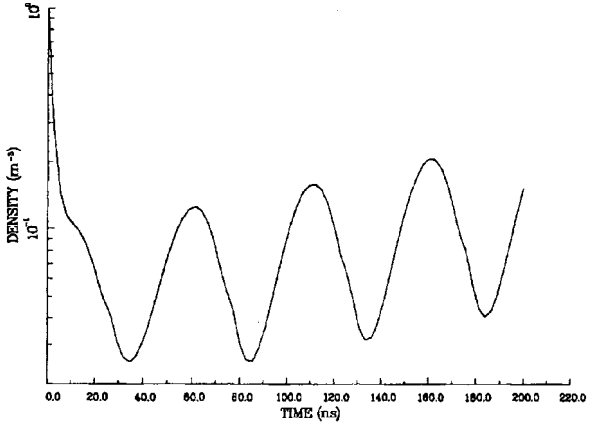

Figure 7. Oscillating electric field with $\omega < \lambda_i$. The electron density is plotted as a function of time for $\delta_{\omega th}$ and $h = 0$. In this case $\omega < \lambda_i$.

the breakdown is defined by the same equation (18), but the effective temperature takes the form[22]:

$$T_{\text{eff}} = \frac{e^2 E_0^2 \nu}{6(\nu^2 + \omega^2)} \tag{40}$$

Here E_0 — is the amplitude of oscillating electric field. We see that equation (40) if $\omega << \nu$ coincide with the same equation for the constant electric field E, only this field is in $\sqrt{2}$ times less due to averaging of E^2 on oscillations. This averaging is clearly seen at Fig. 8. So the threshold amplitude for low frequency electric field should be

$$E_{0th} = \sqrt{2} E_{th}\,, \qquad \delta_{\omega th} = \sqrt{2}\delta_{th} \tag{41}$$

Numerical calculations confirm this results exactly giving $\delta_{\omega th} = \sqrt{2}\delta_{th} \approx 1.8$. Note, that in the nondimensional variables (4) frequency ω takes the form:

$$h_\omega = \frac{mc\omega}{eE_{e0}} \tag{42}$$

We see that the equation (18), (4) in normalized variables takes just the same form as in magnetic field with $h = h_\omega$. The only difference comes from the fact that $\omega_B \propto h/\gamma$, but ω does not depend on γ.

In oscillatory electric field and magnetic field the effective temperature takes a form[22]

$$T_{\text{eff}} = \frac{e^2 E_0^2}{6}\left(\frac{\cos^2\beta}{\nu} + \frac{\sin^2\beta}{2[(\omega-\omega_B)^2+\nu^2]} + \frac{\sin^2\beta}{2[(\omega+\omega_B)^2+\nu^2]}\right) \tag{43}$$

We see, that in this case a gyroresonance effect is possible in conditions when $\beta = 90°$, ν is small enough ($h >> 1$) and frequency ω is close to ω_B at $\gamma \approx 1.3–1.5$.

6. CONCLUSION

Analytical and numerical arguments, presented in Sections 3–4 showed, that the kinetic equation for electrons describing runaway breakdown process in atmospheric

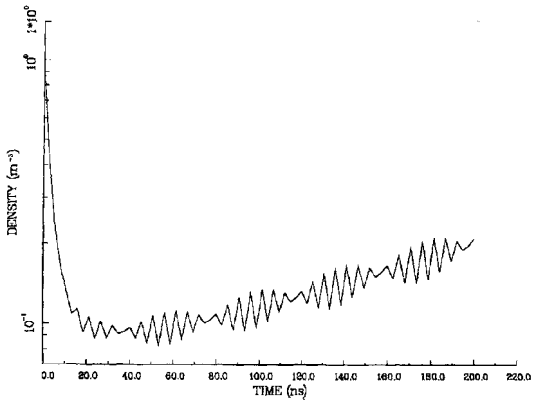

Figure 8. Oscillating electric field with $\omega > \lambda_i$. The electron density is plotted as a function of time for $\delta_{\omega t h}$ and $h = 0$. In this case $\omega > \lambda_i$.

conditions could be significantly simplified and presented in spherical symmetrical form (18). It allowed us to solve this equation and determine breakdown threshold electric field and growth rate. In the first time this problem is consistently solved in the presence of the constant magnetic field, which plays a significant role in the Earth's atmosphere at the heights $z \geq 20$–40 km. [13, 14] In the Table 4 the threshold for a runaway breakdown by vertically directed electric field is presented as the function of height z for northern $E_{th}^{(n)}$ ($\beta \leq 30°$) and equatorial $E_{th}^{(eq)}$ ($\beta \approx 90°$) latitudes. Threshold electric field for the conventional breakdown E_{cth} is given in the Table also. One can see, that in the northern latitude (and midlatitudes) conditions runaway breakdown threshold fields is always much less than conventional

$$E_{th} \ll E_{cth} \tag{44}$$

But in equatorial region the same relation (44) is well fulfilled for the heights $z \leq 50$–60 km only. This fact could be significant for understanding of the nature of high altitude lightning at different latitudes.

We have shown that runaway breakdown in homogeneous atmosphere can take place not only in a constant but in oscillating in time with any frequency electric fields also. The physical nature of this new effect is deeply connected with thermal runaway process. The possibility of existence of runaway breakdown in oscillating electric fields could be significant for interpretation of lower ionosphere ionization during thunderstorms [26] and high altitude lightning mechanism. But the atmosphere at the heights $z \geq 50$ km is strongly rarefied and due to this the spatial inhomogeneity could be significant here. So, a more detailed analysis of this problem is needed which lays out of the frame of present paper.

Table 4. Heights Dependence of Breakdown Parameters

z (km)	$N_m\ cm^{-3}$	$E_{th}^{(n)}$ (V/cm)	$h^{(eq)}$	$E_{th}^{(eq)}$ (V/cm)	E_{cth} (V/cm)
0	2.7 x 10^{19}	2961	0.04	2900	2 x 10^4
10	8.6 x 10^{18}	929	0.126	966	6.4 x 10^3
20	1.8 x 10^{18}	195	0.60	226	1.33 x 10^3
30	3.7 x 10^{17}	40.1	2.92	54	274
40	8.2 x 10^{16}	8.9	13.2	17	60.7
50	2.2 x 10^{16}	2.4	49.1	7.4	16.3
60	6.7 x 10^{15}	0.72	161	3.7	4.9

ACKNOWLEDGMENT

The authors express their appreciations to M. O. Ptitsyn and Yu. V. Medvedev for useful discussions and preliminary numerical calculations. The work was supported by ISTC grant N 480.

REFERENCES

1. C. T. R. Wilson, Proc. Cambridge Philos. Soc. **22,** 34 (1924
2. A. V. Gurevich, JETP, **39,** 1296 (1960) [Sov. Phys. JETP bf 12, 904 (1961)].
3. G. E. Shaw, J. Geophys. Res. **72,** 4623 (1967).
4. D. P. Whitmire, Lett. Novo Cim. **26,** 497 (1979).
5. A. V. Gurevich, G. M. Milikh, R. A. Roussel-Dupreè, Phys. Lett. A **165,** 463 (1992).
6. A. V. Gurevich, G. M. Milikh, R. A. Roussel-Dupreè, Phys. Lett. A **187,** 197 (1994).
7. R. A. Roussel-Dupreè, A. V. Gurevich, T. Tunnel, G. M. Milikh, Phys. Rev. E **49,** 2257 (1994).
8. M. P. McCarthy, G. K. Parks, Geophys. Res. Lett. **12,** 393 (1985).
9. E. K. Eack, Rev. Sci. Instrum. **67,** 2005 (1996).
10. E. K. Eack, W. H. Beasley, W. D. Rust, T. C. Marshal, M. Stolcenberg, J. Geophys. Res. (accepted for publication).
11. E. K. Eack, W. H. Beasley, W. D. Rust, T. C. Marshal, M. Stolcenberg, Geophys. Res. Lett. (1996) (accepted for publication).
12. G. J. Fishman, P. N. Bhat, R. Mallozzi et al., Science **264,** 1313 (1994).
13. A. V. Gurevich, J. A. Valdivia, G. M. Milikh, K. Papadopoulas, Radio Sci. 31, 1541 (1996).
14. R. A. Roussel-Dupreè, R. H. Miller, EOS Trans. AGU 75, 44 (1994).
15. G. M. Milikh, K. Papadopoulas, C. L. Chang, Geophys. Res. Lett. **22,** 85 (1995).
16. V. P. Pasko, K. S. Inan, Y. N. Taranenko, T. F. Bell, Geophys. Res. Lett. **22,** 2127 (1995)
17. Y. N. Taranenko, K. S. Inan, T. F. Bell, Geophys. Res. Lett. **20,** 1593 (1993).
18. Astrophysics of Cosmic Rays (ed. V. L. Ginzburg) Elsevier Science Publish. B. V. (1990).
19. A. V. Gurevich, JETP **38,** 1597 (1960).
20. A. V. Gurevich, Y. N. Zhivlyuk, JETP **49,** 214 (1965).
21. V. Y. Bychenkov, V. P. Silin, S. A. Uryupin, Physics of Plasmas, **10,** 748 (1984).
22. A. V. Gurevich, Nonlinear Phenomena in the Ionosphere, Springer, NY (1978). .
23. A. D. MacDonald, Microwave Breakdown in Gases, NY-London-Sydney, Wiley (1966).
24. A. V. Gurevich, N. D. Borisov, G. M. Milikh, Physics of Microwave Discharges and Artificial Ionized Region in the Atmosphere, Gordon and Breach, Reading (1997).
25. A. V. Gurevich, JETP, **40,** 1825 (1961) [Sov. Phys. JETP 13, 1282 (1961)].
26. U. S. Inan, J. V. Rodriguez, V. P. Idone, GRL **20,** 2355 (1993).

This Page Intentionally Left Blank

NONLOCAL EFFECTS IN STATIONARY AND NON-STATIONARY DISCHARGES

Ivanov V.V., Klopovsky KS., Lopaev D.V., Mankelevich Yu.A.,
Rakhimov A.T., Rakhimova T.V.

Nuclear Physics Institute
Moscow State University
119899 Moscow, RUSSIA

Introduction

At present the interest to non-equilibrium processes in spatially non-uniform low-temperature plasma is stimulated by wide using it in various technologies such as film deposition and etching in microelectronics, lighting technology and etc.

Optimisation of plasma parameters for these aims requires to perform both the experimental investigations and the numerical modelling. Comparison of experimental data with the results of modelling enables to obtain the detailed information about the elementary processes in plasma and to reveal its effect on discharge electrodynamics. In turn for providing the validity of modelling it is required to do testing of the numerical models by the experiment, since for the complex gases the rate constants of many elementary processes are known with the insufficient accuracy or unknown at all. Calculation of electron distribution function (EDF) determining the electron kinetic coefficients and the rate constants is one of the main problem of modelling. In general case EDF is a function of seven variables and can be found by solving the Boltzmann equation:

$$\frac{\partial F(\vec{v},\vec{r},t)}{\partial t} + \vec{v}\frac{\partial F(\vec{v},\vec{r},t)}{\partial \vec{r}} + \frac{e}{m}\vec{E}(\vec{r},t)\frac{\partial F(\vec{v},\vec{r},t)}{\partial \vec{v}} = J(F) \qquad (1)$$

where r - vector radius, v - vector of electron velocity, $J(F) = J_{el}(F) + J_{in}(F)$ – collision integral, defining the change of $F(\vec{v},\vec{r},t)$ in elastic (J_{el}) and inelastic (J_{in}) collisions) $\vec{E}(\vec{r},t)$ a strength of electric field, e and m - charge and mass of electron, respectively.

Because the general effective algorithm for solving equation (1) is absent, one use different simplified approximations. The most often applied approximation concludes in neglecting the spatial non-uniformity of plasma, when one can neglect the second

Electron Kinetics and Application of Glow Discharges
Edited by U. Kortshagen and L. D. Tsendin, Plenum Press, New York, 1998

term in (1). However, this approach is valid when the characteristic dimension L of plasma non-uniformity exceeds the electron energy relaxation length Λ_e. :$L >> \Lambda_e$. When the opposite relation is valid the approximation of spatial uniformity becomes incorrect. Hence electron distribution function $F(\vec{v}, \vec{r}, t)$ is not determined by local electric field and, in this sense, becomes non-local.

There are many discharge physics problems which can not be considered in assumption of local electric field dependence of EDF. The classic problem of this type is a cathode sheath of glow discharge. The existence of such fields in the glow discharge as a negative glow and Faraday dark space is directly connected with the non-locality of electron energy spectrum. Similar problems arise in the stationary RF discharges and the positive column of DC discharge at the lowered pressures where the strong spatially non-uniform field takes place (electrode sheaths in RF discharge, a region of wall ambipolar potential in positive column). As a result EDF should be calculated using equation (1) jointly with the equations of discharge electrodynamics. Solving the spatially non-uniform Boltzmann equation is a complex task even in given electric fields. Therefore the development of effective approaches and methods for the EDF calculations is one of the most actual problem of plasma physics. At the same time the required level of EDF calculation validity must be rather high because EDF can not be very often measured with the satisfactory accuracy.

At last time the different approaches to EDF calculation in the spatially non-uniform fields were developed:

(1) known analytical approaches based on a conservation of total electron energy in almost collisionlless plasma. Namely this approach, at first proposed by Bernstein and Holstein, one often call << non-local>>.

(2) different numerical methods of solving the kinetic equation (1) based on:

a) two-term approximation (TTA)

b) many-term approximation (MTA)

(3) Monte-Carlo technique for direct integrating the electron motion equations.

For the self-consistent simulation of discharge processes one apply:

1') analytical methods, utilising the approach (1)

2') numerical methods with integrating the Boltzmann equation by TTA

3') method of Particle-In-Cell with Monte-Carlo technique (PIC MC) or

4') modified "fast" versions of PIC MC for significant lowering the computer efforts.

Except of the methods based on kinetic approach to electron behaviour description, the methods with approximative accounting for the spatial non-locality of electron energy spectrum are also developed. So in order to take into account the influence of EDF non-locality in drift-diffusion approximation of discharge kinetics one assumes that the ionisation rate and others kinetic coefficients are a function of electron average energy $< \varepsilon >$, which is determined from equation of electron energy transport in the discharge gap. The dependencies of all kinetic coefficients on $< \varepsilon >$ are found by solving the stationary spatially uniform Boltzmann equation.

In this report we will consider an applicability of above-mentioned approaches to EDF calculations description by investigating the stationary discharges in variable and constant electric fields (RF discharge and positive column of DC discharge). As an example of non-stationary discharge where a kinetic description of electrons is also important we will consider a pulsed discharge between dielectric plates with a very small gap. Such discharges are used for phosphor excitation in AC plasma display panel.

Positive column of DC discharge.

Low pressure discharges in electronegative gases are widely used in microelectronics and new material technologies. It strongly increases the interest to the study of electronegative gas plasma at the last years[1–8] .

The difficulties in the study of mechanisms of various processes in electronegative plasma are to a great extent due to insufficient information about the spatial profiles of charged particles (electrons, positive and negative ions), as well as about the electron distribution function (EDF), which can be non-local at low pressure. A study of the problem under consideration is very complicated in RF discharges with complex configuration. For this reason, despite the preferential use of RF discharges in plasmachemical technology, there is a significant interest to the study of the DC glow discharges.

DC glow discharge at low pressure in a long cylindrical tube with the electric field directed axially is appropriate to study (both experimentally and theoretically) the effects of non-locality and anisotropy of the EDF, as well as to examine various elementary processes and chemical reaction in the plasma.

One of the main features of such a discharge is the follows: it is strongly non-equilibrium and non-uniform in radial direction (being uniform along the axial one). As a rule there is no stable discharge glowing in electronegative gases in this geometry does at the value pd parameter lower 0.1 Torr cm.

Calculation of the EDF (which determines rate constants of the main elementary processes and the transport coefficients in plasma) is one of the most important problems in modelling of these discharges. Spatial variations of the EDF can be described in various ways: (1) by solving the parabolic equation for mean energy [3,7] ; (2) by solving the spatially non-uniform Boltzmann equation [3,9] ; (3) by solving the equations of motion for large number of test particles in a given potential (method Monte-Carlo[10], MC), or in self-consistent potential determined by Poisson equation (Particle In Cell Monte-Carlo (PIC MC) technique [11,12]).

For testing the different approaches to modelling of DC discharge we have carried out comprehensive experimental and theoretical investigations of DC discharge positive column in pure oxygen. Note that a structure of cross-sections of electronic scattering on oxygen molecule is such that EDF anisotropy is small even at high energies closed to ionisation potential. It allows to test the applicability of TTA at solving the general Boltzmann equation (1).

A study of oxygen plasma is of fundamental interest for the understanding of plasma electrodynamics in electronegative gases, when the processes with radicals, metastable particles can essentially effect on all discharge parameters. For studying the mutual influence of discharge electrodynamics and plasmachemical processes we have carried out a series of the experiments in which it were measured:

a) axial electric fields, radial profiles of plasma potential and EDF by modulated probe technique;

b) gas and wall temperature;

c) negative ion concentration by laser photodeattachment technique;

d) concentrations of active particles - metastable molecules $O_2(b^1\Sigma_g^+)$, $O_2(a^1\Delta_g$ and atoms $O(^3P)$ by emission spectroscopy and actinometry technique respectively. The DC discharge was formed in a glass tube with the inner diameter of 12mm in a range of pure oxygen pressures 0.15-6 Torr and discharge currents 1-40 mA. The

details of experimental set up and measurements with Langmuir probes are presented in work [13].

We note that non-locality of EDF can be easy experimentally recorded at low gas pressure, when [14–16] the spatial dependence of EDF is determined only by the potential energy of electrons in a space-charge field. The physical basis of this assumption is that the condition $L << \Lambda_e$ is valid at low pressures and the motion of electrons in the space-charge field is a function of the total energy $u(r) = \varepsilon - e\varphi(r)$, where ε and $e\varphi(r)$ are kinetic and potential energies of electron respectively. Hence the experimentally measured EDF at different spatial points has to be identical after the displacement in the energy scale on the difference of plasma potentials in the corresponding points. It has been observed in measurements [17,18] of the EDF in an RF discharge in Ar.

Data of our experiments were a start point to study the applicability of different approximate methods of solving the Boltzmann equation with taking into account the EDF spatial dependence. It is worth noting that a study of EDF non-locality in molecular gases is a difficult problem due to an existence of inelastic processes with low excitation energy thresholds. It is necessary to note that the measurement EDF in electronegative gases is also complicated by the presence of high negative ion concentration. In the experiment [13] $\Lambda_e \gtrsim L$ at p=0.15 Torr and therefore EDF nonlocal effects are more pronounced at this pressure.

Figure.1 represents experimental EDF in a scale of total energy (potential energy is taken on potential on a discharge axis) at three radial positions R_i =0, 3, 5 mm, current density of 5 mA/cm² and different pressures. As it is well seen at pressure of 0.15 Torr the EDF approximation as a function of total energy is quite valid, i.e. $F(r, \varepsilon) = F(u(r))$. EDF's at different radial positions coincide in a scale of total energy up to 13 eV. Note that shifting in radial direction one can observe only such electrons of EDF which have kinetic energy higher than the potential energy at the given point of space. Therefore the low-energy part of the EDF is caused a "cut off" effect. If the pressure increases, EDF's at different point of space start to differ from each other, It show that for certain values of *Rp* the EDF can not be approximated as a function only of the total energy $u(r)$.

The radial profiles of electron average energy are shown in Figure.2 at the same conditions as in Figure.1. It is seen that a spatial region of lowered $< \varepsilon >$ can be directly connected with energy dependence of EDF's. A negative slope of EDF's increases with energy that corresponds to decreasing the average energy of electrons which can penetrate far from the discharge axis. It can be interpreted as an effect of electron << cooling>> by radial field, formed by a space charge. It is interesting to compare the experiment data on EDF with the strict calculations of electron energy spectrum. The applicability of non-local TTA for EDF calculation in spatially non-uniform radial field $E_r(r)$ was analysed from comparison with data of the experiment and MC calculation.

It should be noted that active particles such as atomic oxygen and oxygen metastable molecules have a great influence on oxygen discharge electrodynamics. Besides the ion heating in a strong axial field changes the radial profiles of potential. The complete self-consistent model of oxygen discharge has of course to take into account these processes. In the aims of simplification and correct comparison the applicability of NL TTA was analysed by comparing with the MC calculation in experimentally measured axial and radial fields. In following the analysis of the experimental data was carried out on base of self-consistent model by using the PIC MC technique.

Note, that we have no experimental data about the wall potential φ_W that it was necessary for the calculations in the prescribed electric fields. Therefore, in both NL TTA and MC simulations φ_W were chosen from EDF steady-state condition.

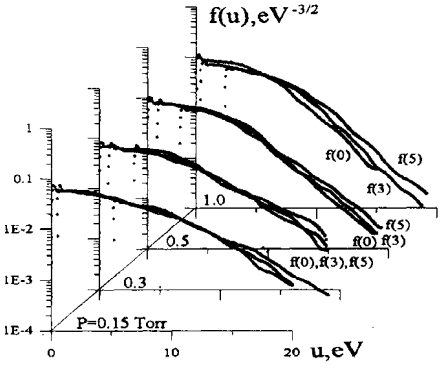

Figure 1. Experimental radial EDF's in a scale of total energy for oxygen DC discharge at 5 mA/cm ². f(0), f(3) and f(5) show the radial position of EDF's in mm from the discharge axis.

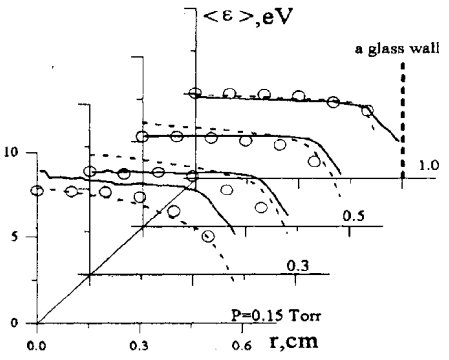

Figure 2. The radial distribution of mean electron energy at the same conditions as in Fig.1. Circles are the experiment data. Solid and dashed lines are MC calculations and NL TTA calculations respectively.

Comparison of calculated and experimental results is represented in Figure.3(a,b). At pressure of 1 Torr $\Lambda_\varepsilon << R$. Therefore one can expect that EDF has to be local excepting only a thin layer nearby the wall. It is well seen that both the experimental and all the calculated results including also local EDF are close. With decreasing the pressure a role of spatial non-locality effects increases. However NL TTA leads to an essentially more high non-locality of electron energy spectrum at high energy than it is observed in the experiment and MC calculation. This discrepancy is connected with the invalid description of wall electron losses (it is necessary to take into account a cone of the losses). However the marked discrepancy in calculated EDF's only slightly influences on ionisation coefficient and other plasma kinetic coefficients. On this reason, even at low pressure the plasma kinetics simulations based on the different approaches to determining the spatially non-uniform EDF practically lead to the same results in integral discharge characteristics. As an illustration of it the calculated radial distributions of electron average energy are shown in Figure.2. As one can see the calculations by NL TTA and MC technique are in good agreement.

To build up a general model of the discharge in spatially non-uniform electric field it is necessary self-consistently to solve Boltzmann equation for EDF, continuity equations for charged and neutral particles and Poisson equation for electric field. Self-consistent

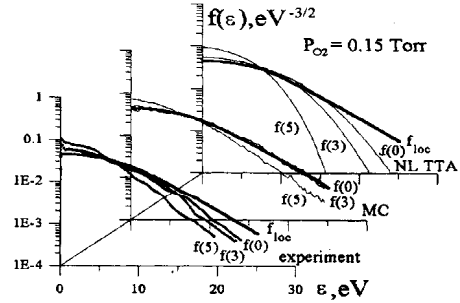

Figure 3a. Comparison of EDF calculated in local field TTA with the experimental ones and calculated by MC tecnique and NL TTA method.

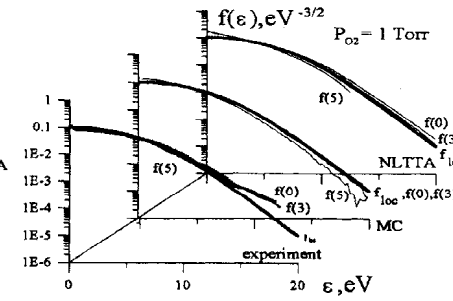

Figure 3b. Comparison of EDF calculated in local field TTA with the experimental ones and calculated by MC technique and NL TTA method

simulation in a wide range of *RN* values requires to use more strict approaches than TTA, for example PIC MC. In our work we have used the fast algorithm of PIC MC (FPIC MC), developed by us for stationary and quasi-stationary (periodic) discharges. FPIC MC is in fact modified PIC MC method. It allows us to perform the calculations with more small account of probe quasi-particles. Thus the statistics was accounted for a great number of time steps that enables to do the calculations on personal computer with PENTIUM processor.

The calculations were performed in a pressure range of 0.15-1 Torr. In order to test our program we used a limited set of plasmachemical reactions. O_2^+ and O^- ions were considered as the main positive and negative ions respectively. The concentrations of active neutral particles - oxygen atoms and metastable molecules were taken from the experiment. The calculations take into account both the ion heating in axial field and its influence on radial ion diffusion and rate constants of detachment processes. Diffusion coefficient of non-equilibrium ion diffusion can be presented by Einstein formula[19]:

$$D_\perp(E_z) = \mu_i k_B T_{i\perp}^{eff}/e \tag{2}$$

$$T_{i\perp}^{eff} = T_g + \xi_\perp m_{red} w^2/k_B \tag{3}$$

where $m_{red} = mM/(m + M)$- reduced mass of ion (m-ion mass,*M*-mass of gas molecule), *w*- a drift velocity, k_B- Boltzmann constant, T_g - gas temperature, $T_{i\perp}^{eff}$ – effective transversal ion temperature and at least

$$\xi_\perp = 1/3(m + M)^2/[m(2m + M)] \tag{4}$$

Two processes of associative detachment:

$$O^-\left(^2P\right) + O\left(^3P\right) \rightarrow O_2\left(X^3\Sigma_g\right) + e \tag{5}$$

$$O^-\left(^2P\right) + O_2\left(a^1\Delta_g\right) \rightarrow O_3\left(^1A_1\right) + e \tag{6}$$

$$\rightarrow O_2\left(X^2\Pi_g\right) + O\left(^3P\right) + e \tag{7}$$

were supposed as the main processes of electron detachment from negative ion O^- (^{2}P).

The best agreement between self-consistent simulation and experimental results for the E_z/N dependence on *RN* parameter was reached when the values of reaction rate constants were taken of 2×10^{-10} cm^3/s and 6 x 10^{-11} cm^3/s, respectively. It should be noted that these rate constants are in the range of known literature data.

However the calculations were shown that:

1) detachment processes have a strong effect on electrodynamics of the discharge;

2) there is a difference of calculated radial profiles of ion concentration and plasma potential from the measured ones.

These differences are conditioned by negative ion kinetics. Note that under our experiment conditions drift-diffusion approach to ion kinetics is quite applicable because a length of the wall potential drop includes about 50 lengths of ion free path. In the calculations of effective ion temperatures we used experimental data on O_2^+ and O^- mobilities. Therefore the influence of resonant charge transfer on O^- transport was also taken into account, i.e. O^- mobility was corrected on gas dissociation degree.

Radial distributions of negative ions in positive column of oxygen DC discharge at current 5 mA are shown in Figure 4[20]. The form of these distributions slightly depends on discharge current so that it allows one to affirm that there is no a clear decomposition of plasma on ion-ion and ion-electron components in the radial direction. However a total ion concentration in turn strongly depends on discharge current and pressure. It is due to a significant contribution of detachment processes into ion kinetics.

The calculated radial profiles of ion concentration are also represented in Figure 4. It is well seen that taking into account the non-equilibrium ion diffusion allows one not only correctly to describe the radial ion distribution and has a great effect on ion concentration too. Thus the investigations of negative ion kinetics have to be accompanied the simultaneous measurements of ion spatial distributions for the correction of experimental data. Obtained data enable us to determine the dependencies of detachment rate constants on "energy" of colliding particles (really on ion temperature):

$$k_1 = 4 \times 10^{-10}(300/T_i^{eff})^{1/2} cm^3/s \tag{8}$$

$$k_2 = 6 \times 10^{-11} + 4 \times 10^{-10}(470/T_i^{eff})^{3/2} exp(-470/T_i^{eff}) cm^3/s \tag{9}$$

where T_i^{eff} effective temperature of O^- ion. Since the ion energy distribution function is anisotropic $T_{i\|}^{eff} > T_{i\perp}^{eff}$ we supposed that T_i^{eff} is the independent average from $T_{i\|}^{eff}$ and $T_{i\perp}^{eff}$:

$$T_i^{eff} = \sqrt{(T_{i\|}^{eff})^2 + 2(T_{i\perp}^{eff})^2} \tag{10}$$

where $T_{i\perp}^{eff}$ is the effective transversal temperature and $T_{i\|}^{eff}$ is the effective axial temperature of O^- ions:

$$T_{i\|}^{eff} = T_g + \xi_{\|} m_{red} w^2/k_B \tag{11}$$

$$\xi_{\|} = 1/3(m+M)(4m+M)/[m(2m+M)] \tag{12}$$

(If to suggest that m is mass of O^- ion and M is mass of O_2 molecule, $T_i^{eff} = \sqrt{2} T_{i\perp}^{eff}$).

These rate constants allowed by the best way to describe the experimental data on negative ion concentrations as a function of discharge current (Figure.5). It should be noted that the rate constants and as a consequence the mechanisms of the detachment reactions (1), (2) were chosen by analysing both the data on potential curves of O_2 and O_2^- molecules and the recent data on potential surfaces of O_3 ozone and O_3^- anion [21–23].

Thus one can conclude that in oxygen where EDF anisotropy is small it is possible to use non-local two-term approximation in solving the Boltzmann kinetic equation. However the use both of the simplified averaged methods based on TTA and of the complete NL TTA in the other electronegative gases (for example CF_4 or SF_6) is rather incorrect.

As an example let's consider self-consistent model of DC discharge positive column8 in pure CF_4. Here like oxygen DC discharge the non-equilibrium ion diffusion takes into account. Owing to high electron affinity to atomic fluorine (F) -3.5 eV (F^- is the main negative ion in given case) only the associative mechanism of detachment is possible:

$$F^- + CF_n \rightarrow e + CF_{n+1} (n = 1, 2, 3). \tag{13}$$

From the experimental study and modelling of the plasma chemical composition, we can conclude that the dominant detaching species should be CF_2 and CF_3 radicals. The concentration of CF is very small, and F-atom is very ineffective as a detaching species.

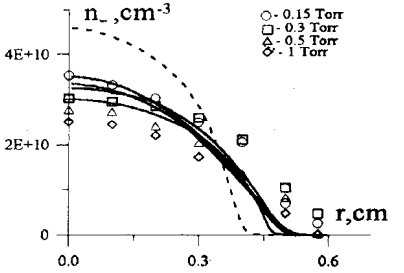

Figure 4. The radial distribution of negative ion density in oxygen DC discharge. Symbols are the experiment data, solid lines are PIC MC simulations. Dashed line shows the same simulation for 0.15 Torr without ion heating (see text).

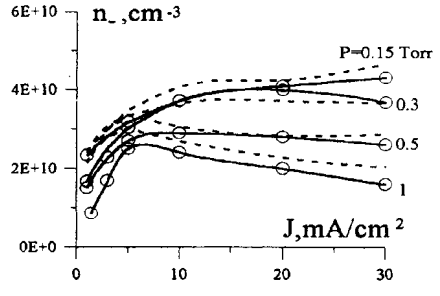

Figure 5. Negative ion concentration on an axis in oxygen DC discharge against the discharge current density. Circles are thee data, solid lines are its fits and dashed lines are PIC MC simulations accounting for the ion heating.

The calculations made for $RN = 10^{16}\,\mathrm{cm}^{-2}$ have shown that we need rather high radical concentrations (about $2 \times 10^{14}\,cm^{-3}$ for $k_{det} = 1 \times 10^{-10}\,cm^3/s$) in order to obtain a good agreement with the experiment. However, so high radical concentrations do not agree with our actinometric measurements of F-atom concentration ($< 2 \times 10^{13}\,cm^{-3}$ for these conditions), since $[CF_2]$ and $[CF_3]$ can be only lower than $[F]$, as can be shown by modelling. Thus the question about the reason for some discrepancy between the experimental data and the results of calculations is not quite clear now, and it needs further study. In the conditions of our experiment, total partial concentration of these radicals is rather small (1%). Therefore, in the most of calculations we did not take into account the processes of detachment.

Calculation results of axial electric fields in positive column are compared with the experimental ones. These results are represented in Figure 6 as a dependence of the reduced field E_z/N on RN parameter. As can be seen from figure, there is a satisfactory agreement between the experimental data and results of calculations in the local approximation for the case of comparatively high pressures ($RN > 10^{16}\,cm^{-2}$). Results of calculations using the non-local approximation have led to practically the same results, so these are not shown in the Figure 6.

Note, that the E_z/N values calculated using the MEE-technique of accounting for the non-locality[7] are very close to those obtained in the local approximation in the whole range of RN studied. For this reason, these data are not shown in Figure 6. However, the radial profiles of the electron concentration and the ionisation rate are somewhat different in these two cases (see below).

For $RN < 10^{16}\,cm^{-2}$, the calculations were carried out using the following discharge models: local and non-local with the usual ion diffusion (i.e. described by the diffusion coefficient determined from the Einstein relation assuming that the ion temperature is equal to the gas one), as well as local and non-local with the non-equilibrium ion diffusion.

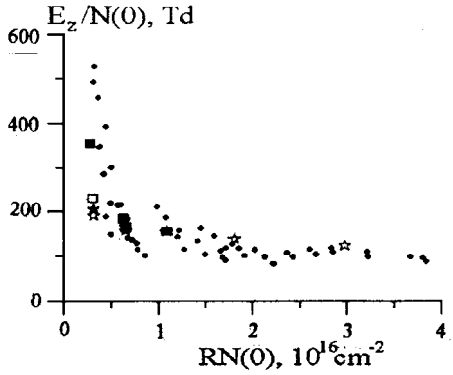

Figure 6. The reduced electric field in CF_4 discharge as a function of RN: experiment[5] (?); calculation via the local model with the usual (*) and non-equilibrium (€) ion diffusion; calculation via PIC MC with usual (+) and non-eqtilhium (■) ion diffusion.

We have also studied the effect of spatial anisotropy of the EDF. Formerly, the anisotropy was usually ignored even in the case of low *RN* (corresponding to high values of E_z/N). This allowed one to use a model based on solution of the Boltzmann equation in the two-term approximation in assumption that the EDF depends on the radial coordinate only through its dependence on the total electron energy (including the potential energy in the radial electric field)[14,15] .

Our results demonstrate that applicability of such model to CF_4 discharge (at low *RN*) is quite doubtful. In the region close to the tube axis due to the axial symmetry the EDF $F(v_r, v_\varphi, v_z)$ depends in fact only on two variables: v_z and $v_p = (v_r^2 + v_\varphi^2)^{1/2}$. This allows us to define a electron distribution function $F(v_p, v_z)$, which is normalised as follows:

$$n_e = \int F(v_p, v_z) v_p dv_p dv_z. \tag{14}$$

Figure.7 shows the function $F(v_p, v_z)$ for the case of low pressure ($p = 0.13 Torr$). The calculations have been made taking into account the non-equilibrium ion diffusion. Figure 7a shows $F(v_p, v_z)$ as a tree-dimensional surface, while in Figure. 7b it is shown as a set of level lines with a constant step. As can be seen from figure 2, the degree of anisotropy is high in all the velocity space. The maximum of the distribution function occurs at $v_p = 0$, but there is a shift along the axial component of about 7×10^7 cms^{-1}. In the region of high electron energies (close to the ionisation potential of CF_4) the function becomes more isotropic. However, even in this region, the ratio of the components of electron energy (for movement along and against the electric field respectively) is about 1/2. If we take into account that the main contribution to the ionisation rate is caused by the electrons with energies close to the ionisation threshold, then we can conclude that nearly all ionisation in CF_4 discharge at low pressure is due to electrons moving in only one direction (against E_z).

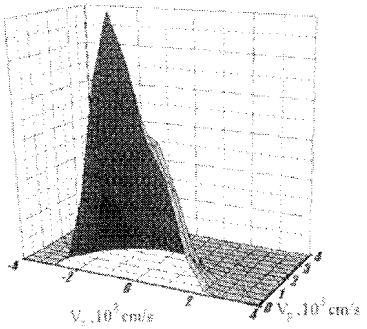

Figure 7a. The EDF in the central region of CF4 discharge as a function of the axial and radial components of the electron velocity via PIC MC.

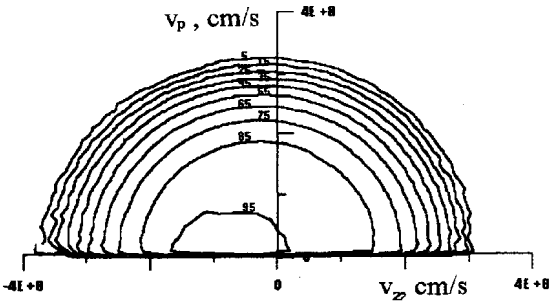

Figure 7b. The same one as in Figure 7a only in the form of level lines with a constant step (the numbers indicate the EDF values as percentages of the EDP maximum).

Let us return to Figure 6 and consider the effect of non-locality and non-equilibrium ion diffusion on the reduced electric field. The influence of both factors is the highest at low *RN* and it rapidly decreases with the increase of *RN*. For $RN = 10^{16}\ cm^{-2}$, all the models (with zero detachment rate) give practically the same results. It is interesting that taking into account the non-locality or the non-equilibrium ion diffusion alone (for the case of low pressure) leads to significantly lower variation of E_z/N than accounting for the both factors simultaneously.

The calculations have shown that non-equilibrium ion diffusion in CF_4 DC discharge like in oxygen DC discharge prevents the formation of a layer of electropositive plasma. Since the detachment processes are negligible in CF_4 plasma, the axial reduced field are very high at low pressures. This leads to more pronounced non-equilibrium ion diffusion effect than in oxygen.

Figure 8 shows the radial profiles of positive and negative ion concentrations (as well as that of radial electric potential φ), which have been calculated using the usual and the non-equilibrium ion diffusion for 0.13 *Torr*. The role of the non-equilibrium diffusion is the strongest in forming the ion radial distributions at low pressure. In this case, there is a widening of the ion radial profiles, as well as the decrease of the concentrations at the tube axis.

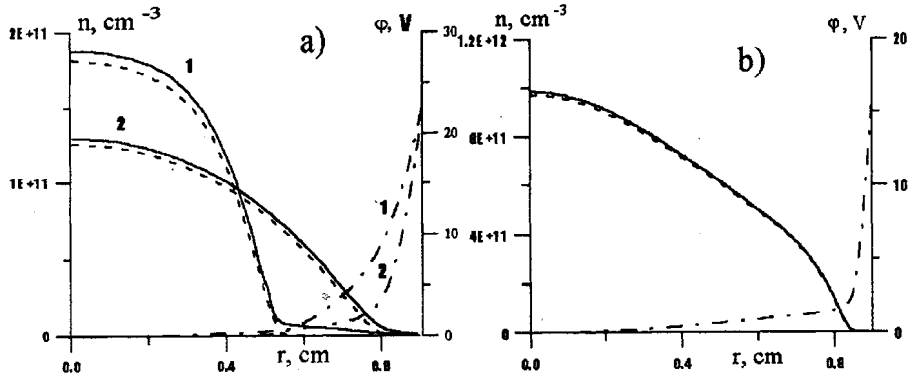

Figure 8. Radial profiles of negative (dashed lines) and positive (solid lines) ions as as well as that of the radial plasma potential in CFDC discharge calculated via PIC MC: 1 - calculation with using the usual ion diffusion, 2 - calculation with using the non-equilibrium ion diffusion. a) P=0.13 Torr, b) P=2.6 Torr.

As notice before we have also performed the applicability analysis of drift diffusion approximation when electron energy spectrum non-locality is introduced through the spatial dependence of mean electron energy (MEE). The radial profiles of electron concentration, mean electron energy and ionisation rate calculated by local, MEE and PIC MC models are shown in Figure 9(a,b,c) respectively at CF_4 pressure of 0.13 *Torr*. The results of MEE and local models are close that leads to the same value of reduced field. However E_z/N in PIC MC model is significantly higher. This corresponds to the twice increase of mean electron energy and, as a consequence, electron density on a discharge axis drops. The difference in ionisation rates is less stressed. In the same time the radial profiles in MEE and PIC MC models are notably more flat than in local model. As it is well seen MEE method incorrectly describes the discharge at low pressures because the electron diffusion loss rate in MEE does not depend on electron energy.

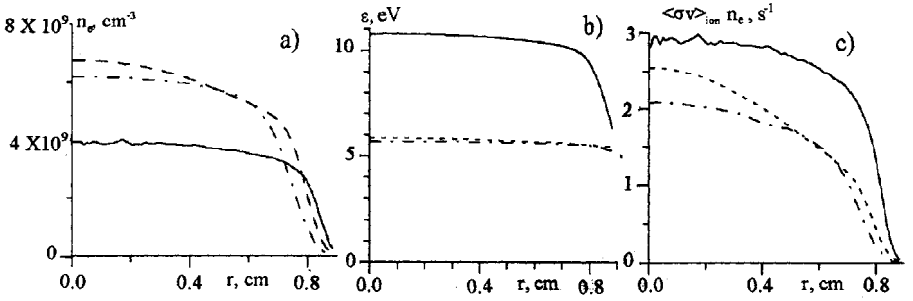

Figure 9. The radial profiles of electron concentration (a), electron mean energy (b), and ionization rate (c) in CF DC discharge at P=0.13 Torr for various models: local feild approximation - dashed lines, MEE - long-short dashed lines, PIC MC - solid lines.

At least it is worth noting again that the developed effective algorithm of modified FPIC MC enables one to carry out a self-consistent simulation of the discharges on personal computers. So the calculation on this self-consistent model requires about 3 hours on the personal computer with PENTIUM processor. The calculations which have been done in the given axial and radial field for oxygen DC discharge required approximately 15 minutes, that is comparable with computer efforts [24], where the normal “nonlocal” approach to electron kinetics description was used.

RF discharge

RF discharges of megahertz frequency range in electropositive (*Ar, He*) and electronegative ($He{:}O_2$, O_2) gases at pressures 3×10^{-2} - 10 *Torr* were the objects of our investigations. The EDF non-local character conditioned by the presence of close electrode sheaths is an essential feature of these discharges. For studying self-consitently the non-locality of EDF we used the following methods:

- solving the spatially non-uniform Boltzmann equation in two term approximation (NL TTA):

$$\frac{\partial F_0\sqrt{\varepsilon}}{\partial t} = -\frac{\partial J_x}{\partial x} - \frac{\partial J_\varepsilon}{\partial \varepsilon} + Q_{el}(F_0) + Q_{in}(F_0) \qquad (15)$$

$$J_x = \varepsilon F_1; \qquad J_\varepsilon = eE(x,t)\varepsilon F_1; \qquad Q_{el} = \frac{2m}{M}\frac{\partial\left(\sigma_m(\varepsilon)\varepsilon^2 F_0\right)}{\partial\varepsilon}\sqrt{\frac{2}{m}}$$

$$F_1 = \frac{1}{3N\sigma_m(\varepsilon)}\left(\frac{\partial F_0}{\partial x} + eE(x,t)\frac{\partial F_\varepsilon}{\partial\varepsilon}\right)\sqrt{\frac{2}{m}} \tag{16}$$

where J_x and J_ε are the fluxes in physical and energy spaces, Q_{el} is the elastic collision integral, Q_{in} - inelastic one;

- mean electron energy method when plasma kinetic coefficients are presented as a function of mean electron energy instead of an electric field strength. (MEE):

$$\frac{\partial n_e < \varepsilon >}{\partial t} = -\frac{\partial}{\partial x}\left(n_e < \varepsilon > \nu_e - \frac{\partial}{\partial x} D_e n_e < \varepsilon >\right) =$$

$$= < \varepsilon > (n_e\nu_e - \frac{\partial}{\partial x} D_e n_e) - \sum_m \nu_m L_m \tag{17}$$

- fast algorithm based on modified Particle In Cell Monte-Carlo technique (FPIC MC) [24].

The main feature of FPIC MC method in RF discharge case is connected with quasi-analytical representation of ambipolar potential dependence on time and space coordinates both in the electrode sheaths and in the central part of the discharge. Besides it was believed that the stationary state of spatial profile of plasma potentials corresponding to the different phases of RF period is a real stationary state of ambipolar potential. The simulation have shown that:

- non-locality effects have a notable influence on RF discharge parameters even at the higher pressure (*He* pd = 10 *Torr cm*)

- the boundary of MEE method applicability is limited by $pd \geq 1$ *Torr cm*. However it should be kept in the mind that the ionisation rate $< \sigma_i v >$ is determined by the "tail" of EDF, whereas $< \varepsilon >$ is determined by the low-energy region. Therefore the ionisation rate presented as a function of the average energy can not reflect the actual relation between these quantities in the discharge.

- the applicability of NL TTA method is limited by a range of $pd \geq 0.3 - 0.5$ *Torr cm.* The restriction of NL TTA applicability at more low pressures-(even at slight anisotropy of EDF) is connected with incorrect description of electron losses on the wall. The correct approach taking into account the electron losses requires to describe EDF in full velocity space that is of course for the frame of TTA.

- the correct simulation of RF discharges at $pd < 0.1$ *Torr cm* under the EDF essential anisotropy or γ - processes conditions is impossible without the strict solution of Boltzmann equation (by using FPIC MC method, for example). More detailed information about these results may be found [12,24,25] ..

Figure 10 (a,b) illustrate the results, obtained in the frame of NL TTA.

We have performed calculations of RF discharge in helium with the following parameters [7] : $\omega/2\pi$ = 10 *MHz*, interelectrode gap d = 1*cm*, j_o = 0.5*mA/cm*², and $N = 3 - 5 \times 10^{17} cm^{-3}$. These calculations revealed that accounting for a spatially non-local electron energy spectrum has a significant effect on the charged particle and electric field profiles in plasma even for pd = 10 *Torr cm.* The study of temporal and

spatial distribution of n_e, $< \sigma_i v > n_e$, $< \varepsilon >$ has revealed that the highest discrepancy in the results is observed in the electrode sheaths where absolute value and gradient of electric field are largest - the calculated values of $< \varepsilon >$ differ by a factor of two, and those of $< \sigma_i v >$ differ by more than an order of magnitude.

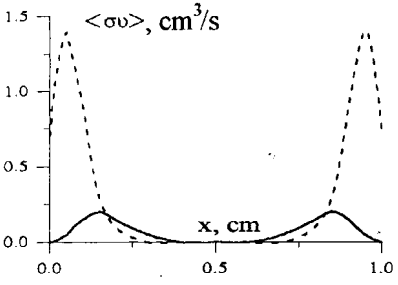

Figure 10a. Averaged over RF period the interelectrode distribution of ionization rate at helium pressure of 10 Torr and j=0.5 mA/cm .²Accounting for the EDF non-locality is shown by solid line.

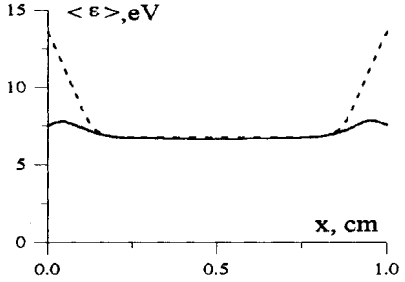

Figure 10b. Averaged over RF period the interelectrode distribution of mean electron energy at the same as in Fig. 10a.

From a practical standpoint it is of more interest to compare the discharge properties averaged over the period of the RF field. Figure 10 shows averaged over a period the distribution of $< \sigma_j v > n_e$ and mean electron energy. The effect of nonlocal spatial behaviour significantly reduces the quantity of $< \sigma_i v > n_e$ near the electrodes and increases it somewhat in the centre of the gap, which is related to the interior of the plasma. The number of particles produced in the volume is found to be different: taking into account the spatial nonlocal behaviour of the distribution reduces it by a factor of two. Figure 11-13 illustrate the results obtained by means of FPIC MC for the experimental conditions [17,24] at the lower pressures 0.03, 0.1 and 1 Torr. Figure II shows the interelectrode distribution of bulk ionisation rate $< \sigma_i v > n_e$ averaged over a RF cycle for this case. This distribution clearly demonstrates the fact that the electron energy spectrum is not spatially local over all the range of the pressure variations. At p = 1 Torr the ionisation rate constant is reached its maximal value in electrode sheath regions, where electric field is high. Nevertheless the ionisation rate is nonlocal that it is well seen in Figure 10. At lowering neutral gas pressure the fast electrons may reach central part of discharge, increasing the ionisation rate in the region with the small electric field strength. It is interesting to note that at low pressure (0.03 Torr) the EDF has an essentially two temperature feature which connected most probably with Ramsauer minimum in elastic cross section.

As it was shown in our calculation [7] under the condition of weak nonlocality the spatial electron-temperature distribution has its maximum near the electrode sheaths, where the electric field is maximum. Therefore we can expect that the maximum of the electron temperature will shift gradually toward the centre of the discharge with the decrease of pressure, whereas the maximum of the electric field will remain inside the sheaths. The experiments [17] show that at p=0.3 Torr, the electron temperature is maximum in the central region of the discharge. However, the electron temperature in the central region of the discharge decreases with the increase of pressure. A two-temperature structure of the EDF is more typical for the electron energy spectrum in given case.

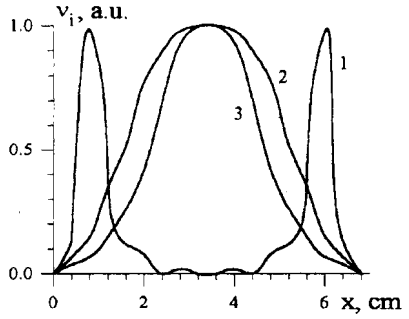

Figure 11. Averaged over RF period the ionization rate in helium RF discharge at the different pressures: 1 - P=1 Torr, 2 - P=0.1 Torr,3 - P=0.03 Torr.[17]

Figure 12 shows the EDFs calculated at the centre of the interelectrode gap. The curves correspond to pressures of p=0.3 Torr and p=0.03 Torr in the experimental conditions [17] and show a good agreement with the experimental data. At p=0.3 Torr, the EDF decreases smoothly in the range ε <10 eV and has a sharp cut-off above the excitation threshold so that the average electron energy is determined by the electrons with energies ε <10 eV. At the same time at p=0.03 Torr the EDF has an unusual bi-Maxwellian form with temperatures $T_1 << T_2$ (where T_1 =1 eV and T_2 =4 eV). Note that at both low and higher pressures the ambipolar potential existing in the plasma forms a potential well for electrons. As a result the low-energy electrons will be trapped in the central region of the interelectrode gap.

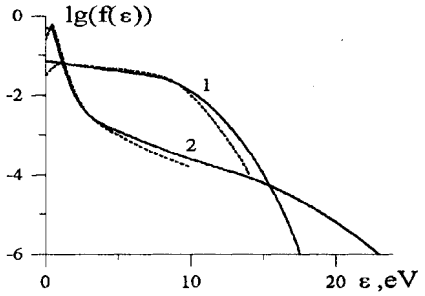

Figure 12. EDF in a center interelectrode gap in argon RF discharge at pressures: 1 - P=0.3 Torr, 2- P=0.03 Torr.Dased lines are the experiment data.[17]

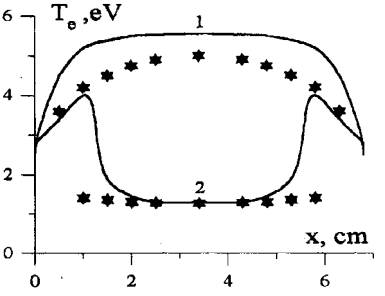

Figure 13. Mean electron temperature distribution in the intereleotrode gap in argon RF discharge at 1 - P=0.3 Torr, 2 - P=0.03 Torr, * - experiment.[17]

For the low-energy electrons the value of the energy mean free path λ_ε is related only to elastic collisions. Consequently in the energy range ε <10 eV for Ar (which is the range where the main energy is stored) the Ramsauer effect can enlarge the slope of the EDF. This fact must be most pronounced at p=0.03 Torr. For the high-energy electrons at pressure 0.3 Torr we have $\lambda_\varepsilon < d$. Therefore the energy losses due to inelastic collisions are sufficiently high. At pressure of 0.03 Torr we have $\lambda_\varepsilon > d$. and, consequently, the fast electrons travel almost without collisions through the entire interelectrode gap. Due to the presence of these electrons in outer regions the temperature in these regions is determined by this fraction of the electrons (T_e =4 eV)

Figure 13 shows the experiment al and calculated spatial distributions of the average electron energy $<\varepsilon>$. One can see that the spatial derivatives of the quantity

$< \varepsilon >$ on the electrode boundary layers are the same for both high (0.3 Torr) and low (0.03 Torr) pressures. Unfortunately at p=0.03 Torr there is no experimental data for the layers thinner than 1 cm whereas the sharp growth in the electron temperature at low pressures should be observed for such layers. Figure 13 shows that there is a more than twofold difference between the calculated values of the average electron energy in the central region of the interelectrode gape and near the electrodes. In an argon plasma, not only the Ramsauer effect but also a stochastic heating can enhance the electron heating in the electrode boundary layers. Therefore it was assumed[17] that the two-temperature form of the EDF is due to both the Ramsauer effect and stochastic heating. However the role of these effects in formation of an unusual EDF shape (which results in the specific temperature dependencies plotted in Figs.13) is not studied in details.

Comparing the experimental and simulation results in oxygen RF discharge we concluded that excitation particle dynamics should be taken into account in self consistent model of this discharge[7]. At low pressures the effects of nondiffusion ion behavior and processes on electrode surfaces may be important as well.

Plasma display panel cell discharge.

Special features of the stationary and quasistationary discharges modelling were analysed in the previous paragraph. It was shown that for certain plasma parameters more simplified methods based on two-term approach for EDF calculations are valid. However, there is a number of non-stationary discharges in non-uniform electric fields, where non-local two-term approach gives only qualitative agreement of the calculated results with experimental data. In such discharges fast electrons from a cathode sheath have a pronounced effect on electrodynamics. Hollow cathode discharges, “open” discharges, PDP cell discharges are the examples of such discharges.

Generally, non-locality effects of the EDF are revealed when the length of electron energy relaxation is comparable with characteristic length of electric field variations. Non-locality effects for discharge gaps of about 1 cm are appeared under low pressure. However non-locality effects may reveal for high pressure discharges with microscopic gaps[26] as in a PDP cell.

Let’s consider for a PDP cell discharge the influence of non-locality effects on discharge electrodynamics and plasma radiation. Model of the discharge consists of two parallel electrodes with the gap of about 100 micrometers. The electrodes are covered with dielectric layers, which in turn are coated with thin MgO layer to reduce discharge breakdown voltage due to high secondary emission coefficient of MgO. The discharge volume is filled with a noble gases mixture[27] . Here we present the calculations for Xe:Ne=90:10 mixture, gas pressure P=560 Torr and initial gap voltage Vs=273.5 V. Self-consistent one-dimensional model of a non-stationary high pressure gas discharge has been developed and used to study the PDP cell operation. In the model the electric field distribution is determined from Poisson equation and electric circuit equation. Simultaneously the continuity equations for electrons, different ions and neutral species of a noble gases mixture are numerically solved. Electron kinetics is simulated using two methods: particle-in-cell Monte Carlo (PIC MC) method and drift-diffusion local approach. Correct electron kinetics simulation requires to solve non-stationary non-uniform Boltzmann equation simultaneously with the solving of other model equations

that is difficult even for a one-dimensional modelling. Since non-locality of EDF mainly deals with cathode beam electrons it would appropriate to use another possibility and to develop the self-consistent hybrid model. Electrons are divided on two groups - fast and slow. Slow electrons as well as ions are described using common drift-diffusion approach [27] :

$$\frac{\partial}{\partial t} n_{eslow} = -\frac{\partial}{\partial z}\Gamma_e + S_e(z,t) \tag{18}$$

$$\frac{\partial}{\partial t} n_i = -\frac{\partial}{\partial z}\Gamma_i + S_i(z,t) \tag{19}$$

$$\Gamma_e = -D_e \frac{\partial}{\partial z} n_{eslow} - n_{eslow}\ \mu_e E \qquad \Gamma_i = -D_i \frac{\partial}{\partial z} n_i + n_i\ \mu_i\ E$$

Here $n_{e\,slow}$ and n_i are the slow electron and i-th ion density, Γ_e and Γ_i are electron and ions fluxes, μ_e, μ_i and D_e, D_i are mobilities and diffusion coefficients of electrons and ions respectively. S_e and S_i are the integral loss-production terms due to different plasma-chemical reactions. For drift-diffusion approach the electron kinetic coefficients are previously determined by solving the Boltzmann equation in two-term approach for all possible ranges of reduced electric fields.

For neutral components the continuity equations are also solved:

$$\frac{\partial}{\partial t} n_k = -\frac{\partial}{\partial z}\Gamma_k + S_k(z,t) \tag{20}$$

where n_k - neutral particle density, $\Gamma_k = -D_k \partial n_k/\partial z$ - neutral particle flux, D_k - diffusion coefficient, $S_k(z,\ t)$- volume input and output of particle k in different plasma chemical reactions taken mainly from [27].

It should be noted that loss-production terms due to different plasma-chemical reactions are calculated using the developed chemical translator that allows one automatically to treat any reaction set.

The continuity equations are added by the Poisson equation for an electric field:

$$dE/dz = 4\pi|q|(n_i - n_{e,slow} - n_{e,fast}) \tag{21}$$

and by the external electric circuit equation:

$$\int_0^d E dz = V_g(t) \tag{22}$$

Dielectric layers are simulated as an additional capacity. The voltage on the gas gap is the difference between external voltage V_s and potential drop V_d on the dielectric layers:

$$V_g(t) = V_s - V_d(t) = V_s - V_d(0) - (\int_0^t j(t)dt)/C_d \tag{23}$$

Standard boundary and initial conditions for charged particles were used.

The behaviour of the fast electrons is determined by solving the non-stationary non-uniform Boltzmann equation. To solve the Boltzmann equation the particle-in-cells Monte-Carlo method adapted for non-stationary discharges is used. Fast electrons can

pass in a slow electron group if two conditions are simultaneously realised $|E(z)| < E_{tr}$, $\varepsilon(z) < \varepsilon_{tr}$. Here $E(z)$ is an electric field in the point z, ε is an electron energy. The threshold electric field - E_{tr} is chosen according to a representation of all electrons in high electric field region as the fast ones. The energy threshold ε_{tr} was close to the lowest threshold of inelastic processes.

Results Temporal and spatial distributions of the calculated electric field, electron density, xenon ion density are shown on Figure 14a-16a (PIC MC method) and Figure 14b-16b (drift-diffusion approach). Calculated time behaviour of such transient discharge can be presented as a follows. At the initial moment the electric field is uniform and is not disturbed by small charge density. Electrons produced in ion collisions with the dielectric layer on the cathode drift to the anode and ionise the gas mixture. The non-compensated charge density is increased and begins to influence on the electric field distribution initially near the anode. The region of quasineutral plasma with low reduced electric field (E/N < 5 Td) is formed near the anode and expanded to the cathode. As a result the discharge positive column and thin cathode sheath, i.e. the region with strong electric field and non-compensated ion density, are formed. The length of cathode sheath (CS) is decreased with time. When the cathode sheath is formed current and charge density in all discharge gap as well as the charge transferred on the dielectric layers are increased. The elevated reduced electric field (~30 Td, see Figure 14) in positive column occurs when discharge current and cathode sheath elec-

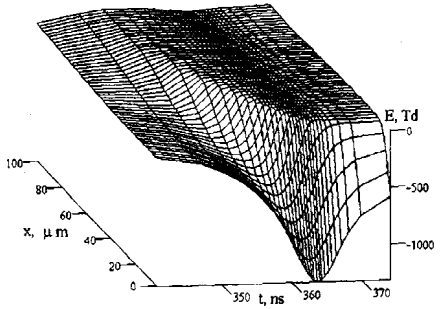

Figure 14a. Time and space variation of electric field. Particle in Cell Monte-Carlo simulation.

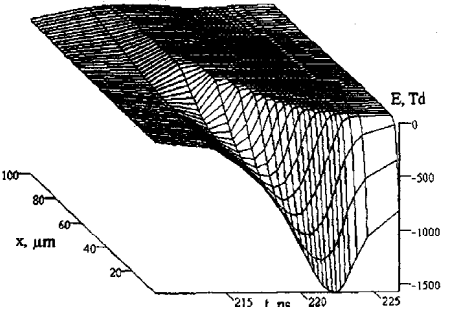

Figure 14b. Time and space variation of electric field Diffusion-drift approach.

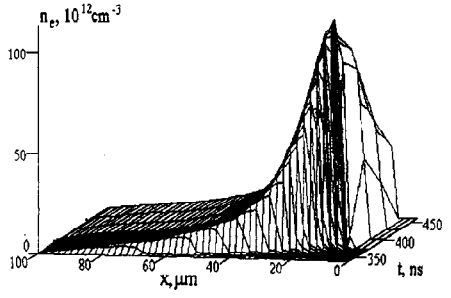

Figure 15a. The same as in Figure 14a only for electron density.

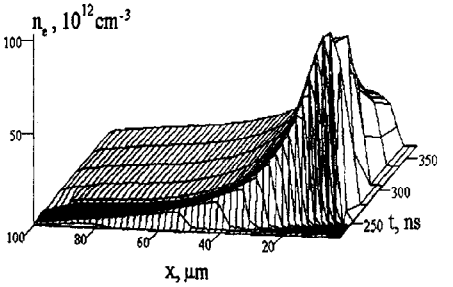

Figure 15b. The same as in Figure 14b only for electron density.

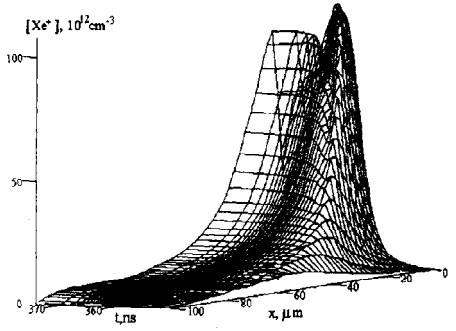

Figure 16a. The same as in Figure 14a only for Xe **ions.**

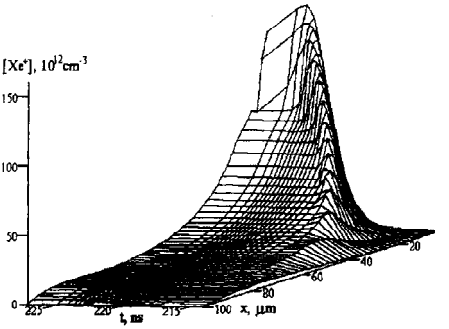

Figure 16b. The same as in Figure 14b only for Xe ions.

tric field reach its maximum. This elevated high field arises because of the necessity to transfer the higher current density. The charges deposited on the dielectric layers reduce the discharge voltage, that lead to plasma decay.

Described discharge dynamics are similar in PIC MC (case ”a”) and drift-diffusion calculations (case ”b”). However there are significant quantitative differences in these cases. The time of cathode sheath formation in PIC MC calculations equals 360 ns that is 1.64 times larger than that in local field calculations as it is well seen in Figure 14. The length of the cathode sheath at the moment of maximal current is 13 and 5 μm in case ”a” and ”b” respectively. The differences in discharge dynamics are associated with the several reasons. First of all the excitation and ionisation rate coefficients calculated by solving the Boltzmann equation in two-term approach (case ”b”) and in PIC MC approach (case ”a”) are substantially different even in low electric fields X0-100 Td. The differences become else more remarkable in the strong field ˜1000 Td, where EDF is substantially anisotropic. Besides EDF is non-local in and near the cathode sheath that is not taken into account in case ”b”.

As it is seen in Figure 15 the electron densities in the positive column where the non-local effects are not important, are slightly distinct (6 $x10^{12}$ and 7 x 10^{12} cm^{-3} at the moment of maximal current) because of different time dependence of current density. Electron densities in the cathode sheath at the moment of maximal current are close for cases ”a” and ”b” that is not obvious and is a result of mutual compensation of two effects taken into account in PIC MC calculations. EDF is substantially anisotropic in high cathode sheath field. Accounting for the anisotropy results in the remarkable decrease of the ionisation rate and as a consequence the maximal electron density. On the other hand there is a notable ionisation due to fast electrons from the CS just in the region of maximal electron density near the boundary of the CS. These effects are responsible for the same level of the electron density maximums despite on the lower ionisation rate. In the local field approach the ionisation occurs in the CS. Beyond the CS the reduced electric field changes a sign and its positive value does not exceed 5 Td in the wide region of plasma -from $x = 5\ \mu m$ up to $x = 42\ \mu m$, x is the distance from the dielectric layer covering the cathode. It should be noted that in PIC MC calculations the positive electric field is higher ˜10 Td and the region of positive field

is extended from $x = 13\ \mu m$ up to $x = 45\ \mu m$. The increase of electric field is due to the necessity to compensate the negative charge transferred by fast electrons up to $x = 30\ \mu m$, see Figure 17. Just the charge transfer results in the formation of negative glow in the stationary discharges. Note that the local approach does not allow one to obtain the negative glow region of stationary discharge.

The non-locality of electron energy spectrum is revealed in the ion density profiles. Second maximum in the *Xe* ion density profile (Figure 16a) farther away from the cathode is just determined by ionisation due to fast electrons from the CS. In the case "b" (see Figure 16b) there is one maximum with it being 1.5 times greater than the first maximum in case "a" and being shifted closer to the cathode. Similar dependencies are observed for neon ion concentration which is one order of magnitude lower than xenon ion density.

As it is seen, time-space behaviour of EDF is of primary importance in the discharge kinetics. The example of EDF is presented on Figure 17: the time dependence of fast electron energy spectrum at the point $x = 10\ \mu m$ in Figure 17a and the space profile of EDF at the moment of maximal current in Figure 17b. The formation of electron quasibeam, i.e. fast electrons which were not subject to inelastic collisions, is clearly seen in Figure 17a. Unlike true beam, its velocity distribution is not unidirectional. Substantial degradation of the beam energy occurs to the moment of maximal electric field (t=361 ns). Despite of it there are electrons with the energy up to 150 eV. Hereafter the substantial depletion of high electron energy spectrum occurs owing to decreasing the electric field. Space degradation of electron beam takes place at the length approximately equal to the CS length, as it is seen in Figure 17b. At the point of $x = 14\ \mu m$ a substantial number of electrons has else the energy higher than *Xe* ionisation potential. It is well seen in Figure 17b that the main part of fast electrons penetrates into the region of positive electric field. On the contrary, for the DDA calculation a mean electron energy in this region does not exceed 4 eV and consequently the ionisation is practically absent.

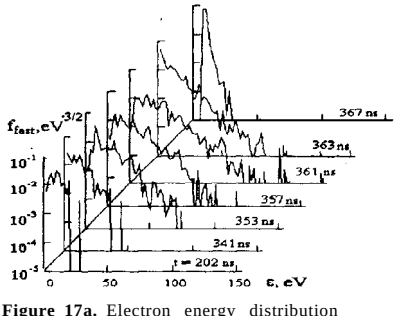

Figure 17a. Electron energy distribution function at a distance of 10μm from cathode at different time moments.

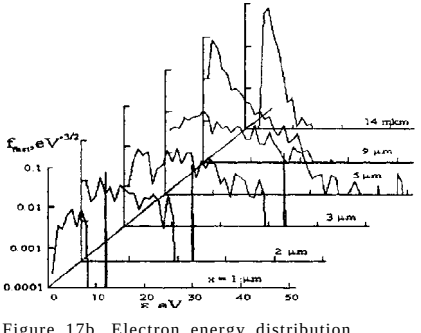

Figure 17b. Electron energy distribution function at different distances from cathode at moment of maximum electric field (t = 361ns).

Time-space distributions of densities of $Xe^*(^3P_1)$ and $Xe^*(^3P_2)$ atoms which are responsible for VUV plasma radiation (resonant emission of Xe^* $(^3P_1)$ atoms and xenon

dimer $Xe_2^*(^3\Sigma_u^+)$) have two maximums, One is located near the cathode, second is located in the quasineutral plasma region. For PIC MC calculations these maximums are farther away from the cathode than for DDA calculations. The concentrations of excited xenon near the cathode are higher for PIC MC calculation (for example $Xe^*(^3P_1) = 2.8\ 10^{14}\ cm^{-3}$ and $Xe^*(^3P_1) = 7.7\ 10^{13}\ cm^{-3}$ for case "a" and "b" respectively). The excited xenon atom concentrations in the quasineutral plasma region are similar for both calculations.

Observed peculiarities can be understood considering the spatial distribution of input power transferred into different inelastic processes and ions. The fraction of full input energy (~90 erg/cm²) transferred into electrons is 37% for case "a" and 44% for case "b". Distribution of integral input energy fractions for the different components:

$$W_i = \iint\limits_{x,t} n_e v_i \varepsilon_i dx dt, \tag{24}$$

are summarised in Table 1.

Table 1.

	Ne^+	Xe^+	$Xe^*(^3P_2)$	$Xe^*(^3P_1)$	Xe^{**}	ion energy
local	11.1%	21%	1.8%	1.1%	7.7%	56%
PIC MIC	1.1%	15%	2.9%	1.8%	14%	63%

The energy redistribution shows a further important difference of two approaches. The energy that goes to *Xe* electronic excitations is higher in PIC MC calculations due to decreasing (in two times) the energy transferred into ionisation of *Xe* and *Ne*. This energy redistribution deals with the more lower effective mean energy of electrons in PIC MC calculations because of the lowered effective electric field with is due to the more longer cathode sheath. Moreover the local approach significantly overestimates mean electron energy in the cathode sheath.

The influence of EDF non-locality effects on the integral plasma characteristics, namely, on radiation power in resonance line (147 *nm*) and dimer band (173 *nm*) is seen in Figure 18. Overall discharge radiation power per unit of electrode surface is equal to:

$$Q_{UV,k}(t) = \int\limits_0^d nk(z,t) nkek dz, \tag{25}$$

Here *k* is the number of the line. As it seen in Figure 18 and mentioned above the radiation power is increased when non-local EDF effect is taken into account.

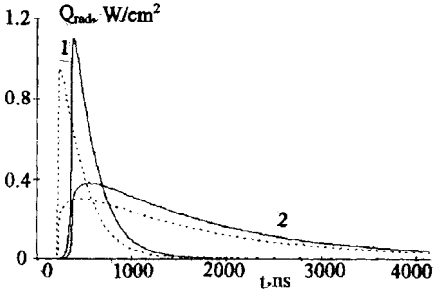

Figure 18. Time dependence of radiation power.
1 - resonance line (147 nm), 2 - dimer line(173 nm).
solid line - PIC MC simulation,
dushed line - diffusion-drift approach.

To the best knowledge of authors it is the first time when the effects of non-locality and anisotropy of EDF on properties of radiative plasma in non-stationary high pressure discharge are analysed. Full self-consistent model of electrodynamics, plasma and neutral kinetics has been developed. Electron kinetics is simulated by solving the Boltzmann equation by PIC MC method and taking into account the electron energy spectrum anisotropy, non-uniform and non-stationary electric field and charge densities distributions. It has been shown that electron energy spectrum is substantially non-local and anisotropic nearby the cathode sheath region. Substantial anisotropy of EDF decreases the ionisation and excitation rates and increases characteristic electrodynamical time of the discharge development. EDF non-locality influences on the redistribution of input energy between electron and ion components and between the different inelastic processes. Considered effects lead to increased plasma radiation in PIC MC calculations than in drift-diffusion approach calculations.

Conclusion

In this report effects of EDF non-locality in stationary and non-stationary discharges are studied using kinetic approaches. Applicability of two-term approach in RF discharges, in positive column of a DC discharge and in plasma display panel (PDP) cell discharge is analyzed. Effective algorithm of self-consistent modeling of stationary and non-stationary discharges is proposed. The necessity of adequate description of negative ion kinetics and transport is demonstrated in the course of the experimental and theoretical investigations of discharges in electronegative gases.

REFERENCES

1. Kono A., Haverlag M., Kroesen G.M.W., de Hoog F.J., 1991, Temporal behaviour of the electron and negative ion densities in pulsed radio-frequency CF_4 plasma, *J. Appl. Phys.* 70:2939.
2. Haverlag M., Kono A., Passchier D., Kroesen G.M.W., Goedheer W.J.,de Hoog F.J.,1991, Measurments of negative ion densities in 13.56-Mhz rf plasmas of CF_4,C_2F_6,CHF_3 and C_3F_8 using microwave resonance photodetachment effects, *J. Appl. Phys.*70:3472.
3. Volynets V.N., Lykyanova A.V., Rakhimov A.T., Slovetsky D.I., Suetin NV., 1993, Experimental and theoretical study of CF_4 DC glow discharge positive column, *J. Phys. D: Appl. Phys..26:647.*
4. Gogolides E., Stathakopoulos M., and Boudouvis A., 1994, Modelling of radio frequency plasmas in tetrafluoromethane(CF4): the gas phase physics and the role of negative ion detachment, *J. Phys. D: Appl. Phys.*27:1878

5. Franklin R.N., Daniels P.G., and Snell J., 1993, Characteristics of electric discharges in the halogens: the recombination-dominated positive column, *J. Phys. D: Appl. Phys.* 26:1638.
6. Franklin R.N., and Snell J., 1994, The recombination-dominated positive column with finite ion temperature, *J.Phys. D: Appl. Phys.* 27: 2102.
7. Feoktistov V.A., Lopaev D.V., Klopovsky K.S., Popov A.M., Popovicheva A.T., Rakhimov A.T., Rakhimova T.V., 1993, Low pressure RF discharge in electronegative gases for plasma processing, *J. of Nucl. Mater.* 200:309.
8. Feoktistov V.A., Ivanov V.V, Popov A.M., Rakhimov A.T., Rakhimova T.V., Slovetsky and Volynets V.N., 1997, The influence of anisotropy and non-locality of the electron distribution function as well as non-equlibrium ion diffusion on the electrodynamics of CF_4 DC discharge at low pressure, *J. Phys. D:Appl. Phys.* 30: 423.
9. Feoktistov V.A., Popov A.M., Popovicheva O.B., Rakhimov A.T., Rakhimova T.V., Volkova E.A., 1991, RF discharge modelling considering time dependence and spatial nonlocality of the electron energy spectrum, *IEEE Trans. on Plasma Sci.* 19:163.
10. Kushner M. J., 1983, Monte-Carlo simulation of electron properties in RF discharges, *J. Appl Phys.* 54:4958.
11. Boswell R.W., Morey I.J., 1989, Self-consistent simulation of a parallel-plate RF discharge, *Appl. Phys. Lett.* 52:21.
12. Ivanov V.V., Popov A.M., Rakhimova T.V. 1995 Spartial structure of microwave discharge in low-pressure argon, *Plasma Phys. Rep.* 21:516.
13. Ivanov V.V., Klopovskii K.S., Lopaev D.V., Muratov E.A., Rakhimov A.T., Rakhimova T.V., 1996, Experimental investigation of nonlocality effects in the electron energy spectrum in an electronegative gas, *JETF Lett.* 68: 537.
14. Bernstein I.B., Holstein T., 1954, Electron energy distribution in stationary discharge, *Phys. Rev.* 94:1475.
15. Tsendin L.D., 1974, Electron energy distribution in current-carrying plasma with transverse inhomogenity, *Sov. Phys.- JETF.* 39:805.
16. Kortshagen U., Parker G.J., Lawler J.E., 1996, Comparision of Monte Carlo simulations and nonlocal calculations of the electron distribution function in a positive coloumn plasma, *Phys. Rev. E* 54:6746.
17. Godyak V.A., Piejak R.B., Alexandrovich B.M. 1992, Measurements of electron energy distribution function in low pressure RF discharges, *Plasma Sources Sci. Technol.* 1:36.
18. Kortshagen U., 1994, Experimental evidence on the nonlocality of the electron distribution function, *Phys. Rev. E.* 49:4369.
19. McDaniel E.W., Mason E.A., The mobility and Diffusion of Ions in Gases (New York: J. Wiley) 1973.22. McDaniel E.W., Mason E.A., The mobility and Diffusion of Ions in Gases (New York: J. Wiley) 1973.
20. Lopaev D.V., Rulev G.B., 1996, Spatial distribution of negative ions in DC discharge plasma in pure O_2 in *"ESCAMPIG 96, Abstracts of ivated lectures and contributed papers. Eropphysics conference abstracts," European Physical Society,* 20E(A):79.
21. Arnold D.W., Xu C., Kim E.H., Neumark D.M., 1994, Study of low-laying electron states of ozone by anion photospectroscopy of O_3^- *, J. Chem. Phys.,* 101(2): 912.
22. Tsuneda T., Nakano H., Hirao K., 1995, Study of low-laying electron states of ozone by multyreferences Mller-Plesset pertrubation method, J. Chem. Phys., 103 (15):6520.
23. Peterson K.A., Mayrhofer R.C., Woods R.C., 1990, The ptential energy and dipole moment surface of NF_2 and O_3^- by complete active space self-consistent field, *J. Chem. Phys.,* 93 (7):5020.
24. Ivanov V.V., Popov A.M., Rakhimova T.V., 1995, New approach to the particle-in-cell method for simulation of low-pressure RF discharge, *Plasma Phys. Rep.* 21:692.
25. Popov A.M.Rakhimov A.T., T.V. Rakhimova, 1993, Self-consistent models of high-frequency low-pressure discharges in electropositive and electronegative gases, *Plasma Phys. Rep.* 19:651.
26. L. F. Weber :Flat Panel Displays and CRT's, 1985, Van Rostand Reinhold, New York.
27. J. Meunier, Ph. Belenguer and J. P. Boeuf, 1995, Numerical model of an AC plasma display panel cell in neon-xenon mixtures, *J. Appl. Phys.* 78:731.

PARTICLE SIMULATION METHODS FOR GLOW DISCHARGES: PAST, PRESENT AND FUTURE, WITH APPLICATIONS

Charles K. Birdsall,[1] Emi Kawamura,[1] Vahid Vahedi[2]

[1]EECS Dept. Cory Hall
University of California
Berkeley, CA
[2]Lam Research Corp.
4650 Cushing Parkway
Fremont, CA

1. INTRODUCTION

Particle simulations of plasmas have been in use since the 1950's for many applications, but only recently for bounded collisional plasmas, such as glow discharges, where neutral particles outnumber charged particles by 2 to 4 orders of magnitude. This paper will review some of the models and techniques used over the past four decades, leading up to our current capability of simulating discharges. Our path will follow the development of first principles, self-consistent many-particle bounded plasma modeling and simulations, mostly particle-in-cell (PIC), with the addition of Monte-Carlo collisions (electrons and ions with neutrals), called PIC-MCC.

Plasma simulations using fluid codes (solving several moments of the Boltzmann equation) tend to run much faster than particle codes, but supply less detail and some times incomplete physics (e.g., ignoring stochastic electron heating). Kinetic codes (solving for the full distribution function from the Boltzmann equation, plus fields from Poisson's equation) tend to run slower, perhaps similar to particle code speeds. (These answers differ among experts and whether in 1, 2, or 3 dimensions.)

It is desirable to keep the first-principle, self-consistent approach in PIC-MCC and to incorporate speed-up mechanisms into PIC-MCC. A very real objective is to make PIC-MCC codes attractive and readily useful by experimentalists who are designing new plasma processing equipment using RF and microwave drives. In order to reach this objective, run times must be on the same order as the time to make experimental changes (time to "cut metal"). We will take such times to be less than a day, perhaps as short as one hour, much shorter than now achieved by one if not two factors of 10.

Our paper will present old and new and combinations of attempts being made to make PIC-MCC codes run faster, that is, to reach equilibrium sooner, on single processor machines. (We are also working on paralleling our codes.) We report on speed gains between 6 and 30 times, using implicit integrations, subcycling, and light

Electron Kinetics and Application of Glow Discharges
Edited by U. Kortshagen and L. D. Tsendin, Plenum Press, New York, 1998

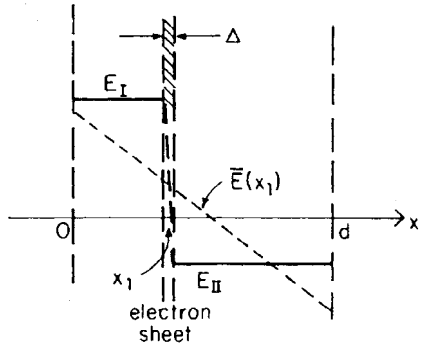

Figure 1. An early electron diode model, with one electron sheet between grounded electrodes, showing the field acting on the sheet as it traverses the diode, as obtained from Gauss' Law. The fields acting on many sheets maybe obtained by superposition (no Poisson solver is needed), allowing one to write the equation of motion for each particle directly. Applied fields may be added. From Birdsall and Bridges (1966).[3]

ions, in combination, on argon and oxygen RF discharges. This is a progress report, with these initial successes, and not a final report.

2. PAST HISTORY, ROUGHLY 1940'S TO 1980

This brief section will be a review of representative contributions in this period, noting particular pre-cursors to PIC and MCC and bounded modeling. More complete reviews may be found in the texts by Roger Hackney and James Eastwood (1981),[11] Charles Birdsall and A. Bruce Langdon (1985)[5] and Toshi Tajima (1989).[14] A more recent review is by Birdsall (1991).[2]

Figure 1 shows an early bounded one-dimensional model, with thin sheet electrons. The force on the sheet is easily obtained from Gauss' Law; and readily extended to multiple sheets. P.K. Tien and J. Moshman (1956)[15] did a $1d1v$ particle simulation, with a similar model, adding a DC bias (to make an electron gun), injecting electrons with a half Maxwellian velocity distribution from the left plane, in order to obtain the high frequency noise current.

Periodic models may be found in the Birdsall and Langdon text,[5] due mostly to John M. Dawson (1962),[7] who made a major contribution by showing that most plasma kinetics may be obtained, in one dimension, with as few as 5 to 10 particles (sheets) in a Debye length. Owen Eldridge and Marc Feix (1962)[8] made complementary contributions. Periodic models also used Gauss' Law to obtain the electric fields to use in the particle equations of motion.

Figure 2 shows a two-dimensional gridded model and flow chart, initiated in the early 1960's, with numerous contributions from the group with Oscar Buneman at Stanford University. The mathematical grid in the plasma region is used to facilitate obtaining the fields from the charge density. Roger Hackney (1965)[10] provided a fast method of solution for Poisson's equation with a grid in $2d$, another essential tool.

Figure 3 shows the flow chart for simulation systems in $1d$, $2d$, and $3d$ using particles and a grid.

The name "particle-in-cell," PIC, originated with Francis Harlow at Los Alamos, in developing fluid codes (1964).[9] Birdsall and Fuss used the name "cloud-in-cell," CIC independently (1969),[4] in order to emphasize the tenuous nature of the finite-sized particles implied by particle weighting to the grid. Langdon provided most of the theory

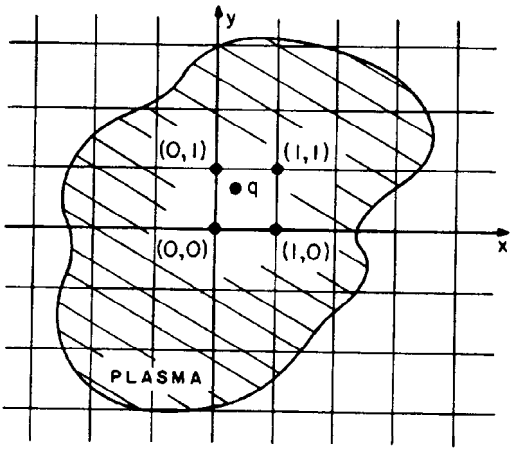

Figure 2. A mathematical grid is set into the plasma region in order to measure the charge and current densities from which the fields will be obtained on the grid. A typical charge q will be "weighted" to the nearby grid nodes, using various splines. From Birdsall and Langdon (1985).[5]

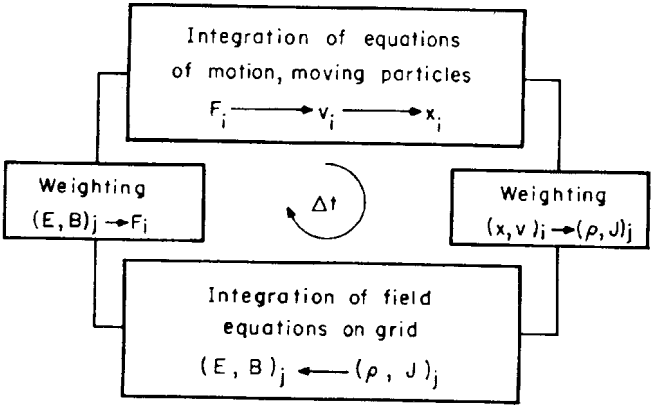

Figure 3. Flow chart for one Δt of the particle-grid method, or PIG. From Birdsall and Langdon (1985).[5]

of finite-size plasma charged particles, with and without a grid, beginning about 1968, well summarized in our text. Richard Morse and Clair Neilson at Los Alamos extended PIC to fully electromagnetic fields (1971).[13]

In the 1960's, 1970's and 1980's there were many publications using PIC codes, for fusion plasmas and many other applications, with a considerable number of refinements. PIC simulation publications were and are mixed right in with theory and experimental articles, indicating strong acceptance of such simulations (and other kinds of simulations as well) by the plasma community.

The major focus on simulation publications continued to focus on the behavior of the plasma bulk or core, ignoring the edges, following the example of nearly all plasma textbooks.

3. RECENT PAST, ROUGHLY 1980 ON

As noted just above, the plasma edge and truly bounded plasmas were relatively neglected up until the 1980's or so. What was going on at the plasma edge was treated as "kitchen physics": not very scientific — perhaps, more realistically, as not readily amenable to scientific understanding, or standard plasma theory techniques. Emission, absorption, sheaths, pre-sheaths, cathodes, anodes, non-Maxwellian velocities, regions that were quite non-neutral, with large fields and potentials etc, were anathema to the plasma community. About 1980, several groups reasoned: All the more reason to start exploring the plasma edge occurred around the world, a challenge which now has grown to a large plasma industry (literally, as 40% of semiconductor manufacturing steps involve plasmas — at the edge!).

Our first real foray into such was a 1983 seminar to construct a bounded plasma model, with real walls (emitting, absorbing), full sheath, external *R, L, C* circuit elements and *V, I* sources. The result is recorded in William S. Lawson (1989),[12] who wrote our PDW1 code in 1983, the predecessor of our Plasma Device codes.

Figure 4 shows a planar 1*d* bounded plasma device, with an external driving circuit, as used in our Plasma Device codes, PDx1 (x = p, planar; c, cylindrical; s, spherical), which are now in world-wide use and free: (see **http://ptsg.eecs.berkeley.edu)** . These are 1*d*3*v*, with many input files for different models, and their own graphics (i.e., self-contained, ready to run).

Figure 5 shows the flow chart for bounded models, with a box for processing particles lost or injected at the boundaries (or possibly in the volume). Another box is added to process elastic and inelastic collisions between charged particles and background neutral gas particles, as needed for discharges.

The PIC Monte-Carlo collision box was presented by Birdsall (1991),[2] as developed in Berkeley (beginning about 1988), by his post-doc, Ian Morey (who had begun collision work with Prof. Rod Boswell at the Australian National Univ., Canberra), M. Surendra (a student of Prof. David Graves, Chem. Engr. Berkeley) and Birdsall's students, Vahid Vahedi, John Verboncoeur, and M. Virginia Alves. A detailed key reference for PIC-MCC is by V. Vahedi and M. Surendra (1995).[19]

The essential difference between the MCC used here and prior Monte-Carlo collision methods (which have random mean free times or mean free paths), is that PIC moves particles only every Δt. The main steps are to use a constant maximum collision frequency ν_{max} (which includes the possibility of a null collision) to obtain the fraction of particles to be collided in a time step Δt, then to randomly divide the colliding charged particles among the different collisions which may occur, then to invert the total and differential cross sections in order to update the speeds and directions of the

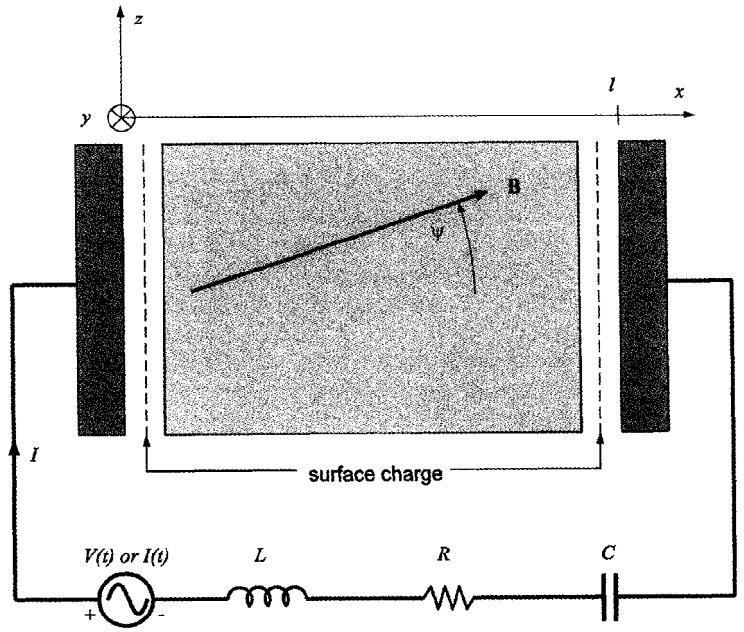

Figure 4. Model for the plasma device code PDP1, showing all of the elements of a whole device, with the plasma between the electrodes and the external driving circuit outside, all solved simultaneously. From Verboncoeur et al. (1993).[20]

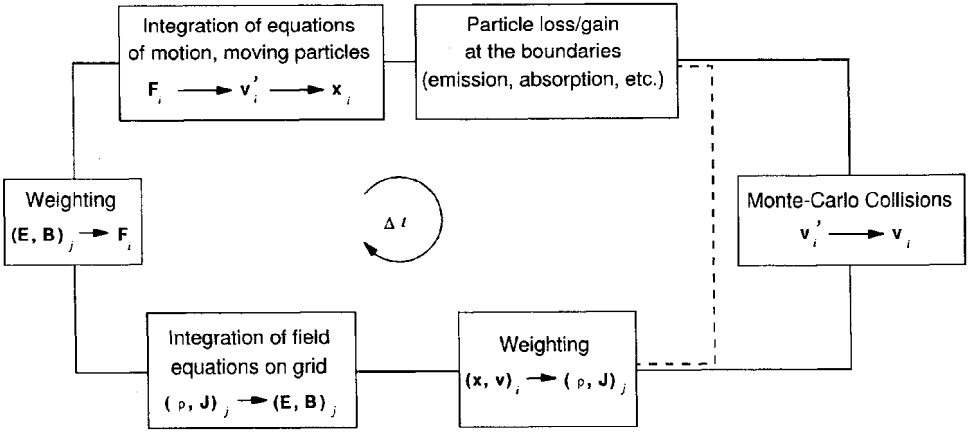

Figure 5. Flow chart for bounded and collisional models. The new "box" beyond that in Figure 3, at the top, is to handle the bookkeeping for particles lost or gained at the walls, and sometimes in the volume. The new "box" at the right is the Monte-Carlo collision processor. From Vahedi and Surendra (1995).[19]

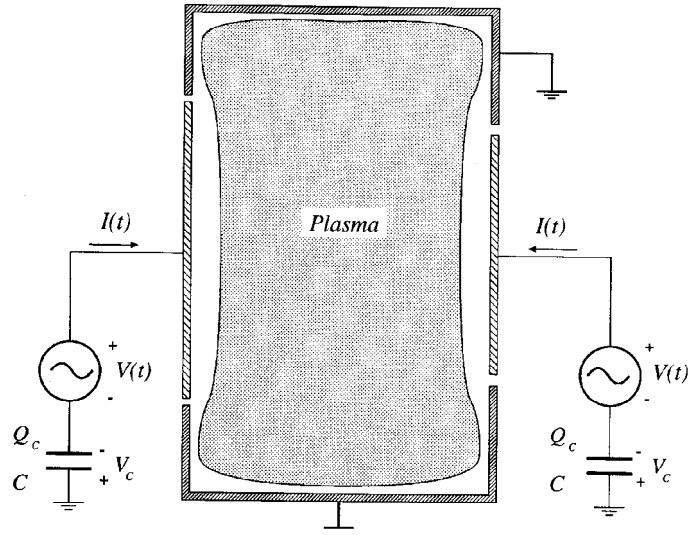

Figure 6. A two dimensional system to be simulated. The top and bottom boundaries are grounded. The left and right hand boundaries may be driven separately, with external circuits having either a voltage source and a (blocking) capacitor or a current source. From Vahedi and DiPeso (1997).[17]

particles. PIC-MCC works efficiently for low pressures and small volumes, where the fraction of particles colliding each Δt is relatively small.

4. VERY RECENT PIC-MCC RESULTS, 1995 ON

Figure 6 shows a two-dimensional model simulated by V. Vahedi and Greg DiPeso (1997).[17] The left electrode might be a silicon wafer, biased, say, by a 13.56 MHz source, and the right electrode might be driven at a higher frequency, as the source of the plasma.

Figure 7 shows another 2*d*3*v* model, this time with an internal grounded grid, from V. Vahedi, J. Norman Bardsley, and G. DiPeso (1995).[16] It was found that the internal grid makes the RF discharge more asymmetric (i.e., has a larger ratio of grounded area to driven area) by providing more grounded surface area for the plasma. This greater asymmetry results in:

(a) lower plasma to ground potential drop;

(b) reduced ion bombarding energy on the grid (and other grounded surfaces);

(c) reduced sputtering from the grid;

(d) larger target sheath width at a fixed pressure, which reduces the ion bombarding energy at the target to compensate for the increased bias voltage.

These results show the power of 2*d*3*v* simulations to complement lab experiments in examining new configurations and exploring (optimizing) over many parameters.

5. COMPARISON OF COMPUTING SPEEDS

Fluid codes work with densities n, velocities v, and temperatures T, as functions of x, y, z, and t for each species, as moments of the Boltzmann equation. A Poisson solver is used for the potential, or the Maxwell set for the fields, with either set solved

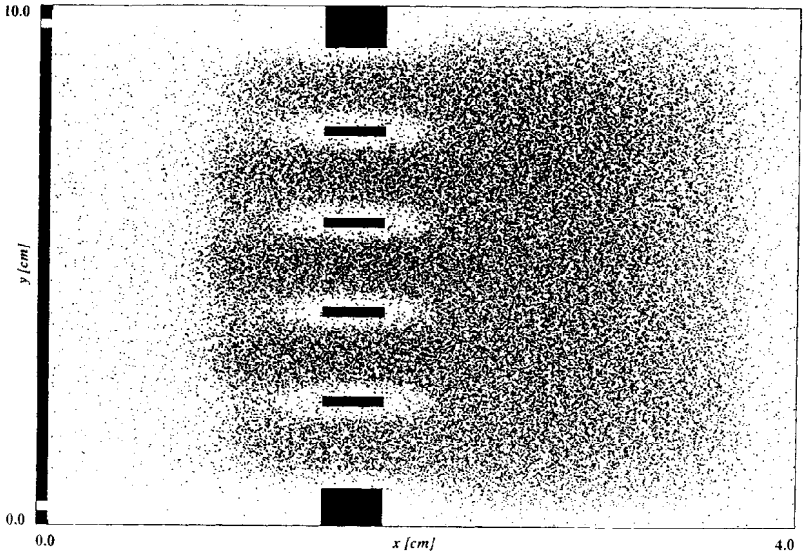

Figure 7. Ions in a two dimensional system which has an internal grid tied to the grounded top-right-bottom electrodes, with the left hand electrode (target for the ions) driven by the RF source. From Vahedi, Bardsley and DiPeso (1995).[16]

on a mathematical mesh overlaying the plasma region. The velocity distributions are drifting Maxwellians. There is a long history of solving fluid equations. Such are usually the fastest codes available.

(An exception in speed is the use of global codes, where all of the variables are spatially averaged, sort of "zero-dimensional," essentially using a set of rate equations. Such may run very fast, and, if available, should be run in advance of all simulations.)

Kinetic codes work with the distribution functions, $f(x, y, z, v_x, v_y, v_z, t)$, for each species, solving the Boltzmann equation, also along with an appropriate potential or field solver. As the number of phase space dimensions increases from $2(x, v_x)$ to the full 6, the difficulty increases and the speed decreases.

Particle codes have already been described earlier.[2,19] These follow individual particles in their own and applied electric and magnetic fields, from first principles, self-consistently, with the collisions done by the MCC null collision method described above. The potentials or fields are obtained on a mesh, much as in the methods above, with appropriate weighting of the particles to the mesh (to obtain ρ and J) and weighting of the (new) fields back to each particle, then advancing the particles. Each computer particle represents, say, a million to a billion real electrons or ions. The simulation must run with a sufficient number of particles in order to minimize the discrete particle noise, and other unwanted effects. There are many $1d3v$ codes in wide use, for many applications. There are quite a few $2d3v$ codes around and not a small number of full $3d3v$ codes. Going from $1d$ to $2d$ involves mostly the field solver, with some thought; going from $2d$ to $3d$ is straightforward. Many species may be used

In their, say, textbook form, usually explicit, PIC codes run appreciably slower than do fluid codes but possibly close to the speed of kinetic codes. Hence, it is most desirable to seek and apply various ways of speeding up PIC and PIC-MCC codes, numerical and physical, in order to compete with other codes. The object is to make first-principles, self-consistent codes run to equilibrium in under one hour, competing with the ability to make changes in the lab. What follows is application of several

known acceleration methods, plus one newer one.

6. METHODS USABLE TO SPEED UP PIC-MCC CODES; APPLICATION TO ACCELERATING RF DISCHARGES TOWARD EQUILIBRIUM

6.1. Motivation

The current "rule-of thumb" on simulation timing is that one needs to run about 1000 RF (or microwave) cycles in PIC-MCC to reach equilibrium, which may be a million time steps, with from 10,000 particles to 10 or 100 times as many. Current explicit PIC-MCC codes, running on single processor moderately fast workstations (e.g., 233 or 500 MHz), do not begin to complete such a run in one hour. (All of our runs, reported in the following, were made on 233 MHz workstations.)

6.2. Base Model: Explicit Integration

Numerous methods for speeding up particle (PIC and PIC-MCC) codes have been published in detail and widely applied, but usually one at a time. See, for example, Table I in Vahedi et al. paper on capacitive RF discharges.[18] We will apply several speed-up methods together to RF discharge simulations. Our base method for comparison is **explicit** coding, with no speed up applied, hence having a speed Gain = 1. Gain measures the gain in speed of a simulation; it is defined as: (sped up run time)/(base run time); a number ≥ 1.

6.3. Implicit, $\Delta t_{\mathbf{implicit}} >> \Delta t_{\mathbf{base}}$

A favorite acceleration comes from implicit methods, which allow much larger time steps, yet maintain stability and accuracy, due to attenuating fields at high frequencies and (usually) at short wavelengths. For these implicit methods, please see the texts by Birdsall and Langdon (1985)[5] (Chap. 9) and by Brackbill and Cohen (1985)[1] (Chaps. 9 and 11); the so-called direct implicit method is used here.

6.4. Subcycling, $\Delta t_i >> \Delta t_e$

With the short time steps used in order to satisfy stability and accuracy conditions for the electrons, the far heavier ions move hardly at all in one electron time step At,. Hence, the ions might be moved less frequently, every kth electron step ($\Delta t_i = k\Delta t_e$), where k may be 10 to 100, depending on the ion mass. Such is called electron subcycling. See the texts Birdsall and Langdon (1985)[5] (Chap. 9) and Brackbill and Cohen (1985)[1] (Chap. 10) for the details.

6.5. Use of Many Processors in Parallel

We are currently in the process of converting our Plasma Device PIC-MCC simulation codes to use on a paralleled network of workstations ("NOW"). With N such in parallel, we might approach a maximum speed-up of N times.

6.6. Use of Much Lighter Ions Initially, $M_{\mathbf{light}} << M_{\mathbf{real}}$, then Reversion to $M_{\mathbf{real}}$

Early on we had decided to try altering the physics (mass, charge, q/m, etc.) such that equilibrium would be reached much faster, in a smaller number of RF cycles.

Recently, Igor Kouznetsov (a student of Prof. Lieberman) showed us how he used much **lighter ion masses** M_{light} in order to speed up his simulations (which mocked a discharge, not RF driven), looking for space-charge effects. The physics for accelerating a discharge to equilibrium is rather simple: reducing the mass of the ions increases their speed, which enables them to reach an equilibrium state in a smaller number of RF cycles, hence less computer time.

The light ion computer run is made in two steps. The first part is with the lighter ions, running until this discharge comes to equilibrium. Then we switch back to the heavier (real) masses M_{real} (keeping the same kinetic energies, by decreasing the ion velocities by $\sqrt{M_{\text{real}}/M_{\text{light}}}$) and run until equilibrium is again reached. (There was a short lived transient in re-starting with the real masses, then a more gradual transition to the final equilibrium.) The hope is that the overall running time is less than that running with M_{real} throughout (it is). Since the speed of the light ions is faster by the factor $\sqrt{M_{\text{real}}/M_{\text{light}}}$, we expect the light ions to reach equilibrium faster than real ions by this factor, the maximum Gain possible, assuming that the second equilibrium is reached relatively quickly.

Increasing the speed of the ions, however, increases the rate of loss of the ions to the walls. This means that we must increase the creation rate (ionization) in order to make up for this increased rate of loss. One way to increase the creation rate was to increase the electron-neutral cross-sections (including ionization) in our code by the factor $\sqrt{M_{\text{real}}/M_{\text{light}}}$. (Note that when we decreased the ion mass, the PDP1 code automatically increased the maximum collision frequency by $\sqrt{M_{\text{real}}/M_{\text{light}}}$.) We then found that we still could not maintain the discharge without also increasing the amplitude of the RF current drive. The required increase in power needs to be estimated from analysis; so far we have made empirical guesses.

6.7. Use of Variable Weights

This is explained under the oxygen runs, as it applies there more than with argon.

6.8. Use of Initial Density Profiles Closer to Equilibrium

This speed-up is to start with initial profiles of electron and ion densities as close to final equilibrium values as we can generate, say, analytically, or from previous runs. The electrons and ions will start with Maxwellian velocity distributions, to be refined next. At this writing, this speed-up has not yet been tried.

6.9. Staying within Time Step Limits, e.g., $v_s \Delta t_s / \Delta x < 1$

Many of the above accelerations stretch the limits on time steps. We list six global cautions in the Tables below that usually must be obeyed in order to obtain stability and accuracy, and to minimize self heating. Most are discussed in the 3 simulation texts noted earlier. Note in the Tables that the higher gains come when we run near these limits.

We are exploring interrelations among these six limits and the number of cells (that is, Δx) and the use or not of digital smoothing of the charge density.

If we assume that fast plasma phenomena are not significant in RF discharge physics, the highest frequency we need to resolve is the RF driving frequency ω_{RF}, and the shortest length we need to resolve is the sheath width s. However, the stability criterion for conventional explicit PIC requires resolving the electron plasma frequency and the electron Debye length: $\omega_{pe}\Delta t \leq 0.2$, $\lambda_{De}/\Delta x \geq 0.3$. Typically, $\omega_{pe} >> \omega_{RF}$ and

$\lambda_{De} << s$ so that in explicit schemes we are forced to pick a much smaller Δt than is necessary to resolve ω_{RF}, and a much smaller Δx than is necessary to resolve s.

Implicit schemes allow us to relax the time constraint above to $\omega_{RF}\Delta t << 1$. They also allow us to relax the constraint on Δx by only requiring us to resolve s rather than λ_{De}. However, implicit schemes are more complex and require more operations than explicit schemes.

An additional accuracy condition which must always be satisfied is for $v_s\Delta t_s/\Delta x < 1$, where v_s is the characteristic velocity of a particle of species s, and Δt_s is the time step of a particle of species s. This ensures that particles will not travel more than one cell per time step and will sample the electric fields properly.

Since MCC only assumes one collision per particle per time step, care must be taken to choose a Δt such that the probability of having a particle collide more than once per Δt is low. The collision probability of the *jth* particle in a time step Δt is

$$P_j = 1 - \exp(-n_{\rm gas}\sigma_T(E_j)v_j\Delta t), \tag{1}$$

where v_j and E_j are the speed and kinetic energy of the jth particle, and $\sigma_T(E_j)$ is its total collision cross section with the target density n_{gas}. Then, the collision probability for n collisions in the same Δt is approximately P_j^n . The number of missed collisions per Δt is then proportional to

$$err = \sum_{l=2,\infty} P_j^l = P_j^2/(1 - P_j). \tag{2}$$

For example, an error of err = 0.01 requires P_j < 0.095 and $n_{\rm gas}\sigma_T(E_j)v_j\Delta t = \nu_j\Delta t <$ 0.1. See Vahid and Surendra (1995).[19] In our Tables below, we calculate

$$\nu_{\max}\Delta t = n_{\rm gas}\max_E(\sigma_{T,s}(E)v_s(E))\Delta t$$

which is larger than all the $\nu_j\Delta t$.

7. APPLICATION TO 100 mT ARGON RF DISCHARGE

Our first step was to examine the 1000 RF cycle "rule of thumb" on our standard explicit argon current driven model, as reported on earlier by V. Vahedi et al. (1993).[18] We did this for his 1*d*3*v* model, at a pressure of 100 mT of argon, with 2 cm electrode spacing, 160 cm² area, current driven by 0.4 A at 13.56 Mhz. The runs were initiated with equal number of electrons and ions, uniform in x, with Maxwellian electrons at T_e = 2 eV, and Maxwellian ions at T_i = 0.03 eV. The initial number of ions and electrons was a little larger than that expected at equilibrium, so that the particle numbers decrease as the run progresses to equilibrium. These runs were made with about 2e4 particles, half electrons, half ions.

7.1. Base Run, Explicit Coding

We ran the base run, explicit coding, for about 1,000 RF cycles, 2 million $\Delta t_{\rm base}$, where $\Delta t_{\rm base}$ = time step for base run. The computing time was about 7.5e4 seconds, roughly 21 hours. However, the actual time for the base model to reach equilibrium, judging from the behavior of the number of particles and other diagnostics, was less, at about 500 RF cycles. We assume that a simulation has reached equilibrium when the number of particles and other diagnostics (i.e., density, electric field, potential profiles, temperature, energy distributions) do not change "appreciably" when we run the simulation longer.

7.2. Implicit Case

As mentioned earlier, implicit coding allows a larger timestep Δt while maintaining numerical stability. We used a timestep of $\Delta t_{\text{implicit}} = 8\Delta t_{\text{base}}$. When run for 1000 RF cycles, the computing time was about 1.9e4 seconds (5.3 hours). Hence, the running time was reduced by a factor of 7.5e4/1.9e4 = 4; Gain = 4. We did not obtain a gain of 8 as might be expected from the 8 times larger Δt because running the code implicitly was roughly twice as costly as running it explicitly. A profile of the explicit and implicit runs showed that the percentage of time spent in the mover was 37% in both cases but the more complex implicit mover took 1.85 times longer per call than the explicit mover. Also even though the collision handler was called only every $8\Delta t_{\text{base}}$, it took 4.5 times as long per call in the implicit case as the explicit case because the number of collisions per call increases with Δt:

$$N_s P_{\text{null},s} = N_s(1 - \exp(-n_{\text{gas}} \max_E(\sigma_{T,s}(E)v_s(E))\Delta t)), \tag{3}$$

where N_s is the number of particles of species s, and $P_{\text{null},s}$ is the maximum fraction of particles of species s which undergo a collision in time Δt. This suggests that at lower pressures, where collision handlers play smaller roles, we can expect higher Gains for implicit runs.

7.3. Implicit and Subcycling Case

A further reduction in time can be gained by subcycling the electrons in the implicit run. As mentioned earlier, this coding chooses $\Delta t_i >> \Delta t_e$. We chose a subcycling factor k = 20, which means that the ions are pushed only every $20\Delta t_e$. When run for 1000 RF cycles, the computing time was about 1.2e4 seconds. This represents a Gain = 1.9e4/1.2e4 = 1.6 over the implicit without subcycling case. The total Gain = 7.4e4/1.2e4 = 6.3 over the base case.

In the non-subcycling case, for every $20\Delta t_e$, we push 20(1e4) + 20(1e4) = 4e5 particles. In the subcycling case, for every $20\Delta t_e$, we push 20(1e4) + 1e4 = 2.1e4 particles. This means that we expect a maximal Gain of about 4e5/2.1e4 = 1.9 from subcycling. (As the subcycling factor k increases, the ion move becomes negligible and the gain approaches 2.) However, only about 1.6 of the expected 1.9 was realized because, like the implicit case, the subcycling did not reduce appreciably the total time spent with the collision handler. This is because, for the ions, even though the collision handler is called only every Δt_i, the number of ion collisions per call is now increased to:

$$N_i P_{\text{null},i} = N_i(1 - \exp(-n_{\text{gas}} \max_E(\sigma_{T,i}(E)v_i(E))k\Delta t_e)) \tag{4}$$

As with the implicit case, at lower pressures we should expect higher gains due to subcycling since the collision handler would play a lesser role. We should also note that albeit small in 1d simulations, the time to calculate fields is also not reduced by subcycling.

8. APPLICATION TO 10 mT ARGON RF DISCHARGE

8.1. Base Run, Explicit Coding

A second explicit base run was made at argon pressure of 10 mT, with larger spacing, 5 cm, and with more current, 0.6 A at 13.56 MHz, same cross-sectional area, 160 cm². As with the 100 mT case, the runs were initiated with an equal number of electrons and argon ions uniform in x, with Maxwellian electrons and ions at T_e = 2 eV and T_i = 0.03 eV. The number of computer particles used in this simulation was roughly 1.3e4 instead of the 2e4 used in the 100 mT simulation. When run explicitly,

Table 1. Argon, 100 mT, Explicit, Implicit, Implicit Plus Subcycled Electrons. Current drive of 0.4 A. The first 256 RF cycles took longer than the succeeding runs, as the initial number of particles was large, then decreased. Note that the implicit gain is not the full time step increase of 8, but about half that, due to the implicit mover taking about twice the time of the explicit mover. The subcycling expected maximum gain is 1.9 (the ion move is not negligible), but about 1.6 is realized, due to the mover not being the only computation

100 mT Argon	**Simulations**		
Model	Base, Δt_{base}	Implicit, $8\Delta t_{\text{base}}$	Implicit, $8\Delta t_{\text{base}}$; Subcycled, $k = 20$
256 RF cycles	24,856 sec	6564 sec	4368 sec
512	17,244 sec	4,299 sec	2721 sec
768	16,613 sec	4032 sec	2507 sec
1024	16,707 sec	4149 sec	2421 sec
Total time	7.5e4 sec 21 hrs	1.9e4 sec, 5.3 hrs	1.2e4 sec, 3.3 hrs
GAIN	**1**	**4**	**6.3**
$v_{te}\Delta t_e/\Delta x < 1$	0.43	1.3	1.3
$v_{\text{imax}}\Delta t_i/\Delta x < 1$	0.013	0.04	0.78
$\nu_e\Delta t_e < 1$	0.076	0.61	0.61
$\nu_i\Delta t_i < 1$	0.0024	0.019	0.38
$\lambda_{De}/\Delta x > 0.3$	2.7	1.0	1.0
$\omega_{pe}\Delta t_e < 0.2$	0.16	1.3	1.3

the discharge reached equilibrium in about 1000 RF cycles. The run took about 5e4 seconds or 14 hours, slightly longer than (1.3e4/2e4)*(time to run 100 mT argon model for 1000 RF cycles).

8.2. Light Mass Case

In our case, when we used $M_{\text{real}}/M_{\text{light}} = 100$, we found that we needed to double the amplitude of the current drive to 1.2 A in order to produce density profiles which were similar to the base case.The light ions reached equilibrium at about 128 RF cycles << 1000 RF cycles. Next, we ran a simulation with the real masses and the original current drive, but using the dump file from the light mass simulation. This simulation only needed an additional 128 RF cycles to reach an equilibrium, which was very close to the equilibrium reached by running the base simulation for 1000 RF cycles. The total running time of the light mass simulation was 1.2e4 seconds which is a factor of 4.1 less than the base simulation running time of 5e4 seconds; Gain = 4.1.

8.3. Light Masses and Implicit

Further reduction in run time can be made by using the implicit mover as described above in the 100 mT case, along with the light mass simulation. We ran the implicit mover with a $\Delta t_{\text{implicit}} = 8\Delta t_{\text{base}}$. The implicit mover reduced the running time by a factor of 4.4 (not by 8), because the implicit code is roughly twice as costly as the explicit code, as noted above. Note that, as expected, the Gain of 4.4 in the 10 mT case is larger than the Gain of 4 in the 100 mT case because, at the lower pressure, less time is spent with the collision handler.

The total Gain in time from using a combination of light masses and an implicit mover is Gain = 4.4 * 4.1 = 19.

Table 2. Argon 10 mT Base, Light Ion, Light Ions Plus Implicit Runs. Current drive of 0.6 A for the base case, with drive of 1.2 A for the light ions. In the light ion runs, the ions move 10 times faster, reaching light ion equilibrium at 128 RF cycles; the next 128 cycles were run with the true mass, reaching equilibrium in another 128 cycles. Note that the combination of light ions and implicit leads to an appreciable gain of 19

10 mT Argon	**Simulations**		
Model	Base, Δt_{base}	Light ions, $M_{real}/M_{light} = 100$	Light ions, plus implicit, $8\Delta t_{base}$
Total time	5e4 sec, 13.9 hrs	1.2e4 sec, 3.3 hrs	2.7e3 sec, 45 min
GAIN	1	4.1	19
$v_{te}\Delta t_e/\Delta x < 1$	0.13	0.13	1.0
$v_{imax}\Delta t_i/\Delta x < 1$	6.7e − 3	0.12	0.96
$\nu_e\Delta t_e < 1$	7.6e − 3	7.6e − 2	0.61
$\nu_i\Delta t_i < 1$	2.4e − 4	2.4e − 3	0.019
$\lambda_{De}/\Delta x > 0.3$	1.0	1.0	1.0
$\omega_{pe}\Delta t_e < 0.2$	0.16	0.16	1.3

9. APPLICATION TO 100 mT OXYGEN RF DISCHARGE

Our third model is a 100 mT current-driven oxygen discharge. As with the 100 mT argon model, the length of the system was 2 cm, the cross-sectional area was 160 cm², and the amplitude and frequency of the current drive was 0.4 A and 13.56 MHz respectively. The oxygen model has three species, electrons, O_2^+ ions and O^- ions. Because oxygen is electronegative, we expect the O_2^+ and O^- population to be much larger than the electron population. Hence, we started the simulation with about 5e4 O_2^+, 5e4 O^- ions and 5e3 electrons. The initial densities were all uniform in x, with Maxwellian electrons at T_e = 2 eV and Maxwellian O_2^+ and O^- at T_i = 0.03 eV.

9.1. Base Run, Explicit Coding

We ran the simulation explicitly for 1000 RF cycles. Because of the large number of particles, the run took 3e5 seconds or 3.5 days (slightly less than (1.05e5/2e4)*(time to run 100 mT argon model for 1000 RF cycles). But, even after 1000 RF cycles, the density profiles were still evolving, suggesting that the simulation did not reach equilibrium. The number of ions in the simulation did not change appreciably over the 1000 RF cycles, but the number of electrons did drop sharply to about 1.5e3 electrons.

9.2. Subcycling Ions

In an argon discharge where there are roughly an equal number of electrons and ions the maximum gain due to subcycling the ions is limited to two. However, in an electronegative discharge the number of ions can be much larger than the number of electrons so that the gain due to subcycling can be far greater. We conducted another oxygen simulation in which we subcycled the electrons by a factor of 80; that is, the ions were pushed only every $80\Delta t_e$. When run for 1000 RF cycles, the computing time was 1.5e4 seconds, representing a Gain of 3e5/1.5e4 = 20 >> 2. For most of our oxygen simulation, we had 5e4 O_2^+, 5e4 O^-, and 1.5e3 electrons. In the non-subcycling case, for every $80\Delta t_e$, we push 80(5e4) + 80(5e4) + 80(1.5e3) = 8.12e6 particles. In the subcycling case, for every $80\Delta t_e$, we push 5e4 + 5e4 + 80(1.5e3) = 2.2e5 particles. This means that we expect a maximal Gain of about 8.12e6/2.2e5 = 37. But, as in the argon case, we obtain a Gain of 20 rather than 37 because, although subcycling reduces

the time spent moving and gathering particles (typically the most costly procedures), subcycling does not reduce the time spent handling collisions or calculating fields.

9.3. Subcycling and Variable Weights

For very electronegative gases, the densities of the ions are much higher than the density of the electron. In our simulation, for every electron there were about 30 O_2^+ and 30 O^- .We require about 1000 electrons in our model in order to reduce numerical noise and to satisfy the condition that the number of electrons per λ_{De} be at least 5. This means that we will have at least 3e4 O_2^+ and 3e4 O^- ions in our simulation. Since moving and gathering particles are typically the costliest procedures, much can be gained by reducing the number of computer particles.

One way to reduce the number of computer particles is to weight the ion superparticles more heavily than the electron superparticle. For example, if an electron superparticle represents 1e8 real electrons, an ion superparticle can represent 1e9 real ions; this is called $w = 10$. Then, instead of requiring 3e4 O_2^+ and 3e4 O^- ions per every 1000 electrons, we can have 3e3 O_2^+ and 3e3 O^- per every 1000 electrons. A variable weighting procedure for oxygen discharges has been developed and implemented by Cooperberg et al. (1994).[6] If there. were no collisions, then the procedure would be fairly straightforward since there would be no interactions involving particles of different weights. But, because of collisions, the weight of each particle is a dynamic variable that is updated every time it undergoes a collision. In order to keep the number of ions low (*i.e.*, maintain their initial weights), it is necessary to set a cap on the number of electrons and ions that is close to their initial values.

In our example, we did a simulation using both subcycling and variable weights. As before, we used a subcycling factor $k = 80$, and we used a variable weight factor $w = 10$. This reduced the number of O_2^+ and O^- from 5e4 each to 5e3 each. So instead of pushing, 5e4 + 5e4 + 80(1.5e3) = 2.2e5 particles every $80\Delta t_e$, we only had to push 5e3 + 5e3 + 80(1.5e3) = 1.3e5 particles every $80\Delta t_e$. This implies a Gain = 2.2e5/1.3e5 = 1.7. The subcycling run with variable weights took 1e4 seconds to run 1000 RF cycles. Compared to the subcycling run without variable weights the Gain = 1.5e4/1e4 = 1.5, very close to the expected gain of 1.7. The total Gain from subcycling and variable weights is Gain = 20 * 1.5 = 30.

Implicit increasing of Δt_e will add little Gain here, as there are relatively few electrons to move, and the implicit mover is roughly twice as costly as the explicit one.

10. FUTURE DEVELOPMENTS

As stated earlier, a major objective is to make first-principles, self-consistent (PIC-MCC) codes run fast enough to be useful to plasma processing machine designers and experimentalists, on their time scale. We take this to mean running at least as fast as experimentalists can “cut metal,” say, in a matter of hours. We have made good progress on single processor machines, with perhaps a factor of 10 to go yet in Gain, some from better physics, and some from better numerics. And, of course, there is more yet to be gained from using many processors in parallel.

The above is a progress report, achieving Gains in time of 6, 20 and 30, over base runs, with runs to equilibrium now taking times like 45 minutes to three hours, beginning to become attractive for design purposes, parameter searching and optimization.

The future is really with us, with faster single processors announced regularly, easier ways to parallel, and so on.

Table 3. Oxygen, 100 mT, Explicit, Subcycling, Subcycling and Variable Weights. Current driven, 0.4 A, length of 2 cm. Electronegative gas, dominated by the positive and negative ions, such that subcycling the electrons works very well, as noted by the gain of 20. However, even at 1024 RF cycles, the density profiles are continuing to evolve, even though the number of particles is changing slowly

100 mT Oxygen Simulations			
Model	Base, Δt_{base}	Subcycling, $k = 80$	Subcycling plus Weighting, $w = 10$
Total time	3e5 sec, 3.5 days	1.5e4 sec, 4.2 hrs	1e4 sec, 2.8 hrs
GAIN	**1**	**20**	**30**
$v_{te}\Delta t_e/\Delta x < 1$	0.22	0.22	0.22
$v_{\mathrm{imax}}\Delta t_i/\Delta x < 1$	$6.2\epsilon-3^{(+)}$; $1.5\epsilon-3^{(-)}$	$0.5^{(+)}$; $0.12^{(-)}$	$0.5^{(+)}$; $0.12^{(-)}$
$\nu_e\Delta t_e < 1$	0.071	0.071	0.071
$\nu_i\Delta t_i < 1$	$8.9\epsilon-4^{(+)}$; $2.3\epsilon-4^{(-)}$	$0.071^{(+)}$; $0.018^{(-)}$	$0.071^{(+)}$; $0.018^{(-)}$
$\lambda_{De}/\Delta x > 0.3$	5.0	5.0	5.0
$\omega_{pe}\Delta t_e < 0.2$	0.043	0.043	0.043

Recently CKB showed our codes to a group including a former grad student, who did some excellent simulations almost 4 decades ago. He ran the former student's problem through very quickly on an ordinary PC, with many diagnostics. The student's reaction was: "There goes my thesis in one minute!" This will happen again, but sooner than waiting 4 decades.

11. CONCLUSIONS

The future is very bright. Our speed-up attempts here, using several known methods all together, plus a new one, plus more to come, will cut single processor workstation run times from days to less than an hour by the end of this year. As a benchmark, our speed-up runs given above took about six weeks of rather intensive computing; our efforts continue. We hope that these speed-ups will be noticed in industries that are now highly empirical. Hopefully, examples will be set by the first laboratories to use simulations for device and machine design; others must follow.

ACKNOWLEDGMENT

We are especially grateful to our long term supporters in advanced simulations and applications, namely AFOSR (for electron beam and plasma devices, of many kinds) and ONR (for plasma edge science support). There also has been continued support from LLNL, plus collaborations in the plasma processing area, for most of a decade, for which are very grateful. We also would like to recognize help from industries; in the recent past, from Samsung, Sumitomo Metals, and Hitachi, with earlier help from Varian, Hughes, and Applied Materials, plus just starting, from Lam Research.

We appreciate the large effort put forth by the organizers, Profs. Uwe Kortshagen and Lev Tsendin, of the NATO Advanced Research Workshop.

REFERENCES

1. J. U. Brackbill and B. I. Cohen. *Multiple Time Scales.* Academic Press (1985).
2. C.K. Birdsall. Particle-in-cell charged-particle simulations, plus monte carlo collisions with neutral atoms, pit-mcc. *IEEE Transactions on Plasma Science*, 19(2):65–85 (April 1991).

3. Birdsall and Bridges (1966).
4. C.K. Birdsall and D. Fuss. Clouds-in clouds, clouds-in-cells physics for many-body simulation. *J. Comput. Phys.*, 3:494-511 (1969).
5. C.K. Birdsall and A. B. Langdon. *Plasma Physics via Computer Simulation.* McGraw-Hill (1985).
6. D. J. Cooperberg, V. Vahedi, and C. K. Birdsall. Pic-mcc with variable particle weights. *Proc. Numerical Simulation of Plasmas Conf. Valley Forge PA 7-9 Sept. 1994, plus PIC-MCC Workshop 9-10 Sept. 1994.* (1994).
7. J.M. Dawson. One-dimensional plasma model. *Phys. Fluids*, 5:445–459 (1962).
8. O. C. Eldridge and M.Feix. One-dimensional plasma model at thermodynamic equilibrium. *Phys. Fluids*, 5:1076-1080 (1962).
9. F. H Harlow. The particle-in-cell computing method for fluid dynamics. *Methods of Comput. Phys.*, 3:319–343 (1964).
10. R. W. Hackney. A fast direct solution of poisson's equation using fourier analysis. *J. Assoc. Comput. Mach.*, 12:95–113 (1965).
11. R. W. Hackney and J. W. Eastwood. *Computer Simulation Using Particles.* McGraw-Hill (1981).
12. William S. Lawson. Particle simulation of bounded 1d plasma systems. *Journal of Computational Physics*, 80(2):253–276 (February 1989).
13. R. L. Morse and C. W. Neilson. Numerical simulation of the weibel instability in one and two dimensions. *Phys. Fluids*, 14:830–840 (1971).
14. T. Tajima. *Computational Plasma Physics, with Applications to Fusion and Astrophysics*. Addison-Wesley (1989).
15. P.K. Tien and J. Moshman. Monte carlo calculation of noise near the potential minimum of a high frequncy diode. *J. Appl. Phys.*, 27:1067–1078 (1956).
16. V. Vahedi, J. N. Bardsley, and G. DiPeso. Simulations of a capacitively coupled plasma source with an internal grid. Technical report, Lawrence Livermore National Lab. (1995).
17. V. Vahedi and G. DiPeso. Simultaneous potential and circuit solution for two dimensional bounded plasma simuation codes. *J. Comput. Phys.*, 131:149–163 (1997).
18. V. Vahedi, G. DiPeso, C.K. Birdsall, M.A. Lieberman, and T.D. Rognlien. Capacitive rf discharges modelled by particle-in-cell monte carlo simulation. i: Anaylsis of numerical techniques. *Plasma Sources Sci. Technol.*, 2:261–272 (1993).
19. V. Vahedi and M. Surendra. Monte-Carlo collision model for particle-in-cell method: Application to argon and oxygen discharges. *Comp. Phys. Comm.*, 87:179–198 (1995).
20. Verboncoeur et al. (1993).

CONVECTED SCHEME SIMULATIONS OF GLOW DISCHARGES

G. J. Parker[1] and W. N. G. Hitchon[2]

[1]Lawrence Livermore National Laboratory
7000 East Avenue, L-418
Livermore, CA
[2]Department of Electrical and Computer Engineering
University of Wisconsin, Madison WI

1. INTRODUCTION

The Convected Scheme (CS) will be reviewed here, with emphasis on recent modifications of the scheme which make it particularly accurate and effective in a variety of different physical situations corresponding to several important classes of discharges. The CS is a numerical scheme for solving the Boltzmann equation which corresponds in some limit to the method of characteristics. [1, 2, 3] It also has features in common with the 'Water Bag' model of Berk and Roberts. [4] The distinct feature of the method is that it relies on physical intuition to build up a numerical scheme which reflects the underlying physics. Focusing attention on individual 'cells' in phase space, the distribution is advanced in time by following the phase space 'fluid' in one initial cell at a time. This allows particle numbers from the initial cell to be conserved exactly, numerically. Various conserved dynamical quantities are also conserved, either by using a mesh based on the conserved quantity or by imposing conservation of that quantity as the fluid from each initial cell is moved around the mesh and replaced on the mesh.

Schemes which conserve energy on a mesh which does not employ the total energy as an independent variable were developed early on. [5, 6] Other schemes which treat scattering processes very accurately were also developed. [7] It has been clear from the outset of this work that it is advantage ous to be able to follow each phase space cell as long as possible, before replacing its contents on the mesh.[8] Collisions disrupt the integrity of the contents of a moving cell, so that they need to be replaced in other cells. Ways in which the particles can be replaced while allowing the rest of the cell to continue being followed without interruption, and without a proliferation of moving cells, are discussed and results presented.

CS simulations have been applied to a number of important classes of plasmas:
1) Self-consistent simulations of ion motion, in presheaths and sheaths. [9]
2) Self-consistent simulations of electrons and ions in (1-space,2-velocity)-simulations of

Electron Kinetics and Application of Glow Discharges
Edited by U. Kortshagen and L. D. Tsendin, Plenum Press, New York, 1998

dc and rf discharges.[5, 6, 8, 10, 7, 11] It was in this context that the importance of including Coulomb collisions between trapped and untrapped electrons in certain dc discharges became apparent. [11]

3) Self-consistent simulations of electrons and ions in positive column plasmas. [12] A mesh and integration scheme which reflect the appropriate conserved dynamical qantities in cylindrical geometry were devised. [13]

4) CS results in (2-space, 3-velocity) independent variables were compared to the predictions of the non-local theory of Tsendin et a1.[14] CS results were also compared to Monte Carlo simulations of swarms [15] and of positive columns. [13] Very good agreement was obtained, especially when a suitable CS was used which employed conserved dynamical variables or which allowed long time steps to minimize mesh errors.

The original purpose of the CS was to develop a physically-based scheme which had the appropriate physics built into the 'microscopic' treatment of the particle motions. The time step is limited, in this case, only by the physical processes - not by the numerical representation of those processes.

As the scheme has evolved, the emphasis has turned to the related issue of how to handle the numerical errors ('numerical diffusion') which occur in a scheme such as this, when cells are moved around a mesh a very large number of times during a simulation. The best strategy for minimizing errors must depend on the physics of the problem, and is probably best stated in terms of the characteristic times of the particle motion.

The first time scales one must consider are for collisionless (or ballistic) motion, $\tau_{\rm ball}$, the time to go a characteristic length (such as the system size) and the times for elastic and inelastic collisions $\tau_{\rm col}^{\rm el}$ and $\tau_{\rm col}^{\rm inel}$. When $\tau_{\rm col}^{\rm el} \ll \tau_{\rm ball}$ one must be sure that numerical diffusion is not a problem during elastic collisions. A simulation which handles both ballistic motion and elastic collisions with little diffusion was presented in [Ref. 11].

In the work which is presented in the last section here, the emphasis is on a problem where particles are relatively collisionless; $\tau_{\rm ball} \ll \tau_{\rm col}^{\rm el} \ll \tau_{\rm col}^{\rm inel}$. In this case we need to follow particles for a large distance without much numerical diffusion. Ideally we would simply follow packets of particles as they move around phase space and never put them back into different cells, except when they undergo collisions, because the process of replacement into other cells usually leads to diffusion. However, we cannot afford to follow vast numbers of such packets. We need to limit their numbers, and the way to limit their numbers is probably to limit the lifetime of the packets, and to put the particles in expired packets into 'younger' packets. The CS 'overlap' rules are used in the replacement of particles, from one packet into another. The issue then becomes how to choose the lifetime of the packets so that efficiency and accuracy are greatest, how to choose when to launch new packets, and sometimes how to ensure that the moving packets completely fill phase space so that we can easily put new particles into them.

One of the simplest ways to launch packets or "moving cells" is to have each moving cell instantaneously coincide with a corresponding fixed cell, and to have the back of one moving cell coincide exactly with the front of the moving cell behind it. This solves the problem of filling phase space, but involves redundancy - there are several moving cells for each fixed cell. These moving cells have the exact same values of the conserved dynamical variables (e.g. angular momentum, total energy) as the fixed cell and for the portion of the moving cells which are within the initial fixed cell, they have the exact same values of kinetic energy as the fixed cell. For example, we could envisage a situation where for any fixed cell we keep track of three or more moving cells, see

Fig. 1. Supposing that three cells is enough. Cell 1 might be a moving cell which has completely left the initial fixed cell which it initially corresponded to. Cell 2 partially overlaps the initial fixed cell and is on the way out. Its front is in contact with the back of cell 1. Cell 3 partially overlaps the initial fixed cell and is on its way in. It will exactly coincide with the fixed cell at the moment cell 2 first leaves the fixed cell. The front of cell 3 is the back of cell 2. The back of cell 3 coincides with the back of the fixed cell at first, but the back of cell 3 will be set loose when cell 3 completely fills the fixed cell. The back of cell 3 will be the front of the next moving cell to be launched.

Particles being replaced in the fixed cell can be put back in cells 2 and 3 - or just whichever is currently overlapping the center of the fixed cell. Replacing only in the moving cell which overlaps the center of the fixed cell leads to less diffusion - and leaves more time for the moving cells to empty out. No particles are replaced in cell 1, so it will be emptied by collisions and we can stop following it after some time. (We may need more than one cell like cell 1 which has left the initial cell and which no longer has particles put back into it. to allow time for these cells to be mostly emptied out.)

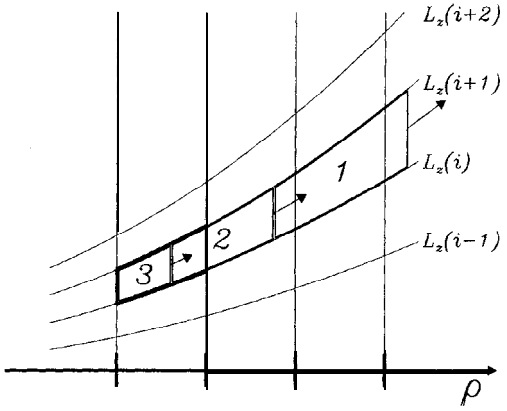

Figure 1. Schematic of the radial ballistic move. Original fixed cell is bounded by constant L_z contours, radial cell boundaries and constant total energy contours (not shown). Direction and speed of moving cell faces are indicated by arrows.

In the last section of this paper, conserved dynamical variables are used to define the mesh - including the total energy. For a fixed potential V the use of the total energy allows the replacement of 'old' packets or scattered particles to be done in a relatively straightforward way with no associated numerical diffusion - see section 3.

The success of the method in describing these different plasmas, in some cases where other simulation methods are not available, shows the utility of the method and illustrates the class of problems for which the CS is suited.

2. PREVIOUS CS SIMULATIONS

i.) A d.c. discharge in helium has been modeled from electrode to electrode, fully kinetically using a self-consistent electric field and including all the physical processes

believed to be important for ions, electrons and neutral atoms.[11] The cathode fall, negative glow, and cathode fall-negative glow boundary develop naturally in the simulation without an internal boundary condition and without breaking the electron energy distribution function in components. Results of the simulation have been compared to precise experimental results for the electric field profile, species densities, and average electron energy. Excellent agreement is obtained demonstrating that the physical model used is both correct and complete.

ii.) The effects of allowing anisotropy in elastic electron collisions with neutral atoms instead of using the momentum transfer cross-section, the effects of using anisotropic distribution in inelastic electron-atom collisions, and the effects of including a Coulomb electron-electron collision operator have been examined.[7, 8] It was shown that changes in any of the collisional models, especially the second and third described above, can make a profound difference in the simulation results. This confirms that many discharge simulations have great sensitivity to the physical and numerical approximations used. Our results reinforce the importance of using a kinetic theory approach with highly realistic models of various collisional processes.

iii.) A numerical procedure which provides an accurate solution of the Boltzmann equation in cylindrical geometry with coordinates $(\rho, \vec{v})$ was developed. [12] The solution method, which is a version of the CS, eliminates some specific sources of numerical diffusion in cylindrical geometry. The velocity is represented as $(v_z,\ v_\perp,\ M)$, where M is a moment arm or 'reduced' angular momentum, $M = \rho \sin \phi$ and ϕ is an azimuthal angle in velocity space (referenced to $\hat{\rho}$). The reasons for all the coordinate choices were discussed. Propagator algorithm(s) for solving the kinetic equation were presented which remove certain numerical errors.

iv.) Kinetic calculations have been employed to model electron behavior in a low-pressure Inductively-Coupled Plasma (ICP) in order to investigate the processes governing the formation of the electron distribution function (EDF).[14] Our approach involved a numerical "propagator" treatment of time-resolved electron motion in five-dimensional phase space (two spatial and three velocity coordinates) based on the "Convected Scheme" (CS).

In the next section, we will describe a version of the CS where the electrostatic potential is constant in time. In this case, the distinction between a "moving" mesh and a "fixed" mesh simplifies, since one can define a mesh which cyclic in the dynamically conserved variables. Instead of launching new moving cells, the fixed cells at each radial position are continuously being exactly overlapped by cells which were "upstream" at an earlier time. The following section describes in some detail how this is implemented in this special case of a time independent electrostatic potential.

3. CONVECTED SCHEME SIMULATIONS OF THE ELECTRON DISTRIBUTION FUNCTION IN A POSITIVE COLUMN PLASMA

In previous work the CS used propagators which were designed to locally conserve appropriate quantities (such as numbers and energy) and the possibility of using long time steps to reduce numerical diffusion. The next set of innovations enable us to eliminate numerical diffusion and associated mesh errors during the ballistic motion entirely. Where possible we use conserved dynamical variables to specify the computational mesh thereby eliminating the need to replace particle densities back onto the mesh at the end of a ballistic (collisionless) step. In this approach, the initial condition of a computational cell (total energy and angular momentum about the *z* axis, say) specifies a unique orbit in phase space. One additional independent variable is used

which is the position or phase in any particular orbit of the cell particles are in- the cell moves around the orbit with the particles. The phase in the orbit of each cell is updated as time passes so the particles can stay in the same computational cell and follow its trajectory without any replacement onto a fixed mesh. Collisions, of course, will couple different trajectories together locally in space. The spatial location of the collision can be determined from the phase and the independent dynamically conserved variables. In this procedure, the distribution function is the main dependent quantity and is computed by integrating forward in time.

In Section 3.1, the coordinate system and computational mesh are introduced and explained. Section 3.2 describes the "ballistic" (collisionless) motion of electrons on the mesh, while Section 3.3 describes electron-neutral atom collisions. Section 3.4 presents the results and comparisons of the CS and MC methods for a dc positive column.

3.1. Coordinate System and Mesh for Electrons in Cylindrical Geometry

In this section, the coordinate system used to describe electron motion is discussed, as well as reasons for choosing it. Then the electron computational mesh is introduced. The computational mesh can be described by many different sets of independent variables. To eliminate computational errors, such as artificial numerical diffusion, a set of variables should be dynamically conserved during the ballistic (collisionless) motion.

In earlier work in cylindrical geometry,[12,14] the coordinate system used was: (ρ, v_z, $v_\perp$, M). Here, ρ is the radial position, v_z is the axial (z) velocity, $v_\perp$ is the speed in the plane perpendicular to z axis and M is a moment arm or "reduced" angular momentum: $M = \rho \sin \phi$, where ϕ is an azimuthal angle in velocity space (referenced to the unit vector $\hat{\rho}$).

This mesh, as was discussed, has some desirable properties. First, it allows the axial motion to be effectively decoupled from the radial motion. This allows an efficient vectorization of the ballistic motion. Second, in the absence of radial and azimuthal electric fields, both $v_\perp$ and M are conserved during ballistic motion. This, in turn, eliminated errors introduced by the finite size of the computational mesh. Finally, in the absence of an azimuthal electric field, the product $v_\perp M$ is conserved.

On the other hand, this set of independent variables has a few undesirable properties. First, once a radial (and/or azimuthal) electric field is present, errors introduced by the finite size of the mesh in $v_\perp$ and M could affect the accuracy of the propagators, since neither are conserved quantities. This problem was addressed by taking small enough cells (a large number) or alternately by taking large time steps Δt so that the error was manageable.

A second and perhaps more serious problem occurred if the time step, Δt, was small so that only a small fraction of electrons in a certain radial cell could move to the adjacent radial cell. The correction for this has been described in detail elsewhere.[8, 12]

In search of a suitable choice of independent variables, one would prefer variables which are conserved during the ballistic radial move. In addition, the systematic error due to numerical diffusion during radial motion should be avoided if possible. In the absence of an azimuthal field, two conserved quantities are the angular momentum about the axial (z) axis,

$$L_z = m\rho v_\perp \sin\phi \tag{1}$$

and the total energy in the plane perpendicular to the z axis,

$$\varepsilon_\perp = \frac{1}{2}mv_\perp^2 + V(\rho) = \frac{1}{2}mv_\perp^2 - e\Phi(\rho). \tag{2}$$

Here m is the mass of an electron, $V(\rho) = -e\Phi(\rho)$ is the potential energy, e is the elementary charge and $\Phi(\rho)$ is the radial electrostatic potential. We choose to keep the axial velocity v_z, along with L_z and $\in_\perp$, since that choice allows us to decouple the axial and radial motion for computational efficiency.

Given L_z and $\varepsilon_\perp$, a trajectory can be determined. The last independent variable must change with time. We choose to use moving cells, so particles stay in these cells. We need a label to indicate where these cells have got to. The elapsed time since passing some reference point on the orbit (or phase) is chosen. In the normal numerical procedure we integrate the particle motion around the orbit by taking discrete time steps and replacing particles on the fixed mesh after each step. The discrete nature of the steps leads to numerical diffusion, since spreading out of the particles takes place each time the particles are put back onto the mesh.

Instead of using discrete steps in the ballistic (or collisionless) motion, the procedure used here involves first following particles around their orbits and accurately calculating and tabulating for future use the time between crossings of successive radial cell faces. This allows us to keep track of where the cells containing particles are at any time during their orbit, without having to put the particles 'into' the radial mesh cells they are passing through during the ballistic motion. This in turn eliminates the numerical diffusion associated with the ballistic motion. Particles which have collisions at some point in their orbit are introduced into the radial cell where the collision occurs. After the collision these particles are restored with a new $L_z, \in_\perp, v_z$, and elapsed time in their new orbit. Other particles will return to their exact initial position after each period (if their motion is periodic).

The details of the construction of the mesh have been given previously.[13] We define a phase space cell by the indices (k, i, n, p) which represents phase space coordinates with total energy $\varepsilon_\perp(k)$, angular momentum about the z axis of L_z (i, k), at time τ (n, i, k) in that orbit and an axial velocity given by $v_z(p)$, where $-N_{v_z} \le p \le N_{v_z}$ and N_{v_z}, is the number of positive v_z cells. ?From these coordinates, all other coordinates (i.e. ρ, v_ρ, v_ϕ, M, etc.) may be derived as needed.

We will see below, that this set of independent variables and the associated mesh alleviate many of the errors associated with the finite size of the computational mesh.

3.2. The Electron Ballistic Move

In the previous section we discussed the independent variables and the associated computational mesh. In this section, we will describe how the collisionless, or "ballistic", move is implemented on the mesh. Here there are two ballistic motions: one in radius and another in the axial direction. We first discuss the radial motion.

By the construction of the mesh, the radial motion is trivial. It consists of looping over all valid $\in_\perp(k)$ and $L_z(i, k)$ and incrementing the boundaries of each τ (n, i, k) cell by the time step Δt. Once τ (n, i, k) exceeds $T(i, k)$ one of two conditions is met. If the $L_z(i,k)$ and $\varepsilon_\perp(k)$ orbit is a confined orbit (i.e. $\in_\perp(k) - V(R) < 0$ and $\rho^{\max}(L_z(i,k)) < R$), it simply means that the cell has completed one orbit and $\tau(n, i, k)$ should be decreased by $T(i, k)$. Otherwise, the phase space cell is in an unconfined orbit (it can reach the outer boundary) and $\tau(n,i,k) > T(i,k)$ means that cell has struck the wall. Those particles in the phase space cell are removed and the cell is 'reset' by decreasing τ (n, i, k) by T(i, k).

It is easily seen that since the particles are not put back on the fixed $\rho(j)$ mesh as they move around the orbit (unless they have a collision) the systematic problem which occurred with small time steps (see Section 3.1) does not occur. Also, since the mesh was created according to the radial electric field (i.e. ($\Phi(\rho)$), there is no inaccuracy in

energy associated with the radial ballistic move. Of course, the computational overhead is small since we are only incrementing the time array ($\tau(n, i, k)$) and checking for outer boundary hits.

We now will describe the axial or z ballistic move. Complete decoupling of the z motion from the radial motion results in a very simple ballistic mover for v_z. In a positive column, the axial field E_z is uniform which simplifies matters further. The (k, i, n, p) initial cell has a mean (i.e. cell centered) velocity $v_z(p)$. After a time step Δt, the moved cell has

$$v_z' = v_z(p) - eE_z\Delta t/m. \tag{3}$$

This moved velocity is typically not equal to the mean v_z in a cell on the mesh. If $\delta v_z = |eE_z\Delta t/m| \sim \Delta V_z$, where ΔV_z is the local spacing of the v_z mesh, then simply splitting the moved cell between two neighboring cells such that $mv_z'^2/2$ is conserved gives a small error, as noted in earlier work.[12] However, if $\delta v_z << \Delta V_z$, then splitting the moved cell can introduce another systematic error. [12] In this work, instead of using a 'fixed' v_z mesh a 'floating' mesh is used to eliminate numerical diffusion and other mesh errors during the ballistic move on the v_z mesh. See Ref. 13.

3.3. The Electron Collision Operator

In the previous section, we described the ballistic or collisionless motion of the electrons. We will now outline the collisional propagator and how it is implemented on the computational mesh. Details of the collision operator were given in Ref. 13.

We can always use moving cells to follow particles until they collide. After each Δt the scattered particles are replaced on the fixed mesh as described here. Unscattered particles continue in the moving cells. The scattered particles are then put into moving cells. We need to have the information as to where the old moving cells are in a form which is convenient for mapping the fixed cells onto the moving cells after the moving cells have moved through multiple time steps. If we can not easily map the fixed cells onto the moving cells after they have moved around, we will have to launch new moving cells after each Δt and follow them until they are emptied by collisions or until we can map them onto each other. The use of conserved dynamical variables makes mapping onto moving cells straightforward. If total energy, for instance, was not a convenient variable, the CS conservative overlap rules allow the mapping to be done when necessary. The mapping of moving cells onto fixed cells is straightforward. Sorting the indices of the reverse mapping would need to be done efficiently in general.

Elastic electron-neutral atom collisions, inelastic electron-neutral atom collisions resulting in excitation and inelastic electron-neutral atom collisions resulting in single-step ionization are included in the electron collision operator. In contrast to previous CS collision operators, the operator used here does not include Coulomb collisions between electrons [7] nor does it incorporate anisotropic scattering of electrons.[7, 12] These two mechanisms could easily be included, however. These simplifications are deliberate because this work is to be used to compare positive column models based on the local field (fluid) approximation, the nonlocal approximation, the convected scheme and other approximations to benchmark Monte Carlo results.

This section completes the description of the propagators needed for the CS.

3.4. Results and Discussion

In the previous four sections we have described the CS mesh and propagators for the ballistic and collisional motion. In this section we present a few results similar to

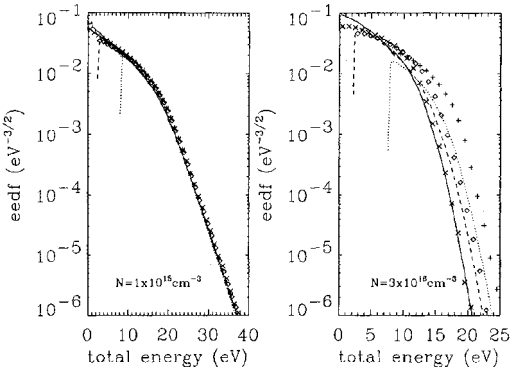

Figure 2. Comparison of EDF's from the MC (symbols) and CS (lines) models. Each EDF is calculated with its self-consistent axial electric field and wall potential. The different curves represent different radial positions: $\rho = 0.06R$, $0.5R$, $0.94R$ are the solid (×), dashed (diamond) and dotted (+) lines, respectively.

those presented in Ref. 13. In these simulations, the radial electrostatic potential is assumed to be harmonic from the center of the discharge to the inner boundary of the last radial cell (there are 25 equally spaced radial cells) such that the potential at that point has fallen 8 volts. In the last radial cell, the potential is harmonic ($\Phi(r) = a + b\rho^2$) such that it is continuous at the inner radial boundary and so $\Phi(R) = V_w$, where V_w is the "wall potential".[13, 16] The axial field, E_z, and V_w are then varied until the electron wall losses are balanced by the ionization rate. Similarly, the ionization rate must also balance the ion loss rate which is approximated from the ambipolar diffusion equation,

$$\frac{D_s}{\Lambda^2}\bar{n} = \overline{n\nu_i} \; . \tag{4}$$

Here $\overline{n\nu_i}$ is the average ionization rate per unit volume, $\Lambda = R/2.405$ is the diffusion length, and $\bar{n}$ is the average electron density. For the ambipolar diffusion coefficient D_s we use an approximation proposed by Ingold,[17] which approaches the free-fall Tonks–Langmuir[18] case in the small $R \times N$ limit as well as the-collision dominated Schottky[19] case in the large $R \times N$ limit: $D_s = D_a/(1 + 2\bar{n}\overline{\nu_i}/(\bar{n}\nu_{cx}))$. Here $D_a \approx k_B T_e \mu_i / e$ is the usual ambipolar diffusion coefficient from the Schottky theory, with $\mu_i = e/M\nu_{cx}$ the ion mobility, $\nu_{cx} = N v_i Q_{cx}$ the ion–neutral charge exchange collision frequency, v_i the thermal speed of the ions and $Q_{cx} = 40 \times 10^{-20}$ m² the charge exchange cross section. The electron temperature T_e is approximated as 2/3 of the mean kinetic energy of the EDF in the discharge center divided by the Boltzmann constant k_B. All simulations were done in an "argon-like" gas and in a tube of radius one centimeter.[13, 16]

In Figure 2, the calculated electron EDF at two different neutral gas pressures are compared to MC[16] results. In these simulations, V_w and E_z agree to within 5% between the two methods and the constraints (i.e. ionization rate balanced by wall loss rate) are in agreement to within 2%. Similar results are also shown in Ref. 13.

4. CONCLUSION

The Convected Scheme (CS) was reviewed, with emphasis on recent modifications of the scheme which make it particularly accurate and effective in a variety of different physical situations corresponding to several important classes of discharges. Detailed

discussion of the algorithm and results for a dc positive column were compared to Monte Carlo simulations and excellent agreement was found.

REFERENCES

1. P. Segur and R. Keller: Journal of Computational Physics, **24,** 43 (1977).
2. J. W. Eastwood: Computer Physics Communications, **43,** 89 (1986).
3. J. W. Eastwood: Computer Physics Communications, **44,** 73 (1987).
4. H. L. Berk and K. V. Roberts:: Methods Comput. Phys., **9,** 88 (1970).
5. T. J. Sommerer, W. N. G. Hitchon and J. E. Lawler: Physical Review Letters, **63,** 2361 (1989).
6. T. J. Sommerer, W. N. G. Hitchon and J. E. Lawler: Physical Review A, **39,** 6356, (1989).
7. W. N. G. Hitchon, G. J. Parker and J. E. Lawler: IEEE Transactions on Plasma Science, **22,** 267 (1994).
8. W. N. G. Hitchon, G. J. Parker and J. E. Lawler: IEEE Transactions on Plasma Science, **21,** 228 (1993).
9. W. N. G. Hitchon and E. R. Keiter: J. Comp. Phys., **112,** 226 (1994).
10. G. J. Parker, W. N. G. Hitchon and J. E. Lawler: Physics of Fluids B, **5,** 646, (1993).
11. G. J. Parker, W. N. G. Hitchon and J. E. Lawler: Phys. Lett A, **174,** 308, (1993).
12. G. J. Parker, W. N. G. Hitchon and J. E. Lawler: Physical Review E, **50,** 3210 (1994).
13. G. J. Parker and W. N. G. Hitchon: Jap. J. Appl. Phys., accepted for publication (1997).
14. V. Kolobov, G. J. Parker and W. N. G. Hitchon: Physical Review E, **53,** 1110 (1996).
15. J. P. Verboncoeur, G. J. Parker, B. M. Penetrante and W. L. Morgan: J. App. Phys., **80,** 1299 (1996).
16. U. Kortshagen, G. J. Parker and J. E. Lawler, Phys. Rev, E, **54,** 6746 (1996).
17. J. H. Ingold: *Gaseous Electronics*, (Academic Press, New York, 1978).
18. L. Tonks and I. Langmuir: Physical Review, **34,** 876 (1929).
19. W. Schottky: Z. Phys., **25,** 635 (1924).

This Page Intentionally Left Blank

MODELING OF A MAGNETIZED PLASMA: THE STATIONARY PLASMA THRUSTER

Jean-Pierre Boeuf, Laurent Garrigues, and Leanne C. Pitchford
Centre de Physique des Plasmas et Applications de Toulouse
Université Paul Sabatier, 118 Route de Narbonne
31062 Toulouse cedex, FRANCE

INTRODUCTION

The properties of closed drift thrusters or stationary plasma thrusters (SPT) make them especially suitable for applications such as satellite station-keeping and orbit transfer. They are characterized by an E×B configuration where the externally applied magnetic field is radial and perpendicular to the axial, self-consistent electric field which accelerates the ions to the exhaust. These thrusters have been studied for more than three decades and are now operating on several Russian satellites. Due to the complexity of electron transport in these devices, the properties of the stationary plasma thrusters are not clearly understood and an important research effort has been undertaken in Europe and in the US to clarify some aspects of the physical mechanisms occurring in these devices and to optimize their operating conditions.

In this paper we present some recent effort to develop numerical models of the SPT. In the first part, the basic parameters which characterize the performances of a thruster are defined. In the second part we describe the stationary plasma thruster and discuss some of the physical phenomena which are not well understood in the SPT. In the third section we briefly review the numerical models which have been developed. In the fourth and fifth section we present a quasi-neutral hybrid model of the SPT that we have developed and show some preliminary results.

CHARACTERIZATION OF A THRUSTER: SPECIFIC IMPULSE AND THRUST

The exhaust velocity of the propellant in electric thrusters can be much larger than in conventional chemical systems, and therefore, from momentum conservation, a much lower mass of propellant is necessary to obtain the same change in the velocity of the satellite[1]. The specific impulse of a thruster is, by definition, equal to the exhaust velocity of the propellant divided by the value of the gravitational constant at the earth's surface, g=9.8 m/s^2. It is therefore expressed in seconds and is about one tenth of the exhaust velocity expressed in m/s.

The thrust is defined as $T = \dot{m} U_s$ where $\dot{m}$ is the mass flow rate and U_s the exhaust velocity of the propellant. The thruster efficiency η is defined by

Electron Kinetics and Application of Glow Discharges
Edited by U. Kortshagen and L. D. Tsendin, Plenum Press, New York, 1998

$\eta = \frac{T^2}{2\dot{m}P}$ where P is the injected power.

Electric thrusters can be divided in three categories[1]: 1) the electrothermal thrusters, 2), the electromagnetic thrusters (magnetoplasmadynamic thrusters) and 3), the ion thrusters (or electrostatic thrusters).

In electrothermal thrusters the propellant is electrically heated and accelerated through the nozzle. The heating can be provided by an electric current flowing through the propellant (arcjet, power in the 10 kW range).

Electromagnetic thrusters are very ambitious devices (power larger than 1 MW) which where first designed for manned interplanetary flights. A variety of electromagnetic thrusters has been proposed. In one of them, the magnetoplasmadynamic thruster, the plasma is compressed by its self magnetic field and its subsequent expansion provides the thrust.

In ion thrusters, positive ions are extracted from a plasma and accelerated to high velocities, generally by a system of grids. The SPT is a particular type of ion thruster which does not require grids to extract the ions from the plasma. A magnetic field perpendicular to the thrust direction induces a large electric field in the plasma, which accelerates the ions to the exhaust. Ion thrusters are characterized by electric powers in the kW range. Figure 1 shows the engine efficiency as a function of specific impulse in typical thrusters.

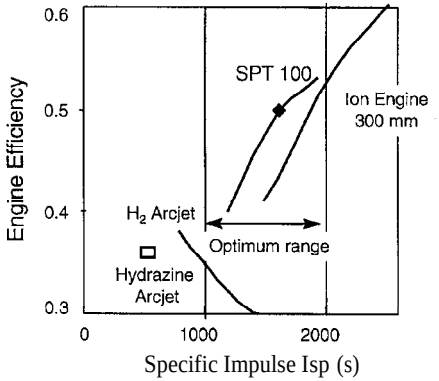

Figure 1. Engine efficiency as a function of specific impulse for different types of thrusters (after Brophy[2])

Stationary Plasma Thrusters are very efficient in the range of specific impulses (1000-2000 s) which is optimum for station-keeping and orbit transfer. The thrust to power ratio in SPT's is relatively large, on the order of 60 mN/kW.

THE STATIONNARY PLASMA THRUSTER: DESCRIPTION AND QUESTIONS

Figure 2 represents schematically the geometry of a SPT. The two coaxial cylinders are in a dielectric material. Xenon is injected from the anode, at the end of the cylinders and on the cathode side, outside the cylinders. We are mainly interested here in the plasma column which is located between the coaxial cylinders. Since the device must work under conditions of relatively low gas density (the xenon density is on the order of a few 10^{13} cm^{-3} close to the anode), and the length of the column is on the order of a few cm (typically 4 cm), the electrons undergo very few collisions from the cylinder entrance, on the cathode

side, to the anode and it would not be possible to sustain a plasma in the column without a better confinement of the electrons. This confinement is provided by a magnetic field created by coils located on the external surface of the cylinder. The magnetic field is generally radial in the exhaust region (cathode side of the cylinders) as indicated in Fig. 2.

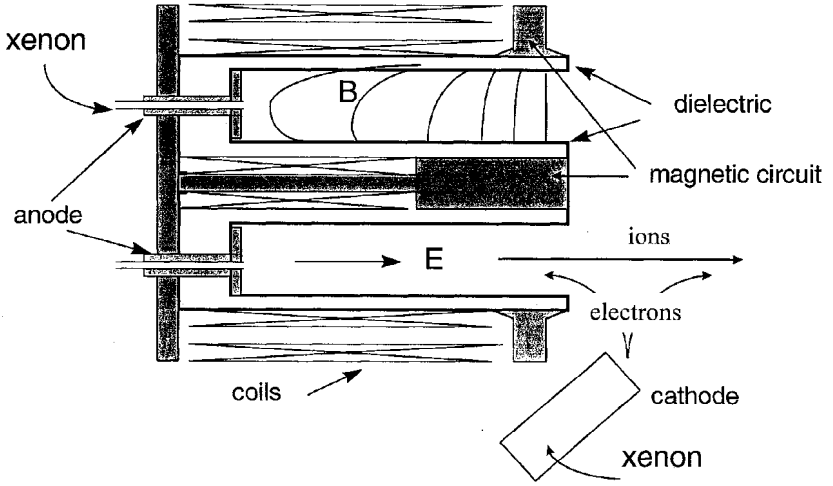

Figure 2. Schematic of a stationary plasma thruster.

Due to the closed electron drift in the E×B field, the Stationary Plasma Thrusters are also called “closed drift thrusters” or “Hall thrusters”.

The electron transit time to the anode is considerably increased by the presence of the radial magnetic field which makes possible intense ionization of the neutral gas. The potential drop in the plasma column is on the order of 200 to 300 V in standard conditions. The positive ions are not sensitive to the magnetic field and undergo practically no collisions in the column. They are accelerated toward the exhaust and reach energies corresponding to a large part of the potential drop across the column.

Typical conditions are:

- xenon flow rate at the anode: 5 mg/s
- radial magnetic field at the exhaust: 200 Gauss (about ten times less at the anode)
- voltage drop across the column: 200-300 V
- discharge current: 5 A
- internal cylinder radius: 3 cm; external cylinder radius: 5 cm
- column length: 4 cm

Several features of the SPT are not well understood. One of them is the conductivity of the column which is higher than what can be expected from the classical collisional conductivity in a transverse magnetic field. The collisional electron mobility perpendicular to a magnetic field line is given by:

$$\mu_e = \frac{e}{m\nu}\frac{1}{1+\frac{\omega_B^2}{\nu^2}}$$

where ν is the electron momentum exchange collision frequency and ω_B the electron cyclotron frequency $\omega_B = \frac{eB}{m}$.

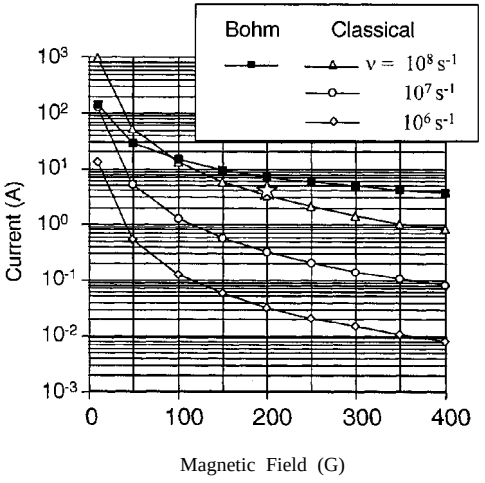

Figure 3. Estimated current in a SPT, as a function of radial magnetic field, for a plasma density of 10^{12} cm^{-3}, electric field of 50 V/cm, 3 and 5 cm cylinder radii, and different values of the electron collision frequencies using a classical mobility (open symbols), and assuming anomalous Bohm conductivity (full symbols). The star represents a typical current measurement under these conditions.

Assuming an electron mobility of this form, the order of magnitude of the current flowing through the device can be estimated by $J_T \approx en\mu_e E$ where n is the plasma density and E the electric field in the column. Plasma density and electric field in the column can be estimated from experimental measurements and are on the order of 10^{12} cm^{-3} and 50 V/cm, respectively. Calculating the current from this estimation of the plasma parameters and mobility gives the results represented in Fig. 3. The typical electron-neutral collision frequency in the SPT is in the 10^6-10^7 s^{-1} range and seems too small to be responsible for the large measured conductivity.

The problem of unexpectedly large conductivity and diffusion across the magnetic field lines in a magnetized plasma is a classical one and some authors[3] proposed that this anomalous transport results from correlated azimuthal variations in density and electric field or to Bohm diffusion[4].

Assuming anomalous Bohm conductivity (i.e. conductivity due to field fluctuations, with an electron mobility of the form $\mu_e \approx \frac{1}{16B}$) gives a current in better agreement with experimental measurements[4]. However it has not been clearly established that Bohm diffusion plays a dominant role in this device and the Russian school of Morozov and Bugrova [5-8] has proposed another interpretation of the observed anomalous conductivity. They point out that although collisions between electrons and heavy particle are not sufficient to explain the large electron mobility, electrons also collide with the dielectric walls [9-15]. Non-specular reflection of electrons and secondary electron emission by electron impact on the dielectric walls could also be responsible for the large measured conductivity (the collisions frequency of electrons with the walls is on the order of 10^8 s^{-1}, which would

give an electron mobility in the correct range (see Fig.2), but only electrons with energy higher than the Debye sheath potential could contribute to this "wall" conductivity).

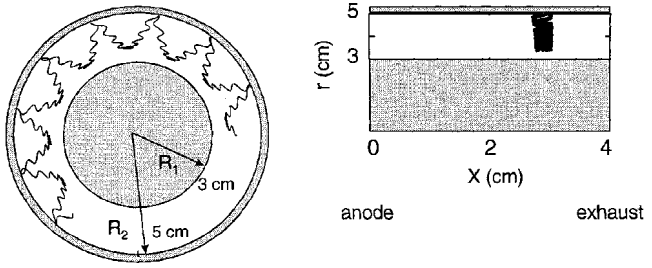

Figure 4. Example of electron trajectories in E×B fields, in the SPT geometry. The electric field is axial and uniform (50 V/cm) and the magnetic field is radial and of the form $B_r = B_0 r/R1$, with $B_0 = 100$ Gauss. The reflection on the wall is supposed to be specular and the electron is trapped.

Kaufman [4] suggested that anomalous diffusion in closed drift thrusters could shift from being caused by bulk fluctuations to being caused by wall effects (or vice-versa), as the magnetic field is increased.

Typical electron trajectories in the SPT are displayed in Figs. 4-6. Figure 4 shows an electron trajectory for a uniform axial field and a purely radial magnetic field (uniform axially and varying as l/r). The electron is supposed to be specularly reflected by the wall (mirror reflection). In these conditions it is easy to show that the electron is trapped along the axial direction and cannot drift to the anode.

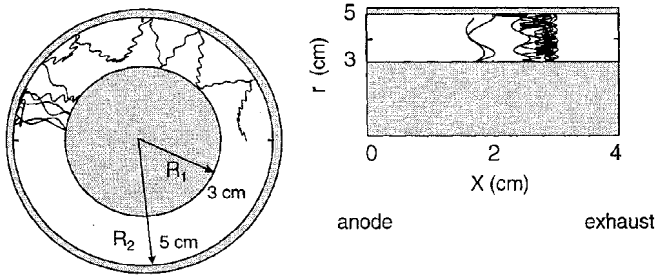

Figure 5. Example of electron trajectories in E×B fields, in the SPT geometry. The electric field is axial and uniform (50 V/cm) and the magnetic field is radial and of the form $B_r = B_0 r/R1$, with $B_0 = 100$ Gauss. The reflection on the wall is diffusive and semi-isotropic. The electron can drift to the anode.

The azimuthal motion of the electron can be seen in Fig. 4. Note that in the example shown in Fig. 4 the electron does not reach the internal wall at R_1. This is a magnetic mirror effect due to the l/r variation of the radial magnetic field.

If the velocity of the electron after the collision with the wall is randomly distributed, there is change in the electron momentum and axial motion is possible. The "collision" with the wall has the same effect as a collision with an atom or a molecule.

Monte Carlo simulations show that the. electron mobility in these conditions has the same form as for electron-atom collisions, i.e.

$$\mu_e = \frac{e}{m\nu}\frac{1}{1+\frac{\omega_B^2}{\nu^2}}$$

where the equivalent momentum exchange frequency for electron-wall collisions can be written as:

$$\nu = C\frac{v_{e,th}}{R_2 - R_1}$$

where $v_{e,the}$ is the electron thermal velocity, and C is a constant. We have performed Monte Carlo simulations in a coaxial cylinder geometry under a uniform axial electric field and a l/r radial magnetic field, assuming diffusing, semi-isotropic reflection on the walls. The electron mobility deduced from these simulations was very well represented by the expression above with a coefficient C equal to 0.3 (the electron energy distribution function was monoenergetic). A mathematical model of wall conductivity by P. Degond[16] confirmed the $\sqrt{Te}/B^2$ dependence of the electron conductivity.

Note than in E×B fields and in the limit $\omega_B >> \nu$, the electron mobility becomes

$$\mu_e \approx \frac{e}{m}\frac{\nu}{\omega_B^2}$$

In contrast with the unmagnetized case, the electron mobility now increases with increasing collision frequency.

When the magnetic field is not purely radial, some electron trajectories may never reach the walls and are trapped in the volume, as can be seen on the example of Fig. 6.

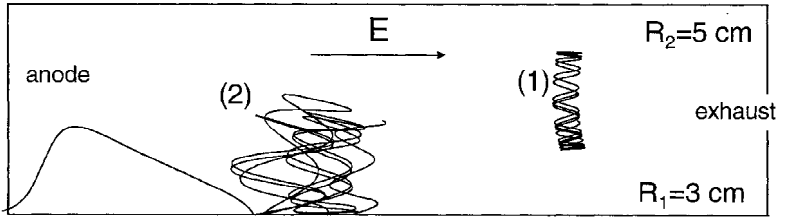

Figure 6. Examples of electron trajectories in the SPT with a uniform axial field, a large radial component of the magnetic field and a non zero axial component of the magnetic field: (1) trapped electron (mirror effect), (2) electron scattered by the wall (non specular reflection).

The fact that Morozov et al. have found that the discharge current is affected by the microscopic structure (rugosity) of the surface of the dielectric walls indicates that "wall conductivity" plays an important role in electron transport to the anode. According to Morozov et al. [5,7,11], secondary electron emission due to electron impact on the dielectric walls also contributes significantly to the overall conductivity. The secondary electron emission coefficient by electron impact becomes larger than 1 for electron energies above typically 20 to 30 eV and a non negligible number of electrons are in this energy range in the SPT.

The concept of wall conductivity can however apply only to those electrons which can overcome the potential barrier of the Debye sheath which is on the order of a few kT_e. The bulk electrons cannot reach the walls and their transport to the anode must be due to collisions or to field fluctuations (Bohm conductivity or sheath oscillations?).

It is not possible, at the moment, with only the help of the models, to demonstrate that the plasma conductivity in the SPT is due to Bohm anomalous diffusion or to electron-wall collisions and the only way to solve this problem is to confront experimental results with simulation results based on different assumptions. All the published models of the SPT therefore assume either classical conductivity (collisions with walls, neutral atoms and ions) or Bohm conductivity.

Other features of the SPT are also far from being clearly understood. For example it appears that under standard operating conditions, the current through the plasma and voltage across the column undergo oscillations at different frequencies (from kHz to MHz) some of them being of large amplitude (in the 10 kHz range). An detailed description of these oscillations is given by Choueiri.[17] One aspect of these oscillations, as predicted by a model, will be described below.

BRIEF REVIEW OF THE NUMERICAL MODELS OF THE SPT

Due to the complexity of electron transport in the SPT, the ideal numerical model would be a particle model in three dimensions. Such a model would be extremely useful to understand the azimuthal motion of the plasma and the possible effects of field fluctuations on electron transport. Such a model is however completely unpractical because it would involve considerable amounts of computation time. This is because the time step in particle models must be smaller than the plasma period (on the order of 2.10^{-11} s) and it would be necessary, in order to reach steady state to follow the time evolution of the system for more than hundreds of microseconds (the transit time of a neutral atom in the SPT is on the order of 100 μs). The plasma period constraint can be overcome by using an implicit particle model but even in this case the task seems formidable.

A few 2D (r-z) particle models have been developed to study charged particle transport in the SPT[18, 19]. Hirakawa and Arakawa[18] took into account the anomalous conductivity by introducing an oscillating azimuthal electric field (due to plasma fluctuations). This assumption was supported by a separate 2D particle simulation in a (r, θ) plane with a uniform axial field where the authors found that the azimuthal electric field and electron density oscillate in the azimuthal direction as suggested by Yoshikawa and Rose[20] and by the experiments of Janes and Lowder.[3] The phase-shift between the field and electron density oscillations was such that the averaged axial electron velocity v_D given by:

$$v_D = \frac{1}{2\pi \overline{n_e}} \int_0^{2\pi} n_e(\theta) \frac{E_\theta}{B_r} d\theta$$

was on the order of the Bohm velocity. Only a few results are presented in the paper of Hirakawa and Arakawa, and the questions of computation time, existence of steady state or current oscillations are not discussed.

A second class of numerical models of the SPT is based on the quasineutrality assumption. The assumption of quasineutrality seems reasonable to describe the plasma column of the SPT except in the Debye sheath near the wall. In a quasineutral model (see next section) Poisson's equation is not solved and the constraints related to the explicit time integration of the transport equations and Poisson's equation are therefore eliminated. This assumption considerably simplifies the numerical aspect of the simulation. In these models electron transport is generally described by fluid equations assuming either Bohm conductivity or classical conductivity including electron-wall collisions. Since the ions are not magnetized, and since the ion mean free path is much larger than the device dimensions, their transport

must be described by free fall equations, using either a fluid model or a particle (or Vlasov) model. Lentz and Martinez-Sanchez [21] developed a transient 1D quasineutral hybrid model of a stationary plasma thruster where a Boltzmann equation was used for ion transport. In the 1D, quasineutral, steady state model of Manzella, [22] ion transport was described by continuity and momentum equations assuming free fall. Similar fluid and hybrid models have been used by Morozov and Savelyev [23]. Komurasaki and Arakawa [24], and Fife[25] developed a 2D, quasineutral, steady state, hybrid model using fluid equations for electron transport and a Monte Carlo simulation for ion transport. Bohm conductivity was assumed for the electrons.

Although the above references show that an effort in numerical modeling of stationary plasma thrusters has started in several laboratories during the last few years, we are still far from having a numerical tool able to give us a clear picture of the operating regime of the SPT and to help optimize this device.

QUASINEUTRAL HYBRID MODELS OF THE SPT

We discuss here the principles of the quasineutral hybrid models of the SPT which have been developed at CPAT. These models are simple and are far from containing all the physics involved in the problem, but they can certainly help understand some aspects of the SPT. We give the principles of the models for steady state and transient situations. The models are illustrated with results from 1D, steady state and transient simulations of a stationary plasma thruster under typical operating conditions.

Principles of a Quasineutral Model

In a quasineutral model the electric field is not deduced from Poisson's equation but from a combination of the charged particle transport equations. The classical concept of ambipolar diffusion for example, is obtained from the assumption of quasineutrality, and by combining the electron and ion momentum transport equation in the drift-diffusion approximation. In a hybrid model of a stationary plasma thruster, the drift-diffusion equation is a reasonable approximation of the momentum transport equation for electrons. Positive ions are collisionless. A natural way of implementing quasineutrality in a numerical model of the SPT would therefore be to proceed as follows:

i) for a given field distribution and ionization rate distribution, the ion free fall equations (fluid or microscopic) are integrated between times t and $t+\Delta t$. This gives the ion density at time $t+\Delta t$.

ii) the neutral atom density at time $t+\Delta t$ is calculated using fluid or microscopic transport equations.

iii) knowing the plasma density from i), the electron continuity and momentum transport equations are used to calculate the field distribution.

iv) the electron energy equation is used to calculate the electron mean energy at time $t+\Delta t$. The distribution of the ionization rate is deduced from the mean electron energy (assuming a given shape of the electron energy distribution function). Proceed to step i).

The details of the equations are given below.

1D Steady State Mode

The 1D model we have developed is based on the simple following assumptions:

i) quasineutrality is assumed

ii) all the quantities depend only on the axial position x parallel to the cylinder axis
iii) the electric field is axial and the magnetic field is radial, with a given axial distribution
iv) the neutral atoms are emitted at the anode and have a constant velocity v_0 in the x direction
v) the positive ions are created by electron impact ionization of the neutral atoms with an initial velocity equal to v_0 ; their velocity is parallel to x and they are collisionless
vi) electrons are described by a continuity equation, a drift-diffusion momentum transport equation, and a phenomenological energy equation.

Using these assumptions, the neutral atoms transport equations reduce to:

$$v_0 \frac{dn_a}{dx} = -S(x) = -n(x) n_a(x) k_i(x)$$

where n_a is the neutral atom density, n is the plasma density and k_i is the ionization rate.

At steady state, the Vlasov equation for ions does not need to be solved since the ion density can be simply written:

$$n(x) = \int_0^x \left[\frac{S(x_0)\, dx_0}{\left(v_0^{\,2} + 2\frac{e}{M}\left(V(x_0) - V(x)\right)\right)^{1/2}} \right]$$

where M is the ion mass and V(x) is the potential at x.

The steady state continuity equations for electrons, positive ions and neutral atoms imply:

$$d\varphi_e / dx = d\varphi_p / dx = -d\varphi_a / dx = S(x)$$

where φ_e , φ_p , and φ_a are the electron, ion, and neutral atom fluxes, respectively. The integration of theses equations give the following current continuity relations:

$$\varphi_p(x) = \varphi_a(0) - \varphi_a(x)$$
$$\varphi_e(x) = \varphi_e(d) - \varphi_a(x) + \varphi_a(d)$$

where d is the abscissa at the exhaust.

The electric field distribution is then obtained from the electron momentum equation. If we neglect electron diffusion, we can simply write:

$$E(x) = -\frac{\varphi_e(x)}{n\mu_e}$$

The potential drop across the column is imposed and the electron flux at the exhaust, i.e. the electron flux entering the column, is deduced from the potential boundary condition:

$$V(d) - V(0) = -\int_0^d E(x)dx$$

the electron mobility is given by the classical expression:

$$\mu_e = \frac{e}{m\nu} \frac{1}{\left(1 + \frac{\omega_B^{\,2}}{\nu^2}\right)}$$

and ν is supposed to be related to electron-wall collisions and is supposed to be given by:

$$\nu = 0.3 \frac{v_{th,e}}{(R_2 - R_1)}$$

where $v_{th,e} = \sqrt{\frac{8kT_e}{\pi m}}$ is the electron thermal velocity, and R_1 and R_2 are the radii of the coaxial dielectric cylinders.

The electron mean energy $\varepsilon_e = \frac{3}{2}kT_e$ is obtained from the phenomenological energy equation:

$$\frac{d\varepsilon_e}{dx} = -eE - \delta\varepsilon_e$$

The parameter δ is taken to be constant and equal to 2 cm^{-1} in the results presented below. δ is an energy relaxation length. This parameter must account for the electron energy losses due to collisions with the walls (including secondary emission) and with the gas atoms. The effect, on the global results, of more realistic forms of the energy loss per unit length is being studied.

Finally, the ionization rate is obtained from the assumption of a Maxwellian distribution function by the relation (see, e.g. Raizer[26]):

$$k_i = \frac{1}{n}\int f_e(x,v)Q_i v\,dv \approx A\left[\frac{8kT_e}{m\pi}\right]^{1/2}(2kT_e + U_i)exp\left[-\frac{U_i}{kT_e}\right]$$

where A is taken to be $3\cdot10^{-17}$ cm^2/eV for xenon.

An under-relaxation iterative method was used to solve the above system of equations.

An example of steady state solution is shown in Fig. 7 for a SPT 100 (L=4 cm, R_1 =3 cm, R_2=5 cm). The electric field and potential distribution, the plasma density, neutral atom density, ionization source term, electron mean energy and imposed radial magnetic field are displayed on this figure. Two distinct regions appear in this figure: a uniform field region 3 cm long, on the anode side, where the ionization rate and plasma density are relatively small, and a non uniform field region where the positive ions are accelerated. The ionization rate is maximum at the interface between this two regions. The maximum plasma density is on the order of 10^{12} cm^{-3}. Note that the neutral atom concentration falls to almost zero after the ionization region, i.e. most of the neutral atoms are ionized. The maximum ion flux at the exhaust in this model is obviously equal to the neutral atom flux at the anode.

In spite of the simplicity of the model, the predicted features are in qualitative agreement with the experimental observations. Some of the quantitative properties (e.g. plasma density, discharge current) of the discharge are also in reasonable agreement with the experiments. However one point which is difficult to extract from the published experimental work is the detailed structure of the electric filed distribution in the conduction region between the anode and the acceleration (non uniform field) region.

The model predicts a rather large (on the order of 50 V/cm), positive electric in that region. Some of the experimental results indicate that the plasma potential reaches a maximum in the conduction region. This would imply a reversal of the axial electric field in that region. The actual field distribution in this region is probably very dependent on the magnetic field distribution. The model described above cannot predict a field reversal since electron diffusion has been neglected.

This model can only describe a steady state discharge or the time averaged properties of the discharge. Since the experiments show that the SPT exhibits current oscillations in a very large frequency band, it is interesting to generalize this model to transient situations. This is described below.

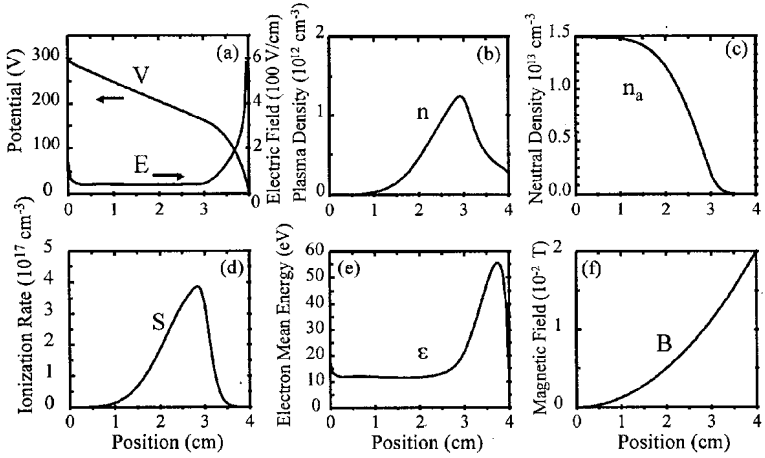

Figure 7. Axial variation of (a) electric field and potential, (b) plasma density, (c) neutral density, (d) ionization source term, (e) mean electron energy, from a 1D quasi-neutral hybrid steady state model of the SPT in the conditions defined by: voltage across the column: 300 V, xenon flow rate: 5 mg/s, dielectric cylinder radii: 3 and 5 cm, radial magnetic field distribution displayed in (f).

1D Transient Model

We are interested here in time scales much longer than the electron transit time. We therefore use the same time independent equations as in the previous section, to describe electron continuity, and momentum and energy transport.

Time dependent equations are used, on the other hand, for neutral atom and ion transport. The neutral continuity equation is now written:

$$\frac{\partial n_a}{\partial t} + \mathrm{v}_0 \frac{\partial n_a}{\partial x} = -n(x) n_a(x) k_i(x)$$

The ion density can no longer be obtained from a simple integral equation and the following Vlasov equation must be solved:

$$\frac{\partial f(x,\mathrm{v}_x)}{\partial t} + \mathrm{v}_x \frac{\partial f(x,\mathrm{v}_x)}{\partial x} + \frac{e}{M} E \frac{\partial f(x,\mathrm{v}_x)}{\partial \mathrm{v}_x} = S_{\mathrm{v}x}(x,\mathrm{v}_x)$$

where

$$S_{\mathrm{v}_x}(x,\mathrm{v}_x) = n(x) n_a(x) k_i(x) \delta(\mathrm{v}_x - \mathrm{v}_0) = S(x) \delta(\mathrm{v}_x - \mathrm{v}_0)$$

f is the ion distribution function, v_x is the x component of the ion velocity, and δ is the Dirac function (the ions are supposed to be created with a velocity equal to v_0). The electron density, n, equal to the ion density (quasi-neutrality)is deduced from the ion distribution function by:

$$n(x,t) = \int f(x,\mathrm{v}_x,t) d\mathrm{v}_x$$

The electron flux is deduced from the continuity equations

$$\frac{\partial \varphi_e}{\partial x} = \frac{\partial \varphi_p}{\partial x}$$

where the ion flux is obtained from the solutions of the ion Vlasov equation.

The neutral atom density and ion distribution function are integrated over one time step using standard upwind numerical schemes. The electric field distribution is recalculated after each time step as above, i.e. using the equations:

$$E(x,t) = -\frac{\varphi_e(x,t)}{n(x,t)\mu_e} \quad \text{and} \quad V(d) - V(0) = -\int_0^d E(x)dx$$

The electron mean energy and the ionization rate are calculated at each time step as before.

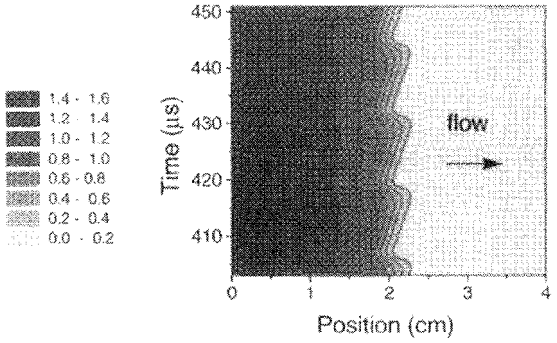

Figure 8. Space and time variations of the neutral atom density in the SPT in the form of contour curves (similar conditions as in Fig. 7, except that the voltage drop across the column is set to 250 V instead of 300 V) obtained from the 1D1V quasi-neutral hybrid model. The anode is located at x= 0 and the exhaust at x=4 cm. The origin in time is arbitrary.

The transient model described above is close to the quasineutral hybrid model of Morozov and Savelyev [23] but some of the assumptions (e.g. form of the ionization rate and the energy loss term) are different.

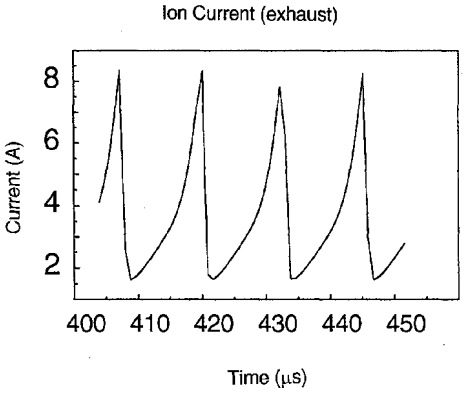

Figure 9. Time evolution of the ion current at the exhaust showing strong oscillations at a frequency on the order of 100 kHz.

This model has been used to study the transient evolution of the device under conditions similar to the steady state example above. The conditions are similar to those of Fig. 7 except for the column voltage drop which is 250 V instead of 300 V

We found that the transient solutions of the system of equations described above exhibit systematic oscillations at a frequency on the order of 100 kHz. The frequency of the oscillations can be changed (in the 20kHz-100 kHz range) by adjusting the parameters characterizing the loss term in the electron energy equation. These oscillations are associated with a small motion of the position of the neutral density gradient as shown in

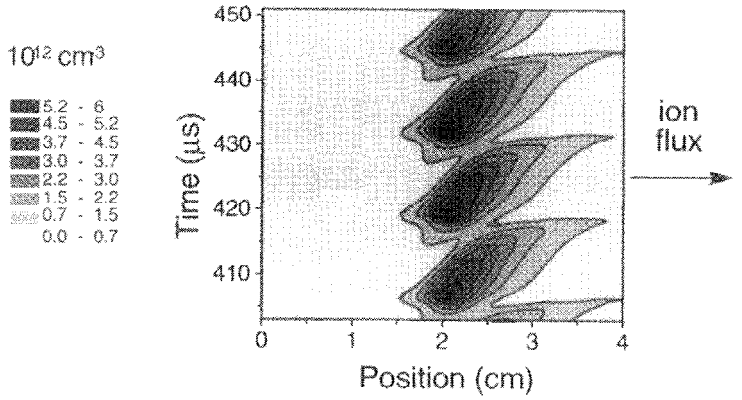

Figure 10. Space and time variations of the plasma density in the SPT in the form of contour curves obtained from the 1D1V quasi-neutral hybrid model (same conditions as Fig. 8). The anode is located at x= 0 and the exhaust at x=4 cm. The origin in time is arbitrary.

The ion current displayed in Fig. 9 exhibits large amplitude oscillations. The oscillations of the position of the neutral density gradient induce a strong oscillation of the ionization source term which leads to strong oscillations of the plasma density (see Fig. 9).

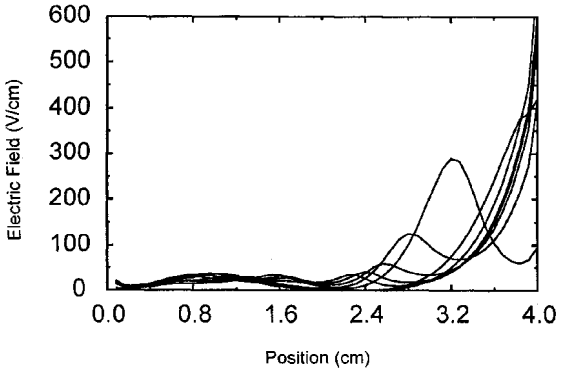

Figure 11. Electric field distribution at different times during one cycle of the current oscillations (same conditions as in Fig. 8).

The qualitative nature of the oscillations and their large amplitude seem to correspond to the reported experimental observations for this frequency range[17,27,28]. The model of

Morozov and Savelyev [23] predicts discharge oscillations which are also in qualitative agreement with the results presented above.

The oscillations of the plasma density are associated with a large amplitude electric field wave as shown in Fig. 11 where the space and time variations of the electric field over one period of the current oscillations are displayed. Figure 12 shows the spatial variations of the ion velocity distribution function at different times, in the form of contour curves. The darker regions of Fig. 12 correspond to larger values of the ion distribution function. The oscillations of the ion flux at the exhaust appear clearly on this figure.

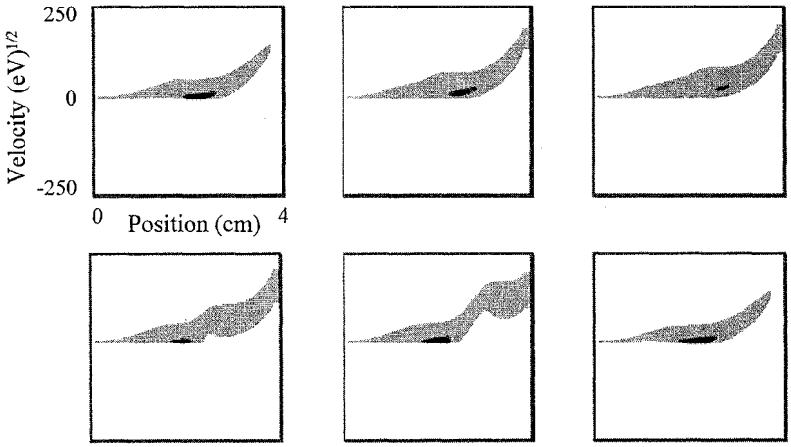

Figure 12. Phase space diagram of the positive ion density at different times during once cycle of the current oscillations (same conditions as in Fig. 8).

CONCLUSION

The mechanisms of electron transport in a Stationary Plasma Thruster are still not clearly understood and numerical or theoretical models cannot at this moment state whether the measured conductivity in this device is due to electron-wall collisions or to field fluctuations.

Simple quasineutral hybrid models of the SPT where the electrons are described as a collisional fluid and ions are assumed to be collisionless have been developed. These models can predict reasonably well the discharge properties when some parameters (electron mobility, electron energy loss coefficient) are adequately adjusted. A transient version of these quasineutral models can reproduce well the low frequency, large amplitude oscillations observed in the SPT. The current oscillations are associated with a small oscillation of the location of the neutral density gradient and ionization source region. More work is however needed to confirm that the model provides the good physical interpretation of the oscillations.

ACKNOWLEDGMENTS

The authors would like to acknowledge the support of CNES in the frame of the "Groupement De Recherche Propulsion Plasma pour Vols Orbitaux".

REFERENCES

1. P. J. Wilbur, R. G. Jahn, and F. C. Curran, Space electric propulsion plasmas, *IEEE Transactions on Plasma Science* 19:1167 (1991).
2. J. R. Brophy, “Stationary plasma thruster evaluation in russia,” Report No. JPL 92-4 (1992).
3. G. S. Janes and R. S. Lowder, Anomalous electron diffusion and ion acceleration in a low-density plasma, *Phys. Fluids* 9:1115 (1966).
4. H. R. Kaufman, Technology of closed-drift thrusters, *AIAA Journal* 23:78 (1985).
5. A. I. Morozov, Y. V. Esinchuk, G. N. Tilinin, A. V. Trofimov, Y. A. Sharov, and G. Y. Schepkin, Plasma accelerator with closed electron drift and extended acceleration zone, *Sov. J. Plasma Phys.* 17:38 (1972).
6. A. I. Morozov, Stationary plasma thruster (SPT) development steps and future perpectives, *23rd International Propulsion Conference,* AIAA-93-101, Seattle, 1993.
7. A. I. Bugrova, V. Kim, N. A. Maslennikov, and A. I. Morozov, Physical processes and characteristics of stationary plasma thrusters with closed electron drift, *22nd International Propulsion Conference,* IEPC-91-079, Viareggio, 1991.
8. A. I. Bugrova, A. V. Desiatskov, V. K. Kharchevnikov, and A. I. Morozov, Main features of physical processes in stationary plasma thrusters, *23rd International Propulsion Conference,* IEPC-93-247, Seattle, 1993.
9. A. I. Morozov and A. P. Shubin, Electron kinetics in the wall-conductivity regime:I, *Sov. J. Plasma Phys.* 10:728 (1984).
10. A. I. Morozov and A. P. Shubin, Electron kinetics in the wall-conductivity regime:II, *Sov. J. Plasma Phys.* 10:734 (1984).
11. A. I. Morozov, Conditions for efficient current transport by near-wall conduction, *Sov. Phys. Tech. Phys.* 32:901 (1987).
12. A. I. Morozov and A. P. Shubin, Analytic methods in the theory of near-wall conductivity:I, *Sov. J. Plasma Phys.* 16:711 (1990).
13. A. I. Morozov and A. P. Shubin, Analytic methods in the theory of near-wall conductivity:II, *Sov. J. Plasma Phys.* 16:713 (1990).
14. A. I. Bugrova, A. I. Morozov, and V. K. Kharchevnikov, Wall-conductivity effects in channel of a closed-drift-circuit plasma accelerator, *Sov. Tech. Phys. Lett.* 9:1 (1983).
15. A. I. Bugrova, A. I. Morozov, and V. K. Kharchevnikov, Experimental investigation of near-wall conductivity, *Sov. J. Plasma Phys.* 16:849 (1990).
16. P. Degond, Un modèle de conductivité pariétale: application au moteur à propulsion ionique, *C.R. Acad. Sci. Paris* 322:797 (1996); P. Degond, On a model of near-wall conductivity and its application to plasma thrusters, to appear in SIAM J. on Appl. Math (1997).
17. E. Y. Choueiri, Characterization of oscillations in closed drift thrusters, *30th Joint Propulsion Conference,* AIAA-94-3013, Indianapolis, 1994.
18. M. Hirakawa and Y. Arakawa, Particle simulation of plasma phenomena in Hall thrusters, *24th International Electric Propulsion Conference,* IEPC-95-164, Moscow, 1995.
19. J. C. Adam and A. Heron, “Modélisation d'un propulseur ionique de type SPT,” unpublished (1996).
20. S. Yoshikawa and D. J. Rose, Anomalous diffusion of a plasma across a magnetic field, *Phys. Fluids* 5:334 (1962).
21. C. A. Lentz and M. Martinez-Sanchez, Transient One Dimensional Numerical Simulation of Hall Thrusters, *29th Joint Electric Propulsion Conference,* AIAA-93-2491, Monterey, 1993.

22. D. H. Manzella, Simplified numerical description of SPT operation, *24th International Electric Propulsion Conference,* IEPC-95-34, Moscow, 1995.

23. A. I. Morozov and V. V. Savelyev, Numerical simulation of plasma flow in SPT, *24th International Electric Propulsion Conference,* IEPC-95-161, Moscow, 1995.

24. K. Komurasaki and Y. Arakawa, Two-Dimensional Numerical Model of Plasma Flow in a Hall Thruster, *Journal of Propulsion Power* 11: 1317 (1995).

25. M. J. Fife, Master of Science Thesis, Massachusetts Institue of Technology, 1995.

26. Raizer, Gas Discharge Physics Springer-Verlag Berlin Heidelberg, (199 1).

27. V. Zhurin, J. Kahn, H. Kaufman, K. Kozubsky, and M. Day, Dynamic characteristics of closed drift thrusters, *23rd International Electric Propulsion Conference,* IEPC-93-095, Seattle, 1993.

28. GDR CNES-CNRS-SEP-ONERA, *Groupement de Recherche "Propulsion Plasma pour Vols Orbitaux"* unpublished results (1996).

DC POSITIVE COLUMN IN THE NONLOCAL REGIME

J. H. Ingold
One Bratenahl Place, Suite 610
Cleveland, OH 44108 USA

INTRODUCTION

The consensus throughout the period 1920-1970 appears to be that the EEDF in the DC positive column is Maxwellian, and that average energy of the electrons is radially invariant. This consensus is supported in review articles by Druyvesteyn and Penning[1] and Francis[2] in which positive column pedagogy is based on Maxwellian EEDF's, although the possibility of non-Maxwellian EEDF's at *low current* is recognized in both review articles. Direct consequences of the Maxwellian EEDF assumption are: (i) Average energy, transport coefficients, and collision frequencies are radially invariant; (ii) Power input per unit volume due to Joule heating and power dissipated per unit volume due to elastic and inelastic collisions are equal in each volume element of the positive column; (iii) Radial effects such as heat flow are negligible. A positive column having these characteristics is said to be operating in the *local regime*, because electron properties are in equilibrium with the axial electric field in each volume element. But what about other EEDF forms? If transport coefficients and collision frequencies are radially invariant, then they can be parametrized by the axial electric field as in a O-D Boltzmann calculation, leading to an improvement over the Maxwellian EEDF assumption. Strictly speaking, when electron-electron collisions can be ignored, then a Maxwellian EEDF results only when the electron-atom momentum transfer collision frequency is independent of electron energy. Realizing that real gases do not have this kind of collision frequency, Blank[3] asks under what conditions can it be assumed that positive column transport coefficients and collision frequencies are radially invariant, similar to conditions found in a drift tube experiment. In agreement with Bernstein and Holstein[4], Blank concludes this assumption is valid for an energy-dependent momentum transfer collision frequency when "the electron energy relaxation distance is small compared with positive column radius." To put this conclusion in perspective, consider a neon-like gas with atomic mass of 20 AMU and electron-atom momentum transfer cross section Q_{ea} of 2.6 Å^2. Blank's condition expressed in mathematical form

Electron Kinetics and Application of Glow Discharges
Edited by U. Kortshagen and L. D. Tsendin, Plenum Press, New York, 1998

is PR >> $0.283\sqrt{M/m}Q_{ea}^{-1}$ = 21 Torr-cm where P is gas pressure in Torr, R is positive column radius in cm, M/m is mass ratio of atoms and electrons, and Q_{ea} is expressed in Å². It is shown later in the present article that the value of PR must be in the range 50-100 Torr-cm for the assumption of radially invariant transport coefficients and collision frequencies in a neon positive column to be valid.

Evidently, when $PR < 0.283\sqrt{M/m}Q_{ea}^{-1}$, the Local Model is not valid. It is argued in [4] that radial effects become important at low pressure, causing electron properties such as average energy, axial drift velocity, etc., to have significant radial variation. In this case, transport coefficients and collision frequencies cannot be parametrized by the axial electric field as in a 0-D Boltzmann calculation, because the axial electric field is independent of radial position. A positive column having these characteristics is said to be operating in the *nonlocal regime*. Radial terms must be taken into account in solving the Boltzmann equation, meaning that a 1-D Boltzmann solution is required in the nonlocal regime.

In an important series of papers beginning in 1974, Tsendin[5] extended the positive column work begun by Bernstein and Holstein and elucidated further by Blank. Tsendin and followers cite several features of the nonlocal model which are different from those of the local model: (i) The Boltzmann relation between electron density $n(r)$, space charge potential $\phi(r)$, and electron temperature θ no longer holds, i. e., $n(r) \neq n(0)\exp[\phi(r)/\theta]$ (ii) There is significant radial variation in average energy of electrons, hence in transport coefficients and collision frequencies; (iii) Likewise, there can be a significant difference between power input by Joule heating and power dissipation due to collisions in a given volume element of the discharge; (iv) To account for (iii), a significant amount of heat must flow inward in the electron gas; (v) Wall potential is much less.

Each of these five different features is corroborated by recently published numerical solutions of the 1-D Boltzmann equation[6]. Features (ii) and (v) are corroborated by additional numerical solutions of the 1-D Boltzmann equation[7] and by other numerical methods, including Monte Carlo (MC) [9], the Nonlocal Approximation[10], and the Convective Scheme (CS) [11, 12]. Table 1 summarizes the comparison of local model calculations[8] with these nonlocal methods. The striking difference in wall potential of the local model compared with that of the nonlocal models strongly suggests that the traditional local model is inadequate at values of PR on the order of unity and less. The purpose of this article is to show that traditional local theory can be extended to the nonlocal regime by adding electron energy balance with radially varying average energy, achieving much better agreement with Reference [6], for example.

Before turning to the subject of the present article—Nonlocal Moment Method—it is instructive to review 1-D Boltzmann methods in use today for analyzing the DC positive column. Methods which do not start with the 1-D Boltzmann equation and the two-term Legendre expansion are not discussed. Those which do can be divided arbitrarily into four categories: (1) Nonlocal Kinetic Method—valid at all PR; (2) Nonlocal Kinetic Approximation Method—valid at low PR; (3) Local Moment Method—valid at high PR, but often used at low PR; (4) Nonlocal Moment Method—valid at all PR. The Nonlocal Kinetic Method is a first principles method which is valid at all values of PR for which the 1-D Boltzmann equation based on the two-term Legendre expansion of the EEDF is valid. The EEDF is denoted by $f(\mathbf{r}, \mathbf{v})$ and the two-term expansion is

$$f(\mathbf{r}, \mathbf{v}) = f_0(r, v) + v^{-1}\mathbf{v} \cdot \mathbf{f_1}(r, v).$$

Measurable properties of the positive column are calculated directly from f_0 and $\mathbf{f}_1$. A prime example of this method was published recently by Uhrlandt & Winkler[6]. The Nonlocal Kinetic Approximation Method[4, 5] is also based on the two-term Legendre expansion of the EEDF. However, solution of the 1-D Boltzmann equation for f_0 and $\mathbf{f}_1$ is avoided by assuming further that f_0 and $\mathbf{f}_1$ can be expanded according to the scheme

$$f_0(r,\epsilon) = f_{00}(\epsilon) + f_{01}(r,\epsilon) + \ldots, \quad \mathbf{f}_1(r,\epsilon) = \mathbf{f_{10}}(r,\epsilon) + \mathbf{f_{11}}(r,\epsilon) + \ldots,$$

where total energy $\epsilon = \frac{1}{2}mv^2 - e\phi(r)$ and f_{00} is given by the O-D Boltzmann equation obtained from the 1-D Boltzmann equation by radially averaging each term, while the radial component of $\mathbf{f}_{10}(r,\epsilon)$ is taken to be zero. The results are similar to those of the First Principles Method at low values of PR, but start diverging near PR = 1. The Local Moment Method, or traditional model, is not based on solution of the 1-D Boltzmann equation, but on moments of it—moments of either the pristine 1-D Boltzmann equation or of the equations for f_0 and $\mathbf{f}_1$. A key assumption of this method is that electrons are in *equilibrium* with the axial electric field, implying that the energy imparted to the electrons by a steady, uniform field is exactly balanced by energy lost in elastic and inelastic collisions with heavy particles *in each volume element of the discharge.* The Nonlocal Moment Method is the subject of the present article, and is discussed in detail in the next section.

Table 1. Comparison of Local Moment Method with Other Methods[a]

GAS TYPE	METHOD	E_z (V/cm)	ϕ_w (V)	$n(0)$ (10^{10}/cc)	$\bar{\nu}_{ii}$ (10^5/sec)	P[b]	REF
HELIUM	NONLOCAL[c]						
PR = 0.045 Torr-cm	MC						
I = 10 mA	CS	48	52	6	450	YES	[11]
R = 1 mm	LOCAL0D[d]	39	84	11	400	YES	[8]
ARGON	NONLOCAL	12	15			NO	[10]
PR = 0.85 Torr-cm	MC	12	18			NO	[9]
$\bar{n}_i = 1\times10^{10}$ cm^{-3}	CS	11	17	2.6	1.1	NO	[12]
R = 1 cm	LOCAL0D	15	52	2.5	2.2	YES	[8]
ARGON	NONLOCAL	6	16			NO	[10]
PR = 0.28 Torr-cm	MC	6	17			NO	[9]
$\bar{n}_i = 1\times10^{10}$ cm^{-3}	CS	6.3	17	2.2	3	NO	[12]
R = 1 cm	LOCAL0D	7.4	53	2.3	3.5	YES	[8]
ARGON	NONLOCAL	1.4	24			NO	[10]
PR = 0.0085 Torr-cm	MC	1.4	24			NO	[9]
$\bar{n}_i = 1\times10^{10}$ cm^{-3}	CS	1.4	24		6.7	NO	[12]
R = 1 cm	LOCAL0D	0.9	64	2.1	5.1	YES	[8]
NEON	NONLOCAL	2.7	41			NO	[5]
PR = 0.1 Torr-cm	MC						
I = 10 mA	CS						
R = 1 cm	LOCAL0D	2.5	59	0.33	7.9	YES	[8]

[a] $-\phi_w$ is wall potential relative to axis; $\bar{n} = (2/R^2)\int n(r)rdr$; $\bar{\nu}_i = (2/R^2)\int n(r)\nu_i(r)rdr/\bar{n}$.
[b] YES in this column means that Poisson's equation is solved self-consistently with equations of motion, etc., to give the radial potential distribution. NO means either that the radial potential distribution is assumed, or that the plasma (ambipolar) approximation $n(r) = n_i(r)$ is assumed.
[c] NONLOCAL means Nonlocal Kinetic Approximation Method
[d] LOCAL0D means Local Moment Method with O-D Boltzmann EEDF.

NONLOCAL MOMENT METHOD

General Remarks

This section deals with extension of the Local Moment Method, or traditional local model, of the DC positive column to the nonlocal regime where electrons are no longer in equilibrium with the axial field. The extension is accomplished by including the energy balance equation obtained by taking the third moment of the 1-D Boltzmann equation after the the two-term Legendre expansion is made. As with the Local Moment Method, the EEDF must be assumed in order to evaluate transport coefficients and collision frequencies appearing in the moment equations. A key assumption of the Nonlocal Moment Method is that transport coefficients and collision frequencies bear the same relation to average energy, which is a function of radial position in the nonequilibrium positive column, as they do in the Local Moment Model—according to a 0-D Boltzmann solution. This assumption is tantamount to assuming a form for the EEDF which depends on electron density, average velocity, and average energy in a particular way that ensures correct values of transport quantities when electrons are in equilibrium with the electric field[13]. This method differs from the Local Moment Method in that average energy, transport coefficients, and collision frequencies can vary across the positive column, even though the axial field does not. This method has several advantages over the Local Moment Method, not the least of which is validity over the entire range of PR, just as with the first principles Nonlocal Kinetic Method. It can be shown that the Nonlocal Moment Method transitions naturally to the Local Moment Method at high values of PR, so it is straightforward to establish the PR range of validity of the Local Moment Method. Due to space limitation, however, discussion of the PR boundary between nonlocal and local regimes is beyond the scope of the present article.

Equations

Formulation of this problem is based on moments of the Boltzmann equation taken after the two-term Legendre expansion is made. This procedure leads to the following equations for the DC positive column with the electron gas characterized by particle density n, particle current density Γ, average energy u, and heat current density $\mathbf{H}$:

$$\mathbf{\Gamma} = -\nabla(nD) - \mu\mathbf{E}n, \tag{1}$$

$$\nabla \cdot \mathbf{\Gamma} = \nu_i n, \tag{2}$$

$$\mathbf{H} = -\nabla(nG) - \beta\mathbf{E}n, \tag{3}$$

$$\nabla \cdot \mathbf{H} = -\mathbf{\Gamma} \cdot \mathbf{E} - \left(2\frac{m}{M}\nu_u u + \nu_x V_x + \nu_i V_i\right) n, \tag{4}$$

where D, μ, G, and β are transport coefficients defined by Allis[14], ν_u is elastic energy exchange collision frequency, $\nu_{x,i}$ is excitation/ionization frequency, and $V_{x,i}$ is excitation/ionization energy. D and μ are the well-known coefficients of particle diffusion and mobility, respectively, while Allis[14] calls G and β the coefficients of heat diffusion and thermoelectricity, respectively. The electric field $\mathbf{E}$ has two components—the imposed axial field E_z, which is independent of r and z, and the radial space charge field $E_r(r)$. The vectors Γ and $\mathbf{H}$ each have axial and radial components which vary with radial position.

Ions with zero temperature, mobility μ_i, mass m_i, and density n_i are characterized by ion momentum balance:

$$\Gamma_r = -\frac{\mu_i}{r}\frac{d}{dr}\left[r\left(\frac{m_i\Gamma_r^2}{en_i}\right)\right] + \mu_i E_r n_i, \tag{5}$$

where it is assumed that $\Gamma_{ir} = \Gamma_r$, reflecting the assumption of a steady state.

Finally, Poisson's equation relating radial space charge field to space charge density is:

$$\frac{1}{r}\frac{d(rE_r)}{dr} = \frac{e}{\epsilon}(n_i - n), \tag{6}$$

where $e = 1.6\times10^{-19}$ C is electronic charge and $\epsilon = 8.85 \times 10^{-14}$ C/V/cm is permittivity.

Equations (1), (2), (5), and (6) form the basis of the Local Model with radially invariant average energy, transport coefficients, etc. Extension of the Local Model to the nonlocal regime is accomplished by the addition of (3) and (4) to account for radial heat flow in the electron gas with radially varying average energy.

The objective of this section is to apply the equations given above to the neon positive column investigated by Urhlandt & Winkler[6], who applied the Nonlocal Kinetic Method to a 0.75 Torr neon discharge in a tube of 1.7 cm radius with a current of 10 mA. They showed that such a discharge operates in the nonlocal regime because power expended in collisions is not equal to the power generated by the external field in each volume element of the discharge. On axis, for example, they found that Joule heating amounts to 6.4 mW/cm^3, while the power expended in collisions amounts to 16 mW/cm^3. To maintain this discharge in the steady state, a significant amount of energy flow from the outer region of the discharge to the inner region is required.

To reach this objective, the approach taken here is to assume a form for the EEDF which depends on electron density, average velocity and average energy in a particular way that ensures correct values of transport quantities when electrons are in equilibrium with the electric field. In other words, transport coefficients are assumed to be functions of radially varying average energy, not of radially constant E_z/N. Still another way of saying this is to say that transport coefficients are parametrized by average energy, not by E_z/N[15]. The parametrization is carried out by solving the 0-D Boltzmann equation and constructing a table of transport coefficients and collision frequencies versus average energy, then solving (1)-(6) for the radial variation of the six quantities—$n(r)$, $n_i(r)$, $u(r)$, $\Gamma_r(r)$, $H_r(r)$, $E_r(r)$.

To solve (1)-(6) by a Runge-Kutta technique, it is convenient to eliminate **E** from (3) by means of (1) to give

$$\mathbf{H} = \frac{\beta}{\mu}\mathbf{\Gamma} + \frac{\beta}{\mu}\nabla(nD) - \nabla(nG),$$

so that

$$H_r = \frac{\beta}{\mu}\Gamma_r + \left(\frac{\beta}{\mu} - \frac{G}{D}\right)D\frac{dn}{dr} - n\left(\frac{\partial G}{\partial u} - \frac{\beta}{\mu}\frac{\partial D}{\partial u}\right)\frac{du}{dr}. \tag{7}$$

The first term on the right represents an energy flow due to convection. The second term on the right represents an energy flow due to diffusion, which can be directed either inward or outward, depending on the relative magnitudes of β/μ and G/D. When the EEDF is Maxwellian, due to electron-electron collisions, for example, then $\beta/\mu - G/D = 0$, resulting in little or no energy flow due to diffusion or conduction.

However, in the case of neon when e-e collisions are ignored, it will be seen that the quantity $\beta/\mu - G/D$ is positive, so. that the energy flow due to diffusion is directed inward, accounting for apparent nonlocal behavior of the low current neon discharge[16]. The third term on the right represents energy flow due to thermal conduction. The quantity

$$n\left(\frac{\partial G}{\partial u} - \frac{\beta}{\mu}\frac{\partial D}{\partial u}\right)$$

is nothing more or less than the thermal conductivity of the electron gas; this quantity is positive so that energy flow due to thermal conduction is directed outward in the neon discharge.

The energy balance equation (4) becomes

$$\frac{1}{r}\frac{d(rH_r)}{dr} = \mu n E_z^2 - \Gamma_r E_r - \left(2\frac{m}{M}\nu_u u + \nu_x V_x + \nu_i V_i\right) n, \tag{8}$$

when the relation $\Gamma_z = -\mu n E_z$ is used to eliminate Γ_z. The second term on the right side of this equation represents a cooling effect due to the radial electron current density flowing against the radial space charge field. This term is neglected in the present treatment because it generally is small compared with the term $\mu n E_z^2$. Γ_r lies between $\mu_i n_i E_r$ and $n_i\sqrt{-2e\phi/m_i}$, where the space charge potential $\phi(r)$ is related to E_r by

$$\phi(r) = -\int_0^r E_r(\rho)d\rho,$$

depending on whether ion motion is limited by ion mobility or by ion inertia. In the mobility-limited case, for example, $\Gamma_r E_r = \mu_i n_i E_r^2$, which is small compared with $\mu n E_z^2$, except, perhaps, very near the wall.

For clarity, the equation system is repeated here. There are six equations to be solved for the six quantities (r), $u(r)$, $n_i(r)$, $\Gamma_r(r)$, $H_r(r)$, $E_r(r)$:

$$\frac{dn}{dr} = \left[D\frac{\partial}{\partial u}\left(\frac{G}{D}\right)\right]^{-1}\left[-\frac{1}{D}\frac{\partial G}{\partial u}\Gamma_r + \frac{1}{D}\frac{\partial D}{\partial u}H_r + \left(\frac{\beta}{\mu}\frac{\partial D}{\partial u} - \frac{\partial G}{\partial u}\right)\frac{\mu}{D}nE_r\right], \tag{9}$$

$$\frac{du}{dr} = \left[D\frac{\partial}{\partial u}\left(\frac{G}{D}\right)\right]^{-1}\left[\frac{G}{D}\frac{\Gamma_r}{n} - \frac{H_r}{n} - \left(\frac{\beta}{\mu} - \frac{G}{D}\right)\mu E_r\right], \tag{10}$$

$$\frac{dn_i}{dr} = \left(\frac{m_i\Gamma_r^2}{en_i^2}\right)^{-1}\left[\Gamma_r\left(\frac{1}{\mu_i} + \frac{2m_i\nu_i}{e}\frac{n}{n_i}\right) - \frac{1}{r}\frac{m_i\Gamma_r^2}{en_i} - n_i E_r\right], \tag{11}$$

$$\frac{1}{r}\frac{d(r\Gamma_r)}{dr} = \nu_i n, \tag{12}$$

$$\frac{1}{r}\frac{d(rH_r)}{dr} = \mu n E_z^2 - \left(2\frac{m}{M}\nu_u u + \nu_x V_x + \nu_i V_i\right) n, \tag{13}$$

$$\frac{1}{r}\frac{d(rE_r)}{dr} = \frac{e}{\epsilon}(n_i - n). \tag{14}$$

Boundary Conditions

Six boundary conditions are needed to specify a unique solution to this set of six first order equations. By symmetry,

$$\Gamma_r(0) = 0,\ H_r(0) = 0,\ E_r(0) = 0. \tag{15}$$

These conditions ensure that

$$\frac{dn}{dr} = 0, \ \frac{du}{dr} = 0.$$

However, because the right side of (11) appears to have a singularity at $r = 0$, conditions (15) alone do not ensure that

$$\frac{dn_i}{dr} = 0.$$

It is necessary to apply l'Hospital's rule to the right side of (11) and impose the condition that the numerator of the resulting quantity be zero at $r = 0$ to ensure zero ion density gradient on axis[17]. Following this procedure gives

$$\frac{\nu_{i0}}{\mu_i} n_0 \left(1 + \frac{3}{2}\frac{\nu_{i0}}{\nu_{im}}\frac{n_0}{n_{i0}}\right) - \frac{e}{\epsilon}(n_{i0} - n_0)n_{i0} = 0, \tag{16}$$

where subscript "0" means "evaluated at $r = 0$" and $\nu_{im} = e/m_i\mu_i$ is the ion-neutral momentum transfer collision frequency.

The remaining two boundary conditions are conditions on Γ_r and H_r that must be satisfied at the wall located at $r = R$, where R is the discharge tube radius. These two conditions follow from the assumption that the wall emits neither electrons nor electron energy back into the discharge. The two conditions are derived from the Legendre expansion for the EEDF as follows. The total current of electrons going in the $-r$ direction at the wall is

$$\Gamma_-(R) = 2\pi \int_0^{-1} \int_0^{\infty} \mu v f(R, \mu, v) v^2 dv d\mu \tag{17}$$

where μ is not electron mobility, but cosine of the angle between **v** and the direction perpendicular to the wall. If no electrons are emitted by the wall, then the total particle current directed inward at the wall must be zero. This condition is expressed mathematically by the equation

$$\Gamma_-(R) = 2\pi \int_0^{-1} \int_0^{\infty} \mu v \left[f_0(R, v) + \mu f_{1r}(R, v)\right] v^2 dv d\mu = 0. \tag{18}$$

Likewise, if no electron energy is emitted by the wall, then the total heat current directed inward at the wall must be zero. This condition is expressed mathematically by the equation

$$H_-(R) = 2\pi \int_0^{-1} \int_0^{\infty} (mv^2/2e) \mu v \left[f_0(R, v) + \mu f_{1r}(R, v)\right] v^2 dv d\mu = 0. \tag{19}$$

When f_0 is Maxwellian, for example, then these conditions become

$$\Gamma_-(R) = \frac{1}{4} n(R) \bar{v}(R) - \frac{1}{2}\Gamma_r(R) = 0$$

and

$$H_-(R) = \frac{1}{3} n(R) \bar{v}(R) u(R) - \frac{1}{2} H_r(R) = 0,$$

respectively, where $\bar{v}(R) \equiv \sqrt{16eu(R)/3\pi m}$ is mean speed. When f_0 is not Maxwellian, then the numerical factors 1/4, 1/3, and $16/3\pi$ are different.

Method of Solution

The set of first order ordinary differential equations (9)-(14) is solved by a Runge-Kutta technique, subject to the set of boundary conditions (15), (16), (18), and (19). Therefore, starting values for all six dependent variables must be selected to find a particular solution. Because boundary conditions (18) and (19) are specified at the wall where $r = R$, values of $u(0)$ and $(dH_r/d_r)_{r=0}$ must be iterated to find the solution which satisfies them. The latter quantity is changed by iterating E_z. Therefore, the solution procedure can be summarized as follows: (i) Set initial values $\Gamma_r(0) = H_r(0) = E_r(0) = 0$; (ii) Guess values of $n(0)$, $u(0)$, and E_z; (iii) Solve (9)-(14) out to $r = R$. If (18) and (19) are not satisfied, then the procedure is repeated with new values of $u(0)$ and E_z. Finally, if discharge current I, defined by the equation

$$I = 2\pi e \int_0^R [\mu(r)n(r) + \mu_i n_i(r)]E_z r dr,$$

is not equal to the desired value, then the entire process is repeated with a new value of $n(0)$.

In the present work, relatively simple expressions for the transport coefficients μ, D, β, and G as functions of u are found from a 0-D Boltzmann solution for the EEDF, as described below.

Parametrization of Transport Coefficients

Transport coefficients and inelastic collision frequencies are parametrized by average energy according to O-D Boltzmann calculations[18]. Because the total cross section for momentum transfer between electrons and neon atoms varies approximately as the 0.2 power of electron energy in the range 1-20 eV, the 0-D Boltzmann transport coefficients can be represented approximately by the simple expressions $\mu N = 1.48 \times 10^{23} u^{-0.7}$ $V^{-1}cm^{-1}sec^{-1}$, $DN = 1.20 \times 10^{23} u^{0.3}$ $cm^{-1}sec^{-1}$, $\beta N = 2.20 \times 10^{23} u^{0.3}$ $cm^{-1}sec^{-1}$, and $GN = 1.34 \times 10^{23} u^{1.3}$ $Vcm^{-1}sec^{-1}$, in this energy range. These values are obtained when the 0-D f_0 is substituted in the recipes for transport coefficients given by Allis[14]. Similar expressions for neon transport coefficients with slightly different exponents of average energy are proposed in Reference [16].

The corresponding inelastic collision frequencies are shown in Table 2. The first six excited levels of atomic neon are lumped together to get excitation frequency $\tilde{\nu}_{igx}$. Density of the lumped excited state is handled in the same way as in Reference [6]. Ionization cross section of the lumped excited state is assumed to be that of Vriens[19].

Table 2. O-D Inelastic Rates.

u (V)	$\tilde{\nu}_{gx}$ (cm^3/sec)	$\tilde{\nu}_{gi}$ (cm^3/sec)
6.0	4.0E-14	3.0E-22
7.0	5.0E-12	7.0E-17
8.0	4.5E-11	1.2E-12
9.0	1.3E-10	1.1E-11
10.0	2.6E-10	4.4E-11
11.0	4.5E-10	1.0E-10
12.0	7.3E-10	1.8E-10

Results and Discussion

Comparison with 1*st* Principles Nonlocal Kinetic Method. To illustrate, the neon positive column described by Urhlandt & Winkler[6] is simulated in the present work. Results corresponding to results shown in their Figures 1, 4, 5a and 5b are shown in Figures 1, 2, 3, and 4, respectively. Figure 1 shows remarkably good agreement between calculated space charge potential $\phi(r)$ an measured $\phi(r)$ which is assumed as input in Reference [6]. Figure 2 shows radial variation of electron/ion density, average

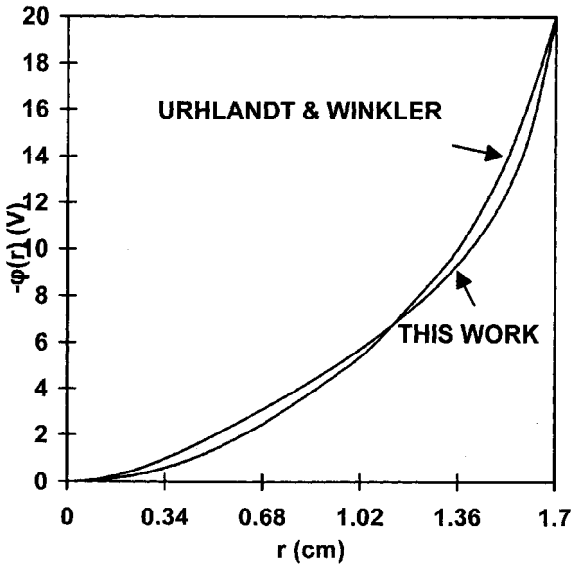

Figure 1: Radial space charge potential $-\phi(r)$. Upper curve is measured potential assumed by Uhrlandt & Winkler, while lower curve is calculated output of the present work. Positive column conditions: 0.75 Torr neon, I = 10 mA, R = 1.7 cm.

energy, radial particle current density, and radial heat current density. These curves are qualitatively similar to those of Urhlandt & Winkler, but there are quantitative differences. For example, inward radial heat current density H_r peaks at about 20×10^{15} V/cm²/sec, whereas the peak value calculated by Urhlandt & Winkler is about 9×10^{15} V/cm²/sec. Figure 3 shows the radial variation of the ionization source, which includes stepwise as well as direct ionization. The total ionization source on axis is about 9×10^{14} $cm^{-3}sec^{-1}$, whereas Urhlandt & Winkler found a value of about $4 \times 10^{14}\,cm^{-3}\,sec^{-1}$. Figure 4 shows the radial variation of power output per unit volume $L(r)$, consisting of elastic and inelastic collision losses, and the power input per unit volume $P(r)$, consisting of Joule heating. Nonlocal behavior is evident in that these two quantities are not equal in each volume element of the discharge, even though their volume integrals are equal. As in previous comparisons, Figure 4 shows different peak values of Joule heating and collision loss compared with those in Reference [6]. The differences between

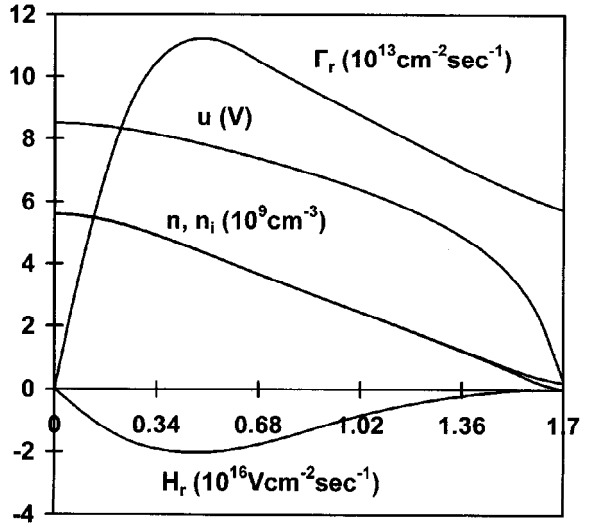

Figure 2: Radial variation of electron properties: electron density $n(r)$, average energy $u(r)$, radial current density Γ_r, radial heat current density H_r. Compare with figure 4 of Reference [6]. Positive column conditions: 0.75 Torr neon, I = 10 mA, R = 1.7 cm.

all of these results and corresponding results of Reference [6] can possibly be made smaller by using the same cross sections used in Reference [6].

According to (7), radial heat current density H_r is the sum of three components—H_{conv}, H_{diff}, and H_{cond}. The three components are defined as

$$H_{conv} \equiv \frac{\beta}{\mu}\Gamma_r, \quad H_{diff} \equiv \left(\frac{\beta}{\mu} - \frac{G}{D}\right) D\frac{dn}{dr}, \quad H_{cond} \equiv -n\left(\frac{\partial G}{\partial u} - \frac{\beta}{\mu}\frac{\partial D}{\partial u}\right)\frac{du}{dr}. \qquad (20)$$

Figure 5 shows the three components of H_r plotted versus r. Note that the convective component is small compared with the other two components, which nearly cancel each other. Identification of radial heat flow as being composed of three components is not done in Reference [6], so comparison of these quantities cannot be made here.

Generally speaking, good qualitative agreement between results of the Nonlocal Moment Method presented here and results of the the first principles Nonlocal Kinetic Method of Urhlandt & Winkler is demonstrated. Proof is given in Table 3, in which a comparison of measurable quantities is made for the four methods listed in the previous section: Method 1—1st Principles Nonlocal Kinetic Method; Method 2—Nonlocal Kinetic Approximation Method; Method 3—Local Moment Method; and Method 4—Nonlocal Moment Method. Entries in the second row of Table 3 are results of Bailey and Bennett [20]. Entries in the third row of Table 3 are obtained by solving the Local Moment Model constructed from the Nonlocal Moment Model by setting du/dr = 0 in (10), solving the resulting equation for H_r, substituting this H_r in (9) to give the

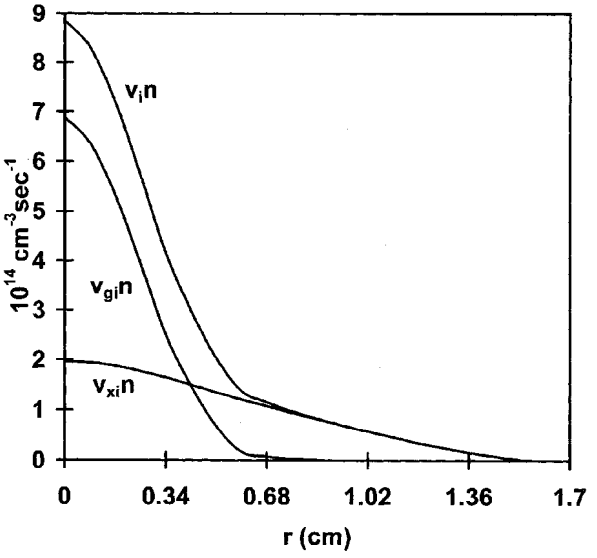

Figure 3: Radial variation of ionization rates: 1 step = $\nu_{gi}(r)n(r)$, 2 step = $\nu_{xi}(r)n(r)$, total $=\nu_{gi}(r)n(r) + \nu_{xi}(r)n(r)$. ν_{xi} based on ionization from 16.62 eV lumped state with parabolic spatial distribution giving average density equal to 10^{-5} times ground state density, similar to Reference [6], and with ionization cross section recommended by Vriens in Reference [19]. Compare with Figure 5a of Reference [6]. Positive column conditions: 0.75 Torr neon, I = 10 mA, R = 1.7 cm.

familiar equation

$$\frac{dn}{dr} = -\frac{1}{D}\Gamma_r - \frac{\mu}{D} n E_r, \tag{21}$$

and solving this equation simultaneously with (11), (12), and (14) while assuming radially invariant transport coefficients and collision frequencies.

Table 3. Comparison of Calculated Measurable Quantities:[a] PR = 1.3 Torr-cm.

Meth	$n(0)$ (cm^{-3})	$\bar{n}$ (cm^{-3})	u(0) (V)	L(0) (V/cm^3/sec)	E_z (V/cm)	ϕ_w (V)	J_w (μA/cm^2)	Source
1	5.8×10^9	2.7×10^9	7.4	1.0×10^{17}	2.17	20.0	9.1	[6]
2	4.5×10^9	1.9×10^9	7.5	1.2×10^{17}	2.53	22.1	7.2	[20]
3	4.4×10^9	1.3×10^9	8.2	1.0×10^{17}	4.25	58.9	14.6	Present
4	5.6×10^9	2.5×10^9	8.5	2.0×10^{17}	2.24	19.9	9.2	Present

[a] E_z and $\phi(r)$ are inputs to 1-D Boltzmann solution, but are calculated outputs in other methods; $\bar{n} = (2/R^2)\int n(r) r dr$; $-\phi_w$ is wall potential measured relative to positive column axis; J_w is ion current density measured at wall.

This table shows that calculated measurable quantities from the Nonlocal Moment Method agree fairly well with those of the Nonlocal Kinetic Method, while those of the other two methods do not agree as well. In particular, the axial electric field is almost twice as large for the Local Moment Method, and the wall potential is about three times

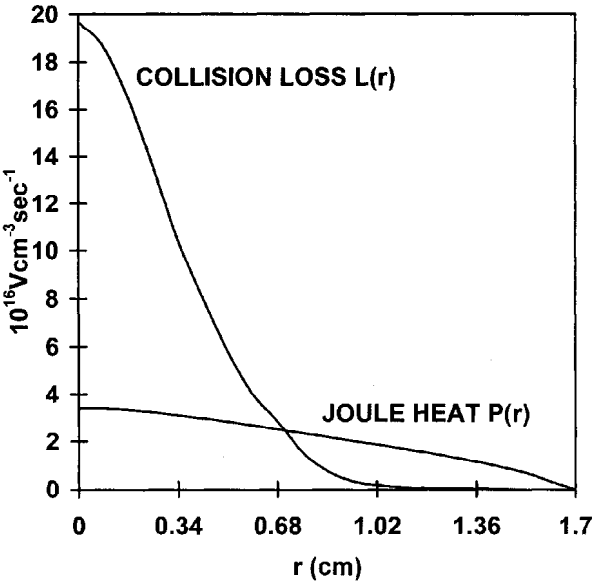

Figure 4: Radial variation of power input due to Joule heating and power output due to collisional losses for the Nonlocal Moment Method. Compare with Figure 5b of Reference [6]. Positive column conditions: 0.75 Torr neon, I = 10 mA, R = 1.7 cm.

larger, as a consequence of average energy u = 8.2 V being constant across the positive column. As mentioned above, it is possible that closer agreement between results of Urhlandt & Winkler's 1-D Boltzmann solution and those of the present Nonlocal Moment solution can be obtained by using the same cross sections they use.

Collision loss $L(r)$ and Joule heat $P(r)$, which are equal for the Local Moment Method, are compared with those for the Nonlocal Moment Method in Figure 6. The halfwidth of the Local Moment $L(r)$ is significantly larger than that of the Nonlocal Moment $L(r)$ because u = 8.2 V is constant across the positive column in the Local Moment calculation, whereas u varies radially in the Nonlocal Moment calculation as shown in Figure 2.

Other Comparisons. In the previous subsection, the Nonlocal Moment Method presented in this article is shown to be in good qualitative agreement with the 1st Principles Nonlocal Kinetic Method. Similarities between the Nonlocal Moment Method formulation and that of other approximate methods have already been cited[13, 15, 16]. The procedure of parametrizing transport coefficients and collision frequencies by average energy instead of by E_z/N in order to apply moment equations to nonequilibrium problems in gaseous electronics is widely used. An early example applying this procedure to a case of spatial nonequilibrium is [16]. Subsequent examples include studies of spatial nonequilibrium in the cathode fall[15], temporal nonequilibrium in pulsed fluorescent lamps[21], nonequilibrium motion in time-of-flight experiments[22], and spatial nonequilibrium near absorbing boundaries[13, 23]. In [16], spatial nonequilibrium in a

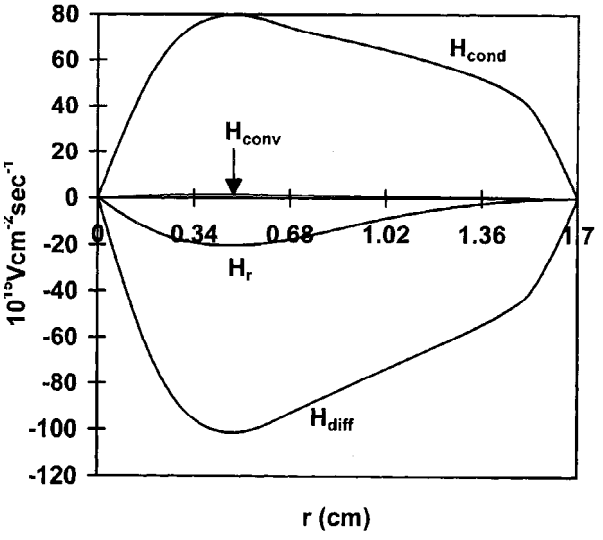

Figure 5: Radial variation of individual components of heat flow. Net heat flow H_r is equal to the sum $H_{conv} + H_{cond} + H_{diff}$. The magnitude of the convective contribution to heat flow is on the order of 1% of the conductive and diffusive contributions. Positive column conditions: 0.75 Torr neon, I = 10 mA, R = 1.7 cm.

neon positive column with PR = 1.4 Torr-cm is studied with a formulation that includes moment equations similar to (9) and (10) and simplifying assumptions of charge neutrality $n = n_i$ and $f_0(\epsilon) \alpha \exp[-(\epsilon/\theta)^2]$. It is suggested in [16] that sometimes a good approximation is obtained by setting both Γ_r and H_r given by (1) and (3), respectively, equal to zero, then eliminating E_r from the resulting equations to get

$$\frac{1}{\beta}\frac{d(Gn)}{dr} = \frac{1}{\mu}\frac{d(Dn)}{dr}.$$

This can be a useful approximation when the momentum transfer collision frequency $\nu_m(\epsilon)$ is expressible as $\nu_m(\epsilon) \alpha \epsilon^{(l+1)/2}$ because transport coefficients μ, D, β, G are then proportional to u^j, where $j = -(l+1)/2$, $(1-l)/2$, $(1-l)/2$, $(3-l)/2$, respectively, allowing analytic integration of the equation above to give u/u_0, = $(n/n_0)^\delta$, where the constant δ is given by

$$\delta = D\left(\frac{\beta}{\mu} - \frac{G}{D}\right)\left[u\left(\frac{\partial G}{\partial u} - \frac{\beta}{\mu}\frac{\partial D}{\partial u}\right)\right]^{-1}$$

The 0-D transport coefficients given above in the subsection called **Parametrization of Transport Coefficients** correspond to l = 0.4 and δ = 0.4. The relation u/u_0 =

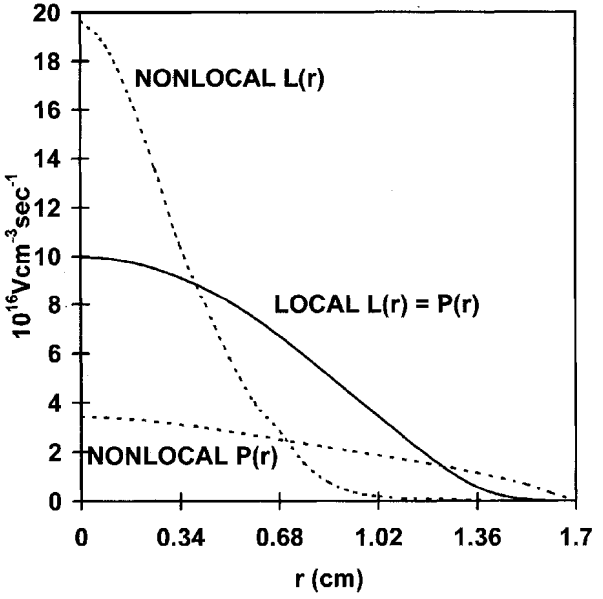

Figure 6: Radial variation of power input due to Joule heating and power output due to collisional losses for the Local Moment Method. Dashed curves same as in Figure 4. Positive column conditions: 0.75 Torr neon, I = 10 mA, R = 1.7 cm.

$(n/n_0)^{0.4}$ is satisfied closely by the Nonlocal Moment Method solutions for $n(r)$ and $u(r)$ shown in Figure 2, even though the approximation $H_r = 0$ is not satisfied as closely as the approximation $\Gamma_r = 0$, as pointed out in Reference [6]. In contrast, $\delta = -2$ when $l = -3/2$, consistent with the conclusion reached in the next section—namely, that u increases with increasing r when $l < -1$.

In addition to these similarities, there are some interesting differences. For example, it is found in [24] that average energy $u(r)$ increases with increasing r in He/Hg and Ar/Hg plasmas with $PR \approx 1$ Torr-cm. This result implies that the second derivative of u with respect to r is greater than 0 on axis. However, (10) predicts the opposite for all plasmas with momentum transfer collision frequency $\nu_m(\epsilon)$ that increases with increasing electron energy ϵ in the energy range of interest, which category includes He/Hg and Ar/Hg mixtures. By differentiating (10) with respect to r and evaluating the result at $r = 0$, the following expression is found:

$$\left[\frac{d^2u}{dr^2}\right]_{r=0} = \left[D\frac{\partial}{\partial u}\left(\frac{G}{D}\right)\right]_{r=0}^{-1}\left[\frac{G}{Dn}\frac{d\Gamma_r}{dr} - \frac{1}{n}\frac{dH_r}{dr} - \left(\frac{\beta}{\mu} - \frac{G}{D}\right)\mu\frac{dE_r}{dr}\right]_{r=0}$$

When the first derivatives appearing in this expression are eliminated by means of (12-14) and (16) and when $\nu_i/\nu_{im} << 1$, then this equation becomes

$$\left[\frac{d^2u}{dr^2}\right]_{r=0} = \frac{1}{2}\left[D\frac{\partial}{\partial u}\left(\frac{G}{D}\right)\right]_{r=0}^{-1}\left(2\frac{m}{M}\nu_u u + \nu_x V_x + \nu_i\left[V_i + \frac{G}{D} - \left(\frac{\beta}{\mu} - \frac{G}{D}\right)\frac{\mu n}{\mu_i n_i}\right] - \mu E_z^2\right)_{r=0}$$

The right side of this equation is dominated by the term proportional to the ratio of electron and ion mobilities—u/u_i—which is on the order of 100 for He/Hg and 1000 for Ar/Hg. Therefore, the right side is negative because $(\beta/\mu - G/D) > 0$ for both gas mixtures. The reader is reminded that the expression for $u'(0)$ given above is exact when the exact result for $f_0(r, \epsilon)$, like the one obtained in Reference [6], for example, is used to calculate transport coefficients. It is possible that the result found in [24] is due to the approximate way in which radial effects are included in the Boltzmann equation.

Mechanism Causing Radial Nonequilibrium. The prevalent speculation about the mechanism responsible for radial nonequilibrium resulting in excess ionization on axis in low *PR* plasmas focuses on the qualitative argument that the radial space charge field accelerates inward-bound electrons sufficiently to cause higher rates of inelastic collisions than encountered in radially uniform plasmas at the same value of E_z/N. If this speculative mechanism be the correct one, then it should occur when f_0 is Maxwellian ($\nu_m(\epsilon)$ independent of ϵ) or sub-Maxwellian ($\nu_m(\epsilon)$ decreasing with increasing ϵ), as well as when it is super-Maxwellian ($\nu_m(\epsilon)$ increasing with increasing ϵ). However, average energy is radially invariant, or nearly so, when f_0 is Maxwellian, and increases with increasing r when f_0 is sub-Maxwellian, according to the analysis of Bernstein and Holstein[4]. Therefore, it appears that the speculation is incorrect. Instead, the mechanism responsible for radial nonequilibrium in a low *PR* plasma with super-Maxwellian f_0 appears to be the inward-bound heat diffusion current density H_{diff}, defined in (20), which carries heat from the outer region of the positive column where Joule heat $P(r)$ is larger than the collision loss $L(r)$ to the inner region where $P(r) < L(r)$, thus augmenting Joule heat generated on axis by the external field. When f_0 is sub-Maxwellian, then $H_{diff} > 0$, average energy increases with increasing r, and there is an ionization deficit on axis, in contradiction to the speculative mechanism mentioned above.

The direction of H_{diff} depends on the quantity $\beta/\mu - G/D$. For momentum transfer collision frequency $\nu_m(\epsilon)$ independent of electron energy ϵ (Maxwellian f_0), this quantity is zero. For $\nu_m(\epsilon)$ increasing with increasing ϵ, this quantity is positive, causing inward heat diffusion and negative gradient in average energy. For $\nu_m(\epsilon)$ decreasing with increasing ϵ, it is negative, causing outward heat diffusion and positive gradient in average energy. Each coefficient in this expression is determined primarily by behavior of bulk electrons, not that of tail electrons. Inward heat flow, for example, causes additional heating over and above Joule heating, increasing average energy in the central region of the positive column over and above the corresponding equilibrium value. The shape of f_0 changes accordingly; there are fewer bulk electrons and more tail electrons, causing excess ionization over and above the corresponding equilibrium value[25]. It doesn't take much additional heating to give significantly more ionization. In the neon case discussed at the beginning of this section, E_z/N = 8.4 Td and $u(0)$ = 8.5 V for the nonequilibrium positive column analyzed by the Nonlocal Moment Method. For the same value of E_z/N in neon, the value of equilibrium average energy is 7.4 V. The corresponding difference in one-step ionization frequency is a factor of about 350 and the difference in excitation frequency is a factor of about 5 for these two values of average energy. Of course, this argument is qualitative, because it is based on the 0-D Boltzmann solution for f_0. However, the same general result can be expected when the exact f_0 of [6] is used to calculate transport coefficients and collision frequencies.

Transition to Local Regime

Transition to the local regime can be investigated by solving (9)-(14) at higher pressure. The solution of these equations for $u(r)$, $L(r)$, and $P(r)$ is shown in Figure 7 for 50 Torr neon pressure. Average energy is practically constant over most of the positive column cross section. $L(r)$ and $P(r)$ are almost equal at each radial position, indicating that the 50 Torr neon positive column can be described adequately by the Local Model.

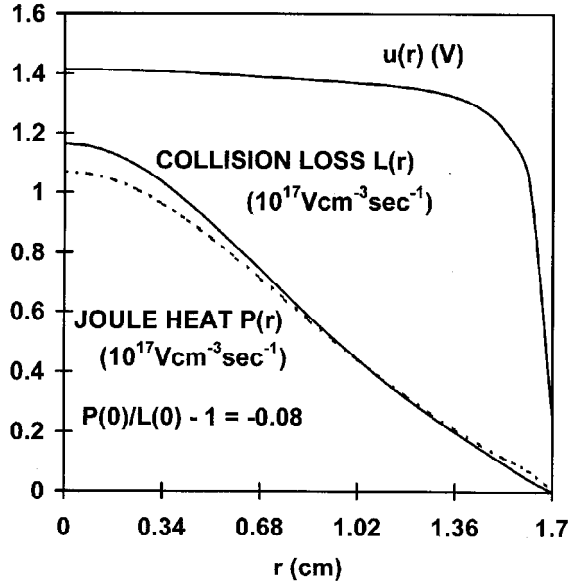

Figure 7: Radial variation of average energy, power input due to Joule heating, and power output due to collisional losses for the Nonlocal Moment Method. The quantity $P(0)/L(0) - 1$ is a measure of the departure from equilibrium. Positive column conditions: 50 Torr neon, I = 10 mA, R = 1.7 cm.

Comparison of measurable quantities for the Local Moment Method and the Nonlocal Moment Method at 50 Torr is shown in Table 4. This table shows. that poor agreement is obtained for wall potential ϕ_w even at 50 Torr, while there is little difference in other measurable quantities.

Table 4. Comparison of Calculated Measurable Quantities:[a] PR = 85 Torr-cm.

Method	$n(0)$ (cm^{-3})	$\bar{n}$ (cm^{-3})	u(0) (V)	L(0) ($V/cm^3/sec$)	E_z (V/cm)	ϕ_w (V)	J_w ($\mu A/cm^2$)
Local Moment	5.5×10^{10}	2.0×10^{10}	1.4	1.0×10^{17}	5.4	14.1	0.4
Nonlocal Mom	6.0×10^{10}	2.1×10^{10}	1.4	1.2×10^{17}	5.3	5.1	0.3

[a] E_z and $\phi(r)$ are inputs to 1-D Boltzmann solution, but are calculated outputs in other methods; $\bar{n} = (2/R^2) \int n(r) r dr$; $-\phi_w$ is wall potential measured relative to positive column axis; J_w is ion current density measured at wall.

CONCLUSIONS

It is concluded from this work that positive column behavior at any pressure can be adequately described by the Nonlocal Moment Method when radial heat flow in the electron gas is taken into account, and when electron transport coefficients and relevant collision frequencies are assumed to be related to radially varying average energy according to 0-D Boltzmann calculations. The Nonlocal Moment Method transitions naturally to the Local Moment Method at sufficiently high values of *PR*. The *PR* range of validity of the four theoretical methods discussed in this article is given in Table 6. The limits of the four ranges of *PR* are arbitrary. The question marks mean that the method can be used in this particular range of *PR*, but it must be recognized that results are inaccurate to some degree or another.

Table 5. PR[a] Range of Validity

Method ↓	$PR < 1$	$1 < PR < 10$	$10 < PR < 100$	$100 < PR$
1st Principles Nonlocal Kinetic	YES	YES	YES	YES
Nonlocal Kinetic Approximation	YES	?	NO	NO
Local Moment	NO	NO	?	YES
Nonlocal Moment	YES	YES	YES	YES

[a] *PR* is expressed in units of Torr-cm.

ACKNOWLEDGMENTS

Special thanks are due Lev Tsendin for leading the author by the hand through derivation of the second term in the expansion of $f_0(r,\epsilon) = f_{00}(\epsilon) + f_{01}(r,\epsilon) + \ldots$, which is the basis of the nonlocal kinetic approximation which he has investigated so thoroughly. In addition, the author wishes to acknowledge assistance of the following people: W. F. Bailey and E. J. Bennett for providing the numerical solution of the Nonlocal Kinetic Approximation Method for neon with *PR*=1.3 Torr-cm and 0-D Boltzmann calculations of neon transport coefficients; Art Phelps and Tim Sommerer for reviewing the manuscript; and Ed Richley for numerous discussions on local model versus nonlocal model. Last, but certainly not least, the author would like to thank Vladimir Kolobov for focusing the author's attention on the nonlocal model.

References

[l] M. J. Druyvesteyn and F. M. Penning, *Rev. Mod. Phys.* 12:87(1940).

[2] G. Francis, "The Glow Discharge at Low Pressure," in *Handbuch der Physik* (Springer, Berlin) ed. by S. Flugge, 22:53(1956).

[3] J. L. Blank, *Phys. of Fluids* 11:1686(1968).

[4] I. B. Bernstein and T. Holstein, *Phys. Rev.* 94:1475(1954).

[5] L. D. Tsendin, *Sov. Phys. JETP* 39:805(1974); *Sov. Phys. Tech. Phys.* 22:1066(1977); *Sov. Phys. Tech. Phys.* 23:890(1978); *Plasma Sources Sci. Technol.* 4:200(1995).

[6] D. Uhrlandt and R. Winkler, *J. Phys. D* 29:115(1996).

[7] C. Busch and U. Kortshagen, *Phys. Rev. E* 51:280(1995).

[8] J. H. Ingold, *Bull. Am. Phys. Soc.* 41:1345(1996), Paper H3B 5.

[9] J. E. Lawler, U. Kortshagen, G. J. Parker, *Ibid.*, Paper H3B 6.

[10] U. Kortshagen, J. E. Lawler, G. J. Parker, *Ibid.*, Paper H3B 7.

[11] G. J. Parker, W. N. G. Hitchon, J. E. Lawler, *Phys. Rev. E* 50:3210(1994).

[12] G. J. Parker, U. Kortshagen, J. E. Lawler, *Bull. Am. Phys. Soc.* 41:1345(1996), Paper H3B 8.

[13] Justification for this approach is given by G. Roumeliotis and L. E. Cram, *J. Phys. D* 22:113 (1989). See also L. E. Cram, *Phys. Rev.* A 43:4480(1991).

[14] See pf. 169 of *Electrons, Ions, and Waves: Selected Works of William Phelps Allis* (MIT Press, Cambridge, MA) ed. by S. C. Brown (1967).

[15] A similar approach is taken by I. Abbas and P. Bayle, *J. Phys. D* 14:649(1981), to study *nonequilibrium* motion of electrons in the cathode fall.

[16] D. Herrmann, A. Rutscher, S. Pfau, *Beit. Plasmaphys.* 11:75(1971). It is noted by these authors that assumption of a Maxwellian f_0 results in radially invariant average energy, approximately, while assumption of a non-Maxwellian f_0 results in radially varying average energy, as noted here.

[17] A similar derivation was given by Allis & Rose in their now classic paper on the transition from free diffusion to ambipolar diffusion, *Phys. Rev.* 93:84(1954).

[18] F. Bailey and E. J. Bennett, private communication, April, 1997. Using ELENDIF, a 0-D Boltzmann code marketed by Kinema Software, P. O. Box 1147, Monument, CO 80132, Bailey and Bennett provided the author with 0-D Boltzmann computation of μ, D, β, G, and collision frequencies versus average energy for neon. The 0-D Boltzmann code ELENDIF is described by W. L. Morgan and B. M. Penetrante, *Computer Physics Communications* 58:127(1990).

[19] L. Vriens, *J. Appl. Phys.* 44:3980(1973).

[20] W. F. Bailey and E. J. Bennett, private communication, May, 1997. See also *Bull. Am. Phys. Soc.* 41:1344 (1996), Paper H3B 3.

[21] J. H. Ingold, "Transient Response of Electrons in a Low Pressure Discharge," Paper V-1, *Third Gaseous Electronics Meeting*, Australian National University, Canberra, 8-10 February 1984. See also "Nonequilibrium Motion of Electrons and Ions Near Absorbing Boundaries," in *Microwave Discharges: Fundamentals and Applications* (Plenum, N. Y.) ed. by C. Ferreira and M. Moisan (1993).

[22] J. H. Ingold, *Phys. Rev.* A 42:950(1990).

[23] J. H. Ingold, *Phys. Rev.* A 43:3086(1991).

[24] M. J. Hartig and M. J. Kushner, *J. Appl. Phys.* 73:1080(1992).

[25] S. Pfau, J. Rohman, D. Urhlandt, R. Winkler, *Contrib. Plasma Phys.* 36:449(1996). Compare curves for the 1-D f_0/n_e on axis and the 0-D F_0 on axis in Figure 6 of this reference.

ON THE RADIAL STRUCTURE OF THE ELECTRON VELOCITY DISTRIBUTION AND RELATED MACROSCOPIC PROPERTIES IN DC COLUMN PLASMAS

R. Winkler and D. Uhrlandt

Institute of Nonthermal Plasma-Physics
D-17489 Greifswald, Germany

INTRODUCTION

The nonisothermal plasma of the axially homogeneous, cylindrical positive column of dc glow discharges represents an attractive example of a spatially bounded inhomogeneous plasma. Several attempts have been made in the past[1-3] as well as are currently [4-14] undertaken to improve the microphysical description and thus the understanding of the significant physical processes occurring in such weakly ionized nonequilibrium plasmas.

These plasmas are usually enclosed by insulated walls. As a consequence a radial space charge field is established in the column to make the confinement and a stable operation of the plasma possible.

An important aspect of the microphysical description of the spatially bounded plasma column is the appropriate treatment of the nonequilibrium kinetics of the active electron component taking into account the specific plasma conditions. Particularly the knowledge of the electron velocity distribution function (EVDF) and of various macroscopic properties of the electrons, which are obtained by appropriate velocity space averages over the EVDF, are of significant importance for the quantitative description of the column plasma.

The occurrence of the space charge field in the column can cause a pronounced radial alteration of the velocity distribution function and of related macroscopic properties of the electrons under certain discharge conditions.

Depending on the special objective of the quantitative plasma description often only a certain part of the electron kinetic quantities is of primary interest. In this respect the isotropic part [1-9] of the per one electron normalized EVDF or the so-called energy distribution function (which can be immediately obtained from the isotropic distribution function) is often of primary interest. This normalized isotropic distribution function already allows to determine several important quantities as the rate coefficients of various inelastic electron-atom collision processes in the plasma. These quantities are then used, for example, to determine the densities of different excited atom and ion species by solving their corresponding particle balance equations.

However a more strict and comprehensive microphysical study of the electron

Electron Kinetics and Application of Glow Discharges
Edited by U. Kortshagen and L. D. Tsendin, Plenum Press, New York, 1998

kinetics in the plasma of the cylindrical positive column requires a more complete treatment [10-14] of the EVDF. In particular the additional determination of the anisotropic part of the EVDF is of large importance. Only the knowledge of the anisotropic distribution function allows a consequent determination of the macroscopic transport of the electrons and of their energy in radial and axial direction and a consistent treatment of the macroscopic particle and energy budget of the electrons in the column plasma.

Thus in an appropriate electron kinetic treatment the action of the axial and radial electric field components, the impact of elastic and various inelastic electron-atom collisions, the collisional ionization in the plasma volume and the electron transport in axial direction and to the insulated tube wall has to be taken into account.

This kinetic problem has been treated by quite different techniques. Mainly in the past and currently too various procedures to solve numerically the complex kinetic equation or analytically an essentially simplified version of the latter have been developed. In last years increasingly simulation techniques as Monte Carlo simulation, particle in cell simulation and convective scheme methods have been adapted.

To avoid the strict solution of this complex kinetic problem different simplifications of the real kinetics of the electrons have been accepted and adopted in the past for the microphysical descriptions of the column plasma. In this context especially the "conventional homogeneous approach" [1, 3, 16] and the "nonlocal approach" [15, 2, 5-10, 16] should be mentioned.

To obtain the per one electron normalized isotropic distribution, in the conventional homogeneous approach the impact of the radial space charge field and of the radial inhomogeneity of the column plasma on the electron kinetics has been neglected. These simplifications have been assumed in the past, since in the central region of the plasma column the radial inhomogeneity of the plasma seems to be less pronounced and the radial electric field becomes small and approaches zero in the column centre due to the rotational symmetry of the plasma. In this approximation[16] the normalized isotropic distribution is determined by solving instead of the complex inhomogeneous kinetic equation the much simpler, homogeneous kinetic equation including with respect to the electric field the sole action of its axial component. To additionally describe the radial density alteration of the electrons, a separate particle balance of the electrons is considered. In this balance radial-independent electron transport coefficients and rate coefficients for the ionization by electron collisions are considered. These coefficients have been determined by the normalized isotropic distribution obtained from the solution of the homogeneous kinetic equation according to the conventional homogeneous approach.

The further approximate treatment of the complex inhomogeneous kinetics of the electrons by the nonlocal approach[15, 2, 6, 7] is based on estimates of the characteristic lengths for spatial energy relaxation by electron-atom collisions in the column plasma of low pressure glow discharges. Such estimates show that the energy relaxation length can be comparable with or even larger than the radius of the discharge column. Therefore it is assumed that the energetic establishment of the electrons in radial direction due to collision processes occurs on a similarly large spatial scale and that the collisional energy dissipation can be approximately taken into account by spatially averaging the inhomogeneous kinetic equation in an appropriate way. Because of the expected weak energetic dissipation in electron-atom collisions it is supposed that the movement of the electrons in the radial electric field and their scattering mainly in elastic collisions take place without remarkable energy loss in collisions and these are the dominant processes which determine the radial alteration of the isotropic distribution in the column plasma. Then the isotropic distribution should essentially depend on the sum

of the kinetic energy and the potential energy of the electrons in the radial electric field, i.e. on the so-called total energy of the electrons, and not additionally on the radial coordinate. Based on these assumptions[15, 2, 6, 7, 16] the complex inhomogeneous kinetic equation is integrated with respect to the radial coordinate at fixed total energy. In this way again a much simpler kinetic equation however with respect to the space of the total energy of the electrons is obtained. The structure of this kinetic equation is very similar to the homogeneous kinetic equation used in the conventional homogeneous approach. By the nonlocal approach the isotropic distribution with the inclusion of the electron density is obtained. The transformation back from the total to the kinetic energy yields a radial alteration of the isotropic distribution from which the per one electron normalized isotropic distribution can additionally be calculated.

Due to the largely contrary assumptions with respect to the energy dissipation by electron-atom collisions, in these two cases of the simplified treatment of the inhomogeneous kinetics of the electrons remarkably different radial structures for example of the isotropic or energy distribution and of the relevant transport and rate coefficients of the electrons are obtained. But in real column plasmas different situations somewhere between these two limits are to expect depending particularly on the efficiency of the collisional energy dissipation of the electrons in the plasmas considered. This dissipation is mainly determined by the density of the ground state atoms and by the magnitude and the energy thresholds of the corresponding collision cross sections of the various electron-atom collision processes in the column plasma under consideration.

However the electron kinetics in the dc column plasma is controlled, in any case, by the above-mentioned complex kinetic problem and the describing inhomogeneous kinetic equation[4, 5, 10-14, 16, 17] whose solution should give the real radial alteration of the EVDF and of the relevant velocity space averaged macroscopic properties of the electrons in the column.

Recently an approach[12, 13, 17] for the numerical solution of this complex electron kinetic equation has been developed which allows in addition to the isotropic distribution especially the determination of the radial anisotropic distribution and thus the analysis of radial particle and energy transport of the electrons as well as of their radially resolved particle and energy balance. Using this approach various studies of the radially dependent kinetics of the electrons have been performed for given axial electric field and radial course of the radial electric field. Both field components have been obtained from measurements under various plasma conditions in different column plasmas.

In the following main aspects of this approach and results on the radial alteration of electron kinetic quantities in various column plasmas obtained by this approach are presented and discussed.

MAIN ASPECTS OF THE KINETIC STUDIES

The basic equation to study the kinetics of the electrons in nonuniform plasma regions is the inhomogeneous, time-independent Boltzmann equation of the electrons

$$\vec{v} \cdot \nabla_{\vec{x}} f - \frac{e_0}{m} \vec{E} \cdot \nabla_{\vec{v}} f = \sum_l C_l^{el}(f) + \sum_l \sum_k C_{lk}^{ex}(f) + \sum_l C_l^{io}(f) \qquad (1)$$

which determines the velocity distribution function $f(\vec{v}, \vec{x})$ of the electrons with $f(\vec{v}, \vec{x}) d\vec{v} d\vec{x}$ being the number of electrons in the interval $d\vec{v} d\vec{x}$ at the position $(\vec{v}, \vec{x})$ in the velocity and coordinate space.

This equation includes by appropriate collision integrals the action of elastic (C_l^{el}), various types (k) of exciting (C_{lk}^{ex}) and ionizing (C_i^{io}) electron-atom collision processes with different atomic species (l) and the impact of a nonuniform electric field $\vec{E}(\vec{x})$ where $-e_0$ and m denote the charge and mass of the electrons. Further less important terms describing the electron collisions of second kind and the electron gain due to ionization in co1lisions between excited atoms, i.e. the chemo-ionization, have been neglected in the kinetic equation for brevity reasons.

As in steady state and in time-dependent plasma conditions approximate solutions of the kinetic equation can be obtained by using orthogonal expansions of the velocity distribution function with respect to the directions $\vec{v}/v$ of the electron velocity $\vec{v}$ in the kinetic equation. Depending on the structure of the electric field, of the expected inhomogeneity in the plasma and of the imposed boundary conditions for the velocity distribution a reduced expansion with respect to one angle coordinate only or a more complex expansion with respect to both angle coordinates of $\vec{v}/v$ has to be used.

The electric field in the axially homogeneous column plasma is a superposition of the constant axial electric field and of the radially varying radial space charge field, i.e. $\vec{E}(r) = E_r(r)\vec{e}_r + E_z\vec{e}_z$. Thus the direction of the total electric field $\vec{E}(r)$ is different from the radial direction in which the inhomogeneity of the plasma column occurs. Therefore an expansion of the velocity distribution in spherical harmonics with respect to both angle coordinates of $\vec{v}/v$ has to be used.

Because of the cylindrical symmetry of the total electric field in the column plasma in the lowest approximation order of this expansion, the so-called two term approximation, the velocity distribution can be represented by the expression

$$f(U, \frac{\vec{v}}{v}, r) = \frac{1}{2\pi}\frac{1}{(2/m)^{3/2}}\left[f_0(U,r) + f_r(U,r)\frac{v_r}{v} + f_z(U,r)\frac{v_z}{v}\right] \qquad (2)$$

with v_r, v_z, $v = |\vec{v}|$ being the radial and axial component and the magnitude of $\vec{v}$ and $U = m v^2/2$ the kinetic energy. This two term approximation includes, in addition to the isotropic distribution $f_0(U, r)$, a radial component $f_r(U, r)$ and an axial component $f_z(U, r)$ of the vectorial anisotropic distribution. Particularly the radial anisotropic distribution allows to describe the particle and energy current density of the electrons in radial direction and thus to reveal significant aspects of the electron confinement by the radial space charge field. In order to describe in an appropriate way the electron loss to the tube wall, the electron generation in the column plasma by various ionization processes, in electron collisions with atoms in the ground state and excited states and additionally in collisions between excited atoms, has to be included in the kinetic equation.

When substituting the expansion (2) into the kinetic equation (1) finally the partial differential equation system[13, 17]

$$\begin{aligned}
&\frac{1}{r}\frac{\partial}{\partial r}\left[r\frac{U}{3}f_r\right] - \frac{\partial}{\partial U}\left[\frac{U}{3}e_0\left(E_r(r)f_r + E_z f_z\right)\right] \\
&-\frac{\partial}{\partial U}\left[\sum_l 2\frac{m}{M_l}U^2 N_l(r)Q_l^d(U)f_0\right] \\
&+\sum_l\sum_k UN_l(r)Q_{lk}^{ex}(U)f_0 + \sum_l UN_l(r)Q_l^{io}(U)f_0 \\
&-\sum_l\sum_k (U+U_{lk}^{ex})N_l(r)Q_{lk}^{ex}(U+U_{lk}^{ex})f_0(U+U_{lk}^{ex},r) \\
&-\sum_l 4(2U+U_l^{io})N_l(r)Q_l^{io}(2U+U_l^{io})f_0(2U+U_l^{io},r) = 0\,,
\end{aligned}$$

$$\frac{\partial}{\partial r} f_0 - e_0 E_r(r) \frac{\partial}{\partial U} f_0 + H(U,r) f_r = 0\,,$$

$$-e_0 E_z \frac{\partial}{\partial U} f_0 + H(U,r) f_z = 0 \tag{3}$$

for the isotropic part $f_0(U, r)$ and the radial and axial anisotropic part $f_r(U, r)$ and $f_z(U, r)$ of the velocity distribution $f(U, \vec{v}/v, r)$ with the coefficient $H(U,r) = \sum_l N_l(r) Q_l^d(U) + \sum_l \sum_k N_l(r) Q_{lk}^{ex}(U) + \sum_l N_l(r) Q_l^{io}(U)$ is obtained. Here are $Q_l^d(U), Q_{lk}^{ex}(U)$ and $Q_l^{io}(U)$ the cross sections for momentum transfer in elastic (d) collisions and the total cross sections for the exciting (ex) and ionizing (io) collisions with various atomic states (l), i.e. with atoms in the ground state and in excited states, of density $N_l(r)$ and mass M_l. The quantities U_{lk}^{ex} and U_l^{io} denote the corresponding energy losses in the inelastic collision processes. The first equation of this system includes terms with the shifted energy arguments $U + U_{lk}^{ex}$ and $2U + U_l^{io}$ due to the different kinds of inelastic collision processes. The special form of the shifted arguments related to the ionization terms is a consequence of the assumption that the remaining kinetic energy has been shared in equal parts among both electrons occurring after each ionizing collision.

If the spatial evolution of the isotropic distribution $f_0(U, r)$ and both components $f_r(U, r)$ and $f_z(U, r)$ of the anisotropic distribution have been determined all significant macroscopic quantities of the electrons can be calculated by appropriate energy space averaging over these distribution functions.

To give some examples, the electron density $n(r)$, the mean energy density $u_m(r)$ (i.e. the mean electron energy times density), the particle and energy current densities $\vec{j}(r)$ and $\vec{j}_e(r)$ and their respective radial and axial components, the energy loss rates $L_l^{el}(r)$, $L_{lk}^{ex}(r)$ and $L_l^{io}(r)$ by elastic collisions and by the various exciting and ionizing collision processes and the particle gain rate $G_l(r)$ by ionizing collisions with the gas component l are represented by the averages [13, 17]

$$n(r) = \int_0^\infty U^{1/2} f_0(U,r) dU, \quad u_m(r) = \int_0^\infty U^{3/2} f_0(U,r) dU,$$

$$\vec{j}(r) = j_r(r)\vec{e}_r + j_z(r)\vec{e}_z,$$

$$j_r(r) = \frac{1}{3}\sqrt{\frac{2}{m}} \int_0^\infty U f_r(U,r) dU, \quad j_z(r) = \frac{1}{3}\sqrt{\frac{2}{m}} \int_0^\infty U f_z(U,r)\, dU,$$

$$\vec{j}_e(r) = j_{er}(r)\vec{e}_r + j_{ez}(r)\vec{e}_z,$$

$$j_{er}(r) = \frac{1}{3}\sqrt{\frac{2}{m}} \int_0^\infty U^2 f_r(U,r)\, dU, \quad j_{ez}(r) = \frac{1}{3}\sqrt{\frac{2}{m}} \int_0^\infty U^2 f_z(U,r)\, dU,$$

$$L_l^{el}(r) = 2\frac{m}{M_l}\sqrt{\frac{2}{m}} \int_0^\infty U^2 N_l(r) Q_l^d(U) f_0(U,r) dU,$$

$$L_{lk}^{ex}(r) = U_{lk}^{ex}\sqrt{\frac{2}{m}} \int_0^\infty U N_l(r) Q_{lk}^{ex}(U) f_0(U,r) dU,$$

$$L_l^{io}(r) = U_l^{io}\sqrt{\frac{2}{m}} \int_0^\infty U N_l(r) Q_l^{io}(U) f_0(U,r) dU,$$

$$G_l(r) = \sqrt{\frac{2}{m}} \int_0^\infty U N_l(r) Q_l^{io}(U) f_0(U,r) dU. \tag{4}$$

Some information about the physics involved in the kinetic treatment can already

be obtained when considering the macroscopic balance equations[13, 17] of the electrons which are consistent to system (3). These are, in particular, the particle and energy balance

$$\frac{1}{r}\frac{d}{dr}(r j_r(r)) = G(r)\,, \quad G(r) = \sum_l G_l(r)\,, \tag{5}$$

$$\frac{1}{r}\frac{d}{dr}(r j_{er}(r)) = P_r(r) + P_z(r) - L^{el}(r) - L^{in}(r)\,,$$

$$P_r(r) = -e_0 E_r(r)\, j_r(r)\,, \quad P_z(r) = -e_0 E_z\, j_z(r)\,,$$

$$L^{el}(r) = \sum_l L_l^{el}(r)\,, \quad L^{in}(r) = \sum_l \sum_k L_{lk}^{ex}(r) + \sum_l L_l^{io}(r)\,. \tag{6}$$

All macroscopic quantities occurring in these balances have already been presented in (4). According to the particle balance the evolution of the radial electron particle current density $j_r(r)$ is directly determined by the radial behaviour of total electron gain $G(r)$ in ionizing collisions. The energy balance says that the difference between the two energy transfer rates $P_r(r)$ and $P_z(r)$ due to the action of the radial and the axial field components $E_r(r)$ and E_z and the energy losses $L^{el}(r)$ and $L^{in}(r)$ due to elastic and inelastic collisions is compensated for by the spatial evolution of the radial energy current density $j_{er}(r)$.

Thus under plasma conditions with largely local energy relaxation an almost complete compensation of the energy transfer rates due to the action of both field components by the total loss in all collision processes should occur at each radial position in the energy balance equation and only a small radial energy current density should be established.

A suitable form of the equation system (3) for its numerical solution is obtained when replacing the kinetic energy U by the total energy $\in$ according to $U(\varepsilon, r) = \in - W(r)$ where $W(r) = e_0 \int_0^r E_r(\tilde{r})d\tilde{r}$ is the potential energy of the electrons in the radial electric field. This transformation and the elimination of the both anisotropic distributions leads to the elliptic differential equation[13, 17]

$$\begin{aligned}
&\frac{1}{r}\frac{\partial}{\partial r}\left[\frac{rU_{\varepsilon r}}{3H(U_{\varepsilon r}, r)}\frac{\partial}{\partial r}\bar{f}_0\right] + \frac{\partial}{\partial \varepsilon}\left[\frac{(e_0 E_z)^2 U_{\varepsilon r}}{3H(U_{\varepsilon r}, r)}\frac{\partial}{\partial \varepsilon}\bar{f}_0\right] \\
&+\frac{\partial}{\partial \varepsilon}\left[\sum_l 2\frac{m}{M_l}U_{\varepsilon r}^2 N_l(r) Q_l^d(U_{\varepsilon r})\bar{f}_0\right] \\
&-\sum_l \sum_k U_{\varepsilon r} N_l(r) Q_{lk}^{ex}(U_{\varepsilon r})\bar{f}_0 - \sum_l U_{\varepsilon r} N_l(r) Q_l^{io}(U_{\varepsilon r})\bar{f}_0 \\
&+\sum_l \sum_k (U_{\varepsilon r} + U_{lk}^{ex}) N_l(r) Q_{lk}^{ex}(U_{\varepsilon r} + U_{lk}^{ex})\bar{f}_0(U_{\varepsilon r} + U_{lk}^{ex} + W(r), r) \\
&+\sum_l 4(2U_{\varepsilon r} + U_l^{io}) N_l(r) Q_l^{io}(2U_{\varepsilon r} + U_l^{io})\bar{f}_0(2U_{\varepsilon r} + U_l^{io} + W(r), r) = 0
\end{aligned} \tag{7}$$

for the isotropic distribution $\bar{f}_0(\varepsilon, r) = f_0(U_{\varepsilon r}, r)$ where here and henceforth the abbreviation $U_{\varepsilon r} \equiv U(\varepsilon, r) = \varepsilon - W(r)$ is used. This elliptic equation includes additional terms with shifted energy arguments due to the exciting and ionizing collisions.

The corresponding equations[13, 17] for the transformed radial and axial anisotropic distribution $\bar{f}_r(\varepsilon, r) = f_r(U_{\varepsilon r}, r)$ and $\bar{f}_z(\varepsilon, r) = f_z(U_{\varepsilon r}, r)$ are

$$\bar{f}_r = -\frac{1}{H(U_{\varepsilon r}, r)}\frac{\partial}{\partial r}\bar{f}_0, \quad \bar{f}_z = \frac{e_0 E_z}{H(U_{\varepsilon r}, r)}\frac{\partial}{\partial \varepsilon}\bar{f}_0\,. \tag{8}$$

The solution of the elliptic equation (7) has to be found on a solution area whose parts of the boundary curve partly depend on the course of the potential energy $W(r)$ of the electrons in the radial space charge field. If the radial course $W(r)$ of the potential energy is known, for example from corresponding measurements, the solution area of the elliptic problem can be fixed. Fig. 1 illustrates for a column plasma with the radius rw the typical shape of this area. The nonrectangular part $\in = W(r)$ of the boundary belongs to zero kinetic energy of the electrons.

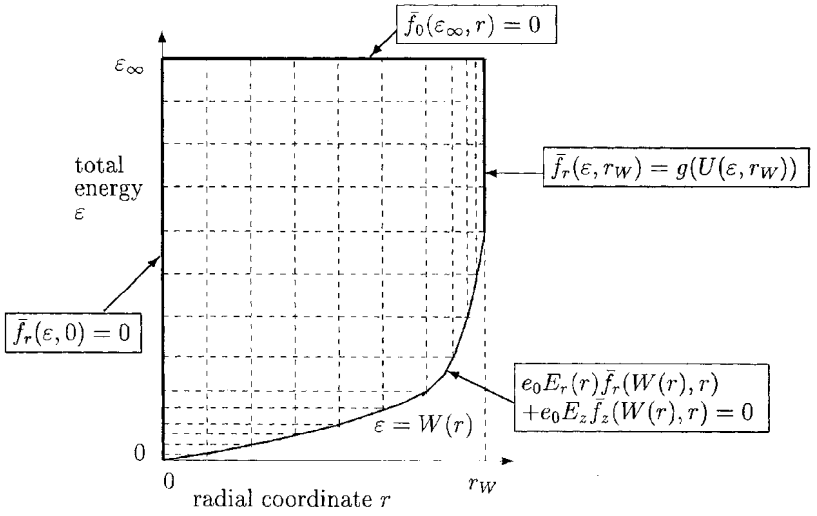

Figure 1. The solution area and the boundary conditions of the elliptic mixed boundary value problem.

Appropriate boundary conditions for the isotropic distribution on all parts of the boundary curve are needed to solve the elliptic problem. Fig. 1 presents additionally the mixed boundary conditions which have been used in the solution procedure. Some of the conditions are formulated by means of the radial anisotropic distribution $\bar{f}_r(\varepsilon, r)$. By using the expression (8), the radial anisotropic distribution can immediately be substituted by the isotropic distribution. Detailed explanations of the various boundary conditions can be found in [13, 12, 17]. However the boundary condition related to the surface of the column plasma will be briefly considered here.

The consistent particle balance (5) requires that all electrons generated by various ionizing collision processes in the cylindrical plasma volume have to be continuously transported to the tube wall in order to maintain a time-independent state. This naturally enforces the occurrence of the radial electron particle current density $j_r(r)$. As shown in (4), the current density $j_r(r)$ is described by an energy space average over the radial anisotropic distribution $f_r(U, r)$ and the latter is coupled via the second equation of (3) or the first equation of (8) to the isotropic distribution. In order to determine the physically relevant solution of (7), the boundary value $g(U) = A \exp(aU^2)$ with $a < 0$ for the radial anisotropic distribution $f_r(U, r_W)$ has been adopted, where a is an appropriate constant. This boundary value describes up to the factor A the energetic distribution of the electron particle current density $j_r(r_W)$ on the tube wall. The constant a in the boundary value allows to vary the contributions from different parts of the energy space of the electrons to their radial particle current density. However, due

to the radial confinement of the electrons by the space charge field, i.e. the reduction of the electron radial movement to the wall by the action of the radial field, it is to expect that the radial electron current close to the plasma surface is carried mainly by the low energy electrons and thus mainly by the low energy part of the anisotropic distribution. For given axial and radial electric field components, related to selected values of the outer discharge parameters, i.e. the gas pressure, the tube radius and the axial discharge current, the value of the macroscopic electron particle current density $j_r(r_W)$ to the tube wall can no longer be freely chosen. Therefore, the factor A is used to adjust the current density onto the wall to the axial discharge current. Further details on this adjustment procedure involved in the solution approach can be found in[13, 17].

But the choice of an appropriate boundary condition for the kinetic problem on the plasma surface remains still an open question and presents currently an object of intensive studies[10, 14].

For the numerical solution of the mixed boundary value problem a nonequidistant rectangle grid is used to derive the discrete representation of the elliptic equation (7) and of the mixed boundary conditions given in Fig. 1 by using a finite difference approach. The discretization of the boundary conditions has been made at grid points on the boundary curves avoiding auxiliary grid points outside of the solution area.

The elliptic equation (7) contains in various collision terms additionally to the density of the ground state atoms the radially varying densities of the atoms in the most populated excited states, i.e. those in the lowest metastable and resonance states. These circumstances enforce to formulate appropriate particle balances for these metastable and resonance atoms too and to determine the self-consistent solution of the elliptic problem and of these particle balances. The self-consistent solution has been obtained using an iterative approach.

The accurate numerical solution of the elliptic problem for specific plasma conditions has been proven to be a laborious task. Using measured values of the axial field strength E_z and of the radial course $W(r)$ of the potential energy for dc plasma columns as input parameters of the kinetic problem, the radial alteration of the velocity distribution and of the various macroscopic quantities of the electrons in different column plasma has been calculated by solving the elliptic mixed boundary value problem together with the particle balances of the most populated excited states.

RADIAL STRUCTURE OF ELECTRON KINETIC QUANTITIES

To illustrate typical aspects of the radial alteration of various kinetic quantities, results of the kinetic studies related to the cylindrical column plasma of glow discharges in the two inert gases neon and krypton and in the He/Xc-mixture with 2 per cent Xe admixture are presented and discussed in the following. With respect to the discharge parameters, i.e. the column radius r_W, the gas pressure p_0 at 0° C and the axial discharge current I_z, the parameter sets r_W = 1.7 cm, p_0 = 75 Pa and I_z = 10 mA for neon, r_W = 2.96 cm, p_0 = 580 Pa and I_z = 0.75 mA for krypton and the further two sets r_W = 2.96 cm, p_0 = 200 Pa, I_z = 8.5 mA and r_W = 2.96 cm, p_0 = 600 Pa, I_z = 20 mA for the He/Xc-mixture, i.e. one discharge condition for each inert gas and two discharge conditions for the mixture, have been selected.

The course of the potential energy $W(r)$ of the electrons in the space charge field $E_r(r)$ and the axial field strength E_z, as obtained from probe measurements[16, 18] in the column plasmas under the specified discharge conditions, are presented for neon, krypton and the He/Xc-mixture in Figs. 2a-c. As mentioned above these quantities

have been used to solve the corresponding elliptic problems. As to be seen from these figures the potential energy on the wall $W(r_W)$ amounts to 21.0 and 14.0 eV in the neon and krypton column and 12.0 and 11.5 eV in the mixture at 200 and 600 Pa, respectively.

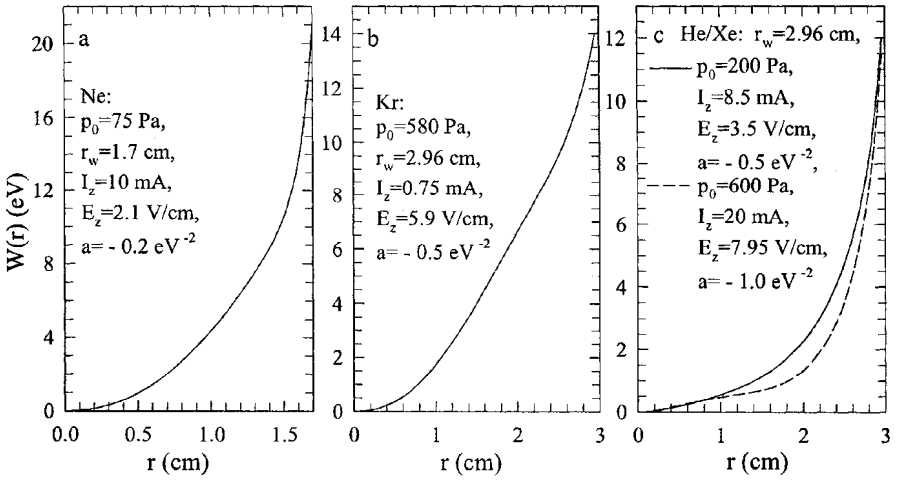

Figure 2. Radial potential energy $W(r)$ and the axial field strength E_z obtained from corresponding measurements and the parameter a used in the boundary value $g(U)$ for four plasma conditions.

For the first two plasma conditions Figs. 3a,b show the calculated radial alteration of the normalized isotropic distribution $f_0(U, r)/n(r)$, i.e. the isotropic distribution additionally normalized on the electron density $n(r)$ at each radial position. The isotropic distributions are presented in their natural (U, r)–space. From Fig. 3a a pronounced radial alteration of the normalized isotropic distribution by several orders of magnitude at higher kinetic energies can be observed in the neon plasma. However, Fig. 3b indicates that a much less pronounced radial alteration of the normalized isotropic distribution is obtained when solving the kinetic equation (7) for the krypton plasma. As illustrated by this figure a slight alteration only of $f_0(U, r)/n(r)$ occurs when going, for example, from the column centre to the radial position $r = 0.77 \cdot r_W$. Already these two examples make obvious that quite different situations with respect to the radial alteration of the normalized isotropic distribution are found in different plasmas and discharge conditions.

Let us consider the radial alteration of both these isotropic distributions, obtained by solving the complex kinetic problem, under the point of view of the above-mentioned simplified approaches for the determination of the isotropic distribution, i.e. the conventional homogeneous approach and the nonlocal approach.

According to the conventional homogeneous approach, often used in the past, the normalized isotropic distribution $f_0(U, r)/n(r)$ is approximately determined by the corresponding homogeneous kinetic equation. By this approach then a per one electron normalized isotropic distribution is obtained which naturally does not depend on the radial coordinate r. Thus it can be concluded that this simplified approach is in obvious contradiction with the behaviour of $f_0(U, r)/n(r)$ found for the neon plasma from the kinetic equation (7), however yields to a certain extent an approximation for the real normalized isotropic distribution in the krypton plasma.

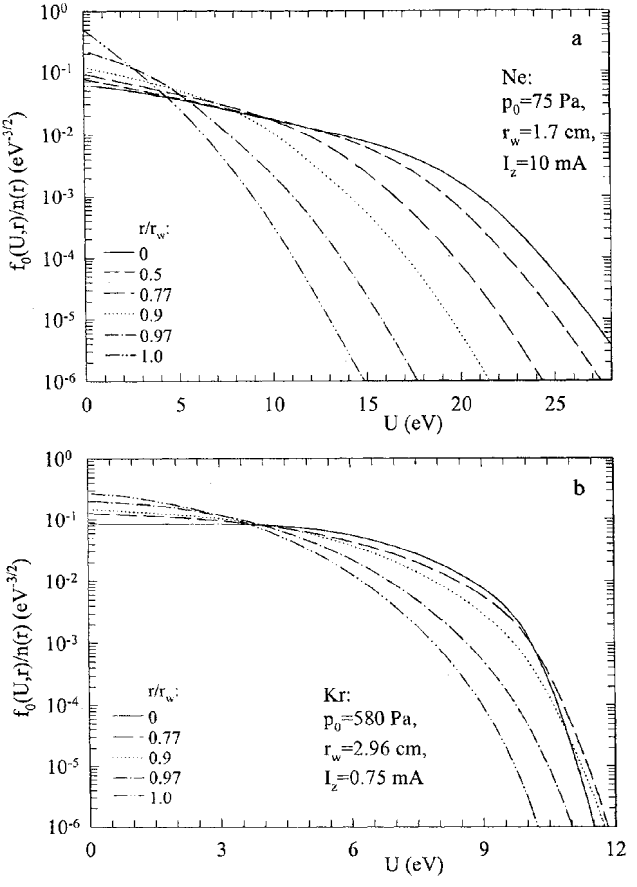

Figure 3. Isotropic distribution $f_0(U, r)/n(r)$ normalized on the electron density $n(r)$ at various radial positions for the neon (a) and for the krypton (b) column plasma.

In order to evaluate the validity of the basic assumption used when applying the nonlocal approach, for the same plasma conditions as considered in Figs. 3a,b the radial alteration of the corresponding isotropic distributions $\bar{f}_0(\varepsilon, r)$ related to the (ε, r)–space is shown in Figs. 4a,b. The respective continuation of the curves by vertical lines marks the position of zero kinetic energy on the total energy scale for different radial positions. Now with respect to the representation by the total energy ε an almost reverse radial alteration of the isotropic distribution compared with that in Figs. 3a,b is obtained. As outlined above the basic assumption of the nonlocal approach is that the isotropic distribution $\bar{f}_0(\varepsilon, r)$ is a function of the total energy ε only, i.e. its dependence on the radial coordinate r can be neglected. A consideration of Figs. 4a,b makes obvious that this simplified approach is now in clear contradiction with the behaviour of $\bar{f}_0(\varepsilon, r)$ found for the krypton plasma, however yields to a certain extent an approximation for the real isotropic distribution in the neon plasma. But even in the latter case radial alterations of almost one order of magnitude remain in the isotropic distribution $\bar{f}_0(\varepsilon, r)$ at higher total energies ε.

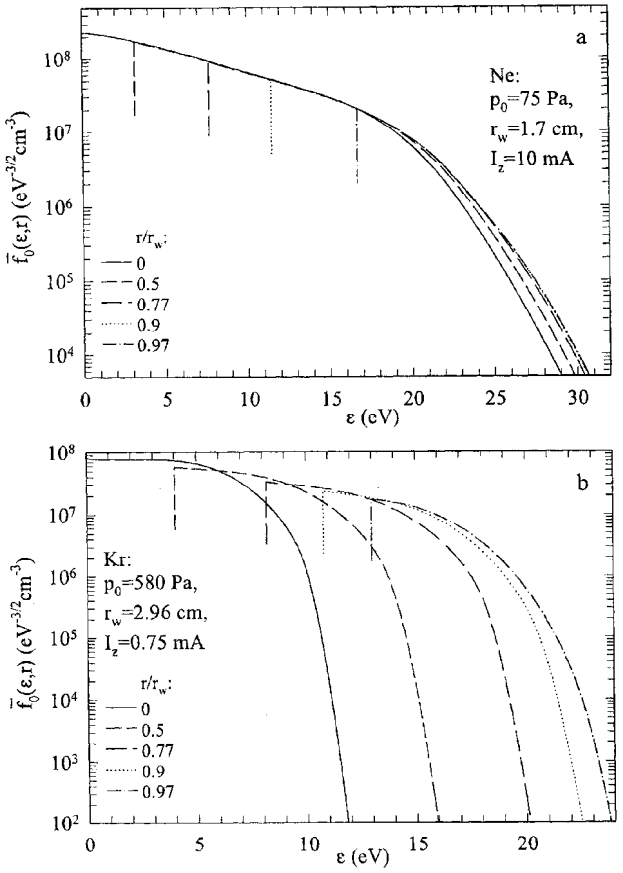

Figure 4. Isotropic distribution $\bar{f}_0(\varepsilon, r)$ at various radial positions for the neon (a) and for the krypton (b) column plasma. The vertical lines indicate the starting points of $\bar{f}_0(\varepsilon, r)$, i.e., the ε value related to zero kinetic energy.

On the basis of the consistent treatment of the radially varying electron kinetics in addition to the isotropic distribution $f_0(U, r)$ the determination of the radial and axial anisotropic distribution $f_r(U, r)$ and $f_z(U, r)$ becomes possible.

Because of the complete neglect of the impact of the radial plasma structure in the frame of the conventional homogeneous approach there is naturally no any way to determine the radial anisotropic distribution. The latter statement holds too with respect to the nonlocal approach since, due to the first equation of (8) and the above-mentioned neglect of the radial dependence of $\bar{f}_0(\varepsilon, r)$, the radial anisotropic distribution formally vanishes. As an immediate consequence the radial transport of the electrons and that of their kinetic energy can not be treated and described by both these simplified approaches. As a further consequence the electron production by ionization in the plasma volume can not be taken into account in the corresponding simplified kinetic equations otherwise an obvious inconsistency would arise. An attempt has been made recently[10] to overcome this inconsistency to a certain extent by inserting an electron loss term

in the kinetic equation of the nonlocal approach which represents the radial upflux of electrons to the tube wall. However, this treatment is incompatible with the vanishing radial transport of the electrons.

Related to the first three of the four parameter sets given above the energy dependence of the isotropic distribution $f_0(U, r)$ and of both anisotropic distributions $f_r(U, r)$ and $f_z(U, r)$ is shown in Figs. 5a-c at the same two values 0.2 and 0.77 of the normalized radial position r/r_W. From these figures a relatively small magnitude of the radial anisotropic distribution compared with the isotropic as well as the axial anisotropic distribution can be seen for all three discharge conditions and at both radial positions. This means there is no any indication that a large anisotropy of the velocity distribution is established in the plasma and that the validity of the two term approximation is lost somewhere in the plasma. Furthermore, in all three cases and at both radial positions, i.e. in the central region and in the surrounding of the discharge wall, always two branches with positive sign at lower and negative sign at higher electron energies occur in the radial anisotropic distribution. This typical behaviour is a distinct reflection of the radial confinement of the electrons by the space charge field.

With respect to the radial alteration of the three distribution components and particularly to the two branches occurring in the radial anisotropic distribution, shown in Figs. 5a-c, it should be underlined that this behaviour is a direct consequence of the interplay between the action of the axial and radial electric field and that of the various collision processes and is not artificially enforced by the choice of the boundary value $g(U)$ for the radial anisotropic distribution. This has been checked, for example, by repeated calculation of the velocity distribution for the same plasma conditions, however for different values of the parameter a involved in the above-given boundary value $g(U)$. An alteration of a in certain limits causes a small alteration of the distribution components however only in the immediate neighbourhood of the tube wall.

To give a further indication, that the specific course of the radial anisotropic distribution is lastly a consequence of the electron confinement by the space charge field and does not sensitively depend on the choice of the boundary value on the plasma surface, the solution of the kinetic problem has been repeated without the inclusion of ionizing collisions in the kinetic equation. The consistent particle balance (5) immediately shows in this case, that the radial particle current density vanishes at each radial position and thus on the plasma surface too. Therefore, the boundary value $g(U)$ has to be replaced by zero and no electron transport onto the wall takes place. However in this case only small modifications of the results are obtained and the typical behaviour of the radial anisotropic distribution remains. This result is illustrated by Fig. 6 for the neon plasma. At one radial position the isotropic distribution as well as the radial anisotropic distribution are compared for the cases with and without inclusion of the ionization processes in the kinetic equation.

As outlined above and already presented in (4), the radial and axial anisotropic distribution determine by appropriate energy space averages the radial and axial components j_r, j_z, j_{er} and j_{ez} of the particle and energy current density $\vec{j}$ and $\vec{j}_e$ of the electrons. The radial alteration of both components of the particle and energy current density are shown in Figs. 7a,b for neon and in Figs. 7c,d for krypton and the He/Xe-mixture at 200 Pa. The comparison of both components of the particle current density shows that the radial current density jr is in all three column plasmas by about two orders of magnitude smaller than the axial current density j_z. The change of the sign in the radial anisotropic distribution with increasing kinetic energy, as illustrated for the same discharge conditions in Figs. 5a-c, leads always to a remarkable compensation of the positive and negative contributions to the integral value in the calculation

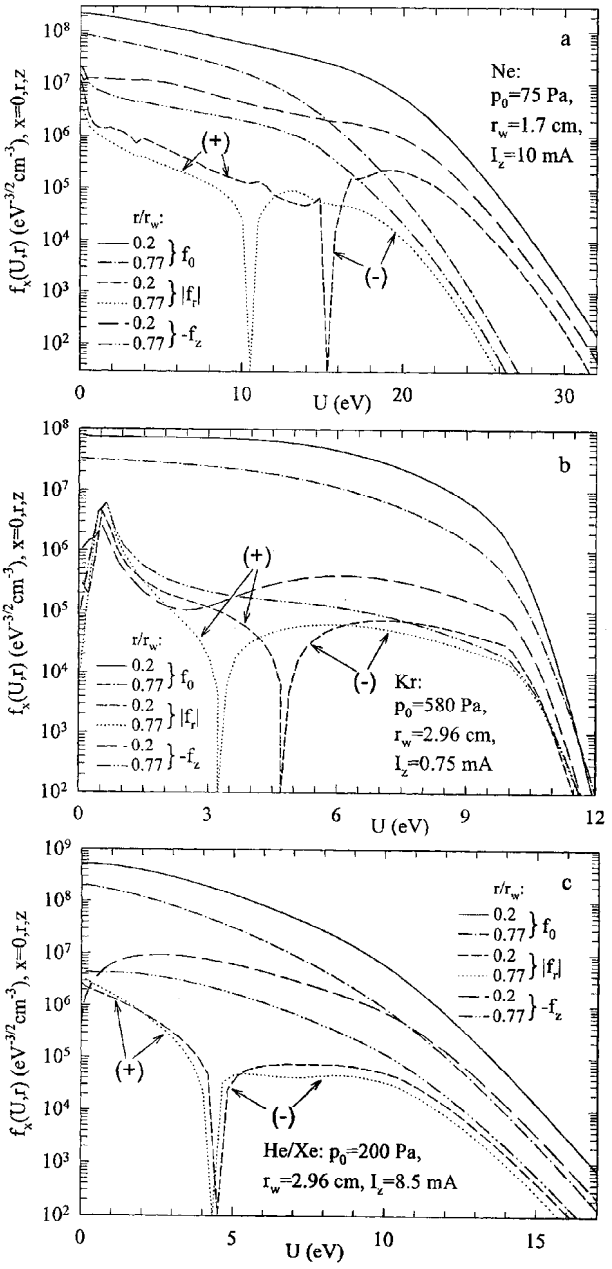

Figure 5. Isotropic distribution $f_0(U, r)$, radial and axial anisotropic distribution $f_r(U, r)$ and $f_z(U, r)$ at two radial positions for neon (a), krypton (b), and for the He/Xe-mixture (c).

of j_r and j_{er} from $f_r(U, r)$. This is lastly a consequence of the fact that always the two contributions to the radial particle current density according to $j_r = j_{rd} + j_{re}$,

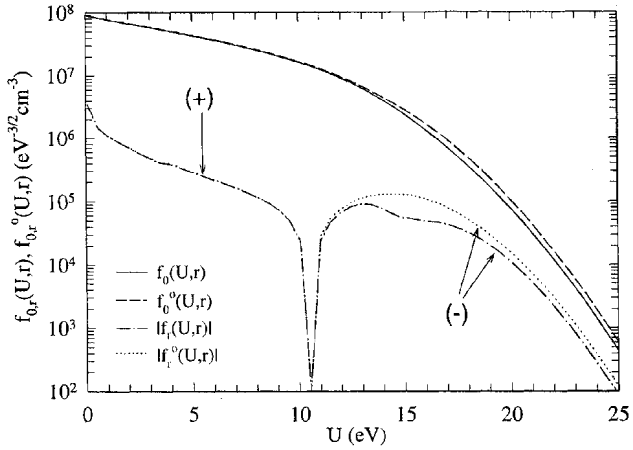

Figure 6. Isotropic distribution $f_0(U, r)$ and radial anisotropic distribution $f_r(U, r)$ at the radial position $r=0.77r_W$ for neon in comparison with the corresponding distribution function f_0^o (U, r) and f_r^o (U, r) determined without the inclusion of ionizing collisions in the kinetic equation.

namely the diffusion part $j_{rd}(r) = -\frac{1}{3}\sqrt{\frac{2}{m}} \int_0^\infty \frac{U}{H(U,r)} \frac{\partial}{\partial r} f_0(U,r)\, dU$ and the field driven part $j_{re}(r) = \frac{1}{3}\sqrt{\frac{2}{m}} \int_0^\infty \frac{U}{H(U,r)} \frac{\partial}{\partial U} f_0(U,r)\, dU\, e_0 E_r(r)$, compensate each other to a large extent. Their representations follow immediately from (3) and (4). These parts are additionally shown for the neon plasma in Fig. 7a. In the same way the diffusion and the field driven part j_{erd} and j_{ere} of the radial energy current density j_{er} can be introduced which are additionally presented for the neon plasma in Fig. 7b. However a detailed comparison of the radial particle with the radial energy current density indicates for each of the plasmas considered that a lesser compensation of the respective diffusion and field driven part occurs with respect to the energy current density. As Figs. 7a-d clearly show, an unexpectedly large radial energy current compared with the radial particle current of the electrons occurs particularly in the neon and krypton plasma and against the expectation the radial energy current flows in all plasmas from the outer column region to the column centre. Thus a larger radial transport of electron energy is required to establish a stable operation of the column plasmas.

Let us further discuss the radial alterations occurring with respect to the energy budget of the electrons in the column plasmas considered. This can be made by considering the various contributions to the energy balance equation (6), i.e. the alteration of the energy transfer rates P_z and P_r caused by the action of the field components E_z and E_r, of the energy losses L^{el} and L^{in} by elastic and inelastic collisions and of the energy source or sink represented by the divergence of the radial energy current density $\mathrm{div}(j_{er}\vec{e}_r) \equiv \frac{1}{r}\frac{d}{dr}(r j_{er})$. For all four plasma conditions specified above, i.e. for neon, krypton and the He/Xe-mixture at 200 and 600 Pa, Figs. 8a-d show the radial alterations of all contributions to the energy balance equation (6) of the electrons.

From Fig. 8a, related to the plasma in neon, it becomes obvious that in the central region of the column plasma the total energy loss in collisions $L \equiv L^{el} + L^{in}$ is about two times the energy gain from the axial field. However outside the central region increasingly the reverse situation occurs. The large difference between the energy gain P_z and the energy loss L at each radial position is compensated for by a large divergence

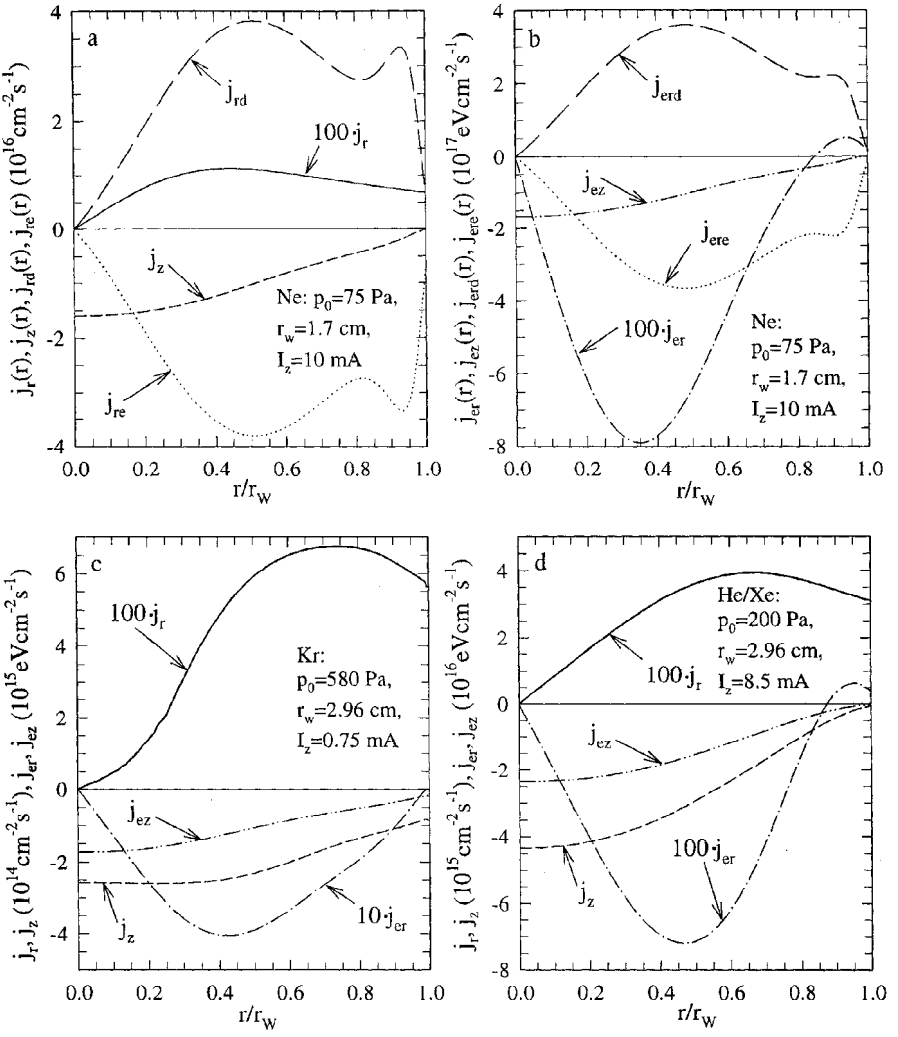

Figure 7. Radial alteration of the radial and axial electron particle current density j_r and j_z, of the radial and axial energy current density j_{er} and j_{ez} for neon (a and b), krypton (c) and for He/Xe-mixture (d). The diffusion part j_{rd} and the field driven part j_{re} of the radial particle current density and the analogous parts j_{erd} and j_{ere} of the radial energy current density are additionally presented for neon (a and b).

of the radial energy current density $j_{er}\vec{e}_r$ of the electrons. The very small contribution P_r of the radial space charge field to the energy balance represents a small cooling of the electrons in the space charge field.

The behaviour of the energy balance terms in the krypton plasma, which is presented in Fig. 8b, is very similar to that in the neon plasma. However the total energy loss in collisions L exceeds now in the central column region the energy input P_z from the axial field by a factor of about 1.5, i.e. by a somewhat reduced factor compared to neon.

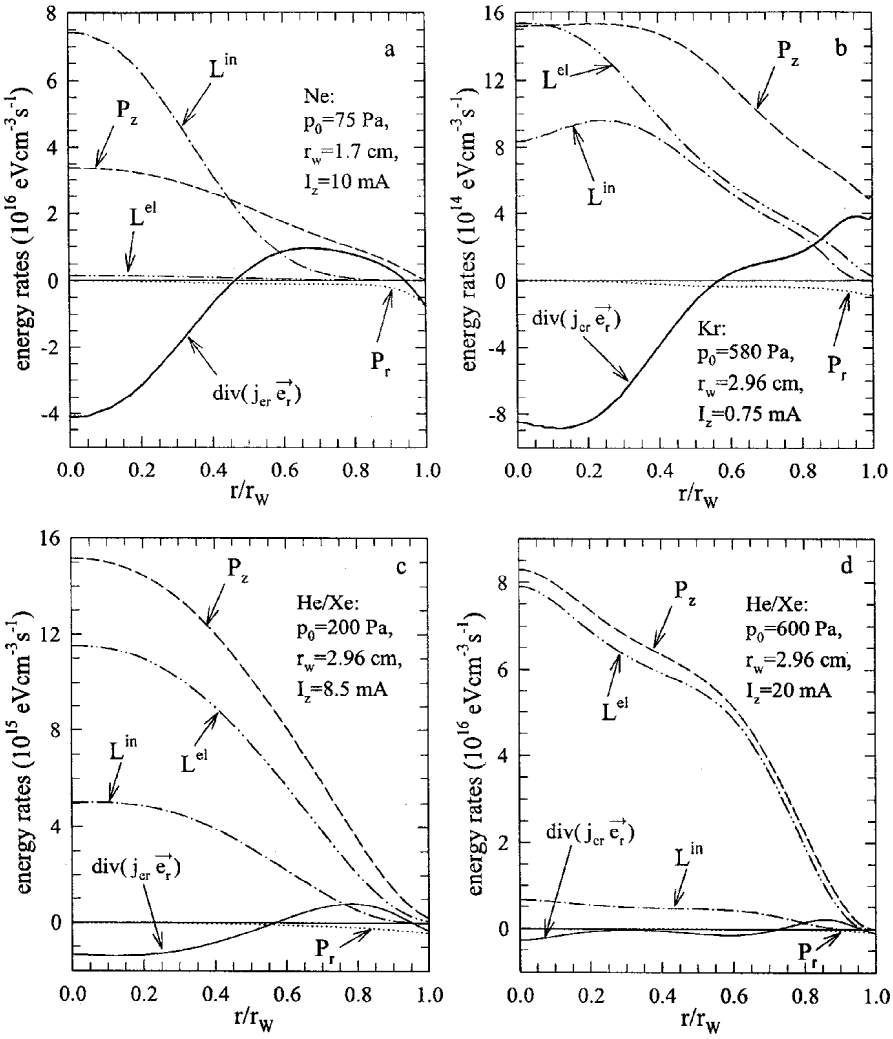

Figure 8. Important terms of the local electron energy balance for neon (a), krypton (b) and for the He/Xe-mixture at 200 and 600 Pa (c and d): divergence of the radial energy current density $j_{er}\vec{e}_r$, axial heating P_z, radial cooling P_r, energy loss in elastic and inelastic electron collisions L^{el} and L^{in}.

The consideration of the results on the spatially resolved energy balance related to the neon and krypton plasma clearly indicates that particularly in the central column region the largest deviations between the local gain and loss of energy occur and a large energy current from the outer to the inner column region is required to satisfy the consistent energy balance. This underlines once more that the various processes inside the plasma mainly determine this somewhat unexpected behaviour of the electrons and that the latter does not be artificially caused by the particular choice made above of the boundary value $g(U)$ for the radial anisotropic distribution.

However the further representations of the energy balance terms in Figs. 8c,d related to the He/Xe-mixture indicate that under these discharge conditions remarkably

smaller differences between the total energy loss in collisions and the energy gain from the axial electric field occur in almost the entire column plasma. In the case of Fig. 8d, related to the higher pressure of 600 Pa, finally an almost local compensation of the energy loss in collisions L and the energy input P_z from E_z is found, and the transport of energy by the radial energy current density is of less importance.

To give some informations concerning the particle budget of the electrons, Figs. 9a,b present, for the column plasma in neon and in the He/Xe-mixture at 200 Pa the radial alteration of the various contributions to the consistent particle balance (5). According to this balance the sum of the electron gain due to the ionization by electron collisions with ground state atoms (G_0) and with excited atoms (G_{ex}) and by the chemo-ionization (G_{ch}) of excited atoms is compensated for by the divergence of the radial electron particle current density div($j_r \vec{e}_r$). It can be observed that the ionization of excited atoms remarkably contributes to the electron production and this is particularly true for the He/Xe-mixture. In this figure the contribution G_{ch} of the chemo-ionization is explicitly presented due to its larger impact on the electron particle balance.

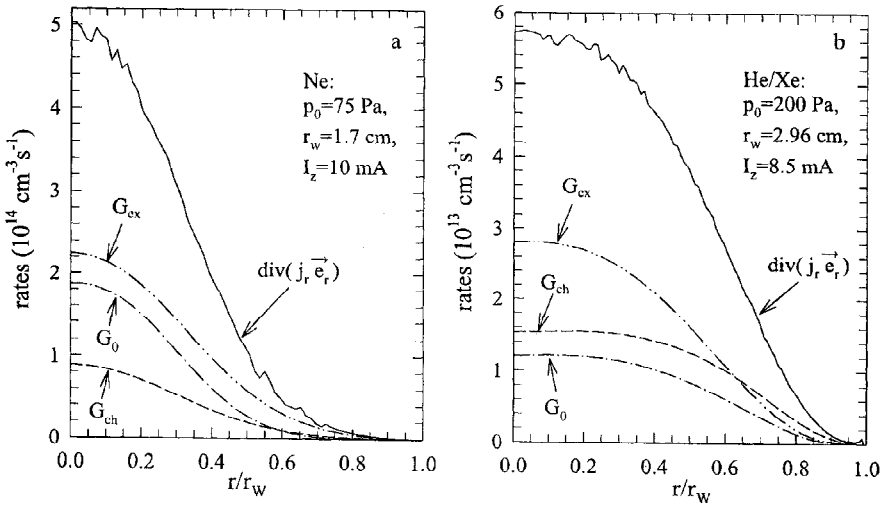

Figure 9. Terms of the local electron particle balance for neon (a) and for the He/Xe-mixture at 200 Pa (b): divergence of the radial current density $j_r \vec{e}_r$ electron production rates due to ionization from the ground state G_0 and excited states G_{ex} by electron collisions, and due to chemo-ionization G_{ch}.

CONCLUDING REMARKS

The various results reported above on the radial alteration of electron kinetic quantities in the dc column plasma of neon, krypton and He/Xe-mixtures have distinctly illustrated that quite different situations with respect to the radial alteration of the isotropic distribution, the radial energy current density and the dominant processes in the energy balance of the electrons can be established.

Depending on the specific plasma conditions considered, the radial behaviour of electron kinetic quantities can be found somewhere between two limiting cases, for

example, between a pronounced radial alteration and an almost radial-independent behaviour of the isotropic distribution normalized on the local electron density or between a pronouncedly nonlocal and an almost local behaviour of the dominant exchange processes occurring in the energy balance of the electrons.

In particular, the results related to the krypton plasma have clearly demonstrated that very complex situations with respect to the kinetics can occur. In this case an almost radial-independent normalized isotropic distribution but still a pronouncedly nonlocal behaviour in the energy balance is found.

It has been further seen that some kinetic properties obtained for the different plasma situations are largely in disagreement with basic assumptions of simplified treatments of the kinetic problem as the conventional homogeneous approach or the nonlocal approach.

REFERENCES

1. D. Herrmann, A. Rutscher, and S. Pfau, Radiale Änderung der Energieverteilungsfunktion der Elektronen im Plasma der positiven Säule elektrischer Entladungen, *Contrib. Plasma Phys.* 11:75, 1971.
2. L. D. Tsendin, Energy distribution of electrons in a weakly ionized current-carrying plasma with a transverse inhomogeneity, *Sov. Phys. JETP* 39:805, 1974.
3. S. Pfau and R. Winkler, Das diffusionsbestimmte Plasma der positiven Säule von Niederdruckentladungen in Neon bei mittleren Ionisierungsgraden von 10^{-8} – 10^{-3}, *Contrib. Plasma Phys.* 20:343, 1980.
4. M. J. Hartig and M. J. Kushner, Radially dependent solutions of Boltzmann's equation in low-temperature plasmas using a modified two-term expansion, *J. Appl. Phys.* 73:1080, 1993.
5. C. Busch and U. Kortshagen, Numerical solution of the spatially inhomogeneous Boltzmann equation and verification of the Nonlocal Approach, *Phys. Rev. E* 51:280, 1995.
6. U. Kortshagen, Electron and ion distribution functions in RF and microwave plasmas, *Plasma Sources Sc. Technol.* 4:172, 1995.
7. L. D. Tsendin, Electron kinetics in non-uniform glow discharge plasmas, *Plasma Sources Sc. Technol.* 4:200, 1995.
8. J. Behnke, Yu. B. Golubovsky, S. U. Nisimov, and I. A. Porokhova, Self-consistent model of a positive column in an inert gas discharge at low pressure and small currents, *Contrib. Plasma Phys.* 36:75, 1996.
9. U. Kortshagen, C. Busch, and L. D. Tsendin, On simplifying approaches to the solution of the Boltzmann equation in spatially inhomogeneous plasmas, *Plasma Sources Sc. Technol.* 5:1, 1996.
10. U. Kortshagen, G. J. Parker, and J. E. Lawler, Comparison of Monte Carlo simulations and nonlocal calculations of the electron distribution function in a positive column plasma, *Phys. Rev. E* 54:6746, 1996.
11. G. J. Parker, W. N. G. Hitchon, and J. E. Lawler, Numerical solution of the Boltzmann equation in cylindrical geometry, *Phys. Rev. E* 50:3210, 1994.
12. D. Uhrlandt and R. Winkler, Radially inhomogeneous electron kinetics in the dc column plasma, *J. Phys. D: Appl. Phys.* 29:115, 1996.
13. D. Uhrlandt and R. Winkler, Radial structure of the kinetics and production of electrons in the dc column plasma, *Plasma Chem. Plasma Process.* 16:517, 1996.
14. L. L. Alves, G. Gousset, and C. M. Ferreira, Self-contained solution to the spatially inhomogeneous electron Boltzmann equation in a cylindrical plasma column, *Phys. Rev. E* 55:890, 1997.
15. I. B. Bernstein and T. Holstein, Electron energy distribution in stationary discharges, *Phys. Rev.* 94:1475, 1954.
16. S. Pfau, J. Rohmann, D. Uhrlandt, and R. Winkler, Experimental and theoretical study of the inhomogeneous electron kinetics in the dc column plasma, *Contrib. Plasma Phys.* 36:449, 1996.
17. D. Uhrlandt, *Zur radial inhomogenen Elektronenkinetik im Säulenplasma der Glimmentladung*, Dissertation, University Greifswald, Germany, 1996.
18. S. Pfau and J. Rohmann, Physical Institute, University Greifswald, Germany, private communication.

ELECTRON KINETICS IN HOMOGENEOUS AND STRATIFIED POSITIVE COLUMN AND ANODE REGION

Yu. B. Golubovskii,[1] V. O. Nekuchaev,[2] and I. A. Porokhova[1]

[1]St.Petersburg University
[2]Uchta Industrial Institute
Ulianovskaia 1, Petrodvorets, St.Petersburg, Russia, 198904

INTRODUCTION

Now the kinetic approach is actively developing for description of various spatially inhomogeneous structures of gas discharge plasmas. The modern state of the problem is reflected in the reviews[1,2] where the convincing argumentation is given for inapplicability of fluid approach and for necessity of successive kinetic analysis for description of such classical plasma objects as, for instance, positive column of a discharge at low pressure and small currents, for cathode and anode regions of glow discharge, for striations, etc.

In the present paper the results of the last works of the authors on experimental and theoretical studies of homogeneous positive column and of anode region of inert gas discharges, as well as of S- and P-striations in the column and near anode are generalizing. The considerable difference between the results of kinetic and fluid approaches is demonstrated on concrete examples.

POSITIVE COLUMN OF NONSTRATIFIED INERT GAS DISCHARGE

For the first time the problem about determination of electron distribution function in radially inhomogeneous plasma of the positive column has been formulated by Bernstein and Holstein[3] and later independently from them by Tsendin[4]. In the papers[5,6] there have been set up the problem on self-consistent description of the positive column of a discharge on the basis of joint solution of Boltzmann kinetic equation for electrons and of equation for field which is the ion motion equation. Most details in the self-consistent kinetic theory of the positive column on example of neon discharge have been discussed in the papers[7,8]. The self-consistent kinetic description consists in finding of the potential profile in which the distribution function has to be formed providing ionization rate, electron density and losses on the wall which are required for maintaining of this field and allowing the current flow through the gas.

The considerable differences in description of discharges at low and high pressures take place. At high pressures, when electron energy relaxation length is shorter than the

Electron Kinetics and Application of Glow Discharges
Edited by U. Kortshagen and L. D. Tsendin, Plenum Press, New York, 1998

tube radius, the electrons are accelerated in longitudinal electric field without noticeable diffusion displacements in radial direction. This permit to neglect the radial gradient of distribution function in kinetic equation. The motion of electrons in radial direction does not influence the distribution function formation with the exception of a small region near the tube walls, the length of which is about the energy relaxation length (local approximation). At low pressures, when the energy relaxation length exceeds the tube radius, the radial diffusive motion of electrons produces the dominant effect on distribution function, and here its form is determined by whole radial profile of potential (nonlocal approximation).

The potential fields of the positive column, where the motion of electrons will be analyzed are schematically shown in Fig.1.

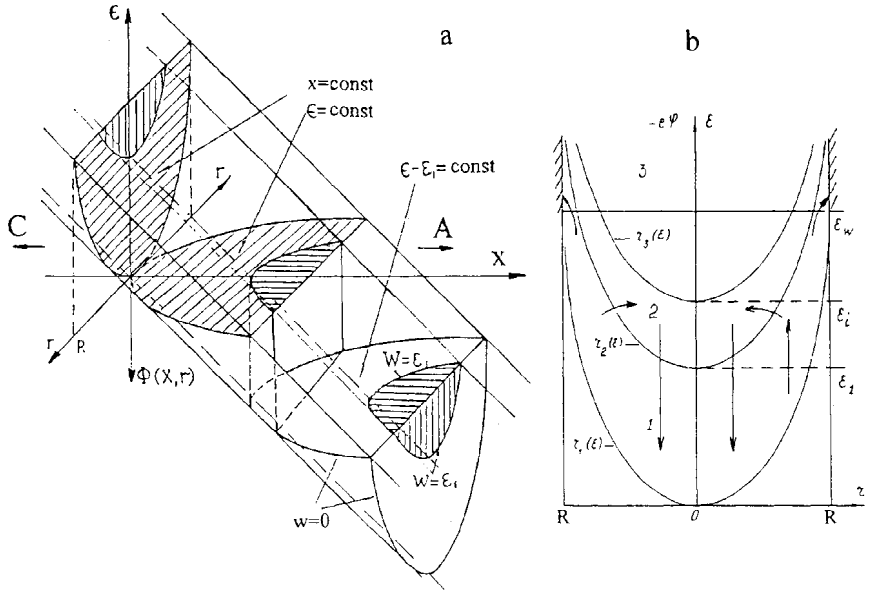

Figure 1: a) Potential field $e\,\Phi(x, r)$ in which the motion of electrons is analyzed. The plane $\epsilon = const$ corresponds to electron motion without energy loss in collisions. Inelastic impacts lead to the jump of electrons with energies $w > \varepsilon_1$ from the plane $\epsilon = const$ on the plane $\epsilon - \varepsilon_1 = const$. b) Potential field $e\varphi(r)$ at $x = const$. The curves $r_1(\varepsilon), r_2(\varepsilon)$ are determined by the equalities $r_1(\varepsilon) : w = 0,\ \varepsilon = e\varphi(x),\ r_2(\varepsilon) : w = \varepsilon_1,\ \varepsilon = \varepsilon_1 + e\varphi(r)$; The numbers 1, 2, 3 correspond to elastic, inelastic and direct ionization regions respectively.

If in electron energy balance the inelastic losses dominate (low pressures) and the electron-electron interactions are negligibly small (small currents), electrons move with conservation of their total energy $\epsilon = w + e\Phi(x, r) = w - eEx + e\varphi(r)$ (w is kinetic and $e\varphi$ is potential energies). On the plane $\epsilon = const$ the electrons are accelerating by the action of the axial field E (diffusion along x axis) and diffusing in radial direction by the action of radial gradients. As electron kinetic energy exceeds the excitation threshold ε_1 the electrons can undergo inelastic collision and jump on the plane $\epsilon - \varepsilon_1 = const$. In the presence of energy loss in elastic collisions and of energy exchange in electron-electron collisions the components of flux in ϵ direction appear. The surface corresponding to electron motion ceases to be a plane, it becomes bent in x and r directions.

For the solution of self-consistent problem it is convenient to write the Boltzmann kinetic equation for isotropic f_0 and anisotropic $\overrightarrow{f_1}$ components of distribution function

on the plane $x = const$ in variables ε, r (Fig. 1b).

The complete system of equations has a form

$$\frac{(eE)^2}{3}\frac{\partial}{\partial\varepsilon}\frac{v^3}{\nu(v)}\frac{\partial f_0(\varepsilon,r)}{\partial\varepsilon}+\frac{1}{3r}\frac{\partial}{\partial r}r\frac{v^3}{\nu(v)}\frac{\partial f_0(\varepsilon,r)}{\partial r}= \\ = v\nu^*(v)f_0(\varepsilon,r)-v'\nu^*(v')f_0(\varepsilon',r), \tag{1}$$

$$\vec{f_1}(\varepsilon,r)=-\frac{v}{\nu(v)}\left(eE\frac{\partial f_0}{\partial\varepsilon}\vec{e_x}+\frac{\partial f_0}{\partial r}\vec{e_r}\right), \tag{2}$$

$$\mathrm{div}j_i=\frac{1}{r}\frac{\partial}{\partial r}rb_in_i(\varphi)\frac{\partial\varphi}{\partial r}=I(\varphi). \tag{3}$$

Here $\nu(v)$ is the transport frequency of elastic impacts, $\nu^*(v)$ is the summarized frequency of inelastic impacts, b_i is the ion mobility, j_i is the ion flux in radial direction, $n_i(\varphi(r))$ and $I(\varphi(r))$ are ion density and ionization rate, $\vec{e_x}$ and $\vec{e_r}$ are the unit vectors in axial and radial directions. The form of Eqs. (1), (2) shows the approximations done: the momentum relaxation considers elastic impacts only and expansion of distribution function is restricted to two terms. The last term in Eq. (1) describes the appearance of slow electrons which have lost energy in inelastic collisions (the transitions inside the cylindrical region (Fig. 1a)). We can unite the low excitation levels of inert gases in one effective level with excitation potential ε_1. Then the velocities v, v' as well as the energies ε, ε' are connected by the relations

$$mv'^2/2=mv^2/2+\varepsilon_1; \qquad \varepsilon'=\varepsilon+\varepsilon_1$$

The kinetic equation (1) should be supplemented by the boundary conditions which can be written in the different ways depending on required accuracy of expectable results. One of the simplest boundary conditions for solution of self-consistent problem are as following

$$\left.\frac{\partial f_0(\varepsilon,r)}{\partial r}\right|_{r=r_1(\varepsilon),\varepsilon<\varepsilon_w}=0; \qquad f_0(\varepsilon,r)|_{\varepsilon\geq\varepsilon_w}=0 \tag{4}$$

These boundary conditions correspond to “black-wall” approximation at energies equal to wall potential $\varepsilon = \varepsilon_w$. The electrons with energies $\varepsilon > \varepsilon_w$ leave fast to the walls, and those with energies $\varepsilon < \varepsilon_w$ are trapped in radial direction by the field of space charge $\varphi(r)$. Under this approximation the electron losses on the wall can be obtained as a flux in energy space at $\varepsilon = \varepsilon_w$. Trapped electrons determine electron density and provide the flowing of axial discharge current.

More precise boundary conditions can be set in the form

$$\left.\frac{\partial f_0(\varepsilon,r)}{\partial r}\right|_{r=r_1(\varepsilon),\varepsilon<\varepsilon_w}=0; \qquad f_0(\varepsilon,r)|_{r=R,\varepsilon\geq\varepsilon_w}=0; \qquad f_0(\varepsilon,r)|_{\varepsilon\to\infty}=0. \tag{5}$$

These conditions correspond to the presence of two almost independent groups of electrons - trapped and free ones with energies $\varepsilon > \varepsilon_w$. The free electrons under this approximation leave to the walls in regime of unipolar diffusion. The lack of such boundary conditions consists of the discontinuity of the derivative $\partial f_0 / \partial r$ at $\varepsilon = \varepsilon_w$ The boundary conditions with continuous derivatives consider the presence of loss cone in the near wall region[9].

To obtain the distribution function it is necessary to know the radial potential profile. Under assumption of quasineutral plasma ($n_i \approx n_e$) it is determined by the

equation (3) where the ionization rate and the electron density should be expressed in terms of the distribution function

$$n_e(e\varphi) = \int_{e\varphi}^{\infty} f_0(\varepsilon, r)\sqrt{\varepsilon - e\varphi}\,d\varepsilon. \tag{6}$$

The ionization term under conditions of low-pressure discharge combines direct $I_d(\varphi)$ and stepwise $I_s(\varphi)$ ionization and ionization in collisions of metastable and resonance atoms $I_m(\varphi)$ (chemoionization). Averaging the direct ionization frequency ν_i over distribution function we obtain the direct ionization rate as a function of potential, ε_i is ionization potential

$$I_d(e\varphi) = \int_{\varepsilon_i + e\varphi(r)}^{\infty} \nu_i(\varepsilon - e\varphi) f_0(\varepsilon, r)\sqrt{\varepsilon - e\varphi}\,d\varepsilon. \tag{7}$$

The four lower metastable and resonance levels of an inert gas atom contribute to stepwise and chemoionizations. The explicit calculation of their rates requires the analysis of the balance equation system for the levels with regard to resonance radiation, diffusion of metastables to the walls, energetic transmissions in collisions with atoms and electrons and radiation processes through upper excited states. Since the influence of ionization processes on distribution function and radial potential is small it is possible to use the approximation of one effective level providing the stepwise ionization and chemoionization. The balance equation for the effective level with density N_m can be approximately written in the form

$$W(e\varphi) = N_m\nu_m + I_s(e\varphi) + I_m(e\varphi) \tag{8}$$

where

$$W(e\varphi) = \int_{\varepsilon_1 + e\varphi(r)}^{\infty} \nu^*(\varepsilon - e\varphi) f_0(\varepsilon, r)\sqrt{\varepsilon - e\varphi}\,d\varepsilon \tag{9}$$

$$I_s(e\varphi) = N_m \int_{\varepsilon_s + e\varphi(r)}^{\infty} \sigma_s(\varepsilon - e\varphi) f_0(\varepsilon, r)(\varepsilon - e\varphi)\,d\varepsilon \tag{10}$$

$$I_m(e\varphi) = N_m^2 k_m \tag{11}$$

Here W is the total number of inelastic impacts, ν_m is the summarized frequency of deactivation of the level N_m connected with metastable diffusion to the walls, effective probability of resonance radiation outcome, etc., rather than with ionization processes. ε_s and σ_s are the threshold and the cross-section of stepwise ionization and k_m is the rate constant of chemoionization. The solution of equation (8) gives the excited atom density N_m which permits to calculate the rates of stepwise ionization (10), of chemoionization (11) and of summarized one $I = I_d + I_s + I_m$.

The system of equations (1)–(3) permits under given external parameters of the discharge – pressure p, current i, radius R, and the constants of elementary processes characterizing the sort of gas - to obtain the internal discharge parameters such as electron distribution function f_0 and $\vec{f_1}$, axial field E and radial potential $e\varphi(r)$, in particular the wall potential ε_w, and thus to reconstruct the potential field shown in Fig.1 and to calculate related macroscopic plasma properties.

The solution of the kinetic equation (1) can be obtained by its averaging over electron radial motions that is justified if electron energy relaxation length exceeds the tube radius.

The energy relaxation length can be defined as a distance at which electrons can diffuse at a time of energy exchange in elastic, inelastic and electron–electron impacts and at a time of accumulation of energy equal to excitation threshold

$$\lambda_\varepsilon \approx \sqrt{D_e\tau}; \qquad D_e \approx \frac{v^2}{3\nu}; \qquad \frac{1}{\tau} = \frac{m}{M}\nu + \nu^* + \nu_{ee} + \frac{1}{\tau_E}; \qquad \frac{1}{\tau_E} = \frac{(eE)^2}{m\nu\varepsilon_1}$$

In this meaning the energy relaxation length defines the spatial scale at which electron distribution function is formed due to collisions of different kind.

$$\lambda_\varepsilon \approx \lambda_e \sqrt{\frac{\nu}{\frac{m}{M}\nu + \nu^* + \nu_{ee} + \frac{(eE)^2}{m\nu\varepsilon_1}\theta(w)}}; \qquad \theta(w) = \begin{cases} 1 & w < \varepsilon_1 \\ 0 & w > \varepsilon_1 \end{cases} \tag{12}$$

At the energies $w < \varepsilon_1$ (elastic region, $\nu^* = 0$) for the discharge at low pressure and small current, when $\frac{m}{M}\nu$ and ν_{ee} are small, the equation (12) gives $\lambda_\varepsilon \approx \varepsilon_1/eE$. At the energies $w > \varepsilon_1$ (inelastic region) $\lambda_\varepsilon \approx \lambda\sqrt{\frac{\nu}{\nu^*}} \approx \sqrt{\lambda\lambda^*}$. And the averaging of kinetic equation is valid when

$$\frac{\varepsilon_1}{eE} > R, \qquad \sqrt{\lambda\lambda^*} > r_2(\varepsilon)$$

here λ, λ^* are electron free paths with respect to elastic and inelastic impacts. At low pressures the first condition is fulfilled well. The relaxation length with respect to inelastic impacts $\sqrt{\lambda\lambda^*}$ exceeds the size of inelastic region $r_2(\varepsilon)$ for energies larger than excitation threshold by the value about $0.25\varepsilon_1\sqrt{\lambda\lambda^*}/R$.

After averaging the equation becomes

$$(eE)^2 \frac{d}{d\varepsilon}\overline{\left(\frac{v^3}{3\nu(v)}\right)}\frac{df_0(\varepsilon)}{d\varepsilon} = \overline{v\nu^*(v)}f_0(\varepsilon) - \overline{v'\nu^*(v')}f_0(\varepsilon + \varepsilon_1) \tag{13}$$

The procedure of averaging is connected with calculations of the integrals over radius of the functions depending on kinetic energy, that demands the knowledge of required potential profile in explicit way. At the first stage the averaging can be done by means of trial potential depending, for instance, on two parameters β and ε_w

$$e\varphi(r) = \begin{cases} \beta\varepsilon_1(r/R)^2 & r < R \\ \varepsilon_w & r = R \end{cases}$$

The distribution function $f_0(\varepsilon)$ obtained thus from the solution of Eq.(13) depends on three parameters of trial potential E, ε_w and β and permits to find $n_e(\varphi)$ and $I(\varphi)$ from the equations (6), (7), (10), (11) and to find new potential profile $\varphi(r)$ from equation (3). The parameters of trial potential were varied in order to satisfy to equality of ion and electron fluxes on the wall, and to balance of charged particles in bulk plasma and of losses on the walls. The obtained solution for distribution function satisfies to kinetic equation (13) and the solution for potential satisfies to ion motion equation (3).

The results of self-consistent solution of the problem with boundary conditions (5) for discharge in neon are shown Fig. 2.

The distribution functions as the functions of total energy ε have explicit radial dependence near wall potential ε_w and at higher energies, such behavior is a consequence of diffusion of free electrons to the walls. As the pressure grows the rate of charged particle losses on the walls decreases, that requires the decrease of ionization rate and hence of the field E/p and of mean energy $\langle w \rangle$. The characteristic energetic scale size of the distribution function drop in inelastic region $kT^* \sim \sqrt{E/p}$ also decreases with the growth of pressure leading to decrease of wall potential ε_w.

The solutions of kinetic equation (1) represented in Fig.2 are obtained with the help of the averaging over radial motions up to the energies $\varepsilon < \varepsilon_w - eER$ and by sewing together with the solution explicitly dependent on radius at the energies $\varepsilon > \varepsilon_w - eER$. This approximation assumes that the condition of distribution function nonlocality is fulfilled in both elastic and inelastic regions. However, at large energies this condition can be broken because of the high values of the frequency of inelastic impacts. That can

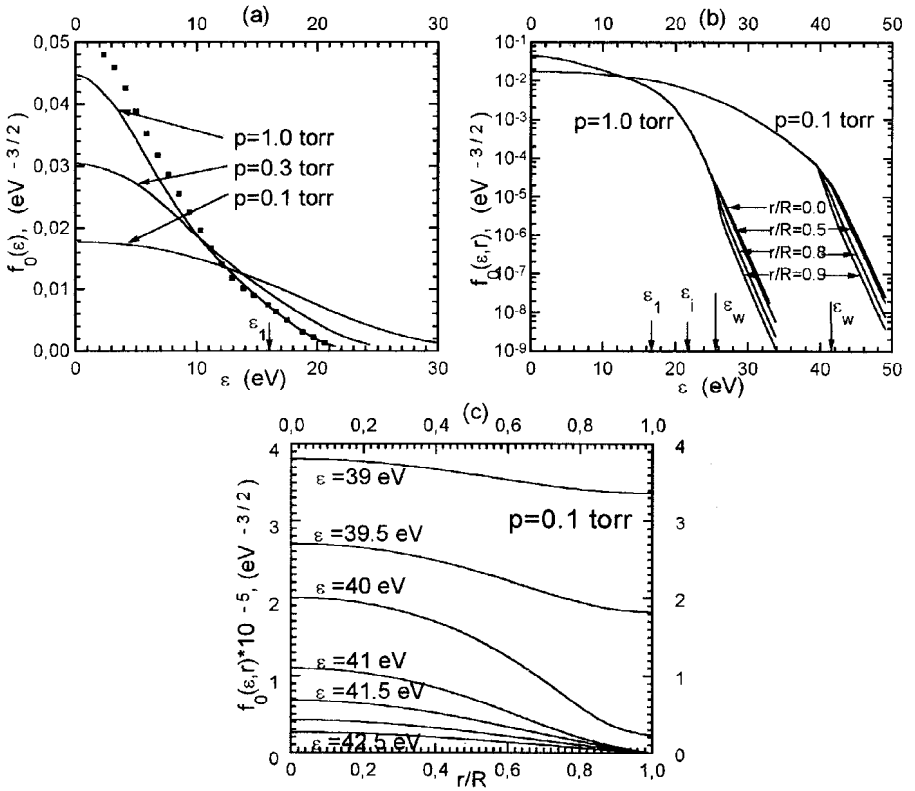

Figure 2. The distribution functions calculated in the self-consistent potential for Ne, $i = 10\ mA$, $R = 1\ cm$ in a) linear, b) logarithmic scales. Dots are experimental results ($p = 1\ torr$, $i = 10\ m\ A$). c)- radial dependence of distribution function near wall potential at $p = 0.1\ torr$.

Table 1. Calculated values of discharge parameters. n_0, I_0, (w_0) and $2\pi R j_R$ are axial values of electron density, ionization rate, average energy and of particle flux to the walls respectively.

	i mA	p torr	E V/cm	ε_w eV	n_0 cm^{-3}	I_0 cm^{-3}s^{-1}	$\frac{2}{3}\langle w_0\rangle$ eV	$2\pi R j_R$ cm^{-1} s^{-1}
Ne	10	0.1	4.01	40.7	$8.5\cdot10^{8}$	$9.7\cdot10^{14}$	9.2	$1.94\cdot10^{15}$
Ne	10	1.0	2.67	25.5	$4.9\cdot10^{9}$	$5.4\cdot10^{14}$	5.6	$0.6\cdot10^{15}$
He	5	0.3	2.32	31.2	$1.0\cdot10^{9}$	$4.5\cdot10^{14}$	6.5	$1.4\cdot10^{15}$
He	35	0.3	1.94	28.8	$8.0\cdot10^{9}$	$3.1\cdot10^{15}$	6.1	$9.9\cdot10^{15}$

result in localization of distribution function in this energy range and in enlargement of electron sinks by inelastic collisions in axial region. This phenomenon has been demonstrated in the paper[10] where kinetic equation (1) has been numerically solved in given potential field without averaging procedure.

The radial distributions of potential, electron density, mean energy and of ionization sources are represented in Fig. 3a,b for neon discharge and in Fig. 3c,d for helium discharge. The values of parameters of the discharges are shown in Table 1.

In neon at lower pressures the direct ionization dominates, at higher pressures the

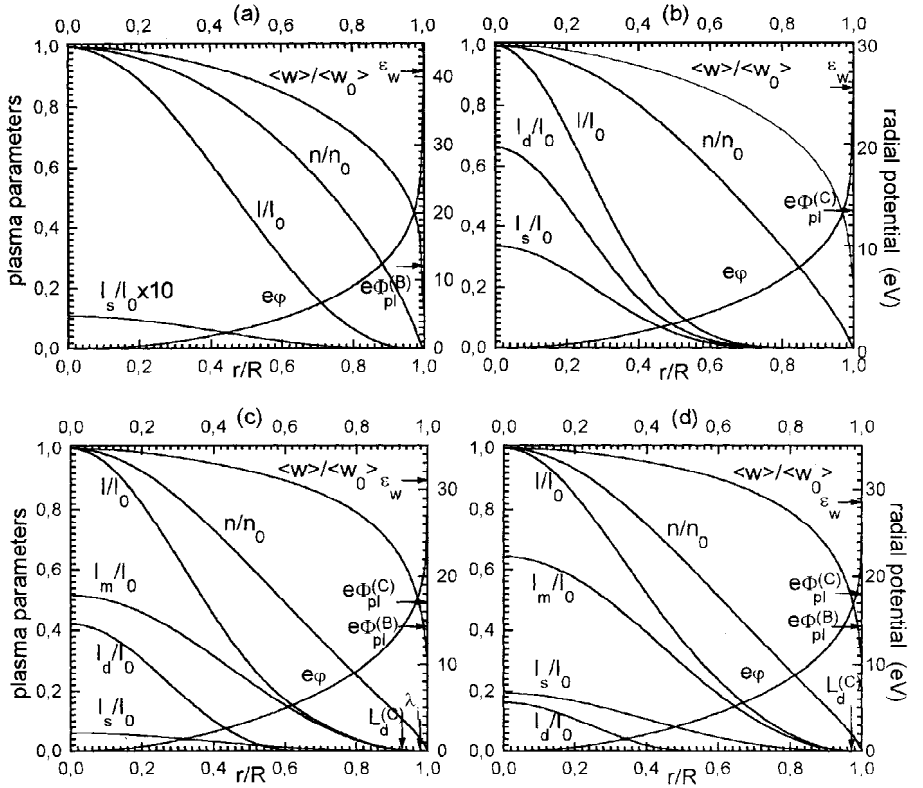

Figure 3. The radial dependencies of electron density n/n_0, mean energy $\langle w\rangle / \langle w_0 \rangle$, direct I_d/I_0, stepwise I_s/I_0, chemoionization I_m/I_0 and of total I/I_0 ionizations, and radial distribution of potential $e\,\varphi(r)$. (ε_w is the value of wall potential). a) Ne, pR = 0.1 *torr* · *cm*, i/R = 10 *mA/cm*, R = 1 *cm*. b) Ne, pR = 1.0 *torr* · *cm*, i/R = 10 *mA/cm*, R = 1 *cm*. c) He, pR = 0.6 *torr* · *cm*, i/R = 2.5 *mA/cm*, R = 2 *cm*. d) He, pR = 0.6 *torr* · *cm*, i/R = 17 *mA/cm*, R = 2 *cm*.

stepwise processes start to play role. In helium discharges chemoionization is dominant. The considerable radial fall of mean energy is observed. The ionization source distributions are noticeably contracted compared to density profile.

The radial profiles of potential represented in Fig.3 have been obtained under assumption of plasma quasineutrality up to the tube wall. The magnitude of the wall potential ε_w consists of two summands: the drop of potential in quasineutral plasma and the potential fall in the near-wall sheath of space charge. The potential fall in plasma $e\Phi_{pl}$ can be estimated in the following way.

Under assumption that the size of the space-charge sheath L_d is smaller than ion free path λ_i (collisionless sheath) we can use the Bohm criterion in the form

$$j_i|_{R-L_d} \approx n_e \sqrt{\frac{\langle w \rangle}{M}}\Bigg|_{R-L_d} \tag{14}$$

This equation determines the value of $e\Phi_{pl}^{(B)}$ and the electron density at the plasma–sheath boundary.

In the opposite case when $L_d > \lambda_i$ (collisional sheath) the potential fall in plasma can be estimated from the following considerations[11]. Beyond the zone of ionization the radial flux of charged particles remains constant and equal to

$$j_r(r) = b_i n(\varphi)\frac{d\varphi}{dr} = const$$

Differentiating this equality we get

$$\frac{d^2\varphi}{dr^2} = -\left(\frac{j_i}{b_i}\right)^2 \frac{1}{n^3(\varphi)}\frac{dn}{d\varphi}$$

Using the Poisson equation $\frac{d^2\varphi}{dr^2} = 4\pi e(n_i - n_e)$ we come to

$$\frac{n_i - n_e}{n} = -\frac{1}{4\pi e}\left(\frac{j_i}{b_i}\right)^2 \frac{1}{n^4}\frac{dn}{d\varphi}$$

By setting $n_i - n_e \sim n$ at the boundary of quasineutral plasma we obtain the equation for determining of $e\Phi_{pl}^{(C)}$ in the case of collisional sheath for unrestricted dependence $n(\varphi)$.

$$-\frac{1}{n^4}\frac{dn}{d\varphi}\bigg|_{e\Phi_{pl}^{(C)}} = 4\pi e\left(\frac{b_i}{j_i}\right)^2\bigg|_{r=R} \tag{15}$$

In the case of Boltzmann distribution of electron density $n(e\varphi) = n_0 \exp(-e\varphi/kT)$ the equation (15) yields

$$e\Phi_{pl}^{(C)} = kT \ln\left(\frac{n_0}{n^*}\right),$$

where

$$n^* = \left[\frac{j_r^2(R)}{4\pi b_i^2 kT}\right]^{1/3}, \qquad L_d = \sqrt{\frac{kT}{4\pi e^2 n^*}} = \left[\frac{b_i (kT)^2}{4\pi e^3 j_r(R)}\right]^{1/3}$$

This case has been discussed in detail in the book[12]. For the real low–pressure inert gas discharge the Boltzmann distribution should be replaced by the dependence given by Eq.(6).

The-potential fall in the sheath of space charge $e\Phi_{sh}$ can be obtained as a remainder between the wall potential ε_w and the plasma potential $e\Phi_{pl}$. Then the size of the space–charge sheath L_d is given by the relation[12].

$$L_d = \left[\frac{9}{32\pi}\frac{b_i (e\Phi_{sh})^2}{e^3 j_r(R)}\right]^{1/3} \tag{16}$$

The length of the sheath $L_d^{(C)}$ is considerably larger than the ion free path λ_i, and consequently the sheath proves to be collisional one.

More correct description of the radial distribution of potential and of the near–wall space–charge sheath formation can be obtained under supplementing of equation system (1)-(3) by Poisson equation. Complete system of equation for calculations of discharge parameters has a form

$$j_i = b_i E_r n_i(\varphi) \qquad \frac{n_i - n_e}{n_e}\bigg|_{r=0} = \frac{I}{4\pi e n_e^2 b_i}\bigg|_{r=0} \tag{17}$$

$$\frac{1}{r}\frac{d}{dr} r j_i = I(\varphi) \qquad j_i(0) = 0 \tag{18}$$

$$\frac{1}{r}\frac{d}{dr}rE_r = 4\pi e(n_i(\varphi) - n_e(\varphi)) \qquad E_r(0) = 0 \tag{19}$$

$$E_r = -\frac{d\varphi}{dr} \qquad \varphi(0) = 0. \tag{20}$$

The equation system (1)–(3), (17)–(20) has been integrated over radius up to the wall, and parameters E, ε_w, β varied until the conditions $j_e(R) = \frac{1}{R}\int_0^R I(\varphi(r))rdr = j_i(R)$ were fulfilled. The results of solution are shown in Fig. 4 on example of discharge in helium.

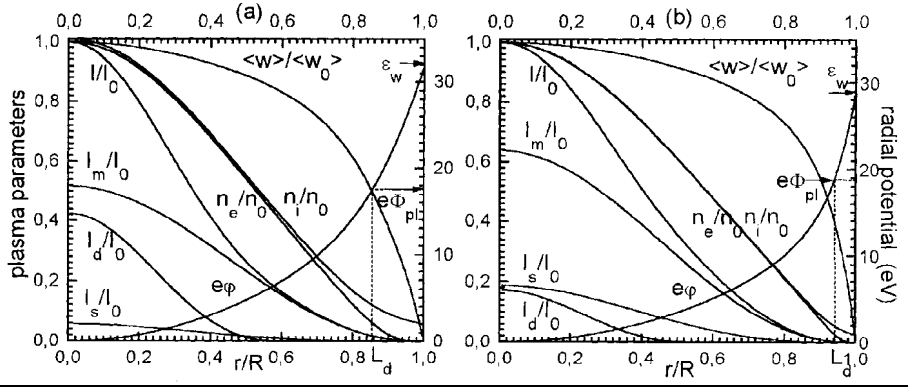

Figure 4. The results of solution of self-consistent problem with respect for plasma deviation from quasineutrality. Designations are the same as in Fig. 3. The potential fall in quasineutral plasma $e\Phi_{pl}$ and the size of the space-charge sheath L_d are determined from the condition $n_e \approx n_i/2$. a) He, $p = 0.3$ *torr*, $i = 5$ *mA*, $R = 2$ *cm*, b) He, $p = 0.3$ *torr*, $i = 35$ *mA*, $R = 2$ *cm*.

The comparison of Fig. 4a, 3c and Fig. 4b, 3d carried out under the same discharge conditions shows that the growth of potential profile near the wall is not so abrupt and sufficiently lengthy sheath of space charge forms. The plasma potential $e\Phi_{pl}$ and the sheath size L_d shown in Fig.4 have been estimated from usual condition $n_e \sim n_i/2$. The value of $e\Phi_{pl}^{(C)}$ obtained from the estimations for collisional sheath by the formula (15) is in good agreement with the potential $e\Phi_{pl}$ (Fig. 4) with accuracy within 5%. The value of the sheath size L_d estimated by the formula (16) proves to be in two times underestimated. Taking account of plasma deviations from quasineutrality weakly influence absolute values and radial distributions of ionization sources as well as charged particle fluxes on the tube wall.

It is interesting to compare the results of calculations by nonlocal theory with those of diffusion theory developed with the same constants of elementary processes. Similar problems have been solved in the papers[13,14] . Assuming that the distribution function can be represented as a product $n_e(r) \cdot f_0(w)$ we can write the kinetic equation for isotropic distribution in neglect of spatial gradients in the form

$$\frac{(eE)^2}{3}\frac{\partial}{\partial w}\frac{v^3}{\nu(v)}\frac{\partial(n_e(r)f_0(w))}{\partial w} = v\nu^*(v)n_e(r)f_0(w) - v'\nu^*(v')n_e(r)f_0(w+\varepsilon_1) \tag{21}$$

The proper calculations of transport coefficients in weakly–ionized plasmas with non-maxwell EDF are described in the book[12] . The diffusion coefficient can be different along and across radial electric field. In neglect of the diffusion coefficient anisotropy

the traditional diffusion theory of the positive column can be developed on the basis of the following set of equations.

$$I_d(n_e, E) = n_e \int_{\varepsilon_i}^{\infty} \nu_i(w) f_0(w) \sqrt{w} dw \tag{22}$$

$$I_s(n_e, E) = N_m n_e \int_{\varepsilon_s}^{\infty} \sigma_s(w) f_0(w) w dw \tag{23}$$

$$b_e = \frac{e}{3}\sqrt{\frac{m}{2}} \int_0^{\infty} \frac{v^3}{\nu} \frac{\partial f_0}{\partial w} dw; \qquad D_e = \frac{1}{3}\sqrt{\frac{m}{2}} \int_0^{\infty} \frac{v^3}{\nu} f_0 dw \tag{24}$$

$$j_i = b_i E_r n_i \tag{25}$$

$$j_e = -b_e E_r n_e - D_e \mathrm{grad} n_e \tag{26}$$

$$j_i = j_e \tag{27}$$

$$\mathrm{div} j_{ir} = I_d + I_s \tag{28}$$

$$\mathrm{div} E_r = 4\pi e(n_i - n_e) \tag{29}$$

$$E_r = -\mathrm{grad}\varphi \tag{30}$$

In Fig. 5 the distribution functions obtained under nonlocal and local approximations are compared.

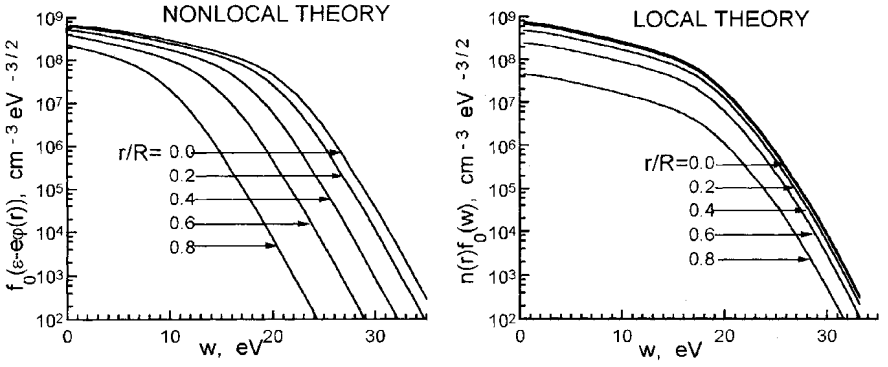

Figure 5. The electrons distribution functions in absolute measure as the functions of kinetic energy and radial coordinate, calculated by nonlocal and local approximations. In nonlocal approximation a considerable deficit of fast electrons at discharge periphery is observed. Ne, $pR = 1$ *torr* $\cdot$ *cm*, $i/R = 10$ *mA/cm*

The important difference consists in sufficient depletion of nonlocal distribution function with fast electrons, especially at receding from the axis towards the wall. This leads to large differences in macroscopic properties of discharge. The comparison of calculation results of plasma parameters by kinetic (nonlocal) and by diffusion (local) theory are shown in Figs. 6,7.

The wall potential and the length of the sheath given by local theory exceed by far those values by nonlocal theory. The plasma potentials differ insufficiently. In the frames of diffusion (local) theory the values of plasma potential $e\Phi_{pl}^{(D)}$ and of potential drop in the sheath $e\Phi_{sh}^{(D)}$ can be estimated as

$$e\Phi_{pl}^{(D)} \approx kT \ln \frac{R}{\lambda_i}, \qquad e\Phi_{sh}^{(D)} \approx kT \ln \sqrt{\frac{M}{m}} \qquad \text{or} \qquad e\Phi_{sh}^{(D)} \approx kT \ln \frac{b_e}{b_i}$$

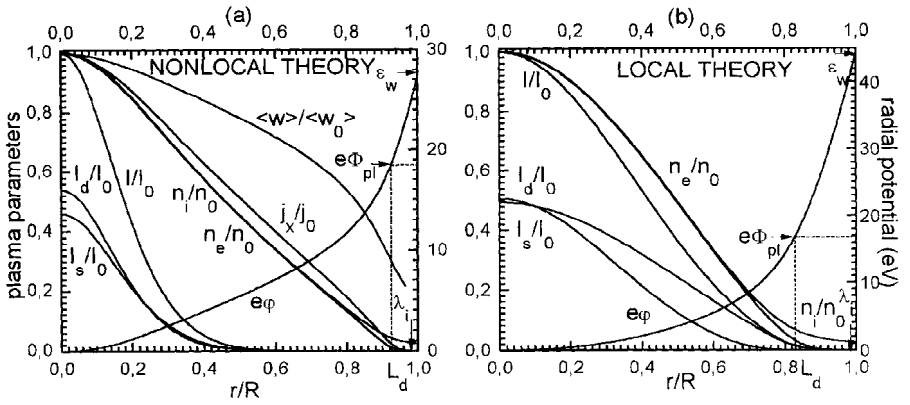

Figure 6. The comparison of calculation results by nonlocal and by local theories for Ne, pR = 1 *torr* · *cm*, i/R = 10 *mA/cm.* The designations are the same as in Fig. 3,4. Radial distribution of axial current density j_x/j_0 in nonlocal theory is wider than radial profile of electron density.

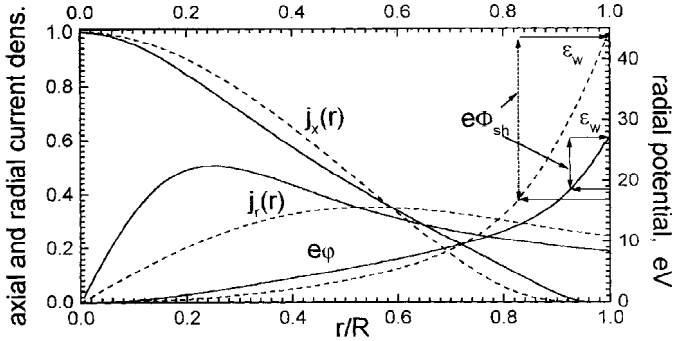

Figure 7. Comparison of calculation results by nonlocal theory (solid lines) and by local theory (dashed lines) for potential distributions $e\varphi(r)$, for radial current densities $j_r(r) \cdot 10^{15}$ $cm^{-2}s^{-1}$, and for normalized by unit axial current densities $j_x(r)$. $j_x(0)$ = 9.8 mA/cm^2 for nonlocal regime and $j_x(0)$ = 11.6 mA/cm^2 for local regime. Ne, pR = 1.0 *torr* · *cm*, i/R = 10 *mA/cm.* The value of potential fall in the space-charge sheath is about 9 *eV* in nonlocal regime and 26 *eV* in local.

These values are in good agreement with those signed in Fig. 6b, 7. The potential drop in the sheath obtained by diffusion model is about three times larger than that by kinetic model. The reason for such large difference in potential drop is connected with assumption of Boltzmann electron distribution in diffusion model, while kinetic model gives much more abrupt functions.

The value of near–wall potential fall is of great importance for numerous applications dealing with ion bombardment, ion etching, etc. On solving of different problems of ion kinetics in the near–surface regions it is necessary to consider the peculiarities of space–charge sheath formation.

The main conclusion following from these investigations is that the physical picture of formation of the positive column of low-pressure discharge can not be described in the frames of fluid model.

ANODE REGION OF NON-STRATIFIED INERT GAS DISCHARGE

In the transitional region between the axially uniform and radially inhomogeneous positive column and the anode covering whole section of the discharge tube a transformation of the potential field of the positive column (Fig.1) into the equipotential surface of the anode takes place. The transitional region includes a disturbed by the anode region of quasineutral plasma which size at low pressures and small currents is about $L \sim \varepsilon_1 / eE$, and a sheath of space charge with a length about Debye radius, where the anode fall of potential is concentrated. This two-dimensionally inhomogeneous anode

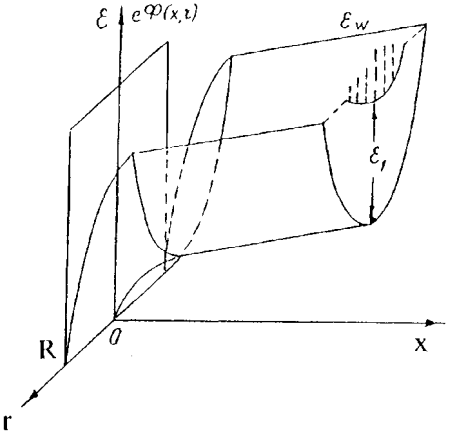

Figure 8. Schematic potential field in the transitional region from the positive column to the equipotential anode.

region is schematically shown in Fig. 8 for the case of the positive anode fall. Visually observed pattern of the discharge radiation at the transition from the positive column to the anode is represented in Fig. 9a.

The surface of the anode is covered by the brightly luminous thin film which then changes into weakly luminous region which is slightly compressed towards the axis and has a length of several millimeters (dark anode space). Then the uniform emission is observed similar to that in the positive column. In spite of the visual homogeneity of the transitional region there are interesting kinetic phenomena connected with a sink of electrons to the anode present. The experimental data show that axial field remains approximately equal to the field in the uniform positive column up to several millimeters from the anode. The distribution of the plasma potential at the discharge axis is shown in Fig. 9b.

The principal questions concerning electron kinetics in the anode region consisting of inhomogeneous quasineutral plasma and space-charge sheath have been considered by Tsendin [15]. The calculations of the distribution functions and of the macroscopic plasma properties as well as comparison with the experimental results are carried out in the papers[16–18] for the discharge in neon.

The distribution function of the axially and radially inhomogeneous quasineutral plasma of the anode region can be obtained from the solution of kinetic equation

$$\frac{\partial}{\partial x}\frac{v^3}{3\nu(v)}\frac{\partial f_0(\varepsilon,x,r)}{\partial x}+\frac{1}{r}\frac{\partial}{\partial r}r\frac{v^3}{3\nu(v)}\frac{\partial f_0(\varepsilon,x,r)}{\partial r}= \tag{31}$$

$$=v\nu^*(v)f_0(\varepsilon,x,r)-v'\nu^*(v')f_0(\varepsilon+\varepsilon_1,x,r)$$

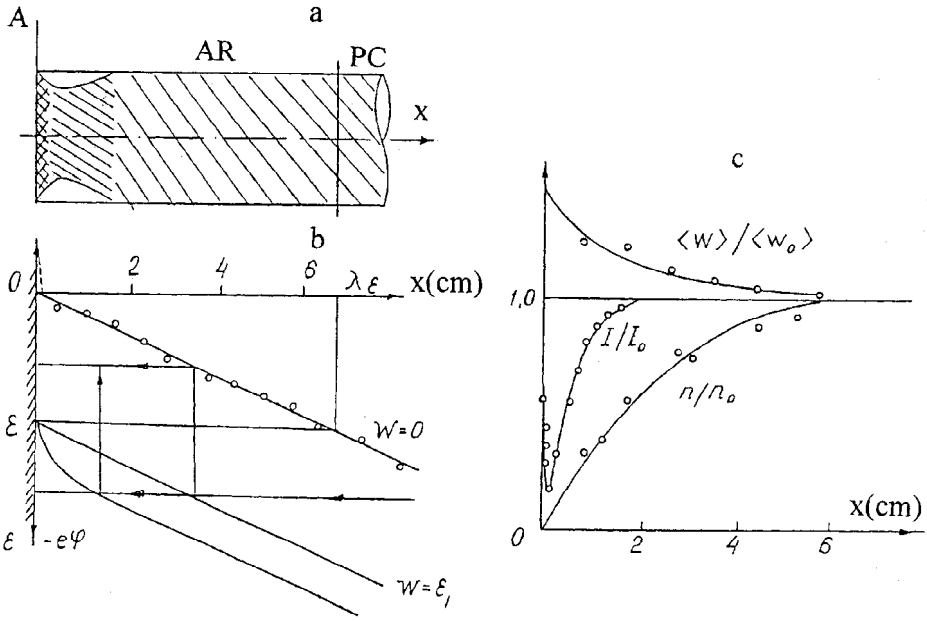

Figure 9. Anode region of glow discharge. a) visually observed radiation pattern, b) approximation of the axial potential in the anode region and trajectories of electron motion. c) axial distributions of mean energy, ionization sources and of mean energy.

The distribution function of the axially and radially inhomogeneous quasineutral plasma of the anode region can be obtained from the solution of kinetic equation
At the first approximation the equation solution can be found in the potential field $e\Phi(x,r) = -eEx + e\varphi(r)$, where E and $e\varphi(r)$ are determined from the solution of the problem about positive column. The presence of the anode absorbing the electrons is taken into account by the zero boundary condition for isotropic distribution function at the anode. This approximation assumes that at the time of ion diffusion to the tube wall their displacement in axial direction is much less than the length of anode region, and the electron free path is shorter compared to diffusive scale $R/2.4$.

Averaging the equation (31) over radial motions of electrons, similar to the problem for positive column, we come to equation

$$\frac{d}{dx}\frac{\overline{v^3}}{3\nu(v)}\frac{df_0(\varepsilon,x)}{dx} = \overline{v\nu^*(v)}f_0(\varepsilon,x) - \overline{v'\nu^*(v')}f_0(\varepsilon+\varepsilon_1,x) \tag{32}$$

$$f_0(\varepsilon,x)|_{x=0} = 0; \qquad f_0(\varepsilon,x)|_{\varepsilon\to\infty} = 0 \tag{33}$$

Since at present stage the problem solution is not directed to calculations of self-consistent potential (Fig. 8), the boundary condition at the wall potential can be replaced by more simple requirement of distribution function vanishing at infinite energies. The solution of Eq. (32) with boundary conditions (33) is shown in Fig. 10a for different distances from the anode, the distribution functions measured at the same points are shown in Fig. 10b.

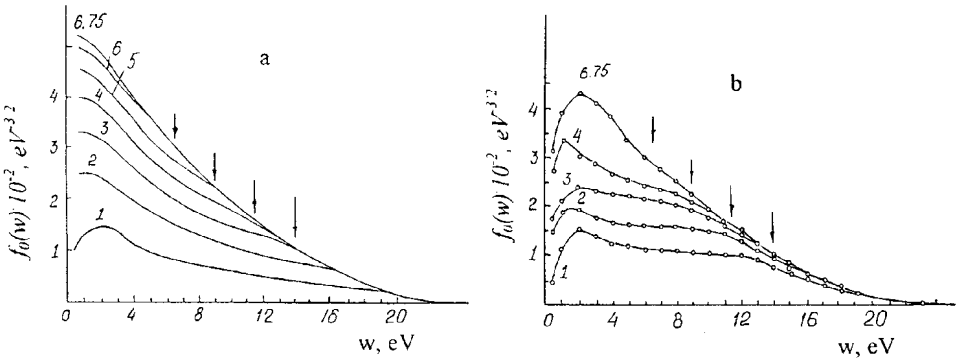

Figure 10. EDF at different points from the anode. Ne, pR = 1 *torr* · *cm*, i/R = 10 *mA*. The numbers at the curves correspond to the distance from the anode in *cm*. a) theory, b) experiment.

By means of calculated distribution functions the electron density, mean energy, total number of excitation processes of levels with different excitation potentials have been calculated as the functions of the distance from the anode. In Fig. 9c the results of measurements and of calculations are compared.

These investigations demonstrate that the disturbing effect of the anode is spreading at considerable distances about energy relaxation length. On approaching to the anode the distribution function becomes depleted by slow electrons at first and then by more and more fast ones. This leads to decrease of electron density and to small growth of mean energy. Up to the distances of about $\sqrt{\lambda\lambda^*}$ (the length of electron energy relaxation in inelastic region) the presence of the anode does not induces the distortion of distribution function tale, this accounts for the visual uniformity of radiation in spite of the decrease of electron density. Close to the anode the distribution function becomes distorted in inelastic region, that causes the abrupt decrease of discharge emission (dark anode space).

The attempts to describe the quasineutral plasma of anode region under considered conditions from the principles of fluid theory in terms of diffusion and mobility seem to be unpromising due to their inability to reproduce the physical picture of the anode region formation.

S- AND P- STRIATIONS IN THE POSITIVE COLUMN

The positive column of a dc glow discharge in inert gases at low pressures and small currents can exist not only in axially uniform state but also in stratified form. In the non-stratified positive column the electron kinetics is analyzed in the radially inhomogeneous potential field and constant axial field E. In the stratified discharges the matter of first rate importance is the analysis of electron kinetics in the spatially periodic potential field $e\varphi(x)$ along the direction of current flowing. Of four known types of striations we shall consider two: S- and P-striations. The length of S-striation is determined by the value $L_s = \varepsilon_s / eE$, (E - is the period averaged electric field strength) where a potential fall ε_s at one spatial period exceeds a little the excitation threshold ε_1. The length of P-striation L_p and the potential fall at one length ε_p are about half as large as in S-striations.

The stratified positive column has been investigated experimentally and theoretically. The probe technique has been used to carry out the measurements of spatio-temporal distribution of plasma potential $e\varphi(x, t)$ and of electron distribution function in different phases of S- and P- striations. In the experimentally measured potential field the kinetic equation has been solved, and the distribution functions obtained by theory have been compared to measured ones.

One of the most important problem for investigation of moving striations is that of correct measurement of axial potential profile. As a rule the measurements of plasma potential have been carried out relative to the grounded anode with a help of immovable probe, which gave temporal distribution of plasma potential $e\varphi(t)$. To reconstruct the spatial profile $e\varphi(x)$ from the temporal profile the argument t has been substituted by the coordinate $x = vt$, (v - is the phase velocity of striations). Such recalculations have led to appearance of the nonmonotonous profiles corresponding to the presence of potential wells [19,20]. However the experimental measurements[21-23] show that in the case of fixed anode potential the propagation of the wave of potential in axial direction must cause the oscillations relative to the anode of plasma potential as a whole. These oscillations have a frequency of striations and amplitude compared with the potential fall on striation length. The using of a mobile probe permits to measure properly the spatio-temporal profile of potential $e\varphi(x, t)$ and to separate the potential of ionization wave and temporal plasma oscillations as a whole. Stewart[21] had moved the anode and cathode simultaneously relative to the immobile probe and thus directly measured the spatial profile of plasma potential. Correct measurements[22–24] show that illusory potential wells of large depth in striations in the positive column are absent in reality.

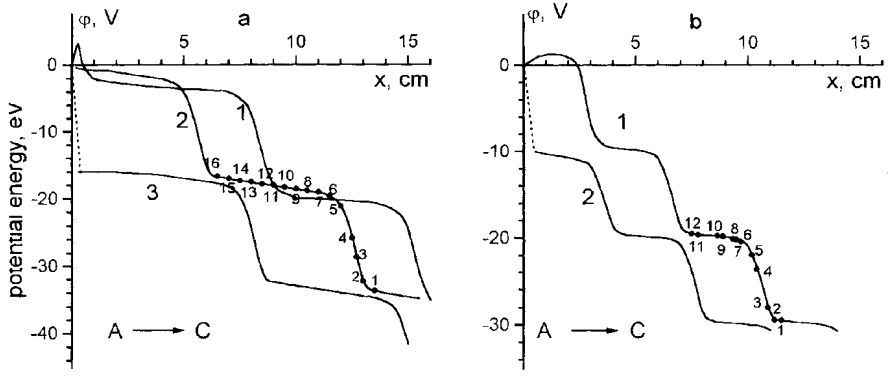

Figure 11. Axial potential for S- (a) and P-striations (b) measured at different times. Wells are dashed. $x = 0$ corresponds to position of the anode. Ne, a) $pR = 2.7$ *torr* $\cdot$ *cm*, $i = 18$ *mA*; b) $pR = 2.24$ *torr* $\cdot$ *cm*, $i = 16$ *mA*.

In Fig.11 the axial potential profiles for S- and P- striations measured in neon in dependence of the distance from the anode at different instants are plotted. It is seen that far from the anode the profiles $e\varphi(x)$ consist of the regions of weak and strong fields, and there are no potential wells. The electron distribution functions measured at 16 points over S-strata length and at 12 points over P-strata length are shown in the Fig. 12a,b, the corresponding points are marked on the curves 2 of the Fig. 11a,b. It can be seen that in S-striation there is one maximum in the election distribution function in the region of weak field that does not practically move over energy (points 9-16). In the transient region from weak to strong field this peak begins to move fast

over energy (points 1,2). Approximately in the middle of the strong field region (points 3,4) a new peak of slow electrons appears in the EDF (~1,5 eV). Further the amplitude of this maxima increases as it moves over energy.

The distribution functions measured in P-striations differ greatly from those in S-striations. The principal difference is that in the region of smooth change of potential there are two maxima in the EDF for P-striations rather than one as it is in S-waves. The distance between these two peaks is approximately equal to the potential period of P-strata ε_p (~10 eV). The experimental pattern of the motion of these two maxima over energy and coordinate in the region of weak (points 7–12) and strong (points 2–5) fields is shown in Fig. 12b for one wave length.

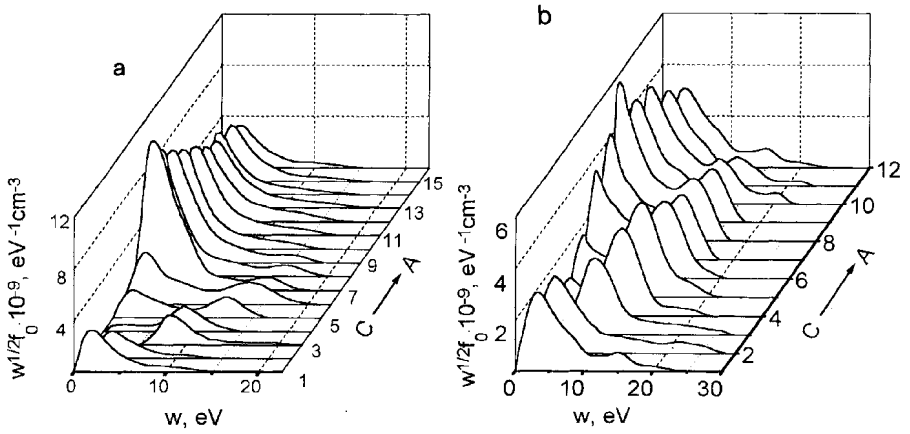

Figure 12. EDF measured for S- (a) and P- (b) striations at different points along discharge axis, marked on the curves 1 in Fig. 11a,b. a) Ne, pR = 2.7 *torr* · *cm*, i = 18 *mA*. b) Ne, pR = 2.24 *torr* · *cm*, i = 16 *mA*.

Such a behavior of experimental distribution functions in S- and P-striations can be interpreted on the basis of nonlocal electron kinetics in spatially periodic electric fields. It should be mentioned that the basic ideas of kinetic approach of EDF formation in striations have been discussed in the papers[25–28]. The kinetic equation for $f_0(\varepsilon, x)$ in variables of total energy $\varepsilon = w + e\varphi(r)$, x for one-dimensional case can be written in the following way

$$\frac{\partial}{\partial x}\left(\frac{v^3}{3\nu}\right)\frac{\partial f_0(\varepsilon,x)}{\partial x} + \frac{\partial}{\partial \varepsilon}\frac{m^2}{M}v^3\nu f_0(\varepsilon,x) = v\nu^*(v)f_0(\varepsilon,x) - v'\nu^*(v')f_0(\varepsilon+\varepsilon_1,x) \quad (34)$$

The analysis of this equation can be considerably simplified by using the "black–wall" approximation $f_0(\varepsilon,x)|_{\varepsilon\geq\varepsilon_1} = 0$ which is valid when inelastic collision frequency ν^* is high enough.

The partial differential equation (34) describes electron diffusion along the coordinate x (acceleration in the longitudinal periodic electric field) and the drift over energy due to elastic collisions. If the elastic impacts are neglected in the equation (34) it becomes an ordinary differential equation and its solution parametrically dependent on

ε can be written as follows

$$f_0(\varepsilon, x) = \Phi(\varepsilon) \int_x^{x_2(\varepsilon)} \frac{\nu(v)}{v^3} dx' = \Phi(\varepsilon) \cdot F_0(w, x) \tag{35}$$

here $x_2(\varepsilon)$ is a potential curve, where kinetic energy is equal to the first level of atom excitation. The integration constant $\Phi(\varepsilon)$ is determined by the boundary condition for the distribution function from the cathode side of the positive column. With energy losses neglected in elastic impacts the motion of electrons on the plane ε, x occurs with constant total energy along the horizontal lines from potential curve $x_1(\varepsilon)$ corresponding to $w = 0$ up to the curve $x_2(\varepsilon)$ where $w = \varepsilon_1$. After inelastic collision an electron jumps upright from the curve $x_2(\varepsilon)$ onto the curve $x_1(\varepsilon)$. All trajectories of electrons are parallel to the axis x on the plane ε, x. Therefore the information about initial electron distribution is transferred at any distance. The recurrence relation for the amplitude of the distribution function

$$\Phi(\varepsilon + \varepsilon_1) = \Phi(\varepsilon) \tag{36}$$

results from the current density being constant at every cross-section $x = const$. In the presence of small energy losses in elastic collisions the electron trajectories on the plane ε, x are spreaded due to dispersion of the energy losses, and information about initial distribution is lost on receding from the point of injection. The final result of spatial relaxation of arbitrary distribution function injected in a uniform field is a distribution formed in this field

$$f_0(w) = \Phi \int_w^{\varepsilon_1} \frac{1}{v^3/\nu} \exp\left\{ - \int_w^{w'} 3 \frac{m^2}{M} \nu^2 \frac{1}{(eE)^2} dw'' \right\} dw'$$

In the spatially periodic field the bunching effect suggested by Tsendin[27] can take place. In presence of small energy losses in elastic collisions the solution of equation (34) can be found by means of expansion with small parameter

$$\theta \approx \frac{m}{M} \left(\frac{\varepsilon_1}{eE\lambda} \right)^2$$

in the form

$$f_0(\varepsilon, x) = f_0^{(0)}(\varepsilon, x) + \theta f_0^{(1)}(\varepsilon, x) + \theta^2 f_0^{(2)}(\varepsilon, x) \tag{37}$$

The function $f_0^{(0)}$ (ε, x) is the solution of equation (34) with $\theta = 0$ and is the same as the expression (35). After the substitution of expansion (37) in the kinetic equation the recurrence relation for the amplitude $\Phi(\varepsilon)$ can be represented in the form

$$\Phi(\varepsilon + 1) = \Phi(\varepsilon) + \theta \frac{\partial}{\partial \varepsilon} \Psi(\varepsilon) \Phi(\varepsilon) + \theta^2 \frac{\partial^2}{\partial \varepsilon^2} C(\varepsilon) \Phi(\varepsilon) \tag{38}$$

The coefficient $\Psi(\varepsilon)$ describes the energy loss in elastic collisions when electrons with the energy ε move from $x_1(\varepsilon)$ to $x_2(\varepsilon)$. The coefficient $C(\varepsilon)$ corresponds to the diffusion coefficient over energy. The slightly varying function $C(\varepsilon)$ can be regarded as a constant. In the spatially-periodic fields the function $\Psi(\varepsilon)$ can be represented as follows

$$\Psi(\varepsilon) = A + \beta(\varepsilon); \qquad A = \frac{1}{\varepsilon_L} \int_0^{\varepsilon_L} \Psi(\varepsilon) d\varepsilon; \qquad \int_0^{\varepsilon_L} \beta(\varepsilon) d\varepsilon = 0$$

$\beta(\varepsilon)$ is the periodic function of energy. The small parameter

$$\theta A = \frac{\varepsilon_L - \varepsilon_1}{\varepsilon_1}; \qquad \varepsilon_L = \int_0^L eE(x) dx$$

L - spatial period of field $E(x)$. Shifting the argument ε in (38) by the value $\theta A\varepsilon_1$ and expanding the coefficients of equation up to terms of the second order in θ, the recurrence relation for the amplitude $\Phi(\varepsilon)$ can be obtained

$$\Phi(\varepsilon - \varepsilon_1 - \theta A\varepsilon_1) - \Phi(\varepsilon) = \frac{\partial}{\partial\varepsilon}\left[\theta\Phi(\varepsilon)\beta(\varepsilon) + \theta^2\left(C - \frac{A^2}{2}\right)\frac{\partial}{\partial\varepsilon}\Phi(\varepsilon)\right] \qquad (39)$$

From the equation (39) the passage to the limit with $\theta \to 0$ to the expression (36) can be easily seen. The right part of equation (39) represents the divergence of the flux over energy consisting of drift and diffusion. The stationary solution corresponds to zero flux in energy space i.e. the drift equalizes the diffusion. In this case the condition of periodicity will be

$$\Phi(\varepsilon - \varepsilon_1 - \theta A\varepsilon_1) = \Phi(\varepsilon) \qquad (40)$$

The amplitude $\Phi(\varepsilon)$ corresponding to the stationary solution, can be written in the following way

$$\Phi(\varepsilon) = B \cdot \exp\int_0^{\varepsilon} \frac{\beta(\varepsilon)}{\theta(C - A^2/2)}d\varepsilon \qquad (41)$$

The final form of the electron distribution function is given by (35) where $\Phi(\varepsilon)$ is determined by (41) and the small additions in the expansion (37) can be neglected. Constant B is determined by the normalization condition on current density.

This model has been used for the calculations of distribution functions in S- and P- striations. Experimentally measured potential profiles (Fig. 11) were approximated by linear staircase functions shown in Fig. 13a for S-strata and in Fig. 13b for P-strata.

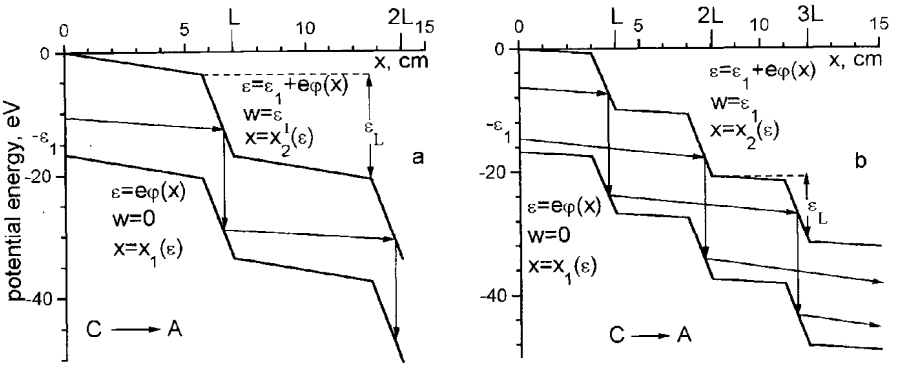

Figure 13. Approximations of potential profiles for S- (a) and P- (b) striations.

As the inequality $\varepsilon_s > \varepsilon_1$ is valid for S-strata there is one resonance trajectory on the energy interval $[0, \varepsilon_1]$ which is shown with arrows in Fig. 13a. For P-strata $\varepsilon_p \approx \varepsilon_s/2 < \varepsilon_1$ and on the same energy interval $[0, \varepsilon_1]$ there are two resonance trajectories shown in Fig. 13b. The distribution functions in variables of kinetic energy w and coordinate x, calculated for S- and P-striations in the potential field of Fig. 13 are shown in Fig. 14a,b. In Fig. 15 the calculated distribution functions for P-strata are compared with measured ones at the different positions along discharge axis.

It can be easily seen that the nonlocal theory describes properly the basic features of the distribution function behavior in S- and P- striations in the positive column of a dc glow discharge.

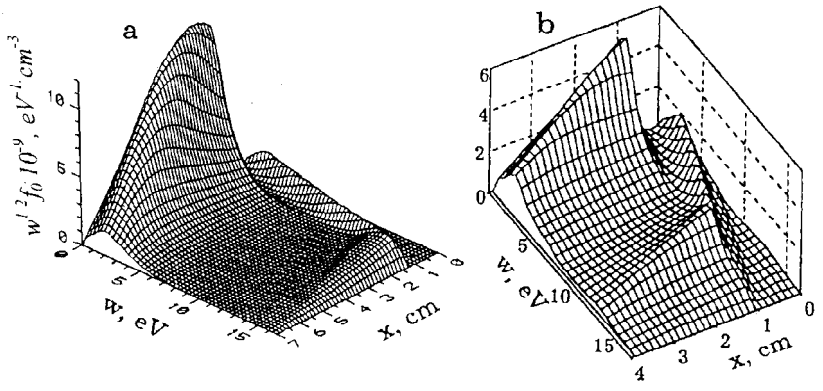

Figure 14. a) EDF calculated in the potential profile shown in Fig. 13a for S-striation. b) EDF calculated in the potential profile shown in Fig. 13b for P-striation.

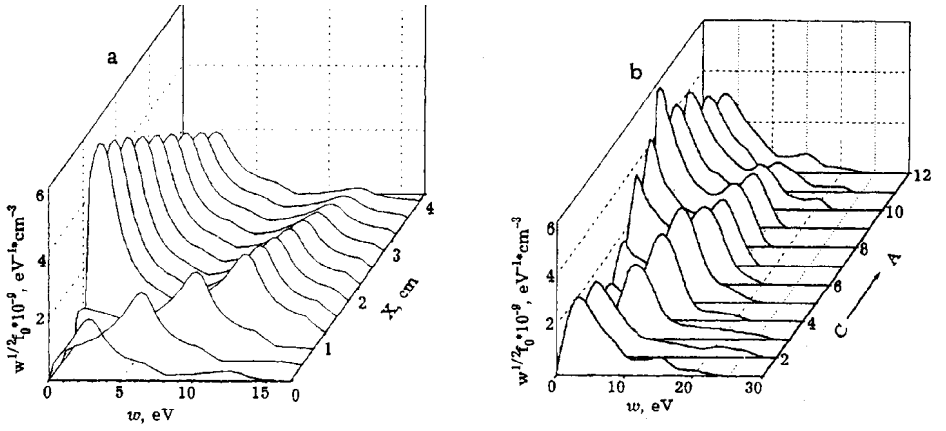

Figure 15. The comparison of calculated a) and measured b) EDFs in P-striations at the points shown in Fig. 1 lb on the curve 1.

S- AND P-STRIATIONS IN THE ANODE REGION

The passage of striations through the anode region of a glow discharge has not been practically investigated. The spatio-temporal dependences of potential in stratified plasma near anode reveal some interesting features (Fig. 11a,b). The most interesting effect which has been found[29] is the appearance of potential profiles with wells adjacent to the anode at certain time intervals (curves 1 in Fig. 11a,b) with synchronous appearance of the explicit peak of slow electrons on the EDF with the energies of fraction of eV. Potential well corresponds to the positive plasma potential with respect to the anode (negative anode drop). The positive anode drop corresponding to potential profile without potential well occurs for the most part of striation period (curves 2 in Fig. 11a,b).

In Fig. 16a the transformation of the experimentally measured EDF is given for moving through the anode region P–striations at different distances from the anode for the potential profile without wells. A decrease of the EDF is seen on approaching to the anode. At first the depletion of the EDF with slow electrons takes place and then

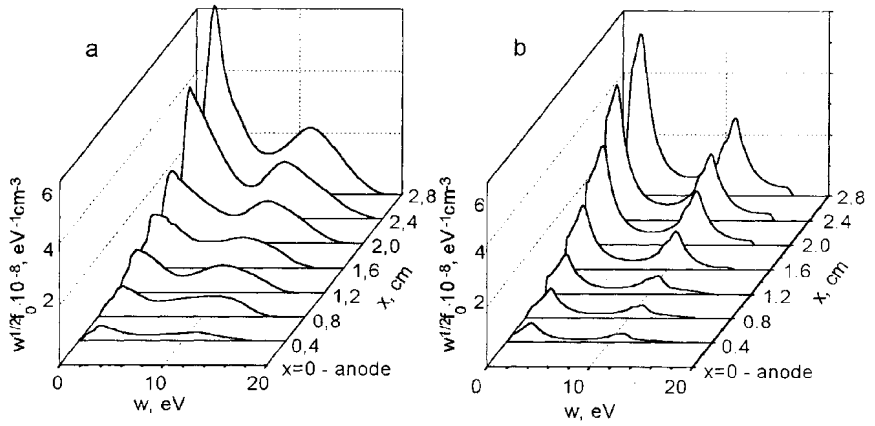

Figure 16. a) EDF measured in P-striations in the near anode region at different distances from the anode for potential profile without well. Ne, pR = 1.4 *torr · cm*, i = 20 *mA*. b) EDF calculated in the near anode region for P-striations. x = 0 corresponds to the anode position.

this process involves more and more fast electrons. At the distance 4 mm the electron density falls by more than one order. The EDF measured in the undisturbed positive column do not reveal the similar decrease and are reproduced quite well from one strata to another at a distance from the anode. The theoretical calculations of EDF in the near–anode region of stratified discharge can be carried out by analogy with stratified positive column on the basis of kinetic equation (34) and equations (35), (41) with the additional zero boundary condition for the EDF at the anode

$$f_0(\varepsilon, x)|_{x=0} = 0$$

The results of EDF calculations for P-strata in the anode region are represented in Fig. 16b. It is clear that the nonlocal theory describes properly the EDF depletion experimentally observed as strata moves to the anode.

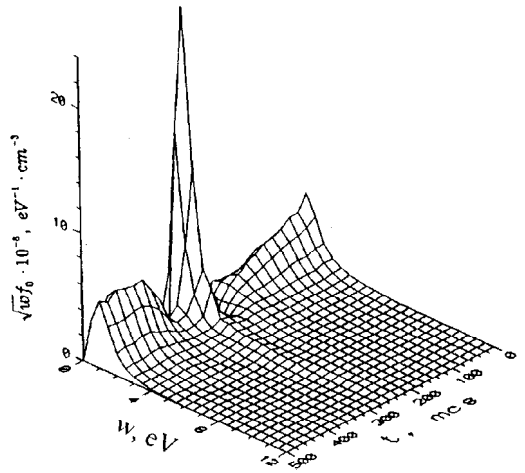

Figure 17. EDF measured in S-striations at the distance 2 mm from the anode at different times. Ne, pR = 2.7 *torr · cm*, i = 18 *mA*.

In Fig. 17 the electron distributions measured for S-strata at the distance 2 mm from the anode approximately corresponding to the center of potential well on the curve

1 in Fig. 11a are shown at different times over strata period (T=500 mcs). It can be seen that at the time interval 260-290 mcs, corresponding to potential well presence there is a sharp peak of slow electrons. The EDFs measured at other points of time, corresponding to potential profiles without wells, do not have the peak of slow electrons. The similar pattern is observed for P-striations. In Fig. 18 the EDF measured in P-

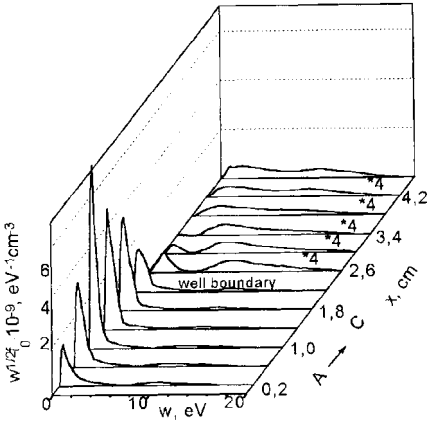

Figure 18. EDF measured in P-striations at different distances from the anode for potential profile with well. Ne, pR = 1.4 *torr · cm*, i = 20 *mA*.

strata at different distances from the anode for the potential curve 1 in Fig. lib are shown. It is clearly seen that within potential well the electron distribution is compressed to the region of small energies. The amplitude of the peak of slow electrons has a maximal value at the middle of the well. On the boundary of the well the shape of the EDF changes abruptly, its amplitude considerably decreases, the peak of slow electrons vanishes and distribution function becomes typical for P-strata in the positive column without well.

The problem of the EDF formation for trapped electrons in the potential wells along direction of a current has been analyzed in the papers[30, 31]. Experimental behavior of EDF in potential wells can be explained on the basis of kinetic equation

$$\frac{\partial}{\partial x}\frac{2}{3}\frac{w^{3/2}}{m\nu}\frac{\partial f_0}{\partial x}+\frac{\partial}{\partial \varepsilon}\left[2\frac{m}{M}\nu w^{3/2}\left(f_0+T_a\frac{\partial f_0}{\partial \varepsilon}\right)\right]+\frac{\partial}{\partial \varepsilon}\left[2\nu_e w^{3/2}\left(A_1 f_0+A_2\frac{\partial f_0}{\partial \varepsilon}\right)\right]=S^* \tag{42}$$

where $\nu_e = \frac{4\pi e^4 n}{m^2 v^3}$ In Λ is the frequency of electron-electron collisions, In Λ is Coulomb logarithm, T_a is the temperature of maxwell distribution of atoms,

$$A_1=\frac{1}{n}\int_0^{\varepsilon} f_0(\varepsilon)\sqrt{\varepsilon}\,d\varepsilon; \qquad A_2=\frac{2}{3n}\left[\int_0^{\varepsilon}\varepsilon^{3/2}f_0(\varepsilon)\,d\varepsilon+\varepsilon^{3/2}\int_{\varepsilon}^{\infty} f_0(\varepsilon)\,d\varepsilon\right],$$

S* is the operator of inelastic collisions.

In the equation (42) in contrast to the equation (34) the electron-electron collisions and the heating of electron in collisions with neutral atoms are taken into account. It has been shown[30] that in presence of potential wells the slow electrons are naturally divided into two almost independent groups: trapped ($\varepsilon < \varepsilon_0$) and free ($\varepsilon > \varepsilon_0$) electrons, where ε_0 is the depth of potential well. If the energy relaxation length with respect to elastic and electron–electron collisions is larger than the size of the well it can be believed that electrons move within the well with constant total energy ε and

the EDF does not depend on coordinate x but depends on total energy ε only. In this case it is possible to average kinetic equation (42) over space and to write

$$\frac{\partial}{\partial\varepsilon}\left[\overline{V_\varepsilon} f_0^t(\varepsilon) + \overline{D_\varepsilon}\frac{\partial f_0^t(\varepsilon)}{\partial\varepsilon}\right] = q(\varepsilon) \tag{43}$$

where

$$\overline{V_\varepsilon} = \frac{1}{L}\int_{x^-(\varepsilon)}^{x^+(\varepsilon)} 2w^{3/2}\left(\frac{m}{M}\nu + A_1\right)dx; \qquad \overline{D_\varepsilon} = \frac{1}{L}\int_{x^-(\varepsilon)}^{x^+(\varepsilon)} 2w^{3/2}\left(A_2\nu_e + \frac{m}{M}\nu T_a\right)dx$$

L is the well size, $x^-(\varepsilon)$, $x^+(\varepsilon)$ are the turn points of electron with energy ε. The sources of electrons $q(\varepsilon)$ describe the appearance of slow electrons within the well due to inelastic collisions of free electrons with energy more than excitation threshold. Equation (10) has a physical sense of continuity equation for the flux which consist of a diffusion with coefficient $\overline{D_\varepsilon}$ and a drift with velocity $\overline{V_\varepsilon}$ where the source is $q(\varepsilon)$.

The experimental data (Fig. 16) show that typical energy of trapped electrons is ~0.3 eV and is much less than the well depth ε_0, that allows to construct EDF of trapped electrons with the zero boundary condition at $\varepsilon = \varepsilon_0$. The solution of equation (43) in this approximation is as follows

$$f_0^t = \int_\varepsilon^{\varepsilon_0} \frac{Q(\varepsilon')}{\overline{D_{\varepsilon'}}}\exp\left[\int_\varepsilon^{\varepsilon'}\frac{\overline{V_{\varepsilon''}}}{\overline{D_{\varepsilon''}}}d\varepsilon''\right]d\varepsilon'; \qquad \text{where} \quad Q(\varepsilon') = \int_0^{\varepsilon'} q(\varepsilon)d\varepsilon. \tag{44}$$

The transition to the maxwell form can be easily seen from the solution (44) for electrons with $\varepsilon < \varepsilon_0$. When electron–electron collisions dominate $\left(\nu_e \gg \frac{m}{M}\nu\right)$ the ratio $\overline{V_\varepsilon}/\overline{D_\varepsilon} \sim T_e$, and f_0^t can be written in the form

$$f_0^t(\varepsilon) = const \cdot e^{-\varepsilon/T_e} \tag{45}$$

For calculation of the electron temperature T_e it is necessary to consider energy balance for trapped electrons which can be obtained by multiplying equation (42) by kinetic energy and integration over energy within the interval $0 \div \varepsilon_0$ and over coordinate within the well size. Finally energy balance equation can be written in the form

$$H_a^* + H_e^* - H_a^d - H_e^d - H_a^V = 0 \tag{46}$$

where $H_a^* \approx \frac{1}{3}\nu_0^*\varepsilon_1^{5/2}(\varepsilon_0/\varepsilon_1)^3 f_0^i(\varepsilon_1)$ is the heating of trapped electrons by means of inelastic collisions of free electrons with $\varepsilon > \varepsilon_1$ yielding slow electrons with energies $\varepsilon - \varepsilon_1$, $H_e^* = 2\nu_e(\varepsilon^i)\varepsilon^i n^t n^i/n$ is the heating due to a cooling of free electrons in collisions with tripped ones, $H_a^d = 2\frac{m}{M}(\nu T_a \varepsilon^{5/2}\partial f_0^t(\varepsilon)/\partial\varepsilon)\Big|_{\varepsilon=\varepsilon_0}$ is the flux of electron energy beyond the boundaries of the well due to collisions with atoms having non-zero temperature T_a, $H_e^d = 2\,\nu_e T_e \varepsilon_0^{5/2}(\partial f_0^t(\varepsilon)/\partial\varepsilon))\Big|_{\varepsilon=\varepsilon_0}$ is the diffusive cooling due to electron–electron collisions within the well, $H_a^V = 2\frac{m}{M}n^t\left(1 - \frac{T_a}{T_e}\right)\langle\nu w\rangle$ describes the energy interchange of trapped electrons in elastic collisions with atoms in the well volume. The final equation of energy balance for the calculation of T_e is as follows

$$2\nu_e(\varepsilon^i)\varepsilon^i\frac{n^t n^i}{n} - \frac{1}{6}\nu_0^*\varepsilon_1^{5/2}\left(\frac{\varepsilon_0}{\varepsilon_1}\right)^3 f_0^i(\varepsilon_1) - 3\frac{m}{M}n^t\left(1 - \frac{T_a}{T_e}\right)\nu(T_e)T_e = 0 \tag{47}$$

It is necessary to know the density of trapped n^t and free n^i electrons, mean energy ε^i and distribution function $f_0^i(\varepsilon_1)$ for free electrons. The value of T_e calculated from the

equation (47) is about 0.34 eV; that is in a quite good agreement with the position of the peak of slow elections in experiment.

On the basis of kinetic equation solution (44) for trapped electrons and (35) for free electrons the EDF can be constructed in the whole energy interval. The idea that electrons are divided on two slightly connected groups described by (44) and (35) allows to find the parameters of these groups: n^t, T_e for trapped electrons and n^i, ε_i for free electrons. The question about temperature and density of trapped electrons can be solved on the basis of joint solution of energy balance and particles balance equations. The balance of particles can be obtained by integrating of kinetic equation (42) over energy at the interval $0 \div \varepsilon_0$ and over coordinate within the well boundaries. The given system of equation permits to find the density n^t and the temperature T_e of trapped electrons by means of the density n^i and the mean energy ε_i of free electrons and thus to calculate the consistent EDF in the whole range of energies.

The particular solution under discharge condition when, $n^t/n^i \approx 1.7$, gives $T_e \approx$ 0.38 eV that is in good agreement with experimental data. In Fig. 19 the comparison of EDF theoretically calculated for trapped and free electrons (solid) with experimental function (dots) is shown. It is clear that theoretical model under consideration qual-

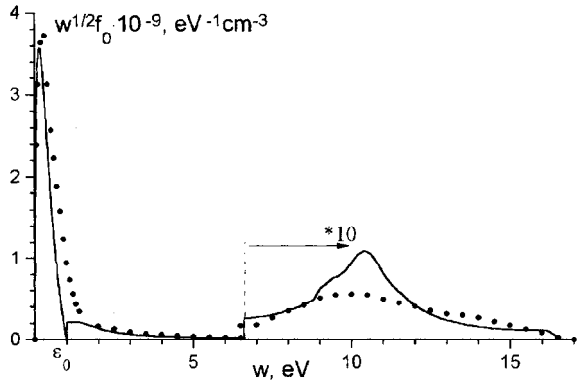

Figure 19. EDF measured (dots) and calculated (solid) in P-striations for potential profile with well. Ne, pR = 1.4 *torr* · *cm*, i = 20 *mA*.

itatively describes electron energy distribution formation in the presence of potential wells. The assumptions of black-wall condition for trapped electrons at $\varepsilon = \varepsilon_0$ and two independent electron groups existence result in break and bend of EDF at $\varepsilon = \varepsilon_0$. The behavior of EDF near ε_0 requires more rigorous analysis of kinetic equation in this region of energies. Nevertheless this model gives a descriptive physical pattern of the EDF formation and relation between of densities and mean energies of trapped and free electrons.

REFERENCES

1. L.D. Tsendin, Electron kinetics in non-uniform glow discharge plasmas, *Plasma Sources Sci. Technol.* 4:200 (1995).
2. V.I. Kolobov and V.A. Godyak, Nonlocal electron kinetics in collisional gas discharge plasmas, *IEEE Transactions on Plasma Science* 23:503 (1995).
3. I.B. Bernstein and T. Holstein, Electron energy distributions in stationary discharges, *Phys. Rev.* 94: 1475 (1954)

4. L.D. Tsendin, Energy distribution of electrons in weakly ionized current-carrying plasma with a transverse inhomogeneity, *Sov. Phys.* JETP 39:805 (1974).
5. L.D. Tsendin and Y.B. Golubovskii, Positive column of a low–density low–pressure discharge. I. Electron energy distribution, *Sov. Phys. Tech. Phys.* 22:1066 (1977).
6. L.D. Tsendin, Positive column of a low–density low–pressure discharge. II. Ion motion and radial potential profile, *Sov. Phys. Tech. Phys.* 48:1569 (1978).
7. J. Behnke, Y.B. Golubovskii and I.A. Porokhova, A self–consistent model of positive column discharge for direct and stepwise ionization, *Proc. XXI ICPIG, Bochum* 2:307 (1993).
8. J. Behnke, Y.B. Golubovskii, S.U. Nisimov and I.A. Porokhova, Self–consistent model of a positive column in an inert gas discharge at low pressures and small currents, *Contrib. Plasma Phys.* 36:75 (1996).
9. U. Kortshagen, I. Pukropski and L.D. Tsendin, Experimental investigation and fast two-dimensional self-consistent kinetic modelling of a low pressure inductively coupled RF discharge, *Phys. Rev. E,* 51:6063 (1995)
10. D. Uhrlandt and R. Winkler, Radially inhomogeneous electron kinetics in the dc column plasma, *J. Phys. D. Appl. Phys.* 29:115 (1996).
11. J. Behnke and Yu.B. Golubovskii, Kinetic description of confined electrons in gas discharge plasma, *Opt. Spektrosk.,* 73:65 (1992).
12. V. A. Rozhanskii and L. D. Tsendin. "Collisional Transport in Partially-Ionized Plasma," Energoatomizdat, Moskow (1988).
13. H. Metze, D.W. Ernie and H.J. Oskam Radial distributions of charged-paticle densities and electric field strength in the positive column, *Phys. Rev.* A 39:4117 (1989)
14. J.F. Behnke, Th. Bindemann, H. Deutsch and K. Becker, Plasma wall interaction in glow discharges, *Contrib. Plasma Phys.* 37 (1997)
15. L.D. Tsendin, Anode region of a glow discharge, *Sov. Phys. Tech. Phys.* 31:169 (1986).
16. Y.B. Golubovskii, V.I. Kolobov and S.H. al Hawat, Anode region of a low-current glow discharge in neon at low pressures, *Sov. Phys. Tech. Phys.* 33:1046 (1988).
17. Y.B. Golubovskii and S.H. al Hawat, The near-anode region of the quasineutral plasma of a low-current glow discharge in neon, *Sov. Phys. Tech. Phys.* 32:25 (1987).
18. Y.B. Golubovskii, S.H. al Hawat and L.D. Tsendin, Electron distribution in the anode region of a low-current discharge in neon, *Sov. Phys. Tech. Phys.* 32:760 (1987).
19. K.F. Bessonova, O.N. Oreshak, E.P. Ostapchenko and V.A. Stepanov, Electron energy distribution investigation in moving striations, *Zh. Tekhn. Fix.* 41:976 (1971).
20. Y.M. Kagan, N.B. Kolokolov, T.A. Krylova and V.M. Milenin, Moving striations in neon, *Sov. Phys. Tech. Phys.* 16:88 (1971).
21. A.B. Stewart, Oscillating glow discharge plasma, *J. Appl. Phys.* 27:911 (1956).
22. Y.B. Golubovskii, V.O. Nekuchaev and N.S. Ponomarev, Formation of EEDF in stratificated discharge, *XIII ESCAMPIG, Poprad, Contr. Pap.* (1996)
23. Y.B. Golubovskii, V.O. Nekuchaev, N.S. Ponomarev and I.A. Porohova, Formation of EEDF in stratified discharge, *Zh. Tekhn. Fix.* 67, (1997).
24. S.W. Rayment and N.D. Twiddy, Time-resolved measurements of electron energy distributions, *J. Phys. D: Appl. Phys.* 2:1747 (1969).
25. T. Ruzicka and K. Rohlena, On nonhydrodynamic properties of the electron gas in the plasma of a dc discharge, *Czech. J. Phys. B,* 22:906 (1972).
T. Ruzicka and K. Rohlena, Electron gas in weakly ionized plasmas, *Invited Paper ICPIG XI, Prague, Czeckoslovakia,* 61 (1973).
27. L.D. Tsendin, Electron distribution function of weakly ionized plasmas in nonuniform electric fields. II. Strong fields (energy balance determined by inelastic collisions) *Sov. J. Plasma Phys.* 8:228 (1982).
28. L.D. Tsendin, Ionization kinetics and ionization waves in neon, *Sov. Phys. Tech. Phys.* 27:407 (1982).
29. Y.B. Golubovskii, V.O. Nekuchaev and N.S. Ponomarev, Trapped and free electrons in the anode region of stratified inert gas discharge, *Contr. Paper ICPIG XXIII, Toulouse* (1997).
30. V.I. Kolobov and L.D. Tsendin, Analytic model of the cathode region of a short glow discharge in light gases, *Phys. Rev,* 46: 7837 (1992).
31. V.A. Shweigert and I.V. Schweigert, Cathode region of a self-maontained glow discharge in helium, *Fix. Plasmy,* 14:347 (1988).

ELECTRON KINETICS IN THE CATHODE REGION OF GLOW DISCHARGES. PLANE AND HOLLOW CATHODES

R. R. Arslanbekov[1] and A. A. Kudryavtsev[2]

[1]Department of Physics, Monash University, Clayton, Victoria, Australia
[2]Institute of Physics, St.Petersburg State University, St.Petersburg, Russia

INTRODUCTION

The electron kinetics in the cathode region determines the principal characteristics of many types of glow discharges. Among them are short plane glow discharges (PGD) and various modifications of hollow cathode discharges (HCD). The key parameter here is the electron distribution function (EDF) which is to be determined in both energy and configuration spaces. The problem of finding the EDF in spatially inhomogeneous plasmas in the presence of complicated electric fields (and also in complex geometries) is highly non trivial. The principal difficulty is connected with the fact that the analysis has to be self-consistent (see, e.g., Ref. 1). In fact, in order to find the inhomogeneous plasma profiles and the electric field in a plasma, it is necessary to know the distribution of charged particle sources, which are determined by the EDF. In its turn, the EDF cannot be found without information about the distribution of the plasma density and electric fields.

At the present time, different straightforward numerical methods exist. They are, e.g., the Monte Carlo methods,[2] the particle-in-cell methods,[3] the convective schemes,[4] the direct solution of the Boltzmann equation,[5] and their modifications and combinations. Application of these methods has revealed good agreement with results of laboratory experiments. However, these methods are often cumbersome and require large amounts of computer time and are unhelpful in developing qualitative understanding. In such a situation, simple and effective approximate methods of (semi-)analytic solution of the electron Boltzmann equation in arbitrary electric fields become very important.[1] Such approaches allow one to obtain simple and physically transparent solutions and can also be helpful in interpreting numerical results. The idea is to divide the configuration and energy space into regions with sharp boundaries and to develop effective methods of treating the electron kinetics in each of these regions separately. Full-scale numerical modeling can be very useful for verification of these approximations. In this paper, some approximations and their applications to glow discharges in the steady-state will be presented. More details can be found in the works of Tsendin (e.g., Refs. 1,6) and references cited in the present paper.

Electron Kinetics and Application of Glow Discharges
Edited by U. Kortshagen and L. D. Tsendin, Plenum Press, New York, 1998

The traditional subdivision of the cathode region (CR) into the cathode dark space (CDS), negative glow (NG) and the Faraday dark space (FDS) is based on optical distinctions. These distinctions are more or less of secondary nature, and it seems more useful and instructive to subdivide the CR into two regions, the ion space charge sheath with strong electric field [where the cathode potential fall (CF) occurs], and the quasineutral plasma region (where the electric field is weak or even changes sign). The sheath occupies the dark space and cathode-adjacent part of the NG, and the plasma consists of the remainder of the NG, FDS and positive column (PC). The difference in nature between the CR and the PC is that the NG and the FDS are sustained by the fast electrons coming from the CF while the PC is sustained by electrons gaining energy in the local field. To describe the electron kinetics in the CR, one can divide electrons into groups according to the role these electrons play in the discharge dynamics: (i) the *fast* electrons which have energies above the first excitation potential, $\in^*$, that is, $w > \varepsilon^*$ and which ionize and excite the gas particles; and the *slow* (or plasma) electrons with energies $w < \varepsilon^*$. The slow electrons can further be subdivided into (ii) the *intermediate* electrons which have energies above several electron temperatures and which are current carriers, and (iii) the *bulk* (ultimate or thermal) electrons which are trapped in the self-consistent electric potential wells and which ensure quasineutrality of the plasma. Since the density and energy of these electron groups differ by many orders of magnitude and vary in completely different ways, it is highly convenient to treat each of these groups separately.

FAST ELECTRONS

The major peculiarity of modeling the fast electrons in the CR is that these electrons are not in hydrodynamic equilibrium with the local electric fields. The reason is that, due to the lack of collisions in the spatially localized CF region, the primary electrons ejected from the cathode and generated in the CF can gain substantial energies in the strong and rapidly varying cathode fields and can even *"run-away"* from collisions. Let us illustrate these statements. It is known from various studies of the fast electron kinetics that the fast EDF can roughly be described by two parameters: (i) the energy-loss function, $L(w)$, which in the range of energies $10 - 10^3$ eV, can be approximated as being energy independent, namely, $L(w) = L_0$; and (ii) the energy loss per ion-electron pair, $\in_0$ (typically, $\in_0 \approx 2\in_i$ with $\in_i$ being the ionization potential). In this approximation, the number of ionizations per unit path (or the Townsend coefficient), α, is given by $\alpha = NL_0/\in_0$, where N is the neutral particle density. Also, the energy relaxation length of an electron with a kinetic energy, w, can be introduced: $\lambda_w = (1/\alpha)(w/\epsilon_0)$. The value of λ_w determines the spatial scale on which the electron energy changes significantly. For typical discharge conditions, the value of λ_w exceeds the characteristic scale of the electric field inhomogeneity, namely, the CF width, d, that is, $\lambda_w >> d$. It follows from this inequality that strong non-locality takes place. In other words, the electrons gain energy in one region of configuration space (CF) and lose it in another region (NG). It is now well understood that, to model the dynamics of the fast electrons, the local field approximation cannot be used and the kinetic approach is necessary. Many numerical methods exist to treat the fast electrons: Monte Carlo methods,[2] direct solution of the Boltzmann equation,[5] and others. There also exist a number of analytical models. One of the simplest analytical models describing the ionization non-locality is that proposed by Kolobov and Tsendin.[7] Let us briefly consider the principal results of this work.

In Ref. 7, a short dc glow discharge is considered. The discharge gap [$0 \le x \le L_d$,

where x is the spatial coordinate and L_d is the discharge gap length (distance between the cathode and the anode)] is divided into three spatially separated regions with sharp boundaries: (i) the CF region or the region of strong electric field, for $0 \le x \le d$, (ii) the NG which is almost field-free due to the efficient ionization by fast electrons, (iii) the Faraday dark space which the fast electrons cannot reach. The Boltzmann equation is the starting equation in describing the kinetics of the fast electrons. Two important simplifications have been made to obtain an analytic solution to this equation. First, it has been assumed that the fast EDF is fully anisotropic, that is, the electrons are only forward scattered in collisions with atoms. Second, a continuous-energy-loss model has been used. These assumptions are valid provided that the kinetic energy of the fast electrons, w, significantly exceeds the energies of atomic electrons, that is, $w >> \in^*$. The kinetic equation for the fast EDF, $F(x, w)$, has then been written in the following form

$$v\frac{\partial F}{\partial x} + v\frac{\partial}{\partial w}\left[-eE(x) - N\mathcal{L}(w)\right] = J(x, w) \tag{1}$$

where v is the electron velocity and $J(x, w)$ is the source term due to generation of electrons. In this model, evolution of the kinetic energy of an electron is governed by the following simple equation [which is the characteristic of Eq. (1)], $dw/dx = -eE(x)-NL(w)$,$E(x)$ is the electric field. The right-hand side of this equation represents an effective force $F(x, w)$ which is the difference of the accelerating force $eE(x)$ and the retarding force $NL(w)$. The force $F(x, w)$ is non-conservative because of the presence of the retarding force. If $F(x, w)$ is positive, the electrons "run-away" from collisions and their kinetic energy permanently increases in the CF. An assumption of an energy-independent loss function, namely, $L(w) = L_0$ can further be made. This allows one to introduce an effective potential $\varphi(x)$ according to the relation $F(x) = -ed\varphi/dx$, where $e\varphi(x) = e\phi(x) - N\mathcal{L}_0 x$ with $\phi(x)$ being the electrostatic potential. The electrons move in this potential conserving their total energy $\in = w - e\varphi(x)$: they are accelerated in the CF (their kinetic energy increases) and they slow down and consequently join the slow electron group in the NG. Assuming that the secondary electrons are born in ionization events with zero energies, the solution to the kinetic equation (1) is found in terms of the total energy $\in$ which represents an independent variable in this model. Using this fast EDF, it is shown that in the CF and NG, the total electron current, j_e (which equals the fast electron current, j_f), is given by $dj_e/dx = \alpha j_e$. This expression corresponds to a generalization of the conventional Townsend approach with the ionization coefficient α = const. The major difference, however, is that the proposed kinetic approach takes into account the ionization non-locality.

Isotropic Fast Electrons

The model of fully anisotropic scattering presented above can be successfully used to describe the kinetics of high energy electrons (w > 100 eV). It is known, however, that the angular distributions of cross-sections, for elastic and inelastic scattering, change within the energy range under consideration (10 – 10^3 eV), going from anisotropic at high energies (w > 100 eV) to isotropic at lower energies (w < 50 eV). In this situation one should also expect changes in the degree of EDF anisotropy as electron energy varies (see, e.g., Ref. 2). The effect of isotropization becomes important in the NG where the electric field (which makes the fast EDF more anisotropic) is absent.

A simple model has been proposed in Ref. 8 to take into account the angular distribution of the fast electrons. It has been shown that at low energies, $w < \in_{is}$ ($\in_{is}$ is the so-called isotropization energy), the momentum of electrons relaxes much

more rapidly than their energy and the EDF for these energies can be regarded as nearly isotropic. The value of $\in_{is}$ depends on the behaviour of the corresponding cross-sections and it is different for each particular gas. For example, $\in_{is} \approx 80$ eV for He and it is expected to be higher for heavy gases where quick isotropization can take place. Using the well-known two-term expansion, the kinetic equation for the isotropic part of the EDF, $F_{is}(\mathbf{r}, w)$ ($\mathbf{r}$ is the spatial coordinate), of the low energy fast electrons ($\in^* \leq w < \in_{is}$) can be written as

$$\nabla \cdot (v D_{tr} \nabla F_{is}) + v \frac{\partial}{\partial w} [-eE - N\mathcal{L}(w)] F_{is} + S[F] v = 0 \qquad (2)$$

where D_{tr} is the fast electron diffusion coefficient and $S[F]$ is the source term determined by the anisotropic EDF of high energy fast electrons, $F(\mathbf{r}, w)$, [see Eq. (1)]. For convenience, the collisional integral in Eq. (2) is written in the form similar to that used above in Eq. (1). Calculations of the spatial profiles of an atomic line (excited mainly by low energy fast electrons, $w \approx$ 20-60 eV) according to Eq. (2) and of an ionic line (excited mainly by high energy anisotropic fast electrons, $w >$ 120 eV) agree well with the experimental data (from Ref. 9) obtained in a cylindrical HCD (see. Fig. 1). The model predicts a marked difference in the spatial behaviour of anisotropic and isotropic electrons, namely, that a strong focusing of the anisotropic electrons takes place at the discharge axis and that the isotropic electrons are distributed more or less uniformly over the NG.

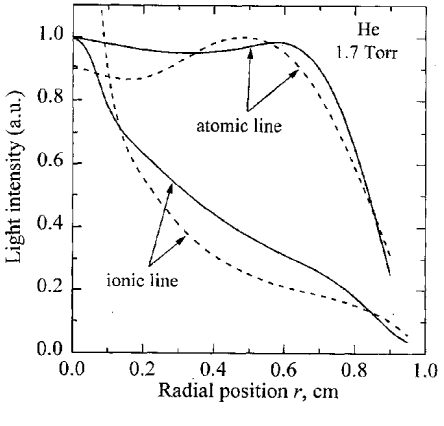

Figure 1. Radial intensity distributions (normalized to their maximum value) of two helium lines: 468.6 nm ionic line and 587.5 nm atomic triplet line at the pressure of 1.7 Torr in a cylindrical HCD in He. Solid lines correspond to the experimental data from Ref. 9 dashed lines are calculations.

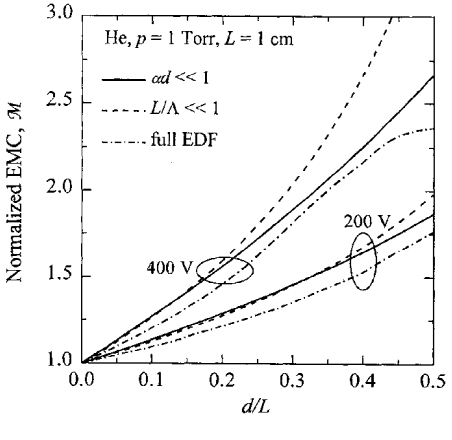

Figure 2. Normalized electron multiplication coefficient, $\tilde{\mathcal{M}}$, as a function of the normalized CF width, d/L, calculated using the approximation of small αd ($\alpha d << 1$), the multipass approximation ($L/\Lambda << 1$), and obtained from a numerical solution of the full kinetic equation from Ref. 11.

The Hollow Cathode Effect

The fast electron kinetics in the CR of a PGD has been studied in details in a number of papers (see, e.g., Refs. 2,4,7). Another issue, in which the fast electron kinetics plays an essential role (see, e.g., Refs. 10,11), is the hollow cathode effect

(HCE). Since there are still some unresolved questions concerning the HCE, we will further consider the HCE in some more detail. The HCE is a very complex multi-parametric phenomenon and there is an extensive literature devoted to it. The most spectacular feature of the HCE is the large increase of the current density, j, which takes place when the intercathode distance, L, is decreased while the discharge voltage, U, is being fixed. (Note that a conventional plane or cylindrical HCD is considered here and later on. For a cylindrical HCD, L corresponds to the tube diameter, D). Hence the HCD can be considered *a priori* as a highly *abnormal* discharge. Another important feature of the HCD is that it operates at voltages which are much lower than those corresponding to an abnormal glow discharge (AGD) at comparable current densities. The HCDs are also characterized by low slope resistance voltage-current (V-I) curves. All these features can be explained by the *improved confinement* of the fast electrons and ions as compared to the usual discharge geometries (e.g., a short PGD).

The important difference between the HCD and PGD is that, in the HCD, there exists a region of a strong reversed field in the opposite CF. Hence, the fast electrons are able to oscillate in the cavity and deposit all their energy into the plasma. Also, while traveling in the opposite CF, they can produce further generations of fast electrons (pendulum effect). The latter effect results in additional ionization being produced: The onset of the HCE occurs when the critical length, $L_c = \Lambda + d$, exceeds the inter-cathode distance, L, that is, $L_c > L$, where $\Lambda = e\phi_c/(\alpha\epsilon_0)$ is the reaching distance of fast electrons with ϕ_c being the cathode potential fall.[11] In Ref. 10, the HCE has been modeled numerically. In Ref. 11, an analytic analysis of the HCE has been proposed.

The results of Ref. 11 indicate that a large rate of ionization in the opposite CFs is essential for the HCE to exist. However, it is known that the HCDs used in practical applications operate at substantial current densities (> 1 mA cm^{-2}) and moderate voltages (< 500 V). In such conditions, the CFs are generally thin ($d << L$) and ionization there is small compared to that in the NG. Hence, the pendulum effect seems to become less significant. So the puzzling question arises: does the HCE still exist when the CFs are thin and ionization there is insignificant ?

In this work, we tried to answer this question and to model the HCE starting from the natural premise of small ionization in the CF, namely, small product αd. This approach is different from the more complicated approach (valid for any αd product) proposed in Ref. 11 in which, even in the multipass approximation when $L/\Lambda << 1$, it is necessary to resolve numerically a spatially averaged kinetic equation. The analytic approach used in the present work allows simple and physically transparent formulae to be obtained for the electron multiplication coefficient (EMC). The approximation of this work however does not rely on small ionization in the opposite CFs since, due to the accumulation of a great number of oscillations, the ionization rate [$\alpha n\alpha d$ with $n(\approx \Lambda/L)$ being the number of oscillations (see below)] can be significant.

Let us calculate the EMC, M, when $\alpha d << 1$. Consider a long PGD with a thin CF and a linearly decreasing electric field, $E(x) = 2\phi_c/d(1 - x/d)$. The anode is supposed to be at a distance $L_d > L$. In this case, Eq. (1) applied in the limit $\alpha d << 1$ (practically, $\alpha d < 0.3 - 0.4$ suffices) yields $M = (e\phi_c/\epsilon_0)(1 + \alpha d/3) + \alpha d$, where the terms of the order of $(\alpha d)^2$ and higher orders have been neglected. The term $e\phi_c/\epsilon_0$ in this equation represents the number of ionizations by a primary electron in the NG with no ionization in the CF ($d = 0$). The term $(e\phi_c/\epsilon_0)/(\alpha d/3)$ describes the number of ionizations in the NG due to the successive generations of secondary electrons in the CF ($d \neq 0$). The third term ad ($\approx e^{\alpha d} - 1$, $\alpha d << 1$) determines the number of ionizations by a primary electron in the CF. Hence, we can now separate the EMC into two parts: $M = M^{NG} + M^{CF}$, where $M^{NG} = e\phi_c/\epsilon_0$ is the EMC in the NG due to

an initial electron started from the cathode, M^{CF} is the EMC due to the fast electron successful generations in the CF. To calculate M^{CF}, we proceed as the following.

One can see from the above expression for M that an electron with an energy $e\phi_c$, increases the number of ionizations by $(e\phi_c/\epsilon_0)/(\alpha d/3)$ when it passes through a CF of width d. It is clear that an electron with an energy w will produce $(w/\epsilon_0)(\alpha d_w/3)$ ionizations, where $2d_w = 2d\sqrt{w/e\phi_c}$ is the path which this electron travels in the opposite CF (forward and back). In the continuous-energy-loss model (see above), the initial electron started from the CF with an energy $w = e\phi_c$, after being decelerated in the NG in a length of $L - 2d$, will come to the boundary of the opposite CF possessing a kinetic energy $w_1 = e\phi_c - \alpha\epsilon_0(L - 2d)$. Therefore, after the primary electron's first passage through the opposite CF, the number of ionizations will increase by $(w_1/\epsilon_0)[2\alpha d_w(w_1)/3]$ en considering a second reflection and so on and summing up over all the possible reflections, one can get

$$\mathcal{M}^{CF} = \frac{e\phi_c}{\epsilon_0}\frac{\alpha d}{3} + \sum_{k=1}^{n}\frac{w_i}{\epsilon_0}\frac{2\alpha d_w(w_i)}{3} \tag{3}$$

where $w_i = w_{i-1} - \alpha\epsilon_0(L - [2d - d_w(w_{i-1}])$. It can be shown from Eq. (3) that $\mathcal{M}^{CF}_{\min} \le \mathcal{M}^{CF} \le \mathcal{M}^{CF}_{\max}$

$$\mathcal{M}^{CF}_{\min} = \frac{e\phi_c}{\epsilon_0} \times \frac{\alpha d}{3}, \text{ when } n = 0 \quad \text{(no reflection)} \tag{4}$$

$$\mathcal{M}^{CF}_{\max} = \frac{e\phi_c}{\epsilon_0} \times \left(\frac{1}{2}\frac{e\phi_c}{\epsilon_0}\frac{d}{L}\right) \quad \text{when } n >> 1 \quad \text{(multiple reflections)}$$

From these equations, it can be concluded that when the multipass regime (when the number of oscillations, n, is large, $n = L/\Lambda >> 1$) is realized, the additional ionization in the CFs is important, that is, $M^{CF} > M^{NG}$, only when $d/L > 2(\epsilon_0/e\phi_c)^{-1}$, that is, when the CF is thick. The multipass regime takes place when the fast electrons lose a small fraction of their energy during a passage through the plasma and so they traverse the plasma many times.

It is then convenient to introduce the normalized EMC, $\widetilde{\mathcal{M}}$, as $\widetilde{\mathcal{M}} = \mathcal{M}/(e\phi_c/\epsilon_0)$, which characterizes the efficiency of ionization in the CFs (e.g., $M = 1$ when ionization in the CFs is absent). Calculations of the EMC using three different approaches are shown in Fig. 2. One can see that the calculations according to the approximation of small ad correspond well to those $\widetilde{\mathcal{M}}$ calculated numerically from the full kinetic equation from Ref. 11. Good agreement is also seen between the results of these two approaches and those obtained from a numerical solution of a spatially averaged kinetic equation in the multipass approximation ($L/\Lambda << 1$). [11] One can observe in Fig. 2 that when $d/L < 0.2$ the fraction of additional ionization does not exceed 20% at $e\phi_c = U =$ 200 V and 40% at $U = 400$ V.

In order to model the HCE, one has to specify the self-sustaining condition (or the current-continuity condition). Due to the specific geometry of the HCD, most of the ions generated the NG return to the cathode. Under the conditions of interest, the major source of electrons is the ion bombardment of the cathode. Hence, in the absence of recombination or other volume losses, the self-sustaining condition in the steady-state can be written as $M(\phi_c, d) = 1/\gamma$, where γ is the secondary electron emission coefficient. To complete the model, we use the well known expression (for a collision dominated CF) for the current density at the cathode surface $j = C\phi_c^{3/2}/(d^2\sqrt{pd})$ where C is a constant.

Results of modeling the HCE in the approximation of small αd are shown in Fig. 3. Experimental conditions from Ref. 12 have been used. One can see that the current amplification factor, j/j_0 (where j_0 is the normal current density [13]), increases by more than two orders of magnitude when L is reduced from 4 cm to 0.3 cm. It is not a surprising result and has been reproduced elsewhere (e.g., Refs. 10,11). The reason is that when L is reduced, the ionization in the NG becomes so efficient that the CF width, d, must decrease to satisfy the self-sustaining condition $M = 1/\gamma$ and j consequently goes up $j \propto d^{-5/2}$. Also, in the multipass regime due to the self-sustaining condition, $d \propto L$ [see Eq. (4)], and hence a decrease of L requires a decrease of d. One can see in Fig. 3 that there is a good agreement with the experimental current density at L = 1.8 cm. V-I characteristics in a large range of current densities (0.5-300 mA cm^{-2}) are presented in Fig. 4 for two cylindrical HCDs in He. The tube diameter D corresponds here to the intercathode distance, L. One can see a good agreement between the calculated V-I curves and those observed experimentally. It is worthwhile to mention the following. It is well known that the HCDs are characterized by V-I curves which have a small slope resistance. In most cases, two different slopes can be observed: a higher slope at low current densities and a lower slope at higher current densities (see Fig. 4). Calculations show that in order to estimate the influence of the additional ionizations in the CF, it is possible to establish a simple rule: when the voltage of the HCD no longer increases (or increases slightly) with current, ionization in the CF can be ruled out. Mathematically, it means that the discharge voltage approaches its "critical" value, $eU_c = \epsilon_0/\gamma$, when ionization in the CF is completely absent. This is of course valid only when other loss mechanisms such as recombination and/or fast electron losses from the cavity are not important.

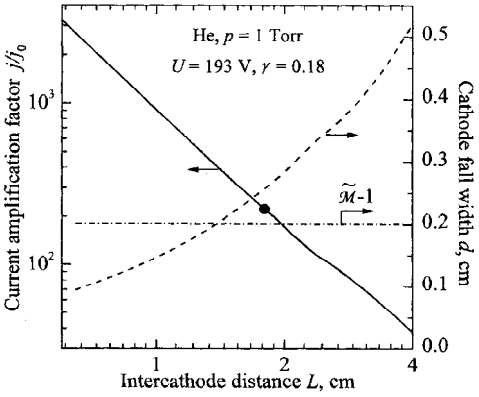

Figure 3. Results of modeling the HCE for the conditions of Ref. 12 using the approximation of small αd. The current amplification factor j/j_0 is plotted vs the intercathode distance, L. The closed circle indicates an experimental point from Ref. 12: $L = D$ = 1.8 cm, j = 0.5 mA cm^{-2} [see Fig. 4(a)].

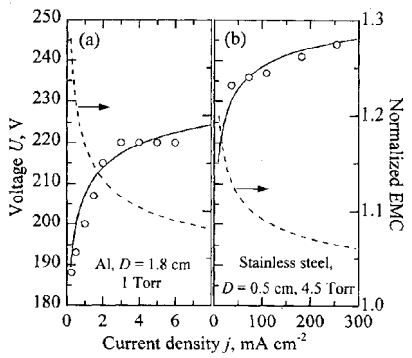

Figure 4. V-I characteristics calculated in the approximation of small αd. Experimental voltage values are shown open circles: (a) from Ref. 12, (b) from Ref. 14. The normalized EMC is shown by a dashed line. γ = 0.18 in the calculations.

We have to point out two other important conclusions which can be drawn from the calculations presented above. First, the HCE has been modeled with only a *small* fraction (< 20%) of additional ionizations in the CFs. Secondly, the HCE has been modeled

with a *linear* electron multiplication in the CF ($M^{CF} \alpha \alpha d$). Hence, we can conclude that for the HCE to exist there is no need for substantial ionization and exponential electron multiplication [11] to occur in the CFs. These latter factors can be important in the early stage of the HCE when the CFs are thick ($d/L > 0.3$) and the current density is low (close to its normal value) or for the HCD operating at high voltages/low secondary electron emission coefficients (or low pressures/small intercathode distance). These latter types of the HCDs are not considered here and they require a special study (e.g., Refs. 15,16). Note, e.g., that for the HCD operating at high-U/low-γ [or low-p/large-(Λ/L) ratio] the fast electron losses from the cavity can be very important. These losses are not taken into account in the present model. Thus for the cases of practical interest (moderate voltages, $U < 500$ V, and substantial current densities, $j > 1$ mA cm^{-2}), additional ionization in the CF can be neglected. These operating conditions are those of the large class of the HCDs which are widely used in analytical[17] and laser [18,19] applications. This means that these HCDs can be modeled with good precision based on the assumption that a monoenergetic electron beam enters the NG with an energy corresponding to the CF potential drop.[8,20,21] These models, of course, cannot explain the HCE. However, within the limits of their validity, these models correctly describe energy integrated characteristics such as the ionization and excitation profiles. Calculations of more precise energy dependent characteristics cannot be done using these crude approximations of anisotropic scattering and continuous-energy-loss.

It is still believed that the pendulum effect leads to a drastic increase in the number of ionization processes.[22] However, as it can be seen from the above calculations, the pendulum effect *does not* result in an increase on number of ionizations because this number ($= 1/\gamma$) is fixed by the self-sustaining condition (see Fig. 3 where $\widetilde{\mathcal{M}} = 1.2$ and it does not vary). Instead, the pendulum effect results in ionization becoming so efficient in the NG that there is no longer need for the electron multiplication to occur in the CFs and hence the CF width reduces and the current density increases.

It can be seen from the above calculations that the HCE exists even if a very small fraction of ionization occurs in the CFs. Moreover, we believe that in the stage of "developed" HCD (when its current density significantly exceeds the normal one and the CFs are thin), any mechanism which results in an increase (even very small) of ionization in the NG when the product pL is decreased can lead to the HCE. This fact thus points out the difficulty in identifying *the* mechanism which is responsible for the HCE in its "developed" stage. We will demonstrate this statement by considering the mechanism of diffusional losses of ions from the discharge cavity.

The ion motion represents another quite independent mechanism of the HCE. If the width of the NG is comparable with (or exceeds) the tube radius, a considerable part of ions in case of the plane cathode is lost to the side tube walls and does not produce electron emission from the cathode. The role of the ion losses is usually neglected while describing the HCE and it is assumed that all the ions generated in the HCD diffuse to the cathode (in the absence of recombination or other volume losses).[11] In order to estimate the rate of ion losses, it can be assumed that their transport is determined by ambipolar diffusion. A diffusion loss coefficient, δ_i, can be introduced, which is roughly equal $H^2/(H^2 + L^2)$ where H is the width of the cathode. Provided that $(H/L)^2 >> 1$, $\delta_i \approx 1$ and the ion diffusional losses can be neglected. The latter condition is not always satisfied (e.g., the experimental set-up in Ref. 23). In order to estimate the effect of these losses, another self-sustaining condition is used, $\delta_i \gamma M = 1$ (see Ref. 11). This expression however is not fully exact since only those ions which are generated in the NG can be lost from the cavity. The ions generated in the CF are collected by the cathode by the strong CF electric fields. The fact that the loss rates are different for the ions in

the NG and the CF can change the situation dramatically. To demonstrate this, one can use the fast EDF obtained above and calculate the fraction of the ions generated in the CF and then introduce the loss of the ions in the NG. It is however interesting to see the effect due to these losses only when the intercathode distance is reduced. In order to do so, we neglect additional ionization in the opposite CF. Keeping in mind that the loss rates in the NG and the CF are different, we should modify the expression $\delta\gamma M = 1$. Let us consider a practical situation which is realized frequently in experiment[23]: a system of two disk cathodes of radius R_c separated by a distance L. In that case, $\delta_i = (R_c/2.4)^2/[(R_c/2.4)^2 + (L_{NG}/\pi)$ where $L_{NG} = L - 2d$ is the NG length. For the case when additional ionization in the CF can be ruled out, one can write the self-sustaining condition as $\mathcal{M}^{CF} + \delta_i \mathcal{M}^{NG} = 1/\gamma$, where $\mathcal{M}^{NG} = e\phi_c/\epsilon_0 \times l_{NG}/\Lambda$ and $\mathcal{M}^{CF} = e\phi_c/\epsilon_0 \times l_{CF}/\Lambda$ are the number of ionizations produced by a primary electron in the NG and CF, respectively; l_{NG} (l_{CF}) is the path of this electron in the NG (CF) which can be calculated easily in a manner similar to that used above to obtain Eq. (3), $l_{NG} + l_{CF} = \Lambda$. It is clear that $l_{CF} \propto d$ so that when the intercathode distance L is decreased, $\delta_i \to 1$ and M^{CF} (and so d) must decrease to satisfy the self-sustaining condition. Hence, an increase in the current density is expected when L decreases. This is similar to the HCE when only the effect of additional ionization in the CF is taken into account. Indeed, in these both cases, the number of ionizations in the NG increases when L reduces and, to satisfy the self-sustaining condition, the number of ionizations in the CF (and so d) must decrease since $d \propto L$. To model this effect quantitatively, we take the following values: R_c = 1.5 cm (see Ref. 23), p = 1 Torr, He gas, $e\phi_c$ = 250 V, γ = 0.2. Results of calculations are presented in Fig. 5. One can see that there is a drastic increase of the discharge current density which results from the decrease of d when L is reduced from 4 cm to 0.75 cm. It is important to note that the effect is observed with the values of the diffusional loss coefficient δ being close to 1 (δ_i varies from 0.75 to 0.9). Therefore, the HCE can be modeled without recourse to any additional ionization in the CF. This result, of course, cannot be considered as being valid by itself and should be considered in conjunction with the mechanism of ionization in the opposite CFs and other competing mechanisms. But this example illustrates that the ion dynamics has comparable importance to the electron dynamics in the HCE. It also proves how complicated the phenomenon of the HCE is and points to necessity of a comprehensive global model of the HCD.

SLOW ELECTRONS

In most numerical models of the CR, the electrons are divided into fast and slow ones. The fast electrons are treated kinetically (Monte Carlo methods, electron Boltzmann equation, etc.). The slow electrons are described using the fluid (or hydrodynamic) approach. Typically, two parameters are used to describe the slow EDF: the electron density, n_e, which is found from the continuity equations and the electron temperature, T_e, which is generally not calculated but is used as an input parameter. In plasmas with weak electric fields (e.g., the NG and FDS), in the elastic energy region, the EDF body (bulk) has the Maxwellian distribution (see below) with a high number density, n_e, and a low mean energy, T_e (< 1 eV). The "hot" tail of the EDF with energies up to ϵ^* is essentially non-Maxwellian. The number of these electrons (usually called the intermediate electrons or hot plasma electrons), n_f, is significantly lower than that of the bulk electrons $[n_f \approx (10^{-3}\text{-}10^{-2})n_e]$ and their mean energy, ϵ_f, is high $(\epsilon_f \approx \epsilon^*/2 \gg T_e)$. Since under typical discharge conditions, the bulk electrons are trapped in the self-consistent electric fields, the intermediate electrons carry the

electron current in the NG and FDS and so play an important role in the formation of the self-consistent electric fields. Moreover, the intermediate electrons are essential in the energy balance of the bulk electrons (see below). Hence, it is important to take into account the existence of the intermediate electrons, which is generally not done in the traditional fluid approach. Since the intermediate electrons cannot be described in the fluid approach in terms of two parameters, namely, n_e and T_e, they must be treated kinetically.

In order to calculate the slow EDF, a kinetic equation is to be derived. The following simplifications can be made. First, in the elastic energy range, the EDF can be treated as isotropic due to the high rate of electron-atom collisions. Second, to simplify the integral of interelectron collisions and write it down in the Fokker-Plank (differential) form, it can be supposed that the EDF body at thermal energies is Maxwellian with the density n_e and temperature T_e. This supposition is valid since, under typical conditions, the interelectron collisions are dominant at thermal energies. Third, one can write down the kinetic equation in variables $\mathbf{r}$ and total energy (kinetic + potential) $\epsilon = w + e\phi_a(\mathbf{r})$ where $\phi_a(\mathbf{r})$ is the ambipolar potential.[6] [Note that it is possible to separate the plasma electric field into the ambipolar electric field which is due to the plasma gradients and the direct (or current carrying) field which originates from an external power supply.] The kinetic equation for the isotropic part of the slow EDF, $f_e(\epsilon, \mathbf{r})$, can be then written down as

$$\nabla \cdot (vD_r \nabla f_e) + \frac{\partial}{\partial \epsilon}\left[v\left(D_\epsilon \frac{\partial f_e}{\partial \epsilon} + V_\epsilon f_e\right)\right] + Q^+(\mathbf{r})R^+(w)v + Q^*(\mathbf{r}, w)v = 0 \qquad (5)$$

where $D_r = (1/3)\lambda v$ is the slow electron diffusion coefficient in configuration space, λ and v are the electron mean free path and velocity, respectively; $D_\epsilon = D_e + D_a + D_E = V_e T_e + V_a T_a + (1/3)(eE_d\lambda)^2\nu_a$ (T_a being the atom temperature) and $V_\epsilon = V_e + V_a \approx w(\nu_e + \delta\nu_a)$ are, respectively, the electron diffusion and friction coefficients in energy space due to interelectron (frequency ν_e), elastic electron-atom (frequency ν_a) collisions and direct electric field E_d (see Refs. 1,24 for more details). The third term in Eq. (5) represents the continuous source (in energy space) of the secondary electrons generated in ionization by fast electron impact with an integral intensity equal to the ionisation rate, $Q^+(\mathbf{r})$; $R^+(w)$ is the energy distribution of the secondary electrons. The fourth term in Eq. (5) is due to processes involving excited particles (e.g., Penning ionization, collisions of the second kind[24]). (Note that the slow EDF is thus directly coupled to the kinetics of ionized and excited particles).

It follows from the kinetic equation (5) that the slow EDF can be separated into two distinct parts, $f_e = f_M + f_f$: (i) the bulk EDF, f_M, which represents the solution of the homogeneous equation, $f_M = C_n \exp(-\int d\epsilon/T)$ where $T(w) = D_\epsilon/V_\epsilon$ is effective temperature and C_n the normalization constant. When the interelectron collisions are dominant, that is, $\nu_e \gg \delta\nu_a$, $T(w) = T_e$, and $f_M \propto n_{e0} \exp(-e\phi_a/T_e) \cdot \exp(-w/T_e)$ which is Maxwell-Boltzmann. The electron density, n_e, can be determined from the ion transport equations and the electron temperature from the corresponding energy balance equation; (ii) the EDF of the intermediate electrons, f_f, which represents the solution of the inhomogeneous kinetic equation and which is essentially non-Maxwellian (see Eq. (6) and Eq. (7) below).

It also follows from the kinetic equation that the relationship between the spatial and energy characteristics of the EDF is determined by the electron energy relaxation length $\lambda_\epsilon = \lambda/\sqrt{\delta(1 + \nu_e/\delta\nu_a)}$ (see Refs. 1,6). The spatial scale on which a significant change of the electron energy takes place is determined by λ_ϵ, and depending on how

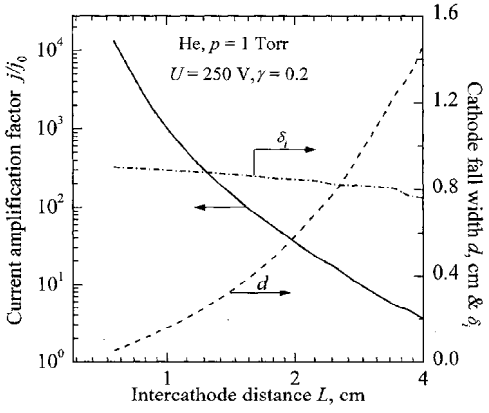

Figure 5. Results of modeling the HCE upon reducing the intercathode distance, *L*. Only the ion diffusional losses are taken into account. Two disk cathodes of radius R_c = 1.5 cm are considered.

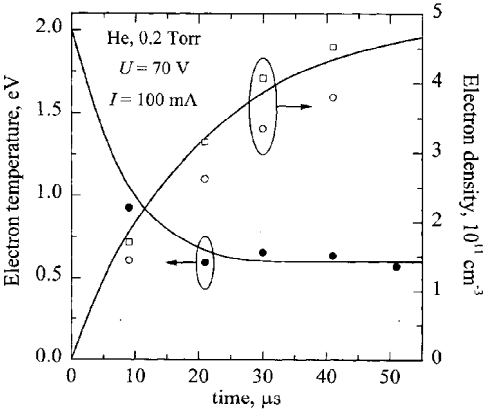

Figure 6. Temporal evolution of T_e and n_e in the beginning of a discharge pulse in the hollow cathode-anode discharge. Symbols correspond to experimental data, lines are calculations.[31]

λ_ϵ relates to the characteristic plasma dimension L_{pl} (e.g., for a cylindrical plasma, $L_{pl} \approx R$) one can consider* the limiting cases specified below (see Refs. 1,6 for details)

In the case when $\lambda_\epsilon << L_{pl}$, that is when electron energy relaxation takes place at a short distance, the terms with spatial gradients of f_e and the potential $\phi_a(\mathbf{r})$, can be neglected in the kinetic equation (5) and the EDF can be found in the *local* approximation. The perturbation of the local EDF due to diffusion to the plasma boundaries shows up only at short distances from the boundaries of the order of $\lambda_\epsilon << L_{pl}$. An approximate expression for the intermediate EDF ($\epsilon > 2 \div 3\, T_e$) in the local regime can be written as

$$f_f(w, \mathbf{r}) = \frac{Q^+(\mathbf{r})}{V_\epsilon} \int_w^{\epsilon^*} R^+(w) dw \qquad (6)$$

where the ionization term only is considered and the difference between the total and kinetic energies is neglected (see Refs. 24-26 for more details).

In the other limiting case when $\lambda_\epsilon >> L_{pl}$, the terms with gradients of the EDF and the potential $\phi a(\mathbf{r})$ became essential, and the regime of the EDF formation is *non-local*, which means that the EDF in a given space region is determined not only by the plasma parameters of this region but also by the whole volume. The term with spatial diffusion is dominant for the trapped electrons (see below) and their EDF is a function of total energy ϵ only, $f_M(\epsilon, \mathbf{r}) = f_M(\epsilon)$. The EDF of the trapped electrons is Maxwell-Boltzmann. Contrary, the balance of the untrapped electrons is determined by escape to the plasma boundaries and their non-local EDF can be approximately written as

$$f_f(\epsilon, r) = Q^+ R^+(w) \tau_{df}(w) [1 - (r/R)^2] \qquad (7)$$

where for simplicity a cylindrical coordinate system is used and $\tau_{df}(w)$ is the time of free diffusion of an electron with an energy w (see Refs. 24,25 for more details).

Let us now illustrate the importance of the kinetic approach to the slow electrons in describing the self-consistent electric fields and the electron temperature.

Self-Consistent Electric Fields and Field Reversal Criteria in the PGD

As has been pointed out above, in spatially inhomogeneous plasmas, the electron distribution function, plasma density profiles, and electric fields must be calculated self-consistently. One of the most interesting examples of such a self-consistent problem is the phenomenon of the field reversal in the PGD when a significant part of the NG and FDS is occupied by a potential well for the thermal electrons.[7,27]

In normal and abnormal PGDs, the non-locality of ionization can be considerable and substantial numbers of charged particles can be generated in the low field region where the plasma density is maximum. The range of a fast electron with a kinetic energy corresponding to the CF potential drop ϕ_c, can be calculated as $\Lambda = e\phi_c/(\alpha\varepsilon_0)$ (see above). This formula gives estimations of the NG length which agree well with experimental results (e.g., see Fig. 3 in Ref. 7). Hence, the position of $x = \Lambda$ can be regarded as a boundary between the NG and the FDS. This position also approximately corresponds to the position of the electron density maximum (n_m). It has been shown in Ref. 7 that the position of the first field reversal (to first order in μ_i/μ_e) is near the end of the NG where the electron density is maximal. The ions, which are generated to the left of this maximum, travel in the NG by ambipolar diffusion to the CF boundary. The region between the NG and PC, where the electron density is still significant, is the FDS. The length of the FDS can be estimated as $L_F \approx l_D \ln(n_m/n_c)$ where l_D is the length on which an ion diffuses during its lifetime and nc is the electron density in the PC (if recombination on the chamber walls is the dominant loss mechanism for the ions, then $l_D \approx R/2.4$). The electric field, E_c, and electron density, n_c, in the PC are determined from the charged particle balance equation which can be written approximately as $I(E_c/N) = n_c/\tau_a$ with I being the ionization rate and τ_a the ambipolar diffusion time, $\tau_a \approx R^2/(5.8D_a)$.

In the case of a long discharge, when the discharge gap length, L_d, exceeds L_F, a second field reversal may occur at the FDS-PC boundary. In that case, a potential well for the slow electrons develops. Its depth, ϕ_t, is of the order of few T_e ($e\phi_t << \epsilon^*$). In the non-local regime when $\lambda_\epsilon >> L_F$ (e.g., $\lambda_\epsilon >> 1$ cm up to few Torr in He) one can separate the slow electron group into two subgroups. The first subgroup consists of the trapped electrons (which are almost all the bulk electrons) with total energies below the trapping potential ϕ_t, that is, $\epsilon \le e\phi_t$, which can only move within a limited space in the discharge cavity determined by the condition $\epsilon \le e\phi_a(\mathbf{r})$. The second subgroup consists of the untrapped electrons (which are practically all the intermediate electrons), with total energies above the trapping potential, that is, $\epsilon > e\phi_t$, which can move to the plasma boundaries and which are the electron current carriers. The particle balance of the untrapped electrons is determined by their sources (Q^+ and Q^*) and free diffusion to the plasma boundaries [see Eq. (7)]. In this non-local regime, the value of the trapping potential can be determined from the condition that, in the steady-state, the flux of electrons entering the energy interval $\epsilon \le e\phi_t$ must be equal to the fluxes of electrons escaping via the sink at $\epsilon = e\phi_t$, through collisions of the second kind and the Coulomb collisions, and through annihilation by recombination.[21,25] Although the trapped electrons constitute the vast majority of the electrons, their contribution to the electron current is zero.[7] The relationship between the spatial distribution of the electron density and the electric potential is given by7: $n_e(x) = n_f(x) + n_M(x)(\exp[-e\phi(x)/T_e] - \exp[-e\phi_t/T_e])$, where n_M is the trapped-electron density. Typically, in the main part of the NG and FDS, the Boltzmann term in this equation dominates and the electric field profile is given by the ambipolar diffusion equation, $E(x) = -T_e/e \cdot d[\ln(n_e)]/dx$. (Note that a significant departure from

this expression for $E(x)$ can take place when the density of the intermediate electrons, n_f, is high[26]). This implies that the reversed field in a short PGD rises monotonically towards the anode and that the depth of the potential well, $e\phi_t$, is determined by the anode potential.

The electron current in the FDS is transported due to diffusion of the intermediate electrons ($e\phi_t \leq \in \leq \in^*$). The distribution function of these electrons is essentially non-Maxwellian and has to be calculated from the kinetic equation as specified above [see Eq. (7)]. Using this EDF, one can roughly estimate the electron current in the FDS as $j_e \approx D_e^{(f)} dn_f/dx$ where $D_e^{(f)}$ is the diffusion coefficient of an electron with an energy $\in f$. The traditional fluid approach employs a division of the slow electron current into the diffusion and mobility components. However, the densities of the trapped and untrapped electrons vary along the FDS in an entirely different manner.[7] Since the electron current is carried only by the untrapped electrons, it is in principle impossible to express j_e in terms of the total electron density and its derivatives. Therefore, the fluid approach is altogether misleading in this case and can result in substantial errors. Moreover, the fact that the fluid approach cannot be used for describing the field reversal follows even from some general considerations. Indeed, in the situation when the field reversal exists, the diffusion term in the electron current is greater than the mobility term, that is, $D_e \nabla n_e > n_e \mu_e E$. It follows immediately from this inequality that the characteristic FDS length, $L_F \approx n_e/\nabla n_e$, is smaller than the electron energy relaxation length, $\lambda_\in \approx T_e/E$, namely, $L_F < \lambda_\in$. In this case, as it has been shown in numerous works devoted to the non-local electron kinetics (see, e.g., Refs. 1,6), the regime of the EDF formation is non-local and a quantitative description requires the kinetic approach.

At elevated pressures (p > 10 Torr, local regime: $\lambda_\in << L_{pl}$), the field reversal in the PGD can be absent.[7] Instead of the electric field which decelerates the electrons, an electric field arises which accelerates the electrons to the anode. A similar situation of the absence of the trapping potential can occur in the longitudinal direction of a long (large *H/R* ratio) cylindrical HCD. [14,25]

In the case of the local regime ($\lambda_\in << L_{pl}$) no distinguishing, in principle, is needed between the untrapped and trapped electrons. However, the fluid approach still cannot be used since it is necessary to know the intermediate EDF to find T_e (see below). In the case of a short PGD or when a second field reversal exists, the value of the trapping potential can be found by equating the electron and ion currents at the plasma boundaries. Also, at high pressures (p > 10 Torr), when the FDS is expected to be very short ($< \lambda_\in \approx 10^{-1}$-$10^{-2}$ cm), abnormally long FDSs (1-3 cm) have been observed. This paradoxical situation could be explained by the transport of charged particles being determined by the so-called *ambipolar drift* when the dependence of the electron mobility, μ_e, on the local electric field (or T_e), $\mu_e(E)$, becomes important.[28] This phenomenon has been observed in the high-pressure high-power gas lasers and it can be important in the plasma display panels operating at high pressures.

Electron Temperature

Knowledge of the electron temperature, T_e, is particularly important in the field-free plasma since the overwhelming majority of electrons there have a Maxwell - Boltzmann distribution. The rates of the major plasma processes thus become directly related to T_e. They are, for example, the rates of ambipolar diffusion, recombination, stepwise processes and many others. Because of the difficulty in predicting the electron temperature using the traditional fluid approach (see below), the value of T_e is usually assigned to 1 eV (e.g., Refs. 29,30) regardless the plasma conditions (gas pressure, dis-

charge current, etc). In some models and model estimations, the value of T_e is assumed to be equal to the gas temperature, T_g, that is, $T_e = T_g = 300$ K (e.g., Ref. 9). The use of these *ad hoc* values of the electron temperature can lead to erroneous predictions of the electron density, metastable density and so on. Indeed, not only can the electron temperature be very different from 300 K or 1 eV but it can also depend strongly on the plasma parameters (gas type, pressure, electron density, etc) (e.g., Refs. 21,25,31).

The fact that the bulk electrons have the Maxwellian distribution can significantly simplify the problem of calculating their mean energy (or T_e). Otherwise, when the form the EDF body is not known *a priori*, a complicated electron Boltzmann equation has to be solved which includes the integro-differential term of interelectron collisions. Hence, the direct solution of the kinetic equation to find T_e (and also n_e) can present difficulties. Instead, the energy balance equation should be used. An important aspect of the problem of finding of T_e in the field-free plasma is that the major source of energy for the bulk electrons is due to collisions with the hot intermediate electrons. Hence, to predict correct values of T_e, it is essential to know the intermediate EDF which must be treated kinetically. This cannot be done within the framework of the fluid approach in which one deals with the energy integrated moments of the EDF.

Multiplying the kinetic equation Eq. (5) by ϵ and then integrating over energy, the energy balance of the Maxwellian electrons can be written as (e.g., Ref. 32)

$$\nabla \cdot (\lambda_e \nabla T_e) + H_r + H_{Q^+} + H_{Q^*} - L_{el} - L_{inel} - L_D = 0 \tag{8}$$

Here, the first term represents conduction cooling with λe being the electron thermal conductivity coefficient; H_r, H_{Q^+} and H_{Q^*} represent, respectively, the energy gains in recombination and in collisions with the intermediate electrons created in ionization by fast electron impact and in interactions involving excited particles;[24] L_{el} and L_{inel} represent the energy losses in elastic collisions with atoms and ions and in inelastic collisions with excited particles (e.g., metastables), respectively. The diffusion cooling is described by L_D which results from the escape of some of the bulk electrons to the absorbing boundaries (e.g., to the anode) and from the work expended in overcoming the ambipolar field in the plasma.[33]

It follows from the energy balance equation (8) that the electron conductivity equalizes the electron temperature over distances $\lambda_T \approx \lambda_\epsilon(n_e = 0) = \lambda/\sqrt{\delta}$ (electron energy is conserved in interelectron collisions). Hence, in the case when $\lambda_T >> L_{pl}$, the electron temperature is uniform and spatial averaging can be performed and the principal term with diffusion can be eliminated in Eq. (8). In the other limiting case when $\lambda_T << L_{pl}$, a local energy balance takes place and the electron temperature is spatially non-uniform.

In equation (8), the principal heating terms [being obtained from the term of interelectron collisions in Eq. (5)] can be represented in a physically transparent form as

$$H_{Q^+} + H_{Q^*} = \int d^3\mathbf{r} \int_{e\phi_a(\mathbf{r})}^{\epsilon^*} V_e f_f d\epsilon = Q^+ E_{eff}^+ + Q^* E_{eff}^* \tag{9}$$

where E_{eff}^+ (E_{eff}^*) characterizes the effective energy transferred to the system of cold bulk electrons in collisions with the hot intermediate electrons created in ionization (in processes involving excited particles) with the corresponding rate $Q^+(Q^*)$ (see Refs. 24,25 for more details). According to Eq. (9), the values of the energy transfer E_{eff}^+ and E_{eff}^* are directly related to the form of the intermediate EDF, $f_f(\epsilon,\mathbf{r})$. Using the results of Ref. 25, it is possible to obtain a crude estimation of E_{eff}^+ as

$$E^{+}_{eff} \approx \frac{\nu_e}{\nu_e + \delta\nu_a + 1/\tau_{df}(\epsilon_f)}\epsilon_f \qquad (10)$$

It can be seen from this equation that the efficiency of the energy transfer is determined by the frequency of collisions, ν_e, between the cold bulk electrons and the hot intermediate ones. In the case when the interelectron collision frequency is high, that is, $\nu_e \gg (\delta\nu_a, 1/\tau_{df})$, the value of the energy transfer is large, $E^{+}_{eff} \approx \epsilon_f$, and consequently T_e can be high. In the other case of weak interelectron interactions, when $\nu_e \ll (\delta\nu_a, 1/\tau_{df})$, the value of the energy transfer is small, $E^{+}_{eff} << \epsilon_f$, and T_e is close to the gas temperature, $T_e \approx T_g$ = 300 K. Hence, depending on the plasma conditions (pressure, electron density, etc), the electron temperature can vary significantly which must be fully incorporated in the plasma models.

Practical Examples

Here we present briefly some examples of the HCDs where the described kinetic model have been applied. Various types of the HCDs have been investigated which allowed us to study different types of glow discharges: from an abnormal PGD with a steep V-I characteristic to the conventional HCD with an almost flat V-I characteristic.[19] All other types of the HCD with non-traditional electrode configurations can be classified as intermediate variants of the glow discharges. They include the HCDs with the anode (or the system of anodes) placed inside the discharge cavity: the hollow-anode-cathode,[18,31] the cage,[21] the segmented,[19] the helical[34] HCDs. Their common feature is an increased rate of charged particle (fast electrons, ions) losses from the discharge cavity as compared to that in the conventional HCDs. This makes them operate at a higher voltage and higher slope resistance than do the conventional HCDs (see Ref. 19 for more details).

Let us first consider the hollow cathode-anode discharge[31] where the discharge device is made up of two closely spaced, square parallelepipeds ($0.8 \times 0.8 \times 4$ cm^3): the outer parallelepiped is an oxide cathode, and the inner one is a grid anode. This type of the HCD is interesting in illustrating some aspects of the non-local electron kinetics. It demonstrates that not only is the electron temperature dependent on the plasma parameters, but also it is determined by the geometry of the discharge device. Since the anode in this system is placed inside the discharge cavity, the untrapped intermediate electrons generated in the NG can easily escape to it, especially when the gas pressure is low and the regime of the slow EDF formation is non-local. Hence, in this condition the hot intermediate electrons do not interact effectively with the cold bulk electrons (for the intermediate electrons, $1/\tau_{df} >> \nu_e$) and the energy transfer E^{+}_{eff} is low [see Eq. (10)]. An example of measurements and calculations of the temporal "evolution of n_e and T_e in this system is presented in Fig. 6. The measured electron temperature and density are reproduced rather well by the model. Even at the low pressure of 0.2 Torr, when the rate of electron cooling in elastic collisions with atoms is small, the observed and predicted values of T_e are small ($\approx$ 0.5 eV in the steady-state), which is explained by E^{+}_{eff} being small. Attempts to calculate T_e in the local approximation (that is, assuming that the intermediate electrons do not diffuse to the walls) have led to the values of T_e being excessively higher than that observed experimentally. As a result of the correct prediction of T_e, good agreement between theory and experiment was also obtained for the electron density (see Fig. 6).

Let us next consider the cage HCD.[21] The cage HCD is formed by a set of alternating rod anodes and cathodes and it is characterized by the large volume of a longitudinally uniform NG plasma of a cylindrical geometry (the plasma radius R =

Table 1. Results of modeling the cage HCD.[21] Comparison of the experimentally observed and calculated (given in parentheses) values of the central electron density n_{e0}, peak factor χ and electron temperature T_e at different gas pressures p. Discharge current I = 30 mA.

p, Torr	1	2	4
n_{e0}, 10^{11} cm^{-3}	0.62 (0.84)	3.2 (4.3)	8.3 (10)
χ	1.9 (2.0)	2.3 (2.1)	3.7 (3.4)
T_e, eV	0.54 (0.58)	0.094 (0.13)	0.061 (0.076)

1.7 cm and height H = 30 cm). One can see in Table 1 that the experimental data obtained by electric probes agree well with the model predictions. The electron density spatial profile is fitted by $n_e(r) = n_{e0}[1 - (r/R)^{\chi}]$ where χ is the electron density peak factor. The election density profile is directly related to the spatial distribution of the ionization profile, $Q^+(r)$, and hence to that of the fast electrons. At low pressures (p < 2 Torr), the fast electrons can easily reach the discharge center, $Q^+(r)$ is uniform and an almost parabolic density profile is observed ($\chi \approx 2$). At higher pressures (p > 3 Torr), the fast electrons cannot travel to the discharge center, a dip develops on the discharge axis, and a flatter (χ > 3) electron density profile is observed. Calculations of the ionization profile, $Q^+(r)$, using the fast EDF obtained above, have allowed us to obtain the electron density profiles and so χ. Another important result is that the electron temperature depends strongly on the gas pressure (see Table 1). This is because of the higher electron cooling rate in collisions with atoms at higher pressures. When such a flat density profile (low ambipolar diffusion rate) and such a low electron temperature exist, recombination may become important, the rate of which varies as $\alpha_r n_e^3$ where $\alpha_r = \alpha_{r0}\, T_e^{-9/2}$. In the regime of purely recombination losses (no diffusion losses), the electron density profile follows the ionization profile and a dip on the density profile can develop.[35] Also, the maximum of the electron density with pressure[14] can be explained by recombination being more important at high pressures. The above mentioned phenomena could not be explained if one considers the electron temperature being constant with varying pressure and being equal to 1 eV (which would underestimate the recombination rate) or to 300 K (which would overestimate it).

CONCLUSIONS

The electron kinetics in the cathode region of glow discharges with plane and hollow cathodes has been analyzed. The following conclusions can be made:

- in order to describe the cathode region of the glow discharges, the kinetic approach is necessary to the entire electron distribution function: both the fast and slow electrons have to be treated kinetically.
- due to the enormous difference in the characteristic energy, space and density scales of different electron groups, it is desirable to have effective (semi-)analytical approaches to each of these groups. Such approaches allow physically transparent results to be obtained. Also, they can be useful in the development of fast computer codes to model laboratory experiment in real time. Full scale direct numerical techniques are important to check the validity of these approaches and to provide quantitative description in conditions when the (semi-)analytical methods cannot be applied.
- using the self-consistent kinetic model, a large class of the glow discharges has been described quantitatively: from the abnormal glow discharges to the conventional hollow cathode discharges, and also a large variety of the intermediate glow discharges.

Some important results are:

(i) it is shown that the hollow cathode effect results from the in crease of the number of ionizations in the negative glow and not in the cathode fall with the total number of ionizations in the discharge cavity remaining constant. The hollow cathode effect could be modeled in the limit of small ionization in the cathode fall. Alternatively, a mechanism of the ion diffusion losses is proposed and shown to be important.

(ii) it is pointed out that knowledge of the electron temperature is crucial in modeling the plasma of the cathode region since the rates of major plasma processes are determined by the electron temperature. It is shown that the electron temperature can vary significantly depending on the plasma parameters (pressure, electron density, discharge geometry) and that the problem of finding the electron temperature is purely kinetic.

(iii) it is shown that to describe quantitatively the self-consistent electric fields in the plasma of the cathode region, it is essential to use the kinetic approach. Such a description is impossible in the framework of the traditional fluid approach which only yields qualitative answers.

(iv) good agreement could be obtained between the predicted and measured plasma parameters (with spatial and energy resolution and also temporal resolution) such as the electron distribution function, the electron density and temperature, the excitation profiles of. different spectral lines.

Acknowledgments

The authors express their deep gratitude to Professor Lev Tsendin for numerous and insightful discussions. This work was supported by INTAS grant N940740 and by RBRF grant N95-0205064.

REFERENCES

1. L. D. Tsendin, Electron kinetics in non-uniform glow discharge plasmas, *Plasma Sources Sci. Technol.* 4:200 (1995).
2. J. P. Boeuf and E. Marode, A Monte Carlo analysis of an electron swarm in a non-uniform field: the cathode region of a glow discharge in helium, *J. Phys. D: Appl. Phys.* 15:2169 (1982).
3. C. K. Birdsall, Particle-in-cell charged-particle simulations, plus Monte Carlo collisions with neutral atoms, PIC-MCC, *IEEE Trans. on Plasma Sci.* 19:65 (1991).
4. T. J. Sommerer, W. N. G. Hitchon, and J. E. Lawler, Self-consistent kinetic model of the cathode fall of a glow discharge, *Phys. Rev.* A 39:6356 (1989).
5. J. V. DiCarlo and M. J. Kushner, Solving the spatially dependent Boltzmann's equation for the electron velocity distribution using flux corrected transport, *J. Appl. Phys.* 66:5763 (1989).
6. L. D. Tsendin, Energy distribution of electrons in a weakly ionized current carrying plasma with a traverse inhomogeneity, *Sov. Phys. JETP* 39:805 (1974).
7. V. I. Kolobov and L. D. Tsendin, Analytic model of the cathode region of a short glow discharge in light gases, *Phys. Rev, A* 46:7837 (1992).
8. R. R. Arslanbekov, A. A. Kudryavtsev, and I. A. Movchan, Spatial and energy distributions of fast electrons in discharges with a cylindrical hollow cathode, *Sov. Phys. Tech. Phys.* 37:395 (1992).
9. I. Kuen, F. Howorka, and H. Störy, Population of excited He states ($3 \leq n \leq 8$) by dielectronic He^+ recombination in dc hollow-cathode discharge, *Phys. Rev. A* 23:829 (1981).
10. J. P. Bouef, Self-consistent models of DC and transient glow discharges, *in*: "Physics and Applications of Pseudosparks" , M. A. Gundersen and G. Schaefer, eds., NATO ASI Series B vol. 219, Plenum, New York (1990).
11. V. I. Kolobov and L. D. Tsendin, Analytic model of the hollow cathode effect, *Plasma Sources Sci. Technol.* 4:551 (1995).
12. A. Lompe, R. Seeliger and E. Wolter, *Ann. Phys. (Leipzig)* 36:9 (1939) (in German).
13. Yu. P. Raizer. "Gas Discharge Physics," Springer, Berlin (1991).

14. J. Mizeraczyk, Axial distributions of the plasma parameters of a longitudinal discharge in helium in hollow cathodes used for lasers, *J. Phys. D: Appl. Phys.* 20:429 (1987).
15. G. Schaefer and K. H. Schoenbach, Basic mechanisms contributing to the hollow cathode effect, *in* Ref. 10
16. K. Frank, Review of superdense glow discharges, *in* Ref. 10
17. R. Mavrodineanu, Hollow cathode discharges, *J. Res. Nat. Bureau Standards* 89:143 (1983).
18. K. Rózsa, Hollow cathode discharges for gas lasers, *Z. Naturforsch.* 35a:649 (1980).
19. R. R. Arslanbekov, R. C. Tobin, and A. A. Kudryavtsev, Self consistent model of high current density segmented hollow cathode discharges, *J. Appl. Phys.* 81:554 (1997).
20. Yu. M. Kagan, Rate of ionisation and density of electrons in a hollow cathode, *J. Phys. D: Appl. Phys.* 18:1113 (1985).
21. R. R. Arslanbekov, A. A. Kudryavtsev, and I. A. Movtchan, Cage discharge: theory and experiment, *IEEE Trans. Plasma Sci.* 24:1079 (1996).
22. K.H. Schoenbach, R. Verhappen, T. Tessnow, F. E. Peterkin, and W. W. Byszewski, Microhollow cathode discharges, *Appl. Phys. Lett.* 68:13 (1996).
23. P. F. Little and A. von Engel, The hollow cathode effect and the theory of glow discharges, *Proc. R. Soc. A* 224:209 (1954). A. Güntherschulze, *Z. Phys.* 30:175 (1924) (in German).
24. N. B. Kolokolov, A. A. Kudrjavtsev, and A. B. Blagoev, Interaction processes with creation of fast electrons in the low temperature plasma, *Physica Scripta* 50:371 (1994).
25. R. R. Arslanbekov, A. A. Kudryavtsev, and I. A. Movchan, Electron density and temperature balance in a cylindrical hollow cathode discharge, *Sov. Phys. Tech. Phys.* 37:1004 (1992).
26. R. R. Arslanbekov, A. A. Kudryavtsev, and I. A. Movchan, Slow electron distribution function in a cylindrical hollow cathode discharge, *Sov. Phys. Tech. Phys.* 37:620 (1992).
27. J. P. Boeuf and L. C. Pitchford, Field reversal in the negative glow of a dc glow discharge, *J. Phys. D: Appl. Phys.* 28:2083 (1995).
28. Y. S. Akishev, F. I. Vysikailo, A. P. Napartovich, and V. V. Ponomarenko, A quasistationary discharge in nitrogen, *High Temp.* 18:216 (1980).
29. M. P. Alberta, J. Derouard, L. C. Pitchford, N. Ouadoudi, and J. P. Boeuf, Space and time dependence of the electric field and plasma induced emission in transient and steady-state hollow cathode discharges, *Phys. Rev. E* 50:2239 (1994).
30. A. Bogaerts and R. Gilberts, Hybrid Monte Carlo-fluid model of a direct current glow discharges, *J. Appl. Phys.* 78:2233 (1995).
31. R. R. Arslanbekov, A. A. Kudryavtsev, Yu. A. Piotrovskii, and Yu. A. Tolmachev, Electronic parameters of a plasma produced by an electron beam in low-pressure helium, *High Temp.* 32:153 (1994).
32. V. E. Golant, A. P. Zhilinsky, and I. E. Sakharov. "Fundamentals of Plasma Physics," John Wiley, New York (1980).
33. N. B. Kolokolov, A. A. Kudryavtsev, and O. G. Toronov, Excited atoms and diffusion cooling of electrons in plasmas, *Sov. Phys. Tech. Phys.* 30:1128 (1985).
34. M. Grozeva and N. Sabotinov, Coil hollow cathode for metal vapor lasers, *Opt. Commun.* 41:57 (1982).
35. V. I. Kirichenko, V. M. Tkachenko, and V. B. Tyutyunnik, Influence of dimensions, cathode material, and gas on the optimum pressure for a cylindrical, hollow-cathode glow discharge, *Sov. Phys. Tech. Phys.* 21:1080 (1976).

A HYDRODYNAMIC DESCRIPTION OF ELECTRONS IN A SPACE-TIME VARYING ELECTRIC FIELD

N. L. Aleksandrov

Department of Physical Mechanics
Moscow Institute of Physics and Technology
141700 Dolgoprudny, Russia

INTRODUCTION

Usually, in gases in a uniform steady electric field far from boundaries, electron transport and rate coefficients are dependent on E/N, the ratio of the electric field strength to the neutral species density, because the energy gain from the field is balanced by the energy loss in collisions. In special cases, the electron properties are also a function of the vibrational temperature of the molecules, T_V, and the degree of ionization $\alpha = n/N$, where n is the electron density. To describe this situation, one uses the local field (or 'equilibrium') approximation which assumes that the electrons are in equilibrium with the local electric field. However, if the electric field (and other parameters) varies rapidly in space or time, then the local energy balance is disturbed. This occurs, for instance, in the cathode fall of a glow discharge, in the head of a streamer, in RF discharges and so on[1]. In addition, one can find the space or time-varying electron density under the conditions of electron swarm experiments[2].

Several approaches have been suggested to study the electron swarm behavior in gases in non-uniform and/or unsteady fields[1-8]. These include a Monte Carlo technique, momentum transfer theory, direct solution of the Boltzmann equation and model analytical approaches. The aim of this paper is to give a hydrodynamic description of electrons in a space-time varying electric field. This approach was suggested by Aleksandrov et al[9] and used initially to study the stability of the gas-discharge plasma. When considering the first-order nonlocality and unsteadiness corrections, the method of interest is simpler than Monte Carlo simulation and other cumbersome approaches. At the same time it consistently takes into account a variety of collisional processes which affect the electron energy distribution.

The basic equations are summarized in section 2. In section 3, the transport and rate coefficients are given for a model system and real gases. A comparison between the results of this method and other approaches is presented in section 4. Some applications of the considered method including a simulation of gas-discharge plasma are given in section 5. Generalizations to other cases are summarized in section 6.

Electron Kinetics and Application of Glow Discharges
Edited by U. Kortshagen and L. D. Tsendin, Plenum Press, New York, 1998

BASIC EQUATIONS

We consider a weakly ionized gas or plasma in an electric field E when the electron energy distribution function (EEDF) is in non-equilibrium. This means that the inequalities $eE\lambda_u > T$ and $\nu_u >> \nu_{ee}$ are valid. Here, e is the electron charge, T is the gas temperature, λ_u is the EEDF relaxation length, ν_u is the frequency of the EEDF relaxation and ν_{ee} is that of the electron-electron collisions. Then, the EEDF is non-Maxwellian and dependent on the reduced electric field E/N and the gas composition. This is true at the low ionization level α ($\alpha < 10^{-6} - 10^{-5}$ in atomic gases and $\alpha < 10^{-4} - 10^{-5}$ in molecular).

We have $\nu_u << \nu_m$ in the most gaseous media at not too high electric fields, where ν_m is the frequency of the electron momentum relaxation. In this case the usual two-term expansion of the electron velocity distribution function in spherical harmonics can be used[2,10]:

$$f(\mathbf{v}) = f_0(v) + \mathbf{f}_1(v)\mathbf{v}/v.$$

We shall restrict ourselves to the practically important situation of $L >> \lambda_m$ and $\tau\nu_m >> 1$, where $\lambda_m = (N\sigma_m)^{-1}$ is the electron mean free path for the momentum transfer, σ_m is the collisional cross section for the momentum relaxation,

$$L \sim \left(\frac{1}{a}\frac{\partial a}{\partial x}\right)^{-1} \qquad \tau \sim \left(\frac{1}{a}\frac{\partial a}{\partial t}\right)^{-1}$$

and a is the EEDF parameter (E/N, n, T_v, etc). Then, the equation describing the spherically symmetrical EEDF $f_0(\varepsilon)$ is written in the form[10]

$$-\frac{1}{nN}\left(\frac{m\varepsilon}{2}\right)^{1/2}\frac{\partial(nf_0)}{\partial t} + \frac{\varepsilon}{3nN\sigma_m}\mathrm{div}\left(\frac{\nabla(nf_0)}{N} - \frac{e\mathbf{E}n}{N}\frac{\partial f_0}{\partial\varepsilon}\right) - \frac{cE}{3nN^2}\frac{\partial}{\partial\varepsilon}\left(\frac{\varepsilon}{\sigma_m}\nabla(nf_0)\right)$$

$$+\frac{1}{3}\left(\frac{eE}{N}\right)^2\frac{\partial}{\partial\varepsilon}\left(\frac{\varepsilon}{\sigma_m}\frac{\partial f_0}{\partial\varepsilon}\right) + S_0(f_0) = 0 \tag{1}$$

where m and $\varepsilon = mv^2/2$ are the electron mass and energy respectively and S_0 is the electron-neutral collision integral. Here, $f_0(\varepsilon)$ is normalized such that

$$\int_0^\infty f_0(\varepsilon)\varepsilon^{1/2}d\varepsilon = 1. \tag{2}$$

The function $\mathbf{f}_1(v)$ is represented by

$$\mathbf{f}_1 = -\frac{\nabla(nf_0)}{nN\sigma_m} + \frac{e\mathbf{E}}{N\sigma_m}\frac{\partial f_0}{\partial\varepsilon}. \tag{3}$$

The collision integral S_0 has the form[2]

$$S_0(f_0) = \frac{2m}{M}\frac{\partial}{\partial\varepsilon}\left[\varepsilon^2\sigma_m(f_0 + T\frac{\partial f_0}{\partial\varepsilon})\right] + \sum_j[(\varepsilon+\varepsilon_j)\sigma_j(\varepsilon+\varepsilon_j)f_0(\varepsilon+\varepsilon_j)$$

$$-\varepsilon\sigma_j(\varepsilon)f_0(\varepsilon)] + S_Q \tag{4}$$

where M is the neutral particle mass. The second term on the right-hand side of equation (4) represents the electron energy loss ε_j in an inelastic collision having a scattering cross section σ_j. The last term describes the processes of electron generation ad loss.

The EEDF in a uniform steady system is obtained from equation (1), neglecting the first three terms. For real gases this equation is to be solved numerically[2,11,12].

An integration of (1) yields the electron density balance equation

$$\frac{\partial n}{\partial t} + \mathrm{div}(n\mathbf{w}) - \mathrm{div}\left[\left(\frac{1}{N}\nabla(ND_T n)\right)\right] = Q \tag{5}$$

where Q represents the processes of electron generation and loss,

$$\mathbf{w} = -\frac{e\mathbf{E}}{3N}\left(\frac{2}{m}\right)^{1/2}\int_0^\infty \frac{\varepsilon}{\sigma_m}\frac{\partial f_0}{\partial \varepsilon}d\varepsilon \tag{6}$$

$$D_T = \frac{1}{3N}\left(\frac{2}{m}\right)^{1/2}\int_0^\infty \frac{\varepsilon}{\sigma_m} f_0 d\varepsilon. \tag{7}$$

The transversal diffusion coefficient D_T is inversely proportional to N (in the gas approximation which is assumed to be valid). The product ND_T is a function of parameter E/N (and in some cases of α and T_v). Therefore, the last term on the left-hand side of equation (5) is the sum of the diffusion flux ($\sim \nabla n$), the 'thermodiffusion' flux ($\sim\nabla E/N$) and other fluxes which are proportional to the gradients of the corresponding parameters.

We consider the gradients of n_e and E/N and time derivative of E/N such that

$$\lambda_u \ll L \tag{8}$$

and

$$\nu_u \tau \gg 1. \tag{9}$$

Then, the ratio of the third term on the left-hand side of equation (5) to the second has an order $\lambda_u/L << 1$. The distribution function correction resulting from the second and third terms of equation (1) changes all fluxes along the electric field. The variation of the diffusion flux causes the well known anisotropy of electron diffusion in electric fields in gases[2,13-15]. The degree of anisotropy is generally of the order 1. Other types of the electron fluxes are expected to be also significantly anisotropic.

We follow the approach suggested previously by Parker and Lowke [13,14] and by Scullerud[15] for the diffusion fluxes and by Aleksandrov et al[4,9] for the other fluxes. In perturbation theory frames under conditions (8) and (9) we look for the solution of equation (1) in the form

$$f_0(\varepsilon) = f_{00}(\varepsilon)\left[1 + b_1(\varepsilon)\mathbf{c}\nabla \ln n + b_2(\varepsilon)\frac{N}{E}\mathrm{div}(\mathbf{E}/N) + b_3(\varepsilon)\mathbf{e}\nabla \ln(E/N) + \frac{b_4(\varepsilon)}{w_0}\frac{\partial \ln(E/N)}{\partial t}\right] \tag{10}$$

where $\mathbf{e} = \mathbf{E}/E$ and the electron drift velocity w_0 is calculated from equation (6) with $f_0 = f_{00}$. The function $f_{00}(\varepsilon)$ obeys the equation

$$\frac{1}{3}\left(\frac{eE}{N}\right)^2 \frac{\partial}{\partial \varepsilon}\left(\frac{\varepsilon}{\sigma_m}\frac{\partial f_{00}}{\partial \varepsilon}\right) + S_0(f_{00}) = 0 \tag{11}$$

and the normalization condition (equation (2)). By substituting equation (10) into (1) and using equation (5), we can derive equations for the expansion coefficients $b_i(\varepsilon)$

$$\frac{1}{3}\left(\frac{eE}{N}\right)^2 \frac{\partial}{\partial \varepsilon}\left[\frac{\varepsilon}{\sigma_m}\frac{\partial(f_{00}b_i)}{\partial \varepsilon}\right] + S_0(f_{00}b_i) = \psi_i \qquad i = 1-4, \tag{12}$$

$$\psi_1 = \frac{2}{3}^{1/2}\left[\frac{\varepsilon}{\sigma_m}\frac{\partial f_{00}}{\partial E} + \frac{\partial}{\partial \varepsilon}\left(\frac{\varepsilon}{\sigma_m} f_{00}\right)\right] + \frac{m^{1/2} w_0 N}{eE}\varepsilon^{1/2} f_{00}$$

$$\psi_2 = \frac{2}{3}^{1/2}\frac{\varepsilon}{\sigma_m}\frac{\partial f_{00}}{\partial \varepsilon} + \frac{m^{1/2} w_0 N}{eE}\varepsilon^{1/2} f_{00}$$

$$\psi_3 = \frac{2}{3}^{1/2} E/N\left[\frac{\varepsilon}{\sigma_m}\frac{\partial^2 f_{00}}{\partial \varepsilon \partial E/N} + \frac{\partial}{\partial \varepsilon}\left(\frac{\varepsilon}{\sigma_m}\frac{\partial f_{00}}{\partial E/N}\right)\right] + \frac{m^{1/2}}{e} E/N \frac{\partial (w_0 N/E)}{\partial E/N}\varepsilon^{1/2} f_{00}$$

$$\psi_4 = \frac{m^{1/2} w_0}{e}\varepsilon^{1/2}\frac{\partial f_{00}}{\partial E/N}.$$

The functions $b_i(\varepsilon)$ obey the condition

$$\int_0^\infty f_{00} b_i \varepsilon^{1/2} d\varepsilon = 0 \qquad i = 1 - 4. \tag{13}$$

Substituting equation (10) into (6), we obtain the electron drift velocity in the unsteady spatially inhomogeneous system

$$\mathbf{w} = \mathbf{w}_0 - \kappa_1 \mathbf{e}(\mathbf{e}\nabla \ln n) - \kappa_2 \mathbf{e}\frac{N}{E}\mathrm{div}(\frac{\mathbf{E}}{N}) - \kappa_3 \mathbf{e}(\mathbf{e}\nabla)\ln(E/N) - \frac{\kappa_4}{w_0}\frac{\partial ln(E/N)}{\partial t}\mathbf{e} \tag{14}$$

where

$$\kappa_i = -\frac{1}{3Nm^{1/2}}\left(\frac{eE}{N}\right)^2 \int_0^\infty \frac{\varepsilon}{\sigma_m}\frac{\partial (f_{00} b_i)}{\partial \varepsilon} d\varepsilon. \tag{15}$$

The coefficients κ_i have the dimensions of diffusion coefficients and describe the effects of inertia (in first order in $(\nu_u \tau)^{-1}$) and of nonlocality (in first order in λ_u / L) in the EEDF. For ν_m = constant it follows from equations (13) and (15) that $K_i = 0$.

The rate coefficient for any electron inelastic process (the excitation of atoms and molecules, ionization, electron attachment and so on) is equal to

$$k = \left(\frac{2}{m}\right)^{1/2} \int_0^\infty f_0 \sigma \varepsilon d\varepsilon \tag{16}$$

where σ is the cross section of the process. Similarly, on substituting equation (10) into (16), we obtain the electron rate coefficient in the unsteady inhomogeneous case

$$k = k_0\left[1 + k_1 \mathbf{e}\nabla \ln n + k_2 \frac{N}{E}\mathrm{div}(\mathbf{E}/N) + k_3 \mathbf{e}\nabla \ln(E/N) + \frac{k_4}{w_0}\frac{\partial \ln(E/N)}{\partial t}\right] \tag{17}$$

where k_0 is calculated from equation (16) with $f_0 = f_{00}$ and

$$k_i = \frac{1}{k_0}\left(\frac{2}{m}\right)^{1/2} \int_0^\infty f_{00} b_i \sigma \varepsilon d\varepsilon \tag{18}$$

According to our approach (see, also,[16]), a hydrodynamic description of electrons in a nonequilibrium weakly ionized plasma reduces to the electron density balance equation (equation (5)) which takes into account the nonlocal and inertial corrections (equations (14) and (17)). To complete a system of equations describing the state of the plasma one should add the balance equation for the number of ions and the ordinary electrodynamic equations. If the gas number density N is not constant, the gas-dynamic equations for neutral component should be also taken into account. The mathematical structure of the resulting system of equations is simpler than the structure of the ordinary system of equations which also contains the balance equation for the average electron energy.

THE TRANSPORT AND RATE COEFFICIENTS OF ELECTRONS

The magnitude and sign of the introduced transport and rate coefficients are governed by the elastic and inelastic collisional cross sections for electrons and may change substantially, depending on the nature of the gas, E/N, α and T_v. Consider these coefficients for a model system and real gases.

A Model of Divergent Collision Integral

In general, equations (11) and (12) must be solved numerically. However, if the collision integral has a divergent form

$$S_0(f) = \frac{1}{v^2}\frac{\partial}{\partial v}(v^3 \nu_u f) \tag{19}$$

these equations can be treated analytically. The collision integral takes this form when the loss of electron energy is dominated by elastic collisions (atomic gases). In molecular gases, the collision integral for rotational and vibrational excitation reduces to the same form under certain conditions.

Let us consider power-law dependences of the frequencies for elastic and inelastic processes on the electron velocity

$$\nu_m = \nu_0 v^p$$

$$\nu_u = \delta \nu_m$$

$$\delta = \delta_0 v^q.$$

Then, the solution of equation (11) is written as

$$f_{00} = \frac{s}{4\pi\alpha^3}\Gamma\left(\frac{3}{s}\right)\exp\left[-\left(\frac{v}{\alpha}\right)^s\right]$$

where Γ is the gamma-function,

$$s = 2p + q + 2$$

$$\alpha = \left[\frac{2s}{3\delta_0}\left(\frac{eE}{m\nu_0}\right)^2\right]^{1/s}.$$

If $p < 3$, the electron drift velocity and the longitudinal diffusion coefficient are[2,13,15]

$$w_0 = \frac{(3-p)eE}{3m\nu_m(\alpha)}\frac{\Gamma\left(\frac{3-p}{s}\right)}{\Gamma\left(\frac{3}{s}\right)}$$

and

$$D_L = D_T + \kappa_1 = D_T + \frac{\alpha^2}{\nu_m(\alpha)}\left\{S + \frac{3-p}{6}\frac{\left[\Gamma\left(\frac{5-p}{s}\right)\Gamma\left(\frac{3}{s}\right) - \Gamma\left(\frac{3-p}{s}\right)\Gamma\left(\frac{5}{s}\right)\right]}{\Gamma^2\left(\frac{3}{s}\right)}\right\}$$

where

$$S = \frac{(3-p)^2}{3s}\frac{\Gamma\left(\frac{3-p}{s}\right)}{\Gamma^2\left(\frac{3}{s}\right)} \times \sum_{i=1}^{\infty}\left[\frac{\Gamma\left(i-1+\frac{5}{s}\right)\Gamma\left(\frac{3}{s}\right) - \Gamma\left(i-1+\frac{p+5}{s}\right)\Gamma\left(\frac{3-p}{s}\right)}{(is-s+p+2)\Gamma\left(i+\frac{3}{s}\right)}\right.$$

$$-\frac{\Gamma\left(i+\frac{5-p}{s}\right)\Gamma\left(\frac{3}{s}\right)-\Gamma\left(i+\frac{5}{s}\right)\Gamma\left(\frac{3-p}{s}\right)}{(is+2)\Gamma\left(i+1+\frac{3-p}{s}\right)}\Bigg].$$

In the one-dimensional case, electron fluxes in a space-time varying electric field are described by the coefficients κ_4 and $D_E = \frac{\partial D_T}{\partial \ln(E/N)} + \kappa_2 +$ These are equal to [4,9]

$$\kappa_4 = -\frac{4w_0^2}{\nu_u(\alpha)(p+2)}\left[\frac{\Gamma\left(\frac{5}{s}\right)}{\Gamma\left(\frac{3-p}{s}\right)} - \frac{\Gamma\left(\frac{p+5}{s}\right)}{\Gamma\left(\frac{3}{s}\right)}\right]$$

$$D_E = S_1\frac{\alpha^2}{\nu_m(\alpha)}$$

where

$$S_1 = 1 - \frac{2p}{s} + \frac{3-p}{3\Gamma^2\left(\frac{3}{s}\right)}\left\{\frac{4(2s+3)}{3(s+2)}\left[\Gamma\left(1+\frac{5-p}{s}\right)\Gamma\left(\frac{3}{s}\right) - \Gamma\left(1+\frac{5}{s}\right)\Gamma\left(\frac{3-p}{s}\right)\right]\right.$$

$$\left.+\Gamma\left(\frac{5}{s}\right)\Gamma\left(\frac{3-p}{s}\right) - \Gamma\left(\frac{5-p}{s}\right)\Gamma\left(\frac{3}{s}\right)\right\}.$$

Real Gases

Calculation of the additional transport coefficients κ_i was carried out for CO, air, Ar, Xe, the CO:Ar mixtures[17], N_2, CO_2 and the N_2:CO_2 mixtures[18] (see, also,[4]). Their dependence on T_v was studied for N_2, CO and CO_2[19,20]. The additional rate coefficients $k_i$were calculated for N_2, CO_2, Ar[21,22] and air[23]. The inelastic processes considered were the excitation of the rotational, vibrational and electronic levels of molecules and atoms, electron attachment and ionization. Details of the numerical method of solving equations for $f_{00}(\varepsilon)$ and $b_i(\varepsilon)$ and the self-consistent sets of electron cross sections have been discussed elsewhere[17-19,24]. These sets satisfy the available swarm experiment parameters.

Figure 1 shows the ratios κ_i/D_T $(i = 2 - 4)$ which were calculated for air as a function of E/N[4,23]. The coefficients κ_i have the same order of magnitude as D_T and are the complicated non-monotonic functions of *E/N*.

The calculated coefficients κ_i are also presented with a dimensionless notation. The values of κ_i are of the order λ_u for $\varepsilon_0 \geq I$, where ε_0 is the characteristic electron energy and *I* is the threshold energy of the considered inelastic process. For $\varepsilon_0 << I$, the rate coefficient is determined by electrons with energy ε such that $I < \varepsilon < I + \Delta\varepsilon$, where $\Delta\varepsilon << I$. Then, considering that the relaxation length for the rate of the inelastic process can be estimated by $eE\lambda_I \simeq I$, the results of the calculation can be expressed in terms of the dimensionless quantity $\tilde{k}_i = k_i eE/I$. The values of $\tilde{k}_3$ and $\tilde{k}_4$ calculated by Aleksandrov et al
refnote23 for air for the excitation of N_2 $(v = 1)$, $N_2(A^3\Sigma_u^+)$, $N_2(C^3\Pi_u)$ and $O_2(a^1\Delta_g)$, ionization of N_2 and O_2 and dissociative electron attachment to O_2 are shown in figures 2 and 3. The values of $\tilde{k}_1$ and $\tilde{k}_2$ are much less than that of $\tilde{k}_3$ and $\tilde{k}_4$.

Two general features are apparent from the comparison in figures 2 and 3: (*i*) for the different processes with $I >> \varepsilon_0$ (the excitation of the electronic levels of N_2, the ionization and the electron attachment to O_2) and for each given i we have nearly the same values of $\tilde{k}_i$ with $\tilde{k}_3 > 0$, $\tilde{k}_4 < 0$ and $d\mid \tilde{k}_i \mid /d(E/N) < 0$; and (*ii*) for the vibrational excitation of N_2 with $I \leq \varepsilon_0$, $\tilde{k}_i$ is a non-monotonic function of *E/N* which may change in sign.

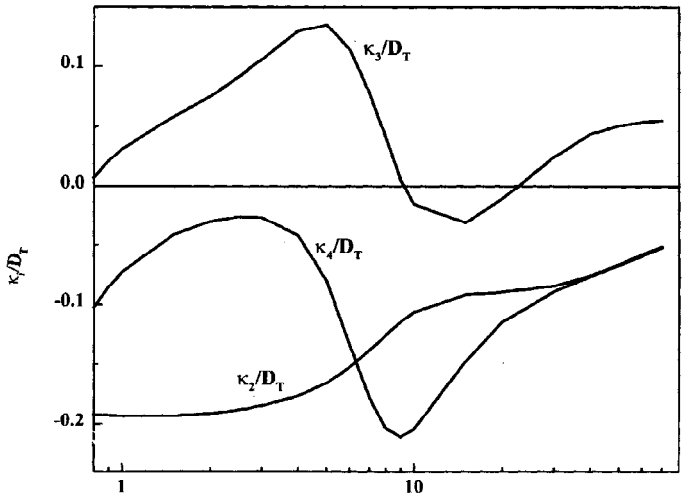

Figure 1. The values of (A) κ_2/D_T, (B) κ_3/D_T, and (C) κ_4/D_T in air versus *E/N*.

These features are not unexpected. For example, the inequality $\tilde{k}_3 > 0$ implies that a positive (along the electric field) gradient of *E/N* results in an increase in the rate of the high-threshold inelastic processes. This may be explained in the following way. If the field is rapidly increasing is space, the local electron-energy balance is perturbed. Then, the ionization and excitation in the low-field region are due to fast electrons streaming across from the high-field region[25]. A similar situation holds when we have $\partial(E/N)/\partial t > 0$. Here, the electrons fail to follow the increasing field; therefore, the high-energy tail of the EEDF is underpopulated and the rate of the inelastic process is less than its steady magnitude corresponding to the given value of *E/N*. As a result, we have $\tilde{k}_4 < 0$. The ratio I/ε_0 increases with decreasing *E/N*, inducing $d \mid \tilde{k}_i \mid /d(E/N) < 0$ because the high-energy tail of the EEDF is relatively more sensitive to the field non-uniformity than its low-energy part.

The *E/N* –dependence of $\tilde{k}_i$ for the vibrational excitation of N_2 molecule is more complicated. The vibrational cross sections in N_2 have a strong peak in the 2–3 eV range. Therefore, the change of sign in the value of $\tilde{k}_i$ results from the relative under – or overpopulation of electrons in the region of the relatively narrow peak in the vibrational cross section during the spatial evolution of the EEDF[25].

COMPARISON WITH OTHER APPROACHES

There have been several previous Monte Carlo simulations[25-27] of the electron properties in highly non-uniform fields excluding boundary effects by the choice of the a priori field profile. To compare these studies with the considered approach, Aleksandrov and Kochetov[21] calculated the non-local field corrections for these conditions with the sets of electron cross sections used for the Monte Carlo simulations cited.

Under non-uniform field conditions Moratz et al[25] gave not only the electron coefficients but also the EEDF, which has much more information for the electron kinetics. Figure 4 represents comparisons of the EEDF calculated by Moratz et al[25] for the field

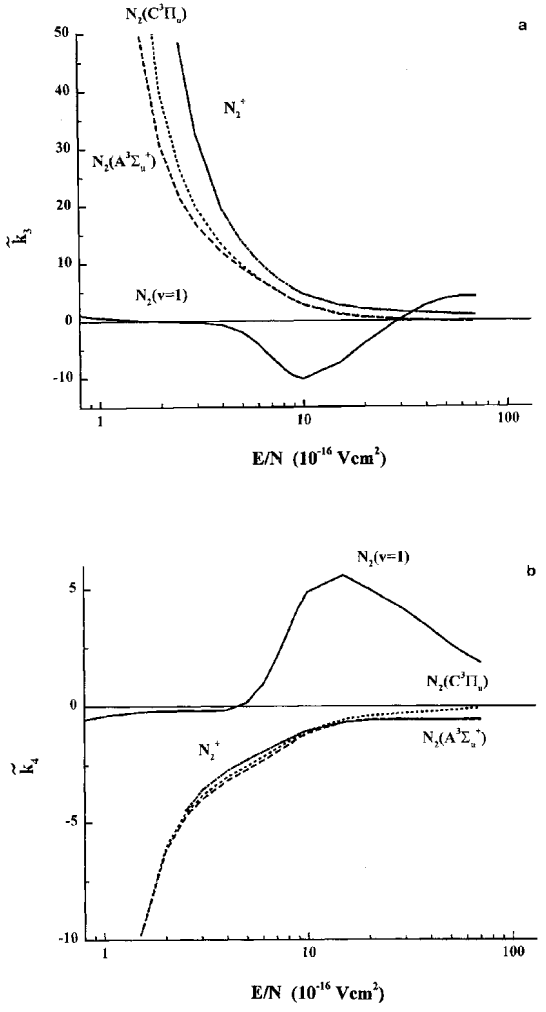

Figure 2. The values of (a) $\tilde{k}_3$ and (b) $\tilde{k}_4$ for N_2 in air[23].

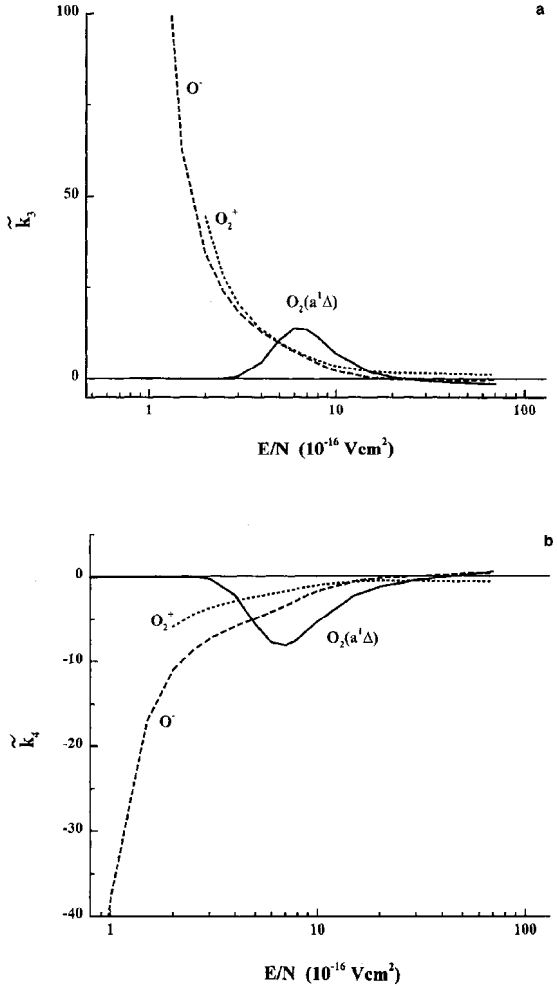

Figure 3. The values of (a) $\tilde{k}_3$ and (b) $\tilde{k}_4$ for O_2 in air [23].

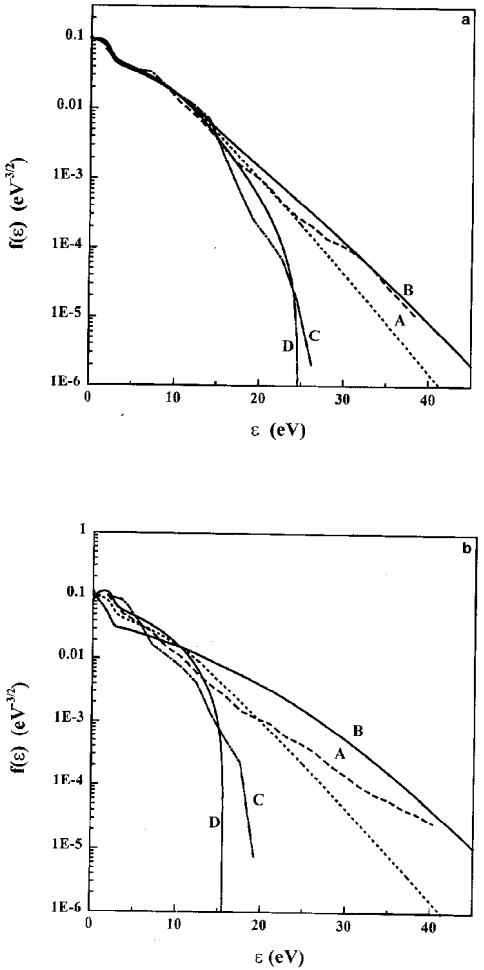

Figure 4. The EEDF in nitrogen for the field slope (a) of 2.67 and (b) 16 kTd cm^{-1} at E/N = 300 Td:(...), local field [25]; A and B, decreased field C and D, increased field. A and C are Monte Carlo simulations [25], B and D are the considered approach.

slopes 2.67 and 16 kTd cm^{-1} at 300 Td (1 Td = 10^{-17} Vcm^2) with the local field distribution and with results by Aleksandrov and Kochetov[21]. The calculations were performed for molecular nitrogen at N = 10^{17} cm^{-3}. It is important that for the field slope 2.67 kTd cm^{-1} both of the non-local approaches give nearly the same ionization coefficients whereas the local ionization coefficient differs from these values by a factor of 1.5–2[21]. A better agreement between the results of the non-local approach and the Monte Carlo simulation is observed for a decreasing field when the high-energy tail of the distribution is more populated by electrons. At higher field slopes the considered approach fails to describe quantitatively the electron behavior in gases.

Aleksandrov et al[22] analyzed the applicability of the considered approach to the description of the electron behavior in an unsteady uniform electric field. To do this, the results of this method were compared with the direct solution of the unsteady Boltzmann equation. Figure 5 shows this comparison for the ionization coefficient k_{on} in N_2 at a pressure of 1 torr, together with the quasi-stationary value of k_{on} and the ratio Ω/ν_u where

$$\Omega = \left| \frac{\partial \ln E}{\partial t} \right|$$

and

$$\nu_u = \frac{w_0^2}{D_T}.$$

The calculations were assumed that, in the time interval from $t = 10^{-8}$ to 3×10^{-8} s, the electric field varied (grew or decreased) linearly with time. The approach which is based on equation (17) gives correct results for the decreasing field even if $\Omega/\nu_u = 0.5$. In the case of a growing field, the agreement with the exact solution is worse; however, even in this case the agreement is sufficiently good, although the quasi-stationary coefficients can differ by factor of two or three from the exact one.

APPLICATIONS OF THE HYDRODYNAMIC DESCRIPTION OF ELECTRONS

Swarm Experiments

Electron swarm experiments are used to measure the electron transport and rate coefficients in a uniform electric field under non-uniform and/or unsteady electron density conditions[2].

The electron coefficients are usually assumed space (or time) independent. Wedding and Kelly[28] measured the spatial variations in the relative excitation rates for two electronic states of molecular nitrogen, namely the 337.1 nm (0,0) band of the second positive system and the 391.4 nm (0,0) band of the first negative system, for a point-source steady-state Townsend discharge. This enables us to compare the results of the calculation[22] of $\tilde{k}_1$ with experimental data. Figure 6 shows the measured radial variation in the ratio of the excited state populations $N(r, z) = n'(r, z)/n''(r, z)$ (n' and n'' refer to the 337.1 and 391.4 nm bands respectively) in a CO_2:N_2:He:CO (6:34:54:6) mixture under the following conditions: $E/N = 3 \times 10^{-15}$ V cm^2, pressure p =0.37 Torr and the axial position z = 2.5 cm.

It should be noted that $N(r, z)$ would be expected to be unity for all radial positions if there were no dependence of the electron rate coefficients on density gradients. However, the ratio of the normalized excited state populations indicates a significant radial variation. At small radii we have $\delta n/\delta z < 0$[28]; this being so, the additional

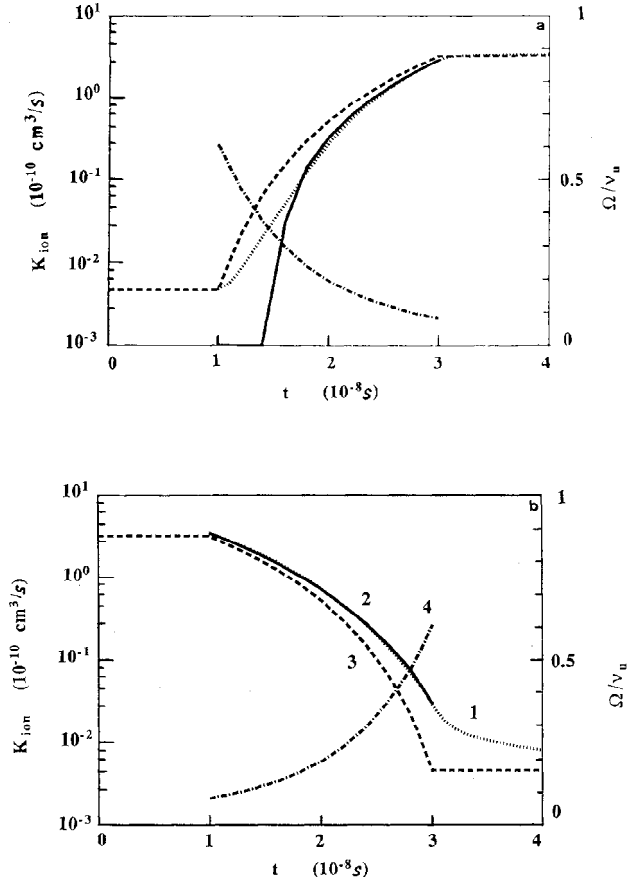

Figure 5. Ionization coefficient in N_2 in (a) increasing and (b) decreasing fields: (1) the exact calculation, (2) the considered approach, (3) the quasi-stationary value, and (4) the ratio Ω/ν_u.

electron diffusion flux increases the energy gained by electrons in the electric field. The rates of the processes with higher thresholds are more sensitive to a variation in the electron energy, resulting in $k_1' < k_1''$ and $N(r, z) < 1$. At larger radii the opposite situation occurs because then we have $\partial n/\partial z > 0$[28].

Using a normalization procedure adopted by Wedding and Kelly and assuming that the density gradient terms are small, then $N(r, z)$ reduces to

$$N(r,z) = 1 - (k_1' - k_1'')\left(\frac{\partial \ln n}{\partial z} - \alpha_T\right)$$

where α_T is the first Townsend ionization coefficient. To compare the measurements with the theory, Aleksandrov and Kochetov[21] calculated k_1', k_1'' and other electron swarm parameters for the conditions mentioned above. The results of this calculation are also shown in figure 6. In this case the electron density was supposed to be given by[28]

$$n(r,z) = \text{constant}\left[\lambda_L z \exp(\lambda_L z) K_{3/2}(s_1)/s_1^{3/2} + A J_0(\gamma_1 r/R)\exp(\beta z)\right] \qquad (20)$$

where

$$\lambda_L = w_0/(2D_L)$$

$$\lambda_T = w_0/(2D_T)$$

$$s_1 = \lambda_L z\left(1 - \frac{2\nu_{ion}}{w_0\lambda_L}\right)^{1/2}\left[1 + \frac{\lambda_L}{\lambda_T}\left(\frac{\lambda_T r}{\lambda_L z}\right)^2\right]^{1/2}$$

$$\beta = \lambda_L\left[1 - \left(1 + \frac{\gamma_1^2}{\lambda_L\lambda_T R^2} - \frac{2\nu_{ion}}{w_0\lambda_L}\right)^{1/2}\right].$$

D_L is the longitudinal diffusion coefficient, ν_{ion} is the ionization frequency, $K_{3/2}(s)$ is a modified Bessel function of the second kind, γ_1 is the first root of the Bessel function $J_0(x)$ and R is the internal radius of the guard rings maintaining a uniform electric field in the experiment. Here, the spatial electron density distribution is described supposing a dipole source at the cathode ($r = 0$, $z = 0$) and a diffuse source of secondary electron production at large radii. A is constant and a measure of the total secondary electron production.

Wedding and Kelly[28] showed that equation (20) is consistent with experiment by choosing A = 0.4 and normalizing the theoretical curve with respect to the experimental one. In contrast to this, the calculation of k_1' and k_1'' gives an absolute value of $N(r, z)$ which agrees closely with the experimental data[28] without any need for normalization.

Evidently, an analysis of the electron rate coefficients under non-uniform electron density conditions can provide new information on the electron properties and an additional possibility for deriving electron-atom (molecule) collision cross sections by comparison of experimental and theoretical electron-swarm findings. This method appears to be particularly appealing because it refers to the electron swarm properties controlled by the high-energy tail of the EEDF and to the high-threshold electron processes.

Stability of A Gas Discharge Plasma

We show that the hydrodynamic approach described above may be used to investigate non-equilibrium plasma instabilities. The diffusion processes decreasing the plasma perturbations, as a rule, have a stabilizing effect. The exception is the so-called

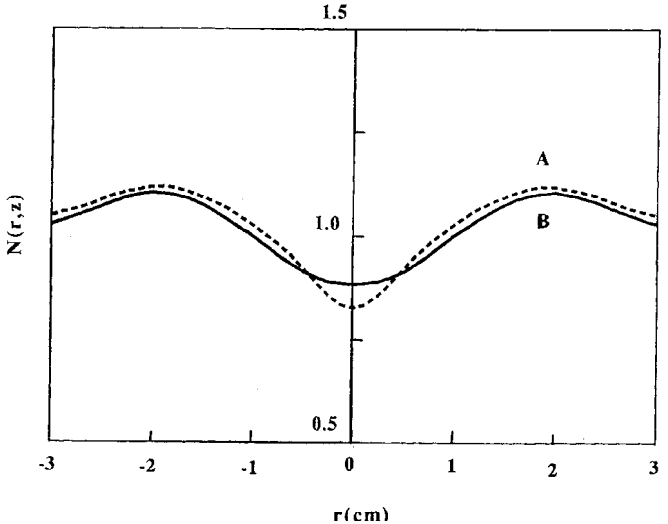

Figure 6. The radial variation in the excited state population ratio N(r,z) for z=2.5 cm: (A) experiment [28] and (B) calculation [21].

thermocurrent instability of a weakly ionized plasma carrying current which is caused by competition between the diffusion and 'thermodiffusion' processes. This type of instability was first predicted by Timofeev [16] who assumed the electron diffusion and thermodiffusion to be isotropic. Taking into account the electron transport anisotropy, this instability was investigated by Aleksandrov et al[4].

The mechanism of the thermocurrent instability is usually explained in the following way. The longitudinal electron flux induced by the gradients of the electron density n and of the parameter *E/N* in the one-dimensional case is equal to

$$\Gamma_D = -D_L \frac{\partial n}{\partial x} - n \frac{D_E}{E/N} \frac{\partial E/N}{\partial x} \tag{21}$$

where

$$D_L = D_T + \kappa_1$$

$$D_E = \frac{\partial D_T}{\partial E/N} + \kappa_2 + \kappa_3.$$

The last term in equation (21) is analogous to the thermodiffusion term in the equilibrium system case because the reduced electric field *E/N* determines the characteristic electron energy. Let us neglect the ion current and consider the time to be long in comparison with the relaxation time of the plasma charge $\tau_M = (4\pi\sigma)^{-1}$ (σ is the electrical conductivity). Then the electric current conservation law

$$enw_0 = \text{constant}$$

results in a simple relation between the electron density gradient and the *E/N* gradient. In this case the ambipolar diffusion flux along the electric field in the two charged-component plasma can be written in the form

$$\Gamma_a = -(D_L - \frac{D_E}{\hat{w}_0}) \frac{\mu_i}{\mu_e} \frac{\partial n}{\partial x}$$

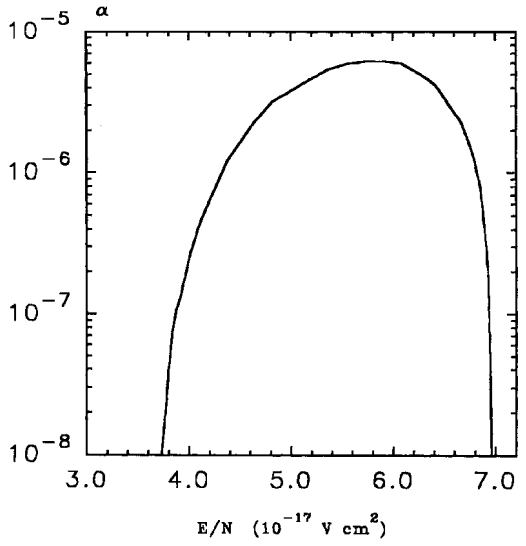

Figure 7. Region of thermocurrent instability for He in $\alpha - E/N$ space.

where μ_i and μ_e are the ion and electron mobilities respectively and

$$\hat{w}_0 = \frac{\partial \ln w_0}{\partial \ln E/N}.$$

According to (22), for

$$D_L \hat{w}_0 < D_E \tag{23}$$

diffusion is replaced by anti-diffusion and the plasma density perturbations are amplified. The instability under consideration is termed the thermocurrent because it is caused by the electron current being proportional to the *E/N* gradient.

It should be noted that the thermocurrent instability takes place only if $\nu_u \tau_M \ll 1$[4]. In the opposite limit the longitudinal ambipolar diffusion is controlled by the plasma quasineutrality violation which always stabilizes the perturbations.

A consistent discussion of the thermocurrent instability should be based on a kinetic treatment because the hydrodynamic approach provides for its growth rate to tend to infinity in the limit of short wavelengths[4]. The threshold of instability development, however, can also be obtained by the hydrodynamic theory. The conclusion from the calculation[4] of the electron transport coefficients that the instability can occur in He at $E/N = (4 - 7) \times 10^{-17}$ V cm² has thus been supported by kinetic calculation by Shveigert[29] on the basis of the inhomogeneous Boltzmann equation.

Akishev et al[30] have obtained experimental confirmation of the occurrence of this instability in He at a pressure of 1-4 Torr. They observed oscillations of the current, the electrode voltage and the potential of probes in a glow discharge. The pressure dependence of the period of the oscillations and the *E/N* instability region were consistent with the conclusions of the theory.

The transport coefficient calculations by Aleksandrov and Kochetov[24,31] indicate that condition (23) is also satisfied in CO_2 at $E/N = (7 - 23) \times 10^{-17}$ V cm² and that an increase in the ionization degree a and in the vibrational temperature of molecules

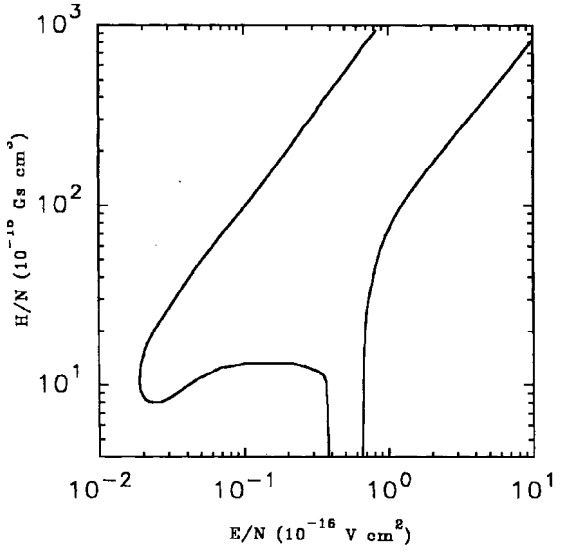

Figure 8. Region of thermocurrent instability for He in $H/N - E/N$ space.

has a stabilizing effect. Figure 7 shows the region of the thermocurrent instability for He in $\alpha - E/N$ space. Evidently, at high values of α the electron-electron interactions tend to drive the EEDF towards a Maxwellian which prevents the development of this instability.

The application of a transverse magnetic field **H** turned out to be favourable to the thermocurrent instability growth[32]. This is associated with the disturbances propagating at an angle to the electric field and with a change in the electron transport parameters, Figure 8 shows the region of the thermocurrent instability for He in $H/N - E/N$ space which was determined at small a from a calculation of the electron transport coefficients in $\mathbf{E} \times \mathbf{H}$ fields[32].

Domain instability of gas discharge plasma which is caused by negative differential conductivity[4,9,33] can also be affected by the non-locality and unsteadiness of the EEDF. This arise, e. g., in mixtures of molecular gases (N_2, CO, CO_2, HCl) with inert gases (Ar, Kr, Xe). Here, in the linear approximation the increment and velocity of the most dangerous long-wave perturbations for $\nu_u \tau_M \gg 1$ are[4,9]

$$\Gamma = -\frac{\hat{w}_0}{\kappa_4} w_0^2$$

$$v = w_0 \frac{D_E}{\kappa_4}$$

where

$$\hat{w}_0 = \frac{\partial \ln w_0}{\partial \ln E/N}.$$

Domain instability develops at $\Gamma > 0$; this is the case at $\hat{w}_0 < 0$ and $k_4 > 0$ or vice versa. The latter can take place in ion-ion plasmas[34]. In electron-ion plasmas with $\hat{w}_0 < 0$, the domain instability causes a bright plane layer moving along the electron drift velocity. Evidently, that the layer can move also in the opposite direction when $D_E < 0$.

A new type of plasma instability takes plase in an electronegative gas when the rate of electron attachment to a molecule strongly increases with the electric field[1,4,33,35,36]. This attachment instability causes solitary layers (domains) with a high electric field and a low electron density (or vice versa) to propagate between the electrodes in the high-pressure discharge in gaseous mixtures containing O_2, CO_2, H_2O or HCl. Both this phenomenon and the instability incluced by negative differential conductivity manifest themselves primarily as oscillations of the electrical current or of the voltage difference across the discharge gap.

In the linear approximation the velocity of long-wave disturbancies can be written as[9,36-38]

$$v = \nu_a \left[\frac{\hat{k}_{a0} - \hat{w}_0}{\hat{w}_0^2} w_0 \tau_M + \frac{\hat{k}_{a0}}{w_0 \hat{w}_0} \left(D_L - \frac{D_E}{\hat{w}_0} \right) + k_{a1} - \frac{k_{a2} + k_{a3}}{\hat{w}_0} \right] \tag{24}$$

where

$$\hat{k}_{a0} = \frac{\partial \ln k_{a0}}{\partial \ln(E/N)},$$

$\nu_a = k_{a0} N$ is the attachment frequency and k_{a0}, k_{a1}, k_{a2} and k_{a3} refer to the attachment rate coefficient. The coefficients k_{a1}, k_{a2} and k_{a3} represent changes in the attachment rate coefficient caused by the spatial evolution of the EEDF in plasmas with n and *E*/*N* gradients (see equation (17)).

The first term in equation (24) represents the transport of plasma disturbances due to the relaxation of the space charge and is of the order $\hat{k}_{a0} w_0 \tau_M \nu_a$. The second and third terms, being of the order of $\hat{k}_{a0} \nu_a \lambda_u$, describe the transport of perturbations due to the nonlocal behaviour of the EEDF and the electron transport and rate coefficients. The importance of any particular term is determined by the parameter $\nu_u \tau_M$ which is equal to the ratio of electric field pressure to electron pressure. For $\nu_u \tau_M >> 1$, the domain propagates from cathode to anode whereas for $\nu_u \tau_M << 1$, the domain may propagate also in the opposite direction. For example, when $\nu_u \tau_M >> 1$, the attachment instability was experimentally studied in an externally-sustained gas discharge in an O2:He mixture[38].

Simulation of Long-streamer Propagation

Streamer propagation is an important discharge phase of the breakdown of a long gas gap. Nowadays the interest in these transient filamentary plasmas is due to their applications to the removal of air-borne toxic chemicals (SO_2, NO_x, etc.).

A great deal of effort has been devoted to computer simulation of the streamer-plasma properties[39-41]. The basic dynamical equations for the streamer propagation are the continuity equations for electrons, ions and active particles, and Poisson's equation for the electric field:

$$\frac{\partial n_e}{\partial t} + \mathrm{div}(n_e \mathbf{v_e}) = Q_e \tag{25}$$

$$\frac{\partial n_p}{\partial t} + \mathrm{div}(n_p \mathbf{v_p}) = Q_p \tag{26}$$

$$\frac{\partial n_n}{\partial t} + \mathrm{div}(n_n \mathbf{v_n}) = Q_n \tag{27}$$

$$\frac{\partial n^*}{\partial t} = Q^* \tag{28}$$

$$\mathrm{div}\mathbf{E} = \frac{e}{\varepsilon_0}(n_p - n_e - n_n). \tag{29}$$

Here n_e, n_p, n_n and n^* are the electron, positive-ion, negative-ion and active-particle densities, respectively, $\mathbf{v_e}$, $\mathbf{v_p}$ and $\mathbf{v_n}$ are the corresponding drift velocities and ε_0 is the permittivity of free space. The terms Q_e, Q_p, Q_n and Q^* describe the production and loss of electrons, positive ions, negative ions and active particles, respectively. The drift velocities and the rate coefficients are usually assumed to be functions of the local reduced electric field *E/N* although there are strong n_e and *E/N* gradients at the streamer head. The effects of nonlocality of the EEDF on the streamer properties were studied by a Monte Carlo technique or momentum transfer theory only for very short (« 1 cm) streamers [42-44].

The hydrodynamic approach described in section 2 was used to simulate much longer streamers in air taking into account the nonlocal and unsteady effects [23]. The 1.5 D (axisymmetrical) simulation model and numerical method used in this calculation were essentially the same as those used by the authors [40,45]. That is, the radius of the streamer channel was assumed to be fixed. Equations (25)-(29) were solved numerically by the finite-difference method with the adapted mesh. The mesh was stretched in the axial coordinate near the anode and in the streamer head, and was uniform in other regions. The electric field was determined from the condition that the streamer space charge is distributed over the cylindrical channel surface. The simulation was performed in a sphere-plane air gap for a spherical anode of 1 cm radius and channel of 0.03 cm radius. The calculation based on the local field approach and that based on the hydrodynamic description of electrons give nearly the same results, although taking into account only the nonlocal effect due to the *E/N* gradient affects the results distinctly. This is because at the streamer head the *E/N* and n_e gradients are in the opposite directions; that is, the various nonlocal effects cancel each other. The same is true at higher pressures. The main conclusion from this calculation is that a long streamer in air at pressures higher than 0.1 bar can be simulated using local approaches.

CONCLUDING REMARKS

Strictly speaking, the approach considered holds for small field and electron density gradients ($\lambda_u << L$) and time derivatives ($\nu_u \tau >> 1$) only. The validity and accuracy of such a treatment for gradients and time derivatives that are not small are not clear in advance. Nevertheless,. when our results are compared with the results of more consistent approaches (Monte Carlo technique, etc.), it is apparent that our approach can also be used for the cases of $\lambda_u \simeq L$ and $\nu_u \tau \simeq 1$ with the corrections for the electron transport and rate coefficients being of the order of unity.

A self-consistent modelling of discharge phenomena taking into account the non-local effects coupled to Poisson's equation for the electric field is a formidable task. This raises the necessity of developing a suitable hydrodynamic-like method incorporating the important kinetic effects. Our approach is intended to provide data necessary for this description of the electron properties in non-uniform and unsteady fields. The method considered here is simpler than Monte Carlo simulation and other cumbersome approaches. It is applicable to a description of the electron kinetics in gases with a variety of electron-atom or electron-molecule scattering processes. Our approach is also more simple and consistent than other hydrodynamic-like approaches which include the balance equation for the average electron energy. This equation is usually written by analogy with the hydrodynamic equations for a highly ionized gas derived by a Chapman-Enskog procedure which is not valid for a nonequilibrium weakly ionized plasma [16].

In this paper we have assumed that the EEDF depends only on the parameter

E/N. When the EEDF depends also on the vibrational temperature of molecules Tv or on the ionization degree α, a new type of corrections to the electron transport and rate coefficients, proportional to ∇T_v, $\frac{\partial T_v}{\partial t}$[4,19,20] and ∇n[4,24], appear. This approach was also generalized to cases of $\mathbf{E} \times \mathbf{H}$ fields[32,46] and electromagnetic waves [47]. Similarly, the ion properties in gases in a strong electric field can be considered[48]. It is interesting that, due to a strong anisotropy of the ion energy distribution function, new corrections proportional to $\mathbf{e}(\nabla \mathbf{e})$ and $\frac{\partial \mathbf{e}}{\partial t}$ ($\mathbf{e} = \mathbf{E}/E$) appear.

REFERENCES

1. Yu. P. Raizer. "Gas Discharge Physics", Springer, Berlin (1991).
2. L. G. H. Huxley and R. W. Crompton. "The Diffusion and Drift of Electrons in Gases", Wiley, New York (1974).
3. K. Kumar, H. R. Scullerud, and R. E. Robson, Kinetic theory of charged particle swarms in neutral gases, Aust. J. Phys. 33: 343 (1980).
4. N. L. Aleksandrov, A. M. Konchakov, A. P. Napartovich and A. N. Starostin, The transport phenomena of charged particles in a weakly ionized gas, in "Khimiya Plazmy", B. M. Smirnov, ed., No.11, Energoatomizdat, Moscow (1984).
5. G. G. Lister, Low-pressure gas discharge modelling, J. Phys. D: Appl. Phys. 25: 1649 (1992).
6. U. Kortshagen, C. Busch, and L. D. Tsendin, On simplifying approaches to the solution of the Boltzmann equation in spatially inhomogeneous plasmas, Plasma Sources: Sci. Technol. 5:1 (1996).
7. V. I. Kolobov and V. A. Godyak, Nonlocal electron kinetics in collisional gas discharge plasmas, IEEE Trans. Plasma Sci. 23:503 (1995).
8. L. D. Tsendin, Electron kinetics in non-uniform glow discharge plasmas, Plasma Sources: Sci. Technol. 4: 200 (1995).
9. N. L. Aleksandrov, A. P. Napartovich, and A. N. Starostin, Transport equations in a nonequilibrium weakly ionized plasma, Sov. J. Plasma Phys. 6: 618 (1980).
10. I. P. Shkarofsky, T. W. Johnston, and M. P. Bachynski. "The Particle Kinetics of Plasmas", Addison Wesley, Reading MA (1966).
11. S. R. Hunter and L. G. Christophorou, Electron motion in low- and high-pressure gases, in: "Electron-Molecule Interactions and Their Applications", vol 2, L. G. Christophorou, ed., Academic, Orlando FL (1984) p.89.
12. N. L. Aleksandrov and E. E. Son, The electron energy distribution and kinetic coefficients in gases in an electric field, in "Khimiya Plasmy", B. M. Smirnov, ed, No.7, Atomizdat, Moscow (1980).
13. J. H. Parker and J. J. Lowke, Theory of electron diffusion parallel to electric fields. I. Theory, Phys. Rev. 181:290 (1969).
14. J. J. Lowke and J. H. Parker, Theory of electron diffusion parallel to electric fields. II. Application to real gases, Phys. Rev. 181: 302 (1969).
15. H. R. Scullerud, Longitudinal diffusion of electrons in electrostatic fields in gases, J. Phys, B: Atom. Mol. Phys. 2:696 (1969).
16. A. V. Timofeev, Hydrodynamic transport equations for a weakly ionized gas discharge plasma, Sov. Phys. Tech. Phys. 15: 140 (1970).
17. N. L. Aleksandrov and A. M. Konchakov, Electron transport coefficients in a weakly ionized nonequilibrium plasma, Sov. J. Plasma. Phys. 7: 103 (1981).
18. N. L. Aleksandrov and A. M. Konchakov, Electron transport coefficients in a weakly ionized nonequilibrium plasma in the CO_2:N_2 mixtures, High Temp. (USSR) 21: 1 (1983).
19. N. L. Aleksandrov and I. V. Kochetov, Electron transport parameters in a weakly ionized gas with vibrationally excited molecules, J. Phys. D: Appl. Phys. 26: 387 (1993).
20. N. L. Aleksandrov and I. V. Kochetov, Electron transport coefficients in a weakly ionized plasma with vibrationally excited molecules, Sov. J. Plasma Phys. 18: 828 (1992).
21. N. L. Aleksandrov and I. V. Kochetov, Electron rate coefficients in gases under non-uniform field and electron density conditions, J. Phys. D: Appl. Phys. 29: 1476 (1996).
22. N. L. Aleksandrov, N. A. Dyatko, and I. V. Kochetov, Rate of inelastic electron processes in a weakly ionized plasma in a nonstationary electric field, Plasma Phys. Rep. 21:763 (1995).

23. N. L. Aleksandrov, E. M. Bazelyan, I. V. Kochetov, and A. M. Okhrimovskyy, The rate of inelastic electron processes in air in a space-time varying electric field, Plasma Phys. Rep. (in press).
24. N. L. Aleksandrov and I. V. Kochetov, Longitudinal diffusion of electrons in weakly ionized gas with Coulomb collisions, J. Phys. D: Appl. Phys. 24: 2164 (1991).
25. T. J. Moratz, L. C. Pitchford, and J. N. Bardsley, Electron swarm behavior in nonuniform fields in nitrogen, J. Appl. Phys. 61: 2146 (1987).
26. N. Sato and H. Tagashira, Monte Carlo simulation of the electron swarm in nitrogen under non-uniform field conditions, J. Phys. D:Appl. Phys. 18: 2451 (1985).
27. Jianfen Liu and G. R. Govinda Raju, The nonequilibrium behavior of electron swarms in nonuniform field in SF_6, IEEE Trans. Plasma Sci. 20:515 (1992).
28. A. B. Wedding and L. J. Kelly, Observation of spatial variations in the energy distribution function for steady-state Townsend discharges, Aust. J. Phys. 42: 101 (1989).
29. V. A. Shveigert, Thermocurrent instability of a glow discharge in helium, Sov. J. Plasma Phys. 14: 739 (1988).
30. Yu. S. Akishev, N. A. Dyatko, I. N. Lopatkin, I. V. Minina, A. P. Napartovich, and I. V. Kochetov, Thermocurrent instability of a glow discharge, in: "Proc. 7th All-Union Conf. on the Physics of Low-Temperature Plasmas", p.261, Fan, Tashkent (1987).
31. N. L. Aleksandrov and I. V. Kochetov, Stability of a nonequilibrium weakly ionized plasma with Coulomb collisions, Sov. J. Plasma Phys. 17: 430 (1991).
32. N. L. Aleksandrov, I. V. Kochetov, and A. M. Konchakov, Instability induced by electron transport in a weakly ionized plasma in $E \times H$ fields, J. Phys. D: Appl. Phys.28: 1072 (1995).
33. A. P. Napartovich and A. N. Starostin, Stability of gas-discharge plasma at high pressures, in: "Khimiya Plazmy", B. M. Smirnov, ed., No.6, Atomizdat, Moscow (1979) p.153.
34. N. L. Aleksandrov and A. M. Okhrimovskyy, Stability of a weakly ionized ion-ion plasma immersed in a strong electric field, Plsma Phys. Rep. 23: 77 (1997).
35. V. L. Nighan, Stability of molecular laser discharges at high energies, in: "Principles of Laser Plasma", G. Bekefi, ed., Wiley, New York (1976).
36. N. L. Aleksandrov and A. P. Napartovich, Phenomena in gases and plasmas with negative ions, Phys. -Usp. 36: 107 (1993).
37. F. I. Vysikailo, Ambipolar drift of a weakly ionized plasma induced by the nonlocality of electron distribution function, Sov. J. Plasma Phys. 13: 111 (1987).
38. N. L. Aleksandrov, I. V. Kochetov, D. A. Mazalov, A. P. Napartovich, A. F. Pal', V. V. Pichugin, and A. N. Starostin, Electron transport coefficients and attachment instability dynamics in a, gas-discharge plasma, Sov. J. Plasma Phys. 18: 758 (1992).
39. A. J. Davies, Discharge simulation, IEE Proc. A 113: 217 (1986).
40. N. L. Aleksandrov, A. E. Bazelyan, E. M. Bazelyan, and I. V. Kochetov, Modeling of long streamers in atmospheric-pressure air, Plasma Phys. Rep.21: 57 (1995).
41. E. M. Bazelyan and Yu. P. Raizer. "Spark Discharge", CRC, New York (1997).
42. E. E. Kunhardt and Y. Tzeng, Development of an electron avalanche and its transition into streamers, Phys. Rev. A 38:1410 (1988).
43. J.-M. Guo and C.-H. J. Wu, Comparisons of multidimensional non-equilibrium and equilibrium fluid and Monte Carlo models for streamers, J. Phys. D: Appl. Phys.26: 487 (1993).
44. J.-M. Guo and C.-H. J. Wu, Two-dimensional nonequilibrium fluid models for streamers, IEEE Trans. Plasma Sci. 21: 684 (1993).
45. N. L. Aleksandrov and E. M. Bazelyan, Simulation of long-streamer propagation in air at atmospheric pressure, J. Phys. D: Appl. Phys. 29: 740 (1996).
46. N. L. Aleksandrov and A. M. Konchakov, Spectrum of the electron cyclotron resonance in an unsteady weakly ionized plasma, Fiz. Plazmy 13: 1390 (1987).
47. N. L. Aleksandrov, A. P. Napartovich and A. N. Starostin, Dielectric permittivity of weakly ionized plasmas in the field of an electromagnetic wave of variable amplitude, in "Proceeding of the XV Int. Conf. on Phenom. Ionized Gases", L. I. Kiselevskiy, ed., Institute of Physics BAS, Minsk (1981).
48. N. L. Aleksandrov, A. P. Napartovich, and A. M. Okhrimovskyy, Ion transport in gases and weakly ionized nonequilibrium plasma in a variable electric field, JETP 82: 214 (1996).

GLOW-LIKE DISCHARGES WITH RUNAWAY ELECTRONS

Leonid P. Babich

Russia Federal Nuclear Center - VNIIEF
"Sarov, 607190, Nizhegorodskii region, Russia

INTRODUCTION

Unspoken opinion restricts the gas-discharge physics by electromagnetic interactions with free electron and photon energy being no more than lower tens of electronvolts. The point is that an idea has been universally adopted according to which the dynamics of breakdown and discharges in dense gases was governed by the entire assembly of electrons moving along the electric force -eE with a drift velocity determined solely by the local value of the reduced field intensity E/N. The chaotic motion of electrons has been considered to dominate over this relatively slow directed motion. This idea originated from a concept of the energy equilibrium of the entire electron assembly with a local E/N. It has being assumed valid however fast the gas discharge process developed. Nevertheless within the line of the gas discharge physics a "thread" of discharge phenomena governed by strongly nonlocal processes, was stretching to develop gradually into an original area recognized presently by scientific community. Wilson was the first who has suggested as early as 1925 that the equilibrium could be violated in sufficiently high electric fields. Thirty years earlier the outset of the era of thermonuclear plasma researches, when the first famous works have been published on the phenomenon known presently as an electron runaway in a rarefied fully ionized plasma governed by Coulomb collisions, Wilson has spoken out and substantiated an idea that electric fields of thunderstorm clouds could accelerate charged particles up to very high energies in the Earth's atmosphere.[1] Furthermore, it seems to be universally admitted that the term "runaway electrons" itself has appeared for the first time only in the scientific literature of the 50's to determine a flux of high-energy electrons accelerated away from a hot plasma core of thermonuclear reactors. Actually it has been introduced by Eddington as early as 1926 in that section of his paper,[2] where he has discussed "the question of the origin of the penetrating radiation found in the earth's atmosphere,...in connection with subatomic energy" as the nature of stellar energy source. At the end of the 20's scientists have not been convinced that the radiation known presently as cosmic rays, originated from extra-terrestrial sources in spite of downward flow of the radiation. The experimental evidences of the cosmic nature of the radiation were not universally adopted. In any case, Eddington "...was somewhat shaken by Wilson's calculations as to run-away electrons in thunderstorms".[2] Proceeding from results of these calculations he considered to be plausible that could produce the observed radiation without involving drastic subatomic processes in stars or interstellar cosmic space.

Electron Kinetics and Application of Glow Discharges
Edited by U. Kortshagen and L. D. Tsendin, Plenum Press, New York, 1998

It seems safe to believe that for the first time the phenomenon of runaway electrons was observed in the 30's in the first experiments performed to search penetrating radiation produced by thunderstorm electric activity, though the results of these observations are commonly considered as statistically insignificant. Exactly Wilson's hypothesis following by these experiments has begun a direction in the gas discharge physics known as highenergy phenomena in dense gases. On account of for years this scientific area was being presented by experiments performed from time to time within so specific field as atmospheric electricity in connection with thunderstorm activity, it happened to be outside the attention of a vast majority of scholars being studied and applied electric discharges in dense gases. Only at the end of 60-th laboratory discharges in gases at the pressure up to 1 atm. were observed to generate runaway electrons of high energies. Exactly the process of electron runaway underlies earlier unknown phenomena and gas-discharge dependencies: (a) high-current glow-like discharges with high degree of spatial homogeneity, [3, 4] (b) production of electrons with anomalous energy, [3, 5] (c) displacement of the minimum of Paschen's curves,[3] (d) inversion of the polarity effect at high values of overvoltage, [6] (c) filamentation of diffuse gas-discharge channels, [7] (d) the effect of utmost voltage.[8] Nonetheless in spite of many interesting consequences were originated on account of runaway electrons to participate in the discharge dynamics, the most intriguing and amazing phenomenon was high-energy runaway electrons themselves to appear in so dense media as the lower layers of the Earth's atmosphere.

FUNDAMENTALS OF NONLOCAL MODEL OF BREAKDOWN IN DENSE GASES

In the present section the author will follow briefly his present day comprehension of ideas having been developed by Babich and Stankevich,[9] and Kunhardt and Byszewski. [10] The case of a "weak" external field with the intensity less than the critical field intensity is the most intricate since a distortion of the external field by space charges is necessary to satisfy both Raethers treatment of breakdown and runaway criterion for electrons with initial energy below the value, at which electron energy losses per unit path hit maximum value nearby to 100 eV. The case of a strong field is rather obvious.

In the framework of the conventional conception assembly averages, such as an average electron energy, ionization frequency and directed (drift) velocity achieve their maxima along the surface of a primary streamer, which is reasonable to define as a surface, where selfconsistent field intensity, as a function of r, is maximum for every given x. Here x is counted along and r transverse to the streamer axis. The maxima are decreasing functions of the angle between the axis and the vector of the local selfconsistent field on the streamer surface with an absolute maximum values at the streamer apex point, where selfconsistent field intensity hits its absolute maximum. As the average electron energy increases to be within the domain of reducing cross-sections, the maximum of the ionization frequency gradually displaces to larger angles. The drift velocity remains maximal at apex point for ever. Thus a filament-like development of the ionization process conserves till electrons at small angles achieve the energy domain of rapidly decreasing ionization frequency. In subsequent stages the streamer channel grows "crown" at large values of the angle.

Let us turn to the nonlocal conception incorporating runaway electrons as a crucial factor governing the discharge dynamics [3, 9, 10] . If proceed from the stochastic definition of runaway electrons, formulated by Kunhardt, Tzeng and Boeuf[11] , the increase of the front field results in a continuous growth of a high-energy tail of the electron distribution, the last being more anisotropic and its tail being longer for small angles. In the framework of the deterministic approach the runaway energy threshold is minimum at the apex. Here the runaway criterion is met first of all, gradually spreading over all streamer front surface. As a result according to Kunhardt and Byszewski an "injection cone" of angles develops with a maximum number

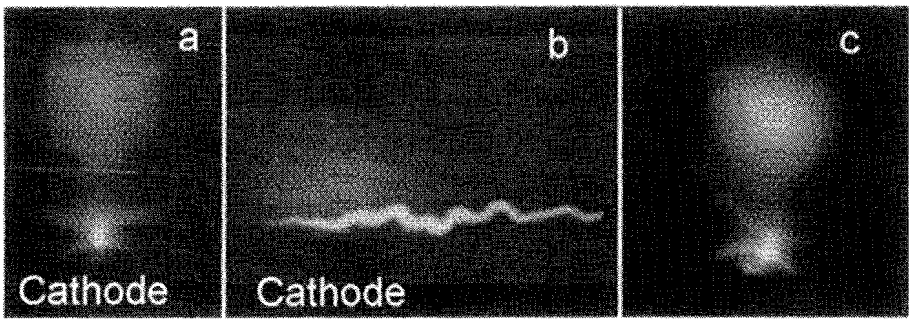

Figure 1. Gow-like discharges in the air at STP conditions: d = 1.5 cm, cathode radius r = 6 mm (a, c). Photochronogram of space-time evolution of the discharge (b)

of runaway electrons on the streamer (avalanche) axis.[10]

Electrons, accelerated away from the moving front surface with a maximum field intensity, relax to a local external field (become "trapped".[10]) Prior to being captured runaway electrons decelerated through the wide energy domain of large ionization frequency, so that they initiate chains of secondary avalanches along a filamentary channel within the injection cone.

This self-consistent process of the field intensification ahead of the channel apex, injection of runaway electrons, secondary avalanche development, and electron acceleration acquires a cone-like behavior. At very high overvoltages the breakdown should develop as a channel with a crown at large angles due to short-range runaway electrons and as a diffuse glow at small angles between the streamer axis and the vector of the local field, and far to an anode due to the preionization of an ambient gas by long-range runaways and overlapping of secondary avalanches prior to their transition to the streamer stage (Fig. 1). So the pictures of the breakdown dynamics are very much alike regardless to the conception (local or nonlocal) used, with the only exception of diffuse glows. The observation below allows to evaluate which one is valid for the particular case. At sufficiently high E/N the average electron energy achieves its maximum over a surface somewhere ahead of the streamer (primary avalanche) front surface defined above. This infers a failure of the local conception, which assumes both surfaces being coincident. The higher is E/N, the earlier the local conception fails in the course of the streamer development and consequently the larger is the distance between positions of the two maxima. Which conception is to be adopted is determined by idiosyncrasies of the particular experiment. Extremely low current pulse rise-time, very high velocity of the ionization propagation, diffuse glow-like forms with high spatial homogeneity, low ionization degree and plasma temperature along with extremely high current density are the most significant features of discharges governed by runaway electrons.

BREAKDOWN AND DISCHARGES AT VERY HIGH OVERVOLTAGES

Results obtained at VNIIEF along the line of experiments started by Tarasova and Khudyakova who reported a production of intensive x-radiation by electric discharges [4] at very high values of the overvoltage in rod to plane air gaps at STP conditions, will be delivered here as the most consistent. Maximum value of idle running HVW used was about 300 kV and rise-time less than 0.6 ns, Storage capacity was charged by microsecond HWV up to about 8 micro-coulombs. This charge determined the initial supply of electrons. As a rule but

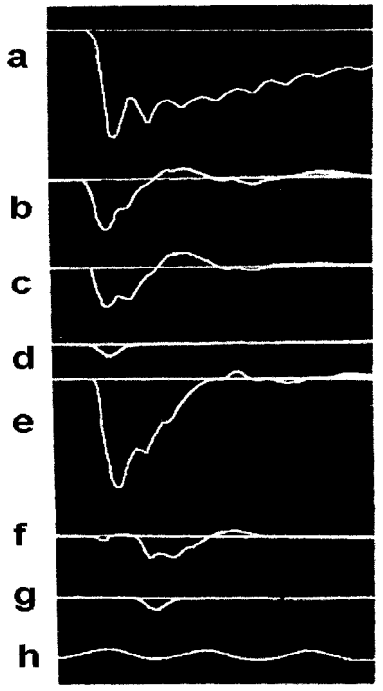

Figure 2. Open-circuit HVW oscilloscope trace U = 240 kV - (a), voltage realized U(t)-(b, e), gas-discharge current I(t) - (c, f), runaway electrons (d, g). Ordinary discharge - (b, c, d), barrier discharge - (e, f, g). Air, STP conditions, d = 1 cm, hemispherical cathode with r = 6 mm. 100 MHz time marker - (h).

not necessary the breakdown occurred at the front of idle running HVW, so that maximum value and rise-time of a pulse U(t) realized over a tested gap, were less than corresponding values for idle running HVW, and depended on a rod geometry and a gas species and density. At STP conditions and interelectrode spacing larger than 1 cm the breakdown developed into a volumetric diffuse glow-like discharge. The glow was separated by a comparatively narrow "dark space" from small one or several bright near-cathode plasmas with a crown seen in Fig. 1. The corresponding oscilloscope traces of U(t) and a current I(t) displayed almost lonely pulses (Fig. 2). Eddy current is seen in Fig. 2f. The similar structure of discharges with a "dark band" was observed by Bychkov et. al. in the air at P=30mTorr.[12]

Their discharges produced intensive x-radiation. At lower d the cathode plasmas grew through the glow to bridge the gap by bright narrow channels, so that oscilloscope traces of realized voltage U(t) and I(t) became oscillatory. At low d the average field intensity U(d)/d increased in spite of decreasing U. The current rise time was estimated to be less than 0.5 ns for either cases. Because a large conductivity current appeared at the voltage U(t) front, the delay time of the breakdown was less than 0.6 ns, indicating that the ionization front propagated with a velocity higher than 0.1c, where c is the light velocity in free space. There were studied plasma characteristics and dynamics of the diffuse glow discharge as the most interesting due to the spatial homogeneity of the plasma within the main volume.[13] The cathode plasma emitted in bands of the second positive system of nitrogen, NII lines, HI

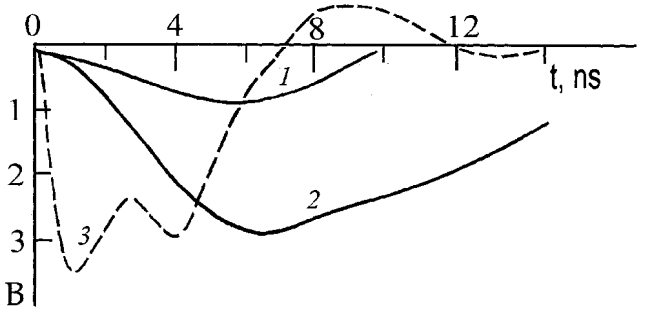

Figure 3. Time dependence of the blackening of a film B(t) produced by the diffuse glow (1) and the emission from the dense cathode plasma (2) measured from the photochronogram displayed in Fig. lb. Oscilloscope trace of the gas-discharge current (3).

line, lines of ions and (or) atoms of a cathode along with a broad continuum. The emission of nitrogen molecules and ions began l-2 ns prior to the appearance of the continuum and metal lines. The electron temperature and the gas ionization degree were 1.8 eV and 0.01, respectively. The diffuse glow emitted only in nitrogen bands, which were the same as from the cathode plasmas. Here the ionization degree was less than 0.00001. Temporal evolution of the light emission is illustrated in Fig. lb. Corresponding blackening of a film used B(t) produced by the diffuse nitrogen glow and cathode plasma emission, are presented in Fig. 3 along with I(t). The duration of the glow almost equaled to that of the current. The lower limit of the glow propagation velocity was estimated to be 0.2c. B(t) due to the glow and emission from the near-cathode domain occurred to be almost equal during the first 0.5 ns, which is the same as the current rise-time.

In view of the nitrogen emission in the cathode region preceded that of the metal atoms, this result implies that during the time shorter than the current rise-time, a faintly glowing streamer-like primary channel developed. Since values of B(t) produced by it and by the volume glow were equal in spite of the near-cathode streamer was many times narrower than the main glowing volume, the energy flux emitted by an unit surface of the streamer, was greater than that of the main volume. Apparently, the streamer was rather power- consuming formation. Electrons were accelerated in front of the streamer to become runaways, and mechanism of polarization self-acceleration came into play, so that subnanosecond pulse of anomalous energy electrons was generated. They preionized the main volume. Homogeneity of the plasma within it resulted from the overlapping of secondary avalanches. In the dark domain the energy of secondary electrons was too large for the molecule excitations due to electron impacts to be sufficiently frequent to provide detectable light intensity.

RUNAWAY ELECTRONS

Subsequent study of the intensive radiation observed by Tarasova and Khudyakova outside the anode of the above discharges at STP conditions, revealed a pronounced anisotropy of the radiation along the axis of the discharge.[5] The voltage was no more than 300 kV. It was too low for the discharges to generate ultra-relativistic electrons which emit the

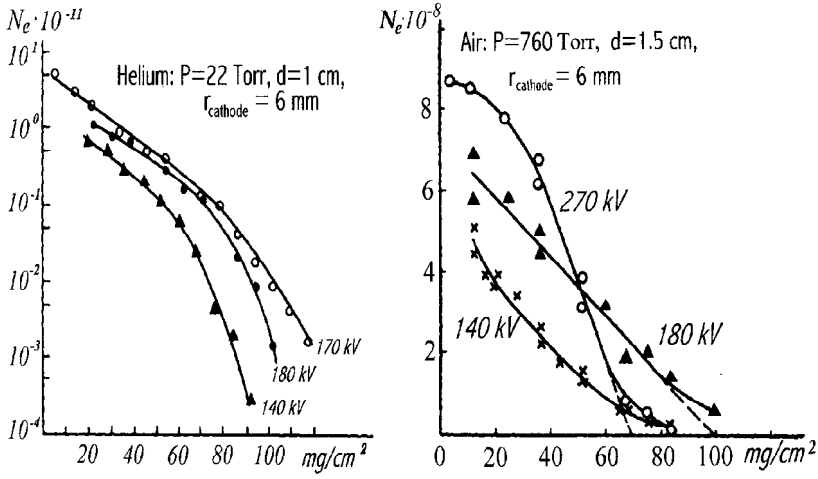

Figure 4. Attenuation curves of runaway electrons in aluminum foils. Figures indicate open circuit voltage. Crossings of dashed lines with axis indicate extrapolated range of runaway electrons.

bremsstrahlung predominantly along the direction of their own motion. Furthermore, a dependence of the observed radiation range on the atomic number Z of an absorber was found to be too weak for x-rays. Both results inferred that Tarasova and Khudyakova detected high-energy runaway electrons rather than x-rays. A comparison of experimental data with calculations on the absorption laws of electrons and x-rays in metallic foils of various Z and density unambiguously confirmed this conclusion.[5]

There was measured a dependence of the runaway electron number on the initial pressure of the air at room temperature for two values of aluminum absorber thickness, allowing to path through for electrons in the energy range above 40 keV and 200 keV respectively. The other conditions were as follows: maximum value of idle running HVW 270 kV, d = 1.5 cm, polished cathode with r = 6 mm. Rather sharp decrease of the electron number measured at low P inferred that the generation of high-energy electrons was governed by volumetric processes rather than by surface ones such as the field emission from a cathode, and apparently was owing to a decrease in the rate of ionizing collisions of electrons, but not only. According to curve obtained for the thicker absorber, some high-energy portion of runaway electron distribution rather weakly depended on P and on U(t) as well. This was the way by which electrons of “anomalous energy” for the first time distinctly revealed themselves.

In this sense absorption curves of runaway electrons occurred to be very illuminative. At lower pressures the curves measured by Tarasova et al.,[5] corresponded to a wide energy distribution. At pressures of the order of hundreds Torr the curves revealed features typical for monoenergetic electrons, i.e. the most steeply decreasing linear section in the middle and the pronounced straggling at the end. Fig. 4 illustrates the curves obtained from discharges in helium at P = 22 Torr and in the air at STP conditions. The linear section allowed to get extrapolated range of electrons and estimate their energy to be 270 keV, which is higher than eU (“anomalous energy”). Babich and Loiko published the most reliable quantitative data on the energy distribution of runaway electrons obtained by the method of magnetic spectroscopy (Fig. 5). [14] The measurements were carried out for discharges in a gap with a conical cathode and a grid anode. Electrons with energies less than 50 keV were absorbed in the window of the vacuum chamber of the spectrometer. Discharges in the air at P higher than

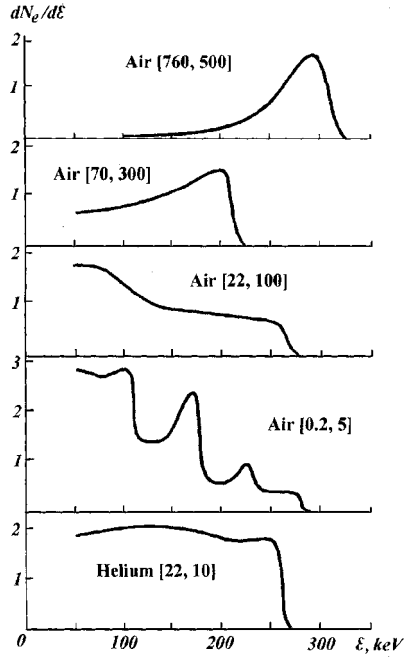

Figure 5. Energy distributions of runaway electrons (arbitrary units): maximum value of idle running HVW 270 kV, air, d = 2 cm, sharp conical cathode with r = 0.2 mm, grid anode; Figures in brackets indicate [pressure in Torr, number of pulses].

Table 1. Anomalous - energy electrons

Interelectrode spacing d, cm		3.5	2	1	0.5
Voltage realized,	kV	210	190	150	130
Peak electron energy,	keV	320	290	260	180
Energy excess,	keV	110	100	110	50

100 Torr generated energy distribution of runaway electrons with a well-defined maximum, whose position shifted to higher energies as P was increased. The value of the peak energy really was higher than eU. The measured width of this distribution W = 60 keV did not change within the pressure range 200-760 Torr. The intrinsic width was essentially less. Since electrons with energies higher than 50 keV have ranges longer than the thickness of the window, the lack of electrons at low energies along with W being less than the peak energy and “anomalous” value of the latter appealed for a mechanism of the electron acceleration unobserved earlier.

At P less than 200 Torr the spike-like energy distribution expanded owing to the generation of a large number of runaway electrons with lower energies. As P was reduced the maximum energy of the distribution initially decreased, and then in agreement with the U(P) dependence it increased backward, reaching at P = 22 Torr the value eU = 270 keV which was the uppermost energy allowed by the ordinary runaway mechanism. Within domain P less than 1 Torr the distribution became a line spectrum reflecting the structure of idle running

HVW oscillations, with the value eU =270 keV being persisted. The value of maximum energy was higher than that at reduced pressures in spite of U at hundreds of Torr was essentially less than maximum value of idle running HVW. This observation also confirms the generation of "anomalous energy" electrons. Table 1 shows maximum values of the voltage realized U and electron energy at the spike maximum at STP conditions for the air. For d longer than 1 cm the energy difference between the peak energy and eU equaled 100-110 keV, while for lower values of d it is less pronounced. It is pertinent to recall that in long gaps the discharge in the air was a volumetric diffuse glow, whereas in gaps with spacing less than 1 cm it was a bright contracted channel.

Experiments with identical accelerating and retarding voltages would allow to obtain the most convincing evidence for the generation of anomalous-energy electrons. A convolution of runaway electron motion and variation of HVW is an unpleasant shortcoming of such experiments. Two gaps with a common grid anode and equal spacing d = 2 cm were arranged. Runaway electrons accelerated within the first gap, passed through the anode into the space domain of the second gap, where they were decelerated by the retarding field and finally detected by a film within a cassette positioned at the second cathode. Wedges were attached to the cassette to estimate final extra energy of electrons traversed the retarding voltage. One and the same HVW was applied to both gaps, so that with the accuracy to the time necessary for an electron to travel the gap spacing (d/c = 0.07 ns) it passed equal accelerating and retarding voltages. Runaway electrons with the energy less than eU never reached the film since they experienced additional energy losses in the air and the cassette. At normal conditions the extra energy occurred to be 90 keV, which is nearly the same as the energy excess from Table 1. The result was concealed by the characteristic time of HVW variation was of the order of the travel time of runaway electrons in both gaps. So magnetic spectrometer measurements are to be considered as the most conclusive. It was of crucial importance to know space and temporal characteristics of runaway electrons in order to identify their origin and understand the way, by which they govern the breakdown and the overall dynamics of the discharge. The transverse structure of runaway electron fluxes was observed to reflect the distribution of emitting plasma spots over the cathode surface. The width of the runaway electron beams at STP conditions appeared to be directly proportional to the gap spacing d. These results inferred that runaway electrons were generated within the cathode region. The width of anomalous energy electron pulse at STP conditions was measured at half-maximum to be 0.5 ns.[14] As the air density was reduced, the width increased to become at P = 10 Torr equal to a half-width of the first oscillation of idle-running HVW (Fig. 2a) due to production of a copious amount of ordinary runaway electrons. To identify the start of a runaway electron generation was of a particular importance. Runaway electrons governed the breakdown as was treated above, provided that they are generated at the stage of primary avalanches or streamers. Otherwise, they are the result rather than one of the crucial causes of the particular way of breakdown. The anomalous energy electrons were detected at the front of the high-voltage pulse U(t). However to connect them with the conductivity current pulse was of more significance. They were assumed to be generated within an initial stage of the fast rise of the current. This was proved to be true with 1ns accuracy by means of a barrier discharge, which allowed to delay the electron emission and onset. The corresponding oscilloscope traces, presented in Fig. 2, show the onset of anomalous energy electrons did coincide with that of the conductivity current. Furthermore, a series of experiments showed that the number of anomalous-energy electrons was essentially independent on the current maximum value in the range 0.2-1.5 kA.[15] A method of two parallel gaps differed by d, was used to study the dependence of the number of anomalous energy electrons on the maximum value of the current. The method allowed to vary the current by means of a variation of the spacing of one of the gaps, with the voltage pulse U(t) was being one and the same over both

Table 2. X-ray dose from anomalous - energy electrons.

Absorber thickness		Dosage, 0.01 mR/pulse	
Polyethylene, mm	Aluminium, mm	measured	calculated
2	0	7.8	7.4
2	0.270	3.6	3.2
2	0.540	2.3	2.5

gaps. The result inferred the duration of the stage responsible for the generation of anomalous energy electrons was reasonable to estimate as (0.2/1.5) times of the current rise time. This product equals to 66 ps, which is far less than the measured magnitude 0.5 ns.

The problem arose to understand the nature of this phenomenon and to find a mechanism responsible for it. It is well-known that high-energy particles are rather usual for highly ionized collisionless rarefied plasmas governed by long-range collective interactions. The generation of such particles by cold collision-dominated gas-discharge plasma with a low ionization degree most likely may be explained by extrapolating the conventional Raether treatment of the breakdown phenomenology, which incorporated localized fields of space charges, to the domain of extremely high electric field intensities. In this sense the proximity of the number of anomalous energy electrons (Fig. 4, air) to the Raethers critical avalanche is very significant. From the very outset of the streamer model of breakdown in dense gases the ionization of a gas and the field intensification at the anode-directed streamer front and associated with it permanent increase of a local drift velocity were considered to be selfconsistent. Actually this collective process one may treat in the framework of the conventional local approach as an electron drift self-acceleration by the edge field soliton, propagating owing to the ionization of a background gas by the swarm of electrons trapped by the soliton itself, and polarization of the resultant plasma. The self-consistency, if being incorporated with the nonlocal approach, infers that under certain conditions runaway electrons can also be trapped by the edge soliton, i.e. the joint motion of the electrons and the soliton coupled due to the ionization, at sufficiently high E/N becomes in fact “pure” (not drift) self-acceleration in the laboratory frame of reference at least within some limited space-time domain of the overall breakdown process. On account of the front field soliton intensity is proportional to the square degree of the streamer length, the energy obtained by runaway electrons on account of the self-acceleration increases as a cubic degree of the streamer length. For sufficiently long and narrow streamer the energy of accelerated electrons can be even larger than the energy eU corresponding to the voltage realized.

X-RAYS PRODUCED BY ANOMALOUS-ENERGY ELECTRONS

Production of x-rays by glow-like discharges at high values of the overvoltage was observed and studied by Stankevich and Kalinin,[18] Kremnev and Kurbatov[16], Bychkov et. al.[12], Byszewski and Reinhold[17], Kolbychev and Samyshkin[19] and other scholars cited in Ref. 3. The most numerous and consistent experimental investigations of this issue were carried out at VNIIEF.

Table 2 illustrates some data on x-ray emission measured under conditions indicated in Fig. 4 right, as follows. The electrons were absorbed in 2 mm thick layer of polyethylene attached outside the anode foil of 8 mm thickness. Aluminum foils were positioned between the polyethylene layer and the dosimeter. The effective energy of x-ray photons was determined from the thickness of the half-attenuation layer to be equal to 14 keV This value being far less than the energy of anomalous-energy electrons 300 keV (Table 1) forced Tarasova et. al. to conclude that the discharges in the air at STP conditions generated a large amount of runaway

electrons with an average energy 1.514 keV.[5] They used relation deduced by Kramers, which actually is valid for the intensity of bremsstrahlung produced in a thin target. Working out from the idea that bremsstrahlung cross section and x-ray absorption coefficient increase as the photon energy decrease, with the absorption coefficient increase indicating the increase of the x-ray input in the dose measured, Babich et. al. supposed that soft x-rays produced by the discharges in the air of atmospheric density was excited by electrons of anomalous energy in the aluminum anode and the absorbing layers.[20] This idea contradicted the Framers relation, because the latter predicted the x-ray energy (2/3)300 keV for anomalous-energy electrons whose energies at the anode are presented in Table. 1. The value 200 keV is much higher than the effective x-ray photon energy 14 keV. To corroborate the idea, there were calculated x-ray spectrum and spectral distributions of intensity and dose of bremsstrahlung produced by anomalous-energy electrons, whose attenuation curve indicated by 270 kV, is presented in Fig. 4. The initial energy of electrons was assumed to be equal to the peak energy as presented in Table 1. Distributions of intensity and dose appeared to be concentrated in the low-energy domain of spectrum in the vicinity of the quantum energy 10 keV far below the spike energy of electrons. The results of integration of the dose distribution are collected in Table 2. The agreement with the measured dose of x-rays is excellent. So the x-ray emission produced by the glow - like discharges at high values of the overvoltage in the air gaps of centimeter range at atmospheric density, was originated from bremsstrahlung of anomalous-energy electrons. Nevertheless the discharges studied were calculated and observed to generate a copious amount of runaway electrons of lower energies which affected the mechanism of the discharges to support volumetric discharge forms.

X-RAY EMISSION FROM VOLUMETRIC DIFFUSE DISCHARGES

The operation time of industrial nanosecond x-ray tubes of nanosecond range is limited by the cathode erosion with subsequent insulator surfaces being covered by metal atoms and dust. To overcome this crucial shortcoming, it is necessary to utilize emission due to gamma-processes. Volumetric gas discharges are necessary to use in order to realize a homogeneous irradiation by positive ions and photons the largest portion of a cathode active surface and thus to avoid the formation of a cathode spot. Loiko et. al.[21] adopted a configuration with a vast plane cathode and a rod anode allowing for the macroscopic electric field to be homogeneous over the cathode surface, with the field intensity being significantly reduced to eliminate the explosion emission. Experiments were carried out with two gas-discharge chambers. Chamber (1) incorporated a plane cathode manufactured of 15 micrometer thick aluminum foil, and a steel hemispherical anode with a diameter of 4 cm. Chamber (2) incorporated 8 micrometer thick aluminum cathode and a cone W-Ni-Cu alloy cathode with r = 3 mm. A plane beryllium window of 1 mm thickness was arranged outside the anode. The interelectrode spacing in either chambers was d = 15 mm. Discharges were performed in helium and air in the pressure range from 0.0001 Torr up to 1 atm. Two HVWs were applied, one with subnanosecond rise-time less than 0.6 ns as illustrated in Fig. 2a, and the other with rise-time of microsecond range. A dosimeter was positioned at the distance 3.5 cm outside the cathode. Measured values of x-ray dose are plotted in Fig. 6. The position of the maximum was determined primarily by the gas species and HVW used. According to curve 4 for microsecond HVW 0.004 Torr was found. The shortening of the rise-time resulted in the displacement of the maximum to the range of higher pressure, as is illustrated by curves 1, 2, 3. The values 1 - 3 Torr for air and 20 Torr for helium were found for the maximum position. The origin of the maximum is rather obvious, though it is due to rather complex interplay of a few reasons. The strong decrease of the dose down to a negligible value at low pressures indicates that production of x-rays measured by Loiko et. al. was due to ionization

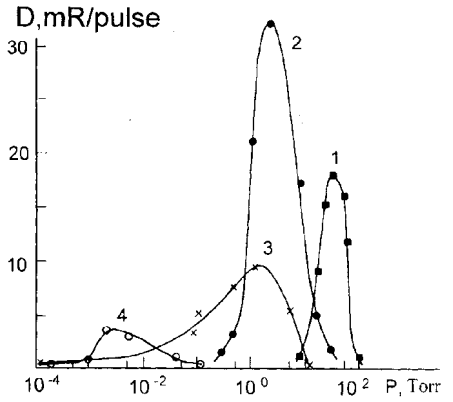

Figure 6. Dependencies of the x-ray dose on the pressure: 1,2- chamber (1), 3, 4 - chamber (2); 1 - He, 2, 3, 4 -air; 1, 2, 3 - open-circuit HVW 250 kV, rise time less than 0.6 ns, 4-u = 110 kV, microsecond rise time.

processes in the gas volume, with the emission was being supported by gamma - processes, though the authors privately communicated that extremely small sparking local spots as if were seen on the cathode plane. At high values of the pressure when the dose was small, the discharge developed in the form of bright contracted channels bridging the gap.

As the pressure was reduced, the channels expanded to become wider, and in the range of the maximum the interelectrode space was filled by spatially homogeneous diffuse glow. These results can be treated as an evidence that volumetric forms of the discharges are consistent with acceleration processes. The maximal dose measured by Loiko et. al., appeared to be only ten times less than that produced by industrial evacuated tubes. It is appropriate to note that neither discharge regime tested nor diode geometry were not optimize to obtain maximal dose and to approach the efficiency of the evacuated tubes.

DISPLACEMENT OF U(Pd) CURVE MINIMUM

Participation of runaway electrons in the breakdown dynamics should manifest itself on the macroscopic level as an adequate behavior of Paschen's curves U(Pd). What occurs with the curve of a particular gas if the overvoltage arises? The first idea but the wrong one is that the curve moves upward so that the position of its minimum (Pd) remains constant. It is well known that the breakdown "on the left hand branch" of the static (dc) Paschen's curve U(Pd) is governed by runaway electrons. The runaway condition for zero-energy threshold, which is the case for the breakdown, appeared to be satisfied, with the minimum value of e(E/P) differing not very much from the maximum value of electron energy losses per unit path reduced to unit pressure L.

Strongly attached gases are the only exception. This implied to go so far as to suggest the validity of the equality e(U/Pd) to maximum value of reduced electron energy losses, which is a fundamental constant for a particular gas. From it one can see that an increase of the overvoltage (decrease of the open circuit HVW rise time) should be accompanied by a rightward shift of the U(Pd) minimum. Fig. 7 shows curves U(Pd), measured in a gap with almost homogeneous geometry and d = 1 cm for three values of rise time: static, microsecond, and subnanosecond.[3]

The shift of the minimum is strongly pronounced. Throughout along the curve for subnanosecond rise time runaway electrons and x-rays were detected. Data are shown from other studies, where x-rays were detected from the air or nitrogen plane to plan gaps at lower

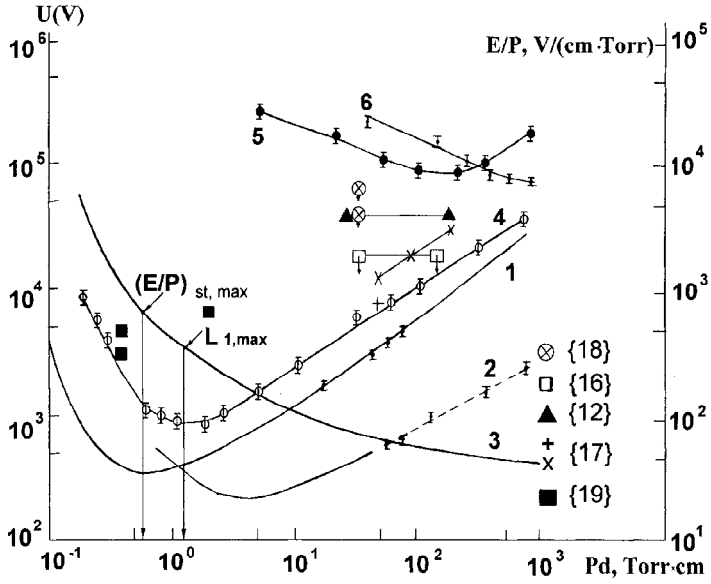

Figure 7. Dependencies U(Pd): 1, 2, 3 - static; 4 - microsecond HVW, 5 and 6 - nanosecond HVW with subnanosecond rise time; 1, 3, 4, 5 - air, 2, 6 - helium; 3 - static E/P.

overvoltage. So the displacement predicted from the conception that the breakdown to govern by runaway electrons, do take place. In its turn this result supports the nonlocal conception of the breakdown in dense gases. In general, the dielectric strength of gases is characterized by a single-parameter family of curves U(Pd, rise time), with the rise time being a parameter. Moreover, this result implies that beside dc U(Pd) curve there exists another fundamental dependence, indicating that for any given open circuit HVW rise time the minimum value of the voltage is directly proportional to the corresponding value of Pd.

INVERSION OF THE POLARITY EFFECT

The outstanding peculiarity of the breakdown in attached gases is the pronounced polarity effect, that is the breakdown voltage in gaps with positive rod to negative plane configuration of electrodes being less than in the event of the opposite polarity. It is believed to be due to a shielding of a negative point by a homopolar space charge. Kovalchuk et. al. observed the effect to inverse for the breakdown in the mixture 0.21 sulphur hexafluoride + 0.79 nitrogen by HWV with a rise time 4 ns.[2 2] This result inferred that at high overvoltage the homopolar space charge was destroyed most likely due to runaway electrons. Babich and Loiko studied the polarity effect in “pure” sulphur hexafluoride, as the outstanding specimen of strongly attached gas, and in the air at STP conditions.[6] The geometry was rod (high-stressed electrode) to plane. The rod active surface was cone with r = 0.2 mm or hemisphere with r = 6 mm. The algebraic values of the breakdown voltage obtained with microsecond HVW, clearly demonstrated the conventional polarity effect. These measurements were followed by experiments with the nanosecond HVW pulses U(t) measured over sulphur hexafluoride and air gaps for variety values of spacing d, indicated that voltage in the air and sulphur hexafluoride differed only by tens of percents rather than by several times as for longer pulses. The polarity effect was observed to inverse both in sulphur hexafluoride and in the air. Like in the air, the breakdown in sulphur hexafluoride was diffuse glow for large values of spacing (d > 5 mm). To support

Table 3. Anomalous - energy electrons in sulphur hexafluoride.

Cathode, radius	Cone (0.2 mm)		hemisphere (6 mm)	
Gas	air	sulphur hexafluoride	air	sulphur hexafluoride
Electron energy, keV	240	270	280	280
U, kV	110	140	180	250
Energy excess, keV	130	130	100	30
Number of electrons: air/sulphur hexafluoride	5		40	

the idea that the inversion of the polarity effect was due to runaway electrons, the number and energy of runaway electrons in sulphur hexafluoride at d = 2 cm and STP conditions were measured. Results obtained are presented in the Table 3 along with the data for the air. Runaway electrons from sulphur hexafluoride proved to be electrons of anomalous energy. Their number occurred to be sufficiently large to govern the breakdown. Thus the diffuse discharges in dense electronegative gases in rod to plane gaps at high overvoltages acquires features similar for the vacuum discharge. This is most likely due to breakdown is governed by the field emission and accelerated (runaway) electrons as in the vacuum. This idea implies that the polarity effect turns over in electropositive gases as well.

COMPUTER SIMULATION OF THE OVERALL DISCHARGE DYNAMICS

Nonlocal approach to electron kinetics in collisional gas discharge plasma was developed by Tsendin,[23] Tsendin and Golubovskii,[24] Kortshagen,[25] Ingold,[26] Kortshagen and Tsendin,[28] and other scholars as was reviewed by Kolobov and Godyak.[27] They considered the case which conventionally is allowed to identify as a weak non-locality. It includes fast beam-like electrons. The case of incorporates runaway electrons. Results on computer simulation of overall dynamics of glow-like diffuse discharge at high overvoltage governed by runaway electrons, were published by Babich and Kutsyk.[29] The calculations were carried out up to the state enabling a comparison with experimental data. The approach of electron energy groups was adopted. Electron energy distribution was divided in three large - scale groups.

The first group incorporated electrons with almost isotropic distribution below some maximum value. It was described by the conventional two-term approximation for the distribution function f(x,v,t). The corresponding set of two equations was reduced to an equation describing the evolution of low-energy component in terms of a local electron number density with a given energy. The second group contained electrons of intermediate energies in the domain below runaway energy threshold. In strong fields the number of particles in this domain is considerable. They move mainly along the lines of electric force -eE. The two-term approximation is violated for them. The simplest statistical approach was invented to describe the kinetics of intermediate energy electrons. It enabled to calculate a fraction of electrons crossing runaway threshold, as a function of the local field intensity. Runaway electrons with energies above the threshold constituted the third group. The dynamics of runaway electrons was described as one- dimensional motion of an equivalent point charge under the action of the local accelerating electric force and the retarding force due to electron-neutral particle interactions. Threshold at any given time instant was calculated from the equality of acceleration and retarding forces for each space zone of the mesh. Drift approximation was adopted to describe the kinetics of positive ions. The first Maxwell equation was solved to calculate the intensity of self-consistent electric field with standard normalization condition to the voltage realized U(t).

Equivalent electric circuit of HWV generator was used to calculate U(t). Field emission was assumed to be a source of electrons from the cathode. At the initial time instant the

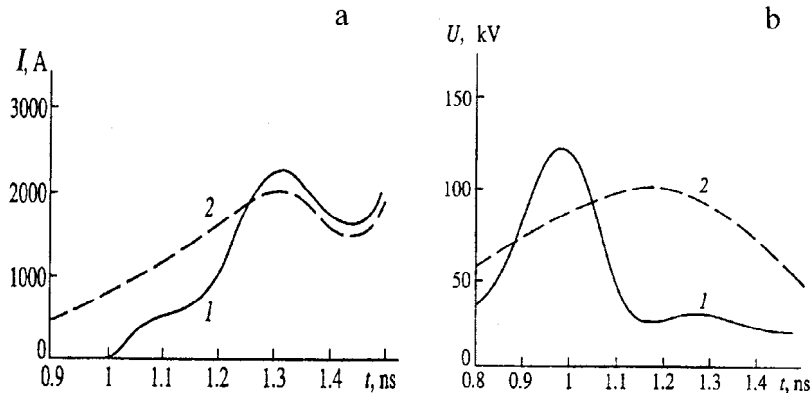

Figure 8. Calculated (1) and measured (2) total conduction current in the gas-discharge gap (a). Calculated (1) and measured (2) voltage across the gas-discharge gap (b). Helium, P = 1 atm.

gas-discharge gap was assumed to be weakly and homogeneously preionized.

A helium gap at P = 1 atm. with plane electrodes (S = 1 squire cm, d = 1 cm) was simulated. Helium was chosen due to its poorest structure of atomic states to simplify calculations of low-energy electrons. Fig. 8 demonstrate calculated and measured current I(t) and voltage U(t). In view of rather good agreement of calculated and measured I(t) the discrepancy between calculated and measured U(t) in all likelihood relates to the experimental precision available. Fig. 9a illustrating calculated current of runaway electrons, indicates that they constitute a substantial portion of the total current. The energy distribution of runaway electrons at the anode presented in Fig. 9b, demonstrates high-energy tail which actually was detected. Large value of the computed runaway electron current proved participation of runaway electrons in the dynamics of glow-like discharges at high values of the overvoltage.

CONCLUSION

The idea for electrons to runaway and the term itself were introduced in the physics of electron-neutral collision dominated plasma as early as the twenties of this century in connection with thunderstorm activity. Presently runaway electrons are acknowledged to govern the breakdown and discharges in a wide range of conditions. Preionization of a gas by runaway electrons with subsequent overlapping of secondary electron avalanches results in the development of volumetric glow-like forms of discharges. Several groups of researchers observed runaway electrons detecting secondary x-ray emission. It was observed that production of penetrating radiation correlated with development of glow-like forms of discharges in a very wide range of the gas density. Loiko succeeded to detect directly runaway electrons at STP conditions at relatively low overvoltage.[3] In a full measure this effect reveals itself at high overvoltages, as the generation of anomalous-energy electrons. At reduced gas density this effect was observed to fade away gradually. A mechanism responsible for their production is not exotic. It follows directly from the approach to the breakdown phenomenon proposed by Raether. Production of anomalous energy electrons was treated on the basis of electron acceleration self-consistent with propagation of the domain with enhanced electric

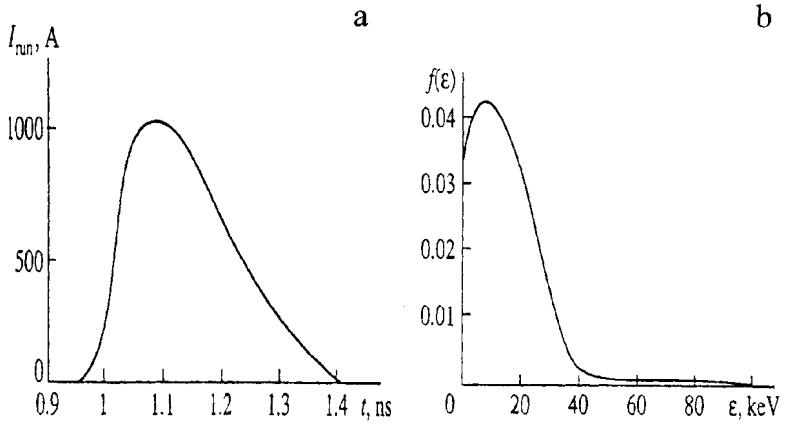

Figure 9. Current of runaway electrons (a). Energy distribution of runaway electrons (b). Helium, P = 1 atm.

field in front of the streamer head. In its turn the observation of anomalous-energy electrons is a direct evidence in favor of Raether treatment of the breakdown phenomenon itself. On the macroscopic level participation of runaway electrons in the breakdown dynamics exposed itself as a rightward displacement of the U(Pd) curve minimum as the overvoltage increased and via the inversion of the polarity effect.

Acknowledgments

The author is grateful to his colleagues Ph.D. Stankevich, Professor Tsukerman, Ph.D. Tarasova., Ph.D. Kutsyk and especially to Ph.D. Loiko for fruitful collaboration.

REFERENCES

1. C.T.R. Wilson, The acceleration of b-particles in strong electric fields such as those of thunderclouds, *Proc. Cambr: Phil. Soc.*, 22: 534, 1925.
2. A.S. Eddington, The source of stellar energy, *Supplement to Nature*, 1 2948, 25, 1926.
3. L.P Babich, T.V. Loiko, and V.A. Tsukerman, High-voltage nanosecond discharge in dense gas at high overvoltage with runaway electrons, *Sov. Phys. Usp.* 33: 521 1990.
4. L.V. Tarasova and L.N. Khudyakova, X-radiation from pulsed discharges in the air, *Sov. Tech. Phys.*, 14: 1148, 1969.
5. L.V. Tarasova, L.N. Khudyakova, T.V. Loiko, and V.A. Tsukerman, Fast electrons and X-rays from nanosecond pulse gas discharges at pressures 0.1-760 Torr, *Sov. Phys. Tech. Phys.*, 19: 351, 1975.
6. L.P. Babich and T.V. Loiko, Some features peculiar for overvoltage breakdown in sulphur hexafluoride gaps, *Proc. ICPIG XX, Piza, Italy*, 2: 46, 1991.
7. S.N. Buranov, V.V. Gorokhov, V.I. Karelin, and P.B. Repin, Fine structure of current channels and accelerated electron beams in high-voltage glow discharge at atmospheric pressure, *Proc. ICPIG XX, Piza, Italy*, 2: 464, 1991.
8. G.F. Kolbychev, An effect of utmost voltage for the breakdown in a gas gap, *Sov. Phys. Tech. Phys.* 27: 326, 1982.
9. L.P. Babich and Yu.L. Stankevich, Criterion of a transition from the streamer mechanism of gas discharge to the continuous electron acceleration, *Sov. Phys. Tech. Phys.* 17: 1333, 1972.
10. E.E. Kunhardt and W.W. Byszewski, Development of overvoltage breakdown at high gas pressure, *Phys. Rev A*, 21: 2069, 1980.

11. E.E. Kunkhardt, Y. Tzeng, and J.P Boeuf, Stochastic development of an electron avalanche, *Phys. Rev. A*, 34: 440, 1986.
12. Yu.I. Bychkov, V.V. Osipov, Yu.A. Kurbatov, and A.G. Filonov, Development of electric discharge in strongly overvoltage gaps at low air pressure, *Sov. Phys. J.*, 16: 46, 1973.
13. L.P. Babich, I.A. Berezin, T.V. Loiko, and M.D. Tarasov, A role of acceleration processes in the formation of nanosecond discharges in dense gases, *Radiophys. Quantum Electron.*, 25: 807, 1982.
14. L.P. Babich and T.V. Loiko, Energy spectra and time characteristics of runaway electrons at nanosecond breakdown in dense gases, *Sov. Phys. Tech. Phys.*, 30: 574, 1985.
15. L.P. Babich, T.V. Loiko, and L.V. Tarasova, On the generation of anomalous-energy electrons by nanosecond discharges in dense gases, *Sov. Phys. Tech. Phys.*, 23: 915, 1978.
16. V.V. Kremnev and Yu. A. Kurbatov, Study of X-radiation from gas discharge in strong electric field, *Sov. Phys. Tech. Phys.*, 17: 626, 1972.
17. W.W. Byszewski and G. Reinhold, X-ray diagnostics of runaway electrons in fast gas discharges, *Phys. Rev A*, 26: 2826, 1982.
18. Yu.L. Stankevich and V.G Kalinin, Fast electrons and X-radiation at the initial stage of pulsed spark discharge in the air, *Sov. Phys. Dokl.*, 12: 1042, 1967.
19. G.F. Kolbychev and E.A. Samyshkin, Study of volumetric gas discharge generating electron beam, *Sov. Phys. Tech. Phys.*, 26: 1185, 1981.
20. L.P Babich, T.V. Loiko, L.V. Tarasova, and VA. Tsukerman, On the origin of X-radiation and fast electrons from nanosecond gas discharges, *Sov. Tech. Phys. Lett.*, 1: 79, 1975.
21. T.V. Loiko, L.V. Tarasova, and V.A. Tsukerman, Application of high-voltage glow discharge to produce nanosecond pulses of X-rays, *Sov. Tech. Phys. Lett.*, 3: 48, 1977.
22. B.M. Kovalchuk, VA. Lavrinovich, G.A. Mesyats et. al., Breakdown in nitrogen and its mixtures with oxygen and sulphur hexafluoride in a strongly non-uniform electric field at nanosecond voltage pulsing, *Proc. ICPIG XVI, Dusseldorf, Germany*, 120, 1983.
23. L.D. Tsendin, Energy distribution of electrons in a weakly ionized current-carrying plasma with a transverse inhomogeneity, *Sov. Phys. JETP*, 39: 805, 1974.
24. L.D. Tsendin and Yu.B. Golubovskii, Positive column of a low-density, low-pressure discharge. I. Electron energy distribution, *Sov. Phys. Tech. Phys.*, 22: 1066, 1977.
25. U. Kortshagen, A non-local kinetic model applied to microwave produced plasmas in cylindrical geometry, *J. Phys. D.*, 26: 1691, 1993.
26. J. Ingold, Nonequilibrium motion of electrons and ions near absorbing boundaries, IN C.M. Ferreira and M. Moisan, editors, *Microwave Discharges. Fundamentals and Applications*, Plenum Press, New York, 1993.
27. V.I. Kolobov and V.A. Godyak, Non-local kinetics in collisional gas discharge plasmas, *IEEE Trans. Plasma Sci.*, 1995.
28. U. Kortshagen and L.D. Tsendin, Fast two-dimensional self-consistent modelling of low-pressure inductively coupled RF discharges, *Appl. Phys. Let.*, 65: 1355, 1994.
29. L.P. Babich and I.M. Kutsyk, Computer simulation of a nanosecond discharge in helium at atmospheric pressure developing in the regime of runaway electrons, *High Temperature*, 33: 190, 1995.

THE DYNAMICS OF FERMI ACCELERATION

M. A. Lieberman

Department of Electrical Engineering and Computer Sciences
University of California
Berkeley, CA

1. INTRODUCTION

1.1. Cosmic Rays: Discovery and Properties

In the morning of August 7, 1912, Austrian physicist Viktor Hess ascended to over five kilometers in a balloon gondola as "an observer for atmospheric electricity."[3,4] During the journey, he made careful measurements of the rate of discharging of three electroscopes, and he noted a several-fold increase in the rate of discharging as the balloon rose in altitude. In his publication in Physikalische Zeitschrift in November 1912, Hess suggested that the results of his observations were best explained "by a radiation of great penetrating power entering our atmosphere from above." Further flights confirmed these findings, and the American physicist Robert Millikan, although initially skeptical of the extraterrestrial origin, introduced the name *cosmic rays.*

It is now generally agreed that the majority of cosmic rays have a galactic origin. The cosmic ray flux is isotropic and of order 1 $\mathrm{cm}^{-2}\ \mathrm{s}^{-1}$, the energy density is approximately 1 eV/cm³, and the lifetime is approximately 107 years. Cosmic rays are mostly protons, but are rich in heavy nuclei compared to solar abundances. The particle energies range from $W \sim 10^{8}$–10^{20} eV, with a power law distribution $N(W) \propto W^{-(2-2.5)}$.

Cosmic rays are believed to originate from supernovas such as the well-studied Crab nebula, which is the remnant of a supernova in 1054 A.D. With one galactic supernova every fifty years within a galactic disk volume of 10^{67} cm³ creating 10^{43} J of fast particles, the energy balance is

$$\frac{10^{43}\ \mathrm{J}}{50\ \mathrm{yrs}} \approx \frac{e \times 1\ \mathrm{eV/cm^3} \times 10^{67}\ \mathrm{cm^3}}{10^{7}\ \mathrm{yrs}}.$$

Measurements of radiation from supernova remnants clearly show the presence of synchrotron radiation, demonstrating the existence of high-energy ($> 10^{11}$ eV) electrons. Exactly how the fast particles are formed and accelerated is not well understood. Early theories emphasized acceleration across high voltages or by means of shock waves.

Electron Kinetics and Application of Glow Discharges
Edited by U. Kortshagen and L. D. Tsendin, Plenum Press, New York, 1998

1.2. Fermi's Proposal

In 1949, Fermi[2] put forth the idea that "cosmic rays are originated and accelerated primarily in the interstellar space of the galaxy by collisions against moving magnetic fields." He went on to assert the basic acceleration mechanism as follows:

> It may happen that a region of high field intensity moves toward the cosmic-ray particle which collides against it. In this case, the particle will gain energy in the collision. Conversely, it may happen that the region of high field intensity moves away from the particle. Since the particle is much faster, it will overtake the irregularity of the field and be reflected backwards, in this case with loss of energy. The net result will be average gain, primarily for the reason that head-on collisions are more frequent than overtaking collisions because the relative velocity is larger in the former case.

Fermi noted that this idea naturally leads to a power law energy distribution, but that it fails to explain in a straightforward way the heavy nuclei observed in the primary cosmic radiation.

2. FERMI ACCELERATION

2.1. Fermi Maps and Dynamical Chaos

The Fermi problem of a particle bouncing between a fixed and an oscillating wall, illustrated in Fig. 1, has become a paradigm problem in dynamics. This model of energy gain by repeated collisions of a particle with an oscillating wall was examined numerically by Ulam and associates,[15] who found that the particle motion appeared to be stochastic, but did not increase its energy on the average. Ulam's result was explained using a combination of analytical and numerical work by subsequent authors. The Fermi problem was treated using an exact area-preserving dynamical mapping for a sawtooth wall velocity by Zaslavskii and Chirikov.[17] Similar studies were performed by Brahic.[1] A "simplified" mapping, in which the oscillating wall imparts momentum to the particle but occupies a fixed position, was introduced by Lieberman and Lichtenberg[10] and studied for arbitrary wall velocities (Ref. 8; see also Ref. 7, Sec. 3.4).

To find the exact mapping dynamics for this system, we introduce a fixed surface of section at some $x =$ const. Defining $u_n = v_n/2\omega a$ to be the normalized velocity and $\theta n = \omega t$ to be the phase of the moving wall at the nth collision with the fixed surface at $x = 0$, then a difference equation for the motion of the particle can be determined in terms of a wall motion $x_w(t) = aF(\psi)$, where F is an even periodic function of the phase $\psi = \omega t$, with period 2π and with $F_{max} = -F_{min} = 1$. We obtain, in implicit form the equations of motion

$$u_{n+1} = u_n + F'(\psi_c), \tag{1a}$$

$$\theta_{n+1} = \psi_c + \frac{[2\pi M - \frac{1}{2}F(\psi_c)]}{u_{n+1}}, \tag{1b}$$

$$\psi_c = \theta_n - \frac{1}{2}\frac{F(\psi_c)}{u_n}. \tag{1c}$$

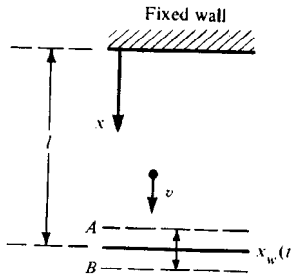

Figure 1. Fermi acceleration in which a particle bounces between a fixed and an oscillating wall.

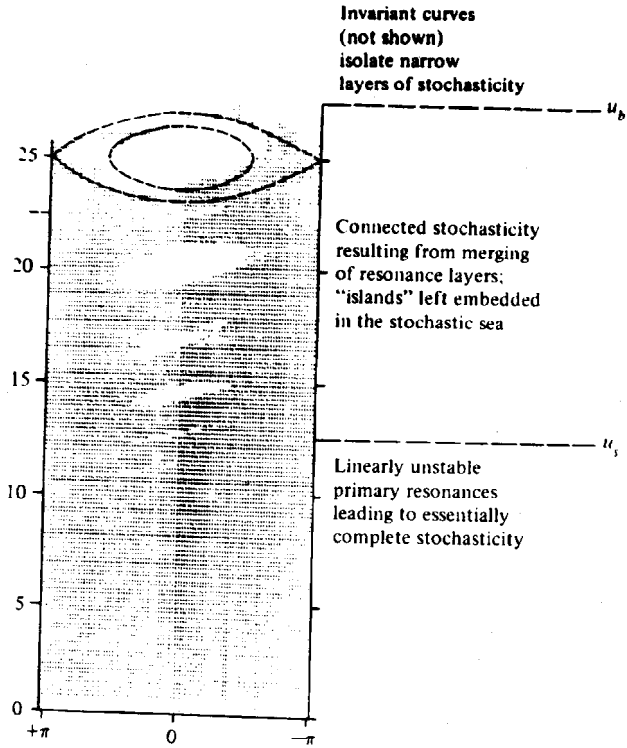

Figure 2. Surface of section for the Fermi problem, showing occupation of phase space cells for 623,000 iterations of a single initial condition. Dashed curves are calculated from secular perturbation theory (after Ref. 10).

Here ψ_c is the phase at the next collision with the moving wall, after the nth collision with the fixed surface $x = 0$; $M = l/2\pi a$, with l the distance between the walls; and $F' = dF/d\psi$ is the velocity impulse given to the ball. In this form it is easy to see that measuring the distance from the fixed wall as x, conjugate to v, then the phase θ is a time-like variable conjugate to the energy-like variable $\omega = u^2$. That is, in the extended phase space $(\psi, x, -\omega, t)$, the choice of a surface $x = 0$ gives an area-preserving mapping for the remaining pair $(-\omega, t)$. As we show in Section 1.2, this implies that a stochastic orbit has a uniform invariant distribution over the accessible (ω, θ) phase space. Hence, assuming all phases are accessible, the energy ω has a uniform invariant distribution.

Because of its implicit form, (1) is not convenient for. numerical or analytical study. Substituting $\omega = u^2$, assuming a sinusoidal wall motion in (1), and expanding to first order in F' (and F), we obtain

$$w_{n+1} = w_n + 2\sqrt{w_n}\sin\theta_n, \tag{2a}$$

$$\theta_{n+1} = \theta_n + \frac{2\pi M}{\sqrt{w_{n+1}}} + \frac{\cos\theta_n}{\sqrt{w_{n+1}}}. \tag{2b}$$

A still simpler form can be constructed if the sinusoidally oscillating wall imparts momentum to the ball, according to the wall velocity, without the wall changing its position in space. The problem defined in this manner has many of the features of the more physical problem. In this simplified form the mapping is

$$u_{n+1} = |u_n + \sin\psi_n|, \tag{3a}$$

$$\psi_{n+1} = \psi_n + \frac{2\pi M}{u_{n+1}} \pmod{2\pi}. \tag{3b}$$

The mapping in (3) serves as an approximation (with suitably defined variables) to many physical systems in which the transit time between kicks is inversely proportional to a velocity. The absolute-value signs in (3) correspond to the velocity reversal, at low velocities $u < 1$, which appears in the exact equations (1). The absolute value has no effect on the region $u > 1$, which is the primary region of interest. For the simplified problem, a proper canonical set of variables are the ball velocity and phase just before the nth impact with the moving wall. The normalized velocity u then has a uniform invariant distribution, as will be seen in Section 1.2.

Transformations of the type (1)–(3) can be examined numerically for many thousands of iterations, thus allowing both detailed knowledge of the structural behavior and statistical properties of the dynamical system to be determined. Figure 2 shows the u–ψ) surface for the simplified Fermi map (3) with $M = 100$ for 623,000 wall collisions of a single trajectory, with an initial condition at low velocity $u_0 \approx 1$. The surface has been divided into 200×200 cells, with a blank indicating no occupation of that cell. We find that the phase plane consists of three regions:

1. a region for large u, $u > u_b = \sqrt{2\pi M}$, in which invariant adiabatic curves predominate and isolate narrow layers of stochasticity near the separatrices of the various resonances;

2. an interconnected stochastic region for intermediate values of u, $u_s \approx \frac{1}{2}u_b < u < u_b$, in which adiabatic islands near linearly stable periodic solutions are embedded in a stochastic sea; and

3. a predominantly stochastic region for small u, $u < u_s$, in which all primary periodic solutions appear to be unstable.

Both regions (2) and (3) exhibit strong or *global stochasticity* of the motion. In the latter region, although some correlation exists between successive iterations, over most of the region it is possible to approximate the dynamics by assuming a *random phase approximation* for the phase coordinate, thus describing the momentum coordinate by a diffusion equation. We explore this question more fully in the next subsection.

2.2. The Fokker–Planck Equation

In regions of the phase space that are stochastic or mostly stochastic with small isolated adiabatic islands, it may be possible to describe the evolution of the distribution function in action space (or velocity space) alone. This is, in fact, the problem of most practical interest. In the Fermi acceleration problem, for example, the motivation was to find a possible mechanism for heating of cosmic rays. The variations in the phases of the particles with respect to their accelerating fields are of little interest except as they are required for determining the heating rates and the final energy distribution.

Let us consider in what sense the evolution of the distribution function $f(u, n)$ can be described by a stochastic process in the action u alone. Clearly we must confine our attention to a globally stochastic region of the phase space in which adiabatic islands do not exist or occupy negligible phase space volume. In such a region, it may be possible to express the evolution of $f(u, n)$, the distribution in u alone, in terms of a Markov process in u [16]:

$$f(u, n + \Delta n) = \int f(u - \Delta u, n) W_t(u - \Delta u, n, \Delta u, \Delta n)\, d(\Delta u), \tag{4}$$

where $W_t(u, n, \Delta u, \Delta n)$, the transition probability, is the probability that an ensemble of phase points having an action u at a "time" n suffers an increment in action Δu after a "time" Δn. If we make the additional assumption that there exists an intermediate time scale $\Delta n >> 1$ such that $\Delta u \ll (f^{-1} df/du)^{-1}$, then we can expand the first argument of the integrand $f W_t$ in (4) to second order in Δu to obtain the Fokker–Planck equation

$$\frac{\partial f}{\partial n} = -\frac{\partial}{\partial u}(Bf) + \frac{1}{2}\frac{\partial^2}{\partial u^2}(Df). \tag{5}$$

For Hamiltonian systems, the friction coefficient B and the diffusion coefficient D are related[6] as

$$B = \frac{1}{2}\frac{dD}{du}, \tag{6}$$

allowing (5) to be written in the form of a diffusion equation

$$\frac{\partial f}{\partial n} = \frac{\partial}{\partial u}\left(\frac{D}{2}\frac{\partial f}{\partial u}\right). \tag{7}$$

Assuming that phase randomization occurs on the time scale Δn, then we can average Δu over a uniform distribution of phases to obtain

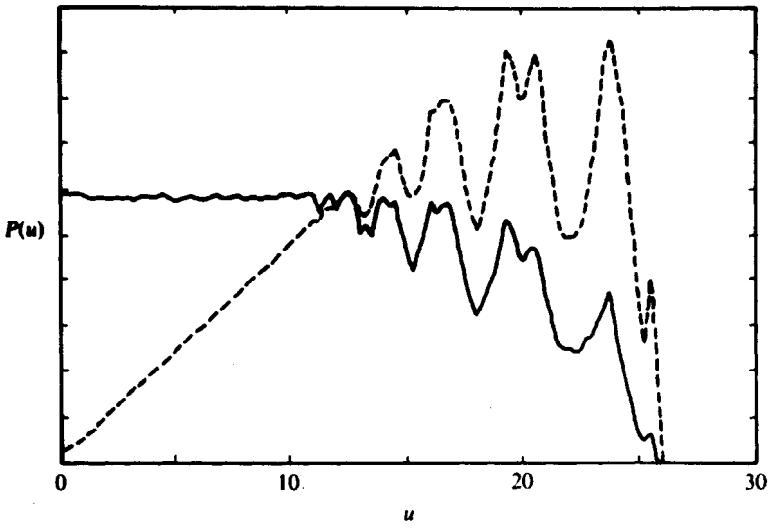

Figure 3. Comparison of velocity distribution $f(u)$ [here $P(u)$] for the simplified Fermi map (3) [solid line] and the exact Fermi map (1) [dashed line] (after Ref. 7).

$$D(u) = \frac{1}{2\pi}\int_0^{2\pi} d\psi[\Delta u(\psi)]^2. \tag{8}$$

$B(u)$ is then obtained directly from (6).

For the simplified Fermi map (3) with sinusoidal velocity, for which $\Delta u = \sin\psi$, we obtain $D = \frac{1}{2}$ and $B = 0$. Hence the Fokker–Planck equation for the velocity distribution is

$$\frac{\partial f}{\partial n} = \frac{1}{4}\frac{\partial^2 f}{\partial u^2}. \tag{9}$$

Similarly, for the Fermi map (2), we obtain

$$\bar{D} = \frac{1}{2\pi}\int_0^{2\pi} 4w\cos^2\theta\, d\theta = 2w \tag{10}$$

and the Fokker–Planck equation for the energy distribution g is, from (7)

$$\frac{\partial g}{\partial n} = \frac{\partial}{\partial w}\left(w\frac{\partial g}{\partial w}\right). \tag{11}$$

To obtain a steady-state solution to the Fokker–Planck equation, we assume perfectly reflecting barriers at $u = 0$ and $u = u_b$. Setting $\partial/\partial n = 0$ in (9) and taking the net flux to be zero, we obtain a uniform invariant distribution in velocity $f(u) = \text{const}$ for the simplified map. For the map (2), we obtain similarly a uniform invariant distribution in energy $g(\omega) = \text{const}$. Introducing the velocity distribution $f(u)$ for (2) through

$$f(u)\,du = g(w)\,dw \tag{12}$$

and using $d\omega = u\,du$, we see that $f(u) = \text{const} \times u$ for (2). In Fig. 3 we compare the numerically calculated distributions for $M = 100$ and 5×10^6 interactions with these

predictions. In the region below $u_s = (\pi M/2)^{1/2} \approx 12.5$, the predictions are verified. Above u_s, the distributions both fall off due to the presence of islands and higher-order correlations in the phase space, with the dips near the island centers.

We can also solve the transient Fokker–Planck equation. For the simplified Fermi mapping (3), with initial conditions of a δ-function at $u = 0^+$, we can solve (9) to obtain

$$f(u,n) = \frac{2}{(\pi n)^{1/2}} \exp\left(-\frac{u^2}{n}\right), \tag{13}$$

which yields the distribution function for the transient heating of the particles. This time development only holds, of course, until the particles begin to penetrate into the region with islands, $u > u_s$.

2.3. Reduction to the Standard Mapping

The complete dynamics, including the transition region with adiabatic islands embedded in a stochastic sea, is very complicated and can only be solved numerically. To gain some understanding of the diffusion in the phase space region where correlations are important, it is convenient to first transform the Fermi map to a local map near a resonance. Taking the simplified Fermi map of (3), we obtain the so-called *standard mapping* by linearization in action space near a given period-1 fixed point. These are located at

$$\frac{2\pi M}{u_1} = 2\pi m, \qquad m \text{ integer}. \tag{14}$$

Putting $u_n = u_1 + \Delta u_n$ and shifting the angle

$$\theta_n = \psi_n - \pi, \qquad -\pi < \theta_n < \pi,$$

then the mapping equations take the standard form

$$I_{n+1} = I_n + K \sin\theta_n, \tag{15a}$$

$$\theta_{n+1} = \theta_n + I_{n+1}, \tag{15b}$$

where

$$I_n = -\frac{2\pi M \Delta u_n}{u_1^2} \tag{16}$$

is the new action and

$$K = \frac{2\pi M}{u_1^2} \tag{17}$$

is the *stochasticity parameter*. We have thus related K to the old action u_1. The conversion from Fermi to standard mapping is illustrated in Fig. 4 for two different values of u_1, leading to two different values of K.

The dynamics of the standard mapping (15) can be considered to evolve on a two-torus, with both θ and I taken modulo 2π. The periodicity of the mapping in I gives rise to a special type of periodic orbit (period-l fixed point) in which I advances by $\pm 2\pi$ every iteration of the mapping. The condition for these so-called *accelerator modes* is that $I_{1l} = 2\pi m$ and $K \sin\theta_{1l} = 2\pi l$, m and l integers, with $l \neq 0$. The accelerator modes are stable provided $|2 \pm K\cos\theta_{1l}| < 2$, which implies that stability

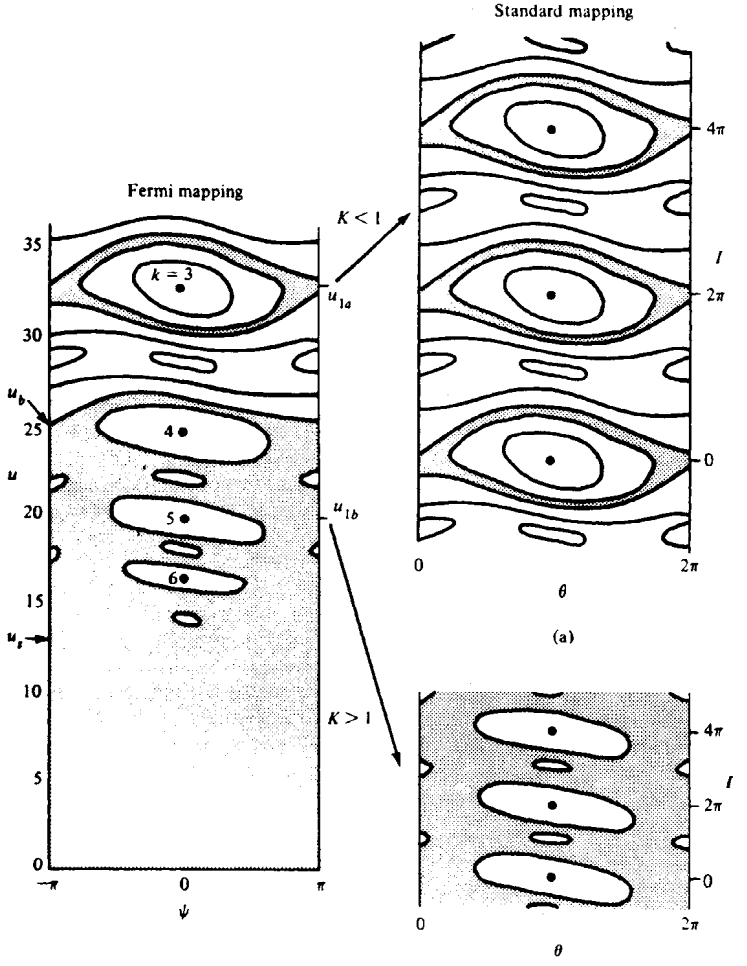

Figure 4. Local approximation of the Fermi mapping by the standard mapping. (a) Linearization about u_{1a} leading to K small and local stochasticity; (b) linearization about u_{1b} leading to K large and global stochasticity (after Ref. 7).

windows for period-l fixed points exist for successively higher values of K as I increases ($\cos\theta_{1l}$ decreases). As we will see below, remnants of these accelerator modes, called *quasi-accelerator modes,* can exist in the Fermi mapping.

The transport coefficients for the standard mapping (15) are $D_I = K^2/2$ and $B_I = 0$. Since this mapping locally approximates the Fermi mapping, we can relate D_I to D for the Fermi mapping. Using $\Delta I = -K\Delta u$, we find that the diffusion coefficients are related by

$$D(u) = \frac{D_I(K(u))}{K^2(u)} \tag{18}$$

2.4. The Effects of Correlations

The island structure embedded in the Fermi stochastic sea is exceeding complex, and, in fact, has fractal properties. We might expect this structure to lead to long

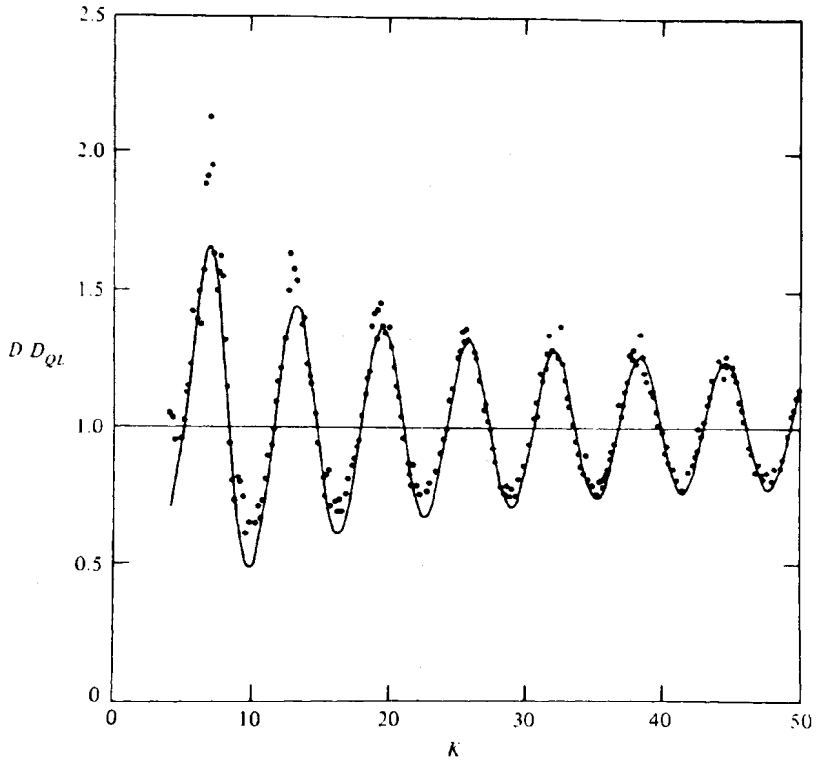

Figure 5. Plot of D/D_{QL} versus stochasticity parameter K. The dots are the numerically computed values and the solid line is the theoretical result in the large K limit (after Ref. 13).

time correlation of stochastic orbits in the neighborhood of adiabatic orbits, and this is in fact what happens. The quasilinear transport coefficients are determined using the random phase assumption applied to a single step jump in the action $\Delta u_1 = u_1 - u_0$. However, as pointed out in Section 1.2, the Fokker–Planck description of the motion is valid only in the limit $n >> n_c$, where n_c is the number of steps for phase randomization to occur. We should therefore consider the jump $\Delta u_n = u_n - u_0$, where $n > n_c$. This was first done using Fourier techniques for the standard mapping in the limit of large K by Rechester and White[13] and for any K by Rechester et al.[14] To order K^{-1}, the result is (Ref. 7, Sec. 5.5a):

$$D_n = D_{QL}[1 - 2\mathrm{J}_2(K) - 2\mathrm{J}_1^2(K) + 2\mathrm{J}_2^2(K) + 2\mathrm{J}_3^2(K)], \tag{19}$$

where $D_{QL} \equiv D_I/2 = K^2/4$ and the J's are Bessel functions. A numerical calculation of D_{50} using 3000 particles is compared with (19) in Fig. 5.[13] There is good agreement, except near the first few peaks of D. As we will see below, these are due to the presence of *accelerator modes*. For K near but greater than the critical value $K_c \approx 0.9716$, one finds numerically that

$$D_\infty \approx 0.1(K - K_c)^3. \tag{20}$$

For $K < K_c$, an adiabatic (invariant) barrier exists and there is no long-time diffusion.

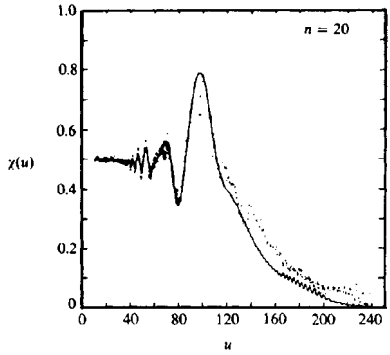

Figure 6. The variance plotted as a function of initial action. Each dot corresponds to a measurement of the diffusion obtained by iterating the Fermi map for 20 iterations. The solid line is the theoretical variance obtained by integrating the Fokker–Planck equation (after Ref. 12).

For the Fermi map in which the phase is randomized within a region of the velocity space for which the local approximation gives a near-constant stochasticity parameter K, it is possible to derive a local (in velocity) diffusion coefficient.[12] In this regime, for which $(1/f)(\partial f/\partial u) \ll K(u)/2\pi$, the diffusion coefficient becomes, using (18),

$$D_\infty(u) = \frac{D_\infty(K(u))}{K^2(u)}. \tag{21}$$

Let us note that if we are interested in using the Fermi map to model a heating mechanism, then particles will generally start at low velocities, where the stable islands have negligibly small area. As the particles are heated they enter regions of phase space within which large islands exist. Without extrinsic stochasticity, the particles will not penetrate these islands. Hence, although the equilibrium distribution is uniform in the ergodic phase space surrounding the islands, the phase-averaged distribution $f(u, n)$ will not be uniform, as is seen in Fig. 3. To correct for this effect, one must divide $D_\infty(u)$ by the fraction ion of phase space occupied by stochastic orbits. The details of the calculation are described in Murray et al.[12]; see also Lichtenberg and Lieberman.[7]

Figure 6 shows a calculation of the variance of $f(u, n)$ determined numerically by directly iterating the Fermi map and by integrating the Fokker–Planck equation with a delta function initial condition at action u_0.[12] There is good agreement between the diffusion theory and the actual behavior of the map.

As noted previously, the standard mapping (15) has stable periodic orbits, the *accelerator modes*, in which the action I advances by $\pm 2\pi$ for every mapping iteration. Such a mode is born at an inverse tangent bifurcation at $K = 2\pi l$ and period doubles at $K = \sqrt{(2\pi l)^2 + 16}$. The first mode ($l = 1$) has the largest stable range of K values and the largest maximum island size, and consequently is most important for modifying the local diffusion. The fixed points are located at $I_l = 2\pi m$, $K \sin \theta_l = 2\pi l$. For each I_l within the window, there are two θ_l's, corresponding to two islands side-by-side whose centers stream up and down in I respectively in the phase space, advancing by $\Delta I = \pm 2\pi l$ each iteration. Hence phase points, trapped within the stable islands about these fixed points, stream rather than diffuse in action, leading to a singularity in the usually defined diffusion. This singularity is clearly visible as an increase in the numerically determined diffusion coefficient at the peaks in D shown in Fig. 5.

For the simplified Fermi map (15), we see from (17) that K depends on u, and therefore the effective K of the mapping of a given trajectory changes as it diffuses or streams. Since K changes, the accelerator modes of the Fermi map are not truly stable,

and may be designated as *quasi-accelerator modes.* The larger the mapping parameter M, the longer the dynamics remains near a given value of K over a range of u-values.

For quasi-accelerator modes, there are two mechanisms by which diffusion is enhanced (Ref. 9; see also Ref. 7, Sec. 5.5d):

1. Particles on locally unstable orbits become trapped on locally stable orbits as they are transported in the direction of increasing stable island size. They then stream through values of u corresponding to increasing and then decreasing island size until they are detrapped at values of u having the same island size at which they were originally trapped.

2. Trajectories near stable islands are only weakly unstable, and therefore shadow the stable trajectories over many mapping periods. This leads to long-time correlations in the phase which again result in streaming.

3. CONCLUDING DISCUSSION

Fermi acceleration has been a fruitful approach to understand the dynamics of the heating of particles by periodic fields. In this work we have reviewed the purely dynamical mechanisms by which such heating takes place. However, let us note that in many applications, such as the heating of electrons in weakly ionized gas discharges, the *extrinsic stochasticity* associated with electron-electron, electron-ion, and electron-neutral collisions can play a critical, and in many cases dominating role. The interplay between the intrinsic dynamical chaos and the extrinsic chaos due to collisions has received much attention both in the dynamics community (see Ref. 7, Sec. 5.6) and in the discharge heating community.[5,11]

The author gratefully acknowledges discussions with R. W. Boswell, V. A. Godyak and A. J. Lichtenberg. This work was partially supported by NSF Grant ECS-9217500 and by the Lam Research Corporation. The author also acknowledges the support of the National Science Foundation Division of International Programs during his sabbatical leave visit to The Australian National University.

REFERENCES

1. Brahic, A. *Astron. Astrophys.* **12,** 98 (1971).
2. Fermi, E. *Phys. Rev.* **75,** 1169 (1949).
3. Friedlander, M. W. *Cosmic Rays,* Harvard University Press, Cambridge (1989).
4. Harwit, M. *Cosmic Discovery — The Search, Scope, and Heritage of Astronomy,* MIT Press, Cambridge (1984).
5. Kagonovich, I. D., V. I. Kolobov and L. D. Tsendin *Appl. Phys. Lett.* **69,** 3818 (1996).
6. Landau, L. D. *Zh. Eksper. Theor. Fiz.* **7,** 203 (1937).
7. Lichtenberg, A. J. and M. A. Lieberman *Regular and Chaotic Dynamics,* Springer-Verlag, New York (1992).
8. Lichtenberg, A. J., M. A. Lieberman and R. H. Cohen *Physica* **1D,** 291 (1980).
9. Lichtenberg, A. J., M. A. Lieberman and N. W. Murray *Physica* **28D,** 371 (1987).
10. Lieberman, M. A. and A. J. Lichtenberg, (1972).
11. Lieberman, M. A. and A. J. Lichtenberg *Principles of Plasma Discharges and Materials Processing,* J. Wiley, New York (1994).
12. Murray, N. W., M. A. Lieberman and A. J. Lichtenberg *Phys. Rev. A* **32,** 2413 (1985).
13. Rechester, A. B. and R. B. White *Phys. Rev. Lett.* **44,** 1586 (1980).
14. Rechester, A. B., M. N. Rosenbluth and R. B. White *Phys. Rev. A* **23,** 2664 (1981).
15. Ulam, S. M., *Proceedings of the 4th Berkeley Symposium on Mathematical Statistics and Probability,* Vol. 3, p. 315 (University of California Press, Berkeley) (1961).
16. Wang, M. C. and G. E. Uhlenbeck *Phys. Rev.* **188,** 416 (1945).
17. Zaslavskii, G. M. and B. V. Chirikov *Soviet Phys. Dokl.* **9,** 989 (1965).

This Page Intentionally Left Blank

APPLICATION OF MAPPING DYNAMICS TO ANALYSIS OF A CAPACITIVE RF DISCHARGE

Allan J. Lichtenberg,[1] Ronald Cohen,[2] and Zuoding Wang[1]

[1]University of California
Berkeley, CA
[2]Lawrence Livermore National Laboratory
Livermore, CA

1. INTRODUCTION

For low pressure capacitive rf discharges stochastic electron heating in the sheath is generally the dominant heating mechanism. Energy is either added or subtracted from each electron as it is reflected from a high voltage sheath, depending on whether the sheath edge is moving toward the plasma (expanding sheath) or away from the plasma (contracting sheath), respectively. The mechanism, originally proposed by Fermi[1] as a method for cosmic ray production, is known as Fermi acceleration. This energy transfer mechanism was applied to rf discharges by Godyak and associates,[2–7] by Akhiezer and Bakai,[8] and by Kushner,[9] using the assumption of phase randomization at each sheath collision. It is well known, however, that depending on the parameters, there is an energy transition between regular and stochastic particle motion, which may serve as a barrier to the heating.[10]

Goedde, Lichtenberg, and Lieberman[11] studied the interaction of the electrons with the sheath and developed a simplified self-consistent discharge heating model. They assumed that the electron energy change from any single collision is small, all electrons interacted with a sinusoidally oscillating sheath, and the only loss mechanism was escape to the walls. For a near-collisionless plasma they determined the discharge parameters for which the particle-sheath interaction had randomized phase at the energies of interest. Using those parameters, they calculated a power-law electron energy probability function (EEPF).

Along with the theoretical development, experiments and particle-in-cell (PIC) simulations have been performed to determine the stochastic heating and the EEPF. In experimental investigations, Popov and Godyak[5] showed the general correctness of the notion that the interaction of the electrons with the plasma sheath can serve as the main source of energy transfer at low pressures. Godyak and associates[6, 7] have measured non-Maxwellian electron distributions in rf capacitive discharges, which, at low pressure, can be approximated by bi-Maxwellian electron distributions or by power-law distributions.

Electron Kinetics and Application of Glow Discharges
Edited by U. Kortshagen and L. D. Tsendin, Plenum Press, New York, 1998

Kushner[9] found, in a Monte-Carlo simulation model, that electron reflection from the oscillating sheaths leads to an enhancement of the high energy tail of the distribution. Subsequent Particle-in-Cell (PIC) Monte-Carlo models have also found electron energy probability distribution functions which can be approximated by either two-temperature Maxwellians or power-law distributions.[12–15]

Because of the Child–Langmuir type of ion distribution in the sheath, the sheath oscillations are non-sinusoidal, and have an amplitude which is much larger than that which would exist if the ions had a uniform density equal to the value at the plasma-sheath interface. This results in enhanced stochastic heating, but also greatly complicates the analysis. Lieberman[16] developed a partially self-consistent heating model in the regime of collisionless ions at high voltages, in which the sheath oscillations are non-sinusoidal, as determined by the ion distribution. In order to make the analysis tractable, the phase of the sheath oscillation at each electron-sheath collision was assumed to be random, and the electron distribution was taken to be Maxwellian. The phase randomization is found to be satisfied by collisional scattering if the pressure is not too low, e.g. for a 10 cm. length Argon discharge at 13.56 MHz applied frequency, if the pressure is 10 mTorr or higher (as we discuss below). The assumption of a Maxwellian EEPF is not, however, justified, as described above. The effect on the heating of using other EEPF's has been explored[17] but the analysis was not fully self-consistent.

To obtain a self-consistent distribution the electron kinetic equation must be solved. Simplified kinetic treatments of plasma discharges have been developed for higher pressures at which the electrons are heated by ohmic heating. The analysis, called a non-local treatment, was originally applied to dc discharges by Bernstein and Holstein[18] and by Tsendin,[19] and has been extended to treat rf discharges by Kaganovich and Tsendin.[20] The basic idea is that electron-neutral scattering can isotropize the electron distribution, but, due to the large mass ratio, does not greatly affect the energy distribution in the elastic energy range. The effect of static potentials does not change the local total electron energy (kinetic plus potential). This formalism allows space and time averages to be performed. Comparisons with simulations and experiments have been made by Kortshagen.[21] The method, as applied to a variety of discharges, has been reviewed by Kolobov and Godyak.[22] Unfortunately, in the presence of sheath heating, at low pressure, there are additional complications that make a kinetic treatment much more difficult. Kaganovich and Tsendin[23] formally introduced the equations required to treat this problem, including an assumption about how the potential structure in the plasma determines the extent to which particles experience the stochastic heating field. However, they did not obtain solutions to the resulting complicated set of equations.

In a separate paper[24] we have introduced additional approximations into the general formalism so that the EEPF, the electron heating rate, and the electron and ion loss rates can be obtained, with a minimum of numerical calculations. Our principal assumption is that the discharge can be stratified into: (1), an energy region in which low temperature electrons are produced by ionization, or injected by excitation and ionization cooling of the hotter species; and (2), an energy region at which the hotter electrons interact with the oscillating sheath to be heated and lost to the electrodes. The hotter and cooler species interchange energy by collisional processes and diffusion across the interface in velocity space. To simplify the calculation, the cooler species are assumed to be held in by a square-well potential. Below the loss boundary and the threshold for excitation the hotter species exhibits a power-law stochastic-heating distribution as found previously.[11] In the region above these energies the tail of the distribution drops more rapidly than a power law, and can be approximated by a

Maxwellian which is usually at a higher temperature than the particles which are not stochastically heated. In addition to the main stochastic sheath heating, there is also ohmic heating which can have an important effect on low energy electrons which do not reach the sheaths. The analysis was not fully self consistent in that a relationship to determine the square-well potential was not available. The use of an experimental electron density supplied the necessary information, and also allowed us to develop a heuristic ansatz for the potential. Here we introduce a self-consistent determination of the potential, in an average sense, which makes the analysis fully self-consistent. A second limitation of our previous analysis is the assumption that the phase of the oscillating wall is randomized between each successive electron bounce. Here we will be more explicit in determining the time for randomization, depending both on the dynamics and on the collisionality.

2. MAPPING DYNAMICS

2.1. Sheath Dynamics

For an applied rf discharge voltage $V = V_{\mathrm{rf}} \cos \omega t$, the voltage across one of the sheaths is, approximately, $V_{\mathrm{sheath}} \approx V_{\mathrm{dc}} + V_1 \cos \omega t, \quad V_1 = V_{\mathrm{rf}}/2$. Using continuity of current and assuming that the electrons move as a body with respect to the rf field, if we ignore ion-space charge in the sheath as a first approximation, the sheath electric field is a constant $E = V_{\mathrm{dc}}/s_0$, and the sheath thickness follows the voltage as

$$s(t) \approx s_0 \left[1 - (V_{\mathrm{rf}}/V_{\mathrm{dc}}) \cos(\omega t)\right]. \tag{1}$$

where s_0 is half of the maximum sheath width as determined from the Child–Langmuir relation. The equation of motion for an electron in the sheath is, then $md^2x/dt^2 = -eV_{\mathrm{dc}}/s_0$. Introducing the dimensionless parameters $a = m\omega^2 s_0^2/eV_{\mathrm{dc}}, \beta = V_{\mathrm{rf}}/V_{\mathrm{dc}}, \epsilon = s_0/L$, and the dimensionless position δ and time, $\delta = x/s_0, \tau = \omega t$, then in terms of these variables, the equation of motion becomes

$$d^2\delta/d\tau^2 = 1/a. \tag{2}$$

Integrating (2) once gives the velocity of an electron as it moves through the sheath

$$\mu(\tau) = \mu(0) - \tau/a, \tag{3}$$

where $\mu \equiv d\delta/d\tau$ is the dimensionless velocity. Integrating again gives the position of an electron as a function of time in the sheath

$$\delta(\tau) - \delta(0) = -\tau^2/2a + \mu(0)\tau. \tag{4}$$

Here $\delta(0) = -\beta \cos \phi$ and $\delta(\tau) = -\beta \cos(\tau + \phi)$ are the positions of the sheath boundary when the electron enters and leaves the sheath. Equation (4) is a transcendental equation for the electron transit time τ for a single pass through the sheath. Using this value of τ in (3) yields the change in velocity due to each interaction with the sheath. This model yields a mapping that to lowest order becomes the simplified Fermi acceleration problem of a ball bouncing between a fixed and an oscillating wall.[10]

2.2. The Mapping

For a collisionless plasma, the motion occurs in two distinct parts: the unperturbed motion through the bulk plasma, where the electron velocity is constant, and the rapidly

varying velocity region in the sheath. The combination of the two regions constitutes a mapping of the velocity and phase of the motion between successive entries into the sheath region, labeled by integers n, $n+1$, etc., with $\mu(0) = \mu_n$ and $\mu(\tau) = -\mu_{n+1}$ in (3). If $\epsilon << 1$ then the zero-order phase advance equation is

$$\phi_{n+1} = \phi_n + 1/\epsilon\mu_{n+1} \tag{5}$$

and to lowest order in τ, (3) yields

$$\mu_{n+1} = -\mu_n + \frac{2(\mu_n - \beta \sin \phi_n)}{1 + \alpha\beta \cos \phi_n}, \tag{6}$$

Eqs. (5) and (6) constitute the lowest order mapping. For measure preservation, the change in phase must also be determined to first order. Furthermore, the variables μ and ϕ are not canonically conjugate in a Hamiltonian sense.[11] For the surface of section at a constant position, the electron energy $\mathcal{E}$ and the crossing time t are canonically conjugate; the equivalent normalized variables are $\varepsilon = \mu^2$ and $\phi = \omega t$. The Hamiltonian mapping is area preserving in these canonically conjugate variables. Assuming $\varepsilon_{n+1} - \varepsilon_n << \varepsilon_n$, expanding (6) for small α, and determining the first-order change in phase in the usual manner[10] to ensure area preservation, (6) and (5) become

$$\varepsilon_{n+1} = \varepsilon_n - 4\beta\sqrt{\varepsilon_{n+1}} \sin \phi_n + 4\alpha\beta\varepsilon_{n+1} \cos \phi_n, \tag{7}$$

$$\phi_{n+1} = \phi_n + \frac{1}{\epsilon\sqrt{\varepsilon_{n+1}}} + \frac{2\beta \cos \phi_n}{\sqrt{\varepsilon_{n+1}}} + 4\alpha\beta \sin \phi_n. \tag{8}$$

Over most of the phase space the last term on the right of (7) is small and can be dropped, along with its area preserving counterpart, the last term in (8). In this approximation the change in velocity in one pass through the sheath is just $\Delta u = u_{n+1} - u_n = -2\omega s_0(V_{rf}/V_{dc}) \sin \phi_n$, which is the impulse approximation of the Fermi acceleration mapping.[10]

The Fermi acceleration mapping has been extensively studied,[10] indicating stochastic heating at low energies in which a random phase assumption holds, an intermediate energy region of somewhat lower diffusion, and an adiabatic barrier (KAM surface) above which the motion is mainly oscillatory. An approximate value of the adiabatic barrier can be found by expanding the mapping around a fixed point to obtain the standard mapping, from which an analytic criterion for the barrier can be obtained[10,11] $\mathcal{E} < \mathcal{E}_B \equiv m\omega^2 s_0 L V_1/V_{dc}$. The dynamics can be visualized by plotting the electron energy versus the sheath phase in a surface of section, conveniently chosen as the plane just after collision with the sheath. We illustrate the phase space in Fig. 1 for typical values of the parameters, as chosen from numerical cases treated in Section 4.

For all cases the discharge length was L = 6.7cm and the applied frequency 13.56 MHz, corresponding to an experiment by Godyak and associates,[6,7] whose results are compared to the theory. Initial conditions at low energy are allowed to diffuse through the available phase space, and the dots represent the particle positions after a specified time. We note the characteristic behavior of a fully accessible low energy followed by some inaccessible islands at intermediate energy and a barrier which prevents diffusion to higher energies. For illustrative purposes a few KAM curves above the barrier are also shown. The criterion tends to somewhat underestimate the barrier. Superposed on the Figures are curves of $\mathcal{E}_{esc} = V_{dc}(1 - \beta \cos \phi)$ which is the energy at which electrons escape to the walls, with the parameters again chosen from the physical examples in Section 4. The losses compete increasingly strongly with the diffusion for $\mathcal{E} > \mathcal{E}_{esc}$, which must be considered in a complete treatment, as described in the next section.

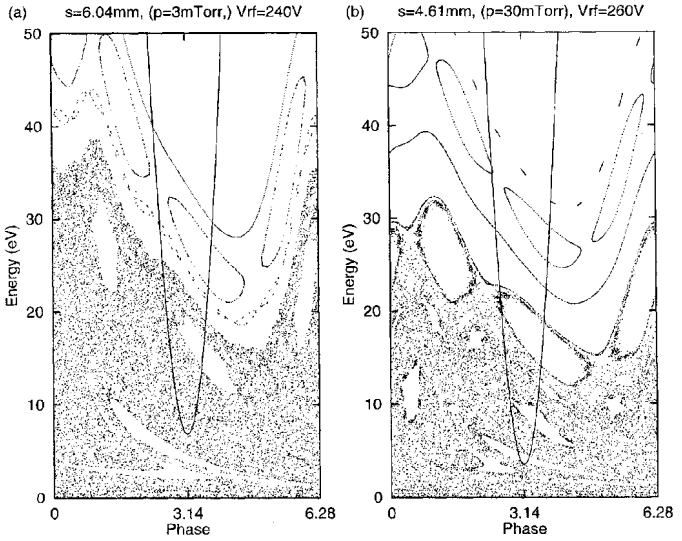

Figure 1. Phase space of the mapping, with no collisions. The dots are occupations after many mapping periods. A loss cone (solid line) is superposed.

2.3. Collisional Effects

In an initial paper [11] the assumed ordering was $\tau_b \ll \tau_c \ll \tau_{esc}$; ; i.e. the collision time for elastic angular scattering of electrons on the neutrals is long compared to the bounce time, but short compared to the escape time. That ordering allowed the mapping to be approximated as collisionless, while the electron distribution could be taken to be isotropic. Except at very low pressure, the second inequality is satisfied. However, the first inequality is generally not satisfied. In our recent paper we made a different assumption to treat the sheath heating, namely that the sheath kicks are phase randomized between each collision of an electron with the wall. As we shall see below, this implies either that the energy is in the range where the collisionless mapping dynamics are phase randomized or where $\tau_c \leq \tau_b$.

The simplest form of the diffusion coefficient in velocity space is

$$D_u = \frac{(\Delta u)^2_{ave}}{2\tau_r} \tag{9}$$

where Δu is the velocity kick, as previously defined, and τ_r is the time for phase randomization.[10] (In the energy variable $\mathcal{E} = \frac{m}{2e}u^2$, provided $\Delta u << u$, we find $D_\mathcal{E}$ by replacing Δu with $\Delta\mathcal{E} = \frac{m}{e}u\Delta u$). For the collisionless mapping in the stochastic region, $\tau_r = \tau_b$. To examine the effect of collisions we first consider the highly collisional regime with $\tau_c \ll \tau_b$. A flux argument then holds. Considering a single velocity class at uniform density n, the flux to the oscillating sheath is $\Gamma = nv$ and the total number of particles in the discharge is $N = nL$. The inverse of the mean frequency of sheath encounters is then approximately

$$\tau_r = N/2\Gamma = L/2u = \tau_b/2 \tag{10}$$

The factor of 1/2 is somewhat of an artifact, since for $\tau_c \approx \tau_b, \tau_r$ may actually increase slightly, and for $\tau_c \ll \tau_b$ the density is not uniform, with $n_0 > n(L)$ also increasing τ_r. A reasonable approximation is that $\tau_r = \tau_b$ (for $\tau_c \leq \tau_b$). For the values of energy for

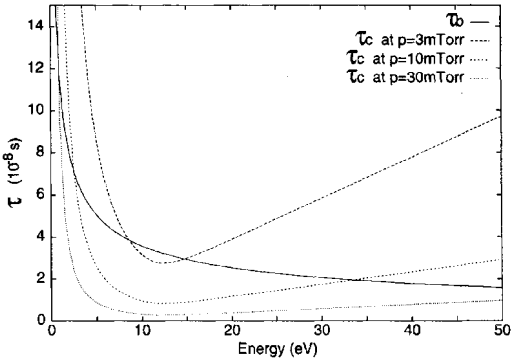

Figure 2. Comparison of the bounce time τ_b with the collisional elastic scattering time τ_c at three pressures.

which $\tau_c \approx \tau_b$ and the mapping dynamics do not randomize the phase, the diffusive rate may decrease. The rate of diffusion at a given energy can, in principle, be determined from a mapping in which collisions are included. Although some approximate values have been obtained in related problems,[10] this has not been done in the present case. The approximation that will be used in our kinetic analysis is that $\tau_r = \tau_c (\text{for } \tau_c \geq \tau_b)$. Because of resonances between the bounce frequency and the sheath oscillation frequency, islands are formed in the phase space, as seen in Fig. 1. These islands can partly maintain the higher diffusion rate in the range $\tau_b < \tau_c < 2\pi/\Omega$ where Ω is the radian frequency of the island motion. This phenomenon, somewhat analogous to the "plateau" regime in toroidal neoclassical diffusion, will not be considered here.

To understand the collisional effects more quantitatively, we use the example of the experimental configuration of Godyak and co-workers,[6,7] which has also been used in our numerical calculations of a parallel plate discharge, with L = 6.7 cm spacing and an argon feedstock gas. The collision times (inverse elastic scattering frequencies) for p = 3, 10 and 30 mTorr are compared to the bounce time in Fig. 2.

We see that at p = 30 mTorr collisional elastic scattering is able to keep the phases randomized over all energies of interest. In contrast, at 3 mTorr collisional randomization of the phase is marginally important, and p = 10 mTorr is an intermediate case.

3. SPATIAL AND TIME AVERAGED KINETIC THEORY

3.1. The Averaged Kinetic Equation

The kinetic equation for the evolution of an EEPF can be written as

$$\frac{\partial}{\partial t} f(x,\vec{u},t) + \nabla_u \cdot \vec{\Gamma}_u(x,\vec{u},t) + \nabla_x \cdot \vec{\Gamma}_x(x,\vec{u},t) = -\nu_{\text{iz}}(\mathcal{E}) f(x,\vec{u},t) - \nu_{\text{ex}}(\mathcal{E}) f(x,\vec{u},t) + C_{\text{en}}(x,\vec{u},t) + S(x,\vec{u},t) \tag{11}$$

where $\vec{\Gamma}_x$ and $\vec{\Gamma}_u$ are fluxes in configuration space and velocity space, respectively; ν_{iz} and ν_{ex} are the ionization and excitation frequencies, respectively, assumed only to be a function of the particle energy $\mathcal{E}$, C_{en} is the electron-neutral atom elastic collision operator; S is the source term corresponding to electrons produced by ionization and electrons which lose energy by inelastic collision with neutral atoms; f is the electron distribution function; and x, $\vec{u}$, t are the position (in one dimension) vector velocity, and time, respectively.

We eliminate the dependence on x by averaging over the bulk plasma, which extends from $x = 2s_0$ to $L - 2s_0$, where the rf voltage is applied between plates at $x = 0$ and $x = L$ and each ion sheath extends over a distance $2s_0$. Then all the terms in (11) remain unchanged in form, except that the spatial flux term becomes

$$\int \nabla \cdot \vec{\Gamma}_x d\vec{x} = u_x[f(\vec{u}, x = L - 2s_0, t)\eta(u_x - u_{v1}(t)) - f(\vec{u}, x = 2s_0, t)\eta(-u_x - u_{v2}(t))] \tag{12}$$

where $u_{v1,2} = [\frac{2e}{m}V_{\rm dc}(1 \pm \beta\cos\phi)]^{1/2}$. For the spatial integration we have taken $f(x)$ to be approximately constant between the ion sheaths. We eliminate the time dependence by averaging over an oscillation period, $\phi \equiv \omega t = 2\pi$. After this time average (11) reduces to

$$\nabla_u \cdot \vec{\Gamma}_u(\vec{u}) + \frac{2}{L - 4s_0}u_x\mathcal{L}(\mathcal{E}_x)f_s(\vec{u}) = -\nu_{iz}f(\vec{u}) - \nu_{ex}f(\vec{u}) + C_{en}(\vec{u}) + S(\vec{u}) \tag{13}$$

Here we have used the same symbol for f after averaging, $f_s = f(x = L - 2s_0)$ with $f_s \neq f$, and $L(\mathcal{E}_x)$ is the fraction of time in one rf period when the positively directed x component of an electron's kinetic energy, $\mathcal{E}_x$ is higher than $V_{\rm sheath}$,

$$\mathcal{L}(\mathcal{E}_x) = \begin{cases} 0 & V_{\rm dc} - V_1 > \mathcal{E}_x \\ \frac{1}{\pi}|\Phi_{\rm loss} - \pi| = \frac{1}{\pi}\cos^{-1}\left(\frac{V_{\rm dc} - \mathcal{E}_x}{V_1}\right) & V_{\rm dc} + V_1 > \mathcal{E}_x > V_{\rm dc} - V_1 \\ 1 & \mathcal{E}_x > V_{\rm dc} + V_1 \end{cases} \tag{14}$$

The electrons are stochastically and ohmically heated, and exchange energy by collisions among themselves, such that

$$\vec{\Gamma}_u(\vec{u}) = \vec{\Gamma}_u^{st} + \vec{\Gamma}_u^{\Omega} + \vec{\Gamma}_u^{ee} \tag{15}$$

We have neglected the small terms arising from the elastic energy loss to the neutrals. The stochastic heating flux can be written as

$$\vec{\Gamma}_u^{st} = -\vec{e}_x D_u \frac{\partial f(\vec{u})}{\partial u_x} \tag{16}$$

where the diffusion coefficient, determined from (9) is

$$D_u^{st} = \frac{\omega^2\beta^2 s_0^2}{\tau_r} \tag{17}$$

and, as described earlier for stochastic dynamics or for $\tau_c < \tau_b, \tau_r = \tau_b = L'/|u_x|$, with $L' = L - 2s_0$; otherwise $\tau_r = \tau_c$. For explicitness, we take $\tau_r = \tau_b$ in the following equations. In our model, stochastic heating is turned off for $\mathcal{E}_x < \Phi$. A step function $\eta(\mathcal{E}_x - \Phi)$ is therefore introduced in the stochastic flux, such that (16) becomes

$$\vec{\Gamma}_u^{st} = -\vec{e}_x\eta(\mathcal{E}_x - \Phi)\frac{\omega^2 s_0^2\beta^2|u_x|}{L'}\frac{\partial f(\vec{u})}{\partial u_x} \tag{18}$$

In addition, s_0 is reduced due to oscillations in the bulk plasma.[16] Subtracting the amplitude of the bulk oscillation caused by the electric field in the plasma, we have the effective sheath amplitude for heating

$$s_0' = s_0 - \frac{e\tilde{E}_p}{m\omega^2} \tag{19}$$

where $\bar{E}_p$, is the average amplitude of rf electric field in the plasma. Ohmic heating produces a flux [20]

$$\vec{\Gamma}_u^{\Omega} = -\vec{e}_x \frac{e^2 E_p^2}{2m^2} \frac{\nu_{\rm el}}{\nu_{\rm el}^2 + \omega^2} \frac{\partial f(\vec{u})}{\partial u_x} \tag{20}$$

where $\nu_{\rm el}$ is the elastic electron-atom collision frequency. Here we use the value of E_p at the center of discharge in the averaged kinetic equation, because ohmic heating is more important for colder electrons, which are trapped near the discharge center. Assuming the distribution function of the cold electrons, which is the predominant component in the center of the discharge, is nearly Maxwellian at temperature T_c, the linearized velocity space flux produced by collisions among the electrons, for $\mathcal{E} > T_c$ is [25]

$$\vec{\Gamma}_u^{ee} \cong -\vec{e}_u \frac{\nu_{ee}}{u^2} \left(\frac{2eT_c}{m}\right)^{3/2} \left(f + T_c \frac{df}{d\mathcal{E}}\right) \tag{21}$$

where $\nu_{ee} = 5 \times 10^{-6} n_{\rm ave} \ln \Lambda T_c^{-3/2}$ is the electron self-collision frequency,[26] with $n_{\rm ave}$ the average density of electrons in units of cm^{-3}. This equation is valid when the distribution function's deviation from a Maxwellian of temperature T_c takes place at energy higher than T_c, i.e., $T_c < \Phi$.

Introducing these fluxes into the kinetic equation we have:

$$-\frac{\nu_{ee}}{u^2}\left(\frac{2eT_c}{m}\right)^{3/2}\frac{d}{du}\left(f + T_c\frac{df}{d\mathcal{E}}\right) - \frac{\omega^2 s_0^2 \beta^2}{L'}\frac{\partial}{\partial u_x}[\eta(\mathcal{E}_x - \Phi)|u_x|\frac{\partial f}{\partial u_x}]$$
$$-\frac{\partial}{\partial u_x}\frac{e^2E_p^2}{2m^2}\frac{\nu_{\rm en}}{\nu_{\rm en}^2+\omega^2}\frac{\partial f}{\partial u_x} + \frac{2h_l u_x g(u_x)\mathcal{L}(\mathcal{E}_x)}{L-4s_0} f = -\nu_{\rm iz} f - \nu_{\rm ex} f + C_{\rm en}(f) + S \tag{22}$$

In the range of pressure we are studying, the frequency of elastic electron-neutral collisions is much higher than those of any other physical processes, in particular, the equivalent escape frequency defined below. Therefore, to the lowest order, $f(\vec{u}) = f(u)$. The equation for $f(u)$ is obtained by averaging (22) over angles thereby annihilating $C_{\rm en}$. Care must be taken when we treat the stochastic heating term and escape term, because Φ is a potential in x. We change the argument from u to $\mathcal{E}$, but use the same symbol for the distribution function. The normalization of $f(\mathcal{E})$ is $f(\mathcal{E})$ is $\int_0^{\mathcal{E}_{\max}} f(\mathcal{E})\sqrt{\mathcal{E}}d\mathcal{E} = n_{\rm ave}$ where $n_{\rm ave}$ is the average density in the bulk plasma. To relate this average density to the central density and to the edge density, we assume a parabolic distribution with central density n_0, dropping to a density n_s at the edge where for low pressures we use[26]

$$n_s = h_l n_0, \quad h_l = 0.86/[3 + 0.0165p(L - 4s_0)]^{1/2} \tag{23}$$

The resulting $n_{\rm ave}$ is, approximately,

$$n_{\rm ave} = \frac{2 + h_l}{3} n_0 \tag{24}$$

and $n_s/n_{\rm ave}$ is obtained using (23). For the escape term, we introduce escape frequency

$$\nu_{\rm es} = \int_0^{\pi} \frac{2}{L - 4s_0} u_x \mathcal{L}(\mathcal{E}_x) \sin\theta d\theta$$
$$= \begin{cases} 0 & (\mathcal{E} < V_{\rm dc} - V_1) \\ \frac{u}{(L-4s_0)\pi}\int_0^{\cos^{-1}\frac{u_0}{u}} \sin\theta\cos\theta\cos^{-1}\frac{V_{\rm dc}-\mathcal{E}\cos^2\theta}{V_1}d\theta = \frac{e}{\pi(L-4s_0)\mu} & (V_{\rm dc} - V_1 < \mathcal{E} \\ \quad \times\left(\sqrt{V_1^2 - (V_{\rm dc}-\mathcal{E})^2} - (V_{\rm dc}-\mathcal{E})\cos^{-1}\frac{V_{\rm dc}-\mathcal{E}}{V_1}\right) & < V_{\rm dc} + V_1) \\ \frac{u}{L-4s_0}\left(\frac{1}{\pi}\int_{\cos^{-1}\frac{u_1}{u}}^{\cos^{-1}\frac{u_0}{u}} \sin\theta\cos\theta\cos^{-1}\frac{V_{\rm dc}-\mathcal{E}\cos^2\theta}{V_1}d\theta\right. & \\ \quad \left. + \int_0^{\cos^{-1}\frac{u_1}{u}} \sin\theta\cos\theta d\theta\right) = \frac{e}{(L-4s_0)\mu}(\mathcal{E} - V_{\rm dc}) & (V_{\rm dc} + V_1 < \mathcal{E}) \end{cases} \tag{25}$$

The source term is also isotropic, i.e. $S(\vec{u}) = S(u)$. We assume that in an ionization process, the new electron has the same kinetic energy as the scattered one, which is one half the difference between the original kinetic energy of the hot electron and $\mathcal{E}_{iz}$. The kinetic energy of an electron after making an inelastic excitation collision with a neutral argon atom is $\mathcal{E} - \mathcal{E}_{ex}$, such that

$$S(\mathcal{E})\sqrt{\mathcal{E}}d\mathcal{E} = 2\nu_{iz}(\mathcal{E}')\sqrt{\mathcal{E}'}f(\mathcal{E}')d\mathcal{E}' + \nu_{ex}(\mathcal{E}'')\sqrt{\mathcal{E}''}f(\mathcal{E}'')d\mathcal{E}'' \tag{26}$$

where $\mathcal{E}' = 2\mathcal{E} + \mathcal{E}_{iz}$ and $\mathcal{E}'' = \mathcal{E} + \mathcal{E}_{ex}$. The inelastic collision frequencies and the elastic electron-neutral collision frequency is given by an analytical formula that fits experimental data.[24]

Substituting these quantities into (22) we obtain the final form of the kinetic equation,

$$-\frac{2}{u}\left(\frac{2e}{m}\right)^{1/2}\nu_{ee}T_c^{3/2}\frac{d}{d\mathcal{E}}\left(f + T_c\frac{df}{d\mathcal{E}}\right) - \eta(\mathcal{E}_x - \Phi)\frac{\omega^2 s_0^2\beta^2}{L'u}\frac{d}{d\mathcal{E}}(\mathcal{E}^2 - \Phi^2)\frac{df}{d\mathcal{E}}$$
$$-\frac{1}{u}\sqrt{\frac{2m}{e}}\frac{e^2E_p^2}{3m^2}\frac{d}{d\mathcal{E}}\left(\frac{\nu_{en}\mathcal{E}^{3/2}}{\nu_{en}^2 + \omega^2}\frac{df}{d\mathcal{E}}\right) = -(\nu_{es} + \nu_{iz} + \nu_{ex})f + S. \tag{27}$$

3.2. Equilibrium Conditions

In a self-consistent analysis, we determine $f(\mathcal{E})$ from input quantities: pressure p, V_1, ω and L.[26] The unknown quantities which must be determined along with $f(\mathcal{E})$ are T_c, Φ, β, n_0 and s_0. We need five physical conditions to determine the five unknown parameters in the equilibrium distribution.

One condition is that the total electron escape rate is equal to the ionization rate,

$$\int_{V_{dc}-V_1}^{\mathcal{E}_{max}} f(\mathcal{E})\nu_{es}\sqrt{\mathcal{E}}d\mathcal{E} = \int_{\mathcal{E}_{iz}}^{\mathcal{E}_{max}} f(\mathcal{E})\nu_{iz}\sqrt{\mathcal{E}}d\mathcal{E} \tag{28}$$

where $\mathcal{E}_{max}$ is the maximum value of energy an electron can reach before escaping. If n_0 and s_0 are known, Eq. (22) determines $f(\mathcal{E})$ at energy higher than $V_{dc} - V_1$, and therefore (28) determines V_{dc} (or β).

A second condition is that the escape rate of ions is equal to that of electrons,

$$\int_{V_{dc}-V_1}^{\mathcal{E}_{max}} f(\mathcal{E})\nu_{es}\sqrt{\mathcal{E}}d\mathcal{E} = \frac{2}{L - 4s_0}n_s u_B \tag{29}$$

which determines Φ if T_c and n_s are known. For a two temperature Maxwellian distribution the Bohm velocity is related to the lower temperature component, $u_B = \sqrt{eT_c/M}$, provided the lower temperature component contains most of the density.[26] There is a transition to a larger value, related to the higher temperature, when the two densities are comparable. Analysis for non-Maxwellian distributions must be similar, but has not been performed. Most of the physics can be captured by using the approximation, $u_B = \sqrt{eT_{ave}/M}$ where T_{ave} is an average temperature defined by $T_{ave} = (2/3)\int f(\mathcal{E})\mathcal{E}^{3/2}d\mathcal{E}/n$.

A third condition requires that the flux leaving the plasma be equal to the flux crossing the sheath, which from Child's law, is

$$2n_s u_B = \frac{2}{e}K_i\epsilon_0\left(\frac{2e}{M}\right)^{1/2}\frac{V_{dc}^{3/2}}{s_m^2} \tag{30}$$

where K_i = 0.82 in Lieberman's model[16] and s_m is the ion sheath width, which corresponds to $s_0(1 + \beta)$ in our model. Equation (30) is usually considered as a relation between n_s and s_m, since the other variables are nearly constant.

A fourth condition is that the total electron distribution cannot be heated by collisions among themselves,[25] leading to

$$\int_{\text{all}} \vec{u} \cdot \vec{\Gamma}_u^{\text{ee}} du^3 = 4\pi\nu_{\text{ee}} \left(\frac{2eT_c}{m}\right)^{3/2} \int_0^{u_{\max}} \frac{1}{u^2} \left(f + T_c \frac{df}{d\mathcal{E}}\right) u^3 du = 0 \tag{31}$$

which can be transformed to the form

$$T_c = \frac{\int_0^{\mathcal{E}_{\max}} f(\mathcal{E}) d\mathcal{E}}{f(0) - f(\mathcal{E}_{\max})} \approx \frac{\int_0^{\mathcal{E}_{\max}} f(\mathcal{E}) d\mathcal{E}}{f(0)} \tag{32}$$

Equation (32) is an implicit relation for T_c, as $f(\mathcal{E})$ is itself a function of T_c, but is rather insensitive to the detailed variation of $f(\mathcal{E})$.

If n_s (or n_0) is given from experiments, the distribution function, containing the parameters V_{dc}, Φ, s_0 and T_c, can be obtained from equations (28), (29), (30), and (32), and the boundary conditions. We previously compared our distribution function to the experimentally determined distribution of Godyak and co-workers, using their measured central densities.[24]

We also used an ansatz $\Phi = cT_c^z T_h^{1-z}$ where z and c are constants, determined from a best fit to the results using the experimental values of n_0. Although this ansatz is physically reasonable, we would like a fully self-consistent theory in which n_s is also determined by the theory. We can use kinetic theory in an averaged sense, consistent with the square well approximation, to do this. We form the approximate average value of the ratio of $n_e(\Phi)$ to n_s as

$$\frac{n_e(\Phi)}{n_s} = \frac{\int_{\mathcal{E}>\Phi}^{\infty} f_s(\mathcal{E})(\mathcal{E} - \Phi)^{1/2} d\mathcal{E}}{\int_0^{\infty} f_s(\mathcal{E}) \mathcal{E}^{1/2} d\mathcal{E}} \tag{33}$$

and relate $n_e(\Phi)$ to $n_i(\Phi)$ by

$$n_e(\Phi) = \alpha n_i(\Phi) \tag{34}$$

where α is an estimate of the ratio of the space-and-time-averaged electron density in the sheath to the space-averaged ion density in the sheath, which can be obtained for a Maxwellian following Lieberman.[16] From Child–Langmuir theory we have

$$\frac{n_i(\Phi)}{n_s} \approx \left(\frac{T_c}{\Phi}\right)^{1/2}. \tag{35}$$

Combining (33)–(35), shifting the coordinates in the numerator of (33) to zero by $y = \mathcal{E} - \Phi$, and approximating the distribution $f(\mathcal{E})$ by

$$f_s(\mathcal{E}) = \begin{cases} Ce^{-\mathcal{E}/T_c} & \mathcal{E} < \Phi \\ Ce^{-\Phi/T_c} e^{(\mathcal{E}-\Phi)/T_h} & \mathcal{E} > \Phi \end{cases} \tag{36}$$

we obtain

$$\frac{e^{\Phi/T_c} \int_0^{\infty} e^{-y/T_h} y^{1/2} dy}{\int_0^{\infty} e^{-\mathcal{E}/T_c} \mathcal{E}^{1/2} d\mathcal{E}} = \alpha \left(\frac{T_c}{\Phi}\right)^{1/2} \tag{37}$$

The integrals are readily evaluated to yield

$$e^{-\Phi/T_c} \left(\frac{\Phi}{T_c}\right)^{1/2} = \alpha \left(\frac{T_h}{T_c}\right)^{3/2} \tag{38}$$

which gives Φ/T_c in terms of T_h/T_c. Thus (30) becomes an equation for n_s.

4. NUMERICAL SOLUTIONS

4.1. Numerical Procedure

We solve the differential equation numerically using a fourth order Runge–Kutta algorithm. To solve $f(\mathcal{E})$, we need to know the source term, which is determined by larger values of $f(\mathcal{E})$, so we integrate from $\mathcal{E}_{max}$. For simplicity, we take $\mathcal{E}_{max}$ to be 200V, which is sufficiently large that it does not significantly influence the solution. The step of integration is 2.5×10^{-3} V. $f(\mathcal{E})$ has two constants to be determined, which can be taken as $f(\mathcal{E}_{max})$ and $f'(\mathcal{E}_{max})/f(\mathcal{E}_{max})$. The first is determined by the normalization of $f(\mathcal{E})$, since the kinetic equation is linear in $f(\mathcal{E})$; and the second is determined by the requirement that there is no flux at $\mathcal{E} = 0$. The eigenvalue problem has two independent solutions, one which increases with $\mathcal{E}$, and one which decreases with $\mathcal{E}$. Since we integrate the equation from $\mathcal{E}_{max}$ to $\mathcal{E} = 0$, the error caused by inappropriate choice of $f'(\mathcal{E}_{max})/f(\mathcal{E}_{max})$ rapidly becomes unimportant in the integration, as long as the value of $\mathcal{E}_{max}$ is large enough. This allows the "boundary" values at $\mathcal{E}_{max}$ to be chosen with considerable flexibility. The differential equation involves s_0, n_0, V_{dc}, Φ and T_c, which are to be determined recursively.

4.2. Numerical Results and Analysis

We compare our results to experimental results of Godyak and co-workers,[6,7] who studied a 6.7 cm discharge with an electrode area of 160 cm,² symmetrically driven by 13.56 MHz rf source. The transverse dimension is sufficiently large that the system can be considered as spatially one-dimensional. Comparison of numerical cases with experimental results have previously been made[24] using the experimentally measured central plasma density to complete the input data.

Using our new results of the modified stochastic heating formula, from (17), and the fully self-consistent calculation, using (38), we can compare our improved theory to previous theory.

From Fig. 2 collisional phase randomization occurs over the entire interesting range of energies at 30 mTorr, and most of the interesting range at 10 mTorr. At 3 mTorr, the dynamical stochasticity is sufficient to maintain the phase randomization as seen in Fig. 1, so the random phase with $\tau_r = \tau_b$ is adequate for all 3 cases.

In Fig. 3 we compare the new method of calculating Φ to our previous ansatz for calculating Φ, to the theory in which the experimental central density n_0 is used, and to the experiments from which the densities are taken. For the new calculation of Φ, $\alpha \approx 0.5$, while for the ansatz $c = 2.25$ and $z = 0.6$. We see that the distributions (EEPFs) using the new calculation of Φ are quite close to the EEPFs using the experimental $n0$, and, somewhat surprisingly, better than the heuristic results using the ansatz. In Table 1 we compare the parameters, corresponding to the three theoretical methods of calculating Φ. The theoretical values of n_0, determined from the self-consistent theory, using (30) are somewhat higher than the experimental values of n_0.

5. CONCLUSIONS AND DISCUSSION

We have developed an approximate kinetic treatment of a low pressure parallel-plane capacitive rf discharge, that specifically treats the stochastic sheath heating of electrons. The approximations are that the EEDFs are bounce averaged, and that the heating and loss processes are sufficiently slow that the electrons are nearly isotropic so that the kinetic equation can be expressed in terms of the single energy variable $\mathcal{E}$.

Table 1. Comparison of Plasma Parameters Using the Three Theoretical Methods

	n_0 (10^8 cm^{-3})	s_0 (mm)	$\mathcal{E}_0$ (eV)	Φ (eV)	T_l (eV)	T_h (eV)
		(a) p = 3 mTorr, V_{rf} = 240 V				
using given n_0	16.0	6.05	6.88	5.46	1.35	7.02
ansatz	11.5	6.54	7.00	7.88	2.05	7.10
Eq. (38)	22.0	5.65	6.96	3.85	0.83	6.99
		(b) p = 10 mTorr, V_{rf} = 165 V				
using given n_0	34.0	4.70	5.54	2.81	0.56	4.83
ansatz	21.0	5.20	5.23	4.70	1.12	4.78
Eq. (38)	56.5	3.57	7.23	2.51	0.55	4.33

In order to make the numerical solutions tractable, the electrons are divided into two classes, a hotter distribution that is heated primarily by the sheath oscillations, and a colder distribution that is prevented from reaching the sheaths by an internal square well potential of magnitude Φ.

For a given feedstock gas, axial dimension between discharge electrodes, and rf driving frequency, the input parameters are pressure p and discharge voltage V_{rf}. After setting the appropriate boundary conditions, there are five internal variables to be solved for, the central density n_0, the dc sheath potential Vdc, the sheath width s_0, the temperature of the low energy species T_c at $\mathcal{E} << \Phi$, and the potential Φ. These

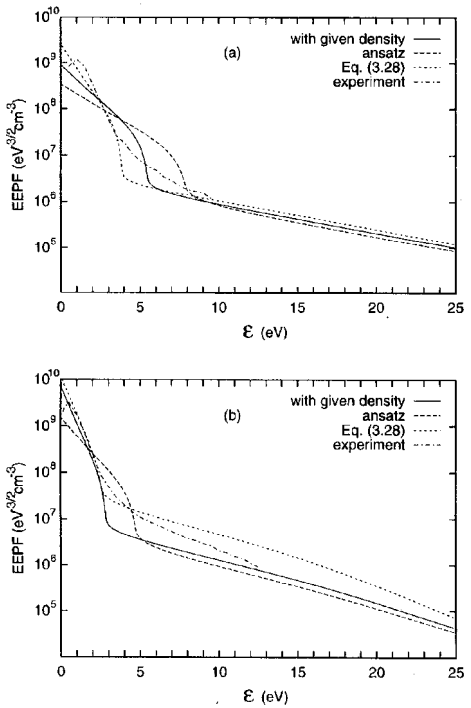

Figure 3. Comparison of the experiment to the three theoretical EEPF's, using the experimental n_0, using the ansatz, and using (38) to calculate Φ: (a) p = 3 mTorr, V_{rf} = 240 V; (b) p = 10 mTorr, V_{rf} = 165 V.

unknowns are expressed in terms of four conservation equations: 1. electron particle balance, 2. charge conservation, 3. collisional energy balance between the hot and cold species, and 4. current conservation (the Child–Langmuir law). A fifth condition required for a complete solution involves the internal potential structure whose details are not readily available. To compare with experimental distributions, we previously used an additional piece of information from the experiments, the central density n_0, or an ansatz on the potential Φ, found from the calculations with known n_0. We have now replaced this ansatz with a self-consistent calculation of an average Φ.

The results of the kinetic calculations capture the main features of the experimental EEPF. Some significant differences are (a) that the transition between the low energy and high energy distributions is sharp, caused by the square well approximation, and (b) that both the high temperature T_h and the cold temperature T_c are higher than in the experiments.

The introduction of a more realistic phase randomization time, depending on the collisionality, has been introduced, but does not significantly change the temperature of the high energy tail of the EEPF. The model may still be overestimating the stochastic heating due to various effects, such as correlations in the dynamical stochastization near the border of stochasticity. The phase randomization due to collisions has been treated in an approximate manner. We are currently working on improvements to the treatment of phase randomization, using the complete mapping dynamics, including collisions.

Other improvements that can be made are an improved stochastic heating calculation, taking the non-sinusoidal sheath motion explicitly into account, and an improved ohmic heating calculation, taking into account the spatial variation of ohmic heating with density, and a more accurate calculation of α.

Finally, we note that, although our analysis has been applied to Argon, the method can be readily extended to treat an electronegative gas. The extension requires only minor modifications of the theory, because the negative ions in the central core plasma are decoupled from the sheath region.

ACKNOWLEDGMENT

The authors would like to acknowledge the many useful conversations with M. A. Lieberman. They thank V. A. Godyak, B. P. Wood, and E. Kawamura for providing unpublished data. The work was partially supported by NSF Grant Phy-9505621.

REFERENCES

1. E. Fermi, "On the origin of cosmic radiation," *Phys. Rev.* 75:1169 (1948).
2. V. A. Godyak, *Soviet Radio Frequency Discharge Research,* Delphic Associates, Falls Church, VA, (1986).
3. V. A. Godyak, "Steady-state low-pressure rf discharge," *Sov. J. Plasma Phys.* 2:78 (1976).
4. V. A. Godyak and A. Kh. Ganna, "Influence of self field on the spatial distribution of a plasma of an rf discharge," *Sov. J. Plasma Phys.* 5:376 (1980).
5. O. A. Popov and V. P. Godyak, "Power dissipation in low-pressure rf discharge plasmas," *J. Appl. Phys.* 57:53 (1985).
6. V. A. Godyak, R. B. Piejak, and B. M. Alexandrovich, "Measurements of electron energy distributions in low-pressure rf discharges," *Plasma Sources Sci. Tech.* 1:36 (1992). (Also, private communication.)
7. V. A. Godyak, V. P. Meytlis, and H. R. Strauss, "Tonks–Langmuir problem for a bi-Maxwellian plasma," *IEEE Trans. on Plasma Sci.,* 23:728 (1995).

8. A. I. Akhiezer, and A. S. Bakai, "Stochastic plasma heating by rf fields," *Sov. J. Plasma Phys.* 2:359 (1976).
9. M. J. Kushner, "Mechanisms for power deposition in $Ar_2Si_4Hs_0$ capacitively coupled rf discharges," *IEEE Trans. on Plasma Sci.* 14:188 (1986).
10. A. J. Lichtenberg and M. A. Lieberman, *Regular and Chaotic Dynamics*, 2nd Ed., Springer-Verlag, N. Y. (1991).
11. C. G. Goedde, A. J. Lichtenberg, and M. A. Lieberman, 'Self-consistent stochastic electron heating in radio frequency discharges," *J. Appl. Phys.* 64:4375 (1988).
12. M. Surendra, D. B. Graves, and I. J. Morey, "Electron heating in low-pressure rf glow discharges," *Appl. Phys. Lett.*, 56:1022 (1990).
13. D. Vender and R. W. Boswell, "Numerical modeling of low-pressure rf plasmas," *IEEE Trans. on Plasma Sci.*, 18:725 (1990).
14. B. P. Wood, "Sheath heating in low pressure capacitive radio frequency discharges," Ph. D. thesis, University of California, Berkeley, November 1991, and private communications.
15. M. Surendra and D. B. Graves, "Electron acoustic waves in capacitively coupled, low-pressure rf glow discharges," *Phys. Rev. Lett.* 66:1469 (1991).
16. M. A. Lieberman, "Analytical solution for capacitive rf sheath," *IEEE Trans. on Plasma Sci.* 16:638 (1988).
17. B. P. Wood, M. A. Lieberman, and A. J. Lichtenberg, "Stochastic electron heating in a capacitive rf discharge with non-Maxwellian and time varying distributions," *IEEE Trans. on Plasma Sci.* 23:89 (1995).
18. I. B. Bernstein and T. Holstein, "Electron energy distributions in stationary discharges," *Phys. Rev.*, 94:1475 (1954).
19. L. D. Tsendin, "Energy distribution of electrons in a weakly ionized current-carrying plasma with a transverse inhomogeneity," *Sov. Phys. JETP* 39:805 (1974).
20. I. D. Kaganovich and L. D. Tsendin, "The space-time-averaging procedure and modeling of the rf discharge, part II: model of collisional low-pressure rf discharge," *IEEE Trans. on Plasma Sci.* 20:66 (1992).
21. U. Kortshagen, "A non-local kinetic model," *J. Phys. D* 26:1691 (1993).
22. V. I. Kolobov and V. A. Godyak, "Nonlocal electron kinetics in collisional gas discharge plasmas," *IEEE Trans. on Plasma Sci.* 23:503 (1995).
23. I. D. Kaganovich and L. D. Tsendin, "Low pressure rf discharge in the free flight regime," *IEEE Trans. on Plasma Sci.* 20:86 (1992).
24. Z. Wang, A. J. Lichtenberg, and R. H. Cohen, "Kinetic theory of stochasticly heated rf capacitive discharges," *IEEE Trans. on Plasma Sci.*, submitted for publication.
25. R. H. Cohen, I. B. Bernstein, J. J. Dorning and G. Rowlands, "Particle and energy exchange between untrapped and electrostatically confined populations in magnetic mirrors," *Nucl. FUS.* 20:1421 (1980).
26. M. A. Lieberman and A. J. Lichtenberg, *Principles of Plasma Discharges and Materials Processing*, John Wiley, N. Y., (1994).

ELECTRON KINETIC AND ELECTRODYNAMIC CHARACTERISTICS OF ICP IN STOCHASTIC HEATING REGIME

Valery Godyak

OSRAM SYLVANIA INC
71 Cherry Hill Drive
Beverly, MA 01915 (USA)

INTRODUCTION

Inductively Coupled Plasma (ICP) sources or inductive discharges are known for over a century.[1] They have been used and studied in last decades mostly in two quite opposite regimes. High pressure (about atmospheric gas pressure) ICPs have been used to generate near equilibrium plasmas[2] while low pressure ICPs (around mTorr pressure range) with non-equilibrium plasmas have been used as ion sources for particle accelerators and as ion thrusters for space propulsion.[3] Recently, interest in low pressure ICPs has been revitalized due to great expectations in using such devices in plasma processing and lighting technology. The ability to achieve a large plasma density at a low gas pressure and the absence of electrodes makes these discharges attractive in development of new technology and stimulates an intensive research activity on the basic plasma phenomena occurring in such discharges.

In an inductive discharge the main interaction of the electromagnetic field with the plasma, and thus rf power dissipation, takes place in the skin layer of thickness δ near the plasma boundary. Depending on gas pressure, plasma density and driving frequency the interaction of electromagnetic field with plasma within the skin layer can be of local or non-local character. The first case corresponds to the classical skin effect for which there is a local coupling between rf current and electric field within the skin layer given by the complex conductivity of cold plasma. The second case corresponds to the so-called anomalous skin effect where electron thermal motion brings spatial dispersion into the relation between rf current and electric field.

The anomalous skin effect is closely related to the collisionless or stochastic electron heating in inductive rf discharges and is widely discussed in recent publications.[4-12] To our knowledge there is only one experimental work by Demirkhanov et al.[13] done over thirty years ago where the anomalous penetration of the rf magnetic field into ICP has been convincingly demonstrated and explained as a result of electron thermal motion dispersing electron momentum acquired in the skin layer into the neighboring plasma. This experimental work has triggered the theoretical study of anomalous skin effect in plasma[14-19] done in 70s. A review of classical and recent works on anomalous skin effect in plasma can be found in ref.(12)

Electron Kinetics and Application of Glow Discharges
Edited by U. Kortshagen and L. D. Tsendin, Plenum Press, New York, 1998

The subject of the present work is an abbreviated review of a recent experimental study of an ICP operating at the lowest pressures where anomalous skin effect and collisionless electron heating may occur. The external ICP parameters (electrical characteristics of the primary coil loaded by the plasma), the electron energy distribution function, the basic plasma parameters and the rf electric field and current distribution have been measured over a wide range of gas pressure, rf power and driving frequency. Taking advantage of the dramatic improvement in diagnostic means achieved for the last 30 years, this study has generated a large experimental data base, which can be used for comparison with the results of ongoing theoretical and modeling activity. New features in the EEDF, rf field phase velocity reversal, phase bifurcation, a second current layer and a negative power absorption are found in these experiments and interpreted as result of a non-local electron dynamics due to electron thermal motion. For the first time, the existence of electron stochastic heating has been directly demonstrated in ICP discharges.

EXPERIMENTAL SETUP AND DIAGNOSTICS

Experiments have been carried out in a cylindrical stainless steel discharge chamber with a Pyrex glass bottom as shown in Fig. 1. The chamber ID was 19.8 cm, its length was 10.5 cm, and the glass thickness was 1.27 cm. A five turn planar induction coil with 12.7 cm OD and 3.8 cm ID was mounted 1.9 cm below the bottom surface of the discharge chamber. To achieve a high degree of azimuthal symmetry, each turn of the coil was made concentric about the center of the discharge chamber with a radial conducting bridge between each turn. The current return lead from the coil was placed 2mm below the bridges to cancel, as much as practically possible, the magnetic field created by the radial component of the coil current along the bridges and thus to minimize perturbation of the coil's azimuthal symmetry.

An electrostatic shield and an air gap between the glass and the coil has practically eliminated capacitive coupling between the induction coil and the plasma to the extent that the rf plasma potential referenced to the grounded chamber was much less than 1 volt. This has significantly improved quality of the Langmuir probe measurement and allowed detection of a low energy peak on the measured EEDF. The coil screening has also made it possible to obtain a large dynamic range (over 60 db) in the magnetic probe measurement and thus to reveal some new features in the electromagnetic field structure behind the skin layer. An aluminum kettle covered the induction coil from below and acted as an rf shield preventing electromagnetic interference on the measurement apparatus and wiring.

Measurements were made at driving frequencies $\omega/2\pi$ = 3.39; 6.78 and 13.56 MHz in an argon discharge at gas pressures of 0.3, 1, 10, and 100 mTorr and at rf power dissipation in the plasma P_{pl} ranging between 6 and 400 W. The discharge power P_{pl} was determined by measuring the power transmitted to the discharge (forward minus reflected power) and subtracting matcher and coil losses which were determined a priori as a function of coil current and temperature. In what follows all mention of power refers to power dissipated in the plasma.

Langmuir probes have been used to measure the electron energy distribution function (EEDF) along the discharge axial direction on the axis and along the radius in the discharge midplane. [20] Also the measurement were done along discharge axial direction at a fixed radial position of 4 cm: near the maximum of the azimuthal rf electric field. The magnetic probe measurements have been done at the same radial position along the axial direction. The plasma density n, the effective electron temperature T_e, the effective electron atom collision frequency in rf field ν_{en}, the effective rf frequency ω_{eff} [21] and the electron mean free path λ_e have been found as corresponding integrals of the measured EEDF.

A two-dimensional magnetic probe has been used for measurement of the radial and axial

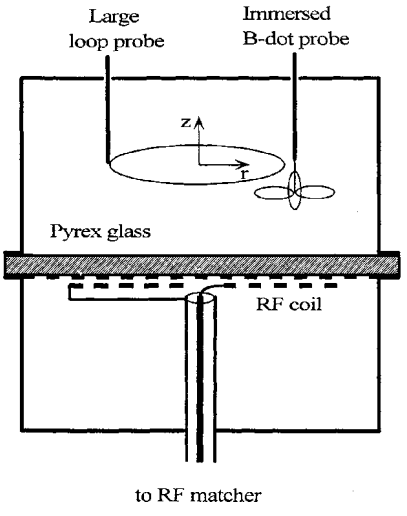

Figure 1. Experimental discharge chamber.

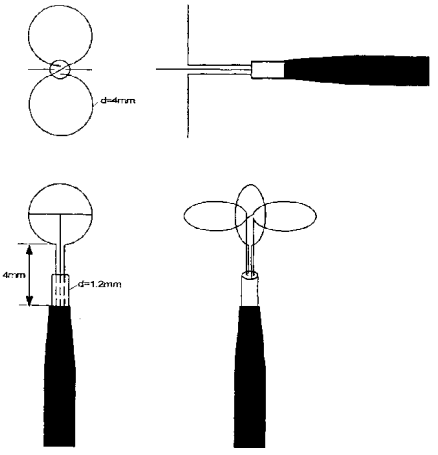

Figure 2. Two-dimensional magnetic probe.

components of the rf magnetic field magnitude and phase along axial direction at fixed radius of 4 cm. These data have been used to infer the azimuthal rf electric field and current density, correspondingly, by spatial integration and differentiation of the magnetic probe signals in the magnitude and the phase domain.[22] The probe has been design to minimize plasma and rf current distortion around the probe. Detailed probe description, signal processing and validation of results obtained with this probe are given in Refs.[23,24]

EXPERIMENTAL RESULTS AND DISCUSSION

EEDF and Plasma Parameters.

The electron energy distributions measured in the maximum of the plasma density distribution on the discharge axis at f = 6.78 MHz over a wide range of the discharge power P_{pl} are shown in Figs. 3 and 4 in terms of the electron energy probability functions (EEPF), correspondingly, for p = 1 mTorr and p = 10 mTorr. EEPFs in Figs 3 and 4 are given in a sequence of doubling rf power. For both pressures the EEPF have a three-temperature structure clearly seen at the lowest discharge power. The EEPFs are depleted at high electron energy in the inelastic energy range. For p = 10 mTorr depletion starts at the lowest argon excitation energy $\epsilon^* = 11.55$ eV since at this pressure argon atom excitation is the major process of electron energy loss. For 1 mTorr depletion starts at energy $\epsilon_w \approx 25$ eV corresponding to the chamber wall potential V_w , since the hot electron escape to the wall is a major factor in the electron energy balance at the lowest gas pressure.

The appearance of a low energy peak in EEPF at small discharge power is a natural consequence of non-local electron kinetics in low pressure rf discharges (capacitive, inductive or wave driven) where the rf power absorption is localized along the plasma boundary.[25-28] Generally, the EEPF structure in a low pressure ICP is similar to and is caused for the same reasons as a low pressure capacitive coupled plasma (CCP). The ambipolar potential, which always exists in a bounded plasma, traps low energy electrons within the plasma center preventing them from participating in the heating process at the plasma boundary (in the skin layer or in the rf sheath). At relatively high plasma density electron-electron (e-e) interaction of the middle energy group with the low energy one equalizes their temperatures and the

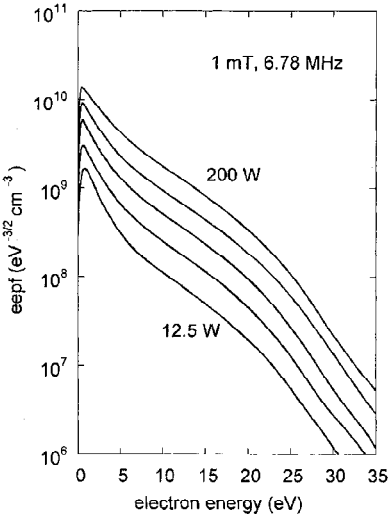

Figure 3. EEPF for p = 1 mTorr. r=0, z=52 cm.

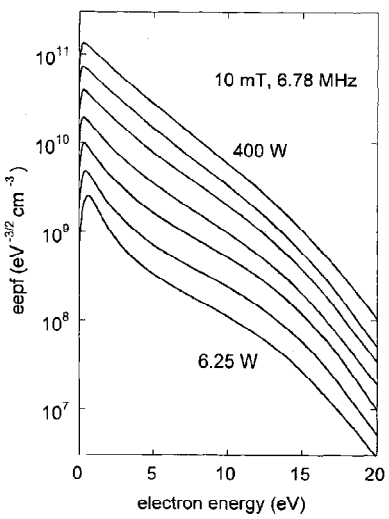

Figure 4. EEPF for p = 10 mTorr. r = 0, z = 4.0 cm.

EEPF at high power approaches a Maxwellian distribution in the elastic energy range.

The plasma density n and effective electron temperature $T_e = 2/3 < \epsilon >$ found as corresponding integrals of the measured EEPF are shown in Figs. 5 and 6 as a function of discharge power. There is a nearly linear dependence of the plasma density on the discharge power with some trend toward saturation at large power. This trend is due to gas heating from the elastic electron-atom and ion-atom collisions resulting in a reduction in the gas density. The power dependence of the electron temperature correlates with that of the EEPF. The growing T_e with power at low power is a result of disappearance of the low energy hump in EEPF due to e-e interaction. At p = 10 mTorr when plasma density is large and electron temperature is small, the two-step ionization process via excited state whose rate is nearly proportional to square of plasma density reduces the electron temperature. These two competing tendencies result in a maximum T_e at intermediate power.

The axial distribution of the plasma density and the effective electron temperature are shown in Figs. 7 and 8, respectively, for 1 and 10 mTorr, P = 100 W and f = 6.78 MHz. At p = 1mTorr the plasma density distribution well matches that given by the Tonks-Langmuir theory for ion free fall regime with the boundary value being about 40% of its maximum at midplane. For 1 mTorr the ion mean free path $\lambda_i \approx 4$ cm and the electron mean free path $\lambda_e \approx 75$ cm. At p = 10 mTorr the maximum in the plasma density distribution shifts out of midplane and plasma density at the boundary is about 20% of its maximum value.

The effective electron temperature at 1 mTorr is growing at plasma boundaries due to trapping of low energy electrons within the minimum of the ambipolar potential. This is not observed at 10mTorr since at this pressure the EEPF is very close to Maxwellian in the elastic energy range and the ambipolar potential does not affect the EEPF shape.

EEPFs along the axial direction at a fixed radius of 4 cm were also measured to evaluate plasma parameters along the path of the magnetic probe diagnostics. These parameters measured at a distance of 1 cm from the glass window (within maximum of the rf current density distribution) are given in Table1 for the collisionless skin layer ($\lambda_e > \delta$) at f = 6.78 MHz together with others relevant parameters.

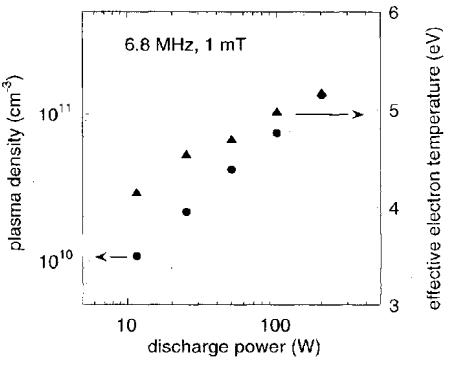

Figure 5. Plasma parameters for p = 1 mTorr.

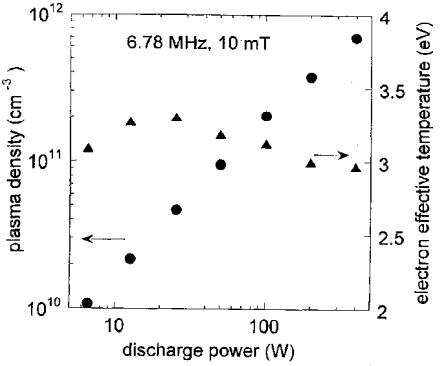

Figure 6. Plasma parameters for p = 10 mTorr.

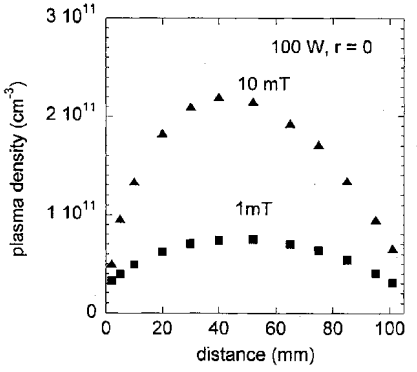

Figure 7. Plasma density axial distribution.

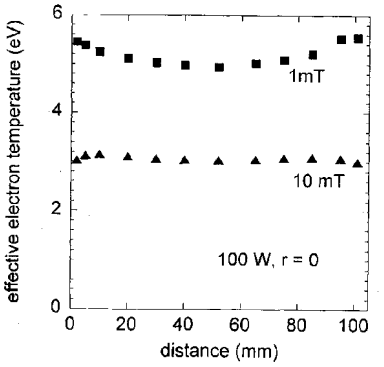

Figure 8. Electron temperature axial distribution.

Table 1. ICP parameters for f= 6.78 MHz at r= 4cm and z= 1cm.

p	P_{pl}	n_1	δ_n	δ_E	ν_{en}	ω_{eff}	ν_{eff}	ν_{st}	v_{rf}
mTorr	W	$10^{10} cm^{-3}$	cm	cm	$10^6 s^{-1}$	$10^7 s^{-1}$	$10^7 s^{-1}$	$10^7 s^{-1}$	$10^7 cm/s$
1	25	1.1	5.1	2.1	7.1	4.4	3.0	1.8	5.5
1	50	2.1	3.6	1.9	6.5	4.4	3.2	2.1	5.6
1	100	4.1	2.6	1.7	5.5	4.4	3.9	2.4	4.9
1	200	8.2	1.9	1.4	4.2	4.4	4.0	2.9	4.6
10	25	2.3	3.5	2.0	52	5.5	5.1	1.6	2.8
10	50	4.8	2.4	1.8	45	5.5	5.3	1.8	2.6
10	100	10	1.7	1.6	36	5.5	5.5	2.0	2.5
10	150	16	1.4	1.4	30	5.5	5.7	2.3	2.5

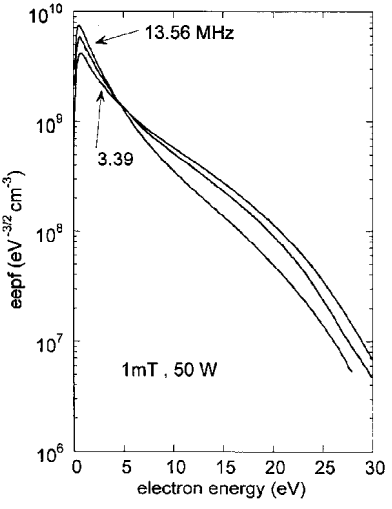

Figure 9. EEPF for different frequencies: 3.39; 6.78 and 13.56MHz, p = 1 mTorr, r = 0, z = 5.2 cm.

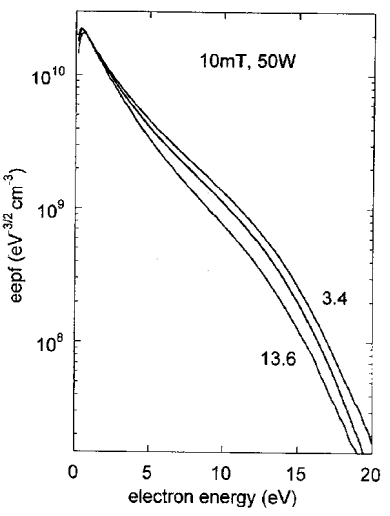

Figure 10. EEPF for different frequencies: 3.39; 6.78 and 13.56 MHz, p = 10mTorr.

Frequency Dependence of EEPF.

Langmuir probe measurements at different frequencies have revealed an essential EEPF dependence on frequency as shown in Figs. 9 and 10. This dependence is more pronounced at smaller discharge power and lower argon pressure. At 100 mTorr and higher pressures no frequency dependence was observed in the measured EEPF.

Integration of the distributions given in Figs. 9 and 10 showed no frequency dependence of the plasma density on the rf frequency at fixed rf power. On the other hand, the effective electron temperature T_e and the temperature of the low energy group T_{el} decreases with rf frequency, while the EEPF shape at high energy (ε ? 10 eV) appears unchanged although its relative magnitude is smaller at higher frequency. Thus, at 1 mTorr T_e is 5.4; 4.7 and 3.7 eV, while T_{el} is 2.9; 2.5 and 2.3 eV, respectively, for frequencies: 3.39; 6.78 and 13.56 MHz.

The increase in electron temperature when frequency goes down, seems to be due to a transition in the electron heating regime in the skin layer from collisional (normal skin effect) to stochastic (collisionless) electron heating (anomalous skin effect). This notion is supported by estimation of the so-called non-locality parameter Λ which shows a departure from the condition of the local collisional electron heating within the skin layer. [14]

$$\Lambda = (\lambda_{eff}/\delta)^2$$

where:

$$\lambda_{eff} = v_{ea}(\nu_{en}^2 + \omega_{eff}^2)^{-1/2}$$

Here, λ_{eff} is the effective electron free path accounting for a change of electron momentum due to collisions and rf field interaction; δ is the characteristic length of rf field penetration, and v_{ea} is the average electron velocity: $v_{ea} = (8T_e/\pi m)^{1/2}$. The value of δ is defined not only by skin effect itself (caused by rf current induced in the plasma) but also by ICP geometry. Note, that in all practical ICP configurations the rf electric field is not homogeneous even in the plasmas absence. Therefore, δ remains limited even at very low

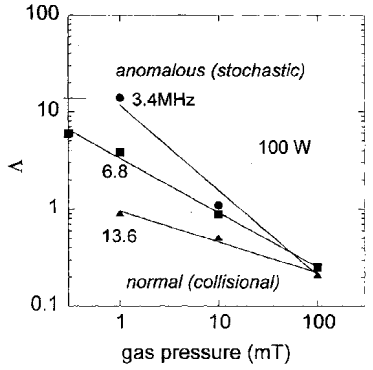

Figure 11. Non-locality parameter versus pressure, r = 4 cm, z = 1cm, P_{pl} = 100W.

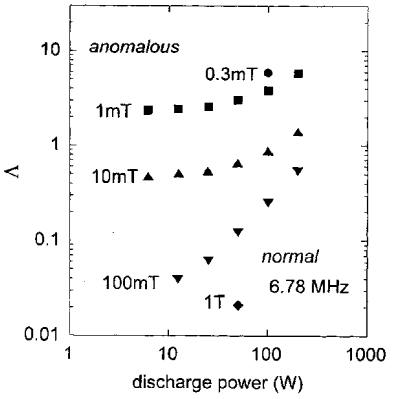

Figure 12. Non-locality parameter versus discharge power, f = 6.78 MHz.

plasma density, and the stochastic heating and many electron kinetic phenomena typical for anomalous skin effect may occur even in the absence of skin effect[6]

When $\Lambda << 1$ the skin effect is normal and rf energy absorption can be adequately described by conductivity of cold plasma. When $\Lambda \geq 1$ the skin effect is anomalous and at $\Lambda >> 1$ the skin effect is strongly anomalous corresponding to a collisionless heating regime.

The values of Λ calculated using the data obtained with Langmuir probe at r = 4 cm and z = 1 cm are shown in Fig. 11 as functions of argon pressure for different frequencies. d was found from an expression similar to that in ref. (7) which is derived for an ICP in a finite length cylindrical metal chamber but accounting for $\omega \neq \omega_{eff}$ and the fact that the induction coil radius is smaller than the chamber radius R.

$$\delta = (c/\omega_p)(\omega_{eff}/\omega)^{1/2}\left[(1+\alpha^2)/b(1+\alpha^2/b^2)^{1/2}\right]^{1/2}$$

where: $\alpha = \nu_{eff}/\omega_{eff}$; $b = 1 + (1+\alpha^2)(c/\delta_0\omega_p)^2(\omega_{eff}/\omega)$ and $\delta_0 \leq R/3.8$ is the characteristic length of rf field decay in vacuum. When the coil radius is equal to the chamber radius, δ_0 = R/3.8. In the limit of low density plasma ($\omega_p \to 0$), $\delta = \delta_0$.

As shown in Fig. 11, the non-locality parameter Λ at p =1 mTorr changes from 0.9 at f = 13.56 MHz to 14 at f = 3.39 MHz clearly showing a transition from a weakly non-local to a strong anomalous skin effect. It is interest to note, that in commonly used ICPs in the mTorr pressure range at 13.56 MHz a strong anomalous skin effect can be achieved only at a very high plasma density ($n > 10^{12} cm^{-3}$). An example of the calculated dependence of A on the discharge power is shown in Fig. 12 for f = 6.78 MHz. At small discharge power (plasma density) when $\delta_p = c/\omega_p \gg \delta_0$, Λ is independent on plasma density and is defined by do. At large discharge power $\delta_p << \delta_0$ and Λ is proportional to the plasma density. For higher gas pressure the linear dependence $\Lambda(P_{pl})$ is achieved at lower discharge power since plasma density is a growing function of the gas pressure.

Electric Field and Current Density Distribution.

Figs. 13 and 14 show the axial distributions of the azimuthal rf electric field and the azimuthal current density measured with the magnetic probe at a fixed radial position of 4 cm in an ICP driven at f = 6.78 MHz. All curves in Figs. 13 and 14 are the result of over 40

measurement points obtained with the 2.5 mm step and are presented here with no smoothing. In all data given in this work the phase is referenced with respect to the E-field measured in vacuum, i.e. 90^0 shifted from the phase of the current in the induction coil.

As shown in Fig. 13 and 14, within the skin layer near the glass window, the rf field decays exponentially and phase decreases linearly as is found from the classical concept of normal skin effect in a conducting medium where: $d\ln E/dz = \delta_E^{-1}$. The normal skin depth in a collisionless plasma $(\nu_{en} \ll \omega)$ is $\delta_p = c/\omega_p$. The values δ_E and δ_p found from Fig. 13 and 14 and probe measurement in the point r = 4 cm and z = 1 cm are shown in Table 1. As shown in Table 1, the values of δ_E and δ_p are essentially different ($\delta_E < \delta_p$). The rf field distribution in vacuum decays exponentially (with z) over most of the chamber with a characteristic length δ_0 = 2.44 cm which is somewhat less than R/3.8 = 2.58 since the coil radius is less than R. The steeper decay in field and in phase beyond the skin layer is a natural consequence of the two-dimensional geometry and non-uniform plasma density distribution in an ICP source with a planar coil. In this experiment the spatial decay of rf field is considerably affected by the geometry of the coil and the chamber (δ_0 and δ_E are comparable).

The rf field and relative phase ϕ behind the skin layer (z ¿, 2 cm) demonstrates anomalous behavior. Here the rf field decays more rapidly and after reaching its first minimum has one or two local maxima followed by a sharp fall to the metal boundary. Meanwhile, the phase either begins to increase, after reaching its minimal value, or sharply falls. This phase evolution corresponds to a dramatic change in the phase velocity $v_{ph} = -\omega(d\phi/dz)^{-1}$ along bounded plasma. In the skin layer it is found from Figs. 13 and 14 that v_{ph} is larger than the average electron thermal velocity v_{th} in the z-direction, $v_{th} = \nu_{ea}/2 = 8.0 \cdot 10^7$ cm/sec for 1 mTorr and $v_{th} = 6.3 \cdot 10^7$ cm/sec for 10 mTorr. With increasing z, v_{ph} decreases and after reaching a minimum it starts to grow again with a reversal of the phase velocity as it passes through the singularity point ($v_{ph} = \pm\infty$ at $d\phi/dz = 0$). Generally, phase velocity falls with plasma density. At the point where the plasma density is large enough (for 1 mTorr at P_{pl} = 200 W and for 10 mTorr at P_{pl} = 120 W) v_{ph} equals v_{th} at some distance from the window as shown in Figs. 13 and 14. At this point the phase starts decreasing rapidly finally reaching a value close to that at smaller P_{pl} but having one more rotation cycle. The phase bifurcation effect is clearly seen in Fig. 14 for 10 mTorr where a relatively small change in the rf power (from. 100 W to 120 W) brings about the dramatic change in the phase evolution.

The non-monotonic rf electric field distribution observed here resembles the distribution of the rf magnetic field in a toroidal inductive rf discharge, first observed by Demirkhanov et. al13 They have explained a non-monotonic decay of the rf magnetic field away from the plasma boundary as a result of electron thermal motion transferring rf electron current from the skin layer to a place deep into plasma (anomalous skin effect). The non-monotonic structure of electromagnetic field in a semi-infinite collisionless plasma has been also found in the kinetic analysis of transverse electromagnetic wave penetrating into bounded plasma.[14, 15] Accordingly, the non-monotonic rf electric field decay found outside the skin layer could be interpreted qualitatively as a superposition of the electric field due to the coil and the electric field induced by the plasma discharge currents, where the plasma currents are those in the skin region (due to skin effect) and those outside this region due to plasma current translated from the skin layer by electron thermal motion. The difference in the phase propagation velocity and the thermal one, together with plasma inhomogeneity and dispersion in the electron velocity can result in a variety of the rf field distribution patterns.

The rf current density J and its phase distribution shown in Figs. 15 and 16 demonstrate the effect of rf current diffusion out of the skin layer with the formation of a second current layer (opposite in direction) near the metal wall. The peak current density in the second layer for p = 1 mTorr at z ≈ 9 cm is just 10 times less than that in the first (skin) layer at z ≈ 1 cm, while the rf electric fields at these particular points (Δz = 8 cm) differs about 50 times. The

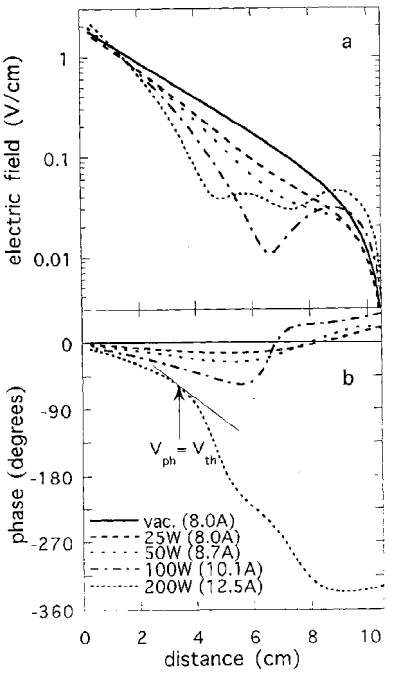

Figure 13. Rf electric field magnitude and phase distribution for f = 6.78 MHz and p = 1 mTorr.

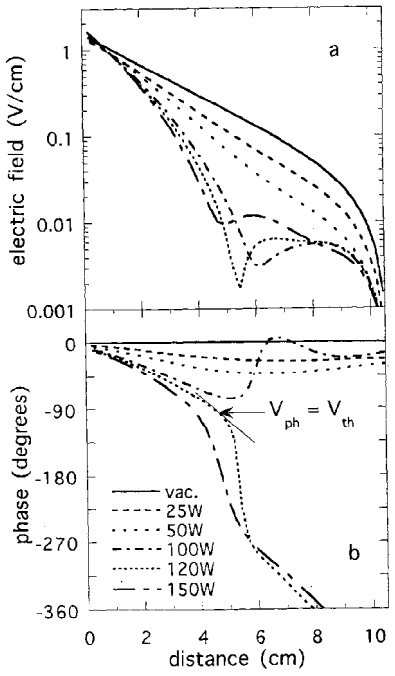

Figure 14. Rf electric field magnitude and phase distribution for f = 6.78 MHz and p = 10 mTorr.

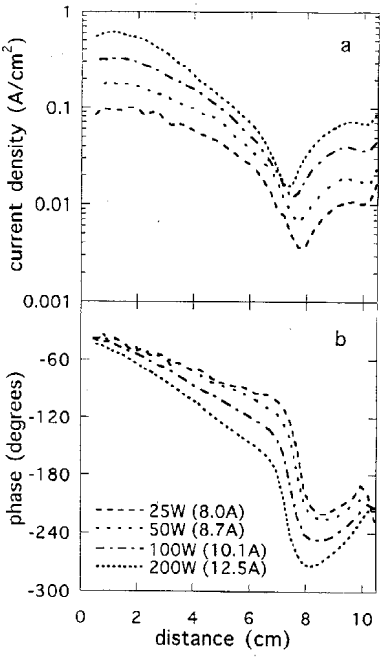

Figure 15. Rf current density magnitude and phase distribution for f = 6.78 MHz and p = 1 mTorr.

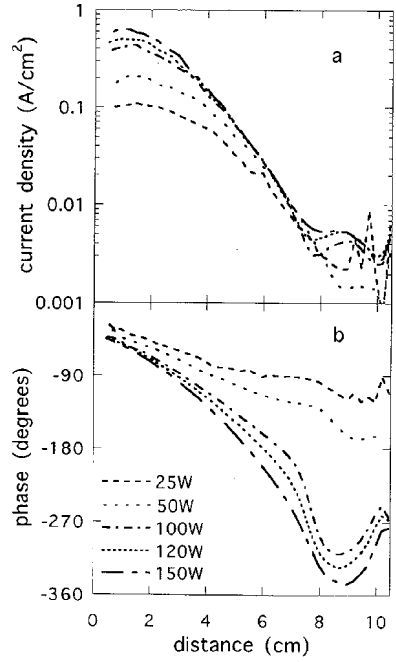

Figure 16. Rf current density magnitude and phase distribution for f = 6.78 MHz and p = 10 mTorr.

phase difference between these points found from Fig. 15 (for different power) is between 180 and 210, which agrees well with the calculated phase of the current transferred by thermal electrons, $\Delta\phi = \omega\Delta z/v_{th} = 240^0$. The similar pattern in the current density distribution is seen for p = 10 mTorr but the second current layer is not so clearly expressed as it is for 1 mTorr. The reason for this is a considerably smaller electron free path and therefore a shorter length of rf current diffusion. Some larger phase shift is seen in the second current layer for p = 10 mTorr since the electron thermal velocity is smaller in this case. Measurements at different pressures showed that the relative value of the secondary maximum in the azimuthal current distribution was about 0.22; 0.1 and 0.01, correspondingly, for 0.3; 1.0 and 10 mTorr.

The existence of the second current layer explains the appearance of a hump in the rf electric field distribution near the wall and its dependence on the rf power. As seen in Fig. 15, the current density in the second layer is proportional to P_{pl}, and so is the nearby rf field (induced by this current) which at small power is comparable to, and at high power is larger than, the rf field penetrated from the skin layer. Note, that the rf field in the skin layer is practically independent of rf power but it attenuates faster deep in the plasma at higher power and plasma density. The rf field induced by the secondary current should also cause (and, in turn, be affected by) rf current in the conductive wall.

The measured rf current density and the plasma density in the skin layer allows one to evaluate the electron oscillatory velocity v_{rf} there. The results given in Table 1 show that at argon pressures of 1 and 10 mTorr the rf drift velocity v_{rf} is essentially smaller than electron averaged velocity v_{ea}.

Anomalous RF Power Absorption.

Having measured the rf electric field and current distributions one can identify the rf power absorption mechanism by comparing the plasma resistivity ρ found in experiment, ($\rho = Ecos\psi/J$) with that calculated from the conductivity of cold plasma ($\rho = Re\left[\sigma_p^{-1}\right]$), where E and J are the magnitude of the rf electric field and current density, and ψ is the phase difference between them. This procedure is equivalent to comparing the effective electron collision frequency ν_{eff} found in experiment (which includes all possible electron energy dissipative processes) with the electron-atom collision frequency in the rf field ν_{en} determined by integrating the product of the electron-neutral cross section and the measured EEDF over energy space.[21]

The plasma resistivity is: $\rho = m\nu_{eff}/ne^2$, thus, $\nu_{eff} = ne^2 Ecos\Psi/mJ$. Calculated values of ν_{eff} and ν_{en} at a distance of 1 cm from glass window (near the maximum in rf current density distribution) are shown in Table 1. At 1 mTorr the values found for ν_{eff} are much larger than ν_{en}. This suggests that at this gas pressure rf power absorption is predominantly collisionless in the skin layer. At 10 mTorr, ν_{eff} and ν_{en} are close to each other, suggesting that rf power absorption is primarily collisional.

It is interesting to compare values of ν_{eff} found in experiment at p = 1 mTorr when $\nu_{eff} >> \nu_{en}$ with a theoretical expression for the stochastic collisionless frequency, $\nu_{st} = v_{ea}/4\delta$ given in ref(7) for a one-dimensional ICP with an exponential rf field profile. Assuming $\delta = \delta_E$, the calculated values of ν_{st} shown in Table 1 appear to be about 0.6 ν_{eff} found in this experiment. The difference between the two can be attributed to the two-dimensional nature of the ICP where the rf field radial inhomogeneity and the electron thermal motion in the radial direction can contribute to non-local collisionless rf power dissipation.

The integral rf power absorption along the electromagnetic field propagation is shown in Figs. 17 and 18 as function of the distance from the window. Here the measured total absorbed power flux is compared with that calculated from the measured E and J distributions assuming collisional power absorption. These comparison shows that the stochastic collisionless

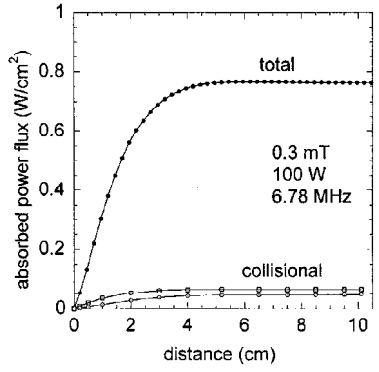

Figure 17. Absorbed rf power flux for p = 0.3 mTorr.

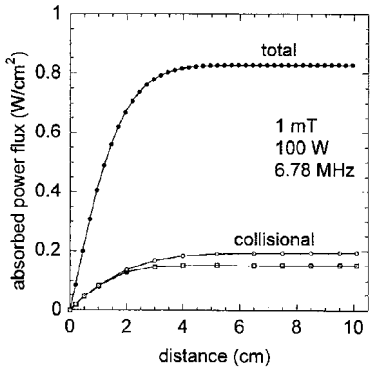

Figure 18. Absorbed rf power flux for p = 1 mTorr.

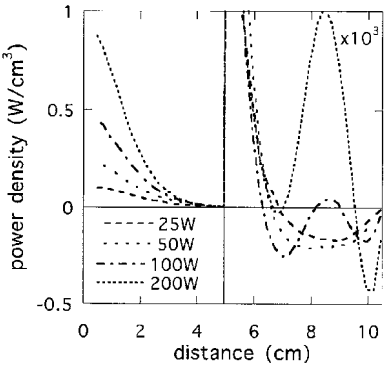

Figure 19. Spatial distribution of rf power absorption for p = lmTorr, f = 6.78 MHz.

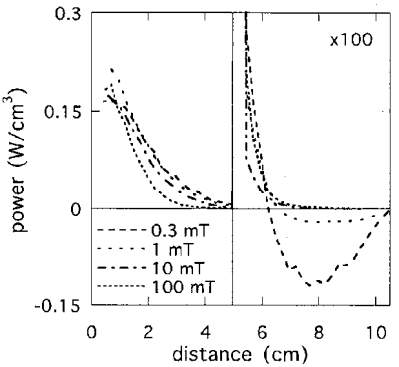

Figure 20. Spatial distribution of rf power absorption for P_{pl} = 50 W, f = 6.78 MHz.

process dominates rf power absorption in these particular cases.

The calculation of the spatial distribution of the absorbed rf power P(z) is shown in Fig. 19 for p = 1 mTorr with various discharge powers and in Fig. 20 at a fixed discharge power of 50 W with various gas pressures. As expected, practically all rf power is dissipated in the skin layer near the window. Far from the window the power absorption for p = 1 mTorr oscillates with distance and even becomes negative. The number of negative peaks on the P(z) space distribution depends on the total rf power absorbed by the plasma: one negative peak at P_{pl} = 25 and 50 W and two at P_{pl} = 100 and 200 W. The negative power absorption occurs in the second current layer where the current phase differs from the local rf field phase by more than 90^0. Here the electrons arriving from the skin layer transfer the energy they acquired in the skin layer back to rf field (local electron deceleration).

The negative power absorption depends on plasma density and frequency. It is most evident at the lowest argon pressure and vanishes at relatively high gas pressure when the electron mean free path is smaller than the chamber length as shown in Fig. 20.

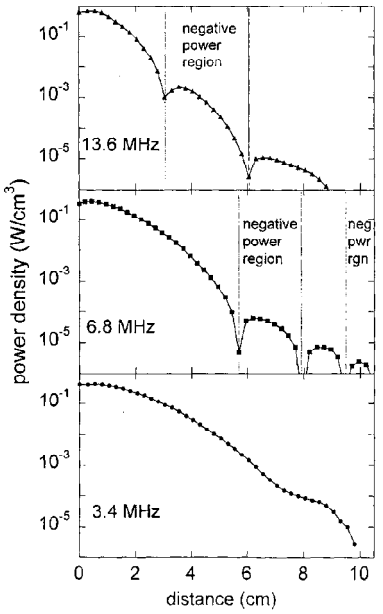

Figure 21. Frequency dependence of rf power absorption for p = 10mTorr, P_{pl} = 100 W.

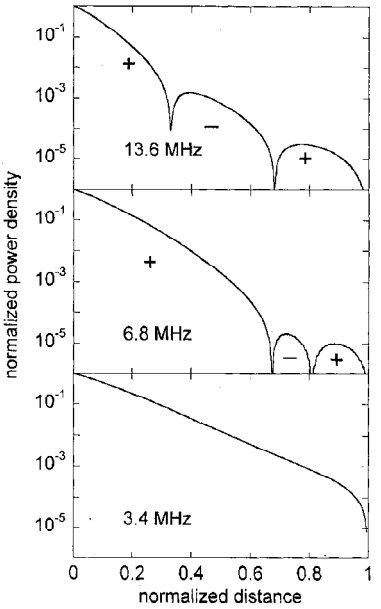

Figure 22. Spatial distribution of rf power absorption calculated by Kolobov.

The frequency dependence of the rf power absorption along the plasma is shown in Fig. 21 for p = 10 mTorr and P_{pl} = 100 W. A transit time resonance is clearly seen in the sequence of the appearance of the first negative power absorption region; the distance d between middle of the skin layer and first zero crossing point corresponds well with the relation: $d = v_{th}/2f$. Note, that apparently there is no negative power absorption at the lowest frequency of 3.39 MHz where anomalous skin effect (large Λ) and electron ballistic phenomena are expected to be greatest. This has a simple explanation: for 3.39 MHz: the electron transit time L/v_{th} is smaller than half the rf field period $(2f)^{-1}$, where L is the chamber length.

Calculation of rf power absorption in our experiment has been performed by Kolobov on the basis of work [15,18] modified to account for the inhomogeneity of the rf field ($\delta_0 \neq \infty$), and the results is shown in Fig. 22. This calculation was done assuming: a) homogeneous plasma, b) Maxwellian EEDF, and c) energy-independent ν_{en}. Although none of these assumptions hold for the experiment, the agreement seems very good.

Another peculiarity in the power absorption at p = 10 mTorr at 6.78 and 13.56 MHz is that the main rf power absorption in the skin layer is mainly collisionally dominated ($\nu_{eff} \approx \nu_{en}$), while deep in plasma the electrons demonstrate non-local electrodynamics typical of anomalous skin effect. This can be understood as a result of plasma inhomogeneity along the propagation of the rf field (see Fig. 7). For dense enough plasma, where $\delta_p < \delta_0$, the non-locality parameter Λ is nearly proportional to the plasma density (see Fig. 12), therefore, rf field interaction with electrons in the skin layer (where Λ is small) is rather local, while deep in plasma (where Λ is large) the interaction is non-local.

CONCLUSION

Electron kinetic and electrodynamic characteristics of ICP have been measured with improved diagnostic means over a wide range of argon pressure, discharge power and fre-

quency. A large data base suitable for comparison with theory and computer experiment has been generated and some new features in ICP characteristics associated with non-local electron kinetics and electrodynamics have been revealed. The large population of low energy electrons (similarly to that in low pressure CCP), the frequency dependence of EEDF and electron temperature, the rf field phase velocity reversal, the phase bifurcation and the second current layer with localized regions of negative power absorption are found to take place over a wide range of gas pressure. These effects are most expressed at the lowest gas pressure of 0.3 mTorr and vanish at about 100 mTorr and higher gas pressures. These observations support the notion that the phenomena reported here can be attributed to near-collisionless electron motion typical for the anomalous skin effect. For the first time, we have demonstrated collisionless rf power absorption and negative power absorption in an ICP through direct measurements of the rf electric field and current in the plasma.

Amazingly, the new features in the rf electric field and current distribution in the ICP observed here were built into the theory of anomalous skin effect[15,18] known for over 25 years, but overlooked. Recently, Wu,[29] Kolobov,[12] Tumer,[30] and Yoon[31] have independently calculated and simulated our experiment and found plausible agreement with our findings.

Acknowledgment

The author thanks R. B. Piejak and B. M. Alexandrovich for their essential contribution to the experimental measurements presented in this lecture. The author also thanks V. I. Kolobov for fruitful discussions.

REFERENCES

1. H. U. Eckert, Proc. 2nd Annual Int. Conf. on Plasma Chemistry and Technology ed. by Boenig, Lancaster, PA: Techonomic Publ., p. 171 (1986).
2. H. U. Eckert, J. Appl. Phys., 43, 2707 (1972).
3. K. H. Groh and H. W. Loeb, J. Propulsion, 7, 573 (1991).
4. M. A. Lieberman and A. J. Lichtenberg, *Principles of Plasma Discharges and Materials Processing*, John Wiley & Sons, Inc., New York, pgs. 390, 555, (1994).
5. M. M. Turner, Phys. Rev. Lett., 71, 1844, (1993).
6. V. A. Godyak, R. B. Piejak and B. M. Alexandrovich, Plasma Sources Sci. & Technol., 3, 169 (1994).
7. V. Vahedi, M. A. Lieberman, G. DiPeso, T. D. Rognlien and D. Hewett, J. Appl. Phys., 78, 1446 (1995).
8. N. S. Yoon, S. S. Kim, C. S. Chang and Duk-In Choi, Phys. Rev. E, 54, 757 (1996).
9. I. D. Kaganovich, V. I. Kolobov and L. D. Tsendin, Appl. Phys. Lett., 69, 3818 (1996).
10. Yu. M. Aliev, I. D. Kaganovich and H. Schluter, Arb. Plasmaphysik, report 51-B3-96, Ruhr University, Bochum (November 1996).
11. V. I. Kolobov, D. P. Limberopoulos and D. J. Economou, Phys. Rev. E, 55, 3408 (1997).
12. V. I. Kolobov and D. J. Economou, Plasma Sources Science & Technol., 6, R1 (1997).
13. R. A. Demirkhanov, I. Ya. Kadish and Yu. S. Khodyrev, Sov. Phys. JETP, 19, 791 (1964).
14. E. S. Weibel, Phys. Fluids, 10, 741 (1967).
15. H. A. Blevin, J. A. Reynolds and P. C. Thonemann, Phys. Fluids, 13, 1259 (1970).
16. M. A. Liberman, B. E. Meierovich and L. P. Pitaevsky, Sov. Phys. JETP, 6, 1737 (1972)
17. Yu. S. Sayasov, Helvetica Physica Acta, 52, 288 (1979)
18. A. N. Kondratenko, RF Field Penetration in Plasma, Atomizdat, Moscow (1979)
19. S. M. Dikman and B. E. Meierovich, Sov. Phys, JETP, 37, 835 (1973)
20. V. A. Godyak, Invited Paper at ESCAMPIG 96, Vol.20E, Part A. pp. IX-XII, published by European Phys. Soc., edited by Lukac, Kozinar and Skalny, Bratislava, Slovakia (1996).
21. G. G. Lister, Y-M. Li and V. A. Godyak, J. Appl. Phys., 79, 8993 (1996).
22. V. A. Godyak and R. B. Piejak., deemed unpublishable in Phys. Rev. Lett.
23. R. B. Piejak, V. A. Godyak, and B. M. Alexandrovich, J. Appl. Phys, 81, 3416 (1997).
24. V. A. Godyak, Invited Paper at 3 rd Intern. Workshop on Microwave Discharges, Abbaye Royal de Fontevraud, France (1997).

25. V. A. Godyak and R. B. Piejak, Phys. Rev. Lett., 65, 996 (1990)
26. A. S. Smirnov and L. D. Tsendin, IEEE Trans. Plasma Sci., 19, 130 (1991)
27. V. I. Kolobov and V. A. Godyak, IEEE Trans. Plasma Sci., 23, 503 (1995)
28. U. Kortshagen, I. Pukropski and M. Zethoff, J. Appl. Phys., 76, 2048 (1994).
29. J. Wu, private communication.
30. M. Turner, private communication.
31. N. Yoon, private communication.

This Page Intentionally Left Blank

COLLISIONLESS ELECTRON HEATING IN RF GAS DISCHARGES: I. QUASILINEAR THEORY

Yu.M. Aliev[1] , I.D. Kaganovich[2] , H. Schlüter,
Experimental Physics II, Ruhr–University, 44780 Bochum, Germany

[1] on leave from Lebedev Physical Institute, Russian Academy of Sciences, 117924 Moscow Russia
[2] on leave from St. Petersburg Technical University, Physical Technical Department, Polytechnicheskaya 29, 195251 St. Petersburg, Russia

INTRODUCTION

Numerous applications of low-pressure gas discharges have recently prompted an interest in mechanisms of electron heating and power deposition in the plasma maintained by radio-frequency (rf) electric fields. A modern trend in plasma technology aims at decreasing the gas pressures down to the millitorr range. For these low pressures it is easier to maintain uniform plasmas with well controlled parameters. Due to the large value of the mean free path (MFP) the main mechanism of electron heating turns out to be a collisionless one rather than the conventional Joule heating dominant for higher pressures.

Being initially studied for a capacitively coupled plasma[1], this mechanism is now widely discussed in application to inductively coupled plasmas (ICP), ECR plasmas, etc. [2]. Initially collisionless heating was studied in a 'kick' model: electron obtains velocity kick in the strong electric field at the discharge periphery, then the phase of velocity kick is randomized either due to collisions in the bulk or due to non-linear mechanism of randomization (Fermi acceleration). As a result diffusion in velocity space arises, and this corresponds to collisionless heating.

In general case the electric field is presented in the whole discharge volume and the separation on periphery region where electron gains energy and a bulk without electric field is not applicable. The other subject of investigation is the heating of trapped in the discharge center electrons in non-uniform plasma buy ambipolar electric field. These electrons also can be heated by collisionless mechanism by weak electric field in the plasma field. For this situation kick model is also not applicable. In this particular situation the use of rigorous quasi-linear theory is necessary. It is based on well known mechanism of collisionless power dissipation - Landau damping (see e.g.

Electron Kinetics and Application of Glow Discharges
Edited by U. Kortshagen and L. D. Tsendin, Plenum Press, New York, 1998

[3]). The resonance particles moving with a velocity close to the wave phase velocity intensively interact with wave fields and receive or lose energy. The result of particle ⇔ wave interaction depends on the shape of the particle distribution function in velocity space. For Maxwellian distributions the wave amplitude decreases, while the particle energy increases. If many waves are excited the power dissipation should be summarized over the spectrum of waves. Such a theory was developed for a weak turbulence in order to explain the mechanisms of anomalous transport phenomena in hot plasma of thermonuclear fusion (see e.g.[4,5]).

But it can also be applied to stable plasmas, when small scale fields with a wide spectrum of wave numbers are excited by an external source. This situation is realized in the cases of Debye screening of longitudinal electric fields or cases of anomalous skin effects for transversal fields. A local spectrum of small scale Langmuir waves appears also in the region of plasma resonances for inhomogeneous plasmas interacting with electric fields capacitively coupled with plasmas (CCPs).

The only particles which are in resonance with a wave are heated by collisionless mechanism. It means that in the regime of collisionless dissipation the form of the electron energy distribution function (EEDF) is sensitive to wave spectrum. If the wave phase velocities are confined in some interval the plateau in the EEDF can be formed[5].

The problem of the plateau formation in the EEDF in the quasilinear theory was investigated first in[6,7]. In[8] it is shown that collisionless heating due to localized plasma oscillations results in plateau formation in the region of high electron energy. Collisions smooth out the plateau and lead to an increased number of high energy electrons[5]. The effect of collisions on electron heating by local plasma oscillations were investigated in [9]. The numerous investigations of EEDF by using a kinetic equation for electrons of a plasma slab with oscillating rigid walls have been performed in[10–12]. This treatment yields a power law energy dependence in the EEDFs. The experimental study of EDF for CCP have been carried out in[13,14].

A quasilinear approach to collisionless electron heating in the regions of plasma resonance in low pressure discharges, sustained by electromagnetic surface waves, is developed in[15,16]. In[17] it is demonstrated that — in view of experimental situations — self-consistent modeling has to account for nonlocal effects[18,19] as well as for collisionless heating. The classification of various regimes of collisionless heating were performed in [20].

In view of the history of successful use of the quasilinear approach as a well established method, particular in hot plasma physics, this paper aims at systematically applying this method also to study collisionless heating in various low temperature plasmas and to summarize existing results using a common basis as well as to gain extended new results. The paper intends to demonstrate that the quasilinear theory is a powerful and easily applicable method for investigations of these type of problems.

This paper is organized as follows: In section II, the derivation of the diffusion coefficient in energy space for uniform boundless plasmas, heated by localized high frequency field is presented. In section III the collisionless heating in inductively coupled plasmas (ICPs) is analyzed for semi-infinite and slab geometry. Both cases can be reduced to the boundless problem with specular reflecting walls. The profile of the electric field under the condition of the anomalous skin effect is found in analytical form and the electric field is shown to oscillate spatially with zero average value. As a result the diffusion coefficient of fast electrons is suppressed, but in the low energy region

it is enhanced in comparison to the case of an exponential profile. For ICPs in slab geometry (of width L) it is demonstrated that the second boundary plays a similar role. In this case the corresponding Fourier spectrum of electric field is discrete ($k_n = \pi n/L$) in contrast to a continuous one for semi-infinite geometry. In section IV the quasilinear theory is applied for capacitively coupled plasmas (CCPs). It is shown that the diffusion coefficient has a clear resonant structure with a main peak at $v = \omega L/\pi$. An analysis of the solutions of the kinetic equation for the EEDF in different regimes of plasma heating is presented. In section V the influence of the ambipolar electric field on the efficiency of collisionless heating is discussed. The general expression for the diffusion coefficient in energy space is obtained for cases both of ICPs and CCPs. The presence of ambipolar electric fields can strongly modify the condition for particle $\Leftrightarrow$ wave resonances. As a consequence the form of diffusion coefficient in energy space is changed, especially for low energy electrons. In a parabolic potential $\Phi = ax^2/2$ the bounce frequency of trapped electrons $(\sqrt{a/m})$ is the same for all energies. So the resonance condition $(\omega = \sqrt{a/m})$ can be fulfilled for one value of a only, and there is no collisionless heating for other values of a. In the general case of a non–parabolic potential the bounce frequency is energy dependent. Section VI contains the conclusion and outlook.

KINETIC THEORY OF COLLISIONLESS ELECTRON HEATING

Separation of the Space and Times scales in the Kinetic Description

First we discuss case when collisionless heating occurs in a small region at the discharge periphery of width $\delta << L$, L being the discharge gap. In the ICP, δ corresponds to the thickness of the skin layer. In a capacitively coupled plasma, this model corresponds to the sheath width smaller then an electron mean free path. For surface wave discharges it corresponds to collisionless dissipation in the narrow region of plasma resonance. In such low pressure discharges the space scale of the electric heating becomes small in comparison to the MFP λ. Under these conditions it is possible to simplify the kinetic description of the plasma by separation of the space scales.

The kinetic equation for the electron velocity distribution function $F(\boldsymbol{r}, \boldsymbol{v}, t)$ is:

$$\frac{\partial \mathcal{F}}{\partial t} + \boldsymbol{v}\frac{\partial \mathcal{F}}{\partial \boldsymbol{r}} + \frac{e}{m}\left(\boldsymbol{\mathcal{E}} + \frac{1}{c}\boldsymbol{v}\times\boldsymbol{\mathcal{B}}\right)\frac{\partial \mathcal{F}}{\partial \boldsymbol{v}} = S(\mathcal{F}) \tag{1}$$

where e and m are the electron charge and mass, respectively, $S(F)$ is the collisional integral, $\varepsilon(\boldsymbol{r}, t)$ is the electric and $ß(\boldsymbol{r}, t)$ is the magnetic field.

The fields can be separated into two parts according to different space scales:

$$\boldsymbol{\mathcal{E}} = \boldsymbol{E} + \tilde{\boldsymbol{E}} \qquad \boldsymbol{\mathcal{B}} = \boldsymbol{B} + \tilde{\boldsymbol{B}} \tag{2}$$

where $\boldsymbol{E}$ and $\boldsymbol{B}$ have spatial scales large compared to λ, while $\tilde{\boldsymbol{E}}$ and $\tilde{\boldsymbol{B}}$ have spatial scales δ small compared to λ (i.e. $\delta << \lambda$). An analogous separation can be performed for the distribution function:

$$\mathcal{F}(\boldsymbol{r}, \boldsymbol{v}, t) = F(\boldsymbol{r}, \boldsymbol{v}, t) + \tilde{F}(\boldsymbol{r}, \boldsymbol{v}, t) \tag{3}$$

where F is averaged over a scale in the order of λ and $\tilde{F}$ describes the deviations of the distribution function on scales smaller than λ. Also the usual quasilinear approximation

$\tilde{F} << F$ is used[4,5]. As a result the kinetic equation (1) can be separated into two parts:

$$\frac{\partial \tilde{F}}{\partial t} + \boldsymbol{v}\frac{\partial \tilde{F}}{\partial \boldsymbol{r}} + \frac{e}{m}\left(\boldsymbol{E} + \frac{1}{c}\boldsymbol{v} \times \boldsymbol{B}\right)\frac{\partial \tilde{F}}{\partial \boldsymbol{v}} = -\frac{e}{m}\left(\tilde{\boldsymbol{E}} + \frac{1}{c}\boldsymbol{v} \times \tilde{\boldsymbol{B}}\right)\frac{\partial F}{\partial \boldsymbol{v}} \tag{4}$$

$$\frac{\partial F}{\partial t} + \boldsymbol{v}\frac{\partial F}{\partial \boldsymbol{r}} + \frac{e}{m}\left(\boldsymbol{E} + \frac{1}{c}\boldsymbol{v} \times \boldsymbol{B}\right)\frac{\partial F}{\partial \boldsymbol{v}} = -\frac{e}{m}\overline{\left(\tilde{\boldsymbol{E}} + \frac{1}{c}\boldsymbol{v} \times \tilde{\boldsymbol{B}}\right)\frac{\partial \tilde{F}}{\partial \boldsymbol{v}}} + S(F) \tag{5}$$

In (4) the collisionless term is omitted, since it is small compared to the second term on the left-hand side: $k\lambda >> 1$. The bar in (5) denotes spatial averaging on scales smaller than λ.

The Form of Quasilinear Integral for Weakly Inhomogeneous Boundless Plasmas

First the case of weakly inhomogeneous boundless plasmas, when $\boldsymbol{E}, \boldsymbol{B} = 0$ and $\tilde{\boldsymbol{E}}$, $\tilde{\boldsymbol{B}}$ are only RF fields, is considered. It correspond to collisionless dissipation in narrow region with a gap width larger than a energy relaxation length, so influence of boundary can be neglected. The electric field is excited at fixed frequency:

$$\tilde{\boldsymbol{E}}(\boldsymbol{r}, t) = \frac{1}{2}\left\{\boldsymbol{E}(\boldsymbol{r})\exp(-i\omega t) + \boldsymbol{E}^*(\boldsymbol{r})\exp(i\omega t)\right\}, \tag{6}$$

where * denotes the complex conjugation.

Under conditions, when the frequency of inelastic collisions ν^* is small compared to the RF ω ($\nu^* << \omega$), the distribution function does not depend on time[19], i.e. $F = F(\boldsymbol{r}, \boldsymbol{v})$, and (4), (5) can be simplified to

$$\frac{\partial \tilde{F}}{\partial t} + \boldsymbol{v}\frac{\partial \tilde{F}}{\partial \boldsymbol{r}} = -\frac{e}{m}\left(\tilde{\boldsymbol{E}} + \frac{1}{c}\boldsymbol{v} \times \tilde{\boldsymbol{B}}\right)\frac{\partial F}{\partial \boldsymbol{v}} \tag{7}$$

$$\boldsymbol{v}\frac{\partial F}{\partial \boldsymbol{r}} = S_{\mathrm{ql}}(F) + S(F) \tag{8}$$

The first term on the right hand side of (8) is well known in the theory of weak turbulent plasmas as the quasilinear collision integral, describing interaction of electrons with waves,

$$S_{\mathrm{ql}}(F) = -\frac{e}{m}\overline{\left\langle\left(\tilde{\boldsymbol{E}} + \frac{1}{c}\boldsymbol{v} \times \tilde{\boldsymbol{B}}\right)\frac{\partial \tilde{F}}{\partial \boldsymbol{v}}\right\rangle} \tag{9}$$

where the $\langle . . . \rangle$ brackets indicate temporal averaging over the wave period $2\pi/\omega$.

Equation (7) can be solved by the Fourier method giving:

$$\tilde{F}(\boldsymbol{k}) = -\frac{ie}{m} \cdot \frac{\boldsymbol{E}(\boldsymbol{k}) + \frac{1}{c}\boldsymbol{v} \times \boldsymbol{B}(\boldsymbol{k})}{\omega - \boldsymbol{k}\boldsymbol{v}} \cdot \frac{\partial F}{\partial \boldsymbol{v}} \tag{10}$$

where $\tilde{F}(\boldsymbol{k})$, $\boldsymbol{E}(\boldsymbol{k})$ and $\boldsymbol{B}(\boldsymbol{k})$ are the Fourier transformations of the functions $\tilde{F}(\boldsymbol{r})$, $\boldsymbol{E}(\boldsymbol{r})$ and $\boldsymbol{B}(\boldsymbol{r})$, respectively:

By inserting (10) into (9) the quasilinear integral for the one-dimensional geometry can be written in the form:

$$S_{\mathrm{ql}} = \delta(x - x_0)\frac{\partial}{\partial v_i} D_{ij}(\boldsymbol{v})\frac{\partial F}{\partial v_j} \tag{11}$$

where the δ–function appears as a result of space averaging and reflects the fact of localization of the heating electric field in the region $x \approx x_0$ with a characteristic scale δ much smaller than λ and

$$D_{ij}(\boldsymbol{v}) = -\frac{e^2\pi}{m^2}\int dk \left[\boldsymbol{E}(k) + \frac{1}{c}\boldsymbol{v}\times\boldsymbol{B}(k)\right]_i \left[\boldsymbol{E}(k) + \frac{1}{c}\boldsymbol{v}\times\boldsymbol{B}(k)\right]_j \operatorname{Im}\left(\frac{1}{\omega - kv_x}\right) \tag{12}$$

is the tensor of the diffusion coefficient in velocity space. For excluding the magnetic field in (12) one can use the Maxwells equations:

$$\tilde{\boldsymbol{B}}(\boldsymbol{k}) = \frac{c}{\omega}\boldsymbol{k}\times\tilde{\boldsymbol{E}}(\boldsymbol{k}) \tag{13}$$

Thus in expression (12) the contribution of the Lorentz force is of the same order of magnitude as that of the electric field[21]. After substituting expression (13) for the magnetic field one gets:

$$D_{ij} = \frac{\pi(2\pi)^n e^2}{2m^2}\int d^n k \frac{k_i k_j}{\omega^2}|\boldsymbol{v}\tilde{\boldsymbol{E}}(k)|^2\delta(\omega - \boldsymbol{k}.\boldsymbol{v}) \tag{14}$$

From (12,14) it can be seen that the role of the Lorentz force is changing the direction of diffusion in velocity space. Without accounting for the Lorentz force the diffusion is in the direction of the electric field, but with accounting for the Lorentz force it is in the direction of wave propagation given by ***k.*** The same result in an one-particle approach was discussed in[21]. The formula (14) has a general form: it is valid for longitudinal waves, too ($\boldsymbol{E}\times\boldsymbol{k} = \mathbf{o}$). This stems from the fact that the electrons receive impulse from the wave impulse directed along ***k*** independent of the type of heating field (transverse or longitudinal).

The relation

$$\operatorname{Im}\left(\frac{1}{\omega - kv_x + i\mathrm{o}}\right) = -\pi\delta(\omega - kv_x), \tag{15}$$

corresponding to the chase resonance between traveling wave and moving electron, was used to obtain expression (14).

It should be stressed that D_{ij} is a nonlocal function of the heating electric field due to the integral representation

$$\boldsymbol{E}(k) = \int \frac{dx}{2\pi}\exp(-ikx)\tilde{\boldsymbol{E}}(x)\,. \tag{16}$$

This type of nonlocality is also discussed in[22].

The simple physical meaning of expression (14) shall be illustrated by the example of plasma heating due to the localized field of a longitudinal wave $\tilde{\boldsymbol{E}}$ (E_x, 0, 0). In this case one obtains from (14):

$$D_{xx} = \frac{\pi^2 e^2}{m^2}\frac{1}{|v_x|}\left|E\left(k = \frac{\omega}{v_x}\right)\right|^2 \tag{17}$$

Expression (17) can be presented in the form

$$D_{xx} = \frac{|v_x|}{4}(\Delta v)^2 \tag{18}$$

where Δv is the amplitude of the velocity kick after interaction with the wave field:

$$\Delta v = \int_{-\infty}^{+\infty} e\tilde{E}_x(x = v_x t)\exp(-i\omega t)dt = \frac{2\pi e}{v_x}E\left(k = \frac{\omega}{v_x}\right) \tag{19}$$

Kinetic Equations for the EEDF

In gas discharge plasmas the anisotropy of the distribution function in velocity space is small due to the elastic collision frequency ν being large compared to the inelastic one (ν^*),[19] i.e. $\nu >> \nu^{**}$. In this case the conventional two-term approach is applicable and for the spherically symmetric part of the EEDF F_0 one has the following equation for one-dimensional geometry:

$$\frac{v^2}{3\nu(v)}\frac{\partial^2 F_0}{\partial x^2} - S^0_{\rm ql}(F_0) - S^*(F_0) = 0 \tag{20}$$

where

$$S^0_{\rm ql}(F_0) = \frac{1}{v^2}\frac{\partial}{\partial v}\left(v^2\mathcal{D}(v)\frac{\partial F_0}{\partial v}\right)\cdot\delta(x - x_0) \tag{21}$$

with

$$\mathcal{D}(v) = \frac{1}{v^2}\frac{\pi^2 e^2}{m^2}\int_{-\infty}^{+\infty}dk\int_0^{\pi}\sin\vartheta\, d\vartheta\int_0^{2\pi}\frac{d\tilde{\Phi}}{4\pi}|\boldsymbol{v}\boldsymbol{E}(k)|^2\delta(\omega - kv_x) \tag{22}$$

is the averaged (over the velocity angles) quasilinear collision integral $S_{\rm ql}$ (11) and $S^*(F_0)$ is the inelastic collision integral.

Expression (22) like (14) has a general form for all types of fields. The Lorentz force in (22) for an isotropic EEDF has vanished and the resulting diffusion coefficient (14) is the same with or without accounting for the Lorentz force. Thus the wave instability discussed in[3,21], which is equivalent to electron cooling, is essential only for anisotropic or non monotonic EEDFs, where the role of the Lorentz force is essential.

Below we summarize the forms of the diffusion coefficients in velocity space for various types of discharges:

1. For the case of transverse em waves ($\boldsymbol{k} \perp \boldsymbol{E}(\boldsymbol{k})$, $\boldsymbol{k} = k\boldsymbol{e}_x$, $\boldsymbol{E}_y = \boldsymbol{e}_y E(\boldsymbol{k})$) — corresponding to an inductive discharge — (22) yields

$$\mathcal{D}(v) = \frac{1}{v^2}\frac{\pi^2 e^2}{m^2}\int_0^{\pi}\int_0^{2\pi}\frac{v_y^2\left|E(k = \frac{\omega}{v_x})\right|^2}{|v_x|}\frac{\sin\theta\, d\theta\, d\tilde{\Phi}}{4\pi}. \tag{23}$$

After integration over $\tilde{\Phi}$ and introduction of $\mu = \cos\theta = v_x/v$, one gets

$$\mathcal{D}(v) = \frac{1}{v}\frac{\pi^2 e^2}{2m^2}\int_{-1}^{1}\frac{(1-\mu^2)\left|E(k = \frac{\omega}{v\mu})\right|^2}{2|\mu|}d\mu. \tag{24}$$

*It corresponds to the case, when a localized em field is excited with a broad spectrum of wavenumber Δk. So the corresponding time of diffusion through the region of wave–particle interaction ($\Delta v \approx \omega/k^2\Delta k$) $- t_i \approx (\Delta v)^2/\mathcal{D}$ is large compared with the collision time $\nu t_i >> 1$. The steady state condition is established on a time $t \approx \nu^{*-1}$. The opposite case corresponds to large anisotropy of the EEDF and can even lead to current drive[23].

2. For the case of a longitudinal electric field ($\boldsymbol{k} \parallel \boldsymbol{E}$, $\boldsymbol{k} = k\,\boldsymbol{e}_x$, $\boldsymbol{E} = E\,\boldsymbol{e}_x$) — corresponding to a capacitive discharge and plasma resonance heating in surface wave plasmas — (22) reduces to

$$\mathcal{D}(v) = \frac{1}{v}\frac{\pi^2 e^2}{m^2}\int_{-1}^{1}\frac{|\mu|}{2}\left|E\left(k = \frac{\omega}{v\mu}\right)\right|^2 d\mu\,. \tag{25}$$

3. For the case of a circularly polarized electric field ($\boldsymbol{k} = k_{y0}\boldsymbol{e}_y + k_x\boldsymbol{e}_x$, $\boldsymbol{E} = E_x\boldsymbol{e}_x + E_y\boldsymbol{e}_y$, $E_y = iE_x = E_0$) — corresponding to SW sustained discharges (generally speaking elliptically polarized) — (22) gives

$$\mathcal{D}(v) = \frac{1}{v^2}\frac{\pi^2 e^2}{m^2}\int_0^{\pi}\int_0^{2\pi}\frac{(v_y^2 + v_x^2)\left|E_0\left(k = \frac{\omega - k_{y0}v_y}{v_x}\right)\right|^2}{|v_x|}\frac{\sin\theta\,d\theta\,d\tilde{\Phi}}{4\pi}\,, \tag{26}$$

where k_{y0} is the fixed wavenumber of the surface wave and $E(k)$ corresponds to the Fourier transformation of the electric field profile $E_0(x)$.

To obtain the EEDF, (20) should be integrated over a small vicinity of the point $x = x_0$. One gets as result:

$$-\frac{v^2}{3\nu(v)}\left.\frac{\partial F_0}{\partial x}\right|_{x=x_0+0} = \frac{1}{2}\frac{1}{v^2}\frac{\partial}{\partial v}\left(v^2\mathcal{D}(v)\left.\frac{\partial F_0}{\partial v}\right|_{x=x_0+0}\right) \tag{27}$$

In obtaining (27) symmetry of plasma heating and EEDF with respect to the space position $x = x_0$ is assumed. Relation (27) should be considered as boundary condition for the equation

$$\frac{v^2}{3\nu(v)}\frac{\partial^2 F_0}{\partial x^2} - S^*(F_0) = 0 \tag{28}$$

describing the space evaluation of the EEDF outside the region of RF power input.

By representing the collisional integral $S^*(F_0)$ in the form

$$S^*(F_0) = -\nu^*(v)F_0(v,x) \tag{29}$$

one obtains from (28):

$$F_0(v,x) = F_0(v)\exp\left(-\frac{x}{\lambda_\varepsilon}\right), \tag{30}$$

where $\lambda_\varepsilon = v/\sqrt{3\nu(v)\nu^*(v)}$ energy relaxation length. Substituting (30) into the boundary condition (27) now results in the equation for the EEDF:

$$v\sqrt{\frac{\nu^*(v)}{3\nu(v)}}F_0(v) = \frac{1}{2}\frac{1}{v^2}\frac{\partial}{\partial v}\left(v^2\mathcal{D}(v)\frac{\partial F_0}{\partial v}\right) \tag{31}$$

Equation (31) has previously been analyzed for the case of localized longitudinal RF fields in the ionosphere[9] and SW produced plasmas[15]. The character of the solutions of (31) essentially depends on the diffusion coefficient $D(v)$. For its determination the space spectra of the heating EM fields have to be known.

In contrast to boundless plasmas considered above gas discharge plasmas are always bounded. Thus, in the next section a procedure of reducing the bounded problem to a boundless one will be developed.

SPACE SPECTRA OF HEATING ELECTRIC FIELDS AND DIFFUSION COEFFICIENTS FOR INDUCTIVELY COUPLED PLASMAS

The Semi–Infinite Plasma

In order to use the results of boundless plasmas, specular reflection of the electrons from the discharge wall ($x = 0$) is assumed:

$$\tilde{F}(v_x, v_y, v_z, x < 0) = \tilde{F}(-v_x, x_y, v_z, x > 0) \tag{32}$$

To reduce the semi-infinite problem to boundless one the continuation of Eq. (7) into the complete x-range ($-\infty < x < \infty$) can be performed. Now the reflected electron is represented by one passing to the region $x < 0$). The kinetic equation is symmetric with respect to electron reflection if the fields are continued by the following *ansatz* see Fig.1:

$$\begin{aligned} \tilde{B}_y(x < 0) &= -\tilde{B}_y(x > 0) \\ \tilde{E}_y(x < 0) &= \tilde{E}_y(x > 0) \\ \tilde{E}_x(x < 0) &= -\tilde{E}_x(x > 0) \end{aligned} \tag{33}$$

and the problem reduces to the case of boundless plasmas *.

Now the possible regimes of shielding the transverse EM field by the semi-space plasma are addressed. In the case of weak collisions ($\omega > \nu$) the field penetrates into the overdense plasma ($\omega \ll \omega_p = (4\pi e^2 n/m)^{1/2}$) over the depth $\delta_0 = c/\omega_p$. For such a regime the frequency of the electric field should be sufficiently high ($\omega > v_T/\delta_0$, with v_T being the thermal electron velocity). A regime of collisionless plasma heating is possible, if the skin length δ_0 does not exceed the MFP λ, i.e. if $v_T > \nu \cdot \delta_0$. In this case one should use the following form for the electric field, continued into the complete x-range to calculate the diffusion coefficient for semi-infinite plasmas:

$$E_y(x) = E_0 \exp\left(-\frac{|x|}{\delta_0}\right), \tag{34}$$

with the Fourier spectrum given by

$$E(k) = \frac{E_0' \delta_0}{\pi(1 + k^2\delta_0^2)}. \tag{35}$$

It should be noted that result (34) corresponds to the absence of power dissipation, accounting for low power dissipation either due to small collisionality or colisionless dissipation results in weak spatial field oscillations and a small EM power flux into the plasma. Substitution of (35) into (22) yields the expression for the diffusion coefficient $D(v)$:

$$\mathcal{D}(v) = \omega\delta_0 v_E^2 g\left(\frac{v}{\omega\delta_0}\right) \tag{36}$$

*It should be mentioned that the approximation of specular boundary reflection ($v_x = -v_x$, $x = 0$) may not be valid in real plasmas, where electrons reflect from the sheath region and penetrate into the sheath by a length $\Delta(v_T) \sim r_D$ (r_D being the Debye radius). If this length is small (i.e. $\Delta(v_T) < v_T/\omega \ll \delta$), the sheath region is not important and formulae for specular reflection are valid. For the opposite case $\delta > \Delta(v_T) \gtrsim v_T/\omega$ the velocity kick (and thus the energy dissipation) is smaller[24].

a)

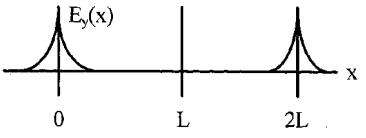

b)

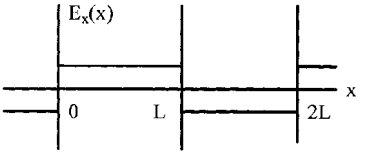

Figure 1. Scheme of electric field continuation: (a) transverse electric field; (b) longitudinal electric field.

where $v_E = eE_0/m\omega$ and

$$g(\tilde{v}) = \frac{1}{4\tilde{v}^3}[(2+\tilde{v}^2)\ln(1+\tilde{v}^2) - 2\tilde{v}^2] \tag{37}$$

which should be used in the kinetic equation (31) for obtaining the EEDF $F_0(v)$.

In the region of low electron energy $(v/\omega\delta_0 \ll 1 \rightarrow \tilde{v} \ll 1)$ one has

$$g(\tilde{v}) \approx \frac{1}{24}\tilde{v}^3. \tag{38a}$$

In the limit of high electron energy $(v/\omega\delta \gg 1 \rightarrow \tilde{v} \gg 1)$ one obtains:

$$g(\tilde{v}) \approx \frac{\ln(\tilde{v})}{2\tilde{v}} \tag{38b}$$

For lower frequencies $\omega^* < \omega < v_{T_e}/\delta_0$ the case of anomalous skin effect[3] is realized $(\omega^* = \nu^3 c^2/\omega_p^2 v_{Te})$, independent of the relation between ω and ν. In this situation the depth of the electric field penetration becomes less than the MFP λ and electrons are heated in a collisionless manner.

If one uses a description of the electric field in the form

$$E_y(x) = E_0 \exp\left(-\frac{|x|}{\lambda_{sk}}\right) \tag{39}$$

where $\lambda_{sk} = (c\mathcal{Z})/(i\omega)$ is chosen from the condition of a correct representation for the power deposition into the plasma with the surface impedance $\mathcal{Z} = 2/3\delta(1 + \frac{1}{3}\sqrt{3}i)$,

where $\delta = b^{-1/3}$ is effective skin depth see Eq.(44) the diffusion coefficient $D(v)$ is:

$$\mathcal{D}(v) = \omega\delta v_E^2 g\left(\frac{v}{\omega\delta}\right) \tag{40a}$$

$$g(\tilde{v}) = \frac{4}{27}\frac{1}{\tilde{v}}\left\langle\left(\frac{1}{2}+\frac{8}{27\tilde{v}^2}\right)\ln\left[\frac{3+\left(1+\frac{27}{8}\tilde{v}^2\right)^2}{4}\right] - \right.$$
$$\left. -\frac{1}{\sqrt{3}}\left(1-\frac{16}{27\tilde{v}^2}\right)\left\{\arctan\left[\frac{1+\frac{27}{8}\tilde{v}^2}{\sqrt{3}}\right]-\frac{\pi}{6}\right\}-1\right\rangle \tag{40b}$$

The function $g(\tilde{v})$ has the following approximation in the region of high electron energy ($\tilde{v} = v/\omega\delta \gg 1$):

$$g(\tilde{v}) \approx \frac{4}{27}\frac{\ln(\tilde{v})}{\tilde{v}} \tag{41a}$$

and in that of low electron energy ($\tilde{v} << 1$):

$$g(\tilde{v}) = \frac{9}{128}\tilde{v}^3 \tag{41b}$$

The exact Fourier transformation of the electric field obtained from the kinetic approach[3] yields:

$$E(k) = \frac{E_0}{\pi L_{sk}\left(k^2 - i\frac{b}{|k|}\right)} \tag{42}$$

where

$$b = \frac{4\pi\omega e^2}{c^2 m}\int v_y \frac{\partial F}{\partial v_y}\delta(v_x)d\boldsymbol{v} \tag{43}$$

In the case of a Maxwellian EEDF one has:

$$b = \frac{2e^2 n\omega}{c^2}\sqrt{\frac{2\pi}{mT}} \tag{44}$$

where n is the electron density and

$$L_{sk} = \frac{2(\sqrt{3}+i)}{3^{3/2}b^{1/3}}. \tag{45}$$

The space dependence of the electric field penetrating into the plasma over the region $0 < x < v_T/\omega$ has the form:

$$E_y(x) = \frac{E_0}{\pi L_{sk} b^{1/3}}\left\{\frac{\pi}{3}\left[(\sqrt{3}\,i+1)\exp\left(i\frac{\sqrt{3}}{2}-\frac{1}{2}\right)xb^{1/3}+\exp\left(-xb^{1/3}\right)\right]\right.$$
$$\left. -2i\int_0^\infty \frac{\xi\exp\left(-xb^{1/3}\xi\right)}{1-\xi^6}d\xi\right\} \tag{46}$$

The last term on the right–hand side of (46) represents the contribution of the branch point $k = 0$ and the exponential terms are a result of the poles in the integration when the inverse Fourier transformation of expression (42) is performed. A plot of $E_y(x)$

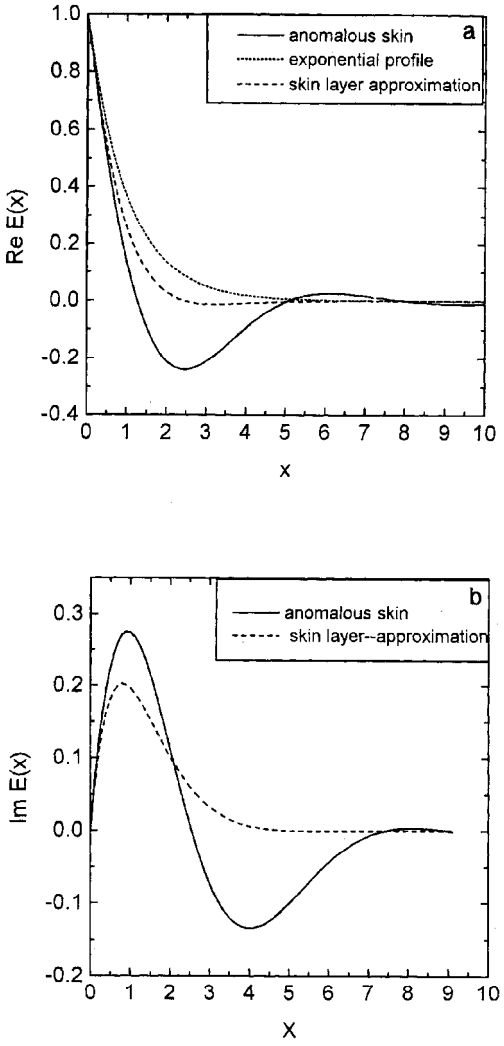

Figure 2. Plot of the electric field at anomalous skin effect as a function of normalized coordinates x/δ_0. The solid curve corresponds to the exact profile of the electric field (46), the dashed one to the exponential profile (34) and the small dashes represent the impedance approximation (39): (a) Real, (b) imaginary part of the electric field intensity.

is presented in Fig. 2. The electric field profile has a oscillatory structure which reflects the existence of power flux into the plasma due to collisionless dissipation. It should be noted that at large distances from the plasma surface $(x > v_{Te}/\omega)$ the influence of electron thermal motion is not important and the electric field penetration becomes purely exponential with a scale length $\delta_0 = c/\omega_p$. But this effect of changing the regime of field penetration can be neglected because at this distance $E_y(x)$ has decreased to a small fraction of its value at the surface if the frequency w is in the range $\omega < (v_T/c)\,\omega_p$ where the anomalous skin effect is applicable.

By substituting expression (42) into (22) one obtains:

$$\mathcal{D}(v) = \omega\delta v_E^2 g\left(\frac{v}{\omega\delta}\right) \tag{47}$$

where

$$g(\tilde{v}) = \frac{9}{64\tilde{v}}\left\{\sqrt{3}\left[\arctan\left(\frac{2\tilde{v}^2-1}{\sqrt{3}}\right)+\frac{\pi}{6}\right] - \frac{1}{\tilde{v}^2}\ln(1+\tilde{v}^6) - \ln\left(\frac{1+\tilde{v}^2}{\sqrt{1-\tilde{v}^2+\tilde{v}^4}}\right)\right\}. \tag{48}$$

In the region of large values of the argument $\tilde{v} >> 1$ the function $g(\tilde{v})$ decays and can be approximated by:

$$g(\tilde{v}) \approx \frac{9\pi}{32\sqrt{3}}\frac{1}{\tilde{v}} \tag{49a}$$

For small values of $\tilde{v} << 1$ (44) goes to zero by the law:

$$g(\tilde{v}) \approx \frac{9}{128}\tilde{v}^3 \tag{49b}$$

In Fig. 3 plot of $g(\tilde{v})$ for different cases of electric field representation is shown. The difference of the diffusion coefficients (49) to (38,41) (see Fig. 3) is essentially due to the oscillating structure of the em field penetrating into the plasma, which is very important for resonant interaction of particles with the field. The reason for this structure of the electric field is the nonlocality of the conductivity $\sigma(k)$. Due to the plasma conductivity an electron current arises and produces magnetic and electric fields in a direction opposite to that of the external em fields. In the local case (σ does not depend on k) this leads to a monotonic decrease of the sum of all em fields, while in the nonlocal case these em fields are shifted towards the plasma and as a result the oscillating structure of the em fields appears.

Another feature of exact description is that

$$\int_0^\infty E(x)\,dx = 0 \tag{50}$$

Note that it follows from (46) that the Fourier component $E(k = 0)$ should be equal to zero, which is in agreement with (42).

The integral of the electric field $\int_0^\infty E\,dx \to 0$, since the electron current has to vanish at large *x*, where the average electron velocity is determined by this integral.

Diminishing of the diffusion coefficient (47) in regions of a high electron velocity $v > \omega\delta$ as a transparent physical meaning. To the electron with such a high velocity the electric field appears as a stationary one. The increase of the electron energy by interacting with the localized electric field is equal to zero, since the spatial integral over electric field is zero.

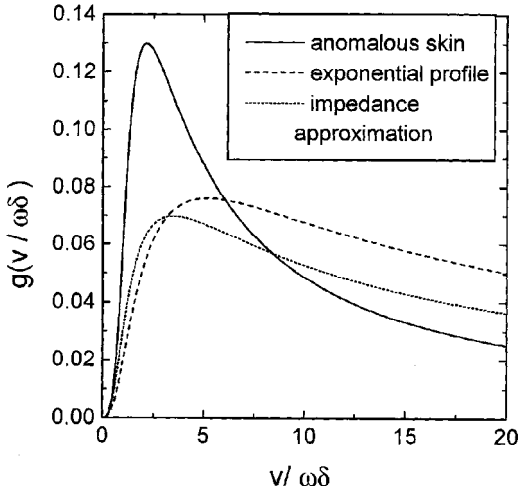

Figure 3. The normalized diffusion coefficient $g = \mathcal{D}/\frac{\delta_0}{2}\omega v_E^2$ as a function of the dimensionless velocity $\tilde{v} = v/\omega\delta_0$ for various models of electric field profile. The solid curve corresponds to the exact profile of the electric field (46), the dashed one to the exponential profile (34) and the small dashes represent the impedance approximation (39).

In the region of high electron energy the diffusion coefficients $D(v)$ (36), (40) decays much less than in the case, when the electric field is described exactly (48). This is a consequence of the fact that in the former two cases the long wave part of the Fourier spectrum of the electric field does not vanish and $E(k = 0) \neq 0$.

The Slab Geometry

Now the case of a uniform plasma slab (of width L) bounded by two plane walls with specular reflection of electrons is considered. For the case $L >> \lambda$ collisionless heating of overdense plasmas occurs only in the nearest vicinity of the walls, while between then the usual Joule heating takes place. By using the method of continuation considered in the previous section the following solution for the EEDF is obtained

$$F_0(v,x) = F_0(v) \cdot \frac{\cosh\left(\frac{x-\frac{L}{2}}{\lambda_\varepsilon}\right)}{\cosh\left(\frac{L}{2\lambda_\varepsilon}\right)} \tag{51}$$

generalizing the result (30) for the case of plasma slabs with symmetrical heating on both walls. The kinetic equation for the EEDF $F_0(v)$ instead of (31) now has the form:

$$v\sqrt{\frac{\nu^*}{3\nu}}\,F_0(v) = \frac{\coth\left(\frac{L}{2\lambda_\varepsilon}\right)}{2v^2}\frac{\partial}{\partial v}\left(v^2\mathcal{D}(v)\frac{\partial F_0(v)}{\partial v}\right) \tag{52}$$

The diffusion coefficient $D(v)$ in (52) is defined by (22). The limit $L >> \lambda_\varepsilon$, corresponds to the case of semi–infinite plasmas and (52) changes to (27). In the opposite limit of

thin slabs ($L << 2\lambda_\varepsilon$), on the right-hand side of (52) a large parameter $2\lambda_\varepsilon/L >> 1$ arises corresponding to more effective heating. In this case (52) takes the form:

$$\nu^* F_0(v) = \frac{1}{v^2}\frac{\partial}{\partial v}\left(\frac{v^2\mathcal{D}(v)}{L}\frac{\partial F_0(v)}{\partial v}\right) \tag{53}$$

Equation (52) expresses the fact that losses of electron energy by inelastic collisions in the plasma volume balances the collisionless heating. It should be noted that in this limit the EEDF is spatially uniform and is equal to $F_0(\varepsilon)$ in spite of the localization of energy input regions near the walls. This limit corresponds to the so called "nonlocal" heating regime of plasmas with space dimensions less than the length of of electron energy relaxation λ_ε[18,19].

If the slab width does not exceed the MFP ($L < \lambda < \lambda_\varepsilon$), the kinetic equation for the EEDF has a form identical to (53) but with the diffusion coefficient

$$\mathcal{D}(v) = \frac{\pi e^2 L}{2v^2 m^2}\sum_{n=-\infty}^{\infty}\int_0^\pi \sin\vartheta\, d\vartheta \cdot \int_0^{2\pi}\frac{d\tilde{\Phi}}{4\pi}\cdot (v_y)^2|E_n|^2\cdot\delta\left(\omega - \frac{\pi n}{L}v_x\right) \tag{54}$$

where

$$E_n = \frac{1}{L}\int_0^L E_y(x)\cos\left(\frac{\pi}{L}nx\right)\,dx \tag{55}$$

is the Fourier transformation of the periodically continued—in accordance with (33)—electric field $E_y(x)$ (with period L).

Expression (54) shows that only particles being in resonance $(v_x = \omega L/\pi n)$ contribute to the collisionless heating in contrast to semi–infinite geometry, where *all* particles contribute to the heating, as can be seen from (14). The reason for such a discrimination lies in the way of stochastization of the em field phase[20]. In the semi-infinite case all electrons undergo collisions in the periphery of the heating region, so subsequent interactions with the em field region happen after several collisions and randomly. Thus all electrons participate in the heating. In the slab geometry ($L < \lambda$) electrons return to the same place in a time much smaller than the time between collisions. So these interactions are correlated and no diffusion in velocity space occurs. The collision frequency does not enter in the expressions for the diffusion coefficient (22) and (54), but the presence of collisions (or other stochastization mechanisms) is necessary for collisionless heating. The situation is similar to the problem of Landau-damping. The different ways of stochastization in semi-infinite and slab geometry result in different diffusion coefficients (22) and (54). For a given velocity v the sum in (54) is over the resonance velocities $v_x = \omega L/\pi n < v$ (see Fig. 4). If $v \ll \omega L/\pi$, only higher n contribute to the integral. For small v the approximation of hard wall and specular reflection can be not valid and the real profile of the potential sheath should be considered (see comment after Eq.(33). It can be shown that the spectrum E_n is always proportional to $1/n^2$, independent of the form of dependence of $E_y(x)$. This behavior is connected to the symmetric continuation of $E_y(x)$ and originates from the jump of the magnetic field component $B_y = -\frac{ic}{\omega}\frac{\partial E_y}{\partial x}$ and is easy to check by twice partially integrating (55). For such a spectrum the sum in (54) can be changed to an integral for low energy electrons ($v < \omega L/\pi$) and the diffusion coefficient takes the form of (22) with the function $E(k)$ corresponding to the Fourier spectrum of the electric field

$$E_y(x) = \begin{cases} E_y(|x|) & -L < x < L \\ 0 & |x| > L \end{cases} \tag{56}$$

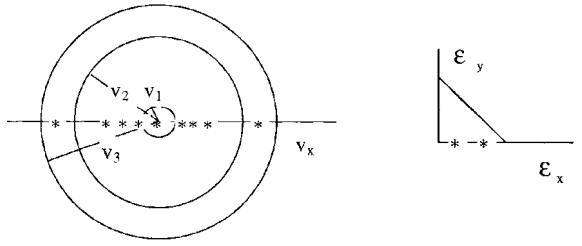

Figure 4. (a) Scheme of velocity space, area of averaging and resonance points. Small velocity v_1 corresponds to the region of many resonances, medium velocity v_2 lies in the region of the second resonance, and large velocity v_3 lies in the region of the first resonance. (b) Scheme of energy space, area of averaging and resonance points with accounting for the ambipolar electric field; no resonance points occur at small energies.

In the region of high electron energy $v \geq \omega L/\pi$) the sum in (54) cannot be transformed into an integral. To demonstrate this the simple case of an exponential profile of the penetrating electric field with skin depth $\delta_0 \leq L$ is considered. The spectrum E_n for this case is

$$E_n = \frac{E_0 \frac{\delta_0}{L}}{1 + \left(\frac{n}{n^*}\right)^2} \tag{57}$$

(with $n^* = L/\pi\delta_0$) and the diffusion coefficient (54)

$$\mathcal{D}(v) = \omega \frac{\delta_0}{2} v_E^2 \, g\left(\frac{v}{\omega\delta_0}\right) \tag{58}$$

is obtained, where

$$g(\tilde{v}) = \frac{1}{2\tilde{v}} \sum_{n > \frac{n^*}{\tilde{v}}}^{+\infty} \frac{1 - \left(\frac{n^*}{n\tilde{v}}\right)^2}{\left[1 + \left(\frac{n}{n^*}\right)^2\right]^2 \cdot n} . \tag{59}$$

For small $\tilde{v}$ ($\tilde{v} < n^*$) the main contribution to the sum in (59) stems from large n so that the sum can be represented by an integral and the result coincides with the result (36) for the case of semi-infinite plasmas.

For large $\tilde{v}$ ($\tilde{v} > n^*$) the sum in (54) yields a smaller diffusion coefficient compared with that in the case of semi–infinite plasmas. This is connected to the effective cut–off at small $k \leq \pi/L$ for the slab geometry.

From the point of view of the one particle approach formula (54) can be interpreted as follows. Passing forward and backward through the slab, an electron obtains a velocity kick. Subsequent kicks are correlated, and the sequence of this kicks leads to no diffusion. The diffusion in the energy space is only due to resonance electrons which

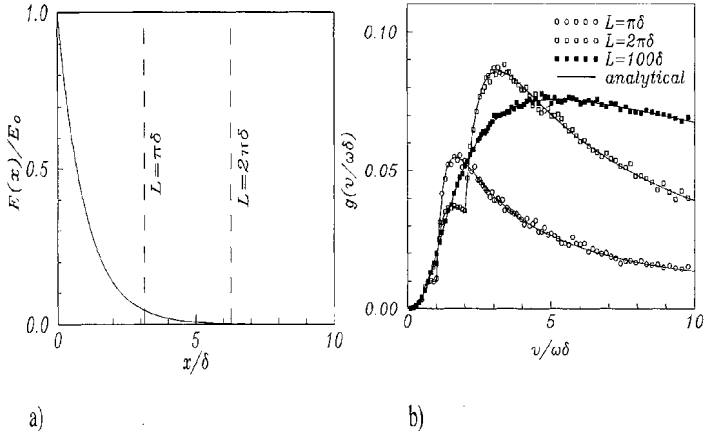

Figure 5. Influence of the second boundary on collisionless heating. (a) profile of the inductive electric field $E = E_0 \exp(-x/\delta)$ with second boundary at $x \equiv L = (\pi; 2\pi)\delta$; (b) normalized diffusion coefficient for an inductive exponential electric field $g = \mathcal{D}/\frac{9}{2}\omega v_E^2$, as a function of the normalised velocity $\tilde{v} = v/\omega\delta$ for different slab widths L. Solid curves correspond to the the analytical formulae (54), symbols to Monte Carlo simulations[25]: black squares: $L \to \infty$ $(100\,\delta)$; circles: $L = \pi\,\delta$; squares: $L = 2\pi\,\delta$.

randomize the phase of velocity kick due to rare collisions. And the diffusion coefficient reads:

$$\mathcal{D}(v) = L \sum_{n=-\infty}^{\infty} \int_0^{\pi} \int_0^{2\pi} \frac{1}{2} \frac{|v_x|}{2L} \frac{(\Delta \boldsymbol{v}_n \cdot \boldsymbol{v})^2}{2v^2} \delta\left(n - \frac{\omega L}{\pi v_x}\right) \frac{\sin\vartheta}{4\pi} d\vartheta d\tilde{\Phi}, \tag{60}$$

$$\Delta v_n = \int_{-\frac{L}{v_x}}^{\frac{L}{v_x}} \frac{e}{m} \tilde{E}(x = v_x t) \exp(-i\omega t)\, dt = \frac{2eL}{m|v_x|} E_n \tag{61}$$

It should be noted that (60) is only valid with accounting for collisions. Without collisions the stochastization for $\omega \gtrsim {}^{\pi v}/_{L}$ usually does not exist, even due to nonlinear effects[20]. The collisions play two important roles:

1. They stochastizate the phase of electron motion with respect to the phase of the electric field and

2. they transfer electrons from non–resonance velocity to resonance and vice versa.

This complex process of electron motion can be considered as diffusion with diffusion coefficient (60). The identity of this diffusion coefficient with the one from the one particle approach is fortuitous, but accounting for nonlinear effects, the results are different [20]. The plot of the normalized diffusion coefficient function $g(v)$ is shown in Fig. 5. The reduction of the diffusion coefficient due to the second boundary for ${}^{\pi v}/_{\omega L} \gtrsim 1$., where correlation effects are important, are clearly seen.

The vanishing of correlation effects for $\nu > \omega L$ was proposed first in[26], but the conclusion that it can occur without collisions is not correct[20,25]. The decrease of the real part of the surface impedance in the slab geometry compared to the semi–infinite one was found in[27] for a case, when the electron density drops exponentially with the width a and a skin depth much smaller than a. The reduction of collisionless heating due to the influence of the second boundary was observed in numerical simulations[28].

For a homogeneous electric field ($E_{n>1} = 0$) the collisionless heating vanishes[29]. In the sum in (54) there is no wave–particle resonance at all for $n = 0$. This can also be understood from the one–particle approach. Since the electric field is continued symmetrically, the motion of the electron in the case of slab geometry can be substituted by the motion in infinite space with a homogeneous electric field, where no condition for collisionless heating occurs. This situation is different for a longitudinal electric field.

CAPACITIVELY COUPLED PLASMAS

CCPs have a more complicated structure than ICPs due to the presence of large oscillating sheaths. For such a situation the approximation of the sheath potential as a moving rigid wall has repeatedly been used (see e.g.[22]). In this model the sheath velocity is $v_{\rm sh} = v_E \cos(\omega t + \tilde{\Phi})$. The electric field in the plasma bulk is neglected.

When MFP $\lambda < L$ we can apply Eq. (18) with velocity kick in the sheath $\Delta v = 2v_E$. After averaging over velocity angle the diffusion coefficient reads

$$\mathcal{D}(v) = \frac{v}{4}(v_E)^2 \tag{62}$$

If the energy relaxation length is larger than discharge gap $\lambda^* >> L$ the kinetic equation has a form (53). The physical meaning of expression (62) can be explained as follows. After reflection from the wall an electron obtains a velocity kick $2v_{\rm sh}$. If the next kick can be considered as randomly with respect to the previous one, diffusion in velocity space and electron heating appear. The randomization can originate from two mechanisms: collisions, when the mean free path of the electrons λ is smaller than the slab width ($\lambda \le L$), and the nonlinear mechanisms of collisionless stochastization[30]. In this case the averaged diffusion coefficient from two sheaths is[12]:

$$\frac{\mathcal{D}}{L} = \frac{1}{2}\frac{1}{4}\frac{v}{L}\left\langle (2v_{\rm sh}(t))^2 \right\rangle \tag{63}$$

Therefore $\frac{\mathcal{D}}{L}$ is the product of a factor ½, the bounce frequency, the squared velocity kick averaged in time and a coefficient ¼ resulting from averaging over the velocity angle.

For $\lambda > L$ the correlation between two following kicks are important. In this case Eq. (60) can be applied. After integration the diffusion coefficient reads:

$$\mathcal{D}(v) = \frac{\omega L}{2\pi} v_E^2 \, g\left(\frac{\pi v}{\omega L}\right) \tag{64}$$

with

$$g(\tilde{v}) = \frac{4}{\tilde{v}^3} \sum_{\substack{n=1,3,5,\dots \\ n > 1/\tilde{v}}} n^{-5} \tag{65}$$

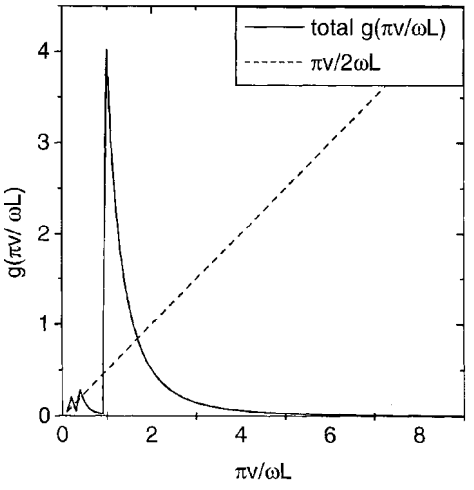

Figure 6. The normalized diffusion coefficient $g = \mathcal{D}/\frac{L}{2\pi}\omega v_E^2$ as a function of the dimensionless velocity $\tilde{v} = \pi v/\omega L$ for CCPs. The dashed curve represents $g = \tilde{v}/2$.

For small $\tilde{v}$ $(v < \omega L/\pi)$ the sum in (64) can be replaced by an integral and $g(\tilde{v})$ is approximated by

$$g(\tilde{v}) = \frac{\tilde{v}}{2} \tag{66}$$

so that

$$\mathcal{D}(v) = \frac{v v_E^2}{4}. \tag{67}$$

Thus in the low energy region the expression for the diffusion coefficient (62) is identical to the result obtained in[12] with an one–particle approach.

In the high velocity region $(v > \omega L/\pi)$ the main contribution in the sum of (65) is due to the first resonance and one obtains

$$g(\tilde{v}) = \frac{4}{\tilde{v}^3} \tag{68}$$

and correspondingly the diffusion coefficient decays $\sim v^{-3}$:

$$\mathcal{D}(v) = \frac{2\omega^4 L^2 v_E^2}{\pi^4}\frac{1}{v^3} \tag{69}$$

From Fig. 6 the large deviation of the quasilinear diffusion coefficient (solid line) from the one obtained without account correlation effect (dashed line) in the region of high electron velocity is evident. It is also possible to transfer the problem into a noninertial system moving with the sheath velocity v_{sh}. In this system there is a

stationary specularly reflecting boundary and an alternating electric field connected to the inertial force:

$$E_x(t) = -\frac{m}{e}\frac{dv_{\rm sh}}{dt} = E_0 \sin(\omega t + \tilde{\Phi}) , \tag{70}$$

Now the quasilinear approach is easily applied and with the help of the continuation method described above (32), (33) it yields the same expression for the diffusion coefficient (54) in ICP.

$$\mathcal{D}(v) = \frac{1}{v^2}\frac{\pi e^2}{2m^2}\sum_{n=-\infty}^{\infty}\int_0^{\pi}\sin\vartheta\, d\vartheta \int_0^{2\pi}\frac{d\tilde{\Phi}}{4\pi} v_x^2 |E_n|^2 \cdot \delta\left(\omega - \frac{\pi n}{L}v_x\right) \tag{71}$$

where

$$E_n = \frac{1}{L}\int_0^L E_x(x)\sin\left(\frac{\pi n x}{L}\right) dx. \tag{72}$$

In the case considered here $Ex(x) = E0$ = constant and Eq.(71) coincide with Eq.(64).

The interesting difference between capacitively and inductively coupled discharges is the different influence of the boundary on collisionless heating. For inductively coupled discharges the reflection from the boundary does not change the correlation between particle motion and electric field, since the influence of the electric field is the same before and after reflection and vice versa. For capacitively coupled discharges when the electric field diminishes the absolute value of velocity before reflection, but increases it after reflection. Consequently there is no collisionless heating with uniform electric fields for slab geometry in the case of inductively coupled discharges, but it does occur in the case of capacitively coupled discharges.

The difference in the nature of the heating field for CCPs and ICPs rests also in the structure of the diffusion coefficient near resonances. In the case of CCPs every resonance gives a well defined peak near $v_n = \pi\omega/Ln$ (see Fig. 6). With increasing v an additional resonance v_n yields at first a considerable contribution, followed, however, by a rapid decrease $\sim v^{-3}$. As a consequence at $v > \pi\omega/3L$ (i.e., $n \leq 3$) the diffusion coefficient is practically determined by the lowest resonance ($n = 1$) and its curve resembles a sequence of peaks (see Fig. 6). For ICPs the peak structure is smoothed out, since every new resonance results only in a small contribution $\sim (v - v_n)^2$ and the decrease of the resonance contributions is also slower than for CCPs ($\sim v^{-1}$). Therefore only the peak of the first resonance is pronounced in the net diffusion coefficient compare Fig.5 and Fig 6.

THE DIFFUSION COEFFICIENTS FOR INHOMOGENEOUS PLASMAS ACCOUNTING FOR STATIONARY AMBIPOLAR ELECTRIC FIELDS

In inhomogeneous plasmas the stationary ambipolar electric field appears which tends to trap electrons in the plasma volume. As a consequence low energy electrons cannot reach the periphery of the discharge, where the RF field is large. Therefore taking into account the ambipolar potential leads to a decrease in the efficiency of heating of low energy electrons. The diffusion coefficient for these electrons is small and the effective temperature of the low energy part of the EEDF can be considerably smaller than that of the higher energy part. For instance, in CCPs EEDFs resembling bi–Maxwellian ones have been observed, with a temperature of low energy electrons

($\varepsilon < 2$eV) ten times smaller than that of high energy electrons ($\varepsilon > 2$eV)[13]. Trapped electrons are heated by the bulk rf electric field. If the mean free path is larger than the plasma slab width ($\lambda > L$), the heating of trapped electrons tends to be collisionless and thus an appropriate quasilinear theory has to be developed.

The presence of the ambipolar electric field results not only in quantitative effects, but in qualitative ones, as we will see it changes the distribution of resonance particles over energy (see Fig. 4b).

First the case of a collisionless slab for CCPs ($\lambda >> L$) will be considered. The kinetic equation (4) for the fast varying part of the distribution function $\tilde{F}(x, \boldsymbol{v})$ with the ambipolar potential $\Phi(x)$ takes the form:

$$-i\omega\tilde{F} + v_x\frac{\partial\tilde{F}}{\partial x} - \frac{e}{m}\frac{\partial\Phi}{\partial x}\frac{\partial\tilde{F}}{\partial v_x} = -\frac{e}{m}\tilde{E}_x\frac{\partial F}{\partial v_x} - \nu\tilde{F} \tag{73}$$

Equation (73) can be simplified by introducing new variables: instead of v_x and x now ε_x and x, where $\varepsilon_x = mv_x^2/2 + e\Phi(x)$[18,19].

The corresponding boundary condition for the distribution function is

$$\tilde{F}(v_x) = \tilde{F}(-v_x), \quad x = x_\pm(\varepsilon_x) \tag{74}$$

The solution of (73) is given by (see e.g. [31])

$$\tilde{F}(x,\varepsilon_x) = e\frac{\partial F(\varepsilon)}{\partial\varepsilon}\exp(i\Omega)\left[-\frac{\int_{x_-}^{x_+}\sin(\Omega^* - \Omega(x'))E_0(x')\,dx'}{\sin\Omega^*} + \int_{x_-}^{x}\exp(-\Omega(x'))E_0(x')\,dx'\right] \tag{75}$$

where

$$\Omega(x,\varepsilon_x) = \text{sign } v_x\int_{x_-(\varepsilon_x)}^{x}\frac{\omega + i\nu\,dx'}{\sqrt{\frac{2}{m}(\varepsilon_x - e\Phi(x'))}} \tag{76}$$

$\Omega^* = \Omega(x_+, \varepsilon_x)$ and the turning points $x_\pm(\varepsilon_x)$ are defined by the relation (see Fig.7)

$$e\Phi(x_\pm) = \varepsilon_x \tag{77}$$

Due to isotropization in collisions the main part of the distribution function $F = F(\varepsilon)$ is the function of the total energy $\varepsilon = e\Phi + \frac{1}{2}mv^2$. After averaging over both x and velocity angle the kinetic equation reads:

$$\frac{d}{d\varepsilon}\overline{\mathcal{D}_\varepsilon}\frac{dF}{d\varepsilon} + \overline{S^*(F)} = 0 \tag{78}$$

The bars indicate averaging over the slab width L. The diffusion coefficient averaged over the angles in velocity space is:

$$\overline{\mathcal{D}_\varepsilon} = \frac{\pi e^2 L}{2}\int_0^\varepsilon\frac{d\varepsilon_x}{m}\sum_n E_n^2(\varepsilon_x)\delta[\Omega^*(\varepsilon_x) - \pi n] \tag{79}$$

with

$$E_n(\varepsilon_x) = \frac{1}{L}\int_{x_-(\varepsilon_x)}^{x_+(\varepsilon_x)}E_x(x)\sin\Omega(x,\varepsilon_x)\,dx \tag{80}$$

Thus (78) with the energy diffusion coefficient (79) appears to be a generalized form of the kinetic equation accounting for collisionless heating. The coefficients E_n are generalized Fourier coefficients (80)*.

Resonances occur, if the time of particle motion from one turning point to another (bounce time) is equal to $nT/2$, where $T = 2\pi/\omega$. This is in accordance with the resonance condition $\Omega^*(\varepsilon_x) = \pi n$, as follows from (79). If the value of $\Omega^*(\varepsilon_x)$ does not exceed π, there are no resonances at all and no collisionless heating occurs. It should be noted that, if the ambipolar potential is approximated by rigid walls, $\Omega^*(\varepsilon_X)$ is proportional to $\pi/\sqrt{\varepsilon_x}$ and the resonance conditions can always be fulfilled. In the case of a parabolic potential, which is realized for low energy electrons trapped near the discharge center and is defined by the potential profile $\Phi(x) = \Phi_0(x/l)^2/2$, the dimensionless period $\Omega^* = \sqrt{(\omega^2 m l^2)/\Phi_0}$ does not depend on the electron energy ε_X and the resonance conditions can be fulfilled in this case for one value of Φ_0/l^2 only. All plasma electrons are in or out of wave-particle resonance. Thus the "degeneracy" could be removed by taking into account the deviation of the ambipolar potential from the parabolic one.

To demonstrate the influence of the ambipolar potential on the energy diffusion coefficient an example for its calculation is given. Usually at the discharge center both the density and the potential profile are parabolic. At the periphery a more rapid decrease of density results in a more rapid increase of ambipolar potential. Therefore the latter is modeled in the form

$$\Phi(x) = \Phi_0(\cosh(x/l) - 1), \tag{81}$$

which is parabolic at the center $|x/l| \lesssim 1$ and higher than parabolic at the periphery (see Fig. 7a). The plot of the dimensionless period

$$\Omega^*(\varepsilon) = \int_{x_-}^{x_+} \frac{\omega dx}{v_x} \tag{82}$$

is shown in Fig. 7b for electrons moving in ambipolar potential (81). In contrast to the case of no ambipolar potential the function $\Omega^*(\varepsilon)$ is finite at small ε. For a given potential (81) e.g. this situation occurs, if $\Phi_0/m\omega^2 l^2 > 1$. For smaller Φ_0 the bounce time is larger and a first resonance $\Omega^* = \pi$ appears. For example for $\Phi_0 = 0.82$ resonance corresponds to a energy $\tilde{\varepsilon} = 0.82 m\omega^2 l^2$. With a given resonance energy the energy diffusion coefficient (76) can be calculated, its plot is shown in Fig. 8.

In Fig. 8 also the energy diffusion coefficient is presented without accounting for the ambipolar potential for a slab width the same as distance between turning points for resonance particles remains the same (i.e. $L = 2x_+(\varepsilon_r)$) (see Fig. 8) *.

The corresponding energy diffusion coefficient is considerably smaller than that with account of ambipolar field.

Indeed, for a purely parabolic profile, the function Ω^* does not depend on ε and $d\Omega^*/d\varepsilon = 0$, so for a resonance in this situation $D\varepsilon \to \infty$. As a consequence the smaller

*Expression (79) for the diffusion coefficient in energy space can also be derived by introducing a new variable—phase $\Omega = \int \frac{dx}{v_x}$ instead of coordinates[32] —and then performing a Fourier transformation on this variable.

*Many resonances exist for small energies, as a result the function $D_\varepsilon(\varepsilon)$ has the form of a ladder function. The value of steps at higher resonances is small $\propto 1/n^5$ and, thus, this cannot be recognized in Fig. 8. The main contribution is due to the first resonance, which corresponds to a energy $\varepsilon = m/2(\omega L/\pi)^2$.

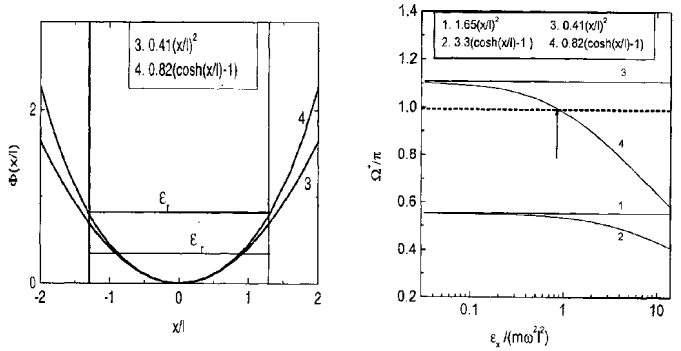

Figure 7. (a) Plot of the ambipolar potential $\Phi(x) = \Phi_0(\cosh(x/l) - 1)$ with $\Phi_0 = 0.82m\omega^2l^2$. $x_\pm(\tilde{\varepsilon}_r) = \pm 1.3l$ are the coordinates of the turning points. Model with no ambipolar field corresponds to the slab width L, so that the discharge area available for resonance particles is the same as before: $L = 2x_+(\tilde{\varepsilon}_r)$. Resonance occurs at the energy $\varepsilon = 0.82m\omega^2l^2$. with and $\varepsilon_r = 2m\omega^2(x_\pm(\varepsilon))^2/\pi^2$ without accounting for the ambipolar potential. (b) Plot of the phase Ω^*/π as function of the normalised energy $\tilde{\varepsilon} = \varepsilon/(m\omega^2l^2)$. For normalized potentials $\tilde{\Phi} = \Phi/(m\omega^2l^2)$ 1. $\tilde{\Phi}(x) = 1.65(x/l)^2$ 2. $\Phi(x) = 3.3(\cosh(x/l) - 1)$, 3. $\tilde{\Phi}(x) = 0.41(x/l)^2$ 4. $\tilde{\Phi}(x) = 0.82(\cosh(x/l) - 1)$

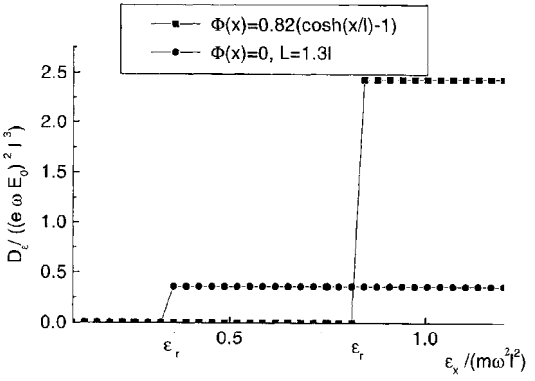

Figure 8. c) Plot of the dimensionless diffusion coefficient $g(\tilde{\varepsilon}) = \mathcal{D}_\varepsilon(\tilde{\varepsilon})/e^2E_0^2\omega^2l^3$ as a function of the dimensionless energy $\tilde{\varepsilon}$ (see Fig. 7b). Solid curve: with ambipolar normalised potential $\tilde{\Phi}(x) = 0.2(\cosh x - 1)$, $\tilde{\Phi}_0 > 1$ corresponds to the absence of resonance particles and $g = 0$. Small dashes: no ambipolar field, but smaller slab width L, so that the discharge area available for resonance particles is the same as before: $L = 2x_+(\tilde{\varepsilon}_r)$.

the nonlinearity of the ambipolar potential (the difference to the parabolic profile) the larger is the diffusion coefficient and, correspondingly, heating.

From kinetic equation (73) the distribution of current in the discharge can be found. The current in the system is determined by the difference $\Delta\tilde{F} = \tilde{F}(|v_x|) - \tilde{F}(-|v_x|)$. Substituting the solution (75) gives

$$\Delta\tilde{F} = 2ie\frac{\partial F}{\partial\varepsilon} \cdot \left[\int_{x_-}^{x} G(x,x',\varepsilon_x)E(x')\,dx' + \int_{x}^{x_+} G(x',x,\varepsilon_x)E(x')\,dx'\right], \tag{83a}$$

with the kernel

$$G(x,x',\varepsilon_x) = -\frac{\sin\Omega(x')\cdot\sin(\Omega^* - \Omega(x))}{\sin\Omega^*}, \tag{83b}$$

Integrating (83a) over the velocity we get an equation for the current in the discharge:

$$J(x) = \int_{x_-}^{x} \Pi(x,x')E(x')\,dx' + \int_{x}^{x_+} \Pi(x',x)E(x')\,dx' \tag{83c}$$

with

$$\Pi(x,x') = \frac{2\pi i}{m}\int_0^\infty \frac{\partial F}{\partial\varepsilon}\int_0^\varepsilon G(x,x',\varepsilon_x)\,d\varepsilon_x\,d\varepsilon \tag{83d}$$

For small collision frequency the current is shifted by $\pi/2$ in phase compared to the electric field, since it is determined by electron inertia.

For ICPs the diffusion coefficient averaged in velocity space is not influenced by the magnetic field, so it can be omitted for $\overline{\overline{\mathcal{D}_\varepsilon}}$ calculation. For the inductive electric field the current is determined by the sum$\Delta\tilde{F} = \tilde{F}(|v_x|) + \tilde{F}(-|v_x|)$. The function $\Delta\tilde{F}$ obeys to the integral equation (83a) with a kernel[2 7]

$$G(x,x') = -\frac{\cos(\Omega(x'))\cdot\cos(\Omega^* - \Omega(x))}{\sin(\Omega^*)}\,\frac{v_y}{|v_x|} \tag{84}$$

the expression for the diffusion coefficient has the form:

$$\overline{\mathcal{D}_\varepsilon} = \frac{\pi e^2 L}{2}\int_0^\varepsilon \frac{d\varepsilon_x}{m}\frac{\varepsilon - \varepsilon_x}{2\varepsilon_x}\sum_n E_n^2\delta(\Omega^* - \pi n) \tag{85}$$

where

$$E_n(\varepsilon_x) = \int_{x_-(\varepsilon_x)}^{x_+(\varepsilon_x)} E_y(x)\cos\Omega(x)\sqrt{\frac{\varepsilon_x}{\varepsilon_x - e\Phi(x)}}\,dx \tag{86}$$

CONCLUSIONS AND OUTLOOK

The quasilinear approach to the description of collisionless electron heating by given high frequency EM fields has been developed. This approach has been shown to be an effective method of providing a common basis for a variety of conditions in gas discharges and obtaining generalized expressions. It was possible not only to summarize the effects obtained and to compare with results previously obtained by a different approach, but also to obtain new and extended results: The comparison to results from the one-particle approach yields agreement in the diffusion coefficient characterizing heating only for the case of low energy electrons. The expressions derived here are valid

also for higher energies. For this region of electron energy a cut–off for the long wave part of the spectrum of heating electric field is required. Accounting for the second boundary of bounded plasma automatically provides such a cut–off. The generalized expressions for bounded plasmas given include the effect of ambipolar electric fields, which can be essential for the effectiveness of collisionless heating.

It should be noted, if the EM in the plasma has also large space scale parts ($\boldsymbol{E} \neq 0$, $\boldsymbol{B} \neq 0$), the complete equation (5) has to be used instead of (8). The influence of static ambipolar fields has been considered. The large space scale and time varying part of the EM give rise to local diffusion coefficients which should be added to nonlocal ones. Modeling of microwave discharges with heating due to two space scales and time varying electric fields has been undertaken in[17]. In general it can be underlined that knowledge of the energy diffusion coefficient gives a good basis for further developments, in particular for calculations of EEDFs needed for specific applications.

Finally it should be noted that the theory used in the present article is not a self consistent quasilinear theory due to neglecting backward influences of the modification of the EEDF on the electric field profile. For the case of surface wave produced plasmas this problem has briefly been discussed in[16] and included in numerical modeling in[17].

Acknowledgments The authors would like to thank Prof. L.D. Tsendin for interest in the work and T. Kaganovich and B. Lehnhoff for the help in numerical calculations and article preparing. The work was supported by Deutsche Forschungsgemeinschaft (SFB 191 and exchange program 438 113/133). I.K. acknowledges a research fellowship of the Alexander von Humboldt Foundation. Also discussions with Prof. A. Shivarova and cooperation within the Volkswagenstiftung contract I/70375 are gratefully acknowledged.

REFERENCES

1. V.A. Godyak, Statistical heating of electrons at an oscillating plasma boundary, *Sov. Phys. Tech. Phys.* 16: 1073 (1972).
2. M.A. Lieberman and A.J. Lichtenberg, “Principles of Plasma Discharges and Materials Processing”, John Wiley & Sons Inc. , New York (1994)
3. A.F. Alexandrov, L.S. Bogdankevich and A.A. Rukhadze, ” Principles of Plasma Electrodynamics”, Springer Series in Electrophysics vol. 9, Berlin–Heidelberg–New York: Springer (1984).
4. A.A. Galeev and R.Z. Sagdeev, “Nonlinear Plasma Theory”, in: M.A. Leontovich (ed.), Reviews of Plasma Physics vol. 7 ,New York–London: Consultants Bureau, (1976).
5. A.A. Vedenov, “Theory of a Weakly Turbulent Plasma”, in: M.A. Leontovich (ed.), Reviews of Plasma Physics vol. 3, New York–London: Consultants Bureau, (1967).
6. A.H. Vedenov, E.P. Velikhov and R. Sagdeev, Nonlinear oscillations of rare plasma, *Nucl. Fusion* 1: 82 (1961).
7. W.E. Drummond and D. Pines, *Nucl. Fusion Suppl.* 3: 1049 (1962).
8. L.M. Kovrizhnykh and A. Sakharov, Electron acceleration in the field of plasma resonance, *Sov. J. Plasma Phys.* 5: 470 (1979).
9. V.V. Vas’kov, A.B. Gurevich, Ja.S. Dimant, Multiply acceleration of electrons in plasma resonance, *Sov. Phys. JETP* 57: 310 (1983).
10. Yu.R. Alanakyan, Fermi acceleration and rf particle heating, *Sov. Phys. Tech. Phys.* 24: 611 (1979).
11. Yu.R. Alanakyan, Electron energy distribution in a free-streaming rf plasma column, *Sov, J. Plasma Phys.* 5: 504 (1979).
12. C.G. Goedde, A.J. Lichtenberg and M.A. Lieberman, Self-consistent stochastic electron heating in radio frequency discharges, *J. Appl. Phys.* 64: 4375 (1988).

13. V.A. Godyak and R.B. Piejak, Abnormally low electron energy and heating-mode transition in a low-pressure Argon rf discharge at 13.56 MHz, *Phys. Rev. Lett.* 65: 996 (1990).
14. U. Buddemeier, U. Kortshagen and I. Pukropski, On the efficiency of the electron sheath heating in a capacitively coupled radio frequency discharges in the weakly collisional regime, *J. Appl. Phys. Lett.* 67: 191 (1995).
15. Yu.M. Aliev, V.Yu. Bychenkov, A.V. Maximov and H. Schlüter, High energy electron generation in surface-wave produced plasmas, *Plasma Sources Sci. Technol.* 1: 126 (1992).
16. Yu.M. Aliev, Some aspects of nonlinear theory of ionizing surface plasma waves, in: CM. Ferreira and M. Moisan (eds.), "Microwave Discharges: Fundamentals and Applications", NATO ASI Ser. B: Phys. vol. 302 (Plenum, 1993), 105–115.
17. Yu.M. Aliev, A.V. Maximov, U. Kortshagen, H, Schlüter and A. Shivarova, Modeling of microwave discharges in the presence of plasma resonances, *Phys. Rev. E* 51: 6091 (1995).
18. I.B. Bernstein and T. Holstein, Electron energy distribution in stationary discharges, *Phys. Rev.* 94: 1475 (1954).
19. L.D. Tsendin, Electron kinetics in non-uniform glow discharge plasma, *Plasma Sources Sci. Technol.* 4: 200 (1995).
20. I.D. Kaganovich, V.I. Kolobov, L.D. Tsendin, Stochastic electron heating in bounded radio-frequency plasmas, *J. Appl. Phys. Lett.* 69: 3818 (1996).
21. R.H. Cohen and T.D. Rognlien, Electron kinetics in radio-frequency magnetic fields of inductive plasma sources, *Plasma Sources Sci. Techn.* 5: 442 (1996).
22. V. Vahedi, M.A. Lieberman, G. Di Peso, T.D. Rognlien and D. Hewett, Analytic model of power deposition in inductively coupled plasma sources, *J. Appl. Phys.* 78: 1446 (1995).
23. M.J. Fish, Confining a tokamak plasma with rf-driven currents, *Phys. Rev. Lett.* 41: 873 (1978).
24. I.D. Kaganovich and L.D. Tsendin, The space-time-averaging procedure and modeling of the rf discharge, part II: model of collisional low-pressure rf discharge, *IEEE Trans. Plasma Sci.* 20: 66 (1992).
25. U. Buddemeier, I. Kaganovich, Collisionless electron heating in RF gas discharges. II. Role of collisions and non-linear effects, *in* this book.
26. A.I. Akhiezer and A.S. Bakai, Theory of stochastic particle acceleration, *Sov. Phys. Dokl.* 16: 1065 (1972).
27. S.M. Dikman and B.E. Meierovich, Theory of the anomalous skin effect in a plasma with a diffuse boundary, *Sov. Phys.–JEPT*, vol. 37, 835 (1973).
28. M.M. Turner, Collisionless electron heating in a inductively coupled discharge, *Phys. Rev. Lett.* 71: 1844 (1993).
29. V.A. Godyak, R.B. Piejak and B.M. Alexandrovich, Electrical characteristics and electron heating mechanism of an inductively coupled argon discharge, *Plasma Sources Sci. Technol.* 3: 169 (1994).
30. R.Z. Sagdeev, D.A. Usikov and G.M. Zaslavsky, "Nonlinear Physics from the Pendulum to Turbulence and Chaos" Chur: Harwood Academic Publishers (1988).
31. M.A. Lieberman, B.E. Meierovich and L.P. Pitaevski, Anomalous skin effect in a plasma with a diffuse boundary, *Sov. Phys. JEPT* 35: 904 (1972).
32. I.D. Kaganovich and L.D. Tsendin, Low pressure rf discharge in the free flight regime, *IEEE Trans. Plasma Sci.* 20: 86 (1992).

This Page Intentionally Left Blank

COLLISIONLESS ELECTRON HEATING IN RF GAS DISCHARGES: II. THE ROLE OF COLLISIONS AND NON-LINEAR EFFECTS

U. Buddemeier and I. D. Kaganovich[1],
Experimental Physics II, Ruhr–University, 44780 Bochum, Germany

[1] on leave from St. Petersburg Technical University, Physical Technical Department, Polytechnicheskaya 29, 195251 St. Petersburg, Russia

INTRODUCTION

A new trend in applications of low pressure discharges is to decrease the pressure below 10 mTorr. For these low pressures the mean free path of electrons (λ) is large (comparable with discharge slab) and collisionless heating dominates Ohmic one. Being initially proposed for plasma heating in [1], it was first explored in gas discharge plasma for a capacitively coupled plasma (CCP)[2-4], and is now widely discussed for application to inductively coupled plasmas (ICP)[5,6]. The classification of various scenaria of collisionless heating has been done in[7]. The similar problem of cyclotron heating were extensively analyzed for magnetic traps (see for example review[8]).

Here we concentrate on the effects of stochastization due to collisions and non-linear effects and investigate theinteraction between them. For a single wave the collisionless heating corresponds to Landau damping. The role of collisions and non-linear effects has been investigated in detail for a single finite-amplitude wave[9,10]. Recently it has been shown that collisions play a key role in Landau damping and have to be accounted for [11]. In a gas discharge plasma the rf electric field is strongly inhomogeneous. The corresponding Fourier spectrum contains many wave vectors. Our aim is to study the electron heating resulting from the interaction with the whole spectrum of waves.

In common models the collisionless heating does not depend on the collision frequency. We demonstrate in a number of examples that collisions play an important role and that collisionless heating depends on collision frequency for some cases.

It is known that in low-pressure discharges electron heating may occur without collisions [1,12]. In absence of collisions the conditions for such a collisionless heating arise if there exists some other phase randomization mechanism. This stochastic heating can only occur if an electron “forgets” the field. phase between subsequent interactions during its dynamic motion. The sequence of non-correlated interactions with the field results in diffusive electron motion along the energy axis toward high energies, i.e. in

Electron Kinetics and Application of Glow Discharges
Edited by U. Kortshagen and L. D. Tsendin, Plenum Press, New York, 1998

the electron heating. In a bounded plasma the situation may be quite different. Due to the presence of plasma boundaries (potential barriers) that specularly reflect the electrons, the phases of subsequent electron interactions with the field may be strongly correlated. Also, the picture essentially depends on the direction of the rf field with respect to the boundaries.

The CCP is sustained by longitudinal — i.e. perpendicular to the boundary — electric field. The ICP is sustained by the electric field along the plasma boundary. It results in velocity kicks along the plasma boundary. If the influence of the rf magnetic field is taken into the account, the kicks are transverse to the boundary[13]. Thus, in general, a variety of heating scenaria may arise.

We consider different mechanisms of the electron heating using a simple model. Let L denote the gap length and $\delta << L$ the layer thickness where electrons interact with the localized rf fields, For a CCP such a model corresponds to a strongly asymmetric discharge with a much larger current density at the powered electrode then at the grounded electrode. δ is the width of the sheath. In the ICP, δ is the skin depth. In addition to the rf fields, a static space-charge field is present, which confines the majority of plasma electrons. We shall approximate its influence in the model by rigid reflecting walls and neglect the ambipolar potential in the bulk. The influence of the bulk potential on the electron collisionless heating was analyzed in[14]. In the plasma bulk electrons experience isotropic collisions, and there shall be no collisions in the δ layer ($\delta << \lambda$).

The electron motion is governed by three frequencies: the frequency of the rf field ω, the collision frequency ν and the bounce frequency $\Omega(vx) = v_x/2L$.

The electron heating is adequately described in terms of the diffusion coefficients in energy space D_ε or velocity space Dv[15]:

$$D_\varepsilon = \left\langle \frac{(\Delta\varepsilon)^2}{2\Delta t} \right\rangle, \; D_v = \left\langle \frac{(\Delta v)^2}{2\Delta t} \right\rangle, \; D_\varepsilon = 2m\varepsilon D_v. \tag{1}$$

They determine the microscopic characteristics of the electron ensemble such as the electron distribution function (EDF) $f(\varepsilon)$ and the power deposition rate into a unit volume of plasma P, which can be expressed in terms of D_ε and $f(\varepsilon)$[7]. The principal part of the EDF $f(\varepsilon)$ satisfies the stationary kinetic equation:

$$\frac{1}{\sqrt{\varepsilon}} \frac{d}{d\varepsilon} \sqrt{\varepsilon} D_\varepsilon \frac{df(\varepsilon)}{d\varepsilon} + St^* f(\varepsilon) = 0, \tag{2}$$

where $St^*f(\varepsilon)$ is the inelastic collision integral. The macroscopic quantities such as the rate of energy input deposition into the unit volume of plasma, P, can be expressed in terms of D_ε and $f(\varepsilon)$:

$$P = \frac{4\sqrt{2}\pi}{m^{3/2}} \int_0^\infty f(\varepsilon) \frac{d}{d\varepsilon} (\sqrt{\varepsilon} D_\varepsilon(\varepsilon)) d\varepsilon. \tag{3}$$

Thus, the energy diffusion coefficient contains all information about the electron heating. We have performed a Monte Carlo simulation at various ω, δ, L, ν and compare its results ($f(v)$, D_ε or D_v) with the quasi-linear theory[14] and analyse non-linear effects.

THE COLLISIONLESS HEATING IN THE CASE $\lambda < L$

If $\lambda < L$, there are many collisions in the gap and subsequent interactions with the electric field (δ-layer) are random. The energy diffusion coefficient can be evaluated as the product of the square of the step of random-walk in energy and the frequency of such steps Ω, which is the average frequency of electron-field interactions[7]. Since the process of velocity isotropisation is faster then the energy loss mechanism in gas discharges, the EDF is isotropic[16]. Thus, the energy diffusion coefficient should be averaged over velocity directions:

$$D_\varepsilon = \frac{1}{2}\left\langle\left\langle \Omega(\Delta\varepsilon)^2\right\rangle\right\rangle, \tag{4}$$

where $\langle\langle ... \rangle\rangle$ means averaging in time and in direction of velocity, $\Delta\varepsilon = m\boldsymbol{v} \cdot \Delta\mathrm{v}$ is the change in absolute value of energy and $\Delta\boldsymbol{v}$ is the kick in velocity.

For example in a CCP $\Delta\varepsilon = mv_x\Delta v_x(t)$ with $\Delta v_x = \Delta v_{x0}\sin\omega t$. Averaging in time and velocity direction gives[3,4]:

$$D_\varepsilon = m^2(\Delta v_{x0})^2 v^3/32L. \tag{5}$$

The expression for the energy diffusion coefficient does not explicitly depend on ν. The role of collisions is only stochastization of subsequent interactions with the δ-layer and isotropisation of the EDF. More precisely the disappearance of ν from the expression for D_ε is the result of averaging over all electrons in a volume. The main contribution to D_ε corresponds to the particles at a distance of the order of one mean free path $\lambda = v/\nu$ from the S-layer. They have the largest possible electron–field interaction frequency which is of the order of ν. The interaction frequency averaged over all particles is of the order $\nu\lambda/L = \Omega$ which does not depend on collision frequency.

THE COLLISIONLESS HEATING IN THE CASE $\lambda >> L$

If $\lambda >> L$, collisions in the gap are rare and subsequent interactions with the electric field are not random (Fig. 1).

Most interactions with the electric field in the δ-layer result in oscillations of the velocity around a constant average value. Only due to collisions there is decorrelation and alternation of the average value and as a result diffusion in velocity space. The main contribution to this diffusion is due to resonances $\omega/\Omega \approx 2\pi n$: the electrons interact with the rf field practically always at the same phase, so kicks are summed up. Due to small divergence from resonance conditions the phase is changing. This results in large oscillations in velocity (Fig. 1). The quasi-linear theory gives the energy diffusion coefficient for this case[14]:

$$D_\varepsilon = \frac{m^2}{8L^2}\sum_n \int v_x^2\,(\boldsymbol{v}\cdot\Delta_0\boldsymbol{v})^2\,\Delta\left(\omega - \frac{\pi n|v_x|}{L}\right)\frac{d\boldsymbol{\Omega}}{4\pi} \tag{6}$$

$$\Delta(\omega^*) = \frac{\nu}{\nu^2+\omega^{*2}},\ \lim_{\nu\to 0}\Delta(\omega^*) = \pi\delta(\omega^*),\ \omega^* = \omega - \frac{\pi n|v_x|}{L} \tag{7}$$

where Ω is the solid angle in velocity space and δ is the Direc function, $\Delta_0 v$ is the amplitude of velocity kick.

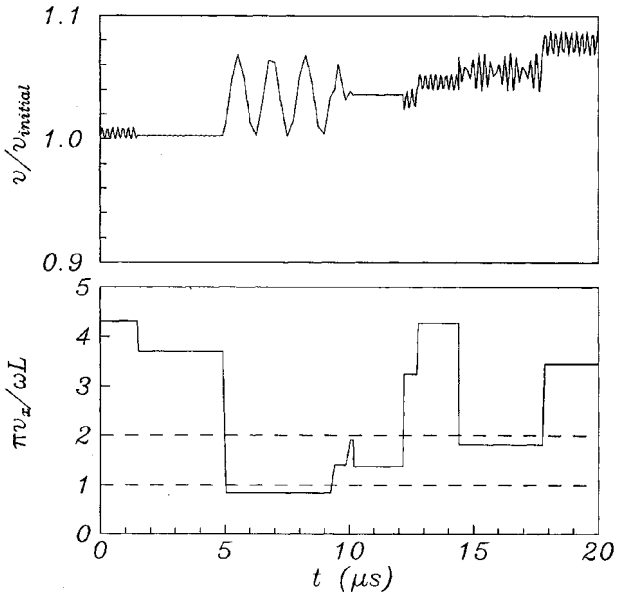

Figure 1. Time evolution of the the velocity $v(t)$ and its x-projection $v_x(t)$ for a model of ICP, velocity kicks are in y-direction: $\omega = 3 \cdot 10^7 s^{-1}$, $\delta = 1cm$, $\nu = 5 \cdot 10^5 s^{-1}$, $L = 3.14cm$, $E_0 = 10V/m$, $v_{initial} = 1.5 \cdot 10^6 m/s$. Dashed lines correspond to first and second resonance.

When $\nu << \omega L/\pi$ there are many resonances enabling the sum to be changed into an integral and the energy diffusion coefficient (6) coincides with (4) [14].

It should be noted that this result is only valid with accounting for collisions. The collisions play two important roles:

1. They stochastizate the phase of electron motion with respect to the phase of the electric field and

2. they transfer electrons from non-resonance velocity to resonance and vice versa.

This complex process of electron motion can be considered as diffusion with a diffusion coefficient (6). The identity of diffusion coefficient (6) with (4) is not general, since accounting for nonlinear effects will change the results as shown below.

We also note importance of three dimensional effects. In the one dimensional case (e.g. in magnetic traps [8]), the situation is quit different: A single collision is not able to move the electrons from a non-resonant velocity to a resonant one and vice versa, since a considerable change of kinetic energy is required. In the three dimensional case, only the projection of the velocity perpendicular to the wall has to be changed. As a result the diffusion coefficient is much smaller in one dimensional case compared to the three dimensional one. More precisely, in one dimensional case the averaging over region of many resonances is to be performed not over D_ε, but over $1/D_\varepsilon$. This is due to modification of EDF near the resonances, where plateaus are formed $\frac{df(\varepsilon)}{d\varepsilon} \approx 0$. Indeed

if we define the averaged diffusion coefficient as

$$< D_\varepsilon >= \frac{\Gamma}{(f_1 - f_2)/(\varepsilon_2 - \varepsilon_1)} \tag{8}$$

where Γ is flux in energy space, and the region $\varepsilon_2 - \varepsilon_1$ includes many resonances. With the use of relation $\Gamma = D_\varepsilon \frac{df}{d\varepsilon}$ we find that [8]:

$$< D_\varepsilon >= \frac{1}{\int_{\varepsilon_1}^{\varepsilon_2} \frac{d\varepsilon}{D_\varepsilon}} \tag{9}$$

As a result the regions of resonances, where D_ε is large do not contribute to average diffusion coefficient (9) and main contribution is due to non-resonant regions with small D_ε. So $< D_\varepsilon >$ is small and proportional to collision frequency. Physically this means that electrons diffuse very fast across the resonance and get stuck in the region between them. In three dimensional case the scattering of electrons allows them to escape from this non-resonant region and participate in farther diffusion.

If $v > \omega L/\pi$ the sum in (6) cannot be transformed into an integral. The main contribution is due to first resonance ($n = 1$) and the diffusion coefficient according to (6) is small compared to that from (4) for $v > 3v_1$, where $v_1 = L\omega/\pi$ corresponds to the velocity of first resonance. This is due to the fact that most electron field interactions result in no heating and compensate each other (Fig. 1). The numerical example is shown in Fig. 2 for an ICP-type field $E_y = E_0 \exp(-x/\delta)$ (without account for the influence of the rf magnetic field). In the Monte Carlo simulation the diffusion coefficients were calculated according to their definition (1) as the ratio of the square of averaged change of energy or absolute value of velocity over some time interval $\Delta t >> 1/\nu, 1/\Omega$.

From Fig. 2 one can see the remarkable influence of a finite gap on the diffusion coefficient. The diffusion coefficients are characterized by a sharp rise at the velocity of first resonance $(v_1/\omega\delta = 1)$. A strong suppression of diffusion compared to the "infinite" gap situation occurs for $v > 3v_1$. The vanishing of correlation effects for $v < \omega L$ (all curves coincide) was proposed first in [1], but the conclusion that it can occur without collisions is not correct. The reduction of collisionless heating due to the influence of the second boundary was observed in numerical simulations [5].

The resonance effect also considerably influences the EDF. Since the flux in energy space $D_\varepsilon\, df/d\varepsilon$ does not change as rapidly as the diffusion coefficient at the first resonance, the derivative $df/d\varepsilon$ decreases above the resonance. This leads to the formation of a sort of plateau on the EDF for $\varepsilon > \frac{1}{2}mv_1^2$. Fig. 3 depicts the EDF resulting from the simulation of a CCP with electron generation (injection) at 0.5eV and loss at 20eV. The flux is constant between these energies. For a collision frequency of $\nu = 5 \cdot 10^7\ s^{-1}$ the mean free path is (MFP) $\lambda \sim 4cm < L$ and electrons return with random phase. This corresponds to the diffusion coefficient (5), which gives a smooth growth of D_ε. For $\nu = 5 \cdot 10^6 s^{-1}$, $\lambda \sim 40cm >> L = 5cm$ and electrons return with correlated phase. The use of (6) gives

$$D_\varepsilon = \frac{(m\Delta v_{x0} v_1^2)^2}{8vL} \tag{10}$$

for $v > v_1$, $v_1 = \omega L/\pi$. Comparing (5) and (10) shows that, the diffusion coefficient of (5) four times smaller than that of (10). The deviation of simulation results from the analytical formula (10) is due to a large value of the velocity kick $\Delta v_{x0}/v \sim 0.5$ so that

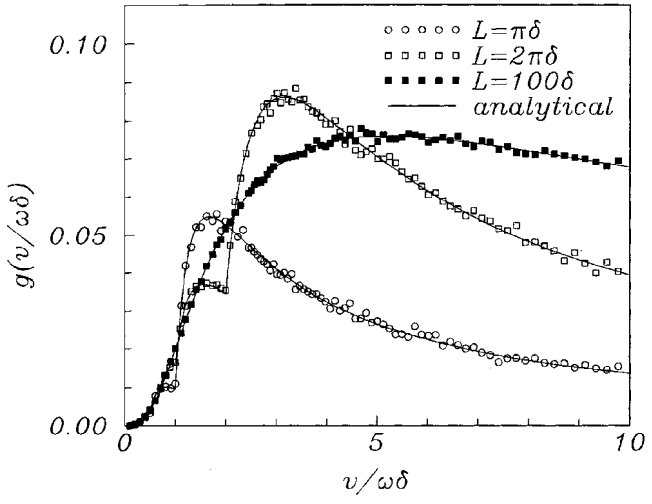

Figure 2. Influence of the second boundary on collisionless heating. Dimensionless diffusion coefficient for this field $g = D_v / \frac{e^2 E_0^2 \delta}{2m^2\omega^2 L}$ as a function of the normalized velocity for different slab widths *L*. Solid curves correspond to the analytical formulae (6), symbols to Monte Carlo simulations.

the sharp rise of D_ε is smoothed out. The first resonance appears at $\varepsilon \simeq 5eV$, above this energy the sort of plateau is formed.

It should be mentioned that this mechanism can be responsible for the formation of a bi-Maxwellian distribution in capacitively coupled discharges as found in experiments [17]. The resonance effects and hence the plateau vanish if $\lambda < 2L$ (Fig. 3).

INFLUENCE OF NONLINEAR EFFECTS ON COLLISIONLESS HEATING.

Nonlinear effects are introduced in the case $\Delta \boldsymbol{v} \parallel \boldsymbol{x}$ by the fact that the bounce frequency itself depends on v_X. The kicks change the bounce frequency in contrast to the case $\Delta \boldsymbol{v} \perp \boldsymbol{x}$. Thus, electrons move out of the resonance. The amplitude of the velocity oscillation (see Fig. 1) in the resonances are limited by a resonance width $\Delta_{rw} v = \Delta v \Omega / \theta$ [15], where θ is characteristic frequency of non-linear oscillations:

$$\theta = \Delta_{rw} v \frac{\omega d\Omega}{\Omega dv} = \sqrt{\Delta v \omega \frac{d\Omega}{dv}} \tag{11}$$

If the resonance width $\Delta_{rw} v$ is larger then the distance between resonances $\delta v = \pi v^2/\omega L$, diffusion in velocity space can occur even without collisions[3,4].

Otherwise, collisions are necessary for diffusion. The non-linear effects should be accounted for by limiting the amplitude of velocity oscillation in resonances. This can be done by using a modified resonant function $\Delta(\omega^*)$, approximated as:

$$\Delta(\omega^*) = \frac{\nu}{\nu^2 + \theta^2 + \omega^{*2}}, \ \lim_{\nu \to 0} \Delta(\omega^*) = \frac{\pi\nu}{\theta} \delta(\omega^*) \tag{12}$$

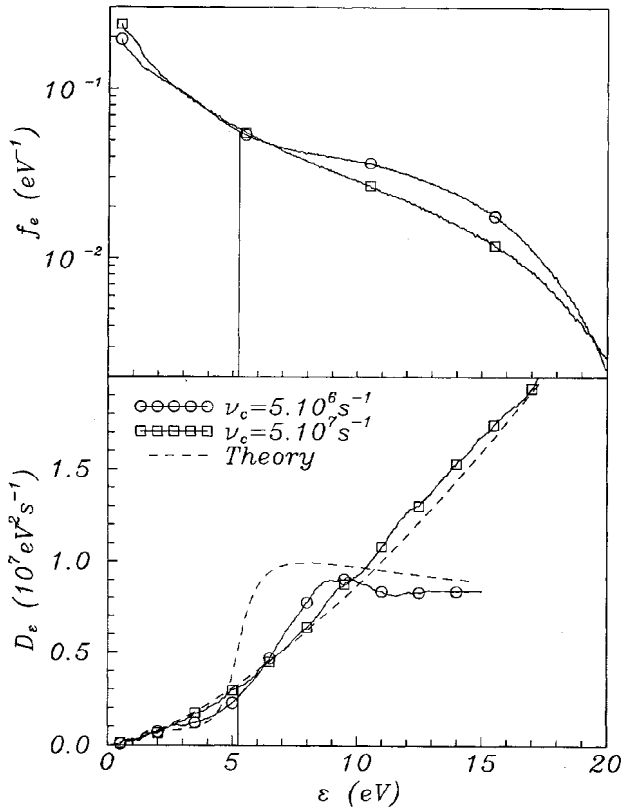

Figure 3. The EDFs (upper part) and energy diffusion coefficients (lower part) obtained in a Monte–Carlo simulation of a CCP with two different collision frequencies. f = 13.56MHz, sheath length 0.6cm and slab width L = 5*cm*. The first resonance is marked by a vertical line.

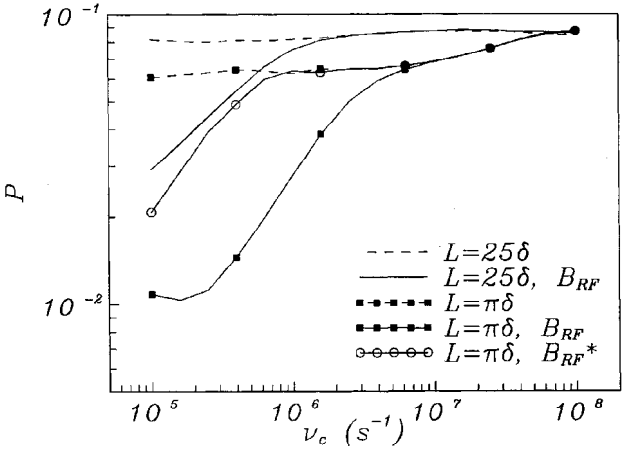

Figure 4. Dimensionless power dissipation, normalized on $\frac{ne^2E_0^2\delta}{m\omega L}$ for the same conditions as in Fig. 2 as function of the collision frequency for two slab widths L with and without account for B_{rf}, $\omega = 6 \cdot 10^7 s^{-1}$, $\delta = 1cm$, $E_0 = 5V/m$ except (*): $E_0 = 0.1V/m$.

A more detailed calculation is performed in[8]. As a result D_ε is proportional to ν (at $\nu < \theta$) and tends to zero with $\nu \to 0$. This is in contrast to the case of transversal kicks, where the non-linear effect is absent, and D_ε remains a constant when $\nu \to 0$.

The non-linear effect is important for the capacitive discharge and inductive discharge with account of magnetic field, where the kicks are along *x*. Fig. 4 is a plot of power dissipation (3) as function of the collision frequency for Maxwell distribution function with electron temperature 3 eV.

If the gap is small ($L = \pi\delta$), the diffusion decreases when $\lambda > 2L$ ($\nu < \Omega \approx 5 \cdot 10^7 s^{-1}$). There is no decrease in the case of the large gap, because the corresponding velocity of first resonance $\nu_1 = \omega L/\pi$ is larger than thermal velocity and decrease of diffusion coefficient is not pronounced. Accounting for B_{rf} leads to a decrease of the diffusion coefficient at $\nu < \theta$ from (11) due to the introduction of the non-linear effect as described above. As a result the curves for power dissipation with and without account for induced magnetic field diverge below $\nu = \theta$. Increasing L or diminishing E_0 decreases θ and hence the critical collision frequency for divergence (see Fig. 4). The typical numbers for θ are : $\theta = 2.3 \cdot 10^7$ in case of $L = \pi\delta$, $E_0 = 5V/m$, and $\theta = 3.2 \cdot 10^6$ in case of $E_0 = 0.1V/m$, $\theta = 2.1 \cdot 10^6$ in case of $L = 25\delta$, $E_0 = 5V/m$.

The results presented in Fig. 4 correspond to two values of electric fields. For small E_0 kicks are small ($\Delta v << v_1$) and D is proportional to ν. For larger value of kicks (Δv comparable with v_1) the dependence of D on ν is even more complex. For example D can have a minimum at some ν and then increase with decreasing ν. The reason for this effect is that many subsequent interactions with the δ-layer can result in a change of v. We discuss these effects elsewhere.

CONCLUSIONS

1. It is shown that when $\lambda > L$, only resonance particles $(\omega L/\pi v_x = n)$ contribute to the heating and as result for large velocities, where the fraction of resonance particles is small, collisionless heating is suppressed.

2. A plateau in the distribution function in the region of first resonance can be observed.

3. At smaller collision frequency the nonlinear effects should be accounted for. If kicks are perpendicular to the discharge boundaries a considerable suppression of collisionless heating appears due to nonlinear effects. In this case collisionless heating is proportional to collision frequency ($D \sim \nu$).

This work was partially supported by the Deutsche Forschungsgemeinschaft (SFB 191 and project KO 1331/4-1,2), and by INTAS grant N 94–0740. I.K. acknowledges Alexander von Humboldt Foundation for a research fellowship. The authors wish to thank Uwe Kortshagen (U. of Minnesota) for valuable discussions.

REFERENCES

1. A.I. Akhiezer and A.S. Bakai, Theory of stochastic particle acceleration, *Sov. Phys. Dokl.* 16: 1065 (1972).
2. V.A. Godyak, Statistical heating of electrons at an oscillating plasma boundary, *Sov. Phys. Tech. Phys.* 16: 1073 (1972).
3. C.G. Goedde, A.J. Lichtenberg and M.A. Lieberman, Self-consistent stochastic electron heating in radio frequency discharges, *J. Appl. Phys.* 64: 4375 (1988).
4. I.D. Kaganovich and L.D. Tsendin, Low pressure rf discharge in the free flight regime, *IEEE Trans. Plasma Sci.* 20: 86 (1992).
5. M.M. Turner, Collisionless electron heating in a inductively coupled discharge, *Phys. Rev. Lett,* 71: 1844 (1993).
6. V. Vahedi, M.A. Lieberman, G. Di Peso, T.D. Rognlien and D. Hewett, Analytic model of power deposition in inductively coupled plasma sources, *J. Appl. Phys.* 78: 1446 (1995).
7. I.D. Kaganovich, V.I. Kolobov, L.D. Tsendin, Stochastic electron heating in bounded radio-frequency plasmas, *J. Appl. Phys. Lett.* 69: 3818 (1996).
8. A.V. Timofeev, Cyclotron oscillations of an equilibrium plasma *in:* "Review of Plasma Physics v.14" ed. B.B. Kadomtsev, Consultants Bureau, New York-London (1989).
9. B. B. Kadomtsev, Landau damping and echo in a plasma, *Sov. Phys. Usp.* 11:328 (1968).
10. J. N. Istomin, V. Karpman, and D. Shkljar, Drag effects when there is resonance interaction between particles and a Langmuir waves in a inhomogeneous plasma, *Sov. Phys. JETP* 42:463(1975).
11. G. Brodin, Non-linear Landau damping, *Phys. Rev. Lett.* 78: 1263 (1997).
12. M.A. Lieberman and A.J. Lichtenberg, "Principles of Plasma Discharges and Materials Processing", John Wiley & Sons Inc. , New York (1994)
13. R.H. Cohen and T.D. Rognlien, Electron kinetics in radio-frequency magnetic fields of inductive plasma sources, *Plasma Sources Sci. Techn.* 5: 442 (1996).
14. Y. M. Aliev, I. D. Kaganovich, and H. Schlüter, Collisionless electron heating in RF gas discharges: I Quasilinear theory, *in* this book
15. R.Z. Sagdeev, D.A. Usikov and G.M. Zaslavsky, "Nonlinear Physics from the Pendulum to Turbulence and Chaos" Chur: Harwood Academic Publishers (1988).
16. A. P. Dmitriev and L. D. Tsendin, Distribution functions of electrons scattered with a large energy loss in an electric field, *Sov. Phys JETP* 54: 1071 (1981).
17. V. A. Godyak and R. B. Piejak, Abnormally low electron energy and heating-mode transition in a low-pressure Argon rf discharge at 13.56 MHz, *Phys. Rev. Lett.* 65: 996 (1990).

This Page Intentionally Left Blank

THE ANOMALOUS SKIN EFFECT IN BOUNDED SYSTEMS

Vladimir Kolobov

Plasma Processing Laboratory
Department of Chemical Engineering
University of Houston
Houston, TX 77204-4792

INTRODUCTION

It is known that an alternating electromagnetic field is damped within a conductor, and both the field and the induced electric current are concentrated near the surface of the conductor. This is called the skin effect. The skin effect is observed if the field frequency ω is lower than plasma frequency ω_p. In simple cases, the nature of the skin effect depends on the relative magnitude of three characteristic lengths[1]: the skin depth δ, the electron mean free path λ, and the length v/ω which an electron traverses during the field period (v is a characteristic electron velocity). If the relationship between the current density $\mathbf{j}$ and the electric field $\mathbf{E}$ is local, $\mathbf{j} = \sigma \mathbf{E}$, the skin effect is called normal. In the nonlocal case, it is said to be anomalaus. The anomalous skin effect, first discovered and thoroughly explored in metals, has been actively studied in radiophysics[2], solid state[3,4] and gaseous plasmas. Recent interest in this problem has been generated by the advent of low-pressure high-density plasma sources sustained by radio-frequency electromagnetic fields. Understanding nonlocal electrodynamics in bounded plasmas is important for the design of these sources.

The high-density plasma sources generate a weakly ionized, non-equilibrium plasma with electron temperature $T_e \approx 5$ eV, and nearly a room temperature of heavy species. At gas pressures $p < 25$ mTorr, electron collision frequency ν is lower than the typical driving frequency $\omega = 8.5 \times 10^7$ s^{-1} (13.56 MHz). For plasma densities $10^{11} - 10^{13}$, the inequality $\omega < \omega_p$ is satisfied within a large margin. The electron mean free path λ becomes smaller than the characteristic size of plasma devices $L \times 10$ cm at $p < 5$ mTorr. Under these conditions, the finiteness of the plasma is very important for electron kinetics and electrodynamics: the electric current at a point depends on the geometry of the system and the distribution of electromagnetic fields in the entire device. In addition, static magnetic field B as weak as 5 Gauss results in electron cyclotron resonance at 13.56 MHz. The electron Larmor radius r_H is comparable to λ at $B \times 1$ G. Gaseous plasma is a perfect medium for basic studies of the skin effect, as precise measurements of spatial distributions of the electromagnetic fields and currents can be

Electron Kinetics and Application of Glow Discharges
Edited by U. Kortshagen and L. D. Tsendin, Plenum Press, New York, 1998

performed in this plasma. Nevertheless, the anomalous skin effect in gas discharges is relatively unexplored in comparison to that effect in metals.

Peculiarities of skin effect in metals are caused by Fermi statistics of conducting electrons and by the complex nature of electron reflection from the boundaries (which is diffuse to some extent). The calculation of λ, one of the basic problems in the theory of metals, usually requires considering electron collisions with phonons (lattice vibrations), other electrons, impurity atoms, and defects of the lattice. The theory of skin effect in metals is relatively well-developed [3]. The experimental studies are often limited to measurements of the reflection and transmission coefficients; contrary to gaseous plasmas, the spatial distributions of the fields inside solid samples are rather difficult to perform. We draw upon advances in the physics of metals to gain insight into discharge plasmas.

The gaseous electronics community has witnessed the advance of high-density plasma reactors for advanced semiconductor manufacturing. The semiconductor industry calls for a plasma in which collisions among particles occur as rarely as possible. Newer plasma reactors operate in the near-collisionless regime where the electron mean free path is comparable to or large than discharge dimensions. The electromagnetic fields in these devices are spatially inhomogeneous even in the absence of the skin effect, with plasma conductivity an integral characteristic of the system. Studies of nonlocal electrodynamics in bounded systems is today's area of active research and a subject where basic plasma physics meets the world of semiconductor manufacturing.

The anomalous skin effect in gas discharge plasmas has been studied since the pioneering works of Demirkhanov et al. [5] and Weibel [6]. A review of classical and recent works has been given in Ref. 7. Our paper describes the state of the art and presents results of recent studies of electrodynamic properties of weakly collisional ICPs.

FORMULATION OF THE PROBLEM

Calculation of the field penetration into a plasma requires self-consistent solution of Maxwell equations for the fields and kinetic equations for the charged carriers that determine the currents induced in the plasma. In the limit $\omega < \omega_p$, the displacement current is small compared to the conduction current, and Maxwell equations (in Gaussian system) have the form of Ampere's law

$$\nabla \times \mathbf{B} = \frac{4\pi}{c}\mathbf{j} \tag{1}$$

and Faraday's law

$$\nabla \times \mathbf{E} = -\frac{1}{c}\frac{\partial \mathbf{B}}{\partial t} \tag{2}$$

For the frequency range of interest, the ion contribution to the current density $\mathbf{j}$ is negligible. We confine ourselves to the case of weak fields when a linear relationship is valid between the electron current density and the electric field.

In calculating the electron current density, we can distinguish two limiting cases. If the characteristic length δ (skin depth) in which the field changes significantly is large compared to the characteristic scale l describing the electron motion (the shortest of λ, r_H, and v/ω), the relationship between $\mathbf{j}$ and $\mathbf{E}$ is given by Ohm's law

$$\mathbf{j} = \hat{\sigma}\mathbf{E} \tag{3}$$

where $\hat{\sigma}$ is the conductivity tensor. The skin effect is said to be normal when the local relationship (3) holds true and the frequency dependence of $\hat{\sigma}$ (temporal dispersion) is weak.

Another limit corresponds to the extreme anomalous skin effect when δ is small: $\delta << l$. In this case, the plasma conductivity is a nonlocal integral operator:

$$j_\alpha(\mathbf{r},\omega) = \int \sigma_{\alpha\beta}(\mathbf{r},\mathbf{r}',\omega)E_\beta(\mathbf{r}',\omega)d\mathbf{r} \tag{4}$$

The field with a β component at a point $\mathbf{r}'$ in the plasma produces a current density with α component and magnitude $\sigma_{\alpha\beta}E_\beta$ at another point $\mathbf{r}$ in the plasma. The main contribution to integral (4) comes from a vicinity of the point $\mathbf{r}$ with a size l. In an infinite plasma, σ is a function of $|\mathbf{r} - \mathbf{r}'|$ only. In this case, performing a Fourier transform reduces integral relation (4) into an algebraic relation in Fourier space

$$j_\alpha(\mathbf{q},\omega) = \sigma_{\alpha\beta}(\mathbf{q},\omega)E_\beta(\mathbf{q},\omega) \tag{5}$$

In a bounded plasma, $\hat{\sigma}$, in general, is a function of $\mathbf{r}$ and $\mathbf{r}'$ separately, and the integral (4) extends only over the plasma volume. In this case, the functional dependence of $\hat{\sigma}$ ($\mathbf{r}$, $\mathbf{r}'$, ω) is determined by the geometry of the system, the nature of electron trajectories, and the configuration of the external fields. Under these conditions, Fourier methods do not generally simplify the analysis. We confine ourselves here to simple cases that allow for semi-analytical solutions. The numerical treatment of this problem by PIC methods [8,9] is beyond the scope of this paper.

To determine $\hat{\sigma}$, one uses the Boltzmann equation for the electron distribution function [10]

$$\frac{\partial f}{\partial t} + \mathbf{v}\cdot\nabla f + \frac{e}{m}\left(\mathbf{E} + \frac{1}{c}\mathbf{v}\times\mathbf{B}\right)\cdot\frac{\partial f}{\partial \mathbf{v}} = -\nu(f - f_0) \tag{6}$$

Here, f_0 is the isotropic part of the EDF and ν is an effective collision frequency. Equation (6) is linearized by setting $f = f_0 + f_1$, where $f_1 << f_0$ is a small anisotropic addition responsible for dc and rf currents in the plasma:

$$\mathbf{j} = e\int \mathbf{v} f_1 d\mathbf{v} \tag{7}$$

Maxwell equations (1) and (2) with the rf current density $\mathbf{j}$ found from (6) and (7) determine electromagnetic fields in the plasma. The steady component of f_1 defines the dc current. The electrostatic field with a potential $\phi(\mathbf{r})$ can be found from the condition of quasi-neutrality.

Consider first an isotropic plasma with no static magnetic field. Since f_0 is a function of electron speed, the term with alternating magnetic field $(\mathbf{v}\times\mathbf{B})\partial f_0/\partial\mathbf{v}$ vanishes, and the equation for the oscillating part of $f_1 \propto \exp i\omega t$ takes the form

$$\mathbf{v}\cdot\nabla f_1 + (i\omega + \nu)f_1 = -e(\mathbf{v}\cdot\mathbf{E})\frac{\partial f_0}{\partial \varepsilon} \tag{8}$$

The electrostatic field is accounted for in (8) by using the total electron energy $\varepsilon = mv^2/2 - e\phi(\mathbf{r})$ as an independent variable. An important difference exists between the nonlocal electron kinetics in collisional and near-collisionless plasmas. In both these cases, the isotropic part $f_0(\varepsilon)$ is an integral characteristic of the system [11]. However, in the collisional plasma, the spatial derivative in (8) is neglected, and both f_1 and $\mathbf{j}$ become functions of the local rf field (local electrodynamics). In the near-collisionless plasma, the spatial derivative in (8) is of principal importance, and both f_1 and $\mathbf{j}$ are integral characteristics of the system (nonlocal electrodynamics).

SKIN EFFECT IN A SEMI-INFINITE PLASMA IN THE ABSENCE OF A STATIC MAGNETIC FIELD

Consider the penetration of an electromagnetic wave with E_y and B_z components into a spatially homogeneous plasma occupying the half-space $x > 0$. Such a model corresponds to an ICP sustained by a planar coil, if the radius R and length L of the chamber are large compared to electron mean free path: $R >> L >> \lambda$. The coil is represented by a surface current $J_S \exp i\omega t$ in the plane $x = 0$. The specular reflection of electrons is assumed at $x = 0$ due to the presence of a potential barrier (space charge sheath) at the boundary.

To calculate the profiles of electromagnetic fields in the plasma, the fields E_y and B_z are continued into the region $x < 0$ by assuming $E_y(-x) = E_y(x)$ and $B_z(-x) = -B_z(x)$. According to (1), the magnetic field at the boundary is proportional to the surface current $B_0 = 2\pi J_s/c$. The complex amplitude of the electric field in the plasma obeys the equation

$$\frac{d^2E_y}{dx^2} = \frac{4\pi i\omega}{c^2} j_y \tag{9}$$

and the boundary condition $E'(\pm 0) = \mp i\omega B_0/c$. The current density in the plasma is

$$j_y(x) = e\int_{v_x>0} d\mathbf{v}\frac{v_y^2}{v_x} f_0' \int_{-\infty}^{\infty} dx' E_y(x') \exp\left(i\gamma|x-x'|\right) \tag{10}$$

where

$$\gamma = \frac{i\omega + \nu}{v_x} \tag{11}$$

and f_0' denotes the first derivative. Performing a Fourier transform on (10) results in Eq. (5) for Fourier components. The Fourier component of the conductivity is

$$\sigma(q,\omega) = \frac{2e^2 i}{\pi}\int_{v_x>0} d\mathbf{v}\frac{v_y^2}{v_x} f_0' \frac{\gamma}{q^2-\gamma^2} \tag{12}$$

We assume an energy-independent collision frequency ν and a Maxwellian EDF $f_0(\varepsilon)$ to obtain

$$\sigma(q,\omega) = -\frac{i\omega_p^2}{4\pi q v_T} Z(u) \tag{13}$$

Here $Z(u)$ is the plasma dispersion function [12], $u = (\omega+i\nu)/(qv_T)$, and $v_T = (2T_e/m)^{1/2}$ is the most probable electron speed. At $v_T \to 0$, when $Z(u) \to -1/u$, Eq.(13) gives the conductivity of cold plasma, σ_0.

A Fourier transform of (9) yields the following for the Fourier component of the electric field $\mathcal{E}(q)$:

$$\left(q^2 + \frac{4\pi i\omega}{c^2}\sigma(q,\omega)\right)\mathcal{E}(q) = \frac{i\omega B_0}{c} \tag{14}$$

It is accounted that the second derivative contains a delta function $2E'(0)\delta(x)$. The spatial distribution of the electric field is found from (14) by the inverse transform

$$E_y(x) = \frac{2}{\pi}\int_0^{\infty} \mathcal{E}(q)\cos(qx)dq \tag{15}$$

The surface impedance of the plasma is defined as *

$$\zeta = \frac{E_y(0)}{B_0} = \frac{2i\omega}{\pi c}\int_0^{\infty} \frac{dq}{q^2 - \frac{\omega_p^2\omega}{c^2 q v_T} Z(u)} \tag{16}$$

*Same name is given to the quantity $\mathcal{Z} = 4\pi\zeta/c$

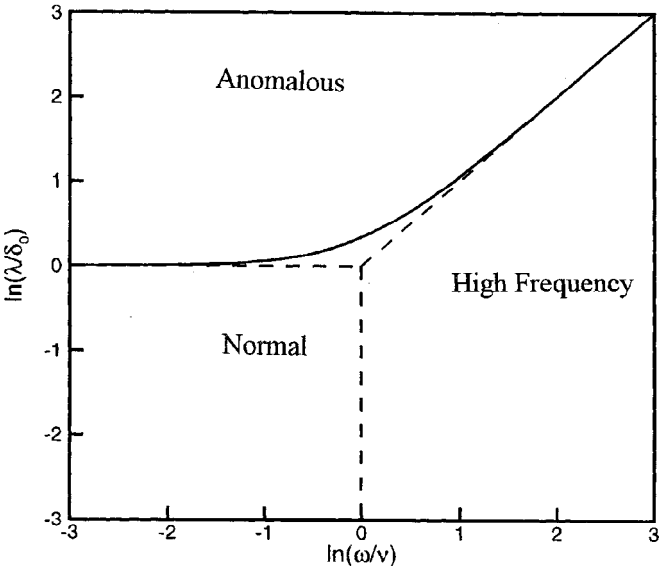

Figure 1. Skin effect in a semi-infinite plasma with no static magnetic field. The solid line, $\Lambda = 1$, corresponds to the boundary of the anomalous skin effect. From Ref. 7.

The real part of ζ, called plasma resistance, determines the energy dissipation in the plasma. The penetration depth of magnetic and electric fields can be introduced as [13]

$$\delta_B = \frac{1}{B_0}\int_0^\infty B_z(x)dx = \frac{ic\zeta}{\omega} \tag{17}$$

$$\delta_E = \frac{1}{E_y(0)}\int_0^\infty E_y(x)dx = \frac{\mathcal{E}(0)}{E(0)} = \frac{ic}{4\pi\zeta\sigma_0} \tag{18}$$

The real and imaginary parts of δ_B and δ_E describe the amplitude and phase of the fields Several regimes of the skin effect can be distinguished (Fig. 1).

Classical Skin Effect

The length $l = v_T/\sqrt{\omega^2+\nu^2}$ defines the distance an electron traverses during the field period or during the time between-subsequent collisions. If the penetration depth δ is larger than l, the effect of thermal electron motion is negligible (weak spatial dispersion of conductivity).. In this case, both electric and magnetic fields are damped exponentially with the skin depth [6]

$$\delta_B = \delta_E = \delta_0/cos(\epsilon/2) \tag{19}$$

where

$$\delta_0 = \frac{c}{\omega_p}\left(1+\frac{\nu^2}{\omega^2}\right)^{1/4}, \epsilon = \arctan(\nu/\omega) \tag{20}$$

At low frequencies, $\omega << \nu$, the skin depth is $\delta_n = (c/\omega_p)\sqrt{2\nu/\omega}$, and the surface impedance is

$$\zeta = (1+i)\left(\frac{\omega\nu}{2\omega_p^2}\right)^{1/2} \tag{21}$$

This regime corresponds to normal skin effect (Fig. 1) and collisional energy dissipation.

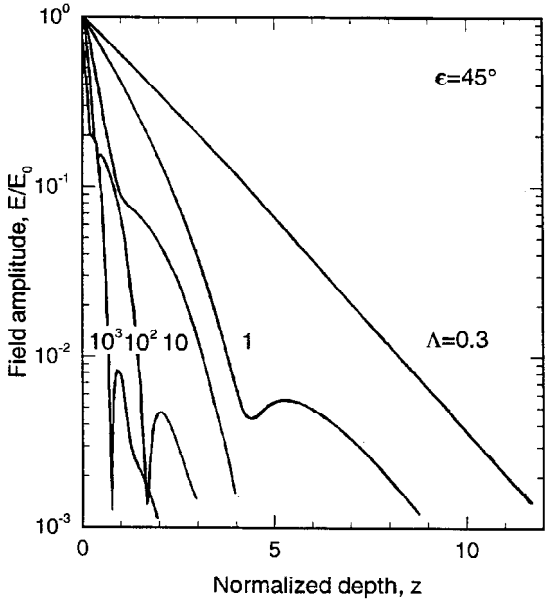

Figure 2. The amplitude of the electric field E as a function of normalized depth z for different Λ and $\nu/w = 1$. From Ref. 6.

In the high-frequency region, $\omega >> \nu$, the (collisionless) skin depth is $\delta_p = c/\omega_p$. The energy dissipation is due to resonant interaction of electrons with velocity $v_x = \omega/q$ and q-th harmonic of the field (Cherenkov resonance). However, the real part of ζ is small compared to the imaginary part [2]

$$\zeta = \frac{\omega}{\omega_p}\left(i + \frac{1}{\sqrt{\pi}}\left(\frac{v_T\omega_p}{c\omega}\right)^3\right) \tag{22}$$

and the wave is reflected from the plasma with small energy dissipation.

The nature of collisionless energy absorption can be understood considering the work performed by electromagnetic forces on electrons in the skin layer[14]. Due to spatial inhomogeneity of the electric field, the electrons change their velocity depending on the field frequency ω and the time $\tau = (qv_T)^{-1}$ they spend in the skin layer[15]. Both electric and magnetic rf fields contribute to this process. Indeed, the magnetic field does not work on electrons and produce no energy change. However, without accounting for the magnetic field, the velocity changes along the direction of the electric field, whereas with accounting for the magnetic field, the velocity component normal to the boundary is altered[16].

Anomalous Skin Effect

Introducing dimensionless coordinate $z = x/l$, Eqs.(13) and (15) can be cast in the form [6]

$$E(z) = \frac{2i\omega l B_0}{\pi c}\int_0^\infty \frac{dk\cos kz}{D(k)} \tag{23}$$

where $k = ql$ is the dimensionless wave number, $D(k) = k^2 + \Lambda Z(is/k)/k$, $s = i\exp(-i\epsilon)$ and

$$\Lambda = \left(\frac{\omega_p v_T}{c}\right)^2 \frac{\omega}{(\omega^2+\nu^2)^{3/2}} \tag{24}$$

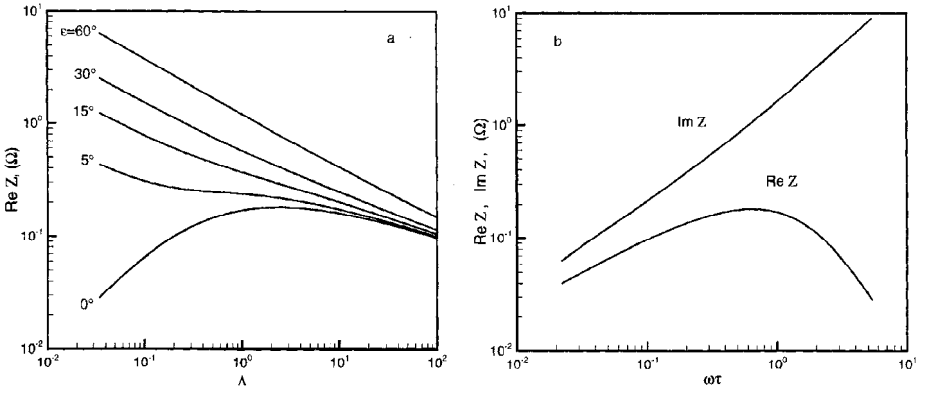

Figure 3. a) Plasma resistance $Z = 4\pi\zeta/c$ plotted versus $\Lambda = (v_T\omega_p/c\omega)^2$ for different ϵ. The low-frequency case corresponds to ($\epsilon = 0$, the high-frequency case corresponds to $\epsilon = \pi/2$; b) The real and imaginary parts of the plasma impedance versus $\omega\tau = c\omega/v_T\omega_p$ for the collisionless plasma.

The parameter $\Lambda = (l/\delta_0)^2$ is a fundamental measure of nonlocality of electromagnetic phenomena in plasmas[17]. The nonlocal effects are pronounced if the effective mean free path l exceeds the classical skin depth δ_0 ($\Lambda > 1$), and they are small otherwise, It is important that Λ becomes small for low and high frequencies and has a maximum at $\omega \approx \nu$. That means that in both low- and high-frequency cases, the penetration of electromagnetic waves into a plasma can be described as a classical skin effect.

The solution $E(\Lambda, s, z)$ depends on the values of parameters Λ and s. Small values of Λ correspond to the normal case. Anomalies (such as nonmonotonic field profiles) begin to be noticeable at $\Lambda > 1$ (Fig.2). For the extreme anomalous skin effect, $\Lambda >> 1$, the penetration depths δ_B and δ_E are entirely different [2]:

$$\delta_B = \frac{2\delta_p}{3}\left(1 + \frac{i}{\sqrt{3}}\right)\left(\frac{\omega_p v_T}{\sqrt{\pi}\omega c}\right)^{1/3} \tag{25}$$

$$\delta_E = \frac{9\delta_p}{8}\left(1 - \frac{i}{\sqrt{3}}\right)\left(1 + i\frac{\nu}{\omega}\right)\left(\frac{\omega_p v_T}{\sqrt{\pi}\omega c}\right)^{-1/3} \tag{26}$$

Notably, the usual expression for the anomalous skin depth corresponds to the characteristic scale of the magnetic field decay. The electric field is damped more rapidly because $|\delta_B| \gg \delta_p \gg |\delta_E|$. Thus, with a decrease of ω, δ_H increases whereas δ_E decreases compared to the high-frequency skin depth δ_P. This can be expected because a constant magnetic field penetrates easily into conductors, whereas a constant electric field is shielded by the space charge.

Figure 3a shows the plasma resistance as a function of Λ for different ϵ. The plasma resistance does not vanish at $\nu = 0$ (curve $\epsilon = 0$); for the extreme anomalous case, the dissipation of energy is independent of ν (lines with different ϵ "converge" for $\Lambda >> 1$). At $\Lambda \gg 1$, $Z(u) \approx i\pi^{1/2}$, and the surface impedance is [2]

$$\zeta = -\frac{2i}{3}\left(1 + \frac{i}{\sqrt{3}}\right)\left(\frac{\omega^2 v_T}{\sqrt{\pi}\omega_p^2 c}\right)^{1/3} \tag{27}$$

The collisionless energy dissipation under the anomalous skin effect is more efficient in comparison with the high-frequency skin effect (Fig.3b). Also, thermal electron motion produces interesting peculiarities in the spatial distribution of the absorbed power.

Figure 4 shows the spatial distribution of the normalized power absorbed in a unit volume of the plasma. The behavior is quite striking. There are regions outside the

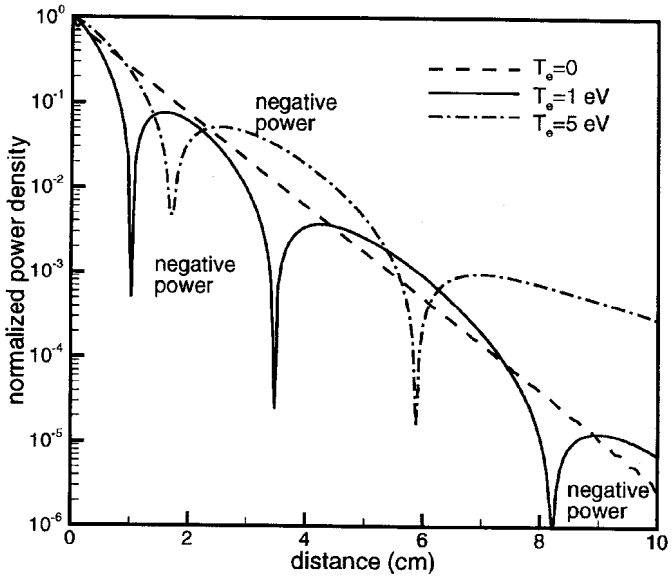

Figure 4. Spatial distribution of magnitude of the normalized power density for different electron temperatures. Plasma parameters: $\omega/2\pi$ = 13.56 MHz, argon p = 1 mTorr, plasma density 2×10^{11} cm^{-3}.

skin layer where the power density is negative; i.e., the energy is transferred from the plasma to the wave. This is possible because the current induced by the field at one point can drift by virtue of thermal electron motion to another point where the field is of opposite phase. In this situation, the current created by a field at one point can give up energy to the field at another point. The net energy transfer at a point is determined by an average over the entire half-space. Although this effect has been known for years [18], its direct experimental observation has not been obtained until recently[19].

We have demonstrated that under conditions of the anomalous skin effect ($\Lambda > 1$) it is impossible to describe the field profile as a damped exponential wave. The complicated distributions of the electromagnetic fields, current density, and power absorption are caused by the thermal motion of electrons. Electrons that have acquired momentum from the fields in the skin layer carry this momentum into the interior of the plasma to a distance of the order of the mean free path. Along the way, they generate a high-frequency current. Both the current density and the fields in the bulk are considerably weaker than they are in the skin layer, yet they vanish only at a depth of the order of the electron mean free path. The profile of the fields at large distances is determined by the high-energy electrons in the tail of the EDF. In the simplest case, the damping of the fields is characterized by two quantities (δ and λ) of different orders of magnitude.

PLANAR PLASMA SLAB

Consider a plasma slab of thickness L with all parameters varying only along the coordinate x. The electrostatic potential $\phi(x)$ confines the majority of electrons in the plasma. The electrons with axial energy $\varepsilon_x = mv_x^2/2 - e\phi(x)$ bounce between the two turning points $x_\pm(\varepsilon_x)$ defined by the equation $e\phi(x_\pm) = \varepsilon_x$. For a rectangular potential well with sharp boundaries at $x = 0$ and $x = L$, Eq.(8) can be solved by Fourier method. The electric and magnetic fields are continued into the region $-L < x < 0$ by

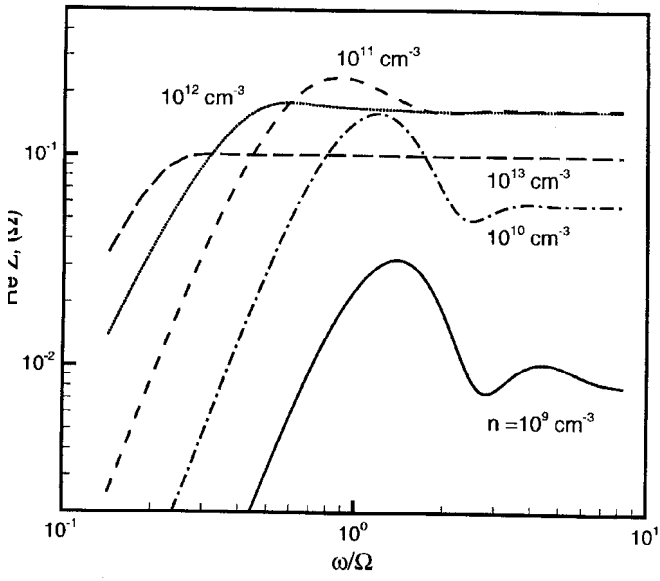

Figure 5. The resistance of a planar asymmetric plasma slab as function of the ratio $\omega/\bar{\Omega}$ for different plasma densities calculated from Eqs. (31) and (32) for collisionless plasma with T_e = 5 eV.

assuming that $B(-x) = -B(x)$ and $E_y(-x) = E_y(x)$, and the problem is reduced to that for an infinite plasma with periodic fields and currents. We seek the electric field in the form

$$E_y(x) = \sum_{n=0}^{\infty}{}' \alpha_n \cos(\pi n x/L) \tag{28}$$

where the prime means that the term $n = 0$ is multiplied by 1/2. Equation (8) gives the oscillating part of the EDF: [2 0]

$$f_1 = e v_y \frac{\partial f_0}{\partial \varepsilon} \sum_{n=0}^{\infty}{}' \alpha_n \frac{(i\omega + \nu)\cos(\pi n x/L) - n\Omega \sin(\pi n x/L)}{(i\omega + \nu)^2 + (n\Omega)^2} \tag{29}$$

where $\Omega = \pi v_x/L$ is the bounce frequency for an electron with velocity v_X. It is seen that f_1 becomes anomalously large at $\nu << \omega$ for electrons with $\omega = n\Omega$. Since Ω is a function of v_x, the resonance frequency ω depends on electron energy.

For a Maxwellian EDF f_0 (ϵ), the rf current density is: [2 0]

$$j_y(x) = \frac{i n_e e^2 l}{m v_T} \sum_{n=0}^{\infty}{}' \frac{\alpha_n}{k_n} \cos(\pi n x/L) Z(is/k_n) \tag{30}$$

where $k_n = \pi nl/L$. The solution of Eq.(9) with the current density (30) gives the Fourier coefficients [2]

(31)

where $D(k)$ is defined after (23) and the value of $\xi = B_z(L)/B_0$ is determined by the conditions at $x = L$. For a symmetric slab with two opposite current layers, $\xi = 1$. For an asymmetric slab with a metallic boundary at $x = L$, the boundary condition $E_y(L) = 0$ gives [2,9]

$$\xi = \sum_{n=0}^{\infty}(-1)^n D^{-1}(k_n) / \sum_{n=0}^{\infty}{}' D^{-1}(k_n) \tag{32}$$

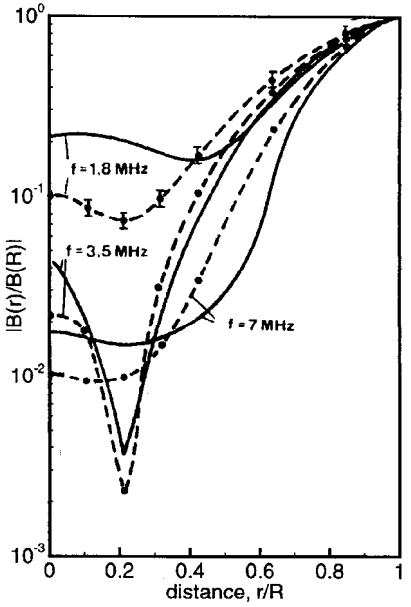

Figure 6. The radial distributions of the amplitude of the magnetic field in a cylindrical argon plasma. Dotted lines show experimental data for p = 10 mTorr, average plasma density $n = 4.2 \times 10^{12}$ cm^{-3} and T_e = 2.1 eV. Solid lines are calculations according to the Sayasov theory for $n = 3 \times 10^{12}$ cm^{-3}) $\nu = 4 \times 10^{7}$ s^{-1}. From Ref. 24.

At $L \to \infty$, the magnetic field at $x = L$ vanishes, $\xi \to 0$, the summation over n goes into an integral

$$\frac{1}{L}\sum_{n=0}^{\infty}{}' \to \frac{1}{\pi}\int_0^{\infty} dk \tag{33}$$

and expressions (28) and (31) coincide with Eq. (23) for semi-infinite plasma.

The finiteness of the plasma is important at $l > L$ when electrons traverse the slab without collisions. In this case, successive electron interactions with the fields can be strongly correlated, and resonance phenomena take place at particular values of plasma density, driving frequency, and slab thickness[21]. In Fig. 5, the resistance $\mathcal{Z} = 4\pi\zeta/c$ of an asymmetric slab is plotted versus $\omega/\bar{\Omega}$, where $\bar{\Omega} = \Omega(v_T)$ is the mean bounce frequency. One can see an oscillating structure of $Re\mathcal{Z}(\omega/\bar{\Omega})$ at low plasma densities with a pronounced maximum at $\omega/\bar{\Omega} \approx 1$ due to bounce resonance. With increasing plasma density, the maximum is shifted towards lower $\omega/\bar{\Omega}$ and gradually disappear. At large $\omega/\bar{\Omega}$, the maximum of $Re\mathcal{Z}$ with respect to n takes place at $\omega\tau \approx 1$ as in a semi-infinite plasma (see Fig. 3b). The maximum of plasma resistance at certain L suggests the optimal conditions for the power absorption[9].

The theory of the anomalous skin effect in a plasma slab with an arbitrary profile of $\phi(x)$ was developed in Ref. 22. The plasma density was assumed as relatively high so that the alternating field attenuated at a distance $\delta << L$ from the boundary. Under these conditions, it is sufficient to know the profile of $\phi(x)$ at the tail of $n_e(x)$, since low-energy electrons do not penetrate into the skin layer. It was found that the surface resistance is a nonmonotonic function of ω in the region $\omega \approx \bar{\Omega} \gg \nu$ due to the finite size of the plasma. Indeed, in a plasma bounded on one side, an electron reflected from the boundary moves into the interior of the plasma until it collides with another particle. In the presence of a second boundary, the electron bounces between the two boundaries

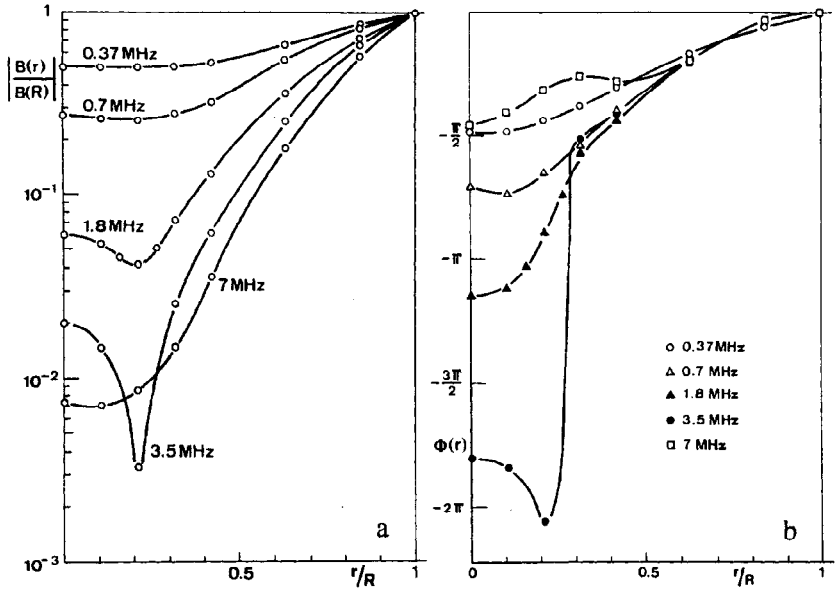

Figure 7. The radial distributions of the amplitude (a) and phase (b) of the rf magnetic field for different driving frequencies in a cylindrical argon plasma. Plasma parameters: p =10 mTorr, $n = 3.6 \times 10^{12}$ cm^{-3}, T_e = 2.1 eV. From Ref. 24

and visits the skin layer with a frequency ω. These phase correlations averaged over the ensemble of electrons cause the resonance behavior of the plasma resistance.

CYLINDRICAL CASE

Two different field configurations are possible in cylindrical geometry. The one with azimuthal electric field E_θ and axial magnetic field B_z corresponds to classical inductively coupled "ring discharges" [2,3]. The other, with azimuthal magnetic field B_θ and axial electric field E_z, corresponds to the pinch configuration.

Electromagnetic fields in ring discharges are produced by rf current in a coaxial coil wrapped around a cylindrical chamber. This current generates a time-varying magnetic field B_z, which induces solenoidal electric field E_θ and rf currents in the plasma. The E_θ field vanishes on the discharge axis due to azimuthal symmetry of the system. In addition to electromagnetic fields, a radial electrostatic field arises to assure the balance of charged particle flow to the wall. The electrostatic field confines the majority of electrons in the plasma. The trapped electrons are reflected by the potential barriers at the plasma-sheath boundaries. The finiteness of the plasma is particularly important for electron kinetics when the radius of the chamber is comparable to or less than the electron mean free path. The finite-size effects and transit-time resonances have been studied in a number of works.

Blevin et al.[25] developed the theory of the skin effect in cylindrical ring discharges. The electrostatic potential was assumed of the form $\phi(r) = -(m/2e)\Omega_0^2 r^2$, and both planar and cylindrical geometries have been analyzed. In planar geometry, the electron bounce frequency in a parabolic potential well is equal to ω_0, independent of axial electron velocity. As a result, strong bounce resonances occur at odd multiples of ω_0. In cylindrical geometry, the resonances occur at even multiples of ω. The parabolic

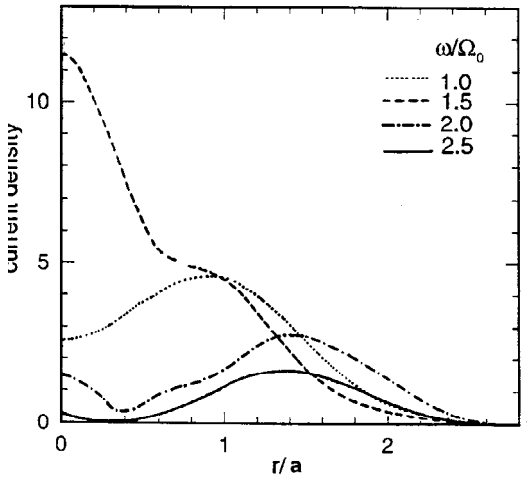

Figure 8. The radial distribution of the rf current density (arb. units) in a cylindrical plasma with a Gaussian profile of the plasma density, $n(r) \alpha \exp(-r^2/a^2)$, where $a = v_T/\Omega_0$, for different values of ω/Ω_0. The rf electric field is directed along the axis of the cylinder [26].

potential corresponds to a Gaussian shape of electron density, $n(r) \alpha \exp(-r^2/a^2)$ with a width $a = v_T\Omega_0$, which is a poor approximation to the real discharges.

Sayasov [17] developed an analytic theory of the skin effect in a cylindrical plasma with a rectangular potential profile $\phi(r)$, for the conditions $\delta << R$, $\lambda << R$. He has shown that for $\Lambda > 1$ the distribution of electromagnetic fields can be represented as a superposition of three fundamental modes

$$B(r) \approx B_0 \sum_1^3 A_n \frac{J_0(k_n r/R)}{J_0(k_n)} \tag{34}$$

Here, J_0 is the Bessel function, k_1, k_2 and k_3 are the three complex roots of the equation $D(k) = k^2 + \Lambda Z(is/k)/k = 0$, and $A_n = k_n/D'(k_n)$ where prime refers to the first derivative. The interference of these modes reproduces all the peculiarities in the spatial distributions of the fields observed in the experiments (see Fig. 6). For instance, the off-axis minimum of $|B(r)|$ appears only at a particular value of driving frequency $\omega \approx \omega_{max}$ and vanishes at low and high frequencies. According to Sayasov's theory, this is the frequency $\omega_{max} = \nu/\sqrt{2}$ at which the fundamental parameter Λ reaches a maximum as a function of ω.

Systematic experimental measurements and comparison with available theories were performed by Joye and Schneider [24] in a cylindrical plasma of radius $R = 4.7$ cm at argon pressure of 10 mTorr. The driving frequency varied in the interval 0.32 – 14 MHz, and the plasma density was between $10^{12} - 10^{13}$ cm^{-3}. Typical experimental results are shown in Fig. 6. It is seen that an off-axis minimum of the magnetic field amplitude is observed only at a particular driving frequency (Fig. 7a). This local minimum vanishes both at low and high frequencies. An abrupt change of the field phase takes place in the position of the minimum (Fig. 7b).

The theory of skin effect in the pinch configuration was developed [26] for a parabolic electrostatic potential $\phi(r)$. Strong bounce resonances were found in this case as well. Fig. 8 shows the radial distribution of the current density for various values of the ratio ω/Ω_0. The anomalous current in the center appears at $\omega/\Omega_0 = 1.5$. Two current layers are seen at $\omega/\Omega_0 = 2.0$ and $\omega/\Omega_0 = 2.5$. The phase of the current density at the center differs from that at the edge by about π; i.e. the current at the center flows in

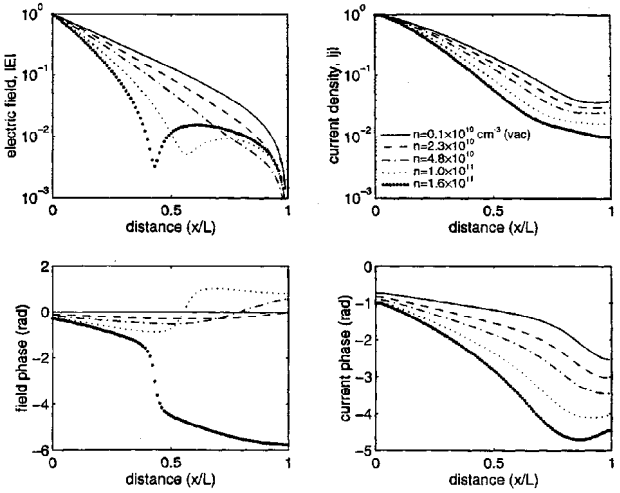

Figure 9. Amplitudes and phases of the rf electric field and current density in a plasma slab calculated from Eqs. (28), (30) and (31) for discharge conditions of Ref. 19. Argon p = 10 mTorr, $\omega/2\pi$ = 6.78 MHz, $T_e \approx 3.2$ eV, L = 10.5 cm, plasma densities n = 2,6.5,11,20 $\times 10^{10}$ cm^{-3}. Other parameters: $\nu = 3 \times 10^7$ s^{-1}, R = 10 cm.

a direction opposite to that of the local rf field.

In the general case, the skin effect in a cylindrical plasma depends on the cylinder radius R, the electron mean free path λ, and the thickness of the skin layer δ. Meierovich [27] analyzed the anomalous skin effect in the pinch configuration for $l >> R$. His theory for metal conductors with specular electron reflection at the boundary is applicable to gaseous plasma with rectangular electrostatic potential $\phi(r)$. The equation for E_z is of the form [27]

$$\frac{d}{d\rho}\rho\frac{dE_z}{d\rho} = \alpha \int_0^1 K(x,x')E_z(x')dx' \tag{35}$$

where $\rho = r/R$, the kernel $K(x, x')$ is given by

$$K(x,y) = \int_0^\infty J_0\left(\frac{k\sqrt{1-x^2}}{x}\right)J_0\left(\frac{k\sqrt{1-y^2}}{y}\right)dk \tag{36}$$

and $\alpha = (R\omega_p/c)i\omega/(i\omega + \nu)$. Notice that in the approximation $\lambda >> R$, electron temperature does not appear in the equations for the field.

The enhanced attenuation of the fields in a cylindrical plasma is observed [28] due to the difference in the dynamics of glancing electrons, which are the ones mainly responsible for the power absorption. These electrons collide much more frequently with the walls in cylindrical geometry than they do in a planar slab, and they spend more time in the skin layer.

PLANAR-COIL GEOMETRY

The ICP sources used for semiconductor processing are usually sustained by a planar coil placed on top of a cylindrical chamber. Typically, $R \approx L$, and the systems are essentially two-dimensional. Thus far, no reliable calculations of the electromagnetic phenomena in such systems have been performed for the weakly collisional regime. The published works have used rather crude approximations that have not been convincingly

justified. By assuming a homogeneous plasma, one can use the Fourier-Bessel series to solve the set of Maxwell-Boltzmann equations. Such an approach was employed by Yoon et al. [29]. However, the radial electron motion was neglected in that work by using an approximation that reduces the calculation of nonlocal conductivity to that of a plasma slab with a radially inhomogeneous electric field. A similar approach was used in Ref. 7. In addition, it was assumed[7] that higher radial modes can be neglected and only the first radial mode $J_1(\alpha_1 r/R)$ with α_1 = 3.8 is important. This innocent assumption makes the formulae look more compact.

With the assumptions of homogeneous plasma, Maxwellian EDF f_0, energy-independent collision frequency, and neglect of radial electron motion, the axial distribution of the electric field can be described by Eq. (28) with replacing $D(k)$ by $D(k)+(\alpha_1 l/R)^2$. The magnetic field and current density are given by the equations of the plasma-slab theory, modified accordingly. In spite of the crude approximations, such a model reasonably describes recent experiments performed by Godyak et al. in weakly collisional argon ICP. In Ref. 7 the calculated spatial distributions of the electric field and current density were compared to the experimental measurements at a pressure 1 mTorr. Figure 9 presents the results of similar calculations for 10 mTorr. The comparison with experimental data [19] shows good agreement. In particular, the calculations reproduce nonmonotonic distributions of electromagnetic fields and current density, bifurcations of field and current phases with changing discharge parameters, the appearance of negative power absorption and its dependence on driving frequency (see Ref.19). However, further advancement of the theory is desirable to relax the used approximations and to develop a generic approach applicable to the treatment of practical plasma sources.

One main assumption of the present model, the neglect of radial electron motion, is justified in the presence of a static magnetic field directed along the discharge axis. When the Larmor radius of electrons is small compared to the chamber radius *R*, the radial electron motion is greatly suppressed and the assumption of one-dimensional electron kinetics serves a good approximation. This model will be used below.

THE EFFECT OF MAGNETIC FIELDS

The application of a static magnetic field gives rise to new physical effects. Electron motion becomes finite in the plane orthogonal to the magnetic field. When the Larmor radius r_H is smaller than electron mean free path, transverse conductivity is much lower than longitudinal conductivity, and the plasma behaves as a dielectric in the plane orthogonal to *B*. The rf electric field orthogonal to *B* can easily penetrate into such a plasma at frequencies $\omega << \omega_H$.

Consider the static magnetic field directed along the x-axis. The magnetic field does not affect the longitudinal component of the conductivity, $\sigma_{\|} = \sigma$, while the transverse component in the bulk of the plasma (for $\omega << \nu$)

$$\sigma_{\perp} = \sigma/(1 + \omega_H^2/\nu^2), \tag{37}$$

decreases with increasing *B* and becomes very small for $\omega_H \gg \nu$: $\sigma_{\perp} \sim \sigma(r_H/\lambda)^2$. Owing to electron collisions with the boundary, the conductivity near the *surface* may be quite different from the bulk conductivity (37). Two cases need to be distinguished with respect to the direction of the magnetic field.

Magnetic Field Parallel to the Boundary

If electrons are scattered diffusively by the boundary (typical for metals), electron

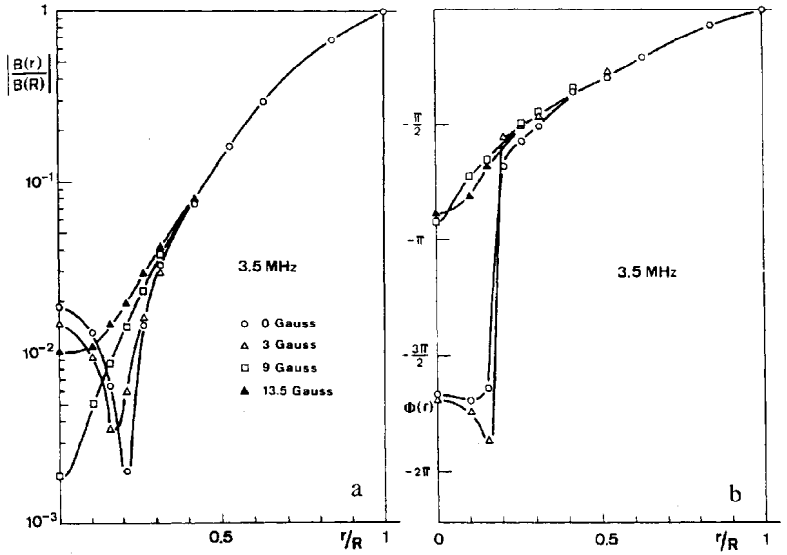

Figure 10. Radial distributions of the amplitude and phase of the rf magnetic field in a cylindrical argon plasma for different values of axial static magnetic field. Plasma parameters: p = 10 mTorr n = 3.4 · 10^{12} cm^{-3}, T_e = 2.1 eV, $\omega/2\pi$ = 3.5 MHz. From Ref.24

momentum is lost in each collision with the boundary. Therefore, the effective collision frequency of electrons in a layer of thickness r_H is equal to the gyro-frequency ω_H. Consequently, within the surface layer,

$$\sigma^s_{xx} \approx \sigma \frac{r_H}{\lambda} \gg \sigma\left(\frac{r_H}{\lambda}\right)^2 = \sigma_{xx} \tag{38}$$

The *surface* conductivity is therefore much larger than the bulk conductivity. High surface conductivity results in the concentration of the current near the boundary, a phenomenon known as the *static skin effect* in metals[3]. In the case of specular reflection from the boundary (as in discharge plasma), electron collisions with the surface do not lead to scattering. The electrons in the boundary layer follow infinite paths and the *surface* conductivity is of the order of the bulk conductivity *without* the magnetic field. In both cases, the principal contribution to the total current is made by a surface layer of thickness r_H. The current practically vanishes at $x > r_H$, and the field and current have different depths of penetration.

At high frequencies, $\omega >> \nu$, there is no dissipation of energy in the absence of a boundary. However, if $\omega > \omega_H$, a specific cyclotron resonance (known as Azbel-Kaner resonance) may occur. Assume that $\lambda > r_H$ and the skin depth is of the order of c/ω_H. For the magnetic field parallel to the surface, there are some electrons that do not collide with the surface and return to the skin layer after each revolution. If the return of these electrons is synchronized with the high-frequency field, and if the frequency ω is equal to or a multiple of the frequency ω_H, the electrons are accelerated in the skin layer by a factor $\lambda/2\pi r_H$. In this case, the skin layer plays a role analogous to the accelerating gap in a cyclotron.

The damping of a high-frequency field is of special nature. In a layer of thickness δ, electrons acquire directed velocity and give rise to a current density. Moving into the plasma bulk, the electrons "congregate" again in a layer of thickness δ at a depth $\approx 2r_H$. The current density has a local maximum at that point and has an opposite sign compared to that in the skin layer. Therefore, if all electrons were to move along orbits of the same radius, the "glancing" electrons would give rise to peaks of the current and

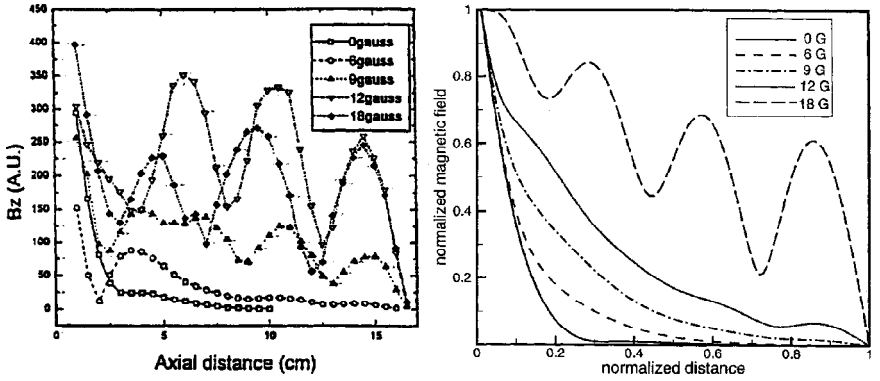

Figure 11. The spatial distribution of the rf magnetic field H_z on the discharge axis for different values of static magnetic field. a) Experimental data[30] in argon for the input power 500 W, p=5 mTorr and $\omega/2\pi$ = 13.56 MHz; b) Our calculations for the same conditions with electron temperature T_e = 4.2 eV and plasma densities taken from the experiment[30].

electromagnetic field at a depth $x = 2r_H$. Such peaks would accelerate new electrons that have "glanced" in the layer at a depth $2r_H$, and this would be repeated at $4r_H$, etc. Due to the presence of orbits of different radii r_H, only a small fraction of electrons "congregates" at any given depth, and the amplitude of field spikes decreases rapidly at each ((stage." The appearance of such field and current peaks gives rise to several macroscopic effects that have been unambiguously proven in metals[3]. The physical origin of the field (current) peaks implies that they should be observed anytime when there is a mechanism selecting a small fraction of electrons whose orbit-diameter scatter is of the order of or less than the skin depth. However, no experimental observation of the field and current splashes in gas discharges has been reported so far.

The influence of a static magnetic field, B_0, was studied for a ring discharge in argon. Fig. 10 shows experimental results for a frequency of 3.5 MHz. The off-axis minimum of $|B(r)|$, observed without static magnetic field, gradually disappears with an increase of B_0. A field as weak as 3G already modifies the position of the local minimum (this field corresponds to $\omega_H/2\pi$ = 8.4 MHz, r_H = 1.6 cm). The off-axis minimum disappears at B_0 = 9G when r_H = 0.53 cm. The effect of the static magnetic field is mostly pronounced when the fundamental parameter Λ has a maximum.

Magnetic Field Perpendicular to the Boundary

When the static magnetic field is perpendicular to the plasma boundary, the incident wave breaks into a sum of right and left circularly polarized components which propagate independently of one another. The interaction of the right-hand polarized wave with electrons exhibits a resonance at the field frequency close to the Larmor frequency of the electrons. In the frequency range $\omega << \omega_H$, weakly damped helicon waves can penetrate into the plasma.

Lee et al. [30] have recently studied the effect of static magnetic fields on a planar ICP. Fig. 11a shows the spatial distribution of the H_z component of the rf magnetic field in argon at a pressure of 5 mTorr, driving frequency 13.56 MHz, and input power 500 W, for different values of static magnetic field B_0. It is seen that static fields of only a few Gauss completely modify the nature of the rf field penetration into the plasma.

Figure 11b presents results of our calculations for the discharge conditions of Ref. 30. Thermal effects parallel to the magnetic field (such as the Doppler shift) are retained

in the calculations, while thermal effects perpendicular to the magnetic field (such as finite Larmor radius) are neglected. In other words, electrons are allowed to move only along the lines of the static magnetic field. The electromagnetic field profiles correspond to azimuthally symmetric, right-hand polarized helicon waves in a cylindrical waveguide [31]. Both E_θ and E_z are zero at the conducting wall. The radial profile of B_z is given by the Bessel function J_0, and the axial profile is found by using the plasma slab theory with σ calculated from Eq. (13)) using $\omega - \omega_H$ in place of ω.

The enhanced penetration of the rf magnetic field into the plasma is due to excitation of helicon waves. The power absorption in ICP under these conditions can be due to Landau damping, cyclotron and Cherenkov resonances, and collisional damping, similar to helicon discharges [31]. A thorough analysis of excitation, conversion and damping of waves in a helicon plasma source driven by azimuthally symmetric antennae was given for the cold plasma [32]. However, the helicon sources usually operate at magnetic fields 20-200 G when $\omega << \omega_H$. The thermal electron motion is important at frequencies below the cyclotron frequency [31]. Lee's experiments [30] give direct evidence of drastic changes produced by weak static magnetic fields in inductively coupled plasmas. It seems that the role of static magnetic fields in ICPs has not been appreciated thus far. The fields of only a few Gauss can greatly enhance the penetration of electromagnetic energy into high-density plasmas and improve characteristics of ICP sources.

The Role of RF Magnetic Fields

Although the question about possible influence of the rf magnetic field on the skin effect in inductive discharges was raised more than 30 years ago [5], clear understanding of the effect is still absent. Most currently used ICP models have ignored the rf magnetic field. Analyzing a single particle motion, Cohen and Rognlien have recently shown [16] the importance of the rf magnetic field on electron dynamics in the collisionless skin layer In a planar geometry, for instance, the canonical momentum $p_y = mv_y - eA_y(x,t)$ is a strict invariant of the electron motion (A_y is the vector potential of the magnetic field). Therefore, the Lorentz force transforms a v_y velocity kick produced by the rf electric field E_y into a v_x kick orthogonal to E_y. In a planar slab, the electron bounce frequency changes after each interaction, which can be of great importance for the collisionless electron heating [33]. However these nonlinear effects disappear in the linear models we have considered and are slured by collisions which are present in any discharge. In the linear approximation, the EDF is calculated by integration along unperturbed electron trajectories, and the effect of the rf magnetic field vanishes in isotropic plasmas. Monte Carlo simulations [34] have revealed a small influence of the rf magnetic field on electron heating in weakly collisional ring discharges. It was pointed out 34 that magnetic field effect may be more important for gas breakdown by inductive fields where nonlinear analysis seems to be necessary.

The effect of the rf magnetic field on the skin effect becomes more important with a decrease of the field frequency ω. Tuszewski [35] has measured the penetration of the rf magnetic field in a low-pressure (5-50 mTorr) cylindrical ICP (R=16.5 cm) driven by a coaxial coil at the relatively low frequency of $\omega/2\pi$ = 0.46 MHz. He found enhanced penetration of the magnetic field compared to the predictions of linear models He described the influence of the rf magnetic field on electron motion by introducing an effective collision frequency $\nu_{eff} = |\omega_H|$, where $\omega_H(r)$ is the amplitude of oscillating gyro-frequency. This approach results in an effective skin depth $\delta_{eff} = \delta_p(2|\omega_H|/\omega)^{1/2}$ if $\omega_H(r)$ exceeds the angular frequency ω and collision frequency ν. However, no quantitative calculations of this effect have yet been reported. The analysis

of nonlinear effects in nonlocal electrodynamics of plasmas remains a subject for further studies.

CONCLUSION

We have described the state of the art of nonlocal electrodynamics of bounded discharge plasmas. We revived classical works on the anomalous skin effect to analyze peculiarities of the electromagnetic phenomena in weakly collisional ICPs. Our calculations corroborated nonmonotonic distributions of the electromagnetic fields and electron current density, the existence of negative power absorption, and other interesting phenomena recently observed in experiments. We have analyzed the effect of weak static magnetic fields on the penetration of rf fields into weakly-collisional ICPs.

The elaboration of nonlocal electrodynamics in bounded systems is important for the development of novel plasma reactors operating at gas pressures below 10 mTorr. Currently used models designed for collisional plasmas do not contain the nonlocal effects we have discussed. Our treatment was based on simple models. Further development of theory and numerical tools is required for simulation of practical devices.

ACKNOWLEDGMENT

The author acknowledges fruitful discussions with D. J. Economou and V.A. Godyak, This work was supported by NSF grant CTS-9216023.

REFERENCES

1. E.M.Lifshitz and L.P.Pitaevskii, *Physical Kinetics,* Pergamon Press, Oxford, 1981.
2. A.N.Kondratenko, *Field Penetration into Plasmas,* Atomizdat, Moscow, 1979, in Russian.
3. I.M.Lifshits, M.Ya.Azbel', and M.I.Kaganov, *Electron Theory of Metals,* Consultants Bureau, New York-London, 1973.
4. P.M.Platzman and P.A.Wolff, *Waves and Interactions in Solid State Plasmas,* Academic Press, New York, 1973.
5. R.A.Demirkhanov, I. Kadysh, and Yu.S.Khodyrev, Sov. Phys. JETP **19,** 791 (1964).
6. E.S.Weibel, Phys. Fluids **10,** 741 (1967).
7. V.I.Kolobov and D.J.Economou, Plasma Sources Sci. Technol. **6,** 1 (1997).
8. M.M.Turner, Phys. Rev. Lett. **71,** 1844 (1993).
9. N.S.Yoon, S.S.Kim, C.S.Chang, and D.-I. Choi, Phys. Rev. E. **54,** 757 (1996).
10. I.P.Shkarofsky, T.W.Johnson, and M.P.Bachinski, *The Particle Kinetics of the Plasmas,* Addison-Wesley, Reading, 1966.
11. V.I.Kolobov and V.A.Godyak, IEEE Trans. Plasma Sci. **23,** 503 (1995).
12. B.D.Fried and S.D.Conte, *The Plasma Dispersion Function,* Academic Press, New York, 1961.
13. K.N.Stepanov, Soviet Phys. JETP **36,** 1035 (1959).
14. I.Holstein, Phys. Rev. **88,** 1427 (1952).
15. V.Vahedi, M.A.Lieberman, G.DiPeso, T.D.Rognlien, and D.Hewett, J. Appl. Phys. **78,** 1446 (1995).
16. R.H.Cohen and T.D.Rognlien, Plasma Sources Sci. Technol. **5,** 442 (1996).
17. Yu.S.Sayasov, Helvetica Physica Acta **52,** 288 (1979).
18. P.M.Platzman and S.J.Buchsbaum, Phys. Rev. **128,** 1004 (1962).
19. V.A.Godyak, Electron kinetics and electrodynamic characteristics of ICP in stochastic heating regime, in *Electron Kinetics in Glow Discharges,* edited by U.Kortschagen and L.D.Tsendin, Plenum Press, Inc., New York, 1997.
20. H.A.Blevin, J.A.Reynolds, and P. Thonemann, Phys. Fluids **13,** 1259 (1970).
21. H.A.Blevin, J.A.Reinolds, and P.C.Thonemann, Phys. Fluids **16,** 82 (1973).
22. S.M.Dikman and B.E.Meierovich, Soviet Physics JETP **37,** 835 (1973).

23. H.U.Eckert, The hundred year history of induction discharges, in *Proc. 2nd Int Conf on Plasma Chem Technol.*, edited by H.V.Boenig, Lancaster, Pennsylvania, 1986, Technomic Publishing Company, Inc.
24. B.Joye and H.Schneider, Helvetica Physica Acta **51,** 804 (1978).
25. H.A.Blevin, J.M.Greene, D.L.Jolly, and R.G.Storer, J.Plasma Phys. **10,** 337 (1973).
26. R.G.Storer, Phys. Fluids **16,** 949 (1973).
27. B.E.Meierovich, Soviet Physics JETP **10,** 782 (1970).
28. A.I.Kondratenko, Soviet Physics-Technical Physics **17,** 584 (1972).
29. N.S.Yoon, S.M.Hwang, and D.-I. Choi, Phys. Rev. E **55,** 7536 (1997).
30. H.-J. Lee, I.-D. Yang, and K.-W. Whang, Plasma Sources Sci. Technol. **5,** 383 (1996).
31. B.M.Harvey and C.N.Lashmore-Davies, Phys. Fluids B **5,** 3864 (1993).
32. K.P.Shamrai, V.P.Pavlenko, and V.B.Taranov, Plasma Phys. Control. Fusion **39,** 505 (1997).
33. I. D.Kaganovich, V.I.Kolobov, and L.D.Tsendin, Appl. Phys. Lett. **69,** 3818 (1996).
34. V.I.Kolobov, D.P.Lymberopoulos, and D.J.Economou, Phys. Rev. E **55,** 3408 (1997).
35. M.Tuszewski, Phys. Rev. Lett. **77,** 1286 (1996).

This Page Intentionally Left Blank

COLLISIONLESS HEATING IN CAPACITIVELY-COUPLED RADIO FREQUENCY DISCHARGES

M. M. Turner

Plasma Research Laboratory
Dublin City University
Dublin
Ireland

INTRODUCTION

Most readers of this volume will be acquainted with the idea of a capacitive discharge, and some will be familiar with ideas about collisionless heating in such discharges. If not, there are several good introductions to the field, and to the focus of contemporary research [1, 2, 3, 4, 5]. These make superfluous any general introduction here. Therefore we turn at once to our theme, which is the origin of the collisionless heating that is generally agreed to occur in capacitive discharges. This collisionless heating becomes an important effect only under restricted circumstances, when the electron collision frequency, ν_e, is comparable to or less than the angular frequency of the discharge current, ω_{rf}, and the electron mean free path λ_e is comparable with the other characteristic dimensions of the discharge, such as the electrode separation L or the maximum sheath width s_m. When these conditions are satisfied, the discharge plasma does not behave in every way as a classical fluid, and effects such as collisionless heating can be expected. As is sometimes remarked, "collisionless" heating is slightly a misnomer, since we usually are dealing with situations where collisions are present, as they must be in a discharge that must sustain itself by ionization, and the relaxation of the electron energy distribution function by these collisions is an important part of the process. A more accurate but also more cumbrous term is "non-Ohmic" heating, meaning heating that cannot be described by a local relationship between the electric field E and the current density J, such as the classical expressions

$$J = \sigma E \tag{1}$$

with

$$\sigma = \frac{e^2 n_e}{m_e(\nu_e + i\omega_r f)}, \tag{2}$$

where m_e is the electron mass, n_e the electron density; this expression for σ is the Langevin or Lorentz conductivity. In this chapter we assume that "collisionless" heating is non-Ohmic heating in the sense that eqn. (1) does not hold, so that "collisionless

Electron Kinetics and Application of Glow Discharges
Edited by U. Kortshagen and L. D. Tsendin, Plenum Press, New York, 1998

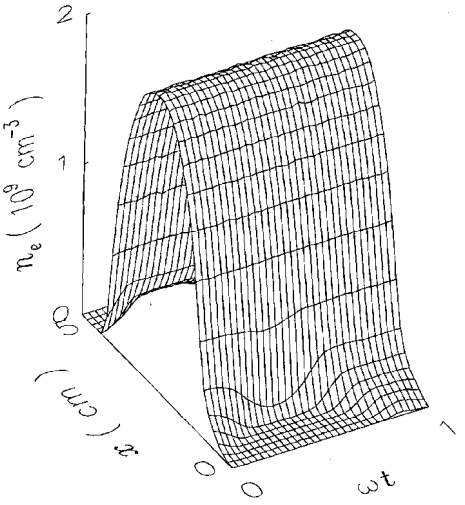

Figure 1. The electron density n_e during a single period of the radio frequency current, showing the flow of electrons in and out of the sheath regions. (Discharge current density $J = 1$ mA cm^{-2}, $\omega_{rf} = 2\pi \times 13.56$ MHz, and pressure $p = 20$ mTorr.)

heating" and "non-Ohmic heating" are synonyms. The evidence that collisionless heating can be important comes in the first case from experiments, such as those of Godyak and his collaborators [4, 6, 7, 8], that attempt to estimate independently the power dissipated in the electrons and the electron collision frequency and density. From the latter parameters the Ohmic heating can be estimated, whence an estimate of the collisionless heating component can be derived. These experiments are inherently difficult, and open to the objection that the Ohmic heating may be underestimated in peripheral parts of the discharge plasma where no measurements are made, but they justify further enquiries. These enquiries have been either theoretical or computational. The computational studies take one of two approaches. The most general make practically no physical assumptions. These are in the spirit of computer experiments, and are generally more or less direct solution of the Boltzmann equation. The results reported in this chapter were obtained from such a simulation based on the particle in cell with Monte Carlo collisions method. Most theoretical studies, and the remaining computational ones, have emphasized the "hard wall" model of the collisionless heating process, the idea of which is as follows. The basic structure of the radio frequency capacitive sheath is indicated in figs. 1 and 2. At any given time the discharge is clearly differentiated into quasi-neutral regions where electrons are present and conduction current dominates, and other regions where there are no electrons and displacement current dominates. The electron-free regions of net positive space charge are referred to as the sheaths, which cyclically expand and collapse as the radio frequency phase advances and the polarity of the current changes. There is a narrow interface region between the sheaths and the quasi-neutral plasma, which can be abstracted to a point s and called the sheath edge. This point oscillates back and forth with velocity u_s. Since the electron temperature is normally small relative to the potential that appears across the sheath, an electron cannot penetrate far beyond the sheath edge without being reflected

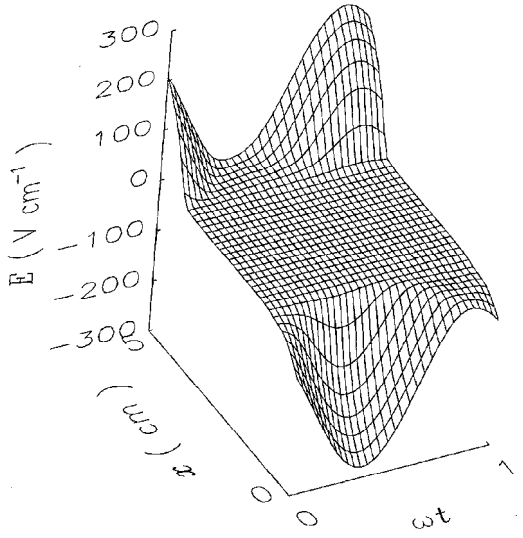

Figure 2. The electric field E during one cycle of the discharge current. (Conditions as in fig. 1.)

back into the plasma. The "hard wall" model represents the sheath edge as an infinite potential barrier that specularly reflects incident electrons. Since this barrier moves at velocity u_s, an electron striking it with an incident velocity u_i is reflected with a change of speed, so that the reflected velocity $u_r = -u_i + 2u_s$. This may or may not lead to a net transfer of energy from the sheaths to the electrons, depending on the assumptions that govern the distribution of u_i. Or, for an individual particle, we may say that the energy exchanged at each collision depends on the phase of the sheath motion where the particle arrives, and the net effect over a long time depends on how this phase changes between sheath reflection events. However although it is certain that there is an electron heating mechanism associated with the oscillatory motion of the sheaths, as fig. 3 shows, there are difficulties with the "hard wall" model. Chief amongst these is the difficulty of demonstrating that there is a non-zero effect. Assuming a particular model of the sheath, which gives a specific form to $u_s(t)$, and assuming that the electron velocity distribution function is a drifting Maxwellian with mean speed u_t and drift velocity u_e, Lieberman[9] shows that average power delivered to the electrons is

$$P = \frac{m_e u_t}{T_{rf}} \int_0^{T_{rf}} dt\,(u_s - u_e) u_s n_e(s), \tag{3}$$

where T_{rf} is the period of the driving frequency and $n_e(s)$ is the electron density at the sheath edge s. Lieberman makes u_e the drift velocity at the maximum extent of the sheath, s_m, but this choice does not conserve conduction current between s and s_m. The current conservation condition in fact imposes $u_e = u_s$, whereupon the integral in

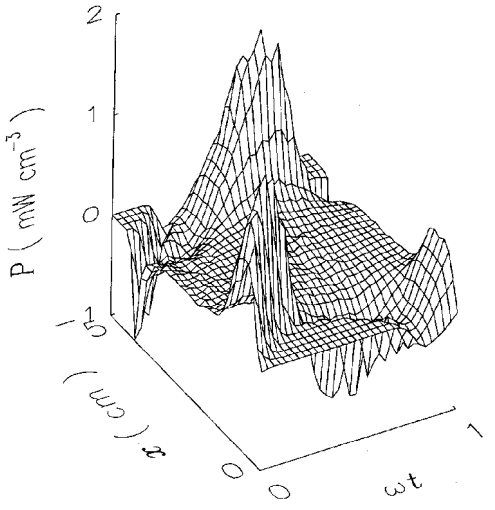

Figure 3. The power deposited in electrons during an rf period, showing the largest effect occuring at the plasma periphery, with heating during expansion of the adjacent sheath and cooling during collapse. (Conditions as in fig. 1 and 2.)

eqn. 3 vanishes identically*. This is reasonable enough, as the movement of the electrons and the motion of the sheath edge are one and the same. It seems to be difficult to construct a "hard wall" model along these lines that predicts a non-zero result for the collisionless power, conserves current everywhere, and avoids difficult assumptions about the electron velocity distribution function. There is an alternative strategy, which is to express the interaction in terms of an energy space diffusion coefficient which can be used in a solution of a simplified (*e.g.* non-local) Boltzmann equation[10, 11]. This procedure usually (but not necessarily) entails the use of some simplified model of the electron-sheath interaction along the lines discussed above. In the remainder of this chapter we take issue with this aspect of such models of the electron heating process. We investigate a periodic model system in which the electron dynamics resemble a capacitive radio frequency discharge in every way except for the absence of a sheath edge. The net heating effect in this model system, however, remains, which we take to be evidence that the sheath edge is not the source of the primary effect[12, 13]. The implications of this result are discussed in a final section.

*If the electric field is zero at $x = s_m$, the electrode is at at $x = 0$, the plasma is neutral for $s < x < s_m$, and the ion density in the sheath is $n_i(x)$, then

$$E(x) = \int_0^{s-x} dx' e n_i(x')/\epsilon_0$$

for $x < s$ and zero otherwise, and the displacement current

$$J_D = \epsilon_0 \frac{\partial E}{\partial t} = e u_s n_i(s)$$

and since the conduction current at the sheath edge is $u_e(s)n_i(s)$, we must have $u_s = u_e(s)$.

SIMULATION PROCEDURE

Particle in Cell Simulation with Monte Carlo Collisions

The basic simulation approach is a fully kinetic procedure using the particle in cell method with Monte Carlo collisions[14, 15]. This technique represents the plasma particles by a tractably small number of computer particles, whose equations of motion are integrated forwards in time using a finite difference procedure with time step Δt. In this work we used an explicit leap-frog algorithm. The field equations, in this case only Poisson's equation, are solved at every time step using a charge density constructed by projecting the contributions of individual particles onto a finite spatial mesh with mesh interval Δx. Bilinear weighting is used for mapping particle data onto mesh points, and *vice versa.* These well-known techniques are fully explained elsewhere. The finite difference parameters Δt and Δx are constrained by the stability and accuracy conditions

$$\omega_p \Delta t \lesssim 0.2 \tag{4}$$

$$\lambda_D / \Delta x \gtrsim 2, \tag{5}$$

which have been carefully respected in the present work. We used typically many tens to a few hundred computer particles per mesh cell in the computations reported here.

Collisions between the plasma particles and the neutral gas were handled using an orthodox null collision Monte Carlo method [16, 17]. For electrons, the collision processes included were elastic scattering [18], two lumped excitation processes [19] and ionization; for ions, elastic scattering and charge exchange scattering[20]. The cross sections were obtained from the indicated references. All scattering was assumed to be isotropic. The collision handling procedure introduces a further constraint on the time step relating to the assumption that there is only one collision per particle per time step, so that the probability of a collision in each time step must be small. This is normally a less important restriction than eqn. (5).

Bounded Model System

The bounded model plasma was formed between a pair of plane parallel electrodes separated by 5 cm. Both electrodes were assumed to absorb all the particles that strike them, and the system was driven by a sinusoidal current source with amplitude J_0 = 1 mA cm^{-2}. We reduced the ion mass to that of helium to accelerate the convergence of the simulation, which was initiated from essentially arbitrary initial conditions and integrated forward in time to a harmonic steady state, in which all quantities may vary over a radio frequency cycle, but are essentially invariant from one cycle to the next. This converged state was typically attained in a few hundred cycles.

Periodic Model System

The aim of the periodic model used here is to isolate the effect of sheath edges by constructing a system that resembles closely the bounded model plasma discussed in the previous section in every way except for the presence of sheaths. This is accomplished by adopting a periodic model which is filled with a quasi-neutral plasma everywhere, but in which the distribution of plasma resembles the envelope of the plasma density in the bounded system. The current density in this periodic model is then forced with the same amplitude as in the bounded system. Only the electron dynamics are of interest

in this case, so the ions are fixed (their mass is infinite), and ionizing collisions are treated as excitation, so, there being no loss mechanisms, the total number of particles in the system is preserved.

Distinguishing Ohmic from Non-Ohmic Heating

It is necessary to make a precise distinction between Ohmic and non-Ohmic heating. The quantity directly calculated by the simulation is an aggregate of several processes that we can distinguish as Ohmic heating, non-Ohmic heating and, in the bounded system, diffusion (or evaporation) cooling. We want to define Ohmic heating as the heating that would be produced if there were a local relation between the electric field and the current density. The simplest such relationship is eqn. 2 but that expression cannot be used in the bounded model system because a large proportion of the heating of interest occurs in the sheath regions where the electron density varies with time. We instead defined the Ohmic heating as the heating that would occur if the plasma satisfied the Langevin equation

$$m_e \frac{d}{dt}(u_e n_e) + e n_e E_{local} + m_e n_e u_e \bar{\nu}_e = 0, \tag{6}$$

which has the same physical content as the Langevin conductivity mentioned above, but involves no assumptions about the time variation of the quantities involved, all of which except the effective electric field E_{local} in eqn. (6) are know from the simulation. We define the Ohmic heating by using eqn. (6) to compute E_{local}, the electric field that would be needed to produce the local drift velocity u_e, and $\langle JE_{local} \rangle$ is then defined as the Ohmic heating. There is a third component of the gross electron heating, which is the energy lost by electrons to the fields as they escape to the walls – under normal circumstances there is always a positive potential between the plasma and the adjacent wall, even when the rf sheath is fully collapsed[21], so that an electron that leaves the plasma must climb this potential and be cooled in the process. (This accounts for the region of net negative heating commonly appearing in simulations next to electrodes, see fig. 9 below.) We have estimated this contribution to the net electron power balance as

$$P_{evaporation} = \frac{1}{T_{rf}} \int_0^{T_{rf}} [\phi(0) J(0) + \phi(L) J(L)]\, dt, \tag{7}$$

where for this computation $\phi(L/2) = 0$.

We can do better in the periodic system. The Langevin equation assumes ν_e independent of ϵ, the electron energy, which is not true for electrons at low energies in argon. An expression for the conductivity that allows for arbitrary electron energy distribution functions $f(\epsilon)$ and arbitrary variation of ν_e with energy is[22, 23]

$$\sigma_e = -\frac{2 n_e e^2}{3 m_e} \int_0^\infty \frac{\epsilon^{3/2}}{\nu_e(\epsilon) + i\omega} \frac{df}{d\epsilon} d\epsilon, \tag{8}$$

This expression is certainly more accurate than eqn. (2), but it can only be applied conveniently to the periodic model, for the reasons noted above in connexion with the Langevin conductivity.

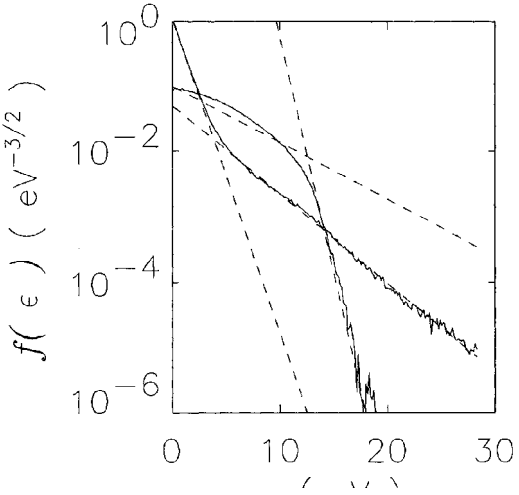

Figure 4. The electron energy distribution function in the bounded model system at the extrema of the pressure range under consideration, 20 mTorr (bi-Maxwellian) and 200 mTorr (Druyvesteyn-like). The dashed lines indicate the temperatures used to characterize these distribution functions in fig. 5, which clearly are crude but serve to emphasize the change in the form of the distribution function.

RESULTS

Bounded Model

As the pressure is changed, the bounded model exhibits a heating mode transition similar to those several times reported in the past [8, 7, 24]. At low pressure, less than 30 mTorr in this context, the heating is dominantly collisionless. As the pressure is increased above 50 mTorr, Ohmic heating displaces collisionless heating as the most important effect, and this is accompanied by characteristic changes in the shape of the electron energy distribution function, as shown in figs. 4 and 5. It is also relevant that the spatial distribution of the effective temperature changes across this range of pressure. At the low end of the pressure range, the temperature is lowest in the bulk plasma and elevated in the sheaths, whereas at high pressure the reserve is the case, as fig. 6 shows, and as experiments confirm, as least so far as the bulk plasma is concerned[25]. This may seem surprising, since it is sometimes suggested that at low enough pressure the thermal conductivity becomes so large as to eliminate any temperature gradients, but this is assuming that the classical expression for the thermal conductivity may be applied, which is not the case (see below). Fig. 7 shows the fraction of the power deposited in the electrons that can be attributed to collisionless heating, using the definition of the collisionless heating given above. Fig. 8 shows an example of the distribution of the heating, showing that both Ohmic and collisionless heating are concentrated at the plasma boundaries.

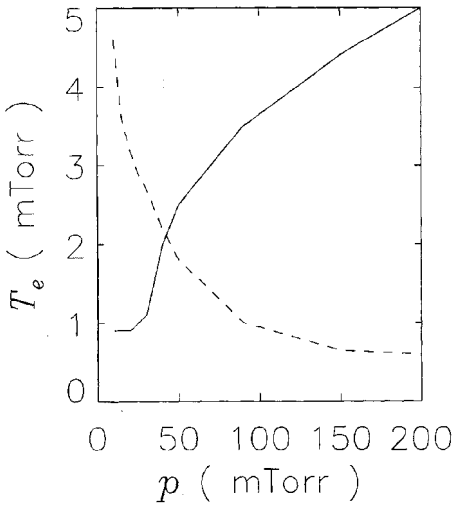

Figure 5. The effective temperatures of the bulk and tail electrons as a function of pressure in the bounded model system, *c.f* fig. 3. Solid line – bulk electrons. Dashed line – tail electrons.

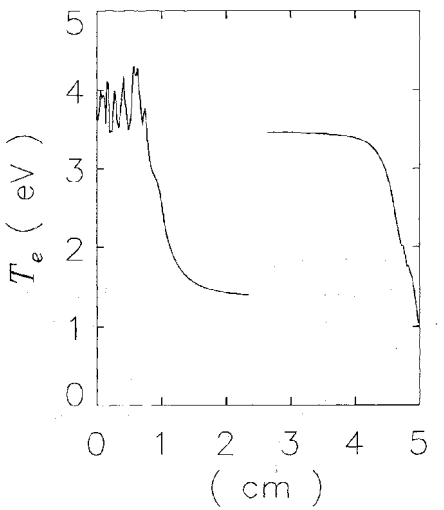

Figure 6. The effective temperatures of the electrons as a function of position at the extrema of the pressure range – 20mTorr (left half of the figure) and 200mTorr (right half of the figure) – showing the marked change in the distribution of temperature.

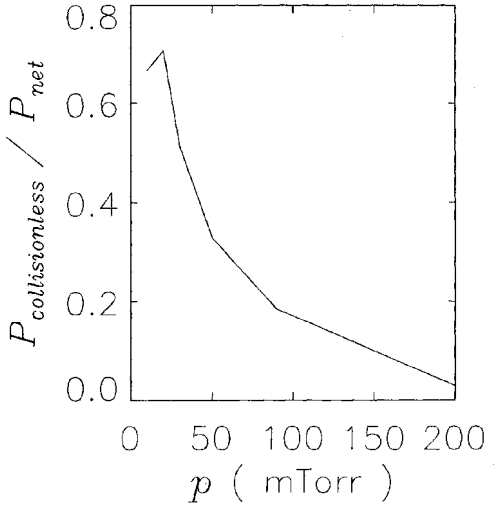

Figure 7. The fraction of the electron heating attributable to collisionless heating, as a function of pressure, using the definitions of different classes of heating mechanism discussed in the text. $(P_{net} = P_{Ohmic} + P_{collisionless} = P_{gross} - P_{evaporation}.)$

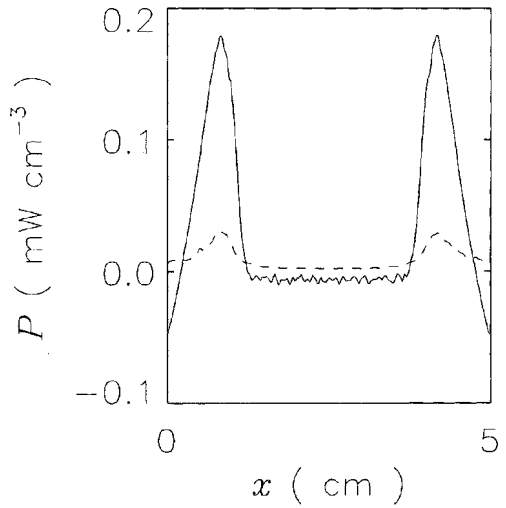

Figure 8. An example showing the low-pressure distribution of the net heating (solid line) and the Ohmic heating (dashed line) for the bounded model system at a pressure of 20 mTorr.

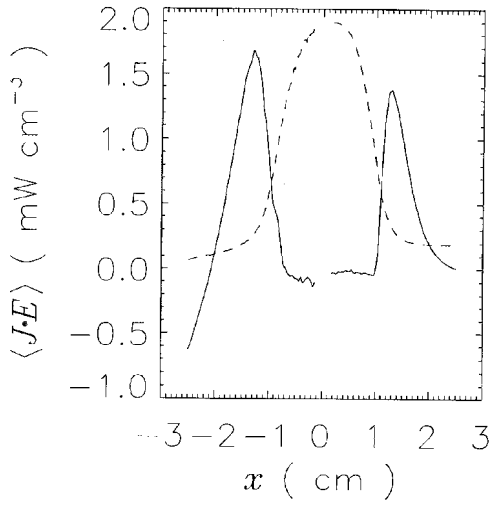

Figure 9. Comparison of the net electron heating in the bounded model system (left half of figure) and the periodic model system (right half of figure), for a gas pressure of 10 mTorr. The solid lines show the electron heating, while the dashed lines are the envelopes of the plasma density, in arbitrary units. To facilitate the comparison, the data for the periodic system have been modified by discarding heating that occurs at times and in places which are electron-free in the bounded system.

Periodic Model

As remarked above, the aim of the periodic model is to represent a system that is similar to the bounded model in every respect except for the presence of sheaths. Figs. 9 and 10 show that this is achieved in a high degree, since both the magnitude and spatial distribution of the electron heating and the mid-plane electron energy distribution functions are closely similar in each case. The mid-plane electron energy energy distribution functions are also remarkably similar, as fig. 10 shows.

DISCUSSION

The comparison of the bounded and periodic model systems shows that the collisionless electron heating is not intimately associated with the sheath edge, but is instead produced by the relatively small fields at the periphery of the plasma. It is obvious that the electric field in the plasma must be non-uniform, because the conduction current density is constant but the plasma density changes, so that the radio frequency electric field amplitude varies as $E \sim 1/n_e$. In any situation where an electric field changes in space and time, there is the possibility of kinetic effects under the general rubric of "transit time heating" [26](the anomalous skin effect is another example). But it is also useful, and consistent with recent work on kinetic or Landau fluid equations[27], to describe this effect in fluid language as an acoustic or pressure effect, in the following way. The physical basis of this argument is the observation that during the radio frequency cycle, electrons flow in and out of the sheath region,

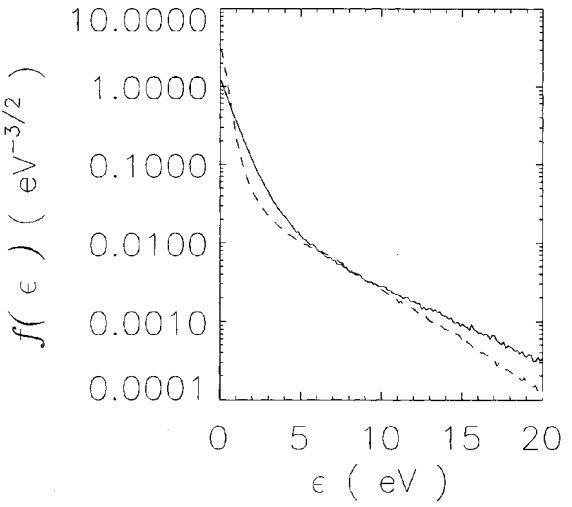

Figure 10. Comparison of the time averaged electron energy distribution functions from the mid-planes of the bounded system (solid line) and the periodic system (dashed line), for the same conditions as fig. 8.

as shown in fig. 1. Since the plasma density in the sheath regions is much less than in the bulk, this flow involves a cyclic expansion and compression of the electron fluid. If the electrons have a finite temperature, then work must be done by the electric field on the plasma during the compression cycle (while the sheath is expanding), and this work will be reversed during the subsequent expansion (when the sheath is contracting). In the absence of dissipative processes, this will not lead to any net work, but only an instantaneous electric field different from that obtained from eqn. (6). If there are dissipative processes, though, the net effect may not be zero. In this connexion the most important dissipative effect is thermal diffusion – the temperature perturbations produced acoustically can decay by diffusion, and in this case the exchange of energy between the fields and the plasma is not reversible. In principle this could be either a net heating or cooling effect, but if the time averaged electron temperature decreases from the sheaths towards the center of the plasma, then this is a heating mechanism. A relatively simple analytical model illustrates the basic effect. The time variation of the electron temperature is governed by the energy balance equation

$$\frac{3}{2}\frac{\partial}{\partial t}\left(n_e k_B T_e\right) + \frac{5}{2}\frac{\partial}{\partial x}\left(u_e n_e k_B T_e\right) + \frac{\partial q_e}{\partial x} + u_e n_e e E + \frac{3}{2}\frac{n_e k_B T_e}{\tau_e} = 0, \qquad (9)$$

where τ_e is some relaxation time associated with *e.g.* inelastic collisions, q_e is the heat flux, and we have assumed the ratio of specific heats $\Gamma = 5/3$†, which is reasonable when there are several collisions per electron per period of the driving frequency, and terms involving the drift energy have been neglected. We further assume that all time variation is at the driving frequency, ω_f, so that each quantity can be written as the sum of a steady state component (e.g. $T_e^{(0)}$), which is given, and a time varying component

†Probably in a more accurate treatment one should solve separate equations for the temperature parallel and perpendicular to the field28

with a complex amplitude (*e.g.* $T_e^{(1)}$) that is to be determined. It is convenient to eliminate the electric field from eqn. (9) using the momentum balance equation

$$m_e n_e \frac{\partial u_e}{\partial t} + \frac{\partial}{\partial x}(n_e k_B T_e) + e n_e E + m_e n_e u_e \nu_e = 0, \tag{10}$$

and to express the heat conduction term as

$$\frac{\partial q_e^{(1)}}{\partial x} = -n_e \bar{D}_e \frac{\partial^2}{\partial x^2}(k_B T_e^{(1)}), \tag{11}$$

where $\bar{D}_e = k_B \bar{T}_e^{(0)}/m_e \bar{\nu}_e$ is the space-averaged classical electron free diffusion coefficient, so that the thermal conductivity $\bar{\kappa}_e = n_e \bar{D}_e$. It is analytically convenient and qualitatively reasonable to choose $T_e^{(0)}(x) = T_0 \cosh(x/x_1)$ and $n_e(x) = n_0 \operatorname{sech}(x/x_0)$ then with these expressions and using the current continuity equation the equation for $T_e^{(1)}$ becomes

$$\frac{d^2}{dx^2} T_e^{(1)} - \alpha^2 T_e^{(1)} = \gamma \left[(3x_0 + 2x_1) \sinh \frac{(x_0 + x_1)}{x_0 x_1} x + (3x_0 - 2x_1) \sinh \frac{(x_0 - x_1)}{x_0 x_1} x \right], \tag{12}$$

where $\alpha^2 = (3/2\bar{\kappa}_e)(1/\tau_e - i\omega_{rf})$, $\gamma = J_0 T_0 / 4 e n_0 \bar{\kappa}_e x_0 x_1$, and J_0 is the current density amplitude. This equation can be solved rather easily for $T_e^{(1)}$, subject to the boundary conditions that $T_e^{(1)}(0) = T_e^{(1)}(L) = 0$. The solutions are essentially "thermal waves" [29] – thermal disturbances that originate in the "sheath" regions penetrate into the bulk plasma. The solutions for $T_e^{(1)}$ can be used to construct the electric fields using eqn. (10), and thereby an approximate expression can be found for the time averaged power delivered to the electrons

$$P \approx \frac{J_0^2 x_0}{e^2 n_0} \left[\frac{5 k_B T_0 \sinh(2L/x_0)}{32 \bar{\kappa}_e (1 + \beta^2)} + m_e \bar{\nu}_e \sinh(L/x_0) \right], \tag{13}$$

where the first term represents the non-Ohmic heating and the dimensionless parameter $\beta = 3\omega_{rf} x_0^2 / 8 \bar{D}_e$ measures the importance of thermal conduction effects. This expression illustrates only certain aspects of the relevant scaling relations that apply to real discharges, because the time independent parts of the spatial distributions are assumed fixed and independent of *e.g.* pressure, but it is notable that the collisionless term is small in the limits $\bar{D}_e \to 0$ and $\bar{D}_e \to \infty$, and, if $\bar{D}_e$ is given by the classical expression mentioned above, these correspond to the high and low pressure limits respectively. However, in the low pressure limit the classical expression is not appropriate because there comes a point where the free diffusion rate becomes transit time limited, so that the diffusion coefficient does not increase indefinitely but is cut off, with an upper limit given by

$$D_e^{(max)} \sim v_{th} \Lambda, \tag{14}$$

where v_{th} is the electron thermal speed and $\Lambda = L/\pi$ is the free diffusion length. This truncation of the thermal conductivity accounts for the presence of large temperature gradients in the low pressure limit of the bounded model, the absence of which is one of the more striking differences between particle and fluid models of low pressure capacitive discharges. These gradients also appear in the periodic model. Fig. 11 isolates the temperature perturbations. The analytic model is in reasonable agreement with the kinetic simulation, as figs. 12 and 13 show. Since n_0, T_0, x_0 and x_1 are parameters in the analytic model, there are just chosen to fit in these comparisons, which therefore test only the computation of $T_e^{(1)}$ and the total heating. This model is consistent with

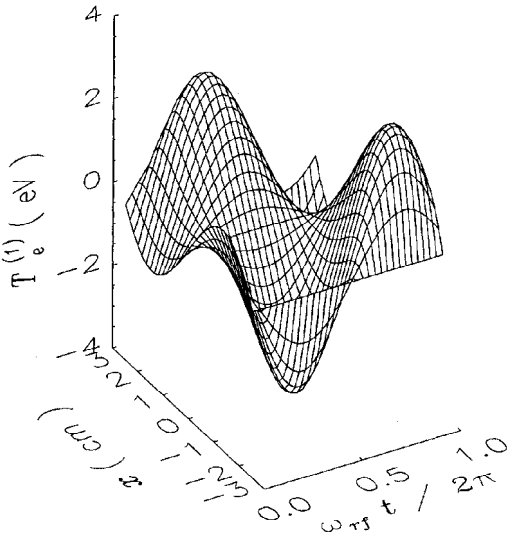

Figure 11. The time varying part of the temperature, $T_e^{(1)}$, for one period of the radio frequency.. The conditions expressed in terms of the parameters of the analytic model are $n_0 = 6 \times 10^8$ cm^{-3}, $J_0 = 10$ mA cm^{-2}, $T_0 = 3$ eV, $x_0 = 0.8$ cm, $x_1 = 0.9$ cm, $\omega_{rf} = 2\pi \times 13.56$ MHz, $\nu_e = 60$ MHz, and $L = 2.5$ cm. The origin of phase for the current is at $t = 0$.

the interpretation of the negative heating effect in the bulk plasma as an acoustic effect by Surendra and Graves [30], the association of the non-Ohmic heating with the pressure term in the fluid equations given by Surendra and Dalvie [28], the connexion between the collisionless heating and the near-sheath bulk plasma field established by Surendra and Vender [31], and the interpretation of Landau damping as an acoustic effect by Hammett and Perkins [27].

CONCLUDING REMARKS

The aim of this chapter has been to show that the "hard wall" approximation is not an adequate description of the collisionless electron heating found in low-pressure capacitive discharges. Rather, we have suggested that this heating should be associated with the inhomogeneous fields in the quasi-neutral plasma, and understood as a transit-time effect at the particle level, or as an acoustic effect in fluid terms. This is consistent with the outcome of other recent simulation-based studies [28, 31]. It is therefore difficult to see how the heating effect can be quantitatively described without a self-consistent description of the fields inside the plasma. A corollary is that it ought to be possible to construct fluid equations that include the collisionless heating component. These would be kinetic or Landau fluid equations [27], which connect Landau damping with the heat conduction term in the fluid equations. Evidently this view of the collisionless heating process connects with the main body of plasma kinetic theory, indeed with the very first work on plasma kinetic theory: Landau was the first to discuss the response of a plasma in the inhomogenous field near a boundary [32, 33].

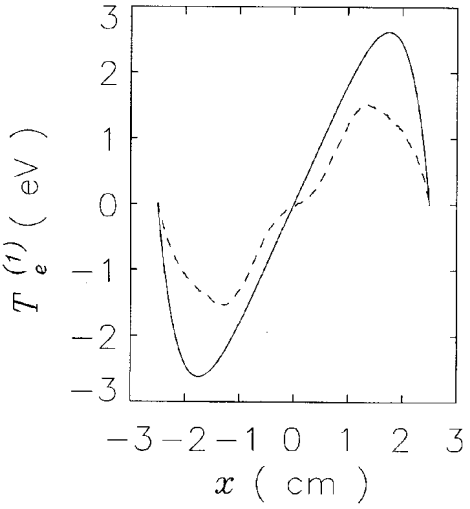

Figure 12. Comparison of the amplitude of $T_e^{(1)}$ from the analytic model (solid line) with the particle simulation result (dashed line). Conditions as in fig. 11.

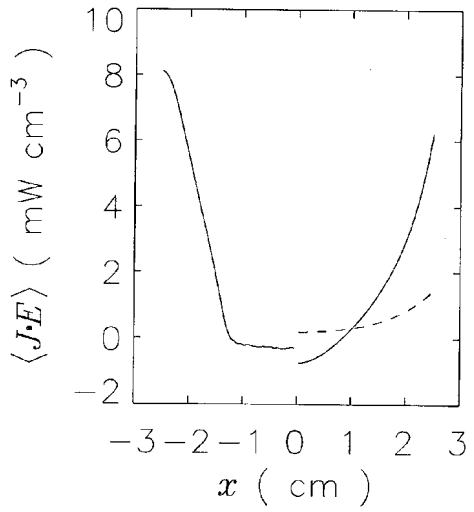

Figure 13. Comparison of the time averaged heating from the analytic model (right half the figure) with the particle simulation result (left half of the figure). The dashed line in the right half of the figure is the Ohmic part of the heating from the analytic model. Conditions as in fig. 11.

REFERENCES

1. M. A. Lieberman and A. J. Lichtenberg. *Principles of Plasma Discharges and Materials Processing.* Wiley, New York, 1994.
2. Y. P. Raizer. *Gas Discharge Physics.* Springer-Verlag, Berlin, 1991.
3. Y. P. Raizer, M. N. Shneider, and N. A. Yatsenko. *Radio-frequency capacitive discharges.* CRC Press, Boca Raton, 1995.
4. V. A. Godyak. *Soviet Radio Frequency Discharge Research.* Delphic Associates, Inc., Falls Church, VA, 1986.
5. D. B. Graves. Plasma processing. *IEEE Trans. Plasma Sci.,* 22(1):31–42, February 1994.
6. O. A. Popov and V. A. Godyak. Power dissipated in low-pressure radio-frequency discharge plasmas. *J. Appl. Phys.,* 57(1):53–58, January 1985.
7. V. A. Godyak and R. B. Piejak. Abnormally low electron temperature and heating-mode transition in a low-pressure rf discharge at 13.56 MHz. *Phys. Rev. Lett.,* 65(8):996–999, August 1990.
8. V. A. Godyak, R. B. Piejak, and B. M. Alexandrovich. Measurements of electron energy distribution in low-pressure rf discharges. *Plasma Sources Sci. Technol.,* 1(1):36–58, March 1992.
9. M. A. Lieberman. Analytical solution for capacitive rf sheath. *IEEE Trans. Plasma Sci.,* 16(6):638–644, December 1988.
10. I. D. Kaganovich and L. D. Tsendin. Low-pressure rf discharge in the free-flight regime. *IEEE Trans. Plasma Sci.,* 20(2):86–92, April 1992.
11. I. D. Kaganovich, V. I. Kolobov, and L. D. Tsendin. Stochastic electron heating in bounded radio-frequency plasmas. *Appl. Phys. Lett.,* 69(25), December 1996.
12. M. M. Turner. Pressure heating of electrons in capacitively-coupled rf discharges. *Phys. Rev. Lett.,* 75(7):1312–1315, August 1995.
13. M. M. Turner, D. A. W. Hutchinson, R. A. Doyle, and M. B. Hopkins. Heating mode transition induced by a magnetic field in a capacitive rf discharge. *Phys. Rev. Lett.,* 76(12):2069–2072, March 1996.
14. C. K. Birdsall and A. B. Langdon. *Plasma Physics via Computer Simulation.* Adam Hilger, Bristol, 1991.
15. R. W. Hackney and J. W. Eastwood. *Computer Simulation Using Particles.* Adam Hilger, Bristol, 1988.
16. C. K. Birdsall. Particle-in-cell charged-particle simulations, plus Monte Carlo collisions with neutral atoms, PIC-MCC. *IEEE Trans. Plasma Sci.,* 19(2):65–85, April 1991.
17. V. Vahedi and M. Surendra. A Monte Carlo collision model for the particle-in-cell method: applications to argon and oxygen discharges. *Comp. Phys. Comm.,* 87:178–198, 1995.
18. J. L. Pack, R. E. Voshall, A. V. Phelps, and L. E. Kline. Longitudinal electron diffusion coefficients in gases: Noble gases. *J. Appl. Phys.,* 71(11):5363–5371, June 1992.
19. K. Tachibana. Excitation of the $1s_5$, $1s_4$, $1s_3$, and $1s_2$ levels of argon by low-energy electrons. *Phy. Rev. A,* 34(2):1007–1015, August 1986.
20. A. V. Phelps. Cross sections and swarm coefficients for nitrogen ions and neutrals in N_2 and argon ions and neutrals in Ar for energies from 0.1 eV to 10 keV. *J. Chem. Phys. Ref. Data,* 20(3):557–573, 1991.
21. D. Vender and R. W. Boswell. Numerical modeling of low-pressure RF plasmas. *IEEE Trans. Plasma Sci.,* 18(4):725–732, August 1990.
22. B. E. Cherrington. *Gaseous Electronics and Gas Lasers.* Pergamon Press, Oxford, 1979.
23. G. G. Lister, Y.-M. Li, and V. A. Godyak. Electrical conductivity in high-frequency plasmas. *J. Appl. Phys.,* 79(12):8993–8997, June 1996.
24, V. Vahedi, C. K. Birdsall, M. A. Lieberman, G. DiPeso, and T. D. Rognlien Capacitive RF discharges modelled by particle-in-cell Monte Carlo simulation. II. Comparison with laboratory measurements of electron energy distribution functions. *Plasma Sources Sci. Technol.,* 2:273–278, 1993.
25. V. A. Godyak and R. B. Piejak. Paradoxical spatial distribution of the electron temperature in a low pressure rf discharge. *Appl. Phys. Lett.,* 63(23):3137–3139, December 1993.
26. J. M. Berger, W. A. Newcomb, J. M. Dawson, E. A. Frieman, R. M. Kulsrud, and A. Lenard. Heating of a confined plasma by oscillating electromagnetic fields. *Phys. Fluids,* 1(4):301–307, July-August 1958.
27. G. W. Hammett and F. W. Perkins. Fluid moment models for Landau damping with application to the ion-temperature-gradient instability. *Phys. Rev. Lett.,* 64(25):3019–3022, June 1990.

28. M. Surendra and M. Dalvie. Moment analysis of rf parallel-plate-discharge simulations using the particle-in-cell with monte carlo collisions technique. *Phy. Rev. E,* 48(5):3914–3924, November 1993.
29. L. D. Landau and E. M. Lifshitz. *Fluid Mechanics*. Pergamon Press, Oxford, 1978.
30. M. Surendra and D. B. Graves. Electron accoustic waves in capacitively coupled, low-pressure rf glow discharges. *Phys. Rev. Lett.,* 66(11):1469–1472, November 1991.
31. M. Surendra and D. Vender. Collisionless electron heating by radio-frequency plasma sheaths. *Appl. Phys. Lett.,* 65(2):153–155, July 1994.
32. L. D. Landau. On the vibrations of the electronic plasma. *J. Phys.,* 10(1), 1946.
33. A. F. Alexandrov, L. S. Bogdankevich, and A. A. Rukhadze. *Priciples of Plasma Electrodynamics.* Springer-Verlag, Berlin, 1984.

MODELING AND DIAGNOSTICS OF LOW PRESSURE INDUCTIVELY COUPLED PLASMAS

Uwe Kortshagen

University of Minnesota
Dept. of Mechanical Engineering
111 Church Street S.E.
Minneapolis, MN 55455, U.S.A.

INTRODUCTION

The new generation of plasma etching tools used in semiconductor processing is based on low-pressure high-density plasma tools. Different concepts have been developed such as electron cyclotron resonance discharges,[1,2] plasmas produced by helicon waves[3, 4, 5] or surface waves, and inductively coupled plasmas (ICP).[6, 7] Advantages of these low-pressure high-density tools are high plasma densities at simultaneously low controllable ion energies.

The large scale uniformity of the plasma is an issue of increasing importance. Future plasma tools have to provide a plasma density uniform to within a few percent over areas of 300 mm or 400 mm in diameter. Even larger uniform plasmas are needed for the processing of flat panel displays. The design of such plasma tools is still mostly performed empirically. However, plasma models are approaching a state, where they can be considered valuable design tools.

The necessity of using kinetic plasma models for low pressure discharges has been widely recognized. A number of approaches have been developed to attack this problem such as Monte-Carlo techniques,[8, 9] the particle in cell with Monte Carlo collision method,[10, 11] and the convected scheme method.[12, 13] However, these methods are computationally very expensive and they largely contribute to the overall computation time of kinetic models. Hence, since kinetic models were frequently considered to be too slow for engineering design studies, also fluid models have been applied to low-pressure high-density discharges. However, a number of experimental results indicate that fluid models may be inappropriate to describe low-pressure plasmas. A main criticism of fluid models is the inherent pronounced coupling of energy input and energy dissipation, i.e., heating in the RF electric field and energy loss in excitation and ionization. Experiments have shown that under low pressure conditions a strong spatial decoupling of these mechanisms can occur exemplified by the observation of maxima in the light emission on the axis of ICP's, where the electric field strength is close to zero.[14] Such effects and others discussed in the further course of this paper can be recovered correctly only from kinetic models.

In this paper we will demonstrate that a kinetic plasma description and fast computer

Electron Kinetics and Application of Glow Discharges
Edited by U. Kortshagen and L. D. Tsendin, Plenum Press, New York, 1998

modeling are not necessarily exclusive items. We will exemplify the technique of fast kinetic modeling for a low pressure ICP system. However, the strategy described in the following can easily be adapted to other plasma situations as has been demonstrated in numerous examples. One key aspect of the plasma model presented below is the use of the "Nonlocal Approximation" (NLA), which was first formulated by Bernstein and Holstein[15] and by Tsendin. [16] We will demonstrate the applicability and accuracy of models based on this approximation by a number of comparisons to experimental results. At the end of this paper, we will also point out some of the shortcomings of the classical NLA and discuss ways to overcome these problems.

The paper is organized as follows: In the next section we give a brief outline of the kinetic plasma model for the low-pressure ICP based on the classical NLA. Then we compare results of this model with experimental results. In the subsequent section extensions of the classical NLA are discussed. Conclusions are presented in the last section.

THE NONLOCAL 2D-KINETIC MODEL OF THE ICP

The plasma model presented in this chapter mainly consists of three modules which are coupled in an iterative numerical scheme to achieve a self-consistent plasma description. The electron kinetics is treated in a module in which the Boltzmann equation is solved within the classical NLA. For the ions a simple fluid model is used. The model is complemented by an electromagnetic module for the determination of the RF induced electric field. We assume that the discharge considered is azimuthally symmetric which implies a spatially two-dimensional treatment.

In a model involving two space dimensions, the electron kinetics module is usually the most tedious part since in addition to the two space dimensions the energy "dimension" has to be considered, too. The assumption that the consideration of one energy dimension is sufficient to describe the electron distribution function (EDF) implies that the EDF is mostly isotropic and that the well-known two-term Legendre approximation can be used.[17] This approximation is usually well applicable in glow discharges, since in most gases the elastic electron–atom collisions are much more frequent than inelastic collisions. An additional simplification in low pressure RF discharges is that quite often the typical time for energy relaxation of the electrons is long compared to the RF period. In this case, the isotropic part of the EDF will be mainly time-independent and the "effective field approximation" can be used. [18, 19] The validity of the NLA relies on a similar argument, namely that the spatial scale of the energy relaxation of electrons in collisions and due to heating is larger than the discharge dimensions.[15, 16] This argument is most restrictive in the energy range where inelastic collisions are possible. The energy relaxation length in this range can be approximated as [16]

$$\lambda_\varepsilon = \sqrt{\lambda_m \lambda^*}, \tag{1}$$

with λ_m, the transport mean free path and λ^* the mean free path for inelastic collisions. If λ_ε is larger than the typical discharge dimension, the total energy of electrons (kinetic plus potential energy in the space charge potential $\Phi(\mathbf{r}) = \Phi(r, z)$) is an (approximate) constant of motion. The total energy ε is a suitable variable for the formulation of the kinetic equations.

Bernstein and Holstein[15] and Tsendin [16] have shown that under these conditions the isotropic main part of the EDF F_0, expressed in total energy, is spatially almost constant: $F_0(\varepsilon, \mathbf{r}) \approx F_0^0(\varepsilon) + F_0^1(\varepsilon, \mathbf{r})$, with $|F_0^0| \gg |F_0^1|$. This spatial uniformity of the EDF as a function of total energy has been demonstrated in a number of theoretical [20, 21, 22] and experimental investigations.[23, 24, 25, 26] Furthermore, the authors demonstrated that the spatially constant main part of the EDF $F_0^0(\varepsilon)$ can be obtained from a spatially averaged kinetic

equation. For our particular case, this equation reads:

$$-\frac{\partial}{\partial\varepsilon}\left(\overline{\frac{v^3}{3\nu_m}E_{eff}^2}\frac{\partial F_0^0}{\partial\varepsilon}\right)=\overline{vC_0(F_0^0)}+\overline{vC_{0,wall}(F_0^0)}, \tag{2}$$

where $\varepsilon = m v^2/2e - \Phi(\mathbf{r})$ is the total electron energy expressed in volt, v is the electron velocity, ν_m is the momentum transfer collision frequency, $E_{eff} = E_0/\sqrt{2}\times\nu_m/(\nu_m^2+\omega^2)^{1/2}$ is the effective field strength for Joule electron heating by the RF field with angular frequency ω, $C_0(F_0^0)$ is the collision integral, and $C_{0,w}$ is the term accounting for the wall losses. The overlined quantities represent averages performed over the part of the volume V_{ac} which can be accessed by electrons with a given total energy, i.e. for which $\varepsilon \geq -\Phi(\mathbf{r})$. The collision integral $C_0(F_0^0)$ includes elastic, inelastic, and Coulomb collisions. The inclusion of the latter is mandatory for the treatment of high-density discharges.

The elastic collision term

$$\overline{u^{1/2}C_{0,el}} = \frac{d}{d\varepsilon}\left(\overline{V}_\varepsilon F_0^{(0)}(\varepsilon)\right), \tag{3}$$

$$\overline{V}_\varepsilon = \frac{1}{V_0}\int_{V_{ac}} \kappa\, u^{3/2}(\mathbf{r})\,\nu_m(u(\mathbf{r}))\,dV, \tag{4}$$

is simplified by neglecting the recoil term, since the gas temperature is usually small compared to the electron energies of interest. The symbol V_0 represents the total volume of the discharge, $\kappa = 2m_e/M_a$ is the energy transfer coefficient for elastic collisions.

The collision term for excitation collisions is given by

$$\overline{u^{1/2}C_{0,ex}} = -\sum_k\left(\overline{u^{1/2}\nu_{ex}^k}(\varepsilon)F_0^{(0)}(\varepsilon) - \overline{u^{1/2}\nu_{ex}^k}(\varepsilon+u_k)F_0^{(0)}(\varepsilon+u_k)\right), \tag{5}$$

with

$$\overline{u^{1/2}\nu_{ex}^k}(\varepsilon) = \frac{1}{V_0}\int_{u(\mathbf{r})\geq u_k} u^{1/2}(\mathbf{r})\,\nu_{ex}^k(u(\mathbf{r}))\,dV. \tag{6}$$

The averaging is performed over the region where the k-th excitation process is possible, i.e. where the kinetic energy $u(\mathbf{r}) = \varepsilon + \Phi(\mathbf{r})$ exceeds the excitation threshold energy of the k-th process u_k. Ionization is treated like an excitation process which means that the production of low energy electrons is neglected.

The collision term for electron-electron collisions is given by a spatially averaged Fokker-Planck term:[27]

$$\overline{u^{1/2}C_{0,ee}} = \Gamma\frac{d}{d\varepsilon}\left[\overline{H}(\varepsilon)F_0^{(0)}(\varepsilon) + \frac{2}{3}\overline{G}(\varepsilon)\frac{dF_0^{(0)}(\varepsilon)}{d\varepsilon}\right], \tag{7}$$

with

$$\overline{H}(\varepsilon) = \frac{1}{V_0}\int_{V_{ac}} dV \int_0^{u(\mathbf{r})} F_0(u',\mathbf{r})u'^{1/2}\,du', \tag{8}$$

$$\overline{G}(\varepsilon) = \frac{1}{V_0}\int_{V_{ac}} dV\left(\int_0^{u(\mathbf{r})} F_0(u',\mathbf{r})u'^{3/2}\,du' + u^{3/2}(\mathbf{r})\int_{u(\mathbf{r})}^{\infty} F_0(u',\mathbf{r})du'\right), \tag{9}$$

$$\Gamma = \left(\frac{2e}{m_e}\right)^{1/2}\frac{e^2}{8\pi\varepsilon_0^2}\ln\Lambda_C. \tag{10}$$

ε_0 is the dielectric constant and In Λ_C is the Coulomb logarithm.

The escape of energetic electrons to the wall has a similar effect on the EDF as inelastic collisions. It leads to a depletion of the high energy part of the EDF. In the total energy picture, only those electrons can be lost to the wall which have a total energy higher than the potential energy at the wall. In order to reach the wall the electrons must have a sufficient amount of energy stored in the motion normal to the wall, which requires that their velocity vector is inside a loss cone with the cone axis pointing normally towards the wall. The loss cone has a solid angle of

$$\delta\Omega(\varepsilon, \mathbf{r}) = 2\pi \left(1 - \sqrt{\frac{(-\Phi_w + \Phi(\mathbf{r}))}{\varepsilon + \Phi(\mathbf{r})}}\right). \tag{11}$$

Φ_w denotes the potential at the wall, which can be space dependent for insulating walls or which is constant for conducting walls. The existence of this loss cone has recently been demonstrated by Monte Carlo simulations.[28]

The wall loss term in Eq. (2) can be written in terms of an effective wall loss frequency ν_w or in terms of a typical life-time τ of electrons with a given total energy in the discharge:

$$\overline{u^{1/2}\nu_w}(\varepsilon) \approx \frac{\varepsilon^{1/2}}{\tau}. \tag{12}$$

The life-time τ has different components. At higher pressures, when the electron motion is collisional, the time for diffusion of an electron to the plasma boundary is the main contribution. At very low pressures, when the electrons almost perform a free flight motion, their life-time in the discharge is determined by the typical free-flight time and the time to be scattered from outside the loss cone into the cone by elastic collisions. As a useful approximation, all these times may simply be added to obtain an expression which covers the entire pressure range. The typical life-time can be written as:

$$\tau = \frac{\Lambda^2}{D_e} + \frac{1}{2}\left(\frac{\Lambda + \lambda_m}{\lambda_m}\right)\frac{4\pi}{\delta\Omega}\frac{1}{\nu_m}, \tag{13}$$

with the diffusion length Λ given by $1/\Lambda^2 = \left[(2.4/R)^2 + (\pi/L)^2\right]$ and D_e the electron diffusion coefficient. A detailed derivation of this expression and a demonstration of its accuracy can be found in Ref. 21.

From the EDF of total energy $F_0^0(\varepsilon)$ one can determine the spatially resolved EDF of kinetic energy $F_0(u, \mathbf{r})$ (expressed in volts) using a "generalized Boltzmann relation":

$$F_0(u, \mathbf{r}) = F_0^0(\varepsilon = u - \Phi(\mathbf{r})). \tag{14}$$

Knowing $F_0(u, \mathbf{r})$, excitation and ionization frequencies can be computed spatially resolved.

The electron kinetics model is complemented by an ion fluid model and the wave equation for the RF electric field. The space charge potential in the plasma is found from a fluid model for the ions. For a high-density plasma the assumption of a quasineutral plasma bulk is well fulfilled. If one limits the consideration to a description of the quasineutral plasma bulk up to the sheath boundary, the solution of the Poisson equation may be avoided and be replaced by using the quasineutrality conditions $n_i = n_e = n$. For pressures of several mTorr and discharge dimensions of several tens of centimeters, the ion motion is usually dominated by collisions. Thus, assuming mobility-limited ion motion the ion momentum and continuity equation can be combined to

$$-\nabla \cdot [n(\mathbf{r}) b_i(|\nabla\Phi(\mathbf{r})|)\nabla\Phi(\mathbf{r})] = n(\mathbf{r})\nu_i(\mathbf{r}), \tag{15}$$

where b_i denotes the field-dependent ion mobility (cf. Ref. 23) and $\nu_i(\mathbf{r})$ denotes the local ionization frequency. This equation is solved subject to the boundary condition that the Bohm criterion is fulfilled at the sheath boundary $e|\nabla\Phi(\mathbf{r})|_{sb}| \cdot \lambda_i = \frac{1}{2}k_B T_{e,scr}$. Here λ_i is the ion mean free path, k_B denotes the Boltzmann constant and $T_{e,scr} = -ek_B^{-1}\left(\partial \ln F_0^0(\varepsilon)/\partial\varepsilon|_{\varepsilon=\Phi_{sb}}\right)^{-1}$ is the so called screening temperature.[29]

The RF electric field for an azimuthally symmetric ICP has only an azimuthal component, $\mathrm{E} = E_\theta \mathrm{e}_\theta$, which can be determined from the complex wave equation. Assuming a harmonic time-dependence of the electric field we get:

$$\left(\nabla^2 - \frac{\omega^2}{c^2}\right) E_\theta(\mathbf{r}) = i\omega\mu_0 \left(\sigma(\mathbf{r}) E_\theta(\mathbf{r}) + j_{coil}\right). \tag{16}$$

Here c is the vacuum speed of light, μ_0 is the vacuum permeability. The symbol j_{coil} is the coil current density and $\sigma(\mathbf{r})$ is the kinetic conductivity of the plasma.[23] The solution of this equation is strongly simplified by the assumption that the plasma is surrounded by metallic walls so that a zero boundary condition can be used.

This set of equations is closed by the normalization condition of the EDF which defines a relation between the plasma density n and the space charge potential $\Phi(\mathbf{r})$,

$$n(\Phi(\mathbf{r})) = \int_0^\infty u^{1/2} F_0(u, \mathbf{r})\, du = \int_{-\Phi(\mathbf{r})}^\infty (\varepsilon + \Phi(\mathbf{r}))^{1/2}\ F_0^0(\varepsilon)\, d\varepsilon. \tag{17}$$

The wall potential, which appears in the definition of the loss cone solid angle Eq. (11) has to be determined by additional, considerations. The restriction of the above model to the quasineutral plasma bulk eliminates the need of solving the Poisson equation. In fact, it is also possible to determine the wall potential without solution of the Poisson equation. In the simpler case that the walls are assumed to be conducting they define an equipotential surface. The. wall potential can be found from the general particle balance that the total ionization I has to be equal to the total wall loss rate W:

$$\begin{aligned} I &= \int dV \int_{u_i}^\infty \nu_i(u) F_0(u, \mathbf{r}) u^{1/2} du \\ &= W = \oint dA \int_{-\Phi_w}^\infty \frac{\delta\Omega(\varepsilon, \mathbf{r})}{4\pi} v F_0(u, \mathbf{r}) u^{1/2} du. \end{aligned} \tag{18}$$

In the slightly more complicated case of dielectric walls the constant wall potential in Eq. (18) has to be replaced by a variable potential $\Phi_w(\mathbf{r})$ which can be determined from the requirement of locally balanced electron and ion current densities to the walls. The wall loss frequency used in the kinetic equation (2) has to be replaced by an average frequency, where the average is performed over the plasma boundaries using the respective space dependent wall potential. Results of this procedure have recently been discussed in Ref. 30.

The iterative numerical scheme used to approach a self-consistent solution of this set of equations was described in great detail in Ref. 23. The use of the various approximations detailed above enables a very efficient modeling of the discharge. Typical computation times for a given set of parameters are of the order of a few minutes on Pentium class computers.

EXPERIMENTAL SET-UP

Predictions of the model presented above have been compared to numerous parameters of an ICP experiment. In the following space resolved measurements of bulk plasma parameters (EDF, plasma density and potential) as well as of particle fluxes from the plasmas will be presented. All measurements have been performed on the experiment sketched in Fig. 1.

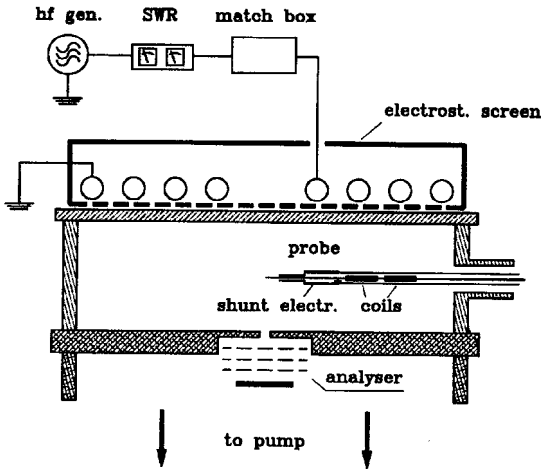

Figure 1. Experimental set–up of the inductively coupled plasma. The height of the discharge vessel is 6 cm, its diameter 15 cm. (Figure from Ref. 23.)

The discharge vessel has a height of $L = 6$ cm and a radius $R = 7.5$ cm. The side wall and the top plate of the vessel were made of glass, the bottom plate was constructed of aluminum. For some measurements presented below, also a dielectric bottom plate can be used. The RF field is induced via a spiral coil with four turns of a bent copper tube. Care was taken to avoid capacitive coupling from the coil by using a Faraday shield. We used a radially slitted copper sheet placed below the coil on the top glass window of the chamber. At the other sides the coil was screened with a solid copper cylinder. A maximum RF power of up to 400 W was coupled to the discharge via a matching network. The RF current to the coil is measured with a current transformer placed close to the induction coil. The RF voltage at the coil is measured with a capacitive voltage divider. The whole system was evacuated by a turbo molecular pump to a base pressure of less than 10^{-6} mbar. During the active plasma phase the system was operated with a constant gas flow.

The EDF measurements were performed using a pulsed probe technique.[31 32] Due to the use of the Faraday shield an RF compensation of the probe was not necessary. Initially, a shunt electrode to increase the plasma–probe capacitance and inductors self-resonant at the excitation frequency have been used.[33, 34, 32] However, in the course of the experiments these measures turned out to be unnecessary. Radial resolution of the measurements was achieved by using a linear, radially movable probe. Axially resolved measurements were performed using a bent probe which was rotated around the discharge center in a plane containing the axis.

The measurements of the IEDs were performed with a standard retarding field analyzer (see e.g. Refs. 35, 36, 37), which is mounted in the grounded bottom plate. The analyzer which is sketched in Fig. 1 consists of three plane parallel grids of 100 mesh (i.e., 100 holes per inch) with 80% transparency, which were produced by an electrogalvanic method. The grids are insulated and mounted with a distance of 7 mm between the adjacent grids. The entrance orifice, which is lying in the electrode plane, has a diameter of 100 μm. The entrance diaphragm is also 100 μm thick so that the ion energy analyzer admits ions impinging under angles up to about 45° from the normal direction. The two outer grids are put to a fixed negative potential, and the middle grid provides the variable positive, ion retarding potential. The collector, which is made of polished stainless steel, is at ground potential like the entrance

plane. The whole analyzer is differentially pumped up to pressures ranging between 10^{-6}-10^{-4} mbar to avoid charge exchange collisions in the analyzer as much as possible. The ion current is measured using a programmable low input impedance picoamperemeter which is equipped with a programmable bipolar voltage source to scan the retarding voltage.

Measurements of the particle current densities flowing to the bottom plate were performed with a probe array mounted into the plate. This array consists of 12 plane stainless steel electrodes with polished surfaces. The diameter of the probe surfaces is 5 mm. The electrodes are arranged on a radius of the discharge with a spacing of 6mm between the centers of two adjacent probes. This array allows the measurement of the total (electron plus ion) current flowing to the probes with a low impedance picoammeter. For the radially resolved measurements of ion impact energies an array of identical ion energy analyzers was used. The design is different from the gridded retarding field analyzer, since the performance of this kind of analyzer depends slightly on the mutual grid alignment. Each analyzer consists of two metal tubes in line and a Faraday cup at its bottom. These elements are separated by a 1 mm thick insulator. The entrance orifice of the analyzer has a diameter of 200 μm and a depth of 1.3 mm. The acceptance angle of the analyzer is 8 degrees with respect to the analyzer axis. It has been shown by Woodworth et al.[38] that in the range of gas pressures considered the majority of ions fall within this limit. The major part of the electrons is lost to the walls of the orifice. Each analyzer has a diameter of 3 mm and a length of 14 mm. The analyzer array is differentially pumped. The first tube of each analyzer (length 2 mm) is set to the ion retarding potential. The second tube (length 7 mm) has a constant potential of -64 V to repel the remaining plasma electrons as well as secondary electrons that can be released at the Faraday cup. More details on these analyzers can be found in Ref. 39.

COMPARISON OF EXPERIMENTAL AND THEORETICAL RESULTS

One of the main simplifications which enables the rapid kinetic discharge modeling is the use of the NLA to the solution of the Boltzmann equation. Hence, a comparison of measured and calculated EDFs may give reassurance on the validity and accuracy of this approximation. Figure 2 presents such a comparison for EDFs measured in the discharge center. The working gas is argon. A convincing quantitative agreement over about three orders of magnitude of the EDF can be observed. In particular, for the lower pressures the agreement of experiment and theory is excellent. For higher pressures some deviations occur, in particular, at low kinetic energies where the experimental EDF does not exhibit such a pronounced peak as has been predicted by the theory. However, it is well-known that the largest problems of the EDF measurements manifest close to zero kinetic energy.

In Fig. 3 the measured axial and radial variation of the EDF is depicted. The EDFs are plotted as functions of total energy. This means that the position of the steep drop of the EDFs on the left of the diagram corresponds to the zero of kinetic energy at a particular position. The shift of this zero of kinetic energy towards higher total energy reflects the increase of the potential energy (decrease of the plasma potential) towards the wall. It is obvious that the different EDFs, when plotted against total energy, almost lie on top of each other. This means that the EDF of total energy is indeed spatially constant, as it is assumed as one basic prerequisite for the validity of the NLA. The results presented in Fig. 3 thus confirm the applicability of the nonlocal approximation. Moreover, the quantitative agreement with the theoretical results (thick curves) is very convincing. These results give good reassurance on the validity of the applied kinetic approach.

Measured and calculated profiles. of the space charge potential and of the electron density are presented in Fig. 4. The electron densities have been obtained by integration of the measured EDF; the space charge potential profile is obtained from the shift of the

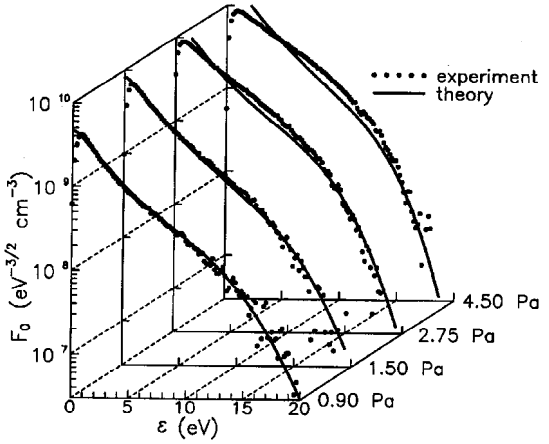

Figure 2. Comparison between measured EDFs and results of the 2D–model in the center of the discharge. (Figure from Ref. 23.)

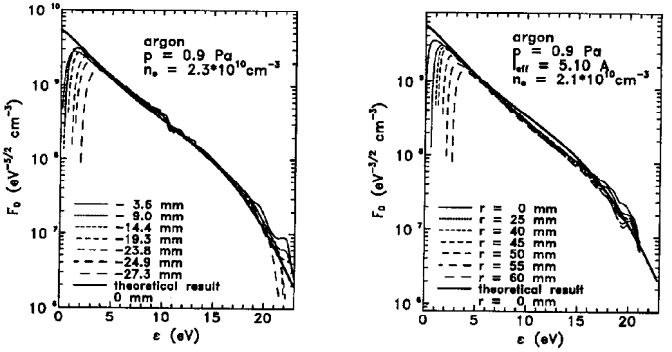

Figure 3. Axial (left) and radial (right) variation of the EDF in the ICP discharge. The thick lines represent the theoretical results. (Figure from Ref. 23.)

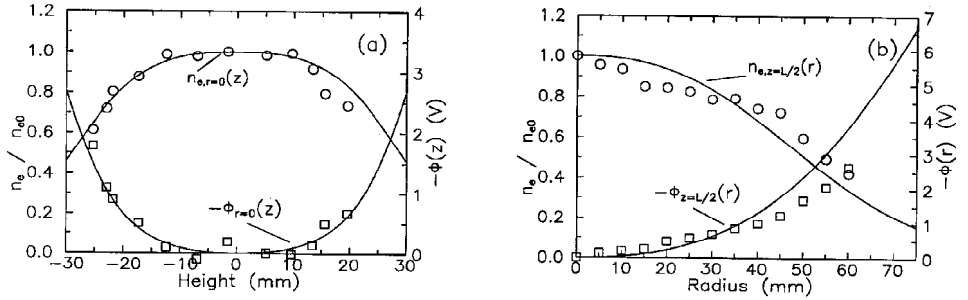

Figure 4. Profiles of the space charge potential and of the electron density for p = 0.9 Pa: (a) axial and (b) radial variation. The solid lines represent the results of the 2D–model. The circles represent the experimental electron density profile, the squares the measured potential profile. (Figure from Ref. 23.)

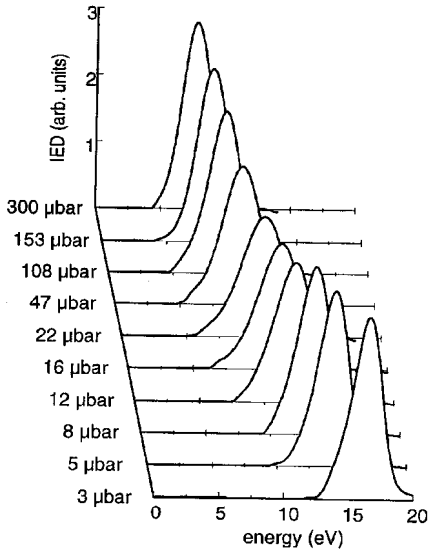

Figure 5. Measured IEDs in an argon ICP for different pressures with an electrostatic screen at a RF power of 200 W. (Figure from Ref. 41.)

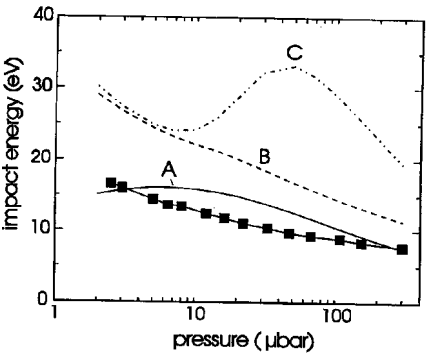

Figure 6. Comparison between measured and calculated peak energies of the IEDs in the ICP discharge. The symbols represent the measurements. Theoretical results: (A): present kinetic model, (B): assuming a Maxwellian EDF with $kT_e = 2\langle u \rangle/3$, and (C): assuming a Maxwellian EDF with the screening temperature. (Figure from Ref. 41.)

zero crossing of the measured second derivatives. Good agreement of the experimental and theoretical results is observed for the radial as well as the axial direction. It is noteworthy that the profiles of the plasma density $n(r, z)$ and of the plasma potential $\Phi(r, z)$ are maximal in the discharge center. The maximum of the energy input is clearly displaced from the center due to the geometry of our discharge and due to the skin effect of the RF field. Actually, the maximum of the RF electric field is located at the position of the coil and the RF field is close to zero on axis. The decoupling of energy input and maxima of density and potential is obvious. The same holds for the light emission. In all our experiments, the light emission was maximal on axis for sufficiently low pressures up to 9 Pa. This is a direct consequence of the nonlocal behavior of the EDF. Even though the electric field is maximal in the plasma periphery, the kinetic energy of the electrons is maximal on axis of the discharge, since the electrons are accelerated by the space charge electric field towards the axis. However, a slight shift of the maximum of the light emission, of the plasma density, and of the potential towards the coil is observed at higher pressures. As will be discussed below, this shift can be correlated to a slight deviation from the fully nonlocal behavior of the EDF.

It is necessary to stress here that all these phenomena cannot be described properly within the framework of a fluid approach, when all the electrons are characterized by the average values of the directed velocity and of the mean energy.[40] In fact, interesting effects become obvious when the fluxes of electrons with a given total energy are discussed. The growth of the accessible volume V_{ac} with increasing total energy corresponds to an outward-directed electron flux as long as ε is less than the excitation threshold energy. At higher energies, however, strongly energy reducing inelastic collisions can occur. Since these are maximum close to the chamber center, an inward–directed flux of the fast electrons with ε larger then the excitation threshold energy arises.

In the following we discuss various aspects of particle fluxes from the plasma. In Fig. 5 ion energy distribution functions measured with the gridded retarding field analyzer are shown. The ion energy distributions are bell-shaped functions with mean ion energies

ranging between 10-15 eV over a wide range of pressures. The absence of low energy ions to the left of the peak suggests that the sheath region, in which the ions experience additional acceleration after the presheath, is collisionless. The mean ion energy is thus given by the potential drop within the sheath plus the energy obtained in the presheath region, which is about half the electron temperature following the Bohm criterion. The present kinetic model allows calculation of these quantities easily. The ion fluid model yields at least a rough value for the potential at the sheath boundary. The wall potential is determined by equating total ionization and wall loss of electrons as described by Eq. (18). Thus the potential drop in the sheath can be determined without solving the Poisson equation in order to find the exact potential profile within the sheath region. Figure 6 shows a comparison of measured mean ion energies to the ion energies found from the above model. Obviously, the agreement is satisfactory. The drop of the mean ion energy can be understood qualitatively as being caused by two effects. The increasing pressure leads to a stronger potential variation and thus more negative potentials at the sheath boundary. However, the increasing pressure also causes a stronger drop of the EDF in the inelastic tail region, which leads to a smaller differential temperature $T_e = e(d \ln F_0^0/d\varepsilon)^{-1}/k_b$. The decreasing differential temperature in the tail leads to more positive wall potentials. The overall potential drop in the sheath thus decreases. For comparison, the wall potentials assuming a Maxwellian EDF are given. Curve B assumes that the temperature can be determined as 2/3 of the mean kinetic energy of the EDF at the sheath boundary, curve C assumes the differential temperature at the total energy corresponding to the potential at the plasma sheath boundary (screening temperature). Obviously, the agreement with the experimental data is poor. The reason is that the assumption of a Maxwellian EDF overestimates the population in the EDF tail, requiring a larger sheath potential drop to sufficiently reduce the electron flux.

Recently, we have also studied the radial variation of fluxes of electrons and ions to the wall of the ICP.[39, 30] It turned out that these fluxes are conceptually different for conducting and insulating walls. Figure 7 shows measurements of the total current, i.e. electron plus ion current, to a conducting bottom wall performed with the flat probe array. The mere fact that the total current is different from zero shows that electron and ion fluxes to the conducting wall are not ambipolar. Of course, a conducting wall allows such locally unbalanced electron and ion fluxes as long as the total electron and ion currents to the conducting walls of the discharge vessel are equal. The positive total current in the central part of the bottom wall indicates that the ion current exceeds the electron current. The electron current dominates in the periphery of the circular wall. This interesting effect can well be understood within the framework of the above model. It is based on the fundamentally different physical mechanisms governing the electron and the ion motion. The ions perform a convective motion driven by the space charge electric field. The shape of the space charge electric field is determined by the plasma density profile so that a strong correlation between the ion flux density and the plasma density profile exists. The ion flux density is determined by the plasma density at the sheath boundary times the Bohm velocity. Since the plasma density profiles for the aspect ratio and the coil configuration of our experiment always peak in the discharge center, the ion current density is maximal on the discharge axis and decreases in radial direction. On the contrary, the electron motion is diffusive and the total energy is a constant of motion, at least approximately. The spatial constancy of the EDF of total energy implies that everywhere within the accessible. volume the density of electrons with a given total energy is the same. In particular, since the wall potential along the conducting bottom wall is constant, the density of electrons with a total energy exceeding the wall potential is also (almost) constant along the wall. This effect leads to an electron current which is radially much more uniform than it has to be expected from the actual plasma density profile. The electron and ion current density obtained from the above model are depicted in Fig. 8.

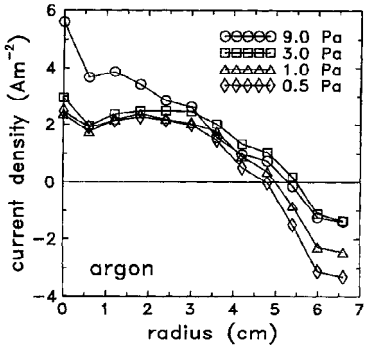

Figure 7. Measured radial profile of the total current (electron plus ion current) flowing from the plasma to a conducting bottom wall. (From Ref. 39)

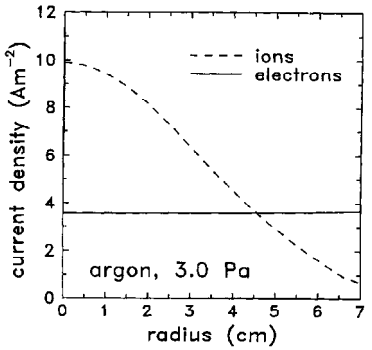

Figure 8. Calculated radial profiles of the electron (full line) and ion current density (dashed line) along a conducting bottom wall. (From Ref. 39)

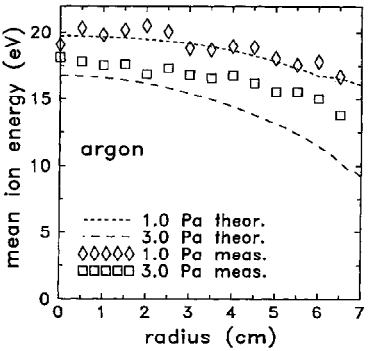

Figure 9. Comparison between theoretical and measured radial profiles of the ion impact energy along a conducting wall. (From Ref. 39)

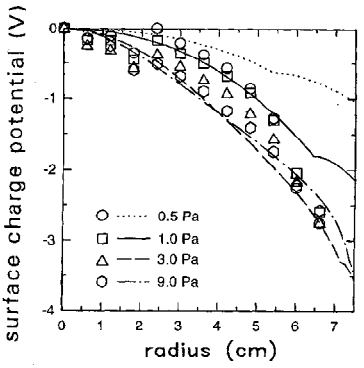

Figure 10. Surface charge profile on an insulating bottom wall. The symbols represent the measurements, the lines show the theoretical results. (From Ref. 30)

The conducting, equipotential wall also causes a radial dependence of the ion impact energies. For the aspect ratio of our discharge, we usually find a considerable drop of the plasma density in radial direction connected to a radial drop of the plasma potential (see Fig. 4). The radial drop of the potential at the sheath boundary and the radially constant wall potential at the conducting wall lead to a radially decreasing sheath potential drop. This effect is supported by the measurements shown in Fig. 9. Since both the potential at the sheath boundary and the wall potential as well as the potential drop in the presheath can be determined from the above model, the radial ion energy profile can also be obtained from the above model. The agreement between theory and measurement is reasonable.

For a nonconducting wall electron and ion current have to be balanced locally. The wall has to develop a surface charge potential profile in order to enforce locally balanced currents. The ion current density is not significantly affected by the wall potential distribution. Thus, the balancing of the currents is achieved by adjusting the electron current. The electron current has to increase on axis in order to match the ion current and it has to decrease in the periphery. Thus the wall has to charge more positively on axis and more negatively in the periphery compared to the equipotential wall. Exactly this effect is seen in the experiment as shown in Fig. 10. On the first glance, it might seem surprising that the potential profile

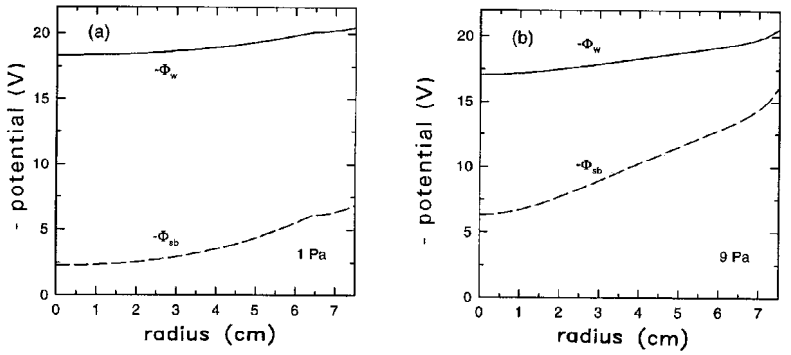

Figure 11. Radial variation of the potential at the sheath boundary Φ_{sb} and at the wall Φ_w. (Figure from Ref. 30.)

is almost independent on the pressure even though this changes from 0.5 Pa to 9.0 Pa. This slight variation is caused by the counteraction of two effects, which are demonstrated by the theoretical results in Fig. 11. On the one hand, the plasma density decreases more rapidly in the radial direction for increasing pressure, since the plasma becomes more collisional. This stronger decrease of the density is related to a stronger radial variation of the potential at the sheath boundary. At lower pressures, when the EDF is still close to a Maxwellian, a radially almost constant sheath potential drop is added to this to determine the profile of the wall potential. For higher pressures the magnitude of the sheath potential drop decreases in the radial direction. The stronger radial decrease of the potential at the sheath boundary combined with the radially decreasing sheath potential drop lead to the comparable profiles of the wall potential. This effect is explained in more detail in Ref. 30.

MODELING OF ICP IN THE REGIME WITH MODEST DEVIATIONS FROM NON-LOCALITY

Even though models based on the classical NLA have been successfully applied to a number of laboratory plasmas, such as the example given above, their actual practical use for plasma modeling of industrial discharges seems at least questionable. Many modern low pressure plasma processing tools are geared towards providing large scale uniform plasmas. This requirement, however, is principally incompatible with operation in the purely nonlocal regime. For instance, operation in the purely nonlocal regime usually implies a pronounced insensitivity of the discharge characteristics to the configuration of the electric field, since the nonlocal EDF is only determined by spatial averages. However, a certain sensitivity of the plasma to the actual field configuration is definitely desirable in order to tailor the plasma density profiles for maximum uniformity. Discharge operation in the purely nonlocal regime usually implies a plasma density maximum close to the geometric center of the discharge, as it was found in our laboratory system. Hence we conclude that modem industrial discharge are explicitly designed to operate in a regime in which the EDF shows at least slight deviations from the purely nonlocal EDF.

In this chapter we present preliminary results of an improved two-dimensional kinetic model which also applies to the regime in which the EDF is no longer a spatially uniform function of total energy. The model uses a hybrid approach to the determination of the EDF from the Boltzmann equation, which was first proposed by Kolobov and Hitchon.[42] However, to our knowledge this method has not yet been implemented in a self-consistent plasma

model.

For many gases, the energy relaxation length usually depends strongly on the energy range considered. For instance, in rare gases electrons with low kinetic energy are only capable of performing elastic collisions, while electrons at high energies are able also to perform inelastic collisions. The energy relaxation length in the "elastic" energy range thus highly exceeds the energy relaxation length in the "inelastic" range. As a consequence, the NLA may still be a good approximation to describe the "elastic" energy range but a poor approximation for the "inelastic" range. Deviations from the nonlocal behavior in the inelastic range are caused by two effects: A strong local electric field strength may locally enhance the energy diffusion of electrons. This effect leads to an elevation of the actual EDF over the level of the nonlocal EDF. Inelastic collisions lead to a local depression of the actual EDF compared to the nonlocal EDF. Exactly this hybrid behavior has been observed in experiments.[25] Thus it seems reasonable to split the solution of the Boltzmann equation into tow steps: At first, the classical NLA is applied to obtain the spatially homogeneous EDF of total energy. In a second step, a more accurate solution for the inelastic energy range is calculated by solving the complete spatially dependent kinetic equation for F_0 *only for the high energy, inelastic part of the EDF*:[42]

$$-\frac{1}{3v}\nabla_{\mathbf{r}}\cdot\left(\frac{v^3}{\nu_m}\nabla_{\mathbf{r}}F_0\right)-\frac{1}{3v}\frac{\partial}{\partial\varepsilon}\left(\frac{v^3}{\nu_m}E(\mathbf{r})^2\frac{\partial F_0}{\partial\varepsilon}\right)=C_0(F_0(\varepsilon))\ . \tag{19}$$

This equation is solved subject to the boundary conditions, which have been described by Busch and Kortshagen.[20] Only at the wall for energies higher than the wall potential we currently use the simplified boundary condition that the EDF has to be equal to the EDF in the nonlocal limit. This assumption seems quiet reasonable, since slight deviations (i.e. F_0^1) from the fully nonlocal EDF (F_0^0) vanish when averaged over the discharge cross-section. In the periphery the EDF is elevated over the level of the nonlocal EDF F_0^0. Thus the choice of using F_0^0 at the wall approximately accounts for the drop of the EDF towards the wall due to the electron wall escape. (However, variation of this boundary condition shows that the density and ionization profiles presented below are not significantly affected by this boundary condition.) Since we expect only slight deviations from the fully nonlocal EDF, we use the nonlocal EDF as a starting point for the iterative solution. Equation (19) is then solved in three dimensions — radial and axial direction as well as total energy. The solution is accelerated using a multi-grid algorithm.[43]

The hybrid approach offers a number of advantages for the numerical solution of the problem. First, the domain of integration is much simpler than in the case that the nonaveraged kinetic equation is solved for the entire energy range. The formulation of the problem in total energy leads to an irregular boundary of the domain of integration at the boundary $\varepsilon = -\Phi(\mathrm{r})$, i.e. $u(\mathbf{r}) = 0$.[20] In the hybrid approach this problem usually does not occur since the accessible volume of electrons with a total energy above the excitation threshold usually includes the entire discharge volume up to the sheath boundaries. Thus the total energy formulation can be used in a domain with only straight boundaries. Moreover, the use of the hybrid method enables the inclusion of Coulomb collisions. It is well-known that Coulomb collisions affect the EDF in the elastic range already at much lower degrees of ionization than in the inelastic range.[44] Thus the elastic energy range of the EDF in a high density plasma tool is frequently close to a Maxwellian while significant deviations from a Maxwellian persist in the tail. To include the nonlinear Coulomb operator into the multi-dimensional solution of the nonaveraged kinetic equation (19) is an extremely difficult problem, which to our knowledge has not yet been addressed. To neglect the Coulomb collisions in the elastic energy range of the EDF also appears to be inappropriate. Thus the hybrid approach offers a practical alternative, since it is easy to include Coulomb collisions in the classical NLA which is used to determine the EDF in the elastic range.

We use the hybrid approach within the framework of the above self-consistent model. The main difference is that the ionization profile is now determined from the inelastic part of the EDF calculated from Eq. (19). We use this model to study a planar inductive RF discharge with a height of 6 cm and a radius of 15 cm. We assume that the electric field is induced by a one turn coil with an inner radius of 10 cm and an outer radius of 12 cm.

Figure 12 demonstrates the transition of the density profile found with the above model. On increasing the pressure, the density profile changes from a profile with on-axis maximum to a profile with a maximum close to the induction coil. Such a transition in the density profile has recently been observed by Stittsworth and Wendt.[45] This transition is induced by a transition from nonlocal to local behavior. However, the ionization profiles shown on the right side of Fig. 12 demonstrate that even for 1.0 Pa deviations from the purely nonlocal behavior exist.

The actual transition from an on-axis density maximum to an off-axis maximum occurs even faster than shown in Fig. 12. Figure 13 demonstrates that only a 10% increase of the pressure is necessary to initiate the transition. From this rapid transition behavior observed in our model we conclude that the transition is enhanced by a positive feedback mechanism. We interpret this transition behavior as follows: In the completely nonlocal regime usually the maximum of the space charge potential is found close to the geometric center of the discharge. This implies that in the nonlocal regime the maximum of the electron density, of the optical emission, and of the ionization rate are also found at the same position, even if the heating electric field is close to zero at this position. The physical reason is that electrons gain energy in the heating electric field and redistribute it across the discharge. However, in approaching the maximum of the potential their kinetic energy increases at the expense of their potential energy, since their total energy is constant. Since the kinetic energy is relevant for ionization processes the ionization rate is maximum at the maximum of the potential. If the pressure is increased, the high energy part of the EDF starts to deviate from the completely nonlocal behavior. In particular it is elevated in regions of high electric field strength which leads to a local increase of ionization as compared to the nonlocal limit. As long as this increase is slight, the potential maximum remains in the discharge center and electrons still gain kinetic energy when they approach the center. However, if the off-center ionization increases such that the maximum of the potential starts to shift off center, the kinetic energy now decreases as the electrons approach the center and it increases as they approach the new off-center maximum of the potential. Thus the ionization is not only increased by the locally high electric field, but this increase is enhanced by the electron's gain of kinetic energy when they fall down the potential hill. This effect has yet to be verified experimentally. It is not clear if effects such as local gas heating, which have been neglected here might counteract this effect. However, the above picture also suggests that a hysteresis might exist, i.e. that the transition occurs at a higher pressure when the pressure is increased and at a lower pressure when the pressure is decreased. However, it should be stressed again that these results are only theoretical and they still have to be supported by experiments.

It should be mentioned that the observed transition cannot be obtained from a classical nonlocal plasma model. The classical NLA tends to always produce on-axis maximum density profiles. In order to reproduce the transition numerically, deviations from the nonlocal EDF have to be included. Finally, it should be mentioned that the occurrence of the transition in the density profile depends strongly on the aspect ratio of the discharge. For the aspect ratio of our experiment (7.5 cm radius and 6 cm height) and our coil configuration, we were not able to find the transition even for the highest pressures of 10 Pa. However, the maximum of the density profile was shifted towards the coil at higher pressures, which is in agreement with experimental observations. For a radius of 15 cm and a height of 5 cm with a one turn coil between 10 cm and 12 cm radius the off-center maximum of the density profile appeared

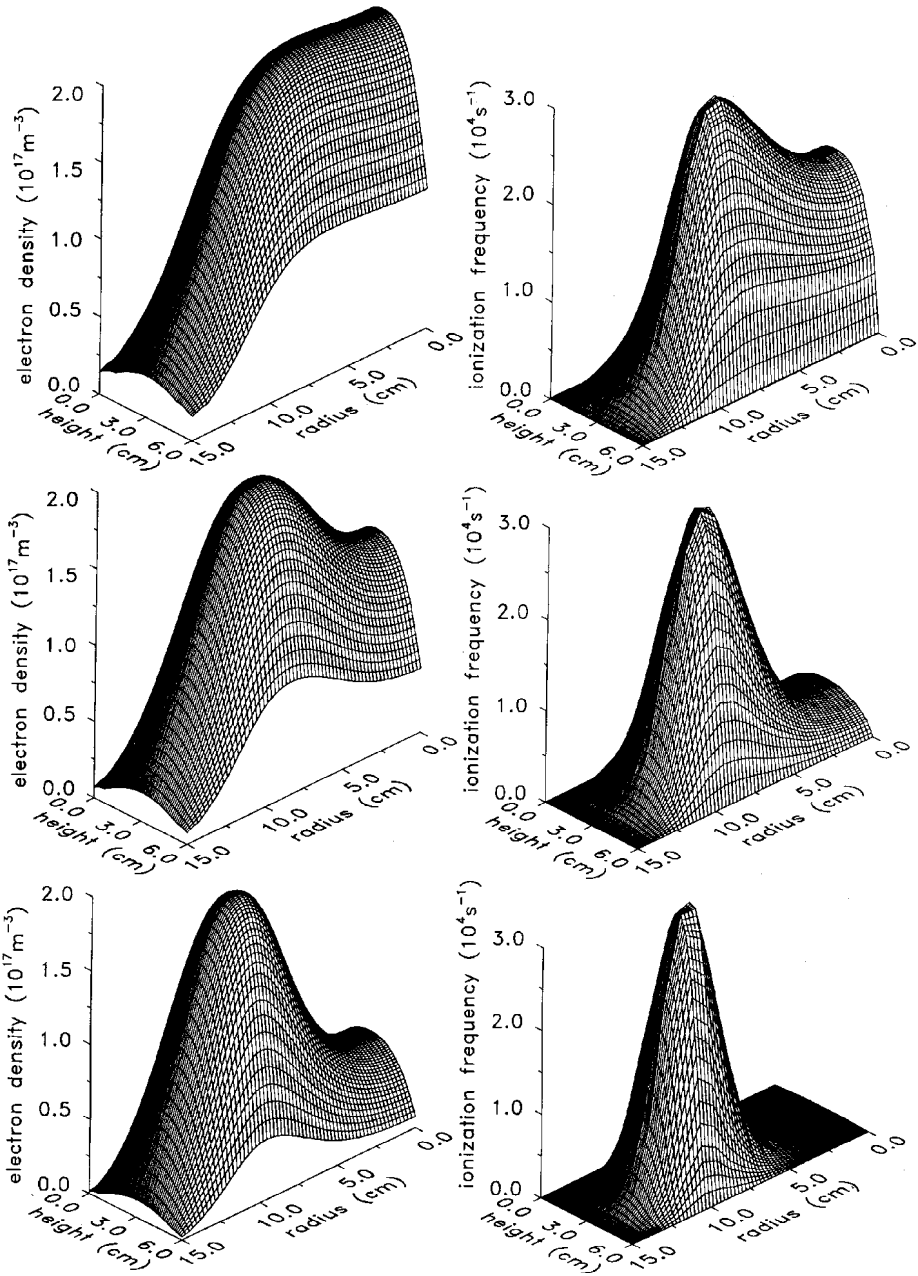

Figure 12. Electron density (left) and ionization frequency (right) for p=1.0 Pa (upper figures), p=1.5 Pa (middle figures), and p=2.0 Pa (lower figures).

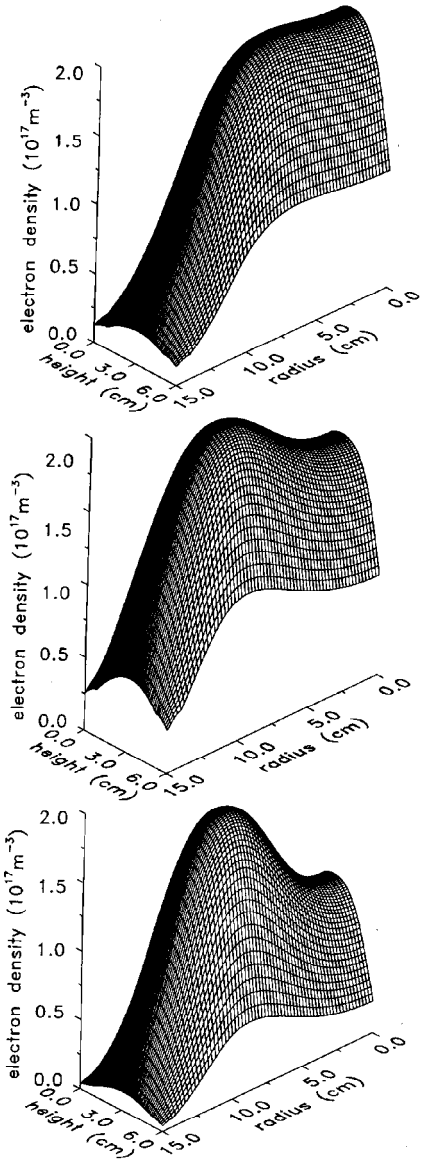

Figure 13. Transition in the density profile for increasing pressure. top: 1.1 Pa, middle: 1.2 Pa, bottom: 1.3 Pa.

already for the lowest pressure considered of 0.5 Pa.

Conclusions

In the present paper we have presented an efficient, two-dimensional kinetic model based on the nonlocal approximation to the solution of the Boltzmann equation. The computational efficiency of the model was achieved by making use of various physically motivated approximations, which are well justified for our laboratory scale plasma. The treatment of the electron kinetics was strongly simplified by making use of the nonlocal character of the EDF and of its time–independence. The problem was essentially reduced to a one-dimensional problem in total energy by the use of the spatially averaged kinetic equation. By taking advantage of the strict division of the discharge volume into the quasineutral plasma and space charge sheaths in high density discharges, we were able to avoid the complicated solution of the Poisson equation. The model allowed a self-consistent plasma description on a usual personal computer within a few minutes.

In spite of the approximations used, the good quantitative accuracy of the model was demonstrated by a number of comparisons to various experiments. The spatial uniformity of the EDF, which is used in the nonlocal model of the electron kinetics, was confirmed in the experiment. Good quantitative accuracy between measured and calculated EDFs was found. The simple model also yields a reasonable description of the ion energies of ions leaving the plasma. The radial distribution of electron and ion fluxes from the plasma to the discharge walls and the development of charging profiles could be explained reasonably with the model presented. The ion motion is driven by the space charge electric field and the ion flux is thus strongly correlated to the plasma density profile. For conducting walls the electron flux from the plasma can be strongly uncorrelated to the plasma density profile. As a consequence, nonambipolar fluxes of electrons and ions occur which are closed by wall currents in the conducting walls. A nonconducting wall enforces locally balanced electron and ion fluxes which can be only achieved by a surface charge profile on the wall.

Finally, we pointed out that in order to address technically relevant industrial discharges, new developments of efficient electron kinetic methods are required. The reason for this is the explicit design of recent high-density discharges to work in a regime with slight deviations from the fully nonlocal regime. Operation in this regime is mandatory in order to achieve large scale uniformity of the plasma. We have implemented a hybrid approach into our self-consistent model in which the elastic part of the EDF is determined using the classical nonlocal approximation and the inelastic part is calculated by the solution of complete kinetic equation formulated in two spatial dimensions and in total energy. This approach also seems to be a practical way to account for the effect of Coulomb collisions on the low energy part of the EDF. This model was successfully applied to describe the transition from on-axis maximum density profiles to off-axis maximum density profiles. This effect is due to the beginning transition from the nonlocal behavior of the EDF to the regime with a slightly local behavior of the EDF if the gas pressure is increased. Our model results indicate that this transition may occur very rapidly due to a positive feedback mechanism.

In conclusion, the hybrid approach seems to be a promising method to achieve rapid kinetic modeling for large-scale low-pressure discharges, which operate in the regime with modest deviations from the full nonlocality. The hybrid model is admittedly more computer-extensive than fully nonlocal models but it still can be solved within several minutes on fast personal computers. Finally, we want to stress again that a number of effects which we have described above are difficult to explain by fluid models such as the nonambipolar electron and ion fluxes to the conducting wall.

ACKNOWLEDGMENTS

The author is grateful to Prof. Lev D. Tsendin, Drs. M. Zethoff and I. Pukropski, and Mr. G. Mümken for their significant contributions to the work presented in this paper. A great part of the work presented in the second and third section has been performed at the Ruhr-University Bochum, Germany.

REFERENCES

1. J. Asmussen. Electron cyclotron resonance microwave discharges for etching and thin-film deposition. *J. Vac. Sci. Technol. A*, 7:883, 1989.
2. O. A. Popov. Characteristics of electron cyclotron responance plasma sources. *J. Vac. Sci. Technol. A*, 7:894, 1989.
3. R. W. Boswell and R. K. Porteous. Large volume, high density rf inductively coupled plasma. *Appl. Phys. Lett.*, 50: 1130, 1987.
4. F. F. Chen. Plasma ionization by helicon waves. *Plasma Phys. Controlled Fusion*, 33:339, 1991.
5. A. J. Perry, D. Vender, and R. W. Boswell. The application of the helicon source to plasma processing. *J. Vac. Sci. Technol. B*, 9:310, 1991.
6. J. H. Keller, J. C. Forster, and M. S. Barnes. Novel radio-frequency induction plasma processing techniques. *J. Vac. Sci. Technol. A*, 11:2487, 1993.
7. J. Hopwood. Review of inductively coupled plasmas for plasma processing. *Plasma Sources Sci. Technol.*, 1:109, 1992.
8. M. J. Kushner. Monte–Carlo simulation of electron properties in rf parallel plate capacitively coupled discharges. *J. Appl. Phys.*, 54:4958, 1983.
9. M. J. Kushner. Application of particle simulation to modeling commutation in a linear thyratron. *J. Appl. Phys.*, 61:2784, 1987.
10. M. Surendra and D. B. Graves. Particle simulations of radio–frequency glow discharges. *IEEE Trans. Plasma Sci.*, 19:144, 1991.
11. C. K. Birdsall. Particle-in-cell charged-particle simulations, plus Monte Carlo collisions with neutral atoms, PIC–MCC. *IEEE Trans. Plasma Sci.*, 19:65, 1991.
12. W. N. G. Hitchon, D. J. Koch, and J. B. Adams. An efficient scheme for convection-dominated transport. *J. of Comput. Phys.*, 83:79, 1989.
13. G. J. Parker, W. N. G. Hitchon, and J. E. Lawler. Kinetic modeling of the α to γ transition in radio frequency discharges. *Phys. Fluids B*, 5:646, 1993.
14. V. I. Kolobov, D. F. Beale, L. J. Mahoney, and A. E. Wendt. Nonlocal electron kinetics in a low–pressure inductively coupled radio-frequency discharge. *Appl. Phys. Lett.*, 65:537, 1994.
15. I. B. Bernstein and T. Holstein. Electron energy distributions in stationary discharges. *Phys. Rev.*, 94:1475, 1954.
16. L. D. Tsendin. Energy distribution of electrons in a weakly ionized current-carrying plasma with a transverse inhomogeneity. *Sov. Phys. JETP*, 39:805, 1974.
17. I. P. Shkarofsky, T. W. Johnston, and M. P. Bachynski. *The Particle Kinetics of Plasmas.* Addison–Wesley, Reading, MA, 1966.
18. L. D. Tsendin. Electron energy distribution in rf electric field. *Sov. Phys. Tech. Phys.*, 22:925, 1977.
19. R. Winkler, H. Deutsch, J. Wilhelm, and Ch. Wilke. Electron kinetics of weakly ionized hf plasmas. I. Direct treatment and Fourier expansion. *Beitr. Plasmaphys.*, 24:285, 1984.
20. C. Busch and U. Kortshagen. Numerical solution of the spatially inhomogeneous Boltzmann equation and verification of the nonlocal approach. *Phys. Rev. E*, 51:280, 1995.
21. U. Kortshagen, C. Busch, and L. D. Tsendin. On simplifying approaches to the solution of the Boltzmann equation in spatially inhomogeneous plasmas. *Plasma Sources Sci.* Technol., 5:1, 1996.
22. V. Kolobov, G. J. Parker, and W. N. G. Hitchon. Modeling of nonlocal electron kinetics in low pressure inductively coupled plasma. *Phys. Rev. E*, 53:1110, 1996.
23. U. Kortshagen, I. Pukropski, and L. D. Tsendin. Experimental investigation and fast two–dimensional self–consistent modelling of a low pressure inductively coupled rf discharge. *Phys. Rev. E*, 51:6063, 1995.
24. K. Wiesemann. Der Einfluß einer Blende auf die Elektronenverteilungsfunktion in einem Gasentladungsplasma: II. Messung der Elektronenverteilungsfunktion in der Nähe der Blende. *Ann. Phys. Leipzig*, 23:275, 1969.

25. V. A. Godyak and R. B. Piejak. Paradoxical spatial distribution of the electron temperature in a low pressure rf discharge. *Appl. Phys. Lett.*, 63:3137, 1993.
26. U. Kortshagen. Experimental evidence on the nonlocality of the electron distribution function. *Phys. Rev. E*, 49:4369, 1994.
27. H. Dreicer. Electron velocity distributions in a partially ionized gas. *Phys. Rev.*, 117:343, 1960.
28. U. Kortshagen, G. J. Parker, and J. E. Lawler. Comparison of nonlocal calculations and Monte Carlo simulations of the electron distribution function in a positive column. *Phys. Rev. E*, 54:6746, 1996.
29. K.-U. Riemann. The Bohm criterion and sheath formation. *J. Phys. D: Appl. Phys.*, 24:493, 1991.
30. U. Kortshagen. Kinetic modeling the charging of nonconducting walls in a low pressure rf inductively coupled plasma. *J. Vac. Sci. Technol. A*, in press.
31. K. F. Schoenberg. Pulsed electrostatic probes as a diagnostic for transient plasmas. *Rev. Sci. Instrum.*, 49:1377, 1978.
32. V. A. Godyak, R. B. Piejak, and B. M. Alexandrovich. Evolution of electron-energy-distribution function during rf discharge transition to the high-voltage mode. *Phys. Rev. Lett.*, 68:40, 1992.
33. A. P. Paranjpe, J. P. McVittie, and S. A. Self. A tuned Langmuir probe for measurements in rf glow discharges. *J. Appl. Phys.*, 67:6718, 1990.
34. G. Dilecce, M. Capitelli, and S. De Benedictis. Electron-energy distribution function measurements in capacitively coupled rf discharges. *J. Appl. Phys.*, 69:121, 1991.
35. J. A. Simpson. Design of retarding field energy analysers. *Rev. Sci. Instrum.*, 32:1291, 1961.
36. S. M. L. Prokopenko, J. G. Laframboise, and J. M. Goodings. Evaluation of an orifice probe for plasma diagnostics. *J. Phys. D: Appl. Phys.*, 5:2152, 1972.
37. S. M. L. Prokopenko, J. G. Laframboise, and J. M. Goodings. Orifice probe for plasma diagnostics. II. Multi-parameter analysis. *J. Phys. D: Appl. Phys.*, 7:355, 1974.
38. J. R. Woodworth, M. E. Riley, D. C. Meister, B. P. Aragon, M. S. Le, and H. H. Sawin. Ion energy and angular distributions in inductively coupled radio frequency discharges in argon. *J. Appl. Phys.*, 80:1304, 1996.
39. G. Mümken and U. Kortshagen. On the radial distribution and nonambipolarity of charged particle fluxes in a nonmagnetized planar inductively coupled plasma. *J. Appl. Phys.*, 80:6639, 1996.
40. L. D. Tsendin. Electron kinetics in non-uniform glow discharge plasmas. *Plasma Sources Sci. Technol.*, 4:200, 1995.
41. U. Kortshagen and M. Zethoff. Ion energy distribution functions in a planar inductively coupled rf discharge. *Plasma Sources Sci. Technol.*, 4:541, 1995.
42. V. Kolobov and W. N. G. Hitchon. Electron distribution function in a low–pressure inductively coupled plasma. *Phys. Rev. E*, 52:972, 1995.
43. W. Hackbusch. *Multi-Grid Methods and Applications.* Springer, Berlin, 1985.
44. U. Kortshagen and H. Schlüter. On the influence of Coulomb collisions on the electron energy distribution function in surface wave produced argon plasmas. *J. Phys. D: Appl. Phys.*, 25:644, 1992.
45. J. A. Stittsworth and A. E. Wendt. Reactor geometry and plasma uniformity in a planar inductively coupled radio frequency argon discharge. *Plasma Sources Sci. Technol.*, 5:429, 1996.

This Page Intentionally Left Blank

FLUID, KINETIC AND HYBRID SIMULATION STRATEGIES FOR MODELING CHEMICALLY COMPLEX INDUCTIVELY COUPLED PLASMAS

Ming Li,[1] Hiroyuki Date,[1,2] and David B. Graves[1]

[1]Department of Chemical Engineering,
University of California, Berkeley, California 94720
[2]Current address: College of Medical Technology,
Hokkaido University, Sapporo 060, Japan

INTRODUCTION

An important application of low pressure plasma modeling and simulation is in the design, optimization and control of plasma material processing tools for semiconductor fabrication. In this context, one must be concerned with developing physically and chemically accurate models of the dominant thin film processing characteristics. In addition, to be most useful, the simulation schemes based on the chosen model should be as computationally efficient as possible. Although plasma and surface chemistry often play dominant roles in plasma processing, these chemical process are activated and heavily influenced by discharge physical processes. Among the most important of these physical processes is electron kinetics.

Electrons play several well-known key roles in plasma processing tools, perhaps the most important of which are the various inelastic collisions with neutrals that sustain the discharge through ionization and that create chemically active free radicals that are vitally important in surface processing. The plasma spatial uniformity is often controlled by ion creation and transport. However, since electrons are responsible for ionization, the spatial profiles of power deposition into electrons and electron energy losses usually strongly affect the ultimate plasma spatial uniformity. Similar comments apply to neutral radicals. This is of the first order of importance in surface processing in which spatial uniformity is essential for proper operation of the tool.

In addition to the indirect effects listed above concerning the importance of electron kinetics in processing plasma, there are increasingly important direct effects as well. For example, in the semiconductor etching applications, the electron energy distribution function (EEDF) at the wafer surface has been identified as a key element in a certain type of charging damage [1, 2, 3]. The proposed mechanism involves electrons charging the insulating photo-resist, resulting in differential electron and positive ion fluxes to feature bottoms, and ultimately leading to charging damage to the device being processed. There is evidence suggesting that this mechanism scales with electron energy: hotter electrons exacerbate the problem. Practical questions regarding ways to minimize this problem revolve around strategies to lower electron energy near the wafer, and inevitably require understanding and control

Electron Kinetics and Application of Glow Discharges
Edited by U. Kortshagen and L. D. Tsendin, Plenum Press, New York, 1998

of electron heating and electron transport.

Relatively recently, a powerful and efficient approach to modeling electron kinetics in low pressure discharges has been reintroduced and applied to a variety of current problems of importance in applications. This method, generally referred to as the "nonlocal" model, was apparently first proposed by Bernstein and Holstein[4] in a study of electron kinetics in the positive column. Tsendin[5], and more recently, Kortshagen and co-workers [6, 7, 8, 9, 10, 11] Kolobov et al.[12], Kolobov and Hitchon [13], Kolobov and Godyak [14], and Tsendin [15] have applied this approach to various problems in gas discharge physics. Under conditions in which the electron energy relaxation length exceeds the system dimensions for all electrons, a very significant simplification of the problem becomes possible if one treats electrons in terms of total energy (kinetic plus electrostatic potential) rather than kinetic energy alone, then performs a spatial average of the spatially dependent electron Boltzmann equation. Given several relatively mild assumptions regarding electron velocity anisotropy, time independence of the isotropic part of the distribution function and the role of stochastic heating, one can obtain the EEDF through the solution of a single ordinary differential equation. This approach offers the promise of kinetic accuracy coupled with striking computational efficiency.

The dramatic increase in computational efficiency, coupled with full spatial kinetic information for electrons, makes the nonlocal approach the obvious technique of choice, but of course only when the assumptions are valid. The major issue appears to be the electron energy relaxation length compared to the system dimensions. Bush and Kortshagen[9], and Kortshagen et al.[11] determined that one can specify the regime of validity of the nonlocal method by examining the product of neutral gas number density (N, m^{-3}) and system characteristic length (R, cm). For argon, if $NR < 3 \times 10^{21}$ ($m^{-3} cm$), then the nonlocal scheme should be valid. For $NR > 3 \times 10^{23}$ ($m^{-3} cm$), a purely local approach is appropriate. The intermediate regime must be described with either the inhomogeneous Boltzmann equation,[9, 11] or with some other self-consistent electron kinetic scheme. Unfortunately, it appears that most applications of greatest interest industrially are in this intermediate regime. For discharges in use for processing microelectronics materials or for flat panel display manufacture, characteristic discharge length scales are on the order of 15 cm or more. Indeed, much discussion in industry currently concerns scaling up existing plasma tools to handle large area substrates, including 300 mm diameter wafers and flat panel display substrates that may exceed 500 mm on a side. Most etching applications generally employ gas number densities between about 3×10^{19} m^{-3} to 3×10^{21} m^{-3}(or 1-100 mtorr for room temperature neutral gas). For even the lowest length scale of R = 15 cm, this translates into $\sim 5 \times 10^{20}$ $m^{-3} cm < NR < 5 \times 10^{22}$ m^{-3} cm, significantly overlapping the range of the difficult intermediate "transition" regime between conditions such that the nonlocal scheme can be used, and conditions in which a purely local approach will be valid. It would appear that the nonlocal approach, while very powerful indeed when it can be used, has significant limitations when discharges of interest in the major industrial applications are considered.

Other approaches to this problem have been to assume some form for the electron velocity distribution function (generally, but not necessarily, Maxwell-Boltzmann), then solve an electron energy balance equation for mean electron energy.[16] Rate coefficients for various electron-neutral collisions, including the all-important inelastic processes, are then expressed in terms of the generally time- and space-dependent electron mean energy. Closely related approaches that rely on electron swarm data and parameterizations in terms of either mean electron energy or reduced electric fields, have also been used and reported in the literature. [17, 18, 19] These approaches, while well understood to be only approximations (sometimes relatively crude approximations) of electron kinetics, have nevertheless proven their value in helping explain and rationalize experimental observations, including in particular the ability to predict spatial gradients in electron rate coefficients. [18, 19] Nevertheless, concerns

persist about the accuracy of models that assume some form for the electron energy distribution function. One alternative is to use either a pure kinetic, self-consistent particle-in-cell / Monte Carlo (PIC/MC) method, or the convective scheme, or some form of hybrid scheme, combining elements of fluid and kinetic treatments for electrons.[20, 21, 22, 23, 24, 25] In this paper, we report on a hybrid fluid-kinetic scheme. A similar scheme, in which the electron kinetic information is obtained from an electron Monte Carlo model has been used by Kushner and co-workers.[2 5]

To illustrate the model, we examine a typical inductively coupled plasma chamber, with radial side coils and with a pure chlorine gas introduced into the chamber. The chosen system has a cylindrical, axisymmetric geometry with 15 cm radius and 6 cm height. The gas pressure is 20 mtorr. No etching occurs in the model, so the distribution of species, while based on a gas in common industrial use, is relative simple. Not all of the database for even this relatively simple system is known, but it serves as a good test case to compare various treatments of electron kinetics. Under the conditions chosen in this example, relatively strong spatial gradients in the EEDF are expected.

Our general strategy is to begin with a solution of conventional fluid equations, obtaining a self-consistent solution of the sustained discharge, including the spatial profiles of the neutral and charged species. Next, the electrostatic and electromagnetic fields and the neutral density profile from this solution are used to recompute the spatial profiles for all electron inelastic rate coefficients and electron transport coefficients. The fluid model is then resolved, except for the electron energy equation (since electron temperature is no longer used). This results in new profiles for all model quantities: electron and ion densities, electrostatic potential and neutral number densities. The electromagnetic field profile is recomputed (since the plasma dielectric properties have changed), then the inhomogeneous Boltzmann equation is resolved. Iterations proceed until convergence has been obtained.

In addition to comparing the solutions based on the pure fluid equations with the fluid-kinetic hybrid model, we have also used another treatment of electron kinetics. We have used a “test particle” electron Monte Carlo method. Kinetic information from the Monte Carlo electrons is obtained from averages over several rf periods. In the Monte Carlo simulations, we use the electrostatic and electromagnetic field profiles and the neutral gas density profiles from the converged hybrid model results.

MODEL DESCRIPTION

Simulation Conditions

The discharge geometry is illustrated in Fig. 1. The plasma is sustained through inductive coupling to electrons. The frequency of the applied rf current is 2 MHZ. No capacitive coupling is applied or is allowed to develop from the coils. The system is cylindrical and axisymmetric (r, z coordinates), and we assume all surfaces are conducting and grounded. The chamber has a 15 cm radius and is 6 cm in axial (z) height. Gas (Cl_2) flows into the chamber along the top walls at r = 13 cm, and is pumped out along the chamber bottom (z = 0) and from r = 10 to r = 15 cm. The results reported in this paper were obtained with a spatial grid with 45 equally spaced nodes radially and 18 equally spaced nodes axially. Pressure is maintained at the approximate desired value by adjusting the effective pumping speed. Inlet gas flow is maintained at 100 sccm. The total power deposition into the discharge was set at 1000 W and the neutral gas pressure was 20 mtorr. The fluid model was initially run to convergence, and the period-averaged electrostatic field ($E_s(r, z)$) and the magnitude of the azimuthal electromagnetic field ($E_\theta(r, z)$) are used as the input for other models. Note that it is assumed that $E_\theta(r,z,t) = E_\theta(r,z)exp(i\omega t)$. In addition, the spatial profiles of Cl and Cl_2 are taken from the converged fluid model as input to the other models. For the

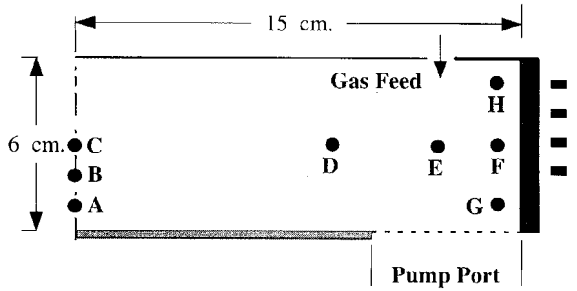

Figure 1. Sectional view of the simplified ICP reactor geometry. The coordinates (*r*, *z*) of the examined points are A(0,1.2), B(0,2.2), C(0,3.0), D(9.0,3.0), E(12.2,3.0), F(14.2,3.0), G(14.2,1.2) and H(14.2,5.2) cm.

conditions we have chosen, the gas is about 90% dissociated, and the Cl concentration profile is nearly flat spatially. Of course, the same collision cross sections are used for each model.[26]

Fluid Model Description

The fluid model we employ for the various species in the discharge has been described in detail elsewhere, so our description here will be brief.[26, 27] In essence, the fluid model assumes that each charged and neutral species (electrons, positive and negative ions, and all neutrals) can be described with a velocity distribution function assuming a (separate) shifted Maxwell-Boltzmann form. The directed component of velocity for each species is obtained from species momentum balance equations, and these incorporate terms for interspecies momentum transfer. The mean thermal energy (or "temperature") for each species comes from the solution of a species energy balance equation. For the neutral species, we generally assume that there is a single temperature characterizing these species, although this assumption can be relaxed. Finally, the species number density results from solution of a species continuity equation. Appropriate boundary conditions are developed and applied for each of the equations. Except for the provision for separate species temperature, this approach is formally identical to a conventional reacting flow model.

Equations for electrostatic and electromagnetic fields are formulated and solved. As described in detail elsewhere[26, 27] , we solve Poisson equation for the electrostatic field in the plasma, and the Helmholtz equations for the rf period-averaged electric field ("θ" or azimuthal component only) resulting from inductive coupling from the external coil. Electron heating is assumed to be resistive (stochastic effects are neglected), and the effects of the rf B-field have not been included. It is known that stochastic heating can play a significant role in inductively coupled plasmas, especially at lower pressures. However, by adjusting the rf current in the external coils until the predicted rf power deposition attains the desired value, the effects of this assumption on the plasma profiles should be minimal.

Electron Kinetics Model

We have chosen to employ the inhomogeneous Boltzmann equation model[7, 10, 11, 14]. It is assumed that electrons can be described with a two-term expansion in spherical harmonics, that the isotropic part of the distribution function is time-independent, and that inductive power deposition can be described using an ohmic model. The latter two assumptions are

also made in the fluid model.

The inputs into the model are the spatial profiles of electrostatic potential, the magnitude and frequency of the inductive electric field, and the effective cross sections for electron-neutral collisions as a function of position and electron energy. Additional details concerning this method, and a summary of the equations, boundary conditions, and numerical solution strategy are included in the Appendix.

Electron Monte Carlo Model

The electron Monte Carlo model begins with the electrostatic potential profile, the electromagnetic field profile and the concentration profiles of Cl and Cl_2. Linear interpolation is used to define the values of the electric fields at locations between nodal grid points. A group of 20,000 (or more) electrons are released at various positions throughout the plasma, with an initial position proportional to the electron density distribution from the hybrid model, and with a Maxwell-Boltzmann distribution at the temperature from the fluid model. We verified that the starting conditions had no effect whatsoever on the steady state solution by choosing many different initial conditions and observing that the final result did not depend on the choice of initial condition. The Monte Carlo technique has been described in detail elsewhere.[28] Briefly the technique uses the free flight time method, in which electrons are advanced a small fraction of mean free path at each time step, and the electron equation of motion is solved explicitly in time. Collisions are considered between electrons and neutral species (Cl and Cl_2), the spatial density profiles for which are determined by the hybrid model. All other collision types have been neglected. These include electron-electron, electron-ion Coulomb collisions, and all superelastic collisions. New electrons are created by electron-impact ionization of neutral species, and are lost on the radial and axial walls. Electrons are also lost to attachment to Cl_2 via the dissociative attachment process.

The results are obtained from sampling this population every 10 time steps (Δt = 0.01×10^{-9} s, where one period $T = 0.5 \times 10^{-6}$ s), at each of the $45 \times 18 = 810$ mesh points in the discharge domain. The electron energy distribution function, rate coefficients for all collisional processes, and the power deposited per electron in the inductive field were collected and averaged. The frequencies of electron gain and loss through collisional and wall processes, and the total number of electrons in the system were recorded through 5 periods that results were averaged.

Hybrid Model Strategy

The self-consistent hybrid model consists of a two-dimensional fluid model described elsewhere[27] for electrons, positive and negative ions, and atomic and molecular neutrals, an electromagnetic field model for the inductive electromagnetic field to solve the Maxwell equations (EM solver), and a electron kinetic model. The electron kinetic model is used to determine the space-dependent EEDF by solving the inhomogeneous Boltzmann equation (two dimensions in space r and z, one dimension for energy). A schematic of the hybrid model is shown in Fig. 2 and described as follow. (1) The self-consistent fluid model (electron continuity and energy equations; ion and neutral continuity and momentum equations; Poisson equation for the plasma potential; and the Helmholtz equations for the inductive electromagnetic field), is run to steady state. (2) The plasma potential $\phi(r, z)$, the magnitude of the inductive electric field intensity ($E_\theta\ r, z$), and the neutral density profiles $n_{neu}(r, z)$ are used to determine the EEDF by solving the inhomogeneous Boltzmann equation. After solving for the EEDF spatial profile, new values of electron mobility ($\mu_e(r, z)$), diffusivity ($D_e(r, z)$), electron flux to the reactor boundary ($\Gamma_e^{wall}(r, z)$), and all electron-neutral inelastic collision rate coefficients ($k_j(r, z)$) are obtained. (3) These new parameters are used when

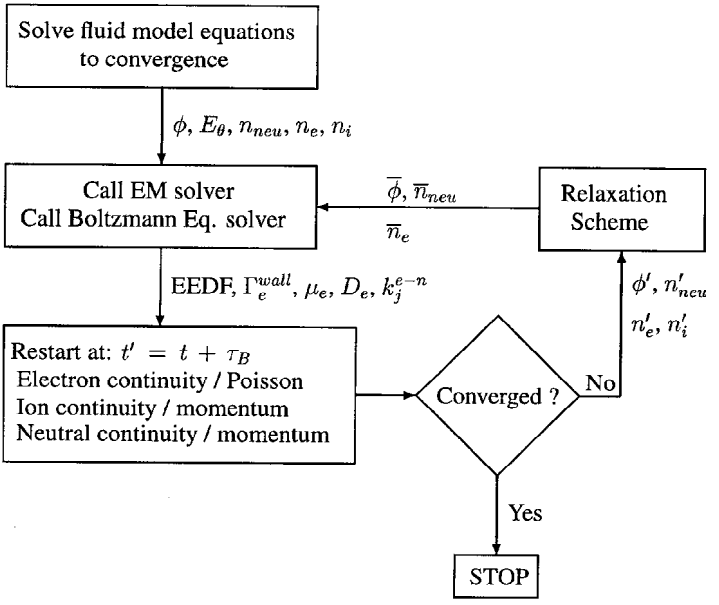

Figure 2. Scheme of the hybrid model strategy

the fluid model is restarted. At this stage, we solve all the fluid equations except the electron energy equation. (4) After some time τ_B, (typically from 0.25 to 2 μs), a convergence test is performed. (5) If the solution is not converged, we calculate the time-averaged plasma potential, neutral and electron density profiles within τ_B and use them in the Boltzmann equation solver and EM solver. Next, steps (2)-(5) are repeated until a converged solution is obtained. The convergence criteria for the simulation are: (a) The oscillations of the peak density of each charged species and the plasma potential within 100 rf cycles are smaller than 0.1%; (b) The total creation and loss of each species, including charged species and neutrals in the reactor balance to within 10^{-2}%.

Generally, the electron mobility $\mu_e(r, z)$ and electron diffusivity $D_e(r, z)$ could be obtained directly from the integration of EEDF by[29]

$$\mu_e(r,z) = \frac{1}{3}\sqrt{\frac{2e}{m_e}}\int_0^\infty \frac{d}{du}\left[\frac{u}{\sum\sigma(u)n_{neu}(r,z)}\right] u^{-1/2}F_0(r,z,u)\,du \tag{1}$$

$$D_e(r,z) = \frac{1}{3}\sqrt{\frac{2e}{m_e}}\int_0^\infty \frac{u^{1/2}}{\sum\sigma(u)n_{neu}(r,z)}F_0(r,z,u)\,du \tag{2}$$

Equation (2) is used to compute D_e, but Eq. (1) results in unacceptable noise, and we resort to the approximate expression,

$$\mu_e(r,z) = e/m_e\nu_{en}(r,z) \tag{3}$$

where $\nu_{en}(r, z)$ is the total collision frequency between electrons and neutrals. It can be obtained by the expression,

$$\nu_{en}(r,z) = \sum_j n_{neu}^j < \sigma_j v > = \sqrt{2e/m_e}\sum_j n_{neu}^j \int_{E_{th}^j}^\infty \sigma_j(u)uF_0(r,z,u)\,du \tag{4}$$

The electron flux to the wall is approximated as

$$\Gamma_e^{wall}(r,z) \;=\; \frac{n_e}{4}\sqrt{\frac{2e}{m_e}}\int_{\phi_s}^{\infty} uF_0(r,z,u)\,du \tag{5}$$

where n_e and F_0 are evaluated at the sheath edge adjacent to the particular-boundary point.

Inelastic electron-neutral rate coefficients are evaluated from,

$$k_j(r,z) \;=<\sigma_j v>=\sqrt{2e/m_e}\int_{E_{th}^j}^{\infty}\sigma_j(u)uF_0(r,z,u)\,du \tag{6}$$

The goal of the hybrid model iteration scheme is to obtain the converged, steady-state solution. The fluid equations are formulated as transient equations, and are integrated in time until the solution stops changing significantly. After the fluid equations have been integrated for time τ_B, we use a time average of the variables over that increment of time in the next call to the Boltzmann equation and EM equation solvers. This is, in effect, a relaxation scheme, and was found to improve the convergence characteristics of the solution strategy.

$$\begin{cases} \overline{\phi}(r,z,t) \;=\int_0^{\tau_B}\phi(r,z)\,dt/\tau_B \\ \overline{n_{neu}}(r,z,t) \;=\int_0^{\tau_B} n_{neu}(r,z)\,dt/\tau_B \\ \overline{n_e}(r,z,t) \;=\int_0^{\tau_B} n_e(r,z)\,dt/\tau_B \end{cases} \tag{7}$$

Variations of the peak values of the plasma potential and charged species density during the iteration for the hybrid model are shown in Fig. 3. Time $t = 0$ corresponds to a converged fluid model solution. All the peak values of the plasma potential and charged species density are unchanged after about 100 μs, and this is taken to be the steady state solution.

RESULTS AND DISCUSSION

Results

A summary of the results from the two models is shown in Figs. 4 and 5 in the form of contour plots. Profiles predicted from the fluid model are plotted on the left half of the figures and the results from the hybrid model are plotted on the right half of the figures. Power deposition profiles are illustrated in Fig. 4a. As expected with the coils at the sides of the chamber, inductive power is localized near the outer radial boundaries. In both cases, 1000W is deposited into electrons. Figure 4c is the corresponding set of plots of the electron density. There is a difference of about a factor of two in the peak density, but the shapes of the profiles from the two models are in reasonable agreement. A difference of about 2V is seen in the plasma potential profiles, but again, the general shapes of the profiles are similar. Ion profiles are shown in Fig. 5, and it can be seen that the results are similar.

The most important comparisons of the models are shown in Figs. 6 and 7. In these figures, the EEDF is plotted from the fluid model (denoted “Maxwellian”), the hybrid model (denoted “Boltzmann”) and from the electron Monte Carlo simulation (denoted “Monte Carlo”). Recall that the electron Monte Carlo simulation was run after the hybrid model was converged. Each of the individual plots corresponds to one spatial location in the plasma, as illustrated in Fig. 1. Points A, B, C, and D are farther from the coils. The Boltzmann solution and the Monte Carlo simulation results are in good agreement. Poorer statistics due to fewer simulated electrons are the cause of the scatter in the EEDF from the Monte Carlo results near the center of the chamber. Nevertheless, the generally good agreement between the Monte Carlo and Boltzmann results helps to justify the assumptions made in the Boltzmann equation formulation. The Maxwellian assumption clearly overestimates the magnitude of the tail of the EEDF. Similar comments can be made for points E-H shown in Fig. 7. Examination of the EEDF at point F and point A illustrates the significant gradient from the zone of electron heating to the center of the chamber.

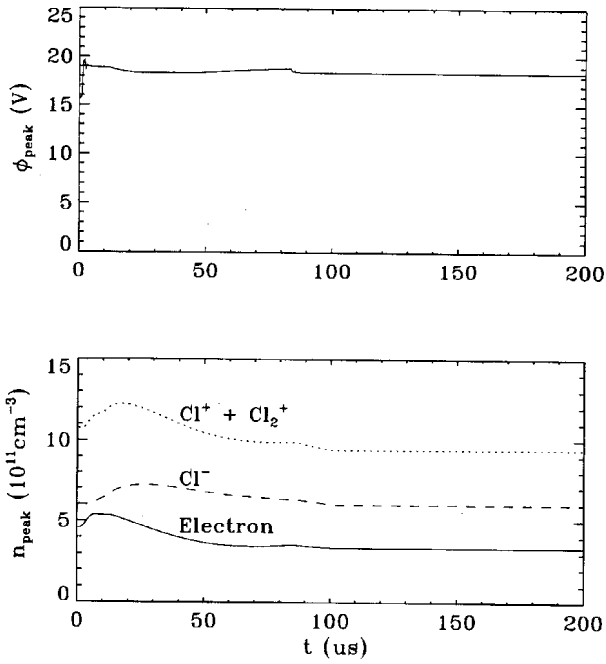

Figure 3. Peak value variations of the plasma potential and all charged species density vs. time for the hybrid model. The operating conditions are 20 mtorr, 1000 W, and T_{neu} = 0.05 *eV*.

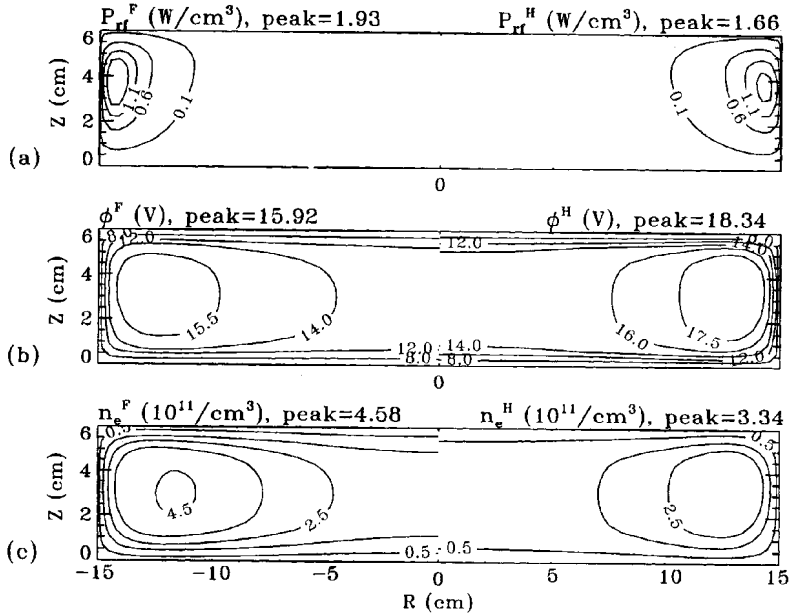

Figure 4. Comparisons the plasma profiles of (a) power deposition, (b) plasma potential, and (c) electron density from the fluid model results (left) with the hybrid model solutions (right). The operating conditions are 20 mtorr, 1000 W, and T_{neu} = 0.05 *eV*.

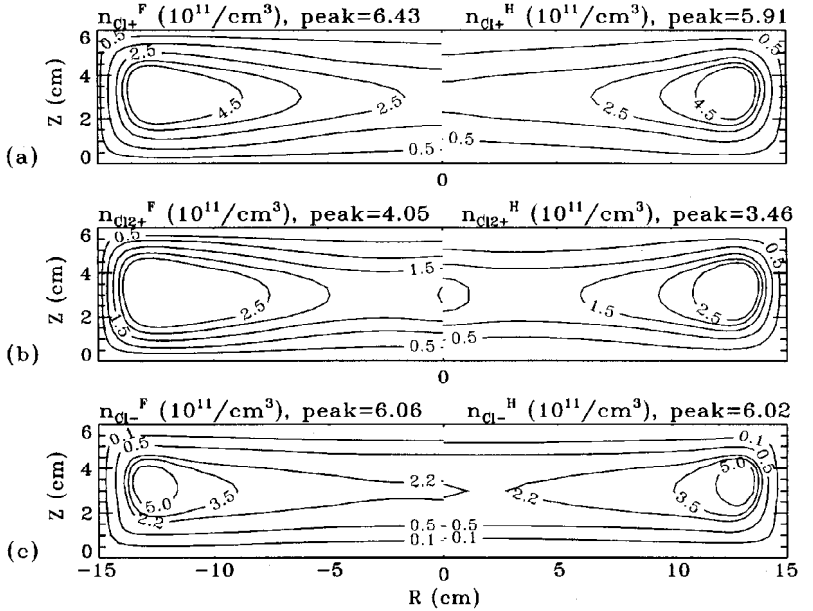

Figure 5. Comparisons the plasma profiles of (a) Cl^+ density, (b) Cl_2^+ density, and (c) Cl^- density from the fluid model results (left) with the hybrid model solutions (right). The operating conditions are the same as Fig. 4.

Discussion

Major concern with regard to a fluid model is usually directed towards the assumption that the EEDF is Maxwell-Boltzmann, or more exactly, that the distribution function can be specified in advance. There is no doubt that the EEDF is not strictly Maxwellian under essentially all conditions of practical interest. This is confirmed in the available measurements of EEDF, usually made with electric probes, as well as simulations that predict distribution functions. [21, 22, 23, 24, 30, 31] Electron-electron collisions are far too infrequent, except for the lowest energy electrons (less than a few tenths of an eV), for anything resembling a Maxwell-Boltzmann distribution to exist for electrons. Of course, collisions with the much colder neutrals are too infrequent to equilibrate electrons with these species either. Since electrons travel in the discharge virtually completely independently of each other, one might imagine that the assumption that electrons equilibrate with one another to single "temperature" at every point in time and space would be very crude approximation indeed. Given the fact that the very important electron-neutral inelastic collisions such as ionization, excitation and molecular dissociation depend on the details of the high energy tail of the EEDF, it could be thought that a fluid model for electrons would have little chance of even qualitatively describing the discharge structure.

In fact, it turns out the electron fluid model is usually not nearly as inaccurate as the foregoing reasoning would suggest, at least if one is concerned primarily with overall discharge structure, predictions of inelastic electron-neutral collision frequencies, etc. Of course, if one is explicitly interested in the EEDF itself, then clearly the Maxwell-Boltzmann assumption is completely inadequate, and recourse must be made to a kinetic description for electrons.

One factor that makes the fluid electron model reasonable accurate is that a self-consistent, self-sustained discharge solution must satisfy the ion balance. Positive ions (ignoring strongly electro-negative gases) that are created throughout the discharge must be lost at boundaries at the same rate, under steady state conditions. Positive ions are usually created by electron impact ionization of neutrals, and are lost by diffusion to the wall bounding the discharge. Both the rate of creation and the rate of wall loss of ions are controlled by electron temperature in a fluid model. Ions are accelerated to their sound speed (the Bohm velocity) at the plasma sheath boundary, and this sound speed is a function of the EEDF.[32] The ionization rate coefficient depends sensitively on electron temperature (generally exponentially), and the Bohm velocity in a fluid model varies as the square root of the electron temperature. Since the fluid description of ion transport to walls is reasonable accurate, the fluid model is constrained to create ions at the same rate, on a volume averaged basis. This constraint forces the electron temperature in a fluid model to generate an ionization rate coefficient that is consistent with the ion loss rate. This value of the electron temperature usually results in a general discharge structure that is reasonable accurate.

CONCLUDING REMARKS

We have presented an iterative hybrid scheme to self-consistently couple a fluid treatment of electron and ion transport, and neutral transport and chemistry, with the inhomogeneous Boltzmann equation for electrons. The EEDF from the Boltzmann equation is used to determine electron transport and rate coefficients and the electron flux to the walls. These quantities are used in the fluid model. The fluid model provides the electron and ion density profiles and the neutral density profiles, to be used by the Boltzmann equation. In the comparison made in this paper, a considerable difference was seen between the assumed Maxwellian EEDF in the fluid model and the results from the Boltzmann solution. In

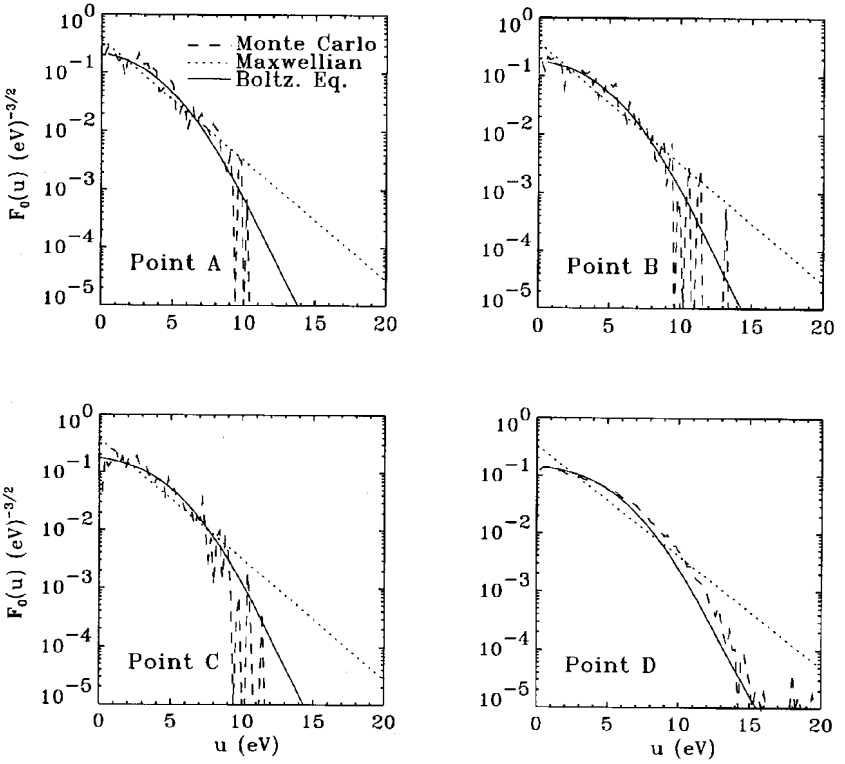

Figure 6. Comparisons of the electron energy distribution function for different electron kinetic treatment: fluid model, inhomogeneous Boltzmann equation, and Monte Carlo simulation at points A, B, C and D in the reactor. The operating conditions are the same as Fig. 4.

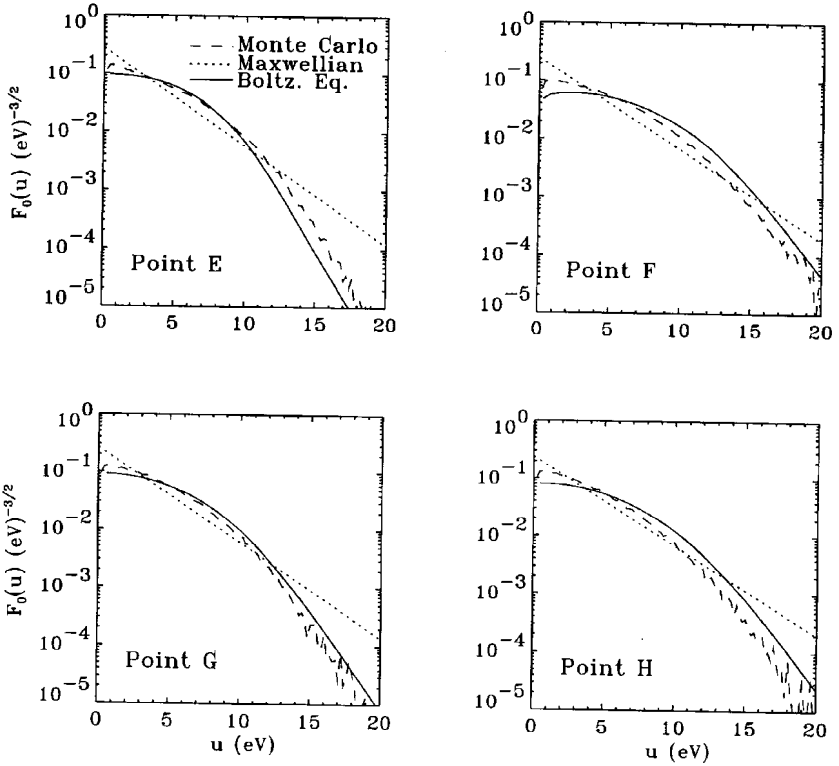

Figure 7. Comparisons of the electron energy distribution function for different electron kinetic treatment: fluid model, inhomogeneous Boltzmann equation, and Monte Carlo simulation at points E, F, G and H in the reactor. The operating conditions are the same as Fig. 4.

spite of this difference, the spatial profiles of the plasma density and plasma potential were qualitatively similar. However, we would not necessarily expect similar agreement in general.

The scheme reported here provides one way to account for the practically important spatial gradients in the EEDF, while keeping the overall computational cost reasonable for a chemically active plasma. It is not difficult to imagine a similar strategy that would include a Boltzmann equation treatment for electron kinetics as one option, and a treatment based on mean electron energy as another option. Depending upon the situation, the trade-off between accuracy and computational cost would dictate which choice is preferred. Another option would be to use an electron Monte Carlo simulation to provide kinetic information for electrons, although our preliminary results suggest that convergence is much slower using a Monte Carlo approach. In any case, a fluid treatment for ions and neutrals seems a likely choice for most simulations that include significant chemistry, and therefore some type of fluid-kinetic hybrid will be common to many simulations of low pressure plasmas use industrially.

INHOMOGENEOUS BOLTZMANN EQUATION

The inhomogeneous Boltzmann equation for the isotropic part of the EEDF have been derived and the complicated collision integrals have been discussed and documented in the literature.[33, 34, 29] At steady state, the inhomogeneous Boltzmann equation with pure electron inductive heating reads:

$$\frac{1}{3}\frac{\partial}{r\partial r}\left[Ar\frac{\partial \tilde{F}_0(r,z,\varepsilon)}{\partial r}\right] + \frac{1}{3}\frac{\partial}{\partial z}\left[A\frac{\partial \tilde{F}_0(r,z,\varepsilon)}{\partial z}\right] + \frac{1}{3}\frac{\partial}{\partial \varepsilon}\left[B\frac{\partial \tilde{F}_0(r,z,\varepsilon)}{\partial \varepsilon}\right] = -\frac{m_e}{2e}\frac{\partial}{\partial \varepsilon}\left[C\tilde{F}_0(r,z,\varepsilon)\right] + F_0(r,z,\varepsilon)\sum_k D_k - \sum_k^{k\neq att,ioniz.} \tilde{F}_0(r,z,\varepsilon+E_{th}^k)E_k - \sum_k^{ioniz.} \tilde{F}_0(r,z,\varepsilon+E_{th}^{ioniz.}+u)E_k^{ioniz.} \quad (8)$$

where

$$A = \frac{v^3}{\nu_m(r,z,u)}, \qquad B = \frac{v^3 E_\theta^2(r,z)}{2\nu_m(r,z,u)}\frac{\nu_m^2(r,z,u)}{\omega^2+\nu_m^2(r,z,u)}$$

$$C = v^3\sum_j (2m_e/m_{neu}^j)\nu_{mj}(r,z,u), \qquad D_k = v\nu_{inelastic}^k(r,z,u)$$

$$E_k = \hat{v}_k\nu_{inelastic}^k(r,z,u+E_{th}^k), \qquad E_k^{ioniz.} = \hat{v}_{ioniz.}\nu^{ioniz.}(r,z,2u+E_{th}^{ioniz.})$$

$$v = \sqrt{2eu/m_e}, \qquad \hat{v}_k = \sqrt{2e(u+E_{th}^k)/m_e}$$

$$\nu_{mj}(r,z,u) = \sigma_m(u)vn_j(r,z), \qquad \nu_{inelastic}^k(r,z,u) = \sigma_k(u)vn_k(r,z)$$

$$\hat{v}_{ioniz.} = \sqrt{2e(2u+E_{th}^{ioniz.})/m_e}$$

$$\nu_{inelastic}^k(r,z,u+E_{th}^k) = \sigma_k(u+E_{th}^k)\hat{v}_k n_k(r,z)$$

$$\nu^{k}_{ioniz.}(r, z, 2u + E^{ioniz.}_{th}) = \sigma_{ioniz.}(2u + E^{ioniz.}_{th})\hat{v}_{ioniz.} n_k(r, z)$$

The first and second term of Eq. (8) stand for the diffusion of electrons in the physical space, the third term is for the heating and diffusion of electrons in the energy space, the fourth term indicates the contribution of elastic collisions, the fifth term is for the local cooling effect of electrons (energy loss) caused by the inelastic collisions at total energy, the sixth and seventh terms are the energy gain of electrons created by the inelastic collisions at higher energy of $\varepsilon + E^{k}_{th}$ for general inelastic collisions and $\varepsilon + u + E^{ioniz.}_{th}$ for ionization. In the above equations, E^{k}_{th} is the threshold energy for the kth inelastic electron-neutral collision type. Symbols ν denotes the collision frequency (s^{-1}); and ω is the angular frequency of the applied RF field; collision cross section is $\sigma(m^2)$; n is neutral species number density (m^{-3}); r is the radial coordinate (m); z is the axial coordinate (m); e is elementary unit of charge (C); m is mass (Kg); and E_θ is inductive electric field (V/m). The subscripts 'e' denotes electrons, 'm' denotes momentum transfer, 'j' denotes the index of the chemical species, and 'k' denotes the index of inelastic collisions.

The lower boundary conditions for Eq. (8) in energy space, which is the minimum total energy with zero kinetic energy, are limited by the local plasma potential. It is hard to know the exact value of $\tilde{F}_0(r, z, \varepsilon = \Phi)$ in advance, therefore we solve the equation of $f_0(r, z, \varepsilon)$ instead of $\tilde{F}_0(r, z, \varepsilon)$ by setting $f_0(r, z, \varepsilon) = u^{1/2}\tilde{F}_0(r, z, \varepsilon)$. Then the boundary conditions for $f_0(r, z, \varepsilon)$ in energy space can be easily given by

$$\begin{cases} f_0(r, z, \varepsilon)\,|_{\varepsilon=\Phi} = 0 \\ f_0(r, z, \varepsilon)\,|_{\varepsilon=\varepsilon_{max}} = 10^{-20} \end{cases} \tag{9}$$

On the axis, due to the symmetric character, the boundary condition is

$$(\partial f_0/\partial r)\,|_{r=0} = 0 \tag{10}$$

On the other reactor walls, we take the similar boundary conditions as (10), which means the electron loss to the walls are neglected.

$$(\partial f_0/\partial r)\,|_{r=R} = 0, \qquad (\partial f_0/\partial z)\,|_{z=0,\,or\,z=h} = 0 \tag{11}$$

NUMERICAL TECHNIQUE FOR SOLVING THE INHOMOGENEOUS BOLTZMANN EQUATION

Mathematically, we use the same grid as the fluid model in physical space, and an energy interval of 0.6 eV with the maximum total energy 30 eV in energy space. A line-by-line TDMA iteration scheme which was developed by Patankar and Spalding[35, 36], was adopted to solve the inhomogeneous Boltzmann equation. For the first few calls of the Boltzmann equation solver (2-5 times), a few hundred iterations are needed to obtain convergence. After that, only a few tens or even a few iterations are needed. The line-by-line TDMA technique is described below. The inhomogeneous Boltzmann equation can be written in the form

$$\nabla \cdot [A \nabla f_0] + \frac{\partial}{\partial \varepsilon}\left[B\frac{\partial f_0}{\partial \varepsilon}\right] + S = 0 \tag{12}$$

As an example, the one-dimensional TDMA method is briefly described. The one-dimensional elliptical equation $\frac{d}{dx}\left[C\frac{dy}{dx}\right] + S = 0$ can be discretized as $a_i y_i = c_i y_{i-1} + b_i y_{i+1} + d_i$ for $1 \le i \le N$ with $c_1 = 0$ and $b_N = 0$. For the recurrence relation,

$$y_i = P_i y_{i+1} + Q_i \tag{13}$$

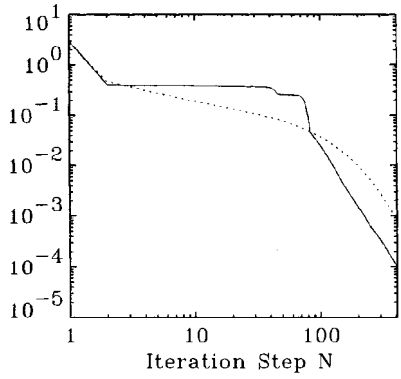

Figure 8. A typical variation of the maximum relative error (solid line) and the residual (dashed line) for the inhomogeneous Boltzmann equation solver.

we have

$$P_N = 0, \qquad y_N = Q_N \qquad if \ i = N \tag{14}$$

$$P_1 = b_1/a_1, \qquad Q_1 = d_1/a_1 \qquad if \ i = 1 \tag{15}$$

where

$$\begin{cases} P_i = b_i/(a_i - c_i P_{i-1}) \\ Q_i = (d_i + c_i P_{i-1})/(a_i - c_i P_{i-1}) \end{cases} \tag{16}$$

Then the iteration can be carried out as follows: (1) calculate P_1 and Q_1 from Eq. (15); (2) calculate P_i and Q_i ($i = 2, N$) from Eq. (16); (3) set $y_N = Q_N$ according to Eq. (14); (4) calculate y_i from $i = N - 1$ to $i = 1$ according to Eq. (13). Steps 1 and 2 are the forward process (from $i = 1$ to $i = N$) in which the boundary condition of the first point at one end comes to the calculation of P_i and Q_i. Steps 3 and 4 are the backward process (from $i = N$ to $i = 1$) in which the boundary condition information of the last point at the other end is gotten in the calculation of y_i.

For multidimensional equations, we use the line-by-line method to get the value of y in each dimension alternatively. In the inhomogeneous Boltzmann equation solver, when the maximum relative error of the EEDF in the physical and energy space between two iteration is smaller than 10^{-4}, we say the EEDF calculation converged.

A typical variation of the maximum relative error
$Max\left[|f_0^n(i,j,k) - f_0^{n-1}(i,j,k)|/|f_0^n(i,j,k)|\right]$
and the residual $\sqrt{\sum_{i,j,k}[f_0^n(i,j,k) - f_0^{n-1}(i,j,k)]^2}$ with the iteration step for the initial calculations of EEDF is shown in Fig. 8.

REFERENCES

1. K. Hashimoto, New Phenomena of Charge Damage Plasma Etching: Heavy Damage only Through Dense-line Antenna, *Jpn. J. Appl. Phys.*, 32:6109(1993).
2. K. Hashimoto, Charge Damage Caused by Electron Shading Effect, *Jpn. J. Appl. Phys.*, 33:6013(1994).

3. S. Sakaimori, T. Maruyama, N. Fujiwara, and H. Miyatake, Evaluation of Electron Shading Build Up Damage Using Metal-Nitride-Oxide-Silicon Capacitors, *Jpn. J. Appl. Phys.*, 36:2521(1997).
4. B. Bernstein and T. Holstein, Electron Energy Distribution in Stationary Discharges, *phys. Rev.*, 94:1475(1954).
5. L. D. Tsendin, *Sov. Phys. -JEPT*, 39:805(1974).
6. U. Kortshagen, Experimental Evidence of the Nonlocality of the Electron Distribution Function, *Phys. Rev. E*, 49:4369(1994).
7. U. Kortshagen, I. Pukropski, and M. Zethoff, Spatial Variation of the Electron Distribution Function in a rf Inductively Coupled Plasma: Experimental and Theoretical Study, *J. Appl. Phys.*, 74:2048(1994).
8. U. Kortshagen and L. D. Tsendin, Fast 2-Dimensional Self-Consistent Kinetic Modeling of Low Pressure Inductively Coupled RF Discharges, *Appl. Phys. Lett.*, 65:1355(1994).
9. C. Bush and U. Kortshagen, Numerical Solution of the Spatially Inhomogeneous Boltzmann Equation and Verification of the Nonlocal Approach for Argon Plasma, *Phys. Rev. E*, 51:280(1995).
10. U. Kortshagen, I. Pukropski, and L. D. Tsendin, Experimental Investigation and Fast Two-Dimensional Self-Consistent Kinetic Modeling of a Low-Pressure Inductively Coupled RF Discharge, *Phys. Rev. E*, 51:6063(1995).
11. U. Kortshagen, C. Busch, and L. D. Tsendin, On Simplifying Approaches to the Solution of the Boltzmann Equation in Spatially Inhomogeneous Plasmas, *Plasma Sources Sci. Technol.*, 5:1(1996).
12. V I. Kolobov, D. F. Beale, L. J. Mahoney, and A. E. Wendt, Nonlocal Electron Kinetics in a Low-Pressure Inductively Coupled Radio-Frequency Discharge, *Appl. Phys. Lett.*, 65:537(1994).
13. V. I. Kolobov and W. N. G. Hitchon, Electron Distribution Function in a Low-Pressure Inductively Coupled Plasma, *Phys. Rev. E*, 52:972(1995).
14. V I. Kolobov and V A. Godyak, Nonlocal Electron Kinetics in Collisional Gas Discharge Plasmas, *IEEE Trans. Plasma Sci.*, 23:503(1995).
15. L. D. Tsendin, Electron Kinetics in Non-Uniform Glow Discharge Plasmas, *Plasma Sources Sci. Technol.*, 4:200(1995).
16. D. B. Graves and K. F. Jensen, A Continuum Model of DC and RF Discharges, *IEEE Trans. Plasma Sci.*, PS-14:78(1986).
17. J.-P Boeuf, Numerical Model of RF Glow Discharges, *Phys. Rev. A*, 36:2782(1987).
18. E. Gogolides, J.-P. Nicolai, and H. H. Sawin, Comparison of Experimental Measurements and Model Predictions for Radio-Frequency Ar and SF_6 Discharges, *J. Vac. Sci. Technol. A*, 7:1001(1989).
19. T. Makabe, F. Tochikubo, and M. Nishimura, Influence of Negative Ions in rf-Glow Discharges in SiH_4 at 13.56 MHz, *Phys. Rev. A*, 42:3674(1990).
20. C. K. Birdsall, Particle-in-Cell Charged-Particle Simulations, Plus Monte Carlo Collisions with Neutral Atoms, PIC-MIC, *IEEE Trans. Plasma Sci.*, 19:65(1991).
21. M. Surendra and D. B. Graves, Electron Acoustic Waves in Capacitively Coupled, Low-Pressure rf Glow Discharges, *Phys. Rev. Lett.*, 66:1469(1991).
22. V. Vahedi, C. K. Birdsall, M. A. Lieberman, G.Dipso, and T. D. Rognlien, Capacitive RF Discharges Modeled by Particle-in-Cell Monte Carlo Simulation. II. Comparisons with Laboratory Measurements of Electron Energy Distribution Function, *Plasma Sources Sci. Technol.*, 2:273(1993).
23. M. M. Turner, Pressure Heating of Electrons in Capacitively Coupled RF Discharge, *Phys. Rev. Lett.*, 75:1312(1995).
24. M. M. Turner and M. B. Hopkins, Anomalous Sheath Heating in a Low Pressure RF Discharge in nitrogen, *Phys. Rev. Lett.*, 69:3511(1992).
25. P. L. G. Ventzek, R. J. Hoekstra, and M. J. Kushner, 2-Dimensional Modeling of High Plasma Density Inductively Coupled Sources for Materials Processing, *J. Vac. Sci. Technol. B*, 12:461(1994).
26. R. A. Stewart, P. Vitello, D. B. Graves, E. F. Jaeger, and L. A. Berry, Plasma Uniformity in High Density Inductively Coupled Plasma Tools, *Plasma Sources Sci. Technol.*, 4:36(1995).
27. J. D. Bukowski, D. B. Graves, and P. Vitello, Two-Dimensional Fluid Model of an Inductively Coupled Plasma with Comparison to Experimental Spatial Profiles, *J. Appl. Phys.*, 80:2614(1996).
28. S. Yachi, H. Date, K. Kitamori, and H. Tagashira, A Multi-Term Boltzmann Equation Analysis of Electron Swarms in Gases — the Time-of-Flight Parameters, *J. Phys. D: Appl. Phys.*, 24:573(1991).
29. V. E. Golant, A. P. Zhilinsky, and I. E. Sakharov. "Fundamentals of Plasma Physics", John Wiley and Sons, Inc., New York(1980).
30. T. J. Sommerer, W. N. G. Hitchon, and J. E. Lawler, Electron Heating Mechanism in Helium RF Glow Discharge — A Self-Consistent Kinetic Calculation, *Phys. Rev. Lett.*, 63:2361(1989).
31. V. A. Godyak and R. B. Piejak, Abnormally Low Electron Energy and Heating — Mode Transition in a Low-Pressure Argon RF Discharge at 13.56 MHz, *Phys. Rev. Lett.*, 65:996(1990).
32. M. A. Lieberman and R. A. Gottscho, Design of High Density Plasma Sources for Materials Processing, *in:* "Physics of Thin Films: Plasma Sources for Thin Film Deposition and Etching," M. Francombe and

J. Vossen ed., Academic Press, New York (1994).
33. P. Shkarofsky, T. W. Johnston, and M. P. Bachynski. “The Particle Kinetics of Plasmas”, Addison-Wesley, Reading, MA(1966).
34. T. Holstein, Energy Distribution of Electrons in High Frequency Gas Discharges, *Phys. Rew.*, 70:367(1946).
35. S. V. Patankar and D. B. Splading, A Calculation Procedure for Heat, Mass and Momentum Transfer in Three-Dimensional Parabolic Flows, *Int. J. Heat Mass Transfer*, 15:1787(1972).
36. S. V. Patankar. “Numerical Heat Transfer and Fluid Flow”, McGraw-Hill, New York (1980).

TRANSPORT AND REACTION IN INDUCTIVELY COUPLED PLASMAS FOR MICROELECTRONICS

D. J. Economou, J. Feldsien, and R. S. Wise

Plasma Processing Laboratory
Department of Chemical Engineering
University of Houston
Houston, TX 77204-4792

INTRODUCTION

Low pressure (0.1 mtorr to 10 torr), cold (gas temperature 300-500 K), weakly ionized (degree of ionization $10^{-6} - 10^{-1}$) glow discharge plasmas are used extensively in the processing of electronic materials, especially for etching and deposition of thin films [1,2]. Such plasmas also find application in surface modification (e.g., hardening, corrosion resistance), lighting, and even environmental remediation. In reactive gas plasmas, electrons are "heated" by an electric field and acquire high enough energies to decompose a flowing feedstock gas into radicals and ions. In plasma deposition, radicals adsorb on the wafer surface where they react to deposit a thin film. The film microstructure and properties (e.g., density, stress) can be influenced by energetic ion bombardment which occurs naturally on all surfaces exposed to the plasma. In plasma etching, radicals adsorb and react on the wafer to form volatile products which desorb and are pumped away by a vacuum system. Again, the surface chemistry can be strongly modified by energetic ion bombardment. Ions bombard the wafer preferentially along the vertical direction, enhancing the reaction rate and inducing anisotropy which is critical for delineating sub-half micron patterns in advanced microelectronic device manufacturing. Controlling the flux, energy distribution, and angular distribution of ions and neutrals bombarding the wafer is of paramount importance in plasma systems. Also, the uniformity of these fluxes over large area (diameter > 200 – 300 mm) wafers is critical for the success of industrial plasma processing equipment.

Up until recently, relatively high pressure (p > 50 mtorr), low plasma density ($n_e < 10^{10} cm^{-3}$) capacitively-coupled systems were used almost exclusively for achieving anisotropic etching. The drive for delineating finer features over larger diameter wafers, however, has resulted in the development of high density plasma (HDP) sources [2]. These reactors operate at low gas pressures (p < 50 mtorr) to improve uniformity and reduce contamination, and high plasma density ($n_e > 10^{11} cm^{-3}$) to deliver a high flux of ions and radicals to the wafer surface, thereby maintaining a high throughput.

Electron Kinetics and Application of Glow Discharges
Edited by U. Kortshagen and L. D. Tsendin, Plenum Press, New York, 1998

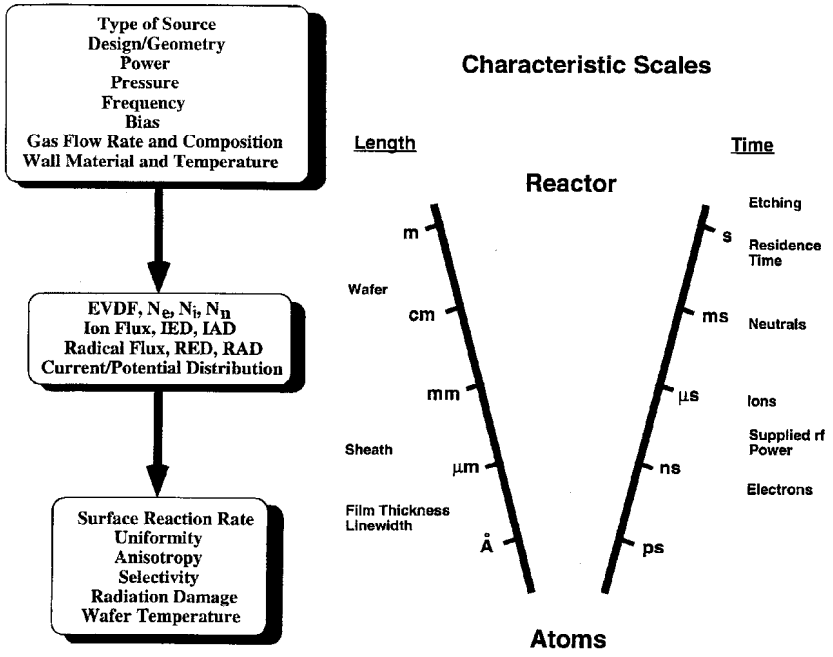

Figure 1. Inputs and outputs (left) and time-length scales (right) in plasma simulation.

Also, low pressure helps anisotropy since the ion mean free path is greater than the sheath dimensions, making ion flow to the wafer directional. There exists a variety of HDP sources including inductively coupled plasmas (ICP), electron cyclotron resonance (ECR), helicon, and helical resonator sources. Practical reactors have relatively large dimensions (10s of cm) and operate with (complex) molecular gas chemistries.

This paper provides a review of recent works on the modeling and simulation of transport and reaction in inductively coupled plasma reactors of the type used for microelectronics manufacturing. An experimentally-verified fluid simulation approach developed by the authors is used to study transport and chemistry effects in a dome-shaped plasma reactor. Multidimensional simulations are emphasized and the importance of making judicious approximations, based on the physics of the system, to reduce the complexity of the problem is stressed.

PLASMA SIMULATION

Problem Statement

The problem statement can be summarized by Figure 1, left. Given a reactor type and configuration, geometrical dimensions and materials of construction, as well as a set of operating parameters (inputs), including feedstock gas composition and flow rate, gas pressure, coil current (or power), excitation frequency, and substrate voltage (or power), determine the following key plasma properties: The electron energy distribution function, the space and time variation of electron, ion, and neutral species densities and velocities, the flux and energy distribution of ions and neutrals bombarding the

electrodes and their uniformity across the electrodes, the power distribution in the plasma, and the potential and current distribution in the system. These variables and their spatiotemporal variation provide insight into the plasma reactor behavior. If the reactor is loaded with a wafer to etch, one is in addition interested in the outputs (figures of merit) including the etch (or deposition) rate, uniformity, anisotropy (shape of microscopic features etched into the wafer), selectivity (rate of etching the film vs. the mask or underlying substrate), radiation damage, and wafer temperature. The level of detail one can obtain depends on the type of simulation used. For example, fluid simulations can't provide the species distribution functions but only averages over the distribution. One can also pose the inverse problem which is much more difficult to solve, that is: given a material to be etched and specifications on the rate, uniformity, anisotropy, and selectivity, determine the reactor configuration, dimensions, and operating parameters to achieve the task.

The problem of plasma simulation is extremely challenging owing to the vast disparity in length and time scales involved (Figure 1, right). Length scales range from atomistic, to microscopic (film thickness, linewidth), to the reactor (wafer) scale. Even if one focuses on reactor scale simulations, as is done in this paper, the presence of the extremely thin sheath in high density plasmas introduces a formidable range of length scales from 10s of μ to 10s of cm. The range of time scales is also extremely wide, from the ns response time of electrons, to 10-100s of ms of heavy species chemistry and gas residence times, to mins for the duration of etching processes.

Plasma Simulation Approaches

Glow discharge plasmas are extremely complex systems in which a plethora of interdependent parameters can influence the process, often in a subtle way. Modeling and simulation of these systems has emerged as a tool for enhancing one's intuition about the physiochemical processes occurring in the plasma, for understanding the complex spatiotemporal plasma dynamics, and for assisting in the design of new reactors or the optimization of existing ones [3]. Simulations of plasma reactors of the type used in the microelectronics industry started to appear only in the 1980s. A number of two-dimensional plasma reactor simulations were reported [4, 5] focusing on the transport and reaction of neutrals only (neutral transport and reaction models). The electron density was assumed to have a uniform or Bessel function profile, and the electron energy was not calculated as a function of space and time in the reactor. These studies did not solve the problem of neutral radical transport and reaction in a self-consistent manner. The radical source terms (by electron-impact dissociation, for example) were estimated and the conservation equations for mass, momentum, and energy transport were solved to obtain the fluid velocity profiles, neutral gas temperature and the concentration distribution of radicals; this is a standard computational fluid dynamics problem. Charged particle transport was not considered, and the effect of plasma gas composition (different than the feedstock gas composition) on the plasma properties was not accounted for.

Up until the early 1990s simulations that solved for the radio frequency (RF) plasma dynamics (so-called glow discharge models) were confined to one spatial dimension (1-D) [6, 7, 8, 9, 10, 11, 12, 13, 14, 15, 16, 17, 18, 19, 20, 21]. In addition most of these simulations did not solve for the transport and reaction of neutrals. Self-consistent RF plasma simulations which solve for the coupled effects of charged and neutral species transport have only been reported within the past several years in 1-D [16, 18, 19] and 2-D [22, 23, 24, 25, 26, 27, 28, 29] and even 3-D [30]. Multidimensional simulations are particularly useful since they can address the important issue of plasma uniformity and the

spatiotemporal plasma dynamics along both the radial and axial direction. However, most 2-D simulations still do not include neutral transport and chemistry and consider noble gases (argon and helium) [31, 32, 33, 34, 35], not reactive gas plasmas. Several 2-D and one 3-D plasma simulations, however, couple the neutral transport and chemistry with the glow discharge in a self-consistent manner [22, 23, 24, 25, 26, 27, 28, 29, 30]. In view of the above discussion, multidimensional self-consistent plasma reactor simulation is of very young age.

There are three kinds of glow discharge simulations: fluid, kinetic and hybrid. Fluid simulations use moments of the Boltzmann equation describing species density, momentum and energy conservation [3, 25, 27, 37]. They require some assumptions regarding the species distribution function to achieve closure of the equations. Kinetic simulations, including Particle-In-Cell with Monte Carlo Collisions (PIC-MCC) [38] or Direct Simulation Monte Carlo (DSMC) [39] yield the particle distribution functions as an output of the simulation. They are considered more accurate than fluid simulations at low pressures when the species mean free path is comparable to or longer than a characteristic length scale (Knudsen number Kn = λ/L) or for highly non-equilibrium situations. However, there is evidence that fluid simulations can perform well even at low pressures for which their assumptions must be scrutinized [40]. Kinetic simulations are computationally intensive as compared to fluid simulations. Hybrid simulations have been developed [16, 18, 28, 41] in an attempt to preserve the accuracy of kinetic simulations and at the same time reduce the computational burden.

When dealing with multidimensional geometries and complex chemistries, "full-blown" self-consisted plasma simulations pose a very challenging task. While "brute force" simulations (for example ones that solve the complete set of conservation equations for all particles) are feasible, they are also labor and time consuming. Judicious approximations, based on the physics of the problem, can reduce the simulation times dramatically. Examples are the space-time averaging used in the non-local approach, or the approximations used to construct rapid plasma simulation tools [41, 42, 43, 44, 45]. (see below).

The Non-Local Approach

A promising approach to calculating the electron distribution function (EDF) in low pressure plasmas is the so-called non-local approach to electron kinetics. This was proposed by Bernstein and Holstein [46], and popularized by Tsendin [47], who initially suggested this approach for the positive column of a DC discharge. Since then, the non-local approach has been applied to a variety of low pressure gas discharge systems [48]. Lately the non-local approach was applied to inductively coupled plasma (ICP) reactor simulation by several authors [41, 49, 50].

For many gas discharges, especially those in monatomic gases, the electron momentum relaxation frequency is much larger that the electron energy relaxation frequency. Under these conditions, the conventional two-term (f_0 and f_1) approximation to the distribution function can be applied, where f_0 and f_1 are the isotropic and anisotropic parts of the distribution function, respectively. Furthermore, for typical conditions, the applied excitation frequency is much larger than the electron energy relaxation frequency. It follows that the isotropic part of the distribution function is time-independent. The Boltzmann equation is then reduced to a time-invariant but space dependent equation for f_0; f_1 is recovered as a derivative of f_0. For the majority of electrons in the discharge, which are trapped by the self-forming electrostatic field, a further simplification is applicable. At low enough pressures, the energy relaxation length for these electrons is large compared to the reactor dimensions. Since electron

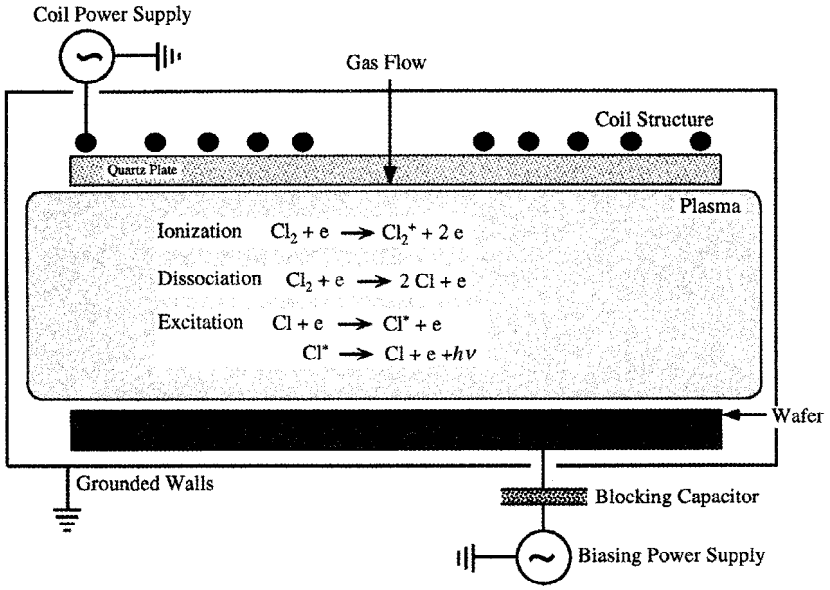

Figure 2. Schematic of an inductively coupled plasma reactor.

heating is a slow process compared to the time scale of electron spatial displacement, the total energy of the electrons (kinetic plus potential) is approximately constant in space. One can then space-average the Boltzmann equation and derive an equation for f_0 as a function of the total electron energy, that does not depend explicitly on the spatial coordinates. This is a tremendous simplification of the Boltzmann equation in multidimensional plasmas. However, the spatial dependence has to be retained for the electrons which have high enough energy to overcome the wall potential and reach the walls (free electrons), or for electrons that have an energy relaxation length smaller than the reactor dimension. For monatomic gases (e.g., argon) this includes electrons with energy above the first excitation potential of the atom.

In molecular gases (e.g., chlorine, sulfur hexafluoride, carbon tetrafluoride) the electron energy relaxation length of trapped electrons is much shorter that in atomic gases because of a plethora of relatively low threshold energy (few eV) collisions (e.g., vibrational excitations). Therefore, as the gas pressure increases, the non-local approach is expected to break down much sooner for molecular gases as compared to atomic gases. Also, for molecular gases, the traditional two-term approximation of the EDF may not be applicable because the inelastic collision cross sections are comparable to or even exceed the elastic collision cross sections.

In addition to spatial non-locality, temporal non-locality of the EDF may be important in low pressure RF plasmas. Temporal non-locality means that the EDF is not, determined by the instantaneous value of the RF field. Instead, different parts of the EDF exhibit various delays with respect to the field. The frequency ranges of interest to temporal evolution of the EDF were studied by Tsendin [79]. Numerical solutions to the time-dependent Boltzmann equation in a uniform electric field have also been performed [52, 53]. The temporal non-locality of the EDF may be important for the operating conditions specific to high density RF plasmas, for which spatial non-locality is also present.

INDUCTIVELY COUPLED PLASMA REACTORS

Inductively coupled plasma (ICP) reactors are particularly attractive because their design is relatively simpler and they are easily scalable to large diameter substrates, [2, 54, 55]. In ICPs the plasma is excited in a cylindrical chamber (r, z, θ) by a solenoidal or planar (stovetop-type) coil powered at radio frequencies, for example 13.56 MHz (Figure 2). The coil current induces a magnetic field which in turn induces an azimuthal (in the θ-direction) electric field that couples power to the plasma, i.e., heats the plasma electrons. For common excitation frequencies (less than the plasma frequency), the electromagnetic fields are absorbed by the plasma within the skin depth. For typical conditions, fields penetrate a few cm into the plasma. The power is deposited non-uniformly in the shape of a toroid. Because of the low pressure, however, species diffusion is facile and the plasma fills the whole reactor. In the absence of any capacitive coupling from the coil, the plasma potential is relatively low (≈ 20 V) thus minimizing unwanted sputtering of the reactor walls. Capacitive coupling from the coil can result in large time-dependent plasma potentials. Similarly, when the wafer platen is biased independently by a separate RF power supply in order to control the energy of ions bombarding the wafer, large time-dependent plasma potentials can be achieved.

Literature Review

Most ICP simulations are for 2-D geometries, although 1-D simulations have also been reported [56, 57]. Recently the first 3-D ICP simulation was published by Kushner et al. [30]. Table 1 gives a sample of published multidimensional ICP reactor scale simulations. The second column indicates the type of electron energy distribution function (EEDF) used in the simulation; Max. is for a Maxwellian distribution, N-L and M-C stand for an EEDF calculated using the non-local approach or a Monte Carlo simulation, respectively, and BE is for a simulation that used an off-line Boltzmann equation solver to calculate the EEDF and the resulting rate coefficients of electron impact reactions. All works in Table 1 except for Kolobov et al. [58] and Economou et al. [39] incorporated a self-consistent solution of the Maxwell equations for the power deposition profiles (third column). The electron heating mechanism (fourth column) was assumed to be either ohmic (i.e., the plasma current is proportional to the local electric field), or hybrid (i.e., anywhere in the range from collisional to collisionless). Most simulations solved Poisson's equation for the electrostatic field (fifth column) although several works assumed electroneutrality in the bulk plasma thus avoiding the need to solve Poisson's equation. Plasma species (electrons, ions, and neutrals, sixth column) were treated either as fluid (F), or kinetically (K), or they were not included in the simulation (n/a).

Stewart et al. [59] used a fluid model to simulate an ICP argon plasma. They used the full momentum equation for ions and the drift-diffusion approximation for electrons. They examined the effect of reactor aspect ratio on ion flux uniformity. A more detailed study of aspect ratio effects on uniformity was conducted by Wainman et al [60].The simulation results compared favorably with experimental measurements. In a more recent work, the fluid model of Stewart et al. [59] was extended to include the mass, momentum, and energy continuity equations for the neutral gas [27]. A chlorine ICP sustained in a GEC reference cell was simulated. The simulation results were in reasonable agreement with measurements. All these simulations assumed Ohmic (collisional) power deposition and neglected non-linear effects such as the ponderomotive force [61]. Also, a Maxwellian EEDF was assumed. Vahedi et al. [62] developed a model for non-collisional electron heating that can be incorporated in ICP simulations using an effective collision frequency approximation.

Kushner et al. have developed a modular approach to simulating ICPs [28, 29, 30]. The simulation consists of an electromagnetics module (EMM), an electron energy module (EEM), and a self-consistent charged species transport and chemistry module. The EEM module has two options. A "fluid" equation for electron energy coupled with an off-line Boltzmann solver which is used to parameterize the electron transport properties and reaction coefficients in terms of the mean electron energy [30], or a Monte Carlo simulation of the electron properties [28, 29]. In the latter case, non-ohmic heating and non-linear effects (e.g., ponderomotive force) are implicitly accounted for. The electric fields are computed using Ohm's law, relating the azimuthal electron current to the azimuthal electric field with the cold plasma conductivity. This limitation was removed later [63]. In the approach of Kushner et al., a neutral hydrodynamic flow module can also be incorporated' to calculate the neutral gas velocity profiles. All these simulations did not resolve the sheath due to the high spatial stiffness. Later, Grapperhaus and Kushner proposed a semi-analytic sheath model that was incorporated into their 2-D hybrid plasma equipment model [64].

Di Peso et al. [61] used the full momentum equation for the electron transport to calculate the azimuthal velocity component of the electrons in an argon ICP. The

Table 1. A sample of published multidimensional inductively coupled plasma simulations. Number next to the author(s) shows reference.

Authors	EEDF	EM	Heating	Poisson	Treatment of Species			Remarks
					e	i	n	
Bukowski et al., 27	Max.	Yes	Ohmic	Yes	F	F	F	
Dai and Wu, 67	N-L	Yes	Hybrid	Yes	K	F	n/a	
DiPeso at al., 61	Max.	Yes	Ohmic	No	F	F	n/a	ponderomotive
Economou et al., 39	Max.	Yes	Ohmic	Yes	F	K	K	DSMC
Kolobov et al., 58	N-L	No	Ohmic	Spec.	K	n/a	n/a	specified EM field
Kortshagen et al., 41	N-L	Yes	Ohmic	No	K	F	n/a	rapid, trapped e
Kushner et al., 30	BE	Yes	Ohmic	Yes	F	F	F	3-D
Lymberopoulos et al., 26	Max.	Yes	Ohmic	Yes	F	F	F	resolved sheath
Paranjpe, 43	Max.	Yes	Ohmic	No	F	F	n/a	rapid, local approx.
Rauf & Kushner, 63	M-C	Yes	Hybrid	Yes	H	F	F	
Stewart et al., 59	Max.	Yes	Ohmic	Yes	F	F	n/a	
Vahedi et al., 62	Max.	Yes	Hybrid	Yes	F	F	n/a	
Wise et al.,44	Max.	Yes	Ohmic	No	F	F	F	rapid
Yang & Wu,36	N-L	Yes	Ohmic	Yes	K	F	n/a	

Legend: EEDF = electron energy distribution function, EM = electromagnetics model, e = electrons, i = ions, n = neutrals, Max. = Maxwellian EEDF, M-C =Monte Carlo, N-L = non-local, BE = of-line Boltzmann equation, F = fluid,, H = hybrid, K = kinetic, n/a = not applicable, Spec. = specified.

authors assumed electroneutrality in the bulk, and ambipolar charge flow in the r and z directions. They neglected electron inertia in the r and z directions, but they included the Lorentz force acting on the electrons due to the RF magnetic field. The effect of this ponderomotive force (also called radiation pressure) is to push charged particles, regardless of sign of charge, against the gradient of the azimuthal electric field, i.e., towards the reactor center. The authors noticed that the ion flux uniformity at the wafer at 5 mtorr was not affected substantially when including the ponderomotive force compared to when that force was neglected; the uniformity was noticeably affected, however, at a pressure of 2 mtorr. They explained this result by noting that as the pressure is lowered, the azimuthal electron velocity component is more out of phase with E_θ and more in phase with the RF magnetic field, making the Lorentz force larger.

Kortshagen et al. [41] used the non-local approach to solve for the self-consistent EEDF in a 2-D argon ICP. They assumed electroneutrality in the bulk plasma and drift-dominated flow of ions, thus turning the ion density continuity equation into an equation for the electrostatic potential. The authors solved a spatially homogeneous Boltzmann equation in terms of the total electron energy. They did not account for the spatial dependence of the EEDF due to the presence of free electrons or due to electrons with energy above the excitation threshold that have a short energy relaxation length. Yang and Wu [36] extended the simulation of Kortshagen et al. by solving the space dependent Boltzmann equation, accounting for both trapped and free electrons. Kolobov et al. [49, 58] also solved the space-dependent Boltzmann equation using specified electromagnetic and electrostatic fields to calculate electron kinetics in a 2-D ICP reactor.

Lymberopoulos and Economou [26] solved the fluid conservation equations for electrons, ions and neutrals for an electronegative (chlorine) plasma to calculate polysilicon etching profiles in an ICP. They made the drift-diffusion approximation to the momentum equations, and assumed a Maxwellian EEDF. They solved for the whole reactor with a refined finite element grid near the walls to resolve the sheaths.

All simulations discussed so far assumed Ohmic heating of electrons by the RF electric field, i.e., the plasma current is proportional to the driving field, the proportionality factor being the (local) plasma conductivity. As the gas pressure is lowered to below some 10 mtorr however (for argon), non-local effects start influencing the power absorption and electron kinetics [65, 66]. In fact, as pointed out by Rauf and Kushner [63], treating the electrons kinetically (e.g., using Monte Carlo simulation or otherwise solving the Boltzmann equation to find the EEDF), and at the same time assuming Ohmic power deposition, can give erroneous results. This inconsistency was rectified by Rauf and Kushner by calculating the plasma current from the Monte Carlo simulation (instead of using Ohm's law) and using this current into Maxwell's equations to calculate the EM fields self-consistently. This way the whole range (from collisional through hybrid [65] to collisionless) of heating regimes and non-local kinetics giving rise to the anomalous skin effect [66] can be captured by the simulation. This approach for studying electron kinetics was also reported by Dai and Wu [67], except that these authors solved the linearized Boltzmann equation for the EEDF and employed an analytic solution of the EM field equations. They also used measured electron temperature and density as input values.

Rapid ICP simulations As mentioned before, judicious approximations based on the physics of the problem can reduce the simulation times dramatically. Paranjpe [43] reported a rapid ICP simulation based on several simplifying approximations. The

author, (a) solved only for the bulk plasma using ambipolar diffusion; (b) applied electroneutrality in the bulk to avoid solving the Poisson equation, and (c) assumed that the electron-impact rate coefficients are a function of the local electric field. He considered an argon plasma without long time scale neutral (metastable in this case) chemistry. These approximations resulted in an extremely fast simulation. However, the ambipolar assumption has been questioned [68], and the local electric field assumption is not applicable at the low pressures of interest. Kortshagen et al. [41] also made use of several simplifying approximations based on the physics of the problem. For example, (a) only the bulk plasma was treated applying a boundary condition at the sheath edge which, due to the thinness of the sheath, essentially coincides with the reactor wall; (b) electroneutrality was applied in the bulk, and (c) the Boltzmann equation was space- and time-averaged resulting in a greatly simplified equation for the EEDF. Again, an argon discharge was employed without metastable chemistry. Both Paranjpe and Kortshagen et al. employed a Maxwell equation solver for the EM fields. Wise et al. [44] and Economou et al. [45] extended these works to include complex chemical reactions in complicated reactor geometries as described below.

A RAPID 2-D SELF-CONSISTENT ICP FLUID SIMULATION

The two-dimensional self-consistent ICP reactor simulation of Wise et al. [44] and Economou et al. [45] employs a modular approach similar to that used for capacitively-coupled [25] and inductively-coupled [26, 29] systems. The simulation begins by solving Maxwell's equations to determine the electromagnetic fields and power deposition for a specified coil current (Figure 3). The power deposition profile is used as input to the electron energy equation to calculate the electron energy or "temperature" and hence the rate coefficients for electron-impact reactions. In turn these are used in the source terms of the neutral and charged species modules. The former is used to

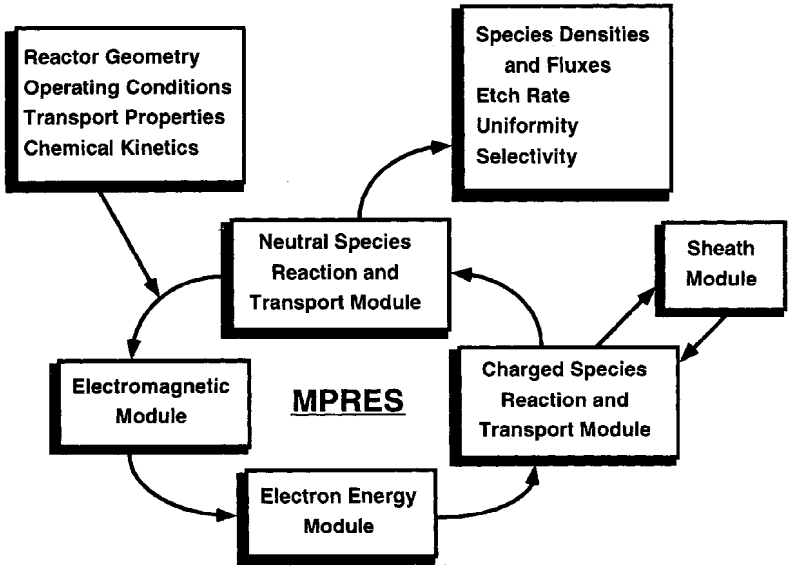

Figure 3. Modular approach used for ICP simulation.

Bukowski et al.[27], the problem has an analog in fluid mechanics, where one couples a (viscous) thin boundary layer solution near the wall to a potential flow (no viscosity) solution extending to much larger distances away from the wall. Fortunately, the sheath in HDPs is collisionless, since the species mean free path at 10 mtorr is on the order of 1 cm, much larger than the sheath thickness. Thus, if one knows the ion (or electron) distribution function at the sheath edge, and the spatiotemporal distribution of the sheath electric field, one can obtain the ion distribution function at the wall.

In order to be consistent with the Bohm criterion for ions, the sheath edge is defined as the point where the ions have been accelerated (presumably by the presheath electric field) to the Bohm velocity, i.e., the presheath is included as part of the bulk plasma. The Bohm flux also provides a boundary condition (applied at the wall because of the thinness of the sheath) for the positive ion continuity equation. The negative ion density was assumed zero at the walls.

Electroneutrality in the bulk plasma If one is not interested in resolving length scales of the order of the Debye length, the electroneutrality constraint in the bulk plasma is applicable.

$$n_e = \frac{1}{e}\sum_i z_i n_i \tag{1}$$

where z_i is the charge on ion i. This is an excellent assumption for the plasmas of interest since the Debye length is exceedingly small (10s of μm) compared to the reactor dimensions. Of course the electroneutrality constraint can't be applied in the sheath, where the Poisson equation has to be solved. Solving Poisson's equation in the whole reactor domain introduces numerical difficulties. When using the electroneutrality constraint, the electron continuity equation is not necessary. The electron density is obtained directly from Equation (1), having solved for all ion densities.

Boltzmann electrons If the Poisson equation is used instead of electroneutrality in the bulk, the electrostatic field can be recovered without recourse to any additional calculate the neutral gas composition. The latter is used to calculate the charged particle densities and the self-consistent electrostatic fields. The calculation is repeated in a cyclic fashion until "convergence". From the converged solution, the self-consistent power deposition, electrostatic potential, electron temperature, charged and neutral species densities and flux, etch rate and uniformity along the wafer radius can be calculated. This modular approach is essentially an equation splitting approach, in order to overcome the disparate time scales of electron, ion, and neutral transport and chemistry. Each of the species is solved in its natural time scale.

In the case of a RF biased substrate (assuming that the bias power is much less than the coil power), a circuit simulation of the plasma which includes the non-linear impedance of the sheath, executed as a post-processing step, can provide the time-dependent plasma potential and information on the energy distribution of ions bombarding the wafer.

The simulation employs a number of simplifying assumptions as described below:

Separation of bulk plasma from sheath In high density plasmas, the sheath thickness is on the order of 10-100s of μ. In contrast, the reactor dimension is typically 10s of cm. This disparity in length scales requires, for any numerical method, a much denser grid near the walls compared to the bulk plasma. The high degree of spatial stiffness ($10^3 - 10^4$) introduces numerical difficulties and results in excessive computation times. For this reason it has become customary to separate the bulk plasma from the sheath [41, 44, 45,] or to avoid resolving the sheath [27, 30, 36]. It then becomes necessary

to device a procedure for "splicing" the sheath to the bulk plasma [64]. As mentioned by assumptions. Since the Poisson equation is not solved in the bulk, the fields are obtained by assuming Boltzmann electrons [2].

$$\mathbf{E}_A = -\frac{\nabla(n_e k T_e)}{e n_e} \tag{2}$$

This expression results from the electron momentum balance equation by assuming inertialess electrons (neglecting the left hand side of the momentum equation) and also dropping the frictional force term. Equation (2) simply states that the electric field force balances the electron pressure force.

Di Peso et al. [61] included the non-linear effect of Lorentz force acting in the direction of $\mathbf{B} \times \mathbf{u}_\theta$. This force becomes more important as the pressure and/or the excitation frequency are lowered. It can be included in the electron momentum balance and therefore end up as an additional term in Equation (2).

Specified EEDF The Boltzmann equation is not solved to compute the EEDF. Instead, the EEDF is specified, normally assumed Maxwellian. The electron energy balance is solved assuming an adiabatic condition for electron temperature at the wall. The Maxwellian assumption is very common in the literature [26, 27, 31, 37, 43]. Measured EDFs in ICPs, however, have a Maxwellian bulk (due to electron-electron collisions), and a depleted tail due to inelastic losses and escape of fast electrons to the walls. Thus a bi-Maxwellian distribution may be more appropriate. A Maxwellian distribution is not expected to have a great effect on ion densities since the ionization rate is self-adjusted to balance the loss rate of ions to the walls; and the latter depends only very weakly on the EEDF. The good agreement with experimental data shown below is an indirect evidence that the Maxwellian EEDF is reasonable for obtaining species densities and their distributions. Other forms of the EEDF may also be used, e.g., Druyvesteyn. The best approach, of course, is to solve the Boltzmann equation for the EEDF. Approximations such as the non-local approach (when applicable), offer tremendous advantages, especially for complex multidimensional geometries. Work along these lines is in progress.

Drift-diffusion for ions The drift-diffusion approximation is made for ions, e.g., ion inertia was neglected. This appears to be a good approximation for Kn < 0.1. Eq. (2) provides the field that drives ions in the plasma. Also, a constant mobility was assumed for ions.

Diffusive Flow for Neutrals The importance of convective vs. diffusive flow of neutrals is determined by the Peclet number $Pe = uL/D$, where L is a characteristic dimension of the system. Away from inlet and exit ports, the characteristic length will be on the order of the reactor dimension. The system will be primarily diffusive when $Pe \ll 1$. For Cl_2 gas in a reactor with $L \approx 0.1$ m and a neutral species diffusivity of $D \approx 5\, m^2 s^{-1}$ at 20 mTorr, the Peclet number will be $Pe \approx 1$ when u = 50 m s^{-1}. Convective gas velocities are not likely to be that high, except for a small region near the gas inlet ports. It follows that gas flow can be approximated as diffusive; this obviates the need for solving the full Navier-Stokes equations which adds to the computational burden. It should be noted that both the diffusivity and the convective velocity scale inversely with gas pressure, so the Pe number is independent of pressure. However, as the pressure is lowered to the point of free molecular flow, the gas diffusion coefficient has no meaning any more. Direct Simulation Monte Carlo (DSMC) can then be applied to solve for the fluid velocity profiles. The boundary condition for neutrals was that the flux at the wall was equal to the reaction rate of neutrals.

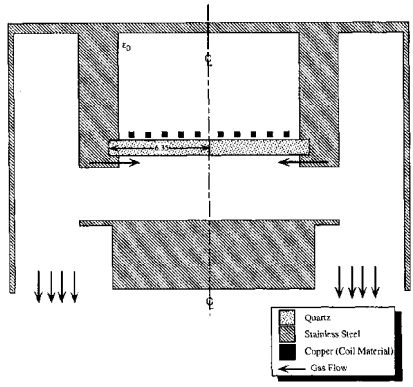

Figure 4. Schematic of the GEC-ICP reference cell.

In summary the following equations, which are listed in reference 26, were used for the ICP reactor model: (a) density continuity for each and every ion and neutral in the system, (b) the drift-diffusion equation for the ion fluxes and diffusion alone for the neutral fluxes, (c) electroneutrality to calculate the electron density, Equation (1) above, (d) Boltzmann relation, Equation (2) above, to calculate the electrostatic fields, (e) an electron energy equation to calculate T_e, and (f) the Maxwell's equations, reduced to one equation for the azimuthal electric field. The cold plasma approximation was used to calculate the power deposition profiles. This system of equations was supplemented with a table of values for the reaction rate coefficients of electron impact reactions as a function of T_e. Analytical approximations can also be used for this purpose, but table interpolation is generally faster. These equations were incorporated into a simulation code named MPRES (Modular Plasma Reactor Simulator [45]) which can be used as a Technology Computer-Aided Design (TCAD) tool for inductively coupled plasma systems.

RESULTS AND COMPARISON WITH EXPERIMENTAL DATA

Application to a GEC Reference Cell and Experimental Validation

The rapid ICP simulation approach was validated against experimental data. The reactor used for comparison of model predictions to data is the Gaseous Electronics Conference reference cell, modified for inductive operation[69]. The 2-dimensional (2-D) cell structure studied here is shown in Figure 4. A quartz plate separates the 5-turn planar inductive coil from the plasma. In practice the gas flow is three dimensional, but the flow rates (10-20 sccm) are quite small for the flow to be diffusive. In the simulation, gas injection was provided as a ring directly below the quartz plate, and the exhaust was located azimuthally below the wafer level.

Except when noted otherwise, all experimental data shown below were obtained by researchers at Sandia National Laboratories in Albuquerque[69, 70]. Line-integrated electron densities were measured by microwave interferometry, spatially resolved electron densities by Langmuir probes, negative ion densities by laser photodetachment and simultaneous detection of the resulting electrons by microwave interferometry, and metastable argon atoms by absorption measurements. Langmuir probes were also used to measure the electron temperature and the plasma potential.

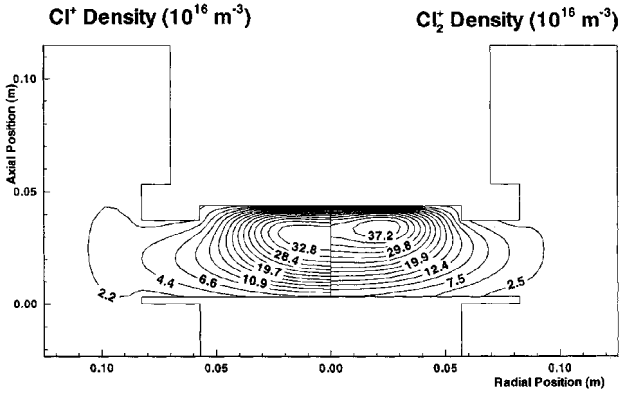

Figure 5. Atomic (left) and molecular (right) chlorine ion number densities under base case conditions.

Chlorine Plasma

The chemistry set used for chlorine is identical to that used earlier[26]. Base case conditions were 20 mTorr pressure (nominal), 180 W deposited in the plasma, 20 sccm flow of pure Cl_2, 13.56 MHz excitation frequency, and no wafer present (i.e. no etching) to allow comparison to available measurements. Heavy species temperatures were not solved for. The ion and neutral gas temperatures were assumed constant at 0.12 eV and 500 K, respectively. The probability of Cl recombination on the walls was taken as 0.1. These parameter values were not "optimized" or "fit" in anyway to the data. They were chosen based on previous experience with calculations or measurements in chlorine plasmas.

Figure 5 shows the Cl^+ and Cl_2^+ densities, which are depleted near the walls of the chamber by losses to the walls. The peak density of Cl^+ is $3.4\text{x}10^{17}\,m^{-3}$, slightly less than the molecular ion (Cl_2^+) peak density ($3.8\text{x}10^{17}\,m^{-3}$). Although the Cl_2 density was lower than that of Cl, the corresponding ions are of comparable magnitude. This is because the ionization threshold for Cl_2 is lower (hence the production rate coefficient is higher) than that of Cl, and also the losses of Cl_2^+ to the walls are lower than those of Cl^+ due to the higher mass of the former ion. The atomic chlorine ion is produced off axis (not shown) but diffuses inwards to peak on axis, where the atomic chlorine neutral density is also highest. Because the molecular chlorine neutral density peaks away from the reactor axis, and Cl_2^+ production also peaks off axis, the established Cl_2^+ profile has a maximum off axis, under the coil where the power deposition is also maximum.

Figure 6, left, shows comparisons of radial profiles of electron density, temperature, and plasma potential measured by a Langmuir probe [69]. A simple one dimensional Langmuir Probe theory was applied due to the small Debye length, and the Langmuir probe measurements were calibrated using microwave interferometry. The plasma is well confined, as evidenced by the drop off in electron density by one order of magnitude by r=10 cm. Given the inevitable uncertainty in the reaction rate coefficients and in the probe measurements, the agreement between predictions and measurements is thought to be good. Notice that there were no adjustable parameters that were varied to fit the data. The trend of predicted electron temperature is very similar to experiment, capturing a slight peak at a radial position corresponding to the centroid of the toroidal power deposition profile. Of interest here is the substantial drop off in electron

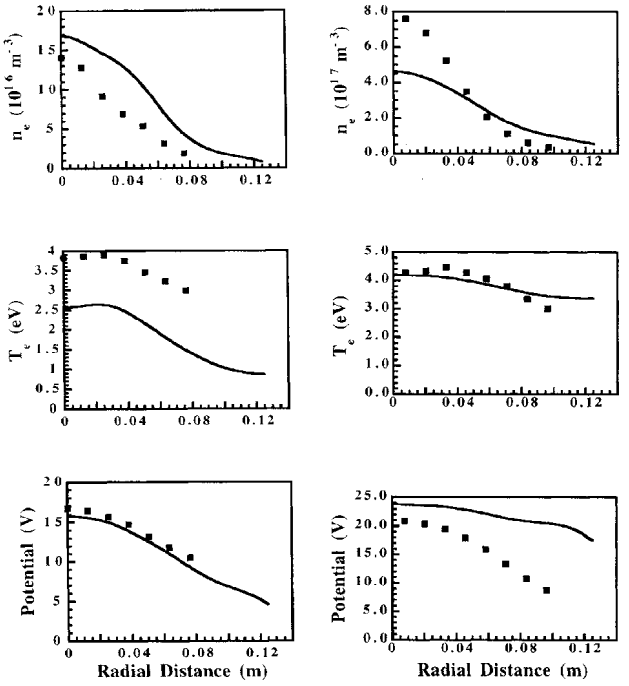

Figure 6. Comparison of simulation predictions (lines) with data (points) for chlorine (left) and argon (right) plasmas.

temperature with position. This is due to the rather small electron energy relaxation length in the 20 mtorr chlorine plasma (see below), which results in a somewhat "local" behavior of the molecular gas discharge.

Figure 7 shows a comparison of the line integrated electron density at the central plane of the discharge, and the Cl^- density at the reactor center versus power. The line integrated electron density was measured by a microwave interferometer; the Cl^- density was measured by photodetachment of Cl^- and subsequent detection of the electrons produced. The simulated electron density increases linearly with coil input power, as expected for a system in which most of the coil power is deposited in the plasma as opposed to the sheaths. The measured electron density increases superlinearly. The agreement with the data is within experimental error. The trend for Cl- increasing with power is in quantitative agreement with experiment to within a factor of two, which is the estimated uncertainty in the photodetachment cross section [70]. Comparison of the measured radial profile of Cl^- was also made for the base case chlorine plasma in the GEC cell. The measured Cl^- density was close to that obtained numerically, approximately $3x10^{17}\,m^{-3}$, at the plasma center. However, there were differences in the shape of the profile. The experiment showed a rather flat profile at the center with a slight increase with radius. The simulation also showed a flat profile at the center, but the negative ion density decreased substantially as a function of radius. The simulation predicted that the negative ions will tend to be confined by the ambipolar fields. We do believe that the negative ion density has to start dropping at some radial position away from the center of the reactor since the plasma is rather well confined (Fig. 7). At this point we can't explain the differences between measurement and simulation.

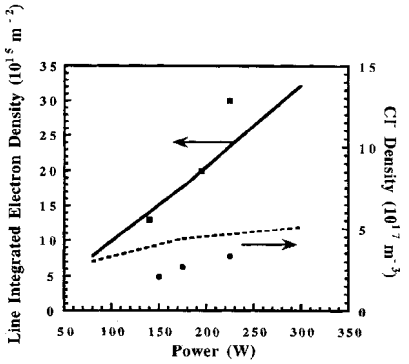

Figure 7. Comparison of predicted (lines) line-integrated electron density and negative ion density at the center of the plasma with experimental data (points).

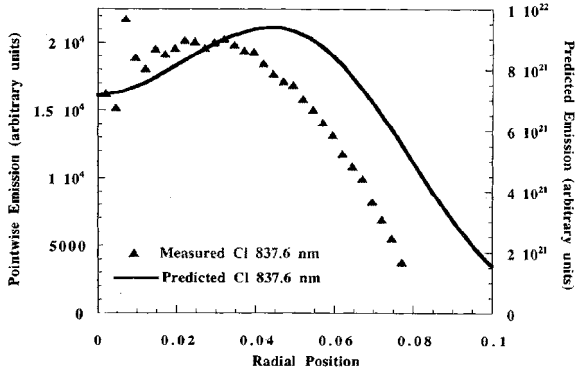

Figure 8. Comparison of predicted (line) plasma emission profile to measurement (points).

Comparisons of optical emission intensity profiles with data taken at the UH-ICP reactor are shown in Figure 8 [71]. The pressure was 15 mtorr and the gas mixture was 80%/20% Cl_2/Ar. The data show some scatter near the centerline due to the method (Abel inversion) used to extract the radial profiles from side-on observations of emission intensity. There is qualitative agreement with the data. However, there is a radial shift in the off-axis maximum between predictions and data. The off axis maximum occurs close to the maximum in power deposition, again signifying some degree of local behavior of the molecular gas plasma.

Argon Plasma

For the Ar plasma, we used the same chemistry as before [72], with the radiative relaxation of the resonant state corrected for the reduced operating pressure in the high density source. Comparison of the Ar plasma density, electron temperature, and electrostatic potential are shown in Figure 6, right. The electron density is predicted to be more diffuse compared to the measured profile, possibly due to the drift-diffusion assumption for ions. Correspondingly, the plasma potential is predicted to be flatter that the measured values (remember that the space charge fields are recovered from the electron density profiles, see Equation 2). The electron temperature gradients are much

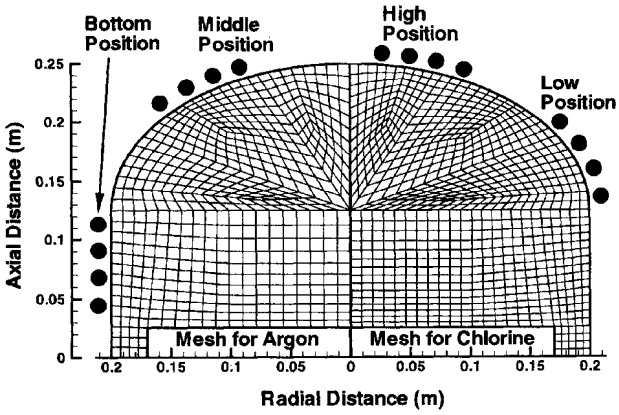

Figure 9. Dome-shaped ICP used for simulations. The finite element grid is also shown.

smaller than in the case of chlorine, due to the much larger electron energy relaxation length (see below).

Comparison of the line-integrated Ar^* density (measured by absorption) was also made for a 10 mtorr, 200 W argon plasma. The simulation considered one (lumped) metastable state and one resonant state, while the data were for the dominant $1S_5$ state [73]. The absolute value of the metastable density was captured by the simulation. The predicted profiles were qualitatively similar with the measured profiles, except that the measurements showed very small values of the integrated density near the bottom electrode. This might be in part due to blocking by the window edge of the probing beam used to do the metastable absorption measurements.

Application to a dome-shaped ICP reactor

The experimentally verified simulation tool was then used to predict plasma transport in a dome-shaped reactor that can accommodate 300 mm-diameter wafers, i.e., an industrial-size reactor (Figure 9). This is an inductively coupled reactor powered by a four-turn solenoidal coil wound around the quartz dome. The coil can be positioned in one of four different locations designated in Figure 9 as high, middle, low, and bottom positions, in descending order from the top of the dome (for each position only half of the coil is shown in Figure 9).

The chosen base case conditions were a total pressure of 10 mtorr, a plasma power of 1000 Watts, no substrate bias, the middle coil position, an excitation frequency of 13.56 MHz, a neutral gas temperature of 500 K, an ion temperature of 0.12 eV, and an inlet gas feedrate of 30 sccm.

The predicted plasma potential and ion (electron) density distributions for argon are shown in Figure 10. The scales for the contour values are shown on the top of the figure. The potential difference in the bulk of the plasma is a few kT_e, as expected. The sheath potential drop over the grounded electrode is about 13 Volts. The ion density peaks on axis and shows a smooth gradient towards the walls, where the density drops by about an order of magnitude at the bottom corner of the reactor. Note the ion density gradients along the electrode surface signifying a non-uniform ion flux to the electrode. The potential and ion density distributions shown in Figure 10 are qualitative similar to those measured in a similar reactor by Tuszewski and Tobin [74]. Quantitative comparison cannot be made because these authors used mixed gas $Ar/O_2/H_2$ discharges.

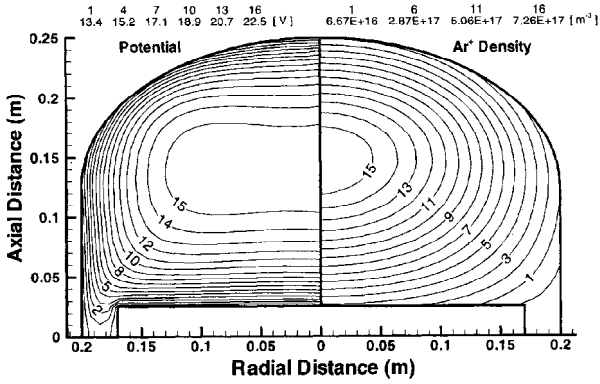

Figure 10. Plasma potential (left) and ion density (right) in an argon plasma.

The electron temperature distribution in argon and chlorine discharges under the same (base case) conditions are shown in Figure 11, for the middle coil position. The striking feature of this plot is the rather weak gradient of electron temperature in argon and the strong gradient in chlorine. This is in part due to the different electron impact

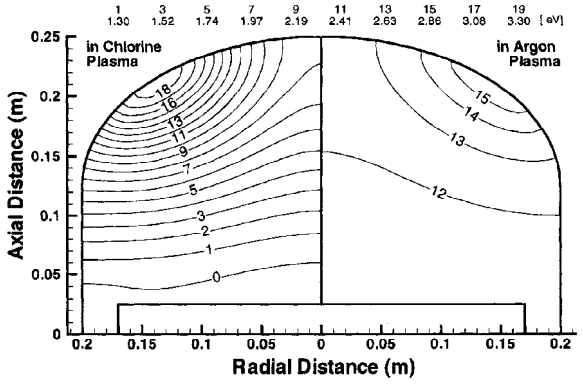

Figure 11. Electron temperature in chlorine (left) and argon (right) plasmas.

reactions occurring in these two kinds of discharges: a noble gas and a molecular gas discharge. A cross section set for molecular chlorine is shown in Figure 12, left [75]. A set for argon is shown on the right side of the same figure [2]. The magnitude of the cross section of low threshold processes is substantial in chlorine, approaching the elastic collision cross section for some energy range. In addition, these processes have a threshold comparable to the electron temperature, i.e., they are inelastic and not quasi-elastic (as for example rotational excitation) collisions. Thus the electron energy relaxation length (λ_e) is expected to be much shorter in chlorine compared to argon. For a pressure of 10 mtorr, λ_e is estimated to be a few cm in chlorine. Therefore, for a reactor length of 20 cm, a strong electron temperature gradient is reasonable. Another reason for the stronger temperature gradients in chlorine compared to argon is the electron density being lower in chlorine (and the electron thermal diffusivity is proportional to the electron density). The strong temperature gradients lead to much more localized plasma production and molecular dissociation (Figure 13, left) near the power deposition zone (near the coils) in the chlorine plasma. Also, the strong

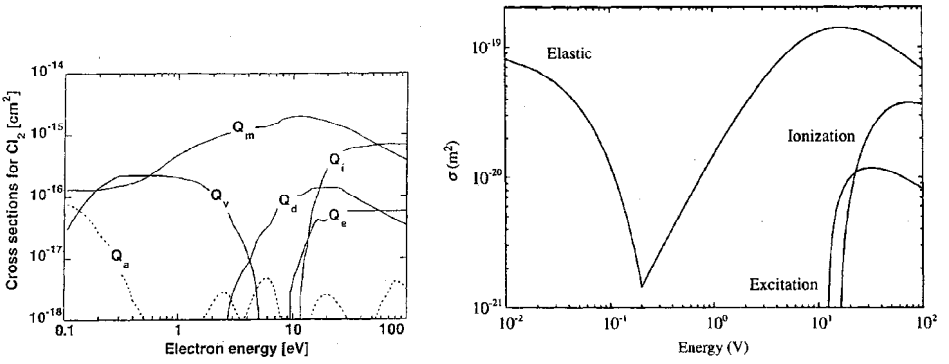

Figure 12. Cross section set for molecular chlorine (left) and argon (right).

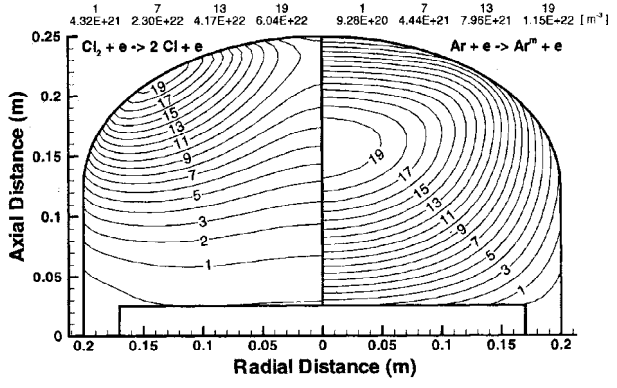

Figure 13. Dissociation rate in chlorine (left) and excitation rate in argon (right) plasmas.

temperature gradients in the chlorine discharge lead to substantially lower electron temperatures over the wafer. This is due to the large distance of the wafer from the power deposition zone. The lower electron temperature may be advantageous for minimizing charging damage of thin film structures on the wafer [76].

In contrast, the first inelastic threshold for argon is around 11.5 eV (ionization of argon metastables with a threshold of 4.2 eV is not shown in the cross section set of Figure 12, right). Hence the electron energy relaxation length for low energy electrons is greater than the reactor dimensions, assuming that metastable collisions do not play a substantial role. The result is much more uniform electron temperature, and an excitation rate peaking on the reactor axis and not near the power deposition zone (Figure 13, right). From the above discussion one concludes that, under these conditions, the chlorine discharge is closer to exhibiting local behavior, while the argon discharge is closer to exhibiting non-local behavior.

The effect of coil location on ion flux uniformity is shown in Figure 14, left, for the argon discharge. Four positions were studied; in addition to the default middle position used in the preceding results, top, low, and bottom coil positions (also shown in Figure 9) were tested. The peak values of the ion flux were $4.20 \times 10^{20} m^{-2} s - 1$, $4.23 \times 10^{20} m^{-2} s - 1$, $4.56 \times 10^{20} m^{-2} s^{-1}$, and $4.64 \times 10^{20} m^{-2} s^{-1}$, respectively. Pressure was kept at 10 mtorr and power was set at 1000 W for all the runs involving the different coil positions. The ion flux uniformity improves steadily and dramatically in going from the upper to the lowest coil positions. This is a result of altering the location of

the plasma generation zone and the ion diffusion length as the coil position is varied. Under the conditions of Figure 14, left, the ion density always peaks on axis. However, having the plasma production zone near the wafer edge (when the coil is at its lowest position), results in more uniform ion density profiles.

In general, the ion flux uniformity depends on the ion production rate, ion diffusion length (this depends not only on the geometry of the system but also on the location of plasma production), reactor aspect ratio, and pressure (which determines the value of diffusivity). These parameters can be lumped into two dimensionless groups (Damkohler number and aspect ratio) that characterize the system behavior. The Damkholer number [77] $Da = k_p n_e L^2 / D$, shows the relative importance of species production (or loss) by gas-phase mechanisms relative to their ability to diffuse away from the source. When $Da > 1$, large concentration gradients may be expected. The Da number in these systems varies depending on the power level (which affects electron density n_e and degree of dissociation) and pressure (which affects neutral density, diffusivity and the rate coefficient for electron impact reactions k_p). The effect of aspect ratio is shown schematically in Figure 15. Given a localized source of species (e.g. radicals), the spatial distribution of these species at steady state will depend on the reactor aspect ratio. Low aspect ratio reactors (tall, small radius) yield a distribution that peaks on axis, while large aspect ratio systems (short, large radius) yield a distribution that peaks off axis. This is because, as the species diffuse radially away from the localized source to try to fill in the central regions of the reactor, they also diffuse towards and lost onto the axial end walls. The final profile is dictated by the relative magnitude of the diffusion lengths, i.e., the aspect ratio. Actually it is the square of the aspect ratio that governs behavior since the diffusion loss "rate coefficient" is inversely proportional to the square of the diffusion length.

The etch rate of polysilicon in a chlorine discharge is a complex convolution of the ion (atomic and molecular) and neutral (atomic and molecular) fluxes bombarding the wafer. Using the surface chemistry model for polysilicon etching proposed by Bailey et al. [78], we calculated the etch rate distribution for the base case conditions. The result is shown in Figure 14, right, for two coil positions. The etch rate is much more uniform for the case of chlorine even for the standard (middle) coil position. Moving the coil to the low position improves uniformity substantially. The corresponding plot for the argon ion flux (Figure 14, left) is still very non-uniform. This demonstrates that chemistry plays a critical role in reaction uniformity across the wafer. These results also demonstrate that reaction uniformity across a wafer can be tailored by optimizing the position of the coils.

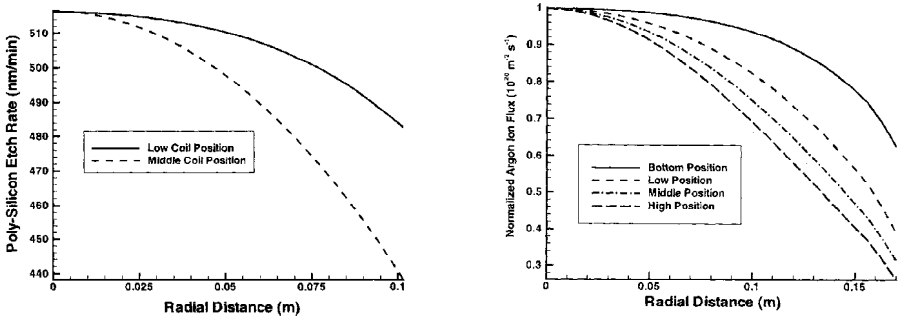

Figure 14. Ion flux uniformity in argon plasma (left) and etch rate uniformity in chlorine plasma (right) across the wafer surface.

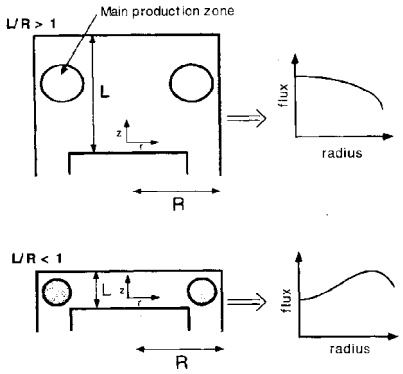

Figure 15. Effect of aspect ratio on flux uniformity along the substrate electrode.

Summary

Modeling and simulation of plasma systems, combined with well-defined experiments, are essential for furthering our understanding of the transport and reaction phenomena occurring in these systems. The problem is exceedingly complicated due to the disparate length and time scales involved, especially when complex chemistries and multidimensional geometries are of interest. Direct solution of the governing equations, or large scale particle simulations are time consuming and are not suitable for rapid turn-around parametric investigations. Judicious approximations, based on the physics of the system, can reduce the complexity of the problem to yield rapid simulation tools. This is particularly important for complex chemistries and complex multidimensional geometries found in practical systems.

We have developed a two-dimensional self-consistent rapid simulation tool for inductively coupled high density plasma reactors. Simulations of complex chemical systems in arbitrary geometries can be performed in a matter of hours on desktop (125 MHz) workstations. Experimental validation of the tool was performed with Langmuir probe, microwave interferometry, laser photodetachment, optical emission, and absorption measurements.

The simulation tool was then used to conduct a parametric study of radial plasma uniformity in a domed-shaped ICP reactor. Using a uniformly spaced four turn solenoidal coil, the ion flux uniformity in the case of argon was steadily improved by moving the coil away from the dome top towards the reactor bottom. Sharper temperature and ionization profiles in the chlorine plasma, however, led to large gradients towards the sides of the substrate if the coils are placed too low on the side of the reactor, so a mid-range coil position produces the best uniformity results. Also, the stronger electron temperature gradients in the case of chlorine (or in the case of any molecular gas) resulted in very low electron temperatures near the wafer when the latter was placed far enough from the power deposition zone. This may be advantageous regarding wafer damage.

DISCUSSION

Improvements to Fluid Model

The following improvements can be made to the fluid model described above to

extend its range of validity to lower pressures. First, a field-dependent ion mobility is more accurate for low collisionality systems. Dropping the drift-diffusion approximation and using the full momentum equation for ions is expected to be even better. This should result in more confined ion density profiles and better agreement with the experimental data, especially for pressures of 10 mtorr and below for argon (see Figure 7, right).

Ohm's law breaks down at low enough pressures where electron kinetics is nonlocal [66]. An improvement in the electromagnetics module, used to calculate the power deposition profiles, can be made by replacing Ohm's law with a more accurate expression for the electron current flowing in the plasma. Several options come to mind: (a) the electron current can be calculated by using the azimuthal component of the momentum balance equation as done by DiPeso et al. [61] (b) The Boltzmann equation can be solved to calculate the electron current. In general, the spatially dependent equation must be solved. When applicable, the spatially independent equation with constant total energy [41], or a combination of spatially independent and spatially dependent parts of the EEDF [36] can provide significant computational savings. (c) A Monte Carlo simulation can be used to calculate the EEDF and the resultant electron current [29, 63]; this is a computationally intensive proposition.

Of course, incorporating any of the above improvements will increase the time required for the simulation to converge. Careful comparisons with analytic or semi-analytic models, fully kinetic simulations, and especially with experimental data need to be made to ascertain the range of validity of the fluid simulation as the pressure is lowered to below 10 mtorr.

Will fluid models become unusable in the future as pressure decreases?

The tendency in the microelectronics industry is to go to even lower pressures. However, it should be kept in mind that it is not pressure, p, alone but the product of pressure and length scale, pL, that determines the range of applicability of a fluid model. (actually the quantity that determines system behavior is NL, where N is the gas density; alternatively one can speak in terms of the Knudsen number.) There is a practical lower limit to pressure in etching and deposition systems, determined by the reaction rate. Let's consider this simple example: polysilicon etching on a 200 mm-diameter wafer at a practical rate of 0.5 μ/min, to generate product $SiCl_4$, requires 56 sccm of Cl_2 flow. Of course one must have a higher flow of chlorine to avoid having a reactor filled with product; let's say 112 sccm. This flow would require a pumping speed of 1400 1/s at the wafer surface to maintain a pressure of 1 mtorr. Due to conductance limitations, the required pumping speed at the pump may be a few times higher, i.e., a huge pump! When the wafer size becomes 450 mm around year 2005, the corresponding figures will be 560 sccm of chlorine flow and 7,000 1/s pumping speed at the wafer. These figures show that an operating pressure less than 1 mtorr is highly unlikely for a practical system. Now, since the pressure is approaching a lower limit but the wafer size keeps increasing, it appears that the product pL will reach a minimum some time in the near future and then it will start increasing. Therefore fluid models are not to become obsolete in the future! On the other hand, kinetic models will always be useful to provide the species distributions functions, i.e., the EEDF of electrons or the energy and angular distributions of ions and neutrals bombarding the wafer.

Ending notes

During the past several years, multidimensional self-consistent plasma simulations

which account for the coupled effects of charged and neutral species transport and chemistry have been developed. These simulations vary in their degree of detail from fluid to kinetic to hybrid simulations. Also, different degrees of approximation are used within the same group (e.g., fluid) of simulations. Detailed comparisons with experimental data are necessary to decide which degree of approximation is adequate for accurate determination of some important quantities such as the species density profiles, and the radical and ion flux and energy uniformity along the electrodes. For example, how low in pressure can the fluid approximation be used, and what is the window of pressure and frequency for which the drift-diffusion approximation is correct?

For complex chemical systems the accuracy of the simulation is limited by the lack of knowledge of cross sections for electron-impact reactions and plasma chemistry. In etch or deposition plasmas, knowledge of surface chemistry is viewed as an even more important limitation. This becomes more acute as the operating pressure decreases. Experiments in well characterized systems, in combination with plasma simulation, will continue to enhance our fundamental knowledge about the plasma dynamics. Many more comparisons with experimental data are needed to ”tune” chemically complex models and provide simulation tools with predictive capabilities over a wider range of operating parameters. Considering that multidimensional self-consistent RF plasma simulations are only several years old, such activity is expected to be more vigorous in the near future.

ACKNOWLEDGMENTS

Thanks are due to V. Kolobov (University of Houston), D. Lymberopoulos (Applied Materials), and T. Bartel, J. Johannes, and M. Riley (Sandia National Laboratories) for helpful discussions. Financial support has been provided by the National Science Foundation and Sandia/SEMATECH. Special thanks to my wife Eleni Patsidou-Economou for helping with the manuscript.

REFERENCES

1. S. M. Rossnagel, J. J. Cuomo, and W. D. Westwood, *Handbook of Plasma Processing Technology,* Noyes Publications, 1990.
2. M.A. Lieberman and A.J. Lichtenberg, *Principles of Plasma Discharges and Materials Processing,* John Wiley and Sons, New York, 1994.
3. M. Meyyappan, editor, *Computational Modeling in Semiconductor Processing* Artech House, 1994.
4. M. Dalvie and K. F. Jensen, J. Vac. Sci. Technol. A, **8,** 1648 (1990).
5. S.-K. Park and D. J. Economou, J. Electrochem. Soc. **137,** 2624 (1990).
6. D. B. Graves and K. F. Jensen, IEEE Trans. Plasma Sci. **PS-14,** 78 (1986).
7. S.-K. Park and D. J. Economou, J. Appl. Phys. **68,** 3904 (1990).
8. A. D. Richards, B. E. Thompson, and H. H. Sawin, Appl. Phys. Lett. **50,** 492 (1987).
9. J.-P. Boeuf and L. C. Pitchford, IEEE Trans. Plasma Sci. **19,** 286 (1991).
10. Y. Oh, N. Choi and D. Choi, J. Appl. Phys. **67,** 3264 (1990).
11. M. Meyyappan and T. R. Govindan, J. Vac. Sci. Technol. A **10,** 1344 (1992).
12. A. P. Paranjpe, J. P. McVittie, S. A. Self, J. Vac. Sci. Technol. A **8,** 1654 (1990).
13. G. R. Misium, A. M. Lichtenberg and M. A. Lieberman, J. Vac. Sci. Technol. A **7** 1007 (1989).
14. W. N. G. Hitchon, T. J. Sommerer and J. E. Lawler, IEEE Trans. Plasma Phys. **19,** 113 (1991).
15. V. A. Feoktistov, A, M. Popov, O. B. Popovicheva, A. T. Rakhimov, T. V. Rakhimova, and E. A. Volkova, IEEE Trans. Plasma Sci. **19,** 163 (1991).
16. N. Sato and H. Tagashira, IEEE Trans. Plasma Sci. **PS-19,** 102 (1991).
17. E. Gogolides and H. H. Sawin, J. Appl. Phys. **72,** 3971 (1992).
18. T. J. Sommerer and M. J. Kushner, J. Appl. Phys. **71,** 1654 (1991).

19. D. P. Lymberopoulos and D. J. Economou, J. Appl. Phys. **73,** 3668 (1993).
20. M. S. Barnes, T. J. Cotler and M. E. Elta, J. Comp. Phys. **77,** 53 (1988).
21. M. H. Wilcoxson and V. I. Manousiouthakis, J. Comp. Phys. **115,** 376 (1994).
22. D. P. Lymberopoulos and D, J. Economou, Appl. Phys. Lett. **63,** 2478 (1993).
23. D. P. Lymberopoulos and D. J. Economou, J. Vac. Sci. Technol. A **12,** 1229 (1994).
24. P. L. G. Ventzek, T. J. Sommerer, R. J. Hoekstra, and M. J. Kushner, Appl. Phys. Lett. **62,** 3247 (1993).
25. D. P. Lymberopoulos and D. J. Economou, J. Res. Natl. Inst. Standards Technol., **100,** 473 (1995).
26. D. P. Lymberopoulos and D. J. Economou, IEEE Trans. Plasma Sci. **23,** 573 (1995).
27. J. D. Bukowski and D. B. Graves, J. Appl. Phys. **80,** 2614 (1996).
28. P. L. G. Ventzek, R. J. Hoekstra and M. J. Kushner, J. Vac. Sci. Technol. B **12,** 461 (1994).
29. P. L. G. Ventzek, M. Grapperhaus and M. J. Kushner, J. Vac. Sci. Technol. B **12,** 3118 (1994).
30. M. J. Kushner, W. Z. Collison, M. J. Grapperhaus, J. P. Holland, and M. S. Barnes, J. Appl. Phys. **80,** 1337 (1996).
31. M. Dalvie, M. Surendra, G. S. Selwyn, Appl. Phys. Lett. **62,** 3207 (1993).
32. F. Young and C.-H. (John) Wu, IEEE Trans. Plasma Sci. **21,** 312 (1993).
33. J. -P. Boeuf and L. C. Pitchford, Phys. Rev. E, accepted.
34. M. H. Wilcoxson and V. I. Manousiouthakis, in *Proceedings of the First International Symposium on Process Control, Diagnostics, and Modeling in Semiconductor Manufacturing,* **95-4,** edited by M. Meyyappan, D. J. Economou, and S. W. Butler, The Electrochemical Society Inc., 1995.
35. J. D. P. Passchier and W. J. Goedheer, J. Appl. Phys. **74,** 3744 (1993).
36. Y. Yang and H. Wu, J. Appl. Phys. **80,** 3699 (1996).
37. A. M. Popov, A. T. Rakhimov, and T. V. Rakhimova, Plasma. Phys. Rep. **19,** 651 (1993).
38. C. K. Birdsall, IEEE Trans. Plasma Sci. **19,** 65 (1991).
39. D. J. Economou, T. Bartel, R. S. Wise and D. P. Lymberopoulos, IEEE Trans. Plasma Sci. **23,** 581 (1995).
40. M. Surendra, Plasma Sources Sci. & Technol. **4,** 56 (1995).
41. U. Kortshagen, I. Pukropski, and L. D. Tsendin, Phys. Rev. E **51,** 6063 (1995).
42. R.P. Brinkman, R.F. Furst, C. Werner, and M. Hierlemann, in *Proceedings of the First International Symp. on Control, Diagnostics, and Modeling in Semiconductor Manufacturing* edited by M. Meyyappan, D.J. Economou, and S.W. Butler, The Electrochemical Society, (1995).
43. A. A. Paranjpe, J. Vac. Sci. Technol. A **12(4),** 1221 (1994).
44. R. S. Wise, D. P. Lymberopoulos, and D. J. Economou, Appl. Phys. Lett. **68,** 2499 (1996).
45. D. J. Economou, R. S. Wise and D. P. Lymberopoulos, in *Plasma Processing XI,* **Vol. 96-12,** edited by G. Mathad and M. Meyyappan, The Electrochemical Society Inc., 1996.
46. I. B. Bernstein and T. Holstein, Phys. Rev. **94,** 1475 (1954).
47. L. D. Tsendin, Sov. Phys. JETP **39,** 805 (1974).
48. V. I. Kolobov and V. A. Godyak, IEEE Trans. Plasma Sci. **23,** 503 (1995).
49. V. I. Kolobov and W. N. G. Hitchon, Phys. Rev. E **52,** 972 (1995).
50. V. I. Kolobov, D. F. Beale, L. J. Mahoney and A. E. Wendt, Appl. Phys. Lett. **65,** 537 (1994).
51. L. D. Tsendin, Sov. Phys. Tech. Phys. **22,** 925 (1977).
52. P. Jiang and D. J. Economou, J. Appl. Phys. **73,** 8151 (1993).
53. M. Capitelli, C. Gorse, R. Winkler, and J. Wilhelm, Plasma Chem. Plasma Process **8,** 399 (1988).
54. J. Hopwood, Plasma Sources Sci. Technol. **1,** 109 (1992).
55. J. H. Keller, J. C. Foster, and M. S. Barnes, J. Vac. Sci. Technol. A, **11,** 2487 (1993).
56. D. P. Lymberopoulos, V. Kolobov, and D. J. Economou, submitted to J. Vac. Sci. Technol.
57. T. E. Nitschke and D. B. Graves, IEEE Trans. Plasmas Sci. **23,** 717 (1995).
58. V. I. Kolobov, G. J. Parker, and W. N. G. Hitchon, Phys. Rev. E, **53,** 1110 (1996).
59. R. A. Stewart, P. Vitello and D. B. Graves, J. Vac. Sci. Technol. B **12,** 478 (1994).
60. P. N. Wainman, M. A. Lieberman, A. J. Lichtenberg, R. A. Stewart, and C. Lee, J. Vac. Sci. Technol. A **13,** 2464 (1995).
61. G. Dipeso, V. Vahedi, D. W. Hewett, and T. D. Rognlien, J. Vac. Sci. Technol. **12,** 1387 (1994).
62. V. Vahedi, M. A. Lieberman, G. DiPeso, T. D. Rognlien, and D. Hewett, J. Appl. Phys. **78,** 1446 (1995).
63. S. Rauf and M. J. Kushner, J. Appl. Phys. **81,** 5966 (1997).
64. M. J. Grapperhaus and M. J. Kushner, J. Appl. Phys. **81,** 569 (1997).

65. V. I. Kolobov, D. P. Lymberopoulos, and D. J. Economou, Phys. Rev. E **55,** 3408 (1997).
66. V. I. Kolobov and D. J. Economou, Plasma Sources Sci. Technol. **6,** 1 (1997).
67. Dai and C.H. (John) Wu, IEEE Trans. Plasma Sci. **24,** 1155 (1996).
68. G. Mümken and U. Kortshagen, J. Appl. Phys. **80** 6639 (1996).
69. P. A. Miller, G. A. Hebner, K. E. Greenberg, P. D. Pochan, and B. P. Aragon, J. Res. Natl. Inst. Standards Technol. **100,** 427 (1995).
70. G. A. Hebner, J. Vac. Sci. Technol. A **14,** 2158 (1996).
71. R. S. Wise, Inductively Coupled Plasma Reactors: Modeling, Simulation, and Experimental Validation, Ph.D. Dissertation, University of Houston (1996).
72. N.L. Bassett and D.J. Economou, J. Appl. Phys. **75** (4), 1931 (1994).
73. K. Greenberg and G. A. Hebner, J. Appl. Phys. **73,** 8126 (1993).
74. M. Tuszewski and J. A. Tobin, J. Vac. Sci. Technol. A **14,** 1096 (1996).
75. E. Meeks and J. Shon, *personal communication,* Sandia National Labs, Livermore, CA.
76. G. S. Hwang and K. Giapis, J. Appl. Phys. **81,** 3433 (1997).
77. D. J. Economou, S.-K. Park, and G. Williams, J. Electrochem. Soc. **136,** 188 (1989).
78. A. D. Bailey III, M. C. M. van de Sanden, J. A. Gregus, and R. A. Gottscho, J. Vac. Sci. Technol. B **13** 92 (1995); see also erratum in J. Vac. Sci. Technol. B **15,** 373 (1997).
79. L.D.Tsendin Sov. Phys. Tech. Phys. **22,** 925 (1977).

NEW TRENDS IN THE KINETIC MODELING OF DISCHARGES IN LOW PRESSURE MOLECULAR GASES

Carlos M. Ferreira and Boris F. Gordiets

Physics Department and Centro de Fisica de Plasmas
Instituto Superior Ténico
1096 Lisboa Codex
Portugal

INTRODUCTION

The non-equilibrium kinetics of low pressure plasmas in molecular gases, such as nitrogen, oxygen, hydrogen and their mixtures, is an active field of research in order to understand the processes occurring in a variety of modern plasma technologies, and also in the atmosphere and the ionosphere. In particular, the knowledge of the volume and the surface kinetics of active species such as N and O atoms, $N(^2D)$, $O_2(a^1\Delta)$, and $N_2(A^3\Sigma)$ metastables, and NO molecules is important to understand the workings of plasma reactors used for chemical synthesis, air pollution cleaning, or surface treatments of various materials. Such knowledge is also important to understand the reentry heating of the Space Shuttle (surface recombination of O and N atoms) and the emissions near the surface of space vehicles in stationary orbits (surface production of gas phase NO and NO_2 excited molecules). Discharges in $N_2 - H_2$ mixtures are currently employed in plasma chemical treatment of materials and can also be used for the chemical synthesis of such molecules as NH, NH_3, and N_2H_2.

In this paper we survey and discuss the main results of recently developed self-consistent models for bulk and surface kinetic processes in low pressure flowing discharges in $N_2 - O_2$ [1-3] and $N_2 - H_2$ [4] mixtures. Detailed comparisons with experimental data are carried out. These models include a large number of physico-chemical reactions enabling one to determine the concentrations of different neutral and ionic species, excited electronic states, and $N_2(X, v)$ and $H_2(X, v)$ vibrational levels, the density N_e of free electrons, their average kinetic energy and transport properties, the electric field, the average (across the tube) gas temperature and the wall temperature.

KINETIC MODEL FOR BULK PLASMA PROCESSES

The models above referred to are one-dimensional, self-consistent and designed to apply to DC flowing glow discharges and post-discharges. The input parameters are the usual externally controlled ones, that is: pressure p (Torr), radius R (cm) and length L (cm) of the

Electron Kinetics and Application of Glow Discharges
Edited by U. Kortshagen and L. D. Tsendin, Plenum Press, New York, 1998

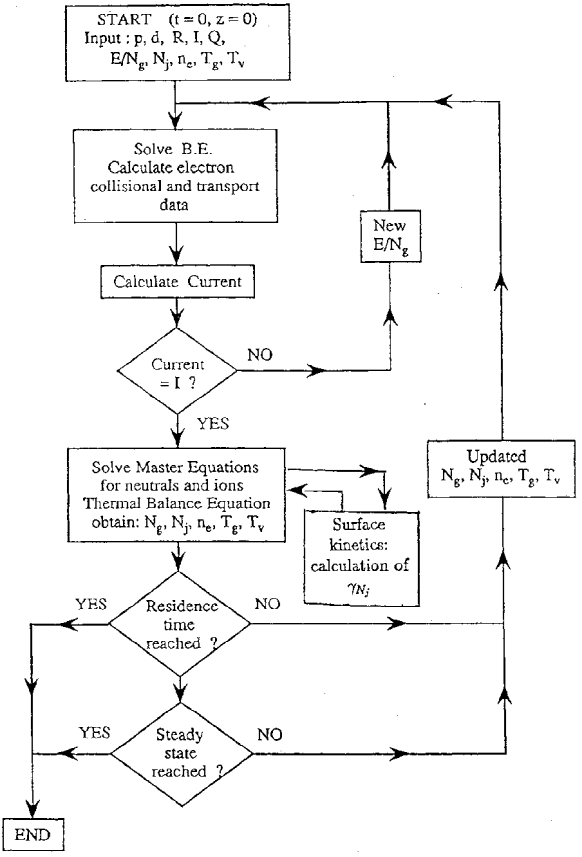

Figure 1. Flow chart of the model.

discharge tube, electric current I (mA), gas flow rate Q (sccm), and initial gas temperature and composition (*i.e.*, the relative oxygen or hydrogen concentration X(%) in a binary mixture with N_2 at the entrance of gas into the discharge zone). The model for $N_2 - O_2$ mixtures gives the possibility to calculate, as a function of the axial coordinate z, the following properties of the bulk plasma: concentrations of N_2, O_2, O_3, NO, N_2O, NO_2, NO_3, N_2O_5 molecules and N, O atoms in the ground electronic states, the populations of electronically excited states $N_2(A^3\Sigma_u^+, B^3\Pi_g, a'^1\Sigma_u^-, a^1\Pi_g, C^3\Pi_u, a''^1\Sigma_g^+)$, $O_2(a^1\Delta_g, b^1\Sigma_g^+)$, $N(^2D, ^2P)$, $O(^1D, ^1S)$, concentration of ions N_2^+, $N_2^+(B)$, N_4^+, O^+, O_2^+, NO^+, O^-, populations of vibrational levels of N_2 molecules in the ground electronic state $X^1\Sigma_g^+$, density of electrons (N_e), their average kinetic $\frac{3}{2}kT_e$ and characteristic energy u_k, electron drift velocity v_d, discharge maintaining electric field E, average gas temperature across the discharge tube, T, and temperature T_w of the tube walls. For $N_2 - H_2$ mixtures, the model predicts the concentrations of N_2, H_2, NH, NH_2, NH_3 molecules and N, H atoms in the electronic ground states, nitrogen ions and excited states as above, an effective high-lying Rydberg state H_2 (R), and ions H_2^+, H_3^+, HN_2^+, H^-, in addition to the same electrical and thermal quantities as for $N_2 - O_2$.

All the above properties are derived from a system of coupled equations for the plasma bulk describing the kinetics of free electrons (homogeneous Boltzmann equation), the vibrational kinetics of N_2 (and H_2) molecules, the kinetics of electronic states of molecules and

Table 1. List of Surface Processes

No.	Process	No.	Process
S1	$N + F_v \rightleftharpoons N_f$	S11	$N + O_S \rightarrow (NO)_S$
S2	$O + F_v \rightleftharpoons O_f$	S12	$N_f + O_S \rightarrow (NO)_S + F$
S3	$N + S_v \rightleftharpoons N_S$	S13	$O + N_S \rightarrow (NO)_S$
S4	$N_f + S_v \rightarrow N_S + F_v$	S14	$O_f + N_S \rightarrow (NO)_S + F$
S5	$N + N_S \rightarrow N_2 + S_v$	S15	$NO + S_v \rightleftharpoons (NO)_S$
S6	$N_f + N_S \rightarrow N_2 + S_v + F_v$	S16	$NO_2 + S_v \rightleftharpoons (NO_2)_S$
S7	$O + S_v \rightleftharpoons O_S$	S17	$(NO)_S + O \rightarrow (NO_2)_S$
S8	$O_f + S_v \rightarrow O_S + F_v$	S18	$(NO)_S + O_f \rightarrow (NO_2)_S + F_v$
S9	$O + O_S \rightarrow O_2 + F_v + S_v$	S19	$NO + O_S \rightarrow (NO_2)_S$
S10	$O_f + O_S \rightarrow O_2 + S_v$		

atoms, the chemical kinetics of heavy neutrals and charged particles, the energy balance of the gas and the charged particle balance determining the maintaining reduced electric field. Empirical formulas have been derived and used for the calculation of the wall temperature T_w. Further, a set of equations for the surface kinetics of *N* and *O* (or *H*) atoms is coupled to the gas phase chemical kinetic equations, which renders the models fully self-consistent.

Figure 1 shows a flow chart of the numerical algorithm used to solve the model equations.

KINETIC MODEL FOR SURFACE PROCESSES

Here, we shall refer only to the model for surface processes in $N_2 - O_2$ mixtures. Details of the model for $N_2 - H_2$, which is quite similar, can be found elsewhere [4]. The basic mechanisms taken into account are the following:

a) Physical adsorption and desorption of *N* and *O* atoms at vacant sites *F*;

b) Chemical adsorption and desorption of both types of atoms and *NO*, NO_2 molecules at vacant chemically active sites *S* on the surface;

c) Surface diffusion of physisorbed N_f and O_f atoms;

d) The reactions of chemisorbed N_S and O_S atoms with gas phase *N*, *O* atoms and *NO* molecules (Eley-Rideal mechanism); and with physisorbed N_f and O_f atoms (Langmuir-Hinshelwood mechanism).

These reactions lead to the formation of gas phase N_2, O_2 and chemisorbed $(NO)_S$, $(NO_2)_S$ molecules. $(NO)_S$ molecules can either be desorbed or react with *O*, O_f to produce $(NO_2)_S$, which by desorption produce gas phase NO_2 molecules. The list of surface processes is given in Table 1.

From the master equations for the surface and gas phase particle concentrations depending on the processes (S1)-(S19), one obtains:

$$\left(\frac{d[N]}{dt}\right)_{wall} = -\frac{\overline{v_N}}{2R}\gamma_N[N] + \frac{2}{R}K'_{-S3}\epsilon\delta\alpha_N, \tag{1}$$

$$\left(\frac{d[O]}{dt}\right)_{wall} = -\frac{\overline{v_O}}{2R}\gamma_O[O] + \frac{2}{R}K'_{-S7}\epsilon\delta\alpha_O, \tag{2}$$

$$\left(\frac{d[NO]}{dt}\right)_{wall} = -\frac{\overline{v_{NO}}}{2R}\gamma_{NO}[NO] + \frac{2}{R}K'_{-S15}\epsilon\delta\alpha_{NO} \tag{3}$$

$$\left(\frac{d[NO_2]}{dt}\right)_{wall} = -\frac{\overline{v_{NO_2}}}{2R}\gamma_{NO_2}[NO_2] + \frac{2}{R}K'_{-S16}\epsilon\delta\alpha_{NO_2}, \tag{4}$$

Herein, the second terms on the right-hand-side describe the surface production of species due to chemical desorption; ϵ is the surface roughness factor; and γ_M is the wall loss probability of the species *M*. For *M* = *N*, *O* this probability is given by, respectively,

$$\gamma_N = \gamma_N^{(1)} + \gamma_N^{(2)} \tag{5}$$

$$\gamma_N^{(1)} = \epsilon\delta(K'_{S3} + K'_{S5}\alpha_N + P_{S4} + P_{S6}\alpha_N); \tag{6}$$

$$\gamma_N^{(2)} = \epsilon\delta(K'_{S11} + P_{S12})\alpha_O \tag{7}$$

$$\gamma_O = \gamma_O^{(1)} + \gamma_O^{(2)} + \gamma_O^{(3)} \tag{8}$$

$$\gamma_O^{(1)} = \epsilon\delta(K'_{S7} + K'_{S9}\alpha_O + P_{S8} + P_{S10}\alpha_O) \tag{9}$$

$$\gamma_O^{(2)} = \epsilon\delta(K'_{S13} + P_{S14})\alpha_N; \quad \gamma_O^{(3)} = \epsilon\delta(K'_{S17} + P_{S18})\alpha_{NO} \tag{10}$$

$$\gamma_{NO} = \epsilon\delta(K'_{S15} + K'_{S19}\alpha_O); \quad \gamma_{NO_2} = \epsilon\delta K'_{S16} \tag{11}$$

The dimensionless probabilities K_j^l and K_j^l for processes involving gas phase species are determined by the following formulas:

$$K'_i = \frac{[S]}{[F]} K_i^0 \exp\left(-\frac{E_i}{T_{gw}}\right); \quad K'_j \equiv P_M = K_M^0 \exp\left(-\frac{E_M^0}{T_{gw}}\right), \tag{12}$$

where *i*=S3,S5,S7,S9,S11,S13,S15,S16,S17,S19; *M* = *N* for *j*=S1, *M* = *O* for *j*=S2. The ratio [*S*]/[*F*] is the fraction of the surface covered by chemically active sites. K_i^0 , K_M^0 are the steric factors; E_i , E_M^0 are the activation energies.

The dimensionless probabilities P_i for surface processes involving physisorbed N_f and O_f atoms (*i*=S4,S6,S8,S10,S12,S14,S18) are determined by the following formulas:

$$P_i = P_M P_i^0 \times [1 + \Psi_M]^{-1} \tag{13}$$

$$P_i^0 = K_{Mi} exp\left(\frac{E_{dM} - E_{DM} - E_i}{T_w}\right); \quad K_{Mi} = \frac{1}{4} K_i^0 \frac{[S]}{[F]} \frac{\nu_{DM}^0}{\nu_{dM}^0} \tag{14}$$

$$\Psi_N = \delta\left(P_{S4}^0 + \alpha_N P_{S6}^0 + \alpha_O P_{S12}^0\right); \tag{15}$$

$$\Psi_O = \delta\left(P_{S8}^0 + \alpha_O P_{S10}^0 + \alpha_N P_{S14}^0 + \alpha_{NO} P_{S18}^0\right) \tag{16}$$

Here, ν_{DM}^0 and E_{DM} , ν_{dM}^0 and E_{dM} are, respectively, the frequency factor and the activation energy for surface diffusion and desorption of species *M*; the factors Ψ_N and Ψ_O describe the influence on the lifetime of N_f and O_f of the surface chemical processes (in addition to desorption).

$$\delta = \frac{1}{(1 + \sum_M \alpha_M)} \tag{17}$$

(with *M* = *N*, *O*, *NO*, NO_2).

The values α_M determine the coverage $\theta_M = \alpha_M \delta$ of chemically active sites by the species *M*:

$$\alpha_N = \frac{(K'_{S3} + P_{S4})\Phi_N}{K'_{-S3} + (K'_{S5} + P_{S6})\Phi_N + (K'_{S13} + P_{S14})\Phi_O} \tag{18}$$

$$\alpha_O = \frac{(K'_{S7} + P_{S8})\Phi_O}{K'_{-S7} + (K'_{S9} + P_{S10})\Phi_O + (K'_{S11} + P_{S12})\Phi_N + K'_{S19}\Phi_{NO}} \tag{19}$$

$$\alpha_{NO} = \frac{(K'_{11} + P_{S12})\alpha_O\Phi_N + (K'_{S13} + P_{S14})\alpha_N\Phi_O + K'_{S15}\Phi_{NO}}{K'_{-S15} + (K'_{S17} + P_{S18})\Phi_O} \tag{20}$$

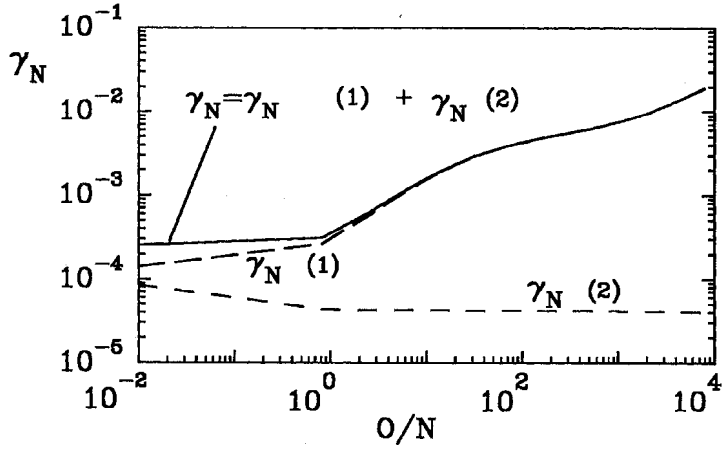

Figure 2. Variation of the probability of wall losses for N atoms *vs.* the ratio $X = [O]/[N]$. $I = 30$ mA. The curves are calculations using the surface reaction model: $\gamma_N^{(1)}$ and $\gamma_N^{(2)}$ are the contributions of the first and the second systems of active sites, respectively, and γ_N is their sum.

$$\alpha_{NO_2} = \frac{(K'_{S17} + P_{S18})\alpha_{NO}\Phi_O + K'_{S19}\alpha_O\Phi_{NO} + K'_{S16}\Phi_{NO_2}}{K'_{-S16}} \tag{21}$$

Here, $\Phi_M(\text{cm}^{-2}\text{sec}^{-1})$ are the fluxes of gas phase atoms or molecules M = N, O, NO, NO_2 to the surface.

Note that the units of K'_{-S3}, K'_{-S7}, K'_{-S15} and K'_{-S16} are $\text{cm}^{-2}\,\text{sec}^{-1}$. These quantities are proportional to the chemical desorption fluxes.

The curves shown on Figures 2 to 4 are calculations from the surface kinetic model of the wall loss probabilities for *N, O, H* atoms, respectively, for the discharge conditions indicated in the captions, using estimated values for the activation energies and parameters $[S]/[F]$, ν^0_{DM}/ν^0_{dM}, K^0_i in equations (12)-(14). Such values have been given in [2,3] for $N_2 - O_2$ discharges and in [4] for $N_2 - H_2$ discharge. The data points on Figure 3 are derived from a fit of the populations predicted from the gas phase kinetic model to the measured ones, using the wall loss probabilities as adjustable parameters. It can be seen that the surface kinetic model provides a satisfactory explanation for the values of these wall loss probabilities.

VIBRATIONAL LEVEL POPULATIONS

Populations of $N_2(X, v)$ Levels

The populations of $N_2(X, v)$ vibrational levels are controlled by the processes:

$$e + N_2(v) \rightleftharpoons e + N_2(w) \quad (v, w \leq 10; |w - v| \leq 8) \quad \text{(e-V processes)} \tag{22}$$

$$N_2(v) + N_2(v') \rightleftharpoons N_2(v-1) + N_2(v'+1) \quad \text{(V-V energy exchanges)} \tag{23}$$

$$N_2(v) + M \rightleftharpoons N_2(v') + M; \quad M = N;\ O;\ H \quad \text{(V-T energy exchanges)} \tag{24}$$

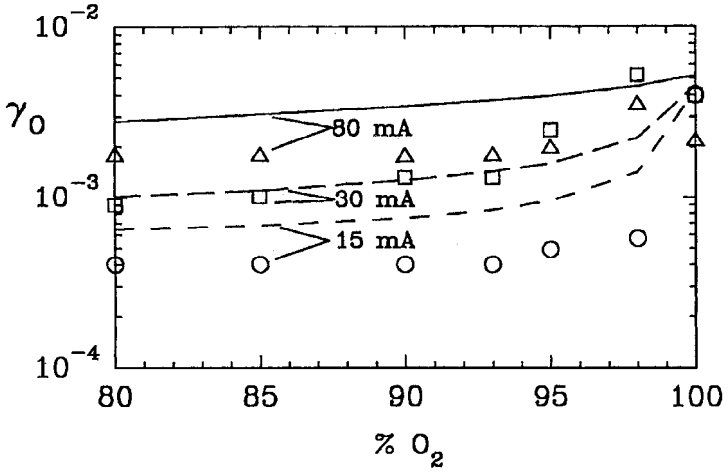

Figure 3. Wall loss probability of *O* atoms in $N_2 - O_2$ discharge *vs.* O_2 percentage, for different currents. Pressure 2 Torr, tube radius 0.8 cm, gas flow rate 100 sccm, distance from gas entrance in discharge 43 cm. Points - from fit to measurements [2]; curves - calculations from surface reaction model.

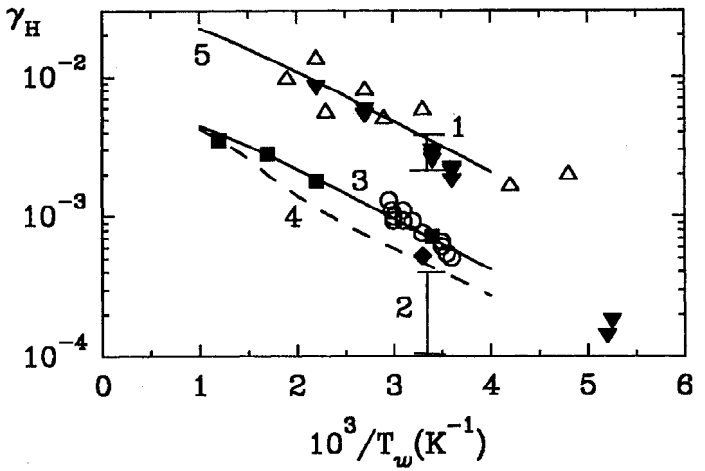

Figure 4. Probability γ_H for wall losses of *H* atoms on pyrex glass as a function of the wall temperature T_w. Points and 1,2 - different experimental data (see [5]); curves 3,4 - calculations for pure $H_2 - H$ system (curve 3) and for $[H]/[N] = 1$ (curve 4). Curve 5 - calculations from present model but for $\in \times [S]/[F]$ five times larger than the value adopted in our model.

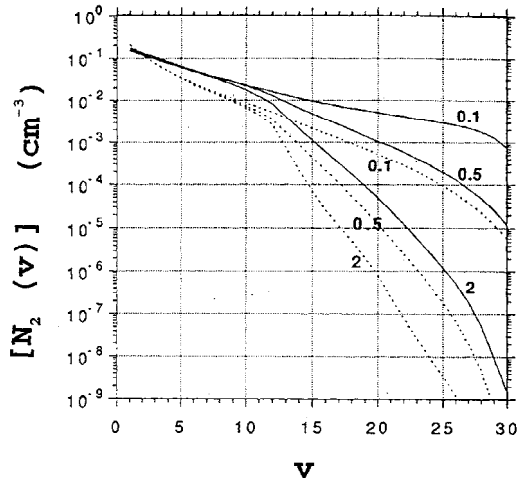

Figure 5. Vibrational distribution of $N_2(X, v)$ molecules calculated for O_2 percentages of 0.1, 0.5 and 2%. Solid and dashed lines are for discharge currents of 80 mA and 30 mA, respectively. The other conditions are the same as in Fig.3

$$N_2(v) + O \rightarrow NO + N \quad \text{(chemical reaction)} \tag{25}$$

$$N + NO \rightarrow N_2(\bar{v} = 3.4) + O \quad \text{(chemical reaction)} \tag{26}$$

Figure 5 shows calculated $N_2(X, v)$ vibrational distributions for various O_2 percentages in $N_2 - O_2$ mixtures. The fast decrease observed in the populations for $v \geq 12$ is due to the chemical reaction (25).

Populations of $O_2(X, v)$ Levels

For the $O_2(v)$ populations it was assumed that

$$T_V^{O_2} \simeq T \tag{27}$$

because the $e - V$ rate coefficients are small and the V-T processes

$$O_2(v) + O \rightleftharpoons O_2(v') + O \tag{28}$$

are very fast.

Populations of $H_2(X, v)$ Levels

Investigation of the H_2 vibrational kinetics is particularly important due to its effects on the H^- concentration through the dissociative attachment reaction

$$e + H_2(v) \rightarrow H + H^- \tag{29}$$

The vibrational populations $H_2(X, v)$ are controlled by the processes:

$$e + H_2(v) \rightleftharpoons e + H_2(w) \quad (v, w \leq 6; |w - v| \leq 3) \quad \text{(e-V processes)} \tag{30}$$

$$H_2(v+1) + N_2(w) \rightleftharpoons H_2(v) + N_2(w+1) \quad \text{(one-quantum V-V' processes)} \tag{31}$$

$$N_2(w+2) + H_2(v) \rightleftharpoons N_2(w) + H_2(v+1) \quad \text{(two-quantum V-V' processes)} \tag{32}$$

$$H_2(v) + H \rightleftharpoons H_2(v-\Delta v) + H; \quad \Delta v \geq 1 \quad \text{(V-T energy exchanges)} \tag{33}$$

$$H_2(B^1\Sigma_u^+) \text{ and } H_2(C^1\Pi_u) \rightarrow H_2(X, v) \quad \text{(cascade processes)} \tag{34}$$

POPULATIONS OF ELECTRONICALLY EXCITED STATES

Metastable $N_2(A^3\Sigma_u^+)$ and $N_2(B^3\Pi_g)$, $N_2(C^3\Pi_u)$ Radiative States

The main processes controlling the $N_2(B)$ population are the following :

$$N_2(B) \rightarrow N_2(A) + h\nu \quad \text{(radiative decay; 1st positive system)} \tag{35}$$

$$e + N_2(X) \rightarrow e + N_2(B) \quad \text{(electron excitation)} \tag{36}$$

$$N_2(B) + N_2(X, v-6) \rightleftharpoons N_2(A) + N_2(X, v) \quad \text{(E-VE exchange)} \tag{37}$$

Deactivation of the $N_2(A)$ + $N_2(B)$ system takes place mainly through the following processes:

$$N_2(A) + \text{wall} \rightarrow N_2(X) \tag{38}$$

$$N_2(A) + N \rightarrow N_2(X) + N(^2P) \tag{39}$$

$$N_2(B) + N_2 \rightarrow N_2(X) = N_2(X) \tag{40}$$

$$N_2(A) + O \rightarrow N_2(X) + O \tag{41}$$

$$N_2(A) + H \rightarrow N_2(X) + H \tag{42}$$

As to the $N_2(C)$ state, the main processes controlling its population are the following:

$$N_2(C) \rightarrow N_2(B) + h\nu \quad \text{(radiative decay; 2nd positive system)} \tag{43}$$

$$e + N_2(X) \rightarrow e + N_2(C) \quad \text{(electron excitation)} \tag{44}$$

$$N_2(A) + N_2(A) \rightarrow N_2(C) + N_2(X) \quad \text{(E-VE exchange)} \tag{45}$$

Metastables $N_2(a'^1\Sigma_u^-)$ and $N_2(a''^1\Sigma_g^+)$

The $N_2(a')$ state plays a very important role in N_2 discharges with a small impurity of O_2 or H_2 due to the associative ionization processes:

$$N_2(a') + N_2(A) \rightarrow e + N_4^+ \tag{46}$$

$$N_2(a') + N_2(a') \rightarrow e + N_2 + N_2^+ \text{ or } e + N_4^+ \tag{47}$$

The main processes controlling the $N_2(a')$ population are the following:

$$e + N_2(X) \rightarrow e + N_2(a') \quad \text{(electron excitation)} \tag{48}$$

$$2N_2(X, v \geq 16) \rightarrow N_2(a') + N_2(X) \tag{49}$$

$$N_2(a') + M \rightleftharpoons N_2(a) + M \tag{50}$$

$$N_2(a') + N_2 \rightarrow N_2(B) + N_2 \tag{51}$$

$$N_2(a') + O_2 \rightarrow N_2(X) + O + O \tag{52}$$

$$N_2(a') + H_2 \rightarrow N_2(X) + H_2 \tag{53}$$

$$N_2(a') + H \rightarrow N_2(X) + H \tag{54}$$

The rate coefficients for processes (46), (47), (54) and the probability for wall losses of $N_2(a')$ have been estimated from our model.

Due to the fast deactivation process

$$N_2(a'') + N_2 \rightarrow N_2(X) + N_2, \tag{55}$$

the $N_2(a'')$ population is small so that stepwise ionization via this state is unimportant.

Radiative Ionic State $N_2^+(B)$

The main processes controlling the $N_2^+(B)$ population are the following:

$$N_2^+(B) \rightarrow N_2^+(X) + h\nu \text{ (radiative decay; 1st negative system)} \tag{56}$$

$$N_2(v \geq 12) + N_2^+(X) \rightarrow N_2(v - 12) + N_2^+(B) \text{ (V-E resonance process)} \tag{57}$$

The importance of processes (57) was first noticed in [6]. This has been confirmed in our work by comparing calculated and measured relative intensities of the 1st negative system versus the O_2 (or H_2) percentage in $N_2 - O_2$ (or $N_2 - H_2$) discharges as shown in Figures 6 and 7.

The fast decrease in the 1st negative system intensity with addition of O_2 (or H_2) is mainly due to a fall down of the pumping via process (57) as the $N_2(v \geq 12)$ populations are quenched through the fast processes

$$N_2(v \geq 12) + O \rightarrow NO + N \text{ for } N_2 - O_2 \text{ discharge} \tag{58}$$

$$N_2(v \geq 12) + H \rightarrow N_2(v' < v) + H \text{ for } N_2 - H_2 \text{ discharge} \tag{59}$$

Radiative State $NO(A)$

The main processes determining the $NO(A)$ population are the following:

$$NO(A) \rightarrow NO(X) + h\nu \text{ (radiative decay; } \gamma \text{ band)} \tag{60}$$

$$N_2(A) + NO(X) \rightarrow N_2(X) + NO(A) \text{ (E-E energy exchange)} \tag{61}$$

The importance of reaction (61) is demonstrated in Figure 8 where a comparison is given of experimental $NO(A)$ relative populations with calculations taking into account either (61) or direct electron excitation

$$e + NO(X) \rightarrow e + NO(A) \text{ (direct electron excitation)} \tag{62}$$

The maximum in $[NO(A)]$ results from the combined effects of an increase in $[NO(X)]$ and a decrease in $[N_2(A)]$ as the O_2 percentage in the mixture grows up.

CHARGED PARTICLE BALANCE AND MAINTAINING FIELD

The main processes determining E/N under the present conditions are the losses of electrons and positive ions by ambipolar diffusion to the wall

$$e; M^+ + \text{wall} \rightarrow M; M = N_2, O_2, H_2, NO, O, H, \tag{63}$$

volume ionization by electron collisions

$$e + M \rightarrow 2e + M^+; M + N_2, O_2, H_2, NO, O, H \tag{64}$$

and the associative ionization processes (46) and (47).

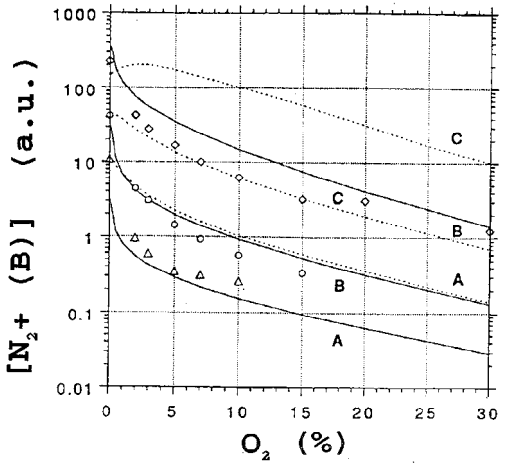

Figure 6. Population of $N_2^+(B)$ state in arbitrary units versus the O_2 percentage for I = 15, 30 and 80 mA. Experimental (points) [1] and theoretical (curves) values were adjusted for pure N_2 and I = 30 mA. The solid and the dashed lines represent calculations with a rate constant $k_v = 10^{-11}$ and $k_v = 10^{-13}$ $cm^3 s^{-1}$, respectively, for all levels $v \geq 12$ in the process (58). The other conditions are the same as in Fig.3.

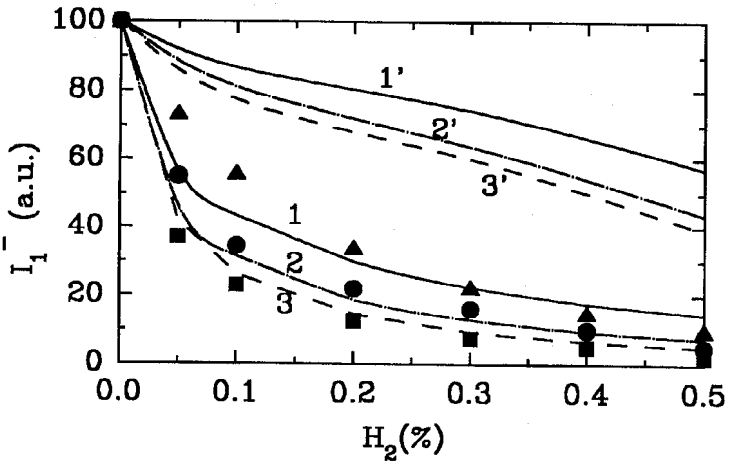

Figure 7. Relative intensity of N_2 1st negative system *versus* H_2 percentage in $N_2 - H_2$ discharge. Measurements [7] are represented by symbols: triangles- 1 Torr; circles - 2 Torr; squares - 3 Torr. Calculations are represented by curves: solid - 1 Torr; chain - 2 Torr; broken - 3 Torr, for two values of the rate coefficient for processes (59): curves 1,2,3 - $k_v \rightarrow 4 \times 10^{-10} (T/300)^{0.5}$ (cm^3/s), asymptotically for $v \geq 23$; curves 1',2',3' - $k_v = 0$. These data are for a distance L = 30 cm from gas entrance in discharge tube, R = 1 cm, Q = 120,340 and 600 sccm, and I = 50 mA.

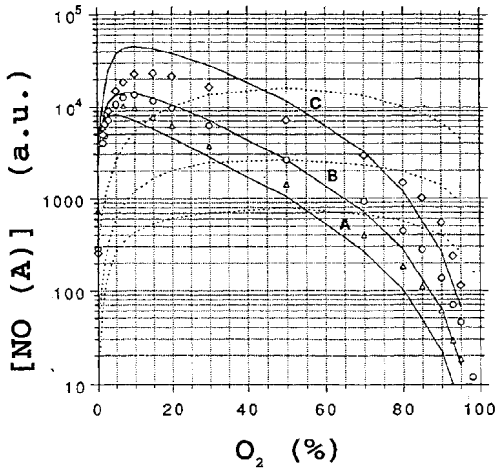

Figure 8. Relative population of $NO(A)$ *versus* O_2 percentage, for I = 15, 30 and 80 mA. Full lines represent the excitation rate of $NO(A)$ by reaction (61) while dashed lines are for direct electron excitation (62). The calculated and experimental values were adjusted for a O_2 percentage of 50% and I = 30 mA. Data points are measurements; triangles: 15 mA; circles: 30 mA and diamonds: 80 mA. Calculations are represented by solid lines. A: 15 mA; B: 30 mA; C: 80 mA. The other conditions are the same as in Fig.3.

Reduced Electric Field E/N in $N_2 - O_2$ Discharge

Figure 9 shows calculated and measured values of the reduced maintaining field in a $N_2 - O_2$ discharge as a function of the O_2 percentage.

The maximum in E/N is related to the importance of associative ionization (46, 47) for very low O_2 percentages. As the latter increases the rate of associative ionization sharply decreases, since the involved excited states $(N_2(X, v \geq 16), N_2(a'))$ are then destroyed by O, O_2, and thus E/N has to rise in order to sustain the discharge. For larger O_2 percentages ($> (5 \div 10)\%$) associative ionization is negligible and the decrease in E/N is due to increased contributions of electron ionization of O, O_2 and NO which have lower ionization thresholds than N_2.

Behavior of E in $N_2 - H_2$ Discharges

Figure 10 shows the relative variation in the maintaining field as a small amount of H_2 is admixed to a N_2 discharge.

The deactivation of upper vibrational $N_2(v \geq 16)$ levels by the process

$$N_2(v) + H \rightarrow N_2(v' < v) + H \tag{65}$$

decreases the pumping of $N_2(a')$ via (49) and, thus, the rate of associative ionization (46), (47). As a result, E has to increase in order to sustain the discharge.

The rate coefficients for processes (46), (47), (49), and (54) could be more accurately determined in present work from the comparison between calculated and experimental E values.

For $X(H_2) > 10\%$, E/N decreases due to the increase in gas density (T decreases due to a higher thermal conductivity) and in the electron ionization rate (due to an enhancement in the EEDF tail).

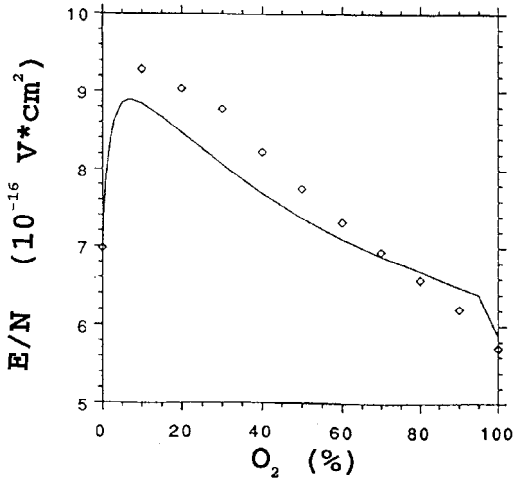

Figure 9. *E/N vs.* O_2 percentage, for *I*=80 mA, *p* = 2 Torr, *Q* = 100 sccm. Points - experiment [1], line - calculations. The other conditions are the same as in Fig.3.

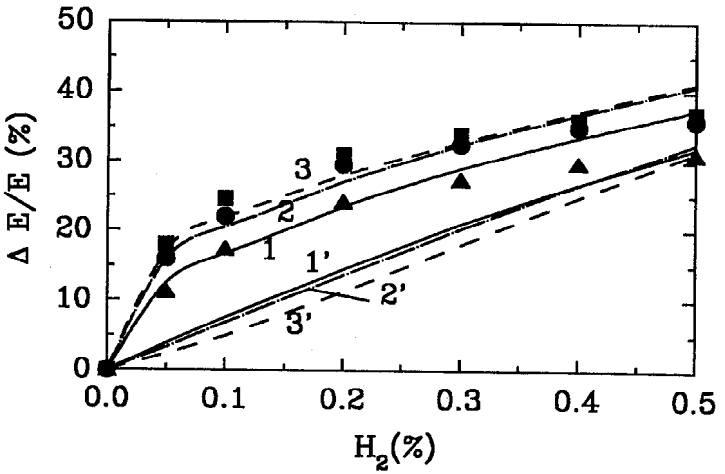

Figure 10. Relative variation of the electric field *E* as a function of H_2 percentage in $N_2 - H_2$ discharge, for *I*=50 mA; *R*=1 cm. Symbols are measurements [7]: triangles - 1 Torr; circles - 2 Torr; squares - 3 Torr. Curves are calculations: solid - 1 Torr; chain - 2 Torr; broken - 3 Torr. Curves 1,2,3 - calculations with process (10), 1',2',3' - without (10). Data shown are for *L* = 30 cm from gas entrance into discharge, flow rates 120, 340 and 600 sccm and pressures 1, 2 and 3 Torr, respectively.

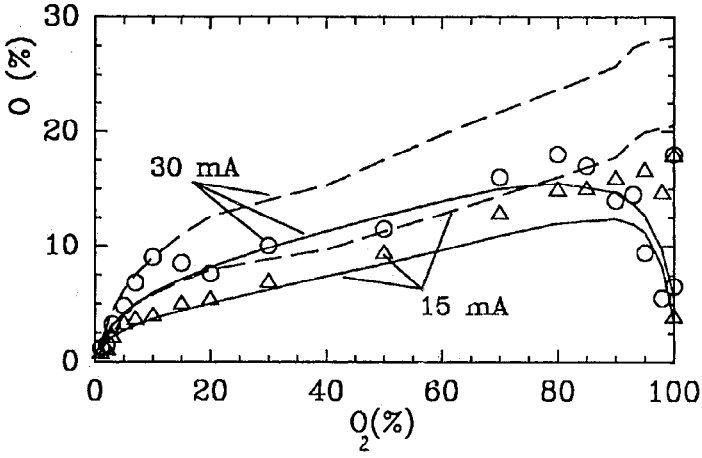

Figure 11. Relative concentration of *O* atoms *versus* O_2 percentage. Data points are measurements [2]. Lines are calculations from the surface reaction model using, respectively, two systems of surface chemically active sites (solid) and only one ordinary system (dotted). The other conditions are the same as in Fig.3.

NEUTRAL PARTICLE POPULATIONS

Discharges in $N_2 - O_2$ Mixtures

Oxygen Atoms. The main processes determining $[O]$ are the following:

$$e + O_2 \rightarrow e + O_2(A, C, c) \rightarrow e + O(^3P) + O(^3P) \tag{66}$$

$$e + O_2 \rightarrow e + O_2(B^3\Sigma_u^-) \rightarrow e + O(^3P) + O(^1D) \tag{67}$$

$$O + \text{wall} \rightarrow \frac{1}{2}O_2 \text{ with } \gamma o \text{ depending on } [O]/[N] \tag{68}$$

$$O + N_2(v \geq 12) \rightarrow NO + N \tag{69}$$

$$N + NO \rightarrow N_2 + O \tag{70}$$

It is to be noted that the rates of processes (69) and (70) nearly balance each other.

Figure 11 shows a comparison of predicted and measured relative concentrations of *O* as a function of the O_2 percentage in a $N_2 - O_2$ discharge.

The increase in [O] as the the amount of O_2 increases is due, first (sharp variation range), to the increase of E/N for small O_2 percentages and, then (smooth variation range), to that of $[O_2]$. For O_2 percentages ≥ 90%, [O] falls down due to an increase in γ_O.

Nitrogen Atoms. The main processes determining $[N]$ are (69), (70) and the following ones:

$$e + N_2 \rightarrow e + 2N \tag{71}$$

$$N + O_2 \rightarrow NO + O \tag{72}$$

$$N + \text{wall} \rightarrow \frac{1}{2}N_2 \text{ or } NO, \text{ with } \gamma_N \text{ depending on } [O]/[N] \tag{73}$$

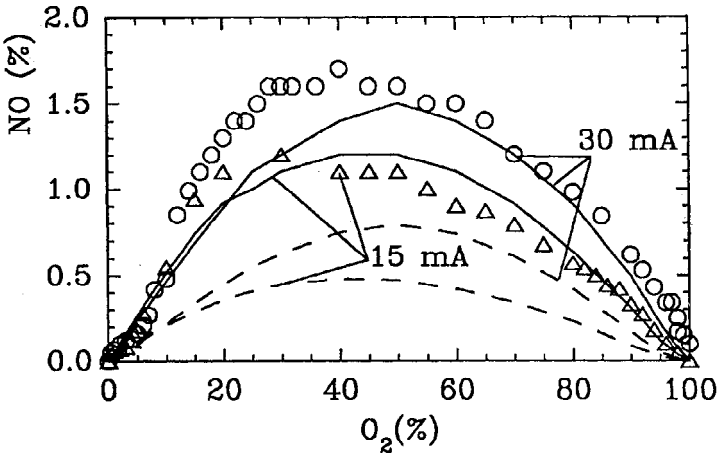

Figure 12. Relative *N* concentration *versus* O_2 percentage. Data points are measurements [1] and lines are calculations. The conditions are the same as in Fig.3.

Figure 12 shows a comparison between predicted and measured relative *N* concentrations as a function of the O_2 percentage.

The maximum of [*N*] at O_2 percentages of ~ 0.5% results from the balance between the increase in the rates of N_2 dissociation (due to the increase in *E*/*N*) and of *N* losses via processes (70) and (72).

Molecules *NO*. The main processes determining [*NO*] are (72)-(75).

Figure 13 shows a comparison between predicted and measured relative *NO* concentrations as a function of the O_2 percentage.

The main reason for the increase in [NO] as $2\% \leq X(O_2) \leq 50\%$ is the decrease in [*N*]. The [NO] decrease for $X(O_2) \geq 50\%$ is due to the decrease in the pumping rate via reaction (69).

It is important to note that agreement with experiment could only be obtained assuming large $\gamma_N = \gamma_N(O/N)$ values.

Discharges in $N_2 - H_2$ Mixtures

Hydrogen and Nitrogen Atoms. The main processes determining [*H*] are the following:

$$e + H_2 \rightarrow e + 2H \tag{74}$$

$$H + \text{wall} \rightarrow \frac{1}{2}H_2 \text{ or } (NH)_S \text{ with } \gamma_H \text{ depending on } [H]/[N] \tag{75}$$

In what concerns [*N*], the main creation and destruction processes are:

$$e + N_2 \rightarrow e + 2N \tag{76}$$

$$e + N \rightleftharpoons e + N(^2D) \tag{77}$$

$$N(^2D) + H_2 \rightarrow NH + H \tag{78}$$

$$N + \text{wall} \rightarrow \frac{1}{2}N_2 \text{ or } (NH)_S \text{ with } \gamma_N \text{ depending on } [H]/[N] \tag{79}$$

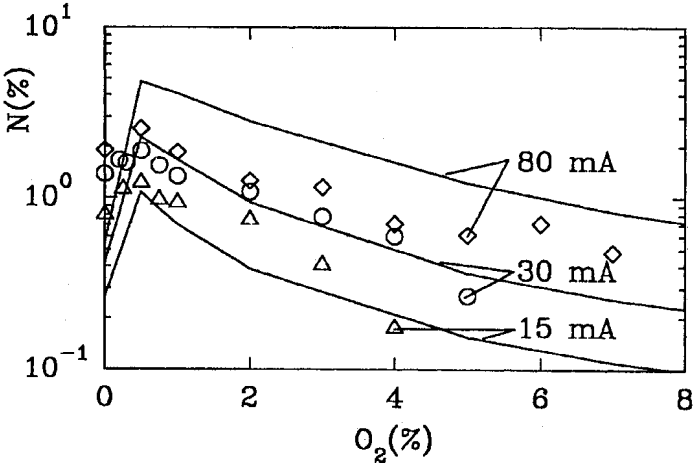

Figure 13. Relative *NO* density *versus* O_2 percentage. Data points are measurements [1,2]. Solid lines are calculations using the surface reaction model. Dotted lines are calculations with small $\gamma_N \leq 10^{-4}$ (only with one system of surface chemically active sites). The other conditions are the same as in Fig.3.

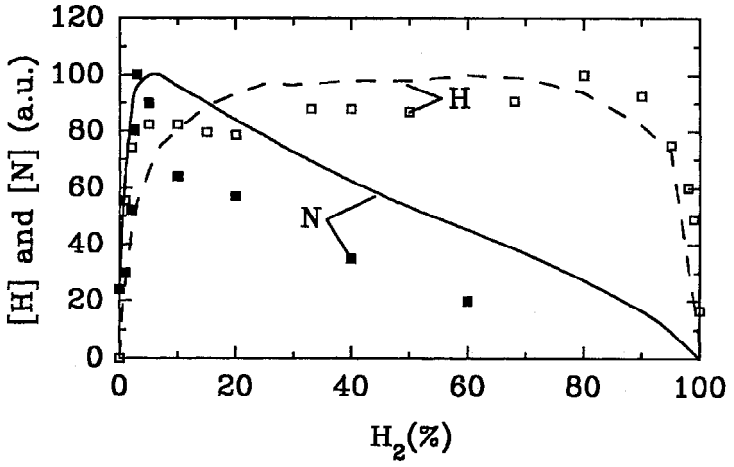

Figure 14. Relative *H* and *N* densities *versus* H_2 percentage in $N_2 - H_2$ post-discharge. Points - measurements [8]; curves - our calculations, for I = 50 mA, R = 0.8 cm, p = 2 Torr, Q = 200 sccm. Measurements and calculations at 20 cm from discharge end. Calculations are normalized to maximum relative experimental values.

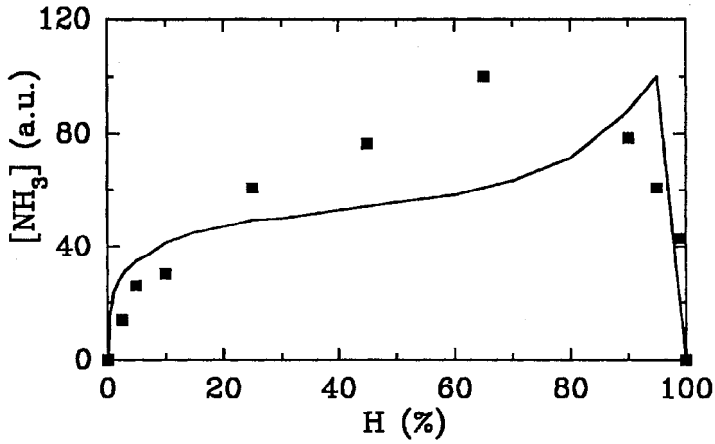

Figure 15. Relative NH_3 density *vs.* H_2 percentage in $N_2 - H_2$ discharge, for I = 50 mA, R = 0.8 cm, p = 2 Torr, Q = 200 sccm. Points - experiment [9]; curves - calculations. Measurements and calculations at 20 cm from discharge end.

Figure 14 shows a comparison between predicted and measured [8] relative concentrations of H and N as a function of the H_2 percentage.

The reasons for the maximum observed in $[N]$ are the maximum in E/N for $X(H_2) \sim 5 \div 10\%$, the decrease in $[N_2]$ and the increase of losses due to processes (77)-(79). Note that the decrease of $[N]$ is quite smooth as compared to the situation observed in $N_2 - O_2$. This is due to the absence, in the present case, of a fast reaction similar to (72) and the fact that γ_N does not increase.

The reason for the fast decrease of $[H]$ for $X(H_2) \geq 80\%$ is an increase in $\gamma_H (H/N)$ by a factor of ~ 2.

Molecules NH_3. The concentration of NH_3 is determined by:

Volume processes:

$$H + NH_2 + M \rightarrow NH_3 + M \tag{80}$$

$$H_2 + NH + M \rightarrow NH_3 + M \tag{81}$$

$$NH_3 + N_2(A) \rightarrow N_2(X) + NH_2 + H \tag{82}$$

$$NH_3 + N(^2D) + M \rightarrow NH_2 + NH \tag{83}$$

Surface processes:

$$H + (NH_2)_S \rightarrow (NH_3)_S \rightarrow NH_3 + S \tag{84}$$

$$H_F + (NH_2)_S \rightarrow F + (NH_3)_S \rightarrow NH_3 + F + S \tag{85}$$

$$NH_2 + (H)_S \rightarrow (NH_3)_S \rightarrow NH_3 + S \tag{86}$$

$$H_2 + (NH)_S \rightarrow (NH_3)_S \rightarrow NH_3 + S \tag{87}$$

Figure 15 shows a comparison between predicted and measured [9] relative NH_3 concentrations in a $N_2 - H_2$ discharge as a function of the H_2 percentage. It is important to

stress that the volume processes for NH_3 production cannot explain the large NH_3 densities ($\sim 10^{12}$ cm^{-3}) measured in low pressure (~2 Torr) $N_2 - H_2$ discharges. The surface processes (84)-(87) play therefore a crucial role in the production of this molecule.

CONCLUSIONS

Self-consistent kinetic models combining volume and surface processes are a new step in the numerical modelling of nonequilibrium plasmas in molecular gases. The developed surface kinetics for dissociated atoms enables one to obtain the dependence of the corresponding wall loss probability γ_M on the relative concentration of gas phase atoms and to explain the changes in γ_M with the composition of the gas mixture.

An important peculiarity of present models is the small number of input parameters – only those externally controlled in real experiments: *R, I, Q* (sccm), *p*, initial gas temperature and composition. This self-consistent approach provides quantitative interpretation of different experiments and an understanding of the role of different processes. It also enables one to estimate or define more accurately some important rate coefficients and parameters. This was achieved in the present work for rate coefficients and parameters determining (see [1]-[4] for details):

– the surface kinetics of *O* and *N* atoms;
– the surface kinetics of *H* and *N* atoms;
– associative ionization of N_2 molecules from $N_2(A, a')$ metastables;
– excitation of $N_2(a')$ from $2N_2(v \geq 16)$;
– deactivation of $N_2(a')$ on walls;
– deactivation of $N_2(a')$ by *H* atoms;
– V-T relaxation of $N_2(X, v)$ molecules by $N_2(X, v) - H$ collisions;
– chemical reaction $N_2(X, v \geq 12) + O \rightarrow NO + N$;
– V-E resonant exchanges via $N_2(X, v \geq 12) + N_2^+(X) \rightarrow N_2(X, v-12) + N_2^+(B)$.

Acknowledgments

This work was supported by the Programme PRAXIS XXI of the Portuguese Ministry of Science and Technology, partly funded by the EU FEDER.

REFERENCES

1. B. Gordiets, C. M. Ferreira, V. Guerra, J. Loureiro, J. Nahorny, D. Pagnon, M. Touzeau, and M. Vialle, Kinetic model of a low-pressure $N_2 - O_2$ flowing glow discharge, *IEEE Trans. Plasma Sci.*, 23:750, 1995.
2. B. Gordiets, C.M. Ferreira, J. Nahorny, D. Pagnon, M. Touzeau, and M. Vialle, Surface kinetics of *N* and *O* atoms in $N_2 - O_2$ discharges, *J. Phys. D: Appl. Phys.*, 29:1021, 1996.
3. B. Gordiets and C. M. Ferreira, Self-consistent modelling of volume and surface processes in air plasma, *AIAA Paper*, N 97-2504, 1997.
4. B. Gordiets, M. Pinheiro, C. M. Ferreira, and A. Ricard, Self-consistent kinetic model for volume and surface processes in low-pressure $N_2 - H_2$ flowing discharges, *J. Phys. D: Appl. Phys.* (in press).
5. J. Lede and J. Villermaux, *J. de Chimie Phys.*, 71:85, 1974.
6. B. Massabieaux, A. Plain, A. Ricard, M. Capitelli, and C. Gorse, Excitation of vibrational and electronic states in a glow discharge column in flowing N_2, *J. Phys. B: Atom. Mol. Phys.*, 16:1863, 1983.
7. S. D. Popa, L. Hochard, and A. Ricard, Production of N_2 radiative states in $N_2 - H_2$ flowing d.c. discharge, *J. Phys. III France*, 7:1331, 1997.
8. J. Amorim, G. Baravian, and A. Ricard, Production of *N, H* and *NH* active species in $N_2 - H_2$ dc flowing discharges, *Plasma Chemistry and Plasma Processing*, 15:721, 1995.
9. J. Amorin, G. Baravian, S. Bockel, A. Ricard, P. Stratil, and G. Sultan, (private communication, to be published).

This Page Intentionally Left Blank

ELECTRON KINETICS IN LOW-VOLTAGE CESIUM-HYDROGEN DISCHARGES

F.G. Baksht, V.G. Ivanov

A.F. Ioffe Physical-Technical Institute, Russia, St.Petersburg, 194021, Polytechnicheskaya 26.

INTRODUCTION

During the past two decades there has been intensive investigation of H^- high current volume-plasma ion sources. In these sources, H^- ions are created in the gas-discharge plasma, mainly due to the dissociative attachment (DA) of thermal electrons to vibrationally excited H_2 $(X^1\Sigma_g^+, v)$ levels [1-3].

Interest in low-voltage (LV) cesium-hydrogen discharge is stimulated by the prospect of utilizing this kind of the discharge as a volume-plasma source of vibrationally excited H_2 molecules and H^- ions. In this paper we shall briefly discuss the results of theoretical investigations of electron-vibration kinetics in Cs-H_2 discharge. In the discharge, the plasma is created by means of a strong ionization of a small cesium additive only, the H_2 vibrational excitation is due to e-v exchange between thermal electrons and H_2 molecules.

The typical potential distribution in a LV discharge is shown in Fig. 1. Here $q\varphi$ is an electron potential energy, φ_1 and φ_2 are the near-electrode voltage drops in narrow Langmuir sheaths.. The typical parameters of the discharge are as follows: interelectrode distance $L \sim$ several mm, molecular hydrogen concentration N_{H_2} $(10^{15}$-$10^{17})\mathrm{cm}^{-3}$; whole cesium concentration $N_{Cs}^{(0)} \sim 10^{14}\mathrm{cm}^{-3}$; thermal electron concentration $n_e < 10^{14}\mathrm{cm}^{-3}$; cathode voltage drop $\varphi_1 < E_d/q$, where $E_d \approx 8.8$ eV is the threshold of H_2 direct dissociation by electron impact.

Two limit modes of LV discharge are essential for further theoretical discussion. The first mode is the discharge in a dense, collisional plasma, where the paths of the beam and thermal electrons are smaller than the gap and the length of the beam energy relaxation due to pair collisions is also less than the gap. In this kind of the LV discharge the fast (beam) electrons and slow (thermal) electrons have a common distribution function (DF), which is the Maxwellian one. In this discharge, the plasma heating mechanism is the pair Coulomb collisions: the energy of a cathode beam is transfered by pair Coulomb collisions from fast electrons to thermal ones.

The second mode is so called Knudsen discharge, where the free paths of beam electrons and their Maxwellization length are greater than the gap. Therefore, the DF of fast electrons is non-Maxwellian. In this kind of the LV discharge, the plasma

Electron Kinetics and Application of Glow Discharges
Edited by U. Kortshagen and L. D. Tsendin, Plenum Press, New York, 1998

heating mechanism is the collisional damping of Langmuir waves, excited by plasma-beam interaction. Usually, this heating mechanism is preferable for the creation of the thermal electron temperature T_e, which is needed for H_2 vibrational excitation and H^- generation by means of DA [3]. In the Knudsen discharge, the needed T_e value may be achieved at a lower cathode emission current density j_1 than in a dense plasma.

CATHODE BEAM RELAXATION IN A DENSE PLASMA OF CESIUM-HYDROGEN DISCHARGE.

The typical hierarchy of the characteristic lengths in near-cathode layer of LV discharge is a follows: $L_0 << l_1 << L_\epsilon << L$. Here L_0 is the thickness of the Langmuir sheath, $l_1 \equiv v_1\tau_p$ is the free path of fast electrons in molecular hydrogen gas, $L_\varepsilon^{(ee)} \equiv \sqrt{D_1\tau_\varepsilon^{(ee)}}$ is the fast electron energy relaxation length due to collisions between fast and slow electrons, i.e. the length of beam Maxwellization, L is the interelectrode distance, τ_p is the momentum relaxation time; $D_1 = \frac{1}{3}l_1v_1$ is the diffusion coefficient of fast electrons and $\tau_\varepsilon^{(ee)} = \varepsilon_1^2/2\pi q^4 v_1 n_e \Lambda$ is the energy relaxation time for electron-electron (ee) collisions, $\varepsilon_1 = m_e v_1^2/2$ is the fast electron energy, n_e is the slow electron concentration, Λ is the Coulomb logarithm and q is the absolute electron charge. In the near-electrode layer of a weakly ionized molecular gas plasma, the energy relaxation of fast electrons occurs not only due to collisions between fast and thermal electrons but also due to the electron-vibration (e-v) and partly to electron-rotation (e-r) and electron-translation (e-t) exchanges. An important feature of these collisions is the fulfillment of the inequality $\tau_\varepsilon^* >> \tau_p$, where τ_ε^* is the respective total energy relaxation time. As a result, the fast electron DF is approximately spherically symmetric during the energy relaxation. The kinetic equation for electron DF of fast electrons has the form

$$-D_1\frac{\partial^2 f_0}{\partial x^2} = I_{ee}\{f_0\} + I_{ev}\{f_0\} + I_{er}\{f_0\} + I_{et}\{f_0\}, \qquad (1)$$

where $f_0(w, x)$ is a spherical part of the fast electron DF in a velocity space. Here the DF is defined as the function of the total electron energy $w = \varepsilon + q\varphi$, the zero potential being at the cathode surface (see Fig. 1). In (1) the collision terms correspond to electron-electron (e-e), electron-vibration (e-v), electron-rotation (e-r) and electron-translation (e-t) exchange. These terms are expressed in the following manner. I_{ee}, I_{er} and I_{et} collision terms are written in the Fokker-Planck approximation as

$$I\{f_0\} = \frac{\varepsilon_1}{\tau_\varepsilon(\varepsilon_1)}\left[\frac{\partial f_0(w,x)}{\partial w} + T_{eff}\frac{\partial^2 f_0(w,x)}{\partial w^2}\right] \qquad (2)$$

Here $T_{eff} = T_e$ and $\tau_\varepsilon = \tau_\varepsilon^{(ee)}$ - for e-e Coulomb collisions; $T_{eff} = T$ and $\tau_\varepsilon = \tau_\varepsilon^{(et)} \equiv (l_1/v_1)(M/2m_e)$ for e-t collisions with heavy particles, M and T being the mass and the translation temperature of heavy particles. $T_{eff} = T_r$ and

$$\tau_\varepsilon = \tau_\varepsilon^{(er)} \equiv \left[\frac{v_1 N_{H_2}}{\varepsilon_1 T_r}\left\langle\sigma_{j,j+2}(\varepsilon_1)(\Delta E_{j,j+2})^2\right\rangle\right]^{-1} \qquad (3)$$

are the rotational temperature of H_2 molecules and the energy relaxation time for e-r exchange [4]. In (3) N_{H_2} is the molecular hydrogen concentration, $T_r \sim T$ is the rotational temperature, $\sigma_{j,j+2}$ is the cross-section of H_2 rotational excitation, $E_{j,j+2}$ is the corresponding energy difference between rotational H_2 levels, symbol <...> denotes the average value over all rotational levels.

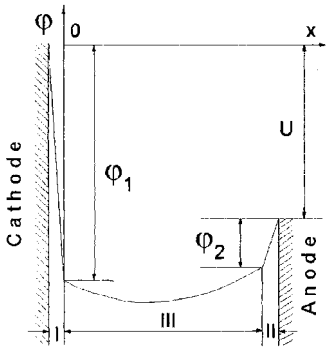

Figure 1.

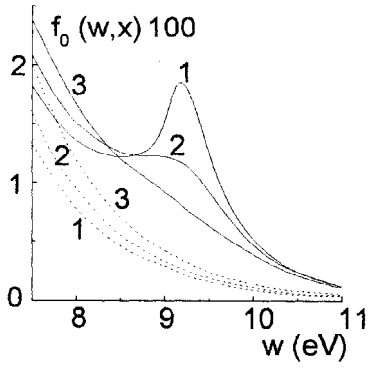

Figure 2.

Figure 1. Potential distribution in low voltage discharge. Near-electrode Langmuir layers (regions I and II) and quasi-neutral plasma (region III).

Figure 2. Fast electron energy distribution function (full curves) and the Maxwellian one (broken curves) at various distances from the emitter: x = 0 (curve 1), x = 0.1 $L_\varepsilon^{(ee)}$ (curve 2), x = 0.25 $L_\varepsilon^{(ee)}$ (curve 3). Cathode emission current j_1 = 30 A/cm². Plasma parameters in the near-electrode layer: p_{H_2} = 10 Torr, $T_1 = T$ = 0.15eV, $n_e / N_{H_2} = 2 \cdot 10^{-2}$, $L_\varepsilon^{(ee)}$ = 0.025cm, $q\varphi_1$ = 9eV, ς = 2. Broken curves correspond to the Maxwellian energy distribution function at the respective distance from the emitter.

Now we shall consider the collision term I_{ev}, which corresponds to e-v exchange. The variation of the electron DF due to e-v exchange is caused only by interaction of fast electrons with low vibrational levels, which populations are sufficiently high. These levels may be considered in harmonic approximation and may be described approximately by means of Boltzmann distribution with vibrational temperature T_v. If $\varepsilon_1 >> \hbar\omega$, the corresponding I_{ev} term may be written as

$$I_{ev}\{f_0\} = -1/\tau_{ev}\{f_0(w,x) - f_0(w+\hbar\omega, x) + \exp(-\hbar\omega/T_v)[f_0(w,x) - f_0(w-\hbar\omega, x)]\}, \quad (4)$$

where $1/\tau_{ev} = v_1 N_{H_2} < \sigma_{v,v+1}(\mathcal{E}_1) >$, symbol <...> denotes the average value over all electron-vibrational excitations $(\sigma_{v,v+1} = (v+1)\sigma_{01}$ [5]). In (4) the 1-st term corresponds $v \to v+1$ molecule excitation and $\varepsilon \to \varepsilon - \hbar\omega$ electron transition, the 4-th term corresponds to reverse transition $(v+1 \to v, \varepsilon - \hbar\omega \to \varepsilon)$; the 2-nd term corresponds to $(v \to v+1, \varepsilon + \hbar\omega \to \varepsilon)$ transition, and the 3-rd term - to reverse process ($v + 1 \to v, \varepsilon \to \varepsilon + \hbar\omega$).

The boundary conditions for equation (1) on the cathode-plasma boundary are written in the form

$$-D_1 \frac{\partial f_0(w,x)}{\partial x}\Big|_{x=0} = j_1 \frac{w}{T_1^2} \exp(-w/T_1) - w/(4\mathcal{E}_1) \cdot v_1 f_0(w,0), (w \geq 0) \quad (5)$$

$$\frac{\partial f_0(w,x)}{\partial x}\Big|_{x=0} = 0, (w \leq 0) \quad (6)$$

where T_1 and T_e are the cathode temperature and the thermal electron temperature in the near-cathode region of plasma, $\varepsilon_1 = q\,\varphi_1$.

The mathematical solution of the problem and the main results concerning the near-electrode layers of a weakly ionized hydrogen plasma are described in [6-14]. The typical calculated fast electron DF is shown in Fig.2 [4]. Calculations are performed for near-electrode plasma parameters, that are usual for the near-cathode layer of a LV Cs-H_2 discharge, at various distances from the emitter: the results are given in dimensionless units. The near-electrode layer was taken to be inhomogeneous with a linear dependence of the slow electron concentration n_e on the distance x from the cathode sheath-plasma boundary. The parameters correspond to the plasma-sheath boundary, T_1 and T being the emitter and heavy particle temperatures. The parameter ζ denotes the value

$$\zeta = \frac{L_\varepsilon^{(ee)}}{n_e} \frac{dn_e(x)}{dx} \Big|_{x=0}$$

The broken curves correspond to the Maxwellian electron DF $f_M(w)$. The fast cathode beam relaxation in the near-cathode layer of quasi-neutral plasma of a LV Cs-H_2 discharge is largely due to e-e collisions, the corresponding relaxation length $L_\varepsilon^{(ee)}$ being about 10^{-2} cm.

Because of quick energy relaxation of fast electron DF in the near-electrode layer of LV cesium-hydrogen discharge, it may be usually proposed that all the electrons have a Maxwellian DF in the main part of the gap of LV Cs-H_2 discharge.

One of the significant results of the calculations is presented in Fig.3, which shows the energy transformation coefficients α_i , which are the proportions of energy transferred from the cathode beam to the various degrees of freedom of molecular hydrogen [14] The curves labelled 4 are very important because they correspond to the electron heating due to pair Coulomb collisions between fast and slow electrons. It is very significant that the e-e collisions (e-e exchange) dominate in LV Cs-H_2 discharges, where $\varphi_1 < 8.8$ V and $n_e / N_{H_2} > 10^{-3}$., This means that nearly the total beam energy is transfered to slow plasma electrons. Thus, in the near-cathode layer the total beam current and nearly the total beam energy are transferred to the core of the Maxwellian electron DF. This current and energy are transferred further along the gap via the respective current and energy fluxes, which can be described by a set of hydrodynamic plasma equations.

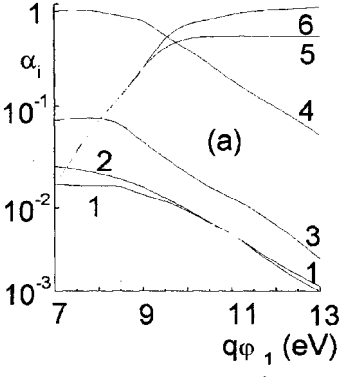

Figure 3a.

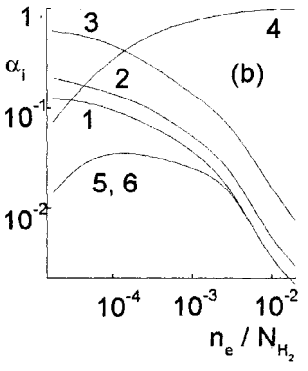

Figure 3b.

Figure 3. Coefficients of energy transformation — the proportions of energy lost by the cathode beam through various collisional mechanisms: e-t exchange (curves 1, e-r exchange (curves 2), e-v

exchange (curves 3), e-e exchange (curves 4), direct H_2 dissociation due to $b^3\Sigma_u^+$ excitation (curves 5), total energy losses due to excitation of $b^3\Sigma_u^+$, $B^1\Sigma_u^+$, $c^3\Pi_u$, $e^3\Sigma_g^+$, $a^3\Sigma_g^+$ states (curves 6). p_{H_2} = 10 Torr, T_e = 1 eV, T = 0.1 eV. (a) Dependence on the cathode voltage drop ($n_e/N_{H_2} = 1.2\cdot10^{-3}$). (b) Dependence on the degree of ionization (φ_1 = 7 V).

THE ELECTRON FLOW AND THE KINETIC REFLECTION COEFFICIENTS AT THE PLASMA-ELECTRODE INTERFACE

Having calculated $f_0(w, x)$, we can find the electron current

$$j = -qD_1 \int_0^\infty \frac{\partial f_0(w,x)}{\partial x}\Big|_{x=0} dw \tag{7}$$

at the plasma boundary. Since the equation (1) and the boundary conditions (5) and (6) are linear with respect to $f_0(w, x)$, we can find the solution in the form of the sum of $f_M(w)$ and two other components: $f_1(w,x)$ and $f_2(w,x)$:

$$f_0(w,x) = f_M(w) + f_1(w,x) - f_2(w,x). \tag{8}$$

Each of component f_1 and f_2 satisfies equation (1) with boundary condition (6) at x=0. The other boundary condition has the form:

$$-D_1\frac{\partial f_1(w,x)}{\partial x}\Big|_{x=0} = \frac{j_1}{q}\frac{w}{T_1^2}\exp\left(-\frac{w}{T_1}\right) - \frac{w}{4\varepsilon_1}v_1 f_1(w,0) \tag{9}$$

$$-D_1\frac{\partial f_2(w,x)}{\partial x}\Big|_{x=0} = \frac{j_{T_e}}{q}\frac{w}{T_e^2}\exp\left(-\frac{w}{T_e}\right) - \frac{w}{4\varepsilon_1}v_1 f_2(w,0) \tag{10}$$

where j_1 and

$$j_{T_e} = \frac{1}{4}qn_e(0)\bar{v}_e\exp(-\varepsilon_1/T_e) \tag{11}$$

are the cathode emission current density and the equilibrium emission current density from plasma to the electrode, $n_e(0)$ is the electron concentration at the electrode-plasma boundary. In (8) the term $f_1(w, x)$ describes the increase of fast electron DF due to the injection of fast electrons from electrode to plasma. The term $f_2(w, x)$ describes the decrease of fast electron DF because of the emission of the fast electrons from plasma to electrode. Substituting (8) in (7) and using (9) and (10), the electron current at the electrode-plasma boundary can be represented in the form of the difference

$$j = j_1(1 - r_1) - j_{T_e}(1 - r_2), \tag{12}$$

where

$$j_1(1 - r_1) \equiv -qD_1 \int_0^\infty \frac{\partial f_1(w,x)}{\partial x} dw \tag{13}$$

$$j_{T_e}(1 - r_2) \equiv -qD_1 \int_0^\infty \frac{\partial f_2(w,x)}{\partial x} dw \tag{14}$$

Here r_1 and r_2 are so called kinetic coefficients of reflection for cathode emission and for the electron emission from plasma to the electrode[6,9].

The kinetic coefficients of reflection satisfy the inequalities: $0 < r_1 < 1$ and $0 < r_2 < 1$. The physical meaning of the coefficients r_1 and r_2 is as follows. If $\tau_\varepsilon^* >> \tau_p$, both the thermal electron emission from plasma, which really reaches the electrode surface, and electrode emission, which really penetrates into the plasma, are depleted as compared with j_{T_e} and j_1. The depletion of thermoemission current from plasma to cathode, which is described by r_2, is caused by the escape of fast electrons from plasma and by the corresponding diminution of fast electron DF in comparison with equilibrium one in near-electrode plasma layer. The range of values of electron kinetic energy ε and coordinate x, in which the number of fast electrons is less than equilibrium one, is shown qualitatively in Fig. 4.

The depletion of the effective current from cathode to plasma in comparison with cathode emission current j_1 is caused by the return of the part of the fast electrons, injected from cathode to plasma, back to the cathode surface due to the frequent momentum relaxation in near-cathode plasma layer.

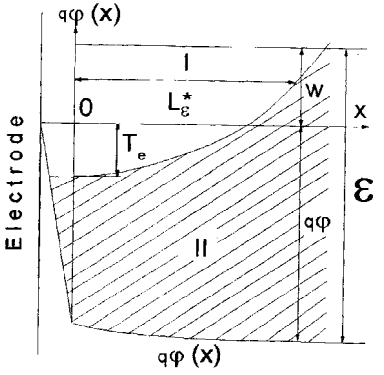

Figure 4.

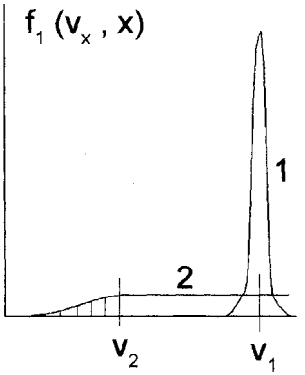

Figure 5.

Figure 4. Range of values of ε and x, in which the distribution function $f_2(w, x)$ differs appreciably from the Maxwell-Boltzmann distribution (I). L_ε^* is the distance, at which energy of the order of T_e has been lost. The hatched part of the diagram (II) corresponds to undisturbed distribution. $w = \varepsilon + q\varphi$.
Figure 5. Cathode beam relaxation in a Knudsen LV discharge. Beam electron distribution function at the cathode-plasma boundary $f_1(v_x, 0)$ (curve 1) and after completion of the plasma-beam interaction $f_1(v_x, \infty)$ (curve 2). The hatched part of the electron DF corresponds to the beam electrons captured into the potential well. $v_1 = \sqrt{2q\varphi_1/m_e}$, $v_2 = \sqrt{2q\varphi_2/m_e}$.

If the main mechanism of the fast electron energy relaxation is the e-e Coulomb collisions in near-electrode layer, the coefficients r_1 and r_2 are the functions of the cathode temperature T_1 and thermal electron temperature T_e : $r_1 = r_1(T_1, T_e)$, $r_2 = r_2(T_e)$. These coefficients satisfy the relation: $r_2(T_e) = r_1(T_e, T_e)$, which is the consequence of the principle of detailed balance: the right side of (12) is equal to zero, if thermodynamical equilibrium exists between the cathode and the plasma, i.e. if $T_1 = T_e$ and $j_1 = j_{T_e}$.

In the limit cases, where $1 - r_1 << 1$ or $r_1 << 1$, the following expressions are valid [6]

$$1 - r_1 = 4/3 \cdot (\varepsilon_1/T_1)^{3/2} \cdot \left(l_1/L_\varepsilon^{(ee)}\right), \qquad (1 - r_1 << 1) \tag{15}$$

$$r_1(T_1, T_e) = (8/\pi) \cdot (T_1/\varepsilon_1)^{3/2} \cdot \left(L_\varepsilon^{(ee)}/l_1\right) \cdot \Psi(T_e/T_1), \qquad (r_1 << 1) \tag{16}$$

where $\Psi(\tau)$ was calculated in [6], $\Psi(1) = 1$. The intermediate case, when $r_1 \sim 1$, is considered in [12], the main results being summarized in [6].

If the degree of ionization is small enough (see Fig. 3b) and the e-v exchange is the main mechanism of the fast electron energy relaxation in plasma, the results are more complicated. Here we shall consider only the expression of $1 - r_1$ in the limiting case, where $1 - r_1 << 1$:

$$1 - r_1 = \frac{4}{3}\frac{l_1}{L_{ev}}\frac{\varepsilon_1}{T_1}\sqrt{[1 - \exp(-\hbar\omega/T_1)] \cdot [1 - \exp(-\hbar\omega/T_v)]} \tag{17}$$

and the expression of r_2 in the limiting case, where $r_2 << 1$

$$r_2 = 8/\pi \cdot \left[(L_{ev}/l_1) \cdot T_e^{3/2} \cdot T_v^{1/2}/(\varepsilon_1\hbar\omega)\right] \cdot \chi(\hbar\omega/T_v) \tag{18}$$

where $L_{ev} = (D_1\tau_{ev})^{1/2}$, $\chi(z)$ is calculated in [6]. $\chi(0) = 1$. If $\hbar\omega << T_1$ and $\hbar\omega << T_v$, the expression (17) leads to

$$1 - r_1 = 4/3(\varepsilon_1/T_1)^{3/2}\left(l_1/L_\varepsilon^{(ev)}\right) \tag{19}$$

and the expression (18) leads to

$$r_2 = 8/\pi \cdot \left(L_\varepsilon^{(ev)}/l_1\right)(T_e/\varepsilon_1)^{3/2} \tag{20}$$

Here $L_\varepsilon^{(ev)} = \left(D_1\tau_\varepsilon^{(ev)}\right)^{1/2}$ and $\tau_\varepsilon^{(ee)}$ is the energy relaxation time for e-v exchange:

$$\tau_\varepsilon^{(ev)} = \left[\frac{v_1 N_{H_2}}{\varepsilon_1 T_v}(\hbar\omega)^2 \langle\sigma_{v,v+1}(\varepsilon_1)\rangle\right]^{-1} \tag{21}$$

(compare with $\tau_\varepsilon^{(er)}$ relaxation time in (3)). Of course, the expressions (19) and (20) are absolutely identical with (15) and (16), $\tau_\varepsilon^{(er)}$ being substituted by $\tau_\varepsilon^{(ev)}$ and T_1 being substituted by T_e in (16). As it was mentioned above, if an electron beam is injected into plasma from cathode, than an excess of fast electrons with an energy of the order of the height of the potential barrier, $q\varphi_1$, forms near the cathode. If the atomic, i.e. cesium, ionization or excitation energy is close to $q\varphi_1$, the excitation or ionization processes are accelerated as a result of an increase of inelastic collisions of the first kind. This phenomenon was discussed in [6,7,15], where the review of the problem was made.

CATHODE BEAM RELAXATION IN THE KNUDSEN PLASMA OF CESIUM-HYDROGEN DISCHARGE

It was mentioned above that the Maxwellization length of fast (cathode beam) electrons in the Knudsen LV discharge is greater than the interelectrode distance L. Therefore, thermal electrons, captured into the potential well, cannot be heated by means of pair Coulomb collisions between them and fast electrons. The details of the thermal electron heating mechanism in a Knudsen LV discharge and its mathematical modelling were described in [16-20]. It was shown that the process of cathode beam relaxation can be described by a quasi-linear theory [21-23]. A quantitative comparison [16-20] showed good agreement between experimental results and theoretical calculations made with one-dimensional quasi-linear equations

$$v_x\frac{\partial f_1(v_x, x)}{\partial x} = \frac{\partial}{\partial v_x}\left(\tilde{D}\frac{\partial f_1(v_x, x)}{\partial v_x}\right) \tag{22}$$

$$\frac{3v_{T_e}^2}{v_x}\frac{\partial\tilde{N}(\omega_p/v_x)}{\partial x} = 2\gamma\tilde{N}(\omega_p/v_x, x) \tag{23}$$

Here $f_1(v_x,x)$ and $\tilde{N}(k_x,x)$ are the one-dimensional distribution function of the cathode beam electrons and Langmuir plasmons[22], k is the plasmon wavevector, $\tilde{D} = \hbar\omega_p^2\tilde{N}(\omega_p/v_x,x)/2m_en_ev_x$ is the quasi-linear diffusion coefficient. The increment 2γ is equal to

$$2\gamma = 2\tilde{\gamma} - 2\gamma_{coll} \equiv \pi\frac{\omega_p}{n_e}v_x^2\frac{\partial f_1(v_x,x)}{\partial v_x} - \frac{\langle v^2/\tau_p(v)\rangle}{3v_{T_e}^2} \tag{24}$$

Here $2\tilde{\gamma}$ and $2\gamma_{coll}$ are the quasi-linear increment and the collisional decrement which occurs due to the collisions between thermal electrons and heavy particles. Averaging in (24) was made over the Maxwellian electron DF of thermal electrons and $v_{T_e} = \sqrt{T_e/m_e}$.

Equations (22) and (23) lead to the energy conservation law:

$$S_1(0) = S_1(x) + \tilde{S}(x) + \Delta S(x), \tag{25}$$

where $S_1(0)$ is the initial energy flux of fast (beam) electrons, $S_1(x)$ and $\tilde{S}(x)$ are the energy fluxes of electrons and plasmons at a distance x from the cathode surface, and $\Delta S(x)$ is the energy transmitted from the Langmuir waves to thermal electrons by means of collisional damping of the waves:

$$\Delta S(x) = 2\gamma_{coll}\hbar\omega_p\int_0^x dx'\int\tilde{N}(k_x,x')\frac{dk_x}{2\pi} \tag{26}$$

We can introduce the energy transformation coefficient, which would be equal to the energy lost by the beam due to the Langmuir wave excitation:

$$\alpha(x) = (S_1(0) - S_1(x))/S_1(0) \tag{27}$$

The following hierarchy of lengths usually takes place in a LV Knudsen Cs-H_2 discharge: $\tilde{L} \le L_{coll} < L$. Here $\tilde{L} = r_{de}qn_ev_{T_e}/I_1$ is the length of quasi-linear relaxation [22] ($\tilde{L} \cong 10^{-2}$cm), $r_{de} = (T_e/(4\pi n_e q^2))^{1/2}$ is the Debye radius, $L_{coll} = 3v_{T_e}^2/2v_1\gamma_{coll}$ is the length of the collisional Langmuir wave damping, I_1 is the cathode emission current. Because $\tilde{L} < L$, the asymptotic form of the beam electron DF $f_1(v_x,\infty)$ is achieved in the gap at a distance $x > \tilde{L}$. The corresponding asymptotic value $\alpha_0 \equiv \alpha(\infty)$ is equal to the share of initial beam energy that was transmitted from the cathode beam to the Langmuir waves. This energy is eventually transmitted to slow electrons largely because of the collisional wave damping or via several other mechanisms [16-20,24-27]. The DF of fast electrons is depicted qualitatively in Fig. 5. Here curve 1 is the initial beam electron DF $f_1(v_x,0)$ at the plasma-cathode sheath boundary, curve 2 is the beam electron DF $f_1(v_x,\infty)$ after the quasi-liner relaxation was completed. The results of $\alpha(x)$ calculations are shown in Fig.6 20, where is the collisional frequency divided by the quasi-liner increment $\Theta = 2\gamma_{coll}/(\pi\omega_p n_1/n_e)$. Because of the comparatively small value of $\Theta(0 < \Theta < 0.2)$ a large proportion of the initial beam energy is transmitted to thermal electrons via the Langmuir wave excitation and their subswquent damping in the plasma.

In addition, the thermal electrons are heated because of the fast electron capture into the potential well. The beam electron DF that corresponds to the captured electrons is shown hatched in Fig. 5, where $v_2 = (2q\varphi_2/m_e)^{1/2}$ and φ_2 is the near-anode potential drop. The corresponding energy transformation coefficient is equal to $\alpha_1 = S_1/S_e(0)$, where S_1 is the energy flux transported by the beam electrons which are captured into the potential well.

CALCULATION OF LOW-VOLTAGE Cs-H_2 DISCHARGE PARAMETERS AND COMPARISON OF THEORY AND EXPERIMENT

In the LV Cs-H_2 discharge, the heated thermal electrons carry out three function in one discharge volume: they ionize Cs atoms, vibrationally excite H_2 molecules and create H^- ions due to DA to rovibrationally excited H_2 molecules, as it was mentioned previously. According to the theoretical calculations [3] and many experimental investigations, the electron temperature $T_e \approx 1$ eV should be attained in the hydrogen plasma for the maximum rate of DA. It is significant that, according to the theoretical predictions, just the same T_e value may be really obtained in a LV Cs-H_2 discharge. The theory of a LV Cs-H_2 discharge in a dense plasma was created in [28-31] . A review of the main theoretical and experimental works is presented in [32] . For the calculation of low-voltage Cs-H_2 dense plasma discharge parameters, the set of hydrodynamic equations was solved with the balance equations to determine the populations $N_v(x)$ of vibrational H_2 levels. The following processes of vibrational level excitation-deexcitation were taken into account: vibration-vibration (v-v) exchange, vibration-translation (v-t) exchange with H_2 molecules and H atoms, e-v exchange, direct dissociation of hydrogen molecule by electron impact from v-levels, DA and inverse associative detachment. Explicit expressions for the rates of these processes were given in [29] . The exchange of excitations between Cs atoms and H_2 molecules, and the stripping of a H^- ions by a vibrationally excited H_2 molecule were also considered. For sufficiently rarefied plasma an additional term for the determination of a vibrational level distribution function was introduced in the balance equations. It corresponds to the surface H_2 de-excitation.

Some results of the calculations are depicted at Fig. 7. One can see that very high value of H^- concentration may be obtained in a LV Cs-H_2 discharge in a dense plasma. But thus H^- concentration corresponds to comparatively high values of emission current density j_1.

Contrary to it, in a rare,Knudsen, plasma the optimum T_e value for H^- generation may be obtained at comparatively low value of emission current density. The theory of a LV Cs- H_2 discharge in Knudsen plasma was created in [33-34] . In this kind of the discharge, plasma is homogeneous. It is first covinient to calculate the parameters of a homogeneous Knudsen Cs-H_2 plasma as a function of thermal electron temperature T_e . For this, the electron-vibration kinetic equations must be solved simultaneously with the balance equations for neutral and charged particles. The calculation procedure was described in [28-29, 33-34] including surface vibration de-excitation .

The calculated negative ion concentration, N_H—(T_e) is shown in Fig. 8. One can see that maximum value of N_H–(T_e) corresponds to $T_e \cong 1.5$ eV and $N_{Cs}^{(0)} \sim (2\text{-}3)10^{14}$ cm^{-3}. It is essential that in this kind of the LV discharge the optimum electron temperature for H^- generation and corresponding high value of negative ion concentration $N_H - \cong 10^{13}$ cm^{-3} are obtained at a moderate value of cathode emission current density $j_1 \leq 10$ A/cm^2, which may be easily achieved in the experimental device. The dependences of the calculated electron temperature T_e and the cathode voltage drop φ_1 upon the anode voltage U are shown in Fig. 9. One can see that the needed optimum value of electron temperature $T_e \cong (1\text{-}1.5)$ eV may be really obtained in a low-voltage mode of operation (corresponding value of a cathode voltage drop $\varphi_1 < 9$ V).

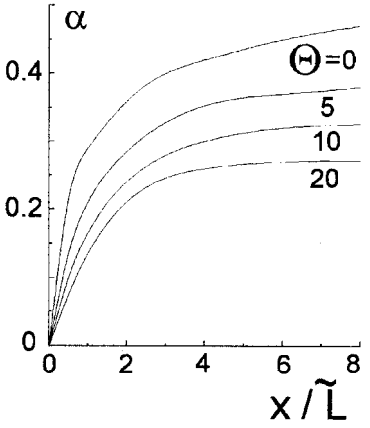

Figure 6.

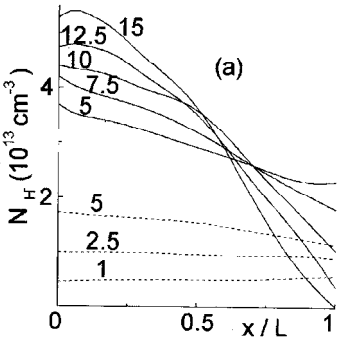

Figure 7a.

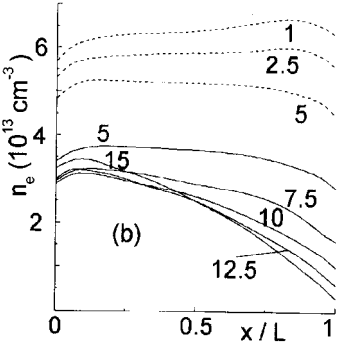

Figure 7b.

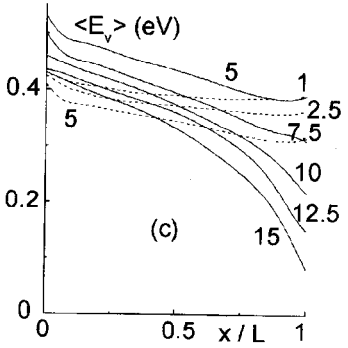

Figure 7c.

Figure 6. Coefficient of the electron beam energy transformation in a Knudsen plasma - the share of the beam energy which is lost via Langmuir wave excitation, $\Theta = 2\gamma_{coll}/(\pi\omega_p n_1/n_e)$.

Figure 7. LV discharge plasma parameter distribution for various hydrogen pressures p_{H_2}. L =0.1cm. Numbers at the curves give the values of p_{H_2} in Torr. φ_1 = 7 V, j_1 = 30 A/cm², $N_{Cs}^{(0)} = 1.5 \cdot 10^{14}\,\mathrm{cm}^{-3}$. Full and broken curves are for the results obtained with and without surface vibrational de-excitation, respectively. $< E_v >$ - mean vibrational energy of H_2 molecule.

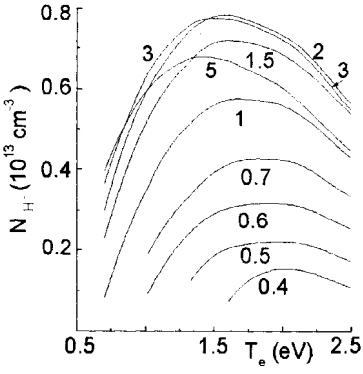

Figure 8.

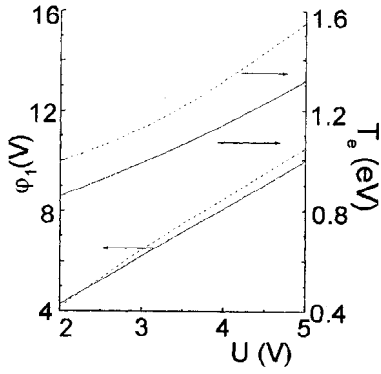

Figure 9.

Figure 8. Dependence of the negative ion concentration on thermal electron temperature T_e . L = 0.1 cm. Total concentration of molecular hydrogen $N_{H_2}^{(0)} = N_{H_2} + N_H/2 = 10^{16}\text{cm}^{-3}$. Total cesium concentration $N_{Cs}^{(0)}$ is shown at the curves in units of 10^{14} cm^{-3}.

Figure 9. Dependence of the cathode voltage drop φ_1 and electron temperature T_e upon the anode voltage. L = 0.1 cm, $N_{H_2}^{(0)}$ = 10^{16} cm^{-3}. Full curves: j_1 = 10 A/cm², $N_{Cs}^{(0)}$ =1.2•10^{14}cm^{-3}. Broken curves: j_1 = 8 A/cm², $N_{Cs}^{(0)}$ = 0.8·10^{14}cm^{-3}.

The experimental investigation of LV cesium-hydrogen discharge was fulfilled in [35-39]. A comparison between the theoretical and the first experimental data [35-38] is shown in Fig. 10-12. The experimental data were obtained by a probe method in a plane diode, the cylindrical probe being parallel to the electrode plane. The probe was shifted by 1 mm with respect to anode in Fig. 10-11 and by 2 mm with respect to anode in Fig.12. For a LV discharge in a dense plasma (Fig. 11-12), the comparison was done at comparatively high current densities: j_1 = 10 A/cm² and j_1 = 18 A/cm². For a LV discharge in a Knudsen plasma (Fig. 12) the comparison was fulfilled at a small current density: j_1 = 2 A/cm².

The dependence of T_e on hydrogen pressure p_{H_2} in strongly ionized plasma is given in Fig. 10 together with the calculations. The experimental and theoretical curves for similar discharge parameters are very close to one another.

The experimental results and theoretical parameter distributions are compared in Fig. 11, which shows a satisfactory agreement for the plasma concentration and the potential values. The measured T_e coincides qualitatively with the theoretical values, but the experimental curves are slightly below the theoretical values (see Fig. 11), because of the boundary effects in the plasma energy balance. A similar effect was observed in a pure Cs LV discharge [6].

For a Knudsen mode of a LV discharge, the data from the probe investigations and the respective theoretical results are given in Fig. 12 for φ_1 and for T_e . We have obtained a good qualitative and nearly quantitative agreement between theory and experiment. The slight difference may be due to the boundary effects, as it was pointed out above.

It is clear from the experimental data that the optimum T_e value for negative hydrogen ion generation in a Knudsen discharge (T_e > 1 eV), indeed, can be easily achieved in an experimental device at comparatively low cathode emission current.

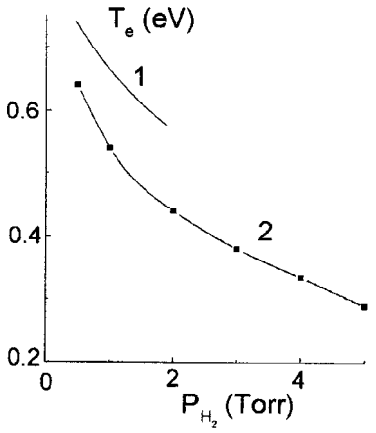

Figure 10.

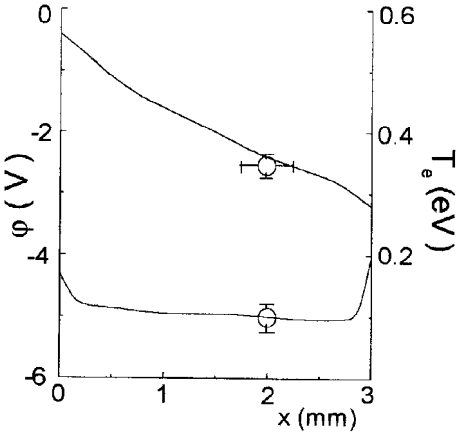

Figure 11a.

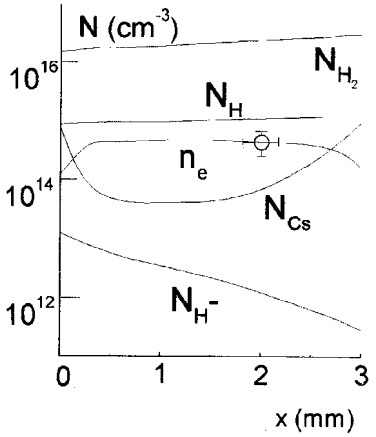

Figure 11b

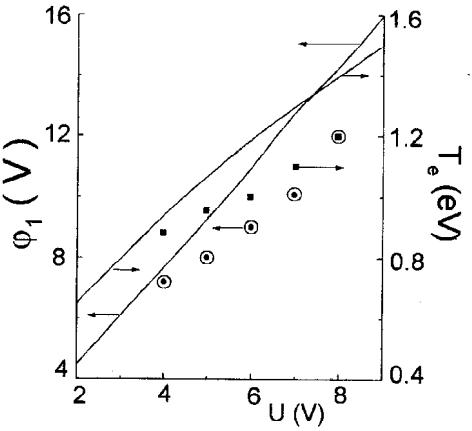

Figure 12.

Figure 10. Experimental and theoretical dependences of electron temperature on hydrogen pressure in a dense plasma LV discharge. 1, theory: j_1 = 10 A/cm², L = 0.5 cm, $N_{Cs}^{(0)}$ = $1.5 \cdot 10^{14}$cm^{-3}, φ_1 = 7 V. 2, experiment: j_1 = 10 A/cm², L = 0.3 cm, $N_{Cs}^{(0)}$ = $1.5 \cdot 10^{14}$cm^{-3}, φ_1 = 7 V.

Figure 11. Comparison between experimental and theoretical plasma parameter distributions in a dense plasma LV discharge. j_1 = 18 A/cm², L = 0.3 cm, p_{H_2} = 3 Torr, $N_{Cs}^{(0)}$ = $5 \cdot 10^{14}$cm^{-3}, φ_1 = 4.5 V.

Figure 12. Comparison between experimental (points) and theoretical plasma parameter distributions in a Knudsen LV discharge. j_1 = 2 A/cm², L = 0.3 cm, $N_{H_2}^{(0)}$ = 10^{15}cm^{-3}, $N_{Cs}^{(0)}$ = $3 \cdot 10^{13}$cm^{-3}.

The good fit between the theoretical and experimental plasma parameters allows the suggestion to be made that real N_{H^-} will fit the theory too. Direct measurement of H^- concentration in LV Cs-H_2 discharges will be the subject of experimental research in the near future.

Acknowledgment. This work is supported by INTAS (Grant 94-316).

REFERENCES

1. E. Nicolopoulou, M. Bacal, and H.J. Doucet. Equilibrium density of H^- in a low pressure hydrogen plasma. J. Phys. 38:1399, (1977).
2, M. Bacal and G.W. Hamilton. H^-, D^- production in plasmas. Phys. Rev. Lett. 42:1538 (1979).
3. J.M. Wadehra. Dissociative attachment to rovibrationally excited H_2. Phys. Rev. A 29:106 (1984).
4. F.G. Baksht, V.G. Ivanov. Electron distribution function in near-electrode layer of molecular gas. Zh.Tekh. Fiz. 54:1870 (1984).
5. A.A. Likalter, A.H. Mnatsakanjan. Molecule vibrational distribution, caused by the collisions between electrons and heavy particles. High Temperature Physics. (in Russian) 11: 202 (1973).
6. F.G. Baksht, G.A. Djuzhev, A.M. Martsinovskiy, B.Ya. Moizhes, G.E. Pikus, E.B. Sonin, V.G. Yuriev. "Thermionic converters and low-temperature plasma". (Russian edn. B.Ya. Moizhes and G.E. Pikus. Nauka, Moscow (1973). English edn. L.K. Hansen, US Department of Energy (1978))
7. F.G. Baksht, V.G. Yuriev. Near-electrode phenomena in low-temperature plasma. Zh.Tekh. Fiz. 49:905 (1979).
8. F.G. Baksht, V.G. Ivanov, V.G. Yuriev. Near-electrode phenomena in low- temperature plasma. XVIII Int. Conf. on Phenomena in Ionized Gases. Invited Papers. Swansea, UK 206 (1987)
9. F.G. Baksht, B.Ya. Moizhes, VA. Nemchinskiy. Calculation of the kinetic coefficient of reflection for thermoelectron current from plasma and semiconductor. Zh.Tekh. Fiz. 37:729 (1967).
10. L.D. Tsendin. About the influence of thermionic emission on the saturation current value. Fiz. Tv. Tela 7: 1078 (1965).
11. F.G. Baksht. Electron energy distribution function in near-electrode layer of weakly ionized plasma. Zh.Tekh. Fiz. 39 : 1594 (1969).
12. F.G. Baksht, V.G. Ivanov. The kinetic coefficient of reflection at the contact between weakly ionized plasma and electrode. Zh.Tekh. Fiz. 40 : 218 (1970).
13. F.G. Baksht. The kinetic coefficient of reflection for the current at the boundary of plasma or semiconductor in the case where electron energy relaxation occurs by inelastic collisions. Zh.Tekh. Fiz. 43 : 30 (1973).
14. F.G. Baksht, V.G. Ivanov, Mechanisms of electron beam energy relaxation in near-electrode layer of low-voltage discharge in molecular hydrogen. Sov. J. Plasma Phys. 12:165 (1986).
15. I.P. Stahanov, V.E. Cherkovets, "Physics of Thermionic Converter" (in Russian) Energoatomizdat, Moscow (1985).
16. F.G. Baksht, A.A. Kostin, A.M. Martsinovskiy, et. al. Electron beam plasma heating and peculiarities of ionization mechanism in Knudsen arc. Pis'ma Zh. Tekh. Fiz. 5:905 (1979).
17. F.G. Baksht, A.A. Bogdanov, V.B. Kaplan et. al. Electron beam plasma heating and peculiarities of ionization mechanism in nonstationary Knudsen arc. Fiz. Plasmy 7:547 (Mar. 1981).
18. A.V. Agapov, F.G. Baksht, B.I. Kolosov et. al. Quasilinear relaxation at strong collisional damping of Langmuir waves. Pis'ma Zh.Tekh. Fiz. 9:583 (1983).
19. F.G. Baksht, A.A. Bogdanov, V.B. Kaplan et. al.Stationary low-voltage plasma-beam Knudsen discharge. Fiz. Plazmy. 10: 881 (1984).
20. F.G. Baksht, B.I. Kolosov, A.A. Kostin et. al. "Mathematical Modelling of the Processes in Low-voltage Plasma-beam Discharge." (in Russian) Energoatomizdat, Moscow (1991).
21. A.A. Vedenov, E.P. Velichov, R.S. Sagdeev. Nuclear Fusion Suppl. 2:465 (1962).
22. V.N. Tsitovich. "Non linear Effects in Plasma" (in Russian) Nauka, Moscow (1967).
23. A.A. Vedenov, D.D. Rjutov. Quasilinear effects in beam instabilities. Problems Plasma Theory. (in Russian) M.A. Leontovich, ed, 6:3 (1972).
24. P.M. Lebedev, I.N. Oniscenko, Yu.V. Tkach, Ya.B. Fainberg, V.I. Shevchenko. Theory of plasma-beam discharge. Fiz. Plazmy. 2:407 (1976).
25. A.A. Ivanov, T.K. Soboleva, and P.N. Jushmanov. Perspectives of plasma-beam discharge utilization in plasma chemistry. Fiz. Plazmy. 3:152 (1977).

26. S.I. Krasheninnikov, V.V. Filjushkin. About the electron beam relaxation in weakly ionized gas of high density. Pis'ma Zh. Eksp. Theor. Fiz. 32:290 (1980).
27. E.B. Mishin, Yu.Ya. Rujhin, V.A. Telegin. "Interaction of Electron Beams with Ionospheric Plasma" (in Russian) Hydrometeoizdat, Leningrad (1989).
28. F.G. Baksht and V.G. Ivanov. Low-voltage discharge in cesium-molecular hydrogen mixture. Sov. Tech. Phys. Lett. 12:278 (1986).
29. F.G. Baksht, L.I. Elizarov, V.G. Ivanov et. al. Low-voltage discharge in a mixture of cesium with molecular hydrogen. Sov. J. Plasma Phys. 14:56 (1988).
30. F.G. Baksht, L.I. Elizarov, V.G. Ivanov. Theory of low-voltage arc in cesium-molecular hydrogen mixture. Sov. J. Plasma Phys. 16:479 (1990).
31. F.G. Baksht, V.G. Ivanov, Generation of negative hydrogen ions and vibrationally excited molecules in a low-voltage cesium-hydrogen discharge. Sov. Phys. Techn. Phys. 37: 223 (1992).
32. F.G. Baksht, G.A. Djuzhev, L.I. Elizarov, V.G. Ivanov, A.A. Kostin, S.M. Shkolnik. Low-voltage discharge in cesium-hydrogen mixture as a source of negative hydrogen ions. IEEE Trans. on Plasma Science 21:552 (1993).
33. F.G. Baksht, V.G. Ivanov, A.A. Kostin. Plasma-beam cesium-hydrogen discharge as a source of negative hydrogen ions. Sov. Techn. Phys. Lett. 18: 399 (1992).
34. F.G. Baksht, V.G. Ivanov, A.A. Kostin. Generation of negative hydrogen ions in a low-voltage plasma-beam cesium-hydrogen discharge. Sov. Phys. Techn. Phys. 38:825 (1993).
35. F.G. Baksht, G.A. Djuzhev, L.I. Elizarov, V.G. Ivanov, A.G. Filatov, S.M. Shkolnik. Experimental investigation of a low-voltage cesium-hydrogen discharge. Sov. Phys. Techn. Phys. 37:959 (1992).
36. F.G. Baksht, G.A. Djuzhev, L.I. Elizarov, V.G. Ivanov, A.G. Nikitin, S.M. Shkolnik. Peculiarities of electron-vibration kinetics in the afterglow of cesium-hydrogen plasma. Sov. Techn. Phys. Lett. 19:716 (1993).
37. F.G. Baksht, V.G. Ivanov, A.G. Nikitin, Shkolnik. Investigation of long-living plasma in the afterglow of low-voltage cesium-hydrogen discharge. Sov. Techn. Phys . Lett, 20: 927 (1994).
38. F.G. Baksht, V.G. Ivanov, A.A. Kostin, A.G. Nikitin, Shkolnik. Plasma beam Knudsen discharge in the mixture of cesium and molecular hydrogen. Sov. Phys. Techn. Phys. 40:851 (1995).
39. A.G. Nikitin, S.M. Shkolnik. The dependence of the kinetics of the decay of low-voltage cesium-hydrogen discharge plasma upon electrodes materials. Sov. Phys. Techn. Phys. 42:110 (1997).

SURFACE WAVE SUSTAINED DISCHARGES

S. Grosse[1], H. Schlüter[1], and M. Schlüter[2]

[1]Inst. f. Experimentalphysik II
[2]Inst. f. Experimentalphysik V
Ruhr-Universität Bochum
44780 Bochum
Germany

INTRODUCTION

A selfconsistent modeling of discharges obviously aims at a full description without requiring prior knowledge or diagnostic determination of any parameter beyond those actually chosen by an operator in the laboratory, i.e. beyond gas type and pressure, geometry and material of discharge tube, electric field frequency and voltage setting of power supply (for simplicity assumed to possess negligible internal resistance). This setting of power supply can be considered here in the case of surface wave (SW) sustained discharges as equivalent to the knowledge of electric field strength right at the beginning of the discharge column.

The electric field strength and its spatial structure throughout the discharge is expected to be provided by the model as well as value and spatial structure of electron density. Actually simultaneous determination and (nonlinear) interdependence of electron density and electric field strength is a particular feature of truly selfconsistent modeling. This implies to go beyond the well known Schottky approximation for the electric field strength which may provide simple estimates, but is degenerate in the electron density and requires prior knowledge of its value.

A model on the basis of ion and electron fluid equations can be condensed to two equations: the electron energy and the electron particle balance equation. The former connects electron temperature and electric field intensity (nonlocally in case of sufficient heat conductivity). The latter, balancing diffusion losses and ionization, should contain nonlinear contributions such as stepwise ionization or at high density recombination in order to avoid the above mentioned degeneracy in electron density. For selfconsistency these two equations of discharge physics have to be augmented by two equations of electrodynamical character: by the proper SW dispersion relation and wave power equation connecting Poynting flux with power transfer to the plasma. Here SW sustained discharges are chosen, which possess well defined electrodynamic boundary

Electron Kinetics and Application of Glow Discharges
Edited by U. Kortshagen and L. D. Tsendin, Plenum Press, New York, 1998

conditions essentially given by field continuity relations at interfaces and which may be considered as simple prototype discharges giving some guidance also for cases with more complicated boundary situations.

For the low degree of ionization encountered in the discharges considered, the electron energy distribution function (EEDF) cannot be expected to be Maxwellian, since energy losses by inelastic processes lowers the tail of distribution with electron–electron interactions being unable to completely counterbalance this effect. Therefore a kinetic model basing the treatment of electron component on numerical solutions of the Boltzmann equation is more accurate than the (in some respect more transparent) electron fluid approach. Moreover more details of atomic (and molecular) processes can be incorporated. The kinetic approach also facilitates the treatment of radial and axial density inhomogeneities which pose a difficult problem and in many situations can be responsible for even qualitative changes in discharge description and behavior.

Below basis and procedure of the model employed will be outlined, before numerical results as well as pertinent observations are discussed. Approximations still used are pointed out and potential improvements are discussed.

KINETIC NUMERICAL MODELING

The density nonuniformity unavoidably present complicates the modeling. Relatively weak axial density gradients are expected and the axial diffusion losses may be considered minor as compared to the radial diffusion, which is essential for the particle losses of a steady state plasma. Therefore, with respect to the axial dimension z, at first local solutions are sought and the selfconsistency between local (cross–section averaged) electron density and z is turned to below in the electrodynamical part of the problem as well as complications arising there in cases.

Thus for the basic equation of kinetic description of the electron component, the Boltzmann equation, two–dimensional solutions should be found (in electron energy u and radial coordinate r). The present development in numerical work aims at using appropriate procedures, such as multi–grid schemes, and at incorporating them into a selfconsistent model. The numerical effort involved is unavoidable for accurate solutions in particular towards higher gas pressures, as will be commented on below. However, when interest is restricted to rather low pressures, an approximation and simplification may be employed. This can be expected to provide reasonable accuracy and correct description of essential trends for sufficiently low products $p \cdot a$ (with p being the gas pressure, a tube radius).

Nonlocal approximation

For rather large ratios of energy relaxation length λ_ε to a the nonlocal approximation has been used to good effect[1], by formulating the problem in total energy $\varepsilon = u - \Phi(r)$ (u being the electron energy in eV, $\Phi(r)$ the ambipolar space charge potential), employing averaging procedures and simplified boundary conditions. Thus, the problem is reduced to a one–dimensional one. The Boltzmann equation for the symmetric zero part of the distribution function $F_0^{(0)}(\varepsilon)$ reads then (with bars denoting

averaging within the discharge cross section):

$$\frac{d}{d\varepsilon}\left(\overline{\mathcal{D}_\varepsilon}\frac{dF_0^{(0)}(\varepsilon)}{d\varepsilon}+\overline{V_\varepsilon}F_0^{(0)}(\varepsilon)\right)$$
$$=\sum_k\left[\bar{\nu}_k^*(\varepsilon)F_0^{(0)}(\varepsilon)-\bar{\nu}_k^*(\varepsilon+u_k)F_0^{(0)}(\varepsilon)(\varepsilon+u_k)\right]+\overline{S_{ee}} \tag{1}$$

where

$$\overline{V_\varepsilon}=\frac{2}{a^2}\varkappa\int_0^{r^*(\varepsilon)}u^{3/2}(r)\nu_m(u(r))r\,dr, \tag{2}$$

$$\bar{\nu}_k^*(\varepsilon)=\frac{2}{a^2}\int_0^{r^k(\varepsilon)}\nu_k(u(r))u^{1/2}(r)r\,dr. \tag{3}$$

The ν_k's stand for inelastic collision frequencies and ν_m for the electron–neutral collision frequency. is $r^*(\varepsilon)$ the turning point radius of electrons travelling in the space charge potential, $r^k(\varepsilon)$ the maximum radius for which the k^{th} inelastic process is possible. χ is the portion of energy transferred at one electron–atom collision. $\overline{S_{ee}}$ is obtained analogously. The retransformed $F_0^{(0)}(u)$ has now a specific r–dependence due to $u = \varepsilon + \Phi(r)$. The diffusion coefficient in energy space is defined by

$$\overline{\mathcal{D}_\varepsilon}=\frac{2}{a^2}\int_0^{r^*(\varepsilon)}(\mathcal{D}_z+\mathcal{D}_r)\,r\,dr \tag{4}$$

with

$$\mathcal{D}_z=\frac{2e}{3m_e}u^{3/2}(r)\frac{|E_z(r)|^2}{2\nu_m(u)}\frac{\nu_m^2(u)}{\nu_m^2(u)+\omega^2}, \tag{5}$$

$$\mathcal{D}_r=\frac{2e}{3m_e}u^{3/2}(r)\frac{|E_r(r)|^2}{2\nu_m(u)}\frac{\nu_m^2(u)}{\nu_m^2(u)+\omega^2}. \tag{6}$$

ω is the wave frequency.

Transit–time heating

As also pointed out in another contribution to this workshop[2], there is noncollisional heating in addition to the collisional one. A corresponding (two–dimensional) diffusion coefficient for energy space is included for the case of SW sustained discharges. As evaluated in some detail previously[1,3], the diffusion coefficients (5) and (6) describing the Joule heating of the plasma by the high frequency electric field can be augmented by a term which is derived from a quasilinear approach based on separation of small/large space scales (similar to the one employed some time ago in treatments of plasma turbulence):

$$\mathcal{D}_{\text{ql}}=\frac{\pi e}{2m_e}u^{3/2}|E_r(r)|^2\tau(u)\exp\left(-4\pi\frac{\tau}{T}\right) \tag{7}$$

In essence expression (7) describes a transit–time heating important here when peaks of the radial high frequency field component $|E_r|$ appear due to strong radial density nonuniformity allowing $\omega_p(r)$ to match the wave frequency ω. Then the transit time τ of electrons passing radially through such peaks acts similar to the collision time τ_c in causing phase decorrelation. The exponential factor in (7) accounts for the fact that the noncollisional heating is effective only for electrons passing quickly as compared to the wave period $T = 2\pi/\omega$. Since contributions from expression (7) modify the attenuation

of the SW, the effective damping of the E_r–component is treated differently from that of the E_z–component, but the field calculations are performed in a way that no more power is taken from the wave as is required for discharge maintenance[1]. It should be stressed that aside from outright field peaks also steep radial ascents of field strength towards the wall contribute and are accounted for. The noncollisional channel of high frequency heating does not provide automatically much enhanced or noticeably changed total heating, since the selfconsistency calls only for as much field intensity as required to cover the plasma losses. It rather provides some redistribution in the heating channels and in the energy distribution function.

Complementation of system

For selfconsistent modeling a closed set of equations has to be considered simultaneously by iterative numerical procedures: in addition to the Boltzmann equation (5) the normalization condition for the electron density $n_e(r)$, connecting the distribution function $F_0^{(0)}(\varepsilon)$ with Φ, the electric field equations and the fluid equations have to be solved. The dispersion relation is obtained from the field equation to which the electrodynamic continuity conditions at the plasma–glass ($r = a$) and glass–vacuum ($r = b$) interface are applied. The fluid equations contain the ambipolar potential $\Phi(r)$, the ion drift velocity, the ionization frequency and the ion–neutral collision frequency. The effect of stepwise processes in the ionization is an *approximation* accounted for by carrying one (effective) excited level with the population density

$$n_{\mathrm{ex}} = \frac{N n_{e_0} \nu_0}{n_{e_0} \nu_L + \mathcal{D}_{\mathrm{ex}} \Big/ \left(\frac{a}{2.4}\right)^2}, \tag{8}$$

where N is the neutral gas density, n_{e_0} the electron density in the center, ν_0 and ν_L are the frequency for ground state ionization and for losses by excitation, respectively, and D_{ex} is the diffusion coefficient of metastables[1].

Electrodynamical part of the model

The comparatively strong radial density nonuniformity can be taken care of by numerical (Runge–Kutta) integration of the field equations for the components E_z and E_r assumed to vary $\propto \exp[-\int_0^z \gamma(z')dz'] \exp(i\omega t)$:

$$\frac{d^2E_z}{dr^2} + \left(\frac{1}{r} + \frac{\gamma^2}{k_n^2(r)} \frac{\frac{d\varepsilon_n(r)}{dr}}{\varepsilon_n(r)}\right) \frac{dE_z}{dr} + k_n^2(r) E_z = 0 \tag{9}$$

$$E_r(r) = -\frac{\gamma}{k_n^2(r)} \frac{dE_z}{dr} \tag{10}$$

with $k_n^2(r) = k_0^2 \varepsilon_n(r) + \gamma^2$ and the index n representing plasma, glass and vacuum. In the plasma $(n = p)$ $\varepsilon_p(r)$ is given by the cold plasma permittivity in good approximation as

$$\varepsilon_p(r) = 1 - \frac{\omega_p^2(r)}{\omega(\omega - i\nu_m(r))}, \tag{11}$$

or somewhat more general by[4,5]

$$\varepsilon_p(r) = 1 + \frac{2e^2 n_e(r)}{3\varepsilon_0 m_e \omega} \int_0^\infty \frac{u^{3/2}}{\omega - i\nu_m(u,r)} \frac{\partial F_0^{(0)}(u,r)}{\partial u} du \tag{12}$$

with $\omega_p(r)$ the plasma frequency.

The radial density profile in $\omega_p(r)$ is obtained by simultaneous (iterative) solution of the other equations of the system. The sheath thickness is usually taken to be small, and Bohm's criterion is used. The above equations (9) and (10) neglect axial density nonuniformity, i.e. the zero order local approach is used and the comparatively slow axial change of the cross–section averaged electron density on $\overline{\omega_p}(z)$ is derived thereafter by integrating the Poynting flux relation:

$$-\text{div Re}\left(\frac{1}{2}\vec{E}(r)\times\vec{H}^{*}(r)\right)=q(r) \tag{13}$$

over a plane across the discharge. q indicates the power loss per unit volume plasma.

The validity and accuracy of the above approach to axial density nonuniformity may call for checking and justification by two– or three–dimensional field calculations including x-dependencies. Especially the complications introduced into dispersion and field structure by strong radial density inhomogeneities and in particular situations when a pronounced "system resonance" arises towards the end of discharge and should be investigated. Details to this are reported elsewhere[6,7]. Moreover some results of such field calculations [7] are discussed below in a separate section.

NUMERICAL RESULTS

Power loss per average electron

The selfconsistent electric field strengths resulting from the above numerical modeling are closely connected to the averaged power loss per electron Θ. This loss averaged over the discharge cross section, required to maintain the discharge (to cover, for instance, the main losses by inelastic atomic processes), can be obtained via energy conservation from the balance to the power input by the high frequency electric field:

$$\Theta=\sum_i\frac{1}{\bar{n}_e}\int_0^\infty\left[\frac{d}{d\varepsilon}\left(\overline{\mathcal{D}_i}\,\frac{dF_0^{(0)}(\varepsilon)}{d\varepsilon}\right)\right]\varepsilon\,d\varepsilon \tag{14}$$

The sum is over the input channels of the E_z, and E_r–field components. Thus the maintenance electric field intensity, averaged over the discharge cross section, is contained in the diffusion coefficients in energy space. From the above mentioned Schottky approximation for diffusion dominated regimes, equating ground state ionization and diffusion particle losses, simple—usually reasonable—estimates of the field intensity can be obtained. However, they are independent of the electron density, what is in contradiction to daily experience when the discharge turned on chosen selfconsistent electric field strength, electron density and power values and their spatial distributions. The discharge formation is obviously a strongly nonlinear phenomenon and for full selfconsistency processes nonlinear in electron density have to be taken into account, even though their contributions may appear, for instance in particle balance considerations, to be small compared to the linear ones.

As relevant nonlinear atomic processes already previously[8] stepwise ionization has been pointed out, as well as its tendency to saturation towards higher electron densities and the influence of recombination which arises finally at very high densities. Another

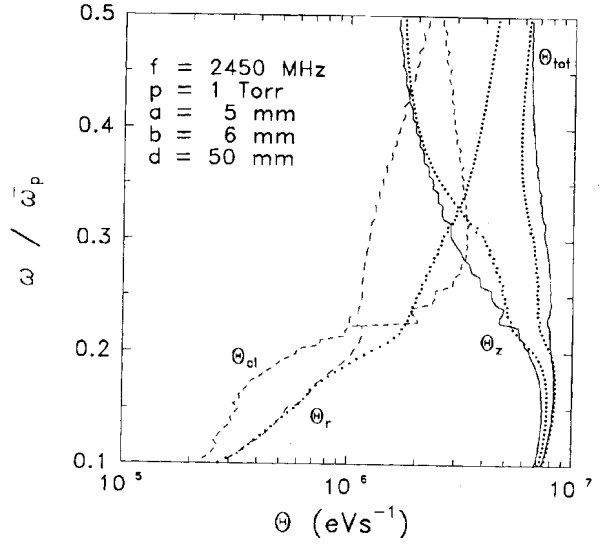

Figure 1. Example of Θ_{total}, Θ_z, Θ_r and Θ_{cl} versus $\omega/\overline{\omega_p}$ in the microwave range. Dotted curves are without the collisionless effect: $\Theta_{cl} = 0$.

(weak) nonlinear effect, accessible in kinetic treatment, is the influence of electron-electron collisions. In addition to these general effects there can be effects more specific to the particular discharge type, here to plasmas maintained by travelling surface waves and their dispersion properties. They are basically contained in a previous fluid approach[8], but elaborated on below in numerical kinetic treatment. In particular the radial penetration of the electric field is changing with the axially varying electron density $\overline{n_e}$ (cross section averaged) along the discharge. This in turn can effect changes in the electron energy distribution function with $\overline{n_e}(z)$, conceivably also of the radial density profile. The resultant variation of Θ may be small, but significant enough for the aspect of selfconsistency pointed out.

Fig. 1 gives an example in the microwave range showing indeed reasonable constancy of 0 as a function of $\omega/\overline{\omega_p} \sim \overline{n_e}^{-1/2}$. The calculations are performed for argon as always in the following. The behavior without inclusion of the noncollisional term according to expression (7) is demonstrated by the dotted curves and conforms to the comments given above. To point out the influence of step–ionization, its role is exaggerated by increasing its excitation rate by a factor. A case at lower frequency is chosen in Fig. 2. Towards low values of $\omega/\overline{\omega_p}$ a decrease of 0 is to be seen as expected.

For the situation considered both in Fig. 1 and Fig. 2, however, another effect is dominant: At higher $\omega/\overline{\omega_p}$ a slight decrease of Θ towards discharge end shows up, even when low ω and small radius a are chosen. It is correlated with a noticeable change in the distribution of θ on the E_z – and E_r–contributions and can indeed be traced to the changes of radial field distributions along the discharge. Fig. 3 depicting $|E|$ for three values of $\omega/\overline{\omega_p}$ for conditions similar to those in Fig. 2 demonstrates that along the discharge (with growing $\omega/\overline{\omega_p}$) the field intensity gets more concentrated near

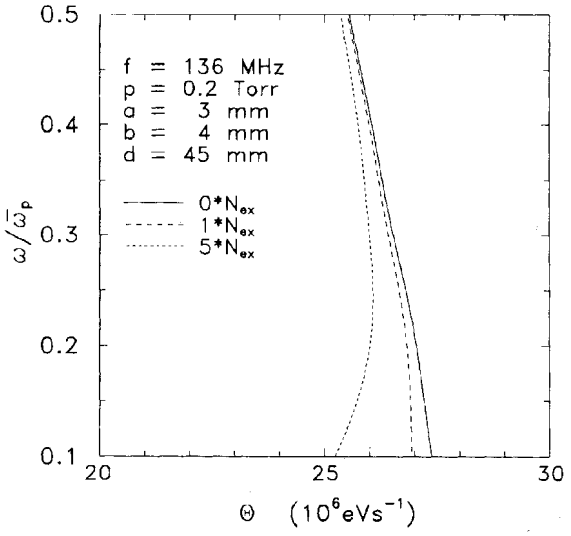

Figure 2. Example of Θ_{total} versus $\omega/\overline{\omega_p}$ at lower frequency. Dotted line with ionization via excited levels, solid without, dashed augmented by factor 5. *d* radius of metal shielding.

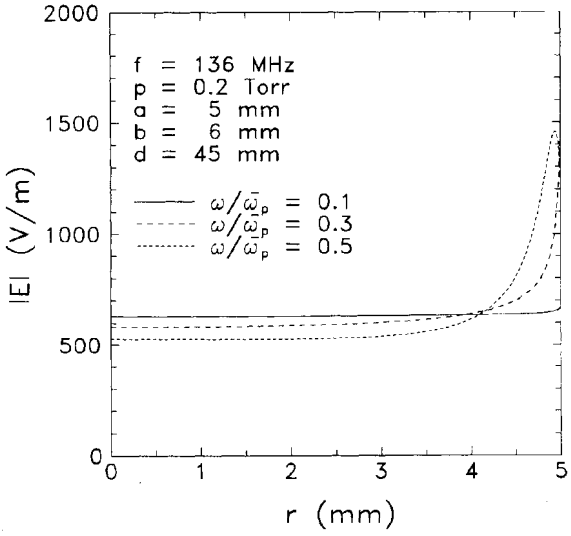

Figure 3. Radial field profiles of total field strength |*E*| for three values of $\omega/\overline{\omega_p}$.

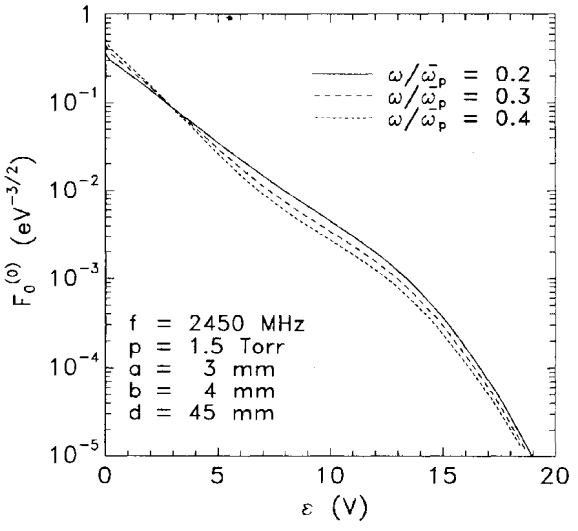

Figure 4. EEDFs $F_0^{(0)}$ at different $\overline{\omega_p}$.

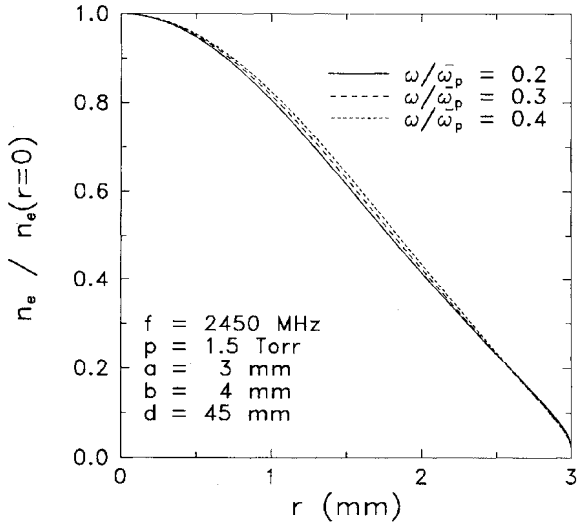

Figure 5. Radial profiles of $n_e(r)$ at different $\overline{\omega_p}$.

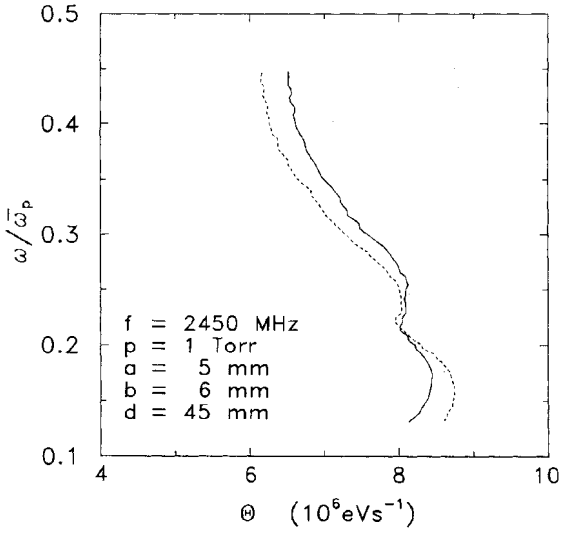

Figure 6. Examples for 0 versus $\omega/\overline{\omega_p}$. - - - with the electron–electron term in eq. (1) reduced by a factor 2.

to the discharge wall. This enters into the formation process of the energy distribution function $F_0^{(0)}$ through the diffusion coefficients (in energy space) D, weakly, but predictably—within the nonlocal approximation used—altering $F_0^{(0)}(\varepsilon)$ with changing $\omega/\overline{\omega_p}$. Fig. 4 for the distribution function and three values of $\omega/\overline{\omega_p}$ indeed shows a situation where $F_0^{(0)}$ towards the discharge end has more particles concentrated at low energies, but with less particles in the range of inelastic losses leading to somewhat reduced Θ at lower $\overline{n_e}$. A case in the GHz range is considered, but a similar behavior can be found at lower frequencies. Thus there is a nonlinear mechanism via changing radial field distributions and resultant distribution functions with $\overline{n_e}$. Variations also in the (diffusion dominated) radial profiles of electron density $n_e(r)$ with $\overline{n_e}$ are usually small, as shown in Fig. 5.

Changes in $F_0^{(0)}$ with $\overline{n_e}$ can also be—partially—caused by electron—electron collisions which have basically a smoothing–out effect in the EEDF. As to the resultant effect on Θ, Fig. 6 (with linear scale) demonstrates from calculations with reduced electron–electron collisions that there is a small influence, but only a partial one and not of the type sought. At low ω the influence of electron–electron collisions is similar and even decreased.

The variation of field distribution with $\overline{n_e}$ affecting the energy distribution function in cases causes the main influence responsible for small variations in Θ. This is supported by the fact that the above effect is weaker for small radii and more pronounced for large radii, which is in line with the concept of changing radial field profiles. Also for higher ω the effect is larger.

EXPERIMENTS ON SPECIFIC FEATURES

Main characteristics of the described modeling are use of the nonlocal approximation and inclusion of even strong radial density inhomogeneities in this approach. So far there are some experimental indications on some specific results of this modeling. They have previously been addressed[9–11] and are only briefly pointed out here.

Measurements of electron energy distribution functions (EEDFs) by probe methods (employing compensation techniques) confirm that in good approximation there is a unique function of total energy as expected for $F_0^{(0)}(\varepsilon)$ from the nonlocal approximation, constituting an envelope to the EEDF's for different radial positions which are shifted in the ε–scale by the corresponding value of ambipolar potential $\Phi(r)$, as e.g. shown and discussed in some detail by Kortshagen[12,13]. Of course, also the expected non–Maxwellian character of the EEDFs, with lowered tail in the inelastic range, is born out by such observations. Since the requirements of nonlocal approximation become strongest towards higher electron energies, systematic studies in this range (for different products $p \cdot a$) will be of great interest.

A rather strong point for the usefulness of the nonlocal approach is gained from comparisons[13] to tomographic measurements of radial line emission profiles[14]. At low $p \cdot a$ results of a nonlocal model are much closer to experimental findings than those of a local model which tends to produce a pronounced maximum in the emission profile before the final drop at the wall due to increased electric field intensities. Such a maximum in the radial emission profile is not or barely observable at low $p \cdot a$, the EEDFs being obviously not drastically affected locally by the field intensities. However, there is still room for improvements in the nonlocal approach suggested by observations, e.g. in the treatment of metastable and step processes. Moreover, towards higher $p \cdot a$ doubtlessly a transition to a local scenario becomes evident in experiment—as expected-and a generalized truly two–dimensional (in u, r) treatment becomes desirable.

As to contribution of noncollisional heating in the presence of strong gradients and even peaks in the radial electric field strength, there is some evidence for the expected bump at the transition to the inelastic range in measured EEDFs at appropriate values of $p \cdot a$, which become apparent towards the end of discharge as predictable[10,11,15].

A direct measurement of peaks in the radial electric field by means of a probe/antenna possesses reduced spatial resolution, but at slightly increased $p \cdot a$ maxima in measured $|E_r|$–contours shifting slightly away from the discharge wall towards the discharge end could be reported, as to be expected for strong radial density inhomogeneity[9–11,15].

There is also support for a change from a linear axial density profile to a steeper axial descent towards discharge end[1,8] from density determinations by microwave interferometry[9,15]. The analysis of perturbations due to the finite ratio of wavelength to radius allows to consider the findings as relevant. There are also supporting observations on this in recent microwave radiometry work[16].

THEORETICAL CHECKS AND IMPROVEMENTS

There are two aspects of the model open to immediate check or improvement.

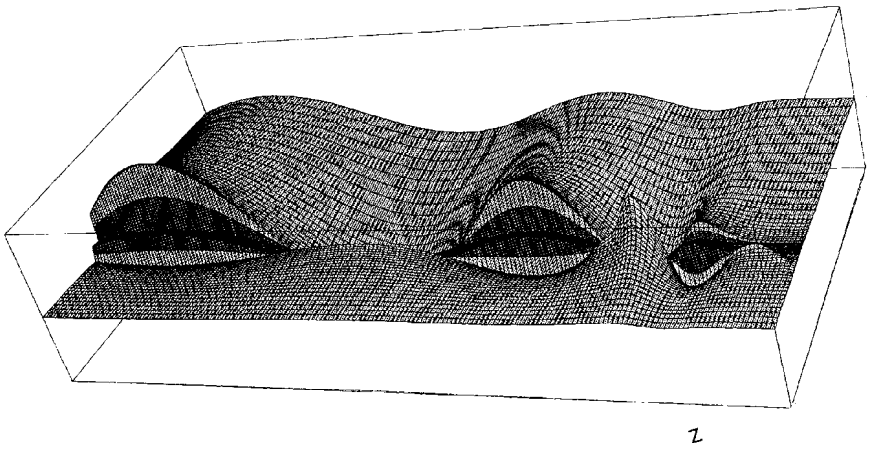

Figure 7. Re(E_r) versus z and r for a linear axial density profile with scale length L = 2.74 cm, radial profile $\propto J_0(\mu \frac{r}{a})$ with μ = 2, 220 MHz, ν_{en}/ω = 0.2, a =5 mm, b = 6 cm, d = 45 mm, shown from z = –44 cm (left) to z = 1 cm (right) with z = 0 at $\overline{\omega_p}^2/\omega$ = 2. r runs from 2.4 mm in the plasma (front) to d = 45 mm at the metallic shield (back).

Influence of $\overline{n_e}(z)$ on field calculations

The assumption of weak influence of axial density variations through $\overline{n_e}(r)$ in the field and dispersion calculations can be checked by three-dimensional numerical studies including both radial and axial density inhomogeneities. This has been recently performed on the basis of numerical solutions of the field equations in integral form, the wave excitation given by a "numerical" surfatron[7]. The required numerical effort is reduced by the use of magnetic boundary conditions suited to the considered azimuthal symmetry and by the use of appropriate variable grids.

Fig. 7 shows an example of a two–dimensional representation (in the r, z plane of Re(E_r)) for a surface wave calculated in this way. In Fig. 8 $|E_r|$ and in Fig. 9 $|E_z|$ are depicted. Calculations of this type confirm that the assumption in the above modeling on the usually weak influence of axial density inhomogeneity is sufficiently warranted even in the case of strong changes brought about by pronounced radial density inhomogeneity and by absorption. This is demonstrated by radial cuts in Fig. 10 for a radially inhomogeneous case and in Fig. 11 for an also radially homogeneous situation. Comparisons are made to simplified calculations neglecting z–dependencies. Differences become only noticeable when a system ("quasistatic") resonance at the discharge end is present and z-positions close to it are considered. They are more pronounced in the radially inhomogeneous case. Even in a situation of rather strong radial density variation (profile parameter μ = 2.4), but with increased damping of ν_{en}/ω = 0.6 (suppressing the formation of a system resonance connected to axial nonuniformity), field peaks due to radial plasma resonances ($\omega_p(r) = \omega$) appear clearly resolved towards the discharge end and are satisfactorily described in both cases, as to be seen in Fig. 12. By Fig. 13 axial cuts of $|E_r|$-field strength are shown when a (modest) radial inhomogeneity (μ = 2.0 as in Figs. 7–10) is present: As compared to calculations with a radially homogeneous density of averaged value the field distribution plasma–vacuum is of course changed.

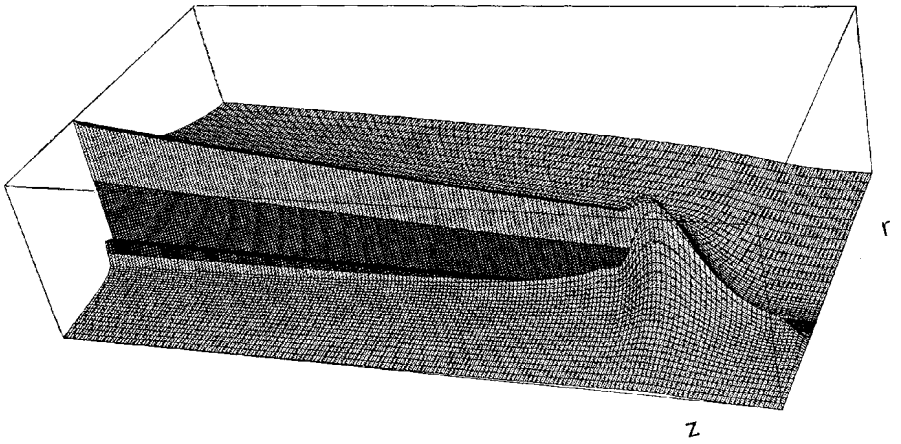

Figure 8. Conditions as for Fig. 7: $|E_r|$ is depicted.

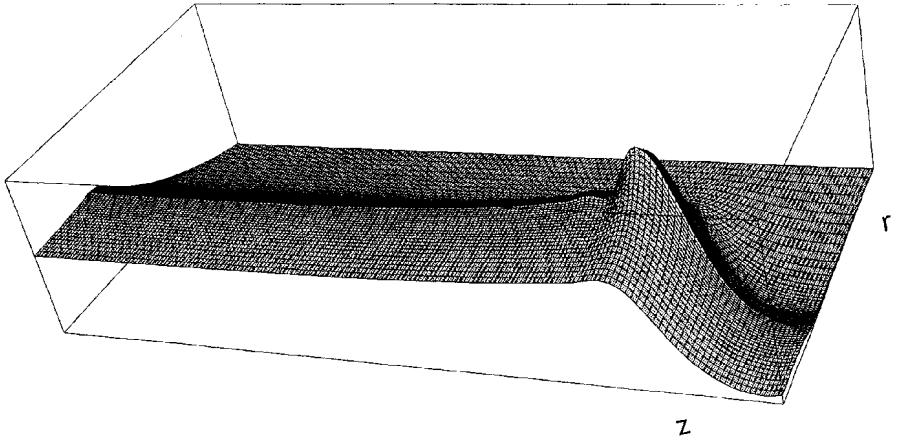

Figure 9. Conditions as for Fig. 7: $|E_z|$ is depicted.

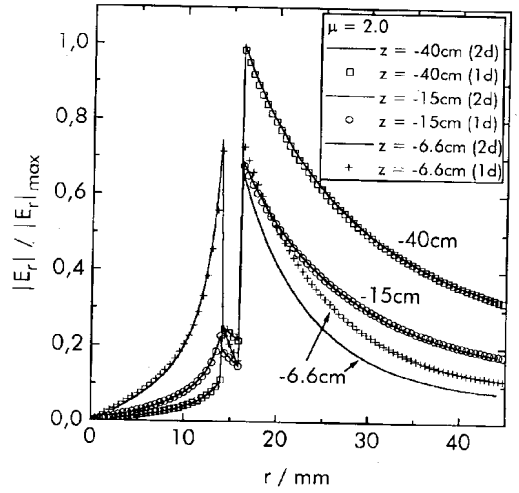

Figure 10. Radial cuts for conditions of Fig. 7 comparing full solutions (2d, solid lines) to one–dimensional ones (1d) neglecting z-dependencies. $\mu = 2$

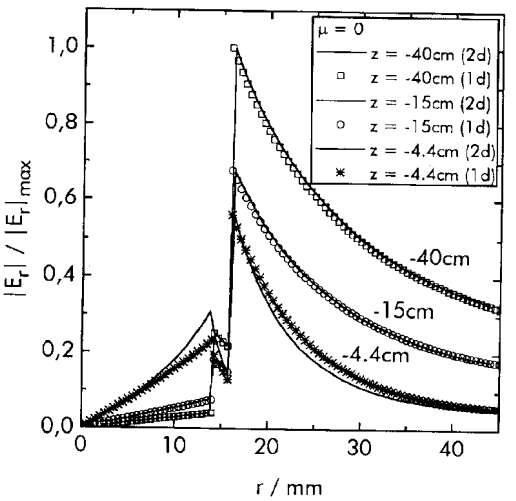

Figure 11. As in Fig. 10, but the radially homogeneous situation ($\mu = 0$) is considered.

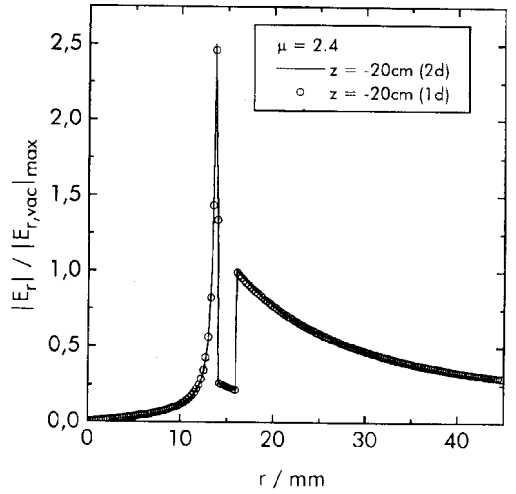

Figure 12. Radial cut at $z = -20$ cm for conditions as before, but $\mu = 2.4$ and $\nu_{en}/\omega = 0.6$.

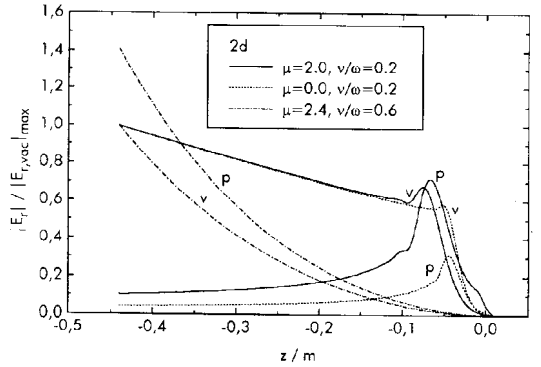

Figure 13. Axial cuts for $|E_r|$ near the wall in plasma (p, $r = a$) and in vacuum (v, $r = b$), both for the case $\mu = 2$ and $\nu_{en}/\omega = 0.2$ with system resonance and for $\mu = 2.4$ and $\nu_{en}/\omega = 0.6$ without system resonance.

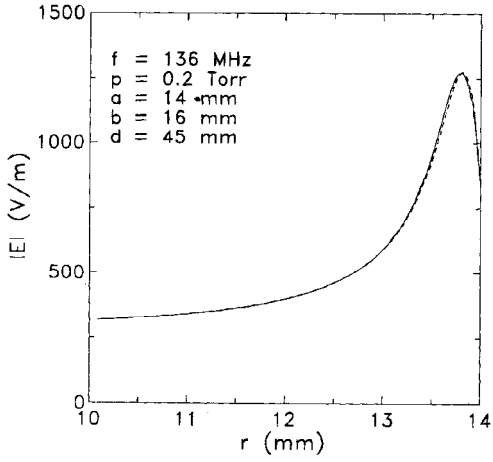

Figure 14. Radial profile of total field $|E|$ selfconsistently calculated with (solid) and without (dashed) ponderomotive potential for a relatively low frequency and $\omega/\bar{\omega_p} = 0.4$.

Moreover the position of the system resonance present starts being affected, since towards discharge end the density values near the wall become more relevant than the simply cross–section averaged value. Included in Fig. 10 is a situation of stronger radial inhomogeneity ($\mu = 2.4$) and larger damping ($\nu_{en}/\omega = 0.6$) when no system resonance shows up.

Influence of ponderomotive effects

The occurrence of relative strong radial field changes reminds of the potential influence of ponderomotive effects. Estimates are possible following previous studies[17] by using a ponderomotive potential $|e||E|^2/\ 4m(\omega^2 + \nu^2)$ and comparing it to the ambipolar potential, predicting usually minor influence. Indeed calculations where the total energy ε is extended in its definition to include this ponderomotive potential confirms the expected small difference within the framework of a nonlocal treatment on this basis as demonstrated in Fig. 14 for a resultant selfconsistently calculated radial $|E|$–profile for a low frequency case. Fig. 15 shows radial density profiles calculated both ways for a case in the GHz range. Fig. 16 demonstrates (in linear scale) corresponding small changes in the Θ–values.

SUMMARY AND OUTLOOK

The modeling outlined for the prototype case of SW allows a selfconsistent description in the microwave and also low frequency range. In particular even strong density inhomogeneities could be facilitated and simplified by the use of a nonlocal approximation. Some specific features resulting from density inhomogeneities and inherent resulting field inhomogeneities, including noncollisional transit–time–type damping, can thus

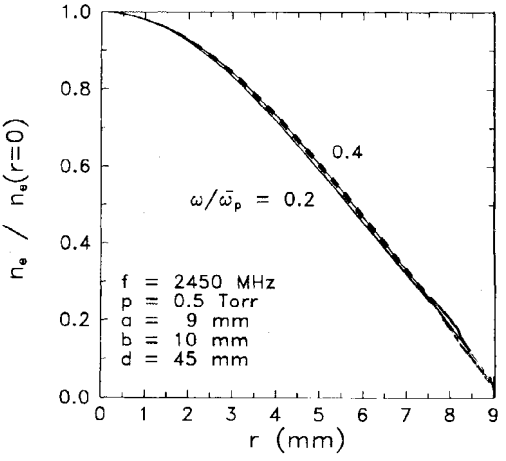

Figure 15. Resulting radial density profiles with (solid) and without (dashed) ponderomotive potential in the GHz regime. $\omega/\overline{\omega_p}$ = 0.2 and 0.4.

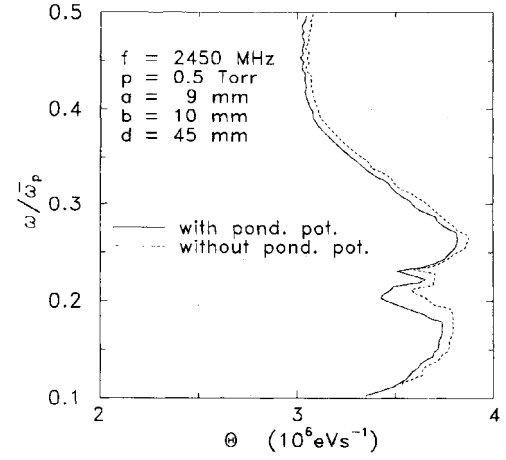

Figure 16. Conditions as in Fig. 15: Θ in linear scale versus $\overline{\omega_p}/\omega$.

be predicted. Relevant experimental observations so far available seem to bear out or at least to be consistent with predictions.

Doubtlessly more observations are desirable. For instance concerning the validity of a nonlocal scenario, more studies on EEDFs towards higher energies seem to be meaningful. Also detailed studies of radial emission profiles appear to promise sensitive checks on this aspect.

As to theoretical improvements required, there is of course always the need for refined incorporation of atomic/molecular physics data, even in the case of inert gases. Of most promise presently are investigations of generalization of the nonlocal approach, e.g. using multi–grid methods and improved boundary conditions on energy fluxes. After all the nonlocal approach is an approximation even in the regime of present use, particularly towards the inelastic energy range, and there are signs for the need of improvement at least in detail. Moreover the transition to the local regime has to be solved quantitatively in a completely selfconsistent way. An interesting detail aspect seems to be the detailed radial structure of energy fluxes for various conditions.

ACKNOWLEDGMENTS

Valuable contributions by Prof. Yu.M. Aliev and Prof. A. Shivarova are gratefully acknowledged, moreover the support by Deutsche Forschungsgemeinschaft and Volkswagenstiftung (grant I/70 375).

REFERENCES

1. Yu.M. Aliev, A.V. Maximov, U. Kortshagen, H. Schlüter and A. Shivarova, Modeling of microwave discharges in the presence of plasma resonances, *Phys. Rev. E* 51:6091 (1995).
2. Yu.M. Aliev, I.D. Kaganovich and H. Schlüter, Collisionless electron heating in RF gas discharges: I. Quasilinear theory, *in:* "Electron Kinetics and Applications of Glow Discharge", U. Kortshagen and L.D. Tsendin, eds., Plenum, New York, in press.
3. Yu.M. Aliev, V.Yu. Bychenkov, A.V. Maximov and H. Schlüter, High energy electron generation in surface–wave–produced plasmas, *Plasma Sources Sci. Technol.* 1:126 (1992).
4. C. Boisse–Laporte, Wave propagation in bounded plasmas, *in:* "Microwave discharges. Fundamentals and Application", C.M. Ferreira and M. Moisan, eds., Plenum, New York (1992).
5. G.G. Lister, Y.–M. Li and V.A. Godyak, Electrical conductivity in high–frequency plasmas, *J. Appl. Phys.* 79:8993 (1996).
6. S. Grosse, M. Georgieva–Grosse, I. Ghanashev and M. Schlüter, Influence of transversal plasma density nonuniformity and collisions on surface wave propagation, *J. Electromagn. Waves and Appl.* 11:609 (1997).
7. M. Schlüter, A numerical solution of 2D plasma surface waves, *J. Phys. D: Appl. Phys.* 30:L11 (1997).
8. Yu.M. Aliev, S. Grosse, H. Schlüter and A. Shivarova, Nonlinearity: basis for selfconsistent modeling of surface wave produced plasmas in diffusion controlled regimes, *Phys. Plasmas* 3:3162 (1996).
9. H. Schlüter, Surface wave sustained microwave discharges in the presence of plasma resonances, *in:* "Microwave Plasma and its Applications. Proceedings of the International Workshop 5–8 September 1994 vol. 2", Y.A. Lebedev, ed., Moscow Physical Society, Zvenigorad (1994).
10. H. Schlüter, Numerical modelling of surface wave discharges in the microwave range, *in:* "Plasma '95. Research and Applications of Plasmas. 2nd National Symposium vol. 2", H. Rotkaehl, ed., Warsaw (1995).
11. H. Schlüter, Selfconsistent modeling of surface wave sustained discharges, *in:* "Proceedings 3rd International Workshop Microwave Discharges: Fundamentals and Applications, Fontevraud, April 20–25, 1997") in press.

12. U. Kortshagen, Experimental evidence on the nonlocality of the electron distribution function, *Phys. Rev. E* 49:4369 (1994).
13. Kortshagen, U., A non–local kinetic model applied to microwave produced plasmas in cylindrical geometry, *J. Phys. D: Appl. Phys.* 26:1691 (1993).
14. J. Margot, M. Moisan and A. Ricard, Optical radiation effciency of surface–wave–produced plasmas as compared to DC positive columns, *Appl. Spectrosc.* 45:260 (1991).
15. S. Grosse, "Untersuchungen an einem mikrowellenangeregten Oberflächenwellenplasma", dissertation, Bochum (1995).
16. G. Himmel, I. Koleva and H. Schlüter, Diagnostics on a pulsed surface–wave discharge, *in:* "Proceedings 3rd International Workshop Microwave Discharges: Fundamentals and Applications, Fontevraud, April 20–25, 1997", in press.
17. Yu.M. Aliev, V.Yu. Bychenkov, M.S. Jovanovic and A.A. Frolov, The kinetic theory of the nonlinear low–frequency response of a collisionless plasma to high–frequency electromagnetic radiation, *J. Plasma Physics* 48:167 (1992).

MOMENTUM TRANSFER THEORY OF ELECTRON TRANSPORT IN $\vec{E} \times \vec{B}$ FIELD

Zoran Lj. Petrović and Slobodan B. Vrhovac

Institute of Physics
University of Belgrade, P.O.Box57,
11001 Belgrade, Yugoslavia

INTRODUCTION

Requirements for an electron transport theory which can serve as the basis for rf discharge modeling are increasingly complex and represent the main obstacle in achieving global plasma processing device modeling. In case of inductively coupled plasma (ICP) modeling[1], additional complication arises from the need to describe the effect of magnetic field and it requires non-linear equations of motion. Development of a simple, reasonably accurate kinetic theory, which on the other hand can describe all the relevant processes, is a desirable option to numerically intensive models. A very good example of great benefits from a simple analytical or semi-analytical theory is application of the non-local theory of Tsendin and Kortshagen[2]. In this paper we develop another aproach to developing a simple kinetic theory which can be used universally. It is the Momentum Transfer Theory (MTT) which has been used in physics of electron and ion swarms to provide physical insight into kinetic phenomena through development of analytical relations[3]. In this paper we restrict ourselves to application of MTT to charged particle transport, electrons in particular.

MTT basically consists of applying Taylor expansion to the rate coefficients at the appropriately determined value of the mean energy. Regardless of its simplicity it allows a reasonably small uncertainty of the calculated data of the order of 10%. While early developments relevant to MTT date back to the work of Wannier[4, 5] and Mason[6] the MTT has been mostly developed by Robson and coworkers.

MTT has been applied to test the validity of Blanc's law for charged particle transport in mixtures of gases having only elastic processes[6, 7, 8]. Inelastic collisions have been included in the single gas MTT and corresponding equations for energy, drift velocity and relationship between the mobility and components of the diffusion tensor were developed[9]. Reactive collisions were included in addition to inelastic and the corresponding effects of attachment, annihilation[10] and ionization[11] on transport coefficients were discussed. MTT was also applied to electron transport in crossed electric and magnetic fields for a case of a single gas with non-reactive collisions[12].

Recently, however, MTT has been developed for a general case of gas mixtures that

Electron Kinetics and Application of Glow Discharges
Edited by U. Kortshagen and L. D. Tsendin, Plenum Press, New York, 1998

include elastic, inelastic and reactive collisions[13] . This theory was applied to study the development of negative differential conductivity (NDC)[13] , the validity of Blanc's law at high E/n_0 [14] , the higher order transport coefficients[15] , electron transport in $\vec{E} \times \vec{B}$ fields [16] and also a time dependent MTT was developed[14] .

In this paper we give a summary of the theory in purely electric field and some phenomena that were studied. Usefulness of MTT in developing analytical formulae is illustrated by the analysis of some of the processes supporting the development of NDC and in calculation of the higher order transport coefficients. We proceed to describe the steady state $\vec{E} \times \vec{B}$ theory and finally we summarize the MTT procedure and possible applications in gas discharge modeling including the development of the time dependent and spatially dependent theory and development of a non-local beam-equation theory[17] .

THEORETICAL EVALUATION- ELECTRIC FIELD ONLY

A swarm of particles of charge *e* and mass *m* is moving with velocity $\vec{v}$ through neutral gas mixtures under the influence of an applied electric field $\vec{E}$. We limit ourselves to electron swarms but most of the results presented here may be directly applied or easily extended to ion swarms, even to neutral swarms. There may be several different (l) constituents of the gas mixture. Let m_α and $\vec{v}_\alpha$ be mass and velocity of molecules of the αth neutral gas, respectively. Let $n(\vec{r},t)$ be the number density of swarm particles and let $n_\alpha(\vec{r},t)$ be the number density of the αth neutral gas. We introduce a standard notation:

$n_0 = \sum_\alpha n_\alpha$ (number density of the gas mixture),
$\mu_\alpha = m\, m_\alpha/(m + m + \alpha)$ (reduced mass),
$M_\alpha = m_\alpha/(m + m_\alpha)$, $M_\alpha^0 = m/(m + m_\alpha)$,
$\vec{v}_{r\alpha} = \vec{v} - \vec{v}_\alpha$ (relative velocity) and
$\varepsilon_\alpha = \frac{1}{2}\mu_\alpha v_{r\alpha}^2$ (energy measured in the center-of-mass reference frame).
The remaining notation is the same as in the paper by Vrhovac and Petrović[13] where a detailed developoment of the theory may be found. The theory presented here is a generalization of the MTT developed by Robson [7, 9, 10, 18] .

The Boltzmann equation for a swarm of particles moving through a gaseous multicomponent medium is[3]:

$$\left[\frac{\partial}{\partial t} + \vec{v}\cdot\frac{\partial}{\partial \vec{r}} + \frac{e}{m}\vec{E}(\vec{r},t)\cdot\frac{\partial}{\partial \vec{v}}\right] f^{\mathrm{mix}}(\vec{r},\vec{v},t) = \sum_\alpha J_\alpha^{\mathrm{mix}}(f^{\mathrm{mix}}, f_\alpha^{\mathrm{mix}}), \qquad (1)$$

where J_α^{mix} is the collision operator which represents the rate of change of the distribution function f^{mix} due to collisions between the swarm particles and molecules of the neutral gas α. All velocity distribution functions are normalized to number densities.

The collision processes included in our analysis are limited to elastic, inelastic and reactive (both attachment and ionization) collisions of individual swarm particles with normal gas molecules. Both momentum and energy loss of swarm particles in elastic collisions arising from the finite mass of gas molecules are taken into account. The gas particles have a non-zero temperature. Momentum exchange in inelastic processes is not ignored and we also include the superelastic terms associated with inelastic processes. The dynamics of ionization collisions is more complicated than that of attachment We ignore the motion of the molecule after ionization, so that the available energy and momentum are divided between the two electrons. Only single ionization is taken into account but the resulting ion can be left in any one of its internal excited states.

Formulation of Moment Equations

The chain of moment equations is derived by multiplying both sides of Eq. (1) by various powers of swarm particle velocity and integrating over velocity space. What we obtain is basically an extention of the moment equations derived by Robson[10] and Robson and Nessr[18] to include gas mixtures by taking appropriately weighted sums of collision terms in momentum equations. In addition a more detailed representation of collisional events is provided including the momentum transfer in inelastic collisions. The starting moment equations are:
Equation of continuity:

$$\begin{aligned}&\frac{\partial}{\partial t}n(\vec{r},t)+\frac{\partial}{\partial \vec{r}}\cdot\left[n(\vec{r},t)\langle\vec{v}\rangle^{\mathrm{mix}}\right]\\&=-n(\vec{r},t)\sum_{\alpha\in I_l}\langle\langle\nu_\alpha^{(A)}(\vec{r},v_{r\alpha},t)\rangle\rangle_\alpha^{\mathrm{mix}}+n(\vec{r},t)\sum_{\alpha\in I_l}\langle\langle\nu_\alpha^{(I)}(\vec{r},v_{r\alpha},t)\rangle\rangle_\alpha^{\mathrm{mix}}\end{aligned}\tag{2}$$

Momentum balance equation:

$$\begin{aligned}&\frac{\partial}{\partial t}\left[mn(\vec{r},t)\langle\vec{v}\rangle^{\mathrm{mix}}\right]+\frac{\partial}{\partial \vec{r}}\left[mn(\vec{r},t)\langle\{\vec{v},\vec{v}\}\rangle^{\mathrm{mix}}\right]-n(\vec{r},t)e\vec{E}(\vec{r},t)\\&=-n(\vec{r},t)\sum_{\alpha\in I_l}\mu_\alpha\langle\langle\vec{v}_{r\alpha}\nu_{0\alpha}^{(m)}(\vec{r},v_{r\alpha},t)\rangle\rangle_\alpha^{\mathrm{mix}}-n(\vec{r},t)m\sum_{\alpha\in I_l}\langle\langle\vec{v}\nu_\alpha^{(A)}(\vec{r},v_{r\alpha},t)\rangle\rangle_\alpha^{\mathrm{mix}}\end{aligned}\tag{3}$$

Energy balance equation:

$$\begin{aligned}&\frac{\partial}{\partial t}\left[\frac{1}{2}mn(\vec{r},t)\left\langle v^2\right\rangle^{\mathrm{mix}}\right]+\frac{\partial}{\partial \vec{r}}\cdot\left[\frac{1}{2}mn(\vec{r},t)\left\langle v^2\vec{v}\right\rangle^{\mathrm{mix}}\right]-n(\vec{r},t)e\vec{E}(\vec{r},t)\left\langle\vec{v}\right\rangle^{\mathrm{mix}}\\&=-n(\vec{r},t)\sum_{\alpha\in I_l}\frac{\mu_\alpha}{m+m_\alpha}\left\langle\left\langle\left[mv^2-m_\alpha v_\alpha^2-(m-m_\alpha)\vec{v}\cdot\vec{v}_\alpha\right]\nu_{0\alpha}^{(m)}(\vec{r},v_{r\alpha},t)\right\rangle\right\rangle_\alpha^{\mathrm{mix}}\\&-n(\vec{r},t)\sum_{\alpha\in I_l}\sum_{s\in I_\alpha^{(in)}}\langle\langle\nu_{s\alpha}(\vec{r},v_{r\alpha},t)\rangle\rangle_\alpha^{\mathrm{mix}}\Delta E_\alpha^s-n(\vec{r},t)\frac{1}{2}m\sum_{\alpha\in I_l}\left\langle\left\langle v^2\nu_\alpha^{(A)}(\vec{r},v_{r\alpha},t)\right\rangle\right\rangle_\alpha^{\mathrm{mix}}\\&-n(\vec{r},t)\sum_{\alpha\in I_l}\left\langle\left\langle\nu_\alpha^{(I)}(\vec{r},v_{r\alpha},t)\right\rangle\right\rangle_\alpha^{\mathrm{mix}}\varepsilon_\alpha^{(I)}-n(\vec{r},t)\sum_{\alpha\in I_l}\sum_{s\in I_\alpha^{(I)}}\left\langle\left\langle\nu_{s\alpha}^{(I)}(\vec{r},v_{r\alpha},t)\right\rangle\right\rangle_\alpha^{\mathrm{mix}}\Delta\varepsilon_{s\alpha}^{(I)}.\end{aligned}\tag{4}$$

Momentum - Transfer Approximation

If we replace the variables $v_{r\alpha}\longrightarrow\varepsilon_\alpha$ in expressions for collisional frequencies, $\nu_\alpha(\vec{r},v_{r\alpha},t)\longrightarrow\tilde{\nu}_\alpha=\tilde{\nu}_\alpha(\vec{r},\varepsilon_\alpha,t)$ and apply Taylor series expansion in the vicinity of ε_α^0 we obtain the MTT balance equations. We assume that Taylor expansion converges rapidly in the neighborhood of ε_α^0. The extended momentum - transfer approximation consists of retention of several terms in Taylor expansion. Momentum and energy loss rates for attachment are calculated using the first two terms and the assumption that the distribution function of swarm particles is shifted Maxwellian. We also assume that the background gas is in the thermal equilibrium (characterized by Maxwellian distribution and temperature T^{mix}). Using momentum - transfer approximation we obtain the equation of continuity

$$\frac{\partial}{\partial t}n(\vec{r},t)+\frac{\partial}{\partial \vec{r}}\cdot\left[n(\vec{r},t)\langle\vec{v}\rangle^{\mathrm{mix}}\right]=-n(\vec{r},t)\tilde{\nu}^{(A)}(\vec{r},\varepsilon^0,t)+n(\vec{r},t)\tilde{\nu}^{(I)}(\vec{r},\varepsilon^0,t)\tag{5}$$

and a more useful form of the momentum and energy balance equations:

$$mn(\vec{r},t)\left[\frac{\partial}{\partial t}+\langle\vec{v}\rangle^{\mathrm{mix}}\cdot\frac{\partial}{\partial\vec{r}}\right]\langle\vec{v}\rangle^{\mathrm{mix}}-n(\vec{r},t)e\vec{E}(\vec{r},t)+\mathrm{div}\hat{P}^{\mathrm{mix}}$$
$$=-n(\vec{r},t)m\langle\vec{v}\rangle^{\mathrm{mix}}\tilde{\nu}_0^{(m)}(\vec{r},\varepsilon^0,t)-n(\vec{r},t)m\langle\vec{v}\rangle^{\mathrm{mix}}\left[\xi^{\mathrm{mix}}\tilde{\nu}_1^{(A)}(\vec{r},\varepsilon^0,t)+\tilde{\nu}^{(I)}(\vec{r},\varepsilon^0,t)\right] \tag{6}$$

$$n(\vec{r},t)\left[\frac{\partial}{\partial t}+\langle\vec{v}\rangle^{\mathrm{mix}}\cdot\frac{\partial}{\partial\vec{r}}\right]\left[\frac{1}{2}m\langle v^2\rangle^{\mathrm{mix}}\right]+\frac{\partial}{\partial\vec{r}}\cdot\left[\hat{P}^{\mathrm{mix}}\langle\vec{v}\rangle^{\mathrm{mix}}+\frac{3}{2}\vec{Q}^{\mathrm{mix}}\right]$$
$$-n(\vec{r},t)e\vec{E}(\vec{r},t)\langle\vec{v}\rangle^{\mathrm{mix}}=-n(\vec{r},t)\left[m\langle v^2\rangle^{\mathrm{mix}}-3kT^{\mathrm{mix}}\right]\tilde{\nu}_{00}^{(m)}(\vec{r},\varepsilon^0,t)$$
$$-n(\vec{r},t)\sum_{\alpha\in I_l}\sum_{s\in I_\alpha^{(in)}}\tilde{\nu}_{s\alpha}(\vec{r},\varepsilon_\alpha^0,t)\Delta E_\alpha^s-n(\vec{r},t)\frac{1}{2}m\left[\langle v^2\rangle^{\mathrm{mix}}-(\langle\vec{v}\rangle^{\mathrm{mix}})^2\right]\xi^{\mathrm{mix}}\tilde{\nu}_1^{(A)}(\vec{r},\varepsilon^0,t)$$
$$-n(\vec{r},t)\sum_{\alpha\in I_l}\tilde{\nu}_\alpha^{(I)}(\vec{r},\varepsilon_\alpha^0,t)\varepsilon_\alpha^{(I)}-n(\vec{r},t)\sum_{\alpha\in I_l}\sum_{s\in I_\alpha^{(I)}}\tilde{\nu}_{s\alpha}^{(I)}(\vec{r},\varepsilon_\alpha^0,t)\Delta\varepsilon_{s\alpha}^{(I)}$$
$$-n(\vec{r},t)\frac{1}{2}m\langle v^2\rangle^{\mathrm{mix}}\tilde{\nu}^{(I)}(\vec{r},\varepsilon^0,t). \tag{7}$$

where $\hat{P}^{\mathrm{mix}}$ is the pressure tensor and $\vec{Q}^{\mathrm{mix}}$ is the heat conductivity vector. Attachment collision rate appears in the form of the first derivative denoted by $\tilde{\nu}_1^{(A)}$[13].

Hydrodynamic Limit and Transport Coefficients

We assume that the swarm has evolved to its hydrodynamic limit (HDL). In HDL, the space - time dependence of all properties is carried by the number density and the swarm can be characterized by time - independent transport coefficients.

The starting point of the hydrodynamic description is the continuity equation for the number density which can be developed by applying gradient expansion to take the form of the diffusion equation:

$$\left[\frac{\partial}{\partial t}+\vec{W}^{\mathrm{mix}}\cdot\frac{\partial}{\partial\vec{r}}-\hat{D}^{\mathrm{mix}}:\left\{\frac{\partial}{\partial\vec{r}},\frac{\partial}{\partial\vec{r}}\right\}+\hat{S}^{\mathrm{mix}}\odot\left(\frac{\partial}{\partial\vec{r}}\right)^3\right]n(\vec{r},t)=-\alpha^*n(\vec{r},t), \tag{8}$$

which can be used to define the transport coefficients: reaction rate α, drift velocity $\vec{W}^{\mathrm{mix}}$, diffusion tensor $\hat{D}^{\mathrm{mix}}$ and, depending on truncation, the higher order coefficients such as skewness $\hat{S}^{\mathrm{mix}}$. Following a procedure similar to that developed by Robson[10] momentum and energy balance equations can be written as:

$$\langle\vec{v}\rangle^{\mathrm{mix}}=\psi_1(\varepsilon^0,(\langle\vec{v}\rangle^{\mathrm{mix}})^2)\left[\vec{E}-\frac{k}{e}\hat{T}^{\mathrm{mix}}\vec{G}\right] \tag{9}$$

$$\langle\langle\varepsilon_\alpha\rangle\rangle_\alpha^{\mathrm{mix}}=\psi_2^\alpha(\varepsilon^0,(\langle\vec{v}\rangle^{\mathrm{mix}})^2)-M_\alpha\frac{3}{2}\vec{q}^{\mathrm{mix}}\vec{G}\frac{1}{\bar{\nu}_{(\varepsilon)}^{\mathrm{mix}}},\quad\alpha\in I_l \tag{10}$$

The functions ψ_1 and ψ_2^α, $\alpha\in I_l$, of Eqs. (9) and (10), respectively, are defined as follows:

$$\psi_1(\varepsilon^0,(\langle\vec{v}\rangle^{\mathrm{mix}})^2)=\frac{e}{m\bar{\nu}_{(m)}^{\mathrm{mix}}} \tag{11}$$

$$\psi_2^\alpha(\varepsilon^0,(\langle\vec{v}\rangle^{\mathrm{mix}})^2) = \frac{1}{2}m(\langle\vec{v}\rangle^{\mathrm{mix}})^2 M_\alpha r^{\mathrm{mix}} + \frac{3}{2}kT^{\mathrm{mix}}M_\alpha\left[\frac{M_\alpha^0}{M_\alpha}+s^{\mathrm{mix}}\right] - M_\alpha\bar{\Omega}^{\mathrm{mix}}, \quad \alpha\in I_l, \tag{12}$$

where we use the notations:

$$\bar{\nu}_{(e)}^{\mathrm{mix}} = 2\tilde{\nu}_{00}^{(m)} + \xi^{\mathrm{mix}}\tilde{\nu}_1^{(A)} + \tilde{\nu}^{(I)} \tag{13}$$

$$r^{\mathrm{mix}} = \frac{2\tilde{\nu}_0^{(m)} + \xi^{\mathrm{mix}}\tilde{\nu}_1^{(A)} + 2\tilde{\nu}^{(I)}}{\bar{\nu}_{(e)}^{\mathrm{mix}}}, \qquad s^{\mathrm{mix}} = \frac{2\tilde{\nu}_{00}^{(m)}}{\bar{\nu}_{(e)}^{\mathrm{mix}}} \tag{14}$$

$$\bar{\Omega}^{\mathrm{mix}} = \frac{\bar{\Lambda}^{\mathrm{mix}}}{\bar{\nu}_{(e)}^{\mathrm{mix}}}, \qquad \bar{\Lambda}^{\mathrm{mix}} = \sum_{\alpha\in I_l}\bar{\Lambda}_\alpha^{\mathrm{mix}} \tag{15}$$

$$\bar{\Lambda}_\alpha^{\mathrm{mix}} = \sum_{s\in I_\alpha^{(\mathrm{in})}}\tilde{\nu}_{s\alpha}\Delta E_\alpha^s + \tilde{\nu}_\alpha^{(I)}\varepsilon_\alpha^{(I)} + \sum_{s\in I_\alpha^{(I)}}\tilde{\nu}_{s\alpha}^{(I)}\Delta\varepsilon_{s\alpha}^{(I)}, \quad \alpha\in I_l \tag{16}$$

$$\langle\langle\varepsilon_\alpha\rangle\rangle_\alpha^{\mathrm{mix}} = M_\alpha\frac{1}{2}m\langle v^2\rangle^{\mathrm{mix}} + M_\alpha^0\frac{3}{2}kT^{\mathrm{mix}}, \quad \alpha\in I_l \tag{17}$$

and

$$\vec{G}(\vec{r},t) = \frac{1}{n(\vec{r},t)}\frac{\partial}{\partial\vec{r}}n(\vec{r},t). \tag{18}$$

If functions $\vec{\omega}^{\mathrm{mix}} = \vec{\omega}^{\mathrm{mix}}(\vec{E})$ and $\varepsilon_\alpha^{\mathrm{mix}} = \varepsilon_\alpha^{\mathrm{mix}}(\vec{E})$, $\alpha\in I_l$, satisfy the following system of equations:

$$\vec{\omega}^{\mathrm{mix}}(\vec{E}) = \psi_1((\varepsilon_\alpha^{\mathrm{mix}})_{\alpha\in I_l},(\omega^{\mathrm{mix}})^2)\vec{E} \tag{19}$$

$$\varepsilon_\alpha^{\mathrm{mix}}(\vec{E}) = \psi_2^\alpha((\varepsilon_\alpha^{\mathrm{mix}})_{\alpha\in I_l},(\omega^{\mathrm{mix}})^2), \quad \alpha\in I_l \tag{20}$$

we can write

$$\langle\vec{v}\rangle^{\mathrm{mix}} = \vec{\omega}^{\mathrm{mix}}\left(\vec{E}-\frac{k}{e}\hat{T}^{\mathrm{mix}}\vec{G}\right), \tag{21}$$

$$\langle\langle\varepsilon_\alpha\rangle\rangle_\alpha^{\mathrm{mix}} = \varepsilon_\alpha^{\mathrm{mix}}\left(\vec{E}-\frac{k}{e}\hat{T}^{\mathrm{mix}}\vec{G}\right), \quad \alpha\in I_l \tag{22}$$

$$\tilde{\nu}^* = \tilde{\nu}^*\left[\varepsilon^0\left(\vec{E}-\frac{k}{e}\hat{T}^{\mathrm{mix}}\vec{G}\right)\right] = \alpha^*\left(\vec{E}-\frac{k}{e}\hat{T}^{\mathrm{mix}}\vec{G}\right). \tag{23}$$

The calculations in MTT proceed by using (19) and (20) to determine the values of mean velocity and mean energy, which are subsequently used to determine the collision

rates from (23). The actual drift velocity in the presence of reactive collisions can be obtained from:

$$\vec{W}^{\text{mix}}(\vec{E}) = \vec{\omega}^{\text{mix}}(\vec{E}) - \frac{k}{e}\hat{T}^{\text{mix}}\frac{\partial\alpha^*(\vec{E})}{\partial\vec{E}}, \tag{24}$$

while the components of the diffusion tensor are determined from:

$$D_{ij}^{\text{mix}} = \frac{k}{e}\sum_{k=1}^{3} t_{ik}^{\text{mix}}\left[\frac{\partial}{\partial E_k}W_j^{\text{mix}} + \frac{1}{2}\frac{k}{e}\sum_{l=1}^{3} t_{jl}^{\text{mix}}\frac{\partial}{\partial E_l}\frac{\partial\alpha^*}{\partial E_k}\right], \quad i,j = 1,2,3 \tag{25}$$

where the effective reaction rate α^* is determined from:

$$\alpha^*(\vec{E}) = \tilde{\nu}^*[\varepsilon^0(\vec{E})] = \tilde{\nu}^{(A)}[\varepsilon^0(\vec{E})] - \tilde{\nu}^{(I)}[\varepsilon^0(\vec{E})]. \tag{26}$$

Equation (25) is a generalized Einstein relation (GER) appropriate to reacting particle swarms in gas mixtures. It is thus a generalization of the GER available in the literature [19, 10].

APPLICATIONS OF ANALYTICAL FORMULAE

Negative Differential Conductivity

Negative differential conductivity (NDC) may be, rather narrowly, defined as a decrease of the drift velocity with an increasing normalized driving field E/n_0. NDC is a kinetic phenomenon which is both of fundamental interest[20, 21, 22] and of interest for a number of applications such as determination of accurate electron scattering cross sections[23] and diffuse discharge switches[24]. A specific form of time dependent NDC was found to exist in rf discharges[25, 26] which may affect power deposition efficiency.

Several explanations of NDC were available in the literature prior to 1984. Those were mostly based on the condition that the Ramsauer Townsend minimum is present[20] and even that the conditions for the NDC and for the breakdown of the two term theory coincide[27]. Earlier theories have included most of the correct ideas[20, 21] in explanation of the NDC but were limited by the accepted assumptions and thus could not cover all its basic aspects. Petrović et al.[28] (PCH) have made a series of model calculations that led them do develop a set of conditions for the shapes of the cross sections that favour NDC. Robson[9] has put the NDC criterion on a much firmer ground by applying MTT.

The conditions developed by PCH and Robson for NDC as summarized by Petrović et al. are:

1. Inelastic processes are necessary;
2. Increasing momentum transfer cross section favours NDC;
3. Decreasing inelastic cross section favours NDC;
4. Occurrence of NDC depends on magnitudes of the factors 2 and 3;
5. Superelastic processes will have a tendency to reduce the NDC.

The above conditions represent what can be regarded as the standard NDC, i.e. the NDC that is induced by the shape of the cross sections under non-reactive swarm conditions. It turned out that the condition 1. was valid only for pure gases[9]. For mixtures it is possible to use two different atomic gases in the mixture under conditions when only elastic collisions are important and still observe NDC[29, 30, 13, 31]. The NDC criterion may be obtained in an analytic form from Eqs. (9) and (10) applied to a

mixture of gases having elastic collisions only. The resulting criterion for a binary mixture [13] is:

$$1-\frac{1}{2}\left[\frac{eE}{m}\right]^2\frac{m_1}{(\tilde{\nu}_{01}^{(m)}+\tilde{\nu}_{02}^{(m)})^2}\frac{d}{d\varepsilon}\left[\frac{\tilde{\nu}_{01}^{(m)}+\tilde{\nu}_{02}^{(m)}}{\tilde{\nu}_{01}^{(m)}+\frac{m_1}{m_2}\tilde{\nu}_{02}^{(m)}}\right]<0. \tag{27}$$

L.h.s. of Eq. (27) is less than zero when collisional frequency of elastic collisions increases rapidly while the mass normalized term describing the energy transfer in elastic collisions should be dominated by the collisional frequency that has a different energy dependence to the dominant cross section. NDC will not occur for low mean energies close to the thermal equilibrium because of the first bracket in the second term. For binary mixtures when $m_1 \ll m_2$ and $\tilde{\nu}_{01}^{(m)} \approx$ const a rapid increase of $\tilde{\nu}_{02}^{(m)}$ with E/n_0 will tend to induce a negative slope of drift velocity provided that n_{01}/n_{02} is sufficiently small. In case that mean energy dependences of collisional frequencies are similar or masses of atoms of the two constituent gases are similar no NDC will develop. What basically occurs in this case is that energy losses in collisions of electrons with lighter atomic gas play the role of the energy contolling inelastic process [13, 30, 31].

In case of a pure gas with inelastic and reactive collisions the criterion for the development of NDC may be written in the form [13] :

$$\frac{d}{d\varepsilon}\left[\varepsilon\tilde{s}_e^{(*)}\right]+\frac{d\bar{\Omega}_e^{(*)}}{d\varepsilon}<0, \tag{28}$$

where

$$\tilde{s}_e^{(*)}=1+\frac{\tilde{\nu}^{(I)}+\frac{2}{3}\varepsilon\tilde{\nu}_1^{(A)}}{\tilde{\nu}_e},\quad \bar{\Omega}_e^{(*)}=\frac{\bar{\Lambda}}{\tilde{\nu}_e}. \tag{29}$$

If we neglect the reactive collisions, the equation (28) becomes identical to the criterion developed by Robson[9]. It is possible to predict easily the effect of superelastic colisions on NDC. In all criteria superelastic collision rates appear with symmetry to the inelastic losses i.e. only the sign is changed. That means that exactly the opposite conditions, i.e. an increase with the mean energy, will be valid for superelastic collisions. While it is difficult to find exact conditions when the shape of cross sections will be such that superelastic process will contribute more to the NDC than the negative effect of inelastic collisions, it may not be impossible. In any case superelastic collisions will reduce the NDC effect as can be seen in Fig. (1) for the case of methane.

The basic difference between Robson's criterion and that of Vrhovac and Petrović is in the first term on the 1.h.s. (See Eq. (28)). That term can be written explicitely as:

$$\frac{d}{d\varepsilon}(\varepsilon\tilde{s}_e^{(*)})=1+\frac{\tilde{\nu}^{(I)}+\frac{2}{3}\varepsilon\tilde{\nu}_1^{(A)}}{\tilde{\nu}_e}+\varepsilon\frac{d}{d\varepsilon}\left[\frac{\tilde{\nu}^{(I)}+\frac{2}{3}\varepsilon\tilde{\nu}_1^{(A)}}{\tilde{\nu}_e}\right]. \tag{30}$$

One should note that attachment and ionization are not equivalent in this criterion, i.e. attachment collision rate is present through it's first derivative $\tilde{\nu}_1^{(A)}$. NDC will be supported by decreasing ionization collision frequency, a condition that is not likely to occur for realistic conditions. However, for the attachment, collision frequency may have a shape that is required to induce the NDC, may even have it for two different E/n_0 below and above the maximum. The requirement is that the rate of change of the slope changes sign to negative values which is commonly realized. One should be warned that this effect promoting the NDC is purely due to the reactive nature of

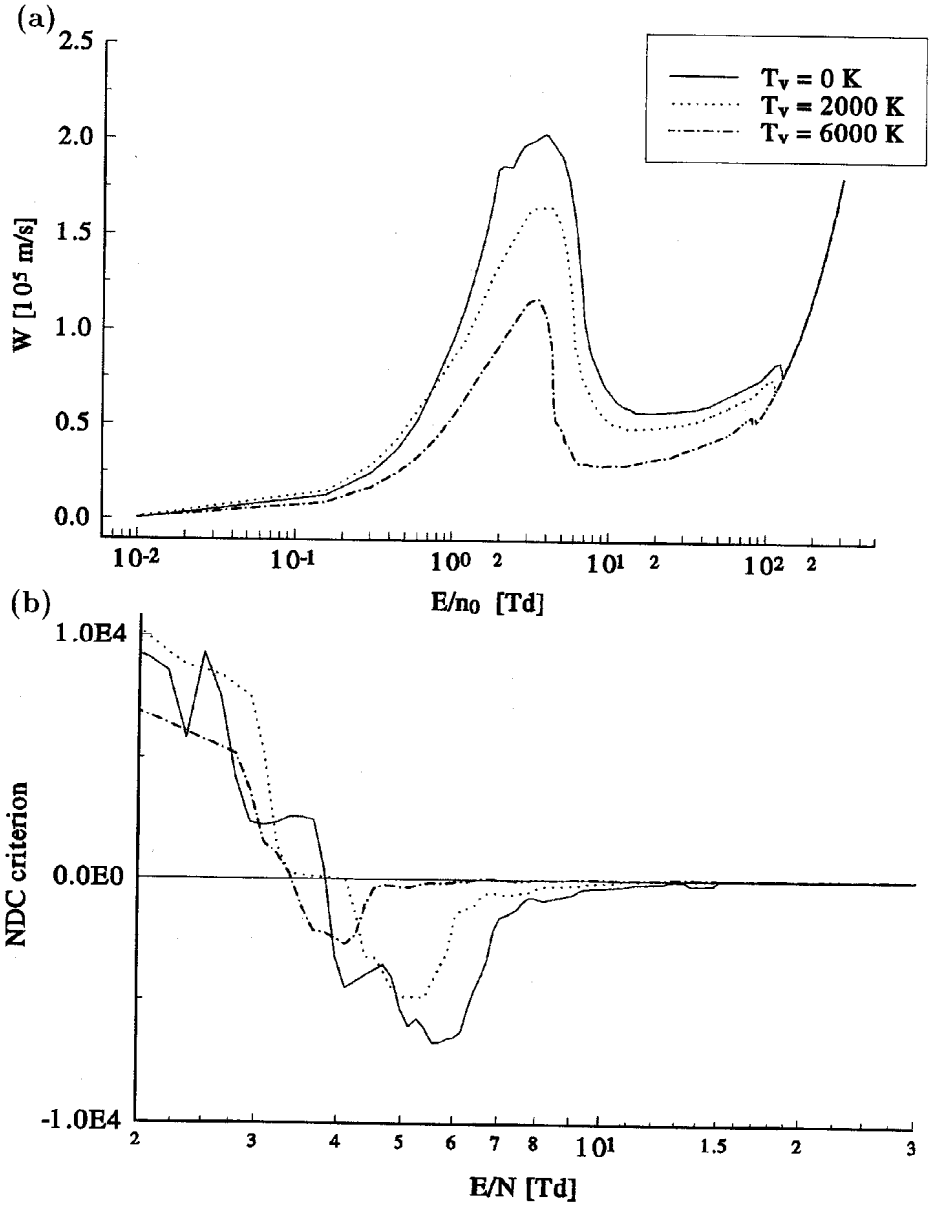

Figure 1. 1. NDC in methane as a function of E/n_0 and non-equilibrium vibrational temperature[25]: a) Drift velocities calculated from the Boltzmann equation; b) The NDC criterion from equation (28) - negative values correspond to NDC and the results are in excellent agreement with calculations.

collisions and should be added to the standard cause of the NDC due to the shape of cross sections. If we make a set of cross sections that gives the mean velocity of electrons just on the verge of NDC then NDC may be induced by changing the nature of one of the inelastic processes into reactive- ionization or by adding attachment. This is shown in Fig. (2).

When reactive collisions are present the drift velocity is different from the mean velocity of electrons [32] and thus the condition for the NDC for drift velocity chages to:

$$\frac{dW}{dE} = \frac{d\omega}{dE} - \frac{1}{e}\frac{2}{3}\left[\frac{d\varepsilon}{dE}\frac{d\alpha}{dE} + \varepsilon\frac{d^2\alpha}{dE^2}\right] < 0, \tag{31}$$

which contains the first term due to the NDC in the mean velocity and the second two terms due to correction for reactive collisions which will affect greatly the occurence and the position of the NDC. If we neglect ionization and all inelastic collisions from Eq. (28) we obtain:

$$1 + \frac{\frac{2}{3}\varepsilon\tilde{\nu}_1^{(A)}}{\tilde{\nu}_e} + \varepsilon\frac{d}{d\varepsilon}\left[\frac{\frac{2}{3}\varepsilon\tilde{\nu}_1^{(A)}}{\tilde{\nu}_e}\right] < 0, \tag{32}$$

which indicates that in the presence of elastic collisions only, even in a single gas, attachment may induce the NDC.

The NDC can thus be indeced by the basic shape of the cross sections (collisional rates) as a function of the energy, by reactive corrections and by reactive collision term as well. It was also discovered that electron-electron collisions may induce the NDC[33] though the effect may be reduced due to the thermalizing effect of electron- electron collisions. We may expect additional causes of NDC due to different kinetic processes and this effect may prove to be one of the most interesting targets for fundamental studies of gas discharge kinetics, with some possible applications[34].

Higher Order Transport Coefficients

Momentum-transfer theory will also be used here to derive approximate expression for higher order transport coefficients of reacting particle swarms in mixtures of gases. Higher order transport coefficients may not be yet required for plasma modeling but can be useful in obtaining the cross section data and removing the discrepancies between the existing sets[35]. Our basic aim is to derive *relationships* between experimentally measurable quatities. In particular, the aim is to obtain semi-quantitative relations between skewness and lower-order transport coefficients.

In the hydrodynamics regime $|\vec{G}|$ is small. We expand functions $\vec{\omega}^{\text{mix}}$ [Eq. (21)] and α^* [Eq. (23)] to the *second* and *third* order in $\vec{G}$, respectively. Substituting these expansions into the equation of continuity [Eq. (2)] leads, after some algebra, to a diffusion equation [Eq. (8)], where

$$S_{ijk}^{\text{mix}} = \frac{1}{2}\frac{k^2}{e^2}\sum_{l=1}^{3} t_{il}^{\text{mix}} \sum_{m=1}^{3} t_{jm}^{\text{mix}} \left[\frac{\partial}{\partial E_m}\frac{\partial}{\partial E_l} W_k^{\text{mix}} + \frac{1}{6}\frac{k}{e}\sum_{n=1}^{3} t_{kn}^{\text{mix}} \frac{\partial}{\partial E_n}\frac{\partial}{\partial E_m}\frac{\partial \alpha^*}{\partial E_l}\right], \quad i,j,k = 1,2,3 \tag{33}$$

is the skewness.

In Eq. (33) $\alpha^* = \tilde{\nu}^{(A)} - \tilde{\nu}^{(I)}$ is the effective reaction rate (attachment) coefficient. Equation (33) establishes the relationship between skewness $\hat{S}^{\text{mix}}$, drift velocity $\vec{W}^{\text{mix}}$

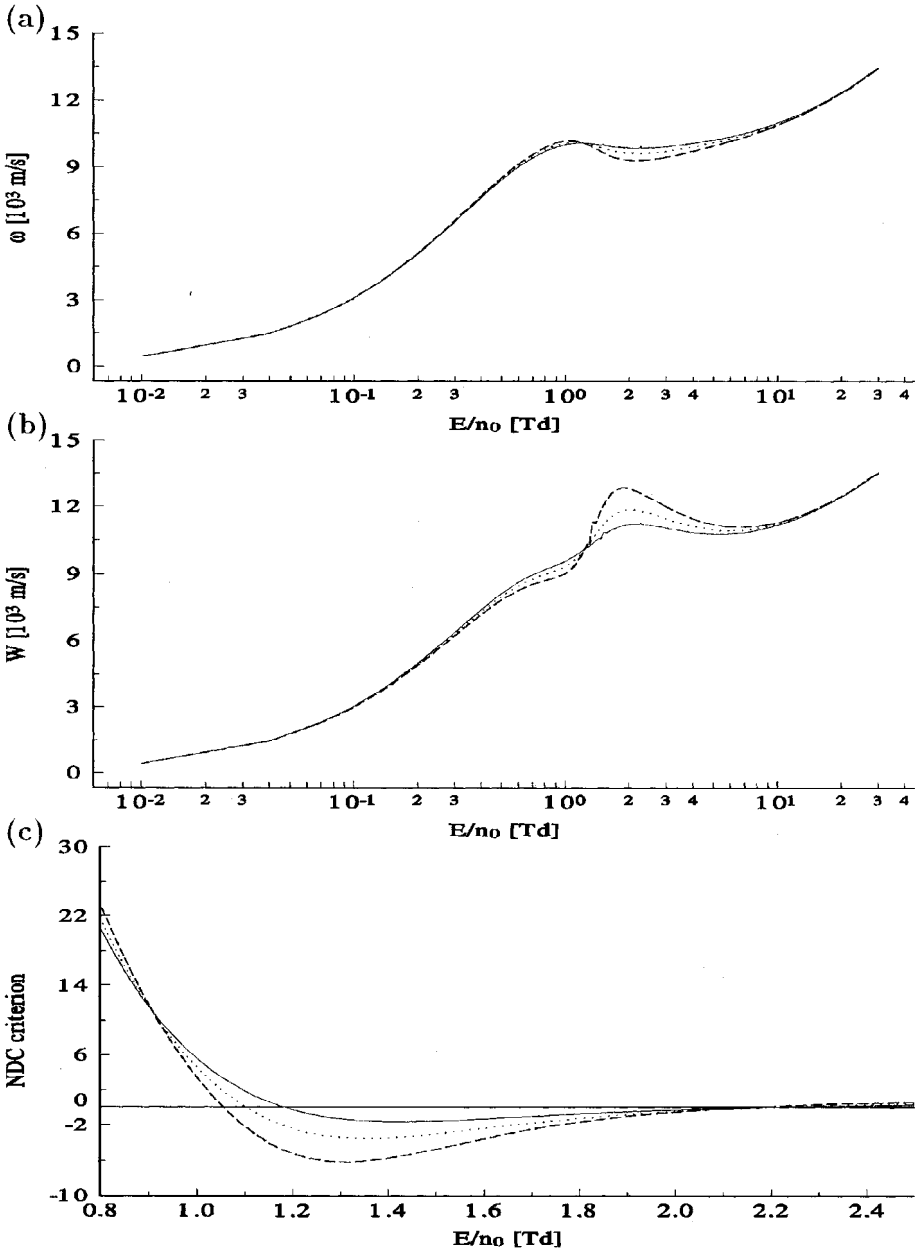

Figure 2. The effect of attachment on drift velocity. A basic set of model cross sections giving a constant drift velocity but no NDC is used[28]. A constant attachment cross section is added with three different values of the cross section: 0.001 $\cdot 10^{-16} cm^2$-solid curve; 0.0016 $\cdot 10^{-16} cm^2$ - dashed curve and 0.0024 $\cdot 10^{-16} cm^2$ - dotted curve. We show the mean velocity (a), the drift velocity (b) and the criterion for NDC (c), all calculated by MTT. The ranges of E/n_0 where NDC occurs are in excellent agreement.

and reaction rate α^*. This equation has the same role that GER play for diffusion. From measurements of drift velocity $\vec{W}^{\text{mix}}$ and reaction rates α^* as a function of the reduced electric field E/n_0, it is possible to predict diffusion coefficients and skewness, as long as the temperature tensor $\hat{T}^{\text{mix}}$ can be estimated. In general, k-th order transport coefficients ($k \geq 2$) depend on $(k-1)$-th derivate of the drift velocity $\vec{W}^{\text{mix}}$ and k-th derivate of the reaction rate α^* with respect to the electric field.

The heat flux in the energy balance equation was neglected in derivation of Eqs. (21). One may thus expect that Eqs. (25) and (33) are not correct in cases where mass of swarm particle is comparable to the mass of gas atoms and that GER should contain an additional factor proportional to the heat flux [19].

When E/n_0's are low enough the mean electron energies are well below the first inelastic threshold and in that case, distribution of electron velocities is nearly isotropic. Hence,

$$t_{ij}^{\text{mix}} = T\delta_{ij} \approx \frac{2}{3}\frac{1}{k}\varepsilon^{\text{mix}}\delta_{ij}, \quad i,j = 1,2,3, \tag{34}$$

where $\varepsilon^{\text{mix}} \approx (1/2)\, m \langle v^2 \rangle^{\text{mix}}$. Using the above assumptions, we can simplify Eq. (33),

$$S_{ijk}^{\text{mix}} = \frac{1}{2}\frac{k^2}{e^2}T^2\frac{\partial}{\partial E_j}\frac{\partial}{\partial E_i}W_k^{\text{mix}} + \frac{1}{12}\frac{k^3}{e^3}T^3\frac{\partial}{\partial E_k}\frac{\partial}{\partial E_j}\frac{\partial \alpha^*}{\partial E_i}, \quad i,j,k = 1,2,3. \tag{35}$$

If we neglect inelastic and reactive processes and assume a constant elastic cross section, $\sigma^{(el)} = \sigma^0/(4\pi)$ = const (hard-sphere model) the well known analytical forms for the drift velocity:

$$W = e^{\frac{1}{2}}\left(\frac{m+m_0}{mm_0^2}\right)^{\frac{1}{4}}\frac{\left(\frac{E}{n_0}\right)^{\frac{1}{2}}}{(\sigma^0)^{\frac{1}{2}}}, \tag{36}$$

and skewness:

$$n_0^2 S_L = \frac{1}{72}e^{\frac{1}{2}}m_0\left(\frac{m+m_0}{mm_0^2}\right)^{\frac{5}{4}}\frac{\left(\frac{E}{n_0}\right)^{\frac{1}{2}}}{(\sigma^0)^{\frac{5}{2}}}. \tag{37}$$

may be obtained.

These formulae are explicitely given in Huxley and Crompton[36]. Results for skewness S_L versus E/n_0 for He, Ne and Ar, calculated on the basis of MTT (i.e. according to Eq. (35)) are in reasonably good agreement with the Boltzmann equation solutions[35].

ELECTRON TRANSPORT IN $\vec{E} \times \vec{B}$ FIELDS

Momentum transfer theory for electrons in a single gas with non-reactive collisions has been first developed by Robson [12]. Independently of his work we have developed MTT which has been extended to include mixtures of gases and reactive collisions. When magnetic field is included the Boltzmann equation has an additional term due to the $\vec{v} \times \vec{B}$ force. This term affects explicitely the momentum balance equation (3) which takes the form:

$$\frac{\partial}{\partial t}\left[mn(\vec{r},t)\langle\vec{v}\rangle^{\text{mix}}\right] + \frac{\partial}{\partial \vec{r}}\left[mn(\vec{r},t)\langle\{\vec{v},\vec{v}\}\rangle^{\text{mix}}\right] - n(\vec{r},t)e\left(\vec{E}(\vec{r},t) + \langle\vec{v}\rangle^{\text{mix}} \times \vec{B}(\vec{r},t)\right)$$
$$= -n(\vec{r},t)\sum_{\alpha \in I_l}\mu_\alpha\langle\langle\vec{v}_{r\alpha}\nu_{0\alpha}^{(m)}(\vec{r},v_{r\alpha},t)\rangle\rangle_\alpha^{\text{mix}} - n(\vec{r},t)m\sum_{\alpha \in I_l}\langle\langle\vec{v}\nu_\alpha^{(A)}(\vec{r},v_{r\alpha},t)\rangle\rangle_\alpha^{\text{mix}}. \tag{38}$$

However, all other equations are affected implicitly including the collision terms. After application of the momentum transfer approximation (MTA) and the hydrodynamic expansion the equations for the mean energy and velocity reduce to:

$$\langle\vec{v}\rangle^{\mathrm{mix}} = \hat{K}(\varepsilon^0, (\langle\vec{v}\rangle^{\mathrm{mix}})^2, \vec{B})\left[\vec{E} - \frac{k}{e}\hat{T}^{\mathrm{mix}}\vec{G}\right] \tag{39}$$

$$\langle\langle\varepsilon_\alpha\rangle\rangle_\alpha^{\mathrm{mix}} = \mathcal{L}^\alpha(\varepsilon^0, (\langle\vec{v}\rangle^{\mathrm{mix}})^2, \vec{B}), \quad \alpha \in I_l \tag{40}$$

where

$$\hat{K} = \frac{1}{\left(\frac{m}{e}\bar{\nu}_{(m)}^{\mathrm{mix}}\right)^2 + B^2}\begin{bmatrix} \frac{\left(\frac{m}{e}\bar{\nu}_{(m)}^{\mathrm{mix}}\right)^2 + B^2}{\frac{m}{e}\bar{\nu}_{(m)}^{\mathrm{mix}}} & 0 & 0 \\ 0 & \frac{m}{e}\bar{\nu}_{(m)}^{\mathrm{mix}} & +B \\ 0 & -B & \frac{m}{e}\bar{\nu}_{(m)}^{\mathrm{mix}} \end{bmatrix} \tag{41}$$

is the mobility tensor and

$$\mathcal{L}^\alpha(\varepsilon^0, (\langle\vec{v}\rangle^{\mathrm{mix}})^2, \vec{B}) = \frac{1}{2}m(\langle\vec{v}\rangle^{\mathrm{mix}})^2 M_\alpha r^{\mathrm{mix}} + \frac{3}{2}kT^{\mathrm{mix}}M_\alpha\left[\frac{M_\alpha^0}{M_\alpha} + s^{\mathrm{mix}}\right] - M_\alpha\bar{\Omega}^{\mathrm{mix}}, \quad \alpha \in I_l. \tag{42}$$

All equations presented here are given for the coordinate system where electric field is along the y-axis, while magnetic field is along the x-axis. It is possible to develop equations for an arbitrary angle between the electric and magnetic fields but in this paper we shall only discuss the situation when the two fields are perpendicular.

It is also possible to establish the analytic equations for the components of the diffusion tensor but the number of these components will depend on the magnitude of the off-diagonal terms of the temperature tensor which is not necessarily diagonal when magnetic field is present.

When reactive collisions are present the mean and the drift velocity are not identical[32] but in the case of the crossed electric and magnetic fields the correction is required only for the drift along the direction of the electric field. Both components of the drift are affected by the reactive collisions indirectly through the value of the mean drift velocity.

While much more complex and difficult to obtain, the analytic MTT forms can be established for $\vec{E} \times \vec{B}$ fields and used to calculate the transport coefficients. It is also possible to establish a numerical procedure on the basis of the balance equations. The main difficulty in completing the MTT for $\vec{E} \times \vec{B}$ fields is the requirement to establish separately the form of the temperature tensor.

In this section we shall only show some of the results of calculations obtained with simple model cross sections[28] .

Figure (3) shows the influence of normalized magnetic field B/n_0 on drift velocities (Figure 3a), mean energy (Figure 3b) and inelastic collision rate (Figure 3c). Increasing field B/N reduces the mean energy at low values of E/n_0 . The influence on the inealstic rate coefficient is similar. Increasing the magnetic field to very high values will completely diminish both components of the drift velocity as well as the mean energy.

In Fig. (4) we show how changing of the nature of one of the collisional processes from inelastic (dashed line) to ionization (solid line) affects the mean velocity and consequently the drift velocity (see Figure 4b). One should note that there is no difference between the mean and the drift velocity of the perpendicular (z) component while the longitudinal and therefore the total drift velocity are both affected by the correction for the reactive collisions. This effect should not be confused with the effect of reactive collisions on the mean velocity which exists for both components.

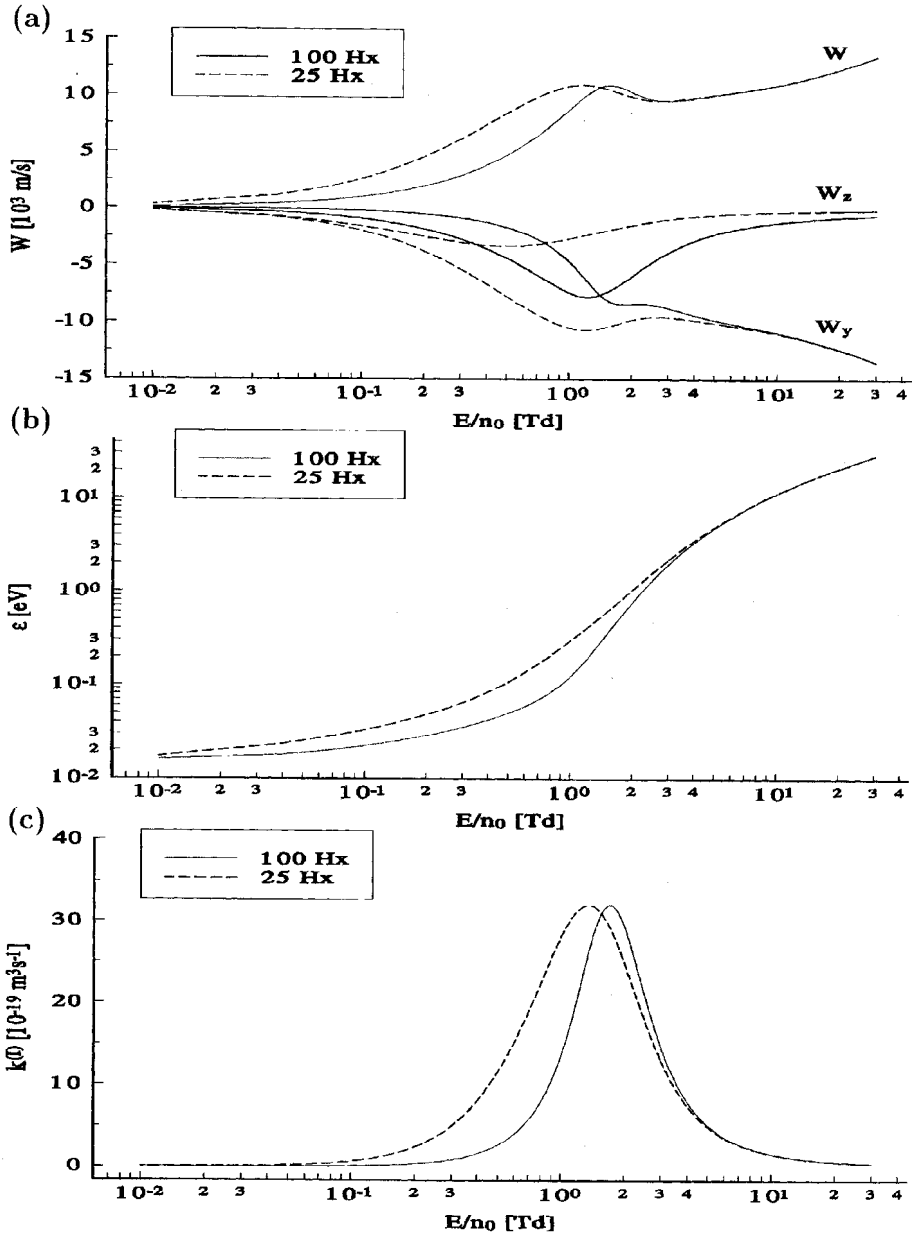

Figure 3. The influence of normalized magnetic field B/N on transport coefficients: a) drift velocity, b) mean energy and c) inelastic collision rate.

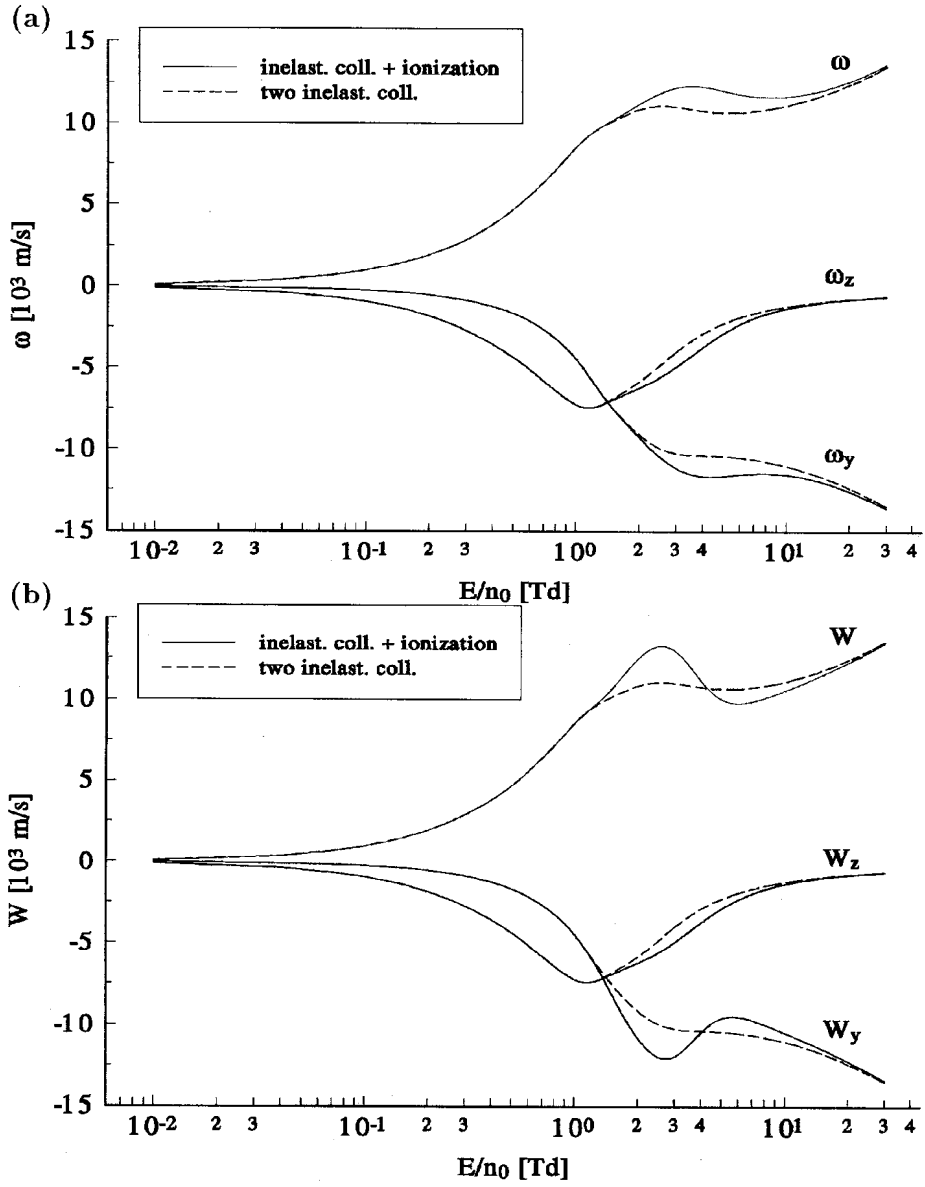

Figure 4. The effect of changing of the nature of one of the inelastic processes from number conserving inelastic (dashed) to reactive (solid). We show the results for the average velocity (a) and drift velocity (b).

POSSIBLE APPLICATION OF MTT IN GAS DISCHARGE MODELING

First we should discuss how one applies the MTT for numerical calculations. On the basis of available cross sections the equations (19) and (20) are solved, i.e. the mean velocity and energy are determined. These values are used to establish the effective rate coefficients (23) from the specific cross sections. In principle MTT should be applied only at the mean energy. Such procedure is not adequate when energy is below or close to the thresholds of inelastic processes. Robson has proposed to use a modified cross section which is equivalent to convolution of the cross section by a Maxwellian distribution function. This procedure allows one to apply MTT when the mean energy is below the threshold for ionization which is usually the case in gas discharges. Yet it appears that for different conditions a far reaching tails of distribution functions are generated[37] which can provide the necessary ionization for maintaining the discharge even when mean energy is well below the ionization threshold.

One should have in mind that analytical formulae and balance equations developed by applying MTT should be applicable regardless of some of the approximations that are used in developing them. Those formulae represent relations between collisional frequencies and driving fields with transport coefficients. Approximations were necessary in order to develop the analytic forms but we may use more accurate collisional frequencies in those formulae. In fact we may also use the experimental data without any loss of generality. In other words the implicit approximations may limit the scope of the formulae and some kinetic phenomena may not be represented but they do not prevent us from using more accurate input data. When such data are applied MTT gives final results of a much higher accuracy which is not surprising, the main source of inaccuracy of MTT results is due to the poor representation of collision frequencies especially close to the threshold. Thus our proposal is to use collision frequencies calculated by other more accurate but numerical methods or measured and renormalize them to effective cross sections. Under such conditions applying a procedure to establish the collision frequency at a single energy will give more accurate final results. Even without such precautions MTT results are usually within 10% of the accurate swarm data, which may be sufficient for gas discharge modeling.

More serious problems arise from the requirement to establish the results for time varying fields. We were able to develop MTT equations for infinite swarms with rf fields, even including the magnetic field. In that case, however, ordinary differential equations have to be solved, but the results are in good agreement with those obtained by other techniques.

In real discharges spatially variable fields leading to non-local electron kinetics have to be taken into account. It is, however, possible to use the MTT to develop equations without the hydrodynamic approximation, which would be partial differential equations. We have been able to derive beam equations from the basic MTT balance equations that are equivalent to beam equations developed by Phelps and coworkers[17] . It means that the non-local electron kinetics can be preserved in MTT.

CONCLUSION

In this paper we describe the development of MTT for electron transport in mixtures of reactive gases. MTT can be extended to time varying and spatially non-uniform fields. The previous work of Robson[9] has been limited to the transport in a single reactive gas and some extensions to mixtures are not trivial.

In order to illustrate the usefulness of the analytic forms derived by MTT we

discuss the negative differential conductivity and higher order transport coefficients for electron swarms. The increasingly popular ICP reactors require modeling of electron transport in crossed electric and magnetic fields. Therefore we describe the development of the MTT for $\vec{E} \times \vec{B}$ fields. This theory can be used to analyze electron transport phenomena but also to calculate the transport coefficients.

Modeling of gas discharges may banefit from MTT in different ways. Analytic forms can help elucidate the relations between various transport coefficients and also the effect of cross section profiles on electron transport. One particularly interesting application of MTT, (not discussed in this paper due to the lack of space) is in deriving corrections for Blanc's law, which gives transport coefficients for mixtures as a function of the coefficients for pure constituent gases. While it has been regarded as inapplicable for electron transport at moderate E/n_0, Blanc's law may become an option for very high E/n_0. Under such conditions the energy distribution functions and scattering cross sections in different gases may be more similar in shape. The values of mean energies would also differ by a lesser degree. At the same time elastic collisions may have an increasing importance in energy transfer which would be dominated by ionization. The reasons for the breakdown of Blanc's law beyond reasonably applicable corrections are diminishing at high E/n_0. On the other hand the data for transport coefficients for such conditions are lacking so a corrected form of Blanc's law would become useful.

It is also proposed here that MTT equations may be used as the basis for faster yet adequately accurate modeling of rf plasmas[38]. The requirement is that the space-time dependence is allowed, while at the same time it should be necassary to maintain the physics necessary to describe the non-locality in space and time. Some developments in our laboratory indicate that it is possible to develop such a theory with some additional effort. Whether it would be useful or not remains to be seen.

In any case MTT, as applied to swarm parameters and in understanding of various kinetic phenomena, is a technique that has contributed significantly to gas discharge modeling. At the moment it has been developed to cover mixtures of reactive gases, to include time dependence and to include the magnetic field in all its aspects[13].

ACKNOWLEDGEMENTS

Authors are grateful to Prof. R. E. Robson for numerous useful discussions and continuous support. We would also like to acknowledge discussions with Dr. K. F. Ness, Prof. T. Makabe, Dr. S. A. Bzenić and many other colleagues.

This work was supported to a small degree by the Ministry of Science and Technology of the Republic of Serbia.

REFERENCES

1. A. Okigawa, Z. Lj. Petrović, M. Tadokoro, T. Makabe, N. Nakano and A. Itoh, "Diagnostics of a non-equilibrium inductively coupled plasmas in argon", *Appl. Phys. Lett.* 69:2644 (1996).
2. U. Kortshagen and L. D. Tsendin, "Fast two-dimensional self-consistent kinetic modeling of low-pressure inductively coupled RF discharges", *Appl. Phys. Lett.* 65: 1355 (1994).
3. K. Kumar, H. R. Skullerud and R. E. Robson, "Kinetic theory of charged particle swarms in neutral gases", *Aust. J. Phys.* 33:343 (1980).
4. G. H. Wannier, "Motion of gaseous ions in strong electric fields", *Bell Syst. Tech. J.* 32:170 (1953).
5. G. H. Wannier, "On a conjecture about diffusion of gaseous ions", *Aust. J. Phys.* 26:897 (1973).
6. E. A. Mason and H. Hahn, "Ion drift velocities in gaseous mixtures at arbitrary field strengths", *Phys. Rev. A* 5:438 (1972).

7. H. B. Milloy and R. E. Robson, "The mobility of potassium ions in gas mixtures", *J. Phys. B: Atom. Molec. Phys.* 6:1139 (1973).
8. J. H. Whealton, E. A. Mason and R. E. Robson, "Composition dependence of ion - transport coefficients in gas mixtures", *Phys. Rev. A* 9:1017 (1974).
9. R. E. Robson, "Generalized Einstein relation and negative differential conductivity in gases", *Aust. J. Phys.* 37:35 (1984).
10. R. E. Robson, "Physics of reacting particle swarms in gases", *J. Chem. Phys.* 85:4486 (1986).
11. R. E. Robson and K. F. Ness, "Physics of reacting particle swarms. III Effects of ionization upon transport coefficients", *J. Chem. Phys.* 89(8):4815 (1988).
12. R. E. Robson, "Approximate formulas for ion and electron transport coefficients in crossed electric and magnetic fields", *Aust. J. Phys.* 47:279 (1994).
13. S. B. Vrhovac and Z. Lj. Petrović, "Momentum transfer theory of nonconservative particle transport in mixtures of gases: General equations and negative differential conductivity", *Phys. Rev. E* 53:4012 (1996).
14. S. B. Vrhovac, Ph.D. thesis, Faculty of Physics, University of Belgrade (1996) (unpublished).
15. S. B. Vrhovac and Z. Lj. Petrović, "Higher order electron transport coefficients from momentum transfer theory", *Europhysics conference abstracts* 20E: 103 (1996).
16. S. B. Vrhovac and Z. Lj. Petrović, "Momentum Transfer Theory of Non - Conservative Charged Particle Transport in Crossed Electric and Magnetic Fields", Proc. XXII ICPIG (International Conference on Phenomena in Ionized Gases), Editors. K. Becker, W. E. Carr and E. E. Kunhardt, Hoboken, 2:39 (1995)
17. A. V. Phelps, B. M. Jelenković and L. C. Pitchford, "Simplified models of electron excitation and ionization at very high E/N", *Phys. Rev. A* 36:5327 (1987).
18. R. E. Robson and K. F. Ness, "Velocity distribution function and transport coefficients of electron swarm in gases. I Spherical decomposition of Boltzmann equation", *Phys. Rev. A* 33:2068 (1986).
19. R. E. Robson, "On the generalized Einstein relation for gaseous ions in an electrostatic field", *J. Phys. B: Atom. Molec. Phys.* 9:L337 (1976).
20. W. H. Long, W. F. Bailey and A. Garscadden, "Electron drift velocities in molecular-gas-rare gas mixtures", *Phys. Rev. A* 13:471 (1976).
21. G. B. Lopantseva, A. F. Pal', I. G. Persiatsev, V. M. Polushkin, A. N. Starostin, M. A. Timofeef and E. G. Treneva, *Sov. J. Plasma Phys*, 5:767 (1979).
22. K. F. Ness and R. E. Robson, "Transport properties of electrons in water vapor", *Phys. Rev. A* 38:1446 (1988).
23. D. L. Mosteller Jr., M. L. Andrews, J. D. Clark and A. Garscadden, "Electron drift velocities in argon - boron tricholoride gas mixtures", *J. Appl. Phys.* 74:2247 (1993).
24. S.R. Hunter, J.G. Carter and L.G. Christophorou, "Electron transport studies of gas mixtures for use in e-beam controlled diffuse discharge switches", *J. Appl. Phys.* 56:3001 (1985).
25. A. Jelenak, J. V. Jovanović, S. A. Bzenić, S. B. Vrhovac, S. S. Manola, B. Tomčik and Z. Lj. Petrović, "The influence of excited states on the kinetics of excitation and dissociation in gas mixtures containing methane", *Diamond and Related materials* 4:1103 (1995).
26. S. A. Bzenić and Z. Lj. Petrović, "Negative differential conductivity for electrons in rf fields", *Europhysics conference abstracts* 20E:101 (1996).
27. P. Kleban and T. H. Davis, "Electron transport in methane gas", *Phys. Rev. Lett.* 39:456 (1977).
28. Z. Lj. Petrović, ,R. W. Crompton and G. N. Haddad, "Model Calculations of Negative Differential Conductivity in Gases", *Aust. J. Phys.* 37:23 (1984).
29. B. Shizgal, "Negative Differential Conductivity of Electrons in He-Xe and He-Kr mixtures", *Chem. Phys.* 147:271 (1990).
30. R. Nagpal and A. Garscadden, "Electron transport in helium-rare gas mixtures", *Appl. Phys. Lett.* 64:1626 (1994).
31. R. V. Chiflikyan, "Negative differential electron conductivity in He-Kr and He-Xe gas discharge plasmas", *Fiz. Plazmi* 22:71 (1996).
32. R. E. Robson, "Transport phenomena in the presence of reactions: Definition and measurement of transport coefficients", *Aust. J. Phys.* 44:685 (1991).
33. N. L. Aleksandrov, N. A. Dyatko, I. V. Kochetov, A. P. Napartovich and D. Lo, "Negative differential conductivity in pure rare gases", *Phys. Rev.* E 53:2730 (1996).
34. N. L. Aleksandrov, A. M. Konchakov, A. I. Napratovich and A. N. Starostin, "Novel mechanism of sound amplification in a weakly ionized gas", *Sov. Phys. JETP* 68:933 (1989).

35. B. M. Penetrante and J. N. Bardsley, Higher - order electron transport in gases, in: “Nonequilibrium Effects in Ion and Electron Transport”, edited by J. W. Gallagher *et al.* (Plenum Press, New York, 1990).
36. L. G. H. Huxley and R. W. Crompton, “The Diffusion and Drift of Electrons in Gases”, Wiley, New York, (1974).
37. V. D. Stojanović, B. M. Jelenković and Z. Lj.Petrović, “Excitation by electrons and fast neutrals in nitrogen discharges at very high electric field to gas number density ratios”, *J. Appl. Phys.* 81:1601 (1997).
38. N. Nakano, N. Shimura, Z. Lj. Petrović and T. Makabe, “Simulations of rf glow discharge in SF6 by the relaxation continuum model: Physical structure and function of the narrow-gap reactive-ion etcher”, *Phys. Rev. E* 49:4455 (1994).

HOT ELECTRONS IN AN EXPANDING MAGNETIZED HYDROGEN PLASMA

D. K. Otorbaev,[1] Zhou Qing, G. J. H. Brussaard, M. C. M. van de Sanden and D. C. Schram

[1]Institute of Chemistry and Chemical Technology
Kyrgyz National Academy of Sciences
Chui prospect 265 A, Bishkek, 720071, Kyrgyz Republic
Department of Physics
Eindhoven University of Technology
P. O. Box 513, 5600 MB Eindhoven, The Netherlands

1. INTRODUCTION

Nonequilibrium hydrogen plasma have been widely used in different research and application fields and have become a promising research subject. In microelectronics hydrogen containing plasmas have been utilized in the thin film deposition,[1] surface cleaning and passivation techniques.[2] It has been shown that high quality diamond films are grown in a hydrogen diluted plasma, and that the atomic hydrogen present in these plasmas is essential for the quality of the films.[3] The research of hydrogen plasmas has also a direct bearing to controlled thermonuclear fusion project. Heating of the fusion plasma by injection of neutral beams produced by neutralization of negative ions from a negative deuterium (hydrogen) ion source has been suggested as a key technology to reach the plasma conditions needed for energy production by thermonuclear fusion.[4]

Hydrogen plasmas can be generated in different kinds of gas discharges, e.g. in DC glow discharges, RF plasmas, microwave plasmas, in a hollow cathode arcs, etc.[5–8] To obtain a high enthalpy flow, it can be also created at higher pressures, e.g. by a so-called cascaded arc,[9] which is a kind of wall stabilized high electron density plasma, and which is the subject of this paper. Previous research shows that the cascaded arc is an ideal design to create a stable arc plasma with high electron density as well as an expanding plasma for both plasma studies and applied research.[10, 11] It has been shown that the expanding cascaded arc plasmas have potential prospect in different application fields; e.g. using a cascaded arc as a light source for spectroscopy,[12] as a particle source for surface modification,[10] silicon and carbon thin film deposition.[13, 14] Mostly noble gases are used to feed the arc plasma, but exceptionally molecular gases like H_2 and SF_6 are added.[15, 16]

The aim of this research is to develop a hydrogen radical source for the rising interest in hydrogen plasma applications. The plasma is first created in a cascaded arc. The treatment plasma is obtained by the expansion of the arc plasma into a low

Electron Kinetics and Application of Glow Discharges
Edited by U. Kortshagen and L. D. Tsendin, Plenum Press, New York, 1998

background pressure vessel. In this paper the low pressure range ($\simeq$5 Pa) is explored in order to reduce plasma recombination. At these lower pressures collisional confinement is not effective and magnetic confinement of electrons and ions is needed to obtain a high electron density expanding plasma. Therefore this work focuses on magnetized expanding hydrogen plasmas at low pressure.

2. PLASMA SOURCE AND EXPANSION

2.1. Cascaded Arc Set Up

The cascaded arc used in. this work consists of three main parts, namely cathode section, cascade plates section and anode section. In this type of arc a plasma is generated in a cylindrical channel consisting of a number of plates. The arc discharge is stabilized by the water cooled channel walls. The power dissipation is relatively high, typically of the order of 5 kW, and the carrier gas (argon, nitrogen, hydrogen) is flowing at a rate typically between 5 and 100 standard cm^3s^{-1} (sccs).[10, 17] The plasma is initiated by the application of a high voltage pulse to the cathode ($V_{pulse} \simeq 1$ kV, $t_{pulse} \simeq 1$ s), and the arc plasma is sustained by drawing a high current (30–100 A) between the cathode tips and the anode at a lower voltage (80–150 V). The arc plasma is always started using pure argon since lower power is needed to generate an argon plasma. By this procedure the lifetime of the cascaded arc set up can be significantly extended. After the argon arc becomes stable, the hydrogen concentration in the flow is slowly increased from 0" until 100", and a pure hydrogen arc plasma is obtained through a transition from an argon arc to a hydrogen arc. The power needed to generate and sustain an arc is determined by arc length, or the number of the cascade plates. The longer the arc, the more the input power is needed. In this experiment, a four plate arc is used.[10, 17]

2.2. Different Regimes of an Expanding Plasma

The arc plasma is first generated in the cascaded arc and then expands into a low pressure vessel (P $\simeq$ 5 Pa) (Figure 1). At moderate pressures in the vessel ($\simeq$ 100 Pa) an expanding hydrogen plasma shows a strong recombination of hydrogen atomic ions.[18] This strong recombination can not be explained by atomic processes. In pure

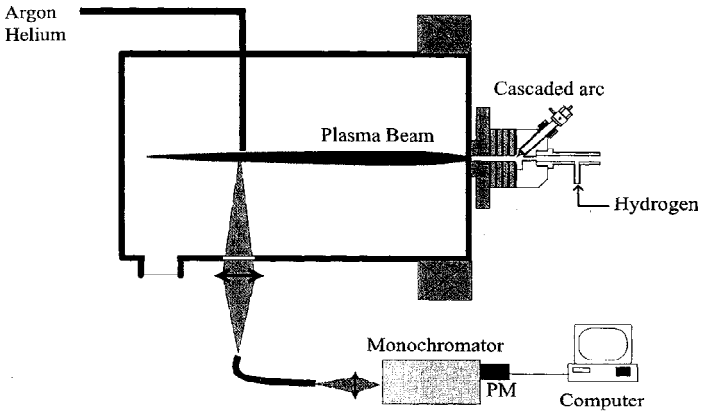

Figure 1. Expanding cascaded arc plasma and the spectroscopy set up, with the geometry, used for the local excitation of the Ar and He spectral lines.

argon plasmas, recombination has been shown to be a relatively weak process.[11] The anomalous recombination of H_2 containing plasma is due to charge exchange of the atomic ion H^+ with H_2 molecules to form the molecular ion H_2^+, which recombines fast by dissociative recombination. In order to avoid the recombination, the charge exchange between the primary H^+ ions and H_2 molecules has to be reduced which can be achieved by decreasing the hydrogen molecule density. However, then the mean free paths become larger the fast diffusion starts to reduce the charged particle density. Therefore a magnetic field is applied to confine the expanding plasma and by this to reduce outward diffusion and thus to increase the plasma density. To obtain a magnetized expanding plasma beam, a magnetic field coil is mounted in front of the cascaded arc.

Two regimes of an expanding plasma can be distinguished depending on the applied magnetic field, which we define as the "atomic" regime and the "molecular" regime. The two regimes can also be reached by varying the pressure suggesting that confinement of the plasma plays an important role. The main feature of the regime at relatively large magnetic fields is that the plasma emits strong hydrogen Balmer lines. There is no observable molecular spectrum in the measured wavelength range. Therefore we name this regime the "atomic" one.[19] The main characteristic of the regime at relatively small magnetic field is that not only hydrogen Balmer lines, but also strong hydrogen molecular lines are observed. We name this regime the "molecular" one. This regime is reached by decreasing the magnetic field (by lowering the coil current I_B from 250 A to 50 A) continuously from the atomic regime. In this paper the results of diagnostics of the molecular regime of an expanding magnetized hydrogen plasma jet will be presented.

3. DIAGNOSTICS

3.1. Optical Emission Spectroscopy

Figure 1 shows the line intensity measuring system used in the experiment. The system consists of a computer controlled two dimensional translation set up, a computer controlled monochromator, a photomultiplier, a quartz fibre, a signal discriminator, TTL converter and a digital counter. The signal is first focused on the detection surface of the quartz fibre by an optical system. Through the fibre, the light signal is transmitted to the monochromator. Behind the exit slit a photomultiplier is positioned. The resulting current pulses are converted into TTL pulses which are counted by the computer. The optical system was calibrated positioning a tungsten ribbon lamp in the vessel, and recording the spectrum at a known true temperature of the ribbon. Figure 2 gives an example of a hydrogen spectrum which is typical for an expanding plasma in the molecular regime.

It can be shown that the plasma under study is optically transparent for the studied atomic and molecular spectral lines. It is known that the optical depth of a plasma, $\overline{kR}$ is the value, which determines the transparency of the plasma. The optical depth can be expressed through the following formula:

$$\overline{kR} = \frac{\sqrt{\ln 2}}{4\pi\sqrt{\pi}} \cdot \frac{\lambda_{pq}^4}{c\Delta\lambda_{pq}} \cdot \frac{g_p}{g_q} \cdot A_{pq} n_q \cdot \mu R, \qquad (1)$$

in which k is the absorption coefficient, n_q is the population density of the lower state of radiative transition, A_{pq} is the absolute radiative transition probability, λ_{pq} is the wavelength of the transition between state p and state q, R is the effective radius of

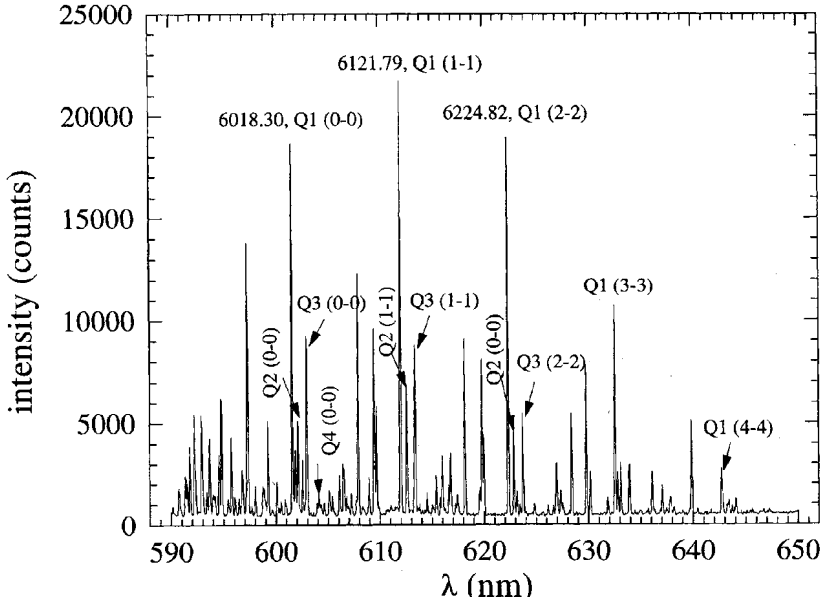

Figure 2. Part of the Fulcher-α spectrum of molecular hydrogen in an expanding plasma. Experimental conditions Q = 8 scc/s, I_{arc} = 50 A, I_B = 50 A, P = 5 Pa, z = 18 cm.

the plasma beam, $\Delta\lambda_{pq}$ is the half width of the emission profile and μ a geometrical factor (for a cylindrical plasma beam, $\mu \simeq 1.2$).[20]

For the spectral lines under investigation, λ_{pq} is in the range of 360 nm to 660 nm, A_{pq} is in the range of 10^3 to $10^7 s^{-1}$. In this experiment, the density of the state H(p = 2) is about $10^{16} m^{-3}$ as will be discussed later, the radius R is about 10^{-2} m and the line width $\Delta\lambda_{pq}$ is on the order of 10^{-11} m. The calculated optical depths for the hydrogen atomic and molecular lines for the present experimental conditions are in the range of 3. 10^{-3} to 10^{-6}, i.e. much less than 1. Therefore all discussed transitions between the hydrogen excited states can be considered as optically thin.

3.2. Langmuir Probes

A Langmuir double probe set up was used to determine electron temperature (T_e) and density (n_e). A potential difference is applied between the two floating probes. The current passing through the probes is measured (cf. Ref. 21):

$$\frac{I_p - I_i^-}{I_i^+ - I_p} = \frac{S_{p1}}{S_{p2}} \cdot \exp\left(\frac{eV_p}{kT_e}\right), \tag{2}$$

with I_p the current trough the probes at applied potential difference V_p, $I_i^{+,-}$ the saturation currents at large positive and negative potentials, and $S_{p1,p2}$ the surfaces of the probes. After plotting the left hand side of equation (2) on a semi-logarithmic scale, the slope at V_p = 0 will yield the electron temperature. The electron (ion) density n_e can be determined from the saturation currents (cf. Ref. 22):

$$I_i = \kappa_i \cdot e \cdot n_e \cdot S_p \cdot \sqrt{\frac{kT_e}{m_i}}, \tag{3}$$

where k_i ($\simeq 0.6$) is a geometrical factor for the ion flow towards the probe,[23] and m_i the ion mass.

Although the electron current to the probe is significantly reduced by the presence of a magnetic field, it is still proportional to the Boltzmann factor $\exp(eV/kT_e)$.[24] Therefore equation (3) remains valid. In Figure 3 the results of T_e and n_e in the molecular regime of an expanding hydrogen plasma, determined by the Langmuir double probe measurements are given. The assumption made in the calculations that H_2^+ is the dominant positive ion in the plasma. In principle it is necessary to verify some requirements of the use of the Langmuir probe theory in a magnetized plasma, since in the magnetic field the trajectories of the charged particles can be disturbed, so the collection efficiency of the charged particles by a probe will be influenced.[22] However, it can easily be shown, that for the particular experimental conditions the basic requirement of the probe theory is still valid, since the Larmor radii both for electrons and for ions are much larger than the Debye length.

4. EMISSION OF FULCHER-α BAND OF H_2 AND GAS TEMPERATURE

Analysis of the relative intensity distribution of the rotational spectral lines of electronically-excited molecules are widely used as a method of determination of the gas temperature of low-temperature plasmas.[5] The parameter to be measured is the rotational excitation temperature T^*_{rot}, which is associated with the molecular distribution over the rotational levels of the excited electronic-vibrational (vibronic) states. The rotational distributions of the electronically-excited molecules were usually similar to a Boltzmann distribution. Therefore it is often assumed that the rotational temperature coincides with the translational gas temperature T_g.[25] However, since at low densities the radiative lifetimes of excited molecules are usually shorter than the characteristic time for rotational relaxation,[26, 27] the relation between rotational temperature and gas temperature requires special attention.

In order to determine the temperature of the neutral particles in an expanding hydrogen plasma (the gas temperature), we measured the rotational distribution of hydrogen molecules of the electronically-excited state $H_2(d^3\Pi_u)$. For this purpose we used the radiative transitions, which correspond to Fulcher-α system of H_2. The Fulcher-α system is the result of radiative transition $H_2(d^3\Pi_u \rightarrow a^3\Sigma_g^+)$, and has been chosen for two reasons. First, the lines of this system in the red part of the visible spectrum are fairly far apart from one another and dominate over the spectral lines associated with other transitions. Second, for the Fulcher-α system all necessary molecular constants have been studied most thoroughly.[28–30] In this section we will discuss the properties of the radiative state $H_2(d^3\Pi_u)$, the excitation mechanism of this state in the conditions of an expanding plasma, and the method of gas temperature determination from analysis of the rotational spectrum of H_2.

4.1. The Fulcher-α Spectrum

For a hydrogen molecule, both the electronic ground state $H_2(X^1\Sigma_g^+)$, and the considered electronically excited states $H_2(d^3\Pi_u)$ and $H_2(a^3\Sigma_g^+)$ belong to Hund's case (b).[31] The triplet splitting in the $H_2(d^3\Pi_u)$ and $H_2(a^3\Sigma_g^+)$ states are negligible.[30] For the $H_2(d^3\Pi_u)$ state the rotational levels split into two components due to A-type doubling, where one is symmetric and applies to para-hydrogen, and the other is antisymmetric and applies to ortho-hydrogen. This results into two distinguishable series of rotational levels denoted as the Π^+ and Π^- components.

Since vibrational and rotational interaction is insignificant in then $H_2(d^3\Pi_u)$ state, the line strengths can be calculated with the Hönl–London formula[25,32]:

$$\begin{aligned} S_{J,J+1} &= \frac{1}{2}J(2t+1) \qquad \text{(P-branch)}, \\ S_{J,J} &= \frac{1}{2}(2J+1)(2t+1) \qquad \text{(Q-branch)}, \\ S_{J,J-1} &= \frac{1}{2}(J+1)(2t+1) \qquad \text{(R-branch)}. \end{aligned} \tag{4}$$

with $t = 0$ for even J' values, and $t = 1$ for odd J' values.

Figure 2 shows an example of a part of the hydrogen Fulcher-α spectrum measured in an expanding hydrogen cascaded arc plasma in the molecular regime.

4.2. Determination of Rotational Temperature

In general the intensity of the radiation between the rotational levels of the electronic-vibrational excited states can be expressed:

$$I_{\prime\to\prime\prime} = n_{p'v'J'} \cdot A_{\prime\to\prime\prime} \cdot h\nu_{\prime\to\prime\prime} \cdot \frac{\Delta\Omega}{4\pi}, \tag{5}$$

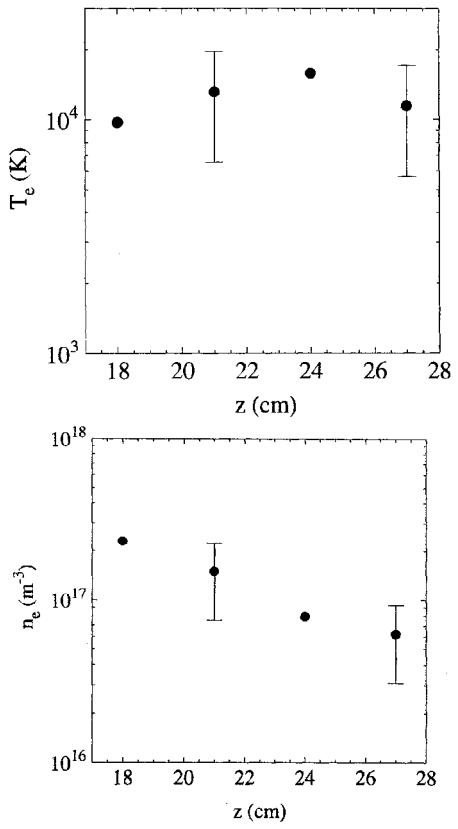

Figure 3. Axial dependencies of the electron temperature (T_e) and electron density (n_e) in the molecular regime of an expanding hydrogen plasma, measured by a Langmuir double probe.

in which $n_{p'v'J'}$ is the population of an electronically excited state p', with vibrational quantum number v', and rotational quantum number J', $v'_{\rightarrow''}$ and $A'_{\rightarrow''}$ are the wavenumber and the transition probability for the given spectral line, $\Delta\Omega$ is the solid angle of observation, h and c are known constants. In the adiabatic approximation, the corresponding transition probability $A'_{\rightarrow''}$ is a product of electronic, vibrational and rotational fractions and can be expressed as[25, 32] :

$$A_{\prime\rightarrow\prime\prime} = \frac{64\pi\nu^3_{\prime\rightarrow\prime\prime}}{3h} \cdot A_{p',p''} \cdot q_{v',v''} \cdot S_{J',J''}, \tag{6}$$

where $q_{v',v''}$ is the so called Franck–Condon factor, which determines the distribution over the vibrational transitions.[25, 32]

In the case that the rotational distribution of the upper state of a molecular radiative transition is a Boltzmann distribution, the intensities of the rotational lines $I'_{\rightarrow''}$ are directly linked to the rotational temperature through:

$$\ln\left(\frac{I_{\prime\rightarrow\prime\prime}}{\nu^4_{\prime\rightarrow\prime\prime} \cdot S_{J',J''}}\right) = -\frac{hc}{kT^*_{\mathrm{rot}}} \cdot F(J') + \mathrm{const}, \tag{7}$$

in which $F(J')$ is the energy of the upper level in cm^{-1}, k is the Boltzmann's constant. The plot of the $\ln(I_{\prime\rightarrow\prime\prime}/\nu^4_{\prime\rightarrow\prime\prime} \cdot S_{J',J''})$ versus the rotational term values $F(J')$ gives a so-called Boltzmann plot. The rotational temperature can be obtained from the slope of this plot.

4.3. Determination of Gas Temperature

In a low pressure plasma, the radiative lifetimes of the molecules in the electronically excited states τ_{rad} are often much shorter than the characteristic time of rotational relaxation τ_{rel}. The only exceptions are the ground state and the metastable states of the molecules. Therefore, the mechanism of excitation of rotational levels in the electronically excited states is important in plasma diagnostics since the determination of the gas temperature is based on the analysis of the relative intensities of the rotational lines in the electronic-vibrational (vibronic) bands of the molecular spectra.

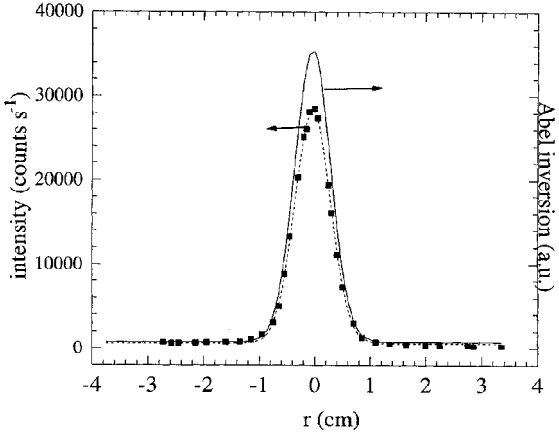

Figure 4. Example of the experimental and radial profiles of the Q1 spectral line of the Fulcher-α transition in an expanding plasma. Experimental conditions Q = 8 scc/s, I_{arc} = 50 A, I_B = 50 A, P = 5 Pa, z = 18 cm. represents the experimental data, - - - represents the Gaussian profile, — represents it after Abel inversion.

The previous investigation[27] shows that in a broad range of plasma conditions a Boltzmann rotational distribution in the ground electronic state of the molecules images to a Boltzmann rotational distribution in the excited electronic states despite the substantial change of angular momentum of a molecule during a direct electron impact. However, due to the fact, that the rotational constants of the ground state B^0 and excited state B' are different, and the difference is especially large for the hydrogen molecule, the rotational temperature of the ground state T^0_{rot} and the rotational temperature of the excited state T^*_{rot} will in general be different. From Eq. (7) and the expression for the rotational term it is easy to obtain a relation between the two temperatures with good accuracy:

$$\frac{T^0_{\mathrm{rot}}}{T^*_{\mathrm{rot}}} = \frac{B^0}{B'}. \tag{8}$$

Therefore to determine the gas temperature of a hydrogen plasma from a rotational spectral line intensity distribution, it is necessary to assume that the hydrogen molecular excited state $H_2(d^3\Pi_u)$ is excited from the hydrogen molecular ground state $H_2(X^1\Sigma_g^+)$ by direct electron impact and decay to $H_2(a^3\Sigma_g^+)$ occurs spontaneously. These two assumptions will be discussed in more detail in the next section.

4.4. Excitation Mechanism and Gas Temperature in an Expanding Hydrogen Plasma

To determine the rotational temperature of an expanding hydrogen plasma in the molecular regime, the first five lines belonging to the Q-branch of the first three diagonal vibrational states of (0–0), (1–1) and (2–2) transitions in the Fulcher-α spectrum have been measured. The measurements were carried out by a lateral scanning of these Q-branch lines at axial positions. from 18 to 30 cm downstream of the arc nozzle.

Figure 4 shows an example of a lateral profile measurement. The procedure of Abel inversion was applied to derive local values of the emission coefficients, and the relative densities of rotational levels of $H_2(d^3\Pi_u)$ state. As can be seen from the measurements, the expanding plasma is strongly confined to a narrow beam with a width approximately equal to 1.5 cm.

The Boltzmann plot for Q (0–0), (1–1) and (2–2) series measured at the center of the beam for z = 18 cm are given in Figure 5. As can be seen the Boltzmann

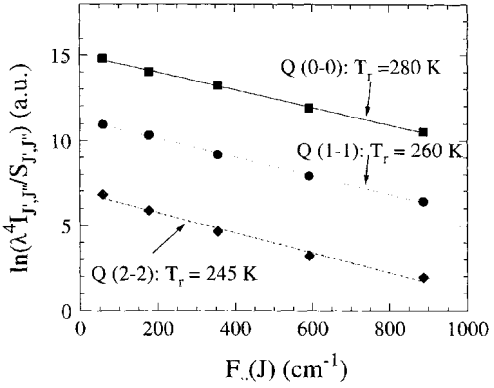

Figure 5. Boltzmann plot of the first five lines of Q-branch in the (0–0) (□), (1–1) (•) and (2–2) (◊) rotational bands of the Fulcher-α system of H_2. Plasma parameters are the same as in Figure 4.

plots give straight lines. This fact indicates that the rotational levels of the excited hydrogen molecules $H_2(d^3\Pi_u)$ follow a Boltzmann distribution. Therefore the rotational temperature T^*_{rot} can be derived from the slope of the Boltzmann plot. The three Q bands are measured independently and T^*_{rot} can be obtained from each of the measured bands. The relatively small difference in the T^*_{rot} values determined from different Boltzmann plots show that the T^*_{rot} value determined in the experiment is accurate (the error is estimated to be smaller than 20").

To draw conclusions for the ground state molecules from the measurements of electronically excited molecules, it is important to know the excitation and de-excitation mechanisms of the radiative excited states. In principle a more detailed analysis of excitation of $H_2(d^3\Pi_u)$ state in an expanding hydrogen plasma is required since both heavy particles and electrons can be involved in the collisional processes. Generally speaking it is a complicated kinetic problem especially for a non-equilibrium molecular plasma, However, in this experiment, the measured rotational excitation temperature of the $H_2(d^3\Pi_u)$ state is very low, $T^*_{rot} \simeq 260$ K (cf. Figure 5). We can conclude that the collisions between the heavy particles are not responsible for the excitation of the hydrogen molecules. The only possible mechanism of the excitation of the hydrogen molecules in this regime is the direct electron impact from the ground state. Such statement can be made because a in low-temperature plasma all effective inelastic collisional processes between heavy particles are exothermic (see, for example, Refs. 5, 34). With that the excess of energy should be distributed among the various degrees of freedom (internal and translational) of the products after the reaction. As a result it should inevitably lead to the nonthermal molecular rotational population.[5, 35, 36] Thus the rotational temperature of excited molecular states should be higher (and often much higher), than the gas temperature. Numerous examples of appearances of “hot” rotational distribution of diatomic molecules, produced by heavy particles interactions in low-temperature plasma have been given in literature.[5, 35, 36] However, for direct electron excitation of the molecules from the ground state, the resulting rotational excitation temperature of the excited molecules should be low (comparable to the gas temperature). Electrons are rather ineffective in rotational (de)excitation because of their small mass.[5, 26, 27]

In the conditions of an expanding plasma the characteristic time between the heavy particle collisions τ_{col} is in the order of 10^{-6} s (the total cross section for the collisions H_2–$H_2(d^3\Pi_u)$ is equal to $\sigma_{col} = 2.3 \cdot 10^{-18}$ m [233]). This characteristic time is much longer than the radiative lifetime of hydrogen molecules in the $H_2(d^3\Pi_u)$ state, which is only about $\tau_{rad} = 31$ ns.[33] Therefore to determine the gas temperature we can use the method mentioned earlier, which is based on the fact that a Boltzmann rotational distribution in the ground electronic state of the molecules images to a Boltzmann rotational distribution in the excited electronic state. According to equation (8), the ratio of the rotational temperatures of the ground state molecules and the rotational temperature of the excited molecules equals the ratio of the rotational constants of the two states. As the ground state $H_2(X^1\Sigma^+_g)$ rotational constant is twice as large as that of the $H_2(d^3\Pi_u)$ state,[25] the gas temperature $T_{gas} = T^0_{rot}$ is approximately twice the rotational temperature T^*_{rot} of the $H_2(d^3\Pi_u)$ state. Therefore the gas temperature in the molecular regime is found to be approximately 520 K.

5. LOCAL EXCITATION OF THE Ar AND He SPECTRAL LINES

It is important to mention the experiments with a local excitation in an expanding hydrogen plasma of the Ar and He spectral lines. In this case the transportation of Ar and He to a particular local point in the plasma has been done through a thin cylindrical

ceramic tube (Figure 1). In the molecular regime of an expanding plasma we observed the appearance of the spectral line of neutral argon Ar I ($7d \rightarrow 4p$)λ = 4876.26 Å and λ = 4887.95 Å, and of ion argon Ar II ($4p^2D \rightarrow 4s^2D$)λ = 4879.86 Å. The excitation potential of these lines ΔE_2 = 15.45 eV, and ΔE_3 = 19.68 eV, respectively. An appearance of the spectral lines with even higher excitation potentials has been observed in the case of helium, namely the spectral lines of He I ($3d \rightarrow 2p$)λ = 5875.70 Å (ΔE_4 = 23.07 eV), and He I ($5d \rightarrow 2p$)λ = 4026.20 Å (ΔE_5 = 24.04 eV). These experimental facts together with the Langmuir probe measurements, observation of the Fulcher-α system of H_2 (excitation potential ΔE = 13.87 eV), with a low rotational temperature ($T^*_{\mathrm{rot}} \simeq 260$ K) of the excited $H_2(d^3\Pi_u)$ molecules, provide a strong evidence of presence of the "hot" electrons in an expanding plasma.

6. CONCLUSION

The rotational temperature of hydrogen molecular excited state $H_2(d^3\Pi_u)$ has been determined by analyzing the relative intensity distribution of the rotational spectral lines of the Fulcher-α system of H_2. A strong hydrogen molecular spectrum, and an estimated low rotational temperature of $H_2(d^3\Pi_u)$ molecules (260 K) indicate that in the molecular regime of an expanding hydrogen plasma the electronic quantum state $H_2(d^3\Pi_u)$ (excitation potential ΔE = 13.87 eV) is excited by a direct electron impact from the ground electronic state $H_2(X^1\Sigma^+_g)$. The gas temperature in the plasma is twice the value of the rotational temperature, i.e. approximately 520 K.

Several clear indications of presence of the "hot" electrons have been observed at the axial position of $\simeq$ 24 cm from the nozzle of the arc. Among them: 1) Langmuir probe measurements ($T_e \simeq 1.4$ eV), 2) appearance of the Fulcher-α system of H2 (excitation potential ΔE = 13.87 eV), 3) low rotational temperature ($T^*_{\mathrm{rot}} \simeq 260$ K) of the excited $H_2(d^3\Pi_u)$ molecules, 4) local excitation in the plasma of Ar I (ΔE = 15.45 eV), and Ar II (ΔE = 19.68 eV) spectral lines, 5) local excitation in the plasma of He I (ΔE = 23.07 eV and ΔE = 24.04 eV) spectral lines.

REFERENCES

1. D. L. Smith, *Thin Films Deposition* (McGraw-Hill Inc., New York, 1995).
2. V. Daniels, Studies in Conservation **26,** 45 (1982).
3. P. K. Bachmann, I. M. Buckley-Golder, J. T. Glass and M. Kamo (ed), *Diamond Films '94* (Elsevier, Amsterdam, 1994).
4. J. G. Alessi and A. Hershcovich (ed), *Production and Neutralization of Negative Ions and Beams* (AIP Conference Proceedings, No. 387, AIP, New York, 1994).
5. V. M. Lelevkin, D. K. Otorbaev and D. C. Schram, *Physics of Non-Equilibrium Plasmas* (Elsevier, Amsterdam, 1992).
6. C. J. Mogab, A. C. Adams and D. L. Flamm, J. Appl. Phys. **49,** 3796 (1979).
7. K. Suzuki, S. Okudaira, S. Nishimatsu, K. Usami and I. Kanomata, J. Electrochem. Soc. **129,** 2764 (1982).
8. H. O. Blom, C. Nender, S. Berg, H. Norstroem, Vacuum **38,** 813 (1988).
9. H. Maecker, Z. Naturforsch. **11a,** 457 (1956).
10. G. M. W. Kroesen, C. J. Timmermans and D. C. Schram, Pure & Appl. Chem., **88,** 795 (1988).
11. M. C. M. van de Sanden, G. M. Janssen, J. M. de Regt, D. C. Schram, J. A. M. van der Mullen and B. van der Sijde, Rev. Sci. Instrum., **63,** 3369 (1992).
12. A. T. M. Wilbers, G. M. W. Kroesen, C. J. Timmermans and D. C. Schram, Meas. Sci. Technol. **1,** 1326 (1990).
13. G. J. Meeusen, R. P. Dahiya, M. C. M. van de Sanden, G. Dinescu, Zhou Qing, R. F. G. Meulenbroeks and D. C. Schram, Plasma Sources Sci. Technol. **3,** 521 (1994).
14. A. J. M. Buuron, D. K. Otorbaev, M. C. M. van de Sanden and D. C. Schram, Phys. Rev. E **19,** 1383 (1994).
15. Zhou Qing, M. J. de Graaf, M. C. M. van de Sanden, D. K. Otorbaev and D. C. Schram, Rev. Sci. Instrum. **65,** 1469 (1993).

16. A. Gleizes, I. Sakalis, M. Razafinimanana and S. Vacquie, J. Appl. Phys. **61,** 510 (1985).
17. Zhou Qing, Ph. D. thesis, Eindhoven University of Technology, The Netherlands, 1995.
18. M. J. de Graaf, R. J. Severens, R. P. Dahiya, M. C. M. van de Sanden and D. C. Schram, Phys. Rev. E., **48,** 2098 (1993).
19. M. C. M. van de Sanden, Zhou Qing, D. K. Otorbaev, M. J. de Graaf, J. C. A. Wevers and D. C. Schram. Proc. V European Workshop on the Production and Application of Light Negative Ions, Dublin, Ireland, 41-47 (1994).
20. H. W. Drawin and F. Emard, Beitr. Plasmaphysik **13,** 143 (1973).
21. F. F. Chen. In book: *Plasma Diagnostic Technique*, edited by R. H. Huddlestone and S. L. Leonard (Academic Press, New York, 1965).
22. D. Bohm, E. H. S. Burhop and H. W. W. Massey. In book: *Characteristics of Electrical Discharges in Mugnetic Fields*, edited by A. Guthrie and R. K. Wakerling (McGraw-Hill, New York, 1949).
23. L. Schott. In book: *Plasma Diagnostics*, edited by W. Lohte-Holtgraven (North-Holland, Amsterdam, 1968).
24. I. H. Hutchinson, *Principles of Plasma Diagnostics* (Cambridge University Press, Cambridge, 1987).
25. G. Herzberg, *Molecular Spectra and Molecular Structure. I. Spectra of Diatomic Molecules* (Van Nostrand, New York, 1955).
26. B. P. Lavrov and D. K. Otorbaev, Opt. Spectrosc. **45,** 859 (1979).
27. D. K. Otorbaev, V. N. Ochkin, S. Yu. Savinov, N. N. Sobolev and S. N. Tskhai, Sov. Phys. JETP Letters **28,** 424 (1978).
28. H. M. Crosswhite, *The Hydrogen Molecule Wavelength Tables of Gerhard Heinrich Dieke* (Wiley-Interscience, New York, 1972).
29. O. W. Richardson, *Molecular Hydrogen and Its Spectrum* (Yale University Press, New Haven, 1934).
30. G. H. Dieke and R. W. Blue, Phys. Rev. **47,** 2611 (1935).
31. F. Hund, Z. Phys. **36,** 657 (1926).
32. I. Kovács, *Rotational Structure in the Spectra of Diatomic Molecules* (Adam Hilger, London, 1966).
33. M. A. Marechal, R. Jost and M. Lombardi, Phys. Rev. A. **5,** 732 (1972).
34. M. J. J. Eerden, M. C. M. van de Sanden, D. K. Otorbaev and D. C. Schram, Phys. Rev. A. **51,** No. 4 (1995).
35. D. K. Otorbaev, V. N. Ochkin, N. G. Preobrazhensky, S. Yu. Savinov, A. I. Sedelnikov and N. N. Sobolev, Sov. Phys. JETP **81,** 1626 (1981).
36. D. W. Setser, D. H. Stedman and J. A. Coxon, J. Chem. Phys. **53,** 1004 (1970).

This Page Intentionally Left Blank

RESONANCE RADIATION TRANSPORT IN GLOW DISCHARGE PLASMAS

J. E. Lawler and J. J. Curry

Department of Physics
University of Wisconsin
Madison, WI, 53706

I. INTRODUCTION

The energy balance of many glow discharge plasmas in atomic gases is dominated by resonance radiation. This is especially true for low pressure Hg and Na plasmas used in lighting applications, e.g., the standard Hg-Ar plasma used in fluorescent lamps releases about 70% of its input power as 254 nm and 185 nm Hg resonance radiation (Jack, 1986). The low pressure Na lamp produces the highest luminous efficacy (200 lumen/Watt) of any commercially available light source (Jack, 1986). Typically this resonance radiation is trapped or imprisoned in the plasma. The use of gas pressures in the mTorr, or higher, range causes a photon to be emitted, reabsorbed, and emitted again many times before it reaches the plasma wall and escapes or is absorbed by the phosphor.

The modeling of this resonance radiation trapping or transport is a fascinating part of plasma modeling. In the remainder of the introduction we will briefly review some of the highlights in the development of realistic resonance radiation transport models. We refer the reader to an excellent and more comprehensive review published by Vermeersch and Wieme (1991) for a more detailed description of historical developments. The second section of this article describes recent progress using the propagator function method for resonance radiation transport simulations (Lawler, Parker, and Hitchon, 1993). The third section describes the recent development of an efficient and highly realistic Monte Carlo code (Anderson et al., 1995) based on the J. S. Lee (1974, 1977, 1982) algorithm for partial frequency redistribution. The algorithm for angle resolved partial frequency redistribution presented by J.S. Lee is sometimes described as “exact” because it is the most realistic available. The Monte Carlo code developed by Anderson et al. (1995) is particularly efficient because it exploits the method of rejection (J. von Neumann, 1951) to eliminate all numerical integration and eliminate the use of ‘look up’ tables. The fourth section of this manuscript reports the use of this efficient Monte Carlo code over a vast region of parameter space. The emphasis is on cylindrical geometry and on resonance radiation from an atomic gas in which the lineshape is determined by a combination of natural or radiative broadening, of Doppler broadening, and of resonance collisional broadening. Results from these highly realistic Monte Carlo simulations are used to construct and test a simple analytic expression for the ratio of the fundamental mode decay rate to the vacuum decay rate of resonance

Electron Kinetics and Application of Glow Discharges
Edited by U. Kortshagen and L. D. Tsendin, Plenum Press, New York, 1998

radiation. This expression is a function of three dimensionless parameters. The expression is shown to be accurate in the low absorbing gas density regime where Doppler broadening dominates the radiation transport, in the intermediate absorbing gas density regime where partial frequency redistribution is important, and in the high absorbing gas density regime where a collision-broadened Lorentz lineshape dominates the radiation transport. In most cases the simple analytic expression agrees with the Monte Carlo results to better than 10%. The analytic formula is accurate to 5% for the most important part of parameter space. The last section of the manuscript is a summary.

Early attempts to model resonance radiation transport were based on modification of the standard equation for diffusive transport (Compton, 1923; Milne, 1926). The 'modified diffusion' approach, proposed by Milne (1926), and improved by Blickensderfer, Breckenridge, and Simons (1976), is reasonably accurate at very low opacity or extremely low absorbing gas density (Romberg and Kunze; 1988). We mention these early attempts to emphasize a key concept: *resonance radiation transport is, with the exception of the very low opacity regime, a non-diffusive transport problem.* At modest absorbing gas density the mean-free-path of a photon emitted at the spectral line center becomes extremely short and the opacity becomes quite large. Most of the transport occurs when a photon is emitted in the spectral line wings. The correct physical picture at high opacity is that the photon is repeatedly emitted and reabsorbed within a very small volume (often comparable to a cubic wavelength) until the photon is emitted in the spectral line wings. Once the photon is emitted in the spectral line wings it will then have a very much longer mean-free-path and then may 'jump' across, or even out of the discharge tube. This physical picture led Biberman (1947) in Russia and Holstein (1947 and 1951) in the USA to construct an integral transport equation. This integral transport equation is 'nonlocal' in real space whereas the older and very limited diffusive transport model is based on a differential equation which is 'local' in real space. Plasma modellers may at first find the concept of nonlocal transport quite unusual until they realize that kinetic theory modeling of particle transport based on the Boltzmann equation is local in real space but nonlocal in velocity space. Essentially all elastic and inelastic collisions, with the exception of those described by Fokker-Planck diffusion, cause particles to 'jump' in velocity space. Integral terms are introduced in the collision terms of the Boltzmann equation to described these jumps. Radiation transport has integral terms to describe real space transport and thus is nonlocal in real space.

Most of the modeling work in the decades after Holstein's and Biberman's seminal 1947 papers was based on the approximation of complete frequency redistribution (CFR). In the CFR approximation it is assumed that the frequency of a reemitted photon is uncorrelated with the frequency of the previously absorbed photon, and the frequency of the reemitted photon is randomly chosen from a probability distribution function given by the emission lineshape. The CFR approximation is usually used with the approximation that the emission lineshape and absorption lineshape are the same. The CFR approximation works quite well over an extended range of absorbing gas density where Doppler broadening dominates transport. Changes in the direction of a photon during an absorption-reemission cycle tend to randomize Doppler shifts. The CFR approximation is extremely realistic at high gas density where a collision-broadened Lorentz lineshape dominates the radiation transport. Work by van Trigt (1969, 1970, 1971, 1976a, 1976b) and by Irons (1979a; 1979b; 1979c) provided solutions to the Holstein-Biberman equation with CFR over a range of geometries, lineshapes, and opacities. As mentioned earlier, a more thorough review and more complete list of references can be found in Vermeersch and Wieme (1991).

Payne et al. (1974) demonstrated the existence of a range of absorbing gas density where the CFR approximation produces significant error. Partial frequency redistribution (PFR) is important in this regime. Payne introduced a modified Holstein-Biberman equation which

allows for the possibility of correlation between the frequency of the previously absorbed photon and the frequency of the reemitted photon. This modified equation is, of course, a more general and more complex equation than the original equation. Various approximations for the PFR function in the modified transport equation have been developed. One of the most popular and simple PFR functions is the Jefferies-White (1960) approximation. A highly realistic PFR algorithm was presented by J. S. Lee (1974, 1977, 1982). Work by Post (1986) provided fundamental mode solutions to the modified Holstein-Biberman equation with a PFR function based on the Jefferies-White (1960) approximation. Post et al. (1986) compared these fundamental mode solutions to experimental results in mercury. Earlier work by Payne et al. (1974) provided specialized transient, or early time solutions for particular excitation sources and geometry. Again we refer the reader to a more thorough review and more complete list of references in Vermeersch and Wieme (1991).

We close this introduction with a discussion of various types of solutions to the resonance radiation transport equation. Plasma modellers working on steady state problems in a simple cylindrical, plane parallel, or spherical geometry are typically interested only in the fundamental mode solution and especially the trapped decay rate for this mode. For example, the radial distribution of electrons in a cylindrical positive column discharge will excite resonance atoms with a similar radial distribution. The steady state radial distribution of resonance atoms will often be indistinguishable from the fundamental mode solution of the original or modified Holstein-Biberman equation. The plasma modeller or diagnostician may be satisfied with simply replacing the natural or vacuum decay rate of the resonance atoms with a trapped decay rate for the fundamental mode (e.g., Phelps, 1959; Doughty and Fobare, 1995). Only an accurate trapped decay rate for the fundamental mode is desired in these problems. There are other classes of problems such as those with localized and/or transient excitation sources or unusual geometries requiring a more sophisticated approach. In some problems of this type it is desirable to compute the temporal and spatial dependence of the density of resonance atoms in a self-consistent fashion with other transport equations. We argue that the propagator function method is most advantageous in such problems. The computational speed of the propagator function method is typically 100 times greater than Monte Carlo methods.

II. PROPAGATOR FUNCTION METHOD IN CYLINDRICAL GEOMETRY

Propagator Function Method with CFR

The propagator function method was introduced by Lawler, Parker, and Hitchon (1993). They used the CFR approximation with a Lorentz lineshape and derived analytic expressions for the propagator function matrix elements in an infinite plane parallel geometry and a hollow spherical geometry at high opacity. The hollow spherical geometry was of interest in modelling the 'ball' of plasma around the hot cathode in a typical fluorescent lamp (Wamsley, Mitsuhashi and Lawler, 1993). The propagator function method was further developed to include PFR and additional geometries by Parker, Hitchon, and Lawler (1993). In this work we shall emphasize results for an infinite cylindrical geometry which are most useful in modelling positive column plasmas. This infinite cylinder has an absorbing boundary at radius $\rho = h$.

In describing the propagator function method with CFR it is useful to start from the Holstein-Biberman equation. The Holstein-Biberman equation may be written as

$$\frac{dn(\mathbf{r},t)}{dt} = p(\mathbf{r},t) - \frac{1}{\tau_v} n(\mathbf{r},t) - \frac{1}{\tau_v} \int d^3r' \frac{n(\mathbf{r}',t)}{4\pi R^2} \frac{\partial T(R)}{\partial R} \tag{1}$$

where $n(\mathbf{r}, t)$ is the density of resonance (excited) atoms, $p(\mathbf{r}, t)$ is the production rate per

unit volume, τ_v is the vacuum radiative lifetime, $\mathbf{R} = \mathbf{r} - \mathbf{r}'$, and the Holstein transmission factor is

$$T(R) = \int_0^\infty d\nu\, g(\nu - \nu_0) \exp\left[\frac{-k_0 g(\nu - \nu_0) R}{g(0)}\right]. \tag{2}$$

The normalized lineshape $g(\nu - \nu_0)$ is defined in the usual fashion such that

$$\int_0^\infty g(\nu - \nu_0) d\nu = 1 \tag{3}$$

where ν is the frequency of the radiation, ν_0 is the line center frequency, and k_0 is defined as the line center absorption coefficient. The Holstein transmission function for a pure Lorentz lineshape is very simple

$$T(R) = I_0(k_0 R/2) \exp(-k_0 R/2). \tag{4}$$

The large $k_0 R$ or high opacity limit of this expression is even simpler

$$T(R) \simeq (\pi k_0 R)^{-1/2}. \tag{5}$$

A propagator function

$$Q(R) = -\frac{1}{4\pi R^2}\frac{\partial T}{\partial R} = -\nabla_R \cdot \left[\frac{\hat{\mathbf{R}}}{4\pi R^2} T(R)\right] + \delta(\mathbf{R}) \tag{6}$$

is most conveniently defined as used by Parker, Hitchon, and Lawler (1993). This propagator is actually slightly different from the propagator defined in the original work by Lawler, Parker, and Hitchon (1993) in that it does not include the radiative decay term. This is to make the spatial propagator similar for the CFR and PFR treatments. The next step is to introduce a real space mesh (with a total of n_s cells numbered by j or i) to vectorize the transport equation. In an infinite cylindrical geometry a set of concentric cylindrical shells uniformly spaced in radius is most convenient. The density of excited atoms $n(\mathbf{r}, t)$ is now approximated as

$$\sum_{i=1}^{n_s} N_i(t) \delta(\mathbf{r} - \mathbf{r}_i) \tag{7}$$

where $N_i(t)$ is the number of excited atoms per unit length in the z direction in the spatial cell i, the production rate per unit volume is approximated as

$$\sum_{i=1}^{n_s} P_i(t) \delta(\mathbf{r} - \mathbf{r}_i), \tag{8}$$

and Q is represented by a matrix. The simulation is advanced in time using

$$N_j(t + \Delta t) = P_j(t)\Delta t + (1 - \frac{\Delta t}{\tau_v}) N_j(t) + \sum_{i=1}^{n_s} Q_{j,i} N_i(t) \frac{\Delta t}{\tau_v} \tag{9}$$

with the usual choice for Δt of τ_v. The matrix elements $Q_{j,i}$ can be expressed, assuming a Lorentz lineshape and high opacity, in terms of the integral

$$M_b(u) = u \int_{-\infty}^{+\infty} dz \int_0^{2\pi} d\phi \frac{1}{4\pi R^2} \frac{1}{\sqrt{\pi k_0 R}} \hat{\rho} \cdot \hat{R} \tag{10}$$

where $R^2 = u^2 + b^2 - 2ub\cos\phi + z^2$. If $u > b$ this integral represents the probability of the photon escaping to the region outside the cylindrical surface $\rho = u$ after emission at $\mathbf{r}_i' = (i - \frac{1}{2})(\frac{h}{n_s})\hat{\rho} = b\hat{x}$ (i.e. $\hat{\rho}$ along Cartesian axis $\hat{x}$). If $u < b$ the absolute value of this integral represents the probability of the photon being absorbed inside the cylindrical surface at $\rho = u$.

The z integral is analytic using trigonometric substitutions and is done first. The remaining ϕ integration leads to the derivative of a Gaussian hypergeometric function yielding

$$M_b(u) = \begin{cases} \frac{(\Gamma(\frac{1}{4}))^2}{3\pi(2k_0u)^{1/2}} \sum_{n=0}^{\infty}(2n+\frac{1}{2})\left[(\frac{1}{4})_n\right]^2 \frac{(b/u)^{2n}}{(n!)^2} & \text{if } u > b \\ \frac{-2(\Gamma(\frac{1}{4}))^2}{3\pi(2k_0b)^{1/2}} \sum_{n=1}^{\infty} n\left[(\frac{1}{4})_n\right]^2 \frac{(u/b)^{2n}}{(n!)^2} & \text{if } b > u \end{cases} \tag{11}$$

where $(\frac{1}{4})_n = [1 \times 5 \times 9 \times \cdots \times (4n-3)]/4^n$ for $n \geq 1$ and $(\frac{1}{4})_0 = 1$ and where $\Gamma(\frac{1}{4}) = 3.625\,609\,91$. Both sums can be shown to converge absolutely, though numerous terms must be taken when $u \sim b$. Alternatively, Press et al. (1989) give efficient and accurate routines for evaluating derivatives of hypergeometric functions with $u \sim b$ using path integrals.

The actual matrix elements are

$$Q_{j,i} = \begin{cases} \delta_{ij} + M_b((j-1)\frac{h}{n_s}) - M_b(\frac{jh}{n_s}) & \text{if } 1 \leq j \leq n_s \\ M_b(h) & \text{if } j = n_s + 1 \end{cases} \tag{12}$$

where h is the radius of the absorbing cylindrical wall. Note' that $\sum_{j=1}^{n_s+1} Q_{ji} = 1$ which is equivalent to a statement that the propagator conserves photons during a time step.

The propagator function matrix elements with a Lorentz lineshape and CFR are even simpler in an infinite plane parallel geometry and in a (hollow) spherical geometry (Lawler, Parker, and Hitchon, 1993).

A few points should be stressed here. First, a natural choice for the time step Δt is the vacuum lifetime τ_v, which is accurate if the density is much greater than $p(\mathbf{r}, t)\tau_v$ and changes slowly in a vacuum lifetime. This choice of Δt is inaccurate under some circumstances. One example requiring a smaller Δt would be the study of 'early time' $(t \sim \tau_v)$ behaviour after an abrupt turn-on of $p(\mathbf{r}, t)$. This is because when $\Delta t = \tau_v$ the above equation assumes all the excited atoms emit a photon after one vacuum lifetime. Early time behaviour can be studied, provided the time step is a small fraction of τ_v. Fractional errors are found at time t of $\sim \Delta t/t$ in the studies of early time behaviour after an abrupt turn-on of $p(\mathbf{r}, t)$. Secondly, other effects can be included between iterations of the above equation. For example, collisional quenching could be included in a straightforward manner.

Propagator Function Method with PFR

In describing the propagator function method with PFR it is useful to start from the modified transport equation of Payne et al. (1974)

$$\frac{dn(\mathbf{r}, x, t)}{dt} = p(\mathbf{r}, x, t) - \frac{1}{\tau_v} n(\mathbf{r}, x, t) - \frac{\bar{k}}{\tau_v} \int_{-\infty}^{+\infty} dx' \int_V d^3r'\, n(\mathbf{r}', x', t) H(x, x') \frac{\exp(-k(x')R)}{4\pi R^2} \tag{13}$$

where x is the reduced frequency difference from the line center at ν_0 given by

$$x = \frac{(\nu - \nu_0)}{\nu_0(2k_BT/Mc^2)^{1/2}}. \tag{14}$$

In the expression for x, the quantity c is the speed of light, k_B is Boltzmann's constant T is the absolute temperature, and M is the atomic mass. The change from real frequency, ν, to reduced frequency, x, is desirable because typically the Voigt lineshape is used in the transport equation with PFR. In the equation for radiation transport, $n(\mathbf{r}, x, t)$ is the number of resonance or excited atoms per unit volume and per unit unit frequency, $n(\mathbf{r}, t) = \int_{-\infty}^{+\infty} n(\mathbf{r}, x, t)\, dx$ is the number of resonance (excited) atoms per unit volume, $p(\mathbf{r}, x, t)$ is the production rate per unit volume per unit frequency, $p(\mathbf{r}, t) = \int_{-\infty}^{+\infty} p(\mathbf{r}, x, t)\, dx$ is the production rate per unit volume, τ_v is the vacuum lifetime as defined earlier, $\bar{k} = \int_{-\infty}^{+\infty} k(x)\, dx$ is the absorption coefficient integrated over reduced frequency, and $H(x, x')$ is the angle-averaged frequency redistribution function. The reader is advised that other authors have used different definitions for k_0. We use k_0 for the line center absorption coefficient and note that $k(x) = k_0 g(\nu - \nu_0)/g(0)$. Typically, the Voigt lineshape is used in defining $k(x)$ for a simulation with PFR, $k(x) = \bar{k} L_V(x)$ with

$$L_V(x) = \frac{a_\nu}{\pi^{3/2}} \int_{-\infty}^{+\infty} \frac{\exp(-w^2)}{(x-w)^2 + a_\nu^2}\, dw, \tag{15}$$

and

$$\int_{-\infty}^{+\infty} L_V(x)\, dx = 1. \tag{16}$$

This lineshape leads to the equation $\bar{k} = \pi a_\nu k_0$ in the limit of small Doppler contribution to the Voigt lineshape, where a_ν is the Voigt parameter (half-width at half-maximum of the Lorentz contribution to the Voigt lineshape divided by $\nu_0(2k_BT/Mc^2)^{1/2}$). It is relatively simple to recover the original Holstein-Biberman equation from the modified transport equation with PFR by taking this limit with CFR.

Propagators

$$Q(x', R) = \frac{k(x')\exp(-k(x')R)}{4\pi R^2} = -\nabla_R \cdot \left[\frac{\hat{\mathbf{R}}}{4\pi R^2}\exp(-k(x')R)\right] + \delta(\mathbf{R}) \tag{17}$$

and

$$J(x, x') = \frac{\bar{k}}{k(x')} H(x, x') \tag{18}$$

are defined, yielding

$$\frac{dn(\mathbf{r}, x, t)}{dt} = p(\mathbf{r}, x, t) - \frac{1}{\tau_v} n(\mathbf{r}, x, t) + \frac{1}{\tau_v} \int_{-\infty}^{+\infty} J(x, x')dx' \int_V n(\mathbf{r}', x', t) Q(x', R) d^3r' \tag{19}$$

This allows one to calculate the radiation transport by considering two distinct processes. The first is a spatial movement of the radiation. That is, once the photon is emitted, it travels a distance described by $Q(x', R)$. Once the radiation is reabsorbed, the excited atom will emit another photon with, generally, a different frequency given by $J(x, x')$.

Actual implementation requires that a mesh be defined in real space (with a total of n_s cells, numbered by i or j) and in reduced frequency space (with a total of n_x cells, numbered l or m). Let $\mathbf{r}_i$ and x_l denote the centers (or suitable means) in cell i and l respectively. The density of excited atoms $n(\mathbf{r}, x, t)$ is now approximated as $\sum_{i=1}^{n_s} \sum_{l=1}^{n_x} N_{i,l}(t)\delta(\mathbf{r} - \mathbf{r}_i)\delta(x - x_l)$, where $N_{i,l}$ is the total number of excited atoms in cell (i, l), or the number per unit length in

the z direction for infinite cylindrical geometry. Analogously, the total production rate P*i,l* in this cell is now assumed to be concentrated at r*i, xl* as well. Substitution of these expressions in equation(19), and integration over a 'final' cell (*j, m*) results in a set of *nsnx* differential equations,

$$\frac{dN_{j,m}(t)}{dt} = P_{j,m}(t) - \frac{1}{\tau_v} N_{j,m}(t) + \frac{1}{\tau_v} \sum_{l=1}^{n_x} J_{m,l} \sum_{i=1}^{n_s} Q_{l,j,i} N_{i,l}(t) \tag{20}$$

where the operators *Q* and *J* are now represented by matrices.

The integral over the final cell (*j, m*) which isolates the time derivative of *Nj,m* also serves to define the matrix elements of the propagators *J* and *Q*. The matrix element *Ql,j,i* is essentially the probability that a photon emitted from the location r' *i* with reduced frequency x' *l* will be absorbed in the spatial cell *j*. Certain mesh errors are introduced by the approximation that all the photons from the spatial cell *i* are emitted from r' *i* at the center of the cell. Under most circumstances these mesh errors are negligible. Under some circumstances it is desirable to reduce these mesh errors by either slightly modifying the definition of r'*i* or by defining *Ql,j,i* in terms of an average over several points in the source cell *i*. On the other hand, numerical diffusion is decreased by emitting photons from the cell centers. Similar comments apply to the matrix element *Jm,l* of the propagator for frequency redistribution. A formal derivation of propagators in terms of averages over source cells follows from a slightly different approximation for vectorizing the radiation transport equation. Sums of 'box' functions rather than delta functions are used to approximate *n*(r, *x, t*) and *P*(*r, x, t*).

These coupled equations are to be advanced in time with time step Δt,

$$N_{j,m}(t+\Delta t) = P_{j,m}(t)\Delta t + (1 - \Delta t/\tau_v) N_{j,m}(t) + \sum_{l=1}^{n_x} J_{m,l} \left[\sum_{i=1}^{n_s} Q_{l,j,i} N_{i,l}(t) \right] \Delta t/\tau_v. \tag{21}$$

The matrix describing radiation transport, followed by the matrix describing frequency redistribution, are used to advance the number of excited atoms in each cell in time. The resulting number of excited atoms in each cell is then augmented by the production of new excited atoms during the time step.

A simple conservation condition requires

$$1 = \sum_{m=1}^{n_x} J_{m,l}. \tag{22}$$

Similarly,

$$1 > \sum_{j=1}^{n_s} Q_{l,j,i}. \tag{23}$$

The difference from unity, as in the CFR case, is simply the fraction of photons that have hit a boundary, and thus escaped from the system. In a simulation for a geometry with only one absorbing boundary, the matrix element *Ql,j,i* with $j = ns + 1$ represents the probability that a photon emitted from location r′ with reduced frequency *x¢l* will escape to the absorbing boundary. With only one absorbing boundary, equation (23) becomes

$$1 = \sum_{j=1}^{n_s+1} Q_{l,j,i}. \tag{24}$$

Expressions for the spatial propagator matrix elements in cylindrical, plane parallel, and spherical geometries are derived by Parker, Hitchon, and Lawler (1993). A method for generating the frequency space propagator matrix elements using a Jeffries-White (1960)

approximation for PFR is also presented by Parker, Hitchon, and Lawler (1993). The generation of frequency space propagator function matrix elements using a more realistic algorithm for PFR is discussed by Molisch et al. (1995). The full power of the propagator function method is demonstrated in a simulation with time dependent localized excitation on the axis of a cylinder (Parker, Hitchon, and Lawler, 1993). The density of excited atoms is seen to evolve in time after the localized source is turned on, until a steady state distribution is reached. The spatial distribution of excited atoms is not a fundamental mode in steady state due to the localized excitation. The density of excited atoms decays after the localized excitation source is turned off. The spatial distribution approaches a fundamental mode at late times.

III. ADVANCED MONTE CARLO SIMULATIONS IN CYLINDRICAL GEOMETRY

Monte Carlo simulations are attractive because such simulations are easy to code and because they are free from all, except statisitical, errors within the framework of a particular model. The J. S. Lee (1974, 1977, 1982) algorithm for PFR is the most realistic available. The Monte Carlo code developed by Anderson et al. (1995) using the Lee approximation is more efficient than the original codes developed by Lee (1974, 1977, 1982) in that it uses the method of rejection (von Neumann, 1951) to avoid any numerical integration or 'look up' tables. This more efficient code is described in the following paragraphs.

The initial radial coordinate, *pi*, of the excited atom is chosen using a random number so that a desired production rate per unit volume or initial density of excited atoms is reproduced on the average. The position is recorded, and the frequency of the emitted photon is chosen from the Voigt profile. Let the reduced frequency x be as defined in the preceding section. Parker et al. (1991) described an efficient random frequency generator for a Voigt profile. Specifically, a normally distributed random number, *xDoppler*, with a variance of one is chosen in the range of $-\infty$ to $+\infty$. Many computer software packages have a library function for generating normally distributed random numbers with a variance of one. This random number divided by $\sqrt{2}$ corresponds to a randomly chosen reduced frequency in a Doppler profile. Random numbers *w*1 through *w*7 uniformly distributed in the range 0 to 1 are chosen. The first of these is used to determine the reduced frequency in the Lorentzian profile:

$$w_1 = \int_{-\infty}^{x_{Lorentz}} \frac{a_\nu}{\pi} \frac{1}{y^2 + a_\nu^2}\, dy \tag{25}$$

where av is the Voigt parameter defined earlier (Lorentzian half-width at half-maximum divided by $\nu_0\sqrt{(2k_BT/Mc^2)}$) and $x_{Lorentz}$ is a reduced frequency. This analytic integral yields

$$x_{Lorentz} = a_\nu \tan[\pi(w_1 - 0.5)]. \tag{26}$$

The resultant randomly chosen reduced frequency from a Voigt lineshape is given by

$$x_{Voigt} = x_{Lorentz} + \frac{x_{Doppler}}{\sqrt{2}}. \tag{27}$$

The distance the photon goes before being absorbed is given by

$$D = \frac{-\ln(w_2)}{\bar{k}L_V(x_{Voigt})} = -\ln(w_2)\frac{\sqrt{2k_BT/M}}{N_0\pi r_e c f_{lu}\lambda_0 L_V(x_{Voigt})} \tag{28}$$

where *Lv*(*xvoigt*) is the normalized Voigt profile, $\int Lv(y)dy = 1$, which is evaluated using an analytic approximation based on a complex error function. In the preceeding equation *N*0

is the density of the ground state atoms, *re* is the classical radius of the electron, flu is the absorption oscillator strength, and $\lambda 0$ is the resonance transition wavelength. Emission of radiation is assumed to be isotropic, so the cosine of the polar angle is given by $\mu i = 2w3 - 1$ and the azimuthal angle is given by $\phi i = 2\pi w4$. The new radial position of the resonance atom is then found using

$$\rho_{i+1} = [\rho_i^2 + D^2(1 - \mu_i^2) + 2D(1 - \mu_i^2)^{1/2}\rho_i \cos \phi_i]^{1/2}. \tag{29}$$

Note that the $\phi = 0$ axis is oriented along the direction of $\hat{\rho}_i$. If the pi+1 radius is outside the cylinder, the frequency and time taken (or number of steps) since the initial production of the photon are recorded. A new resonance atom is generated. If the photon did not escape, then the new position pi+1 of the resonance atom is recorded. The probability of a dephasing collision during a radiative lifetime is

$$P_c = \left[1 + \frac{65.71 g_l}{N_0 \lambda_0^3 g_u}\right]^{-1}. \tag{30}$$

This equation is based on Corney's (1977) expression for resonance collisional broadening. The expression for the Voigt parameter including natural, or radiative, broadening and resonance collisional broadening is

$$a_\nu = \frac{1 + \lambda_0^3 N_0 g_u/(65.71 g_l)}{4\pi \nu_0 \tau_v (2k_B T/Mc^2)^{1/2}}. \tag{31}$$

Similarly,

$$\bar{k} = \frac{g_u \lambda_0^2 N_0}{8\pi g_l \tau_v \nu_0 (2k_B T/Mc^2)^{1/2}} = \frac{\pi r_e c f_{lu} \lambda_0 N_0}{(2k_B T/M)^{1/2}}. \tag{32}$$

If $w5$ is less than Pc the photon is reemitted using a random reduced frequency from a Voigt profile as described above. Otherwise the resonance atom did not have a dephasing collision and the frequency in the lab frame of the reemitted photon must be determined using appropriate Doppler shifts. The direction of the photon which excited the resonance atom at pi+1 is updated using

$$\phi_i' = \phi_i - \arcsin\left[\frac{D(1 - \mu_i^2)^{1/2} \sin \phi_i}{\rho_{i+1}}\right]. \tag{33}$$

This information is used in a Doppler shift calculation if no dephasing collision occurs.

The Doppler shift determination is one of the more intricate parts of the code. First, the axial velocity of the absorbing atom along the absorbed photon's trajectory must be randomly selected from the distribution

$$f(u_a) = \frac{1}{L_V(x_{Voigt})}\left[\frac{a_\nu}{\pi^{3/2}} \frac{\exp(-u_a^2)}{a_\nu^2 + (x_{Voigt} - u_a)^2}\right] \tag{34}$$

where u_a is the reduced axial velocity (axial velocity divided by $\sqrt{2k_B T/M}$), , and where L_V is a normalized Voigt profile. The operator used to select a random u_a from this distribution depends on $x_{V_{oigt}}$. The code uses the same approximation used by Jong-Sen Lee (1977) for $|x_{V_{oigt}}| > 5$. The distribution for these large $x_{V_{oigt}}$ is approximated

$$f(u_a) \simeq \frac{1}{\sqrt{\pi}} \exp\left[-(u_a - \frac{1.0}{x_{Voigt}})^2\right] \tag{35}$$

and the normally distributed random number generator is called, the result is divided by $\sqrt{2}$, and then shifted by adding $1.0/x_{V_{oigt}}$. Von Neumann's (1951) method of rejection is used

for $1.5 \leq |x_{Voigt}| \leq 5$. The trial function for this range of $|x_{Voigt}|$ is different from that used by Jong-Sen Lee in order to avoid numerical integration and look up tables. A trial function $f_t(u_a) \geq f(u_a)$ where

$$f_t(u_a) = \begin{cases} -f(-1)u_a \exp(1.0 - u_a^2) & \text{if } u_a < -1.0 \\ \max[1.5f(0), f(|x_{Voigt}| - 0.25)] & \text{if } -1 \leq u_a \leq |x_{Voigt}| - 0.25 \\ f(|x_{Voigt}| - 0.25)\frac{1+(0.25/a_\nu)^2}{1+[(u_a-|x_{Voigt}|)\frac{1}{a_\nu}]^2} & \text{if } |x_{Voigt}| - 0.25 < u_a \end{cases} \tag{36}$$

is used. Note that the indefinite integral

$$F_t(u_a) = \int_{-\infty}^{u_a} f_t(y)\, dy \tag{37}$$

is analytic in each region. Furthermore, the function F_t is easily inverted so that a trial u_a can be chosen using

$$u_a = F_t^{-1}\{w_6 F_t(\infty)\}. \tag{38}$$

This u_a is accepted if

$$w_7 < \frac{f(u_a)}{f_t(u_a)} \tag{39}$$

otherwise it is rejected and the two preceding steps are repeated. When a u_a is accepted, it is multiplied by the sign of x_{Voigt}. The trial function used by Anderson et al. (1995) has a significant advantage over that used by Jong-Sen Lee (1982) in that it avoids any numerical integration and any look up tables. Finally for $|x_{Voigt}| < 1.5$ the method of rejection is used with the same trial function used by Jong-Sen Lee (1982)

$$f_t(u_a) = \frac{1}{\pi^{3/2} L_V(x_{Voigt})}\left[\frac{a_\nu}{a_\nu^2 + (x_{Voigt} - u_a)^2}\right]. \tag{40}$$

Equations 37, 38, and 39 are used with this trial function.

After the axial velocity of the absorbing atom is determined, the normally distributed random number generator is used with appropriate $1/\sqrt{2}$ scaling to determine the transverse component ut of the reduced velocity of the absorbing atom. The frequency of the photon is then Doppler shifted into the rest frame of the atom. The reemitted photon direction (μ_{i+1}, ϕ_{i+1}) is chosen from an isotropic distribution and the frequency of the reemitted photon in the lab computed using a Doppler shift from the rest frame of the atom, specifically

$$x_{i+1} = x_{Voigt} + u_a(\hat{\mathbf{n}}_{i+1} \cdot \hat{\mathbf{n}}_i' - 1.0) + u_t\sqrt{1.0 - (\hat{\mathbf{n}}_{i+1} \cdot \hat{\mathbf{n}}_i')^2} \tag{41}$$

where

$$\hat{\mathbf{n}}_{i+1} \cdot \hat{\mathbf{n}}_i' = \mu_{i+1}\mu_i + \sqrt{1 - \mu_{i+1}^2}\sqrt{1 - \mu_i^2}\cos(\phi_{i+1} - \phi_i'). \tag{42}$$

Fundamental mode decay rates are determined by recording the 'late time' escape rate (after the initial density has decayed more than a factor of ten) using a spatially uniform initial density of resonance atoms. Anderson et al. (1995) used the Monte Carlo code

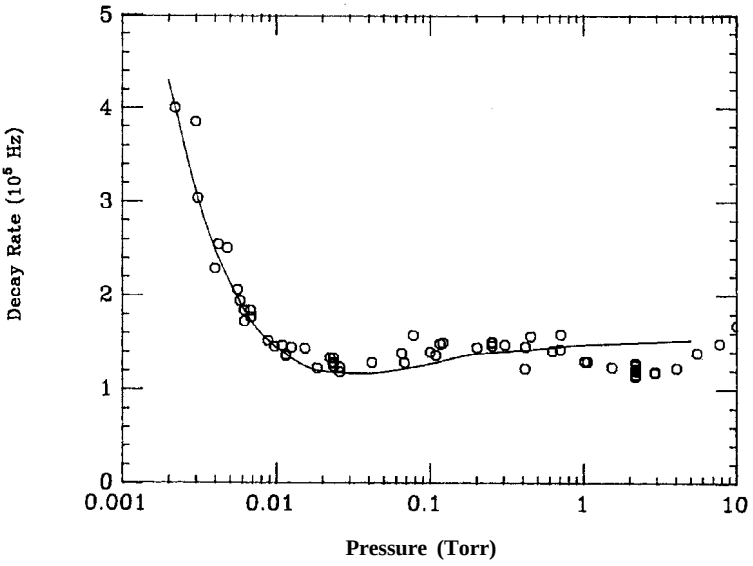

Figure 1. Trapped decay rate of the fundamental mode for the xenon 147 nm resonance radiation as a function of pressure at 40°C. The line is from the Monte Carlo simulations of Anderson et al. (1995). The symbols are from the experiment of Vermeersch et al. (1991).

with an improved experimental oscillator strength for the resonance line of Xe to compare to experimental measurements on the fundamental mode trapped decay rates of the Xe resonance level. Quite good agreement with experiment was found as shown in Figure 1. The second dip in the trapped decay rate near 3 Torr ($N_0 \approx 10^{17}$ cm^{-3}) is not due to PFR. Vermeersch et al. (1991) suggest that it is due to quasistatic resonance collisional broadening and this seems very likely correct. This highly realistic Monte Carlo code made it possible to determine the 147 nm resonance line output of low pressure Xe positive column discharges and surface wave discharges by measuring the population of the Xe resonance level using absorption spectroscopy (Doughty and Fobare, 1995; Gibson, Kortshagen, and Lawler 1996).

IV. ANALYTIC EXPRESSION FOR THE FUNDAMENTAL MODE DECAY RATE

It is desirable to have a simple analytic expression for the fundamental mode decay rate in cylindrical geometry which is accurate for all absorbing gas densities. Toward that end we have run a large number of Monte Carlo simulations using the code developed by Anderson et al. (1995). These simulations cover a factor of 100 in column radius, a factor of 100 in Doppler width, and a factor of 10,000,000 in gas density. Results from these Monte Carlo simulations are presented in this section and compared to a simple analytic formula for the fundamental mode decay rate in cylindrical geometry.

A careful inspection of the original (CFR) and modified (PFR) Holstein-Biberman equations indicates that the ratio of the fundamental mode decay rate over the vacuum radiative decay rate can be parametrized in terms three dimensionless parameters. This ratio of the fundamental mode decay rate, A_t, over the vacuum radiative decay rate, $1/\tau_v$ is sometimes called the escape factor (Irons 1979a; 1979b; 1979c). The first dimensionless parameter we choose is the reduced density,

$$N_r = N_0 \lambda_0^3, \tag{43}$$

which is the number of absorbing gas atoms per cubic wavelength. This parameter is contained in the expressions introduced earlier for the probability of a dephasing collision during a radiative lifetime. The second dimensionless parameter,

$$a_{\nu 0} = [4\pi \nu_0 \tau_v (2k_B T/Mc^2)^{1/2}]^{-1}, \tag{44}$$

is the Voigt parameter at the limit of low gas density. This Voigt parameter has been introduced earlier. In the limit of low gas density the Lorentz half-width at half-maximum in the Voigt parameter is the vacuum radiative decay rate, $1/\tau_v$, divided by 4π. The third dimensionless parameter is the reduced radius,

$$H_r = h/\lambda_0, \tag{45}$$

of the cylinder which is defined to be the radius divided by the wavelength of the resonance radiation. By expressing the analytic formula in terms of these three dimensionless parameters, it becomes simpler and more easily applied to other gases besides Xe.

In constructing the analytic formula we focus on $a_{\nu 0} = 0.0160$ which is appropriate for the Xe I resonance line at 147 nm and a typical discharge lamp operating temperature of 40°C. This value of $a_{\nu 0}$ is not too different than the value for the resonance lines of other rare gases, for example the 58.4 nm line of He I has $a_{\nu 0} = 0.0185$ at a temperature of 40°C. We have also run Monte Carlo simulations for an order of magnitude larger and smaller values of $a_{\nu 0}$. Simulations are run for three values of reduced radius: $H_r = 1.22 \times 10^5$, $H_r = 1.22 \times 10^4$, $H_r = 1.22 \times 103$. These reduced radii correspond to physical radii of 18 mm, 1.8 mm, and 0.18 mm respectively for the Xe I resonance line. Simulations are run for many values of reduced density ranging from $N_r = 9.79 \times 10^{-7}$ to $N_r = 4.90 \times 10^2$ in steps of $\times 2, \times 5$, and $\times 10$. These reduced densities correspond to gas pressures of 1×10^{-7} Torr to 5 Torr at 40°C. This range of gas densities produces ratios of the trapped decay rate of the fundamental mode over the vacuum decay rate, $A_t \tau_v$, ranging from approximately 0.9 to the asymptotic solution for high gas density. Monte Carlo results for $a_{\nu 0} = 0.0160$ are presented in Table 1 with the ratio of the analytic formula over the Monte Carlo results in brackets. All Monte Carlo results are from runs with 10,000 or more late decays and thus have statistical errors no larger than a few percent. Monte Carlo results for $a_{\nu 0} = 0.160$ and $a_{\nu 0} = 0.00160$ are presented in Tables 2 and 3, respectively.

Our analytic formula is constructed from analytic solutions to the Holstein-Biberman equation with CFR in two limiting cases. The first case corresponds to the limit of low absorbing gas density where Doppler broadening dominates the transport. The high opacity analytic solution for the fundamental mode decay rate as derived by Holstein (1947b) and refined by van Trigt (1976) and others is

$$(A_t \tau_v)_d = \frac{1.575}{\bar{k}h\sqrt{\ln(\bar{k}h/\sqrt{\pi})}}. \tag{46}$$

This expression can be rewritten as

$$(A_t \tau_v)_d = \frac{1.575}{Z\sqrt{\ln(Z\sqrt{\pi})}} \tag{47}$$

where

$$Z = N_r a_{\nu 0} H_r \frac{g_u}{2g_l}. \tag{48}$$

Table 1. Monte Carlo results for the ratio of the trapped decay rate of the fundamental mode over the vacuum decay rate, $(A_t\tau_v)_{mc}$,with a_{v0} = 0.0160 for the three values of the reduced radius H_r. The number in brackets is the ratio of the analytic formula, $A_t\tau_v$, over the Monte Carlo result, $(A_t\tau_v)_{mc}$.

N_r	$(A_t\tau_v)_{mc}$		
	H_r = 1.22 x 10^5	H_r = 1.22×10^4	H_r = 1.22×10^3
9.79×10^{-5}	8.61×10^{-1} [1.04]		
1.96×10^{-4}	7.61×10^{-1} [1.04]		
4.90×10^{-4}	5.59×10^{-1} [1.02]		
9.79×10^{-4}	3.68×10^{-1} [0.99]	8.64×10^{-1} [1.03]	
1.96×10^{-3}	2.06×10^{-1} [0.96]	7.62×10^{-1} [l.04]	
4.90×10^{-3}	7.88×10^{-2} [0.98]	5.52×10^{-1} [1.03]	
9.79×10^{-3}	3.57×10^{-2} [1.01]	3.70×10^{-1} [0.98]	8.64×10^{-1} [1.03]
1.96×10^{-2}	1.63×10^{-2} [1.04]	2.06×10^{-1} [0.97]	7.65×10^{-1} [1.04]
4.90×10^{-2}	6.09×10^{-3} [1.04]	7.84×10^{-2} [0.99]	5.56×10^{-1} [1.02]
9.79×10^{-2}	3.04×10^{-3} [1.04]	3.60×10^{-2} [1.01]	3.66×10^{-1} [0.99]
1.96×10^{-1}	1.58×10^{-3} [1.04]	1.65×10^{-2} [1.03]	2.07×10^{-1} [0.96]
4.90×10^{-1}	7.86×10^{-4} [1.02]	6.17×10^{-3} [1.05]	7.91×10^{-2} [0.98]
9.79×10^{-1}	5.33×10^{-4} [1.01]	3.22×10^{-3} [1.02]	3.58×10^{-2} [1.01]
1.96	4.41×10^{-4} [0.99]	1.91×10^{-3} [0.99]	1.69×10^{-2} [l.00]
4.90	4.38×10^{-4} [0.97]	1.40×10^{-3} [1.00]	7.28×10^{-3} [0.95]
9.79	4.69×10^{-4} [0.97]	1.44×10^{-3} [0.98]	4.80×10^{-3} [1.01]
1.96×101	5.10×10^{-4} [0.97]	1.56×10^{-3} [0.97]	4.42×10^{-3} [1.05]
4.90×101	5.29×10^{-4} [1.00]	1.70×10^{-3} [0.96]	5.11×10^{-3} [0.98]
9.79×101	5.45×10^{-4} [1.00]	1.72×10^{-3} [0.99]	5.53×10^{-3} [0.95]
1.96×102	5.52×10^{-4} [1.00]	1.77×10^{-3} [0.98]	5.51×10^{-3} [0.98]
4.90×102	5.62×10^{-4} [0.99]	1.77×10^{-3} [0.99]	5.64×10^{-3} [0.98]

Table 2. Monte Carlo results for the ratio of the trapped decay rate of the fundamental mode over the vacuum decay rate, $(A_t\tau_v)_{mc}$, with $a_{v0} = 0.160$ for the three values of the reduced radius H_r. The number in brackets is the ratio of the analytic formula, $A_t\tau_v$, over the Monte Carlo result, $(A_t\tau_v)_{mc}$.

N_r	$(A_t\tau_v)_{mc}$		
	$H_r = 1.22 \times 10^5$	$H_r = 1.22 \times 10^4$	$H_r = 1.22 \times 10^3$
9.79×10^{-6}	8.78×10^{-1} [1.02]		
1.96×10^{-5}	7.91×10^{-1} [1.02]		
4.90×10^{-5}	6.04×10^{-1} [0.99]		
9.79×10^{-5}	4.15×10^{-1} [0.98]	8.79×10^{-1} [1.02]	
1.96×10^{-4}	2.44×10^{-1} [0.96]	7.90×10^{-1} [1.02]	
4.90×10^{-4}	9.67×10^{-2} [0.99]	6.09×10^{-1} [0.98]	
9.79×10^{-4}	4.72×10^{-2} [0.97]	4.11×10^{-1} [0.99]	8.81×10^{-1} [1.02]
1.96×10^{-3}	2.29×10^{-2} [0.95]	2.41×10^{-1} [0.98]	7.94×10^{-1} [1.01]
4.90×10^{-3}	9.46×10^{-3} [0.89]	9.87×10^{-2} [0.98]	6.02×10^{-1} [0.99]
9.79×10^{-3}	5.03×10^{-3} [0.86]	4.68×10^{-2} [1.00]	4.10×10^{-1} [0.99]
1.96×10^{-2}	2.71×10^{-3} [0.88]	2.26×10^{-2} [1.00]	2.40×10^{-1} [0.98]
4.90×10^{-2}	1.23×10^{-3} [0.99]	9.39×10^{-3} [0.95]	9.85×10^{-2} [0.99]
9.79×10^{-2}	6.81×10^{-4} [1.16]	5.12×10^{-3} [0.92]	4.73×10^{-2} [1.00]
1.96×10^{-1}	4.32×10^{-4} [1.22]	2.88×10^{-3} [0.92]	2.30×10^{-2} [1.00]
4.90×10^{-1}	3.15×10^{-4} [1.17]	1.60×10^{-3} [0.93]	1.04×10^{-2} [0.89]
9.79×10^{-1}	3.33×10^{-4} [1.10]	1.25×10^{-3} [0.97]	6.27×10^{-3} [0.86]
1.96	3.63×10^{-4} [1.11]	1.22×10^{-3} [1.02]	4.76×10^{-3} [0.87]
4.90	4.41×10^{-4} [1.04]	1.35×10^{-3} [1.04]	4.46×10^{-3} [0.96]
9.79	4.67×10^{-4} [1.05]	1.51×10^{-3} [1.01]	4.68×10^{-3} [1.00]
1.96×10^{1}	5.11×10^{-4} [1.01]	1.58×10^{-3} [1.03]	5.04×10^{-3} [1.00]
4.90×10^{1}	5.34×10^{-4} [1.01]	1.70×10^{-3} [1.00]	5.34×10^{-3} [1.00]
9.79×10^{1}	5.48×10^{-4} [1.00]	1.74×10^{-3} [1.00]	5.43×10^{-3} [1.00]
1.96×10^{2}	5.54×10^{-4} [1.00]	1.75×10^{-3} [1.00]	5.60×10^{-3} [0.99]
4.90×10^{2}	5.61×10^{-4} [0.99]	1.77×10^{-3} [1.001	5.53×10^{-3} [1.01]

Table 3. Monte Carlo results for the ratio of the trapped decay rate of the fundamental mode over the vacuum decay rate, $(A_t\tau_v)_{mc}$, with $a_{v0} = 0.00160$ for the three values of the reduced radius H_r. The number in brackets is the ratio of the analytic formula, $(A_t\tau_v)$, over the Monte Carlo result, $(A_t\tau_v)_{mc}$.

N_r	$(A_t\tau_v)_{mc}$		
	$H_r = 1.22 \times 105$	$H_r = 1.22 \times 104$	$H_r = 1.22 \times 103$
9.79×10^{-4}	8.63×10^{-1}[1.03]		
1.96×10^{-3}	7.62×10^{-1}[1.04]		
4.90×10^{-3}	5.48×10^{-1}[1.02]		
9.79×10^{-3}	3.60×10^{-1}[0.97]	8.68×10^{-1}[1.03]	
1.96×10^{-2}	2.03×10^{-1}[0.92]	7.60×10^{-1}[1.04]	
4.90×10^{-2}	7.71×10^{-2}[0.92]	5.54×10^{-1}[1.01]	
9.79×10^{-2}	3.47×10^{-2}[0.95]	3.63×10^{-1}[0.96]	8.64×10^{-1} [1.03]
1.96×10^{-1}	1.56×10^{-2}[0.98]	2.01×10^{-1}[0.93]	7.60×10^{-1} [1.04]
4.90×10^{-1}	5.45×10^{-3}[1.02]	7.56×10^{-2}[0.94]	5.55×10^{-1} [1.00]
9.79×10^{-1}	2.59×10^{-3}[1.03]	3.46×10^{-2}[0.95]	3.67×10^{-1} [0.95]
1.96	1.24×10^{-3}[1.07]	1.58×10^{-2}[0.96]	2.03×10^{-1} [0.92]
4.90	5.52×10^{-4}[1.14]	5.70×10^{-3}[0.96]	7.76×10^{-2} [0.90]
9.79	3.95×10^{-4}[1.23]	2.84×10^{-3}[0.96]	3.62×10^{-2} [0.88]
1.96×10^{1}	3.98×10^{-4}[1.17]	1.58×10^{-3}[1.09]	1.70×10^{-2} [0.86]
4.90×10^{1}	4.99×10^{-4}[0.99]	1.25×10^{-3}[1.23]	6.93×10^{-3} [0.90]
9.79×10^{1}	5.40×10^{-4}[0.95]	1.46×10^{-3}[1.08]	4.61×10^{-3} [1.08]
1.96×10^{2}	5.58×10^{-4}[0.96]	1.68×10^{-3}[0.98]	4.50×10^{-3} [1.11]
4.90×10^{2}	5.60×10^{-4}[0.98]	1.74×10^{-3}[0.98]	5.30×10^{-3} [0.99]

The second case corresponds to the limit of high absorbing gas density where resonance collisional broadening dominates the lineshape and the transport. The high opacity analytic solution derived by Holstein (1951) and refined by others (including van Trigt, 1976) is

$$(A_t\tau_v)_{rc} = 0.196\sqrt{\lambda/h} = 0.196/\sqrt{H_r}. \tag{49}$$

In order to reproduce the Monte Carlo results we modify the opacity function, Z, by using

$$Z_m = \frac{Z}{1.0 + \frac{\sqrt{a_{\nu 0}}Z}{Z+2} + \frac{0.573N_r(a_{\nu 0})^{1.25}(H_r)^{0.75}}{N_r(a_{\nu 0})^{1.15}\sqrt{H_r}+10.5}}. \tag{50}$$

The formula for the case where Doppler broadening dominates transport is modified as

$$(A_t\tau_v)_{dm} = \frac{1.575}{1.575 + Z_m\sqrt{\ln(1.4 + Z_m/\sqrt{\pi})}}. \tag{51}$$

The formula for the case where resonance collisional broadening dominates transport is also modified as

$$(A_t\tau_v)_{rcm} = P_c^{0.1}\frac{0.196}{\sqrt{H_r}}. \tag{52}$$

Finally, these formulae are combined as

$$A_t\tau_v = \sqrt{(A_t\tau_v)_{dm}^2 + (A_t\tau_v)_{rcm}^2 - 0.89(A_t\tau_v)_{dm}(A_t\tau_v)_{rcm}}. \tag{53}$$

This analytic formula is accurate within ±5% for $a_{\nu 0}$ = 0.0160. It is accurate to ±23% for values of $a_{\nu 0}$ which are an order of magnitude larger and smaller as shown in Tables 2 and 3.

V. SUMMARY

Methods for calculating resonance radiation transport in glow discharge plasmas are reviewed. Emphasis is given to the recently developed propagator function method, and to a recently developed Monte Carlo code which is both efficient and highly realistic. The Monte Carlo code is used to determine the resonance radiation trapped decay rate for the fundamental mode in cylindrical geometry over a vast region of parameter space. An analytic formula is devised to approximate the Monte Carlo results.

REFERENCES

Anderson, H.M., Bergeson, S.D., Doughty, D.A., and Lawler, J.E., 1995, Phys. Rev. A **51,** 211.
Biberman, L.M., 1947, Zh. Eksp. Teor. Fiz. **17,** 416.
Blickensderfer, R.P., Breckenridge, W.H., and Simons, J., 1976, J. Phys. Chem. **80,** 653.
Compton, K.T., 1923, Phil. Mag. **45,** 750.
Corney, A., 1977, "Atomic and Laser Spectroscopy," Oxford: Clarendon.
Doughty, D.A. and Fobare, D.F., 1995, Rev. Sci. Instrum. **66,** 4834.
Gibson, N.D., Kortshagen, U., and Lawler, J.E., 1997, J. Appl. Phys. **81,** 1087.
Holstein, T., 1947, Phys. Rev. **72,** 1212.
Holstein, T., 1951, Phys. Rev. **83,** 1159.
Jack, A.G., 1986, Low Pressure Mercury and Sodium Lamps, *in:* "Radiative Processes in Discharge Plasmas", NATO ASI Series B **149,** J.M. Proud and L.H. Luessen, eds., Plenum, New York.
Irons, F.E., 1979, J. Quant. Spectrosc. Radiat. Transfer **22,** 1; *ibid.* **22,** 21; *ibid.* **22,** 37,
Jeffries, J.T. and White, O.R., 1960, Astrophys. J. 132, 767.
Lawler, J.E., Parker, G.J., and Hitchon, W.N.G., 1993, J. Quant. Spectrosc. Radiat. Transfer **49,** 627.
Lee, J.S., 1974, Astrophys. J. **192,** 465.

Lee, J.S., 1977, Astrophys. J. **218,** 857.
Lee, J.S., 1982, Astrophys. J. **255,** 303.
Milne, E.A., 1926, J. London Math. Soc, **1,** 40.
Molisch, A.F., Parker, G.J., Oehry, B P., Schupita, W., and Magerl, G., 1995, J. Quant. Spectrosc. Radiat. Transfer **53,** 269.
von Neumann, J., 1951, NBS Appl. Math. Series **12,** 36.
Parker, G.J., Hitchon, W.N.G., and Lawler, J.E., 1993, J. Phys. B **26,** 4643.
Payne, M.G., Talmage, J.E., Hurst, G.S., and Wagner E.B., 1974, Phys. Rev. A **9,** 1050.
Phelps, A.V., 1959, Phys. Rev. **114,** 1011.
Post, H.A., 1986, Phys. Rev. A **33,** 2003.
Post, H.A., van de Weijer, P., and Cremers, R.M.M., 1986, Phys. Rev. A **33,** 2017.
Press W.H., Flannery B.P., Teukolsky, S.A., and Vetterling, W.T., 1989, ch 4, *in:* Numerical Recipes: The Art of Scientific Computing, Cambridge University Press, New York.
Romberg, A. and Kunze, H.J., 1988, J. Quant. Spectrosc. Radiat. Transfer **39,** 99.
van Trigt, C., 1969, Phys. Rev. **181,** 97.
van Trigt, C., 1970, Phys. Rev. A **1,** 1298.
van Trigt, C., 1971, Phys. Rev. A **4,** 1303.
van Trigt, C., 1976a, Phys. Rev. A **13,** 726.
van Trigt, C., 1976b, Phys. Rev. A **13,** 734.
Vermeersch, F. and Wieme, W, 1991, Calculation of resonance radiation trapping, in: "Optogalvanic Spectroscopy", Inst. of Physics. Conf. Ser. **113,** 109.
Vermeersch, F., Schoon, N., Desoppere, E., and Wieme, W, Experimental investigation of the imprisonment of the ($^3P_1 - ^1S_0$) 146.96 nm resonance radiation in xenon, 1991, *in:* "Optogalvanic Spectroscopy", Inst. of Physics. Conf. Ser. **113,** 133.
Wamsley, R.C., Mitsuhashi, K., and Lawler, J.E., 1993, Phys. Rev. E **47,** 3540.

This Page Intentionally Left Blank

OPTICAL CHARACTERIZATION OF RF INDUCTIVELY COUPLED PLASMAS

A. E. Wendt[1,2] , D. F. Beale[3], W. N. G. Hitchon[1,2] , E. Keiter[4], V. Kolobov[5], L. Mahoney[6], A. A. Pierre[2] and J. Stittsworth[7]

[1]Dept. of Electrical and Computer Engineering
[2]Engineering Research Center for Plasma-Aided Manufacturing
University of Wisconsin - Madison
Madison, WI 53706
[3]currently at Lam Research Corp., Fremont, CA
[4]currently at University of Illinois, Urbana, IL
[5]currently at University of Houston, Houston, TX
[6]currently at Diamonex, Allentown, PA
[7]currently at Hewlett Packard Corp., Corvallis, OR

INTRODUCTION

RF inductively-coupled plasmas (ICP) provide a rich resource for studying electron kinetics in low pressure discharges. Coupling of rf power to the electrons results from interaction with some combination of inductive and capacitive electric fields, and is spatially nonuniform. Power is absorbed by the electrons through both collisional (ohmic) and collisionless (stochastic) heating. Depending on operating conditions, electron energy may be expended locally, near where heating took place, or non-locally. Creation of plasma may be dominated by single-step electron impact ionization from ground state neutrals, or through a two-step process involving metastables. These are just a few examples of factors affecting discharge operation, and this study of these phenomena is framed in the context of identifying factors that govern the spatial uniformity of the plasma density, an issue of great importance in the use of ICP discharges in plasma processing applications [1, 2].

The focus of this investigation is argon discharges in a planar rf ICP system. The discharge is confined to a cylindrical volume bounded by grounded walls and at one end, a flat quartz window through which rf power is coupled. Power is delivered at 13.56 MHz through a flat spiral or circular antenna flush against the quartz window outside of the vacuum. For many of these experiments, a spoked Faraday shield was inserted between the antenna and the quartz window to minimize the contribution of capacitive coupling to the discharge power.

Discharge properties have been characterized over a range of operating conditions. Specifically, we have varied discharge pressure and power, as well as the dimensions of

Electron Kinetics and Application of Glow Discharges
Edited by U. Kortshagen and L. D. Tsendin, Plenum Press, New York, 1998

the cylindrical plasma volume. Discharge characterization consists of detailed spatial maps of optical emission intensity and plasma parameters measured with Langmuir probes, as well as absorption spectroscopic measurements of argon metastable concentrations. These measurements are consistent with "non-local" electron heating in ICP discharges, and raise new questions about the details of ICP discharge dynamics. The latter is most dramatically illustrated in the azimuthal striations in discharge intensity reported in the last section of this chapter.

Experimental observations are examined through a two dimensional model of the ICP discharge that has been developed based on non-local kinetic theory. By taking advantage of slow electron energy diffusion at low pressures, a simplified kinetic model is possible by approximately treating the electron energy as a constant of the motion. This approach provides improves improved accuracy over fluid models[3] and improved speed over other kinetic approaches for electron motion, such as Monte Carlo[4].

R-Z SPATIAL PROFILES OF OPTICAL EMISSION

Spatially resolved optical emission spectroscopy (OES) has been employed to examine electron impact excitation in a planar ICP argon discharge. Because of the short lifetimes of the excited argon states probed, emission profiles can be considered an accurate reflection of spatial profiles of excitation rate. These measurements may also be considered a qualitative probe of the ionization rate spatial distribution. Although total ionization rates and excitation rates may differ dramatically, the two may be expected to have similar spatial structure, as both will be sensitive to spatial variation of the tail of the electron energy distribution function (EEDF).

Two-dimensional maps of emission in the *r-z* plane of the cylindrical chamber have been constructed through Abel inversion of the line-integrated emission measurements. The plasma was generated in a cylindrical volume 14 cm long by 23 cm diameter. A 1.27 cm thick quartz window and a Faraday shield separate the plasma from the four-turn aluminum antenna, powered at 13.56 MHz. Emission intensity was measured for parallel chords through 1 cm slots at three axial locations centered at 4.2, 8.8 and 13.1 cm from the quartz window. Measurements at axial positions closer to the window were impossible because the line of sight was mechanically obstructed. For each axial position, emission intensity was recorded for four chords, with the first intersecting the discharge axis and separated by 2 cm in the transverse direction.

Measurements shown in Figure 1 were made at 10 and 50 mTorr, and 200 watts rf power. Optical transitions at 912.5 and 867.1 nm were observed. Both cases show an off-axis peak below the antenna, in the region of maximum heating, the 10 mTorr case shows a secondary local maximum on-axis near the discharge center. Langmuir probe measurements made under identical operating conditions[5] in the same reactor show a single maximum in electron density near the discharge center, and a maximum in average electron energy off-axis near the antenna. In all cases, the location of peak emission (and thus peak excitation rate) corresponds to the location of peak average electron energy found by Mahoney *et al.*[5], rather than the location of maximum electron density. This maximum is attributed to localized electron heating.

In the 10 mTorr case, a secondary peak is observed on-axis, suggesting the effect of non-local electron kinetics. This feature appears in the 10 and 20 mTorr cases, and in the 100 mTorr, 200 W case. This peak is thought not to be associated with localized electron heating, but with three other possible factors. First, the secondary peak in emission intensity coincides with the location of peak plasma potential[5]. As a result, we may expect an enhancement at low pressures. Collisionless trapped electrons have

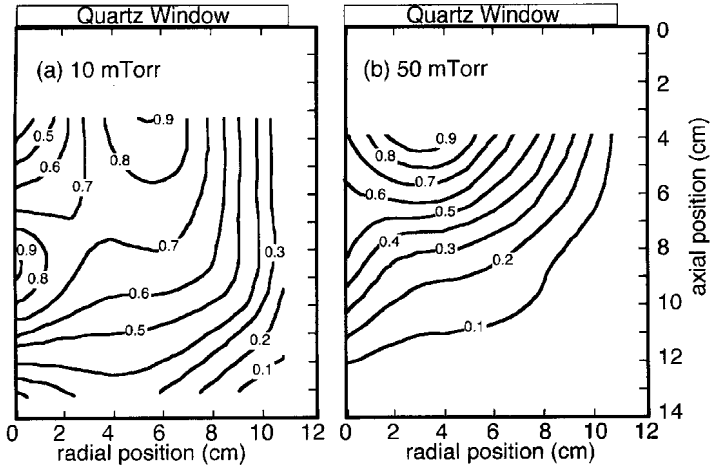

Figure 1. Contour plots of relative optical emission intensity in the *r-z* plane of argon ICP discharges for (a) 10 mTorr, 200 watts, and (b) 50 mTorr, 200 watts. While both cases exhibit maxima near the antenna, the 10 mTorr case shows a second maxima near the discharge center.

a minimum in potential energy there, and therefore a maximum in kinetic energy and excitation probability[6]. Second, measurements of electron density also show a peak in this location[5]. Since the excitation rate is proportional to electron density, this may also be a factor in the observed peak. Finally, if excitation to the emitting states is dominated by a two-step process, the argon metastable concentration is another contributing factor.

NON-LOCAL ELECTRON KINETICS-BASED DISCHARGE MODEL

A self-consistent model of ICP electron kinetics capable of describing the spatially-resolved electron distribution function and the relevant energy transfer processes has been developed. In particular, the electron energy balance is described by Coulomb collisions between electrons as well as heating, spatial diffusion and inelastic collisions. Excitation rate spatial profiles are captured in this model and can be attributed to non-local effects and explained in terms of the spatial scale lengths and, in particular, the energy loss lengths for the main collision processes.

The non-local approach to electron kinetics provides an appropriate description for weakly collisional plasmas, approaching the accuracy of kinetic techniques with the simplicity of fluid methods. This is achieved by reducing the kinetic equation to an ordinary differential equation in a single variable. Rather than following electron trajectories of individual electrons, the non-local approach represents the electron density distribution in the aggregate. More specifically, non-local models resolve the spatial and energy dependence of the isotropic electron energy distribution function F_0. Physically, due to the low frequency of collisions at low pressure (less than 50 mTorr in Ar), electrons traverse a large part of the reactor vessel before losing energy. This permits the non-local approximation that electron total energy depends only weakly on distance from the heating region. In the collisionless limit, total electron energy $\epsilon = \epsilon_k - e\phi(r, z)$ is a constant of the motion for confined electrons.

The electron energy distribution function is calculated using the non-local kinetics technique that was developed by Bernstein and Holstein[7] and Tsendin *et al.*[8, 9], and which has recently been used for discharges at moderate and low neutral pressure[6, 10].

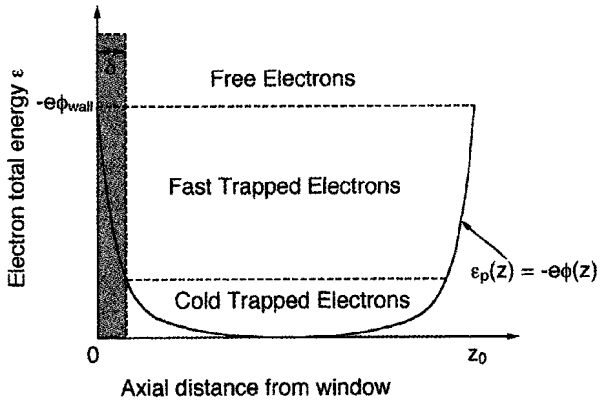

Figure 2. Since electron total energy is approximately conserved, electrons can be categorized by total energy. Cold trapped electrons are not heated by the rf electric field, as they are confined away from the strong field region by the ambipolar potential well. Fast trapped electrons are also confined by the ambipolar field, but can reach the high-field region. Only free electrons, which have energy greater than the plasma potential, can escape from the discharge.

Many previous model assumed that the electron velocity distribution is nearly isotropic, and that the electron total energy $\in$ is an approximate constant of the motion. This assumption is relaxed in this study in order to resolve the spatial distribution of the hot electrons. Spatial variation in the energy distribution of the hot electrons is likely to have significant implications for discharge uniformity for conditions under which the electron mean free path for inelastic collisions can be smaller than the discharge dimensions, as is the case here. This approach enables an accurate treatment of Coulomb collisions between electrons, which are a vital part of the electron energy balance.

Since conservation of total electron energy is the premise of the non-local approach, we categorize classes of electrons according to this parameter, as shown in Figure 2. The lowest energy electrons in the system are trapped electrostatically and are unable to reach the rf electric field heating the plasma, thus the name “cold trapped” electrons. Electrons that are confined electrostatically but are energetic enough that their range of motion reaches to within a skin depth of the quartz window are heated by the rf fields, distinguishing these “fast trapped” electrons from the cold trapped electrons. Finally, the “free” electrons have sufficient energy that they are not confined electrostatically and can escape to the chamber walls.

The organization of the simulation is illustrated in Figure 3. SimGen©, a partial differential equations solver[11], is used to solve all finite difference equations. The solver is based on the multidimensional Newton’s method for solving non-linear equations.

Electron Energy Distribution Function

For electrons below the 11.5 eV threshold energy for electron-neutral inelastic collisions, the total electron energy $\in$ is approximately conserved, as electron-electron and quasi-elastic collisions change their energy very slowly.

For both cold and hot trapped electrons in low pressure argon discharges, the inelastic mean free path $\lambda_{\in}$, is large compared to the dimensions of the chamber used in this study (~ 10 cm). Because electrons carry energy gained from the rf field

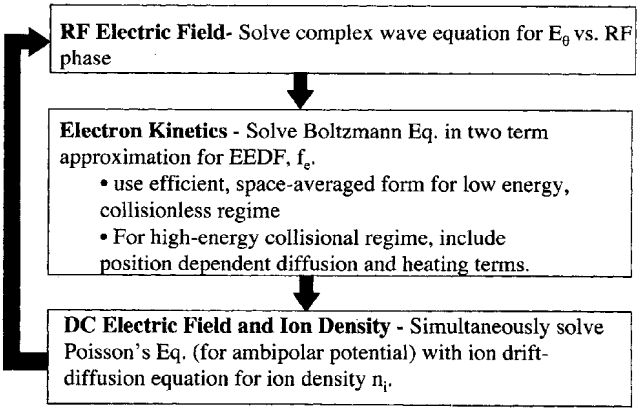

Figure 3. The simulation is organized into three modules.

throughout their accessible volume, the Boltzmann equation is equivalent, to a good approximation, to its spatially averaged form. The method used for spatial averaging involves averaging over the volume V_ϵ accessible to an electron with total energy ϵ.

A time-averaged version of the Boltzmann equation is solved in the case of near-isotropic electron energy distribution function f_e. The velocity dependence of f_e is approximated using the first two terms of the Legendre polynomial expansion:

$$f_e(\vec{v},\vec{r},t) = \sum_k P_k(\cos\theta) F_k(v,\vec{r},t). \tag{1}$$

In the following discussion $F_0(\epsilon, r, z)$ is the zero order isotropic term of the expansion, where the independent variable has been changed from velocity to total energy $\epsilon = \epsilon_k - e\phi(r,z)$. Electron kinetic energy is ϵ_k and potential energy $\epsilon_p(\vec{r}) = -e\phi(\vec{r})$.

The space-averaged kinetic equation is:

$$\frac{\partial}{\partial\epsilon}\left[\left(\overline{D}_{ee} + \overline{D}_E + \overline{D}_N\right)\frac{\partial F_0}{\partial\epsilon} + \left(\overline{V}_{ee} + \overline{V}_N\right)F_0\right] = \left(\overline{V}^*(\epsilon) + \sqrt{\epsilon}\nu_{wall}(\epsilon_k)\right)F_0(\epsilon) - \overline{V}^*(\epsilon+\epsilon^*)F_0(\epsilon+\epsilon^*), \tag{2}$$

where ϵ^* is the inelastic threshold, D_{ee} and V_{ee} are Coulomb coefficients, described below, ν_{wall} is the approximate wall loss frequency described by Kortshagen *et al.*[10], D_E, D_N and V_N, and V^* are associated with electron energy diffusion due to heating by the rf electric field, elastic collisions, and inelastic collisions, respectively, and an overline represents a spatial average. At low energy this reduces to:

$$\frac{\partial F_0}{\partial\epsilon} + \frac{\overline{V}_{ee} + \overline{V}_N}{\overline{D}_{ee}}F_0 = 0 \tag{3}$$

Heating and cooling of electrons through Coulomb collisions are accounted for in the kinetic equation through D_{ee} and V_{ee}, respectively, defined as

$$D_{ee} = \frac{16\pi\sqrt{2}\nu_{ee}}{3n_e m^{5/2}}\left[\int_0^{\epsilon_k}\epsilon_k^{3/2}F_0\,d\epsilon_k + \epsilon_k^{3/2}\int_{\epsilon_k}^{\infty}F_0\,d\epsilon_k\right], \tag{4}$$

and

$$V_{ee} = \frac{4\pi\nu_{ee}}{n_e}\int_0^{\epsilon_k}F_0\sqrt{\epsilon_k}d\epsilon_k, \tag{5}$$

where ν_{ee} is the Coulomb collision frequency[12]. Though weak in absolute magnitude as compared to heating by rf fields, energy diffusion by Coulomb collisions is significant because they provide the only heating mechanism for cold trapped electrons. The power is initially deposited in the more energetic electrons, since they are the only ones that can reach the high-field region. At a pressure of 10 mTorr and typical observed electron densities on the order of $n_e = 10^{11}$ cm^{-3}, Coulomb collisions keep the distribution nearly Maxwellian. Once electrons have sufficient energy to reach the heating region, heating from the electric field becomes dominant.

For the highest energy electrons, the approximation that the inelastic collision length is long compared to the chamber length is no longer valid. These "fast" electrons constitute less than 5% of all electrons in this model. The spatial averaging procedure is not correct for fast electrons. These electrons have a significant effect on the ionization rate profile and provide the entire electron flux to the walls. The model described here includes these effects, representing an improvement over other self-consistent non-local models.

The kinetic equation for fast electrons must be written as a function of spatial coordinates:

$$\nabla_r(vD_r\nabla_r F_0^1(\epsilon,r,z)) + \frac{\partial}{\partial\epsilon}vD_E\frac{\partial F_0^1(\epsilon,r,z)}{\partial\epsilon} = S. \tag{6}$$

Here the spatial diffusion coefficient is $D_r = \frac{v^2}{2\nu_m}$ and

$$D_E = \frac{(eE_{eff}(r,z))^2}{3\nu_m} \tag{7}$$

is termed the energy diffusion coefficient. S represents the net number of electrons per unit time scattered in a unit phase space volume by collisions. Included are momentum transfer electron-neutral collisions, inelastic electron-neutral collisions, Coulomb collisions and electron loss to the chamber walls.

Care must be taken in matching the distribution function in the energy range where the space-averaged equation is solved for trapped electrons to the region where the local (non-averaged) equation is solved for the free electrons. The matching is carried out by equating the distribution functions at the energy boundary. The boundary is placed at an energy which is sufficiently low that the spatial diffusion term dominates the energy diffusion term. At this boundary in energy, there is a discontinuous change in E_θ, as the spatially averaged electric field is used at lower energies and the local field is used at higher energies. This discontinuity in E_θ does not produce a significant non-physical discontinuity in F_0 if the spatial diffusion term in the kinetic equation dominates over the electric field term.

Fluid Formulation for Ions

A fluid description is used to model ion behavior in the ICP discharge. The ion equation of motion used includes electric field and quasi-elastic terms: $M\frac{\partial v}{\partial t} = eE - Mv\nu_{mi}$. Here ν_{mi} is the ion-neutral collision frequency. For ions in thermal equilibrium, this can be recast as an ion drift-diffusion equation:

$$\Gamma_i = -D_i\nabla n_i + n_i\mu_i(E)E - \frac{1}{\nu_{mi}}\frac{\partial\Gamma_i}{\partial t}, \tag{8}$$

with the diffusion term arising from averaged behavior over many collisions. Here Γ_i is the ion flux, D_i is the ion diffusion coefficient and $\mu_i(E)$ is the electric field dependent ion mobility. The ion inertia is neglected in this simulation, leading to

inaccuracies in the sheath region for low-pressure, high-density plasmas. Ion motion in the sheath region is approximated by using a a velocity dependent mobility derived from experimental measurements [13].

Potential ø throughout the discharge is determined by solving Poisson's equation,

$$\nabla^2\phi(r,z) = \frac{e}{\epsilon_0}\left(n_e(\phi(r,z)) - n_i(r,z)\right), \tag{9}$$

simultaneously with the drift-diffusion equation. The inclusion of Poisson's equation allows us to rigorously calculate the wall potential.

A straightforward central difference approach is used to solve Poisson's equation simultaneously with the ion continuity equation. Unfortunately, using a standard central difference scheme is not advisable for solving for the ion flux Γ_i. Due to the approximately exponential dependence of the plasma density on the potential, very small mesh spacing would be required to solve the ion continuity equation with standard finite difference methods. The finite difference technique of Scharfetter and Gummel is employed instead[14]. This method, which uses an exponential interpolation between mesh points, is stable on a coarser mesh than the conventional method used elsewhere[4, 10].

RF Electric Field

The rf electric field responsible for electron heating is determined by currents both in the planar antenna and in the plasma. In this simulation, we assume azimuthal symmetry, so that the rf electric field, E_θ, is oriented in the azimuthal direction. E_θ is determined from the complex wave equation

$$\nabla^2 E_\theta = i\omega(J_{coil} + J_{plasma}). \tag{10}$$

It is assumed that the plasma responds linearly to the field, and that time-dependence of all quantities is sinusoidal. The current density in the plasma is defined by $J_e = -n_e e < \vec{v} >$, determined by integrating over the distribution function calculated in the electron kinetic module. Power deposition is modeled by Ohmic heating, i. e.,

$$P = \frac{1}{2} Re(J^*_{plasma} E_\theta). \tag{11}$$

Model Predictions of Excitation Rate Profiles

The ICP system simulated was the same as that for which optical emission spatial maps were made experimentally. The dimensions of both the plasma volume and the ICP antenna are given in the section describing optical emission experiments above. Simulations were run at 10 mTorr and 50 mTorr argon for comparison with optical emission data. Results showing *r-z* contour plots of electron impact excitation rate of argon are depicted in Figure 4. Since the observed emitting states are short-lived, spatial maps of excitation rate should be strongly correlated with optical emission profiles. It can be seen in Figure 4 that the model reproduces the experimentally observed shift in location of the excitation rate maximum as the pressure is increased from 10 mTorr to 50 mTorr. The shift in excitation rate toward the antenna can be attributed to the reduction in thermal conductivity for the electrons as the pressure is increased.

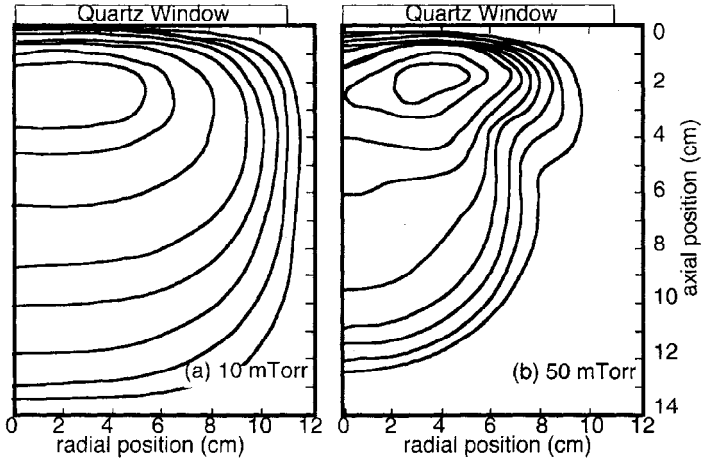

Figure 4. Spatial maps (r-z) of relative excitation rates in argon ICP discharges, for pressures of a) 10 mTorr and b) 50 mTorr. Excitation exhibits a peak near the center of the discharge in the low-pressure, diffusion-dominated "regime," but reaches a maximum closer to the antenna at higher pressures. This reproduces the qualitative features seen in the optical emission measurements.

ARGON METASTABLES

Argon metastables potentially play an important role in plasma production and plasma uniformity in argon ICP discharges. Spatial profiles of ionization rate may be quite different depending on whether ionization is dominated by single-step or two-step processes. Since metastables are long-lived and not confined electrostatically, they may diffuse throughout the volume, even if they are produced locally. In addition, their ionization energy is significantly lower than that for ground state argon, so that ionization is possible in regions where energetic electrons are absent. Therefore, depending on the concentration of argon metastables, they may have an impact on plasma uniformity.

To address this question, measurements of argon metastable concentrations have been compared with predictions of the model described above, and we conclude that under some conditions, metastable concentrations are high enough to have an effect.

Argon metastable concentrations were measured in the same system as the optical emission measurements described previously. Optical absorption spectroscopy in the visible range of the electromagnetic spectrum was used to measure line densities of Ar metastables. When a plasma is probed in transmission by the light from a broadband light source (in this case, a xenon arclamp), traversal of the discharge introduces absorption features into the otherwise smooth arclamp spectrum. The result is a modified arclamp spectrum where intensity is reduced only at certain wavelengths, characteristic of the absorber species. Each peak in the absorption spectrum reflects the absorption of photons by individual atoms at a wavelength corresponding to the energy of an allowed electronic transition for that atom. In this mode, the signal reaching the detector is a superposition of the arclamp intensity distribution along with the emission spectrum of the plasma itself. Although in the optical emission experiments the plasma line emission was the desired signal, in absorption spectroscopy this portion must be subtracted out to isolate the absorption features. The subtraction is accomplished by placing a mechanical chopper wheel in front of the xenon arclamp to selectively block the arclamp signal at periodic intervals. By gating the detector appropriately, signals

can be recorded with and with out the arclamp, and subtracted. An absorption spectrum is obtained by subsequently subtracting the spectrum of the lamp in the absence of plasma.

The height of each spectral peak is a direct function of the concentration of the absorbing species, and can be used to infer its line density, integrated along the path of the beam. The absorption coefficient is determined from the reduction in spectral intensity $I(\nu)$, as described (for a homogeneous medium) by:

$$I(\nu) = I_0(\nu) \exp\left[-\gamma(\nu)L\right],$$

where ν is optical frequency and L is the path length. In turn, the absorber volume concentration is directly related to the absorption coefficient, according to

$$\gamma(\nu) = \frac{h\nu_0}{c} B_{ik} N f_i \left(1 - \frac{g_i N_k}{g_k N_i}\right) G(\nu).$$

In this expression, N is the volume density of a particular species (in this case argon atoms) and f_i is the fraction in the absorbing state i (such as a particular metastable level). The values g_i and g_k are the statistical weights for the lower and upper states of the transition, respectively, and B_{ik} is the Einstein coefficient for the transition, with an associated centerline frequency, ν_0 (in Hz). Einstein coefficients for the transitions investigated here were obtained from Wiese *et al.*[15]. Finally, $G(\nu)$ is the normalized lineshape function characterizing the spread of the absorption feature about the centerline frequency.

Optical absorption spectroscopy is applied here to determine argon metastable concentrations in an ICP discharge for pressures ranging from 5 mTorr to 50 mTorr and discharge powers from 50 to 400 watts.

System Description

The optical absorption system makes use of a xenon arc lamp as a light source[16, 17, 18]. A block diagram of the optical system is shown in Figure 5. The absorption spectrum is imaged on a multichannel detector (EG&G Park Model 1812 photodiode array) at the output of the 0.5 m Jarell Ash spectrometer (Model 82020), configured with an Echelle grating with a blaze angle of 63 degrees.

The area under the curve of an absorption feature determined from the absorption spectrum is referred to as the equivalent width of the feature, W_ν (Hz), and is a function of the absolute concentration of the absorbing species. The exact functional relationship between the equivalent width and the absorption coefficient is called the curve-of-growth:

$$W_\nu = \int_{-\infty}^{+\infty} \left[1 - \exp\left\{-\int_0^L \gamma(\nu)dx\right\} d\nu\right]$$

Results

The concentration of each of the four sublevels in the argon 4s manifold were measured as a function of pressure and discharge power. The argon flow rate was held constant at 12.5 sccm for all experiments. Experiments were conducted at 50,100,150, 200, 300 and 400 watts of rf net forward power, measured with a Bird Electronics Model 43 inline watt meter located between the rf supply and matching network. Thus, these power levels include power dissipated in the matching network and antenna, and are greater than the power delivered to the plasma. Argon pressures examined were 5,

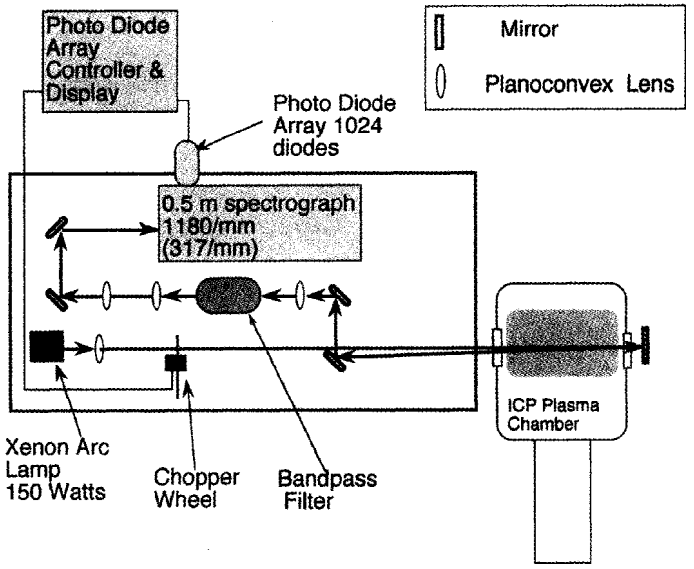

Figure 5. Two-pass xenon arc lamp based optical absorption spectroscopy system for measurement of argon metastable concentrations.

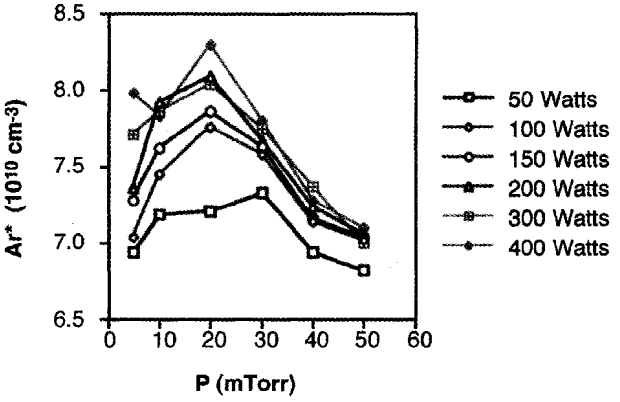

Figure 6. Pressure dependence of argon metastable concentration for various power levels. Concentrations represent a sum of measured contributions of the $1s_2$, $1s_3$, $1s_4$ and $1s_5$ levels.

10, 20, 30, 40 and 50 mTorr. Results are shown in Figure 6. The concentrations plotted are discharge averages calculated from the measured line densities by dividing by the path length of the beam through the plasma. Spatial variation in the metastable concentration is expected due to diffusion and loss at the walls. Thus peak densities near the chamber center are expected to be somewhat higher than the average values reported here.

The steady-state concentration of metastables results when creation and loss rates exactly balance. As pressure is increased, changes in electron density and temperature are likely to affect the metastable concentration in opposite ways. The production rate of metastables is proportional to the electron density, which increases with pressure, but

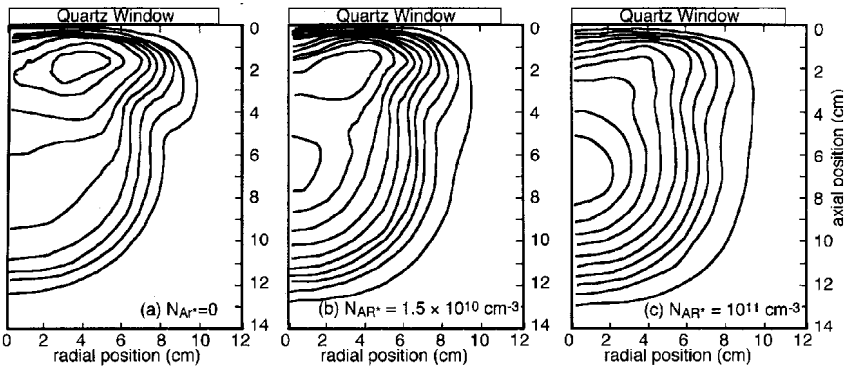

Figure 7. Effect of metastables on excitation rate spatial profiles, for 200 watts rf power and 50 mTorr argon pressure. Profiles were calculated for a uniform metastable concentration of (a) 0 cm^{-3}, (b) 1.5×10^{10} cm^{-3} and (c) 10^{11} cm^{-3}.

also decreases as the electron temperature decreases with increasing pressure. Although a detailed accounting of all the reactions contributing to creation and loss of metastables is nontrivial (see, for example, Kannari *et al.*[19]), these two factors may be sufficient to provide a qualitative explanation for the pressure dependence observed. Namely, at low pressures, the rise in metastable production with increasing pressure outweighs the-decrease associated with the reduction in electron temperature. However, at higher pressure, decreased production due to decreasing electron temperature wins out, and metastable concentration decreases.

Simulation - Effect of Metastables on Excitation Rate

The model described above was used to evaluate whether the measured metastable levels are sufficient to have a significant effect on excitation and ionization rate spatial profiles. An *ad hoc* approach was used to get a qualitative estimate of the effect of metastables. A uniform metastable population of specified concentration was superimposed on the system, and the simulation was run to equilibrium with the inclusion of excitation and ionization of metastables. Spatial maps of excitation rate obtained in the simulation are shown in Figure 7.

The range of metastable concentrations imposed on the simulation was chosen to approximately match those observed experimentally. The simulation results suggest that the observed metastable concentrations, on the order of 10^{10} to 10^{11} cm^{-3}, are sufficient to have a significant effect on discharge spatial structure.

AZIMUTHAL STRIATIONS

Azimuthal striations in planar rf inductively coupled plasmas are another phenomenon that may shed light on the electron kinetics in these discharges[20]. Specifically, we have observed strong azimuthal variation in the visible optical emission from a planar rf inductively coupled plasma, corresponding to azimuthal modulation in neutral excitation due to electron impact collisions. Observations were made in an argon discharge generated with a single-turn loop antenna in a cylindrical volume with a relatively high aspect ratio. A comparison to positive column striations in a dc glow

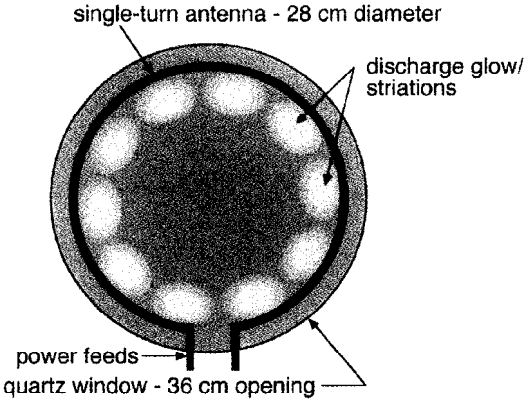

Figure 8. Geometry of plasma volume and discharge structure when striations are present.

discharges shows some similarities, although a complete explanation will require consideration of rf effects.

The argon plasma observed in this study was confined to a cylindrical volume 36 cm in diameter by 2.5 cm high, inside a much larger vacuum chamber. The volume is bounded at one end by a quartz vacuum window and at the other by an aluminum plate with a 1 cm wide radial slot for diagnostic access. The radial boundary is defined by a cylindrical tube made of perforated aluminum sheet. The antenna used for inductive power coupling to the plasma is a 28 cm diameter single-turn circular loop that rests on the quartz window. The antenna was driven at 13.56 MHz at 85 mTorr argon pressure and power of 300 watts measured with a Bird wattmeter between the power supply and matching network.

Azimuthal structure was observed visually through the quartz window separating the induction antenna from the plasma, with a line of sight almost parallel to the system axis. A gap of several centimeters is present in the circular antenna at the location of the connection point for the external leads. The discharge glow was always restricted to a ring-shaped region with radius slightly smaller than that of the antenna, and with a large dark region in the center. Ten striations around the ring were observed, with an approximate spatial period of 7.5 cm, as illustrated in Figure 8. The striations were stationary for as long as minutes at a time, but were also observed to move at random intervals, and completely faded away after 20-30 minutes of continuous discharge operation, suggesting that heating of the chamber walls by the discharge, and the associated outgassing of contaminants, may have an important impact on the striations.

Electrostatic trapping of electrons both axially and radially in this discharge is likely to contribute to formation of azimuthal striations. The electron density, n_e, at and in the vicinity of the discharge axis has been found to be negligible [20, 21], and both n_e and the plasma potential have peak values off-axis glowing ring. Thus, electrons are confined in the region of strong azimuthal rf electric field and their motion is channeled electrostatically into the azimuthal direction. Striations were not observed in lower aspect ratio systems, in which the plasma potential typically has a maximum on the discharge axis. Electron collisions are also likely play a role the formation of striations, as striations were not observed at pressures less than 30 mTorr, below which inelastic mean free paths become significant compared to the system length and striation spatial period.

Although striations in planar rf ICP discharges are not yet well understood, striations have been studied extensively in other types of discharges in a pressure range that includes the pressure of the case reported here[22, 23]. These include axial striations in the positives columns and azimuthal striations in the anode glow (anode spots) of dc glow discharges. Although both the anode spots observed in dc glow discharges and the ICP striations show structure in the azimuthal direction, the mechanisms are probably quite different. The cause of the ICP striations is more likely to be similar to that of striations observed in positive columns of glow discharges. In the case of the positive column, striations are the result of ionization waves, with feedback between axial modulations in plasma density, axial dc electric field, electron energy distribution function and ionization rate. The spatial period of the striation in the positive column corresponds approximately to the distance λ^* in the dc electric field electrons must accelerate to acquire kinetic energy equal to the excitation energy. Striations occur when $\lambda^* \gg \lambda_\epsilon$, the energy relaxation length for electrons in the inelastic energy range, so that once an electron has reached the excitation threshold energy it travels a relatively short distance before giving it up in an inelastic collision.

There are both similarities and differences between the conditions under which striations are observed in the ICP system and the glow discharge positive column. Field magnitudes in ICP discharges under similar conditions have been found to have peak values of 4 to 5 V/cm, so the requirement that $\lambda^* \gg \lambda_\epsilon$ is satisfied. However, the temporal oscillation of the ICP induction fields at the rf frequency suggest a significant departure from the positive column. In electric fields of this magnitude, electrons cannot accelerate to the inelastic threshold energy in a single rf cycle. Thus, while the observed ICP striations are likely to arise from ionization waves as in the positive column, there are differences in the mechanism associated with the time oscillation of the rf ICP fields. We therefore conclude that positive column theory, while possibly providing a partial explanation, does not provide a complete description of ICP striations.

ACKNOWLEDGEMENTS

This work supported in part by NSF Grant #EEC8721545

REFERENCES

1. J. B. Carter, J. P. Holland, E. Peltzer, B. Richardson, E. Bogle, H. T. Nguyen, Y. Melaku, D. Gates, and M. Ben-Dor. Transformer coupled plasma etch technology for the fabrication of subhalf micron structures. *J. Vac. Sci. Technol. A,* 11:1301, 1993.
2. J. Hopwood. Review of inductively coupled plasmas for plasma processing. *Plasma Sources Sci. Technol.,* 1:109, 1992.
3. R. A. Stewart, P. Vitello, D. B. Graves, E. F. Jaeger, and L. A. Berry. Plasma uniformity in high-density inductively coupled plasma tools. *Plasma Sources Sci. Technol.,* 4:36, 1995.
4. P. L. G. Ventzek, R. J. Hoekstra, and M. J. Kushner. 2-dimensional modeling of high plasma-density inductively-coupled sources for materials processing. *J. Vac. Sci. Technol. B,* 12:461, 1994.
5. L. J. Mahoney, A. E. Wendt, E. Barrios, C. J. Richards, and J. L. Shohet. Langmuir probe characterization of planar inductive radio frequency plasma sources for materials processing. *J. Appl. Phys.,* 76:2041, 1994.
6. V. I. Kolobov, D. F. Beale, L. J. Mahoney, and A. E. Wendt. Non-local electron kinetics in an inductively coupled radio frequency discharge. *Appl. Phys. Lett.,* 65:537, 1994.
7. I. B. Bernstein and T. Holstein. Electron energy distributions in stationary discharges. *Phys. Rev.,* 94: 1475, 1954.

8. I. D. Kaganovich and L. D. Tsendin. The space-time-averaging procedure and modeling of the rf discharge, part II:model of collisional low pressure rf discharge. *IEEE Trans. on Plasma Science,* 20:66, 1992.
9. I. D. Kaganovich and L. D. Tsendin. Low pressure rf discharge in the free-flight regime. *IEEE Trans. on Plasma Science,* 20:86, 1992.
10. U. Kortshagen, I. Pukropski, and L. D. Tsendin. Experimental investigation and fast 2-dimensional self-consistent kinetic modeling of a low-pressure inductively-coupled rf discharge. *Phys. Rev. E,* 51:6063, 1995.
11. K. Kramer and W. N. G. Hitchon. A highly flexible tool for large scale computational problems in applied physics. *Computer Phys. Comm.,* 85:167, 1995.
12. B. E. Cherrington. *Gaseous Electronics and Gas Lasers.* Pergamon, New York, 1979.
13. A. Fiala, L. Pitchford, and J. P. Boeuf. Two-dimensional, hybrid model of low-pressure glow discharges. *Phys. Rev. E,* 49:5607, 1994.
14. D. L. Scharfetter and H. K. Gummel. Large-signal analysis of a silicon read diode oscillator. *IEEE Trans. Electron Devices,* ED-16:64, 1969.
15. W. L. Wiese, J. W. Brault, K. Danzmann, V. Helbig, and M. Kock. Unified set of atomic transition probablilities for neutral argon. *Phys. Rev. A,* 39:2461, 1989.
16. R. C. Wamsley, K. Mitsuhashi, and J. E. Lawler. High-sensitivity absorption-spectroscopy in glow discharge plasmas. *Rev. Sci. Instrum.,* 64:45, 1993.
17. R. G. Wamsley, J. E. Lawler, J. H. Ingold, L. Bigio, and V. D. Roberts. Absorption spectroscopy on Hg^+ and excited Hg in Hg-Ar discharges. *Appl. Phys. Lett.,* 57:2614, 1990.
18. R. C. Wamsley, K. Mitsuhashi, and J. E. Lawler. Ionization balance in the negative glow of a Hg-Ar hot-cathode discharge. *Phys. Rev. E,* 47:3540, 1993.
19. F. Kannari, M. Obara, and T. Fujioka. An advanced kinetic model of electron-beam-excited KrF lasers including the vibrational relaxation in KrF*(B) and collisional mixing of KrF*(B,C). *J. Appl. Phys.,* 57:4309, 1985.
20. J. A. Stittsworth and A. E. Wendt. Striations in a radio frequency planar inductively coupled plasma. *IEEE Trans. on Plasma Science,* 24:125, 1996.
21. J. A. Stittsworth and A. E. Wendt. Effect of chamber geometry on plasma uniformity in a planar inductively coupled rf argon discharge. *Plasma Sources Sci. Technol.,* 5:429, 1996.
22. V. I. Kolobov and V. A. Godyak. Non-local electron kinetics in collisional gas discharge plasmas,. *IEEE Trans. Plasma Sci.,* 23:503, 1995.
23. Yu. B. Golubovskii, V. I. Kolobov, and Sh. Kh. al Hawat. Anode region of low-current glow discharges at low and high pressures. *Sov. Phys. Tech. Phys.,* 35:747, 1990.

EXPERIMENTAL STUDIES OF RF SHEATHS

W.G. Graham and C.M.O. Mahony

The Department of Pure and Applied Physics
The Queen's University of Belfast
Belfast BT7 1NN
Northern Ireland

INTRODUCTION

The sheath is of paramount importance in rf-driven plasmas. It is critical to the fundamental nature of the plasma in acting as a conduit for energy input to the plasma, determining energy and particle flux to and from surfaces and thus controlling plasma-surface interactions. In rf-driven plasmas the electrode sheaths are dynamic, responding to the time-varying electrode voltage. In a simple model of a capacitive discharge, while the electric field strength may change, it is considered to always point away from the plasma and at all times to decrease in strength monotonically with distance from the driven electrode.

Electrons in the sheath are accelerated towards the plasma in these electric fields and subsequently reach energies sufficiently high to excite gas atoms and so produce regions of bright emission generally associated with the sheath edge. Therefore excitation studies, derived from optical emission measurements, can provide information about electric fields and sheath dynamics. There have been many reports of time-resolved emission measurements for 13.56 MHz driven plasmas, some for the gases used here [1-13].

The electrode and plasma potentials have both dc and ac components. As will be discussed later these can be measured by appropriate electrostatic probe and voltage monitoring techniques so that the time dependent behaviour of the electrode potential relative to the plasma can be determined. Here rf driving voltage and the plasma potential measurements have been correlated with spatially and temporally resolved emission measurements to provide an additional insight into the sheath dynamics of a 13.56 MHz asymmetric capacitively driven plasma. In particular the sheath behaviour with different operating gases, namely H_2, D_2, He and Ar has been contrasted and compared.

EXPERIMENTAL DETAILS

The present measurements were made in the UK GEC (Gaseous Electronics Conference) rf reference reactor [14]. This is a parallel plate device with two 102 mm diameter electrodes separated by 25.4 mm. The upper, aluminium electrode and the stainless steel vacuum vessel were grounded. The plasma was created by capacitively coupling rf voltages at 13.56 MHz,

Electron Kinetics and Application of Glow Discharges
Edited by U. Kortshagen and L. D. Tsendin, Plenum Press, New York, 1998

Table 1. Wavelengths, transitions and radiative lifetimes of the atomic states observed. Also shown is the central wavelength and the FWHM bandwidth of the filters used.

	H_2, D_2	He	Ar
Wavelength (nm)	656	587	750
Transition	3p-2s	2p-3d	4s-4p
Lifetime (ns)	7.6	14.1	21.5
Filter (nm)	657±11	587±7	750±20

to the lower, stainless steel electrode. In the present measurements peak-to-peak rf voltages of up to 700 V were applied producing plasma input powers of up to 120 W and discharge currents of up to 3 A. The operating pressures, ranging from 6.7 to 133 Pa (50 to 1000 mTorr), were measured using a capacitance manometer.

At any time during the rf cycle the electrode potential relative to the plasma is given by

$$V_{\mathrm{Ep}}(t) = V_{\mathrm{Edc}} + V_{\mathrm{Erf}} - V_{\mathrm{pdc}} - V_{\mathrm{prf}} \tag{1}$$

The terms and how each was measured are discussed below.

The power input to the plasma was measured as specified for GEC reactor reference conditions [14]. Time resolved plasma currents and electrode voltages (V_{Erf}) were recorded using standard derivative probes. A reference output from the rf matching unit was used to trigger and so synchronize all the time-resolved measurements. The dc component of the electrode potential (V_{Edc}), the dc bias, was recorded directly from the rf matching unit display. The ac component of the plasma potential (V_{prf}) was measured using a capacitive probe technique [13,15,16]. A standard passively compensated Langmuir probe technique was used to measure the time-averaged plasma potential (V_{pdc}) and other time-averaged plasma parameters. The measured time-averaged electron energy distribution functions (eedf) are complex, depend on the gas pressure and input power and are generally not described by a single Maxwellian. The mean energy of the electrons derived from the measured eedfs varies from 0.1 to 10 eV.

Over the present operating conditions the measured electron densities varied ranged from 1×10^9 to $5 \times 10^{10}\,\mathrm{cm}^{-3}$, the electron plasma frequencies calculated from these density measurements varied from 300 MHz to 2 GHz. The ion plasma frequencies, calculated from the electron density range for each gas, varied in Ar from 1 to 7 MHz and in H_2 (assuming the dominant ion is H_3^+) from 7 to 17 MHz. Thus the assumption that the ions do not respond to the rf driving frequency, while valid in the present Ar, He and D_2 plasmas may not be valid under all conditions in H_2. The temporal behaviour of fast electrons, i.e. those with sufficient energy to excite the gas atoms to the electronic state from which emission is observed (see Table 1), was determined from time and space resolved emission spectroscopy. The emission intensity depends on electron and gas atom densities, their energy distributions and excitation cross sections. Assuming the gas density is spatially and temporally uniform then emission is indicative of the fast (typically greater than at least 10 eV) electron behaviour.

Measurements were made using an Oriel Instruments Instaspec V (ICCD) with a spatial resolution of about 1 mm and time resolution < 2 ns. A 30 mm wide vertical section through the centre of the plasma was imaged onto the front plane of the ICCD. The optical arrangement produced a depth of field of 18 mm. Filters selected the appropriate emission lines (Table 1).

The time variation of the light emission intensity $I(t)$ was measured, generally over two rf cycles at 2 ns intervals. It is the time dependence of the optical excitation $E(t)$ which

reflects the time-dependent behaviour of the electrons. This was found from the measured emission signal $I(t)$ by deconvolution with the effective lifetime τ_{eff} of the observed states

$$E(t) = I(t) + \tau_{\text{eff}} \frac{dI(t)}{dt} \qquad \tau_{\text{eff}} = \frac{\tau}{1 + \tau k_q N} \tag{2}$$

where τ is the radiative lifetime of the excited state (Table 1), k_q the collisional quenching rate constant and N the neutral gas number density. In the present analysis quenching effects were ignored. We believe this analysis to result in an uncertainty of less than 1 ns [13].

RESULTS AND DISCUSSION

The space and time resolved excitation data for Balmer-alpha excitation shown in Fig. 1 are typical of those for hydrogen. Results in D_2 are similar. Figs. 2 and 3 show typical excitation results for Ar and He. The most obvious difference in the excitation data from the three gases is the close-to-electrode excitation observed in H_2 . Such regions of excitation have previously been reported in H_2 and H_2-containing gas mixtures [6,7,10,12,13,17-19]. The double emission structure is observed through all the present operating conditions in pure hydrogen and quantitatively identical structure is observed when operating with deuterium.

As has been discussed in more detail previously [13], the near electrode excitation can be seen to occur when the electrode is at its least negative with respect to the plasma. In fact the present measurements (Fig. 1) show that, in contrast to He and Ar, in H_2 the electrode goes positive with respect to the plasma. This observation supports the proposal that the near electrode emission in H_2 is associated with electric field reversal for a portion of the rf cycle [10], i.e. there is a period during the rf cycle when electrons are accelerated towards the electrode, causing excitation of, and so emission from, gas atoms near the electrode.

All the gases exhibit a region of excitation at a greater distance from the driven electrode than the close-to-electrode emission in H_2 (Figs. l-3). This is often referred to as the bulk emission. The location of the excitation maximum is different for each gas (Figs. l-3). However for all gases at the same input power the distance of the maximum from the driven electrode is found to vary with pressure (P) as $P^{-0.5\pm0.1}$. The dependence on input power at constant pressure is much less pronounced.

The bulk excitation maximum occurs as the electrode voltage becomes increasingly negative with respect to the plasma. At constant power the phase at which the excitation occurs remains relatively constant for H_2 and He. In Ar the excitation occurs later and the phase at which it occurs changes with pressure. At the excitation maximum the electrode-plasma potential difference is always greater than 150 V. However there appears to be no simple relationship between the two.

In Ar there is some preliminary evidence for a discontinuity in the excitation behaviour between 100 and 250 mTorr, where the measured eedfs indicate the transition from a stochastic to ohmic heating mechanism occurs [20]. Presently there is insufficient data in H_2 and He to confirm this.

CONCLUSIONS

The correlation between the temporal variation in plasma excitation and electrode and plasma potential measurements through the rf driving voltage period have been investigated. The near electrode emission observed here and by others in capacitively coupled 13.56 MHz driven H_2 plasmas is correlated with sheath field reversal. The distance of the bulk excitation maximum from the electrode is found to vary systematically with pressure for all gases. The

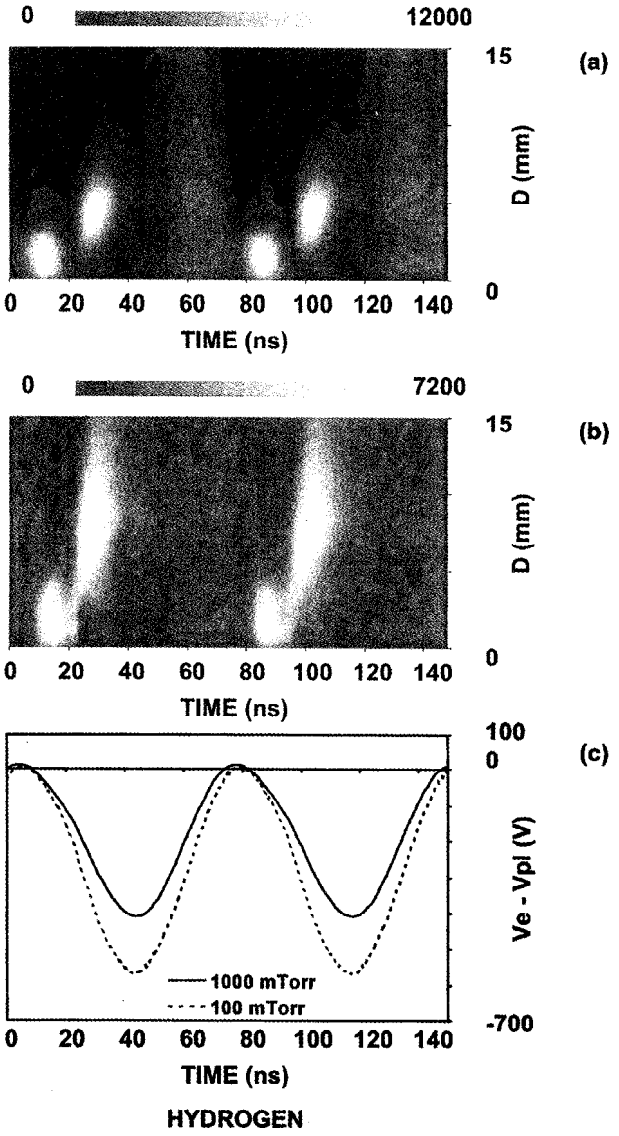

Figure 1. (a) and (b) spatially and temporally resolved Balmer alpha (653.3 nm) excitation from a hydrogen plasma operating with a forward directed rf power of 30 W and gas pressures of 250 and 1000 mTorr respectively. (Note that the full electrode spacing is 25 mm.) (c) The temporal dependence of the driven electrode potential relative to the plasma, calculated from $V_{Ep}(t) = V_{Eg}(t) - V_p(t)$ under the same conditions. (See text.)

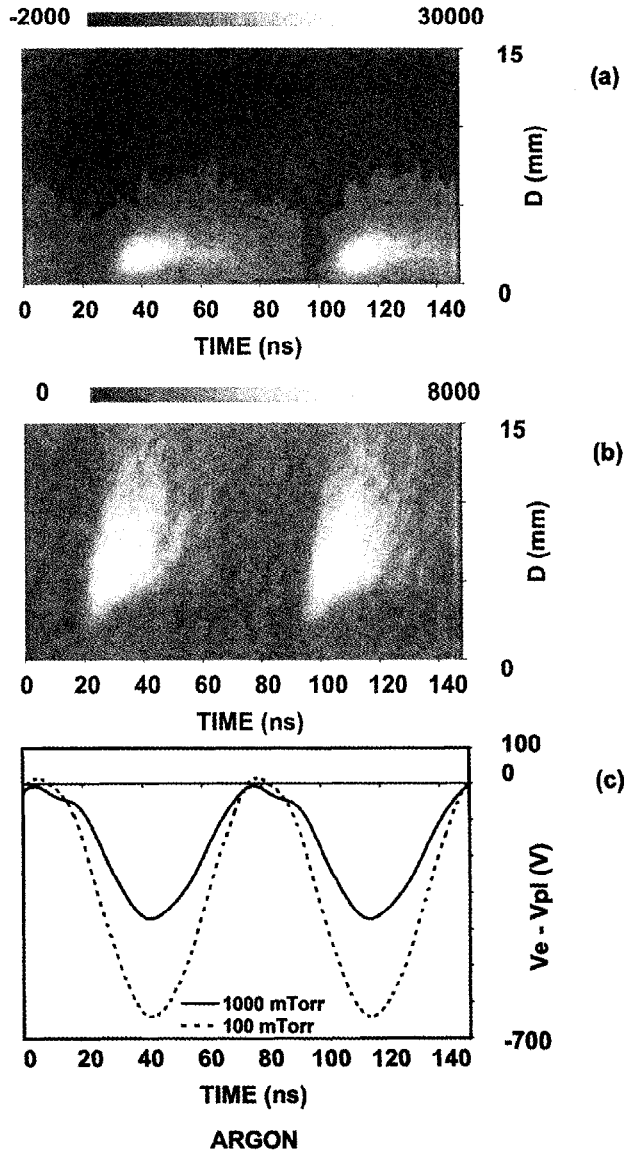

Figure 2. (a) and (b) spatially and temporally resolved 750.4 nm excitation from an argon plasma operating with a forward directed rf power of 30 W and gas pressures of 100 and 1000 mTorr respectively. (Note that the full electrode spacing is 25 mm.) (c) The temporal dependence of the driven electrode potential relative to the plasma, calculated from $V_{Ep}(t) = V_{Eg}(t) - V_p(t)$ under the same conditions. (See text.)

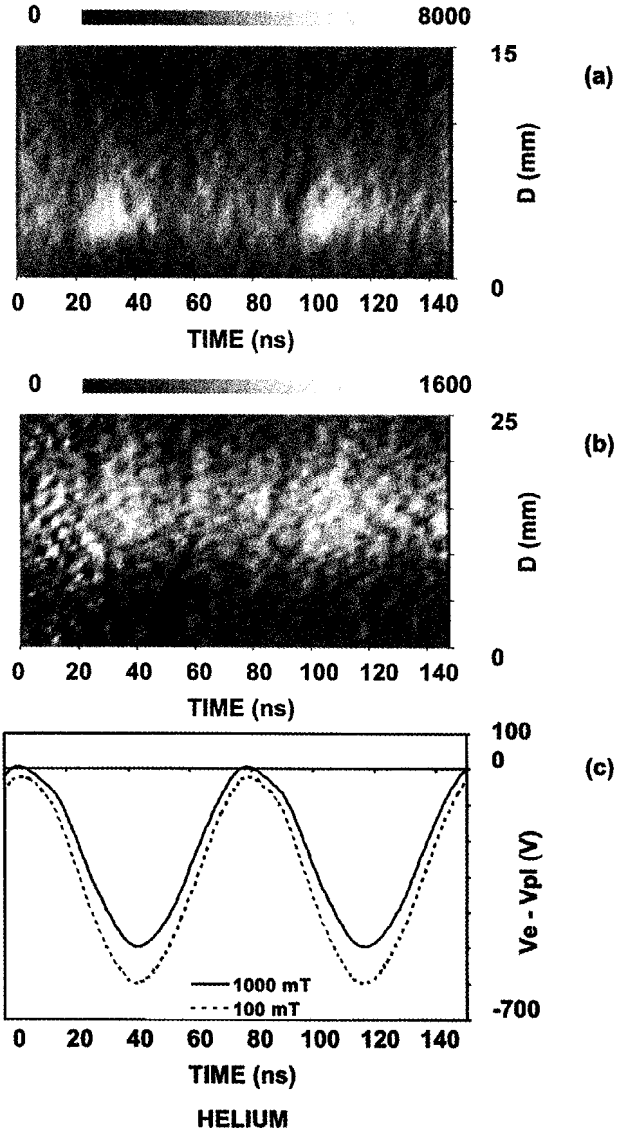

Figure 3. (a) and (b) spatially and temporally resolved 587 nm excitation from an helium plasma operating with a forward directed rf power of 30 W and gas pressures of 100 and 1000 mTorr respectively. (Note that the full electrode spacing is 25 mm.) (c) The temporal dependence of the driven electrode potential relative to the plasma, calculated from $V_{Ep}(t) = V_{Eg}(t) - V_p(t)$ under the same conditions. (See text.)

dependence on input power at constant pressure is much less pronounced. The bulk excitation occurs as the electrode voltage relative to the plasma becomes increasingly negative. In Ar there is some preliminary evidence for a discontinuity in excitation behaviour where the measured eedfs indicate the transition in heating mechanism occurs.

Acknowledgements

The authors wish to acknowledge the assistance of Caith McGrath and Declan McSherry and Jill McFarland in obtaining the capacitive probe and Langmuir probe data respectively. This work is supported by the Engineering and Physical Sciences Research Council.

REFERENCES

1. R. M. Barnes and R. J. Winslow, Spatial and temporal emission spectroscopy of a radio-frequency capacitively coupled low pressure oxygen plasma. *J. Phys. Chem.* 82: 1869, 1978.
2. G. de Rosny, E. R. Mosburg, J. R. Abelson, G. Devaud and R. C. Kerns, Evidence for a time dependent excitation process in silane radio frequency glow discharges. *J. Appl. Phys.* 54:2272, 1983.
3. V. M. Donnelly, D.L. Flamm and R.H. Bruce, Effects of frequency on optical-emission, electrical, ion and etching characteristics of a radio- frequency chlorine plasma. *J. Appl. Phys.* 58:2135, 1985.
4. P. Bletzinger and C. A. De Joseph Jnr,Structure of rf parallel-plate discharges, *IEEE Trans. Plasma Sci.* PS-14:124, 1986.
5. D. L. Flamm and V. M. Donnelly, Time-dependent excitation in high- and low- frequency chlorine plasmas. *J. Appl. Phys.* 59: 1052, 1986.
6. F. Tochikubo, A. Suzuki, S. Kakuta, Y. Terazono and T. Makabe, Study of the structure of rf glow discharges in SiH_4/H_2 by spatiotemporal optical emission spectroscopy: influence of negative ions. *J. Appl. Phys.* 68:5532, 1990.
7. F.Tochikubo, T. Kokubo, S. Kakuta, A. Suzuki and T. Makabe, Investigation of the high-frequency glow discharge in Ar at 13.56 MHz by spatiotemporal optical emission spectroscopy., *J. Phys. D* 23: 1184, 1990.
8. W. E. Koehler, R. J. Seeboeck and F. Rebentrost, Time resolved study of the bulk plasma of a 13.56 MHz discharge in argon. *J. Phys. D* 24:252, 1991.
9. M. Shimozuma, G. Tochitani and H. Tagashira, Optical emission diagnostics of H_2+CH_4 50 Hz-13.56 MHz plasmas for chemical vapor deposition. *J.Appl. Phys.* 70:645, 1991.
10. F. Tochikubo, T. Makabe, S. Kakuta and A. Suzuki, Study of the structure of radio frequency glow discharges in CH_4 and H_2 by spatiotemporal optical emission spectroscopy. *J. Appl. Phys.* 71:2143, 1992.
11. S. Djurovic, J. R. Roberts, M. A. Sobolewski and J. K. Olthoff, Absolute spatially- and temporally - resolved optical emission measurements in rf glow discharges in argon. *J. Res. Natl. Inst. Stand. Technol.* 98:159, 1993.
12. O. Leroy, P. Stratil, J. Perrin, J. Jolly and P. Belenguer, Spatiotemporal analysis of the double layer formation in hydrogen radio frequency discharges. *J. Phys. D* 28:500, 1995.
13. C. M. O. Mahony, R. Al Wazzan and W. G. Graham, Sheath dynamics observed in a 13.56 MHz-driven plasma. *Appl. Phys. Lett.* (to be published).
14. P. J. Hargis Jr. , K.E. Greenberg, P.A. Miller, J.B. Gerardo, J.R. Torczymski, M.E. Roley, G.A. Hebner, J.R. Roberts, J.K. Olthoff, J. R. Whetstone, R.J. Van Brunt, M.M. Sobolewski, H.M. Anderson, M.P. Splichal, J.L. Mock, P. Bletzinger, A. Garscadden, R.A. Gottscho, G. Selwyn, M. Dalvie, J.E. Heidenreich, J. W. Butterbaugh, M.L. Brake, M. L. Passov, J. Pender, A. Lujan, M.E. Elta, D.B. Graves, H.H. Sawin, M.J. Kushner, J. T. Verdeyen, R. Horwath and T.R. Turner, The Gaseous Electronics Conference radio-frequency reference cell: A defined parallel-plate radio-frequency system for experimental and theoretical studies of plasma-processing discharges. *Rev. Sci. Instrum.* 65:140 1994.
15. S.E. Savas and G. Donohoe, Capacitive probes for rf process plasmas. *Rev. Sci. Instrum.* 60:3391, 1989.
16. E.Y. Wang, D. Diebold, P.Nonn, J. Pew, W.Q. Li, P. Probert, R. Breun, R. Majeski, S.L. Wan, and N. Hershkowitz., An improved capacitive divider probe for plasma potential measurements in the Phaedrus tokamak. *Rev. Sci. Instrum.* 62:1494, 1991.
17. N. Mutsukara, K. Koyabashi and Y. Machi, Monitoring of a radio- frequency glow-discharge plasma. *J. Appl. Phys.* 66: 468, 1989.

18. S. Kakuta, T. Kitajima, Y. Okabe and T. Makabe, Experimental study of very- high-frequency plasmas in H_2 by spatiotemporally resolved optical emission spectroscopy. *Jpn. J. Appl. Phys.* 33: 4335, 1994.
19. S.B. Radovanov, K. Dzierzega, J.R. Roberts and J.K. Olthoff, Time - resolved Balmer-alpha emission from fast hydrogen atoms in low pressure, radio-frequency discharges in hydrogen. *Appl. Phys. Lett.* 66: 2637, 1995.
20. V.A. Godyak and R.B. Piejak, Abnormally low electron energy and heating-mode transition in a low-pressure argon rf discharge at 13.56 MHz. *Phys. Rev. Lett.* 65:996, 1990.

TIME RESOLVED MEASUREMENTS OF PULSED DISCHARGES: THE ROLE OF METASTABLE ATOMS IN THE AFTERGLOW.

Lawrence J. Overzet and Jennifer Kleber

Plasma Applications Laboratory
The University of Texas at Dallas
P. O. Box 830688, EC33,
Richardson, TX 75083-0688

ABSTRACT

The electron and ion densities, electron temperatures, and electron energy probability functions (EEPF) of modulated-power glow discharges through argon and helium in the Gaseous Electronics Conference reference reactor have been measured using an RF compensated Langmuir probe and microwave interferometer. RF power was capacitively coupled to the glow and square wave amplitude modulated with a 50% duty cycle and 100% modulation depth. The time resolution of the probe was approximately 10 μs and of the interferometer better than 1μs. We found that a metastable-metastable ionization reaction can produce hot electrons in the EEPF. In addition this reaction can cause the electron density to increase in the afterglow rather than decrease as one might first expect. By moving the Langmuir probe along the diameter of the chamber it was determined that the electron density decreases more quickly between the electrodes by diffusion. This gives rise to a plasma density in argon which becomes somewhat donut shaped during the afterglow and causes the glow to re-ignite from the edges into the center. The electron temperature at re-ignition in helium discharges can become larger than that at steady state in the active glow. It quickly relaxes to the steady state value. This effect is not nearly as pronounced in argon.

MOTIVATION AND BACKGROUND

Modulated power discharges (also called pulsed discharges) have exhibited advantages over continuous glows in a wide variety of circumstances. Researchers have found that the discharge chemistry can be altered,[1-4] the properties of deposited films can be altered,[5,6] the processing rate can be maintained despite the lower average power,[7-9] dust particle formation can be reduced[6,10] and trenching notching and charging damage can also be reduced.[11-14] At least some of these advantages are derived from how the plasma turns on and off.

Electron Kinetics and Application of Glow Discharges
Edited by U. Kortshagen and L. D. Tsendin, Plenum Press, New York, 1998

We wanted to examine the reasons why pulsed discharges could act so differently from their continuous glow counterparts and so we began to study how the glows ignite and decay in simple chemistries. We started by investigating noble gas discharges (since they exhibit as little chemistry as possible in a glow discharge) and measured: the electron density by both microwave interferometer and Langmuir probe, the floating potential, plasma potential, electron temperature, electron energy probability function, RF current, voltage, power and plasma impedance as well as the ion flux to a grounded electrode.

What we found is that metastable excited state atoms, "metastables," play an important role in the turn off of inert gas plasmas affecting both the electron density and the Electron Energy Probability Function (EEPF). We also found that diffusion effects in the Gaseous Electronics Conference (GEC) reference reactor are significant during the afterglow period. Diffusion effects cause the electron density to remain large outside the electrode edges for a longer time than inside the electrode radius because the effective diffusion length, Λ, is larger there. This can force the discharge to re-ignite at the electrode radial edges first. We will demonstrate that these effects can be modeled and understood using data from a time resolved Langmuir probe (LP) and microwave interferometer (MWI) in conjunction with one another and that the electrons produced from metastable-metastable ionization reactions could be found in the measured EEPF.

EXPERIMENTAL APPARATUS

The experiments were all performed in a Gaseous Electronics Conference (GEC) reference reactor.[15] Our reactor has 4" diameter steel electrodes, approximately a 12" chamber diameter and a 1" inter-electrode spacing. The upper electrode is the shower-head gas inlet and also acts as the driven electrode. RF power at 13.56 MHz is supplied by a Hewlett Packard 3314A function generator and ENI A300 power amplifier through a matching network. The output of the function generator was square wave amplitude modulated with a period of 2 ms, a 50% duty cycle and 100% modulation depth. The power amplifier (and matching network) can follow the amplitude modulated signal from the function generator reasonably well. It introduces a rise time to full power from zero of approximately 0.3 μs and from full power to zero of approximately 0.5 μs when connected to a precision 50 W load.[16] Our experience with this reactor indicates that both plasma initiation and decay require at the very least a two order of magnitude longer time than this. We shall define t = 0 to be the time when the function generator signal turns on and the plasma first begins to ignite; as a consequence, the RF power to the plasma is turned off and the afterglow period begins at t = 1000 μs.

The Langmuir probe system used to obtain these results has been described in detail elsewhere.[17] It is a single cylindrical probe made of either tungsten or platinum with a length of approximately 1 cm, and a radius of between 0.1 and 0.2 mm. The probe tip is forced to float with the RF fluctuations of the plasma potential by a second capacitively coupled electrode in close proximity because the probe to plasma impedance is much smaller than the probe to ground impedance at RF frequencies. (This electrode takes the form of a sleeve for our LP.) The LP is capable of a time resolution of approximately 10 μs (measured FWHM) and a spatial resolution of approximately the length of its tip. The LP electronics can be triggered to measure at certain times during the cycle of the square wave amplitude modulation by using a delay generator. In addition to the LP measurements, a microwave interferometer is used to measure the plasmas time-varying density.[18, 19] The MWI measures a volume-averaged electron density and its results generally agree with those of the LP near the glow center for

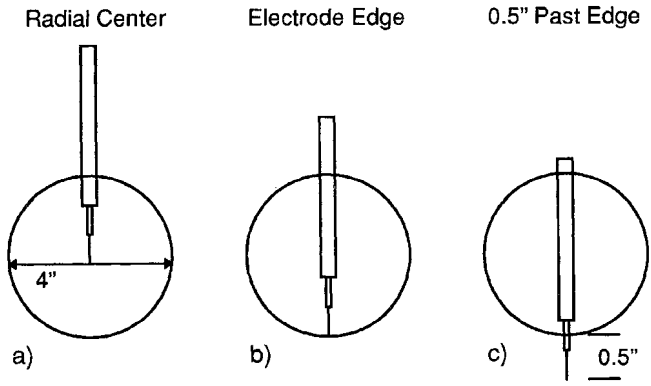

Figure 1. The definitions of various positions for the LP. The circle represents the electrode outer radius for the GEC reactor. The thin line represents the LP tip and is about 1 cm long. The glass body of the probe is the larger dimension rectangle and the smaller rectangle between the glass body and probe tip represents a metal sleeve used for passive RF compensation of the probe. (This is required by the RF fluctuations of the plasma potential.)

active discharges.[18] The MWI is noninvasive, but, it can not give us spatially resolved results.

Glow discharges in argon, helium or argon-helium mixtures at pressures between 100 and 500 mTorr and flow rates of approximately 20 to 30 sccm were generated in the GEC cell with RF voltages between 50 and 700 V zero to peak across the electrodes. The MWI was used to measure the time-varying electron density and the LP was used to measure the plasma potential (V_p), floating potential (V_f), electron density (n_e), ion density (n_p), and electron effective temperature (kT_e) at up to 48 points during the 2 ms cycle. The majority of the data points were concentrated early in the plasma turn-on and turn-off. It was difficult to measure plasma parameters with the LP at very early times in the plasma ignition and at very late times in the afterglow when the plasma density was very small. The dc bias voltage generated by the unequal electrode areas likely caused the plasma sheath to touch the LP in this instance causing the difficulty. The LP was also used to measure the EEPFs when the plasma was first ignited, at steady state in the active glow, and in the afterglow. While the LP was centered axially between the reactor electrodes, the measurements were repeated for five radial positions: at the electrode center, at the radial edges of the electrodes, and 0.5", 1.5", and 2" away from the edges of the electrodes. (See Fig. 1.) EEPFs were not obtained 2" away from the edges of the electrodes.

RESULTS AND DISCUSSION

The normalized electron densities of pulsed discharges in argon and helium as measured using the MWI are shown in Figs. 2 and 3. The electron densities were normalized to that during the RF on period in order to facilitate comparison. In addition, the helium results were obtained using a 10 ms pulsing period while the argon results had to be taken using a 50 ms period. Noting this difference in the time scales allows one to clearly see how much faster the helium processes are compared to those in argon. There are a couple of points to note. First, the electron density rise at plasma turn-on in helium is much faster than that in argon, reaching steady state within

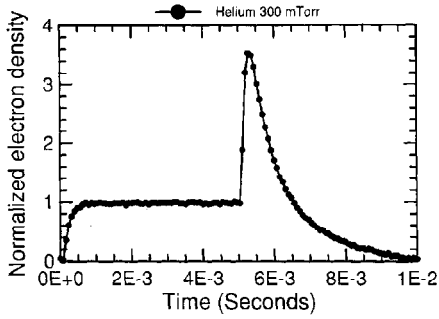

Figure 2. The normalized electron density in a helium discharge. The electron density rises rather than decreasing when the RF excitation is turned off at 5 ms. The electron density does decrease after first rising in the afterglow and is nearly zero by 10 ms.

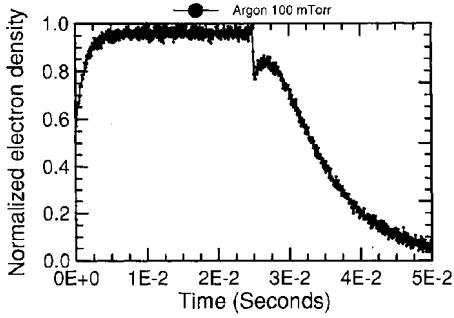

Figure 3. The normalized electron density in an argon discharge. When the RF excitation is turned off at 25 ms the electron density first decreases momentarily then rises rather than decreasing. The electron density does decrease to less than 10% of the on-time value by 50 ms.

0.7 ms, while the same rise requires nearly 7 ms in argon. Second, the electron density overshoot immediately following turn-off in helium is much larger than that for argon and occurs on a much shorter time scale. Finally, while the electron density in helium increases immediately at discharge turn-off, the argon glows electron concentration first decreases, then increases before finally decreasing to zero. The reasons for the electron density rise in the afterglow as well as the differences between argon and helium can be explained by comparing the results from a LP and MWI.

This is done for helium first and is plotted in Fig. 4. There is one item to note about Fig. 4 before making these comparisons. The time scale of the measurements has been changed to a 2 ms period from 10 ms. The LP collected data too slowly if the pulse period was 10 ms, so we used a 1 ms on-time and off-time. This causes the electron density to be non-zero at the end of the RF-off period.

In Figure 4, one can see three important differences as well as a few similarities

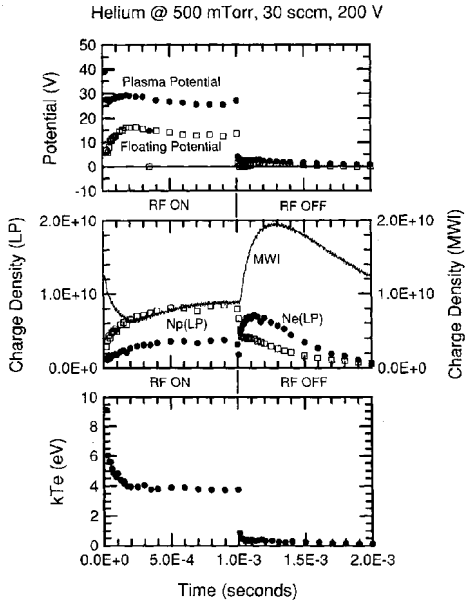

Figure 4. The plasma parameters measured by LP (plasma potential, floating potential, electron density (Ne(LP)), ion density (Np(LP)), and electron "temperature") and MWI (electron density (MWI)) as a function of time in a helium discharge at 500 mTorr, 30 sccm and 200 Volts RF amplitude. The LP was placed in the radial and axial centers of the glow.

between the electron and ion densities estimated using the LP and the MWI. For example, both the LP and the MWI indicate that the electron density increases at plasma turn-off (indicated as "RF-OFF" on the figure). On the other hand, the ion density estimated from the LP indicates a decrease at plasma turn-off. We believe that the ion density estimation is in error. The ion density should also rise in the afterglow because plasma neutrality has to be maintained and the ion density measurement is less reliable than the electron density measurement. There are two reasons why the ion density measurement is less reliable early in the afterglow. First, the electron temperature is changing rapidly during this period and causes the Debye length to be changing rapidly as well. This causes problems in estimating the ion density from the ion saturation current using Laframboise theory. Second, the floating and plasma potentials decrease rapidly as the electron temperature drops and can cause a transient current to flow between the RF compensation electrode and ground. This current is large enough to affect the ion saturation current measurement (because of its small magnitude) but is too small to seriously impact the electron saturation current. These effects make the ion density estimate less reliable and consequently it will not be discussed further.

There must be net ionization resulting from a source other than energetic electrons in the moments after the RF excitation is turned off since both the LP and MWI indicate that the electron density is increasing rather than decreasing (requiring net electron production) and the LP indicates that the electron temperature is decreasing extremely quickly during the same time. The only energy source that makes reasonable

sense is metastable excited state atoms.[20,21] Metastables have enough stored energy that an electron-ion pair can be produced when they collide and react. In addition, the resulting electron is ejected with a reasonably well defined kinetic energy. The electron will be produced with between 15 and 16.7 eV for a reaction between two helium metastables, between 7.3 and 7.9 eV for two argon metastables and between 4.1 and 4.9 eV if a helium metastable collides with an argon ground state atom. These reactions are written below.

$$\begin{aligned} 2He(M) &\Rightarrow He^{+} + He + e^{-}(15.05,\ 15.85,\ 16.65\ eV) \\ 2Ar(M) &\Rightarrow Ar^{+} + Ar + e^{-}(7.3 - 7.9eV) \\ Ar + He(M) &\Rightarrow Ar^{+} + He + e^{-}(4.06,\ 4.86\ eV) \end{aligned} \tag{1}$$

We should be able to find the signature of metastable reactions in the Electron Energy Probability Function (EEPF) during the afterglow period because these reactions produce well defined electron kinetic energies. This signature was found and is shown in Fig. 5. One can clearly see that the EEPF at the end of the RF-on period (1000 μs in Fig. 4) extends out to very large energies for helium and is reasonably Maxwellian in form. There is a significant deviation from Maxwellian near low energies that may be a result of the plasma sheath resistance, or the probe having missed the actual plasma potential by a few volts. The large numbers of high energy electrons during the active glow mask the electrons produced by metastable-metastable ionization reactions; however, the electron average energy has dropped dramatically within 20 μs of RF turn-off due to the light mass of helium atoms, and as a result, a peak around 15 eV becomes clearly visible in the EEPF. This peak has to be the result of two helium metastables colliding to produce an electron-ion pair and is gone by 200 μs into the afterglow (for the probe positioned between the electrodes.) One should note that there is no peak in the EEPF near 20 eV. Superelastic collisions between helium metastables and electrons could cause a peak around this energy, but, it should be more difficult to identify for two reasons. First, this peak in the EEPF is smoothed both by electron elastic collisions (after the superelastic collision) and by the low energy spread of the EEPF. The latter spreading occurs because the 20 eV energy in the metastable atom is added to the kinetic energy already possessed by the electron. As a consequence, the kinetic energy of the electron after a superelastic reaction is not as well defined as after a metastable-metastable ionization reaction. Second, it is probable that superelastic electrons would simply create another metastable atom in a second inelastic collision and thereby ”help” in metastable atom diffusion. Electrons produced in metastable ionization reactions (at 15 eV) can not do this. In any case, there is no evidence of superelastic collisions in the EEPF and as a consequence, we will ignore this process in our modeling to follow.

A second difference, that is evident in Fig. 4, is that the LP electron density is always smaller than that indicated by the MWI. The electron density results do not have to agree between the LP and MWI since the LP measurements are spatially resolved while the MWI measurements are spatially averaged. The LP results correspond to a small region around the probe tip, while the MWI gives results that are averaged over the length between the transmit and receive horns. This includes the region where the LP sits as well as the regions outside the electrodes, which we will call “ballast” regions since the volume there is quite large compared to the volume between the electrodes. In this case however, the discrepancy between the two techniques is partly because the pressure was 500 mTorr and causes the LP results to have problems with self shielding. (The ion mean free path and probe radius are becoming too close in magnitude.[18]) It

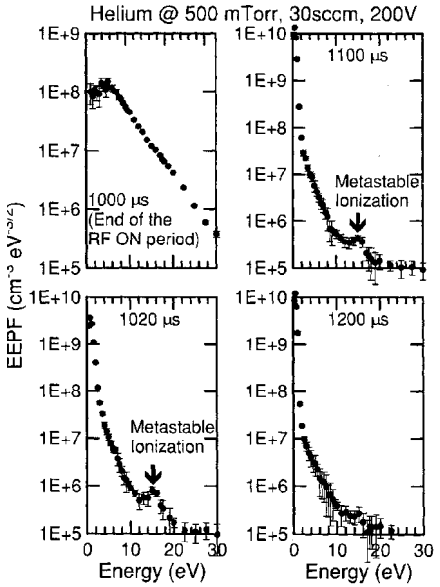

Figure 5. The Electron Energy Probability Functions (EEPF) measured using the LP in a helium discharge at 500 mTorr, 30 sccm and 200 Volts RF amplitude. The RF source is just about to be turned off at 1000 μs. The high energy electrons produced in metastable ionization reactions are clearly visible at 20 and 100 μs into the afterglow, but, are gone by 1200 μs (200 μs into the afterglow).

may also be due to some sheath resistance effects on the probe.[17] Finally, the MWI calibration is set for steady state plasmas in the GEC reactor, but changes in the electron density distribution of the afterglow could cause the MWI to overestimate the electron density.

The third difference between the LP and MWI measurements, evident in Fig. 4, is a matter of timing. The LP indicates that the electron density maximum occurs approximately 200 μs earlier in the afterglow than the MWI indicates. This is a significant difference between the two techniques because both have much better time resolution than 200 μs and the plasma parameters change slowly after the first 20 μs indicating that both techniques should be accurate. In particular, the electron temperature drops extremely quickly at the start of the afterglow, but kT_e has become small and nearly constant within a few tens of microseconds and the LP results should no longer be affected by its initial rapid decrease (and the rapid changes in the associated plasma and floating potentials.) The solution to this apparent discrepancy lies in the limitations of the two measurement techniques. The MWI is a spatially averaged technique, while the LP is spatially resolved. We will start with a simple model of the electron density time dependencies in order to make the importance of these limitations clearer.

The simplest differential equations for fitting the electron density in the afterglow using metastables as an ionization source and neglecting superelastic collisions (or more accurately assuming that superelastic collisions only contribute to metastable diffusion) are:

$$\frac{dn_e}{dt} = -D_a(T_e)\{\frac{n_e}{\Lambda^2}\} + \beta n_m^2 \qquad (2)$$

for the electron density as a function of time and

$$\frac{dn_m}{dt} = -D_m\{\frac{n_m}{\Lambda^2}\} - 2\beta n_m^2 \tag{3}$$

for the metastable atom density as a function of time. Here n_e is the electron density, n_m is the metastable atom density, Λ is the effective diffusion length, and β is the metastable atom reaction rate constant. D_m is the metastable atom diffusion coefficient and $D_a(T_e)$ is the ambipolar diffusion constant for electrons which depends upon the electron temperature. We estimate that the effective diffusion length, Λ, of a lowest order diffusion mode will vary as a function of position due to the geometry of the GEC reactor, and as a consequence will have to be a fitting parameter. (A should be smallest between the electrodes and largest in the center of the ballast regions.) D_m and $D_a(T_e)$ were estimated as 960 and 810 cm^2/s.[20] Further the exact values of $D_a(T_e)$ and D_m are not particularly important since they are always divided by Λ^2 (an adjustable parameter.) We also assumed that $D_a(T_e)$ is a constant since the measured electron temperature decreases very fast in the afterglow and has reached a small, nearly steady state value before the LP can begin to measure the electron density increase. Finally, β has been measured by Kolokolov and Blagoev,[22]

The metastable atom density equation can be solved analytically and the electron density equation is easiest to solve numerically using the initial metastable atom density, $n_m(0)$, and A as fitting parameters. The result of this fitting procedure is shown in Fig. 6. The fitting parameters were $n_m(0) = 2.95 \times 10^{11} cm^{-3}$ and $\Lambda = 0.5$ cm. The fit to the LP data taken at the center of the electrodes is reasonably good as well as precise. The latter is demonstrated by the fact that a variation in A of only 10% causes a very noticeable degradation in the fit. Greenberg and Hebner measured a metastable concentration of $2.6 \times 10^{11} cm^{-3}$ under similar conditions which has to be considered very good agreement.[20]

The same measurements can also be taken with the LP situated outside the edge of the electrodes (in the ballast region). These are shown in Fig. 7 where it becomes immediately evident that the peaks in the electron densities measured by the LP and MWI now occur at the same time position. (The MWI measurements are nearly identical with those in Fig. 4 since it does not depend upon the LP position.) Fitting the LP measured electron density again results in the fit parameters $n_m(0) = 1.47 \times 10^{11} cm^{-3}$ and $\Lambda = 0.63$ cm. Note that the initial metastable atom density is smaller and that the effective diffusion length is larger than before. It is expected that the diffusion loss of electrons in the ballast regions is slower because the volume is larger, the walls are further away and as a consequence, the effective diffusion length should be larger than that between the electrodes. Therefore, electron production by metastable atoms can dominate losses and ensure net production for a longer period of time in the afterglow even though the initial metastable atom density is smaller. As the metastable density decreases, a time is inevitably reached when metastable ionization can no longer produce more electrons than are lost and the peak is reached. It is also clear that the spatial averaging of the MWI is significantly affected by the electrons in the ballast regions and that this is why it indicates an electron density peak later than that of the LP in Fig. 4.

This diffusion effect also carries over to the end of the off-period. There is a slightly larger electron density remaining in the ballast regions at the end of the off period than there is in the region between the electrodes. This can be noted by comparing the LP results for the electron density at 2 ms between Figs. 4 and 7. There are fewer than $1 \times 10^9 cm^{-3}$ electrons at 2 ms in Fig. 4 and slightly greater than that in Fig. 7. As a consequence, the discharge ignites from both the ballast and inter-electrode

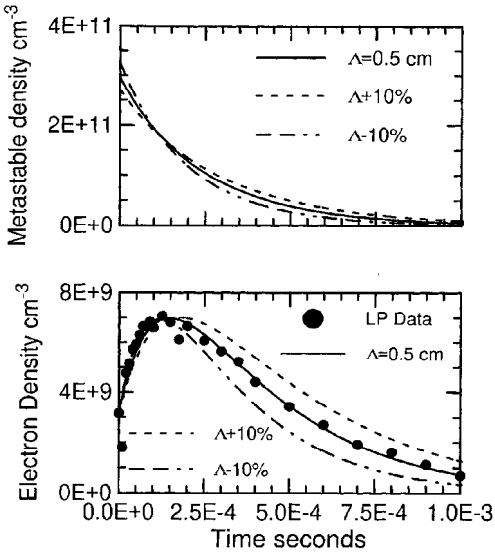

Figure 6. The fit to the LP electron density measurements using the simple differential equation formulation in the text. The result of the fit is an effective diffusion length and the metastable density as a function of time in the afterglow. The fit is clearly degraded by a variation in the effective diffusion length of only 10%. The initial metastable density is also determined with good precision, however, the accuracy of both is probably not as good.

regions and eventually concentrates in the central electrode region. This also helps to explain the final characteristic difference between the LP and MWI results displayed in Fig. 4 and occurring at discharge turn-on. The electron density measured by the MWI is decreasing while that measured by the LP is increasing initially. The MWI sees electrons being driven out of the ballast regions by the RF heating. As the electron temperature increases, the electron loss rate increases in the ballast regions and the MWI catches this behavior. Interestingly, the LP also catches this behavior to some extent in Fig. 7.

Argon discharges can be investigated in the same fashion which can help to explain why these pulsed glows act significantly differently than those through helium. These measurements are presented in Fig. 8 for an argon discharge at 100 mTorr, and an RF voltage amplitude of 105 Volts. Please note again that the modulation period is 2 ms rather than the 50 ms period used in Fig. 3 because of the LP. There are two inaccuracies in the data of this figure to discuss before we begin the comparisons. First, The LP sometimes had difficulties obtaining the plasma and floating potentials at very early times in the turn-on. This could cause the results to be inaccurate and in particular the electron temperature to be overestimated. An example of this problem occurs at 40 ms into the turn-on in Fig. 8. The electron temperature there was estimated from the LP to lie between 4.8 and 6.5 eV but is bounded by T_e measurements at 10 μs and 50 μs in the range of 2 to 3 eV. The electron temperature should not have such a wild dependence, as a consequence, the measurements at 40 μs are likely to be erroneous and have only been included in this graph for completeness. Likewise, the LP has increasing difficulty in determining floating and plasma potentials as the plasma decays in the afterglow and the electron density vanishes. This also can cause the electron temperature measurements to become erroneous. This overestimation can

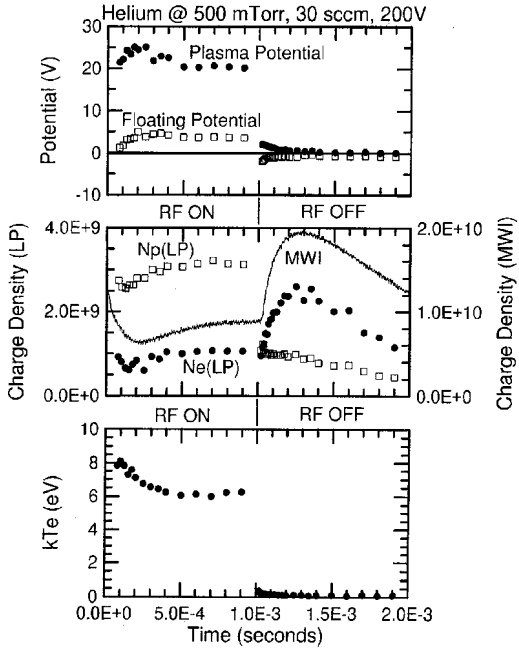

Figure 7. The plasma parameters measured by LP (plasma potential, floating potential, electron density (Ne(LP)), ion density (Np(LP)), and electron "temperature") and MWI (electron density (MWI)) as a function of time in a helium discharge at 500 mTorr, 30 sccm and 200 Volts RF amplitude. The LP was placed in the axial center of the glow, but was displaced from the radial center by 3.5". (1.5" outside the electrodes.)

be compounded by the fact that the dc bias voltage remains on the driven electrode late into the afterglow and causes the sheath in front of that electrode to expand and even touch the LP as the electron density decreases. The result can be seen in Fig. 8 at times greater than 1200 μs. There the LP indicates that T_e is increasing, but, in reality the electron density has become too small for the probe to make reliable measurements. Again, we kept these results simply for completeness.

What is good to note in Fig. 8 is the large discrepancy between the electron density behaviors measured by the LP and MWI at the beginning of the afterglow. While the LP indicates an electron density that is clearly decreasing quickly, the MWI indicates that the spatially averaged electron density decreases some initially and then begins to increase. This is very similar to what was found in Fig. 3. We noted there that while the electron density in helium increased immediately at discharge turn-off, the argon glows electron concentration first decreased, and then increased. The reason for this difference is now clearly found in the LP measured electron density between the electrodes. That density decreases to zero quickly in the case of argon, but, increased in the afterglow for helium. The reason why is found in the electron temperature of the early afterglow. The electron temperature decreases extremely quickly at the start of the afterglow for helium, but, decreases much slower for argon. The 10x larger mass of the argon atom prevents it from cooling the electrons through elastic collisions as quickly as the helium atoms can cool them. The loss rate of electrons in the afterglow, which depends upon $D_a(T_e)$, remains large in the argon afterglow longer than in the helium afterglow and as a consequence it takes time before the electron temperature

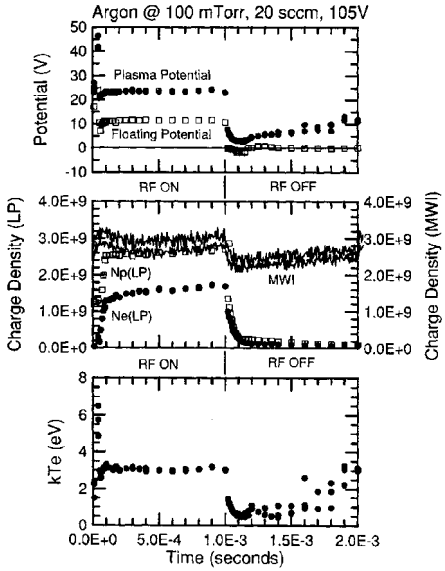

Figure 8. The plasma parameters measured by LP (plasma potential, floating potential, electron density (Ne(LP)), ion density (Np(LP)), and electron "temperature") and MWI (electron density (MWI)) as a function of time in an argon discharge at 100 mTorr, 20 sccm and 105 Volts RF amplitude. The LP was placed in the radial and axial center of the glow.

decreases enough for the production rate by metastables to overcome the loss rate. When it does, the electron density begins to rise.

We can see that metastable ionization is occurring during the afterglow and between the electrodes, even though the electron density measured by the LP simply decreases to zero there, by examining the EEPFs. These are shown in Fig. 9. [23] The RF excitation is on for the first EEPF at 900 μs and the large numbers of energetic electrons mask the contribution to 7.3-7.9 eV electrons from metastable ionization. Even though the electron temperature has not decreased nearly as much in argon in the first 50 to 100 μs of the afterglow as it does in helium (see Fig. 5) a clear peak in the EEPF indicates that metastable ionization is occurring. It became difficult to measure the EEPF after 1150 μs because the LP could not accurately measure the plasma potential as discussed earlier. One other phenomenon is explained with the information obtained from Fig. 8. We had noted on Figs. 2 and 3 that the electron density rises faster in the helium glow at discharge turn-on. Looking at the electron temperature as a function of time during the turn-on for both argon and helium glows helps to show why this occurs. There is a large increase in the electron temperature in the helium discharge at turn-on which did not occur in the argon discharge. The increased electron energy causes increased ion production in the helium glow at ignition and therefore the electron density increases more quickly than that in argon.

CONCLUSIONS

We have demonstrated that a combined diagnostic approach to examining plasma

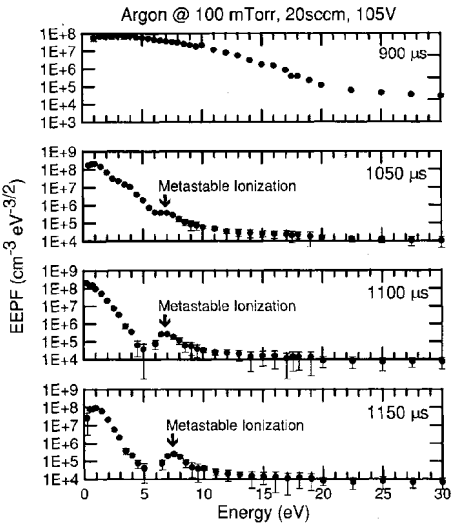

Figure 9. The Electron Energy Probability Functions (EEPF) measured using the LP in an argon discharge at 100 mTorr, 20 sccm and 105 Volts RF amplitude.[ref. 23] The RF source is on at 900 μs. (It is turned off at 1000 μs.) The high energy electrons produced in metastable ionization reactions are just barely visible at 50 μs into the afterglow (1050 μs). They are clearly visible at 100 and 150 μs into the afterglow.

ignition and turn-off could provide information that is not available with either technique alone. In particular, we found that metastable excited state atoms play an important role in the turn-off of helium and argon plasmas in the GEC reactor. They can cause the electron density to increase in the afterglow rather than decrease, they can significantly impact the electron energy probability function (EEPF) and they can cause the glow to remain larger in the ballast regions outside the electrode radial edges longer than between the electrodes.

ACKNOWLEDGMENTS

The authors wish thank B. Cherrington for considerable assistance and advice as well as C. Bowles for assistance in obtaining the data. This material is based upon work supported by the National Science Foundation under Grant No. ECS-9257383 and The State of Texas Advanced Research Program under Grant No. 009741-043.

REFERENCES

1. S. Samukawa and S. Furuoya, Time-modulated electron cyclotron resonance plasma discharge for controlling generation of reactive species, *Appl. Phys. Lett.* 63:2044 (1993).
2. K. Takahashi, M. Hori and T. Goto, Control of fluorocarbon radicals by on-off modulated electon cyclotron resonance plasma, *Jpn. J. Appl. Phys.* 32:L1088 (1993).
3. H. Sugai, K. Nakamura, Y. Hikosaka and M. Nakamura, Diagnostics and control of radicals in an inductively coupled etching reactor, *J. Vac. Sci. Technol.* A 13:887 (1995).
4. A. Howling, L. Sansonnens, J.-L. Dorier and Ch. Hollenstein, Time-resolved measurements of highly polymerized negative ions in radio frequency silane plasma deposition experiments, *J. Appl. Phys.* 75:1340 (1994).

5. L. Overzet, J. Verdeyen, R. Roth and F. Carasco, The effects of modulation on an RF discharge in silane and on the deposited a-Si:H, *in:* "Plasma processing and synthesis of materials," D. Apelian and J. Szekely eds., Materials Research Society, Pittsburgh, PA vol.98 p.321 (1987).
6. Y. Watanabe, M. Shiratani, Y. Kubo, I. Ogawa, and S. Ogi, Effects of low frequency modulation on RF discharge chemical vapor deposition, *Appl. Phys. Lett.* 53:1263 (1988).
7. R. Boswell and D. Henry, Pulsed high rate plasma etching with variable Si/SiO_2 selectivity and variable Si etch profiles, *Appl. phys. Lett.* 47:1095 (1985).
8. R. Boswell and R. Porteous, Etching in a pulsed plasma, *J. Appl. Phys.* 62:3123 (1987).
9. C. Charles, R. Boswell, and H. Kuwahara, SiO_2 deposition form oxygen silane pulsed helicon diffusion plasmas, *Appl. Phys. Lett.* 67:40 (1995).
10. C. Courteille, J-L Dorier, Ch. Hollenstein, L. Sansonnens, and A. Howling, Partial-depth modulation study of anions and neutral in low-pressure silane plasmas, *Plasma Sources Sci. Technol.* 5:210 (1996).
11. S. Samukawa and T. Mieno: Pulse-time modulated plasma discharge for highly selective, highly anisotropic and charge free etching, *Plasma Sources Sci. Technol.* 5:132 (1996).
12. T. Ahn, K. Nakamura, and H. Sugai, Negative ion measurements and etching in a pulsed-power indiuctively coupled plasma in chlorine, *Plasma Sources Sci. Technol.* 5:139 (1996).
13. S. Samukawa and T. Tsukada, Effect of a multiple-cusp magnetic field on electron confinement in a pulse-time-modulated plasma, *Appl. Phys. Lett.* 69:3330 (1996).
14. T. Shibayama, H. Shindo, and Y. Horiike: Silicon etching by alternating irradiations of negative and positive ions, *Plasma Sources Sci. Technol.* 5:254 (1996).
15. P. J. Hargis, K. E. Greenberg, P. A. Miller, J. B. Gerardo, J. R. Torczynski, J. R. Roberts, J. K. Olthoff, J. R. Whetstone, R. J. Van Brunt, M. A. Sobolewski, H. M. Anderson, M. Splichal, J. L. Mock, P. Bletzinger, A. Garscadden, R. A. Gottscho, G. Selwyn, M. Dalvie, J. E. Heidenreich, J. W. Butterbaugh, M. L. Brake, M. L. Passow, J. Pender, A. Lujan, M. E. Elta, D. B. Graves, H. H. Sawin, M. J. Kushner, J. T. Verdeyen, R. Horwath and T. R. Turner, The GEC RF Reference Cell: A parallel-plate radio frequency system to study plasma-processing discharges, *Rev. Sci. Instrum.* 65:140 (1994).
16. L. Overzet and F. Leong-Rousey, Time-resolved power and impedance measurements of pulsed radiofrequency discharges, *Plasma Sources Sci. Technol.* 4:432 (1995).
17. M. Hopkins, Langmuir Probe Measurements in the Gaseous Electronics Conference RF Reference Cell, *J. Res. Natl. Inst. Stand. Technol.* 100:415 (1995).
18. L. Overzet and M. Hopkins, Comparison of electron-density measurements made using a Langmuir probe and microwave interferometer in the Gaseous Electronics Conference reference reactor, *J. Appl. Phys.* 74:4323 (1993).
19. L. Overzet, Microwave Diagnostic Results from the Gaseous Electronics Conference RF Reference Cell, *J. Res. Natl. Inst. Stand. Technol.* 100:401 (1995).
20. K. Greenberg and G. Hebner, Electron and metastable densities in parallel-plate radio-frequency discharges, *J. Appl. Phys.* 73:8126 (1993).
21. P. Miller, J. Verdeyen, and B. Cherrington, Behavior of He(2 ^3S) metastable atoms in weakly ionized helium plasmas, *Phys. Rev. A* 4:692 (1971).
22. N. Kolokolov and A. Blagoev, Ionization and quenching of excited atoms with the production of fast electrons, *Phys. Uspekhi* 36:152 (1993).
23. L. Overzet, B. Smith, J. Kleber and S. Kanakasabapathy, Negative ion extraction from pulsed discharges, Jpn. *J. Appl. Phys.* 36:2443 (1997).

This Page Intentionally Left Blank

RADIO FREQUENCY CAPACITIVE SHEATH DIAGNOSTICS BY TIME RESOLVED MEASUREMENTS OF FAST ELECTRONS

A.S.Smirnov, K.E.Orlov

Plasma Physics Department, St.Petersburg State Technical University, Polytechnicheskaya 29, St.Petersburg, 195251, RUSSIA

INTRODUCTION

Widespread application of diode type reactors in modern semiconductor technology has stimulated an extensive study of low-pressure capacitively coupled RF discharges. This type of discharges has been studied experimentally, theoretically (by analytical and semi-analytical methods) and by numerical simulation. The main purpose of these efforts is to understand the physical processes involved, and the mechanisms of the discharge conditions which influence the plasma chemistry and the plasma-surface interaction. However, this problem is still far from solution. On the one hand, it can be attributed to a lack of proper correlation between theoretical and experimental results. Theoretical models are usually based on the assumptions which can not be tested directly by experiment. Simulation results are strongly affected by the values of cross sections of different processes which are not known with sufficient accuracy. On the other hand, experimentally measured parameters (such as loaded power, voltage drop, electron density, particle fluxes to electrodes, electron distribution function, etc.) are usually integral characteristics, averaged over time and/or space. Different theories may predict close coincidence of integral parameters and very precise measurements are needed to distinguish between them. To improve situation time resolved local parameters must be measured and compared with the theoretical predictions.

Time-resolved energy distribution of charged particles impinging on the electrodes is an important characteristic of RF-discharge plasma. Electron and ion bombardment can strongly affect surface processes, such as film growth, etching, etc. Since charged particles in low pressure discharges are produced in the plasma column and accelerated in the sheaths, time-resolved energy distribution functions provide an important information about physical processes in positive column and electrode sheaths. Multigrid retarding field analyzers were widely used for energy distribution function (EDF) measurements of the ions[1] electrons[2,3] impinging on electrode in RF-discharge. Under the experimental conditions the particle fluxes are actually being averaged over large number of the electric field periods, though all theoretical models[4,5] predict that plasma electrons can be impinging on electrode only during the small part of period when plasma-sheath boundary is close to the electrode. Modulation of the ion and

Electron Kinetics and Application of Glow Discharges
Edited by U. Kortshagen and L. D. Tsendin, Plenum Press, New York, 1998

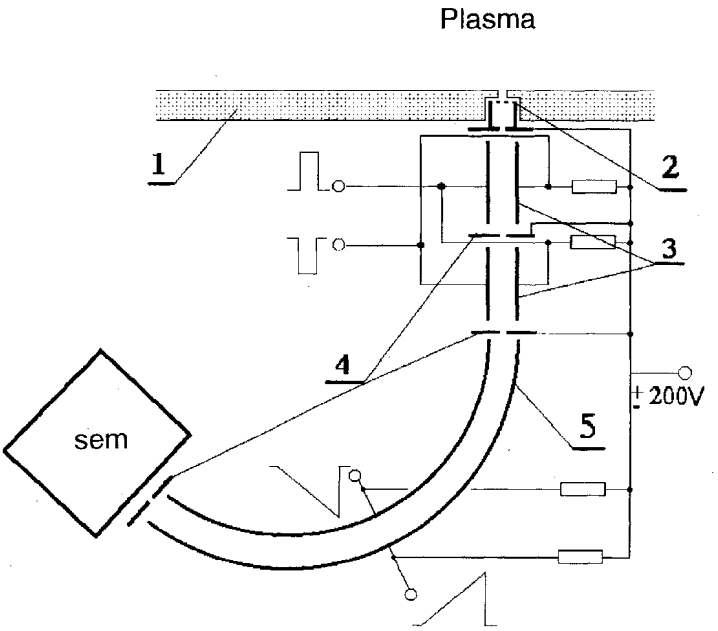

Figure 1. Experimental setup. l-grounded electrode, 2-grid, 3-electronic gate, 4-slits, 5-energy analazer, SEM-secondary electron multiplier.

electron flux by the driving frequency and harmonics was observed in[6]. In these works, time and energy spectra were obtained in separate experiments, so it is impossible to know in which phase the particles of a definite energy are born and come to electrode, though all the inferences are based on such effects. In this paper, we report the results of time resolved measurements of electron EDF by 130° cylindrical electrostatic energy analyzer.

EXPERIMENTAL SETUP

The sketch of the experimental setup is presented in fig.1. Discharge was burned between parallel plate electrodes 20 cm in diameter separated by 2-6 cm. Energy analyzer was placed in high vacuum chamber behind the grounded electrode. Electrons from plasma were extracted through the 1 mm diameter orifice. After accelerating up to 200 eV by positively charged grid retarding ions kept moving through electronic gate to energy analyzer. Particles which passed energy analyzer were detected by the secondary electron multiplier. A voltage of 400 V applied to the gate plates were deflected electrons with energies less than 1500 eV. For the EDF measurements, gate was tuned by 10 ns strobe, which was synchronized with the RF voltage. Varying the strobe delay we could measure the EDF in different electric field phases. The second pair of gate plates was used to compensate particle displacement in residual voltage when the gate was opened. Energy resolution was 4%. Experiments were carried out in Argon 13.56 MHz RF discharge in pressure range 3-50 mTorr and power range 15-90 W. Gas pressure in discharge and high vacuum chamber, loaded power, discharge current and voltage oscillograms and dc self-bias voltage were controlled.

RESULTS AND DISCUSSION

Electron distribution function is reported earlier[3] to correspond to the two groups of electrons. The first one is a group of low energy, "thermal" plasma electrons, which are impinging on electrode when space-charge sheath vanishes. Plasma electrons have a Maxwellian-type distribution[3] with temperature of about 9 eV. A distribution of the fast electrons proves to be more interesting. The typical fast electron EDF in different current phases for Argon discharge are presented in fig.2. In fig.3 time-resolved spectra are compared with that obtained with long duration gate pulse covering ½ of the current circle. In these figures, one can see two specific features of the spectra. The first one is an asymmetry of the spectra obtained in phase when electrons move to the electrode (t<65ns in fig.2) and when electrons move from the electrode (t<70ns in fig.2). This asymmetry results from the klystron-effect occurring on the electron path through the positive column [7]. The second one is a rather complex structure of the energy spectra, which is more pronounced in low pressure (fig.3). We will discuss these features independently.

For analysis of the fast electron spectra let us consider the simplest model based on the following assumptions: (i) the fast electrons are γ - electrons which are emitted from the powered electrode and accelerated in the sheath; (ii) γ - electron flux from the powered electrode is independent of time; (iii) the electron plasma frequency in the sheath is much larger than the driven frequency, hence the time of electron flight through the sheath is much smaller than the RF period and independent of the phase; (iv) the electron energy is equal to the sheath voltage at the moment when electron is crossing the sheath boundary; (v) scattered electrons are not detected; (vi) discharge current is sinusoidal.

Under these assumptions, if we know sheath voltage, we know the energy distribution of the electrons started at any time from the sheath boundary. Hence, the time and the energy distribution for the electrons reached the grounded electrode can be calculated. The results of the calculations are presented in fig.2. It could be seen that calculations provide a correct form of the energy distributions.

All these calculations were made under the assumption that the sheath voltage is proportional to $(1 + cos(\omega t))$. Any other choice of voltage-time dependence produced the electron energy spectra essentially different from those recorded in the experiment. Since electron scattering cross-section decreases with the energy increase [8], the intensity of electron flux decreases with energy. To take this into account, the calculated spectra were normalized as to scattering probability.

Let us consider the structure of the fast electron energy spectra. Electron disribution function f is given by

$$f = \frac{dN}{d\epsilon}, \tag{1}$$

where N is the number of electrons detected, e is electron energy. This expression can be transformed to

$$f = \frac{dN}{dt}\frac{d\epsilon}{dt} = \frac{dN}{dt}\frac{1}{d\epsilon/dt}. \tag{2}$$

At low pressure and short electrode gap scattering and klystron-effect can be neglected. Thus, N equals to the number of electrons ejected from the electrode surface and $\frac{dN}{dt}$ is constant (assumptions ii, iii). Since, electron energy is determined by the sheath voltage U:

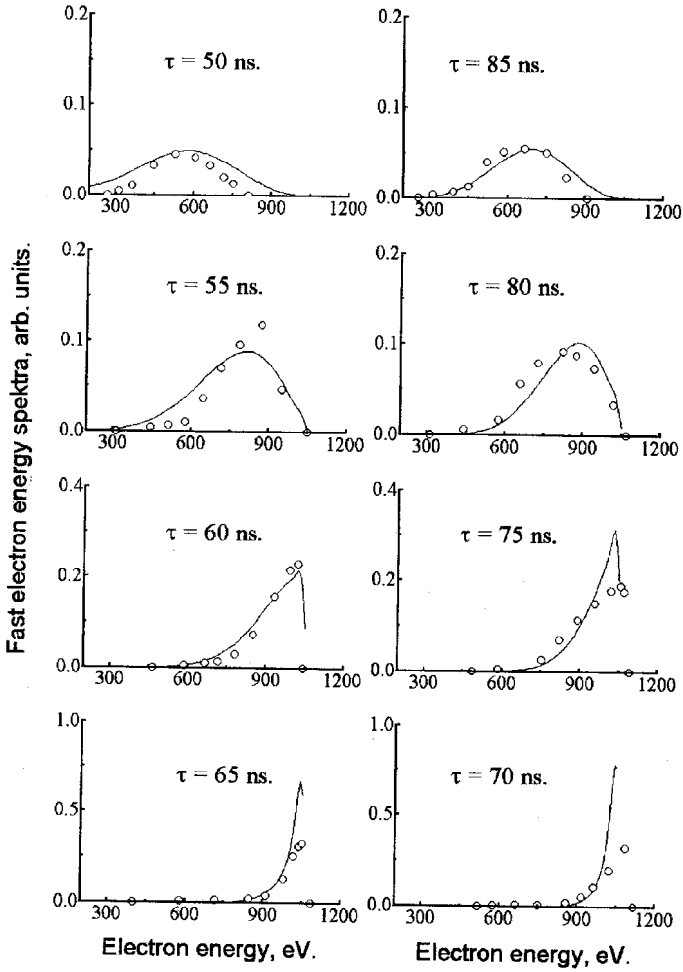

Figure 2. Time-resolved fast electron energy distribution function. Ar, p=40mTorr, U=525V, W=52Watt. Circles-experiment, solid line-calculation.

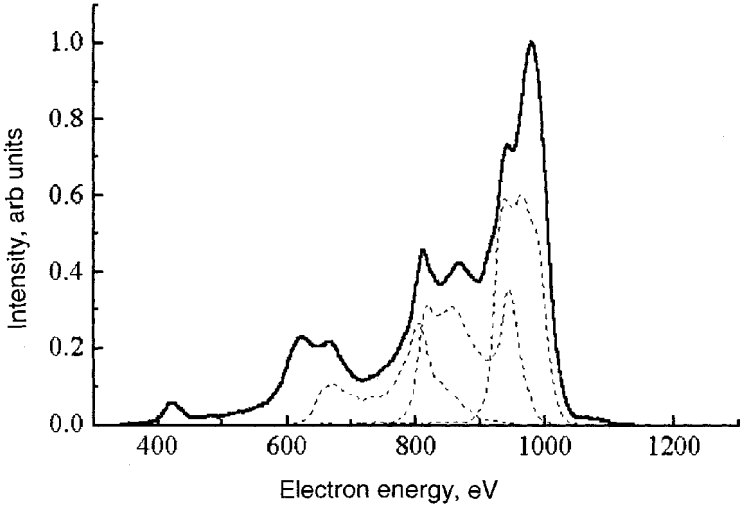

Figure 3. Fast electron energy distribution function. Dashed lines-time resolved measurements, solid lines-measured over of 1/2 RF period.

$$\in = eU. \tag{3}$$

we can obtain

$$f = \frac{C}{dU/dt}\ , \tag{4}$$

where C is a constant. By integrating (4) we obtain the sheath voltage-time dependence:

$$\frac{1}{C}\int f(eU)dU = t(U)\ . \tag{5}$$

Results of these calculations together with the curve $(1 + cos(\omega t))$are presented in fig.4. Evidently, the calculated voltage can be approximated by $(1 + cos(\omega t))$with reasonable accuracy. The higher harmonics (up to n=8) of the driven frequency can be easily seen. Peaks on electron distribution function are the result of these harmonics.

CONCLUSIONS

Time resolved fast electron energy spectra were measured. Asymmetry of the spectra was observed for the phases, when the plasma boundary moves towards the electrode and in the opposite direction. This effect is interpreted as convergence and divergence of the electron trajectories in x-t plane (klystron-effect). Effect of electron scattering was manifested by the decreasing of the electron flux with energy. Modulation of electron energy spectra resulting from the higher harmonics in the sheath voltage was observed.. Sheath voltage wave-form was calculated from the electron energy spectra. Sheath voltage can be approximated by $(1 + cos(\omega t))$. Sheath voltage contains higher harmonics (up to n=8). These harmonics may be related to the temporal and spatial modulation of the ion profile in the sheath.

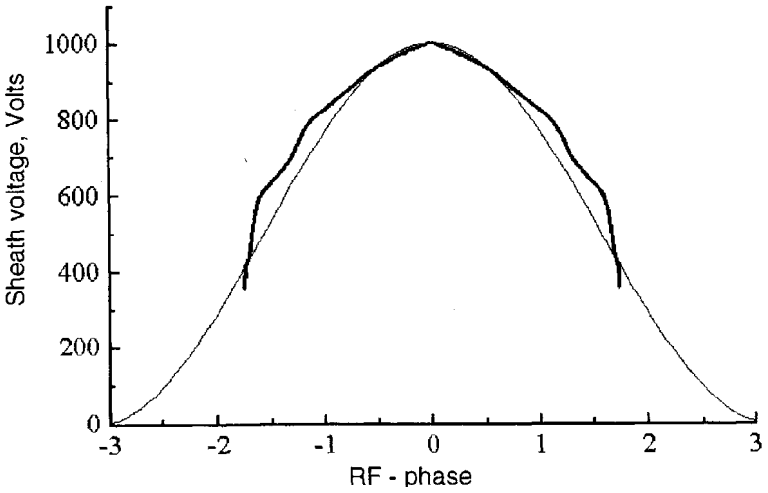

Figure 4. Sheath voltage waveform. Bold line-calculated from fast electron EDF, narrow line-(1+cos(wt)).

ACKNOWLEDGMENTS

This research was supported by INTAS (grant N-94-740), RFRF (grant N-96-02-16918) and International Atomic Energy Agency (contract N 9238).

REFERENCES

1. C.Böhm, J.Perrin, Retarding-field analyzer for measurements of ion energy distributions and secondary electron emission coefficients in low pressure RF discharges. Rev. Sci. Instrum, 64: 31 (1993).
2. H.R.Koenig, L.I.Maissel, Application of RF discharge to sputtering. IBM J. Res. Develop. 14:168 (1970).
3. A.S.Smirnov, K.S.Frolov, A.Yu.Ustavschikov, Energy and time distribution of charged particles bombarding the electrode in a radio-frequency discharge. Sov.Phys.: Tech.Phys.Lett. 21,9:705 (1995).
4. A.S.Smirnov, L.D.Tsendin, The space-time-averaging procedure and modelling of the RF discharge. IEEE Transactions on Plasma Science, 19:130 (1991).
5. M.A.Lieberman, A.J.Lichtenberg. “Principles of Plasma Discharges and Materials Processing,” N.Y. Willey (1994).
6. C.Wild, P.Koidl, Ion and electron dynamics in the sheath of radio-frequency glow discharge. J.Appl.Phys., 69:2909 (1991).
7. A.S.Smirnov, K.S.Frolov, A.Yu.Ustavschikov, Energy distribution of charged particles impinging on ground electrode in RF-discharge, Proc. 11-th Int. Conf. on Gas Discharges and Their Applications. 2:38 (1995).
8. F.J. de Heer, R.H.J. Jansen, W. van der Kaay, Total cross sections for electron scattering by Ne, Ar, Kr and Xe. J.Phys. B: Atom. Molec. Phys., 12,6: 979 (1979).

PROBE METHOD FOR INVESTIGATION OF ANISOTROPIC PLASMA

A. P. Mezentsev, A. S. Mustafaev, and V. L. Fedorov

Department of Physics
St. Petersburg Mining Institute
St. Petersburg Russia

1. INTRODUCTION

Anisotropic plasma is rather a rule than exclusion in the practice of plasma investigations. Actually, the existence of plasma created either by electric current photoexcitation, or by any other methods means conveyance of energy or particles to it. Consideration for this factor only causes local fluxes that determine some direction in space, which, in the first approximation, is the local axis of axial symmetry.

Also, any actual plasma object is spatially limited, and the boundary conditions cause withdrawal of particles from plasma, which also tells on the local direction of the symmetry axis. Thus, for example, axially symmetric plasma is realized in a positive column of an electric discharge with the symmetry axis, in the first approximation coinciding with the local direction of the electric field strength. In beam plasma, the predominant direction of particles motion will be the symmetry axis too. Thus, axially symmetric description takes into account some important specific features of plasma, and this description may be considered as the next approximation after the spherically symmetric one.

In this paper we consider the possibilities of the probe technique in investigations of axisymmetric low-temperature plasma. The greatest attention is paid to determination of the electron velocity distribution function, which is the main dependence that determines many important plasma parameters.

2. REPRESENTATION OF THE ELECTRON VELOCITY DISTRIBUTION FUNCTION IN AXIALLY SYMMETRIC PLASMA

The electron velocity distribution function in an axisymmetric plasma, specified in a spherical co-ordinate system with the polar axis directed along the local axis of plasma symmetry, can be expressed as a Legendre-polynomial expansion[1]:

$$f(v,\theta) = \sum_{j=0}^{\infty} f_j(v) P_j(\cos\theta), \tag{1}$$

Electron Kinetics and Application of Glow Discharges
Edited by U. Kortshagen and L. D. Tsendin, Plenum Press, New York, 1998

where v and θ are the magnitude of velocity and the polar angle, respectively; P_j (cos θ) is the j-th Legendre polynomial.

The series converges absolutely and uniformly if $f(v, \theta)$ is twice continuously differentiable. The first two coefficients of the series are of particular interest. Indeed, the orthogonality of the Legendre polynomials implies that (apart from a multiplicative factor) the coefficient $f_0(v)$ uniquely determines the distribution of the electrons with respect to the velocity modulus, and is responsible for excitation and ionization processes. The coefficient $f_1(v)$ is uniquely related to the convective velocity of the electrons and to the density of the electron current in the plasma. Together with the first two coefficients, the rest of the expansion coefficients specify the detailed angular dependence of the distribution function and may be of interest in studies of electron scattering in collisions, and in analyzing specific features of population of Zeeman atomic levels in excitation acts. The indicated properties of the Legendre components of the distribution function make the expansion (1) preferable as compared with expansions in other known orthogonal polynomials. Also note that the representation of the distribution function (1) with only the first two terms is known as the Lorentz approximation and is often employed to analyze currents flowing through plasmas.

3. PROBE MEASUREMENTS OF THE LEGENDRE COMPONENTS OF THE ELECTRON VELOCITY DISTRIBUTION FUNCTION[2-4]

3.1. Plane One-Sided Probe

One surface of a plane one-sided probe collects electrons, while the opposite side is insulated. We can use such probes to approximate small surface elements of probes of arbitrary shape, and this is the primary reason for our interest in them.

We assume that all the conditions for the applicability of the Langmuir probe method are satisfied, except that the distribution function is anisotropic, i. e., we will assume that the Debye screening radius is much less than the characteristic probe dimension, and that the latter is less than the electron free path; the probe surface absorbs all of the electrons that reach it, and there are no secondary processes connected with emission of charged particles on the surface. Then, if the probe potential U is negative relative to the local potential of the surrounding plasma, the electron current density is given by:

$$j(eU) = \frac{2e}{m^2} \int_0^{2\pi} d\varphi_1 \int_{eU}^{\infty} \varepsilon d\varepsilon \int_0^{\arccos\sqrt{\frac{eU}{\varepsilon}}} f(\varepsilon, \theta_1, \varphi_1) \cos\theta_1 \sin\theta_1 d\theta_1, \tag{2}$$

where e, m, and e are the electron charge, mass, and kinetic energy, respectively; θ_1 and φ_1 are the polar and azimuthal angles in a spherical co-ordinate system with polar axis z along the outer normal to the collecting plane of the probe; The distribution function $f(\varepsilon, \theta_1, \varphi_1)$ is normalized to the electron concentration.

Differentiating expression (2) twice with respect to the parameter U, we find that:

$$j''_U(eU) = \frac{e^3}{m^2} \int_0^{2\pi} f(eU, \theta_1 = 0, \varphi_1) d\varphi_1 -$$

$$- \frac{e^2}{m^2} \int_0^{2\pi} d\varphi_1 \int_{eU}^{\infty} \frac{\partial}{\partial U} f(\varepsilon, \theta_1 = \arccos\sqrt{\frac{eU}{\varepsilon}}, \varphi_1) d\varepsilon. \tag{3}$$

The subsequent analysis depends on the specific location of the probe and on the plasma symmetry. We will consider a plane one-sided probe oriented so that the plasma symmetry axis has the polar and azimuthal angles Φ_0 and φ_0, respectively, in the spherical co-ordinate system with the polar axis coinciding with the outer normal to the probe surface; and the chosen direction of electrons motion is characterized by θ_1 and φ_1, as above. The angle between the indicated directions will be θ (in our previous notations), and the Legendre polynomials for it are determined by the known addition theorem[4]:

$$P_j((\cos\theta) = P_j(\cos\theta_1)P_j(\cos\Phi_0)+$$

$$+2\sum_{m=1}^{j}\frac{(j-m)!}{(j+m)!}P_j^m(\cos\theta_1)P_j^m(\cos\Phi_0)\cos m(\varphi_1-\varphi_0), \tag{4}$$

where $P_j^m(\cos\theta_1)$ are the associated Legendre functions.

Using the representation of the distribution function in the form of expansion in Legendre polynomials and the addition theorem, we find upon integrating over the angular co-ordinate in expression (3) that:

$$j_U''(x,\Phi_0) = 2\pi\frac{e^3}{m^2}\sum_{j=0}^{\infty}F_j(x)P_j(\cos\Phi_0), \tag{5}$$

$$F_j(x) = f_j(x) - \int_x^{\infty} f_j(\varepsilon)\frac{\partial}{\partial x}P_j\left(\sqrt{\frac{x}{\varepsilon}}\right)\mathrm{d}\varepsilon, \quad j = 0,1,2,\ldots, \tag{6}$$

where $x = eU$; U is the probe potential with respect to plasma.

In the particular case of isotropic plasma, only the first term in sum (5) is nonzero. Consideration for this term leads to the known Druyvesteyn formula that connects the second derivative of the probe current density with respect to the probe potential with the distribution function.[5] Relations (5) and (6) can be used to calculate the first coefficients in representation (1). Indeed, suppose that the upper limit ∞ in the sum (1) can be replaced by some finite $j = N$. If we then measure $j_U''(eU)$ for N different angles Φ_0, relation (5) will give a system of algebraic equations for the $F_j(x)$.

To make the set of equations (5) well-posed, orientation angles for the probe in plasma should be specially chosen. One can show that the set will be sufficiently well-posed in the case, when the angles Φ_0 are determined by the following relation:

$$\cos\Phi_{0k} = 1 - 2k/l,\ k = 0, 1, 2, \ldots, l. \tag{7}$$

Now we consider integral equations (6). Note two facts that make them different from the well studied Volterra equation: (1) the integral entering the equation has the infinite limit of integration; (2) the kernel of the integral equation has singularity at $x = 0$. Consequently, it is necessary to introduce the corresponding limitations, in order to use the known theory of the Volterra equations.[6]

Note that the infinite value of the upper integration limit in expressions (6) may be replaced by the finite value E, if the distribution function is close to zero for the energies above E. The point of singularity of the equation kernel at $x = 0$ and its vicinity should be excluded from the domain where the solution is sought.

With consideration for the made limitations, one can determine analytical solutions for equations (6). Indeed, for Volterra integral equations, a solution can be specified by means of resolvent kernels. For equations (6), under made limitations, we obtain:

$$f_j(x) = F_j(x) + \int_x^E R_j(x,\varepsilon)F_j(\varepsilon)\mathrm{d}\varepsilon, \quad j = 0, 1, 2, \ldots . \tag{8}$$

One can show that the resolvent kernels have the form[3] :

$$R_j(x,\varepsilon) = \frac{1}{x}\sum_{n=0}^{[j/2]} C_{jn}\left(\frac{\varepsilon}{x}\right)^{\frac{j-2n-1}{2}} \tag{9}$$

$$C_{jn} = (-1)^n 2^{-(j+1)}\frac{(2j-2n)!}{n!(j-n)!(j-2n)!}(j-2n), \tag{10}$$

where j = 0, 1, 2, . . .; [j/2] = j/2 for even, and [j/2] = (j – 1)/2 for odd j.

The first three resolvent kernels are

$$R_0 = 0, \quad R_1 = \frac{1}{2x}, \quad R_2 = \frac{3}{2}\varepsilon^{1/2}x^{-3/2}. \tag{11}$$

Thus, the problem of determination of Legendre components of the electron velocity distribution function can be solved by means of measurements made by a plane Langmuir probe.

3.2. Cylindrical Probe

Because of their simplicity, cylindrical probes are the ones most often used in plasma diagnostics. We consider a cylindrical probe with arbitrary orientation in axisymmetric plasma. Let the axis of the cylinder make an angle λ with the axis of plasma symmetry, and choose an auxiliary spherical co-ordinate system with the polar axis normal to the plane containing the symmetry axes of the plasma and the cylinder. The direction of the plasma symmetry axis in the auxiliary co-ordinate system is specified by polar and azimuthal angles $\theta = \pi/2$ and $\varphi = 0$, while the direction of the normal to some element of the probe surface — by angles θ_2 and $\varphi_2 = (\lambda \pm \pi/2)$. As above, the angle between the normal and the plasma symmetry axis is Φ_0, and

$$\cos\Phi_0 = \sin\theta_2 \cos\varphi_2 . \tag{12}$$

Using the relation for Φ_0, we integrate expression (5) over the surface S of the cylindrical probe:

$$I_U''(eU) = \frac{2e^3 S}{m^2}\sum_{j=0}^{\infty} F_{2j}(eU)\int_0^{\pi} P_{2j}(\sin\theta_2 \sin\lambda)\mathrm{d}\theta_2. \tag{13}$$

The terms with odd indices integrate to zero because the corresponding Legendre polynomials are odd functions of their argument.

As before, if the upper limit ∞ in the sum (1) can be replaced by some finite j = N, then measurements of the corresponding number of angles form an algebraic set of equations from (13) which permits to determine only even coefficients in series (1) by means of the method described above. However, the matrix of coefficients is less well-posed than for the case of a plane probe, and it is preferable to use plane probes in order to find f_{2j} more accurately.

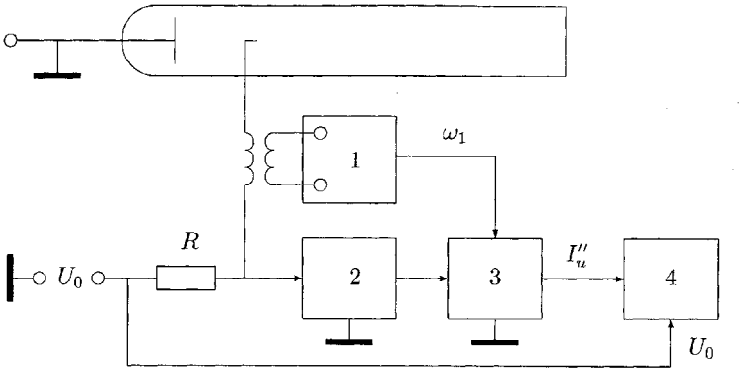

Figure 1. Principal scheme of experimental setup for measurements of the second derivative of the probe current with respect to its potential. 1 — oscillator of the differentiating signal, 2 — narrow-band amplifier, 3 — synchronous detector, 4 — analogous recorder.

4. EXPERIMENTAL TECHNIQUE

Presently, there are several methods for experimental determination of the second derivative of the probe current with respect to the probe potential.[7, 8, 26] These methods are based on modulation of the probe potential by a small-amplitude signal of some time structure, and subsequent analysis of harmonic components of the probe current. Paper Ref. 9 presents sufficiently complete review of the methods.

Along with a constant bias U_0, an alternating voltage ΔU with a small amplitude (the differentiating signal) is introduced in the probe circuit.

We used the differentiating signal with the profile

$$\Delta U = a(1 + \cos \omega_1 t) \cos \omega_2 t \, (\omega_2 \gg \omega_1) \tag{14}$$

proposed earlier in Ref. 7. In this case, expanding the probe current in powers series with respect to the small parameter ΔU, we obtain the following expression for the amplitude of the harmonic of the probe current at the frequency ω_1:

$$A_{\omega_1} = \frac{a^2}{2} I''_U + \frac{7}{64} a^4 I''_U + \ldots . \tag{15}$$

For a sufficiently small "a," one may neglect the second term, and the harmonic amplitude $A_{\omega 1}$ of the probe current coincides with the second derivative of the probe current with respect to the probe potential, with the accuracy up to a constant multiplier.

Figure 1 gives the experimental setup we used.

The differentiating signal was introduced in the probe circuit by means of a transformer with small interwinding capacitance. The transformer was made without a ferromagnetic core. The voltage proportional to the probe current was taken off at the small resistor included in the probe circuit and was amplified by a narrow-band amplifier. Separation of the harmonic component of the probe current with the frequency ω_1 was performed by means of a synchronous detector. The reference voltage was fed to the detector from the master oscillator. The signals proportional to I''_U and U_0 were fed to an analogue recorder.

To calibrate the installation and obtain the absolute values of I''_U we used a thoriating signal with the frequency ω_1 of a known amplitude fed to the input of the amplifier.

Recently, a scheme for determination of the second derivative of the probe current with respect to the probe potential was proposed, in which the volt-ampere probe characteristic is recorded with subsequent numeric differentiating by means of a computer.[10, 26] However, noise stability of the proposed scheme was not analyzed, and its advantages over the modulation schemes were not shown.

The probe measurements were performed both in plasma of the positive column,[12–14] and in a plasma-beam discharge in helium.[4, 15—18] Plasma of the positive column was produced in a glass discharge tube of round cross-section 3 cm in diameter and 25 cm in length. Plasma of the beam discharge was produced in the volume limited by a metal cylinder 11 mm in diameter; the length of the discharge gap varied in the range 10–15 mm. The source of electrons was heated impregnated cathode 10 mm in diameter.

The devices were thoroughly pumped out down to the residual gas pressure of 10^{-8} Torr, and then were filled with spectrally pure helium. Training of discharge tube provided high stability of the discharge parameters during time periods up to 5 hours. Variations of the value of the discharge current did not exceed 1 mA for the 500 mA current, variations of the voltage drop across the discharge gap did not exceed 0.1 V in this case. These measure provided reproducibility of results not worse than 0.5 percent. The signal/noise ratio was about 200.

The measurements were performed by means of a plane one-sided probe 0.5 mm in diameter produced of tantalum foil 25 μm thick. One side of the probe was coated with aluminum oxide layer baked in vacuum. The probe could be moved along the discharge axis by means of a micrometric drive and change its orientation by the angles from 0 to 180°. The error of the probe initial setting was ±05°. The range of helium pressures was 0.1–2.5 Torr and of the discharge currents — from 100 to 500 mA.

5. MEASUREMENTS OF LEGENDRE COMPONENTS OF ELECTRON VELOCITY DISTRIBUTION FUNCTION IN A POSITIVE COLUMN OF DISCHARGE IN HELIUM[12—14]

Theoretical estimations of the role of collisional processes in the positive column of an electric discharge performed with consideration for the value of the electric field strength lead to the conclusion about high degree of isotropy of the electron distribution function.[1, 11]

This conclusion is indirectly confirmed by measurements of the probe characteristic for different orientations of a cylindrical probe and very weak dependence of this characteristic on the probe orientation.[14] However, apparently no direct investigations of the anisotropy degree of the distribution function were performed. Below we present results of experimental determination of the distribution function Legendre components obtained by means of a plane probe and confirming the conclusion about isotropy of the electron velocity distribution function in the positive column of electric discharge in the first approximation. We recorded the second derivatives of the probe current with respect to the probe potential I''_U under discrete orientations of the normal to the probe surface with respect to the axis of the discharge tube, corresponding to the angles 0, 45, 90, 135, and 180°.

Figure 2 presents the Legendre components of the distribution function determined on the basis of the measured values of I''_U. Numeric values of the Legendre component

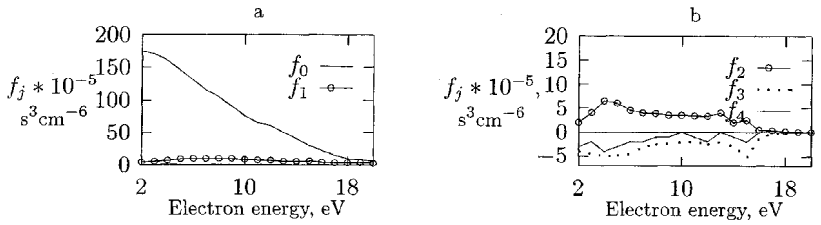

Figure 2. Energy dependence of Legendre components of the electron velocity distribution function f_j in plasma of a discharge positive column in Helium; p_{He} = 0.5 Torr, the discharge current I = 0.5 A.

f_1 are considerably less than the corresponding values of f_0. Also, the values of the Legendre components f_2, f_3, and f_4 are small. This fact indicates high degree of isotropy of the electron velocity distribution function in the positive column of the electric discharge. Thus, the electron distribution function may be assumed isotropic at least in the first approximation. To control the accuracy of determination of the Legendre component f_1, we compared the directly measured value of the discharge current with the value of the discharge current calculated on the basis of experimentally measured values of f_1 with relation[1]:

$$j = \frac{4\pi}{3} e \int_0^\infty v^3 f_1 \mathrm{d}v. \tag{16}$$

Table 1 gives the comparison results. It is easily seen that the values of the discharge current calculated and determined in the way described above differ no more than by 10 percent. Satisfactory agreement between calculated and experimental values of the discharge current indirectly indicates the reliability of determination of the Legendre component f_1 of the electron velocity distribution function.

6. INVESTIGATION OF THE ELECTRON VELOCITY DISTRIBUTION FUNCTION IN BEAM DISCHARGE PLASMA IN HELIUM [4,15—18]

Near the cathode of the discharge tube, the conditions are realized, under which the electron velocity distribution function is highly anisotropic. Usually, this domain of the dark cathode space and plasma in this domain are called beam ones, thus underlying the fact that the group of electrons with directed motion is observed here.

Table 1. Comparison of Experimental and Calculated Values of the Discharge Current for Different Helium Pressures

P, Torr	*I*, mA (experiment)	*I*, mA (calculation)
1	590	565
1	500	470
0.5	514	454
0.5	236	258
0.5	110	110
0.2	404	355
0.2	252	240
0.2	102	119
0.2	50	52

$S_j(v, z, t)$ and $f_1(v, z, t)$ depend only on the modulus of the electron velocity v, coordinate z along the symmetry axis, and time t. The Legendre components S_j and f_j are related by the system of kinetic equations[19]:

$$\frac{\partial f_j}{\partial t} + v\frac{\partial}{\partial z}\left[\frac{j+1}{2j+3}f_{(j+1)} + \frac{j}{2j-1}f_{(j-1)}\right] -$$

$$-\frac{eE}{m}\frac{j+1}{2j+3}\frac{1}{v^{j+2}}\frac{\partial}{\partial v}(v^{j+2}f_{(j-1)}) - \frac{eE}{m}\frac{j}{2j-1}\frac{1}{v^{1-j}}\frac{\partial}{\partial v}(v^{1-j}f_{(j-1)}) + S_j = 0, \qquad (17)$$

where E is the electric field strength; $j = 0, 1, 2, \ldots$.

It is easy to see that the set of kinetic equations permits to determine the Legendre components of the collision integral S_j, if f_j and E have been measured.

Moreover, if measurements are carried out in a positive column of axisymmetric stationary electric discharge, additional and considerable problem simplifications are possible. Indeed, in this case [13] and when the density of discharge current is small, we find that $f_0 \gg f_1 \gg f_2$. Thus, sufficient accuracy is reached when only two first equations are left in the system of kinetic equations (assuming $f_j > 2 = 0$). Besides, note that, as a rule, the field term in the kinetic equations is considerably greater than the diffusion term at the symmetry axis of the discharge in a positive column, i. e.:

$$\frac{eE}{3m}\frac{1}{v^2}\frac{\partial}{\partial v}(v^2 f_1) \gg \frac{1}{3}v\frac{\partial}{\partial z}f_1. \qquad (18)$$

This also permits to simplify the kinetic equations. Thus, in these conditions the set of kinetic equations is reduced to two comparatively simple equations:

$$-\frac{eE}{3m}\frac{1}{v^2}\frac{\partial}{\partial v}(v^2 f_1) + S_0 = 0, \qquad (19)$$

$$-\frac{eE}{m}\frac{\partial}{\partial v}(f_0) + S_1 = 0. \qquad (20)$$

These equations show that it is sufficient to measure f_0, f_1 and E in order to calculate S_0 and S_1. Above we showed that the Legendre components f_0 and f_1 may be determined by using a plane probe. The probe method also permits to determine the electric field strength E.[11] Thus, all values necessary for calculation of the Legendre components S_0 and S_1 of the collision integral may be experimentally determined.

Figure 4 presents the results of determination of the Legendre components S_0 and S_1 of the collision integral for helium pressures 0.5 and 1.0 Torr.

First of all, it is necessary to note that the Legendre component S_0 is close to zero at least with the accuracy reached in the performed experiments (Figure 4a). The obtained values of the Legendre component of the collision integral S_0 agree with the conception that elastic electron-atom collisions in the positive column of the electric discharge make the dominating contribution in the collision integral. It is known[20] that the Legendre component S_0 of the collision integral should be equal to zero exactly in the approximation of immovable atoms and only elastic electron–atom collisions.

Now we consider the Legendre component S_1 of the collision integral. It is seen from Figure 4b that the component S_1 substantially depends on the gas pressure, and its value increases with the pressure growth. Also note that the value of the Legendre component S_1 is determined with comparatively small errors. This is connected with the fact that this component is simply related to the electron velocity distribution function, and with considerable value of S_1. Thus, in the positive column of the electric discharge, it is possible to measure Legendre components of the collision integral, and the component S_1 is determined with the highest accuracy. Measuring the Legendre components of the collision integral permits to study collisional processes with participation of electrons directly in plasma conditions.

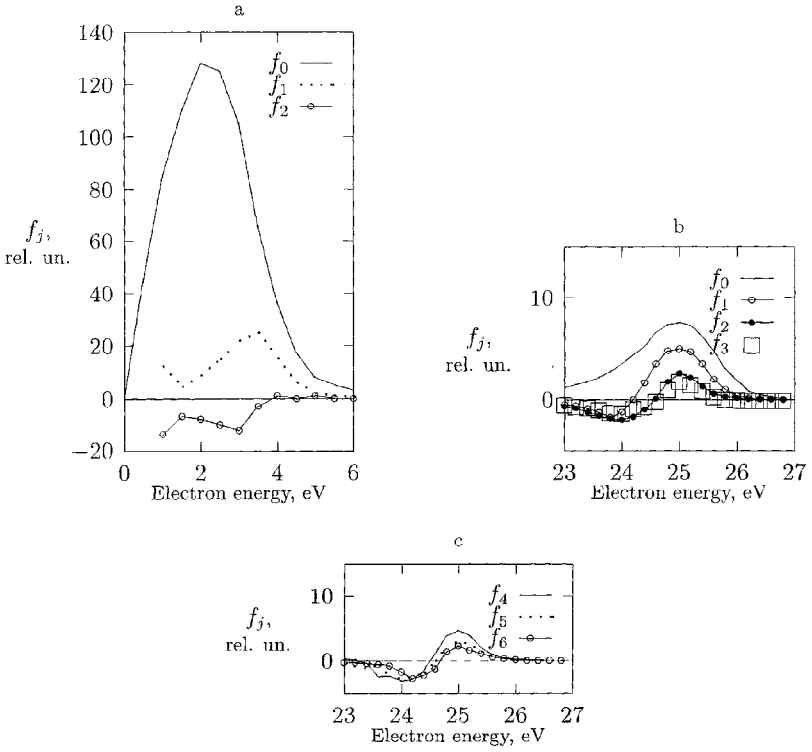

Figure 3. Legendre components of the electron velocity distribution function f_j in Helium plasma-beam discharge; p_{He} = 2 Torr, the discharge current I = 0.128 A.

Figure 3 presents the Legendre components of the distribution function determined in the beam plasma at the distance of 2.5 mm from the cathode, under the pressure of 2 Torr and the discharge current of 0.128 A.

It can be easily noticed that the Legendre components differ from zero for two energy ranges, 0–5 eV and 24–26 eV. At low energies, the Legendre component f_0 dominates over the rest ones (Figure 3a), and this indicates isotropy of the distribution function (in the first approximation). In the energy range 24-26 eV (Figure 3b,c), the Legendre components of indices up to 6 inclusively have the same order of magnitude, this indicating anisotropy connected with the, beam of electrons of this energy not scattered from the moment of the beginning of their motion from the cathode. Study of the processes of the electron beam decay depending on the discharge conditions in works Refs. 15–18 permitted to find the criteria that determine the relaxation length of the distribution function separately in energies and momenta, and to find out the role of walls of the discharge gap and the near-wall potential drop on formation of the electron velocity distribution function.

7. MEASUREMENT OF LEGENDRE COMPONENTS OF ELECTRON–ATOM COLLISION INTEGRAL[13]

Both the integral of electron–atom collisions in axisymmetric plasma and electron velocity distribution functions can be represented by Legendre series, whose coefficients

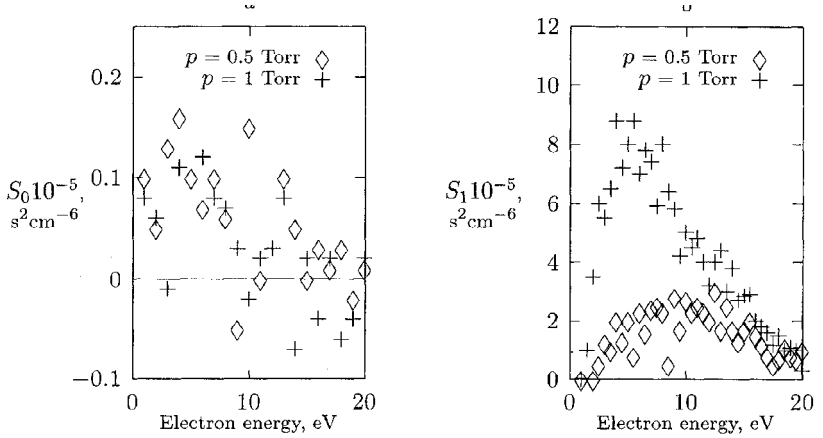

Figure 4. Energy dependence of Legendre components of the electron-atom collision integral ($a - S_0$, $b - S_1$) in a discharge positive column for different Helium pressures and electron concentrations: p_{He} = 0.5 Torr and ne = 1.5 × 10^{11} cm^{-3}; p_{He} = 1 Torr and n_e = 1.9 ×10^{11} cm^{-3}.

8. DETERMINATION OF ENERGY DEPENDENCE OF THE TRANSPORT CROSS-SECTION OF ELECTRON-ATOM COLLISIONS[13, 17]

Measurements of Legendre components of the collision integral and of the electron distribution function open the opportunity to determine the energy dependence of transport cross-section of electron-atom collision. Presuming that the conditions are actually realized in the positive column of electric discharge, under which the major contribution to S1 is made by elastic electron-atom collisions, then in the approximation of immovable atoms the expression for S_1 is[20]:

$$S_1 = N_a \sigma^t_{ea} v f_1, \tag{21}$$

where σ^t_{ea} is the transport cross-section of electron-atom collisions, N_a is the atom concentration.

Relation (21) shows that measurement of S_1, f_1, and N_a makes possible the determination of the value of the transport cross-section σ^t_{ea}. The determination of the σ^t_{ea} dependence on the electron energy is simpler apart from a multiplicative factor. It can be performed by measuring S_1 and f_1 only, and was carried out in the present work. Figure 5 shows the σ^t_{ea}, dependence on the electron energy and the results obtained by other authors. Our measurements are fixed by the value of the cross-section for 4 eV obtained in paper Ref. 21. The obtained dependence of the cross-section on energy agrees with results of other researchers[22, 23] within the accuracy of experimental errors.

9. MEASUREMENT OF ELECTRON CONVECTIVE VELOCITY[24]

Electron convective velocity is formed in plasma due to the action of electric field or to gradient of electron concentration. It determines many plasma electrical parameters.

The electron convective velocity is formed in electron collisional processes and in collective interactions between charged plasma components. Therefore, experimental determination of the electron convective velocity provides a way to study relative rates

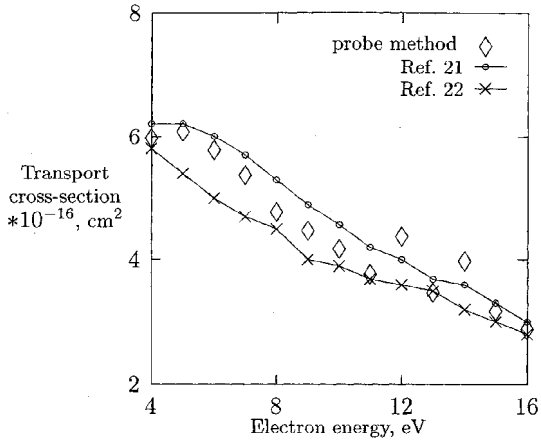

Figure 5. Transport cross-section of elastic scattering of electrons on Helium atoms.

of these processes. If one of these processes dominates in specific plasma conditions, its separate study becomes possible.

The Legendre component f_1 is known[1] to determine the asymmetry of the distribution function and is responsible for the electron convective velocity averaged over the motion directions:

$$< v_z >_{conv} = \frac{1}{3}\frac{v f_1}{f_0}. \tag{22}$$

If the positive-column electric discharge plasma is homogeneous along the discharge tube axis (which is generally the case) and if the dominating way of relaxation of stationary electron velocity distribution function is pair collision processes, the Legendre components f_0 and f_1 are related comparatively simply[20]:

$$f_1 = \frac{eE_z}{m\nu}\frac{\partial f_0}{\partial v}, \tag{23}$$

where ν is the transport frequency of collisions, m is the electron mass, E_z is the electric field strength at the discharge tube axis.

Analysis of equations (22) and (23) shows that it is possible to determine not only the convective electron velocity, but also to estimate the role of pair collision processes in formation of the distribution function.

Indeed, the convective velocity may be determined with relation (22), in which experimental values of the Legendre components f_0 and f_1 are used. On the other hand, it is possible to measure the value of f_0 only, and to calculate f_1 on the basis of relation (23). Information on the transport frequency of electron–atom collisions is necessary in this case.[21] Figure 6 presents the dependences of the electron convective velocity on energy, obtained by the described methods. One can easily see that the values of the electron convective velocity, experimentally determined and calculated with the use of the data on the cross-section of elastic electron–atom collisions, coincide for the helium pressure of 0.5 Torr , i. e., collisional processes dominate under this pressure. Considerable differences beyond experimental errors are observed for the pressure of 0.2 Torr. It is also necessary to note that the transport free path of electrons for elastic electron–atom collisions becomes comparable with the radius of the discharge tube at the pressure of 0.2 Torr. The observed differences in the values of the electron

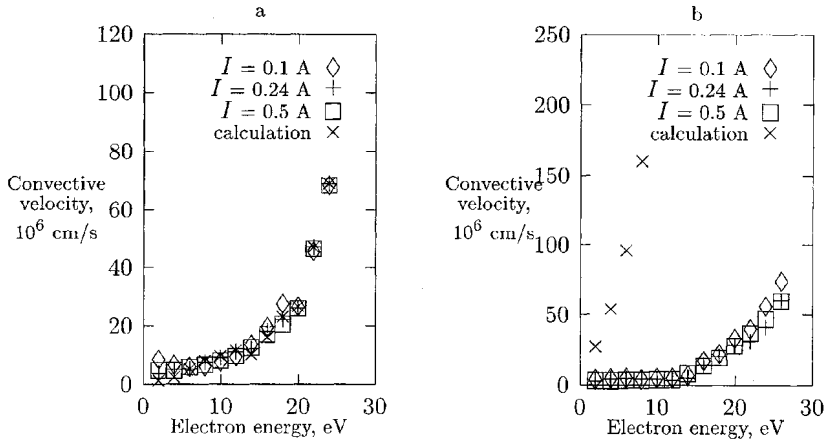

Figure 6. Dependence of the convective velocity on electron energy in plasma of the positive column of a Helium discharge for different discharge currents I and Helium pressures p_{He}. a–p_{He} = 0.5 Torr, b–p_{He} = 0.2 Torr.

convective velocity in this regime may be connected with the influence of collective interelectron interactions, which have comparable or even higher intensity than pair collisional processes.

10. COMPARATIVE ANALYSIS OF INTENSITY OF COLLISIONAL AND COLLECTIVE INTERACTIONS IN FORMATION OF ELECTRON DISTRIBUTION FUNCTION[25]

Collisional processes are taken into account in the kinetic equation by means of the collision integral. The processes of collective interaction of charged particles enter the kinetic equation as the term that includes the electric field strength. Indeed, if the plasma charged components move correlatively, then the volume charge created by them causes the electric field, which in its turn influences the motion of the charged particles. Consider the kinetic equation (17) for the Legendre component S_1. In this equation, it is necessary to consider the values E, f_1 and S_1 as sums of constant and time-dependent parts:

$$E = \overline{E} + \widetilde{E}; \quad f_1 = \overline{f}_1 + \widetilde{f}_1; \quad S_1 = \overline{S}_1 + \widetilde{S}_1. \tag{24}$$

Besides correlated components, the time-dependent parts take into account random fluctuations, which are necessarily present in plasma. As above, we assume that $f_2 << f_1$ in the discharge positive column. Also, let the varying components be small

equation and averaging over time, for a stationary positive column spatially homogeneous along the discharge axis we obtain:

$$\overline{S}_1 - \left\langle \frac{e\widetilde{E}}{m}\frac{\partial \widetilde{f}_0}{\partial v} \right\rangle = \frac{e\overline{E}}{m}\frac{\partial \overline{f}_0}{\partial v}. \tag{25}$$

The right-hand side of this equation includes the values $\overline{E}$ and $\overline{f}_1$ averaged over time. They may be determined within the probe method. The left-hand side is the sum

of the Legendre component $\overline{S}_1$ of the collision integral and the correlation expression responsible for collective interactions of charged particles in plasma. The correlation expression may be assumed as the measure of intensity of the collective interactions of charges particles. The Legendre component $\overline{S}_1$ of the collision integral in the left-hand side of equation (25) can be calculated, if electron–atom collisions are the dominating process of its formation. This is generally the case for a positive column of an electric discharge. The expression for $\overline{S}_1$ with consideration for elastic collisions only was presented above (21). It is clear from this relation that information about the transport cross-section of electron–atom collisions, the concentrations of atoms in the normal state, and the Legendre component of the distribution function $\overline{f}_1$ are sufficient for determination of the Legendre component $\overline{S}_1$ of the collision integral.

Thus, there is a principal possibility for comparison of intensity of collisional and collective processes that take place in plasma of an electric discharge positive column. Below, we show, using a discharge in helium as an example, that the intensity of the collective interaction processes of electrons substantially depends on the gas pressure, and these processes are switched on with decrease of pressure within a narrow pressure interval. After switching on, the collective interactions have dominating influence on the processes in the positive column.

Figure 7a presents the results of determination of the value $\overline{S}_1 - e/m\langle\widetilde{E}\partial\widetilde{f}_0/\partial v\rangle$ under the discharge current of 260 mA and helium pressure of 0.7 Torr. The same figure gives calculated values for the value $\overline{S}_1$. It can be easily seen that, for the conditions used in the experiment, the difference of the presented dependences is small and does not exceed the measurement error. Therefore, we can conclude that the correlation term in the kinetic equation $\langle\widetilde{E}\partial\widetilde{f}_0/\partial v\rangle$ is negligibly small. Thus, collisional processes dominate in formation of the positive column plasma parameters under the indicated experimental conditions.

Figure 7b presents similar dependences for the helium pressure 0.2 Torr. Comparison of the dependences presented here permits to conclude that no even qualitative agreement between experimental and calculated values is observed under the specified discharge conditions. This indicates the dominating role of collective processes in formation of parameters of the discharge positive column. It is interesting to note that the influence of collective interactions is especially significant in the range of small electron energies, and the contribution of collective interactions is considerably lower for the electron energies above 12 eV.

Thus, in dependence on the discharge conditions, two regimes of the electric discharge are realized: the collisional regime and the regime of collective interactions. Transition from one regime to the other takes place in a narrow range of discharge conditions.

11. CONCLUSIONS

The electron velocity distribution function in axisymmetric plasma is completely determined by functional coefficients of the expansion in Legendre polynomials. Experimental determination of finite number of the expansion coefficients is possible by means of the probe method, and measurements for a number of specified orientations of a plane one-sided probe in plasma is necessary to do this.

Measurements by means of a plane two-sided and cylindrical probes permit to determine the expansion coefficients with even indices. Measurements by a spherical probe permit to determine the distribution function in the velocity modulus, and are insensitive to plasma anisotropy.

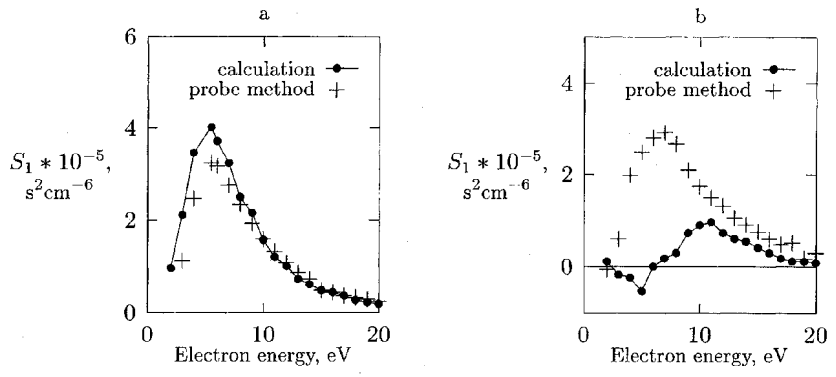

Figure 7. Energy dependence of calculated and experimental values of the electron–atom collision integral S_1 in plasma of a Helium positive column for the discharge current I = 0.26 A and different Helium pressures: a–p_{He} = 0.7 Torr, b–p_{He} = 0.2 Torr.

In a positive column of an electric discharge, the Legendre components of the electron velocity distribution function f_0 and f_1 may be determined with sufficient accuracy, and the components with higher indices are small. This indicates isotropy of the distribution function. The Legendre component f_0 determines distribution of electrons in the velocity modulus, and is responsible for the processes of ionization and excitation. The Legendre component $f_1$determines the process of electron current.

In plasma of low-voltage beam discharge, electrons are represented by two energy groups: isotropic with low energy and anisotropic with substantially higher energy. For anisotropic group of electrons, the Legendre components of the distribution function with indices up to six and higher can be determined. Investigations of the Legendre components of the distribution function open the possibility to study the processes of relaxation of electron beams in plasma separately in energies and momenta.

Application of the probe method and of the Boltzmann kinetic equation to a stationary positive column permits to find the Legendre components S_0 and S_1 of the collision integral. The highest accuracy of the determination is reached for the Legendre component S_1. Its measurements permit to find the energy dependence of the transport cross-section of elastic electron–atom collisions.

Comparison of experimentally determined and calculated values of the Legendre component S_1 of the collision integral permits to judge about the relative contribution of collective interactions of charges particles in formation of discharge parameters. The collective processes of interaction are switched on, if the electron transport free path becomes comparable with the radius of the discharge tube.

REFERENCES

1. Huxley L and Crompton R 1974 *Diffusion and Drift of Electrons in Gases.* Wiley, New York.
2. Fedorov V L 1985 *Sov.Phys.-Tech.Phys.* **30** (6) 554–556.
3. Fedorov V L and Mezentsev A P 1987 *Sov.Phys.-Tech.Phys.* **32** (3) 363–365.
4. Lapshin V F and Mustafaev A S 1989 *Sov.Phys.-Tech. Phys.* **34** (2) 150–156.
5. Druyvesteyn M J 1930 *Z. Phys.* **64** 781–91.
6. Volterra V 1982 *Theory of Functionals, Integrals and Integral Equations* Moscow: Nauka.
7. Malyshev G M and Fedorov V L 1953 *Doklady AN SSSR* **92** 269–71.
8. Hiroshi Amemiya and Kazuo Shimizu 1974 *Jap. J. Appl. Phys.* **13** 1035–6.
9. Demidov V I, Kolokolov N B and Kudryavtsev A A 1996 *Probe Methods for Investigation of Low-temperature Plasma* Moscow: Energoizdat.

10. Woods R and Sudit I 1994 *Phys. Rev. E* **50** 2222–38.
11. Granovsky V L 1952 *Electric Current in Gas* Moscow: GITTL.
12. Mezentsev A P 1987 *Probe Measurements in Anisotropic Plasma* Autoref. Cand. Thes. Leningrad: LGU.
13. Mezentsev A P, Mustafaev A S, Lapshin V F and Fedorov V L 1986 *J.Phys.* B:*At.Mol.Phys* **20** L723–L729.
14. Mezentsev A P, Mustafaev A S and Fedorov V L 1988 *J. Phys.* D:*Appl. Phys.* **21** 1464–66.
15. Mustafaev A S and Mezentsev A P 1986 *J. Phys.* D:*Appl. Phys.* **19** L69–73.
16. Lapshin V F, Mezentsev A P and Mustafaev A S 1989 *J. Phys.* D: *Appl. Phys.* **22** 857–9.
17. Lapshin V F, Mezentsev A P and Mustafaev A S 1989 *In: Ionization Processes with Participation of Exited Atoms* Leningrad: LGU 156–93.
18. Baksht F G, Lapshin V F and Mustafaev A S 1995 *J. Phys.* D: *Appl. Phys.* **28** 669–93, 694–700.
19. Gurevich V E and Shvartsburg A B 1973 *Nonlinear Theory of Propagation of Radiowaves in Ionosphere* Moscow: Nauka.
20. Golant V E, Zhilinsky A P and Sakharov S A 1977 *Basics of Plasma Physics* Moscow: Atomizdat.
21. Kumar K 1984 *Phys. Rep.* **112** 321–75.
22. Sinfailam A L and Nesbet R K 1972 *Phys. Rev.* **46** 2118–29.
23. Burke P G, Cooper J W and Ormonde S 1969 *Phys. Rev* **183** 245–58.
24. Mezentsev A P, Mustafaev A S and Fedorov V L 1988 *Sov. Phys.-Tech. Phys.* **33** (6) 642–646.
25. Mezentsev A P, Stepanov Yu L and Fedorov V L *Sov. Phys.-Tech. Phys 42 (4) 341–345.*
26. *Shimizu K and Amemiya H 1977 J. Phys. E **10** 389–91.*

This Page Intentionally Left Blank

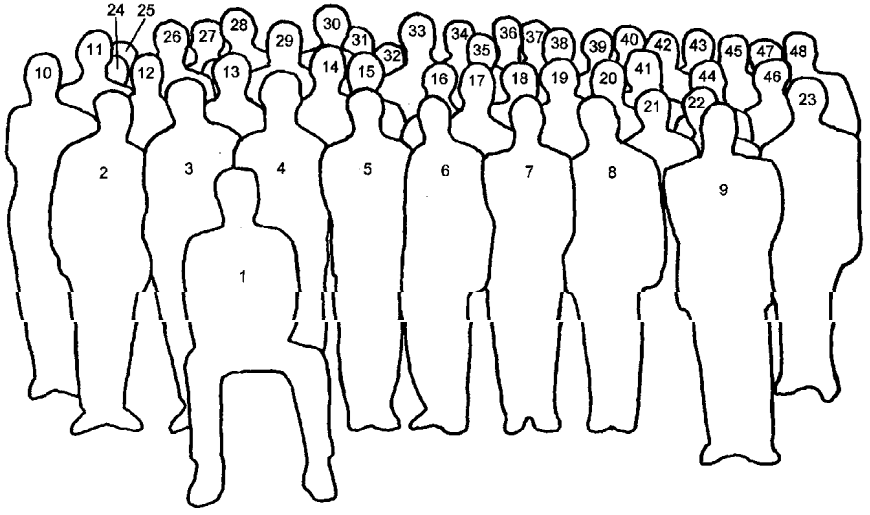

Group photo of workshop participants: 1: G. Hagelaar, 2: Yu. Aliev, 3: V. Shibkov, 4: D. Otorbaev, 5: D. Graves, 6: A. Lichtenberg, 7: A. Wendt, 8: V. Kolobov, 9: U. Kortshagen, 10: S. Berezhnoi, 11: K. Orlov, 12: V. Godyak, 13: D. Lymberopoulos, 14: L. Overzet, 15: W. Graham, 16: V. Ivanov, 17: M. Turner, 18: A. Bogaerts, 19: J.-P. Boeuf, 20: N. Dyatko, 21: V. Kouznetsov, 22: S. Nisimov, 23: Yu. Golubovskii, 24: A. Baryshnikov, 25: I. Porokhova, 26: L. Babich, 27: G. Parker, 28: J. Lawler, 29: Z. Petrovic, 30: M. Lieberman, 31: S. Pancheshnyi, 32: R. Winkler, 33: A. Starikovskiy, 34: D. Economou, 35: L. Alves, 36: A. Okhrimovskiy, 37: E. Quandt, 38: V. Guerra, 39: D. Lopaev, 40: I. Kaganovich, 41: Ph. Ingold, 42: J. Ingold, 43: A. Chervyakov, 44: D. Uhrlandt, 45: C. Ferreira, 46: V. Nekuchaev, 47: A. Ender, 48: R. Franklin. Illness prevented L. D. Tsendin from participating in the workshop. He is not depicted on the photo. This photo is reproduced by courtesy of Dr. V. Kolobov.

This Page Intentionally Left Blank

INDEX